CODEN: JASMAN 4966

THE JOURNAL of the Acoustical Society of America

Vol. 104, No. 1 July 1998

SOUNDINGS SECTION

(Continued)

CONTENTS—*Continued from preceding page*

(Continued)

CONTENTS—*Continued from preceding page*

ACOUSTIC SIGNAL PROCESSING [60]

PHYSIOLOGICAL ACOUSTICS [64]

PSYCHOLOGICAL ACOUSTICS [66]

SPEECH PRODUCTION [70]

SPEECH PERCEPTION [71]

(Continued)

CONTENTS—*Continued from preceding page*

SOUNDINGS

This front section of the *Journal* includes acoustical news, views, reviews, and general tutorial or selected research artcles chosen for wide acoustical interest and written for broad acoustical readership.

ACOUSTICAL NEWS—USA

Elaine Moran
Acoustical Society of America, 500 Sunnyside Boulevard, Woodbury, New York 11797

Editor's Note: *Deadline dates for news items and notices are 2 months prior to publication.*

New Fellows of the Acoustical Society of America

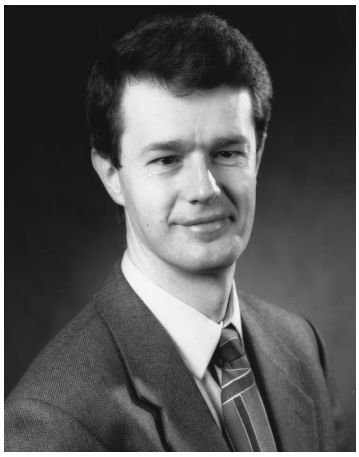

Xavier Boutillon—For research in the physics of musical instruments.

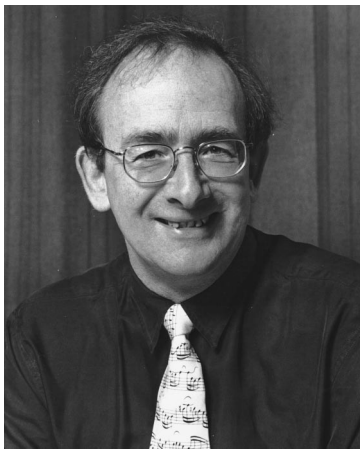

C. J. Darwin—For contributions to the understanding of perceptual grouping processes in hearing and speech.

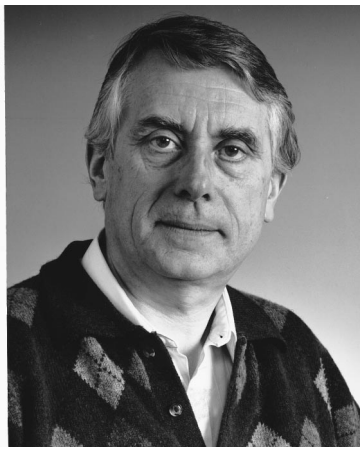

Jos J. Eggermont—For research in neural responses to acoustic signals.

Timothy Leighton—For contributions to bubble acoustics.

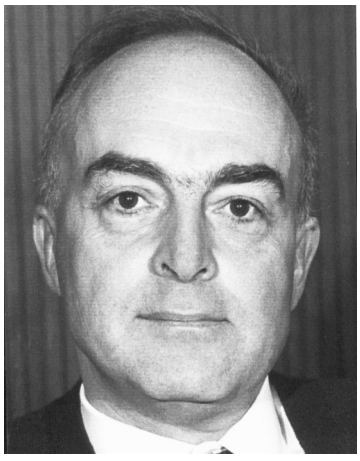

Jacques Reisse—For contributions to sonochemistry.

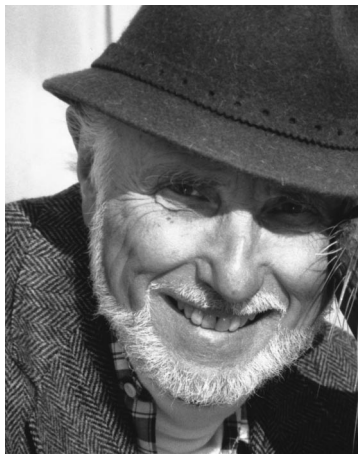

Ronald Schusterman—For contributions in marine mammal audition and psychoacoustics.

 0001-4966/98/104(1)/1/8/$15.00

Kawan Soetanto—For contributions in education and microbubble acoustics.

Kevin Williams—For contributions to measurement and modeling in ocean acoustics.

Appreciation to the 1997 reviewers of manuscripts submitted to the *Journal*

The quality and dependability of the information contained in the articles and letters published in the *Journal of the Acoustical Society of America* are assured through the competent peer reviewing contributed by the reviewers that our Associate Editors enlist each year. The reviews show evidence of the reviewers' diligence and dedication to the Society and to their profession. In appreciation to the reviewers for these anonymous services to the *Journal* and its authors during 1997, the Editor-in-Chief gratefully publishes their names in alphabetical order without identification of the review specialities or of the articles that they reviewed. Fifty-six percent of these reviewers also reviewed in 1996. In such a long list (1423) some errors and omissions are certain to occur. If you reviewed any *Journal* article or letter in 1997 but your name has been omitted (or misspelled), please accept our apology and send a correction promptly to the Editor-in-Chief. Thank you.

DANIEL W. MARTIN
Editor-in-Chief

1997 JASA Peer Reviewers

Abawi, A. T.
Abbas, P. J.
Abdala, C.
Abel, S. M.
Achenbach, J. D.
Adcock, J.
Agullo, J.
Akay, A.
Akeroyd, M. A.
Albert, D. G.
Alers, G. A.
Alexandrou, D.
Alku, P.
Allard, J. F.
Allen, J.
Allen, J. B.
Allen, P.
Alwan, A. A.
Amme, R. C.
Amundsen, L.
Anderson, A. L.
Andruski, J. E.
Angel, Y. C.
Apfel, R. E.
Arnott, W. P.
Arvelo, J. I., Jr.
Ashmead, D. H.
Ashmore, J. F.
Askenfelt, A. G.
Assaad, J.
Assmann, P. F.
Atalla, N.
Atchley, A. A.
Attenborough, K.
Au, W. W. L.
Audoin, B.
Augspurger, G. L.
Awbrey, F. T.
Ayers, R. D.
Ayres, T. J.
Büyükaksoy, A.
Baboux, J. C.
Bacon, S. P.
Badiey, M.
Badin, P.
Baer, R. N.
Baer, T.
Baggeroer, A. B.
Bahr, R. H.
Bai, M. R.
Bailey, P. J.
Baker, C. R.
Ballato, A.
Bamnios, T.
Bao, C.
Bar-Cohen, Y.
Barber, B. P.
Barbour, D. K.
Barger, J. E.
Barron, M.
Barry, W. J.
Bartram, J. F.
Bass, H. E.
Baste, S.
Bastien, F.
Batra, R.
Baum, S. R.
Bayon, A.
Beauchamp, J. W.
Bedard, A. J.
Beddor, P. S.
Belegunda, A. D.
Belinsky, B. P.
Bell, T. S.
Bell-Berti, F.
Benjamin, K. C.
Beran, M. J.
Beranek, L. L.
Berg, B. G.
Berge, T.
Berke, G.
Berkhout, A. J.
Berkson, J. M.
Berman, D. H.
Bernstein, L. E.
Bernstein, L. R.
Berry, D.
Berryman, J. G.
Berthelot, Y. H.
Besieris, I. M.
Beslin, O.
Best, C. T.
Bhat, R. B.
Bilsen, F. A.
Birdsall, T.
Bishop, G.
Bissinger, G. A.
Bjorno, I. K.
Blamey, P. J.
Blauert, J.
Bleistein, N.
Boettcher, F. A.
Bohn, O-S.
Bohne, B. A.
Bond, L. J.
Bondaryk, J. E.
Boone, M. M.
Booth, N. O.
Boothroyd, A.
Borgiotti, G. V.
Bork, I.
Borup, D. T.
Bosmans, I.
Bouchard, M.
Boulanger, P.
Bowles, A. E.
Boyle, F.
Bradley, C. E.
Bradley, J. S.
Bradlow, A. R.
Braga, A. M. B.
Braida, L. D.
Brass, D. N.
Breazeale, M.
Breeding, J. E., Jr.
Brennan, M. J.
Brewster, J.
Briers, R.
Briggs, G. A. D.
Briggs, K.
Brissaud, M.
Broad, D. J.
Broadhead, K.
Brock, L. M.

Bronkhorst, A. W.
Brooke, G.
Brown, A. M.
Brown, C. H.
Brown, C. J.
Brown, M. C.
Brownell, W. E.
Browning, D. G.
Brugge, J. F.
Bruggeman, J. C.
Brunson, B.
Bryne, C. L.
Bucaro, J. A.
Bucker, H. P.
Buckingham, M. J.
Buckley, K.
Buell, T. N.
Bunnell, H. T.
Burdisso, R. A.
Burgess, J. C.
Burkard, R. F.
Burnett, D. S.
Burns, E. M.
Burroughs, C. B.
Busch-Vishniac, I. J.
Buss, E.
Butler, J. L.
Buus, S.
Byrd, D. M.
Cacace, A. T.
Cahn, J.
Campanella, A.
Campbell, N.
Canèvet, G.
Candy, J. V.
Canlon, B.
Cantrell, J. H.
Carcione, J. M.
Carey, W. M.
Cariani, P. A.
Carlyon, R. P.
Carney, L.
Carstensen, E. L.
Carter, C.
Castagnède, B.
Castellanos, P. F.
Castelli, E.
Cato, D. H.
Cawley, P.
Cazals, Y. A. G.
Ceperley, P. H.
Chéenne, D.
Chadwick, R. S.
Chafe, C.
Chai, J. F.
Chambers, J. P.
Champlin, C.
Champoux, Y.
Chamuel, J. R.
Chand, D.
Chandiramani, K. L.
Chapman, C. H.
Chapman, D. M. F.
Chapman, N. R.
Chapman, R.
Charette, F.
Charpie, J. P.
Chatterjee, M.
Chaturvedi, P.
Cheeke, D.
Cheng, A. C. H.
Cheng, L.
Chertoff, M. E.
Chevalier, Y.
Chew, W. C.
Cheyne, S.
Childers, D.
Chimenti, D. E.
Chin-Bing, S. A.
Chinnery, P. A.
Chisolm, T.
Chiu, C.-S.
Cho, Z. H.
Choi, M-S.
Chotiros, N. P.
Chu, D.
Chu, W. T.
Chu, Y. C.
Church, C. C.
Ciocca, V.
Clark, C.
Clark, W. W.
Clarke, E. F.
Clarkson, M. G.
Clay, C. S., Jr.
Cleveland, R. O.
Clifton, R.
Cochrane, N.
Cohen, D. S.
Colburn, H. S.
Collins, L. M.
Collins, M. D.
Colosi, J. A.
Coltman, J. W.
Colton, D.
Colton, R. H.
Commander, K. W.
Conklin, H. A., Jr.
Conoir, J. M.
Constable, R. T.
Cook, P. R.
Cooper, A. J.
Cooper, N. G. F.
Copley, D. C.
Cops, A.
Cornuelle, B.
Corsaro, R. D.
Cotaras, F. D.
Cote, A. F.
Cottingham, J. P.
Couchman, L. S.
Coulouvrat, F.
Cox, D.
Coyette, J. P.
Craik, R. J. M.
Cranen, B.
Craster, R. V.
Crawford, A.
Crawford, D. H.
Cray, B. A.
Creamer, D. B.
Crighton, D. G.
Crum, L. A.
Culling, J. F.
Cummings, A.
Cunefare, K. A.
Cuomo, F. W.
Curtis, A.
Cuschieri, J. M.
Cywiak, M.
Dacol, D.
Dai, H.
Daigle, G. A.
Dalebout, S.
Dallos, P.
D'Amico, A.
Dancer, A. L.
Danicki, E.
Daniloff, R. G.
Dannenberg, R.
Darling, T. W.
Darwin, C. J.
Dassios, G.
Datta, S. K.
Dau, T.
David, P. M.
Davies, H.
Davies, W. J.
Davis, A. M. J.
Davis, K.
Davis, S.
Dawson, T. W.
Deane, G. B.
Deavenport, R.
de Billy, M.
de Boer, E.
de Cheveigné, A.
DeFerrari, H. A.
Degtyar, A.
Dehandschutter, W.
DeJong, K. J.
Delaney, P. A.
Del Balzo, D. R.
Delsanto, P. P.
Denardo, B.
Deng, L.
DeSanto, J. A.
Desmet, C.
Dickey, J. W.
Dimitriodis, E. K.
DiNapoli, F.
Ditri, J. J.
Divenyi, P.
Dixon, T. L.
Docherty, G.
Doherty, K.
Dolan, D. F.
Don, C. G.
Donaldson, G. S.
Donohue, K. D.
Dooling, R. J.
Dorban, D.
Dorman, M. F.
Dosso, S. E.
Dougherty, M. E.
Dowell, E. H.
Dowling, D. R.
Dozier, L. B.
Dragonette, L. R.
Drullman, R.
Drumheller, D. S.
D'Spain, G. L.
Dubno, J. R.
Dubus, B. B.
Duda, R. O.
Duda, T. F.
Duifhuis, H.
Dunn, F.
Dunn, M. L.
Dutoit, T.
Dwyer, R. F.
Dzieciuch, M. A.
Easwaran, V.
Eddington, D. K.
Eddins, D. A.
Edmonds, P. D.
Eggermont, J. J.
Ehrlich, S. L.
Eiss, N.
Eldred, K.
Eller, A. I.
Elliott, S.
Ellis, D. D.
Elmore, P.
El-Raheb, M.
Embleton, T. F. W.
Eom, H. J.
Erskine, F. T.
Espinoza-Varas, B.
Espy-Wilson, C. Y.
Evans, R. B.
Evans, W. E.
Everbach, E. C.
Every, A. G.
Ewart, T. E.
Fabre, J. P.
Fahey, F. J.
Fahey, P. F.
Fahnline, J. B.
Fantini, D. A.
Farag, N. H.
Farassat, F.
Farmer, D. M.
Faulkner, A.
Fawcett, J. A.
Fay, R. R.
Fechter, L.
Feit, D.
Feng, L.
Ferguson, B. G.
Ferri, A. A.
Ferrigno, G.
Festen, J.
Feth, L.
Feuillade, C.
Field, R. A.
Fields, J.
Filippi, P. J. T.
Finch, R. D.
Finegold, L. S.
Finette, S. I.
Finnveden, S.
Fisher, F. H.
Fishman, L.
Fitzgerald, J. W.
Flanagan, J. L.
Flatte, S. M.
Flege, J. E.
Fletcher, N.
Florentine, M.
Fofonoff, N.
Formby, C. C.
Forrest, K. M.
Fortunko, C. M.
Fourakis, M. S.
Fourcin, A. J.
Fowler, C. A.
Fowlkes, J. B.
Fox, R. A.
Frampton, K. D.
Franchek, M. A.
Francois, R. E.
Franke, S. J.
Frazer, L. N.

Fredberg, J.
Freedman, A.
Freyman, R. L.
Friberg, A.
Frisk, G. V.
Frison, T.
Frizzell, L. A.
Fu, Q.-J.
Fujimura, O.
Fuller, C.
Furukawa, S.
Gabillet, Y.
Gabrielson, T. B.
Grabrielsson, A.
Gadd, C. W.
Gade, A. C. S.
Gaitan, D. F.
García-Bonito, J. J.
Gardner, D.
Garrelick, J. M.
Garrett, S.
Gatehouse, S.
Gaumond, C. F.
Gaunaurd, G. C.
Gauss, R.
Gauteses, A. K.
Geer, J.
Geisler, C. D.
George, J.
Geratt, B. R.
Gerdes, F.
Gerstoft, P.
Gibson, L. J.
Giguere, C.
Gilbert, K. E.
Gilkey, R. H.
Giordano, N. J.
Gitza, O.
Glegg, S. A.
Gleich, O.
Gobl, C.
Gockel, H.
Goldstein, J. L.
Goldstein, L. M.
Good, M.
Goodman, R. R.
Gorga, M. P.
Gorman, M. R.
Goss, S. A.
Gottfried, T. L.
Gough G. O.
Govindarajan, K. K.
Gracewski, S. M.
Grantham, D. W.
Grattan, K. T. V.
Green, K.
Greenberg, S.
Greenleaf, J. F.
Greenwood, D. D.
Griesinger, D.
Grose, J. H.
Grosh, K.
Guenther, F.
Guigou, C.
Guinan, J. J.
Gummer, A. W.
Gunalp, N.
Guo, Q.
Guo, Y.
Gusev, V.
Guy, R. W.
Guyer, R. A.
Högberg J.
Haberman, R. C.
Hackney, C. M.
Haddadin, O. S.
Hafter, E. R.
Hall, J. L.
Hall, M. D.
Hall, M. V.
Hall, T. J.
Hallaj, I.
Hallock, Z. R.
Hallworth, R. J.
Hamilton, M.
Han, W.
Handel, S.
Handel, S. J.
Hanna, T. E.
Hansen, C.
Hansen, R. K.
Hanson, H. M.
Harari, A.
Harari, I.
Harding, A.
Harley, T.
Harrington, J.
Harris, G. R.
Harris, J. G.
Harris, K. S.
Harrison R. V.
Hartmann, W. M.
Hartung, K.
Hasegawa-Johnson, M.
Hassan, E.
Hastings, M. C.
Havelock, D. I.
Hawks, J.
Hayek, S. I.
Hazony, D.
He, S.
Heaney, K.
Hedberg, C.
Heffner, R. S.
Helfer, K. S.
Heller, L. M.
Hellman, R.
Hellman, W.
Henderson, B.
Henderson D.
Henning, G. B.
Henyey, F. S.
Herman, I. G. C.
Hermes, D. J.
Herrmann, F. J.
Hertrich, I.
Herzel, H-P.
Hewitt, M. J.
Heyliger, P.
Hickling, R.
Hill, N.
Hillenbrand, J. M.
Hillion, P.
Hinich, M. J.
Hirayama, M. S.
Hirschberg, A.
Hixson, E. L.
Hodgkiss, W. S.
Hodgson, M. R.
Hoekje, P. L.
Hoffmann, T. L.
Hogden, J.
Hoit, J. D.
Holford, R.
Holland, C. K.
Holland, C. W.
Holliday, D. V.
Hollien, H.
Hollman, K. W.
Holt, R. G.
Home, J. K.
Honarvar, F.
Honda, K.
Hoole, P.
Horner, J. L.
Horst, W.
Hossack, J. A.
Hosten, B.
House, A.
Houston, B. H.
Houtgast, T.
Houtsma, A. J.
Howarth, T. R.
Howe, B. M.
Howe, M. S.
Howell, P.
Hua, Y.
Huang, H.
Huang, W.
Hubbard, A. E.
Hudson, J. A.
Hudspeth, A. J.
Hukin, R.
Humes, L. E.
Hunten, D.
Hunten, M. R.
Hurdle, B. G.
Huron, D.
Hutchins, C. M.
Hutchins, D. A.
Hutchinson, J. R.
Hutter, K.
Hwang, W. S.
Idogawa, T.
Ih, J-G.
Ih, Y-S.
Imaizumi, S.
Imhof, M. G.
Insana, M. F.
Ioup, J.
Irino, T.
Isabelle, S. K.
Isakson, S.
Ishii, R.
Ivakin, A. N.
Iverson, P.
Iwasa K. H.
Jackson, D. R.
Jackson, J.
Jaffe, J. S.
Jamieson, D. G.
Jansson, E. V.
Jarzynski, J.
Jech, J. M.
Jenkins, J. J.
Jensen, F. B.
Jezequel, L.
Job, R. F. S.
Johnson, D. H.
Johnson, D. L.
Johnson, K. A.
Johnson, L.
Johnson, M.
Johnson, P.
Jones, D. F.
Jones, K. E.
Jun, S-A.
Junger, M. C.
Kabal, P.
Kadambe, S.
Kaernbach, C.
Kaiser, J.
Kalashnikov, A. N.
Kallivokas, L. F.
Kaltenbach, J. A.
Kaminsky, I.
Kanaun, S.
Kargl, S. G.
Karnell, M. P.
Karra, C.
Kates, J. M.
Kawahara, H.
Kazys, R.
Keefe, D. H.
Keer, L. M.
Keiffer, R. S.
Keith, W. L.
Kelly, J. B.
Keltie, R. F.
Kempster, G. B.
Keolian, R.
Kergomard, J.
Ketten, D. R.
Kewley-Port, D.
Kidd, G.
Kidd, G. D., Jr.
Kil, H-G.
Killion, M. C.
Kim, D. O.
Kim, K. Y.
Kimball, C. V.
Kimberley, B.
Kindel, J.
King, D. B.
King, M. E.
Kingston, J. C.
Kinney, W.
Kipke, D. R.
Kirby, R.
Kirlin, L.
Kiselev, A. P.
Kistler, D.
Kitzing, P.
Kleiner, M.
Kleunder, K. R.
Kline, R. A.
Klinke, R. H.
Klump, G. M.
Knio, O. M.
Ko, S. H.
Koch, R. A.
Koehnke, J.
Kohlrausch, A.
Kokkorakis, J. C.
Kollmeier, B.
Konishi, M.
Konzelman, C. J.
Koopman, G. H.
Koopmans-van Beinum, F. J.
Kopec, J. W.
Koppel, C.
Kossl, M.
Kröger, B. J.
Kraman, S. S.

Kreiman, J.
Kriegsmann, G. A.
Krieman, J. E.
Krishnaswamy, S.
Krolik, J. L.
Krylov, V.
Krysac, L. C.
Kuc, R.
Kuehn, D. P.
Kuhl, P. K.
Kuhn, G. F.
Kuhnicke, E.
Kujawa, S. G.
Kulkarni, A.
Kumar, A.
Kundu, T.
Kuperman, W. A.
Kuttruff, H.
Kuwada, S.
Kwon, Y-P.
Lacerda, F. P.
Ladd, D. R.
Lafleur, L. D.
Lakhtakia, A.
Laloe, F.
Lam, Y. W.
Lane, S. A.
Langley, R. S.
Larraza, A.
Larson, E. G.
Larsson, C.
Lasky, R. E.
Lataitis, R. J.
Lauchle, G. C.
Laulagnet, B.
Lauriks, W.
Lavrentyev, A. I.
Lawrie, J. M.
Learned, R. E.
Lee, C. P.
Lee, H.
Leeper, H. A.
Lees, S.
Leishman, T. W.
Lenhardt, M.
LePage, K. D.
Lerner, R. M.
L'Esperance, A.
Letcher, S. V.
Levitt, H.
Levy, M.
Lewis, E. R.
Lewis, T.N.
Li, K. M.
Li, Y-L.
Liang, Y-C.
Liew, K. M.
Lightfoot, J.
Liljencrants, J. C. W. A.
Lim, C. W.
Lim, R.
Lin, F.
Lin, Q.
Lin, Y. K.
Lindblom, B. E. F.
Linjama, T. T.
Liss, J. M.
Litovsky, R. Y.
Liu, G-R.
Liu, Q-H.
Lizzi, F.
Lo Vetri, J.
Lofstedt, R.
Loftman, R. C.
Loizou, P. C.
Long, G. R.
Loughlin, P. J.
Love, R. H.
Lowe, M. J. S.
Lu, I-T.
Lu, J-y.
Lu, Y.
Lucas, R. J.
Luce, P. A.
Lucero, J. C.
Ludlow, C. L.
Luschei, E. S.
Lutfi, R. A.
Lynch, J. F.
Lyons, A. P.
Macaskill, C.
Macaulay, M. C.
Mackersie, C.
Mackertich, S.
MacLennan, D. N.
Madden, J.
Madden, J. P.
Madigosky, W. M.
Madsen, E. L.
Maher, R.
Mahshie, J. J.
Maidanik, G.
Makris, N. C.
Maling, G. C.
Mammano, F.
Mann, A.
Mann, J. A., III
Manning, J. E.
Manuel, S. Y.
Mapes, T. J.
Maranda, B.
Margoliash, D.
Margolis, R. H.
Marler, P. R.
Marsh, A. H.
Marsh, E.
Marshall, B.
Marshall, H.
Marston, P. L.
Martin, D. W.
Maruszewski, B.
Massaro, D. W.
Masson, P.
Mast, T. D.
Matsukawa, M.
Matsunaga, T. O.
Mattei, P. O.
Matula, T.
May, B. J.
Mayer, W. G.
Maynard, J. D., Jr.
McAdams, S. E.
McAninch, G. L.
McBride, W. E.
McCall, K. R.
McCammon, D. F.
McCartin, B. J.
McClean, M.
McClements, D. J.
McCoy, J. J.
McDaniel, S.
McDonald, B. E.
McFadden, D.
McIntosh, J.
McIntyre, M. E.
McKisic, M. J.
Mead, D. J.
Meador, D.
Means, S.
Meddis, R.
Medwin, H.
Meegan, G. D.
Mehler, J.
Mei, C.
Meirovitch, L.
Mellert, V.
Meredith, R.
Mermelstein, P.
Mershon, D. H.
Meynial, X.
Michalopoulou, E.
Middlebrooks, J. C.
Migliori, A.
Mignerey, P.
Mikata, Y.
Mikhalevsky, P. N.
Milios, E. E.
Miller, D. L.
Miller, E. L.
Miller, J. G.
Miller, J. L.
Miller, R. D.
Mills, D. M.
Ming, R.
Mire, C.
Moebius, B.
Moffett, M. B.
Molz, E. B.
Monahan, E. C.
Mongeau, L.
Montgomery, A.
Moore, B. C. J.
Moore, J. A.
Mooshammer, C.
Morfey, G. L.
Morgan, D. R.
Mori, K.
Morimoto, H.
Moser, P. J.
Mote, C. D., Jr.
Mountain, D. C.
Moura, J. M. F.
Mozurkewich, G.
Muehleisen, R.
Muir, T. G., Jr.
Mullennix, J. W.
Munhall, K. G.
Munjal, M. L.
Myer, L.
Myers, M.
Myrberg, A. A., Jr.
Na, J.
Nabelek, A. K.
Nagem, R. J.
Naghshineh, K.
Nagy, P. B.
Nair, S.
Nakamura, A.
Namba, S.
Narayanan, S. S.
Narins, P. M.
Nayfeh, A. H.
Nearey, T.
Nederveen, C. J.
Neely, S.
Neff, D. L.
Nefske, D. J.
Nejade, A.
Nélisse, H.
Nelken, I.
Nelson, D. A.
Nelson, J. T.
Nelson, P. A.
Nelson, P. B.
Nero, R. W.
Neuman, A.
Neuman, A. C.
Newcomb, J.
Newhouse, V. L.
Newman, R. S.
Nhieu, M. T. V.
Nicolas, J.
Nightingale, T. R. T.
Nittrouer, S. N.
Noble, W.
Nolan, F.
Nolle, A. W.
Nolte, L. W.
Nord, L.
Nordebo, S.
Norris, A. N.
Norton, G. V.
Norton, S. J.
Nossek, J. A.
Novarini, J.
Nowicki, S.
Nuttall, A. L.
Nyborg, W. L.
Nye, P. W.
Nygaard, L. C.
O'Brien, W. D.
Ochmann, M.
Oden, J. T.
Odom, R. I.
O'Donnell, M.
Oertel, D.
Ogden, P.
Ogi, H.
Oguz, H.
Ohde, R. N.
O'Keefe, J. P. M.
Olsson, P.
Omoto, A.
Ophir, J.
Orduna-Bustamante, F.
O'Reilly, O.
Orr, M.
Orris, G. J.
O'Shaughnessy, D. D.
Ostrovsky, L.
Owsley, N.
Oxenham, A. J.
Ozard, J. M.
Ozdamar, O.
Pace, N. G.
Pagneux, V.
Palmer, A. R.
Palmer, C.
Palmer, D.
Pan, G. J.
Pan, J.
Panneton, R.
Papadakis, E. P.
Park, Y. C.

Parncutt, R.
Parra, J. O.
Parvulescu, A.
Pasterkamp, H.
Pastore, R. E.
Patterson, R. D.
Patuzzi, R.
Pavic, G.
Pavlovic, C.
Payton, K. L.
Pecorari, C.
Peirlinckx, L.
Pelorson, X.
Perrott, D. R.
Peters, M.
Peters, R. W.
Petitjean, B.
Pezerat, C.
Pflug, L. A.
Phillips, D. P.
Photiadis, D. M.
Pichora-Fuller, K.
Pickering, N. C.
Pierce A. D.
Piercy J. E.
Pierucci, M.
Pinnington, R. J.
Piquette, J. C.
Pisoni, D. B.
Pitre, R.
Pitton, J.
Plack, C. J.
Plona, T.
Plotkin, E.
Podlesak, M.
Polcari, J. J.
Polka, L.
Pollard, H. F.
Pols, L. C. W.
Ponton, C. W.
Pope, L. D.
Popper, A. N.
Porter, M. B.
Powell, A.
Powers, J. M.
Prasad, M. G.
Preston, J. R.
Preves, D.
Pride, S. R.
Prieve, B.
Prosen, C. A.
Prosperetti, A.
Protopapas, T.
Pruitt, J. S.
Psencik, I.
Puckette, M.
Purcell, A.
Pyle, R. W., Jr.
Rabinkin, D. V.
Rabinowitz, W. M.
Radlinski, R. P.
Rafaely, B.
Rajan, S. D.
Rakerd, B.
Ramig, L.
Randorf, J.
Rankovic, C.
Rasmussen, K. B.
Raspet, R.
Recasens, D.
Reed, C. M.
Rees, A.
Reichard, K. M.
Relkin, E.
Remington, P. J.
Renlie, L.
Reynolds, S.
Rhode, W. S.
Ribner, H. S.
Rice, D.
Richards, V. M.
Richardson, B. E.
Richardson, M. D.
Richardson, W. J.
Ricker, D. W.
Ricks, D. C.
Ridgway, S. H.
Rink, J.
Risset, J-C.
Robb, M. P.
Roberts, B.
Roberts, G. W.
Roberts, R. A.
Robinson, D.
Robinson, H. C.
Rodet, X.
Rodgers, O. E.
Rogers, J. C.
Rogers, P. H.
Rolt, K. D.
Rose, J. H.
Rose, J. L.
Rose, R.
Rosen, S.
Rosenberg, A. P.
Rosenblum, L. D.
Rosowski, J. J.
Rossi, M.
Rossing, T. D.
Rouseff, D.
Royster, L. H.
Royston, T.
Rubin, P. E.
Ruckman, C. E.
Ruggero, M. A.
Rumerman, M. L.
Ruppel, T.
Russell, I. J.
Sabatier, J. M.
Sablik, M. J.
Safaeinili, A.
Salomons, E. M.
Saltzman, E.
Sammelmann, G. S.
Sandell, G. J.
Santos-Sachi, J. R.
Sapienza, C. H.
Sarkar, T. K.
Sarkissian, A.
Sas, P.
Scaife, R.
Scales, J.
Scharf, B.
Schechter, R. S.
Scheirer, E.
Scherer, K. R.
Scherer, R. C.
Schindel, D. W.
Schlauch, B.
Schlauch, R. S.
Schmidt, H.
Schmidt-Nielson, A.
Schmiedt, R.
Schoenberg, M.
Schoentgen, J.
Schomer, P. D.
Schreiner, C. E.
Schroder, M. R.
Schroeter, J.
Schumacher, R. T.
Schuster, G. T.
Sehgal, C.
Seiler, J. P.
Seiner, J. M.
Sekijama, K.
Selamet, A.
Seneff, S.
Seriani, G.
Sessarego, J.-P.
Seybert, A. F.
Shadle, C. H.
Shaffer, L. H.
Shamma, S.
Shang, E-C.
Shaw, E. A. G.
Shaw, L.
Sheft, S.
Shen, I. Y.
Shenderov, E. L.
Shepherd, K. P.
Shera, C.
Sherman, C. H.
Shields, F. D.
Shih, C-L.
Shin, D. C.
Shinn-Cunningham, B. G.
Shipp, T.
Shirron, J. J.
Shung, K. K.
Shuvalov, A. L.
Shuyu, L.
Siegel, J. H.
Siegmann, W. L.
Sigalas, M. M.
Silverberg, L. M.
Silverman, H. F.
Simmons, J. A.
Simpson, H.
Sinclair, A. N.
Sinex, D. G.
Sinha, D. N.
Sinnott, J. M.
Skelton, E. A.
Slaney, M.
Slutsky, L. J.
Smeele, P. M. T.
Smith, C.
Smith, G.
Smith, G. B.
Smith, K. B.
Smith, K. V.
Smith, L.
Smith, S. T.
Smith-Olinde, L.
Smoorenberg, G. F.
Smurzynski, J.
Smyshlyaev, V. P.
Snell, K. B.
Snyder, S.
Soenarko, B.*
Soize, C.
Soldatos, K. P.
Sommerfeldt, S. D.
Sommers, M. S.
Sondhi, M. M.
Song, H. C.
Sorkin, R.
Soulodre, G. A. J.
Spens, K-E.
Spies, M.
Spiesberger, J. L.
Spindel, R. C.
Stamnes, J. J.
Stanton, T. K.
Steele, C. R.
Steinberg, B. D.
Stellmack, M. A.
Stepanishen, P. R.
Stephen, R. A.
Stergiopoulos, S.
Sternlicht, D. D.
Stevens, K. N.
Stinson, M. R.
Stoll, R. D.
Story, B. H.
Stover, L. J.
Strickland, B.
Strickland, E. A.
Strik, H.
Strong, W. Y.
Stroud, J. S.
Strybel, T. Z.
Stusnick, E.
Sugimoto, N.
Sumbatyan, M. A.
Summers, I.
Summers, V.
Sun, J.
Sundberg, J. E. F.
Sussmann, H.
Suter, A.
Suzuki, H.
Svensson, U. P.
Svirsky, M. A.
Swami, A.
Swanson, D. C.
Swift, G. W.
Swingler, D. N.
Szwerc, R.
Szymko, Y. M.
Takahashi, D.
Talmadge, C.
Tamura, M.
Tanaka, H.
Tanaka, N.
Tang, D.
Tappert, F. D.
Tarnow, V.
Taylor, S. M.
Telschow, K.
Ternstrom, S.
Tew, R. H.
Tewary, V. K.
Tezuka, K.
Thijssen, J. M.
Thompson, C.
Thompson, D. J.
Thompson, D. W.
Thompson, P. O.
Thompson, R. B.
Thompson, R. P.
Thompson, S. C.
Thompson, D. J.
Thornton, R.

Thorsos, E.
Thurston, R.
Tiede, M.
Tiersten, H.
Tindle, C. T.
Ting, T. C. T.
Tittmann, B. R.
Titze, I. R.
Tjaden, K. K.
Todd, N.
Tohkura, Y-i.
Tolomeo, J. A.
Tolstoy, A.
Tolstoy, I.
Toole, F. E.
Trahey, G.
Trahiotis, C.
Tran, B. N.
Trine, T. D.
Trinh, E. H.
Troeger, R.
Tsvankin, I.
Tubis, A.
Tugnait, J. K.
Tuller, B. H.
Turgut, A.
Twersky, V.
Tyack, P. L.
Tyler, R. S.
Ungar, E. E.
Uscinski, B. J.
Vagle, S.
Vakakis, A. F.
Van Buren, A. L.
Van Den Abeele, K.
Van den Berg, P. M.
van der Heijden, M.
van de Par, S.
van Dijk, P.
van Hengel, P. W. J.
van Hoesel, R. J. M.
van Santen, J.
van Son, R.
Van Tasell, D. J.
Varadé, A.
Vardoulakis, I.
Varnett, D. M.
Vatikiotis-Bateson, E.
Veksler, N. D.
Vercoe, B.
Verheij, J. W.
Vermeir, B.
Vermeir, G.
Vidmar, P. J.
Vieira, M. N.
Viemeister, N. F.
Visscher, W. M.
Vorlander, M.
Voronovich, A. G.
Waag, R. C.
Wable, J.
Wagner, J. W.
Wagstaff, R.
Wake, M.
Waldstein, R. S.
Walker, W. F.
Walton, J. P.
Wang, B-T.
Wang, C-Y.
Wang, L.
Wang, P. P.
Wang, T. B.
Wang, X.
Wang, Y. J.
Washburn, K.
Waterhouse, R. V.
Watkins, W.
Weaver, R. L.
Webb, H.
Weber, D. L.
Weinberg, H.
Weisenberger, J.
Weismer, G. G.
Weiss, L. G.
Wells, J. C.
Wenzel, E. M.
Werby, M.
Werker, J. F.
Werner, L. A.
West, R.
Wesbury, J. R.
Westervelt, P. J.
Weston, D. E.
Westwood, E. K.
Whalen, D. H.
White, D.
White, M. J.
White, P.
Wickesberg, R. E.
Wiederhold, M. L.
Wightman, F. L.
Williams, E. G.
Willott, J. F.
Wilson, D. K.
Wilson, O. B., Jr.
Wilson, T. E.
Winsberg, S.
Wirgin, A.
Wogram, K.
Wolf, S. N.
Wong, G. S. K.
Wong, K. M.
Woodhouse, J.
Worcester, P.
Wright, B. A.
Wright, W.
Wu, J.
Wu, S. F.
Wu, T. T.
Wu, T. W.
Wursig, B.
Xu, P-c.
Xu, Y.
Yamamoto, T.
Yang, T. C.
Yang, Y.
Yano, H.
Yates, T. W.
Yoder, T. J.
Yogeswaren, E.
Yoshikawa, S.
Yost, W. A.
Yost, W. T.
Young, E. D.
Zabolotskaya, E. A.
Zagaeski, M.
Zahorian, S. A.
Zajac, D. J.
Zakarauskas, P.
Zeng, F-G.
Zeqiri, B.
Zhou, G.
Zhou, J-X.
Zhu, Q.
Zhu, Z.
Zingarelli, R. A.
Ziolkowski, R. W.
Ziomek, L. J.
Ziv, M.
Zolotov, E. M.
Zuckerwar, A. J.
Zurek, P. M.
Zwislocki, J. J.

*Also in 1996, omitted.

Eight medals awarded to students during 1997

In 1997 the twelfth year of the Robert Bradford Newman Student Award Medal Program, eight students were selected to receive the medal ''For Merit in Architectural Acoustics.'' All recipients attended architectural schools previously represented by medalists in past years, including Princeton University and the University of Florida where two students were recipients of medals this year.

Following is a list of the recipients of medals and their projects:

Michelle L. Amt
Princeton University
Acoustical Oppositions In a Performing Arts Center: Building as Narrative

Gabriel Caunt
University of Kansas
A Practical Study of Auralization Using EASE and EARS Software

Karen Timms Godsey
Clemson University
Community Theatre for Greenville, SC

Christopher R. Herr
University of Florida
An Acoustical History of Theaters and Concert Halls

Travis L. Hicks
Princeton University
Acoustical Oppositions in a Performing Arts Center: Building as Narrative

Jacob E. Kain
Massachusetts Institute of Technology
Concept Development for Performing Arts Center: Acoustical Integrity

Shannon L. McKee
Roger Williams University
Falmouth Playhouse on Cape Cod, MA

David Prince
University of Florida
Variation of Room Acoustics: Measurements as a Function of Source Location and Directivity

Neil Shade Awarded 1997 Schultz Grant

The 1997 Theodore John Schulz Grant for Advancement of Teaching and Research in Architectural Acoustics has been awarded to Neil Thompson Shade, President and Principal Consultant of Acoustical Design Collaborative, Ltd. of Falls Church, Virginia.

The grant money will be used to develop a Sound Design Guide for instructional use by faculty and students in schools of architecture. The Design Guide will cover the basics of sound systems design, its integration within buildings, and requirements for contract documents.

Mr. Shade states, ''With rising public expectations on the performance quality of reproduced sound in building, I am hoping the Design Guide will enable students, faculty and practicing architects to more fully understand fundamental electro-acoustic principles and be able to successfully integrate these systems within buildings, achieving a level of technical performance equal to other building systems.''

USA Meetings Calendar

Listed below is a summary of meetings related to acoustics to be held in the U.S. in the near future. The month/year notation refers to the issue in which a complete meeting announcement appeared.

1998

7–12 July — Vienna and the Clarinet, Ohio State Univ., Columbus, OH [Keith Koons, Music Dept., Univ. of Central Florida, P.O. Box 161354, Orlando, FL 32816-1354; Tel.: 407-823-5116; E-mail: kkons@pegasus.cc.ucf.edu].

12–15 July — Transportation Research Board A1F04 Summer Meeting on Transportation Related Noise and Vibration, Tallahassee, FL [Win Lindeman, Florida Department of Transportation, 605 Suwannee St., M.S. 37, Tallahassee, FL 32399-0450; Tel.: 850-488-2914; Fax: 850-922-7217; E-mail: win.lindeman@dot.state.fl.us].

9–14 Aug. — International Acoustic Emission Conference, Hawaii [Karyn S. Downs, Lockheed Martin Astronautics, P.O. Box 179, M.S. DC3005, Denver, CO 80201; Tel.: 303-977-1769; Fax: 303-971-7698; E-mail: karyn.s.down@lmco.com].

13–17 Sept. — American Academy of Otolaryngology—Head and Neck Surgery, San Francisco, CA [American Academy of Otolaryngology—Head and Neck Surgery, One Prince St., Alexandria, VA 22314; Tel.: 703-836-4444; Fax: 703-683-5100].

18–19 Sept. — 6th Annual Conference on Management of the Tinnitus Patient, Iowa City, IA [Richard Tyler, Univ. of Iowa, Dept. of Otolaryngology—Head & Neck Surgery, 200 Hawkins Dr., C21GH Iowa City, IA 52242; Tel.: 319-356-2471; Fax: 319-353-6739; E-mail: rich-tyler@uiowa.edu].

12–16 Oct. — 136th meeting of the Acoustical Society of America, Norfolk, VA [ASA, 500 Sunnyside Blvd., Woodbury, NY 11797; Tel.: 516-576-2360; Fax: 516-576-2377; E-mail: asa@aip.org, WWW: http://asa.aip.org].

1999

15–19 March — Joint meeting 137th meeting of the Acoustical Society of America/Forum Acusticum [Acoustical Society of America, 500 Sunnyside Blvd., Woodbury, NY 11797; Tel.: 516-576-2360; Fax: 516-576-2377; E-mail: asa@aip.org; WWW: asa.aip.org].

27–30 June — ASME Mechanics and Materials Conference, Blacksburg, VA [Mrs. Norman Guynn, Dept. of Engineering Science and Mechanics, Virginia Tech, Blacksburg, VA 24061-0219; Fax: 540-231-4574; E-mail: nguynn@vt.edu; WWW: http://www.esm.vt.edu/mmconf/]. Deadline for receipt of abstracts: 15 January 1999.

REPORTS OF RELATED MEETINGS

This Journal department provides concise reports of meetings that have been held by other organizations concerned with acoustical subjects; and of meetings co-sponsored by the Acoustical Society but planned primarily by other co-sponsors.

World Marine Mammal Science Conference

Monaco, 20–24 January 1998
Sponsored by the Society for Marine Mammalogy and the European Cetacean Society

The World Marine Mammal Science Conference (WMMSC) marked the first meeting cosponsored by the United States-based Society for Marine Mammalogy and The European Cetacean Society. The joint meeting was the 12th Biennial Conference on the Biology of Marine Mammals, and the 12th Annual Conference of the European Cetacean Society. Over 1150 participants from nearly 60 countries attended the 5-day event, which featured roughly 600 scientific presentations. As is common at these meetings, acoustics and audiology featured prominently in many of the sessions. Specifically, there was one plenary talk, two oral sessions (10 papers), and a comprehensive poster session (37 presentations) devoted exclusively to topics in acoustics and underwater noise. In the plenary session, Dr. Darlene Ketten provided a succinct summary of current concerns and scientific investigations *vis-á-vis* the effects of man-made noise on marine mammals. Presentations during concurrent sessions included updates on bottlenose dolphins (*Tursiops truncatus*) whistle contour analyses, investigation of killer whale (*Orcinus orca*) dialects using neural networks, and reports on projects underway to investigate hearing sensitivity of bottlenose dolphins and white whales (*Delphinapterus leucas*) at depth. Poster presentations ran the gamut from call repertoire description (for a variety of species), to acoustic measures of body growth in a photo-identified sperm whale (*Physeter macrocephalus*). Enthusiasm for continued development of passive acoustic techniques to locate and census marine mammals was evidenced by several presentations where acoustics was either combined with visual surveys, or used alone, to detect animals over broad temporal and spatial scales.

Eight workshops preceded the conference, three of which focused on acoustic-related topics, including: (1) bioacoustic signal processing; (2) reducing cetacean bycatches using acoustic deterrents; and (3) assessing behavioral impacts of human activities on marine mammals. The workshops provided a forum for open-ended discussions on specific topics, and an opportunity for scientists active in these specialized fields to exchange ideas and research protocols. Many of the topics discussed at the workshops were revisited during a special symposium session entitled ''Recent Advances in Marine Mammal Acoustics; Noise Pollution, Habitat Degradation and Policy Making,'' convened on the fourth day of the conference. Speakers at the symposium provided summary presentations on marine mammals hearing capabilities, behavioral disruption caused by anthropogenic noise, and U.S. government policy *vis-á-vis* marine mammals and noise pollution.

In addition to these specific sessions, papers on the effects of the Acoustic Thermometry Ocean Climate (ATOC) study sound source on marine mammals, and the use of acoustic data in conjunction with photo-identification or genetic techniques were interspersed throughout the proceedings, especially in sessions focused on ''Behavior.'' Also, use of autonomous hydrophone arrays (including the U.S. Navy SOSUS hydrophones) for whale call detection, and development of new hardware and software to automate call detection were in strong evidence in sessions devoted to ''Surveys & New Techniques.'' Overall, this conference again underscored the importance of acoustic techniques to the study of marine mammals, and its recent strong emergence in applications to field research.

A complete listing of WMMSC presentations and authors are available on The Society for Marine Mammalogy web page (http://pegasus.cc.ucf.edu/~smm); follow the WMMSC Presentations link. Conference abstracts books are available from Dr. Anne Collet, a key member of the Conference Committee. Contact her directly (Center de Recherche sur les Mammiferes Marins—Musee Oceanographique, Port des Minimes, La Rochelle 17000 France; e-mail: crmm@univ-LR.fr) to determine the cost of the books plus shipping and handling.

SUE E. MOORE
SAIC, Maritime Services Division
3990 Old Town Ave., #105A
San Diego, CA 92110-2931 USA
(e-mail: sue.ellen.moore@cpmx.saic.com)

 0001-4966/98/104(1)/17/1/$15.00

OBITUARIES

This section of the Journal publishes obituaries concerning the death of Fellows of the Society and other acousticians eminent in the world of acoustics. When notified, the Editor-in-Chief solicits a summary of the person's life and contributions from an ASA member thoroughly familiar with the details, if possible. If a promised obituary is never received, a brief obituary notice may be published later.

George Chertock • 1914–1997

George Chertock, a Fellow of the Society and a member of Phi Beta Kappa and Sigma Xi, died 29 December 1997, in suburban Washington, DC, after a series of illnesses.

Dr. Chertock was born in New York City 1 August 1914. He graduated from high school during the great depression of the 30s and found it necessary to work while attending evening classes at the uptown campus of the College of the City of New York, where he received a B.S. in Physics in 1939. He remained at the College as a teaching assistant for a year before accepting a government job in 1940 at the National Bureau of Standards. In Washington, he continued his physics education in the evening, receiving a M.A. in 1943 at the George Washington University with a dissertation, ''The Hydrogen Content of White Dwarf Stars,'' and then a Ph.D. at the Catholic University of America in 1952 with a dissertation, ''The Flexural Response of a Submerged Solid to a Pulsating Gas Bubble,'' the latter based on work performed at the David Taylor Model Basin (DTMB) after he transferred from the Bureau in 1946.

At DTMB, he became the Structural Mechanics Laboratory expert on the response of ship structures to the large-amplitude pressure transients developed by underwater explosions and air blasts. He was one of the DTMB contingent at the Crossroads and Wigwam tests conducted in the Pacific to determine the effectiveness of ''atomic'' bombs against naval vessels. Some years later, he contributed to the investigation of the sinking of the submarine, SCORPION, attempting to determine whether the hull had exploded or imploded by analyzing underwater acoustic transients coincidentally observed with listening sonar equipment.

Chertock changed his interests from large-amplitude transients to small-amplitude steady-state sound pressures when he joined the Department of Acoustics and Vibration in 1962. He was one of the early theorists exploiting the use of spheroidal wave functions and integral equations to solve acoustic radiation problems, and published many papers and reports on these topics, all of them models of clarity and accuracy. He spent a sabbatical year, 1966–67, in the Department of Applied Mathematics and Theoretical Physics of the University of Cambridge in England working on mathematical methods for solving acoustic radiation problems. He retired from DTMB in 1982.

Those of us who worked with George have missed his participation in our technical discussions ever since his retirement, and we will continue to miss him. There have been many times when we have thought, ''What would George have to say about this?'' We also miss his participation in what had been famous lunchtime debates, when he could excite all of us while sometimes deliberately arguing an opposing opinion on a controversial subject.

Dr. Chertock is survived by Esther, his wife of 60 years, daughters Barbara Ziony and Evie Tinkham, and three grandchildren.

M. STRASBERG

Paul S. Veneklasen • 1916–1996

Paul Schuelke Veneklasen, a Fellow of the Society, died at home on 21 May 1996 after a stubborn battle with cancer. Paul was born on 10 June 1916 in Grand Haven, Michigan, and moved to Wilmette, Illinois, where he graduated from high school. His B.S. in 1937 and M.S. in 1938 at Northwestern University were in Physics, Mathematics, and Aeronautical Engineering. World War II interrupted his doctoral physics program with Prof. Vern O. Knudsen at UCLA, where he was a teaching assistant.

As a civilian with the Office of Scientific Research and Development at Duke University, he did research on acoustical location of artillery. He then went to the Electroacoustics Laboratory at Harvard University, where he assisted Leo Beranek in the development and testing of voice communication equipment in high-level noise, and of ear protection devices.

After the war Paul returned in 1946 to California for research at Altec-Lansing Corporation on a commercial condenser microphone, and on loudspeakers for motion picture sound systems. In 1947 he became an independent acoustical consultant, and founded Western Electro-Acoustic Laboratory, upon which his successful acoustical career was built.

His varied projects included environmental noise measurement, aircraft and industrial noise control, pulse jet acoustics, miniaturization of electroacoustic components, and the acoustical design of many auditoriums, theaters, and recording studios including notably the Los Angeles Music Center, the Seattle Opera House, and Wolf Trap Farm Park. As a musician and acoustician Paul practiced ''Science in the Service of the Arts.''

Paul Veneklasen has a long history of contributions to his profession in the Acoustical Society of America, often presenting papers at Society meetings on architectural acoustical design, modeling techniques, and sound reinforcement. His first *Journal* article (1948) was about instrumentation for the widely used Western Electric 640-AA condenser microphone. Paul served the *Journal* as Associate Editor for Architectural Acoustics from 1959 to 1963. He was a Distinguished Lecturer at the Society's Wallace Clement Sabine Centennial Symposium (1994), speaking on ''The Challenge of Design for the Performing Arts'' (see the Proceedings, pp. 280–286). Nine patents were issued with Paul listed as inventor.

Paul Veneklasen's interests beyond acoustics were wide ranging, including astronomy, history, aeronautics, photography, sailing, choral music, musical instrument design, philosophy and morality, health, and medicine. Paul was often outspoken in his views and he acted according to his convictions.

In his family relationships he instilled creativity through mentoring and many family projects. He is survived and will be long remembered by an extended family including his wife Elizabeth and her family, sons Lee and Mark and grandsons, former wife Louise, and his Associates. A memorial session in Architectural Acoustics, honoring Paul Veneklasen, was held during the recent 134th Meeting of the Society in San Diego, California on 4 December 1997.

JOE ORTEGA

BOOK REVIEWS

James F. Bartram
94 Kane Avenue, Middletown, Rhode Island 02842

These reviews of books and other forms of information express the opinions of the individual reviewers and are not necessarily endorsed by the Editorial Board of this Journal.

Editorial Policy: *If there is a negative review, the author of the book will be given a chance to respond to the review in this section of the Journal and the reviewer will be allowed to respond to the author's comments. [See ''Book Reviews Editor's Note,'' J. Acoust. Soc. Am.* ***81****, 1651 (May 1987).]*

Encyclopedia of Acoustics

Malcolm J. Crocker, Editor-in-Chief

John Wiley & Sons, Inc., New York, NY 10158.
4 vols. xxiv +2017 pp. Price $395.00.

Acoustics Handbook

Malcolm J. Crocker, Editor-in-Chief

John Wiley & Sons, Inc., New York, NY 10158.
xviii +1461 pp. Price $195.00.

We have here the four-volume *Encyclopedia of Acoustics*, released in the middle of 1997, and its derivative, the single-volume *Acoustics Handbook* that came out in February of this year. *Encyclopedia* constitutes a long-needed, monumental overview of nearly the entire field of acoustics. The editor-in-chief, Malcolm J. Crocker of Auburn University, spent nearly a decade in organizing contributions from many of the most prominent experts in many branches of acoustics.

The genesis of the encyclopedia traces back to the early 1980s when Crocker discussed the need for a comprehensive compilation of acoustical topics with Tony Embleton, Manfred Heckl, William Lang, Bruce Lindsay, Richard Lyon, and Ted Schultz. But work did not begin in earnest until the close of that decade when Crocker organized an editorial board that reads like a veritable *Who's Who in Acoustics*, including Robert F. Apfel, Leo L. Beranek, Per V. Brüel, William J. Cavanaugh, Sir James Lighthill, Bruce Lindsay, Richard Lyon, Alan Powell, Thomas D. Rossing, etc. The board helped Crocker to formulate the organization of the encyclopedia and the topics to be covered (thanks in part to the PACS classification of subjects used by *JASA*). The contributor list is just as impressive, including Allan D. Pierce in linear acoustics, Larry Crum in sonochemistry and sonoluminescence, James Lighthill in aeroacoustics, Ira Dyer and David Feit on underwater sound, Eric E. Ungar on vibration, Richard H. Lyon on statistical methods, A. Harold Marshall and William J. Cavanaugh on architectural acoustics, W. Dixon Ward on pyschoacoustics, Thomas D. Rossing on music and percussion instruments, Per V. Brüel on measuring instruments, Elmer L. Hixson and Ilene Busch-Vishniac on transducers, to name only a few. Moreover, the contributions were checked by more than three hundred highly qualified reviewers.

As pointed out in the foreword by Sir James Lighthill, ''not one out of the 18 parts is self-sufficient; on the contrary, links to the subject matter are...emphasized through cross-references.'' He further paid the compliment of comparing the significance of the encyclopedia with that of Lord Rayleigh's monumental opus, *The Theory of Sound*, originally issued in two volumes in 1894 and 1896, respectively. Only time can tell if Sir James's prognosis is correct, but the odds are that it will be.

The text of the *Encyclopedia of Acoustics* is divided into 18 main parts, with each part assigned to a member of the editorial board. These 18 parts contain a total of 166 chapters. Each chapter covers a specific aspect of that part's main topic. For example, Part I deals with general linear acoustics, subdivided into chapters on the mathematical theory of wave propagation, ray acoustics for fluids and for structures, interference and steady-state scattering of sound waves, speed of sound in fluids, standing waves, etc.

Part I opens with the first chapter Introduction, written by the editor himself (Crocker); it provides a succinct overview of the acoustical fundamentals—viz., plane waves, impedance, 3-D wave equation, sound intensity and power, decibels, the phenomena of reflection, refraction, scattering, and diffraction, modeling techniques (wave, ray, and energy acoustics), boundary waves, standing waves, waveguides, lumped elements, etc. The linearization process establishing wave equations is handled in Allan Pierce's Chapter 2, along with a discussion of mathematical properties of wave propagation. In Chapter 3, D. E. Weston delved into ray (or geometric) acoustics for fluids, which traces its ancestry to Huygens' principle. The applicability and the limitations of the methodology are well outlined. Although brief, Leopold B. Felsen's Chapter 4 on ray acoustics for structures proved to be more satisfying in its coverage of the spectral foundations of ray theory, synthesis of modal fields, waveguides, and submerged elastic structures, along with a bibliography more extensive than that rendered in the preceding chapter. Interference and steady state scattering, the speed of sound in fluids, standing waves, waveguides, and steady-state radiation from sources (monopoles, dipoles, quadrapoles, multipoles, pulsating spheres and cylinders, circular pistons) comprise the subjects of Chapters 5–9, respectively. Transient radiation is extremely well described by Peter Stepanishen in Chapter 10. So is the acoustical interaction between structures and fluids (J. H. Fahy, Chapter 11). Boundary waves (Ivan Tolstoy, Chapter 12), acoustic lumped elements used as analogies to electrical circuit elements in depicting the behavior of sound interacting with physical structures considerably smaller than the impinging acoustic wavelength (Robert E. Apfel, Chapter 13), the finite element and boundary element methodologies of acoustic modeling (Chapters 14 and 15), and acoustic modeling of ducted source systems (M. G. Prasad and Malcolm J. Crocker, Chapter 16) complete the scope of Part I.

Part II delves into nonlinear acoustics and cavitation (David T. Blackstock and Malcolm J. Crocker, Chapter 17); equations of nonlinear acoustics (Blackstock alone, Chapter 18); finite-amplitude waves in fluids (D. G. Crighton, Chapter 19); parameters of nonlinearity in acoustic media (E. Carr Everbach, Chapter 20); finite-amplitude waves in solids (Mack A. Breazeale, Chapter 21); nonlinear standing waves in cavities. Chapter 25 on cavitation by Werner Lauterborn and Chapter 26 on sonochemistry and sonoluminescence by Kenneth Suslick and Lawrence Crum contain exceptionally good descriptions.

Part III (Aeroacoustics and Atmospheric Sound) features Sir James Lighthill's introduction to aircraft noise including supersonic boom), propagation of sound through steady mean flows, sheared stratified winds, acoustic streaming (Chapter 27), and Alan Powell's Chapter 28 on different types of aerodynamic and jet noises; followed by chapters in the interaction of fluid motion and sound, acoustic streaming, shock waves, blast waves, and sonic booms. Chapter 32 (by Louis C. Sutherland and Gilles A. Daigle) is especially outstanding for its comprehensive coverage of atmospheric sound propagation as affected by atmospheric absorption, ground surface impedance, relative humidity, etc. The subject of infrasound which occurs in natural phenomena such as earthquakes, volcanic eruptions, avalanches, wind, and meteors constitutes the last chapter of Part III.

Part IV deals with underwater acoustics, with an introduction by Ira Dyer followed by chapters on the basics of oceanography, propagation of sound in the ocean and in marine sediments, attenuation effects (forward scattering, volume scattering, and backscattering), sound radiation from marine structures, quantitative ray methods for scattering, and ''practical'' chapters on target strength of fish, underwater noise sources, ship and platform noise, propeller noise, underwater explosive sound sources, ocean ambient noise, sonar systems, oceanographic and navigational instruments, acoustic telemetry, transducers, and nonlinear sources and receivers. In Chapter 50 treating navigational instruments, no mention is made of the GPS (global positioning system) which uses satellite technology to provide location which constitutes a vital part of oceanographic information.

 0001-4966/98/104(1)/19/3/$15.00

Volume 2 of *Encyclopedia* begins with Part V (ultrasonics, quantum acoustics, and physical effects of sound). Topics include methods of measuring ultrasonic velocities, relaxation processes phonons in crystals, quasicrystals, and Anderson localization, surface waves in solids (the principles of which are used to study thin film technology), and other effects such as the quantum Hall effect and magnetoelastic interaction. Chapter 59 by Gary A. Williams describes the unusual wave modes (first, second, third, and fourth sound) in near $-0°$ K liquid helium. The thermal effects existing in sound waves can be harnessed through thermoacoustic engines to generate acoustic power from heat or to produce refrigeration from acoustic power—this is described in Chapter 61 by Gregory W. Swift.

Part VI concerns mechanical vibrations and shock. Fundamentals of vibration are developed from Hooke's and Newton's law, along with energy relations and variational principles. An overview is supplied on the principles of analytical and experimental methods applied to vibrating systems with extension to multi-degree-freedom systems (Chapter 63 by Paul J. Remington), followed by discussions on vibrations of one- and two-dimensional continuous systems, nonlinear vibration, random vibration, shock analysis, and design (Chapters 64–67). Acoustic emission constitutes a valuable tool for evaluating structures and this is described in Kanji Ono's Chapter 68. The effects of high-intensity sound on structures, vibration isolation and damping, vibration measurements and instrumentation, machine, monitoring of machine vibration, structure-borne (rods, beams, thin plates, cylindrical and spherical shells, and pipes) energy flow, and active vibration control are the remaining topics covered in Part VI.

Part VII (Statistical Methods in Acoustics) has the fewest numbers of chapters, with a very brief introduction to statistical methods in acoustics, followed by more thorough treatments of response statistics of rooms (for reverberation decay properties) and statistical modeling of vibrating systems.

The effects of noise and its control are treated in Part VIII. There are ten chapters, which treat criteria and rating measures for noise, hearing protection devices, sources of noise emission, generation of noise in machinery, procedures to cut down on machinery noise, and means of identifying noise sources, the relatively new method of active noise control which generates out-of-phase noise to countermand (i.e., at least partially cancel) the effect of the offending noise through superpositioning of sound waves, methods of predicting sound power levels of industrial machinery, airport noise, and surface transportation noise. This section concludes with Chapter 89 on community response to environmental noise. It would have been a good idea to display model codes which could aid communities in legislating noise levels in different municipal zones.

In Volume 3, architectural acoustics is treated in Part IX, which deals with the fundamentals of sound absorption in enclosures and building codes. Chapter 94 by Gregory C. Tocci ranks importantly in its explanation of ratings, e.g., A-weighted SPL, SIL (speech interference level), L_{eq}, L_{xx}, L_{dn}, CNEL (community noise equivalent level), room criterion curves, sound absorption coefficient α, NRC, etc. In addition, descriptors are explained: e.g., reverberation time T_{60}, room constant R, articulation index AI, etc. Descriptors and ratings used in ISO and selected European and Asian standards and regulations are also discussed. Chapter 96 should prove valuable to architects and engineers with a summarization of acoustical guidelines for building design, according to the building categories (dwelling work/study areas, meeting/hospitality spaces, theaters, houses of worship, industrial regions, transport space, or arena). U.S. building codes are covered in Chapter 97, including BOCA, ICBO, and SBCCI. Workers outside the U.S. can refer to a potentially valuable set of tables listing the criteria of the acoustical codes in ten different nations. Noise control for mechanical and ventilation systems are dealt with in Chapter 98: the level and character of sound for principal types of mechanical equipment used in typical buildings, data for the different operating conditions of various types of equipment, and vibration isolation measures.

Part X delves into the more esoteric topics of statistical theory of acoustic signals and acoustic holography. Alan J. Piersol's treatment of the statistical theory of acoustic signals in Chapter 100 is extremely well done with the definition of probability distribution, time-domain, frequency domain, joint, and other functions in spectral signals. Equally good is Chapter 101 by John C. Burgess on the methods of acquiring valid signal data, and on choosing methods of data reduction such as FFT and DFT. In Chapter 102, acoustical holography refers to the method of recording sound waves two-dimensionally and applying the recording to reconstruct the entire sound field in a three-dimensional space.

The topics of the physiology of hearing and of psychoacoustics are covered in Parts XI and XII, respectively. The eleven chapters (103–113) of Part XI summarize the facts and the ever-changing operational hypotheses in physiological acoustics. Separate chapters deal with the outer ear, middle ear, and the inner ear. The other chapters approach the physiological topic from the disciplinary viewpoints of anatomy, biochemistry, and pharmacology. Chapter 113 is quite unusual—it deals with neuroethology, which is premised on the philosophy that the vocal and the auditory systems have evolved together for acoustic communication and echolocation. This field also entails understanding of the neural mechanism for processing sounds, including speech.

The fourth and final volume of *Encyclopedia* holds interest for those involved in speech communication, musical acoustics, bioacoustics, animal bioacoustics, acoustical measuring gear, and transducers.

Speech communication (Part XIII) consists of six chapters (124–129), with overviews of the subtopics of models of speech production, speech perception (how the listener processes the speech signal), acoustical analysis of speech through spectral analysis and parametric extraction, techniques of speech coding (entailing quantization, scalar, and vector coders) which convert speech into digital codes with minimal loss of information and provide the basis for machine recognition of speech. Chapters 128 and 129 clarified very well for this reviewer the principles underlying voice recognition programs, e.g., computer voice dictation programs that convert into written words inside a word-processing program.

Part XIV centers on music and musical instrumentation—which includes the human singing voice and electronically generated music. Separate chapters treat bowed string instruments (131); plucked stringed instruments (132); woodwind instruments, which involve air columns, key mechanisms, and reed generators (133); and brass instruments. Chapter 135 by Thomas D. Rossing is superb in his description of percussion instruments. He discusses modes of ideal and real membranes, membrane instruments such as the kettledrum, the Indian drum, and various types of two-headed drums. Vibrating bar instruments are also described, including marimbas, xylophones, vibes, chimes, cymbals, gongs, and tamtams, Caribbean steel pans, and bells. Chapter 136 by Gabriel Weinreich treats pianos and other stringed keyboard instruments, string dynamics, structural differences between the harpsichord and the piano. Jürgen Meyer describes pipe and reed organs, flue pipes, harmoniums, accordions, and harmonicas (Chapter 137). In Chapter 138, William Morris Hartmann deals with the relatively new topic of electronic and computer music. Analog synthesis traces back to the Moog synthesizer of the 1960s and the digital synthesizer was pioneered by Max Matthews shortly afterwards. In early 1970s J. M. Chowning came out with the FM algorithm synthesizer which proved to be quite cost-effective. The last chapter (139) on music, by Johan Sundberg, describes the human singing voice. Topics include subglottal pressure and breathing activity patterns and underlying generation of song. Special types of singing are described: Western operatic, overtone singing, the higher-pitched Chinese operatic, belting (à la Ethel Merman), and choral.

Bioacoustics, the subject of the six chapters (140–145) of Part XV, deals with the characteristics of sound propagation in biological media, the physiological effects of ultrasound, use of acoustics for medical diagnostics and acoustical imaging, and effects of vibration and shock on humans. This generally involves bioultrasonics in which the frequency range of interest covers 20 kHz to 2 GHz. In Chapter 41 on the acoustical characteristics of biological media, a discussion is given on ultrasound propagation in living tissues as they relate to tissue imaging and the effects produced during chemical therapeutic procedures. In Chapter 142, the mechanisms of the biological effect of ultrasound are described. Three classes of interactions have been identified: thermal, mechanical, and cavitation. Medical diagnosis through acoustical means is described in Chapter 143. Some techniques are fairly old, such as the use of the stethoscope and some are newer such as the measurement of arterial blood flow through ultrasound Doppler effect and phonocardiography. There occurs a wide range of sounds, those emanating from the heart, lungs, blood flow, muscles, acoustic fetal stimulation. Chapter 144 lays out acoustical medical imaging instrumentation, time elements of imaging and imaging acquisition, signal processing, Doppler detection, and display modes. The effects of vibration and shock on people are covered in Chapter 145. The sources of vibration and shock, the physiological/pathological responses, biodynamic prediction modeling, and protective measures (very briefly) are described.

However there appears to be little, if any, mention of using ultrasound as a therapeutic tool, given that it is being applied for dental plaque removal, pulverization of kidney stones, treatment of aching muscles, reaming of blood vessels to counter the effect of arteriosclerosis, etc. Another chapter would be needed to supply the appropriate overview.

Animal bioacoustics (Part XVII, Chapters 146–153) deals with the sounds made by various animal species, viz., land and marine vertebrate animals, insects, amphibians, birds, bats, and non-human primates. Hearing capabilities, sound production, the physiology, and mechanisms of hearing are described.

Acoustical measurements and instrumentation are treated in Part XVII. There are individual chapters on sound level meters, sound intensity measurements, and on calibration of pressure and gradient microphones.

Transducers constitute the last segment, Part XVIII, with discussions of general transducer principles Chapter 159 (Elmer L. Hixson and Ilene J. Busch-Vishniac), loudspeaker design (Bradley Starobin's Chapter 159, covering driver design, cabinetry, crossover networks, and measurements but not different types of drivers such as electrostatic panels and ribbon drivers), horns (Chapter 161 by Vincent Salmon), different types of microphones (Chapter 162, again by Busch-Vishniac and Hixson), sound reinforcement (Chapter 163, a very good exposition by David L. Klepper and Larry S. King that treats microphones, control and preamplification, amplification and loudspeaker layout, equalization and the increasingly important methodology of time delay for treating unfavorable building acoustics, and design procedures), magnetic recording procedures (a very brief Chapter 164), digital audio recording (the basis for CDs and DVDs, Chapter 165), and hearing aid design (Chapter 166, which includes the problems of receiver sensitivity, bandwidth, frequency response shaping, background noise, and distortion).

According to Robert L. Argentieri, John Wiley's senior editor in charge of these two publications, *Acoustics Handbook* was spun off from *Encyclopedia of Acoustics*

> ''because of a professed need by individuals...for a single-volume, low-priced work. In order to make a smaller one-volume handbook out of the larger encyclopedia we focused on trimming away topics that were either esoteric or highly theoretical in nature and/or not of general interest to the main audience...of designers, engineers, and scientists. Thus coverage of topics such as bioacoustics and animal bioacoustics were cut back as well as coverage of underwater acoustics.''

How does the *Handbook* differ from the *Encyclopedia*? For a starter, let us consider size. *Handbook* measures 7 cm in thickness versus a combined total of 12 cm for the four volumes of the encyclopedia. The 19.2 cm×24 cm page size of the *Handbook* contrasts with the *Encyclopedia's* 22 cm×28 1/2 cm. Because the page layout in the same articles are identical in the two publications, the print in the *Handbook* had to be made smaller, about 3/4 that of the *Encyclopedia*. Incidentally, in the table of contents for the *Encyclopedia*, Part VI (Mechanical Vibrations and Shock) is incorrectly listed as Part IV, actually following Part V in all four volumes, but the Roman numbering is correct in the *Handbook*.

In the *Handbook*, two parts from *Encyclopedia* have been eliminated, namely Part XV (Bioacoustics) and XVI (Animal Bioacoustics), and roughly 20% of the remaining chapters eliminated. A new chapter on analyzers is added to the *Handbook*, but cross-referencing to the omitted chapters are retained. The *Handbook* contains 16 main parts subdivided into 113 renumbered chapters. For the benefit of the prospective purchaser deciding between the two publications, we list here the chapters in the *Encyclopedia* that have been omitted in the *Handbook*:

Part I (General Linear Acoustics)
- Chapter 4: Ray Acoustics for Structures
- Chapter 12: Boundary Waves

Part II (Nonlinear Acoustics and Cavitation)
- Chapter 22: Nonlinear Standing Waves in Cavities

Part III (Aeroacoustics and Atmospheric Sound)
- Chapter 30: Acoustic Streaming

Part IV (Underwater Sound)
- Chapter 35: Essential Oceanography
- Chapter 36: Propagation of Sound in the Ocean
- Chapter 37: Propagation in Marine Sediments
- Chapter 38: Attenuation by Forward Scattering: Measurements and Modeling
- Chapter 39: Volume Scattering in Underwater, Acoustic Propagation
- Chapter 40: Backscattering from Rough Surfaces and Inhomogeneous Volumes
- Chapter 43: Quantitative Ray Methods for Scattering
- Chapter 44: Target Strength of Fish
- Chapter 47: Underwater Explosive Sound Sources
- Chapter 52: Transducers
- Chapter 53: Nonlinear Sources and Receivers

Part V (Ultrasonics, Quantum Acoustics, and Physical Effects of Sound)
- Chapter 59: Wave Modes in Liquid Helium

Part VI (Mechanical Vibrations and Shock)
- Chapter 70: Effects of High Intensity Sound on Structures

Part VII (Statistical Methods in Acoustics)
- This section is unaffected

Part VIII (Noise: Its Effects and Control)
- Chapter 82: Determination of Noise Emission of Sound Sources

Part IX (Architectural Acoustics)
- Chapter 95: Sound Propagation in Work Spaces
- Chapter 97: Noise Control in U.S. Building Codes
- Chapter 102: Acoustic Holography

Part XI (Physiological Acoustics)
- Chapter 104: Auditory Function
- Chapter 109: Physiology of the Auditory Nerve
- Chapter 110: Anatomy of the Central Auditory Nerve Systems
- Chapter 111: Electrophysiology of the Central Systems
- Chapter 112: Biochemistry and Pharmacology of the Auditory System
- Chapter 113: Parallel-Hierarchical Processing of Complex Sounds for Specialized Auditory Function

Part XII (Psychological Acoustics)
- Chapter 117: Functions of the Binaural System
- Chapter 121: Perception of Complex Waveforms
- Chapter 122: Adaptation in the Auditory Systems
- Chapter 123: Hearing Thresholds

Part XIII (Speech Communication)
- Chapter 126: Speech Perception

Part XIV (Music and Musical Acoustics)
- Chapter 132: Stringed Instrument: Plucked
- Chapter 135: Percussion Instruments
- Chapter 137: Pipe and Reed Organs
- Chapter 138: Electronic and Computer Music
- Chapter 139: Human Singing Voice

Part XV (Bioacoustics)—entire section eliminated
- Chapters 140–145

Part XVI (Animal Bioacoustics)—entire section eliminated
- Chapters 146–153

Part XVII (Acoustical Measurements and Instrumentation, now Part XV in *Handbook*)
- Only part in the Handbook to have a chapter not in the *Encyclopedia*—J. Pope's Chapter 107: Analyzers

Part XVIII (Transducers, now Part XVI in *Handbook*)
- Chapter 161: Horns
- Chapter 163: Public Address and Sound Reinforcement Systems
- Chapter 166: Hearing Aid Transducers

In Chapter 107 exclusive to the *Handbook*, descriptions are rendered of sound level meters, analogue and digital frequency analyzers, rms and peak detectors, different types of filters (high pass, low pass, bandpass, and band reject), Nyquist frequency, aliasing and antialiasing filters, FTT spectrum analyzer characteristics, and multi-channel analysis. Signal terminologies are also provided.

In most respects the typical acoustician may find the one-volume sufficient, as a majority of the chapters are reproduced in their entirety from the encyclopedia. However, acousticians working for the U.S. Navy Research Laboratory or a Bell Lab or those dealing with the physiology and the effect of acoustics of animals, or musical instrument researchers would probably prefer the *Encyclopedia* to the *Handbook*, even just for the reference listings alone. We should also mention here that the volumes of the *Encyclopedia* are purchasable only as a set, not individually.

In brief, either publication is a must-have for the practicing acoustician.

DANIEL R. RAICHEL

CUNY Graduate School
Mechanical Engineering Department
City College of New York
New York, New York 10031

REVIEWS OF ACOUSTICAL PATENTS

Daniel W. Martin
7349 Clough Pike, Cincinnati, Ohio 45244

The purpose of these acoustical patent reviews is to provide enough information for a Journal reader to decide whether to seek more information from the patent itself. Any opinions expressed here are those of reviewers as individuals and are not legal opinions. Printed copies of United States Patents may be ordered at $3.00 each from the Commissioner of Patents and Trademarks, Washington, DC 20231. Reviewers for this issue:

Reviewers for this issue:

GEORGE L. AUGSPURGER, *Perception Incorporated, Box 39536, Los Angeles, California 90039*
MAHLON D. BURKHARD, *31 Cloverdale Heights, Charles Town, West Virginia 25414*
HARVEY H. HUBBARD, *325 Charleston Way, Newport News, Virginia 23606*
SAMUEL F. LYBARGER, *101 Oakwood Road, McMurray, Pennsylvania 15317*
D. LLOYD RICE, *11222 Flatiron Drive, Lafayette, Colorado 80026*
WILLIAM THOMPSON, JR., *The Pennsylvania State University, University Park, Pennsylvania 16802*

5,511,044

43.25.Gf THRUST PRODUCING APPARATUS

B. B. Bushman, assignor to Lockheed Corporation
23 April 1996 (Class 367/191); filed 19 October 1991

A device for producing thrust consists of a closed cylindrical chamber within which a standing acoustic wave is established along the chamber axis by transducers mounted at the ends of the chamber. This standing wave is characterized by pressure maxima at the ends of the chamber and a pressure node at the midpoint of the chamber. An intake port is mounted in the chamber wall at this midpoint location, and fluid is drawn in because of the low pressure there. Discharge ports are located near the ends of the chamber, and fluid is pumped out of the chamber because of the elevated pressure at those positions.—WT

5,381,382

43.30.Yj NOISE SHIELDED HYDROPHONE

R. A. Marshall, Ft. Pierce, FL
10 January 1995 (Class 367/20); filed 19 August 1993

The sensor element **60** within one hydrophone element **40** of a towed line array of such hydrophones is rendered more immune to noise generated by turbulent boundary layer excitation of the interconnecting cable **32** by the introduction of acoustic scatterers **80** into both the front and back ends of the hydrophone body **40**. These scatterers may be material having an acoustic

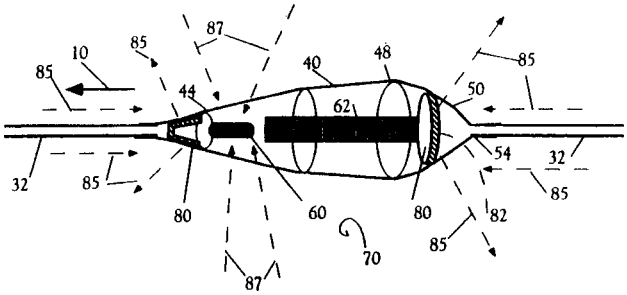

impedance much greater than that of the body material (e.g., stainless steel) or much less (e.g., air-filled foam). The scatterers are sized and shaped to fit within the hydrodynamic contour of the body and the front one, in particular, cannot extend in the axial direction to an extent that it affects the response of the sensor element **60** in the lateral direction.—WT

5,566,132

43.30.Yj ACOUSTIC TRANSDUCER

R. S. James *et al.*, assignors to the United States of America
15 October 1996 (Class 367/163); filed 11 December 1995

The motor section of a class IV flextensional transducer is configured as two, more or less identical, stacks of piezoceramic plates **20** and **40** that are terminated at their central positions by metal end plates **30** and **50**. The two stacks are colinearly aligned and connected together by threaded stud(s) **34** and nut(s) **60**. This arrangement allows for prestressing the stacks after

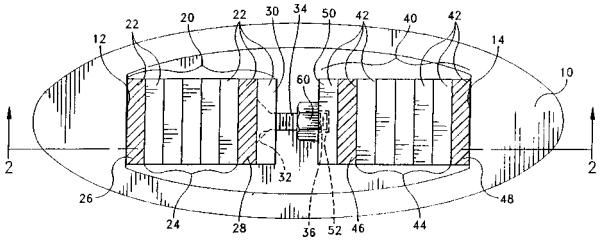

they have been placed within the shell **10** and also for ease of removal of any stack should it be damaged. Of course, since the electromechanical coupling is greatest at the midpoint of the entire stack, as it vibrates in the fundamental length mode, and since there is no piezoceramic at that point, the coupling coefficient of this design will be low.—WT

5,579,286

43.30.Yj QUIET GEOPHYSICAL CONSTRUCTION PRACTICES FOR REDUCED DIAMETER STREAMERS

R. D. Skorheim, assignor to Whitehall Corporation
26 November 1996 (Class 367/154); filed 22 November 1994

It is suggested that some of the transducer elements in a towed array can be physically moved (the mechanics of accomplishing these moves is not discussed) to mitigate against some nearby source of noise interference, but the elements must always be moved in pairs, symmetrically with respect to the geometric center of the set of elements, in order not to disturb the position of the acoustic center of the array.—WT

5,579,287

43.30.Yj PROCESS AND TRANSDUCER FOR EMITTING WIDE BAND AND LOW FREQUENCY ACOUSTIC WAVES IN UNLIMITED IMMERSION DEPTHS

D. D. M. Boucher and Y. LeGall, assignors to L'Etat Francais
26 November 1996 (Class 367/167); filed in France 27 May 1994

A double tonpilz transducer is mounted in a rigid hollow shell. The two radiating faces of the transducer seal the ends of the shell but an opening in the shell wall communicates the surrounding ambient pressure to the internal cavity of the shell. This internal cavity contains one or more bladders filled with a fluid which is more compressible than the surrounding fluid.—WT

5,706,249

43.35.Mr PANEL SPACER WITH ACOUSTIC AND VIBRATION DAMPING

William B. Cushman, Pensacola, FL
6 January 1998 (Class 367/1); filed 1 April 1996

This patent discloses three different types of grids that can be used as spacers between solid panels used for construction. The purpose is to enhance the natural damping characteristics of the combination of panels. In the example shown, the grid between panels **10** and **20** has nub spacers **30** which contact both panels and which are held in place by filament webbing

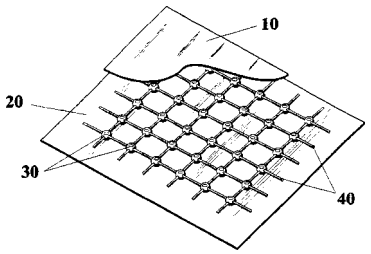

40. A polymer material such as nylon can be used. As the nub spacers are squeezed by the vibration of one panel relative to the other panel, energy is transmitted laterally through the filament structure and into the intervening air space where viscous damping at clearances between the filaments and the panels can add to the overall damping effect.—DWM

5,492,014

43.35.Yb ULTRASONIC TRANSDUCER FOR MONITORING ACOUSTIC EMISSIONS

Dov Hazony, assignor to J. W. Harley, Incorporated
20 February 1996 (Class 73/644); filed 3 January 1994

The transducer is intended for sensing and measuring acoustic events in an environment subject to magnetic and electric fields. Accordingly, the

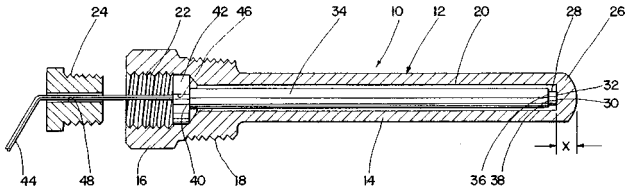

piezoelectric element **28** is shielded within outer jacket **12**. The outer surface of the tip **26** is convex to form a wide angle acoustic lens.—MDB

5,493,618

43.38.Ar METHOD AND APPARATUS FOR ACTIVATING SWITCHES IN RESPONSE TO DIFFERENT ACOUSTIC SIGNALS

Carlile R. Stevens and Dale E. Reamer, assignors to Joseph Enterprises
20 February 1996 (Class 381/110); filed 7 May 1993

The patent describes in some detail an acoustically activated switch device. The device is juxtaposed between an electrical power outlet and the appliance to be turned on or off. A microphone in the device provides electrical signals that are interpreted by a microcontroller which in turn activates switches. The switch can be ''taught'' to respond to particular sounds.—MDB

5,483,501

43.38.Fx SHORT DISTANCE ULTRASONIC DISTANCE METER

K. T. Park and M. Toda, assignors to The Whitaker Corporation
9 January 1996 (Class 367/140); filed 29 April 1994

The effects of transducer ringing in a short distance ultrasonic distance meter are mitigated by the introduction of a modified excitation signal which, during the ringing phase, causes the transducer to vibrate in opposition to how it would naturally vibrate, thus effectively canceling all vibration.—WT

5,491,879

43.38.Fx PROCEDURE TO POLARIZE AT LEAST ONE ZONE OF A FOIL OF FERROELECTRIC MATERIAL TO PRODUCE A POLARIZED ELEMENT FOR PIEZOELECTRIC OR PYROELECTRIC TRANSDUCERS

Francois Bauer, assignor to Institut Franco-Allemand de Recherches de Saint-Louis
20 February 1996 (Class 29/25.35); filed in France 6 January 1993

The patent describes a method of polarizing selected areas of a foil of ferroelectric material. Electrodes are deposited on opposite surfaces of the foil so that the zone to be polarized extends between these two electrodes. The zone to be polarized is compressed and a variable voltage is applied across the electrodes.—MDB

5,682,435

43.38.Ja APPARATUS COMPRISING A BAFFLE AND A LOUDSPEAKER AND LOUDSPEAKER FOR USE IN THE APPARATUS

Marcus G. M. De Wit and Michiel A. A. Schallig, assignors to U.S. Philips Corporation
28 October 1997 (Class 381/188); filed in European Patent Office 4 November 1994

A loudspeaker frame is deliberately made springy rather than rigid. It is designed for use with a mounting baffle of known properties (such as a plastic TV housing). Transmission of vibrations from the loudspeaker to the cabinet can be reduced by 20 dB or so.—GLA

5,696,357

43.38.Ja BASS-REFLEX LOUDSPEAKER

Bradely M. Starobin, assignor to Polk Investment Corporation
9 December 1997 (Class 381/156); filed 25 August 1995

Several vents are used, having ducts of varying lengths so that no single half-wave pipe resonance is emphasized. In addition, vent geometry is calculated to minimize radiation of the depth-mode cabinet resonance.—GLA

5,701,358

43.38.Ja ISOBARIC LOUDSPEAKER

John T. Larsen and James R. Larsen, both of Blue Springs, MO
23 December 1997 (Class 381/202); filed 25 October 1995

Domes **14** and **16** (shown slightly separated) are edge-driven by independent voice coils. The two are connected in opposing polarity so that the assembly functions as an oscillating sphere. ''The present invention provides an isobaric loudspeaker with superior frequency response that does not suffer from sound cancellation, does not require a baffle and is more efficient than prior art sub-woofer loudspeakers and 360-degree loudspeakers.'' Perhaps one out of the four.—GLA

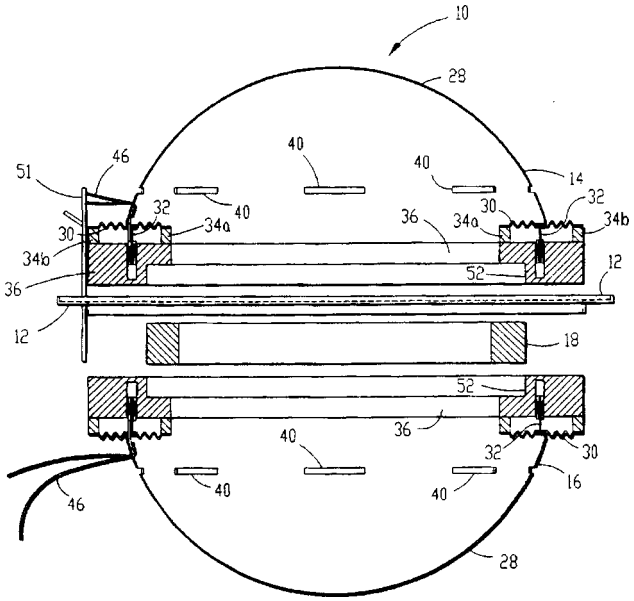

5,694,476

43.38.Lc ADAPTIVE FILTER FOR CORRECTING THE TRANSFER CHARACTERISTIC OF ELECTROACOUSTIC TRANSDUCER

Wolfgang Klippel, Thousand Oaks, CA
2 December 1997 (Class 381/96); filed in Germany 27 September 1993

The inventor's earlier work disclosed practical methods of reducing loudspeaker distortion with nonlinear filters. Pretraining was required to match a filter to a particular loudspeaker. This latest scheme uses a feedback

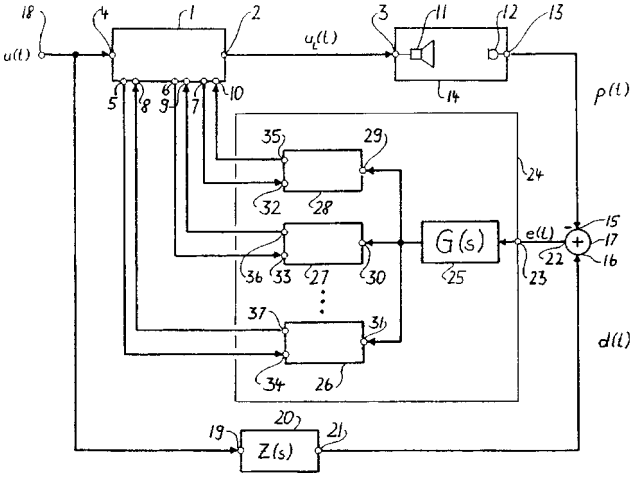

sensor **12**, a reference filter **20**, and a parametric filter **1** that has an additional output for every controllable linear or nonlinear parameter. Thus the system maintains the desired transfer function, including distortion cancellation, during normal operation.—GLA

5,701,344

43.38.Lc AUDIO PROCESSING APPARATUS

Tetsuya Wakui, assignor to Canon Kabushiki Kaisha
23 December 1997 (Class 381/1); filed in Japan 23 August 1995

This apparatus, intended for use in outdoor recording applications, is a two-channel stereophonic processor that attenuates only unnecessary wind noise without cutting off desired low-frequency audio signals.—GLA

5,706,356

43.38.Lc AUDIO PROCESSOR

Gaylord K. Walden, Fontana, CA
6 January 1998 (Class 381/13); filed 1 May 1996

Recording studios are filled with various outboard processors that, ''maximize,'' ''emulate,'' ''compel,'' ''stress,'' ''fatten,'' ''de-ess,'' ''excite,'' ''saturate,'' ''harmonize,'' ''humanize,'' ''flange,'' ''modulate,'' ''overdrive,'' and ''finalize'' an audio signal. The patent describes a processor that can be added to the list, but is also is intended for use in playback applications such as motion picture sound. Dynamic noise reduction is combined with nontraditional expansion and compression ''...to produce a warmer, more natural reproduction of the music while reducing noise levels.''—GLA

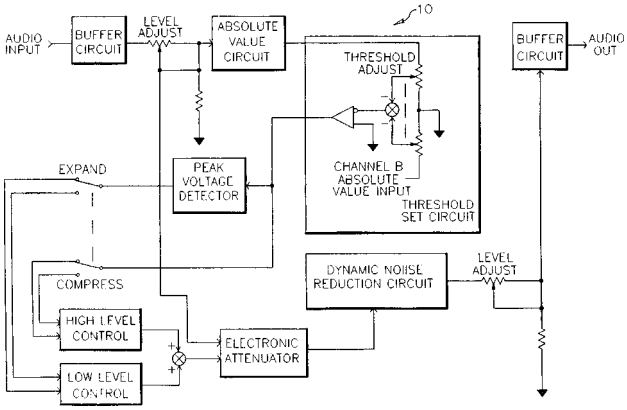

5,666,185

43.38.Ne METHOD FOR RECORDING A DIGITAL AUDIO SIGNAL ON A MOTION PICTURE FILM

Kentaro Odaka, assignor to Sony Corporation
9 September 1997 (Class 352/27); filed in Japan 14 October 1991

This is a continuation of patent 5,471,263. Digital audio signals and a conventional analog audio track are recorded on film. Error-encoded digital audio is arranged sequentially in a crosswise direction.—GLA

5,677,752

43.38.Ne DIGITAL SOUND RECORDING ON MOTION PICTURE FILM

Shinji Miyamori *et al.*, assignors to Sony Corporation and Sony Cinema Products Corporation
14 October 1997 (Class 352/5); filed in Japan 7 December 1993

This companion of patent 5,677,753 (reviewed below) enlarges upon Sony's digital recording method to include surround sound information with minimal risk that playback will be lost due to scratches.—GLA

5,677,753

43.38.Ne DIGITAL SOUND RECORDING ON MOTION PICTURE FILM

Shinji Miyamori *et al.*, assignors to Sony Corporation and Sony Cinema Products Corporation
14 October 1997 (Class 352/5); filed in Japan 7 December 1993

This is a companion of patent 5,677,752 (reviewed above). Using the techniques described in these patents, ''...it becomes possible to compensate for sound interruption even if the recording area of audio data of one of the channels is destroyed by long burst error and becomes unreproducible.''—GLA

5,491,747

43.38.Si NOISE-CANCELLING TELEPHONE HANDSET

Charles S. Bartlett *et al.*, assignors to AT&T Bell Corporation
13 February 1996 (Class 379/433); filed 30 September 1992

Whereas noise-cancelling is usually associated with microphone (i.e., transmitter) design in telephone and similar applications, this patent addresses design of the output transducer, i.e., receiver. There is a noise-cancellation microphone in the earpiece housing which extends outwardly to fit into the user's outer ear. Associated noise-cancellation circuitry responds to the ambient noise to produce a noise-reduction signal which is optimally phase related to the ambient noise signal.—MDB

5,687,231

43.38.Si ARTICULATED HEADSET

Phillip A. Gatty *et al.*, assignors to ACS Wireless, Incorporated
11 November 1997 (Class 379/430); filed 3 May 1996

The communication headset shown includes two curved housings that rotate with respect to one another to allow the headset to be held firmly in place over one ear of the user. One housing supports a microphone boom; the other houses a receiver element. Feedback between the receiver and the

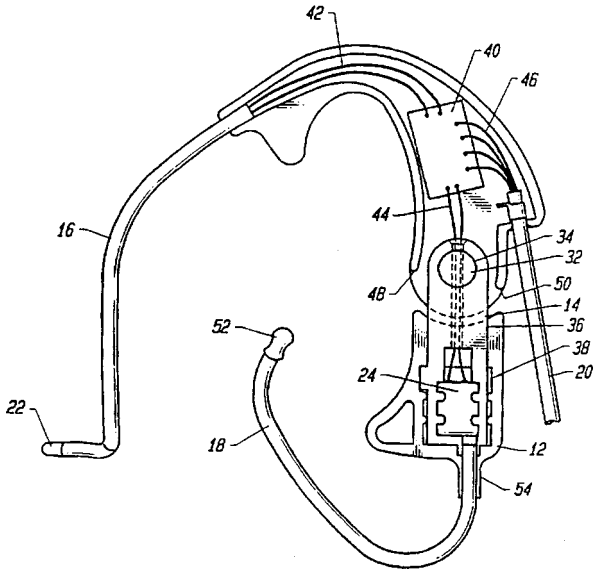

microphone is reduced by an elastomer friction hinge. The receiver element is encapsulated by an elastomer to further reduce feedback.—SFL

5,694,475

43.38.Si ACOUSTICALLY TRANSPARENT EARPHONES

James H. Boyden, assignor to Interval Research Corporation
2 December 1997 (Class 381/68.5); filed 19 September 1995

The patent shows an earphone supported on an eyeglass frame. The sound from the earphone is delivered through tubing into the ear canal. The tip at the end of the tubing that fills the canal is sufficiently porous that sound reaching the ear directly is also transmitted with moderate efficiency.—SFL

5,710,823

43.38.Tj HOWLING REMOVER HAVING CASCADE CONNECTED EQUALIZERS SUPPRESSING MULTIPLE NOISE PEAKS

Yuichi Nagata *et al.*, assignors to Yamaha Corporation
20 January 1998 (Class 381/83); filed in Japan 9 September 1994

The patent title might well apply to C. P. Boner's narrow-band equalization process developed more than 30 years ago. However, the computerized Yamaha system detects feedback frequencies and then tunes appropriate filters automatically.—GLA

5,671,287

43.38.Vk STEREOPHONIC SIGNAL PROCESSOR

Michael Anthony Gerzon, assignor to Trifield Productions Limited
23 September 1997 (Class 381/17); filed in the United Kingdom 3 June 1992

This pseudo-stereo scheme uses some of the principles developed by this late inventor in his work with ''sound field'' stereophonic recording and reproduction. Like other Gerzon patents, the writing is clear and informative with plenty of math for those who can appreciate it.—GLA

5,684,881

43.38.Vk SOUND FIELD AND SOUND IMAGE CONTROL APPARATUS AND METHOD

Mitsuhiko Serikawa *et al.*, assignors to Matsushita Electric Industrial Company
4 November 1997 (Class 381/86); filed in Japan 23 May 1994

The apparatus falls into the general category of phantom surround channel reproduction. That is, virtual sound sources are produced via head transfer functions from conventional left and right loudspeakers. Such systems often produce a convincing illusion only to a listener located exactly on the centerline. A new method of calculating filter coefficients is described that broadens the effective listening area.—GLA

5,701,346

43.38.Vk METHOD OF CODING A PLURALITY OF AUDIO SIGNALS

Jurgen Herre *et al.*, assignors to Fraunhofer-Gesellschaft zur Forderung der Angewandten Forschung e.V.
23 December 1997 (Class 381/18); filed in Germany 18 March 1994

Left, right, and center channels are combined by joint stereophonic coding, and then decoded to provide simulated decoded signals. These are matrixed with the two surround channels by means of a special ''compatibility matrix'' to form compatible signals, suitable for decoding by existing decoders. The process conforms with the coding standard MPEG-2.—GLA

5,574,699

43.38.Zp FIBER OPTIC LEVER TOWED ARRAY

F. W. Cuomo, East Providence, RI
12 November 1996 (Class 367/149); filed 31 October 1983

A small diameter towed hydrophone array comprises many miniature fiber-optic lever hydrophones **22** axially spaced within a fluid filled, acoustically transparent tube **27** and held at defined axial positions by plastic holders **24**. Each hydrophone **22** contains a number of equal length transmit fibers **29a** and receive fibers **29b** that connect with the source fiber bundle **26a** and the signal processor fiber bundle **26b**, respectively. Each hydrophone is of the lever type where the input light is reflected from a mirror

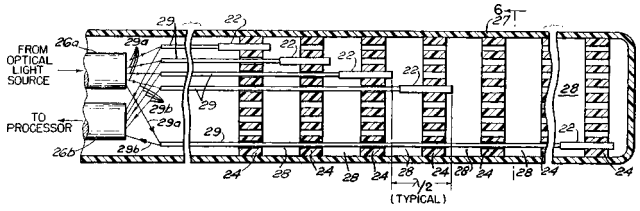

whose position, and hence the phase of the reflected light, is modulated by either the acoustic pressure at the mirror position or the gradient thereof. These mirrors are coupled to the fiber ends by clear optical elastomer compounds. The fill fluid is acoustically transparent and has a density such as to render the whole structure neutrally buoyant. The diameter of a typical hydrophone **22** could be less than 0.05 in. The system is not affected by temperature changes and is very insensitive to static pressure variations.—WT

5,689,194

43.40.Le ACOUSTIC MOTOR CURRENT SIGNATURE ANALYSIS SYSTEM WITH AUDIO AMPLIFIED SPEAKER OUTPUT

Reginald D. Richards *et al.*, assignors to Framatome Technologies, Incorporated
18 November 1997 (Class 324/772); filed 19 April 1996

Motor current signature analysis amplifies small electrical variations produced by friction and load, and then compares them with a library of known signatures to give information about aging or abnormal operating conditions. The system employs a spectrum analyzer plus a means for stepping up infrasonic signals into the audible range so that they can be heard by a human operator.—GLA

5,381,381

43.40.Rj FARFIELD ACOUSTIC RADIATION REDUCTION

M. A. Sartori and J. A. Clark, assignors to the United States of America
10 January 1995 (Class 367/1); filed 30 September 1993

A system for reducing the far-field acoustic radiation from an arbitrarily shaped, but closed, shell structure is described. A number of sensors in the near field of the vibrating structure measure the near-field acoustic radiation. A programmable controller then uses these data to predict the far-field acoustic radiation and to generate a set of control signals that are used to excite a number of acoustic radiators suspended within the structure. This additional airborne acoustic energy generated within the structure then modifies the near-field acoustic radiation external to the structure in such a way that it also reduces the far-field acoustic radiation.—WT

5,490,422

43.40.Yq ACCELERATION SENSOR

Jun Tabota *et al.*, assignors to Murata Manufacturing Co.
13 February 1996 (Class 73/514.34); filed in Japan 19 March 1993

''An acceleration sensor having a specific insensitive direction along which no acceleration is detectable and an insulated case supporting the acceleration sensor body. The acceleration sensor body is so mounted on the insulated case that the insensitive direction is along a direction which is neither parallel nor perpendicular to a surface of the insulated case to be mounted on an external device.'' The acceleration sensor body is formed by a bimorph piezoelectric ceramic element.—MDB

5,613,520

43.50.Gf DEVICE FOR DAMPENING VIBRATION AND NOISE IN HYDRAULIC INSTALLATIONS

Alfons Knapp, assignor to the Masco Corporation
25 March 1997 (Class 137/625.17); filed in Italy 22 June 1993

This patent relates to the reduction of noise from mixer valves and similar hydraulic appliances. The incompressibility of the water is compensated for by the addition of air pockets enclosed in envelopes of a flexible elastomeric material. Possible deterioration of the envelopes is avoided by positioning them so that they are in communication with the main flow but not in contact with the flowing water.—HHH

5,614,699

43.50.Gf AUTOMOBILE EXHAUST NOISE SUPPRESSOR

Haruki Yashiro *et al.*, assignors to Nissan Motor Company
25 March 1997 (Class 181/254); filed in Japan 9 May 1994

This patent relates to the reduction of exhaust noise from internal combustion engines of automobiles. Significant features are passive acoustical absorbing materials, resonating chambers, and variable inner geometry to better accommodate a range of exhaust flow volumes.—HHH

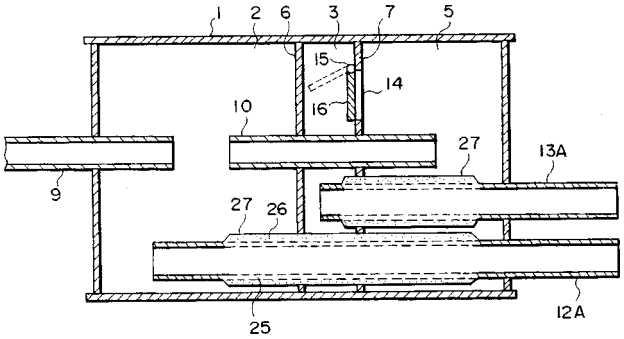

5,625,511

43.50.Gf STEPPED SPINDLE MOTOR SHAFT TO REDUCE DISK DRIVE ACOUSTIC NOISE

Peter E. Brooks *et al.*, assignors to International Business Machines Corporation
29 April 1997 (Class 360/99.08); filed 11 January 1995

This patent relates to a spindle motor shaft having various geometric features for controlling the torsional vibrations and associated noise of disk drives. Such geometrical features as circumferential grooves, radial slots, and transverse holes are made use of in order to allow the torsion mode frequencies of the shaft to be beneficially tuned away from the driving frequency of the motor.—HHH

5,626,199

43.50.Gf PNEUMATIC IMPACT TOOL HAVING IMPROVED VIBRATION AND NOISE ATTENUATION

Edgar G. Henry *et al.*, assignors to T. C. Service Company
6 May 1997 (Class 173/211); filed 5 July 1995

This patent relates to the reduction of noise and vibration of hand operated power tools having reciprocating work members such as chisels and hammers. A hand held cylindrical outer housing incorporates a reciprocating inner member which actuates the work piece. Detailed features which are significant in reducing vibrations and associated noise are a pair of oppositely biased coil springs, a pneumatic chamber with a volume of air compressed by rearward movement of the inner member, and conventional O-ring seals made of elastomeric materials and fitted to the reciprocating inner member.—HHH

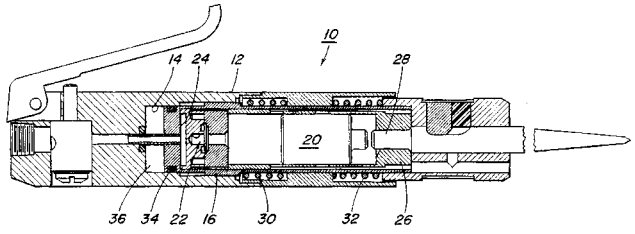

5,681,145

43.50.Gf LOW-NOISE, HIGH EFFICIENCY FAN ASSEMBLY COMBINING UNEQUAL BLADE SPACING ANGLES AND UNEQUAL BLADE SETTING ANGLES

Michael J. Neely *et al.*, assignors to ITT Automotive Electrical Systems
28 October 1997 (Class 416/203); filed 30 October 1996

This patent relates to the control of noise from the cooling fan assemblies of automotive vehicles. Unequal circumferential blade spacing angles and unequal blade setting angles are said to be effective in reducing the tonal content of the cooling fan noise and thus making it less objectionable.—HHH

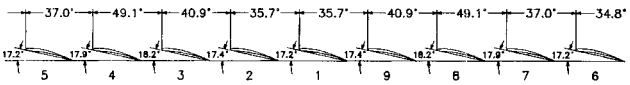

5,696,358

43.50.Gf APPLIANCE MUFFLER

Michael Pfordresher, Jensen Beach, FL
9 December 1997 (Class 181/198); filed 7 July 1995

This patent relates to the control of noise from small household appliances such as blenders. The motor and air circulating fan are enclosed in a structure which is arranged for air cooling of the motor. Passive absorption materials such as neoprene, polystyrene foam, synthetic rubber, or other foamlike materials are applied to some of the interior surfaces.—HHH

5,689,571

43.55.Lb DEVICE FOR PRODUCING REVERBERATION SOUND

Mineo Kitamura, assignor to Kawai Musical Instrument Manufacturing Company
18 November 1997 (Class 381/63); filed in Japan 8 December 1994

Although intended for use with electronic musical instruments, the reverberation algorithms described are suited to more general applications as well. Early reflections and subsequent general reverberation are simulated by independent processors, providing more accurate approximations of natural reverberation as well as generating sophisticated artificial effects. The lengthy patent document includes numerous flow charts and address tables but is relatively easy to follow.—GLA

5,703,797

43.58.Fm METHOD AND APPARATUS FOR TESTING ACOUSTICAL DEVICES, INCLUDING HEARING AIDS AND THE LIKE

Timothy M. Russell, assignor to Frye Electronics, Incorporated
30 December 1997 (Class 364/576); filed 13 October 1994

A method and apparatus for testing hearing aids under actual conditions of use is shown, where a microprocessor is programmed to generate a warbled pure tone and to provide analyses of the signal. The generated

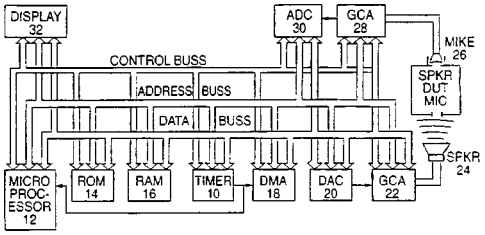

signal and a simplified signal from the hearing aid are analyzed by use of a digital Fourier transform to arrive at the transfer function of the device in a setting approximating the environment of use with results independent of extrinsic noise.—SFL

5,696,833

43.66.Ts HEARING AID HAVING EXTERNALLY CONTROLLED AMPLIFIER GAIN AND METHOD OF USING SAME

Norman P. Matzen and Mead Killion, assignors to Etymotic Research, Incorporated
9 December 1997 (Class 381/60); filed 20 March 1995

The patent shows a method of detecting internal acoustic feedback during the assembly of a hearing aid of the type for which the gain decreases markedly as the input level increases. Ambient noise in the assembly area

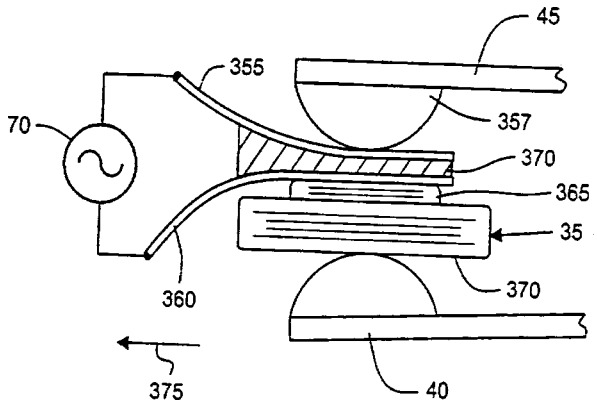

can lower the gain sufficiently to prevent internal acoustic feedback detection that would otherwise appear and be corrected by the assembler. A control circuit in the hearing aid is made responsive to a signal superimposed on the dc power supply to maintain the high gain condition during assembly.—SFL

5,699,435

43.66.Ts MICROPHONE PROBE TUBING

Mead Killion, assignor to Etymotic Research, Incorporated
16 December 1997 (Class 381/60); filed 20 March 1995

A probe tube is shown which permits measurement of sound-pressure level in an ear canal closed by an earmold. In contrast to a round probe tube that leaves openings at its sides, the probe tube shown in the patent has tapered sections extending on each side of its central hole that provide a sealed condition for probe tube testing.—SFL

5,701,348

43.66.Ts ARTICULATED HEARING DEVICE

Adnan Shennib and Richard Urso, assignors to Decibel Instruments, Incorporated
23 December 1997 (Class 381/68.6); filed 29 December 1994

The patent shows a hearing aid that fits into the ear canal. To place the receiver close to the tympanic membrane in a curving ear canal, it may be

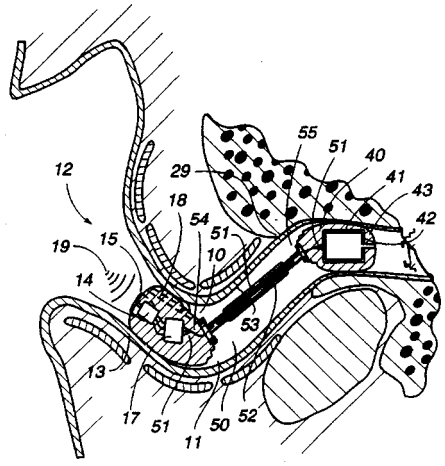

joined to the microphone-amplifier section by an articulating member containing conducting means.—SFL

5,692,104

43.72.Ar METHOD AND APPARATUS FOR DETECTING END POINTS OF SPEECH ACTIVITY

Yen-Lu Chow and Erik P. Staats, assignors to Apple Computer, Incorporated
25 November 1997 (Class 395/2.62); filed 31 December 1992

This voice detection system makes use of a variety of techniques, including power level, magnitude sum, zero-crossings, and vector quantization to determine a steady-state portion of the signal spectrum as computed from incoming speech frames. Voice activity is indicated when the spectrum of an incoming frame is sufficiently different from that of the steady-state portion.—DLR

5,696,873

43.72.Ar VOCODER SYSTEM AND METHOD FOR PERFORMING PITCH ESTIMATION USING AN ADAPTIVE CORRELATION SAMPLE WINDOW

John G. Bartkowiak, assignor to Advanced Micro Devices, Incorporated
9 December 1997 (Class 395/2.25); filed 18 March 1996

This is an improvement to the well-known autocorrelation method of pitch analysis. Prior to pitch detection, a comparison of short-term to long-term power levels serves to detect the transition from voiceless condition to voiced speech. That transition triggers a temporary widening of the autocorrelation window, decreasing the likelihood of false correlation peaks due to signal energy from the first formant.—DLR

5,696,877

43.72.Bs PATTERN RECOGNITION USING A PREDICTIVE NEURAL NETWORK

Ken-Ichi Iso, assignor to NEC Corporation
9 December 1997 (Class 395/2.41); filed 10 May 1990

This is a time-dependent neural network organized specifically for speech recognition. Both the time sequence of past acoustic vectors and a

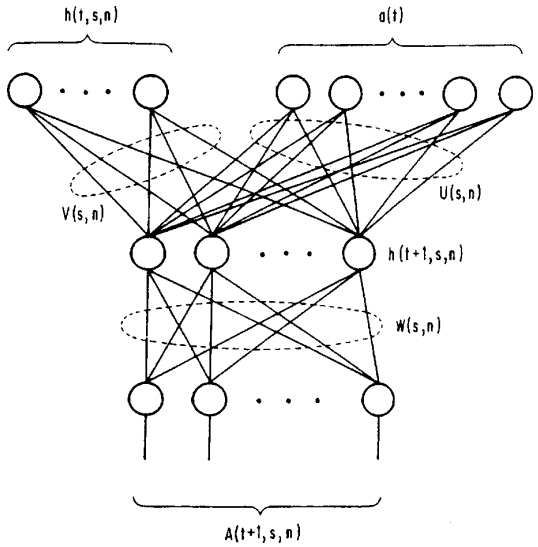

sequence of reference network states are available as network inputs. The training procedure involves adjusting the network state sequence so as to minimize the differences between those states and the speech vectors.—DLR

5,687,285

43.72.Dv NOISE REDUCING METHOD, NOISE REDUCING APPARATUS AND TELEPHONE SET

Keiichi Katayanagi and Masayuki Nishiguchi, assignors to Sony Corporation
11 November 1997 (Class 395/2.35); filed in Japan 25 December 1993

This telephone noise reduction system operates by computing the rms power in each incoming speech frame and compares this value to several thresholds. The idea is to reduce the signal level when the input consists of

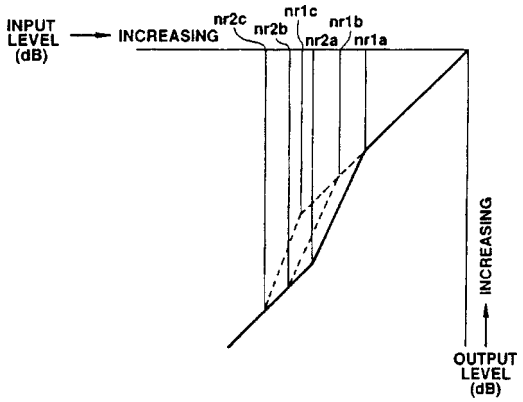

higher-level noise, leaving low-level noise and speech portions unchanged. The figure shows an example mapping of the input/output power level relationship.—DLR

5,687,284

43.72.Gy EXCITATION SIGNAL ENCODING METHOD AND DEVICE CAPABLE OF ENCODING WITH HIGH QUALITY

Masahiro Serizawa and Kazunori Ozawa, assignors to NEC Corporation
11 November 1997 (Class 395/2.31); filed in Japan 21 June 1994

This code excited (CELP) speech coder uses two parallel codebooks. A fixed codebook contains a set of LP spectral responses. The second adaptive codebook contains excitation vectors. Incoming speech frames are

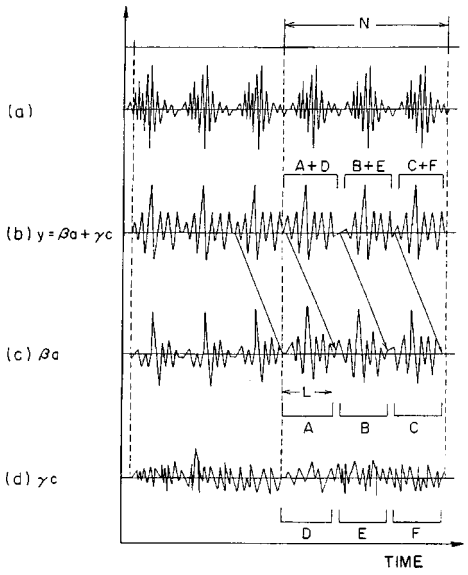

matched by a search of the fixed codebook, the resulting codes being used to select excitations from the second. Speech frames are divided into two or more subframes to improve the analysis of higher pitch frequencies, whenever the period is less than a subframe length.—DLR

5,689,615

43.72.Gy USAGE OF VOICE ACTIVITY DETECTION FOR EFFICIENT CODING OF SPEECH

Adil Benyassine and Huan-Yu Su, assignors to Rockwell International Corporation
18 November 1997 (Class 395/2.28); filed 22 January 1996

The patent describes a method for reducing the bitrate of a communication system by efficient coding of background noise to be played by the receiver during nonspeech periods. The transmitter analyzes the noise and occasionally, only when the spectral characteristics change, sends a compact frame describing the new background filler material.—DLR

5,696,875

43.72.Gy METHOD AND SYSTEM FOR COMPRESSING A SPEECH SIGNAL USING NONLINEAR PREDICTION

Shao Wei Pan *et al.*, assignors to Motorola, Incorporated
9 December 1997 (Class 395/2.28); filed 31 October 1995

This vocoder system is similar to a typical linear predictive coder except that at least one nonlinear prediction term is included with the acoustic coefficients vector. The nonlinear term may be either a sinusoidal component in the case of a voiced frame or a random noise component for an unvoiced frame.—DLR

5,696,879

43.72.Gy METHOD AND APPARATUS FOR IMPROVED VOICE TRANSMISSION

Troy Lee Cline *et al.*, assignors to International Business Machines Corporation
9 December 1997 (Class 395/2.69); filed 31 May 1995

This low bitrate speech coding system is of the type sometimes referred to as a phonetic vocoder. Input speech is recognized as text, the text is transmitted along with some speaker characteristic information, and the speech is reconstructed by text-to-speech (TTS) at the output. With the

speech quality limited by both recognition and TTS technologies, such systems have not yet gained much acceptance but continue to be attractive because of the extremely low bitrates achievable.—DLR

5,709,207

43.72.Kb AUDIO INFORMATION INCORPORATED WITHIN MRI PULSE SEQUENCES

Jeffrey L. Duerk *et al.*, assignors to Case Western Reserve University
20 January 1998 (Class 128/653.2); filed 20 March 1996

''Audio information is spoken into a microphone and saved in digitized form in an electronic file. The digitized information is converted into a format which is usable within a particular MRI [Magnetic Resonance Imaging] system. Thereafter, an electronically stored pulse sequence, usable

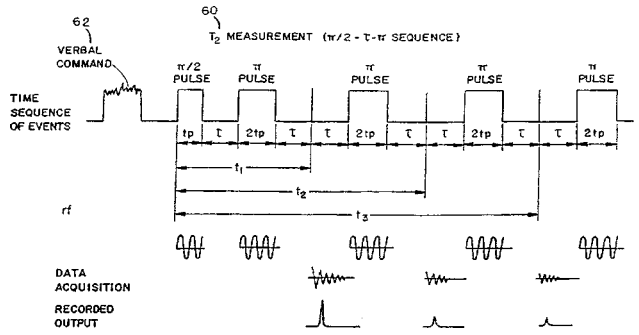

within the selected MRI system is selected and edited to incorporate the converted digitized verbal information and appropriate header information. When the edited pulse sequence is operated by the MRI system, audio information is projected which can be heard by the human ear using the elements of an existing MRI system.''—DWM

5,687,288

43.72.Ne SYSTEM WITH SPEAKING-RATE-ADAPTIVE TRANSITION VALUES FOR DETERMINING WORDS FROM A SPEECH SIGNAL

Stefan Dobler and Hans-Wilhelm Ruehl, assignors to U.S. Phillips Corporation
11 November 1997 (Class 395/2.64); filed in Germany 20 September 1994

This template-based word recognizer constructs a type of mapping of trained templates by computing distance measures between sequential frames in time and between corresponding frames from templates provided

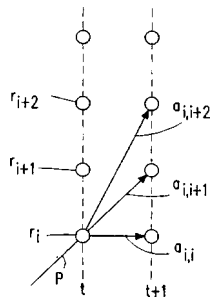

by other speakers. During recognition, a scoring process allows the test pattern to be fit into the mapping in a way that differences in speaking rate and pronunciation can be smoothed over.—DLR

5,689,617

43.72.Ne SPEECH RECOGNITION SYSTEM WHICH RETURNS RECOGNITION RESULTS AS A RECONSTRUCTED LANGUAGE MODEL WITH ATTACHED DATA VALUES

Matthew G. Pallakoff *et al.*, assignors to Apple Computer, Incorporated
18 November 1997 (Class 395/2.64); filed 14 March 1995

Many current speech recognizers use a context-free or similar syntax structure as a recognition language model. This enhancement adds markings to specific nodes in the syntax which identify their position in the syntactic structure. When a phrase matches a path through the syntax and is thus recognized, the system returns the syntactic markers along with the words themselves. An application program can use these markers to speed up text parsing or to make the appropriate control decisions.—DLR

5,692,097

43.72.Ne VOICE RECOGNITION METHOD FOR RECOGNIZING A WORD IN SPEECH

Maki Yamada *et al.*, assignors to Matsushita Electric Industrial Company
25 November 1997 (Class 395/2.5); filed in Japan 25 November 1993

This word recognizer (word spotter) is based on the recognition of sequential phonetic patterns in the speech input. As incoming frames are spectrally analyzed, dynamic programming is simultaneously applied to a set of phonetic templates, tracking the input phonetic sequence. During training, a threshold is computed such that posterior probability similarities for each speech frame will be positive for frames from the target word and negative for frames of other words. In operation, a score accumulates as frames are rated as above or below the threshold.—DLR

5,694,520

43.72.Ne METHOD AND DEVICE FOR SPEECH RECOGNITION

Bertil Lyberg, assignor to Telia AB
2 December 1997 (Class 395/2.63); filed in Sweden 29 June 1994

This speech recognition system includes a pitch tracker to produce intonation profiles and a dictionary which includes a tone structure pattern for each word. Following word recognition, the intonation profile is matched to the word's tone pattern, providing information related to syntactic structure and the speaker's dialectal variation.—DLR

5,687,287

43.72.Pf SPEAKER VERIFICATION METHOD AND APPARATUS USING MIXTURE DECOMPOSITION DISCRIMINATION

Malan Bhatki Gandhi *et al.*, assignors to Lucent Technologies, Incorporated
11 November 1997 (Class 395/2.56); filed 22 May 1995

A well-known method of speaker-independent speech recognition uses a type of hidden Markov model (HMM) based on continuous mixture probability density functions. In this patent, it is noted that different speakers saying the same word tend to activate specific components of the mixtures in such HMMs. This fact is used to build up ''mixture profiles'' specific to the speaker, providing a means to discriminate between a registered speaker and an impostor.—DLR

5,689,616

43.72.Pf AUTOMATIC LANGUAGE IDENTIFICATION/VERIFICATION SYSTEM

Kung-Pu Li, assignor to ITT Corporation
18 November 1997 (Class 395/2.41); filed 19 November 1993

This language identification system is based on an underlying speaker identification system. Speech samples of various languages are collected from speakers with relatively similar voice characteristics. This allows the

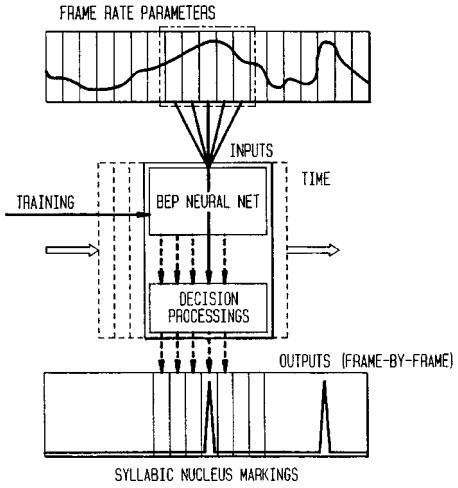

language differences to be highlighted in the comparison. Instead of short-term analysis frames, syllable nuclei are isolated to focus the analysis on vowel formant patterns.—DLR

5,696,878

43.72.Pf SPEAKER NORMALIZATION USING CONSTRAINED SPECTRA SHIFTS IN AUDITORY FILTER DOMAIN

Yoshio Ono *et al.*, assignors to Panasonic Technologies, Incorporated
9 December 1997 (Class 395/2.59); filed 17 September 1993

This technique for speaker normalization uses an estimate of the speaker's vocal tract length to compute a nonlinear frequency warping of the spectral information. Polynomial roots are extracted from an LP analysis

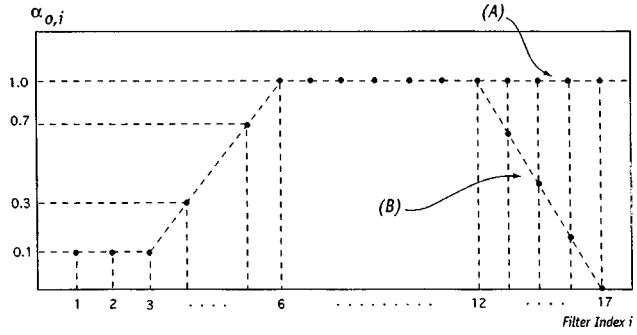

and a tract length parameter is adjusted to minimize an error criterion. A frequency mapping function is then applied to the spectral coefficients to obtain the normalized spectrum.—DLR

5,710,387

43.75.Tv METHOD FOR RECOGNITION OF THE START OF A NOTE IN THE CASE OF PERCUSSION OR PLUCKED MUSICAL INSTRUMENTS

Andreas Szalay, assignor to Yamaha Corporation
20 January 1998 (Class 84/663); filed in Germany 12 January 1995

When electronic tone syntheses are started under the control of audio frequency signals from percussion or plucked musical instruments, it is necessary for the tone synthesizer to have a reliable indication of the onset time of the audio signal. Although the onset occurrence can easily be detected by using a threshold circuit to detect when the instrument output signal exceeds a threshold value, this method is inadequate for instruments having a wide dynamic range (ppp to fff). The threshold detector will also fail to detect the start of individual percussive tones played in rapid succession. In the present patent an ''envelope curve following function'' is derived from the instrument audio signal which compares the instantaneous amplitude to an earlier value, so that a jump in the amplitude ratio defines for the synthesizer the beginning of a new percussive tone. This approach assumes that the input tone signals decay with time, a fairly safe assumption for percussion or plucked musical instruments.—DWM

5,712,438

43.75.Tv ELECTRONIC MUSICAL INSTRUMENT WITH CLASSIFIED REGISTRATION OF TIMBRE VARIATIONS

Takuya Nakata, assignor to Yamaha Corporation
27 January 1998 (Class 84/622); filed in Japan 31 October 1994

In this electronic musical instrument a matrix of memory locations stores tone timbres (presumably spectra), with each column assigned to an instrument type (e.g., piano, strings, reeds) and each row assigned to different ''versions'' of the instrument or instruments in the column. For example, the reed column could include spectra for different reed instruments (arranged in a sequence by formant frequency?).—DWM

5,714,705

43.75.Tv ARPEGGIATOR

Tetsushi Kishimoto and Tsuyoshi Sakata, assignors to Roland Corporation
3 February 1998 (Class 84/651); filed in Japan 19 September 1995

In an electronic keyboard musical instrument, automatic playing of arpeggios (sequences) of musical tones based upon chords played by the musician, have been available for at least 20 years [see Bunger Patent 3,718,748 reviewed J. Acoust. Soc. Am **60**, 1242 (1976)]. However, in the present patent the timing of the sequence can follow a predetermined rhythmic pattern instead of equal spacing in time, and the amplitude of successive individual tones can also be varied as prescribed in the rhythmic pattern.—DWM

Measurements with reticulated vitreous carbon stacks in thermoacoustic prime movers and refrigerators[a)]

Jay A. Adeff, Thomas J. Hofler, and Anthony A. Atchley
Physics Department, Naval Postgraduate School, Monterey, California 93943

William C. Moss
Lawrence Livermore National Laboratory, Livermore, California 94551

(Received 4 June 1997; accepted for publication 9 February 1998)

Reticulated vitreous carbon has been successfully used as a stack material in thermoacoustic prime movers and refrigerators. It is a rigid glassy carbon material, with a porous spongelike structure. Test results indicate peak pressure amplitudes of up to 32% in a prime mover, and refrigeration performance comparable to that of a traditional plastic roll stack. © *1998 Acoustical Society of America.* [S0001-4966(98)05505-2]

PACS numbers: 43.10.Ln, 43.35.Ud [HEB]

INTRODUCTION

he stack is considered to be the most important part of the thermoacoustic engine. However, until now, those wishing to build a practical thermoacoustic prime mover or refrigerator have had a limited choice of stack materials; the plastic roll stack, such as developed by Hofler[1] as shown in Fig. 1, the wire mesh stack described by Reed,[2] and metal or ceramic honeycombs having square[3] and hexagonal[4] channel sections. These stacks, while simple in concept, can be very labor intensive or costly for the casual low budget researcher to fabricate. Recently, a new stack geometry, the ''pin stack,'' was introduced by Swift and Keolian.[5] The pin stack has, possibly, the ideal geometry for a thermoacoustic engine. Unfortunately, it is currently the most difficult stack to fabricate and may have some other potential disadvantages mentioned below.

Reticulated vitreous carbon (RVC) was suggested as a stack material by one of the authors (Moss), and has been found to have many advantages and very few disadvantages. RVC is manufactured by Energy Research and Generation (ERG), Inc.[6] It is an open pore foam material composed solely of vitreous carbon as can be seen in Fig. 2. In addition to being relatively inexpensive, light weight, and easy to machine, it has a temperature limitation of 300 °C in air and 3500 °C in an oxygen-free atmosphere, and has low thermal conductivity and a reasonably high specific heat. ERG also claims that RVC has a very high ''void volume'' or porosity of about 97%. Neither the plastic or metal roll stack nor the wire mesh stack possess all of these properties. Because of its random fibrous structure, RVC has no ''straight through'' optical paths. This serves to block, or at least reduce, infrared radiation back to the cold end and may also reduce the heat leak caused by acoustic streaming; another claim that cannot be made for stacks having a regular and periodic geometry.

Design and construction of a thermoacoustic engine is not a trivial task. It was therefore decided that instead of designing a prime mover and refrigerator specifically for RVC stack measurements, existing devices could be used to test the suitability of RVC as a thermoacoustic stack material. Because of the difficulty in developing theoretical models for RVC stacks, the approach here is strictly empirical. We will report the results of measurements of the performance of several RVC stacks with different pore sizes.

A most elementary method was employed for picking an appropriate RVC material for use in our thermoacoustic engines. The manufacturer grades the material according to the average number of pores per linear inch, or ppi. In other words, if one looks at the surface of an RVC block and counts the number of pores in 1 in. in any given direction, this is the ppi value. RVC was available to us in 100, 80, 60, 45, 30, 20, 10, and 5 ppi. The same measurement of effective pores per inch can be made with a parallel plate stack simply by counting the number of channels per inch across the end of the stack, or it can be approximated by taking the reciprocal of the sum of the plate thickness and plate separation in inches. For example, if a parallel plate stack has a plate thickness of 0.003 in. and a plate separation of 0.015 in., the corresponding porosity would be 1/0.018 ppi, or 56 ppi.

As a starting point, an RVC stack was chosen with a ppi value roughly equal to the effective ppi value of a parallel plate or roll stack known to have good performance. Given the lack of a computational model for the RVC structure, it is valuable to have a simple and relatively effective (as we shall see) means to determine the correct sizing. This is in contrast to the empirical results for stainless steel mesh stacks in thermoacoustic engines[1,2] where the optimal geometry values are somewhat surprising.

I. EXPERIMENTAL APPARATUS

The first set of measurements taken were in a sealed prime mover, illustrated in Fig. 3, which was designed by Hofler and Gardner, and first described by Castro.[7] It was originally designed to test the effectiveness of heat exchangers in a very high amplitude acoustic environment. This device is a half-wavelength sealed resonator that is designed to use low variable pressure neon gas. This allows for relatively

[a)]''Selected research articles'' are ones chosen occasionally by the Editor-in-Chief that are judged (a) to have a subject of wide acoustical interest, and (b) to be written for understanding by broad acoustical readership.

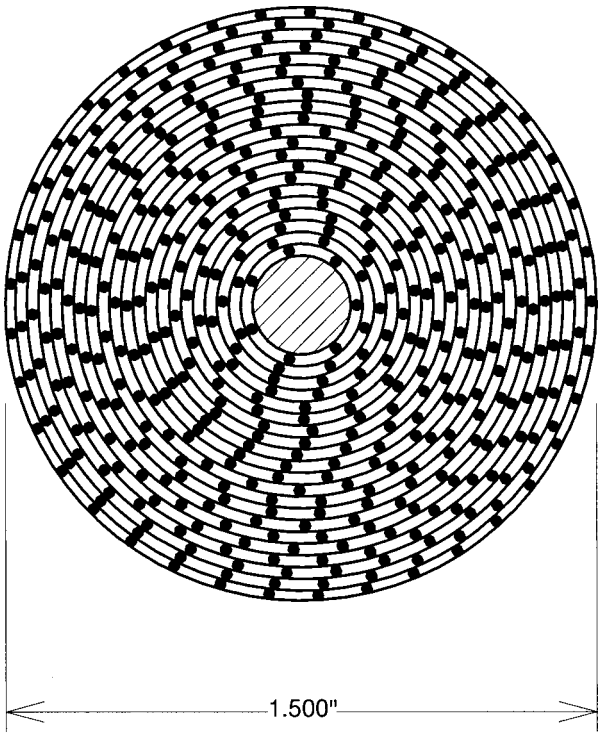

FIG. 1. The plastic roll stack seen edge-on and backlit.

low input heater power with high acoustic amplitudes, as well as adjustable penetration depth. In addition, a moveable plunger is located at the pressure antinode to allow the stack's location in the standing wave to be adjusted. Measurements were taken with the warm end of the stack at $kx = 0.070$, 0.137, and 0.174 rad. An internal pressure transducer, located on the plunger, was used for measuring both the internal mean pressure and the dynamic acoustic pressure amplitude. Thermocouples were placed internally on the heat-exchanger fins and at various points on the outside of the resonator. The cold end of the resonator is placed in a liquid nitrogen bath to anchor the cold heat-exchanger's temperature at 78 K, while the hot heat exchanger is heated by two electrical resistive heater cartridges. The actual internal cold heat-exchanger temperatures were generally considerably higher than that of the liquid nitrogen, because the design did not anticipate the magnitude of the acoustic pressure amplitudes and resulting heat flows through copper parts having limited thermal conductance. Control of the experiment is semiautomated by using a temperature controller to operate the heater cartridges and maintain a constant temperature at the hot heat exchanger. As the mean pressure is gradually increased from about 2 kPa, the device reaches ''onset'' and spontaneously begins to oscillate. As the mean pressure is increased further, the increasing intensity of the acoustic pressure oscillations draws more heat from the hot heat exchanger, which is rejected at the cold heat exchanger. Thus the heat supplied by the heater cartridges must increase in order to maintain the constant temperature difference.

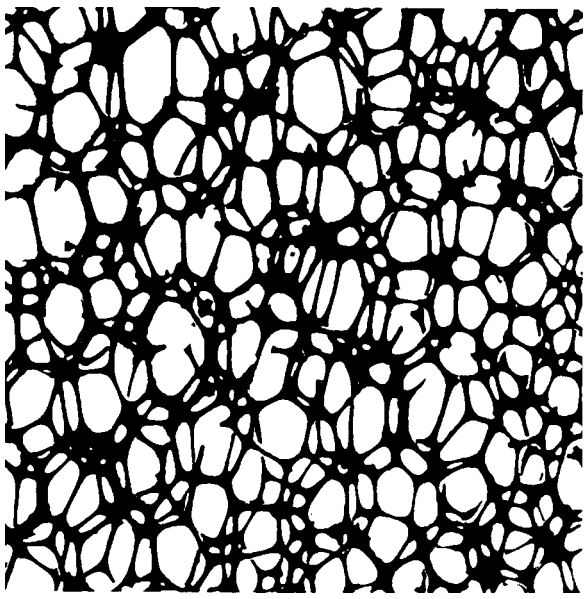

FIG. 2. Enlarged view of RVC showing the open cell reticulated structure.

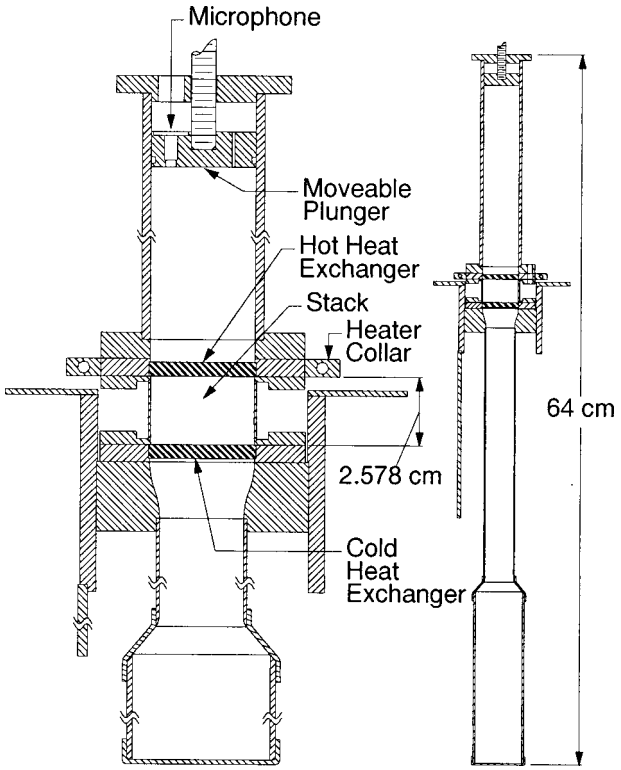

FIG. 3. Section drawing of the sealed prime mover apparatus, designed for high amplitude and relatively low heat power.

The second set of measurements taken were in a small sealed refrigerator, illustrated in Fig. 4, which is a modification of Hofler's original refrigerator.[1] This refrigerator, first described by Brooks,[8] was designed for small temperature spans with the aid of a computer model for thermoacoustic engines, developed by one of the authors (Hofler). This device consists of a quarter wavelength resonator, driven by an electrodynamic loudspeaker at the pressure antinode. It normally operates with a plastic roll stack and is pressurized with 620 kPa of helium. It is typically capable of providing up to 10 W of cooling power at 0 °C with a temperature span of 35 °C and a coefficient of performance (COP) of approximately one.[9]

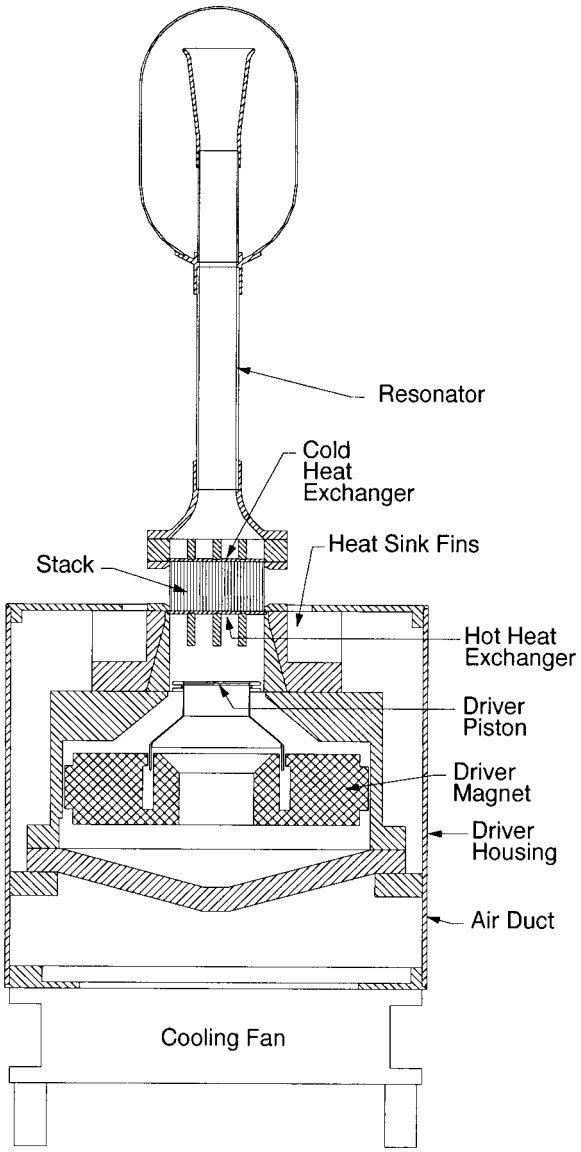

FIG. 4. Section drawing of the demonstration refrigerator.

II. PRIME MOVER MEASUREMENTS

For the prime mover, the plastic roll stack used by Castro[7] had a plate thickness of 0.102 mm and a plate separation of 0.711 mm for a sum of 0.813 mm. The reciprocal of this is 31 pores per inch. We therefore chose to begin our measurements with a 30-ppi RVC stack. Later, we tried a 20-ppi RVC stack because Reed's measurements with wire mesh stacks[2] indicated that more open stacks work better in this apparatus.

The procedure for these tests was to place an RVC sample stack into the resonator, purge the vessel of any air, and then fill it with pure neon to a pressure of about 2 kPa. The cold end was then submerged in liquid nitrogen, and the heater cartridges in the hot end were turned on and placed under the control of an analog temperature controller to maintain the hot heat-exchanger's temperature at approximately 300 K. The mean pressure in the resonator was then slowly increased until onset was reached. The system was allowed to equilibrate for about 10–15 min at which time the hot and cold heat-exchanger temperatures, acoustic and mean pressure, frequency, and heater input power were measured. The mean pressure was then increased slightly, the system allowed to equilibrate again, and another set of data recorded, and so on up to a mean pressure of about 80 kPa. The same test was conducted with the plunger at different positions. In addition, a set of data points was taken holding the mean pressure constant at 50 kPa, but varying the plunger position.

In characterizing the performance of the RVC prime mover stack, we examined two important parameters, the acoustic pressure amplitude and the ''efficiency.'' The acoustic pressure amplitude P_0 is expressed in rms values and given relative to the mean pressure P_m in the resonator, or P_0/P_m. We use rms rather than the usual peak values here because of the occasional presence of some moderate distortion in the acoustic pressure waveform which was measured with a true rms voltmeter. The issue of efficiency is more complicated, however, because the only acoustic load is the wall loss inside the resonator, which we were not able to measure. Therefore, a value for quasiefficiency, $\mathrm{Eff}_{\mathrm{Quasi}}$ derived by Hofler and Reed[1,2] is used which assumes similar loading for each of the different stacks and which is intended for comparison purposes only.

The following derivation for the quasiefficiency follows Reed[10] exactly and begins with Swift's equation for the total resonator dissipation power $\dot{E}$ for a plane-wave resonator:

$$\dot{E}=\frac{1}{4}\frac{P_0^2}{\rho_m a^2}\,\omega\pi RL\left[\delta_\kappa\frac{\gamma-1}{1+\epsilon_s}\left(1+\frac{2R}{L}\right)+\delta_\nu\right]. \tag{1}$$

Where P_0 is the rms dynamic pressure amplitude, ρ_m is the mean density, a is the speed of sound, ω is the angular frequency, δ_κ and δ_v are the thermal and viscous penetration depths, γ is the ratio of specific heats, and the radius and length of the resonator are given by R and L. The available surface heat capacity is ϵ_s, which for these experiments is very small compared to 1 and can be ignored. Then, by using $\rho_m a^2=\gamma P_m$, Eq. (1) becomes

$$\dot{E}\approx\left(\frac{\pi R}{4\gamma}\right)\left(\frac{P_0}{P_m}\right)^2 P_m\omega L\left[\delta_\kappa(\gamma-1)\left(1+\frac{2R}{L}\right)+\delta_\nu\right]. \tag{2}$$

The geometry of the prime mover is such that the term $2R/L$ is much less than 1 and can be ignored. Using the definition of the Prandtl number, Pr,

$$\delta_\kappa=\frac{\delta_\nu}{\sqrt{\mathrm{Pr}}}, \tag{3}$$

Eq. (2) can be rewritten as

$$\dot{E}\approx\left(\frac{\pi R}{4\gamma}\right)\left(\frac{P_0}{P_m}\right)^2 P_m\omega L\,\delta_\nu\left[\left(\frac{\gamma-1}{\sqrt{\mathrm{Pr}}}\right)+1\right]. \tag{4}$$

Collecting all the constants, Eq. (4) can be written as a proportionality:

$$\dot{E}\propto\left(\frac{P_0}{P_m}\right)^2 P_m\omega L\,\delta_\nu. \tag{5}$$

Since the dynamic viscosity is nearly independent of the pressure, the viscous penetration depth can be expressed as

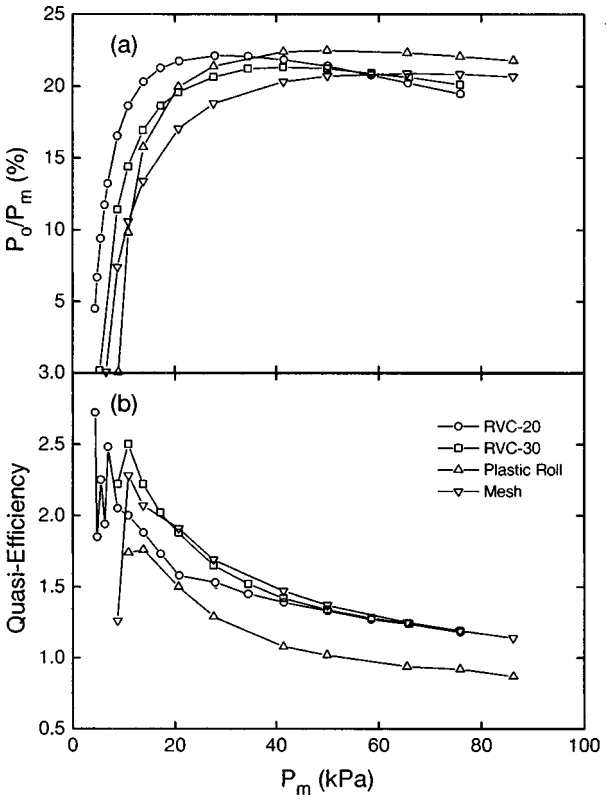

FIG. 5. Measured performance of the thermoacoustic prime mover comparing four different stacks at position $kx=0.070$. (a) Pressure ratio and (b) quasiefficiency plotted against mean pressure.

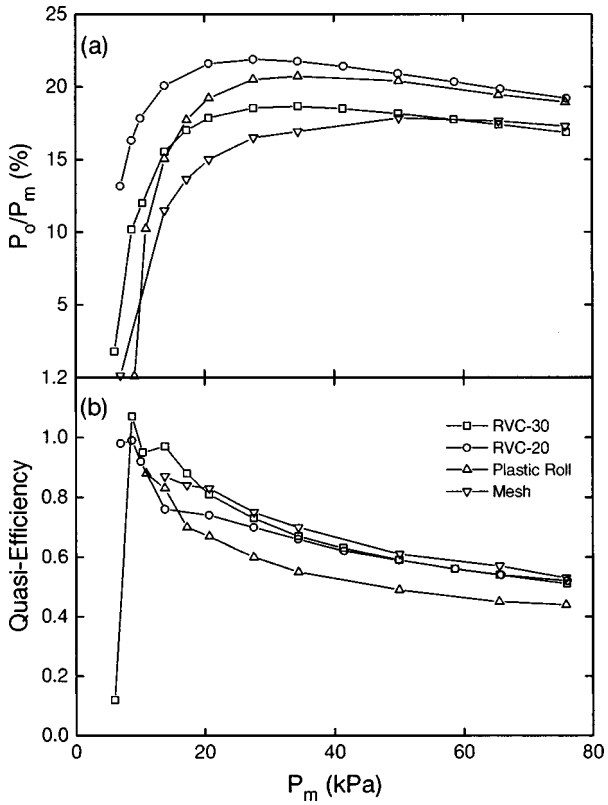

FIG. 6. Measured performance of the thermoacoustic prime mover comparing four different stacks at position $kx=0.137$. (a) Pressure ratio and (b) quasiefficiency plotted against mean pressure.

$$\delta_\nu = \sqrt{\frac{2\eta}{\omega\rho}} \propto (\omega\rho_m)^{-1/2} \propto (\omega P_m)^{-1/2}. \tag{6}$$

Proportionality (5) then becomes

$$\dot{E} \propto \left(\frac{P_0}{P_m}\right)^2 L(\omega P_m)(\omega P_m)^{-1/2} = \left(\frac{P_0}{P_m}\right)^2 L\sqrt{\omega P_m}. \tag{7}$$

Note that the L dependence is for a constant diameter resonator at uniform temperature. In this case $\omega \propto 1/L$, so then

$$\dot{E} \propto \left(\frac{P_0}{P_m}\right)^2 \frac{1}{\omega}\sqrt{\omega P_m} = \left(\frac{P_0}{P_m}\right)^2 \sqrt{\frac{P_m}{\omega}}. \tag{8}$$

The efficiency, Eff, is defined as the resonator losses divided by the heat input

$$\mathrm{Eff} = \frac{\dot{E}}{Q_{\mathrm{Hot}}}. \tag{9}$$

Therefore a quasiefficiency, $\mathrm{Eff}_{\mathrm{Quasi}}$, can be defined as

$$\mathrm{Eff}_{\mathrm{Quasi}} = \frac{(P_0/P_m)^2\sqrt{P_m/2\pi f}}{Q_{\mathrm{Hot}}}, \tag{10}$$

where f is frequency. This quasiefficiency, as shown in Figs. 5(b), 6(b), and 7, has units of $\sqrt{\mathrm{kPa/Hz}}/\mathrm{W}$. This expression assumes a linear system where the resonator dissipation has a quadratic amplitude dependence, and it accounts for pressure and resonator length variations.

It should be noted that we expect that nonlinearities such as flow separation do occur at higher amplitudes and therefore the resonator dissipation increases more rapidly than quadratic at the higher amplitudes. While caution should be exercised in comparing quasiefficiencies at dramatically different amplitudes, a stack that produces higher quasiefficiency values at an equal or higher amplitude is truly more efficient.

The value Q_{Hot} in Eq. (10) is formed by subtracting the heater power measured below acoustic onset, which is essentially an apparatus heat leak, from the heater power measured above onset. The heat leak is generally much smaller than the typical heater power above onset, except at the lower mean pressure and amplitude combinations. Typical heat

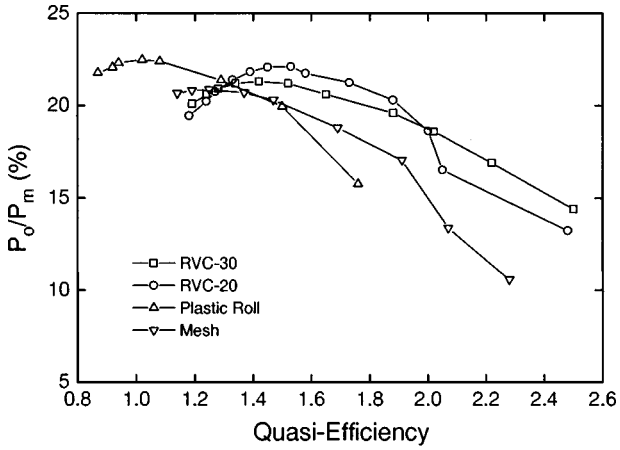

FIG. 7. Comparison of measured P_0/P_m with respect to quasiefficiency for the prime mover with the stack at position $kx=0.07$, for all four stacks.

leaks are in the 15–20 W range, whereas the highest heater powers were in the 250 W range. Estimated uncertainty in the heater power measurements near the heat leak level were between 0.5 and 1.0 W.

The pressure amplitude performance of the RVC stack was very encouraging, as may be seen in Figs. 5(a) and 6(a), showing the ratio P_0/P_m versus mean pressure for two different plunger positions. A comparison is made to the original plastic roll stack used by Castro[7] and the best stainless steel mesh stack used by Reed.[2] At the closest plunger position and at lower mean pressures, the 20-ppi RVC stack performed the best, followed by the 30-ppi RVC stack, then the stainless mesh stack, and finally the plastic roll stack. Only at the higher mean pressures did the plastic roll stack begin to surpass the other stacks. However, as the plunger was pulled back, effectively moving the stack farther from the pressure antinode, the superiority of the 20-ppi RVC stack became quite pronounced. Its performance at low mean pressures surpassed the other stacks considerably, and slightly surpassed the plastic roll stack at the higher mean pressures. The trend continued as the stack was moved farther away from the pressure antinode. The conclusion from these graphs is that under many of the conditions tested the 20-ppi RVC stack offered higher acoustic pressure amplitudes than the other stack materials. Only at the closest stack positions with higher mean pressures was the RVC stack clearly inferior to the plastic roll stack and the wire mesh stack.

Even more interesting are the results of the quasiefficiency plots in Figs. 5(b) and 6(b). The data points at low mean pressure are not very reliable because of the heat leak subtraction discussed above. This was exacerbated by the extremely low onset pressures achieved with the RVC stacks and the correspondingly low heater cartridge power levels. For mean pressures above 10 kPa, however, the data becomes acceptable. With the plunger all the way in, and the stack closest to the pressure antinode, we can see in Fig. 5(b) that the RVC and stainless mesh stacks were clearly superior to the plastic roll stack. Because some of these comparisons are being made at different pressure amplitudes, we can expect that a stack that has both higher quasiefficiency and higher pressure amplitude should have higher true efficiency than a stack with lower quasiefficiency and lower pressure amplitude. We therefore concluded that the 20-ppi RVC stack should have slightly higher true efficiency at the lower mean pressures, while the plastic roll stack should have slightly higher true efficiency at the higher mean pressures relative to what is shown in Fig. 5(a). This gave us a confident assessment that the 20-ppi RVC stack was slightly better than the plastic roll stack, and at least as good as the wire mesh stack.

With the plunger pulled back to the second position, the same behavior was noted as in the closest position. Because the 20-ppi RVC stack always had the highest acoustic pressure amplitudes at this plunger position, we concluded that the true efficiency for this stack was even higher relative to the plastic roll stack than is already seen in Fig. 6(b), while the 30-ppi RVC stack and the mesh stack had lower true efficiencies because they always produced lower acoustic pressure amplitudes. Again, we were confident that the 20-ppi RVC stack was superior to the plastic roll stack, and at least as good as the wire mesh stack. The results were similar for the farthest stack position, even though we do not present them here.

Another interesting way to summarize the performance of these stacks is illustrated in Fig. 7 showing P_0/P_m versus quasiefficiency for the closest plunger position. Ideally, one would want a stack that delivers a high acoustic pressure amplitude ratio, P_0/P_m, as well as high efficiency. In fact, this graph shows that the 20- and 30-ppi RVC stacks delivered higher pressure amplitudes at higher efficiencies than the plastic roll stack.

III. REFRIGERATOR MEASUREMENTS

The procedure used for quantifying the performance of the thermoacoustic refrigerator was to first run the device with no externally applied heat load until it reached its ultimate cold temperature. A data point was taken consisting of hot and cold heat-exchanger temperatures, and the acoustic pressure amplitude and driver volume velocity along with the phase between them. A known heat load was then applied to the cold heat exchanger and the refrigerator's temperatures were allowed to equilibrate again, after which the same data points were recorded with the addition of the external heat load. The refrigerator was operated at a constant drive current level of 1.85 A and a constant frequency of 645 Hz. This was done in order to duplicate the conditions under which the unit was originally tested by Berhow.[9]

The previously mentioned data was reduced down to two important parameters, the temperature ratio T_c/T_h, and the coefficient of performance (COP), both as a function of the total heat load on the cold end of the refrigerator. The total heat load included the heat leak from the hot end of the refrigerator to the cold end of the refrigerator due to conduction by the walls of the resonator vessel, the stack, and the helium gas, the insulation heat leak, and any external heat load added to quantify its performance. The external heat load was applied via a resistive electrical heater and was very simple and straightforward to measure. The nuisance heat leak was measured by running the refrigerator until it reached its ultimate cold temperature and then shutting it off and measuring the warm up rate, which if the resonator is well insulated, is an exponential function. From this data a thermal time constant is derived which, along with the heat capacity of the cold end, gives a heat leak in W/°C. The temperature ratio is also very straightforward to measure, while the COP can be obtained from the simple relation:

$$\mathrm{COP} = Q_{\mathrm{total}}/W,$$

where Q_{total} is the total heat load, in watts, on the refrigerator and W is the acoustic power, or work flow, into the resonator. The rms P_o/P_m values were typically between 2.5% and 3.5% for these tests.

The RVC results for our low-powered refrigerator were not as favorable as they were for the prime mover, and might reflect the fact that the RVC stacks were simply inserted into an engine that had been optimized for use with a particular parallel plate geometry stack, and which was designed for use as a demonstration aid rather than a solid thermoacous-

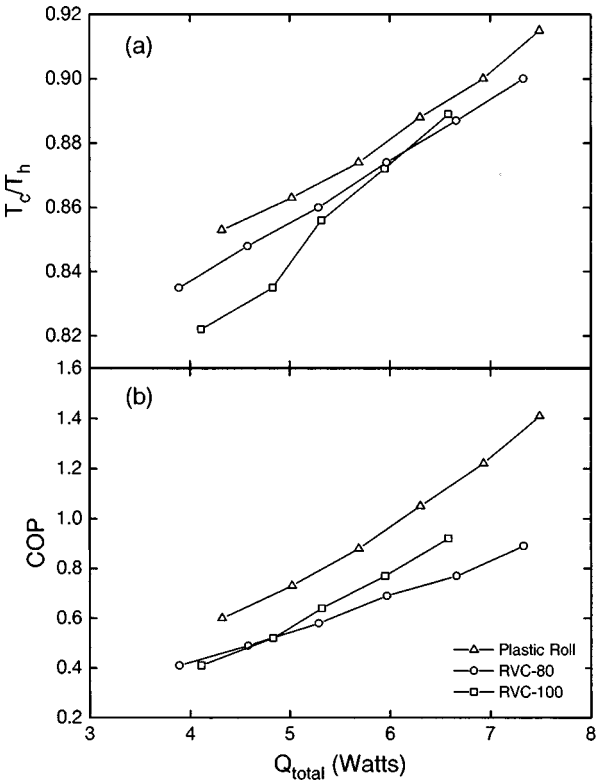

FIG. 8. Measured performance of the thermoacoustic refrigerator at a mean pressure of 620 kPa, comparing three different stacks. (a) Temperature ratio and (b) coefficient of performance against total refrigerator load Q_{total}.

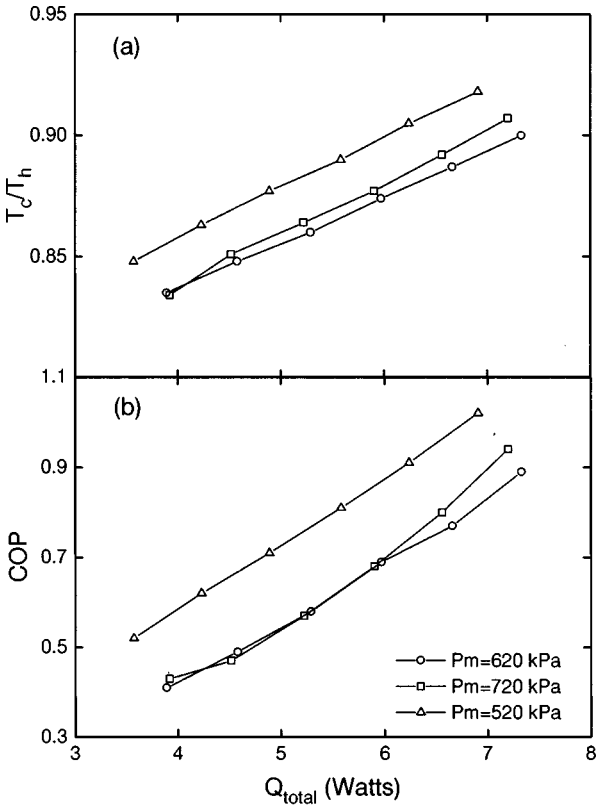

FIG. 9. Measured performance of the thermoacoustic refrigerator with an 80-ppi RVC stack, comparing three different mean operating pressures. (a) Temperature ratio and (b) coefficient of performance plotted against total refrigerator load Q_{total}.

tics test engine. Also, the refrigerator lacked the adjustment provided by the plunger in the prime mover apparatus.

The first set of measurements were taken at a mean pressure of 620 kPa with pure helium, which is the normal operating pressure with the plastic roll stack. The roll stack used in this engine is made from polyester film with a thickness of 0.051 mm, a layer separation of 0.254 mm, and a spacer interval of 5 mm. An RVC porosity of 80 ppi was initially chosen based on these numbers, with 60 and 100 ppi being the secondary choices. Figure 8 shows the results for the temperature ratio (T_c/T_h) and COP as a function of total heat load Q_{total} for the plastic roll stack and for the 80- and 100-ppi RVC stacks. The 60-ppi stack is not included here because it produced negligable refrigeration power, and no data was taken with an applied heat load. Our measurements indicate that while the temperature ratio for a given heat load was slightly lower with both RVC stacks, indicating higher available cooling powers, the plastic roll stack still held the edge in efficiency, giving higher COP's. However, based on this data, it is not clear if one of the two RVC stacks was generally superior to the other.

The second set of measurements taken with the refrigerator consisted of varying the mean pressure up and down by 100 kPa from the normal 620-kPa operating pressure, and taking the same data as before. Unfortunately, due to a sudden driver failure, we were only able to obtain this data for the 80-ppi RVC stack. Figure 9(a) shows that the 80-ppi stack has higher cooling power available at the higher mean pressure of 720 kPa, but Fig. 9(b) shows that it is more efficient at the lower mean pressure of 520 kPa, as evidenced by the higher COP. In fact, when we looked at the COP relative to Carnot (COPR) we found that the refrigerator with the 80-ppi stack had a COPR 1.05 times higher at 520 kPa than at 720 kPa at the lower heat loads, while at the higher heat loads the COPR's were the same. The higher efficiency at lower mean pressure is probably an indication that the 80-ppi stack has too large of a pore size to be operated efficiently at 620 kPa, since lowering the mean pressure to 520 kPa increases the thermal penetration depth and makes more of the gas in the channels productive. The increment of 100 kPa was also perhaps too large to allow us to find an ideal operating pressure, but it does serve to point out the performance trends associated with varying penetration depth.

IV. CONCLUSIONS

Based on these measurements, we believe that RVC has a definite potential as a low cost, easy to fabricate material suitable for use in all types of thermoacoustic prime movers and refrigerators. Further investigation is still needed to determine exactly which combinations of stack and resonator dimensions and gas parameters, including the use of gas mixtures, would yield optimum performance. Currently, measurements are being taken on precompressed samples of RVC in a high-temperature and high-pressure prime mover, in an attempt to decrease the extremely high porosity of the RVC and thereby increase the heat capacity of the stack. The only drawback we have found to RVC, thus far, is that because it is extremely brittle, a loose fitting stack can vibrate

against the heat exchangers enough to cause the filaments to break. However, even if the RVC stack never substantially surpasses the overall performance of the parallel plate stack, it has other advantages that still make it an attractive material. RVC could also become potentially more cost competitive compared to other materials like plastic roll and stainless steel mesh, given enough demand for the product.

ACKNOWLEDGMENTS

This work was supported by the Office of Naval Research and by the Naval Postgraduate School. Assistance was also provided by the Lawerence Livermore National Laboratory. We would also like to thank Energy Research and Generation, Inc. for their help in supplying us with reticulated vitreous carbon for our experiments.

[1] T. J. Hofler, ''Thermoacoustic refrigerator design and performance,'' Ph.D. dissertation, Physics Department, University of California at San Diego, 1986; T. Hofler, J. Wheatley, G. W. Swift, and A. Migliori, ''Acoustic cooling engine,'' U.S. Patent No. 4,722,201 granted 1988.

[2] M. S. Reed and T. J. Hofler, ''Measurements with wire mesh stacks in thermoacoustic prime movers,'' J. Acoust. Soc. Am. **99**, 2559 (1996).

[3] W. P. Arnott, H. Bass, and R. Raspet, ''General formulation of thermoacoustics for stacks having arbitrarily shaped pore cross sections,'' J. Acoust. Soc. Am. **90**, 3228 (1991).

[4] G. W. Swift, ''Analysis and performance of a large thermoacoustic engine,'' J. Acoust. Soc. Am. **92**, 1551 (1992).

[5] G. W. Swift and R. M. Keolian, ''Thermoacoustics in pin-array stacks,'' J. Acoust. Soc. Am. **94**, 941 (1993).

[6] Energy Research and Generation, Inc., 900 Stanford Avenue, Oakland, CA 94608.

[7] N. Castro, ''Experimental heat exchanger performance in a thermoacoustic prime mover, Master's thesis, Naval Postgraduate School, Monterey, California, 1993.

[8] B. R. Brooks, ''Construction of a thermoacoustic refrigerator demonstration apparatus,'' Master's thesis, Naval Postgraduate School, Monterey, CA 1994.

[9] T. J. Berhow, ''Construction and performance measurement of a portable thermoacoustic refrigerator demonstration apparatus,'' Master's thesis, Naval Postgraduate School, Monterey, California, 1994.

[10] M. S. Reed, ''Measurements with wire mesh stacks in thermoacoustic prime mover,'' Master's thesis, Naval Postgraduate School, Monterey, California, 1996.

Application of pulse compression techniques to broadband acoustic scattering by live individual zooplankton[a)]

Dezhang Chu and Timothy K. Stanton
Department of Applied Ocean Physics and Engineering, Woods Hole Oceanographic Institution, Woods Hole, Massachusetts 02543-1053

(Received 30 July 1996; accepted for publication 15 January 1998)

Distinct frequency dependencies of the acoustic backscattering by zooplankton of different anatomical groups have been observed in our previous studies [Chu *et al.*, ICES J. Mar. Sci. **49**, 97–106 (1992); Stanton *et al.*, ICES J. Mar. Sci. **51**, 505–512 (1994)]. Based mainly on the spectral information, scattering models have been proposed to describe the backscattering mechanisms of different zooplankton groups [Stanton *et al.*, J. Acoust. Soc. Am. **103**, 236–253 (1998b)]. In this paper, an in-depth study of pulse compression (PC) techniques is presented to characterize the temporal, spectral, and statistical signatures of the acoustic backscattering by zooplankton of different gross anatomical classes. Data collected from various sources are analyzed and the results are consistent with our acoustic models. From compressed pulse (CP) outputs for all three different zooplankton groups, two major arrivals from different parts of the animal body can be identified: a primary and a secondary arrival. (1) Shrimplike animals (*Euphausiids* and decapod shrimp; near broadside incidence only): the primary one is from the front interface (interface closest to the transducer) of the animal and the secondary arrival is from the back interface; (2) gas-bearing animals (*Siphonophores*): the primary arrival is from the gas inclusion and the secondary arrival is from the body tissue (''local acoustic center of mass''); and (3) elastic shelled animals (*Gastropods*): the primary one is from the front interface and the secondary arrival corresponds to the subsonic Lamb wave that circumnavigates the surface of the shell. Statistical analysis of these arrivals is used to successfully infer the size of the individual animals. In conjunction with different aspects of PC techniques explored in this paper, a concept of partial wave target strength (PWTS) is introduced to describe scattering by the different CP highlights. Furthermore, temporal gating of the CP output allows rejection of unwanted signals, improves the output signal-to-noise ratio (SNR) of the spectra of selected partial waves of interest, and provides a better understanding of the scattering mechanism of the animals. In addition, it is found that the averaged PWTS can be used to obtain a more quantitative scattering characterization for certain animals such as siphonophores.
 [S0001-4966(98)02105-5]

PACS numbers: 43.10.Ln, 43.60.Cg, 43.60.Gk, 43.30.Ft, 43.30.Sf [JLK]

INTRODUCTION

Zooplankton aggregations often contain a diverse collection of animals of different anatomical groups, species, and sizes. Because of this diversity as well as the strong dependence of acoustic scattering by individual zooplankton upon acoustic frequency, and geometrical and physical properties of the animals, it is difficult, if not impossible, to make accurate predictions of zooplankton biomass by using a single frequency sonar. Sophisticated technology and scattering models are required for accurate estimates of biomass. Sonar systems with two or more discrete frequencies have been applied successfully to biomass estimation (Holliday *et al.*, 1989; Holliday and Pieper, 1995) and animal behavior estimation (Chu *et al.*, 1993) of simple populations containing a single species. Laboratory and shipboard experiments involving a combination of narrow band and broadband transducers have been conducted (Chu *et al.*, 1992; Stanton *et al.*, 1993b, 1998a) and much progress has been achieved in characterizing the zooplankton scattering. The broadband signals used in these reported experiments were a linear frequency-modulated signal (a ''chirp'') that continuously covers an octave band of frequencies. A broadband scattering signal is extremely powerful in analyzing and characterizing the signatures of the scattered signal which, in turn, leads to an understanding of the inherent scattering mechanisms.

There are two major domains in which broadband signals can be analyzed: frequency domain and time domain. Our previous studies (Chu *et al.*, 1992; Stanton *et al.*, 1993a, 1993b, 1994a, 1994b, 1998b) mainly focused on the frequency or spectral analysis. There are many advantages of using spectral analysis, such as to automatically reject the noise outside the frequency band of interest (out-of-band noise). In addition to the spectral analysis, temporal analyses also provide useful information. One of the most important features of the time series analysis is that for a broadband signal, a higher time-domain resolution, $1/B$, where B is the bandwidth of the signal, can be obtained through various forms of signal processing. For a sufficiently broad bandwidth of the signal (or equivalently, a sufficiently short pulse length), the different parts of an individual animal can be

[a)]''Selected research articles'' are ones chosen occasionally by the Editor-in-Chief, that are judged (a) to have a subject of wide acoustical interest, and (b) to be written for understanding by broad acoustical readership.

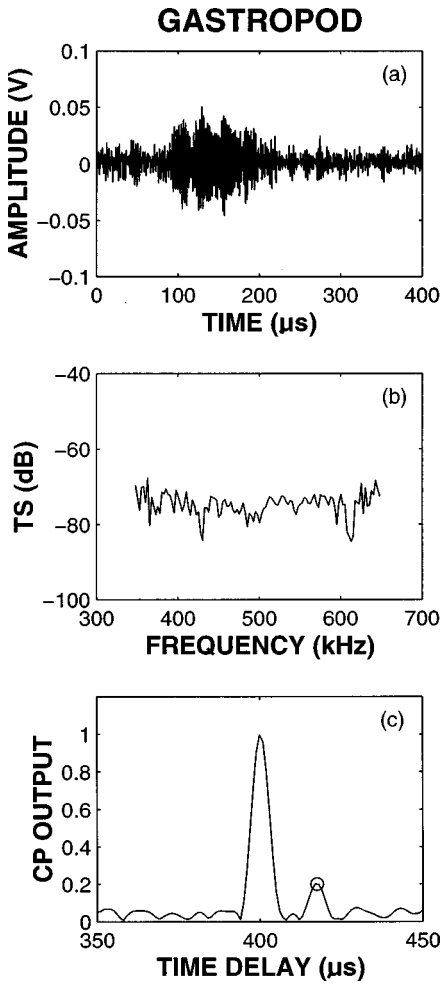

FIG. 1. Single ping backscattered signal from a 2-mm-long gastropod. (a) Time series; (b) target strength versus frequency; (c) compressed pulse (CP) output. The secondary arrival (circled peak) is clearly seen in (c) but its influence in the spectral domain is not noticeable in (b). The transmit signal is a chirp signal swept from 300 kHz to 700 kHz over 200 μs.

resolved acoustically. Ideally, in a noise-free environment, i.e., the signal-to-noise ratio (SNR) approaches infinity, the acoustic impulse response of the target can be obtained via either direct deconvolution (in the time domain) or the Fourier transform/Inverse Fourier transform process (in the frequency domain).

A combination of electrical noise of the data acquisition system and ambient noise in the water detected by the receiver degrades the quality of the data. Increasing the transmit power can help offset these effects but that improvement is restricted by the limitations of the power amplifier and transmit transducers. For a constant transmit power, the wider the bandwidth of the transmitter, the weaker the transmitted power spectral density, and hence the lower the SNR in the spectral domain at the receiver. In zooplankton applications, especially when an individual animal is involved, the received signal could be very noisy. As an example, the scattered signal by a 2-mm-long gastropod (*Limacina retroversa*, an elastic shelled animal) is shown in Fig. 1. Figure 1(a) is the time series of the received backscattering signal for a single ping and Fig. 1(b) is its power spectrum. The transmit signal is a linear frequency modulated signal (chirp) swept from 300 kHz to 700 kHz over 200 μs. Noise is quite apparent in the raw time series and results in some of the ''hashness'' in the power spectrum.

It is well known that when a long-wideband signal is used, i.e., $BT \gg 1$, where B is the bandwidth and T is the pulse length, the output SNR can be increased by applying pulse compression (PC) techniques. With this process, the length of the original signal is reduced which provides improved temporal resolution. One pulse compression technique, the matched filter (MF), maximizes the output SNR by cross-correlating the received signal with a noise-less replicate of the transmit signal. Figure 1(c) illustrates the compressed pulse (CP) output after cross-correlating the received raw backscattering time series in Fig. 1(a) with the applied transmit signal (details of this analysis are given in Sec. II B). Here the output SNR and temporal resolution are clearly improved and two distinct arrivals can be identified. The primary arrival (largest) corresponds to the specular component of the backscattering from the front interface of the animal and the secondary arrival (circled peak) corresponds to a subsonic Lamb wave that circumnavigates the surface of the shell and sheds back to the reciver (Stanton *et al.*, 1998b). Had this been a true MF, the output would have been a sinc-like function. Since the scattering characteristics of the target were not incorporated into the processing, the actual output departs form the idealized MF output (i.e., resulting in multiple highlights). This deviation contains information regarding the scattering properties of the target.

Given the potential advantages of using PC techniques with broadband scattered signals by zooplankton, we present in this paper a study of the performance of PC processing in the context of acoustic scattering by zooplankton with the purpose of extracting more useful information acoustically. Since MF processing is, in part, a basis for this analysis, the background of MF's is given briefly in Sec. I. In Sec. II, different theoretical considerations of PC processing involving zooplankton scattering are studied. CP outputs of the backscattering data from different zooplankton groups collected from various sources are presented and analyzed in Sec. III, and finally, the conclusions are drawn in Sec. IV in which the advantages of using PC techniques in the application of zooplankton scattering are summarized.

I. BACKGROUND OF MATCHED FILTER PROCESSING

Matched filters are widely used in radar and sonar applications (Price, 1956; Siebert, 1956; Parvulescu, 1961; Cook and Bernfeld, 1967; Clay, 1987; Thorne *et al.*, 1994, 1995), and their theoretical background can be found in many references (Van Vleck and Middleton, 1946; Turin, 1960; Van Trees, 1968; Whalen, 1971; Robinson, 1980; Winder and Loda, 1981). In this section, only a brief review of the theory and its application to the class of signals used in our experiments will be presented.

Matched filters are designed to maximize the output SNR for a given input SNR when noise is present. Assume that a time series $x(t)$ is composed of two components: a signal $s(t)$ and noise $n(t)$ [i.e., $x(t)=s(t)+n(t)$], and is fed into a filter whose impulse response is $a(t)$. The filtered output $y(t)$ can be expressed as

$$y(t)=x(t)*a(t)=s(t)*a(t)+n(t)*a(t), \tag{1}$$

where the symbol ''*'' denotes convolution. The ratio of the instantaneous power of the signal to that of the noise at time τ is

$$\Gamma(\tau)=\frac{(\int_0^\tau a(t)s(\tau-t)dt)^2}{\langle(\int_0^\tau a(t)n(\tau-t)dt)^2\rangle}. \tag{2}$$

Maximizing Eq. (2) with respect to the filter $a(t)$ results in (Whalen, 1971)

$$\int_0^\tau a(\xi)r_n(t-\xi)d\xi=k_c s(\tau-t), \tag{3}$$

where r_n is the autocorrelation function of the random noise and k_c is a normalization constant. If the noise is white, r_n becomes a delta function, the above equation reduces to

$$a(t)=k_c s(\tau-t). \tag{4}$$

Such a filter is called a *matched filter* since its coefficients are ''matched'' to the applied signal $s(t)$. Equation (4) shows that a MF is merely a time reversed sequence of the original signal. Since a convolution with a time reversed function is mathematically equivalent to the correlation with that function without time reversal, a MF is also referred to as a *correlator*. Substituting Eq. (4) into Eq. (1) and dropping the time shift τ, we have

$$\begin{aligned} y(t)&=x(t)*s(-t)\\ &=k_c s(t)*s(-t)+k_c n(t)*s(-t)\\ &=k_c r_{ss}(t)+k_c s(t)\otimes n(t), \end{aligned} \tag{5}$$

where ''$\otimes$'' stands for correlation and $r_{ss}(t)$ is the autocorrelation function of the signal $s(t)$. For white noise, $n(t)$, the second term in Eq. (5) tends to zero. It can be proven that the time-domain resolution of a MF output is approximately equal to $1/B$, and the processing gain—the ratio of output SNR to input SNR is proportional to $2BT$, where B is the bandwidth and T is the pulse length of the applied signal (Turin, 1960).

One of the widely used signals to provide a high processing gain is a chirp signal because of its uniform coverage of frequencies within a given band. An ideal ''up-sweep'' chirp, a signal whose instantaneous frequency increases linearly with time, can be represented in the following form:

$$u(t)=\begin{cases}\cos(\omega_0 t+\alpha t^2), & 0\leqslant t\leqslant T,\\ 0, \quad \text{otherwise}, \end{cases} \tag{6}$$

where ω_0, α, and T are the initial angular frequency, sweep rate, and pulse length, respectively. It can be shown that for $\sqrt{\alpha}T\gg 1$, the analytical expression of the MF output of Eq. (6) is approximately

$$R_f(\tau)\simeq\tfrac{1}{2}\cos[(\omega_0+\alpha T)\tau]\mathrm{Sinc}(\alpha\tau T), \tag{7}$$

where τ is the time delay, $R_f(\tau)$ is the autocorrelation function of a continuous signal modulated by a rectangular window function and is defined in more general terms in Eq. (A2) of Appendix A. The Sinc function in Eq. (7) is defined as $\mathrm{Sinc}(x)\equiv\sin(x)/x$. The above approximate expression is based on the conditions that $\sqrt{\alpha}T\gg 1$ and $\tau\ll T$. The cosine term acts as a carrier signal whose angular frequency is the center angular frequency of the original chirp, $(\omega_0+\alpha T)$, while the term involving the Sinc function is the envelope of the MF output. An example of the time series $u(t)$ and its corresponding MF output are shown in Fig. 2(a) and (b), where $f_0=300$ kHz, $\alpha=2\pi\times10^9$ s^{-2}, and $T=200$ μs (these parameters are sometimes used in our zooplankton scattering experiments). The resultant bandwidth is about 400 kHz. The envelope of the MF output is computed from the Sinc function in Eq. (7) and plotted with the thick solid line. Strong sidelobes are observed in Fig. 2(b) which are due to the sharp edges of the signal.

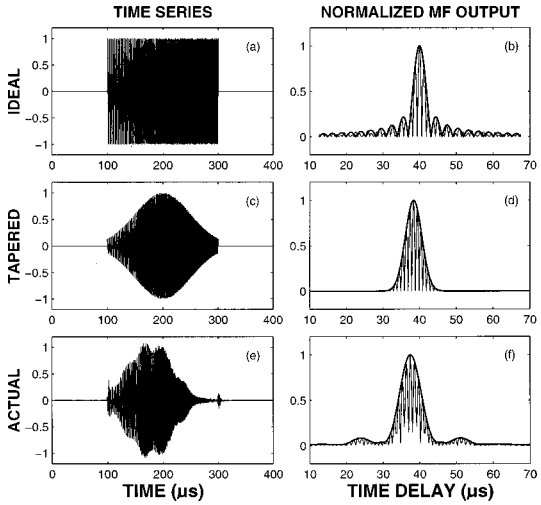

FIG. 2. Time series and MF outputs of various kinds of signals. (a), (b) Ideal chirp (300 kHz to 700 kHz up sweep) with $f_0=300$ kHz, $\alpha=2\pi\times10^9$ s^{-2}, and $T=200$ μs. The envelope (thick line) of the MF output is computed from the Sinc function in Eq. (7). (c), (d) Gaussian-tapered chirp with $\beta=2\times10^8$ s^{-2} and the other parameters are the same as in (a). The envelope of the MF output (thick line) is computed from Eq. (10). (e), (f) Actually measured chirp signal received in the calibration mode illustrating the system response to the transmit signal given in (a). In each plot in the right column, the thick solid line is the demodulated MF output and the thin line is the full rectified MF output before demodulation.

In reality, due to the nonuniform band-limited frequency response of most transducers such as the ones used in our experiments, the transmitted signal is typically tapered on its rising and falling edges. Such a signal can be reasonably approximated by an untapered chirp signal given by Eq. (6) modulated by a Gaussian envelope symmetric about $t=T/2$

$$u_g(t)=u(t)e^{-\beta(t-T/2)^2}, \tag{8}$$

where β is a constant that controls the degree of tapering. For $\sqrt{\beta}T\gg1$, the analytical expression of its MF output becomes (Appendix A)

$$R_f(\tau)=\frac{1}{4T}\sqrt{\frac{2\pi}{\beta}}\,e^{-[(\beta^2+\alpha^2)/2\beta]\tau^2}\cos[(\omega_0+\alpha T)\tau]. \tag{9}$$

The limiting condition of $\sqrt{\beta}T\gg1$ corresponds to the case when the leading and trailing edges of the chirp are negligibly small at the beginning and end of the window function, respectively; that is, the windowed signal has the appearance of varying smoothly in time. The MF output in

Eq. (9) has the same carrier signal as the untapered chirp case but with a Gaussian envelope given by

$$R_{\text{env}}(\tau) = \frac{1}{4T}\sqrt{\frac{2\pi}{\beta}}\, e^{-[(\beta^2+\alpha^2)/2\beta]\tau^2}. \tag{10}$$

Figure 2(c) and (d) shows this Gaussian tapered chirp time series and its MF output with a tapering coefficient $\beta = 2\times 10^8\ \text{s}^{-2}$, where the thick line is the envelope computed using Eq. (10). For the purpose of comparison, the actual received transmit signal used during our 1994 cruise and its MF output are shown in Fig. 2(e) and (f). The modulation of its amplitude is due to the frequency response of the combination of the acoustic transducers and the data acquisition system described in Stanton *et al.* (1998a). The thick solid line is the envelope of the MF output (i.e., demodulated MF output). As expected, the Gaussian modulation widens the main lobe and reduces the sidelobe levels of the MF output [Fig. 2(d) and (f)]. Comparison of the time series and the MF output of the Gaussian tapered chirp with those of the actual received signal indicates that the Gaussian tapered chirp describes the actual received signal reasonably well.

II. BASIC CHARACTERISTICS OF PULSE-COMPRESSED SCATTERED SIGNALS

Since the scattering impulse response of a target is typically unknown, it is, in general, impossible to determine a real ''replicate'' of the received scattered signal and hence the signal will never be truly ''matched'' as in the case described above for MF processing. However, deviations of the received scattered signal from the expected output for the idealized (matched) case, can provide useful information about the target after processing. For example, if the idealized replicate is constructed assuming that the target is a point scatterer but the target is in fact of finite size, then the CP output will consist of multiple arrivals or ''partial waves'' from the target. This is in contrast to the expected single return from a point scatterer. The separations between the multiple arrivals may be related to the size of the target. In addition to the effects due to a finite body, there will be multiple arrivals due to a collection of multiple targets which will also affect the performance of the PC processing. While the mathematical treatment of both cases is similar, we will focus on the different characteristics of the CP output when the scattering from a single target is involved. Special attention will be focussed on relating the physics of the scattering to the deviations.

In many signal detection applications (Van Vleck and Middleton, 1946; Price, 1956; Siebert, 1956; Parvulescu, 1961), the absolute level and the shape of the CP output may not necessarily be as important as the accuracy of the arrival times of the detected echoes and their relative levels. However, to characterize the acoustic scattering by zooplankton of different groups, not only is the timing important but also the absolute level of the scattering, such as the target strength (TS). To determine the TS from a CP output of a scattering signal, special care must be taken. In the following part of this section, the basic scattering equations are presented and then incorporated into PC processing.

A. Basic scattering equations

For a backscattering geometry, ignoring the attenuation in water, the far field received pressure time series $p_{\text{bs}}(t)$ for an individual target due to a point source is

$$p_{\text{bs}}(t) = \frac{s_0(t-t_0)}{r^2} * f_{\text{bs}}(t), \tag{11}$$

where $t_0 = 2r/c$, r is the distance between the transmitter (receiver) and the target, and c is the sound speed in water. $s_0(t)$ is the source function and $f_{\text{bs}}(t)$ is the backscattering impulse response of the target. Its Fourier transform $P_{\text{bs}}(f)$ can be expressed in terms of the backscattering amplitude F_{bs}, which is the Fourier transform of the scattering impulse response f_{bs}, as,

$$P_{\text{bs}}(f) = S_0(f)\frac{e^{2ikr}}{r^2}P_{\text{bs}}(f) = P_0(f)\frac{e^{ikr}}{r}F_{\text{bs}}(f), \tag{12}$$

where S_0 is the Fourier transform of the source function s_0, and k is the wave number of the transmit signal. $P_0 = S_0 e^{ikr}/r$ is the incident wave at the target. For far field applications, P_0 can be treated as a plane incident wave. Notations of lower case and upper case are chosen to be consistent with the convention for time/frequency Fourier pairs. Here F_{bs} corresponds to the backscattering amplitude f_{bs} in our previous papers involving scattering models (e.g., Stanton *et al.*, 1993a, 1993b, 1998b).

Target strength is defined in terms of the differential backscattering cross section σ_{bs} and the backscattering amplitude F_{bs} as (Clay and Medwin, 1977)

$$\text{TS} = 10\log_{10}\sigma_{\text{bs}} = 20\log_{10}|F_{\text{bs}}| \quad \text{dB re: 1 m}^2. \tag{13}$$

The scattering amplitude F_{bs} is a measure of the scattering ability of a target at a range of 1 meter subject to a plane incident wave and can be expressed in terms of directly measurable quantities of transmit and received voltages as

$$F_{\text{bs}} = \frac{V_{\text{bs}}^{(r)}}{V_{\text{cal}}^{(r)}}\frac{V_{\text{cal}}^{(t)}}{V_{\text{bs}}^{(t)}}\frac{r_{\text{bs}}^2}{r_{\text{cal}}}, \tag{14}$$

where V is the Fourier transform of the voltage, r_{bs} is the distance between the transducers and the target in backscattering mode, and r_{cal} is the distance between the transmitter and the receiver in bistatic calibration mode, superscripts t and r stand for transmit and receive, respectively, and subscripts bs and cal stand for backscattering mode and calibration mode, respectively. In the backscattering mode, two closely spaced transducers are used, one for transmission and the other for reception. In the calibration mode, the same two transducers are separated by a distance of r_{cal} and facing each other (Stanton *et al.*, 1998a).

To accurately estimate the frequency dependent TS, the characteristics of the compressed pulse in both time and frequency domains need to be studied.

B. Time domain—Cross correlation

As mentioned above, if the received signal $s(t)$ in Eq. (1) is the scattered signal from a target, it is no longer an exact replica of the transmitted signal $s_0(t)$, but a convolution of $s_0(t)$ with the scattering impulse response of the tar-

get $f_{bs}(t)$ plus a noise component $n(t)$. Since the scattering impulse response is a complicated function of the geometric and physical properties of the target, it is not practical to find a function that truly matches the received scattering signal $f_{bs}*s_0$ as a replica required by MF processing. An alternative candidate is the transmit signal. Since the transmit signal does not truly match the received scattering signal, to distinguish between the true MF processing and the processing using the transmit signal as the replica, we call such a nonideal MF processing pulse compression (PC) processing and its output compressed pulse (CP) output.

The resultant output in this scattering case can then be expressed as

$$y(t) \simeq k_c s_0(t) \otimes \left(\frac{1}{r^2} f_{bs}(t) * s_0(t-t_0) + n(t) \right), \tag{15}$$

$$= \frac{k_c}{r^2} r_{ss}(t-t_0) \otimes f_{bs}(t) + k_c r_{sn}(\tau), \tag{16}$$

where k_c is a proportionality constant, τ is time delay, r_{ss} is the autocorrelation function of $s_0(t)$, r_{sn} is the cross-correlation function of $s_0(t)$ and $n(t)$, and t_0 is defined in Eq. (11). In obtaining Eq. (16) from Eq. (15), we have used the results of Eq. (B7) in Appendix B. For white noise that is of sufficiently low level, the second term on the right hand side is small compared with the first term and Eq. (16) can be written approximately as

$$y(\tau) = \frac{k_c}{r^2} r_{ss}(t-t_0) \otimes f_{bs}(t). \tag{17}$$

For the special case where the scattering impulse response is a delta function $f_{bs}(t) = \delta(t)$ (which corresponds to a point scatterer of uniform response), the resultant CP output $y(\tau)$ will be a simple product of a scaling constant and the autocorrelation function of the transmit signal. This ideal case represents true matched filtering.

If the scattering impulse response $f_{bs}(t)$ is not a single impulse but involves a number of impulsive arrivals separated in time, then it can be written in terms of a sum of those arrivals (Ehrenbreg *et al.*, 1978):

$$f_{bs}(t) = \sum_{j=1}^{N} f_{bs}(t-\Delta_j),$$

$$= \sum_{j=1}^{N} k_{s_j} \delta(t-\Delta_j), \tag{18}$$

where the difference in spreading loss among the arrivals is ignored, N is the total number of arrivals, and Δ_j is the difference of arrival time between the jth arrival and the reference time $t_0 = 2r/c$. For an applied chirp signal given in Eq. (6), the CP output of the scattering described above is a superposition of a series of Sinc-function-like arrivals with different amplitudes. If the separation time between arrivals is greater than $1/B$, where B is the band width of the chirp signal, these N arrivals can be resolved in the time domain after processing. For a more general case where $f_{bs_j}(t-\Delta_j)$ is an arbitrary function (Thorne *et al.*, 1995), the CP output yields

$$y(\tau) = \frac{k_c}{r^2} \sum_{j=1}^{N} r_{ss}(t-t_0) \otimes f_{bs_j}(t-\Delta_j). \tag{19}$$

C. Frequency domain—Spectrum average

To further understand how PC processing can improve the output SNR, we express Eq. (16) as a summation of two integrals over frequency

$$y(\tau) = y_1(\tau) + y_2(\tau),$$

$$= \frac{k_c}{r^2} \int_{-\infty}^{\infty} F_{bs}(f) R_{ss}(f) e^{i\omega(\tau-t_0)}\, df$$

$$+ k_c \int_{-\infty}^{\infty} N(f) S_0(-f) e^{i\omega\tau}\, df, \tag{20}$$

where $F_{bs}(f)$, $R_{ss}(f)$, $S_0(f)$, and $N(f)$ are the Fourier transforms of the backscattering impulse response $f_{bs}(t)$, the autocorrelation function $r_{ss}(t)$, the transmit signal $s_0(t)$, and noise $n(t)$, respectively.

Clearly, the right-hand side of Eq. (20) is in the form of the inverse Fourier transform. By taking the Fourier transform of both sides of Eq. (20), the scattering amplitude F_{bs} can be obtained. However, directly taking the Fourier transform of $y(\tau)$ in Eq. (20) is equivalent to reversing the PC processing (Appendix C), and thus *reduces* the SNR back to that of the original signal. In other words, we cannot improve our estimate on the frequency dependent scattering amplitude F_{bs}.

However, evaluating the CP output $y(\tau)$ given by Eq. (20) at $\tau = t_0$, we obtain,

$$y(t_0) = \frac{k_c}{r^2} \int_{-\infty}^{\infty} F_{bs}(f) R_{ss}(f) df, \tag{21}$$

where the term associated with noise, $y_2(\tau)$, is neglected. Equation (21) is simply a weighted averaging process over a frequency band (band-limited case). Assuming F_{bs} has a slowly varying phase over the frequency band of interest, and since the weighting function $R_{ss}(f) = S_0^* S_0$ is always a real function, all frequency components of the integrand are in phase and add up constructively resulting in an enhanced signal level. In contrast, for random noise described by the second term of Eq. (20), the phase of its Fourier components can be described as randomly and uniformly distributed over $[0\ 2\pi]$. Such random noise always mismatches the filter, hence all frequency components tend to add destructively resulting in a reduced noise level. It is the constructive addition for a matched signal and the destructive addition for random noise in the frequency domain that makes a PC processing improve the output SNR in the time domain.

1. Single nonideal arrival

As discussed in Sec. I B, the ideal case is when the scattering impulse response is a delta function, i.e., $f_{bs}(t) = k_s \delta(t)$, in the case of a point scatterer (the Fourier transform of the arrival is $F_{bs}(f) = k_s$). The CP output is a simple integration of R_{ss} over the entire frequency domain. In this case, the power density of the transmit signal is added constructively since the phase of the scattering transfer function

$F_{bs}(f)$ is zero. However, in reality due to the finite size of any actual targets, the scattering impulse response $f_{bs}(t)$ will never be an ideal delta function, but a function that spreads out in the time domain and whose amplitude and phase spectra are functions of frequency. The CP output $y(t_0)$ of such a function is expected to be smaller than that due to a delta function having the same ''strength'' (i.e., the integration of the scattering impulse response $f_{bs}(t)$ over the time it spans).

In this section, the influences of a nonideal scattering function on its CP output will be studied. The analysis can provide guidance in interpreting the results based on the CP outputs. A triangle function is chosen as the scattering impulse response since it can be easily changed from a delta function to a non-ideal impulse response with a finite bandwidth by simply varying the spread of the triangle function. Its strength is kept at unity; i.e., the area under the triangle is equal to 1 and the peak value at $t=0$ increases as the spread τ of the scattering impulse response decreases. For $\tau \to 0$, the triangle function approaches a delta function with unit strength. Its Fourier transform can be expressed as (Bracewell, 1986):

$$F_{bs}(f)=\left(\frac{\sin(\omega\tau/4)}{\omega\tau/4}\right)^2, \tag{22}$$

where $\omega=2\pi f$ is the angular frequency. To evaluate the performance of the PC processing due to the impulse response given by Eq. (22), a ratio function can be defined as,

$$R_f(\tau)=20\log_{10}\left(\frac{y_f(t_0)}{y_d(t_0)}\right), \tag{23}$$

where $y_d(t_0)$ is the CP output at $\tau=t_0$ using a delta function as the scattering impulse response and $y_f(t_0)$ is the CP output at $\tau=t_0$ using a triangle impulse response. Figure 3 shows the dependence of R_f upon the spread of the scattering impulse responses. For a scattering impulse response having spreads of 4 μs and 8 μs, the CP output levels are reduced by 1.5 dB and 5 dB, respectively, which indicates that for a scattered signal having the same strength but having a different spread, the output levels of a CP could differ by as much as several dB.

As discussed before, $y(t_0)$ is a weighted average of the impulse response of the received backscattering signal over the frequency bandwidth. In some applications, we may be only interested in an averaged scattering level over a certain frequency band. For example, in Fig. 4 of Stanton *et al.* (1998a), an averaged TS over a frequency band from 400 to 500 kHz is computed to characterize the scattering by an individual gastropod over that frequency band.

To analyze a particular band of interest, we integrate Eq. (21) within a specified frequency window resulting in a partial PC operation. To evaluate the performance of this partial PC processing, we define the ratio $R_p(f_T)$, which measures the deviation of the weighted average from its true average as:

$$R_p(f_T)=20\log_{10}\left|\int_{f_0-f_T/2}^{f_0+f_T/2}F_{bs}(f)R_{ss}(f)df/\Lambda(f_T)\right|, \tag{24}$$

where f_0 and f_T are the center frequency and the width of the frequency window, respectively, and $\Lambda(f_T)$ is a normalization factor defined as

$$\Lambda(f_T)=\frac{1}{f_T}\int_{f_0-f_T/2}^{f_0+f_T/2}F_{bs}(f)df\int_{f_0-f_T/2}^{f_0+f_T/2}R_{ss}(f)df. \tag{25}$$

It is apparent from Eq. (24) that if the scattering impulse response is a delta function, its Fourier transform $F_{bs}(f)=1$ and $R_p(f_T)$ is independent of the window width f_T. However, for a scattering impulse response that deviates from a delta function, $R_p(f_T)$ is no longer independent of f_T. Figure 4 illustrates the dependence of $R_p(f_T)$ on the width of the frequency window f_T, where the scattering impulse response is assumed to be a 10-μs triangle function and the frequency window is centered at 500 kHz. Three different transmit signals are used: (1) chirp without Gaussian tapering (dash-dotted); (2) chirp with Gaussian tapering (dashed); and (3) actually received signals in the calibration mode (solid). It can be seen that the deviation increases as the window width increases. For a window width less than 100 kHz, all three transmit signals have similar deviations less than 0.08 dB, while for a 300-kHz frequency window, there are deviations of about 2.2 dB for the Gaussian tapered and measured chirps and 0.2 dB for the untapered chirp. Again, we see that a Gaussian-tapered chirp gives similar results as the actual transmit signal.

Figure 4 suggests that the narrower the frequency window, the better the estimate of the average scattering response over that window. However, the narrower frequency window will degrade the performance of the PC, i.e., it reduces the output SNR. Figure 5 shows the influence of the frequency window on the SNR. The transmit signal is an actually measured calibration signal shown in Fig. 2(e). To compute the averaged output SNR from a windowed CP output, random noise is added to maintain the SNR at 11 dB before applying a PC.

The output SNR approaches a constant level (about 20 dB) as the width of the frequency window increases. From Figs. 4 and 5, we can conclude that to improve the SNR, it is important to average over as wide a frequency band as possible. However, if a more accurate estimate of the scattering response at a particular frequency is desired, a narrower window PC processing is required. In other words, there is a trade-off in selecting the most appropriate window width.

2. Multiple arrivals from a single target

If the scattering function is a superposition of multiple arrivals separated in the time domain and given by Eq. (19), we rewrite Eq. (21) as,

$$y(\tau)=\frac{1}{r^2}\sum_{j=1}^{N}k_{cj}\int_{-\infty}^{\infty}F_{bs}^{(j)}(f)R_{ss}(f)e^{i\omega(t-t_j)}\,df, \tag{26}$$

where $t_j=2r_j/c=t_0-\Delta_j$, t_0 and Δ_j are defined in Eqs. (11) and (18).

For a special case that $N=2$, we define a ratio function

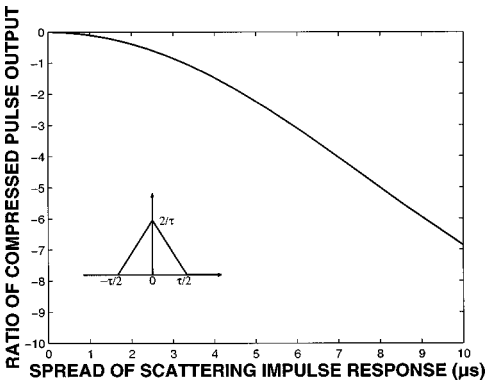

FIG. 3. Influence of the spread of a triangle scattering impulse response on the CP output. The transmit signal is an untapered chirp swept from 300 kHz to 700 kHz over 200 μs shown in Fig. 2(a). The area of the scattering impulse response function is kept at unity.

$$R_T(\Delta)=20\ \log_{10}\left|\frac{\int_{-\infty}^{\infty}R_{ss}(f)(F_{\mathrm{bs}}^{(1)}(f)+F_{\mathrm{bs}}^{(2)}(f)e^{i\omega\Delta})df}{\int_{-\infty}^{\infty}R_{ss}(f)df}\right|, \tag{27}$$

where $\Delta=\delta_2-\delta_1$ is the time separation between the two arrivals. Figure 6 shows the influence of the separation between two arrivals of the same strength on the CP output. The transmit signal is an untapered chirp shown in Fig. 2(a), and the received backscattered signal is the superposition of two ideal delta functions having the same strength, i.e., $F_{\mathrm{bs}}^{(1)}=F_{\mathrm{bs}}^{(2)}=1$.

From Fig. 6, we find that $R_T(0)$ is 6 dB when the two arrivals coincide in time and tends to 0 dB as the separation tends to infinity. Note that for a separation between two arrivals greater than $1/B=2.5$ μs, the fluctuation of $R_T(\Delta)$ is less than 2 dB. Figure 6 suggests that when the separation between two arrivals is less than the time domain resolution of the CP, the echoes are not resolvable. In other words, a large output of the PC processing could result from a strong scattering from a single arrival or a constructive addition of multiple arrivals whose separations in time are smaller than $1/B$. This implication is very important in interpreting the scattering data when PC processing is involved.

D. Partial wave target strength (PWTS)

In Eq. (13), F_{bs} is expressed as the total scattered wave from the target, without distinguishing between the various partial waves that make up that signal. To help understand the scattering mechanism of interest, in the case when the echoes (arrivals) can be resolved in the time domain, a partial wave target strength (PWTS) can be introduced to include only partial scattering waves from a subset of the scatterer:

$$\mathrm{TS}_{pw}=20\log_{10}\left|\sum_{j}^{N_j}F_{\mathrm{bs}}^{(j)}\right|, \tag{28}$$

where N_j is the number of partial waves of interest corresponding to the number of arrivals of the CP output. $F_{\mathrm{bs}}^{(j)}$ is the partial wave scattering amplitude or Fourier transform of a single (jth) arrival. By replacing $V_{\mathrm{bs}}^{(r)}$ and $V_{\mathrm{cal}}^{(r)}$ in Eq. (14) with the Fourier transforms of their cross correlations with

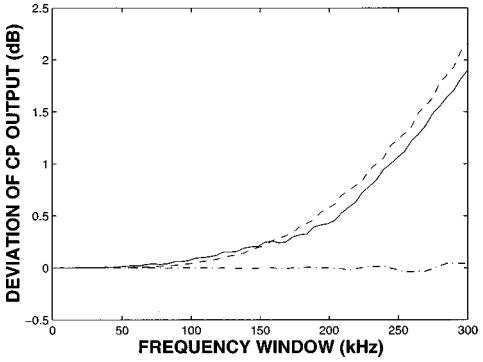

FIG. 4. Influence of the width of the frequency window on the target strength averaged over that window. The scattering amplitude, $F_{\mathrm{bs}}(f)$ in Eqs. (24) and (25) is the Fourier transform of a triangle function with a 10 μs spread. Three transmit signals are used in the computations: ideal (untapered) chirp (dash-dotted), Gaussian tapered chirp (dashed), and actually measured chirp (received signal in the calibration mode) used in the experiment (solid).

the transmit signal, $R_{\mathrm{bs}}^{(r)}$ and $R_{\mathrm{cal}}^{(r)}$, respectively, the summation of all partial waves of interest is given by

$$\sum_{j}^{N_j}F_{\mathrm{bs}}^{(j)}=\frac{V_{\mathrm{cal}}^{(t)}}{V_{\mathrm{bs}}^{(t)}}\frac{r_{\mathrm{bs}}^2}{r_{\mathrm{cal}}}\frac{\Sigma_j^{N_j}R_{\mathrm{bs}(j)}^{(r)}}{R_{\mathrm{cal}}^{(r)}}, \tag{29}$$

where $R_{\mathrm{bs}(j)}^{(r)}$ is the Fourier transform of the cross correlation of the jth received scattering arrival with the calibration signal and can be chosen to include the partial waves of interest. $R_{\mathrm{cal}}^{(r)}$ is the Fourier transform of the autocorrelation of the calibration signal. For a linear system, the ratio $V_{\mathrm{cal}}^{(t)}/V_{\mathrm{bs}}^{(t)}$ can be considered approximately as a constant over a usable frequency band.

In many cases, the highest SNR is more desirable than the precise partial wave target strength at a particular frequency. To obtain the highest SNR of a partial wave, we can use the peak value of the partial wave (arrival) obtainable from the CP output. As discussed in Sec. II C, this peak value corresponds to a weighted average of a single partial wave [Eq. (21)] in the frequency domain. The averaged scattering amplitude of such a partial wave (jth arrival) can be obtained directly from the CP output,

$$\begin{aligned}\langle\sigma_{\mathrm{bs}}^{(j)}\rangle&=\langle|F_{\mathrm{bs}}^{(j)}|^2\rangle,\\&=\left\langle\left|\frac{V_{\mathrm{cal}}^{(t)}}{V_{\mathrm{bs}}^{(t)}}\frac{r_{\mathrm{bs}}^2}{r_{\mathrm{cal}}}\frac{R_{\mathrm{bs}(j)}^{(r)}}{R_{\mathrm{cal}}^{(r)}}\right|^2\right\rangle,\\&=\left|\frac{V_{\mathrm{cal}}^{(t)}}{V_{\mathrm{bs}}^{(t)}}\frac{r_{\mathrm{bs}}^2}{r_{\mathrm{cal}}}\frac{y_{\mathrm{bs}(j)}^{(r)}(t_j)}{y_{\mathrm{cal}_{\max}}^{(r)}}\right|^2,\end{aligned} \tag{30}$$

where $\langle\ .\ \rangle$ stands for averaging over frequency, $y_{\mathrm{bs}(j)}^{(r)}(t_j)$ is the cross correlation of the jth received scattering arrival at $\tau=t_j$ time lag, and $y_{\mathrm{cal}_{\max}}^{(r)}$ is the maximum peak value of the autocorrelation of the calibration signal. In Eqs. (29) and (30), index j represents the partial wave scattering contribution from the jth arrival in the time domain. Note that by assuming $V_{\mathrm{cal}}^{(t)}/V_{\mathrm{bs}}^{(t)}$ is a constant over the frequency band of interest, the average partial wave scattering cross section over the frequency band can be achieved by a simple ratio of CP outputs. The averaged PWTS from the jth arrival can then be defined as

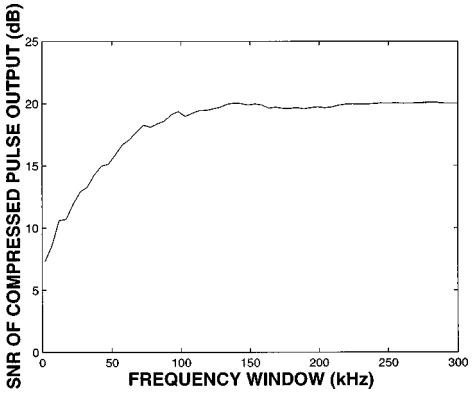

FIG. 5. Influence of the width of the frequency window on the output SNR of PC processing. The transmit signal is the measured signal shown in Fig. 2(e), while random noise is added to the original signal. The ratio of the signal amplitude (peak-to-peak) to the standard deviation of the noise is 5 and the resultant SNR is about 11 dB. 100 realizations are used in the computation.

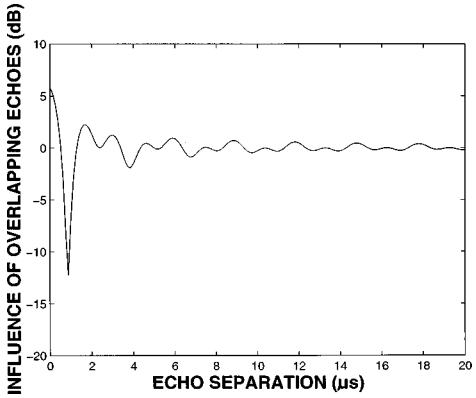

FIG. 6. Influence of the separation of two arrivals on the average target strength computed from Eq. (27). The transmit signal is an untapered chirp signal swept from 300 kHz to 700 kHz over 200 μs shown in Fig. 2(a).

$$\langle \mathrm{TS}_{pw}^{(j)} \rangle \equiv 10 \log_{10} \langle |F_{\mathrm{bs}}^{(j)}|^2 \rangle. \tag{31}$$

From the discussion associated with Fig. 3, a possible error of up to several dB in estimating the ''true'' average target strength can be introduced if the spread of the ''true'' scattering impulse response is as large as a few micro seconds. However, for a scattering impulse response with a shorter length, the error is insignificant and may be neglected.

III. DATA ANALYSIS AND DISCUSSIONS

In this section, experimental scattering data from live individual zooplankton will be analyzed using three different approaches: temporal, spectral, and statistical analyses.

The data were collected during two ship cruises, September 27–October 5, 1993 and September 21–September 30, 1994 on or near Georges Bank (near Cape Cod, Massachusetts), and two series of laboratory tank experiments conducted at Woods Hole Oceanographic Institution (WHOI) in 1990 and at Naval Underwater Warfare Center (NUWC) in Newport, RI, from the end of 1991 to the beginning of 1992.

During the two cruises, a 1.5-m-high by 2.4-m-diameter cylindrical tank was mounted on the deck of the ship. A transducer array was mounted on the bottom of the tank looking upward. The array comprised nine closely spaced transducer pairs for 1993 and 13 pairs for 1994, with frequencies ranging from 50 kHz to 2 MHz including four broadband transducer pairs whose center frequencies are 250 kHz, 500 kHz, 1 MHz, and 2.25 MHz, respectively. Linear chirps were applied to all of the broadband transducers. Live animals were carefully tethered and put into the acoustic beam at a fixed range (50 cm above the transducers) in the tank. One or more transducer pairs were used for obtaining the backscattering data from each animal. Detailed descriptions of the experimental setup and procedures can be found in Stanton *et al.* (1998a).

For the laboratory experiments, at NUWC, a one-cycle 500 kHz pulse was applied to the transducer, while a chirp signal centered at 500 kHz was used for the WHOI experiment [detailed descriptions of the experiments can be found in Chu *et al.* (1992) and Stanton *et al.* (1994a,b, 1998a)]. The bandwidth of the transmitted chirp signal was 400 kHz and the pulse length was 200 μs. Because of a much shorter pulse length used in the NUWC experiment, the PC processing gain is expected to be lower than that when using a chirp signal.

For all experiments, the calibrations were done in a bistatic mode with two transducers facing each other. In the scattering measurements, the configuration was still bistatic but the same transducers were mounted closely next to each other to approximate a true backscattering geometry.

In the following analysis, zooplankton from three anatomical groups are studied in the experiment, namely, shrimp-like animals (euphausiids and decapod shrimp) whose average length and diameter are about 30 mm and 4 mm, respectively; gas-bearing animals (siphonophores) whose diameter of the gas inclusion and body length are about 1 mm and 30 mm, respectively; and elastic shelled animals (gastropods) whose length and diameter are 2 mm and 1 mm, respectively. The shapes of these animals can be found in Stanton *et al.* (1994b). These three animal groups correspondingly represent three different boundary conditions: fluid/fluid boundaries, a bubble embedded in a fluid-like body, and an elastic shell in a fluid medium. Since the transmit pulse length is only 200 μs, the Doppler shift due to animal movement can be ignored.

Before analyzing the CP output data in terms of the scattering physics of the targets, we need to examine the various sources of contamination in the experiment that could lead to errors or ''false targets'' in the output. The CP output that will be used in the following analysis includes two major arrivals: primary and secondary arrivals. For shrimplike animals such as euphausiids near broadside incidence, the primary arrivals (scattering from the front interface) and secondary arrivals (scattering from back interface) are often of comparable level and the contamination is insignificant. However, there is always a largest arrival in company with several smaller arrivals in the CP output for the siphonophores or gastropods. If we define the largest and second largest peaks as the primary and the secondary arrivals, respectively, it is found that the secondary arrivals are much weaker than the primary arrivals.

In general, the primary arrivals are reliable and easily identified while the secondary arrivals, except for euphaus-

iids, are much weaker and exhibit larger variability in both arrival time and peak value. Therefore, they are more likely to be contaminated by echoes from the tether and microstructure, as well as system noise and artifacts of the PC processing itself (sidelobes). In addition to these possible sources of contamination, superglue was used to affix the tether to the gastropod which added another potential source of error [superglue was required when the animal was too small (1–2 mm long) to be tied to the tether]. Appendix D presents the results of the numerical simulations used to evaluate the error caused by the tether, microstructure, superglue, and the artifacts of the PC processing. It is found that even when a moderate noise component is added to the actual received signal, the major source of error is due to the artifacts of the PC processing. The artifacts can be greatly reduced if we only choose the pings in such a way that when the amplitude of the secondary arrival is greater than 10% of that of the primary arrival and when the secondary arrival occurs at points other than where the largest processing sidelobe occurs. In general, by using a PC technique, some low SNR backscattering data that were otherwise considered as unreliable in a spectral analysis can provide much useful information.

A. Temporal characteristics—Resolving partial waves

1. Shrimplike animals (euphausiid and decapod shrimp)

In a series of our previous studies, it was found that a shrimplike animal can be viewed as a weak scatterer and be modeled acoustically as the superposition of various rays:

$$F_{\mathrm{bs}} \sim F_{\mathrm{FI}} + \sum_j b_j e^{i2k\epsilon_j}, \tag{32}$$

where F_{bs} is the total backscattering amplitude, b_j is the amplitude of the jth arrival and ϵ_j is the corresponding distance between the ''acoustic center of mass'' and the reference plane (zero phase plane). The first term F_{FI} corresponds to the scattering from the front interface of the animal, while the second term represents the total contributions from the other parts of the body (Stanton *et al.*, 1993a, 1993b, 1998a). In the case of broadside or near broadside incidence, the second term quite often involves only one ray that penetrates the front interface into the body, bounces back from the back interface, passes through the front interface again and finally back to the receiver as shown in Fig. 7(a). The latter is shown to be reasonably approximated by Re^{iks} (Stanton *et al.*, 1993a, 1993b), where R is the plane wave reflection coefficient from a plane interface, k is the wave number, and s is the round trip distance between the front and the back interfaces [$2\overline{AB}$ in Fig. 7(a)]. Since the acoustic properties of the animal such as density and sound speed of the animal are very close to those of the surrounding fluid (water), the two rays have comparable strength. The phase difference of the two rays that arrive at the receiver is a function of frequency. In a plot of backscattering amplitude versus frequency, it produces an oscillatory pattern due to constructive (when the two rays are in phase) and destructive (when the two rays are out of phase) interferences. The nulls produced by destructive interactions could be as deep as 30 dB and sometimes have a regular spacing (Chu *et al.*, 1992). Under other conditions when changes in shape and/or orientation give rise to multiple arrivals from different parts of the animal body, the pattern may be irregular (Stanton *et al.*, 1998a). This variability in pattern has greatly limited our ability to accurately interpret broadband scattering data with a standard spectral analysis.

PC processing is an alternative way to approach this problem as it helps (temporally) resolve the various sources of scattering. Figure 8(a) shows a single ping backscattering signal from a 2-cm-long euphausiid, while Fig. 8(d) is its TS versus frequency plot. Partly due to the bandwidth limitation, no pattern can be clearly seen. In contrast, the CP output for the same ping is plotted in Fig. 8(g) showing two distinct arrivals with comparable strength. The time difference between the two arrivals corresponds to the round trip time required for the acoustic wave, after penetrating the animal body, traveling from the front interface to the back interface and returning. This result supports our previously proposed simple two-ray model that describes the (near broadside) backscattering from a weakly scattering elongated object such as a euphausiid (Stanton *et al.*, 1993a, 1998b), i.e., the first arrival corresponds to the echo from the front interface while the second corresponds to the echo from the back interface. Note that the time difference between the two arrivals in Fig. 8(a) is much larger than the separation of the two arrivals shown in Fig. 8(g) (the former is about 65 μs and the latter is about 6.5 μs while the average cylindrical diameter of the animal is about 4 mm). The null in the time series in Fig. 8(a) stems from a natural interference between two comparable chirp arrivals.

2. Gas-bearing animals (Siphonophore)

A siphonophore has a gas inclusion embedded in an elongated weakly scattering body. The acoustic scattering model for a siphonophore can be written approximately as

$$F_{\mathrm{bs}} \sim F_{\mathrm{GAS}} + F_{\mathrm{TISSUE}}, \tag{33}$$

where F_{GAS} and F_{TISSUE} represent scattering from the gas inclusion and body tissue, respectively. The second term on the right-hand side of Eq. (33) is the superposition of all rays scattered from the body tissue. A schematic scattering diagram for a siphonophore is illustrated in Fig. 7(b). A typical time series, its spectrum, and the corresponding CP output are shown in Fig. 8(b), (e), and (h), respectively. The largest peak of the CP output from this animal is due to the backscattering from the gas inclusion. The second largest peak which arrives before the main peak (pre-arrival) is interpreted as the scattering from the body tissue. This interpretation was based on the observation using a video camera that the main tissue portion of the animal was closer to the transducer than the bubble inclusion for these data. A time difference of 16.5 μs obtainable from Fig. 8(h) corresponds to a spatial distance of about 12.4 mm. This distance can be interpreted as the distance between the gas bubble and the ''local acoustic center of mass'' of the body [d in Fig. 7(b)]. This ''local acoustic center of mass'' could be a large glint or the superposition of several glints arriving at approximately the same time. The spatial distance of 12.4 mm is a

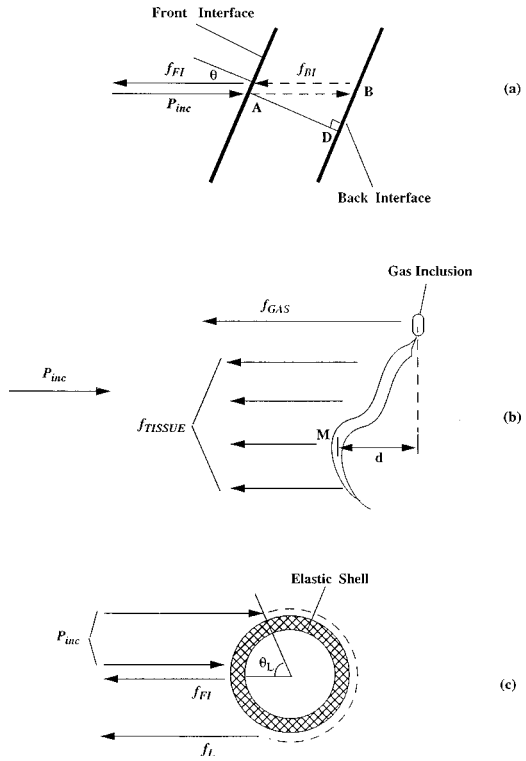

FIG. 7. Schematic diagram of scattering mechanisms for animals from three different zooplankton groups. (a) Euphausiid; (b) siphonophore; and (c) gastropod.

reasonable number for the curled animal whose body length is 26 mm when fully extended.

3. Elastic shelled animals (Gastropod)

A gastropod is a marine snail and has a hard elastic shell. For such a hard-shelled object, the incident wave hardly penetrates the shell or is greatly attenuated. However, other types of acoustic waves can be generated with a shell. A typical time series, its spectrum and its CP output are plotted in Fig. 8(c), (f), and (i), respectively. The primary arrival in the CP output plot (the largest peak) corresponds to the specular component of the backscattering from the front interface much like the cases for the euphausiid and siphonophore. There is also a secondary arrival, the event following the primary arrival (circled peak), corresponding to another kind of acoustic wave. For a time difference of 15 μs (round trip) measured in Fig. 8(i), assuming a sound speed of 1500 m/s, the corresponding spatial distance is 11.3 mm. This spatial distance is much larger than the outer physical dimensions (the animal is about 2 mm long and 1 mm in diameter with a shell thickness about 5 μm) of the gastropod from which the data were collected.

One reasonable explanation is that the hard elastic shell is capable of supporting surface elastic waves that travel at a speed lower than that of the sound speed in the surrounding fluid (Stanton *et al.*, 1998b). This subsonic wave is known as the zeroth order antisymmetric Lamb wave (Zhang *et al.*, 1992). For a subsonic surface wave, the ''landing/launching'' angle θ_L is $\pi/2$; i.e., the acoustic wave that impinges on the shell tangentially will generate a subsonic Lamb wave that circumnavigates the elastic shell and sheds back to the receiver as shown in Fig. 7(c).

As a result, the acoustic backscattering model for this hard shell object can be expressed as

$$F_{\mathrm{bs}} \sim F_{\mathrm{FI}} + F_{\mathrm{Lamb}}, \tag{34}$$

where F_{FI} and F_{Lamb} represent scattering from the front interface of the animal and from the subsonic Lamb wave, respectively. Note that besides the two major peaks, there are some smaller arrivals in Fig. 8(i). These peaks are possibly due to scattering by a combination of other features of the animal and microstructure as well as from sidelobe artifacts of the PC processing discussed in Appendix D.

B. Spectral characteristics—Improving the SNR

As discussed above, if there is more than one arrival from the target, the signal $f_{\mathrm{bs}}(t)$ can be decomposed into a sum of a number of arrivals described in Eq. (19). If, by using PC processing, the echoes from different parts of an animal as well as from other scatterers such as microstructure can be resolved in the time domain, the time series can be gated in such a way that only the arrivals of interest are included. Such a gating rejects the resolvable unwanted arrivals which include echoes from microstructure and partial waves that may not be of interest. If we treat the unwanted arrivals together with the background white noise as the total effective noise, the resultant SNR could be improved from $E_w/(N_{\mathrm{white}}+E_{uw})$ to E_w/N_{white}, where E_w and E_{uw} are energies of wanted and unwanted arrivals, respectively, and N_{white} is the power density of the white noise.

The time series for three different zooplankton groups and their corresponding spectra are shown in Fig. 9, where the truncated time series and their corresponding spectra are plotted with thicker solid lines. For each animal, only two arrivals or partial waves are chosen, i.e., $N_j=2$ in Eq. (28). The spectra of the truncated time series can be considered as PWTS defined in Eq. (28). These spectra (thicker lines) are optimized outputs in that only the two major arrivals that dominate the scattering are included and most of the unwanted echoes stemming mainly from microstructure reverberation as well as some in-band noise are windowed out. As a result of the truncation, the hashy structure of the original spectra (thinner lines) has been removed, which indicates an improved SNR of the desired signal. The resultant spectra clearly illustrate the interferences between two rays, especially for the siphonophore whose original spectrum was too noisy to see the regular interference pattern due to the two rays.

In Fig. 9, since only one rectangular time window is used for each time series, we refer to this process as a ''truncation.'' However, in general, it is more appropriate to use the terminology ''windowing'' or ''gating'' to describe the process since multiple time windows can be used to include any number of wanted arrivals as long as the arrivals can be resolved. The number of time windows used in the process and the type of windowing depends on the purpose of the analysis.

Since spectral analysis automatically eliminates the out-of-band noise in the frequency domain while windowing of

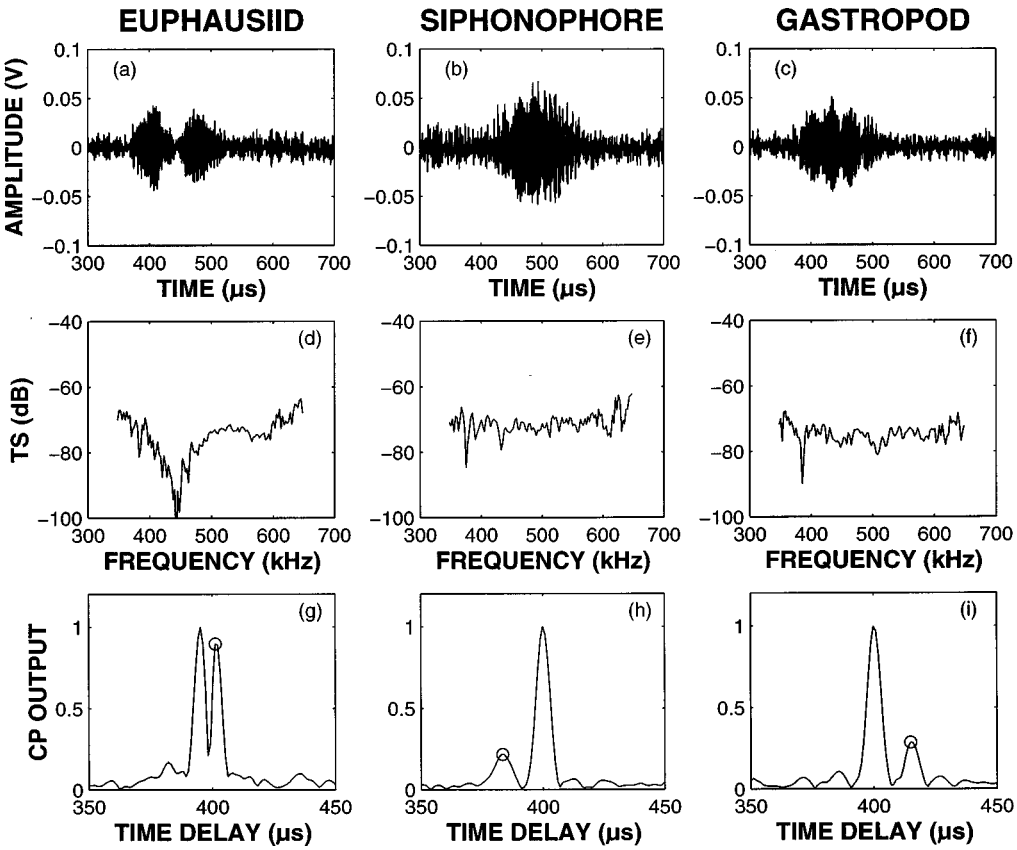

FIG. 8. Single ping analysis from three different zooplankton groups. (a), (d), and (g) for euphausiid; (b), (e) and (h) for siphonophore, and (c), (f) and (i) for gastropod. First row is the time series, second row is the target strength versus frequency, and the third row is the envelope of the CP output where the circled peaks are the secondary arrivals. The transmit signal is a chirp signal shown in Fig. 2(e). Note that the separation between the two major peaks in (g) (6.0 μs) is much smaller than that observed in the corresponding time series in (a) (65 μs).

the CP output can filter out some unwanted in-band signals in the time domain, the resultant PWTS in this process is expected to have a better output SNR as shown in Fig. 9.

C. Statistical characteristics

Since the scattering by live animals is a stochastic process, a statistical analysis of the time series of the CP output is required. This analysis provides at least two types of information: distributions of time difference between two major arrivals and their amplitude ratio (Tables I and II). To eliminate data with unacceptably high contamination due to noise and inherent sidelobe artifacts of the PC processing, we reject the pings whose SNR is below a certain level and whose amplitude ratio of the primary arrival (the largest peak) to the secondary arrival (the second largest peak) is larger than a preset threshold. This threshold is chosen to be the ratio of the main lobe to the largest sidelobe when the PC processing is performed on the received chirp signal in the calibration mode with no target present. As shown in Fig. 2(f), this ratio is about 10 in a noise-free situation and is purely due to the (processing sidelobe) artifacts of the PC operation (Appendix D).

1. Animal characterization

The histograms of the time difference and the amplitude ratio of primary-to-secondary arrivals for animals from three different zooplankton groups are shown in Fig. 10.

For a euphausiid, the histogram of the time difference between the first and second arrivals is narrowly distributed [Fig. 10(a)]. In contrast, the histograms for a 26-mm-long siphonophore [Fig. 10(c)] and a 2-mm-long gastropod [Fig. 10(e)] are more spread out and peaked at values greater than 10 μs.

In terms of the amplitude histogram, the euphausiid has the narrowest distribution (note that the scale for the euphausiid is different from those for the siphonophore and gastropod), and the siphonophore has the widest amplitude distribution. Table I summarizes the statistics of the time differences and amplitude ratios for the three different animals shown in Fig. 10.

2. Sizing animals

Certain dimensions of the animals can be estimated by examining the temporal separation between CP arrivals and relating those times to the dimensions using a scattering model. The accuracy of the estimates are limited, in part, by the temporal resolution of the signal. For example, for a chirp signal with a bandwidth of 250 kHz (a composite bandwidth due to the transmitter/receiver combination), the duration of the received signal can be compressed to about 4 μs, which corresponds to a spatial resolution of 3 mm in water for backscattering.

The histogram of the time difference and the amplitude ratio of primary-to-secondary arrivals from 200 pings for a

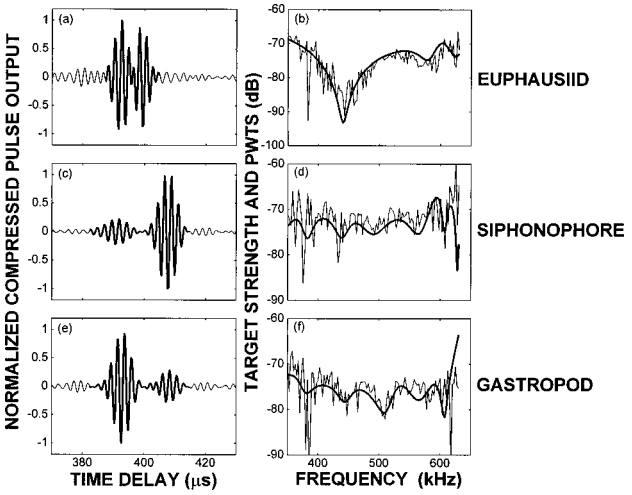

FIG. 9. Partial wave target strength (PWTS) for animals from three different zooplankton groups. (a) and (b) for euphausiid; (c) and (d) for siphonophore; and (e) and (f) for gastropod. The plots on the left column are normalized CP outputs (no demodulation). The thin lines are the original CP outputs while the thick lines are the filtered CP outputs using an optimum rectangular time window. The plots on the right column are TS (thin lines) and PWTS (thick lines). The TS is computed using Eq. (C2) while the PWTS is calculated using Eq. (28) and involves the filtered CP outputs. The transmit signal for all three animals is a chirp signal shown in Fig. 2(e). The partial wave analysis involves a window that includes the two main echoes and filters out echoes or noise outside the window.

25-mm-long euphausiid (*meganyctiphanes*) are shown in Fig. 10(a) and (b) (first row). The minimum value of the time difference in the histogram is 4.74 μs. Assuming that the minimum time difference corresponds to the case when the animal is oriented at broadside incidence, we use this value to estimate the average cylindrical diameter of this weakly scattering animal to be 3.6 mm (which is the same as the measured diameter of 3.6 mm). This agreement of the inferred animal size with that actually measured indicates that it is possible to size animals by using a PC technique. In the amplitude ratio histogram, the maximum value is around 1.1, which is a reasonable value for a weakly scattering target.

Table II lists the comparisons between the measured diameters of euphausiids and decapod shrimp and those computed from the time difference corresponding to the peak value of the histogram of the CP outputs similar to Fig. 10(a) and (b). Due to a combination of system noise and the limitation of the temporal resolution, the peak (mode) histogram values were used for Table II rather than the minimum values. The data were collected during the two cruises on Georges Bank and the two laboratory tank experiments as described at the beginning of this section. From Table II, we see that except for sample #4 the size of all animals are overestimated. This is due, in part, to the fact that the peak (mode) histogram values were used instead of minimum values. Another contribution to an overestimation is from the fact that the least time difference corresponds to the case in which the incidence is truly broadside [θ=0 in Fig. 7(a)]. For all angles of incidence away from broadside, the dimension of the cross section in the incident plane is increased by a factor of 1/cos θ resulting in an increased travel time.

For the NUWC data (sample #4), since only a one-cycle pulse (2 μs) was used, the output SNR was lower (since the SNR is proportional to the product of the bandwidth and the pulse length as discussed in Sec. I) and possible noise contamination in the sizing result is expected. The final overall results still agree reasonably well with the measured data, with relative errors less than 28%.

TABLE I. Summary of statistics for three different animal groups. Δ_t: time difference between two arrivals in CP output (minimum time for euphausiid), σ_t: standard deviation of Δ_t, ρ_a: amplitude ratio of two arrivals, and σ_a: standard deviation of ρ_a.

	Euphausiid	Gastropod	Siphonophore
Δ_t (μs)	4.74	17.37	(−)14.21
σ_t (μs)	0.72	3.77	6.80
ρ_a	1.03	5.65	6.67
σ_a	0.47	1.29	1.98

The histograms of the time difference and the amplitude ratio from 200 pings for a siphonophore are shown in Fig. 10(c) and (d) (second row). In plotting the histograms, we have used the ''pre-arrivals'' as the chosen secondary echoes representing the scattering from the body tissue since the video camera recording reveals that the main portion of the body tissue of the animal was closer to the transducer than the gas inclusion. The time difference at the peak of the histogram corresponds to a separation of 10.7 mm which should be compared with the 26-mm body length of the animal. The animal was partially curled during the experiment and the 10.7-mm value is consistent with scattering off an intermediate part of the body. Further studies show that the time differences between the main peak and ''post-arrival'' are more randomly distributed and the amplitudes of the latter are lower than those of the pre-arrivals which suggests that post-arrivals are likely resulting from randomly distributed micro-structure.

Figure 10(e) and (f) shows the histograms of the time difference and the amplitude ratio for a gastropod. As previously discussed, the secondary arrival is always a post-arrival since it corresponds to a subsonic Lamb wave that circumnavigates the elastic shell and then sheds back to the receiver and always arrives later than the primary arrival. Further work is required toward understanding the variability of the speed of the subsonic wave with respect to acoustic

TABLE II. Comparison of animal size between measured and that inferred (''computed'') from CP output. The inferred animal sizes are the values corresponding to the peaks (mode values) of the histograms based on measured time differences between primary and secondary arrivals from CP outputs.

Sample #	Species	Measured L (mm)	Measured $\langle D \rangle$ (mm)	Inferred $\langle D \rangle$ (mm)
1	Euphausiid[a]	30.0	3.6	4.7
2	Euphausiid[a]	30.3	3.7	4.8
3	Euphausiid[b]	34.0	3.5	4.8
4	Decapod Shrimp[c]	25.0	4.5	3.9
5	Decapod Shrimp[d]	17.8	3.0	3.8
6	Decapod Shrimp[d]	26.1	4.4	4.4

[a]1994 cruise data (shipboard).
[b]1993 cruise data (shipboard).
[c]October 1992–February 1993 NUWC laboratory data (on land).
[d]1990 WHOI laboratory data (on land).

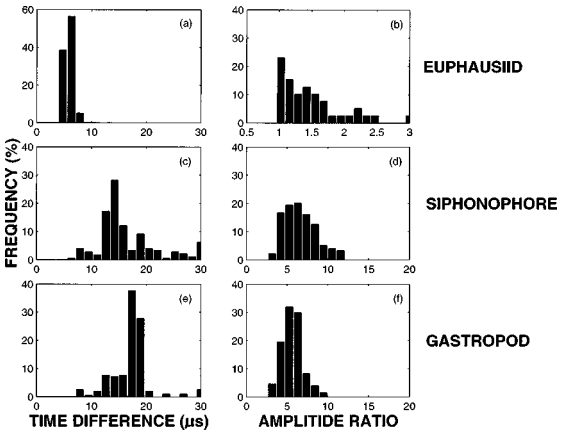

FIG. 10. Statistics of the CP outputs for animals from three different zooplankton groups. (a) and (b) for euphausiid; (c) and (d) for siphonophore; (e) and (f) for gastropod. The plots in the left column are histograms of time difference between the primary and secondary arrivals while the plots on the right are histograms of the peak amplitude ratios of the primary to the secondary arrivals. The transmit signal for all three animals is a chirp signal shown in Fig. 2(e).

frequency, shell thickness, size, orientation, and material properties before we can assess our ability to estimate size from the time difference information.

D. Relation between averaged TS and PWTS

Another interesting result is the comparison of the backscattering by the siphonophore with and without its gas inclusion. About 5-dB difference in average target strength was observed in Stanton *et al.* (1998a). The statistics of CP outputs for the siphonophore with and without gas is shown in Fig. 11, where the left three plots (first column) are for the siphonophore with gas as indicated in the figure while the other three are for the siphonophore without gas. Since the backscattering for the siphonophore without gas is weaker, to improve the SNR and obtain a more reliable estimate, we have used Eq. (31) to compute the PWTS of the largest arrival averaged over a frequency band. The largest arrivals for the two sets of data analyzed: one corresponds to the echoes from the gas when the whole (with gas) siphonophore is involved, and the other corresponds to the tissue when the gas-less animal is involved. Comparison of Fig. 11 and Fig. 5 in Stanton *et al.* (1998a) shows that the average values of TS for the siphonophore with and without its gas inclusion are about 1.7 dB and 6.7 dB higher than the averaged PWTS of the largest arrivals in the corresponding cases shown in Fig. 11(c) and (d). These differences can be explained as follows: for the siphonophore with its gas inclusion, since only the primary arrival (scattering from gas inclusion) is used to compute the averaged PWTS, the contribution from the body tissue is excluded. From Stanton *et al.* (1998b), it is found that the body tissue contributes about 1/3 of the total scattered energy. Thus excluding the body tissue scattering will result in a 1.8-dB drop $[10\log_{10}(2/3)]$ in estimated PWTS, which is close to the measured value of 1.7 dB.

For the case without the gas inclusion, Stanton *et al.* (1998b) used six rays with equal scattering strength but with randomly and uniformly distributed phases to simulate the statistical nature of the backscattering from the body tissue (no gas) of a siphonophore. If we choose one of these six rays to be the primary arrival (it is considered as the secondary arrival in the case where the gas inclusion is not removed), the exclusion of the other five rays would make the averaged PWTS about 7.8 dB $(10\log_{10}6)$ lower than the case when all rays are included [Fig. 5 in Stanton *et al.* (1998a)]. This predicted 7.8-dB difference based on the six-ray model with equal strength cannot explain a 6.7-dB reduction in the averaged PWTS as shown in Fig. 11(d). The six-ray model used in Stanton *et al.* (1998b) was satisfactory to describe the scattering from the body tissue of the animal since it agreed with the measured echo (Rayleigh-like) PDF reasonably well.

Further simulations show that the degree of agreement between data and the model is not inherently very sensitive to the number of rays involved in the statistical model as long as the number of rays exceeds five. However, since Fig. 11 is generated from the dominant ray only, the difference between the averaged TS and the averaged PWTS of the dominant arrival (scattering from the ''local acoustic center of mass'') is very sensitive to the number of rays that make up the total echo. A 6.7-dB difference mentioned above implies an 80% energy loss, which in turn suggests that a model with five rays of equal strength is more plausible in describing the scattering from the body tissue of this particular gas-bearing siphonophore under these experimental conditions. The echo amplitude PDF from five rays with equal strength is also Rayleigh-like (but less so than with six rays). The inclusion of only one out of five rays results in a $10\log_{10}(5)\simeq 7.0$-dB reduction in PWTS, which is a reasonable value as compared with the actually measured value of 6.7 dB. This difference in number of rays to model the scattering by the tissue does not affect the results in Stanton *et al.* (1998b) given the granularity of the measured echo PDFs.

From Fig. 10(c) and (d), it can be seen that the histograms of the scattering amplitude are not Rician PDFs [which well described the total echoes at a particular frequency in Stanton *et al.* (1998b)]. This is because the data used to generate the histograms are obtained from the CP outputs (peak value) which is the integration over a frequency band, whereas a Rician PDF describes the echo statistics for CW-like signals.

IV. SUMMARY

Pulse compression processing is a powerful tool for applications of acoustic scattering by live individual zooplankton as it improves the output SNR and temporal resolution of the echoes. Characteristics of the CP outputs of broadband scattering signals are studied in terms of the features of the scattered signals from acoustic targets. Broadband acoustic backscattering data from various experiments involving three animal groups are analyzed using the PC technique. The in-depth studies of temporal, spectral, and statistical characteristics of the CP outputs are presented in this paper. The following conclusions are made based on these studies:

(1) The results presented in this paper support our previously proposed ray models for the three different zooplankton groups based on the dominant scattering mecha-

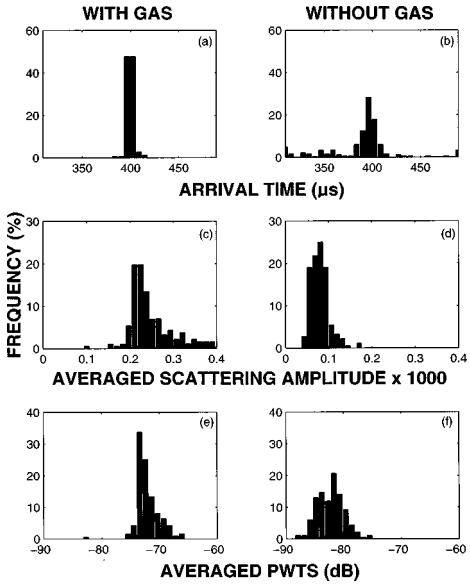

FIG. 11. Statistics of CP outputs from a siphonophore with and without gas inclusion. The averaged scattering amplitude [Eq. (30)] and its corresponding PWTS [Eq. (31)] are computed using the peak value of the primary arrival. The transmit signal is a chirp signal shown in Fig. 2(e).

nisms which depend on the different boundary conditions: (a) Shrimplike animals: one ray from the front interface and the others from other parts of the body. For near broadside incidence, a two-ray model adequately describes the dominant scattering features much of the time, where one ray is from the front interface and the other is from the back interface; (b) gas-bearing animals: one ray from the gas inclusion and the others from body tissue, the latter can sometimes be approximately represented by an equivalent ray scattered from the ''local acoustic center of mass'' of the body tissue; and (c) elastic shelled animals: one ray from the front interface and the other from the circumferential subsonic Lamb wave.

(2) Using an optimum window function based on the CP output, a partial wave contribution can be obtained to only include the dominant scattering features of interest and to eliminate certain unwanted signals. The TS based on such a windowed partial wave(s) can be characterized by the PWTS. As a result, the temporally gated CP output has been shown to dramatically improve the SNR of the corresponding frequency spectrum. A prerequisite condition for the windowing is that the echoes observed in the CP output must be resolved.

(3) The statistical studies on CP outputs demonstrate the ability of using the PC technique to size an individual animal and to differentiate zooplankton from different groups. The distinct characteristics of zooplankton from different groups (Table I) suggest the possible applications of the PC technique to zooplankton classification.

(4) The comparative study of the averaged PWTS versus the average TS of gas-bearing animals (siphonophore) allows a more quantitative estimate of the energy partition of the partial waves scattered from a single target and helps improve our understanding of the scattering mechanism.

The results presented in this paper have broader applications in that this technique can easily be extended to other areas such as fisheries acoustics.

ACKNOWLEDGMENTS

This work was supported by the National Science Foundation under Grant No. OCE-9201264 and the U.S. Office of Naval Research under Grant Nos. N00014-89-J-1729, N00014-94-1-0452, and N00014-95-1-0287. This is Woods Hole Oceanographic Institution contribution No. 9413.

APPENDIX A

For a chirp signal with a Gaussian envelope defined in Eq. (8), where the function $u(t)$ is given by Eq. (6), we can express a cosine by two exponential functions

$$\cos z = \frac{e^{iz}+e^{-iz}}{2}. \tag{A1}$$

The autocorrelation function of $u(t)$ is

$$\begin{aligned} R(\tau) &= \frac{1}{T}\int_{-\infty}^{\infty} u^*(t-\tau)u(t)w(t)dt, \\ &= \frac{1}{4T}\int_{-\infty}^{\infty}(e^{i\phi_0-A_0}+e^{-i\phi_0-A_0}) \\ &\quad \times(e^{i\phi_\tau-A_\tau}+e^{-i\phi_\tau-A_\tau})w(t)dt, \\ &= R_1(\tau)+R_2(\tau)+R_3(\tau)+R_4(\tau), \end{aligned} \tag{A2}$$

where $w(t)$ is a window function that depends on the pulse length T and the time delay variable τ. The above terms are defined as follows:

$$\begin{aligned} &\phi_0=\omega_0 t+\alpha t^2, \quad \phi_\tau=\omega_0(t-\tau)+\alpha(t-\tau)^2, \\ &A_0=\beta(t-T/2)^2, \quad A_\tau=\beta(t-\tau-T/2)^2, \end{aligned} \tag{A3}$$

and

$$\begin{aligned} R_1(\tau) &= \frac{1}{4T}\int_{-\infty}^{\infty} e^{i(\phi_0+\phi_\tau)-A_0-A_\tau}w(t)dt, \\ R_2(\tau) &= \frac{1}{4T}\int_{-\infty}^{\infty} e^{i(\phi_0-\phi_\tau)-A_0-A_\tau}w(t)dt, \\ R_3(\tau) &= \frac{1}{4T}\int_{-\infty}^{\infty} e^{-i(\phi_0+\phi_\tau)-A_0-A_\tau}w(t)dt, \\ R_4(\tau) &= \frac{1}{4T}\int_{-\infty}^{\infty} e^{-i(\phi_0-\phi_\tau)-A_0-A_\tau}w(t)dt. \end{aligned} \tag{A4}$$

Since $R_3(\tau)=R_1^*(\tau)$ and $R_4(\tau)=R_2^*(\tau)$, Eq. (A2) is then

$$R(\tau)=2\,\mathrm{Re}\{R_1(\tau)+R_2(\tau)\}. \tag{A5}$$

For simplicity, we use a rectangular window function $w(t)$ of width T. Substituting Eq. (A3) into Eq. (A4) and rearranging the exponential of the integrand, we have

$$R_j(\tau)=\frac{1}{4T}\int_{-\infty}^{\infty} e^{i(A_jt^2+B_jt+D_j)}\omega(t)dt,$$

$$=\frac{1}{4T}\int_{0}^{T-\tau} e^{i(A_jt^2+B_jt+D_j)}dt, \tag{A6}$$

where $j=1,2$ and

$$A_1=2(\alpha+i\beta),\quad A_2=2i\beta,$$

$$B_1=2\omega_0-2\alpha\tau-2i\beta(T+\tau),$$

$$B_2=2\alpha\tau-2i\beta(T+\tau), \tag{A7}$$

$$D_1=\alpha\tau^2-\omega_0\tau+i\beta\left(\frac{T^2}{2}+\tau^2+T\tau\right),$$

$$D_2=-\alpha\tau^2+\omega_0\tau+i\beta\left(\frac{T^2}{2}+\tau^2+T\tau\right).$$

Equation (A6) can be rearranged into the form of a Fresnel integral with a complex argument,

$$F(z)=\int_{z_1}^{z_2} e^{i(\pi/2)w^2}\,dw,$$

$$=C(z_2)+iS(z_2)-C(z_1)-iS(z_1), \tag{A8}$$

where $C(z)$ and $S(z)$ are sine and cosine Fresnel integrals (Abramowitz and Stegun, 1965). Equation (A5) becomes

$$R(\tau)=\frac{1}{2T}\sum_{j=1}^{2}\ \mathrm{Re}\left\{\sqrt{\frac{\pi}{2A_j}}\,e^{i(4A_jD_j-B_j^2)/4A_j}[C(H_{Uj})\right.$$

$$\left.-C(H_{Lj})+iS(H_{Hj})-iS(H_{Lj})]\right\}, \tag{A9}$$

where

$$H_{Uj}=\left(T-\tau+\frac{B_j}{2A_j}\right)\sqrt{\frac{2A_j}{\pi}},$$

$$H_{Lj}=\frac{B_j}{2A_j}\sqrt{\frac{2A_j}{\pi}}. \tag{A10}$$

Since $|R_j(\tau)|\propto\sqrt{\pi/2|A_j|}$, for $\alpha\gg\beta$, $R_2(\tau)\gg R_1(\tau)$, Eq. (A9) can be expressed approximately as

$$R(\tau)\approx\frac{1}{2T}\,\mathrm{Re}\left\{\sqrt{\frac{\pi}{2A_2}}\,e^{i(4A_2D_2-B_2^2)/4A_2}F_{sc}\right\},$$

$$=\frac{1}{4T}\sqrt{\frac{\pi}{\beta}}\,e^{-[(\beta^2+\alpha^2)/2\beta]\tau^2}\,\mathrm{Re}\{e^{i(\omega+\alpha T)\tau-i\pi/4}F_{sc}\}, \tag{A11}$$

where

$$F_{sc}=C(H_{U2})-C(H_{L2})+iS(H_{U2})-iS(H_{L2}) \tag{A12}$$

and

$$H_{U2}=\sqrt{\frac{2i\beta}{\pi}}\left(\frac{T-3\tau}{2}-i\,\frac{\alpha}{2\beta}\,\tau\right),$$

$$H_{L2}=\sqrt{\frac{2i\beta}{\pi}}\left(-\,\frac{T+\tau}{2}-i\frac{\alpha}{2\beta}\,\tau\right). \tag{A13}$$

It can be shown that $F_{sc}\approx\sqrt{2}e^{i\pi/4}$, thus we can obtain an approximate expression for $R(\tau)$

$$R(\tau)\approx\frac{1}{4T}\sqrt{\frac{2\pi}{\beta}}\,e^{-[(\beta^2+\alpha^2)/2\beta]\tau^2}\cos[(\omega_0+\alpha T)\tau]. \tag{A14}$$

It can be seen that $R(\tau)$ is a Gaussian modulated sine wave with a carrier angular frequency $\omega_0+\alpha T$, which is the same as that for an ideal chirp case given by Eq. (7) but with a Gaussian envelope,

$$R(\tau)_{\mathrm{env}}=\frac{1}{4T}\sqrt{\frac{2\pi}{\beta}}\,e^{-[(\beta^2+\alpha^2)/2\beta]\tau^2}, \tag{A15}$$

which is the same as that given by Cook (1967).

This result shows that the envelope of the CP output of a Gaussian envelope chirp is also Gaussian when the leading and trailing edges of the chirp signal are smoothly varying. Equation (A14) can also be obtained by applying the method of steepest descent to Eq. (A6).

APPENDIX B

For real functions $f(t)$ and $g(t)$, the correlation function $r_{fg}(\tau)$ is defined as

$$r_{fg}(\tau)=f(t)\otimes g(t),$$

$$=\int_{-\infty}^{\infty}f(t-\tau)g(t)dt. \tag{B1}$$

By denoting $F(f)$ and $G(f)$ as the Fourier transforms of $f(t)$ and $g(t)$, it is well known that

$$f(t)*g(t)\Leftrightarrow F(f)G(f),$$

$$f(t)\otimes g(t)\Leftrightarrow F(-f)G(f), \tag{B2}$$

where the operation symbols ''$*$'' and ''$\otimes$'' stand for convolution and correlation, respectively. The symbol ''$\Leftrightarrow$'' represents equivalency between the different domains (time and frequency). Since $f(t)$ is a real function, we have

$$F(-f)=F^*(f), \tag{B3}$$

where F^* is the complex conjugate of F. Using Eqs. (B1)–(B3), we can obtain the following relation:

$$f(t)*(g(t)\otimes h(t))\Leftrightarrow F(f)G^*(f)H(f)$$

$$=(F^*(f)G(f))^*H(f)$$

$$\Leftrightarrow(f(t)\otimes g(t))\otimes h(t). \tag{B4}$$

Thus

$$f(t)*(g(t)\otimes h(t))=(f(t)\otimes g(t))\otimes h(t). \tag{B5}$$

Similarly, we can derive

$$(f(t)*g(t))\otimes h(t)=f(t)\otimes(g(t)\otimes h(t)), \tag{B6}$$

$$f(t)\otimes(g(t)*h(t))=(h(t)\otimes f(t))\otimes g(t). \tag{B7}$$

The following relations can also be obtained in a straightforward way:

$$(f(t)\otimes g(t))\otimes h(t)=(h(t)\otimes g(t))\otimes f(t), \tag{B8}$$

$$f(t)\otimes(g(t)\otimes h(t))=g(t)\otimes(f(t)\otimes h(t)). \tag{B9}$$

APPENDIX C

The frequency response of a compressed backscattering signal can be obtained by taking the Fourier transform of Eq. (15)

$$Y(f)=\frac{k_c}{r^2}F_{\mathrm{bs}}(f)R_{ss}(f)e^{-i\omega t_0}+k_cR_{sn}(f), \tag{C1}$$

where $F_{\mathrm{bs}}(f)$, $R_{ss}(f)=S_0^*(f)S_0(f)$, and $R_{sn}(f)=S_0^*(f)N(f)$ are the Fourier transforms of the signal $f_{\mathrm{bs}}(t)$, autocorrelation $r_{ss}(t)$, and cross correlation $r_{sn}(t)$, respectively. $S_0(f)$ and $N(f)$ are Fourier transforms of the transmit signal, $s_0(t)$, and noise, $n(t)$, respectively. The power spectrum of the backscattering is then obtained by multiplying $Y^*(f)$ on both sides of Eq. (C1) and normalizing by $(k_c/r^2)^2R_{ss}(f)R_{ss}^*(f)$:

$$\begin{aligned}P(f)&=\frac{r^4Y(f)Y^*(f)}{k_c^2R_{ss}(f)R_{ss}^*(f)}\\&=\frac{[F_{\mathrm{bs}}(f)R_{ss}(f)e^{-i\omega t_0}+r^2R_{sn}(f)][F_{\mathrm{bs}}^*(f)R_{ss}^*(f)e^{i\omega t_0}+r^2R_{sn}^*(f)]}{R_{ss}(f)R_{ss}^*(f)}\\&=F_{\mathrm{bs}}(f)F_{\mathrm{bs}}^*(f)+\frac{F_{\mathrm{bs}}(f)N^*(f)e^{-i\omega t_0}}{S_0^*(f)}r^2+\frac{F_{\mathrm{bs}}^*(f)N(f)e^{i\omega t_0}}{S_0(f)}r^2+\frac{r^4N(f)N^*(f)}{S_0(f)S_0^*(f)}\\&=|F_{\mathrm{bs}}(f)|^2+2r^2\frac{\mathrm{Re}\{F_{\mathrm{bs}}(f)S_0(f)N^*(f)e^{-i\omega t_0}\}}{S_0(f)S_0^*(f)}+\frac{|r^2N(f)|^2}{|S_0(f)|^2}.\end{aligned} \tag{C2}$$

The last expression in Eq. (C2) can be proven to be equivalent to that obtained by applying a standard spectral analysis to the original (unprocessed) time series. This result indicates that directly taking a Fourier transform of the CP output cannot improve the SNR of the signal in the frequency domain compared with a standard spectral analysis.

APPENDIX D

To evaluate the influence of the tether and the superglue used with the gastropods in the shipboard scattering experiments, data were collected without the presence of any animal in the acoustic beam. Only the tether and a small drop of superglue attached to it were in the acoustic beam. It was observed that the scattering contribution from the superglue was much larger than that from the tether. Since superglue was used only for the gastropod scattering experiment, our analysis of assessing signal contamination is based on the data associated with the configuration for the gastropod experiment.

The primary arrivals in CP outputs for siphonophores and gastropods are always very strong and can be considered as reliable echoes from the animals. This observation is consistent with the result of Stanton *et al.* (1998a). In that analysis, it is found that within the usable frequency band, the target strength of the combination of the tether and superglue is at least 6 dB lower than those from the gastropods used in the experiment which implies the SNR of the received scattering signal is always 6 dB higher than the background noise (tether, microstructure and other noise).

However, since the secondary arrivals are usually much smaller than the primary arrivals (except for shrimplike animals), a crucial concern to our CP analysis is that whether the secondary arrivals are real and reliable or whether they are contaminated by the presence of the tether, superglue (when it was used), and the microstructure, or even an artifact of PC processing.

One data set that involves only the tether and a small drop of superglue attached to the tether is used to evaluate how these factors affect our CP analysis. The data were acquired after a gastropod was carefully removed from the water (superglue was not visible on the removed animal). The transmitted signal was a chirp sweeping from 300 kHz to 700 kHz over a 200-μs period as shown in Fig. 2(e). To simulate a worst case, random noise with a constant SNR of

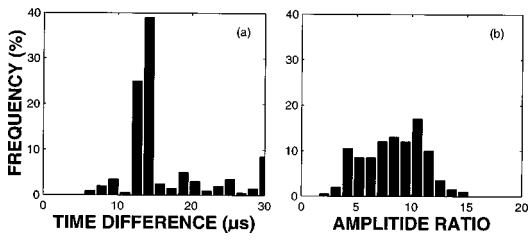

FIG. D1. Study of the influence of the superglue, the tether, microstructure, and artifacts of PC processing on the CP output. The histograms are obtained from the CP outputs from 200 pings. Random noise is added in such a way that the SNR of each ping is kept constant at 6 dB. The signal here refers to the largest echo of the reverberation time series when no animal is attached to the tether. The transmit signal is a chirp signal shown in Fig. 2(e).

6 dB is added to each ping. In this case, the signal is the reverberation from the tether, microstructure, and superglue. The ''replicate'' of the signal used in the PC processing is the received signal in calibration mode shown in Fig. 2(e).

The statistics of the CP output of 200 pings of reverberation only (no animal) is shown in Fig. D1, where the time difference between primary and secondary arrivals and amplitude ratio of primary to secondary arrival are given in Fig. D1(a) and (b), respectively. The secondary arrivals are determined by selecting the second largest peak of the CP time series output regardless of whether the peak corresponds to the pre- or post-arrival. The time difference and the amplitude ratio shown in Fig. D1 are centered at 14 μs and 9–10, respectively. From Fig. 2(f) (calibration mode), the time difference between the primary and the secondary arrivals is found to be 13.5 μs, and the amplitude ratio of the two arrivals is 11. Since the signal in Fig. 2(e) is the direct arrival from the bistatic calibration (where the tether and superglue are absent) and has a very high SNR, the influence of microstructure is weak and can be readily ignored. Thus it is reasonable to assert that the secondary arrivals in Fig. 2(f) stem from edges of the time series and are essentially (sidelobe) artifacts of the PC process as mentioned in Sec. I. Comparison of Fig. D1 and Fig. 2(f) reveals that the inclusion of tether and superglue as well as microstructure does not have a significant effect on the CP output (both time difference and amplitude ratio remain the same). We conclude that the error of our CP analysis is dominated by the artifact of the PC and the influence of the tether and the superglue on the CP output is not significant.

Abramowitz, M., and Stegun, I. A. (**1965**). *Handbook of Mathematical Functions* (Dover, New York).

Bracewell, R. N. (**1986**). *The Fourier Transform and Its Applications* (McGraw-Hill, New York).

Chu, D., Stanton, T. K., and Wiebe, P. H. (**1992**). ''Frequency dependence of sound backscattering from live individual zooplankton,'' ICES J. Mar. Sci. **49**, 97–106.

Chu, D., Foote, K. G., and Stanton, T. K. (**1993**). ''Further analysis of target strength measurements of Antarctic krill at 38 kHz and 120 kHz: Comparison with deformed cylinder model and inference of orientation distribution,'' J. Acoust. Soc. Am. **93**, 2985–2988.

Clay, C. S. (**1987**). ''Optimum time domain signal transmission and source location in a waveguide,'' J. Acoust. Soc. Am. **81**, 660–664.

Clay, C. S., and Medwin, H. (**1977**). *Acoustical Oceanography: Principles and Applications* (Wiley–Interscience, New York).

Cook, C. E., and Bernfeld, M. (**1967**). *Sonar Signals* (Academic, New York).

Ehrenbreg, J. E., Ewart, T. E., and Morris, R. D. (**1978**). ''Signal processing techniques for resolving individual pulses in a multipath signal,'' J. Acoust. Soc. Am. **63**, 1861–1865.

Holliday, D. V., Pieper, R. E., and Kleppel, G. S. (**1989**). ''Determination of zooplankton size and distribution with multi-frequency acoustic technology,'' Journal du Conseil International pour L'Exploration de la Mer **46**, 52–61.

Holliday, D. V., and Pieper, R. E. (**1995**). ''Bioacoustical oceanography at high frequencies,'' ICES J. Mar. Sci. **52**, 279–296.

Parvulescu, A. (**1961**). ''Signal detection in a multipath medium by M.E.S.S. processing,'' J. Acoust. Soc. Am. **33**, 1674.

Price, R. (**1956**). ''Optimum detection of random signals in noise, with application to scatter-multipath communication,'' IRE Trans. Inf. Theory **IT-2**, 125–135.

Robinson, E. A. (**1980**). *Geophysical Signal Analysis* (Prentice-Hall, Englewood Cliffs, NJ).

Siebert, W. Mc. (**1956**). ''A radar detection philosophy,'' IRE Trans. Inf. Theory **IT-2**, 204–221.

Stanton, T. K., Chu, D., and Wiebe, P. H. (**1998a**). ''Sound scattering by several zooplankton groups. I. Experimental determination of dominant scattering mechanisms,'' J. Acoust. Soc. Am. **103**, 225–235.

Stanton, T. K., Chu, D., and Wiebe, P. H. (**1998b**). ''Sound scattering by several zooplankton groups. II. Scattering models,'' J. Acoust. Soc. Am. **103**, 236–253.

Stanton, T. K., Clay, C. S., and Chu, D. (**1993a**). ''Ray representation of sound scattering by weakly scattering deformed fluid cylinders: Simple physics and application to zooplankton,'' J. Acoust. Soc. Am. **94**, 3454–3462.

Stanton, T. K., Chu, D., Wiebe, P. H., and Clay, C. S. (**1993b**). ''Average echoes from randomly oriented random-length finite cylinders: Zooplankton models,'' J. Acoust. Soc. Am. **94**, 3463–3472.

Stanton, T. K., Wiebe, P. H, Chu, D., and Goodman, L. (**1994a**). ''Acoustic characterization and discrimination of marine zooplankton and turbulence,'' ICES J. Mar. Sci. **51**, 469–479.

Stanton, T. K., Wiebe, P. H., Chu, D., Benfield, M. C., Scanlon, L., Martin, L., and Eastwood, R. L. (**1994b**). ''On acoustic estimates of zooplankton biomass,'' ICES J. Mar. Sci. **51**, 505–512.

Thorne, P. D., Brudner, T. J., and Water, K. R. (**1994**). ''Time-domain and frequency-domain analysis of acoustic scattering by spheres,'' J. Acoust. Soc. Am. **95**, 2478–2486.

Thorne, P. D., Water, K. R., and Brudner, T. J. (**1995**). ''Acoustic measurements of scattering by objects of irregular shape,'' J. Acoust. Soc. Am. **97**, 242–251.

Turin, G. L. (**1960**). ''An introduction to matched filters,'' IRE Trans. Inf. Theory **IT-6**, 311–329.

Van Trees, H. L. (**1968**). *Detection, Estimation, and Modulation Theory* (Wiley, New York), Pt. III.

Van Vleck, J. H., and Middleton, D. (**1946**). ''A theoretical comparison of the visual, aural, and meter reception of pulsed signals in the presence of noise,'' J. Appl. Phys. **17**, 940–971.

Whalen, A. D. (**1971**). *Detection of Signals in Noise* (Academic, New York).

Winder, A., and Loda, C. J. (**1981**). *Space-time Information Processing* (Peninsula, Los Altos, CA), pp. 153–156.

Zhang, L. G., Sun, N. H., and Marston, P. L. (**1992**). ''Midfrequency enhancement of the backscattering of tone bursts by thin elastic shells,'' J. Acoust. Soc. Am. **91**, 1862–1874.

Ultrasonic pulse propagation in inhomogeneous one-dimensional media

N. Cretu
Catedra de Fizica, Universitatea Transilvania din Brasov, Brasov, Romania

P. P. Delsanto
INFM—Dip. Fisica, Politecnico di Torino, Torino, Italy

G. Nita
Catedra de Fizica, Universitatea Transilvania din Brasov, Brasov, Romania

C. Rosca
Catedra de Rezistenta si Vibratii, Universitatea Transilvania din Brasov, Brasov, Romania

M. Scalerandi
INFM—Dip. Fisica, Politecnico di Torino, Torino, Italy

I. Sturzu
Catedra de Fizica, Universitatea Transilvania din Brasov, Brasov, Romania

(Received 10 October 1997; accepted for publication 23 March 1998)

The propagation of acoustic or ultrasonic pulses and waves in 1-D media with continuous inhomogeneities due to spatial variations in density, Young modulus, and/or cross section of the propagation medium is discussed. A semianalytical approach leads to a general form of the solution, which can be described by a function, whose Taylor expansion is absolutely convergent. The special case of a periodic inhomogeneity is studied in detail and the dispersion law is found. It is also shown that a finite width pulse is generally not broken down by the inhomogeneity, even though its law of motion is perturbed. A numerical treatment based on the Local Interaction Simulation Approach (LISA) is also considered, and the results of the simulations compared with the semianalytical ones.
 [S0001-4966(98)00807-8]

PACS numbers: 43.20.−f [ANN]

INTRODUCTION

The topic of acoustic wave propagation in inhomogeneous media is very challenging both from a theoretical and an experimental point of view. It also acquires practical relevance, since several experimental techniques and applications (e.g., in nondestructive evaluation) are based on the interaction between propagating acoustic (or ultrasonic) pulses and local inhomogeneities.

While the propagation of electromagnetic pulses in inhomogeneous media has been widely studied, less attention has been devoted to the case of acoustic pulses. Lekner[1,2] and Nayfeh[3] have discussed the propagation of sound in a medium with planar stratification, described by means of discontinuities in the wave speed[1,3] or in its spatial derivative.[2] Jeng and Liu[4] have considered point sources in media with elastic properties varying both with the square root and with the square of the distance. The problem of reflection from inhomogeneities has been studied by Bremmer,[5] Meyer[6] and Gingold[7] for media with propagation velocity varying with the distance. The reflection from an inhomogeneous space has been discussed by Brekhowskikh.[8]

More recently, Oberle and Cammarata[9] have derived an equation of motion for a one-dimensional medium with constant density and an x-dependent elastic modulus. A general form of solution is obtained as an infinite series with unknown coefficients and a specific solution is found for media whose elastic constants vary linearly with x. In the wave equation, it may be preferable to assume as x dependent the elastic constants, rather than the velocity. In fact, since inhomogeneities cause dispersions in finite width pulses, the propagation velocity becomes an ill-defined parameter.

The treatment of Ref. 9 is restricted to media with uniform density and width. Since also the density and width of the specimen may vary with x, it is desirable to adopt a more general treatment. Also, a perturbative approach has been introduced to solve the problem by McIntyre and co-workers in Ref. 10. However, a completely analytical solution of the problem is not possible in the general case. A valid alternative may be a semianalytical solution, based on an expansion of the pulse in an infinite series, whose coefficients may be calculated numerically through iteration equations, usually in the (k,ω) domain. Another possibility is the numerical simulation in the (x,t) domain of the pulse propagation by means of the Local Interaction Simulation Approach (LISA).[11]

The knowledge of dispersive and reflective properties of media with elastic inhomogeneities is of paramount importance in several applications. For instance, multilayered structures and/or composites may be modeled as continuous inhomogeneous media. The latter may be described as structures with periodic variations in space of the Young modulus and density, with periodicity equal to the distance between successive fiber bundles.[10] Also, technical devices, such as ultrasound concentrators (used, e.g., for drilling), are based on the amplification of a pulse due to variations in the cross section of the device.[12] A method for computing the optimal

length and shape of the tool for obtaining maximal amplification may be an advantageous substitute for the existing empirical techniques.[13]

In Sec. I, a semianalytical approach, based on Fourier and Taylor expansions of both the solution and the inhomogeneity, is presented, leading to iteration equations for the expansion coefficients in the (x,ω) domain. Numerical results obtained applying this approach are presented in Sec. II, for monochromatic waves (in the high- and low-frequency domain) and for finite width pulses. In Sec. III, numerical simulations in the (x,t) domain using the LISA method are discussed and compared with the semianalytical solutions.

I. SEMIANALYTICAL APPROACH

Let us consider an elastic semi-infinite bar with a symmetry axis, which we shall call x axis. We assume that its density ρ, width (cross section) S and Young modulus E may vary, albeit with a certain regularity, with x. The problem of an ultrasonic longitudinal wave propagating along the x direction may then be reduced, at least as a first approximation or in a perturbation treatment, to the one-dimensional wave equation

$$f(x)u_{tt}(x,t)=\partial_x(g(x)u_x(x,t)), \tag{1}$$

where $u(x,t)$ is the particle displacement and

$$\begin{aligned} f(x)&=\rho(x)S(x)=f_0(1+\eta_1 p(x)),\\ g(x)&=E(x)S(x)=g_0(1+\eta_2 q(x)), \end{aligned} \tag{2}$$

where f_0 and g_0 are the values corresponding to a ''reference'' homogeneous bar. By choosing properly the two functions $p(x)$ and $q(x)$, Eq. (1) can describe

(i) a bar with x-dependent Young modulus ($\eta_1=0$);
(ii) a bar with x-dependent density ($\eta_2=0$);
(iii) a bar with x-dependent cross section [$\eta_1=\eta_2$ and $p(x)=q(x)$]; or any combination thereof.

Introducing in Eq. (1) a Fourier transform for $u(x,t)$,

$$u(x,t)=\frac{1}{2\pi}\int_{-\infty}^{\infty}\tilde{u}(x,\omega)e^{-i\omega t}\,d\omega, \tag{3}$$

we obtain, for each Fourier component $\tilde{u}(x,\omega)$,

$$\omega^2 f(x)\tilde{u}(x,\omega)+\partial_x(g(x)\tilde{u}_x(x,\omega))=0. \tag{4}$$

Equation (4) may be solved directly. However, as already remarked in Ref. 9, the problem becomes more tractable after a Taylor expansion for $f(x)$, $g(x)$ and $\tilde{u}(x,\omega)$:

$$f(x)=\sum_{n=0}^{\infty}a_n(x-x_0)^n, \tag{5}$$

$$g(x)=\sum_{n=0}^{\infty}b_n(x-x_0)^n, \tag{6}$$

$$\tilde{u}(x,\omega)=\sum_{n=0}^{\infty}c_n(\omega)(x-x_0)^n. \tag{7}$$

By substituting Eqs. (5)–(7) into Eq. (4), one obtains, after some calculations, a recurrence relationship for the coefficients $c_k(\omega)$ $(k\geqslant 2)$:

$$\begin{aligned} c_{n+2}=-\frac{1}{(n+1)(n+2)(1+\eta_2 b_0)}\Bigg((1+\eta_1 a_0)\frac{\omega^2}{v^2}c_n\\ +\sum_{m=1}^{n+1}\Bigg(\eta_1 a_m\frac{\omega^2}{v^2}c_{n-m}+\eta_2 b_m\\ \times(n+1)(n-m+2)c_{n-m+2}\Bigg)\Bigg), \end{aligned} \tag{8}$$

where $v=\sqrt{g_0/f_0}$ represents the phase velocity of a wave traveling in the reference homogeneous bar. The initial values c_0 and c_1 are given by

$$c_0=\tilde{u}(x_0,\omega)=\int_{-\infty}^{\infty}u(x_0,t)e^{i\omega t}\,dt,$$

$$c_1=\left.\frac{\partial\tilde{u}(x,\omega)}{\partial x}\right|_{x=x_0}.$$

Using a retardation condition for the injection of the pulse in $x=x_0$,

$$u(x,t)=\Phi(t-x/v), \tag{9}$$

it follows that

$$\begin{aligned} \tilde{u}(x,\omega)&=\int_{-\infty}^{\infty}\Phi(t-x/v)e^{i\omega t}\,dt\\ &=e^{i\frac{\omega}{v}(x-x_0)}\tilde{u}(x_0,\omega). \end{aligned} \tag{10}$$

Consequently,

$$c_1=i\frac{\omega}{v}\tilde{u}(x_0,\omega)=i\frac{\omega}{v}c_0. \tag{11}$$

Therefore, given c_0, i.e., given $u(x_0,t)$ for a single point x_0, each coefficient c_k can be determined. As a result, $\tilde{u}(x,\omega)$ may be evaluated for any ω and any x, inside the convergence radius of the Taylor expansion. If the interval (x_0,x_F), in which Eq. (1) needs to be solved, extends beyond the convergence range, successive Taylor expansions can be performed to cover it entirely.

An optimal speed-up may be obtained in the numerical implementation of the method, by dividing the interval (x_0,x_F) into many suitably small intervals Δx, in which the Taylor expansions are performed. Thus very few Taylor components are required for each interval Δx and the total CPU time for the calculation may be reduced. As shown in the Appendix, five to ten Taylor components are generally sufficient, if a suitably fine discretization of the integration interval is introduced (steps from about 0.005λ to 0.02λ).

The numerical continuation of the function is, of course, based on an approximate solution, with an associated error, which is also expected to propagate from one interval to the following ones. However, as shown in the Appendix, the

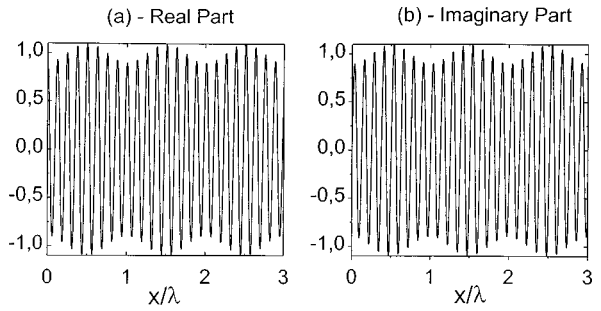

FIG. 1. Real and imaginary parts of a monochromatic wave for $\omega = 10\pi/\lambda$, $\eta_1 = 0$ and $\eta_2 = 0.5$.

degradation in accuracy does not increase with the number of intervals, ensuring a good convergence of the proposed numerical technique.

II. RESULTS AND DISCUSSION

We now apply the semianalytical method described in the previous section to study the propagation of pulses of different shapes in inhomogeneous media. We approximate the propagating pulse as a continuous superposition of monochromatic waves

$$u(x,t) = \mathrm{Re}\left(\sum_{\omega} \tilde{u}(x,\omega) e^{-i\omega t} \Delta\omega \right), \tag{12}$$

where it is assumed that a proper discretization of ω has been performed in the interval $(-\infty, \infty)$ and used in the summation.

Starting from an analysis of the propagation of the individual monochromatic components, we wish to assess the effect of a periodic inhomogeneity of the kind

$$\begin{aligned} f(x) &= f_0 \left(1 + \eta_1 \cos\left(\frac{2\pi}{\lambda} x \right) \right), \\ g(x) &= g_0 \left(1 + \eta_2 \cos\left(\frac{2\pi}{\lambda} x \right) \right), \end{aligned} \tag{13}$$

where λ (henceforth called ''inhomogeneity period'') represents the spatial periodicity of the specimen. The case of linear x dependence has been also analyzed with a different method by Oberle *et al.*[9] Their results have been confirmed by our present study.

A. Propagation of the monochromatic components

In Figs. 1 and 2 the behavior of the individual Fourier components is investigated for low and high frequencies in the case $\eta_1 = 0$ and $\eta_2 = 0.5$.

In Fig. 1, the real and imaginary parts of $\tilde{u}(x,\omega)$ are reported for $\omega = 10\pi/\lambda$. In both plots we observe periodic oscillations modulated both in amplitude and phase. The real and imaginary parts are respectively even and odd functions of x with a period equal to the one of the inhomogeneity. Writing the monochromatic wave $u_\omega(x,t)$ as

$$u_\omega(x,t) = A(x,\omega) e^{i\Phi(x,\omega,t)}, \tag{14}$$

where $\Phi(x,\omega,t) = \phi(x,\omega) - \omega t$, we can define the ''pseudo-wave-number'' $k(x,\omega)$ and the phase velocity $v_\Phi(x,\omega)$ as

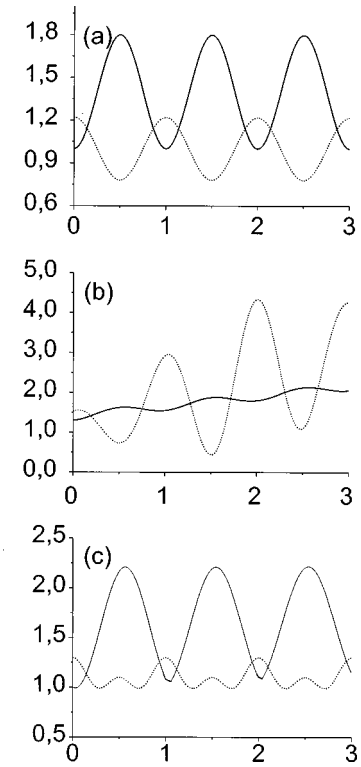

FIG. 2. Relative amplitude (solid line) and phase velocity (dashed line) versus x/λ for monochromatic waves of (a) high frequency ($\omega = 10\pi/\lambda$); (b) intermediate frequency ($\omega = \pi/\lambda$); and (c) low frequency ($\omega = 0.1\pi/\lambda$). $\eta_1 = 0$; $\eta_2 = 0.5$.

$$k(x,\omega) = \frac{\partial \phi(x,\omega)}{\partial x}, \quad v_\Phi(x,\omega) = \frac{\omega}{k(x,\omega)}. \tag{15}$$

In Fig. 2(a)–(c), $A(x,\omega)/A_0$ and $v_\Phi(x,\omega)/v$ are plotted versus x/λ for a high- ($\omega = 10\pi/\lambda$), an intermediate- ($\omega = \pi/\lambda$) and a low- ($\omega = 0.1\pi/\lambda$) frequency monochromatic wave, respectively. Here A_0 is the initial amplitude of the monochromatic signal. In the present context we call low frequencies those for which the wave period is much larger than the inhomogeneity period, i.e.,

$$\frac{2\pi}{\omega} \sqrt{\frac{g_0}{f_0}} \gg \lambda. \tag{16}$$

Choosing units for which $g_0 = f_0$, this condition is equivalent to $\omega \ll 2\pi/\lambda$. Vice versa, for high frequencies $\omega \gg 2\pi/\lambda$.

The behaviors of the phase velocity and relative amplitude in the three frequency domains look very different. For high frequencies [see Fig. 2(a)], both quantities can be described as sinusoidal functions with period λ. In the intermediate region [see Fig. 2(b)], due to resonance effects, they are no longer periodic in space and the difference from the corresponding variables in the homogeneous case increases with x. In the low-frequency region [Fig. 2(c)] they are again periodic, with the same period as the inhomogeneity, but no longer sinusoidal. Completely analogous is the behavior of the pseudo-wave-number, not plotted for brevity.

The dispersion law for the case $\eta_1 = \eta_2 = 0.2$ is depicted in Fig. 3, where the phase velocity and amplitude are plotted versus $\omega/10\pi\lambda$ for $x = 3\lambda$. We observe no dispersion for

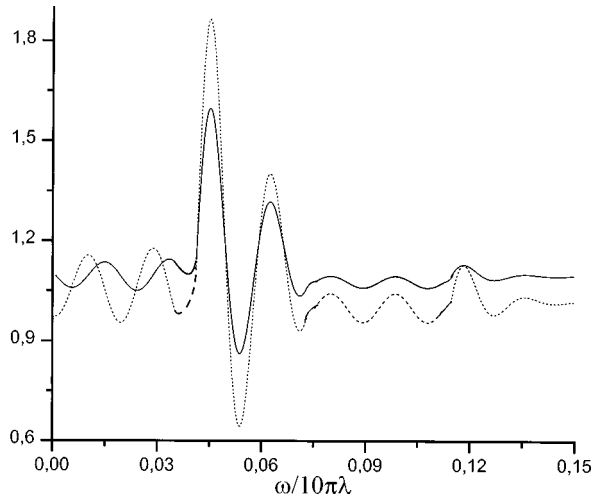

FIG. 3. Relative amplitude (solid line) and phase velocity (dashed line) versus $\omega/10\pi\lambda$ for $x=3\lambda$, and $\eta_1=0, \eta_2=0.2$.

high- and low-frequency components, since at the end of each inhomogeneity period both the amplitude and the phase velocity assume again the initial value, as in a homogeneous bar. However, we can observe a significant dispersion in the intermediate frequency range, for which the phase velocity increases during each inhomogeneity period, leading to significant distortions in finite width pulses.

B. Propagation of finite pulses

We have also applied the method described in Sec. I to study the propagation of several kinds of finite pulses in inhomogeneous media. The initial condition $u(0,t)$ has been used for the determination of the initial conditions for the Fourier components $\tilde{u}(0,\omega)$. An inverse Fourier transform of the components at any x allows the determination of the propagated pulse at any x and t.

Figure 4 displays six snapshots of the propagation of an initially Gaussian pulse in the case $\eta_1=0$ and $\eta_2=0.2$. The initial condition for its Fourier components is assumed to be

$$c_0(\omega)=Ae^{-\omega^2/4}, \tag{17}$$

with $A=1$. The pulse is not losing its shape altogether, but modifies it periodically following the inhomogeneity period. Also, the group velocity is not constant: e.g., the displacement of the peak position is approximatively $0.37x/\lambda$ from $t=24$ to $t=28$ a.u., but approximatively $0.26x/\lambda$ for an equal time interval between $t=32$ and $t=36$. The dispersion appearing in the snapshots at $t=24,28,36$ and 40 is due to the intermediate frequency components, which are relevant in the description of the Gaussian pulse.

The law of motion of the pulse (peak position versus time) displays a periodic oscillation of the peak position around the value expected in the homogeneous case (set equal to zero), as shown in Fig. 5(a). The relative group velocity and peak amplitude for the same pulse versus x/λ are reported in Fig. 5(b). Both plots are periodic in space with the same period as the inhomogeneity. The amplitude maxima grow up slowly with distance due to the dispersion of the intermediate frequency components. The maxima are

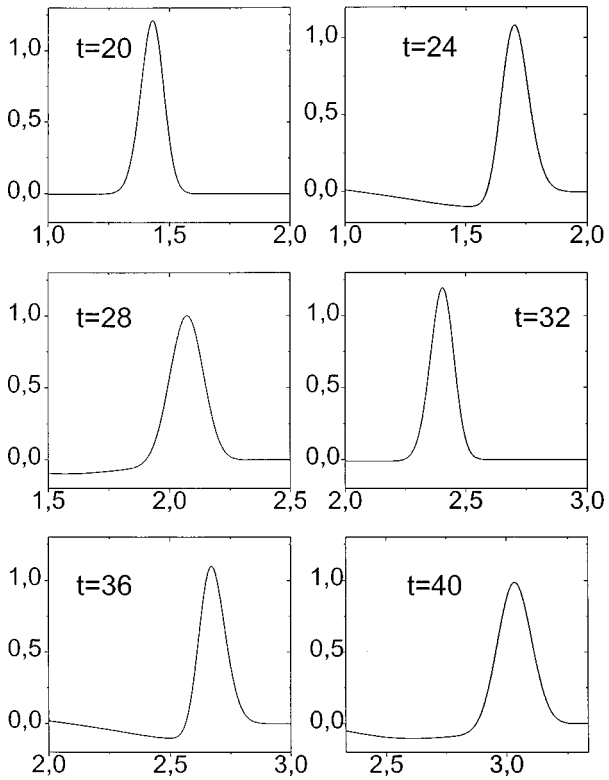

FIG. 4. Snapshots at different times (in a.u.) of the propagation of an initially Gaussian pulse, in the case $\eta_1=\eta_2=0.2$.

slightly shifted from the expected position $x=(2n+1)\lambda/2$. We also observe that the amplitude maxima do not correspond exactly to the group velocity minima.

The propagation of a Gaussian-modulated cosine pulse, which is of interest for applications as a probing signal in the field of ultrasonic nondestructive evaluation (NDE), is illustrated in Fig. 6 for the case $\eta_1=\eta_2=\eta=0.5$. The initial condition for its Fourier components is

$$c_0(\omega)=Ae^{-(\omega-\omega_0)^2/4}, \tag{18}$$

where $\omega_0=60\pi/\lambda$. We observe that no dispersion appears (since the contribution of low-frequency components is negligible), even though, inside each inhomogeneity period, an asymmetry arises and the amplitudes and distances between secondary peaks vary. The law of motion and the pulse amplitude and group velocity are plotted in Fig. 7. The behavior is still periodic, but quite different from the one shown in

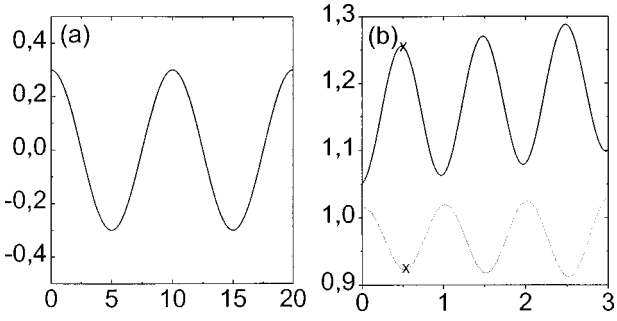

FIG. 5. (a) Law of motion (peak position minus x/λ vs t); (b) relative amplitude (solid line) and phase velocity (dashed line) versus x/λ for a source Gaussian pulse, in the case $\eta_1=0, \eta_2=0.2$.

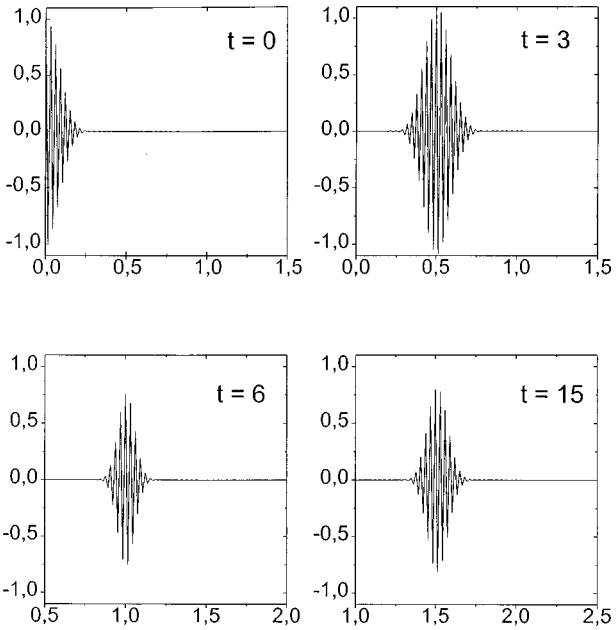

FIG. 6. Snapshots at different times (in a.u.) of the propagation of a Gaussian-modulated cosine pulse, centered around the frequency $\omega_0 = 60\pi/\lambda$, in the case $\eta_1 = \eta_2 = 0.5$.

Fig. 5 for a Gaussian pulse and a spatial inhomogeneity involving only the Young modulus. Both group velocity and amplitude have a deformed highly asymmetric cosine behavior. Such a behavior is typical for the case of inhomogeneity due to cross section variation and has been found also for other kinds of pulses.

In Fig. 8, the relative amplitude of the main peak of a Gaussian-modulated cosine pulse (centered around the frequency $\omega_0 = 60\pi/\lambda$) is plotted versus $\eta = \eta_1 = \eta_2$. As expected, the amplitude maxima do not increase linearly with η. We observe that the positions of the amplitude maxima (not reported in the plot) depend only on the inhomogeneity period and (almost) coincide with the cross-section minima. These results have an important practical application to the determination of the optimal length of ultrasonic concentrators for obtaining maximal amplification.

III. COMPARISON WITH A NUMERICAL SIMULATION

As already mentioned in the Introduction, a completely numerical approach may be used as an alternative to the semianalytical method described and applied so far. The propagation of a finite width (or semi-infinite) pulse may be

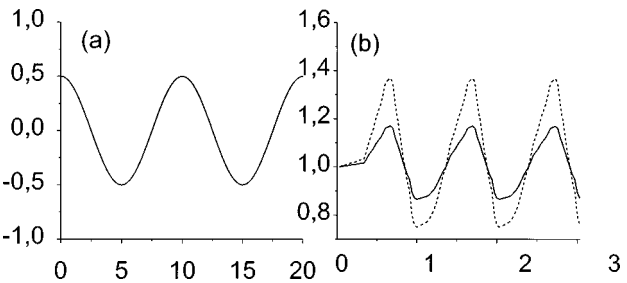

FIG. 7. (a) Law of motion; (b) relative amplitude (solid line) and phase velocity (dashed line) versus x/λ for a Gaussian-modulated cosine pulse, in the case $\eta_1 = \eta_2 = 0.5$.

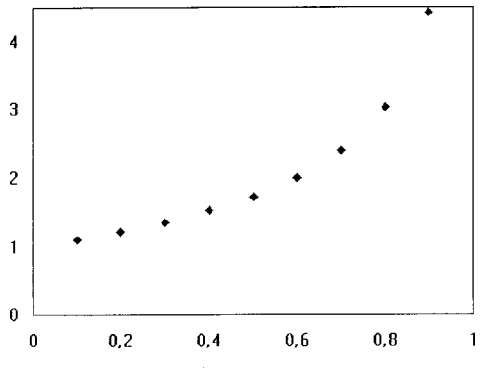

FIG. 8. Relative amplitude versus $\eta = \eta_1 = \eta_2$ for a Gaussian-modulated cosine pulse.

simulated directly in the (x,t) domain, by means of the Local Interaction Simulation Approach (LISA)[11] both at the 1-D level and, in the case of a specimen with x-dependent cross section, through a more realistic 2-D or 3-D calculation. The CPU time required for such simulations (even in 2-D or 3-D, if a massively parallel computer is utilized) is remarkably small (depending, of course, on the size of the specimen and required accuracy). Therefore, LISA may be quite advantageous with respect to the method proposed in the previous sections. However, it must be remarked that the CPU time required for a semianalytical approach is almost entirely devoted to the computation of the monochromatic components, which, once computed, may be used again for additional calculations, concerning different pulse shapes, since they depend only on $f(x)$ and $g(x)$. In this case, the solution becomes considerably faster and the advantages of the LISA approach are correspondingly reduced.

In addition, the reliability of the results of a completely numerical solution may be jeopardized by problems of convergence and stability. In fact, a thorough analysis of the convergence and stability properties of a given discrete scheme (such as the one used in LISA simulations), performed, e.g., by means of the standard Von Neumann approach,[14] may become exceedingly difficult, especially for nonelementary choices of the functions $f(x)$ and $g(x)$.

Thus, the availability of semianalytical solutions (such as the one illustrated before) becomes an efficient tool for testing the convergence of LISA or other discrete schemes, to be used in the simulations. Alternatively, convergence may be confirmed empirically by means of a comparison between the results of two schemes with different orders of accuracy.[15]

By discretizing space and time with unit steps ϵ and τ, respectively, Eq. (1) becomes

$$u_i^{t+1} = 2u_i^t - u_i^{t-1} + \frac{1}{f_i}\left(\frac{\tau^2}{\epsilon^2} g_i (u_{i+1}^t - 2u_i^t + u_{i-1}^t) + \frac{\tau^2}{2\epsilon^2}(g_{i+1} - g_{i-1})(u_{i+1}^t - u_{i-1}^t)\right), \tag{19}$$

where $u_i^t = u(i\epsilon, t\tau)$ and similarly for g_i and f_i. To guarantee convergence and stability, the choice of ϵ and τ cannot be arbitrary. We have found, in the course of many numerical

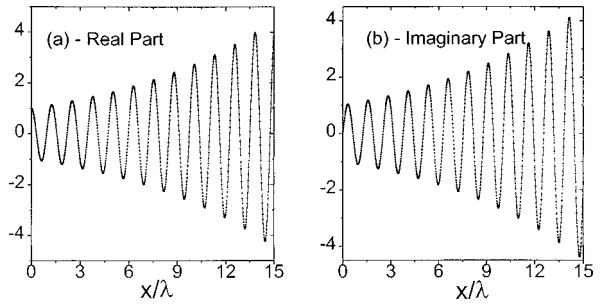

FIG. 9. Real and imaginary parts of a monochromatic wave for $\omega = 10\pi/\lambda$, for a medium with exponentially decreasing cross section. The solid line represents the semianalytical solution, while the dots are the results of a numerical simulation.

experiments, that $\epsilon = 1$ and $\tau = 0.5$ represent a satisfactory choice for a wide range of initial pulses and inhomogeneities. In all cases we have obtained solutions, which were almost entirely coincident with the results of the semianalytical calculations.

As an example we report the case of propagation of a semi-infinite sine wave injected from the left edge of a specimen with $f(x) = 1$ and $g(x) = 1 + 0.2\exp(-x/\lambda)$. In Fig. 9, we have compared the results obtained using the proposed semianalytical technique (continuous line) with the ones obtained by a numerical simulation (dots). We observe an excellent agreement between the two solutions. For the sake of completeness, we remark that in the case of exponential variation of the rod cross section, it is possible to propagate properly only components with frequency larger than a given critical value, which depends of course on the choice of η and λ.

IV. CONCLUSIONS

In this contribution we have considered the propagation of acoustic (or ultrasonic) waves in inhomogeneous 1-D media. A typical example could be an elastic bar, whose density and/or Young modulus and/or cross section vary with x with a certain regularity, e.g., sinusoidally or exponentially. A semianalytical method, based on a Taylor series expansion, has been used, leading to iteration equations for the determination of the coefficients of the Fourier transform of the solution. A formal solution is obtained, which is valid for any medium whose inhomogeneity is described by a function with absolutely convergent Taylor expansion.

The method has been applied to study the propagation first of monochromatic waves, then of several finite pulses: Gaussian, sinusoidal and Gaussian-modulated sinusoidal. Also, both linear and sinusoidal inhomogeneities (in the density, Young modulus and/or cross section) have been considered. The results have been compared with those obtained by means of the Local Interaction Simulation Approach (LISA). The agreement has been found to be very good in all cases. The respective advantages of the two treatments have also been discussed.

It has been found that the propagated pulse presents some properties, which are independent on the pulse shape. The peak amplitude shows periodic oscillations with the same periodicity as the inhomogeneity, and the law of motion of the pulse is periodic around the corresponding one for a reference homogeneous medium. The phase velocity is periodic for high- and low-frequency components, while it is generally increasing (or decreasing) for intermediate frequencies, where strong resonance effects appear.

ACKNOWLEDGMENTS

This work has been partly supported by the EC Program Copernicus No. ERBCIPACT940132.

APPENDIX: ACCURACY OF THE NUMERICAL TECHNIQUE

An *a priori* determination of the accuracy of the proposed numerical technique can be obtained estimating the propagation of the truncation errors of the Taylor expansion from the kth to the $(k+1)$th interval in the analytical continuation. The error, due to the truncation of the Taylor expansion after N terms in a given (e.g., the kth) interval Δx, is given by

$$E_k = \frac{1}{(N+1)!}\frac{d^{N+1}u}{dx^{N+1}}\Delta x^{N+1}.$$

Using Eqs. (8) to (11), the initial conditions for the $k+1$th interval become

$$C_{k+1} = A_k C_k + \frac{1}{N!}\Delta x^N \alpha_k \Delta,$$

where

$$C_k = \begin{pmatrix} c_0^k \\ c_1^k \end{pmatrix}, \quad A_k = \begin{pmatrix} f_k g_k \\ m_k n_k \end{pmatrix},$$

$$\alpha_k = \frac{d^{N+1}u}{dx^{N+1}}, \quad \Delta = \begin{pmatrix} \dfrac{\Delta x}{N+1} \\ 1 \end{pmatrix},$$

where f_k, g_k, m_k and n_k are suitable operators, which may be explicitly obtained from Eq. (8). Assuming α_k to be constant (equal to α), E_k is independent from k. Since the problem is linear, a good estimate for the total error at the end of the kth interval is given by

$$\delta u_{k+1} = \alpha \frac{\Delta x^N}{N!}\Delta\left(1 + \sum_{m=0}^{k-1}\prod_{j=0}^{m} A_{k-j}\right).$$

It is thus possible to choose the minimum value of N, consistent with the required accuracy.

However, for practical purposes, a numerical evaluation of the accuracy may be more useful. Since we are looking for a solution of Eq. (4) in the form of a complex function $\tilde{u}(x,\omega)$, we can write it as $A(x,\omega)\exp(i\varphi(x,\omega))$. Substituting it into Eq. (4), the solution for the imaginary part leads to the following conservation law:

$$F(x) = g(x)A^2(x)\frac{d\varphi(x)}{dx} = \text{const.}$$

The quantity F(x) may be evaluated numerically at any point and provide a useful test of the accuracy of the results. In Fig. A1, the quantity $(F(x) - F(0))/F(0)$ is reported against

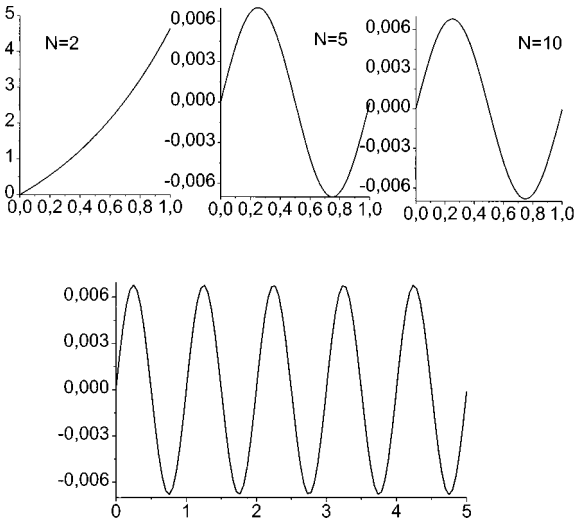

FIG. A1. Numerical error versus x/λ for different values of the number of Taylor components N and $\Delta x = 0.001\lambda$. The bottom plot ($N = 10$) shows that the error remains bounded when the propagation length increases.

x/λ for different choices of N and for $\Delta x = 0.001\lambda$, in the case of a periodic inhomogeneity with $f(x) = \sin(\omega t)$ and $g(x) = 1$. We observe large numerical errors increasing very quickly for $N = 2$, while almost no improvement is obtained if the number of terms in the Taylor expansion goes from 5 to 10. The bottom plot of Fig. A1 shows that the error varies periodically and remains bounded when the propagation length is increased.

[1] J. Lekner, ''Reflection and transmission of compressional waves: Exact results,'' J. Acoust. Soc. Am. **87**, 2325–2331 (1990).
[2] J. Lekner, ''Reflection and transmission of compressional waves in stratification with discontinuities in density and/or sound speed,'' J. Acoust. Soc. Am. **88**, 2876–2879 (1990).
[3] A. H. Nayfeh, ''The general problem of elastic wave propagation in multilayered anisotropic media,'' J. Acoust. Soc. Am. **89**, 1521–1531 (1991).
[4] S. K. Jeng and C. H. Liu, ''Wave propagation in media with dimensional quadratic refractive index profile,'' J. Acoust. Soc. Am. **81**, 1732–1740 (1990).
[5] H. Bremmer, ''The W.K.B. Approximation as the First Term of a Geometric-Optical Series,'' Commun. Pure Appl. Math. **4**, 105–115 (1951).
[6] R. E. Meyer, ''Gradual Reflection of Short Waves,'' SIAM (Soc. Ind. Appl. Math.) J. Appl. Math. **29**, 481–492 (1975).
[7] H. Gingold and J. She, ''Reflection of sound waves by sound speed inhomogeneities,'' J. Acoust. Soc. Am. **91**, 1262–1269 (1992).
[8] L. M. Brekhovskikh, *Waves in Layered Media* (Academic, New York, 1980).
[9] R. Oberle and R. C. Cammarata, ''Acoustic pulse propagation in elastically inhomogeneous media,'' J. Acoust. Soc. Am. **94**, 2947–2953 (1993).
[10] J. S. McIntyre, C. W. Bert, and R. A. Kline, *Wave Propagation in a Composite with Wavy Reinforcing Fibers*, in *Review of Progress in Quantitative Non Destructive Evaluation, Vol. 14*, edited by D. O. Thompson and D. E. Chimenti (Plenum, New York, 1995), pp. 1311–1318.
[11] P. P. Delsanto *et al.*, ''CM Simulation of Ultrasonic Wave Propagation in Materials: I the 1-D case,'' Wave Motion **16**, 65 (1992); ''CM Simulation of Ultrasonic Wave Propagation in Materials: II the 2-D case,'' Wave Motion **20**, 295 (1994); ''CM Simulation of Ultrasonic Wave Propagation in Materials: III the 3-D case'' Wave Motion **26**, 329–339 (1997).
[12] P. A. A. Laura and R. H. Gutierrez, ''Vibrations of an Elastically Restrained Cantilever Beam of Varying Cross Section with Tip Mass of Finite Length,'' J. Sound Vib. **108**, 123–131 (1986); E. Eisner, ''Design of sonic amplitude transformers for high magnification,'' J. Acoust. Soc. Am. **35**, 1367–1377 (1963).
[13] N. Cretu, G. Nita, C. Rosca, I. Sturzu, and M. Scalerandi, ''Shape Optimization for Ultrasonic Concentrators,'' work in progress.
[14] J. C. Strickwerda, *Finite Difference Schemes and Partial Difference Equations* (Wadsworth-Brooks, New York, 1989).
[15] P. P. Delsanto and M. Scalerandi, ''Discretization Schemes for the Simulation of Non Linear Propagation Equations,'' in *Proceedings of the Int. Symp. on Hydroacoustics and Ultrasonics*, edited by A. Stepnowski and E. Kozaczka (1997), pp. 65–71.

Time analysis of immersed waveguides using the finite element method

Anne-Christine Hladky-Hennion and Régis Bossut
IEMN (UMR 9929 CNRS), département ISEN, 41 Boulevard Vauban, 59046 Lille Cedex, France

Michel de Billy
Groupe de Physique des Solides, Universités Paris 6 et 7, Tour 23, 2 Place Jussieu, 75251 Paris Cedex 05, France

(Received 10 October 1997; accepted for publication 24 February 1998)

The propagation of acoustic waves in immersed waveguides has been previously studied with the help of the finite element method, using the ATILA code [A. C. Hladky-Hennion *et al.*, J. Sound Vib. **200**, 519–530 (1997)]. But this method, which is a modal analysis, essentially concerns the case of rectilinear, infinite, and uniform waveguides. Thus this paper deals with another way of solving the problem of wave propagation along waveguides, with the help of a time analysis using finite elements. First, the theoretical formulation is presented for immersed structures. Then, Plexiglas and brass wedge guides, of different apex angles, are considered. When immersed in water, these wedges generate either propagating or radiating wedge waves. The finite element results, using a time analysis, are compared to the previous finite element results, using a modal analysis and to the experiments, leading to a good agreement. Thus the approach can be easily extended to other waveguides whatever their cross sections. © *1998 Acoustical Society of America.*
[S0001-4966(98)02306-6]

PACS numbers: 43.20.Hq, 43.20.Mv [ANN]

INTRODUCTION

Analysis of the propagation of acoustic waves in guides had an increased interest during the 1970s, because such waves can be used in signal processing and information storage applications. Particularly, flexural wedge waves, propagating along the tip of an ideal sharp elastic wedge, attracted considerable interest because these waves are dispersionless; their propagating velocity is lower than the Rayleigh wave velocity and the acoustic energy is confined at the tip of the wedge guide. As the boundary conditions of the problem are complex, it is difficult to use a simple model to study the propagation of acoustic waves in guides. In 1969, Ash *et al.*[1] suggested using a simple wedge as a guiding structure. Then, Moss *et al.*[2] established an analytical model limited to simple geometry of linear wedges. Lagasse[3] applied the finite element method to analyze the propagation of the acoustic waves in an infinite waveguide of arbitrary cross section. The technique is original because the problem is reduced to a bidimensional problem, where only the cross section of the guide is meshed using finite elements. The method has been extensively applied to wedges.[4,5] Mc Kenna *et al.*[6] used the approximations of plate theory to study the guided elastic modes that can propagate along the tip of a wedge. More recently, wedge waves have again attracted interest: Krylov *et al.* have developed an approximate analytical solution based on geometrical-acoustic methods or ray tracing,[7,8] applied to truncated or curved wedges. Chamuel[9,10] has measured the effect of water loading on transient waves propagating along a wedge for applications in geophysics and underwater acoustics, whereas Jia *et al.*[11] and Auribault *et al.*[12] have experimentally studied the truncation and the curvature influence on the wedge wave velocity. Moreover, Bonnet-Ben Dhia *et al.*[13] have studied the theoretical existence of localized waves in wedges.

The finite element method has already been used for the analysis of acoustic waves for in vacuum or immersed guides,[14–16] with a view to finding either propagating or radiating modes. It was an interesting innovation because, to our knowledge, theoretical or numerical modeling of the immersed solid wedge has not yet been developed in the general case. The method previously developed, which is a modal analysis, concerns the study of the propagation of acoustic waves along rectilinear, infinite, and uniform waveguides. In the method, the problem is reduced to a bidimensional problem, where only the cross section of the guide is meshed using finite elements, following Lagasse's original technique.[3] Thus the method does neither allow the study of a waveguide with a defect on the surface, nor the study of a waveguide with a nonuniform cross section, nor the study of reflection waves at the end of the wedge. In all these cases, the whole tridimensional guide has to be meshed, because there is no more symmetry for the structure or for the excitation in the wedge direction. Therefore, a time analysis has been developed in the ATILA finite element code.

This paper presents the way to solve the problem of the propagation of wedge waves, with the help of a time analysis. First, it presents the theoretical formulation for immersed structures, which leads to the resolution of a second order differential system of equations, which has been incorporated in the ATILA finite element code. Then, the time analysis for wedge guides made of Plexiglas and of brass is performed. Immersed in water, wedges can generate either propagating or radiating wedge waves, as a function of the apex angle.[15,16] The finite element results are compared to

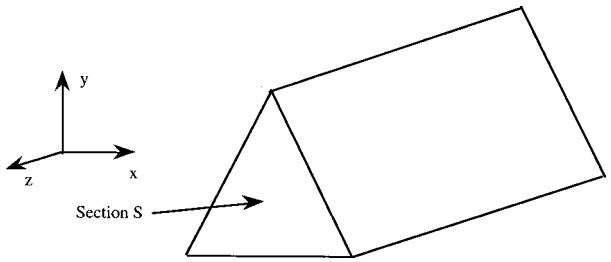

FIG. 1. Rectilinear waveguide, infinite, and uniform in the z direction.

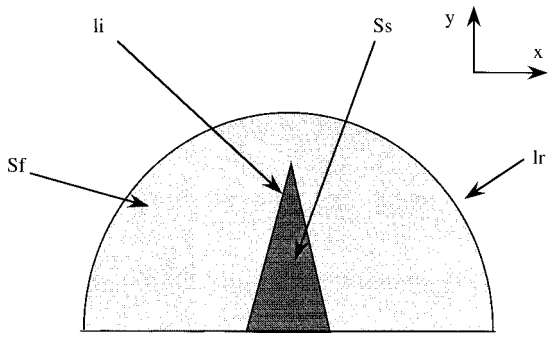

FIG. 2. Traces in the xy plane of the finite element domain. Presentation of the solid part, the fluid part, the solid–fluid interface, and of the radiating fluid boundary.

previous finite element results, using a modal analysis[15,16] and to the experiments,[17] leading to a good agreement. The vizualization of the waves propagating or radiating in the fluid authorizes a good knowledge of the problem. Finally, indications are given on how this approach can be extended to waveguides of any cross section, for applications in signal processing devices, in geophysics, and in underwater acoustics, as well as in surface physics.

I. GENERAL MATHEMATICAL FORMULATION

A. Description of the problem

The mathematical model presented in this part allows the time analysis of a rectilinear waveguide, immersed or not in water, infinite and uniform in the z direction. But the method can be applied to any structure, whether bidimensional or tridimensional, in vacuum, or immersed. The section of the waveguide, which is denoted S, is set in the xy plane (Fig. 1). An excitation is applied on section S. Thus a wedge wave propagates at the top of the wedge, in the wedge direction. In all the cases, the time dependence is implicit in the equations ($e^{j\omega t}$).

B. Finite element system of equations

In the case of a modal analysis, it is possible to find the propagation modes of acoustic waves in an infinite waveguide or arbitrary cross section, using only a bidimensional mesh in the xy plane and to reconstitute the whole solution.[3,14–16] But, in the case of a time analysis, a tridimensional mesh has to be used for the study, because the excitation has no symmetry in the z direction.

The waveguide of a given length is meshed with the finite element method. The whole domain contains a solid part Ω_s and a fluid part Ω_f, which are divided into elements connected by nodes. The notations are defined in Fig. 2, where the trace of the tridimensional fluid domain Ω_f in the xy plane is represented by the S_f surface, the trace of the tridimensional solid domain Ω_s in the xy plane is represented by the S_s surface. In the xy plane, the whole domain is split as follows:

(i) The fluid domain S_f and the solid domain S_s are divided into elements connected by nodes.

(ii) The fluid part and the solid part are separated by the interface line l_i, trace of the S_i surface in the xy plane.

(iii) A line containing the radiating or boundary elements, l_r, is limiting the finite element mesh, trace of the S_r surface in the xy plane.

With an harmonic analysis, the general system of equations associated to this problem is[18]

$$\begin{bmatrix} [K]-\omega^2[M] & -[L] \\ -\rho_f^2 c_f^2 \omega^2 [L]^T & [H]-\omega^2[M_1] \end{bmatrix} \begin{pmatrix} \underset{\sim}{U} \\ \underset{\sim}{P} \end{pmatrix} = \begin{pmatrix} \underset{\sim}{F} \\ \rho_f c_f^2 \phi \end{pmatrix}, \quad (1)$$

where $[K]$ and $[M]$ are, respectively, the stiffness matrix and the mass matrix for the Ω_s solid domain. In the case of a solid material with losses, the stiffness matrix is complex[19] and is denoted by $[K_{uu}]+j\omega[C_{uu}]$, where the $[K_{uu}]$ and $[C_{uu}]$ matrices are frequency independent.[20] $[H]$ and $[M_1]$ are, respectively, the compressibility and the mass matrices for the Ω_f fluid domain. $[L]$ is the interface matrix and represents the coupling between the fluid and the solid domains on the S_i surface, the trace of which in the xy plane is the l_i line. ''T'' stands for matrix transposition. ρ_f and c_f are, respectively, the density and the sound speed in the fluid. ω is the angular frequency. $\underset{\sim}{F}$ contains the nodal values of the applied forces. ϕ contains the nodal values of the pressure normal derivative on the external fluid boundary Ω_f. $[K]$, $[M]$, $[H]$, $[M_1]$, $[L]$, $\underset{\sim}{F}$, and ϕ, respectively, result from the merging of the elementary matrices and the vectors $[K^e]$, $[M^e]$, $[H^e]$, $[M_1^e]$, $[L^e]$, F^e, and ϕ^e. The unknowns of the system are U and P, the vectors of the nodal values of the displacement field in the Ω_s solid domain and of the pressure in the Ω_f fluid domain.

A nonreflecting condition is added to system (1), on the S_r surface of the mesh, the trace of which in the xy plane is the l_r line. It allows limiting the finite element mesh of the fluid part. As the surface is assumed to stand in the far field, the relation between the vector of the nodal values of the normal pressure derivative ϕ and the vector of the nodal values of the pressure field $\underset{\sim}{P}_\infty$ on the external fluid boundary S_r is[21]

$$\phi = -[\alpha + jkR][D]\,\frac{\underset{\sim}{P}_\infty}{R}, \quad (2)$$

where R is the radius of the external fluid boundary, k is the wave number, and $[D]$ is the monopolar radiating matrix,

which only depends on the interpolation functions in the elements. The α term is equal to 1 when the structure is tridimensional or when it is an axisymmetrical structure. The α term is equal to 1/2 in the case of a plane strain analysis. This nonreflecting condition is valid if the external fluid boundary is inside the far field area ($kR \gg 1$).

In the case of a cylindrical external fluid boundary, the far field pressure can be expressed in terms of the Hankel function of first kind and second order, the asymptotic value of which is given below:

$$p(R,k) = p_0(k) H_0^{(2)}(kR) \rightarrow p_0(k) \sqrt{\frac{2}{\pi kR}}\, e^{-j(kR-\pi/4)}.$$

$$kR \gg 1. \tag{3}$$

Considering an external excitation written as a prescribed displacement or a prescribed force, the monopolar radiating condition is included in system (1) which becomes

$$\begin{bmatrix} [K_{uu}] + j\omega[C_{uu}] - \omega^2[M] & -[L] \\ -\rho_f^2 c_f^2 \omega^2 [L]^T & [H] - \omega^2[M_1] + \dfrac{\rho_f c_f^2}{R}[\alpha + jkR][D] \end{bmatrix} \begin{pmatrix} \underset{\sim}{U} \\ \underset{\sim}{P} \end{pmatrix} = \begin{pmatrix} \underset{\sim}{F} \\ \underset{\sim}{0} \end{pmatrix}. \tag{4}$$

Considering a time analysis, the system of equations (4) is modified, replacing the jk terms by $(1/c)(\partial/\partial t)$. It becomes[20,22]

$$\begin{bmatrix} [M] & [0] \\ \rho_f^2 c_f^2 [L]^T & [M_1] \end{bmatrix} \begin{pmatrix} \ddot{\underset{\sim}{U}} \\ \ddot{\underset{\sim}{P}} \end{pmatrix} + \begin{bmatrix} [C_{uu}] & [0] \\ [0] & [D_1] \end{bmatrix} \begin{pmatrix} \dot{\underset{\sim}{U}} \\ \dot{\underset{\sim}{P}} \end{pmatrix} + \begin{bmatrix} [K_{uu}] & -[L] \\ [0] & [H] + [D_0] \end{bmatrix} \begin{pmatrix} \underset{\sim}{U} \\ \underset{\sim}{P} \end{pmatrix} = \begin{pmatrix} \underset{\sim}{F} \\ \underset{\sim}{0} \end{pmatrix}, \tag{5}$$

with

$$[D_0] = \frac{\alpha \rho_f c_f^2}{R}[D] \quad \text{and} \quad [D_1] = \rho_f c_f [D].$$

System (5) is solved with the help of classical algorithms of resolution of a second order differential system of equations.[23,24] It is solved with iterative methods, with a constant time increment. In all the following examples, isoparametric elements are used, with quadratic interpolation along element sides.

II. VALIDATION OF THE MODEL: IMMERSED PULSATING SPHERE

A. Analytical model

In this section, a stiff sphere, the radius of which is denoted by a, is immersed in a fluid. The density in the fluid is denoted ρ_f and the sound speed denoted c_f. Considering a pulsating sphere, the speed on the surface of the sphere is constant for any θ angle, equal to V_0. Classically,[25] the pressure is given as a function of the distance r from the center of the sphere and the ω angular frequency as following:

$$p(r,\omega) = -\rho_f c_f e^{-jk(r-a)} \frac{ka^2}{(1+jka)jr} V_0 e^{j\omega t}. \tag{6}$$

With a view to computing the time analysis of the problem, the inverse Fourier transform is performed on Eq. (6) and the pressure impulse response is

$$\text{if } t < \frac{r-a}{c_f} \quad p(r,t) = 0,$$

$$\text{if } t > \frac{r-a}{c_f} \quad p(r,t) = \frac{-\rho_f c_f a}{r} \left\{ \delta\left(\frac{r-a}{c_f}\right) - \frac{c_f}{a} e^{-\beta c_f/a} \right\} V_0 \tag{7}$$

$$\text{with} \quad \beta = t - \frac{r-a}{c_f}.$$

If the displacement on the surface of the sphere depends on time:

$$u(t) = U_0(1 - \cos\,\omega t), \quad t > 0, \tag{8}$$

then, the speed is

$$v(t) = U_0 \omega\, \sin\,\omega t, \quad t > 0. \tag{9}$$

The pressure at a distance r from the center of the sphere is the convolution product of the pressure impulse response of Eq. (7) by $v(t)$ of Eq. (9). The pressure is equal to zero if $t < (r-a)/c_f$ and, if $t > (r-a)/c_f$ it is equal to

$$p(r,t) = U_0 \frac{\rho_f c_f}{r} \left[a\omega\, \sin\,\omega\tau - \frac{c_f \omega}{\omega^2 + c_f^2/a^2} \times \left\{ \omega e^{-c_f \tau/a} - \omega\, \cos\,\omega\tau + \frac{c_f}{a}\, \sin\,\omega\tau \right\} \right], \tag{10}$$

with $\tau = t - (r-a)/c_f$.

B. Results

In this section, a sphere, the radius of which is equal to 0.1 m, is immersed in water. A sinusoidal displacement,

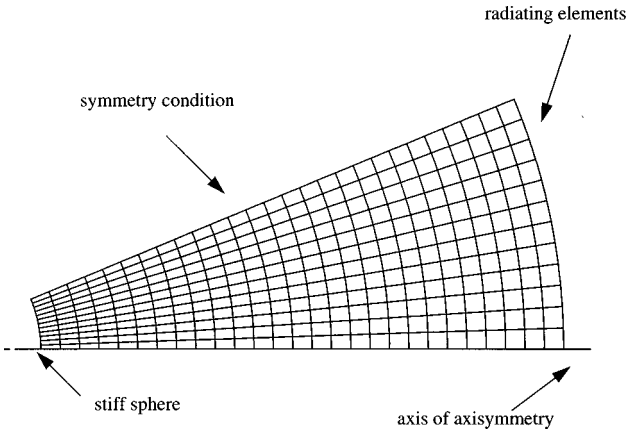

FIG. 3. Finite element mesh of the stiff pulsating sphere.

similar to Eq. (8), is prescribed on the surface of the sphere. The problem is easily solved with the help of Eq. (10). It is also possible to solve the problem with the help of the finite element method. Figure 3 presents the finite element mesh of the problem. Because the sphere is assumed to be stiff, it does not appear on the mesh, which only includes the fluid part. Because of the symmetry of the problem, an axisymmetrical analysis is performed and only 1 over 32 of the fluid part is meshed, applying appropriate boundary conditions. In Fig. 3, the external fluid boundary is at 0.5 m from the center of the sphere and contains the radiating elements, which allows to limit the mesh of the fluid part, with the help of a nonreflecting condition.

For $ka=1$, Fig. 4 presents the variations of the pressure as a function of time, at three different distances from the center of the sphere: $r/a=1$, $r/a=3$, and $r/a=5$. The full lines correspond to the analytical results and the marks correspond to the finite element results. The agreement is perfect between the results, thus validating the finite element model.

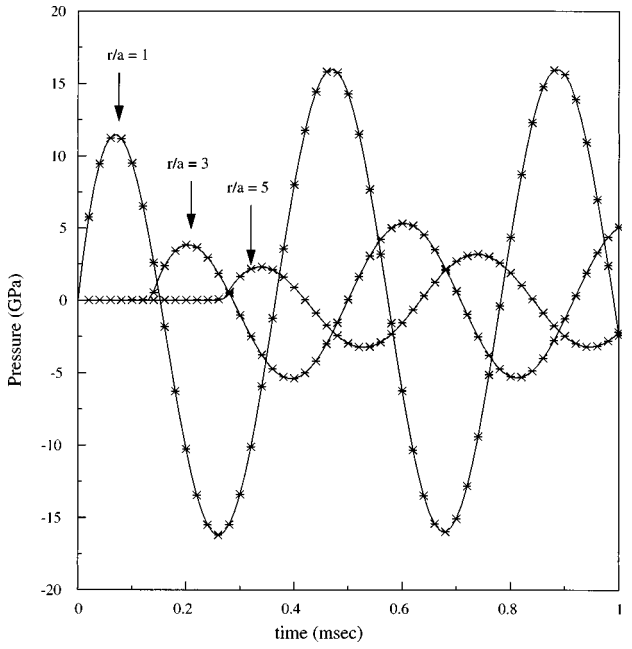

FIG. 4. Variations as a function of time of the pressure at a distance r from the center of the pulsating sphere. $ka=1$. Full lines: analytical results, marks: finite element results.

TABLE I. Physical constants of the material.

Material	Young's modulus (Pa)	Density (kg/m^3)	Poisson's ratio	Rayleigh wave velocity (m/s)
Brass	$1.04\ 10^{11}$	8600	0.3429	1986
Plexiglas	$5.85\ 10^{9}$	1180	0.3343	1271

III. WEDGE GUIDE IN VACUUM

A. General presentation

Surface acoustic waves propagating along an elastic wedge were originally studied in the 1970s.[2–6] In an idealized infinitely sharp wedge, two types of wedge waves are possible: symmetric modes and antisymmetric flexural modes (ASF modes). The latter modes are particularly attractive because of the properties recalled in the introduction. Thus the wedge waves are of important interest in signal processing devices,[4] geophysics and underwater acoustics,[9,10] as well as in solid surface physics.[2,7] More recently, wedge acoustic waves traveling along the tip of cylindrically curved surfaces have been experimentally and theoretically studied,[12,14] the influence of the wedge truncation has been quantified,[11,14,26,27] and the effect of the fluid loading has been evaluated in the case of immersed wedges.[9,10,15–17,28]

Many wedges, made of different materials, have been experimentally and theoretically studied and general trends are stated.[15–17] When the wedges are in vacuum, the wedge waves are propagating in the wedge direction and are evanescent in the perpendicular plane; they are not radiating. When the wedges are immersed, wedge waves can be either propagating, if their velocity is lower than the sound speed in water, or radiating, if their velocity is greater than the sound speed in water.

In this paper, Plexiglas and brass wedges are studied with the help of the finite element method, as a function of the apex angle, between 30° and 90°. The physical constants of these materials used for the calculation are presented in Table I. With a view to studying the antisymmetrical flexural modes, only half of the cross section is meshed, by applying a specific boundary condition on the bisector plane. In all the cases, the length of the mesh is 54 mm and the height is 10 mm. Figure 5 presents the finite element mesh of the tridimensional wedge, when the apex angle is equal to 60° (half-apex angle meshed=30°). A prescribed displacement is applied on the front face of the wedge, which is presented in Fig. 6. It corresponds to the displacement of the first wedge mode, previously obtained with the help of a modal analysis.[14] The displacement is applied with the help of a square pulse, the duration of which is 0.002 ms. The calculation is performed with the help of the finite element method with a 0.00025-ms step.

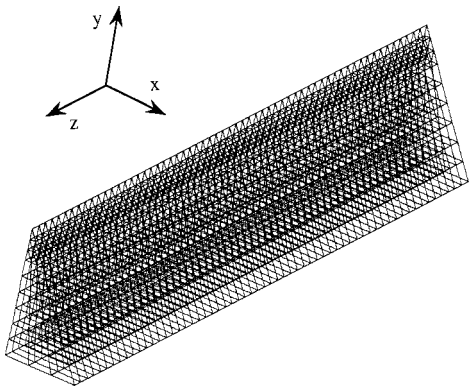

FIG. 5. Tridimensional mesh of the wedge, with an apex angle equal to 60° (half-apex angle meshed=30°).

B. Results

In this section, the propagation velocity of the first ASF mode is studied, as a function of the apex angle. For each apex angle, the wedge wave velocity is calculated, by noticing the position of the maximum of the displacement at the top of the wedge as a function of time. For Plexiglas and brass samples, Fig. 7 presents the variations of the wedge wave velocities as a function of the angle at the top of the wedge. The finite element results, obtained with the help of the time analysis, are compared to results previously obtained with a modal analysis[15] and to the experiments.[17] For large apex angles, the wedge wave velocity is close to the Rayleigh wave velocity.[3] The agreement is good between the results for large angles but the difference between the numerical results is higher for small angles. For small angles, many wedge waves are propagating at the top of the wedge. This is in agreement with previous studies which pointed out that several wedge waves can propagate.[4] But, in that case, the time analysis results are roughly estimated, the separation between the different waves being gradual.

In the case of a 30° Plexiglas wedge, Fig. 8 presents the displacement field at the top of the wedge at different instants. This figure allows a good vizualisation of the separation of the first two waves.

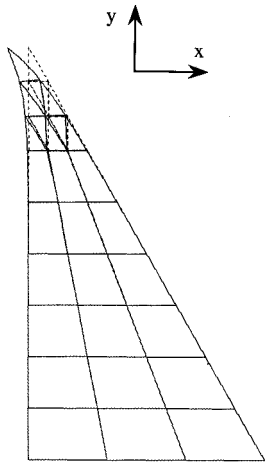

FIG. 6. Displacement field prescribed on the front face of the wedge. Apex angle=60°. Dashed lines correspond to the rest position.

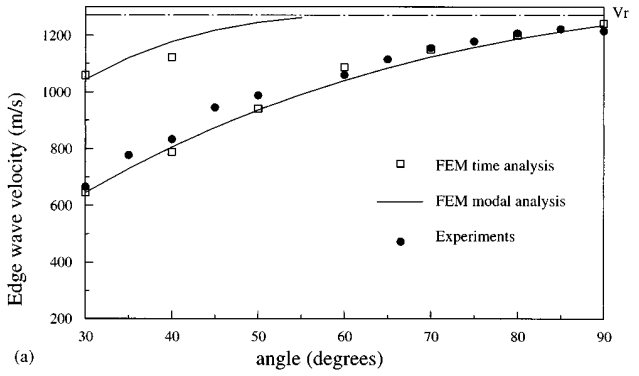

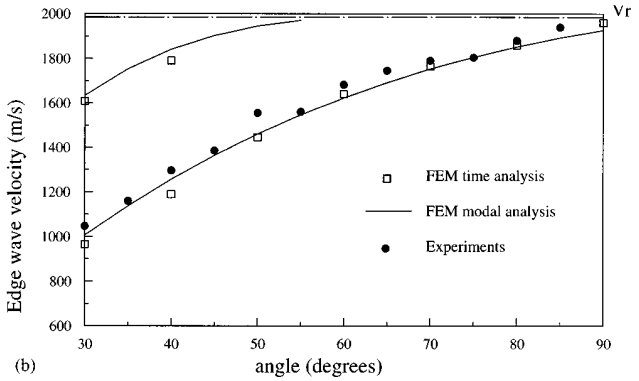

FIG. 7. Variations of the wedge wave velocities, as a function of the apex angle of the in vacuum wedge. White squares: finite element results, using a time analysis; full lines: finite element results, using a modal analysis; black circles: experimental results. (a) Plexiglas wedges; (b) brass wedges.

In the case of a 60° Plexiglas wedge, Fig. 9 presents the displacement field at the top of the wedge at different instants. This figure shows that only one wedge wave is propagating.

IV. WEDGE GUIDE IMMERSED IN WATER

A. General presentation

The previous Plexiglas and brass wedges are now immersed in water. The apex angle varies, from 30° to 90°. Figure 10 presents the mesh of the cross section of the immersed wedge, when the top angle is equal to 60° (half-apex angle meshed=30°). Once again, half of the wedge is meshed, with an appropriate boundary condition on the bisector plane for solid and fluid nodes, to study antisymmetrical flexural modes. In all the cases, a 54-mm-length and 10-mm-height wedge is meshed. The radius of the external fluid boundary is equal to 20 mm. The excitation is a prescribed displacement field on the front face of the wedge, that corresponds to the displacement field of the first wedge mode, presented in Fig. 6. The displacement is the same as in vacuum. The calculation is performed with the help of the finite element method with a 0.00025-ms step.

B. Results

Plexiglas and brass wedges, with apex angles between 30° and 90°, are considered. For each value of the apex angle, the wedge wave velocity is calculated. Figure 11 pre-

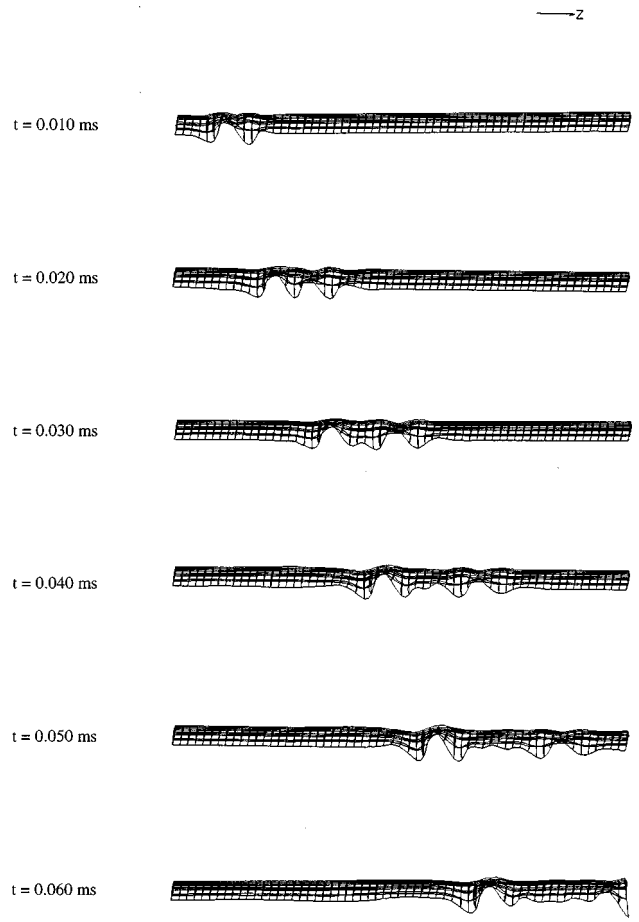

FIG. 8. Top view of the displacement at the top of the wedge between $t = 0.010$ ms and $t = 0.060$ ms. Apex angle=30°. Wedge made of Plexiglas.

sents a comparison between the variations of the wedge wave velocities as a function of the top angle, calculated with the time analysis, obtained with the modal analysis and measurements. The agreement is good between the three different determinations, especially for large apex angles. For small apex angles, because several wedge waves are mixed, the calculation of the velocity with the time analysis is more approximate and implies a shift on the results. The comparison between the data in Fig. 7 and the data in Fig. 11 points out that, in all the cases, the water loading implies a decrease in the wedge wave velocity, which is greater for small angles. In the case of Plexiglas samples, for a large apex angle (90°), the wedge wave velocity seems to be the Stoneley–Scholte wave velocity,[15] whereas for brass samples, the wedge wave velocity for a 90° apex angle seems to be the Rayleigh wave velocity, like in the case of in vacuum wedges.

In the case of immersed Plexiglas samples, the wedge waves are subsonic: They propagate along the wedge direction and do not radiate in the perpendicular plane. The displacement field at the top of the wedge is similar to the displacement field when the Plexiglas samples are in vacuum (Figs. 8 and 9).

In the case of immersed brass samples, the results confirm that below 60°, the wedge waves are subsonic: They propagate in the wedge direction but are attenuated in the perpendicular plane. Above 60°, the wedge waves are supersonic: They propagate along the wedge direction but are attenuated, they are radiating in the perpendicular plane.

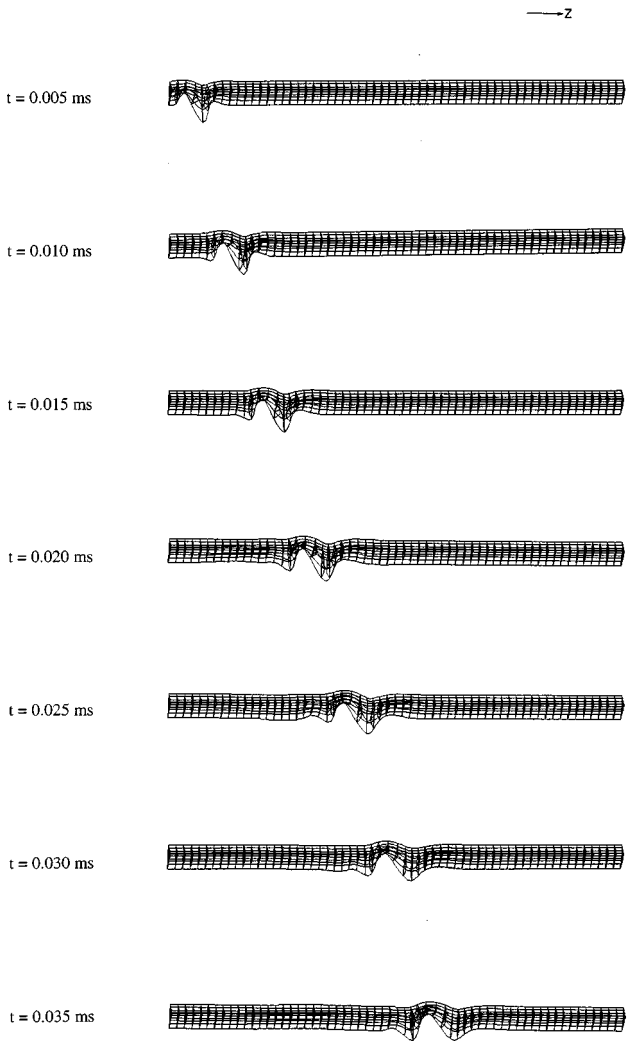

FIG. 9. Top view of the displacement at the top of the wedge between $t = 0.005$ ms and $t = 0.035$ ms. Apex angle=60°. Wedge made of Plexiglas.

For a 40° apex angle wedge made of brass, Fig. 12 presents the variations of the displacement at the top of the wedge as a function of time and of the position along the wedge. In that particular case, this representation is the best way to see the propagating and the attenuated waves. When

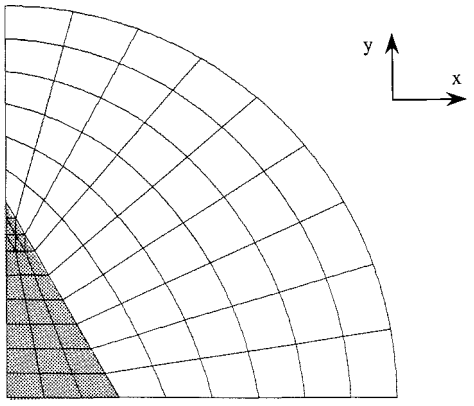

FIG. 10. Finite element mesh of the cross section of the immersed wedge. Apex angle=60°. The gray part corresponds to the wedge.

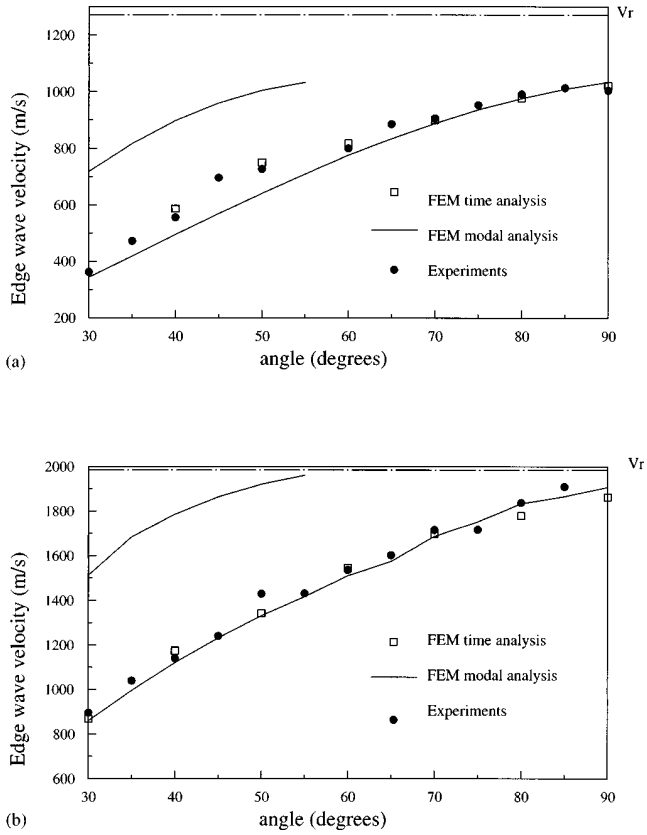

FIG. 11. Variations of the wedge wave velocities, as a function of the apex angle of the wedge, immersed in water. White squares: finite element results, using a time analysis; full lines: finite element results, using a modal analysis; black circles: experimental results. (a) Plexiglas wedges, (b) brass wedges.

the wedge is in vacuum, two propagative wedge waves exist. Immersed in water, the first ASF wedge wave is obtained, propagating along the wedge direction. In Fig. 12, the second ASF wedge wave still exists, it is faster than the previous one but is attenuated. This wave is supersonic: It is propagating but is attenuated in the direction of propagation of the wedge wave, it is radiating in the perpendicular plane. Because its amplitude is low, its velocity is not calculated with the time analysis.

For a 60° top angle wedge made of brass, Fig. 13 dis-

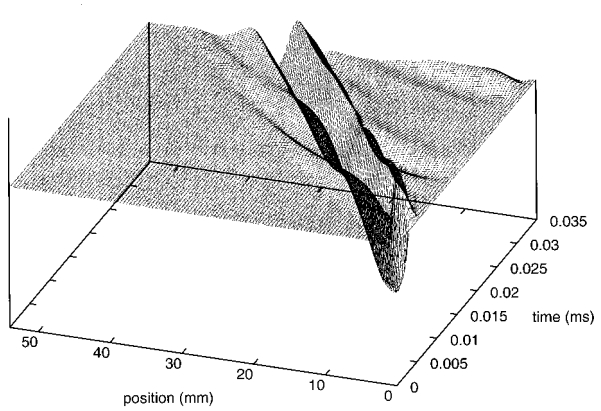

FIG. 12. Variations of the displacement at the top of the wedge as a function of time and of the position along the wedge. Apex angle: 40°. Wedge made of brass immersed in water.

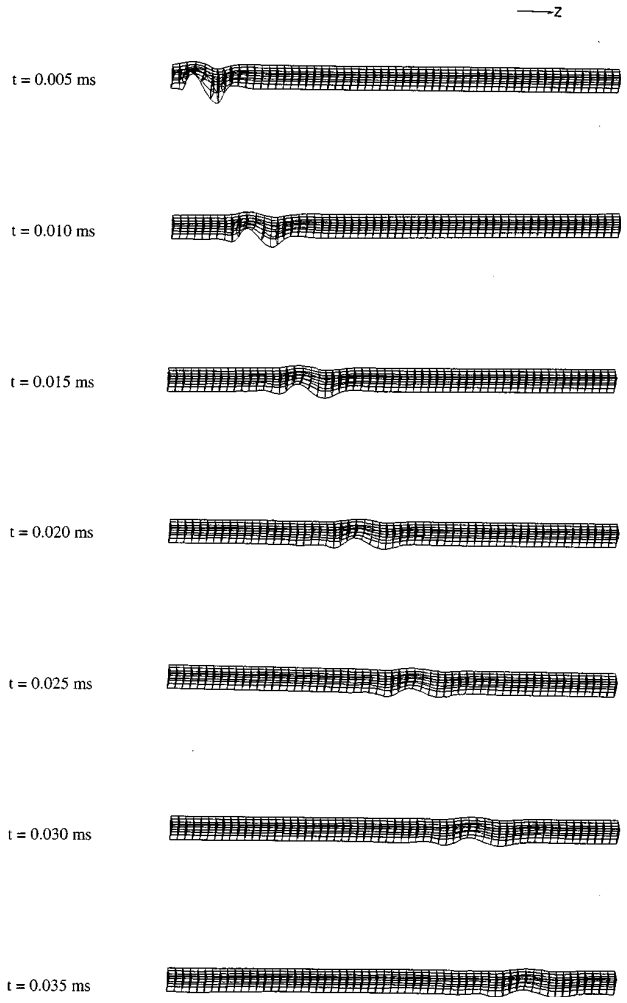

FIG. 13. Top view of the displacement at the top of the wedge between $t = 0.005$ ms and $t = 0.035$ ms. Apex angle=60°. Wedge made of brass immersed in water.

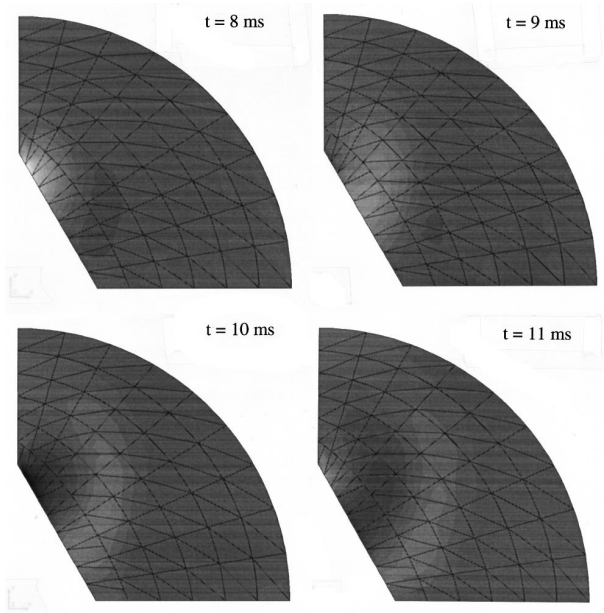

FIG. 14. Pressure field in the $z = 9$ mm plane, when the radiating wave is going through. Apex angle=60°. Wedge made of brass immersed in water. The white part corresponds to a negative pressure, the gray part to a pressure equal to zero, the black part to a positive pressure.

plays the displacement field at the top of the wedge at different instants: It clearly shows that the first ASF wedge wave is propagating but its amplitude is decaying. In that case, the wedge wave is supersonic: It is attenuated in the wedge direction and is radiating in the perpendicular plane. Figure 14 presents the pressure field in the cross section of the wedge, at $z=9$ mm, at different instants, when the wave is going through. It shows that the flexural displacement of the wedge implies a radiating wave in the surrounding fluid, which is antisymmetric to the bisector plane.

V. CONCLUSION

In this paper, the study of wedge waves propagating along in vacuum or immersed wedges has been performed with the help of a time analysis, using the finite element method. The formalism has been presented shortly. Then, after the validation of the method in the case of a stiff pulsating sphere, the method has been applied to Plexiglas and brass wedge guides. The agreement between finite element results using the time analysis and the previous finite element results using a modal analysis and the experiments demonstrates the accuracy of the model. There are several advantages to solve this problem with a time analysis: first a good vizualisation of the propagating or radiating waves, allowing a simple comprehension of the physical effects, and second, the possibility to mesh any waveguide, with any uniform or nonuniform cross section, immersed or not immersed, by simply building tridimensional meshes.

In addition, the time analysis can be used for other original research topics. In the case of wedge guides, the method can be applied to study wedges with apex angles greater than 90°. In that case, wedge waves are not located at the top of the wedge[2] and the wedge modes obtained with a modal analysis are artifacts of calculation.[2,14] A time analysis can be useful to determine how the energy is distributed in the wedge and if the wedge wave is attenuated. Moreover, the method can be applied to study the conversion of modes if a defect appears at the top of the wedge or if there is reflection at the end of the sample.[29] Finally, the method can be used for the study of any solid structure immersed in water, with a prescribed displacement field or a prescribed force.

[1] E. A. Ash, R. M. De La Rue, and R. F. Humphryes, ''Microsound surface waveguides,'' IEEE Trans. Microwave Theory Tech. **MTT-17**, 882–892 (1969).

[2] S. L. Moss, A. A. Maradudin, and S. L. Cunningham, ''Vibrational edge modes for wedges with arbitrary interior angles,'' Phys. Rev. B **8**, 2999–3008 (1973).

[3] P. E. Lagasse, ''Higher-order finite element analysis of topographic guides supporting elastic surface waves,'' J. Acoust. Soc. Am. **53**, 1116–1122 (1973).

[4] P. E. Lagasse, I. M. Mason, and E. A. Ash, ''Acoustic surface waveguides-analysis and assessment,'' IEEE Trans. Microwave Theory Tech. **MTT-21**, 225–236 (1973).

[5] P. E. Lagasse, ''Analysis of a dispersion free guide for elastic waves,'' Electron. Lett. **8**, 372–373 (1972).

[6] J. McKenna, G. D. Boyd, and R. N. Thurston, ''Plate theory solution for guided flexural acoustic waves along the tip of a wedge,'' IEEE Trans. Sonics Ultrason. **SU-21**, 178–186 (1974).

[7] V. V. Krylov, ''Wedge acoustic waves: new theoretical and experimental results,'' in *Proceedings of the II International Symposium on Surface Waves in Solids and Layered Structures*, Varna, Bulgaria (World Scientific, Singapore, 1990), pp. 174–189 (1989).

[8] V. V. Krylov and A. V. Shanin, ''Influence of elastic anisotropy on the velocities of acoustic wedge modes,'' Sov. Phys. Acoust. **37**, 65–67 (1991).

[9] J. R. Chamuel, ''Influence of elastic anisotropy on the velocities of acoustic wedge modes,'' Report JRC-10-90, Sonoquest Advanced Ultrasonic Research, 1990.

[10] J. R. Chamuel, ''Ultrasonic studies of transient seismo-acoustic waves in bounded solids and liquid/solid interfaces,'' Report JRC-34-91, Sonoquest Advanced Ultrasonic Research, 1991.

[11] X. Jia and M. de Billy, ''Observation of the dispersion behavior of surface acoustic waves in a wedge waveguide by laser-ultrasonics,'' Appl. Phys. Lett. **61**, 2970–2972 (1992).

[12] D. Auribault, X. Jia, M. de Billy, and G. Quentin, ''Study of surface acoustic waves guided by a metallic cylindrical wedge using laser-ultrasonic techniques,'' J. Phys. (Paris), Colloq. **C5, Suppl. III-4**, 737–740 (1994).

[13] A. S. Bonnet-Ben Dhia, J. Duterte, and P. Joly, ''Guided waves of the surface of a locally deformed elastic half-space,'' Actes of the 4th French Congress of Acoustics, Vol. 2, 821–824 (1997).

[14] A. C. Hladky-Hennion, ''Finite element analysis of the propagation of acoustic waves in waveguides,'' J. Sound Vib. **194**, 119–136 (1996).

[15] A. C. Hladky-Hennion, P. Langlet, and M. de Billy, ''Finite element analysis of the propagation of acoustic waves along waveguides immersed in water,'' J. Sound Vib. **200**, 519–530 (1997).

[16] A. C. Hladky-Hennion, P. Langlet, R. Bossut, and M. de Billy, ''Finite element modelling of radiating waves in immersed wedges,'' J. Sound Vib. (accepted for publication).

[17] M. de Billy, ''On the influence of loading on the velocity of guided acoustic waves propagating in linear acoustic wedges,'' J. Acoust. Soc. Am. **100**, 659–662 (1995).

[18] J. N. Decarpigny, ''Application de la méthode des éléments finis à l'étude de transducteurs piézoélectriques,'' thesis, Université des Sciences et Techniques de Lille, 1984.

[19] R. Holland, ''Representation of dielectric, elastic, and piezoelectric losses by complex coefficients,'' IEEE Trans. Sonics Ultrason. **SU-14**, 18–20 (1967).

[20] R. Bossut, ''Modélisation en transitoire pour moteurs piézoactifs,'' Report CR 8214, Institut Supérieur d'Electronique du Nord, 1995.

[21] J. Assaad, ''Modélisation des transducteurs piézoélectriques haute fréquence à l'aide de la méthode des éléments finis,'' thesis, Université de Valenciennes et du Hainaut-Cambrésis, 1992.

[22] P. M. Pinsky, L. L. Thompson, and N. N. Abboud, ''Local high-order radiation boundary conditions for the two-dimensional time-dependent structural acoustics problem,'' J. Acoust. Soc. Am. **91**, 1320–1335 (1992).

[23] O. C. Zienkiewicz, *The Finite Element Method* (McGraw-Hill, New York, 1979), 3rd ed.

[24] N. M. Newmark, ''A method for computation of structural dynamics,'' Proc. Am. Soc. Civ. Eng. **85**, EM3, 67–94 (1959).

[25] P. M. Morse, *Vibration and Sound* (McGraw-Hill, New York, 1948), 2nd ed.

[26] P. E. Lagasse, M. Cabus, and M. Verplanken, ''The influence of truncation on dispersion of wedge guides,'' IEEE Ultrason. Symp. 121–124 (1974).

[27] V. V. Krylov, ''Geometrical-acoustics approach to the description of localized vibrational modes of an elastic solid wedge,'' Sov. Phys. Tech. Phys. **35**, 137–140 (1990).

[28] V. V. Krylov, ''Propagation of wedge acoustic waves along wedges imbedded in water,'' Ultra. Symp. Cat. #94, CHO 793–796 (1994).

[29] M. de Billy, ''On the scattering of antisymmetrical edge modes,'' J. Acoust. Soc. Am. **101**, 3261–3269 (1997).

Numerical evaluation of the far-field directivity pattern using the fast Fourier transform

Jamal Assaad and Jean-Michel Rouvaen
Institut d'Electronique et de Microélectronique du Nord (IEMN), UMR CNRS 9929, OAE Department, Université de Valenciennes et du Hainaut Cambrésis, le Mont Houy, BP 311, 59304–Valenciennes Cedex, France

(Received 30 July 1996; revised 20 January 1998; accepted 10 February 1998)

The far-field directivity pattern can be computed using the fast Fourier transform (FFT) algorithm. Numerical implementation of the angular spectrum approach (ASA) is generally used to compute the pressure field. The aim of this paper is to demonstrate that the discrete far-field pressure can be only computed by the calculation of the DFT of the normal velocity. In fact, using the asymptotic expression of the Rayleigh's integral, which is also the solution of Helmholtz equation, it will be shown that the analytical far-field pressure is given by the Fourier transform of the normal velocity. Guidelines for the selection of sampling interval and the size of the baffle in which the source is mounted will be given. Then this paper shows that the size of baffle influences the angular resolution at which the far field is computed and when the source is oversampled the computed discrete pressure becomes better. Numerical results concerning a transducer that exhibits harmonic oscillations will be considered and discussed.
[S0001-4966(98)00106-4]

PACS numbers: 43.20.Rz, 43.20.Bi, 43.40.Rj [JEG]

INTRODUCTION

In many applications (acoustical imaging, nondestructive testing,...), the far-field directivity pattern is the most interesting characteristic of a transducer. In fact, the measurement of these patterns can be simply performed. The fast Fourier transform (FFT) has been previously used[1,2] in order to compute the radiation from unbaffled finite plates. The angular spectrum approach (ASA) can be used to compute the near-field and the far-field pressures. This technique has been previously used by several authors.[1–6] For example Williams *et al.*[1] have used it to evaluate the pressure field of the rectangular plate. Recently, Wu *et al.*[5,6] have analyzed the errors due to DFT and discretization. They have used the same expressions to analyze the errors in the near field and the far field. The aim of this paper is to show that, in the far-field zone, a simpler expression can be used. This expression allows fast computation and gives guidelines for the choice of the sampling interval and the size of baffle in which the source is mounted.

The computed pressure field via angular spectrum decomposition can be found in many papers.[1–6] Reference 3 and Wu's recent paper[5] give a good description of the angular spectrum approach (ASA). Moreover, they give an extensive review of the literature associated with the concept of ASA. Thus this description will not be recalled here. Finally, we will use practically the same notations as Ref. 5.

In the first section, the far field is computed by only the evaluation of the discrete Fourier transform (DFT) of the normal velocity, in other words, its angular spectrum. In the second section, the piston mode case will be discussed. In this case, errors due to the use of DFT and discretization (frequency aliasing, half-sample length phase shift error, and spatial aliasing) will be shown and discussed. Numerical results concerning a transducer that exhibits harmonic oscillations will be considered and analyzed. Guidelines for fixing the different necessary parameters for the numerical implementation of the ASA, in order to get the far-field pressure, are given. In addition, the influence of the guard band (D-2A region, see Fig. 1) region is given. It will be shown that the size of this guard band influences only the angular resolution at which the far field is computed. In other words, the far-field pressure computed using the FFT becomes undersampled if the size of this region is not correctly chosen. The case of oversampling the source will be considered and discussed.

I. FAR-FIELD PRESSURE

Figure 1 describes an acoustic harmonic source (or transducer) of width $2A$ mounted in a rigid wall. The length of the transducer (along y axis) is assumed to be infinite. Then the two-dimensional radiation problem will be considered. The harmonic state $\exp(-j\omega t)$ will be assumed and retained as reference. The pressure $p(x,z)$ is given by

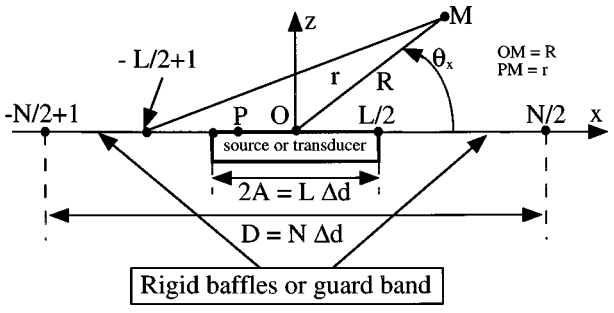

FIG. 1. Geometry and notation used for the calculation of the acoustic field.

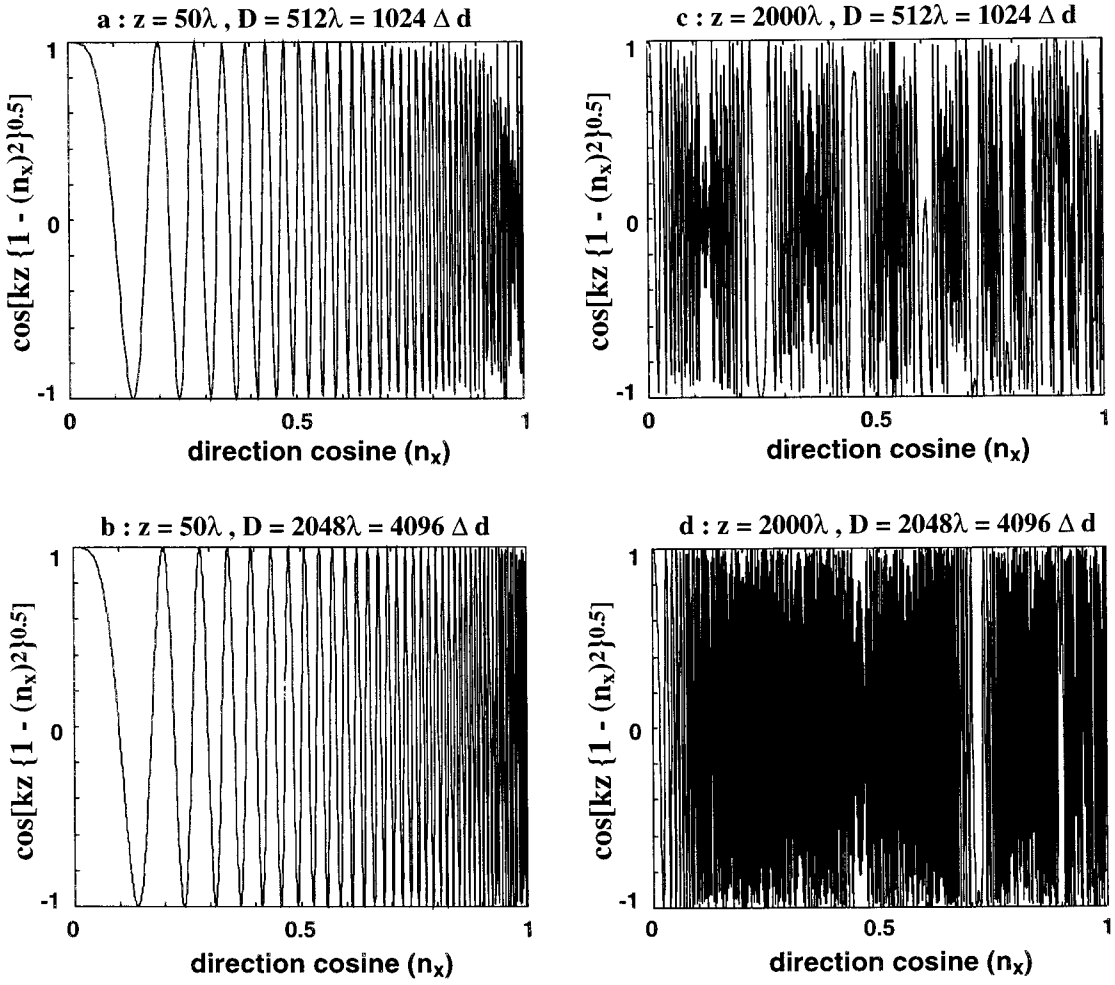

FIG. 2. Real part of Green's function, normalized by $\{1-(n_x)^2\}^{0.5}$, for pressure field computed at two ordinates ($z=50\lambda$ and $z=2000\lambda$).

$$p^a(x,z)=\frac{k\rho c}{2}\int_{-\infty}^{+\infty}\nu(x')H_0^{(1)}(kr)dx', \tag{1}$$

where k is the wave number, $\nu(x')$ is the normal velocity in the source plane $z=0$, and $H_0^{(1)}(kr)$ is the zeroth-order Hankel function, x and z are the coordinates of the field point M, and r gives the position of the field point with respect to running point P (see Fig. 1). The upper index a refers to the analytical expression. Using the convolution theorem, the pressure field for $z\geqslant 0$ can be written as

$$p^a(x,z)=\frac{k\rho c}{2}\int_{-\infty}^{+\infty}\frac{V(f_x)}{f_z}\exp[j2\pi(xf_x+zf_z)]df_x \quad \text{with } k_{x,z}=2\pi f_{x,z}=kn_{x,z}, \tag{2}$$

where $V(f_x)$ is the Fourier transform of $\nu(x)$, n_x ($n_x=\cos\theta_x$) and n_z are the direction cosines,

$$k_z=k\sqrt{1-n^2}, \quad \text{if } k^2\geqslant k_x^2$$
$$=jk\sqrt{n_x^2-1}, \quad \text{if } k^2<k_x^2. \tag{3}$$

The discrete form of the pressure as given by Eq. (2) can be written as

$$p_D(i_x\Delta d,z)=\frac{\Delta f\rho c}{\lambda}\sum_{m_x=-N/2+1}^{N/2}\frac{V(m_x\Delta f)}{U}\times\exp\left[2j\pi\left(i_x\frac{m_x}{N}+zU\right)\right], \tag{4a}$$

with

$$U=(1/(\lambda)^2-(m_x\Delta f)^2)^{0.5} \quad \text{and} \quad n_x=\lambda m_x\Delta f, \tag{4b}$$

where $V(m_x\Delta f)$ is the DFT of $\nu(x)$, λ is the wavelength, Δd is the sampling interval ($\Delta d=1/F_s$, F_s being the spatial sampling frequency) used to sample the source, Δf is equal to $1/N\Delta d$, and $m_x=-N/2+1,...,N/2$. The lower index D refers to the discrete expression. Reference 5 can be referred to for more details concerning the above equation. Time computation can be reduced if the FFT is used to compute $V(m_x\Delta f)$, but generally the value of N must be great, thus a significant amount of time is necessary to compute the field. Equation (2) gives an exact pressure while Eq. (4) is the discrete form of the exact one.

Generally, the far-field pressure is very interesting for many applications. Thus in the following the far-field zone will be always considered. To derive a simple analytical expression for the far-field pressure, Eq. (1) will be considered. In the far field Eq. (1) can be written as:[7]

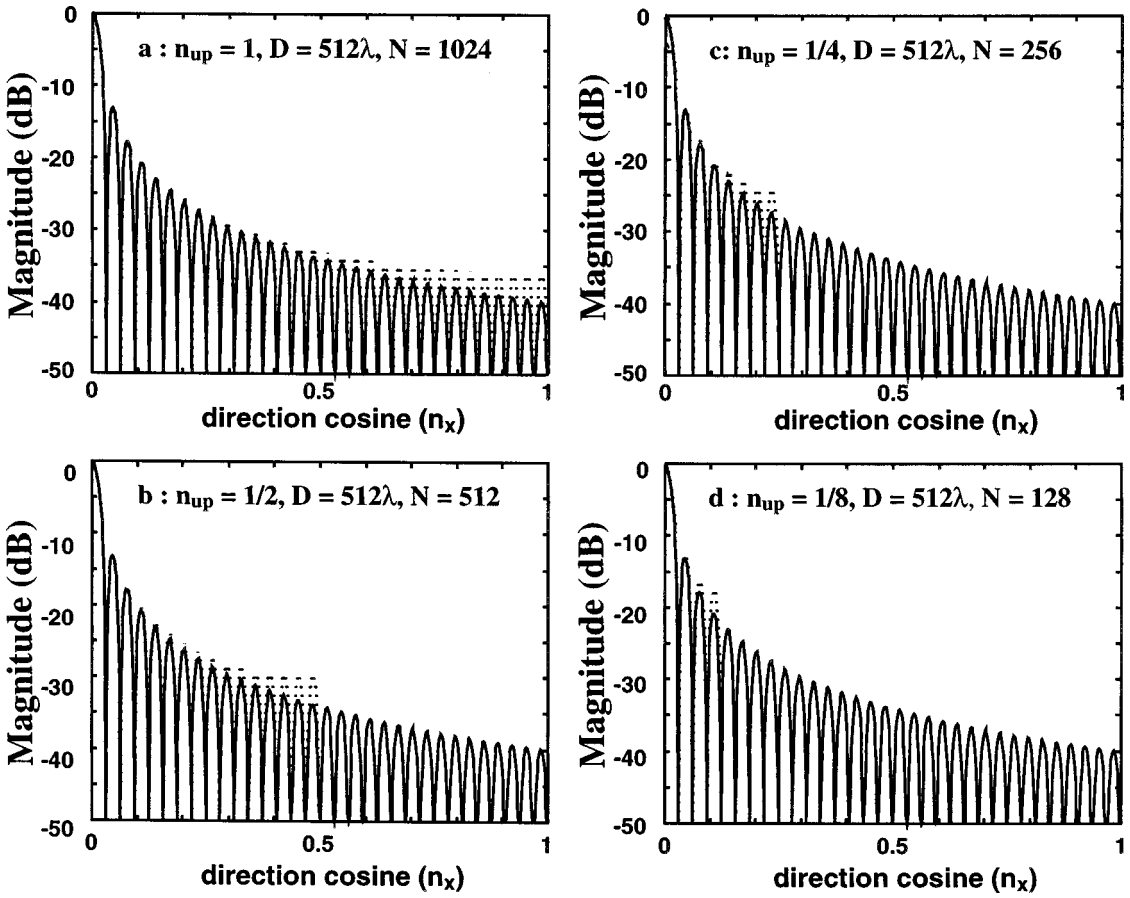

FIG. 3. Far-field pressures versus $n_{up}<1$ for a transducer of width $2A=32\lambda$, mounted in a rigid wall of width $D-2A$ with $D=512\lambda$, and working in piston mode. Solid and dotted lines describe the analytical far-field pressures [Eq. (17)] and DFT result [Eq. (18)].

$$p^a(R,n_x)=p_0\int_{-\infty}^{+\infty}\nu(x)e^{-j2\pi x(n_x/\lambda)}\,dx, \tag{5}$$

with

$$p_0=\frac{k\rho c}{2}\,\tilde{H}(kR)$$

$$\text{and}\quad \tilde{H}(kR)=\sqrt{\frac{2}{\pi kR}}\exp[-j(kR-\pi/4)], \tag{6}$$

where R gives the position of the field point with respect to the origin O of the transducer (Fig. 1). For convenience the polar coordinates (R,θ_x) are used. Equation (5) is valuable for $R>(2A)^2/\lambda$. In fact, three zones can be distinguished: the near-field $[R<(2A)^2/\lambda]$, the Fresnel zone $[R\sim(2A)^2/\lambda]$, and the far-field zone.[4,7] It should be noted that in Eq. (5), $n_x=\cos(\theta_x)$ must always be lower than unity in absolute value (i.e., $|n_x|\leqslant 1$). In fact, the far field as given by Eq. (5) is only valuable in the half-domain defined by $z>0$ and the far-field evanescent waves are completely removed since they play rigorously no role. The far-field pressure as given by Eq. (5) can be computed as

$$p^a(R,n_x)=p_0V(f_x)$$

$$=p_0\int_{-\infty}^{+\infty}\nu(x)e^{-2j\pi xf_x}\,dx \quad \text{with}\quad f_x=\frac{n_x}{\lambda}. \tag{7}$$

Equation (7) is well known and has been always used to compute the far field. In addition, it has been shown, with the help of the finite element method, by using Helmholtz's equation and its exact solution obeying the Sommerfeld radiation condition, that Eq. (7) gives the exact far-field pressure.[7] Thus in the far field, Eq. (2) can be replaced by Eq. (7). Finally, Eq. (7) shows that the far-field pressure is proportional to the FT of the normal velocity. For example, in the case of piston mode [i.e., $\nu(x)=\nu_0=$constant], the famous relation

$$p^a(R,\theta_x)=p_0'\,\text{sinc}(kA\cos\theta_x)\quad\text{with}\quad p_0'=2p_0A \tag{8}$$

is obtained.

Practically, Eq. (7) can be numerically implemented with the help of the FFT. Due to discretization and the use of the FFT some errors appear. These errors are discussed in the second section using the discrete form of Eq. (7) and Eq. (2). Using the discrete form of Eq. (2), i.e., Eq. (4), the numerical implementation of the ASA can be obtained. Recently, in two-dimensional radiation problems, Eq. (4) has been used for direct implementation of the ASA[5,6] in the near field as well as in the far-field zone. But, in the far-field zone it's better to use the discrete form of Eq. (7) [see Eq. (15) or Eq. (16) below] instead of the discrete form of Eq. (2), i.e., Eq. (4), for the following reasons: (i) in Eq. (4) there is a pole at $n_z=0$; (ii) the direct use of the discrete form of Eq. (7) allows fast computation and able to give the guidelines for

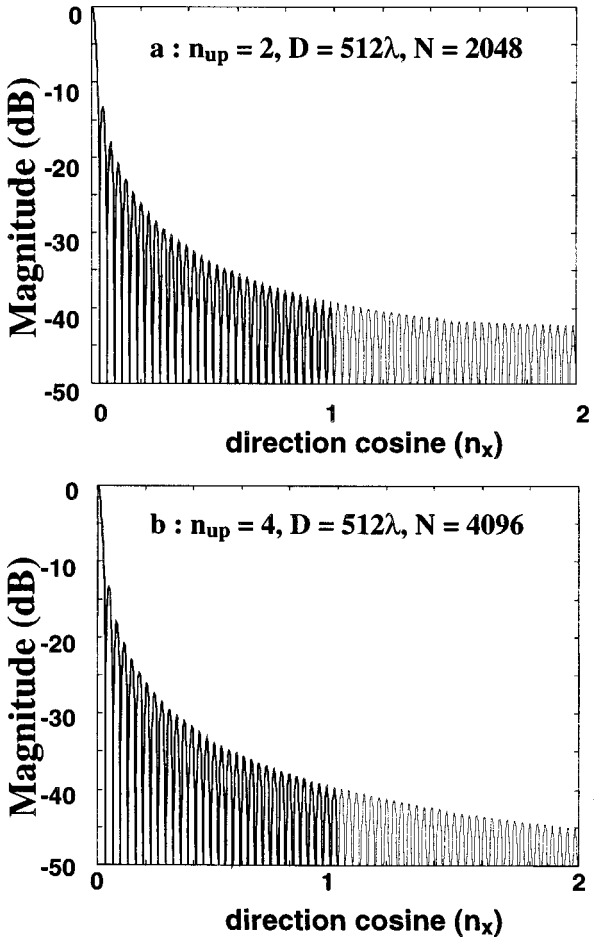

FIG. 4. Far-field pressures versus $n_{up}>1$ and for $2A=32\lambda$ and $D=512\lambda$. Thick and thin lines describe the analytical far-field pressures [Eq. (17)] and DFT result [Eq. (18)]. The normal velocity is assumed constant.

the choice of D (i.e., guard band with $2A$ fixed); and finally, (iii) a large value of N is necessary in order to correctly sample the Fourier transform of Green's function, $\exp(ikz\sqrt{1-n_x^2})/(k\sqrt{1-n_x^2})$. Figure 2 gives the real part of the $\exp(ikz\sqrt{1-n_x^2})$ term in the near field [$z=50\lambda$, Fig. 2(a) and (b)] and in the far field [$z=2000\lambda$, Fig. 2(c) and (d)]. Figure 2(a) and (c) is obtained by taking $\Delta n_x=2/N=1/512$, while Fig. 2(b) and (d) is obtained by taking $\Delta n_x=2/N=1/2048$. In fact, Δn_x gives the angular resolution at which the plane wave components are calculated [see Eq. (29) in Ref. 4]. As the imaginary part, in each case, look very similar to the real part, only the last one is given. It is interesting to note that for $\Delta n_x=2/N=1/512$, the Green's function is undersampled especially for $z=2000\lambda$. For $z=50\lambda$, it undersampled only for n_x near unity ($n_x\approx 1$). Thus if Eq. (4) is used to compute the far field, a large value of N is necessary. In this case, the phase of the Green's function becomes more oscillating. For these reasons, the far field pressure, calculated over the maximum angular range ($-1<n_x\leqslant 1$) with the help of Eq. (4), is not in good agreement with the analytical one[4–6] because of the presence of oscillating ripples [see Fig. 3(b) in Ref. 4 and Fig. 4(b) in Ref. 6]. Recently, Wu *et al.*[6] have proposed to modify the value N in the lower and upper limits of the sum in Eq. (4) for eliminating these ripples. This new value, termed as optimum (N_0), is given by[6]

$$N_0=N\,\sin\left[\mathrm{Arctan}\left(\frac{D}{2z}\right)\right]. \tag{9}$$

For D (see Fig. 1) very small with respect to z, N_0 will converge to zero as z increases. For example, if z becomes infinite and D stays fixed, N_0 becomes equal to zero, and then Eq. (4) with $N=N_0=0$ cannot be used. In other words, Eq. (9) is not suitable in the far field and only useful in the Fresnel zone because in the near field $N_0\approx N$.

In Refs. 3–6, no consideration has been devoted to the ''guard band'' region or $D-2A$ region (see Fig. 1). Guard band refers to an intentional region of zero-padding exterior to the source region ($2A$) that is to say the value of D with $2A$ fixed. In fact, using Eq. (4) it is hard to see the influence of the value of D in the far-field zone. This influence will be easily shown here by the using of Eq. (7).

II. APPLICATIONS

In some experimental cases, harmonic vibrations can propagate at the transducer surface.[8] Thus let assume that the normal velocity is given by

$$\begin{aligned}\nu(x)&=\nu_0\,\cos(2\pi f_l x), \quad \text{if } |x|\leqslant A \text{ with } \lambda_l=l\lambda\\ &=0, \quad \text{if } |x|>A,\end{aligned} \tag{10}$$

where λ_l is the harmonic wavelength. In this case, using Eq. (7) the analytical far-field pressure is given by

$$p^a(R,n_x)=\frac{p_0'}{2}\left\{\mathrm{sinc}\left[\frac{2\pi A}{\lambda}\left(n_x+\frac{1}{l}\right)\right]+\mathrm{sinc}\left[\frac{2\pi A}{\lambda}\left(n_x-\frac{1}{l}\right)\right]\right\}. \tag{11}$$

The discrete form of Eq. (7) is given by

$$p_D(R,m_x\Delta f\,)=p_0V_D(m_x\Delta f\,), \tag{12a}$$

with

$$n_x=m_x\lambda\Delta f=\frac{m_x\lambda}{N\Delta d}, \tag{12b}$$

where V_D is the DFT of the normal velocity and $m_x=-N/2+1,...,N/2$. It should be noted that this expression is periodic in m_x with period N. Then $p_d(R,m_x\Delta f\,)$ is computed over a single period. Moreover, for $m_x=N/2$ the upper direction cosine value, which will be named n_{up}, is equal to $\lambda\Delta fN/2$ and since $\Delta f=1/(N\Delta d)$ we obtain $n_{up}=\lambda/(2\Delta d)$. When Δd is equal to one half-wavelength (Nyquist criterion) n_{up} equals unity. Using Eq. (12), the angular resolution at which the pressure far field is calculated is computed as

$$\Delta n_x=\lambda\Delta f=\frac{2n_{up}}{N} \text{ with } n_{up}=\frac{\lambda}{2\Delta d}. \tag{13}$$

If the classical sampling (see Appendix A) and the discrete Fourier transform (DFT) of $\nu(x)$:

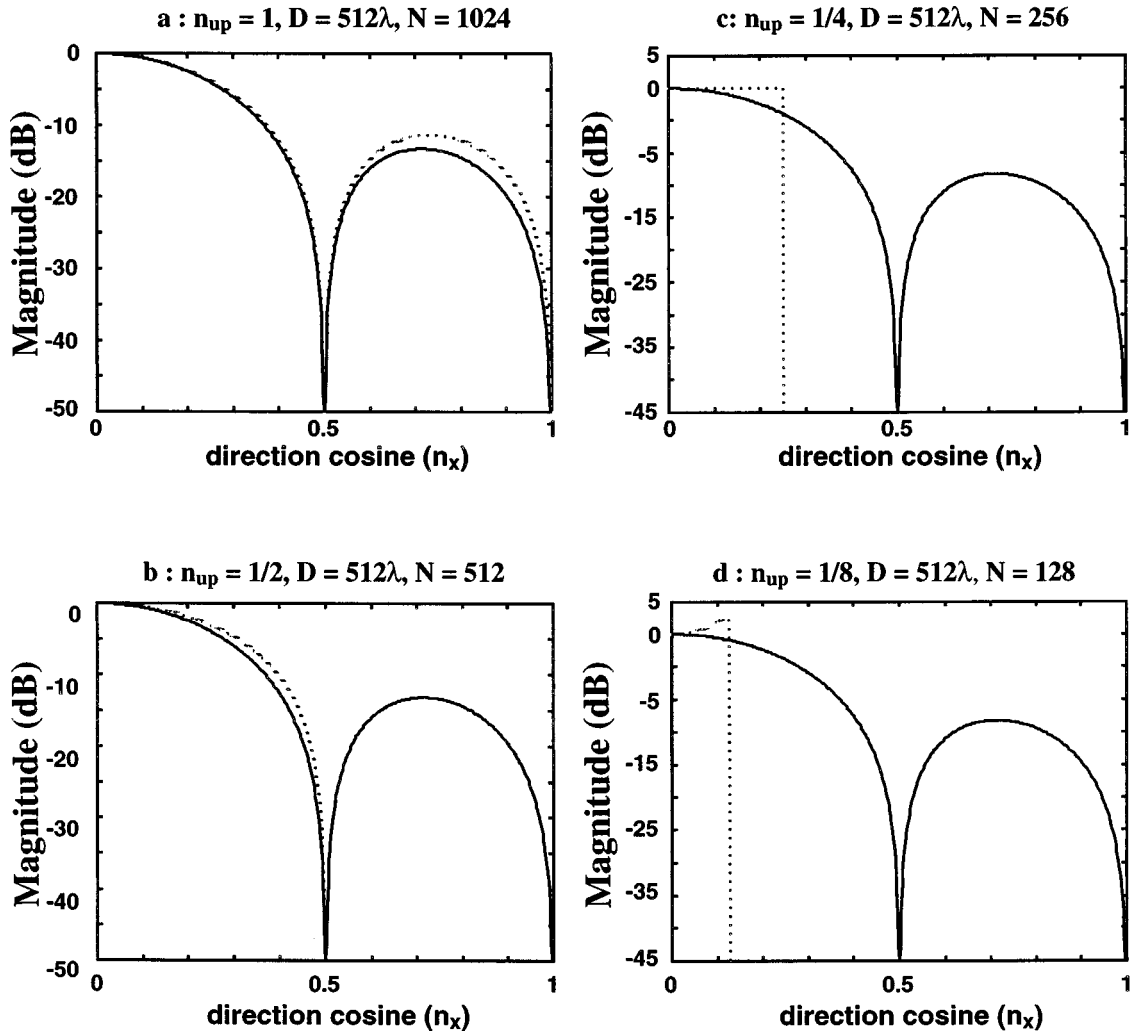

FIG. 5. Same as Fig. 3 except that $2A=2\lambda$.

$$V_D^c(m_x\Delta f\,)=\Delta d\sum_{i_x=-N/2+1}^{N/2}\nu(i_x\Delta d)\exp\left(\frac{-2j\pi m_x i_x}{N}\right) \tag{14}$$

are used to compute the pressure, then the discrete far-field pressure is given by

$$p_D^c(R,m_x\Delta f\,)=\frac{p_0'}{2}\,[X_-e^{-j2\pi(m_x-\kappa)\phi/N}+X_+e^{-j2\pi(m_x+\kappa)\phi/N}], \tag{15a}$$

with

$$X_\pm=\left\{\frac{\sin(\pi L(m_x\pm\kappa)/N}{L\,\sin(\pi(m_x\pm\kappa)/N}\right\}\quad\text{and}\quad\kappa=\frac{N}{2n_{\rm up}l}, \tag{15b}$$

where $A=L\Delta d$, $f_l=1/\lambda_l=\kappa\Delta f$ and ϕ is equal to 1/2 when L is even and equal to 0 when L is odd.

Instead of classical sampling, the sampling and hold can be also used (see Appendix A). In this case

$$p_D^h(R,m_x\Delta f\,)=p_D^c(R,m_x\Delta f\,)\,\mathrm{sinc}\left(\frac{\pi m_x}{N}\right), \tag{16}$$

where the upper index (c or h) refers to the classical (c) and hold (h) sampling, respectively. The computed pressures with the help of Eqs. (15) and (16) are referred as the DFT and DSFT (discrete sinc Fourier transform) based results, respectively.

In the following, for comparison purposes, the analytical solution pressures will be always computed at $n_x=\cos\theta_x=2n_{\rm up}m_x'/N$ with $m_x'=-N/(2n_{\rm up}),\ldots,N/(2n_{\rm up})$ in order to maximize the angular range, i.e., $|n_x|\leqslant 1$. In addition, the angular resolution at which the analytical pressure far field is calculated is also equal to $\Delta n_x=2n_{\rm up}/N$ [see Eq. (13)]. In other words the analytical solution will be undersampled when $n_{\rm up}$ is less than unity.

For n_x values greater than $n_{\rm up}$, the DFT pressure based results are not shown, since it is known that they are periodic (see Appendix B) with period $2n_{\rm up}$ (for $m_x=N/2$, $n_x=n_{\rm up}$, and thus a period N in m_x corresponds to a period $2n_{\rm up}$ in n_x). Finally, as the analytical pressures and DFT based results are even functions, only results corresponding to $n_x\geqslant 0$ will be shown.

A. Piston mode

In this case, the normal velocity is assumed to be constant (i.e., piston mode, $\kappa=0$), then the far-field pressures, as given by Eqs. (11), (15), and (16) simplify to

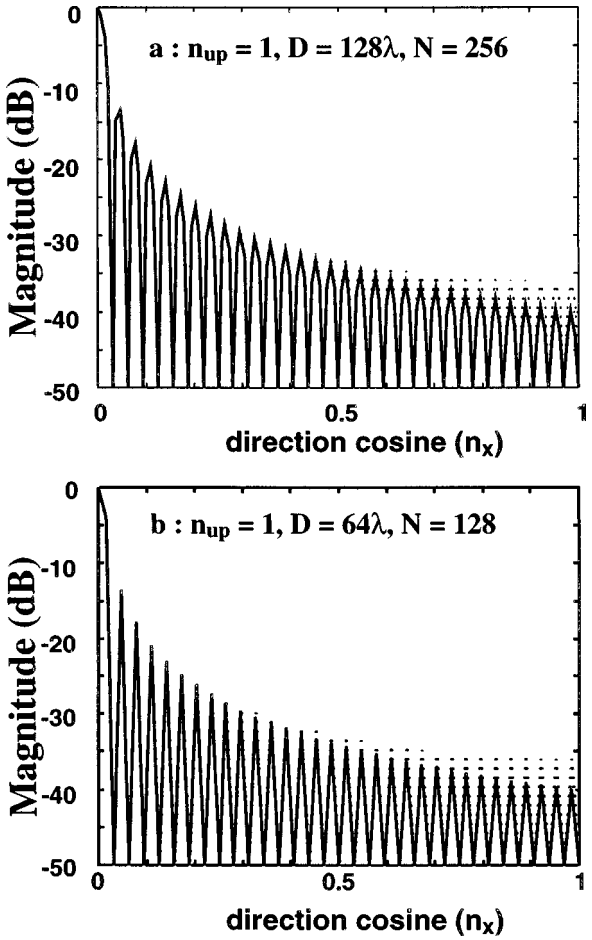

FIG. 6. Far-field pressures versus D keeping $n_{up}=1$ for the previously described transducer of width $2A=32\lambda$. Solid and dotted lines describe the analytical far-field pressures [Eq. (17)] and DFT results [Eq. (18)]. The normal velocity is assumed constant.

$$p^a(R,m_x'\Delta f\ )=p_0'\ \mathrm{sinc}\left(\frac{\pi L}{N}\ m_x'\right), \tag{17}$$

$$p_D^c(R,m_x\Delta f\ )=p_0'\left\{\frac{\sin(\pi L(m_x/N)}{L\ \sin(\pi(m_x/N)}\right\}e^{-j2\pi m_x\phi/N}, \tag{18}$$

and

$$p_D^h(R,m_x\Delta f\ )=p^a(R,m_x\Delta f\ )e^{-j2\pi m_x\phi/N}\ \text{ for }\ n_{up}\leqslant 1. \tag{19}$$

It is interesting to note that when the source plane shifts by half-sample length due to discretization, only the phase of the field pressure as given by Eq. (19) is shifted by the same amount, but its magnitude remains unchanged. So, to the contrary of Wu *et al.*'s[5] method, no supplementary multiplicative phase-correction term is needed to compute the magnitude of the far-field pressure. Moreover, if we multiply the right-hand side of Eq. (19) by $\exp(2j\pi m_x\phi/N)$ the half-sample length phase shift error can be removed. Also, an exact expression for the real part and imaginary part of the far-field pressure can be obtained. In fact, in Ref. 5, an exact angular spectrum is obtained but not an exact pressure. In the far-field zone and for $\theta_x=\pi/2$ (i.e., on the z axis) and by using the DSFT based results, some ripples have been observed in Refs. 5 and 6. But, using Eqs. (17), (18), and (19) for $\theta_x=\pi/2$, we can say immediately that the three pressures give the same result (i.e., no ripples).

In the following the numerical results are normalized by p_0'. In order to study the influence of n_{up}, D and L several cases will be considered.

1. Influence of n_{up} with D and L fixed

Figure 3 displays the far-field pressures for a transducer with $2A=32\lambda$ (as in Wu's paper[5]), for different values of n_{up} and by keeping $D=512\lambda$ (i.e., $D=$constant). In Fig. 3 solid lines and dotted lines describe the analytical far-field pressure magnitude [Eq. (17)] and the DFT based results [Eq. (18)], respectively. It is interesting to note that, for $n_x<n_{up}/2$, good results are obtained if $L=2n_{up}L_p>1$, where L_p is defined by $2A=L_p\lambda$ (see below). For $n_{up}/2<n_x<n_{up}$ there are some small differences between the analytical solution and the DFT based results. It must be noted that using the DSFT based results (which is, in this case, equivalent to the analytical pressure for n_x and $n_{up}<1$) the previous small errors can be corrected at the expense of a significant computation time (N complex products to be performed). The interest of such procedure is questionable for engineering applications, these errors being hardly measurable. Moreover, a true piston mode may never be obtained and the normal velocity has always sinusoidal components for which, as will be shown later, the previous correction fails.

One may also take a value of Δd smaller than $\lambda/2$ (the source is then oversampled) for the DFT based results. In order to show the influence of the oversampling ($n_{up}>1$) let assume $n_{up}=\alpha/2$ with $\alpha\geqslant 2$ ($\Delta d=\lambda/\alpha$), $D=512\lambda=N_\alpha\Delta d$, and $2A=32\lambda=L_\alpha\Delta d$ (A and D are assumed fixed). Two cases are considered. In the first case assume that $\alpha=2$ (Nyquist criterion), then we have $N_2=1024$ and $L_2=64$. In the second case assume that $\alpha=4$ then $N_4=2048$ and $L_4=128$. The first case corresponds to results shown by Fig. 3(a). In the second case, the source is oversampled ($n_{up}=2$). The corresponding results are shown in Fig. 4(a). Results corresponding to $\alpha=8$ are also presented in Fig. 4(b) with the horizontal axis stopped at a value $n_x=2$ for viewing convenience. It is interesting to note that we have always N_α/L_α constant. But the magnitude of the DFT based results [Eq. (18)] is given by

$$|p_D^c(R,m_x\Delta f\ )|=p_0'\left|\frac{\sin(\pi L_\alpha(m_x/N_\alpha)}{L_\alpha\ \sin(\pi(m_x/N_\alpha)}\right|. \tag{20}$$

As α increases, the $L_\alpha\ \sin(\pi(m_x/N_\alpha)$ term is more and more well approximated by the $(\pi L_\alpha(m_x/N_\alpha)$ term, i.e., the aliasing errors become smaller and smaller and the difference between the DFT based results and the analytical results becomes more and more negligible. In addition, for $\alpha=4$, the direction cosine is equal to 2 (i.e., $\cos\theta_x=2$) then for $m_x\geqslant N_\alpha/4$ ($\cos\theta_x\geqslant 1$) the computed value must be rejected. In fact, the analytical solution as given by Eq. (7), as said before, does not contain evanescent waves.

2. Influence of the size of the source (i.e., 2A)

To show the influence of the width $2A$ of the source on the choice of n_{up}, $2A$ is taken equal to 2λ (i.e., $2A=2\lambda$

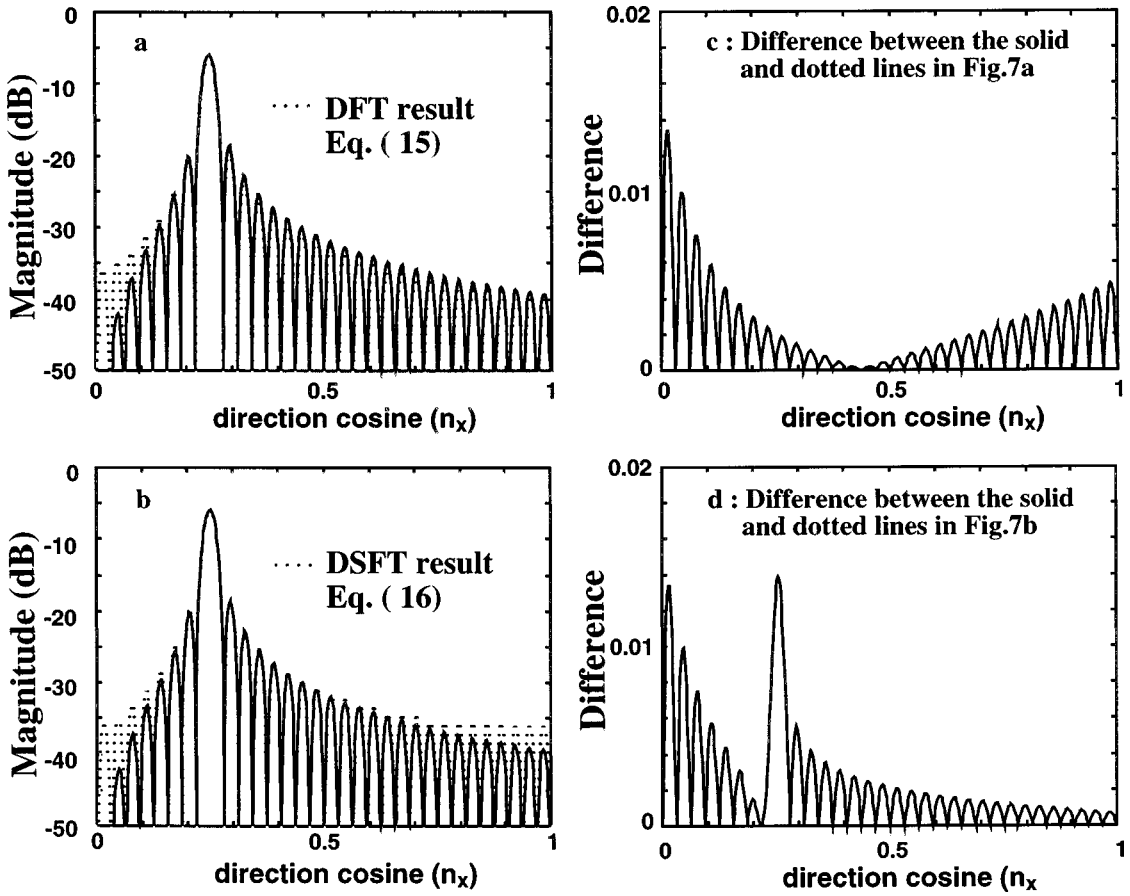

FIG. 7. Far-field pressures in the harmonic mode case for $D=512\lambda$, $n_{up}=1$, $N=1024$, and $l=4$. Dotted lines in (a) and (b), respectively, describe DFT and DSFT based results; while solid lines give the analytical solution [Eq. (12)]. The difference between the analytical solution and the DFT and DSFT based results are shown in (c) and (d), respectively.

$=L_p\lambda$), $D=512\lambda$. As in Fig. 3, Fig. 5 shows the pressures versus n_{up}. Good agreement between theoretical and DFT values are observed for $n_x<n_{up}/2$ in Fig. 5(a) and (b), which satisfy the condition $L=2n_{up}L_p>1$. When this condition fails, as in Fig. 5(c) and (d), the DFT values become erroneous. In fact, taking $D=N_p\lambda$ as $n_{up}=2\lambda/\Delta d$ the following two relations $N=2n_{up}N_p$ and $L=2n_{up}L_p$ are obtained. Then using Eq. (18) the magnitude of the DFT based results can be rewritten as

$$|p_D^c(R,m_x\Delta f\,)|=p_0'\left|\frac{\sin\left(m_x\pi\,\dfrac{L_p}{N_p}\right)}{2n_{up}L_p\,\sin\left(\dfrac{m_x\pi}{(2n_{up}N_p)}\right)}\right|. \qquad (21)$$

For $2n_{up}L_p<1$, and as $m_x/(2n_{up}N_p)<1$ ($m_x=0,...,n_{up}$), it can be easily shown that $|p_D^c(R,m_x\Delta f|\geqslant p_0'$.

3. Influence of the guard band (or D)

In order to study the influence of guard band D ($D=N\Delta d$), Fig. 3(c) ($D=512\lambda$, $N=256$) and Fig. 3(d) ($D=512\lambda$, $N=128$) are considered. In addition, as it has been said before, the angular resolutions [Eq. (13)] at which the pressures are computed by using Eqs. (17) and (18), i.e., the analytical and DFT based results, are taken the same. Figure 6 displays the far-field pressure, keeping $n_{up}=1$, for two different values of D [$D=128\lambda$ and $N=256$ for Fig. 6(a); $D=64\lambda$ and $N=128$ for Fig. 6(b)]. In Fig. 6(a) and (b), the angular resolution Δn_x [Eq. (13)] is equal to 1/128 and 1/64, respectively. Comparing Fig. 3(c) to Fig. 6(a) and Fig. 3(d) to Fig. 6(b) we may infer that, by reducing D and keeping N constant, a maximum range can be obtained. In addition, when D decreases keeping N constant and $n_{up}=1$, the computed pressure becomes undersampled [see Fig. 3(a) and Fig. 6]. But the discrete computed pressures (DFT based results) at $n_x=2m_x/N$ stay the same. Reference 6 does not give the same conclusions. In Appendix B some comments are presented concerning replicated sources.

Using the above examples guidelines for the choice of Δd and D can be found. In fact, knowing $2A$ in terms of λ, Δd can be found by the choice of the upper angular range [i.e., $n_{up}=\lambda/(2\Delta d)$] and D can be obtained from the desired angular resolution because the angular resolution is equal to $2/N$.

B. Harmonic mode

The harmonic wavelength is taken equal to 4λ (i.e., $l=4$, $\kappa=128$). Thus the far-field pressure exhibits a main lobe in the direction cosine $n_x=1/l=0.25$. $2A$ and D are taken, respectively, equal to 32λ and 512λ. In this case Eq. (19) does not apply. Thus the frequency aliasing and a half-sample length phase shift error in the angular spectrum cannot be removed. Using Eqs. (15) and (16) the far-field

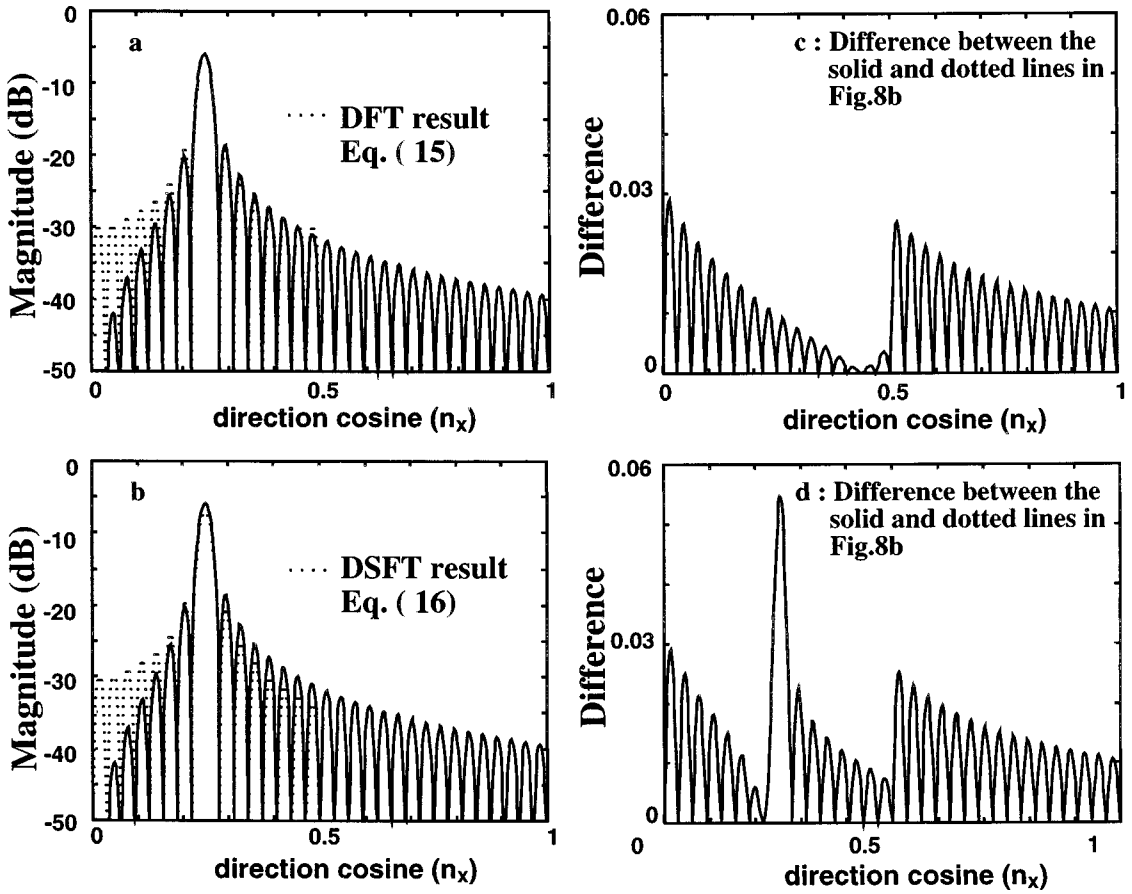

FIG. 8. Same as Fig. 7 except that the angular range is assumed to be equal to 1/2 ($n_{up}=1/2$, $N=512$).

pressure is then computed for $n_{up}=1$ and presented in Fig. 7(a) and (b), respectively, by dotted lines. The analytical solution is obtained by the use of Eq. (12). The difference between the analytical solution and ASA results (i.e., DFT and DSFT results) are presented in Fig. 7(c) and (d). Figure 8 is obtained by using the same parameters as for Fig. 6 but n_{up} is taken equal to 1/2. It should be noted for $n_x=0.25$, the difference is significant when the DSFT angular spectrum is used. Thus as said before, the DSFT do not correct the aliasing errors and the DFT gives best results. By the inspection of Figs. 7 and 8, we can say that, when n_{up} decreases the difference increases. Thus n_{up} must be chosen greater than or equal to $1/l$. The choice of N can be obtained from the desired angular resolution.

III. CONCLUSION

In the far-field zone, it has been shown that the discrete form of Eq. (7) allows fast computation and gives best results. It allows to find guidelines for the choice of the sampling interval and the size of guard band. Using the discrete form of this equation some errors appear. Two examples have been considered: piston mode and harmonic mode. For real transducers, the normal velocity always contains harmonic oscillations. Then, it has been shown that the DFT based results must be used. By using the DFT some errors appear. These errors have been discussed by considering different cases. It has been shown that the DFT based results are correct over the interval $[-n_{up}/2,\ n_{up}/2]$. In the exterior of this interval, the difference between the analytical solutions and the DFT based results are small. In the general case (i.e., piston mode and harmonic mode) these small errors can be reduced if the source is oversampled. In addition, it has been shown that the size of guard band influences only the resolution at which the pressure field is computed. Finally, the proposed method can also be extended to three-dimensional radiation problems. In fact, the normalized far-field directivity pattern of a piston source whose size is given by $[2A,\ 2A]$ and located at the (x,y) plane, is equal to $\mathrm{sinc}(Ak_x)\mathrm{sinc}(Ak_y)$.

APPENDIX A: CLASSICAL AND HOLDING SAMPLING

To use the ASA, the source (Fig. 1) must be sampled. As for signals there are a lot of methods to sample the normal velocity distribution $\nu(x)$ in the source plane $z=0$ (Fig. 1). The classical sampling of $\nu(x)$ can be mathematically described by

$$\nu^c(x)=\Delta d \sum_{i_x=-N/2+1}^{N/2} \nu(i_x\Delta d)\,\delta(x-i_x\Delta d), \tag{A1}$$

where δ is the Dirac function (Fig. 1). The sample and hold of $\nu(x)$, that has been proposed by Wu *et al.*,[5] is mathematically described by[9]

$$\nu^h(x)=\Delta d \sum_{i_x=-N/2+1}^{N/2} \nu(i_x\Delta d)\,\delta(x-i_x\Delta d)*\mathrm{rect}\left(\frac{x}{\Delta d}\right), \tag{A2}$$

with

$$\text{rect}\left(\frac{x}{\Delta d}\right)=1, \quad \text{if } |x|\leqslant\frac{\Delta d}{2}$$
$$=0, \quad \text{elsewise}, \tag{A3}$$

where* denotes the convolution product. In the above two equations, the upper index (c or h) refers to the classical (c) and hold (h) sampling, respectively. It should be noted that if $\Delta d\rightarrow 0$ then $\nu^h\rightarrow\nu^c$. This mathematical presentation is useful because it indicates the physical interpretation of the used sampling. In fact, in Eq. (A2) the value of $\nu(m_x\Delta d)$ is kept constant over the interval $[-\Delta d/2,\ \Delta d/2]$. Using the two previous expressions, it is simple to show that the discrete forms of the analytical Fourier transform (FT) of $\nu(x)$ are given by:

$$V_D^c(m_x\Delta f\ )=\Delta d\sum_{i_x=-N/2+1}^{N/2}\nu(i_x\Delta d)\exp\left(\frac{-2j\pi m_x i_x}{N}\right) \tag{A4}$$

and

$$V_D^h(m_x\Delta f\ )=V_D^c(m_x\Delta f\ )\text{sinc}\left(\frac{\pi m_x}{N}\right), \tag{A5}$$

where $\Delta f=1/(N\Delta d)$. Equation (A4) is the DFT of the normal velocity and Eq. (A5) gives the DSFT's (Discrete Sinc-Fourier Transform) angular spectrum. Equation (A5) has been proposed by Wu *et al.*[5] to obtain an exact angular spectrum.

APPENDIX B: SOME CONSIDERATIONS FOR REPLICATED SOURCES

It is well known that if a general function $f(u)$ is sampled with a period Δu, its Fourier transform (FT) or inverse Fourier transform $F(\eta)$ becomes periodic with period $\Delta\eta=1/\Delta u$. Thus in our case, the normal velocity is sampled at Δd, then the far-field pressure, which is the FT of this velocity, is periodic with period $\Delta f_x=1/\Delta d$. This period corresponds to a period in angular range equal to $\lambda\Delta f_x$ (or equivalent to $2n_{\text{up}}$). In fact, assuming that $N\rightarrow+\infty$, then the FT of Eq. (A1) can be rewritten as

$$V^c(f_x)=V(x)*\sum_{i_x=-\infty}^{+\infty}\delta\left(x-\frac{1_x}{\Delta d}\right)=\sum_{i_x=-\infty}^{+\infty}V\left(x-\frac{i_x}{\Delta d}\right). \tag{B1}$$

Then using Eq. (7), the discrete pressure is given by

$$p^c(R,n_x)=\sum_{i_x=-\infty}^{+\infty}p^a(R,n_x-2i_xn_{\text{up}}). \tag{B2}$$

This equation indicates that the discrete pressure is obtained by summing up the FT of $\nu(x)\exp[(2j\pi x/\lambda)(2i_xn_{\text{up}})]$. This induces errors (aliasing) inherent to the use of sampling. These errors becomes small when $n_{\text{up}}=\lambda/(2\Delta d)$ is greater than unity (the source is then oversampled). In fact, and from Eq. (B1), we can say that the replicated spectra will be located far from the original spectrum when $n_{\text{up}}>1$. For this reason the computed pressures in Fig. 4 are in best agreement with the analytical one. Effects in Eq. (B2) are classical in signal processing and described in many classical books. In addition, similar relations concerning replicated spectra have been obtained by Hah *et al.*[10] Moreover, Eq. (1) in Ref. 6 is not identical to Eq. (B2). For more details see Ref. 11.

[1] E. G. Williams and J. D. Maynard, ''Numerical evaluation of the Rayleigh integral for planar radiators using the FFT,'' J. Acoust. Soc. Am. **72**, 2020–2030 (1982).

[2] E. G. Williams, ''Numerical evaluation of the radiation from unbaffled, finite plates using the FFT,'' J. Acoust. Soc. Am. **74**, 343–347 (1983).

[3] D. P. Orofino and P. C. Pedersen, ''Efficient angular spectrum decomposition of acoustic sources-Part I: Theory,'' IEEE Trans. Ultrason. Ferroelectr. Freq. Control **UFFC-40**, 238–249 (1993).

[4] D. P. Orofino and P. C. Pedersen, ''Efficient angular spectrum decomposition of acoustic sources-Part II: Results,'' IEEE Trans. Ultrason. Ferroelectr. Freq. Control **UFFC-40**, 250–357 (1993).

[5] P. Wu, R. Kazys, and T. Stepinski, ''Analysis of the numerically implemented angular spectrum approach based on the evaluation of two-dimensional acoustic fields. Part I. Errors due to the discrete Fourier transform and discretization,'' J. Acoust. Soc. Am. **99**, 1339–1348 (1996).

[6] P. Wu, R. Kazys, and T. Stepinski, ''Analysis of the numerically implemented angular spectrum approach based on the evaluation of two-dimensional acoustic fields. Part II. Characteristics as a function of angular range,'' J. Acoust. Soc. Am. **99**, 1339–1348 (1996).

[7] J. Assaad, J-N. Decarpigny, C. Bruneel, R. Bossut, and B. Hamonic, ''Application of the finite element method to two-dimensional radiation problems,'' J. Acoust. Soc. Am. **94**, 562–573 (1993).

[8] J. Assaad, C. Bruneel, J-N. Decarpigny, and B. Nongaillard, ''Electromechanical coupling coefficients and far-field radiation patterns of lithium niobate bars (Y-cut) used in high-frequency acoustical imaging and nondestructive testing,'' J. Acoust. Soc. Am. **94**, 2969–2978 (1993).

[9] J. Assaad and J.-M. Rouvaen, ''Comment on Analysis of the numerically implemented angular spectrum approach based on the evaluation of two-dimensional acoustic fields. Part I and Part II,'' J. Acoust. Soc. Am. **101**, 3800–3803 (1997).

[10] Z. G. Hah and K. M. Sung, ''Effect of spatial sampling in the calculation of ultrasonic fields generated by piston mode,'' J. Acoust. Soc. Am. **92**, 3403–3408 (1992).

[11] J. Assaad and J.-M. Rouvaen, ''Some considerations concerning replicated spectra,'' J. Acoust. Soc. Am. **104**, 380–382 (1998).

Temperature dependence of ultrasonic Grüneisen parameter and ultrasonic attenuation in alkali halides

G. G. Sahasrabudhe
Department of Physics, R. K. N. Engineering College, Nagpur 440 013, India

S. D. Lambade
Department of Physics, Y. C. College of Engineering, Wanadongri, Nagpur 441 110, India

(Received 9 August 1996; accepted for publication 12 March 1998)

Temperature dependence of ultrasonic attenuation and ultrasonic Gruneisen parameter are investigated in alkali halides in the range 80–300 K. The calculations use a computer program, developed by the authors, for implementing Nava's modified formulation of Woodruff's theory. These calculations are done for NaCl, NaF, and LiF for longitudinal and shear waves along the [100], [110], and [111] directions. Compared to calculations based on original Mason formulation, it was found that in most cases the results are in better agreement with the experimental data. The results also help to throw some light on relative merits of different theories of attenuation. © *1998 Acoustical Society of America.* [S0001-4966(98)05706-3]

PACS numbers: 43.25.Dc [MAB]

INTRODUCTION

In the past a considerable amount of work, both theoretical and experimental, has been done in investigating the temperature dependence of acoustic attenuation in alkali halides.[1–10] Experimental studies[3–6] reveal that the dislocation mechanism yields a negligible contribution to the ultrasonic absorption in well-annealed crystals of alkali halides, and the contribution of thermoelastic losses, too, is exceedingly small. Thus the class of alkali halides is ideally suited for the study of ultrasonic absorption by phonon–phonon interactions as the absorption is determined almost exclusively by this mechanism.

The calculation of temperature dependence of acoustic damping in the Akhiezer regime has been studied in NaF, NaCl, NaBr,[7–9] KCl, KBr, and KI[6,10] using Mason's theory.[2] In a recent study by Nava *et al.*[11] the attenuation was calculated at room temperature using a modified formulation of theory of Woodruff *et al.*[12] for 12 nonconducting cubic crystals, including the halides NaCl, KCl, LiF, and NaF.

However, all these investigations employ Mason's scheme in which the various averages of the mode Grüneisen numbers γ_{ij} are evaluated over a small, fixed set of thermal phonon modes along the pure mode directions. A computer program recently developed by us[13] facilitates the calculation of these averages over the entire spectrum of thermal phonon modes. The flexibility of our program allows the calculation of these averages using either Mason's formulation[13–15] or Nava's formulation[16] by selecting appropriate weights. The motivation and aim of developing this program was that such a program would facilitate a theoretical investigation of different models in different solids on one hand, and, on the other, it could have the flexibility of incorporating new refinements in these models at any stage. In this work we apply our program to estimate the temperature dependence of Nava's ultrasonic Grüneisen parameter (UGP) and ultrasonic attenuation in NaCl, NaF, and LiF. The calculations are presented for longitudinal and shear waves along the [100], [110], and [111] directions in the range 80–300 K. We have found that, in most cases, the present calculations show much less departure from experimental data compared to calculations based on the original Mason formulation. This is true even if Mason calculation is done with the full integral instead of with just a sum over pure modes.

I. THEORY AND COMPUTATION

In dielectric solids an important source of acoustic absorption in the range $\Omega\tau \ll 1$ (where Ω is the angular frequency of the acoustic wave and τ is the thermal phonon relaxation time) is the Akhiezer mechanism, whereby the thermal phonon gas extracts energy from the acoustic wave through anharmonic interactions. Akhiezer's original theory[17] was modified first by Woodruff and Ehrenreich and then by Mason and Bateman, using fundamentally different approaches. Woodruff's expression for attenuation is a function of mode specific heats, and involves complex averages of the anharmonic parameters which describe the strain dependence of the lattice vibrational frequencies over the Brillouin zone. Mason's expression, derived in the anisotropic continuum limit, involves thermal energy and nonlinearity constant, which is a function of the second-, and third-, order elastic constants (SOEC and TOEC) of the solid.

Although Mason's theory has been most widely used in its original format to account for the temperature dependence of attenuation in a variety of solids,[18–21] its conceptual basis has been questioned by Barrett and Holland[22] who contended that the correct derivation of the starting equation used by Mason should lead to Woodruff's expression for attenuation coefficient.

Recently Nava *et al.* have suggested a modified formulation of Woodruff's theory, based on the use of UGP which is able, at least formally, to clarify the origin of the temperature dependence of attenuation. Their expression for attenuation coefficient for a wave of polarization j and propagation direction $\mathbf{K}$ is

 0001-4966/98/104(1)/81/5/$15.00

$$A_j\left(\frac{\mathrm{Np}}{\mathrm{cm}}\right)=\left[\frac{3\Omega^2\kappa_{\mathbf{K}}T}{\rho V_j^3 c^2}\right]\Gamma^2, \tag{1}$$

where $\kappa_{\mathbf{K}}$ is the thermal conductivity along **K**, T is the absolute temperature, ρ is the density, V_j and c are the sound wave and the Debye average velocities, respectively, and Γ^2 is the effective UGP. This parameter is an average of GP for each phonon mode $(\mathbf{q},i)$ weighted by their thermal conductivity $\kappa_{\mathbf{K}}(\mathbf{q},i)$ and is formally given by the expression

$$\Gamma_j^2=\frac{\Sigma_{\mathbf{q},i}\Gamma_{ij}^2(\mathbf{q},i)\kappa_{\mathbf{K}}(\mathbf{q},i)}{\Sigma_{\mathbf{q},i}\kappa_{\mathbf{K}}(\mathbf{q},i)}, \tag{2}$$

with

$$\Gamma_{ij}^2=\left(\frac{c^2}{\beta_i^2}\right)\left[\gamma_{ij}^2-\langle\langle\gamma_{ij}\rangle\rangle\gamma_{ij}\left[1-\frac{\beta_i^2}{V_j^2}\right]\delta_{jL}\right] \tag{3}$$

and

$$\kappa_{\mathbf{K}}(\mathbf{q},i)=\tfrac{1}{3}C_i\beta_i^2\tau_i\,. \tag{4}$$

Here all properties of the thermal phonon of a given branch i are assumed to depend on the phonon wave vector **q**, β_i is the component of the phonon group velocity $\mathbf{V}_i$ along **K**, C_i is the mode specific heat, γ_{ij} is the mode generalized GP, $\langle\langle\gamma_{ij}\rangle\rangle$ is the specific heat weighted average for all modes in the Brillouin zone, and δ_{jL} is the Kronecker delta. The last two terms in Eq. (3) represent the contribution to Γ_{ij}^2 for longitudinal waves $(j=L)$ from local phonon relaxation effects with the last standing for the classical thermoelastic contribution.

Nava *et al.* assume an anisotropic elastic continuum model in which the **q** dependence of the phonon properties is neglected and γ_{ij} are simply given by linear combinations of SOEC and TOEC.[23] They further assume a constant phonon relaxation time deduced from the thermal conductivity by $\tau=3\kappa/C_v c^2$, C_v being the total specific heat. Under these approximations Eq. (3) reduces to

$$\Gamma_j^2=\langle\gamma_{ij}^2\rangle-\langle\gamma_{ij}\rangle[\langle\gamma_{ij}\rangle-\langle\gamma_{ij}\beta_i^2/\mathbf{V}_j^2\rangle]\delta_{jL}\,, \tag{5}$$

where

$$\langle a_{ij}\rangle=\sum_i C_i a_{ij}/C. \tag{6}$$

Assuming further that all phonon modes contribute equally to the specific heat, Nava *et al.* approximate the averages indicated in Eq. (6) by simple numerical averages; for example,

$$\langle\gamma_{ij}\rangle=\sum_i n_i\gamma_{ij}/N, \tag{7}$$

where n_i is the number of pure thermal modes coupled to the sound wave through γ_{ij} and N is the total number of modes in the forward hemisphere. Mason's scheme of counting these modes is followed.

Thus it can be seen that although the averages of mode γ's indicated in Nava *et al.*'s formulation are defined by considering the mode specific heats as the weights the calculations reported by Nava *et al.*[11] have been performed using approximate simple numerical averages, following Mason's scheme. Our program facilitates a more complete calculation of Nava *et al.*'s modified formulation of Woodruff's theory by performing the specific heat weighted averages of mode γ's over the entire spectrum of thermal phonon modes. Moreover, the calculation of the average $\langle\gamma_{ij}\beta_i^2/V_j^2\rangle$ is performed correctly in our program by evaluating the component β_i of the phonon group velocity along the sound wave propagation direction for each phonon mode. β_i has not been used in this sense by Nava *et al.* although it is defined like this.

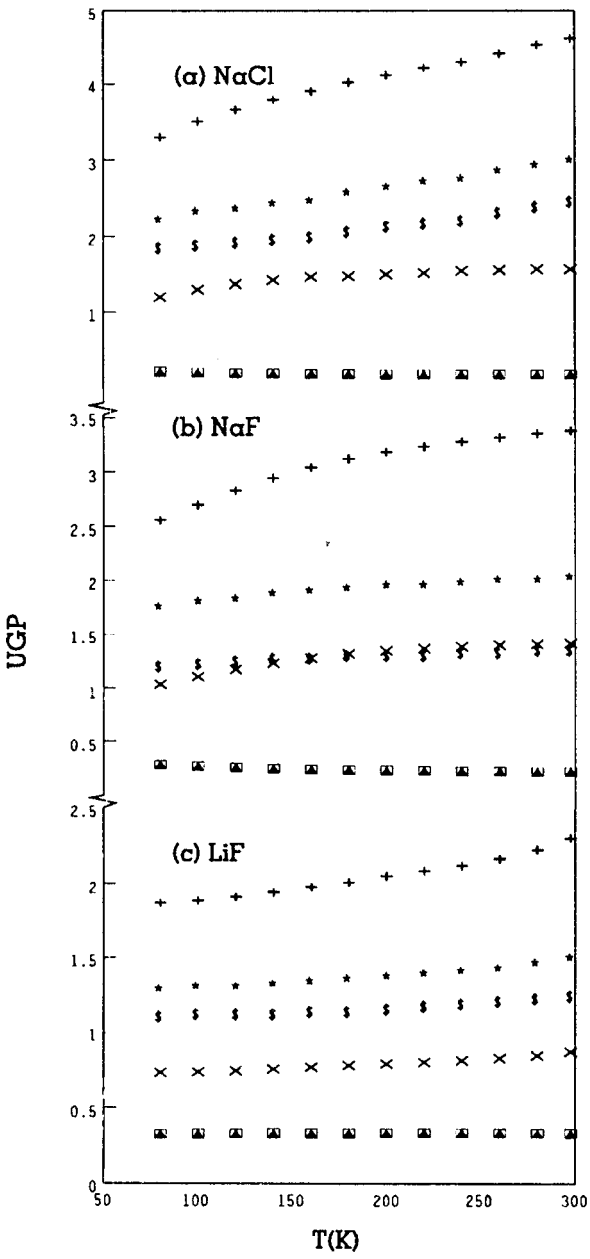

FIG. 1. Temperature dependence of ultrasonic Grüneisen parameter for different directions. +: [1$\underline{00}$] long.,*: [110] long., $: [111] long., □: [100] shear, ×: [110] shear [110], ▲: [110] shear [001].

The computer program developed by us is based on the Brugger–Fritz[24] scheme of integration over the length of the wave vector followed by double angular integration over all directions. In this scheme the continuum model is assumed. This means that the excitation of optic modes can be ne-

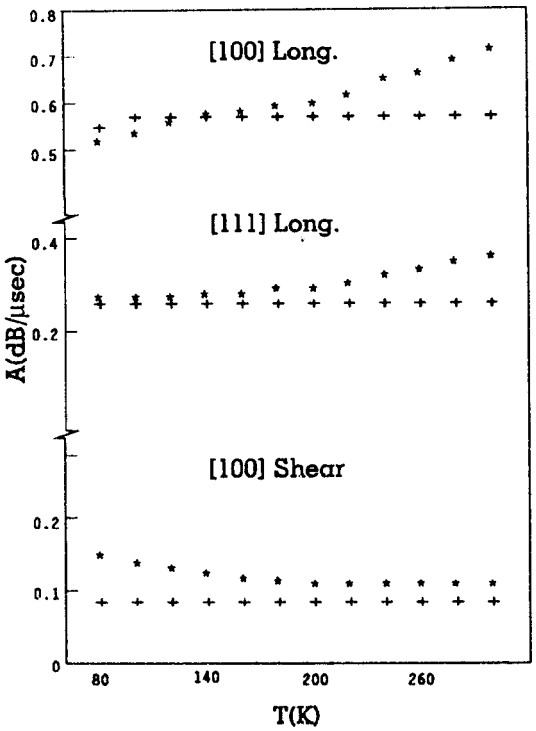

FIG. 2. Temperature dependence of ultrasonic attenuation in NaCl at 170 MHz. *: values calculated using Nava's formulation, +: experimental values from Ref. 8.

glected and the branch index for the mode takes only three values. The acoustic modes obey Debye distribution function and the maximum value of the length of the wave vector in any direction is the Debye radius $(6\pi^2/V_0)^{1/3}$, where V_0 is the volume of the primitive unit cell. The volume of the Debye sphere equals that of the first Brillouin zone.

We have checked the consistency of results using different single and multiple integration routines.[25] In our program the number of directions for which γ_{ij} are evaluated is determined by a convergence criterion for the numerical approximation of the appropriate integral. The minimum number of directions considered in the present study was 800. For shear waves $\langle\gamma\rangle$ was found to be consistently less than 10^{-6} with the imposed convergence criterion in all the cases studied. This points to the essential correctness of the numerical approximation to the full integral.

The UGP and attenuation along different directions were calculated using expressions in Eqs. (5) and (1), respectively, by taking into account the temperature dependence of each parameter contained in these expressions. The experimental data of room temperature densities and of temperature dependence of thermal expansion coefficient, thermal conductivity, and SOEC were taken from the literature.[26–30] The sets of TOECs reported by us earlier[14,15] are used. The wave velocities and Debye average velocities were obtained using the experimental SOEC and density data and the relevant expressions.[31] The results of these calculations are compared with the experimental temperature-dependent attenuation data available in the literature.

For NaCl the attenuation values measured by Merkulov *et al.*[8] at 170 MHz are used. It should be noted here that Merkulov *et al.* have not specified the accuracy of their measurements although these authors mention the substantial difficulties in measurements at low temperatures. For LiF such measurements are reported by Mason[2] and Avdonin *et al.*[5] Avdonin's measurements have an error of 20%. Hanson[3] too has measured the attenuation in LiF and found that the attenuation was independent of temperature down to 60 K within $\pm 30\%$. The attenuation values of Hanson calculated using quadratic frequency dependence of attenuation, which was observed by both Hanson and Avdonin at room temperature, are also included here for comparison with the results of our calculation. Avdonin *et al.*[5] have reported that the damping in NaF crystal varies in a way similar to that observed in LiF crystals. The experimental values used here for NaF are obtained by using the room temperature attenuation values for NaF and the temperature variation of relative attenuation for LiF.

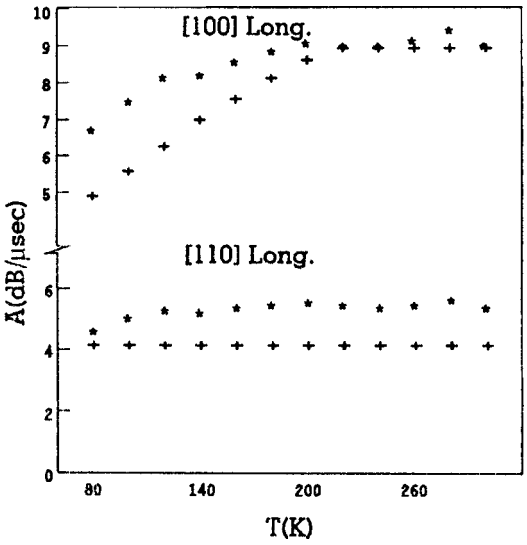

FIG. 3. Same as in Fig. 2 for NaF at 800 MHz. Experimental values from Ref. 5.

II. RESULTS AND DISCUSSION

The temperature dependence of UGP calculated using our program for different directions of propagation and po-

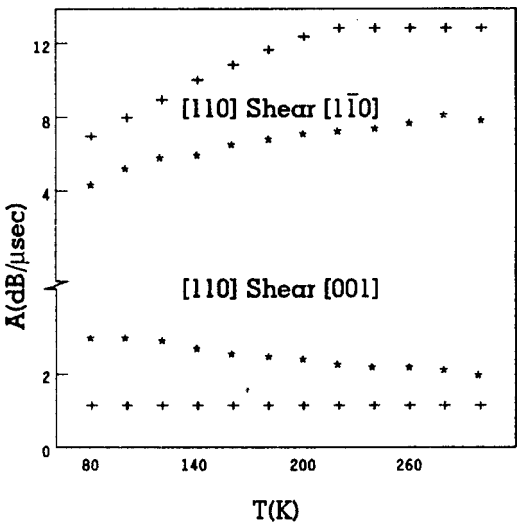

FIG. 4. Same as in Fig. 3.

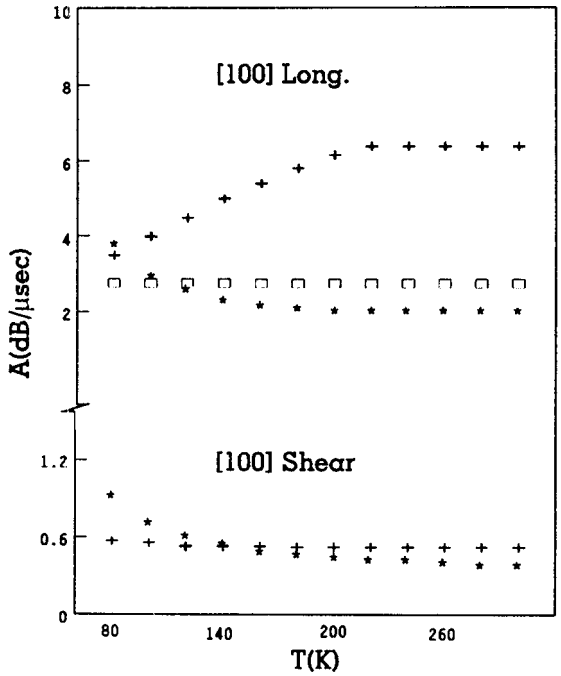

FIG. 5. Same as in Fig. 2 for LiF at 800 MHz (for [100] shear wave, $f = 480$ MHz). Experimental values from Ref. 5 for longitudinal wave and from Ref. 2 for shear wave. □: experimental values from Ref. 3.

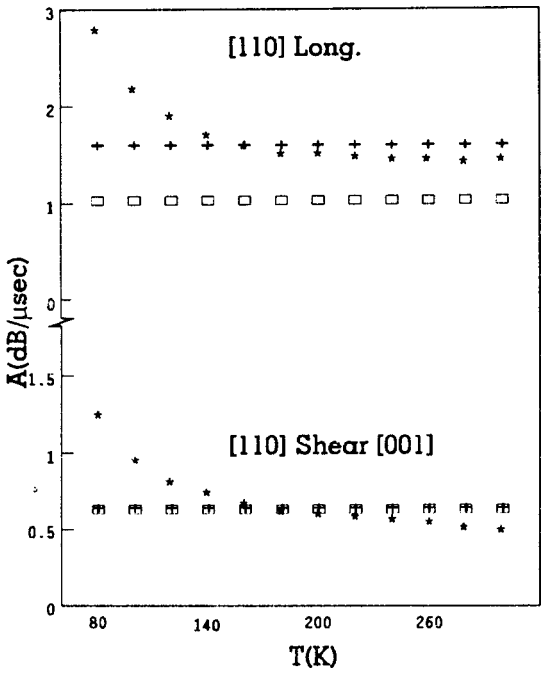

FIG. 6. Same as in Fig. 5, $f = 800$ MHz.

larization is shown in Fig. 1. It can be seen from this figure that the longitudinal waves and the shear wave polarized along the [110] direction exhibit larger magnitude and greater temperature dependence of UGP than the shear waves polarized along the [001] direction. These results are in qualitative agreement with the observations of Nava *et al.*[32] who have used the experimental attenuation data to extract the temperature dependence of UGP in the case of Ge, Si, MgO, and SiO_2. The UGPs determined in this way contain the effects of temperature on the average anharmonicity of the lattice as sampled by the sound waves.

The results of our calculation of temperature dependence of attenuation are presented in Figs. 2–7. These figures must be interpreted in the light of the errors in measurements of attenuation mentioned above as well as the fact that measurements on the same material by different workers show a fair amount of variation, as, for example, in the case of LiF.[3,5] Also, we have found that these results are in better quantitative agreement with experiment than those based on Mason's scheme and reported earlier by us.[14,15] This is illustrated in Fig. 8 discussed below. Moreover, it should be mentioned here that a more complete calculation of attenuation using Nava *et al.*'s theory requires much more knowledge than is available of the parameters τ, γ_{ij}, and β_i. The **q** dependence of τ and γ_{ij}, for example, which is neglected in the present analysis, can throw more light on the present investigation.

The increase of attenuation at low temperatures that is observed for all directions in the case of LiF and for shear waves polarized along [001] in the case of NaCl and NaF was investigated using the Born–von Karman model instead of the Debye model in our program and it was found that the discrepancy could be reduced. However, the improvement was too small. It should be noted here that our earlier calculation[14,15] using Mason's theory incorporating the refinement suggested by Merkulov *et al.*,[4] did not show this discrepancy for longitudinal modes. However, for shear waves a slight increase at low temperature was observed with this calculation, too. Use of the experimental data on the temperature dependence of TOECs should aid further investigation of the temperature dependence of attenuation in these compounds.

It may be recalled here that Barrett and Holland, in their criticism of Mason's theory, have pointed out that a more rigorous derivation of Mason's theory should result in the

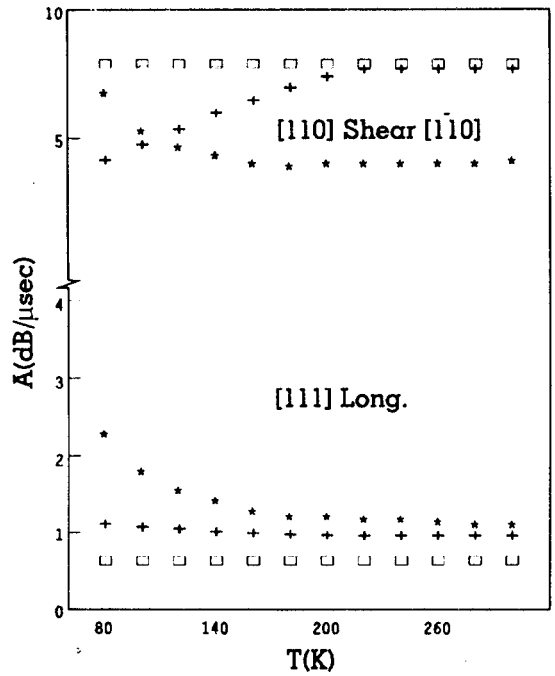

FIG. 7. Same as in Fig. 5, $f = 800$ MHz.

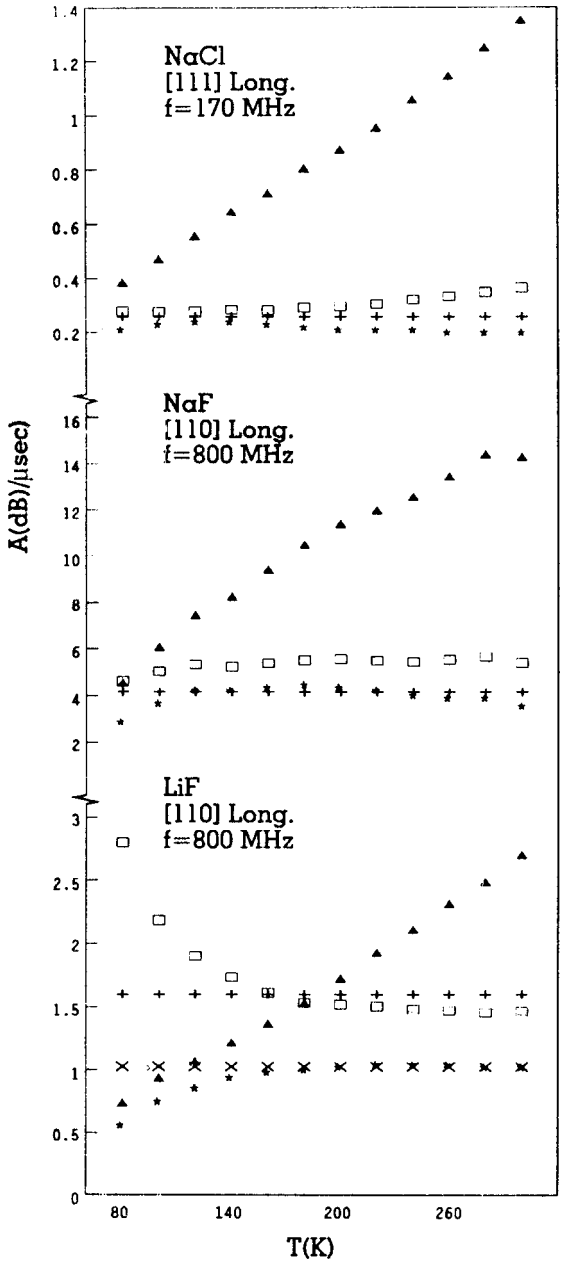

FIG. 8. Comparison of results obtained using different schemes of calculation. ▲: values calculated using Mason's pure mode scheme. *: values calculated using our program with Mason–Merkulov scheme,[14,15] □: values calculated using our program with Nava's scheme (present work). +: experimental values from Refs. 5 and 8. For LiF × denotes the experimental values by Hanson (Ref. 3).

specific heats $C(i)$ appearing in the final expression, rather than the energies $E(i)$, leading to the more rigorous Woodruff expression for attenuation coefficient. In our earlier investigations and the present one we have observed that the use of Merkulov *et al.*'s refinement in Mason's theory and of Nava *et al.*'s modified scheme of calculation of Woodruff's theory both lead to quite a close agreement with the experiment.

For longitudinal waves the results obtained using these two different formulations are found to be in better accord with each other than those obtained for transverse waves. Figure 8 illustrates this comparison in different compounds for those directions for which the two approaches show the closest agreement. In this figure results obtained using Mason's pure mode scheme are also included in order to bring out our observation that the present calculations are, in most cases, far nearer the experiment than those based on original Mason formulation. This is something we have found to be true in all the other materials we have investigated earlier. Thus the results obtained by us so far indicate essential validity of some of the objections raised against Mason's theory by Barrett and Holland.[22] The discrepancy observed for transverse waves is being investigated by incorporating the dispersion of acoustic modes in Nava's calculation. More experimental data regarding attenuation of shear waves should be useful in this investigation.

[1] L. G. Merkulov, Sov. Phys. Acoust. **5**, 444–450 (1960).
[2] W. P. Mason and T. B. Bateman, J. Acoust. Soc. Am. **40**, 852–862 (1966).
[3] R. C. Hanson, J. Phys. Chem. Solids **28**, 475–483 (1967).
[4] L. G. Merkulov, R. V. Kovalenok, and E. V. Konovodehenko, Sov. Phys. Solid State **11**, 2241–2248 (1970).
[5] Y. Ya. Avdonin, V. V. Lemanov, I. A. Smirnov, and V. V. Tikhonov, Sov. Phys. Solid State **14**, 747–752 (1972).
[6] D. N. Joharapurkar, S. Rajagopalan, and B. K. Basu, Phys. Rev. B **37**, 3101–3104 (1988).
[7] S. K. Kor and Kailash, Nuovo Cimento **8D**, 615–623 (1986).
[8] L. G. Merkulov, R. V. Kovalenok, and E. V. Konovodehenko, Sov. Phys. Solid State **13**, 968–973 (1971).
[9] S. K. Kor and R. P. Khare, Acustica **56**, 280–282 (1984).
[10] S. K. Kor, R. R. Yadav, and Kailash, J. Phys. Soc. Jpn. **55**, 207–212 (1986).
[11] R. Nava and J. Romero, J. Acoust. Soc. Am. **64**, 529–532 (1978).
[12] R. O. Woodruff and H. Ehrenreich, Phys. Rev. **123**, 1553–1559 (1961).
[13] S. D. Lambade, G. G. Sahasrabudhe, and S. Rajagopalan, Phys. Rev. B **51**, 15 861–15 866 (1995).
[14] S. D. Lambade, G. G. Sahasrabudhe, and S. Rajagopalan, J. Phys. Chem. Solids **57**, 217–223 (1996).
[15] S. D. Lambade, G. G. Sahasrabudhe, and S. Rajagopalan, J. Appl. Phys. **78**, 6525–6533 (1995).
[16] S. D. Lambade, G. G. Sahasrabudhe, and S. Rajagopalan, Acoust. Lett. **18**, 146–150 (1995).
[17] A. Akhiezer, J. Phys. (Moscow) **1**, 277–287 (1939).
[18] W. P. Mason, in *Physical Acoustics*, edited by W. P. Mason and R. N. Thurston (Academic, New York, 1964), Vol. IIIB, Chap. 6.
[19] M. Nandanpawar and S. Rajagopalan, Phys. Rev. B **18**, 5410–5412 (1978).
[20] S. S. Shukla and S. S. Yun, J. Acoust. Soc. Am. **70**, 1713–1716 (1981).
[21] S. K. Kor and R. K. Singh, Acustica **80**, 83–87 (1994).
[22] H. H. Barrett and M. G. Holland, Phys. Rev. B **1**, 2538–2544 (1970).
[23] K. Brugger, Phys. Rev. A **137**, 1826–1827 (1965).
[24] K. Brugger and T. C. Fritz, Phys. Rev. **157**, 524–531 (1967).
[25] H. M. Antia, *Numerical Methods for Scientists and Engineers* (McGraw-Hill, New York, 1991), pp. 240–260.
[26] *American Institute of Physics Handbook* (McGraw-Hill, New York, 1972), 3rd ed.
[27] A. V. Petrov, N. S. Tsypkina, and Yu. A. Lonachev, Sov. Phys. Solid State **16**, 39–42 (1974).
[28] J. T. Lewis, A. Lehoczky, and C. V. Briscoe, Phys. Rev. **161**, 877–887 (1967).
[29] C. V. Briscoe and C. F. Squire, Phys. Rev. **106**, 1175–1177 (1957).
[30] W. A. Bensch, Phys. Rev. B **6**, 1504–1509 (1972).
[31] R. Truell, C. Elbaum, and B. Chick, *Ultrasonic Methods in Solid State Physics* (Academic, New York, 1969), pp. 14–15.
[32] R. Nava, M. P. Vecchi, J. Romero, and B. Fernandez, Phys. Rev. B **14**, 800–807 (1976).

Theory of acoustic streaming generated by ultrasonic Lamb waves

Zhemin Zhu, Xiaoliang Zhao, and Gonghuan Du
Institute of Acoustics and State Key Lab of Modern Acoustics, Nanjing University, Nanjing 210093, People's Republic of China

Junru Wu
Department of Physics, University of Vermont, Burlington, Vermont 05405

(Received 21 July 1997; revised 31 March 1998; accepted 20 April 1998)

A theory on acoustic streaming generated by Lamb waves propagating in a thin composite membrane was developed. Using this theory, the mass-transport velocity in water, which is loaded on a 4-μm-thick membrane, due to Lamb waves at 4.7 MHz was calculated. The results are in good agreement with the experimental values measured by Moroney *et al.* [Appl. Phys. Lett. **59**, 774 (1991)]. © *1998 Acoustical Society of America.* [S0001-4966(98)06307-3]

PACS numbers: 43.25.Nm [MAB]

INTRODUCTION

Lamb waves in a solid or a thin film have been found useful in nondestructive evaluations[1] and microsensing.[2] Recently, a Lamb wave sensor (LWS) made by microfabrication was used to pump fluids and transport solids in a small-scale system.[3] The pumping of water was induced by 4.7-MHz Lamb waves traveling in the LWS that is essentially a 4-μm-thick composite membrane of silicon nitride and piezoelectric zinc oxide. The pumping speed of water, that is in contact with the surface of the LWS, was found to be proportional to the square of the radio frequency drive voltage applied on LWS. When the amplitude of the lowest antisymmetric mode (A_0 mode) Lamb wave was 6.5 nm, and the pumping speed was measured to be 100 μm/s. This effect is very attractive especially in applications such as mass transportation and heat conduction in a micoscale system.

Moroney *et al.*[3] noticed that the pumping was caused by acoustic streaming and calculated the pumping velocity to be about 80 μm/s using a simple nonloading (no liquid loaded on the LWS) first-order ultrasonic Lamb wave field and the second-order mass-transport velocity equation developed by Longuet-Higgins.[4]

In this paper, we make use of a model[5] that a thin plate is loaded with a compressible viscous liquid layer developed by us previously and the results of the first-order ultrasonic field in the viscous liquid produced by Lamb waves predicted by a rigorous propagation theory, to calculate the acoustic streaming speed and speed distribution induced by the A_0 mode and S_0 mode (the lowest symmetric mode) Lamb waves. Comparison between our theoretical values of the A_0 mode and Moroney *et al.* experimental results is presented. The difference of the streaming fields caused by the A_0 mode and S_0 mode Lamb waves is also discussed.

I. FIRST-ORDER FIELD

To calculate acoustic streaming, which is a second-order quantity, produced by Lamb waves, we first have to know the first-order sound field in the liquid excited by Lamb waves in the thin film. For mathematical simplicity, we consider the following situation: An isotropic solid thin plate of thickness $2d$ extends to infinity in both x and y directions and bordered both on the top and bottom with an infinitely large homogeneous viscous liquid layer of thickness h (Fig. 1). The dispersion of the above situation has been derived by Zhu and Wu.[5] Here we briefly review the process as follows.

In a solid, we have

$$u_s=\frac{\partial\varphi_s}{\partial x}-\frac{\partial\psi_s}{\partial z},\quad w_s=\frac{\partial\varphi_s}{\partial z}+\frac{\partial\psi_s}{\partial x}, \tag{1}$$

where φ_s, ψ_s are the velocity potential functions of longitudinal and shear waves in the film and u_s and w_s are, respectively, x and z components of the particle velocity in the solid. In a liquid boundary layer, we have

$$u_{Li}=\frac{\partial\varphi_{Li}}{\partial x}-\frac{\partial\psi_{Li}}{\partial z},\quad w_{Li}=\frac{\partial\varphi_{Li}}{\partial z}+\frac{\partial\psi_{Li}}{\partial x}, \tag{2}$$

where φ_{Li} and ψ_{Li} are the scalar velocity potential and the y component of the vector velocity potential, respectively (for the top liquid layer subscript $i=1$ and for the bottom layer, $i=2$); u_{Li} and w_{Li} are, respectively, x and z components of the particle velocity. The potential functions of φ_s, ψ_s, and φ_{Li} all satisfy the Helmholz equation and ψ_{Li} is related to the vorticity in a liquid boundary layer and satisfies a diffusion equation as follows:

$$\begin{aligned}
&\nabla^2\varphi_s+k_l^2\varphi_s=0,\\
&\nabla^2\psi_s+k_t^2\psi_s=0,\\
&\nabla^2\varphi_{Li}+k_{Li}^2\varphi_{Li}=0,\\
&\frac{\partial\psi_{Li}}{\partial t}-\left(\frac{\mu_L}{\rho_L}\right)\nabla^2\psi_{Li}=0,
\end{aligned} \tag{3}$$

where $k_l=\omega/c_l$, $k_l=\omega/c_t$, $k_L=\omega/c_L$, $c_l=\sqrt{\mu/\rho_s}$, $c_l=\sqrt{(\lambda+2\mu)/\rho_s}$, λ and μ are the elastic Lame constants of the solids, ρ_s is the density of the solid, and c_L, μ_L, and ρ_L denote the speed of sound, viscosity, and density of the liquid, respectively.

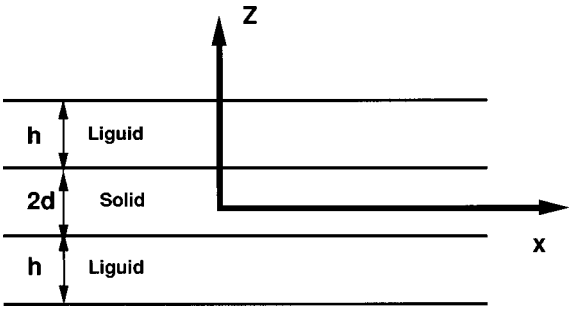

FIG. 1. Illustration of the system and coordinates.

We assume that the harmonic traveling waves (in the x direction) have the forms:

$$\begin{aligned}
\varphi_s &= [A_s \cdot \cosh(qz) + B_a \cdot \sinh(qz)]e^{i(kx-\omega t)},\\
\psi_s &= [D_s \cdot \sinh(sz) + C_a \cdot \cosh(sz)]e^{i(kx-\omega t)},\\
\varphi_{L1} &= A_1 \sin\{\gamma[z-(d+h)]\}e^{i(kx-\omega t)},\\
\psi_{L1} &= B_1 \cdot e^{-m(z-d)} \cdot e^{i(kx-\omega t)},\\
\varphi_{L2} &= A_2 \cdot \sin\{\gamma[z+(d+h)]\}e^{i(kx-\omega t)},\\
\psi_{L2} &= B_2 \cdot e^{m(z+d)} \cdot e^{i(kx-\omega t)},
\end{aligned} \tag{4}$$

where k is the wave number of the traveling wave, $q = \sqrt{k^2 - k_l^2}$, $s = \sqrt{k^2 - k_t^2}$, $\gamma = \sqrt{k_L^2 - k^2}$, $m = (1-i)/\delta$, δ is the boundary layer thickness given by $\delta = \sqrt{2\mu_L/\omega\rho_L}$. Equations (4), which are solutions of Eq. (3), should satisfy the boundary conditions at the liquid–solid interfaces: (1) Both normal and tangential components of the particle velocity should be continuous. (2) Both normal and tangential components of the stress tensor should be continuous. Noting that due to the symmetry of the system, we have $A_1 = A_2$ and $B_1 = B_2$. Thus for symmetrical modes, we obtain

$$\begin{aligned}
&(k^2+s^2)\cosh(qd)A_s + 2iks \cdot \cosh(sd)D_s - \frac{\rho_L}{\rho_s} k_t^2 \sin(\gamma h)A_1 = 0,\\
&2ikq \cdot \sinh(qd)A_s - (k^2+s^2)\sinh(sd)D_s - \frac{i\omega\mu_L}{\mu_s} m^2 B_1 = 0,\\
&q \cdot \sinh(qd)A_s + ik \cdot \sinh(sd)D_s - \gamma \cos(\gamma h)A_1 - ikB_1 = 0,\\
&ik \cdot \cosh(qd)A_s - s \cdot \cosh(sd)D_s + ik \cdot \sin(\gamma h)A_1 - mB_1 = 0,
\end{aligned} \tag{5a}$$

and for antisymmetrical modes, we have

$$\begin{aligned}
&(k^2+s^2)\sinh(qd)B_a + 2iks \cdot \sinh(sd)C_a - \frac{\rho_L}{\rho_s} k_t^2 \sin(\gamma h)A_1 = 0,\\
&2ikq \cdot \cosh(qd)B_a - (k^2+s^2)\cosh(sd)C_a - \frac{i\omega\mu_L}{\mu_s} m^2 B_1 = 0,\\
&q \cdot \cosh(qd)B_a + ik \cdot \cosh(sd)C_a - \gamma \cosh(\gamma h)A_1 - ikB_1 = 0,\\
&ik \cdot \sinh(qd)B_a - s \cdot \sinh(sd)C_a + ik \cdot \sin(\gamma h)A_1 - mB_1 = 0.
\end{aligned} \tag{5b}$$

Thus dispersion relations for symmetrical and antisymmetrical and modes can be derived and are given respectively by Eqs. (6a) and (6b):

$$\det \begin{vmatrix}
(k^2+s^2)\cosh(qd) & 2iks\cosh(sd) & \frac{\rho_L}{\rho_s}k_t^2\sin(\gamma h) & 0\\
2ikq\sinh(qd) & -(k^2+s^2)\sinh(sd) & 0 & i\omega m^2\frac{\mu_L}{\mu_s}\\
q\sinh(qd) & ik\sinh(sd) & k_z\cos(\gamma h) & ik\\
ik\cosh(qd) & -s\cosh(sd) & -ik\sin(\gamma h) & m
\end{vmatrix} = 0, \tag{6a}$$

$$\det \begin{vmatrix}
(k^2+s^2)\sinh(qd) & 2iks\sinh(sd) & -\frac{\rho_L}{\rho_s}k_t^2\sin(\gamma h) & 0\\
2ikq\cosh(qd) & -(k^2+s^2)\cosh(sd) & 0 & -i\omega m^2\frac{\mu_L}{\mu_s}\\
q\cosh(qd) & ik\cosh(sd) & -k_z\cos(\gamma h) & -ik\\
ik\sinh(qd) & -s\sinh(sd) & ik\sin(\gamma h) & -m
\end{vmatrix} = 0. \tag{6b}$$

Meanwhile, x and z components of the first-order particle velocity in the top liquid layer u_{L1} and w_{L1} can be derived from Eq. (2) as

$$u_{L1}=\{ikA_1\cdot\sin\{\gamma[z-(d+h)]\}+m\cdot B_1e^{-m(z-d)}\}e^{i(kx-\omega t)},$$
$$w_{L1}=\{\gamma A_1\cdot\cos\{\gamma[z-(d+h)]\}+ik\cdot B_1e^{-m(z-d)}\}e^{i(kx-\omega t)}, \tag{7}$$

where the relationship between A_1 and B_1 can be derived from Eq. (5). The detailed calculation results are given in the Appendix.

II. ACOUSTIC STREAMING

The Eulerian acoustic streaming velocity $\mathbf{u}_2$, a second-order term, is described by an equation which is derived by Nyborg[6] and accurate up to second order:

$$\mu_L\nabla^2\mathbf{u}_2=\nabla p_2-\mathbf{F}, \tag{8}$$

where $\mathbf{F}$ is the effective source force of the streaming (actually, it is a force per unit volume) and related to the first-order term $\mathbf{u}_1$ by

$$-\mathbf{F}\equiv\rho_0\langle(\mathbf{u}_1\cdot\nabla)\mathbf{u}_1+\mathbf{u}_1\cdot(\nabla\cdot\mathbf{u}_1)\rangle. \tag{9}$$

Here $\langle X\rangle$ means ''time average of X.'' The streaming velocity measured by Moroney *et al.* using small particle tracers is called the Lagrangian streaming velocity or the mass-transport velocity $\mathbf{U}$, which is related to $\mathbf{u}_2$ by[7,8]

$$\mathbf{U}=\mathbf{u}_2+\left\langle\left(\int\mathbf{u}_1\cdot\nabla\right)\mathbf{u}_1\right\rangle. \tag{10}$$

So after determination of the first-order velocity and noting $\nabla\cdot\mathbf{u}_2\approx0$,[9] we can calculate the x-component of the source force F_x, which is relevant to the experiment, by using Eq. (9). Specifically,

$$F_X=-\rho_0\,\mathrm{Re}\left[u_{L1}\left(\frac{\partial u_{L1}}{\partial x}\right)^*+\frac{1}{2}u_{L1}\left(\frac{\partial w_{L1}}{\partial z}\right)^*+\frac{1}{2}w_{L1}\left(\frac{\partial u_{L1}}{\partial z}\right)^*\right], \tag{11}$$

where the symbol Re[ ] means to take the real part of the expression, and $(X)^*$ denotes the complex conjugate of X. Noting that F_x is approximately only a function of z and $\nabla p_2\approx0$, from Eq. (8), we can calculate the x-component of $\mathbf{u}_2$, u_{2x}, by

$$u_{2x}=-\frac{1}{\mu_L}\int\int F_X\,dz'\,dz. \tag{12}$$

Consequently, we obtain the x component of $\mathbf{U}$ as

$$U_x=u_{2x}+\frac{1}{2}\cdot\mathrm{Re}\left[\frac{u_1}{-i\omega}\cdot\left(\frac{\partial u_1}{\partial x}\right)^*+\frac{w_1}{-i\omega}\cdot\left(\frac{\partial u_1}{\partial z}\right)^*\right]. \tag{13}$$

So the x-component of the streaming velocity can be evaluated as the sum of these above two parts with boundary conditions that at the surface of plate $U_x=0$.

III. NUMERICAL RESULTS AND DISCUSSIONS

Here we choose parameters of a typical LWS application for calculations: The thickness of a water layer is 0.25 mm, the thickness of the ZnO plate is 4 μm, $\rho_s=5680$ kg/m^3, $\rho_L=1000$ kg/m^3, $\mu_L=0.001\,329$ kg/m s, and the frequency of the Lamb wave $f=4.7$ MHz. Thus $K_l\cdot d=0.02$. Let us consider two examples: Streaming produced by A_0-mode and that by S_0-mode Lamb waves.

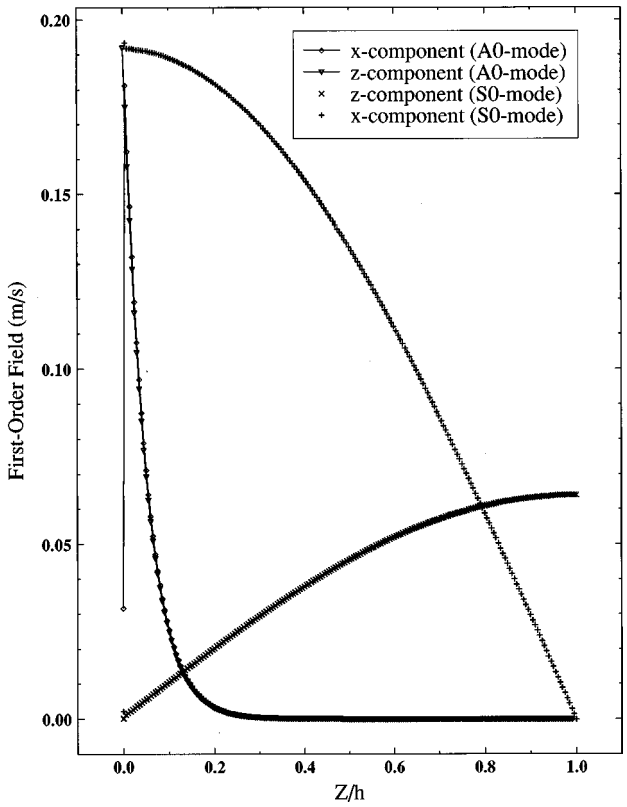

FIG. 2. First-order sound fields in the liquid versus Z/h.

A. First-order fields and the effective source forces

The x-component, u_l, and z-component, w_1, of the A_0 mode and S_0 mode of the abovementioned parameters have been calculated and shown in Fig. 2. The main difference between the two modes is that the wave in the liquid is an evanescent wave for the A_0 mode; it decays exponentially beyond the boundary layer, while that for the S_0 mode is a propagating wave (it is called a leaky wave). This is because the phase velocity of the A_0 mode is smaller than the speed of sound in water and that of the S_0 mode is greater than the speed of sound in water.

Based on the above results, we then calculated the effective source forces due to the A_0 mode and S_0 mode F_x vs Z/δ as shown in Fig. 3 (here $Z=z-d$). For the same amplitude of Lamb waves in the solid, The peak value of F_x of the A_0 mode is much higher than that of S_0 mode. Consequently as shown later the streaming velocity of the A_0 mode is greater too.

B. Streaming induced by Lamb waves

Using Eqs. (1), (2), (4), (11), (12), and (13) we have calculated streaming or the mass-transport velocities versus Z/h generated by the A_0 mode and S_0 mode when the amplitudes of both modes are 6.5 nm. The results are shown in

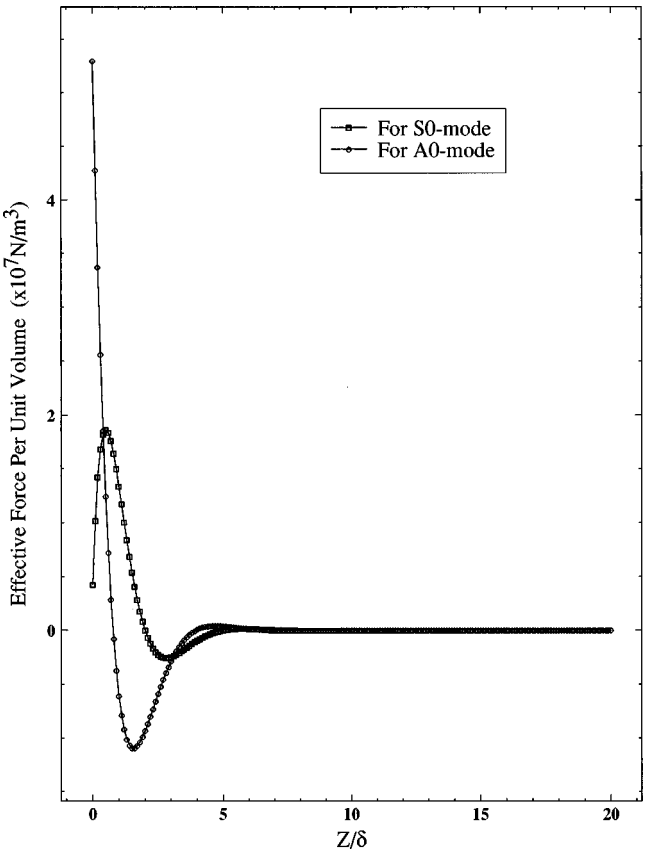

FIG. 3. Effective forces versus Z/δ.

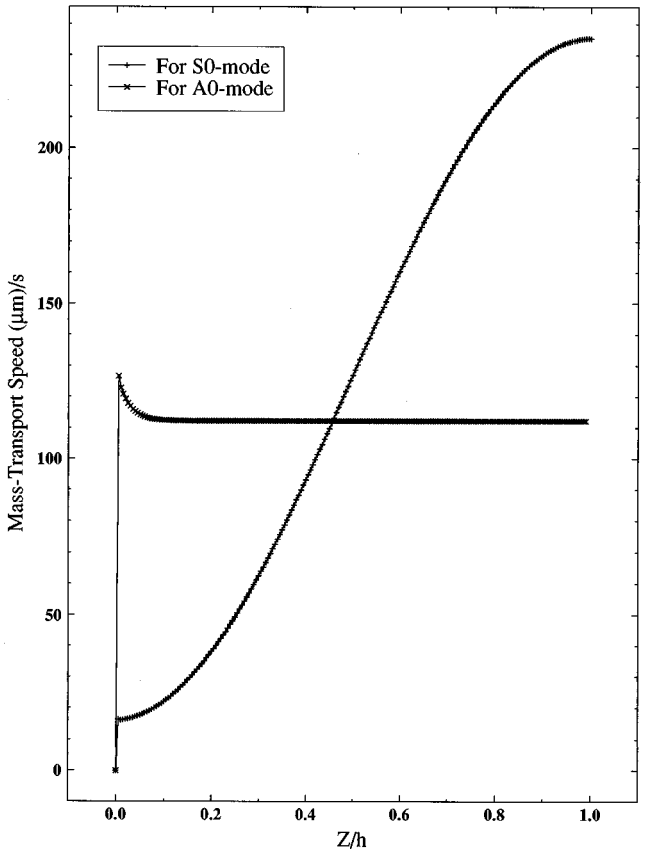

FIG. 4. Mass-transport velocities versus Z/h.

Fig. 4. For the A_0 mode, the mass-transport velocity increases to a maximum value within the boundary layer and then decays and approaches to an asymptotic value. For the S_0 mode, it is an increasing function of z.

For the A_0 mode, the asymptotic value for this case is 110 μm/s, which is in good agreement with the experimental value (100 μm/s) measured by Moroney *et al.*

IV. SUMMARY

Using the elastic Lamb wave propagation and acoustic streaming theories, we have calculated the mass-transport velocity in a liquid layer loaded on a LWS generated by the A_0 mode and S_0 mode Lame waves. The results of the A_0 mode case agrees favorably with the experimental results.

Finally, the two sides loading mode was used in this paper in order to simplify the mathematical treatment. For actual LWS applications, only one liquid layer is loaded on the top of the plate. Our previous results indicated that the approximation is valid and the error induced by the approximation is insignificant.[10,11]

APPENDIX

We assume the first three equations of (5a) or (5b) are independent.

For the A_0 mode Lamb waves:

$$A_1=\Delta_a\cdot B_a, \quad B_1=\Delta_b\cdot B_a,$$

where

$$\Delta_a=\frac{(k^2+s^2)\left(1+\frac{k^2+s^2}{k_t^2}\frac{\rho_s}{\rho_L}\right)\cdot\sinh(qd)\cosh(sd)-2qs\left(1+\frac{2k^2}{k_t^2}\frac{\rho_s}{\rho_L}\right)\cdot\cosh(qd)\sinh(sd)}{k_t^2\,\sin(\gamma h)\cdot\left[\left(\frac{\rho_L}{\rho_s}+\frac{k^2+s^2}{k_t^2}\right)\cdot\cosh(sd)-\frac{2\gamma s}{k_t^2}\cdot\cot(\gamma h)\sinh(sd)\right]}, \tag{A1}$$

$$\Delta_b=i\cdot\frac{k_t^2 q\cdot\cosh(qd)\cosh(sd)+\frac{\rho_s}{\rho_L}\frac{\gamma}{k_t^2}\cot(\gamma h)[(k^2+s^2)^2\,\sinh(qd)\cosh(sd)-4k^2qs\cdot\cosh(qd)\sinh(sd)}{k\cdot k_t^2\,\sin(\gamma h)\cdot\left[\left(\frac{\rho_L}{\rho_s}+\frac{k^2+s^2}{k_t^2}\right)\cdot\cosh(sd)-\frac{2\gamma s}{k_t^2}\cdot\cot(\gamma h)\sinh(sd)\right]}. \tag{A2}$$

Here, B_a can be determined by the wave amplitude ζ_0 (the normal displacement amplitude on the surface of the plate) as

$$B_a = \left| \frac{\omega \cdot \zeta_0}{\gamma \Delta_a \cos(\gamma h) + ik\Delta_b} \right|. \tag{A3}$$

For S_0 mode Lamb wave:

$$A_1 = \Delta_a \cdot A_s, \quad B_1 = \Delta_b \cdot A_s,$$

where

$$\Delta_a = \frac{(k^2+s^2)\left(1+\frac{k^2+s^2}{k_t^2}\frac{\rho_s}{\rho_L}\right)\cdot\cosh(qd)\sinh(sd) - 2qs\left(1+\frac{2k^2}{k_t^2}\frac{\rho_s}{\rho_L}\right)\cdot\sinh(qd)\cosh(sd)}{k_t^2 \sin(\gamma h)\cdot\left[\left(\frac{\rho_L}{\rho_s}+\frac{k^2+s^2}{k_t^2}\right)\cdot\sinh(sd) - \frac{2\gamma s}{k_t^2}\cdot\cot(\gamma h)\cosh(sd)\right]}, \tag{A4}$$

$$\Delta_b = i\cdot\frac{k_t^2 q\cdot\sinh(qd)\sinh(sd) + \frac{\rho_s}{\rho_L}\frac{\gamma}{k_t^2}\cot(\gamma h)[(k^2+s^2)^2\cosh(qd)\sinh(sd) - 4k^2 qs\cdot\sinh(qd)\cosh(sd)}{k\cdot k_t^2 \sin(\gamma h)\cdot\left[\left(\frac{\rho_L}{\rho_s}+\frac{k^2+s^2}{k_t^2}\right)\cdot\sinh(sd) - \frac{2\gamma s}{k_t^2}\cdot\cot(\gamma h)\cdot\cosh(sd)\right]}, \tag{A5}$$

and also, A_s is determined by tangential displacement amplitude ξ_0 as

$$A_s = \left| \frac{\omega \cdot \xi_0}{ik\Delta_a \sin(\gamma h)} \right|. \tag{A6}$$

[1] A. H. Nayfeh, *Wave Propagation in Layered Anisotropic Media* (North-Holland, Amsterdam, 1995).
[2] E. W. Wenzel and R. M. White, IEEE Trans. Electron Devices **35**, 735 (1988).
[3] R. M. Moroney, R. M. White, and R. T. Howe, Appl. Phys. Lett. **59**, 774 (1991).
[4] Longuet-Higgins, Philos. Trans. R. Soc. London, Ser. A **245**, 535 (1953).
[5] Z. Zhu and J. Wu, J. Acoust. Soc. Am. **98**, 1057 (1995).
[6] W. L. Nyborg, in *Physical Acoustics*, edited by W. P. Mason (Academic, New York, 1965), Vol. 2B, Chap. 11, p. 265.
[7] J. Lighthill, J. Sound Vib. **61**, 391 (1978).
[8] J. Wu and G. Du, J. Acoust. Soc. Am. **101**, 1899 (1997).
[9] C. E. Bradley, J. Acoust. Soc. Am. **100**, 1399 (1996).
[10] J. Wu and Z. Zhu, J. Acoust. Soc. Am. **91**, 861 (1991).
[11] Z. Zhu, J. Wu, J. Li, and W. Zhou, Sens. Actuators A **49**, 79 (1995).

Measurements of the two-frequency mutual coherence function for sound propagation through a turbulent atmosphere

David I. Havelock, Michael R. Stinson, and Gilles A. Daigle
Institute for Microstructural Sciences, National Research Council, Ottawa, Ontario K1A 0R6, Canada

(Received 14 February 1996; revised 5 March 1998; accepted 18 March 1998)

An array of 32 microphones spanning 675 m of range was used to measure the frequency coherence for pulse signals propagating through atmospheric turbulence near the ground. Frequency coherence is the correlation between the fluctuations in received signals of different frequencies as expressed through the two frequency mutual coherence function evaluated at the same point in space and time. The experiments were conducted for frequencies between 200 and 1000 Hz under both downward and upward refracting propagation conditions. Measurements and theory are shown to be in good agreement for line-of-sight propagation. In the acoustic shadow region the frequency coherence bandwidth shows a strong dependence on mean frequency. The effects of refraction and diffraction, which cause wandering in the pulse arrival time and broadening of the pulse width, respectively, are clearly distinguished. The measurements provide experimental characterization of signal fluctuations for sound fields propagating outdoors. They are important for acoustic remote sensing and detection applications and for the validation of theoretical and numerical developments in sound propagation modeling. [S0001-4966(98)00507-4]

PACS numbers: 43.28.Fp, 43.60.Cg [LCS]

INTRODUCTION

A pure-tone source propagating through a random medium to a distant receiver will exhibit fluctuations about the unperturbed values of its phase and magnitude. Two tones propagating simultaneously will exhibit fluctuations which become less correlated with each other as the frequency separation between the tones increases. The degree of coherence between two such tones observed at a single receiving point is quantified here by the *frequency coherence* which is defined in terms of the more general two-frequency mutual coherence function.[1,2] In communications theory, this phenomenon is characterized by the ''coherence time-bandwidth,'' which determines a bound on the rate at which information can be transmitted over a channel. In optical and electromagnetic propagation[3] the coherence bandwidth is the quantity of practical interest, as it can be measured by intensity analysis of pulse propagation. In acoustics, the instantaneous phase and magnitude of a propagating signal is more readily observed and so the coherence between the fluctuations of two tones is of greater interest.[4] Indeed, we will see that within an acoustic shadow region the frequency coherence varies significantly with the mean frequency of the signal and so cannot be determined by pulse intensity analysis, as is common practice in the study of optical and electromagnetic propagation.

The coherence bandwidth constrains the available information relating the phase and magnitude of harmonics of a signal. For sound propagation outdoors the coherence bandwidth is limited at longer ranges. This reduces the performance of algorithms which relate signal frequencies coherently (as in the trans-spectral coherence technique,[5] for example) for remote sensing applications such as source detection, localization, and identification. On the other hand, since atmospheric turbulence is responsible for limiting the coherence bandwidth, knowledge of the coherence bandwidth can be used to estimate statistical parameters of the turbulence.

Classical theory[1,6] describes frequency coherence for tones propagating through turbulence in the geometrical optics regime, where magnitude and phase fluctuations are small for each tone, as well as in the saturated regime, where magnitude fluctuations have reached a limiting value of about 6 dB and phase fluctuations are larger than 2π. Unfortunately, these formulations are based on forward-scattering analysis in line-of-sight propagation and do not apply to acoustic shadow regions.

There have been few reported measurements of statistics, other than sound-pressure levels, for sound propagation outdoors to complement existing theoretical work. Furthermore, recent advances in sound propagation modeling[7] have not yet been examined with respect to how well the higher-order statistics of the models compare with measurements, largely because of the lack of available measurement data. The frequency coherence measurements reported here, together with previous investigations into other statistics,[8–12] improve this situation. New opportunities for realistic acoustic modeling of sound propagation outdoors and for the inverse problems of acoustic remote sensing and acoustic probing of atmospheric turbulence will arise from systematic measurements of important sound-field statistics and parameters.

In this paper, measurements of frequency coherence during downward refracting and upward refracting (shadow) conditions are made for sound propagation near the ground. Measurements are made using a large acoustic array at a small airfield.[10,13–15] The results are shown to compare well with the classical theory for forward scattering for the geometrical optics regime and the saturated regime. Within the acoustic shadow region the frequency coherence bandwidth is shown to have a strong dependence on mean frequency.

The theory is outlined in Sec. I, followed by a description of the experiment and processing in Secs. II and III. The results are discussed in Sec. IV.

I. THEORY

A. Frequency coherence

An acoustic source, generated by a signal $s(t)$, propagating through a turbulent atmosphere will result in a stochastic sound field $p(\mathbf{x},t)$. For a pure-tone source $s(t) = S_0 \exp(i\omega_0 t)$, with angular frequency ω_0 and amplitude S_0, the sound field $p(\mathbf{x},t)$ can be expressed as the product of a stochastic *reduced wave function*, $\psi(\mathbf{x},t,\omega_0)$ and the source signal $s(t)$; that is, $p(\mathbf{x},t)=\psi(\mathbf{x},t,\omega_0)s(t)$.

The reduced wave function represents the fluctuations in the received sound field. When the turbulence causes only small fluctuations in the sound field the expected value of $S_0\psi$ approximates the sound pressure in the absence of turbulence. The reduced wave function is sometimes normalized with respect to the unperturbed sound field,[16] however, this is not appropriate for shadow regions or interference nulls where there is little or no received signal in the absence of turbulence. Interpreting the turbulent atmosphere as a time-varying linear system, the reduced wave function is the instantaneous transfer function between the source and receiver.

For a more general source signal $s(t)=\int S(\omega)\exp(i\omega t) \times d\omega$, the sound field at a point $\mathbf{x}$ is

$$p(\mathbf{x},t)=\int \psi(\mathbf{x},t,\omega)S(\omega)\exp(i\omega t)d\omega. \tag{1}$$

Each component signal frequency ω_i has a corresponding reduced wave function $\Psi(\mathbf{x},t,\omega_i)$. The *two-frequency mutual coherence function* Γ for the reduced wave function at two selected positions, times, and frequencies $(\mathbf{x}_1,t_1,\omega_1)$ and $(\mathbf{x}_2,t_2,\omega_2)$ is defined as[1,2]

$$\Gamma(\mathbf{x}_1,\mathbf{x}_2;t_1,t_2;\omega_1,\omega_2)=\langle \psi^*(\mathbf{x}_1,t_1,\omega_1)\psi(\mathbf{x}_2,t_2,\omega_2)\rangle, \tag{2}$$

where the asterisk (*) indicates complex conjugation and the angle brackets $\langle\cdots\rangle$ indicate expected value in the ensemble sense. Note that the *mutual coherence function*[3] is similarly defined without the frequency dependence.

We are interested in the special case of Γ evaluated at a single point in space and time $(\mathbf{x},t)=(\mathbf{x}_0,t_0)$, and so we define here the *frequency coherence*

$$C(\omega_1,\omega_2)=\frac{|\Gamma(\mathbf{x}_0,\mathbf{x}_0;t_0,t_0;\omega_1,\omega_2)|}{\langle|\psi(\mathbf{x}_0,t_0,\omega_1)|^2\rangle^{1/2}\langle|\psi(\mathbf{x}_0,t_0,\omega_2)|^2\rangle^{1/2}}. \tag{3}$$

This definition is based on ensemble averages but under suitable conditions, as discussed in Sec. III, C can be estimated from measurable values.

The frequency coherence C generally decreases with increasing frequency separation $\Delta\omega=(\omega_2-\omega_1)$ and so we use the criterion

$$C(\omega,\omega+\Delta\omega)<\frac{1}{e}, \quad \text{for } |\Delta\omega|\geqslant\omega_{\text{bw}} \tag{4}$$

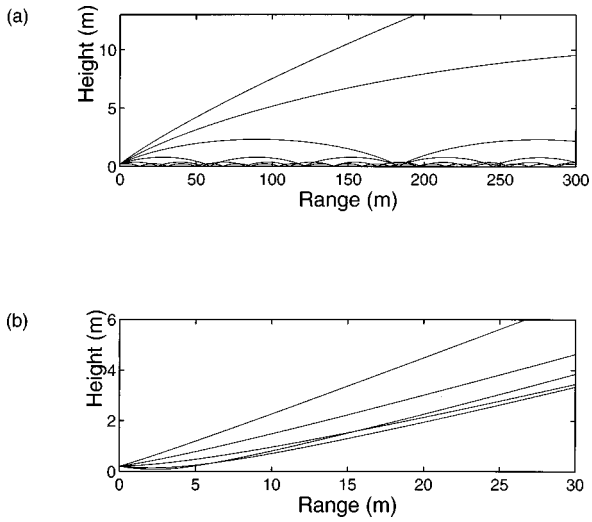

FIG. 1. Ray traces indicating the downward (a) and upward (b) refracting conditions during the tests. The source is positioned 0.2 m above the ground. Ray curvature is greatest near the ground.

to define the *frequency coherence bandwidth* ω_{bw} at ω.

A pulse propagating through a turbulent atmosphere will broaden, and the reciprocal of the frequency coherence bandwidth indicates the extent of this broadening. Although pulse broadening can also be due to nonlinear propagation[17] or ground impedance,[18,19] in these cases the effect is systematic rather than random and does not affect the frequency coherence as defined in Eq. (3).

B. Functional form of the frequency coherence

We consider two principle propagation conditions, (a) downward refraction and (b) upward refraction, as shown in Fig. 1. The (vertical) refraction pattern is determined by the mean vertical sound-velocity profile, which is often predominantly determined by either wind or thermal effects. For the data considered here the wind dominated over thermal effects. Figure 1 is based on measured wind and temperature data during the two test conditions considered in this paper.

During downward refraction conditions a direct ray exists between the source and receiver. This condition can occur during downwind propagation or thermal inversion (positive temperature gradient with height). The term *line-of-sight* propagation refers to the existence of a direct acoustic ray path between source and receiver. At sufficient range during downward refracting conditions, there may be more than one ray path between the source and receiver, each with a different number of ground reflections. The effect of multiple paths and their interaction with the ground is beyond the scope of this paper, but a related analysis has been done by Birdsall and Khan[20] for a moving source underwater.

Two regimes within line-of-sight propagation conditions are considered; the geometrical optics regime and the saturated regime. In practical terms, the former applies to shorter ranges and the latter to longer ranges in this analysis. These regimes have been described in detail within the literature[1,2,6] for propagation in the absence of impedance boundaries or unsteady multipath. We will follow the development of Flatté[1] and Dashen.[16]

During upward refraction conditions an acoustic shadow region is generated near the ground, within which there is no direct ray path between source and receiver. This condition occurs during upwind propagation, during thermal lapse (negative temperature gradient with height), or when the source is substantially occluded by a major terrain structure such as a hill. Although this condition may occur more frequently in situations of practical interest, theoretical developments within this regime are not as well developed as for line-of-sight propagation.

A brief review of theory for frequency coherence in the geometrical optic regime, the saturated regime, and the acoustic shadow region is presented for comparison with the measured data.

1. Geometrical optics regime

The geometrical optics regime is a domain of propagation parameters in which diffraction effects can be ignored and propagation from source to receiver can be approximated by a (possibly refracting) ray path. This regime is typically encountered during propagation in the atmosphere where ranges are less than a few hundred meters, turbulence levels are moderate, refraction is downward, and signal frequencies are below 500 Hz. (For lower frequencies the regime may extend further.)

Theoretical analyses[6,16] indicate that signal fluctuations in the geometrical optics regime have Gaussian log-amplitude and Gaussian phase fluctuations in the received signal. The amplitude fluctuations are small and the phase fluctuations correspond to perturbations in the propagation time along the acoustic ray. The frequency coherence in the geometrical optics regime is[16]

$$C_{\text{geom}}(\omega_1,\omega_2)=e^{-(1/2)(\Delta\omega\Phi/\omega_0)^2}, \tag{5}$$

where the frequency separation is $\Delta\omega=\omega_2-\omega_1$, the mean signal frequency is $\omega_0=(\omega_2+\omega_1)/2$, and the turbulence strength parameter $\Phi^2=(\omega_0/c_0)^2\,\langle|\int \eta\, ds|^2\rangle$ is the variance of the integral of the fluctuations in the index of refraction η along the propagation path ds, times the square of the mean signal wave number ω_0/c_0. In the geometrical optics regime the value of Φ^2 can be obtained by measuring the variance of the received phase for a pure-tone source signal. The frequency coherence bandwidth $\omega_{\text{bw}}=\sqrt{2}\omega_0/\Phi$ is large in this regime (on the order of ω_0). Since Φ varies as $\omega_0\sqrt{R}$, where R is the propagation range, the coherence bandwidth ω_{bw} is independent of ω_0 and decreases with range as $1/\sqrt{R}$. Figure 2 (dotted curves) shows the predicted frequency coherence in the geometrical optics regime at ranges of 100, 675, and 3000 m, based on $\Phi=0.14\sqrt{R}$ at 500 Hz, as determined from the measurement data in Sec. IV A.

A single pulse propagating in the geometrical optics regime will arrive at the receiver with very little pulse broadening, but with considerable variation (pulse wander) in the pulse arrival time. The root-mean-square (rms) of the pulse wander is $\sqrt{2}/\omega_{\text{bw}}$.

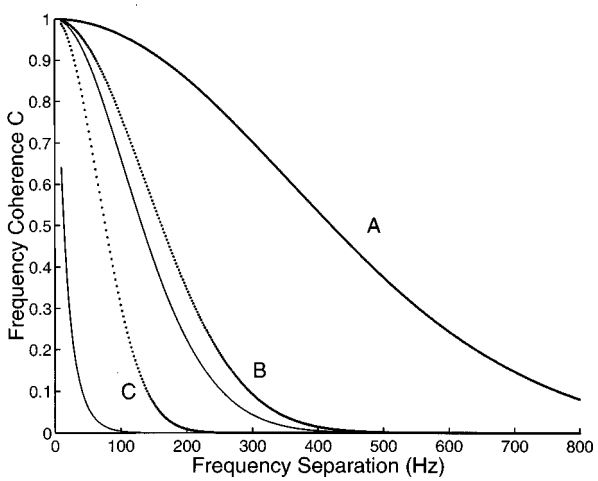

FIG. 2. Predicted frequency coherence using the geometrical optics regime formulation of Eq. (5) (dotted curves · · · ·) and the saturated regime formulation of Eq. (6) (solid curves ———) for ranges of 100 m (A), 675 m (B), and 3000 m (C) with parameter values determined from the measured data in Sec. IV A. The dotted and solid curves are coincident in case (A).

2. Saturated regime

In the saturated regime, diffraction effects are significant and the fluctuations due to turbulence are more dramatic. This regime is typically encountered during propagation at ranges beyond a few hundred meters for frequencies above a few hundred hertz. (For higher frequencies, saturation may occur at closer ranges.)

Theoretical analyses such as that of Tatarskii[6] or Dashen[16] suggest that the sound field observed in the saturated regime is characterized by phase fluctuations which are uniformly distributed between $\pm\pi$ and sound-pressure level fluctuations of approximately ± 6 dB. The real and imaginary part of the acoustic pressure each follow Gaussian distributions and the square-magnitude pressure follows the exponential distribution[11] (i.e., the χ_2^2 distribution).

Propagation from source to receiver in the saturated regime cannot be treated as a single ray path, but it can be treated as an ensemble of *micropaths*.[16] In this formulation, each micropath contributes a randomly delayed version of the source signal and the resultant fluctuations in the signal at the receiver are mainly due to interference between the micropaths. In this regime the frequency coherence has the form.[16]

$$C_{\text{sat}}(\omega_1,\omega_2)=e^{-(1/2)(\Delta\omega\Phi/\omega_0)^2}Q\left(\frac{\Delta\omega}{\xi_0}\right), \tag{6}$$

where $\xi_0=\omega_0^2L^2/\Phi^2Rc_0$ is a convenient normalizing factor, L is the characteristic length of the turbulence (the spatial coherence length), R is the distance between source and receiver, c_0 is the unperturbed speed of sound, and the micropath bandwidth function Q has the form

$$Q(x)=\left|\frac{\sqrt{ix}}{\sin\sqrt{ix}}\right|. \tag{7}$$

The function $Q(x)$ is shown in Fig. 3. The value of ξ_0 is independent of frequency because Φ is proportional to ω_0.[16] Equation (6) generalizes Eq. (5) since within the geometrical

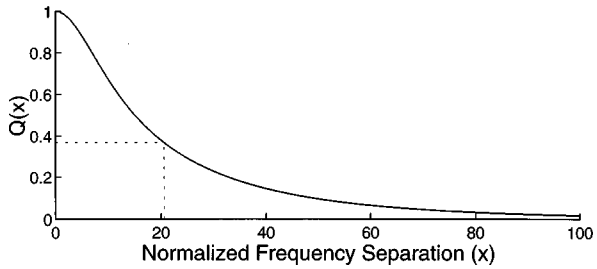

FIG. 3. The function $Q(x)=|\sqrt{ix}/\sin\sqrt{ix}|$ governing the frequency coherence in the saturated regime according to Eq. (6). The $1/e$ point, as indicated, occurs at $x\approx 20.6$.

optics regime the value of ξ_0 is small and the first factor dominates while within the saturated regime the second term dominates. The value of Φ cannot be obtained by measuring the received signal phase fluctuations in the saturated regime, as it can in the geometrical optics regime, because the phase fluctuations are primarily due to the interference between micropaths rather than the variations in the index of refraction along a single propagation path.

From Fig. 3 the $1/e$ point of Q occurs at approximately 20.6, hence in the saturated regime

$$\omega_{\mathrm{bw}}\approx 20.6\,\frac{\omega_0^2 L^2}{\Phi^2 R c_0}. \tag{8}$$

The solid curves in Fig. 2 show the predicted frequency coherence according to Eq. (6) with $\Phi=0.014R$ (at 500 Hz) and $L=6$ m, as determined from the experimental data in Sec. IV A. Notice that as the range increases, the second factor in Eq. (6) begins to dominate over the first factor (dotted curves).

In the saturated regime a short pulse will arrive at the receiver with a width of approximately $1/\omega_{\mathrm{bw}}$. This pulse spread may greatly exceed the wander between successive pulses, which is $\sqrt{2}\omega_0/\Phi$, as caused by the first factor in Eq. (6). As discussed in Sec. IV A the distinction between pulse spread and pulse wander can be observed and used to demonstrate the relative contributions of the two factors in Eq. (6).

3. Acoustic shadow region

The formulation of the frequency coherence bandwidth in the previous sections is applicable to line-of-sight acoustic propagation and does not apply to an acoustic shadow region. Tatarskii has argued (for a coherent scattering volume) that the frequency coherence bandwidth for scattered pulses is of the form[6]

$$\omega_{\mathrm{bw}}=\frac{c_0}{2d\,\sin(\theta/2)}, \tag{9}$$

where d is the height of the scattering volume, c_0 is the speed of sound, and θ is the scattering angle.

When both the source and receiver are on the ground, the dominant scattering region occurs near the shadow boundary midway between the source and receiver.[21] In this geometry, the scattering angle θ is twice the slope of the shadow boundary at the scattering region. This slope varies only slightly at ranges beyond a few hundred meters and it is typically less than 5°.[22]

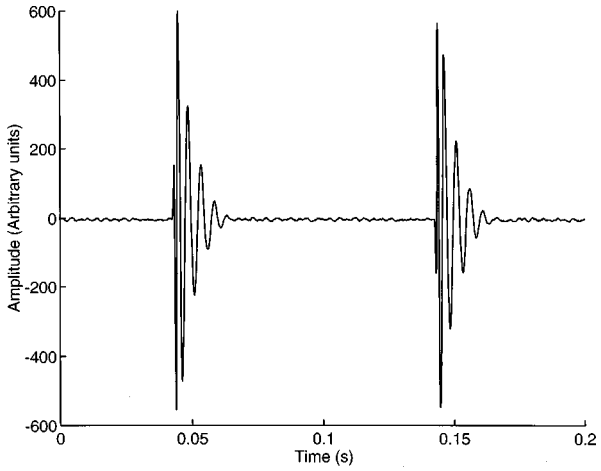

FIG. 4. One complete cycle of the source time series, consisting of two pulses of opposite phase.

To first order, the height of the first Fresnel scattering zone is $d_1\cong\lambda/2\,\tan(\theta/2)+O(\lambda^2/R)$ when θ is less than 45°, where $\lambda=2\pi c_0/\omega_0$. Higher-order terms of order λ^2/R are negligible for $R>100\lambda$. Using d_1 as an estimate for the height of the scattering volume, the frequency coherence bandwidth is $\omega_{\mathrm{bw}}\cong\omega_0/2\pi$; accordingly, the frequency coherence bandwidth within a shadow region will depend upon the mean frequency and will be independent of range. This is contrary to the line-of-sight situation.

II. DATA COLLECTION

The experiment was conducted at Pendleton Airport, a private airfield about 50 km from Ottawa in a rural area. The data collection for this experiment is similar to that reported by Havelock *et al.*[10] for spatial coherence measurements. The runway is about 700 m long with an asphalt surface. The surrounding grounds are cultivated fields with low trees in the distance. There are no buildings or structures to provide significant acoustic scattering.

Sound velocity profiles were calculated, based on similarity laws,[13] using temperature and wind velocity data collected during the tests from sensors on a 10-m tower at the test site. The acoustic data being considered here were obtained under two distinct meteorological conditions, (a) downward refraction (downwind propagation with wind speed 5 m/s, mean temperature 20 °C, and overcast skies) and (b) upward refraction (upwind propagation with wind speed 5 m/s, mean temperature 22 °C, and partly cloudy skies). The estimated ray paths based on the measured meteorology for the downward and upward refracting conditions are shown in Fig. 1(a) and (b), respectively.

The source signal was generated by bandpass filtering either a 5- or 10-Hz square wave to obtain a time series consisting of alternating positive and negative pressure pulses. The 3-dB corner frequencies of the bandpass filter were approximately 200 and 1000 Hz. Figures 4 and 5 show the time series and power spectrum as observed at a sensor

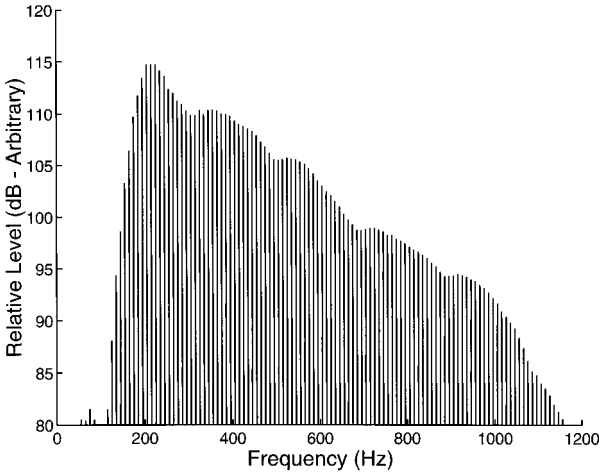

FIG. 5. A high-resolution power spectrum of the source signal, displaying a series of tones uniformly spaced in frequency between 200 and 1000 Hz. The power spectrum was generated using a Hamming window applied to approximately 8 s of data.

75 m in front of the source. For the downward refracting case a filtered 5-Hz square wave was used and for the upward refracting case, to obtain a better signal-to-noise ratio, a filtered 10-Hz square wave was used. The source signals were recorded on DAT and replayed through four speakers, each with a single 15-in. (38 cm) driver, placed on the ground in a line perpendicular to the direction of propagation. The height of the center of the drivers was 28 cm above the ground and the distance between the adjacent centers was 57 cm. The source signal was monitored by a reference microphone positioned on the ground 25 m along the axis of symmetry in front of the speakers. Source levels were approximately 125 dB (*re*: 20 μPa) referred to 1-m distance and the signal-to-noise ratio was generally greater than 20 dB.

The receiving array of 27 microphones was arranged in a straight line parallel to the direction of propagation and along the center of the runway at ranges from 50 to 675 m from the source. (Microphone spacing was nominally 25 m, with some variations at longer ranges.) The sensitivity of the six microphones closest to the source was electronically attenuated 10 dB relative to the other microphones in the array. The microphone signals were passed by cables to an equipment trailer, which was approximately 200 m from the array, where they were filtered, multiplexed, digitized, and then stored on digital tape for off-line processing. Data were recorded in 5-min segments at 8 kHz per channel with 12-bit resolution. Further details of the data collection are reported elsewhere.[10]

III. DATA PROCESSING

The digitized data $f(n)$ from a microphone were segmented into M frames $f_m(n)=f(N_m+n)$ of length $N=4096$ or 8192 samples, where n is the sample index, m is the frame index, and N_m is the start sample as discussed below. The magnitude of the normalized cross-spectral matrix (CSM) is then calculated as

$$|A(k_1,k_2)|=\frac{|\Sigma_{m=0}^{M-1}F_m^*(k_1)F_m(k_2)|}{(\Sigma_{m=0}^{M-1}|F_m(k_1)|^2)^{1/2}(\Sigma_{m=0}^{M-1}|F_m(k_2)|^2)^{1/2}}. \tag{10}$$

where $F_m(k)$ is the discrete Fourier transform (DFT) of $f_m(n)$. The terms in the summation in the numerator of Eq. (10) above will sum coherently if the values of N_m are chosen so that each frame starts at the same place in the period of the source signal. To achieve this, the frame start sample N_m is chosen so that

$$N_m=\left\lfloor\left\lfloor\frac{mN\tau_s}{\tau_p}+\frac{1}{2}\right\rfloor\frac{\tau_p}{\tau_s}\right\rfloor, \tag{11}$$

where the floor brackets $\lfloor\cdots\rfloor$ indicate integer truncation toward zero, τ_s is the data sampling period, and τ_p is the period of the source signal.

The source signal contains tones separated by 10 Hz (downward refraction) or 20 Hz (upward refraction). To resolve these peaks in the spectrum, DFT (frame) sizes of $N=8192$ and $N=4096$ were used, respectively, obtaining spectral resolution of approximately one-tenth the tone spacing. The normalized cross-spectral matrix was computed using only the spectral bin closest to each harmonic peak.

To correct for a very small, but important, systematic error in the clock frequencies, the 10-Hz source frequency for the downward refracting case was decreased by 0.101 mHz and the 5 Hz source frequency for the upward refracting case was increased by 1.650 mHz. The random variations in the clock sampling time are less than a single sample interval and are negligible.

We intend to use the CSM A to estimate the frequency coherence C defined in Eq. (3). It can be shown that (under certain assumptions, as discussed below)

$$|C(\omega(k_1),\omega(k_2))|\cong|A(k_1,k_2)|, \tag{12}$$

where $\omega(k)$ is the angular frequency corresponding to the DFT spectral index k and the approximation is in the sense that C is the expected value of the measured A.

Fluctuations in the propagation channel cause the spectral lines in the received signal to broaden and, if the width of the broadened lines exceeds the separation between lines, entries in the CSM will involve contributions from more than two frequencies. This will cause departure from equality in Eq. (12). Furthermore, variations in the amount of (expected) line broadening from frequency to frequency and the inclusion of decorrelation effects due to the finite temporal extent of the spectral estimation window can also degrade the relationship.

Measurements of the temporal autocorrelation for single tone signals, at the frequencies of interest, at the experiment site 30 min prior to these frequency coherence tests showed autocorrelation times at all ranges and frequencies of at least several seconds for downward refracting propagation and about 1/4 s for upward refraction propagation. The autocorrelation time in seconds is approximately equal to one-half the reciprocal of the bandwidth, in hertz, of the broadened harmonic tones. Accordingly, the harmonic tone separations of 10 and 20 Hz are adequate to ensure that the broadened tones do not overlap. Furthermore, at least for the downward

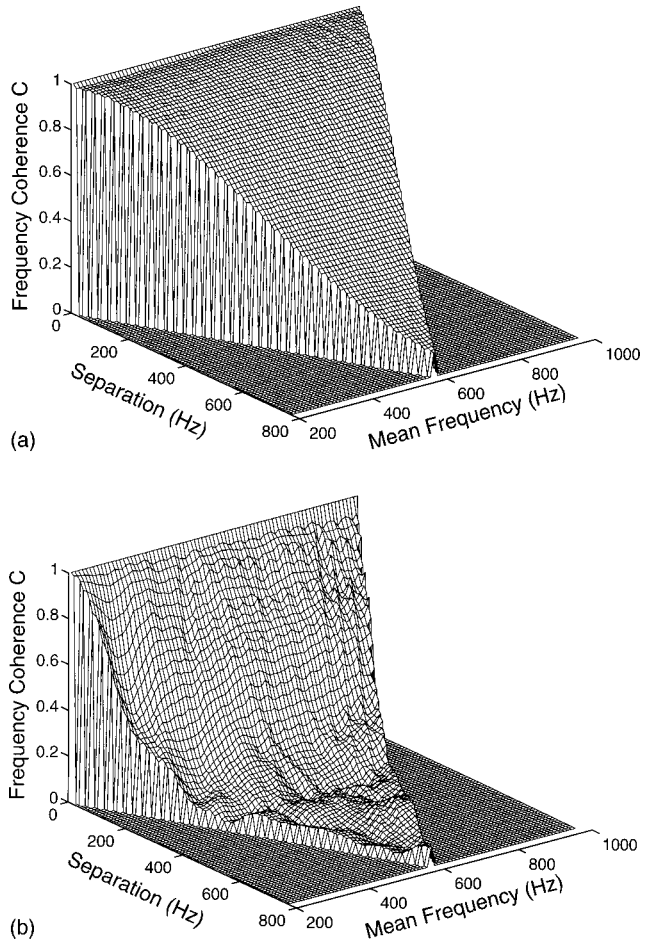

FIG. 6. Frequency coherence as a function of mean frequency and frequency separation for downward refracting conditions at 100-m range (a) and at 675-m range (b).

refraction case, the frame duration is much shorter than the temporal coherence time. In the upward refraction case, a balance was sought between the conflicting requirements of adequate spectral resolution and a frame duration which does not exceed the temporal coherence.

To demonstrate the distinction between pulse spread and pulse wander in the received signal, a method was used to remove the pulse wander prior to computing the frequency coherence. The position of the pulse in each frame was estimated and then the waveform was shifted so that the relative position of the pulse was constant from frame to frame. Details of the technique are not essential here and are omitted but the basic principle is to determine and remove a linear phase trend from the DFT coefficients. Data processed in this manner are referred to here as *phase detrended* data.

IV. DISCUSSION

A. Line-of-sight propagation

For line-of-sight propagation, when a direct ray path exists between source and receiver, the frequency coherence will follow Eq. (5) at shorter ranges (within the geometrical optics regime) and Eq. (6) at longer ranges (within the saturated regime). In Fig. 6(a) and (b) the measured frequency coherence is shown as a function of mean frequency ω_0 $=(\omega_1+\omega_2)/2$ and frequency separation $\Delta\omega=\omega_2-\omega_1$ for sensors at ranges of 100 and 675 m. The signal frequencies are restricted between 200 and 1000 Hz, so the available range of ω_0 decreases as $\Delta\omega$ increases. Measurement data for the frequency coherence therefore exist only on a triangular region of the horizontal axes in the figure. For points outside this triangular region, the values in the plot are set to zero. The data are smoothed with a 3×3 averaging window. As predicted by theory, the frequency coherence drops off more rapidly with increasing frequency separation at the longer range and depends upon the frequency separation only.

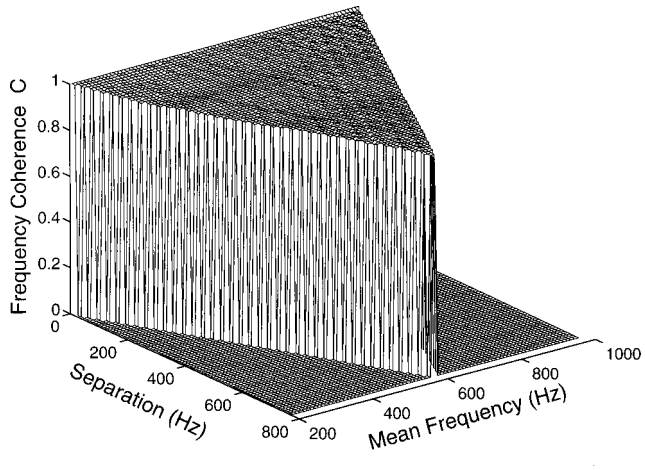

FIG. 7. Phase detrended frequency coherence as a function of mean frequency and frequency separation for downward refracting conditions at 100 m, showing the effect of removing time-of-arrival fluctuations from the received pulse.

To illustrate the distinction between the mechanisms for frequency decorrelation in the geometric optics and the saturated regimes, the normalized cross-spectral matrix was recalculated using phase detrended spectra which has the pulse wander removed, as discussed at the end of Sec. III. The frequency coherence for the phase detrended data at 100 m is shown in Fig. 7. The data are smoothed with a 3×3 averaging window. The correlation is approximately unity at all analysis frequencies, indicating that diffraction effects are minimal and that propagation time (wind speed) fluctuations account for essentially all of the frequency decorrelation. At the longer range, phase detrending is not as effective because diffraction effects, as represented by the factor Q in Eq. (6), are more significant.

In Fig. 8 the frequency coherence as a function of frequency separation is shown for ranges of 100 and 675 m. This plot was obtained by averaging the frequency coherence shown in Fig. 6(a) and (b) along lines of constant frequency separation. Using Eqs. (5) and (8), a good fit is obtained between the predicted (dotted) and the measured frequency coherence at both 100- and 675-m ranges by using $L=6$ m and $\Phi=1.4\Phi_0$, where the reference turbulence strength $\Phi_0(\omega,R)$ is unity at 100 m and 500 Hz, and varies as $\omega\sqrt{R}$ with range R and signal frequency ω. The sensitivity of the predicted coherence to values of Φ and L are indicated in Fig. 8 by the error bars which span the range of predicted values obtained within the parameter ranges $\Phi/\Phi_0=1.4$

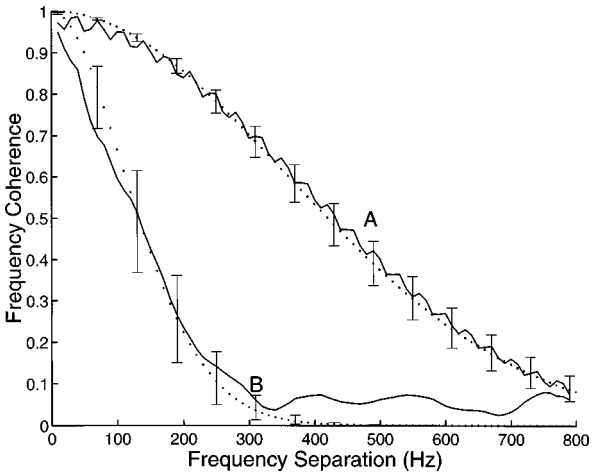

FIG. 8. Frequency coherence as a function of frequency separation is obtained for downward refracting conditions by averaging the surfaces in Fig. 6 along lines parallel to the diagonal. Measured data for 100 m (A) and 675 m (B) are shown as solid curves (———). Predictions based on parameters determined from the experimental data are shown as dotted curves (···). The error bars indicate the sensitivity to parameter value adjustments (as explained in the text).

± 0.1 and $L = 6 \pm 1$ m. Thus using the measured frequency coherence data, it is possible to estimate two important parameters of the prevailing turbulence with some precision. Unfortunately, direct meteorological measurement of the estimated parameters is not available and so the accuracy of these parameter estimates cannot be determined. Note that the error bars are used to indicate parameter sensitivity in the prediction and are not related to measurement errors.

The geometrical optics regime and the saturated regime are formally defined[1] as parameter regions in Λ-Φ space, as described in Table I, according to whether the parameters Φ, Λ, and $\Lambda\Phi^2$ are less than or greater than unity, where $\Lambda = Rc_0/6\omega_0 L^2$ is the so-called diffraction parameter which increases with increasing significance of diffraction effects. (For completeness, we note that the unsaturated region $\Lambda > 1 > \Phi$ is called the Rytov extension regime.) Using the estimated parameter values $\Phi/\Phi_0 = 1.4$ and $L = 6$ m for 100- and 675-m ranges, Φ, Λ, and $\Lambda\Phi^2$ fall within the intervals indicated in Table II for the frequencies of interest. Accordingly, the received signal at 100 m is within the geometrical optics regime, while the signal at 675 m is within the saturated regime. Within the saturated regime, a further distinction is made between the partially saturated regime, where $\Lambda\Phi^2 > 1 > \Lambda\Phi$, and the fully saturated regime, where $\Lambda\Phi > 1$. Since $\Lambda\Phi \approx 1.2$ for the data at 675 m, it falls (marginally) within the fully saturated regime.

The measured frequency coherence bandwidth for each sensor in the array is plotted as a solid line in Fig. 9, showing the bandwidth as a function of range R. (The data for the sensors at 50 and 200 m are omitted.) The frequency coherence bandwidth ω_{bw} at each sensor is calculated according to Eq. (4), after some smoothing of the frequency coherence curve.

TABLE I. Propagation regimes.

Geometrical optics:	$\Lambda\Phi^2 < 1$ and $\Lambda < 1$
(Fully) saturation:	$\Phi > 1$ and $\Lambda\Phi > 1$
Partial saturation:	$\Lambda\Phi^2 > 1$ and $\Lambda\Phi < 1$
Rytov extension:	$\Phi < 1$ and $\Lambda > 1$

TABLE II. Estimated values of turbulence parameters.

	100 m (geometrical optics)	675 m (saturated)
Φ	0.5–2.8	1.4–7.3
Λ	0.02–0.13	0.17–0.85
$\Lambda\Phi^2$	0.04–0.20	1.7–9.0

The dotted curve in Fig. 9 is the frequency coherence bandwidth for the geometrical optics regime, as calculated using Eqs. (4) and (5) with the estimated parameter values for Φ/Φ_0 and L discussed above. The dashed curve in Fig. 9 is the micropath bandwidth from Eq. (8) using the same estimated parameters. As range increases the micropath bandwidth curve decreases more rapidly than the curve for the frequency coherence bandwidth based on the geometrical optics regime. Eventually, at ranges beyond those plotted in Fig. 9, the curves cross and the frequency coherence bandwidth, as given by Eq. (6) for the saturated regime, is dominated by the micropath bandwidth factor.

The conspicuous rise in the frequency coherence bandwidth for the measured data at about 300 m is not explained. Plots of frequency coherence bandwidth ω_{bw} versus range for other datasets on different days with downward refracting conditions show a wide variation in the rate of decrease in ω_{bw} with R. In some cases the bandwidth decreases below the available resolution within a range of only a few hundred meters, while in other cases the bandwidth exceeds 800 Hz even at long ranges. The results reported here were selected because the wind strength was relatively stable throughout the measurement and the results fell within the resolution limitations of the experiment.

B. Acoustic shadow region

Existing theory in the literature provides less information about the frequency coherence in the acoustic shadow

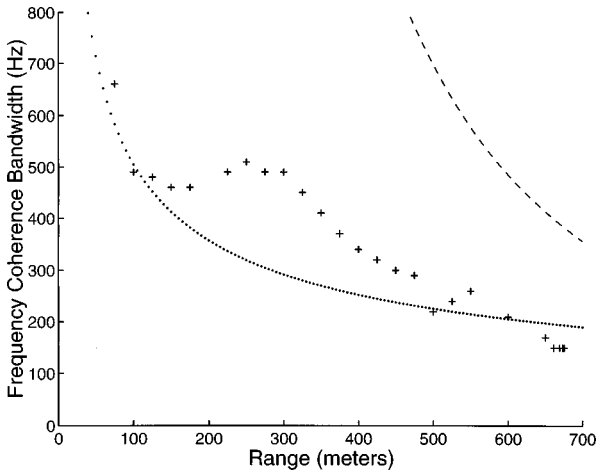

FIG. 9. Measured frequency coherence bandwidth as a function of range for downward refracting conditions (crosses +) is shown with the predicted frequency coherence bandwidth for the geometrical optics regime (dotted curve ···) and the micropath bandwidth due to diffraction effects (dashed curve ---).

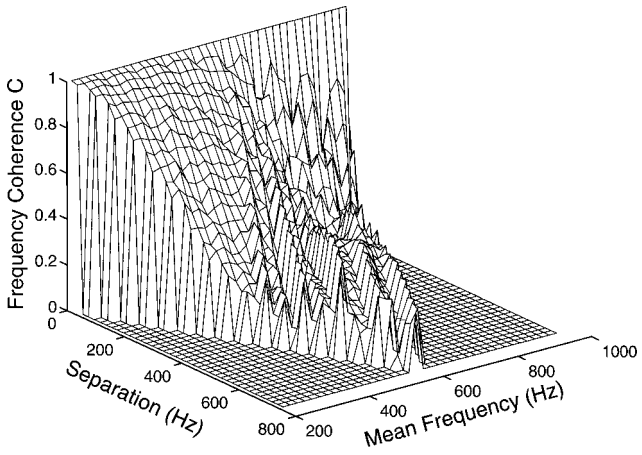

FIG. 10. Frequency coherence as a function of mean frequency and frequency separation for upward refracting conditions at 100-m range.

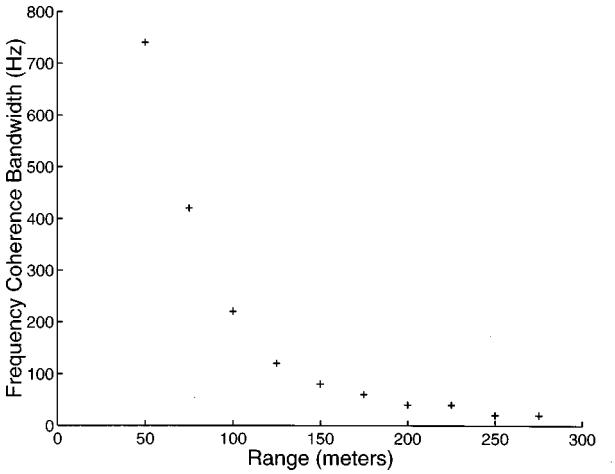

FIG. 11. Averaged frequency coherence bandwidth plotted as a function of range for upward refracting conditions.

region than in the line-of-sight region. Figure 10 shows the measured frequency coherence at a range of 100 m during upward refracting conditions. The frequency coherence is seen to be strongly dependent upon the mean frequency, as well as the frequency separation. This is thought to be a result of the rapidly decreasing ratio of diffracted (''coherent'') to scattered (''incoherent'') energy with increasing frequency in the vicinity of the shadow boundary.

Phase detrended spectra for the shadow region data did not display significantly different frequency coherence than the unadjusted data; this is consistent with there being strong diffraction effects within the shadow region.

The frequency coherence deep within the shadow region (not illustrated) decreases to small values at frequency separations which are less than the 20-Hz frequency resolution of this experiment. A frequency coherence bandwidth of less than 20 Hz is considerably less than that estimated using the size of the first Fresnel zone ($d=d_1$) in Eq. (9) where, for example, $\omega_{\rm bw}\approx 80$ Hz for $\omega_0=500$ Hz. Using numerical simulations, Stinson *et al.*[21] have shown that the vertical height of the dominant scattering region (for 500 Hz at 700-m range) is about 60 m. This is much larger than the height of the corresponding Fresnel zone, which is about 2 m. Applying this value of 60 m to the bandwidth estimate in Eq. (9), and noting that the slope of the shadow boundary in Fig. 1 suggests a value of 0.2 for $\sin(\theta/2)$, we obtain an estimate for the frequency coherence bandwidth at 500 Hz of 15 Hz, which is more consistent with the measurements.

In Fig. 11, the frequency coherence at each sensor is averaged across frequencies to obtain a plot of the mean frequency coherence as a function of range. This provides a comparison with Fig. 9 and illustrates how rapidly the frequency coherence decreases with range in the shadow region.

V. SUMMARY

A large acoustic array has been used to measure frequency coherence at ranges up to 675 m for signal frequencies in the range 200–1000 Hz. Both upward and downward refracting propagation conditions have been examined. Measurements for downward refracting conditions have been compared with existing theory for line-of-sight propagation. For line-of-sight propagation at short ranges (100 m), fluctuations in the propagation time is seen to be the principal mechanism for reduced frequency coherence bandwidth. At longer ranges (675 m), diffraction effects become more important and the frequency coherence bandwidth becomes quite small. It was verified that for line-of-sight propagation the frequency coherence is dependent on frequency separation alone and is independent of mean frequency. Excellent agreement is shown between the shape of the theoretical and experimental frequency coherence curves for line-of-sight propagation. Examination of the dependence of frequency coherence bandwidth on range for line-of-sight propagation showed deviations from predicted values. It has been demonstrated that the turbulence strength Φ and the turbulence coherence length L can be estimated from the frequency coherence measurements.

Measurements for upward refracting conditions, where an acoustic shadow region is generated, have been compared to a simple scattering model. It was shown that in the vicinity of the shadow boundary (100 m) the frequency coherence bandwidth depends upon the mean frequency. Deeper within the shadow region (675 m), the frequency coherence bandwidth is less than 20 Hz over the entire frequency band being considered.

This investigation is applicable to the assessment of critical performance elements of acoustic remote sensing systems outdoors and provides additional criteria against which the realism of simulations and propagation prediction codes might be evaluated.

ACKNOWLEDGMENTS

The cooperation of the Gatineau Flying Club and the use of their facilities are greatly appreciated. The comments of the reviewers and Associate Editor were very helpful.

[1] *Sound Transmission Through a Fluctuating Ocean*, edited by S. M. Flatté (Cambridge U.P., Cambridge, England, 1979).
[2] A. Ishimaru, *Wave Propagation and Scattering in Random Media* (Academic, New York, 1978), Vols. I and II.

[3] R. M. Gagliardi and S. Karp, *Optical Communications* (Wiley, New York, 1979).
[4] A. Derode and M. Fink, ''The notion of coherence in optics and its application to acoustics,'' Eur. J. Phys. **15**, 81–90 (1994).
[5] P. G. Vaidya and M. J. Anderson, ''Use of the trans-spectral-coherence technique to separate signals from noise,'' J. Acoust. Soc. Am. **89**, 2370–2378 (1991).
[6] V. I. Tatarskii, *The Effects of the Turbulent Atmosphere on Wave Propagation* (Keter, Jerusalem, 1971).
[7] K. Attenborough, S. Teherzadeh, H. E. Bass, X. Di, R. Raspet, G. R. Becker, A. Güdensen, A. Chrestman, G. A. Daigle, A. L'Espérance, Y. Gabillet, K. E. Gilbert, Y. L. Li, M. J. White, P. Naz, J. M. Noble, and H. A. J. M. van Hoof, ''Benchmark cases for outdoor sound propagation models,'' J. Acoust. Soc. Am. **97**, 173–191 (1995).
[8] G. A. Daigle, T. F. W. Embleton, and J. E. Piercy, ''Propagation of sound in the presence of gradients and turbulence near the ground,'' J. Acoust. Soc. Am. **79**, 613–627 (1986).
[9] G. A. Daigle, T. F. W. Embleton, and J. E. Piercy, ''Line-of-sight propagation through atmospheric turbulence near the ground,'' J. Acoust. Soc. Am. **74**, 1505–1513 (1983).
[10] D. I. Havelock, X. Di, G. A. Daigle, and M. R. Stinson, ''Spatial coherence of a sound field in a refractive shadow: Comparison of simulation and experiment,'' J. Acoust. Soc. Am. **98**, 2289–2302 (1995).
[11] D. K. Wilson, J. C. Wyngaard, and D. I. Havelock, ''The effect of turbulence intermittency on scattering into an acoustic shadow zone,'' J. Acoust. Soc. Am. **99**, 3393–3400 (1996).
[12] J. M. Noble, H. E. Bass, and R. Raspet, ''The effects of large scale atmospheric inhomogeneities on acoustic propagation,'' J. Acoust. Soc. Am. **92**, 1040–1046 (1992).
[13] M. R. Stinson, ''Importance of the near-ground sound speed profile in prediction of sound fields in a refractive shadow,'' J. Acoust. Soc. Am. **98**, 2924 (1995).
[14] D. I. Havelock, ''Measuring the effects of turbulence,'' Can. Acoust. **22**, 127–128 (1994).
[15] D. I. Havelock, ''A large microphone array for outdoor sound propagation studies,'' J. Acoust. Soc. Am. **96**, 3245 (1994).
[16] R. Dashen, ''Path integrals for waves in random media,'' J. Math. Phys. **20**, 894–920 (1979).
[17] P. Boulanger, R. Raspet, and H. E. Bass, ''Sonic boom propagation through a realistic turbulent atmosphere,'' J. Acoust. Soc. Am. **98**, 3412–3417 (1995).
[18] A. J. Cramond and C. G. Don, ''Impulse propagation in a neutral atmosphere,'' J. Acoust. Soc. Am. **81**, 1341–1352 (1987).
[19] I. P. Chunchuzov, G. A. Bush, and S. N. Kulichkov, ''On acoustical impulse propagation in a moving inhomogeneous atmospheric layer,'' J. Acoust. Soc. Am. **88**, 455–461 (1990).
[20] T. G. Birdsall and F. Khan, ''Implications of multipath propagation for two-frequency coherence measurements,'' J. Acoust. Soc. Am. **78**, 105–111 (1985).
[21] M. R. Stinson, D. I. Havelock, and G. A. Daigle, ''Simulation of scattering by turbulence into a shadow region using the GF-PE method,'' Proceedings of the 6th International Symposium on Long-Range Sound Propagation, Ottawa, Canada, 1994 (1994), pp. 283–295.
[22] J. E. Piercy, T. F. W. Embleton, and L. C. Sutherland, ''Review of noise propagation in the atmosphere,'' J. Acoust. Soc. Am. **61**, 1403–1418 (1977).

Improved Green's function parabolic equation method for atmospheric sound propagation

Erik M. Salomons
TNO Institute of Applied Physics, P.O. Box 155, 2600 AD Delft, The Netherlands

(Received 10 February 1997; revised 22 March 1998; accepted 31 March 1998)

The numerical implementation of the Green's function parabolic equation (GFPE) method for atmospheric sound propagation is discussed. Four types of numerical errors are distinguished: (i) errors in the forward Fourier transform; (ii) errors in the inverse Fourier transform; (iii) errors in the refraction factor; and (iv) errors caused by the split-step approximation. The sizes of the errors depend on the choice of the numerical parameters, in particular the range step and the vertical grid spacing. It is shown that this dependence is related to the stationary phase point of the inverse Fourier integral. The errors of type (i) can be reduced by increasing the range step and/or decreasing the vertical grid spacing, but can be reduced much more efficiently by using an improved approximation for the forward Fourier integral. The errors of type (ii) can be reduced by using a numerical filter in the inverse Fourier integral. The errors of type (iii) can be reduced slightly by using an improved refraction factor. The errors of type (iv) can be reduced only by reducing the range step. The reduction of the four types of errors is illustrated for realistic test cases, by comparison with analytic solutions and results of the Crank–Nicholson PE (CNPE) method. Further, optimized values are presented for the parameters that determine the computational speed of the GFPE method. The computational speed difference between GFPE and CNPE is discussed in terms of numbers of floating point operations required by both methods. [S0001-4966(98)03407-9]

PACS numbers: 43.28.Fp, 43.20.Fn, 43.50.Vt [LCS]

INTRODUCTION

The parabolic equation method is a powerful computational method for sound propagation in inhomogeneous media. The method has been used for underwater acoustics,[1,2] and was adapted for atmospheric acoustics by Gilbert and White.[3] The wide-angle parabolic equation method of Gilbert and White is based on an implicit Crank–Nicholson extrapolation of the sound field, and therefore this method is referred to as the Crank–Nicholson parabolic equation method (CNPE method). The extrapolation step in the CNPE method is limited to a fraction of the wavelength. As a consequence, the computing time of the CNPE method increases sharply with frequency. The computing time for a complete sound spectrum may be several hours on current computers.

Recently, Gilbert and Di[4,5] developed a fast Green's function method for computing atmospheric sound propagation. The method was referred to as the Green's function parabolic equation method (GFPE method). The extrapolation step in the GFPE method may be considerably larger than the wavelength. Computing times of the GFPE method are considerably smaller than computing times of the CNPE method. Gilbert and Di reported speed-up factors of the order of 100.

Two factors that determine the power of a computational method for atmospheric sound propagation are accuracy and computational speed. These factors are not independent of each other. In general, the computational speed increases if a less accurate solution is required. In this paper we discuss the accuracy and the computational speed of the GFPE method. We present optimized values for parameters of the GFPE method. Further, we compare different numerical implementations of the GFPE method, with considerable differences in numerical accuracy.

The most important result of this paper is that the accuracy of the GFPE method, at fixed values of the range step and the vertical grid spacing, can be improved by using an improved approximation for the forward and inverse Fourier integrals, based on the midpoint rule of numerical integration. It should be emphasized that the accuracy of the GFPE method with the standard approximation for the Fourier integrals can always be improved by using a smaller vertical grid spacing. It has been shown that accurate results can be obtained with the GFPE method with the standard approximation for the Fourier integrals, for several benchmark cases.[4–6] Hence, in a sense, the improved approximation for the Fourier integrals improves the efficiency rather than the accuracy of the GFPE method. It will be shown that the improvement of the efficiency is surprisingly large in some cases, e.g., corresponding with a reduction of computing time by a factor of the order of 10.

I. THEORETICAL FORMULATION

We consider a system with a monopole source in a refracting atmosphere above a finite-impedance ground surface. It is assumed that the system has a rotational symmetry around the vertical z axis through the source, i.e., azimuthal derivatives of the sound field are neglected. Therefore, the computation can be performed in two dimensions, in the rz plane, with r the horizontal distance to the source.

Starting from the three-dimensional Helmholtz equation in cylindrical rz coordinates for the harmonic sound pressure p, the following far-field approximation[7] can be derived for the quantity $q=pr^{1/2}$:

$$\frac{\partial^2}{\partial r^2}\,q(r,z)+\frac{\partial^2}{\partial z^2}\,q(r,z)+k^2(z)q(r,z)=0 \tag{1}$$

with $k(z)=\omega/c(z)$ the wave number, where ω is the angular frequency and c the sound speed. We assume here that the sound speed depends only on the height z. Equation (1) shows that q satisfies a two-dimensional wave equation.

We substitute $\phi=\exp(-ik_r r)\,q$, where k_r is a reference wave number, and neglect the term $\partial_r^2\phi$, to obtain the following one-way wave equation from Eq. (1):

$$\frac{\partial\phi(r,z)}{\partial r}=\frac{i}{2k_r}\left(\frac{\partial^2}{\partial z^2}+(k^2-k_r^2)\right)\phi(r,z). \tag{2}$$

This equation is often referred to as the narrow-angle parabolic equation.[1,2] A more accurate wide-angle parabolic equation for atmospheric sound propagation was derived by Gilbert and White.[3] The wide-angle parabolic equation can be solved numerically, by a finite-difference extrapolation of the sound-pressure field in positive r direction, using an implicit Crank–Nicholson algorithm.[3,8] In this case, the computational method is referred to as the Crank–Nicholson PE method (CNPE method). The finite-difference range step in the CNPE method should not exceed about $\lambda/10$, where λ is the wavelength. At high frequency, the range step is small, and computing times of the CNPE method are large.

In the ''fast'' PE method, or Green's function PE (GFPE) method,[4,5] the extrapolation is based on an algorithm that is described in the following. The range step in the GFPE method may be much larger than a wavelength.

The derivation of the GFPE method by Gilbert and Di[4] is based on the spectral theorem of functional analysis. Here we present an alternate derivation that starts from the Rayleigh II integral[9,10] for the field $q(r,z)$ at point $(r_1=r_0+\Delta r,z_1)$ in terms of an integral over the vertical line at $r=r_0$:

$$q(r_1,z_1)=2\int_0^\infty\left(\frac{\partial g(r,z;r_1,z_1)}{\partial r}\,q(r,z)\right)_{r=r_0}dz, \tag{3}$$

which follows from the Kirchhoff–Helmholtz integral equation[11] (using an integration path that contains the line $r=r_0$ and that is closed at infinity). Here $g(r,z;r_1,z_1)$ is the Green's function at (r,z) due to a monopole at (r_1,z_1), and satisfies:

$$\left(\frac{\partial^2}{\partial r^2}+\frac{\partial^2}{\partial z^2}+k^2(z)\right)g(r,z;r_1,z_1)=-\delta(r-r_1)\,\delta(z-z_1). \tag{4}$$

As we assumed that the medium is independent of r, so that $k=k(z)$, we can write the Green's function as $g(\Delta r,z,z_1)$. We introduce the Fourier transform of the Green's function,

$$G(\kappa,z,z_1)=\int g(\Delta r,z,z_1)\exp(-i\kappa\Delta r)\,d(\Delta r).$$

Here the radial wave number κ is the Fourier variable conjugate to the range r. The inverse Fourier transform formula,

$$g(\Delta r,z,z_1)=(2\pi)^{-1}\int G(\kappa,z,z_1)\exp(i\kappa\Delta r)\,dk,$$

is now substituted in Eq. (3). This gives the following equation for extrapolation of the field $q(r,z)$ from r to $r+\Delta r$ (using the notation z for z_1 and z' for z):

$$q(r+\Delta r,z)=\frac{1}{\pi i}\int_{-\infty}^{\infty}\exp(i\kappa\Delta r)\,\kappa\,d\kappa \times\int_0^\infty G(\kappa,z,z')q(r,z')\,dz'. \tag{5}$$

The Green's function $G(\kappa,z,z')$ is the solution of the Fourier transformed version of the Helmholtz equation (4):

$$\left(\frac{\partial^2}{\partial z^2}+k^2(z)-\kappa^2\right)G(\kappa,z,z')=-\delta(z-z'). \tag{6}$$

Equation (5) can also be derived from the spectral theorem of functional analysis.[4] From Eq. (5), Gilbert and Di[4] derived the following equation for extrapolation of the field $\phi(r,z)$ from r to $r+\Delta r$:

$$\begin{aligned}\phi(r+\Delta r,z)=\exp\left(i\,\frac{\Delta r\,\delta k^2(z)}{2k_r}\right)&\\ \times\Bigg[\frac{1}{2\pi}\int_{-\infty}^{\infty}&[\Phi(r,k')+R(k')\Phi(r,-k')]\\ \times\exp(i\Delta r(\sqrt{k_r^2-k'^2}-k_r))\,&e^{ik'z}dk'\\ +2i\beta\Phi(r,\beta)&\\ \times\exp(i\Delta r(\sqrt{k_r^2-\beta^2}-k_r))\,&e^{-i\beta z}\Bigg],\end{aligned} \tag{7}$$

with

$$\Phi(r,k)=\int_0^\infty\exp(-ikz')\,\phi(r,z')\,dz' \tag{8}$$

the spatial Fourier transform of $\phi(r,z)$. These two equations are the basic equations of the GFPE method. In Eq. (7), Δr is the finite-difference range step, $R(k')=(k'Z_g-k_0)/(k'Z_g+k_0)$ the plane-wave reflection coefficient, with Z_g the normalized ground impedance and k_0 the wave number at zero height, and $\beta=k_0/Z_g$ is the surface-wave pole in the reflection coefficient. Further, $\delta k^2(z)$ is defined by

$$k^2(z)=k_r^2+\delta k^2(z). \tag{9}$$

Thus the squared wave number is split into a constant contribution k_r^2 and a contribution $\delta k^2(z)$ that varies with height. We use $k_r=k_0$ in this paper, unless indicated otherwise. It should be noted that range-dependent profiles $k^2(z)$ can be taken into account by changing the profile between successive range steps.[4]

The right-hand side of Eq. (7) is the product of an exponential refraction factor and the sum of three terms. The first term represents the direct sound wave, the second term represents the sound wave reflected by the ground, and the third term represents the surface wave. For a system without a ground surface, the second and the third term are absent. In this case, Eq. (7) can be derived directly from the narrow-

TABLE I. Values of the absorption parameter A. For intermediate frequencies, linear interpolation is applied.

f (Hz)	$\leqslant 16$	31.5	63	125	250	500	$\geqslant 1000$
A (m^{-1})	0.1	0.2	0.3	0.4	0.5	0.5	1.0

angle parabolic equation (2), and is known as the Fourier split-step algorithm for solving the narrow-angle parabolic equation. In other words, the GFPE method reduces to the Fourier split-step algorithm, for a system without a ground surface. The Fourier split-step algorithm has been widely used in ocean acoustics.[1,2] We conclude that the GFPE method yields a solution for the sound field that may be considered as a solution of the narrow-angle parabolic equation.

The accuracy of the Fourier split-step algorithm may be improved by replacing the exponential refraction factor given in Eq. (7) by the following factor:[1,4,12]

$$\exp(i\Delta r[k(z)-k_r]). \tag{10}$$

In the next section it will be shown that this replacement also slightly improves the accuracy of the GFPE method.

II. NUMERICAL IMPLEMENTATION

The GFPE method is based on a step-by-step extrapolation of a harmonic field $\phi(r,z)$ in the positive r direction, using Eqs. (7) and (8). A rectangular grid in the rz plane is used, with grid spacings Δr and Δz. We use $\Delta z=\lambda/10$, where λ is the wavelength of the field. The boundaries of the system are at the ground surface at $z=0$ and at the top at height $z_{\text{top}}=M\Delta z$, where M is an integer. To eliminate spurious reflections from the top surface, we use an absorption layer just below the top surface, between height z_{top} and height $z_{\text{abs}}=m\Delta z$, where m is an integer. For the absorption layer we use a thickness ranging from 50λ to 100λ, so that $M-m$ varies between 500 and 1000. Within the absorption layer, we add an imaginary part $A[(z-z_{\text{abs}})/(z_{\text{top}}-z_{\text{abs}})]^2$ to the wave number $k(z)$, with A a factor that varies with frequency between 0.1 and 1 (see Table I).[4] We use a Gaussian starting function $\phi(z)$ at range $r=0$ at the source:[1]

$$\phi(z)=\sqrt{k_r}\left(\exp\left[-\frac{k_r^2}{2}(z-z_s)^2\right]+\frac{Z_g-1}{Z_g+1}\exp\left[-\frac{k_r^2}{2}(z+z_s)^2\right]\right), \tag{11}$$

where z_s is the source height. The first term represents the direct field and the second term the field reflected by the ground.

The Fourier integrals in Eqs. (7) and (8) are approximated by discrete Fourier sums, which are efficiently evaluated by the fast Fourier transform (FFT) algorithm. We will consider two approaches for this approximation.

In the first approach, we discretize the height z and the wave number k [the two integration variables in Eqs. (7) and (8), omitting the primes for simplicity] as follows:

$$z_j=j\Delta z \quad \text{with} \quad j=0,1,\ldots,N-1 \tag{12}$$

and

$$k_n=n\Delta k \quad \text{with} \quad n=0,1,\ldots,N/2,-N/2+1,-N/2+2,\ldots,-1 \tag{13}$$

with $N=2M$, and $\Delta k=2\pi/(N\Delta z)$ the wave number spacing. The positive values of k are used for $\Phi(r,k)$ in Eq. (7), the negative values are used for $\Phi(r,-k)$. The Fourier integral (8) is approximated as follows:

$$\Phi(r,k_n)\approx\left[\sum_{j=0}^{N-1}\exp(-ik_nz_j)\phi(r,z_j)\right]\Delta z, \tag{14}$$

where the factor in rectangular brackets is the discrete Fourier transform of $\phi(r,z)$. This is the usual method for approximating a Fourier integral by a discrete Fourier sum.[13] For $\Phi(r,-k)$, Eq. (14) holds with k_n replaced by $-k_n$. The two functions $\Phi(r,k_n)$ and $\Phi(r,-k_n)$ for $n=0,1,\ldots,M-1$ are obtained from a single Fourier transform of size $N=2M$. For the function $\Phi(r,\beta)$ in Eq. (7), Eq. (14) is used with k_n replaced by β. The evaluation of $\Phi(r,\beta)$ requires a single summation of N terms. The extrapolation step is completed by the computation of $\phi(r+\Delta r,z_j)$ using Eq. (7). This requires an inverse Fourier transform of size N. For the inverse Fourier integral an approximation analogous to Eq. (14) is used. After each extrapolation step, $\phi(r,z_j)$ is set equal to zero for $j=M,\ M+1,\ldots,N-1$, in order to eliminate the coupling between the top surface and the ground surface introduced by the periodicity assumed by the Fourier transform. This can also be understood from the fact that the heights z_j with $j=M,\ M+1,\ldots,N-1$, correspond with negative heights (by the periodicity), and we need only positive heights since the lower limit of the integral (8) is $z=0$.

An alternate approach for computing the Fourier integrals is based on the ''midpoint rule'' for numerical integration.[14] This rule yields the following approximation for the Fourier integral (8):

$$\begin{aligned}\Phi(r,k_n)&\approx\left[\sum_{j=0}^{N-1}\exp(-ik_n[z_j+\Delta z/2])\phi(r,z_j+\Delta z/2)\right]\Delta z\\&=\left[\sum_{j=0}^{N-1}\exp(-ik_nz_j)\phi(r,z_j+\Delta z/2)\right]\\&\quad\times\exp(-ik_n\Delta z/2)\Delta z,\end{aligned} \tag{15}$$

where the factor in rectangular brackets is the discrete Fourier transform of $\phi(r,z+\Delta z/2)$. By means of numerical examples, it will be shown below that Eq. (15) yields more accurate results than Eq. (14) does. The accuracy of Eq. (15) originates from the choice of the z coordinates at the center of the integration intervals, i.e., halfway between neighboring grid points z_j and z_{j+1}. Thus Eq. (15) uses heights $0.5\Delta z,\ 1.5\Delta z,\ 2.5\Delta z,\ldots$, whereas Eq. (14) uses heights 0, $\Delta z,\ 2\Delta z,\ldots$. Therefore, the lower limit $z=0$ of the Fourier integral (8) is represented more accurately by Eq. (15) than by Eq. (14). For the inverse Fourier integral an approximation analogous to Eq. (15) is used. It should be noted that we found a similar improvement of the accuracy by using Simpson's rule of integration[14] instead of the midpoint rule. Gilbert and Di[15] reported an improvement of the accuracy by using the trapezoidal rule.[14] We found that the improvement with the trapezoidal rule is similar to the improvement with

TABLE II. Parameters of the four test cases. In all cases, the source height is 2 m and the receiver height is 2 m.

	Test case 1	Test case 2	Test case 3	Test case 4
atmosphere(1)	nonrefracting	nonrefracting	downward refracting	downward refracting
ground(2)	absorbing	reflecting	absorbing	reflecting

(1) nonrefracting atmosphere: c=constant
downward refracting atmosphere: logarithmic sound speed profile (16)

(2) reflecting ground: $Z_g=\infty$ at all frequencies
absorbing ground: $Z_g=51.94+51.73i$ at frequency 10 Hz
$Z_g=16.73+16.06i$ at frequency 100 Hz
$Z_g=6.336+4.229i$ at frequency 1000 Hz

the midpoint rule. The improved accuracy of all three integration rules (midpoint, Simpson and trapezoidal) originates from a more accurate representation of the lower limit $z=0$ of the Fourier integral (8).

Equation (15) shows that the improvement of the GFPE method requires only a shift of the grid point heights and the inclusion of an exponential phase factor at each range step. This causes a negligible increase of computing times.

III. TEST CASES

To study the accuracy of different implementations of the GFPE method, we consider the four test cases defined in Table II. For these four cases, we will compare numerical results of the transfer function as a function of horizontal range, up to ten kilometers, for three frequencies: 10, 100, and 1000 Hz. The transfer function is defined as the sound-pressure level relative to free field [this means that the level is corrected for the attenuation $20\lg(r)$ due to spherical spreading, and for the attenuation due to molecular absorption in the atmosphere].

In test case 1, the atmosphere is nonrefracting and the ground can be considered as representative for grassland. The ground impedances specified in Table II were computed with a four-parameter model of Attenborough,[16] using a flow resistivity of $300\ \mathrm{kPa\cdot s\cdot m^{-2}}$, a pore shape factor ratio of 0.75, a grain shape factor of 0.5, and a porosity of 0.3. In test case 2, the atmosphere is nonrefracting and the ground is reflecting (for example, a water surface can be considered as a reflecting surface). In test case 3, the same ground is used as in test case 1, and a downward refracting atmosphere is used with a logarithmic sound speed profile:

$$c(z)=c_0+b\ \ln\left(\frac{z}{z_0}+1\right) \tag{16}$$

with ground-level sound speed $c_0=343$ m/s, refraction velocity $b=1$ m/s, and ground roughness length $z_0=0.1$ m. This profile can be considered as a realistic profile for the atmosphere above open ground areas. In test case 4, a reflecting ground is used and the same sound speed profile as in test case 3.

We performed computations with the GFPE method and with the CNPE method, for the four test cases and the three frequencies. The CNPE results are used as a reference, for estimating the accuracy of GFPE results. Numerical parameters of the CNPE computations are given in Table III. For the test cases 1 and 2, with a nonrefracting atmosphere, we also have analytic solutions. The analytic solution for test case 2 follows directly from the fact that the sound field is the sum of two spherical fields, one originating at the source and the other originating at the image source. The analytic solution for test case 1 was computed with a well-known asymptotic expression for the sound field of a monopole source above a finite-impedance ground plane, valid in the limit of grazing incidence.[17] We used series expansions for the numerical evaluation of the complementary error function in this expression.

It should be noted that we also performed computations for the benchmark cases for outdoor sound propagation models, defined by Attenborough *et al.*[6] From these computations we reached similar conclusions as the conclusions given in the following.

IV. ANALYSIS OF NUMERICAL ERRORS

In this section we analyze numerical errors in GFPE results for the test cases defined in the preceding section. We distinguish four types of errors:

(1) errors in the forward Fourier transform, Eq. (8);
(2) errors in the inverse Fourier transform in Eq. (7);
(3) errors in the exponential refraction factor;
(4) errors caused by the split-step approximation.

Figure 1 demonstrates errors in the forward Fourier transform, for test cases 1 and 2, at frequency 100 Hz. The figure shows GFPE results computed with the standard Fourier

TABLE III. Numerical parameters of the CNPE computations.

Frequency f (Hz)	Grid spacing $\Delta r,\Delta z$(m)	System height M in grid spacings	Thickness M-m of absorption layer, in grid spacings	Sample range r (m)
10	2	4000	1000	10,20, . . . ,10 000
100	0.33	4000	1000	10,20, . . . ,10 000
1000	0.033	8000	1000	10,20, . . . ,5000

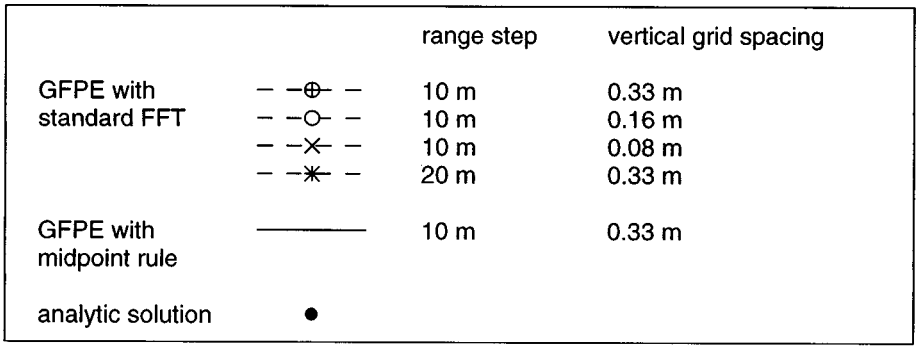

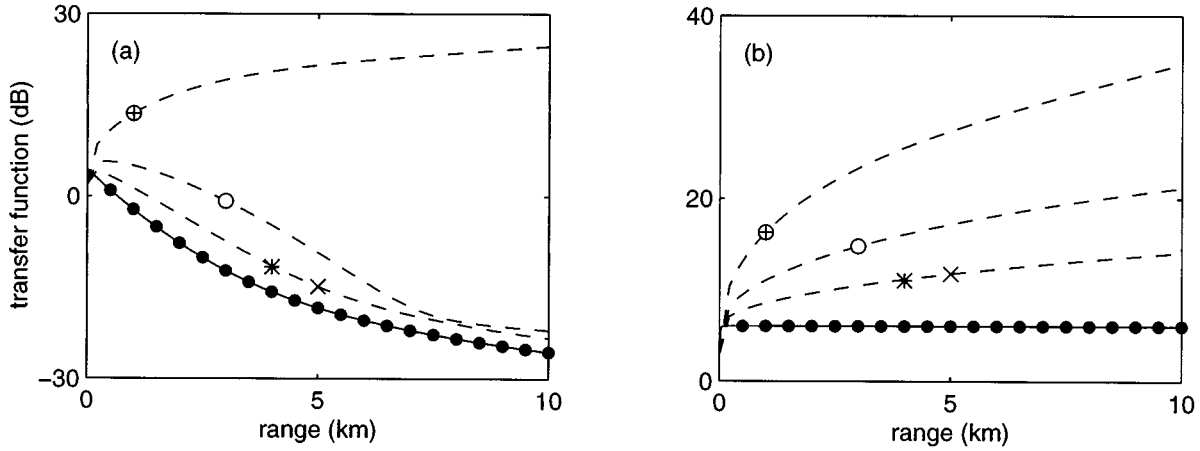

FIG. 1. The transfer function as a function of range, computed with the standard Fourier transform and with the improved Fourier transform based on the midpoint rule, at frequency 100 Hz, for test case 1 (a) and test case 2 (b).

transform [Eq. (14)], GFPE results computed with the improved Fourier transform [Eq. (15)] based on the midpoint integration rule, and analytic results. Results of the improved GFPE method are in excellent agreement with the analytic solution (and also with CNPE results, not shown here), with errors less than 0.1 dB. Results of the standard GFPE method deviate considerably, with errors up to 50 dB at a range of 10 km. We found similar results for the frequencies 10 and 1000 Hz, and also for the test cases 3 and 4 (although the errors for the cases 1 and 3 at 1000 Hz are smaller than for the other cases and frequencies). The figure shows that the error decreases with decreasing vertical grid spacing and with *increasing* range step. The figure shows also that the error is reduced by the same amount upon doubling the range step or decreasing the vertical grid spacing by a factor of 4. This is explained in the following.

The main difference between the standard Fourier transform (14) and the improved Fourier transform (15) is the factor $\exp(-ik_n\Delta z/2)$. The difference between $\phi(r,z)$ and $\phi(r,z+\Delta z/2)$ is negligible, as $\phi(r,z)$ is a smooth function of height. The factor $\exp(-ik_n\Delta z/2)$ causes a phase shift of all the elements $\Phi(r,k_n)$. However, the inverse Fourier transform in Eq. (7), and hence the function $\phi(r,z)$, is determined only by the elements with wave number k_n near the point of stationary phase. This is illustrated in Fig. 2. The graphs in this figure show the summand of the inverse Fourier transform and the cumulative sum, after a single range step of 100 m, for frequency 100 Hz, $M=16\,384$, a nonrefracting atmosphere, a reflecting ground, and a receiver height of 12 m. The summand is (with $\beta=0$):

$$S(k_n)=\frac{\Delta k}{2\pi}\left(\Phi(r,k_n)+R(k)\Phi(r,-k_n)\right)\times\exp(i\Delta r(\sqrt{k_r^2-k_n^2}-k_r))\exp(ik_nz) \tag{17}$$

and the cumulative sum is

$$C(k_n)=\sum_{m=0}^{n}S(k_m), \tag{18}$$

where the index m runs from $m=0$ to $m=n$ in the order indicated in Eq. (13). The complete sum is $\phi=C(k_N)$, as illustrated by the open circles in the lower four graphs in Fig. 2.

The upper two graphs in Fig. 2 show that the summand oscillates rapidly for $k_n\uparrow k_r$ and $k_n\downarrow -k_r$ ($k_r=\omega/c=1.85\,\mathrm{m}^{-1}$ at frequency 100 Hz), while the evanescent waves for $|k_n|>k_r$ have virtually zero amplitude in this case. The discrete sampling of the rapidly oscillating summand causes errors in the cumulative sum, i.e., in the inverse Fourier transform. To eliminate these errors, we multiply the summand by the following window function:

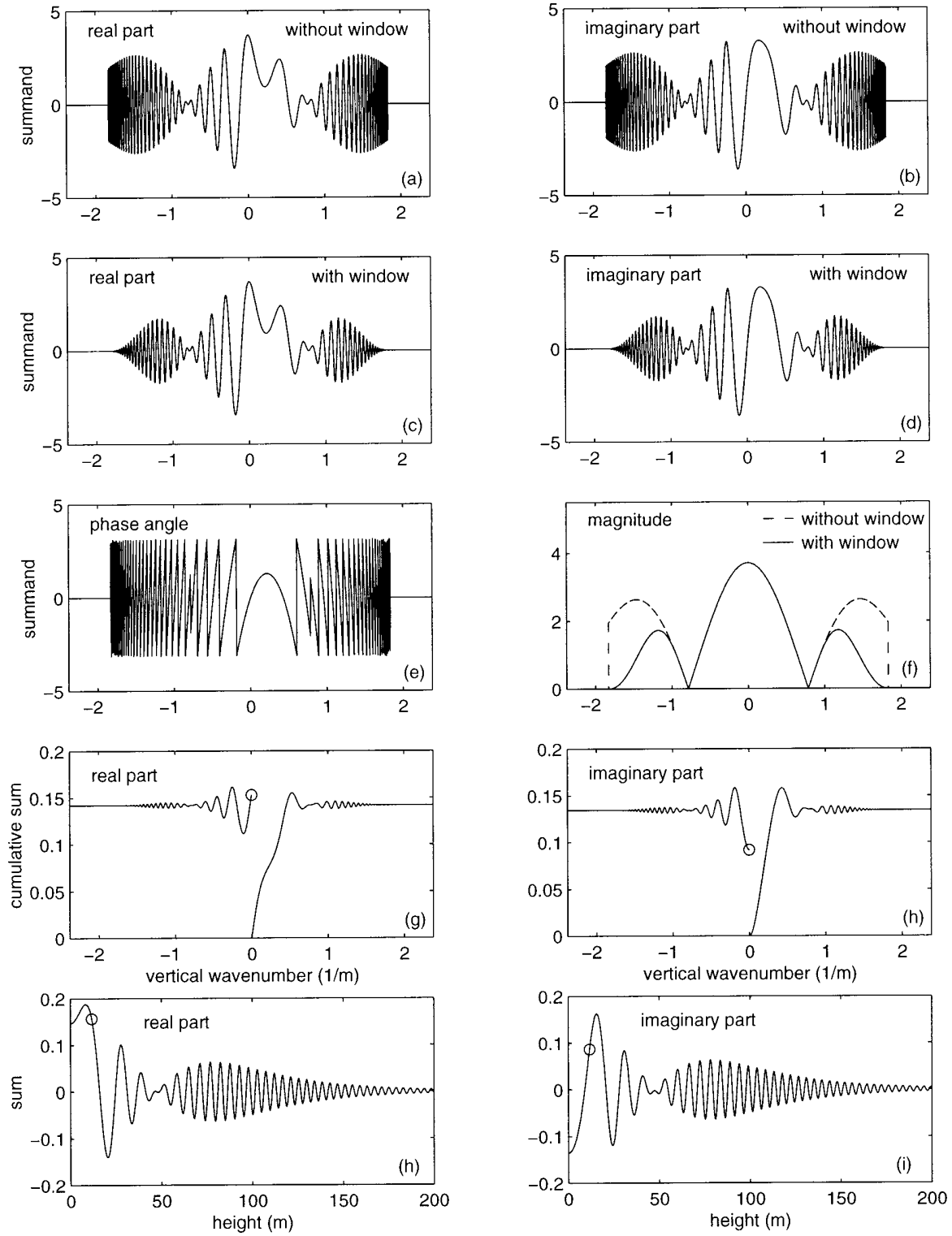

FIG. 2. Summand of the inverse Fourier transform and cumulative sum [(a)–(h)] after a single range step of 100 m, for frequency 100 Hz, $M=16\,384$, nonrefracting atmosphere, reflecting ground, and receiver height 12 m. The lower two graphs [(h) and (i)] show the real and imaginary part of the sum $\phi(z)$ after the first range step.

$$w(k)=\begin{cases} 1, & \text{for } |k|<0.5\,k_r, \\ \cos^2\left(\dfrac{\pi}{2}\dfrac{|k|-0.5\,k_r}{0.5\,k_r}\right), & \text{for } 0.5\,k_r\leqslant|k|\leqslant k_r, \\ 0 & \text{for } |k|>k_r. \end{cases} \tag{19}$$

As the sum is dominated by the wave numbers near the point of stationary phase (this can be seen by comparing the graphs in Fig. 2 for the phase angle of the summand and the cumulative sum), the window function does not affect the sum as long as the stationary phase point is not near the region where $w(k)<1$. In this case, the window function merely suppresses numerical errors caused by the discrete sampling of the rapidly oscillating summand (an example of these errors will be given below). The window function may be considered as a numerical filter in k space.

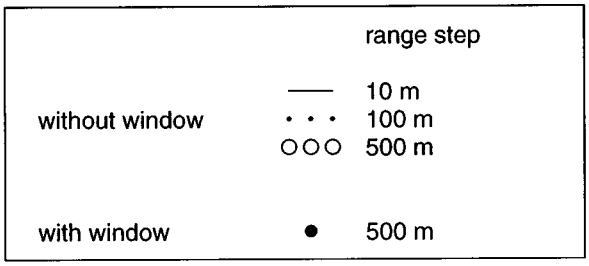

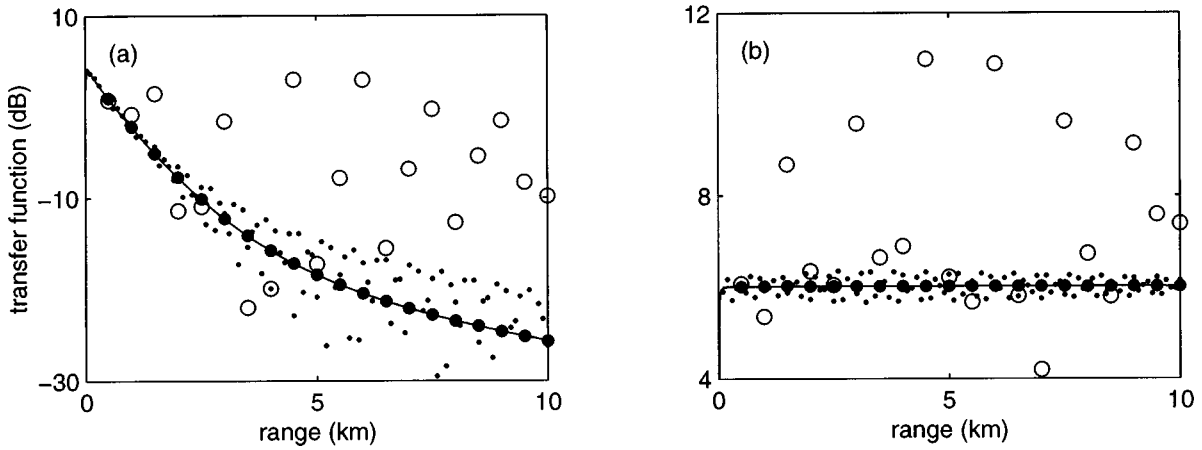

FIG. 3. The transfer function as a function of range, computed with and without a window in the inverse Fourier integral, at frequency 100 Hz, for test case 1 (a) and test case 2 (b).

The location of the point of stationary phase can be obtained from the variation of the phase Ψ of the summand $S(k)$:

$$\frac{d\Psi(k)}{dk} = \frac{d}{dk}\,(\Delta r(\sqrt{k_r^2 - k^2} - k_r) + kz), \tag{20}$$

where we have neglected the slow variation of the function $\Phi(r,k)$ with k. From $d\Psi/dk = 0$ we find that the point of stationary phase occurs at wave number:

$$k = \frac{z}{\sqrt{z^2 + \Delta r^2}}\, k_r\,. \tag{21}$$

In the example shown in Fig. 2, we have $z = 12$ m and $\Delta r = 100$ m, so that the point of stationary phase is located at $k = 0.18\ \mathrm{m}^{-1}$, in agreement with the graph of the phase of the summand.

We return to the error in the standard Fourier transform (14). As explained before, this error can be considered as originating from a spurious factor $\exp(-ik_n \Delta z/2)$ in the function $\Phi(r,k_n)$, at every range step. We can estimate how the error varies with the range step Δr and the vertical grid spacing Δz. From Eq. (21) we find that we can set $k_n \approx z k_r/\Delta r$ in the factor $\exp(-ik_n \Delta z/2)$, for $z \ll \Delta r$. So the phase shift introduced by the spurious factor is proportional to Δz and inversely proportional to Δr. The number of range steps is also inversely proportional to Δr. Therefore, the error is proportional to Δz and inversely proportional to $(\Delta r)^2$. This explains the variation with Δz and Δr of the GFPE results computed with the standard Fourier transform, shown in Fig. 1. We conclude that the error in standard GFPE results can be reduced by choosing a smaller vertical grid spacing or a larger range step. The errors are reduced more efficiently, however, by using the improved Fourier transform (15). For all results presented in the following we used the improved Fourier transform.

While the errors described in the foregoing occur for small range steps (typically a few wavelengths), there is a second type of errors that occur in the inverse Fourier transform, for large range steps (typically a hundred wavelengths). These errors originate from the discrete sampling of the rapidly oscillating summand of the inverse Fourier transform, as mentioned before (see Fig. 2). The ''frequency'' of the oscillations increases with increasing range step, so that the errors in the inverse Fourier transform also increase with increasing range step. As was explained in the foregoing, the errors can be eliminated by using the window function (19) in the inverse Fourier transform. Figure 3 shows an example of this elimination of errors, for frequency 100 Hz. When the window function is used, the GFPE method is accurate for a range step as large as at least 500 m at frequency 100 Hz, for a nonrefracting atmosphere.

It should be noted that one should be careful in using the window function. The window function may be different from $w = 1$ only for wave numbers where the cumulative inverse Fourier sum oscillates around a constant value (this is not the case at low frequency).

Next we consider the test cases 3 and 4, with a downward refracting atmosphere. The accuracy of GFPE results

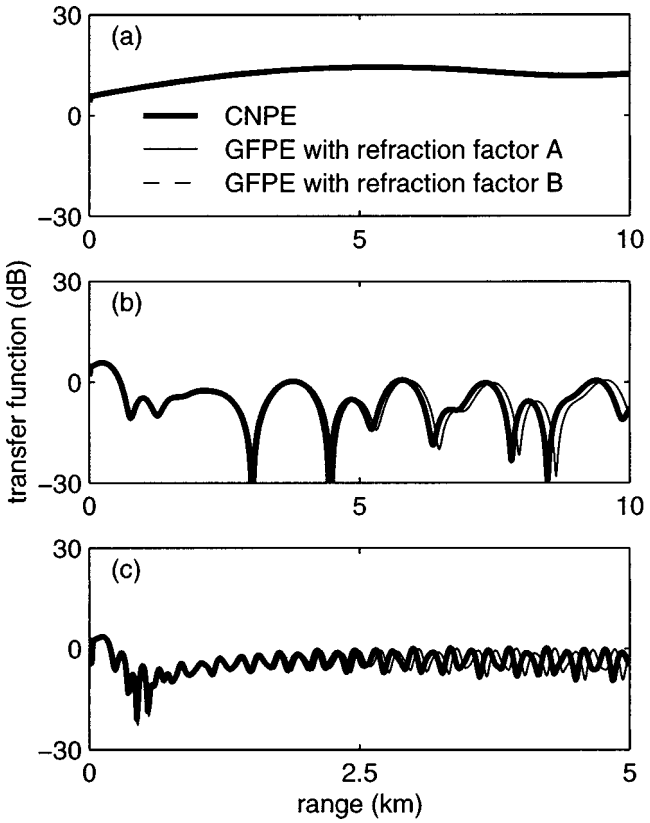

FIG. 4. The transfer function as a function of range, computed with refraction factor A [Eq. (7)] and with refraction factor B [Eq. (10)], for test case 3, at three frequencies: 10 Hz (a), 100 Hz (b), and 1000 Hz (c). The dashed curves are indistinguishable from the CNPE curves.

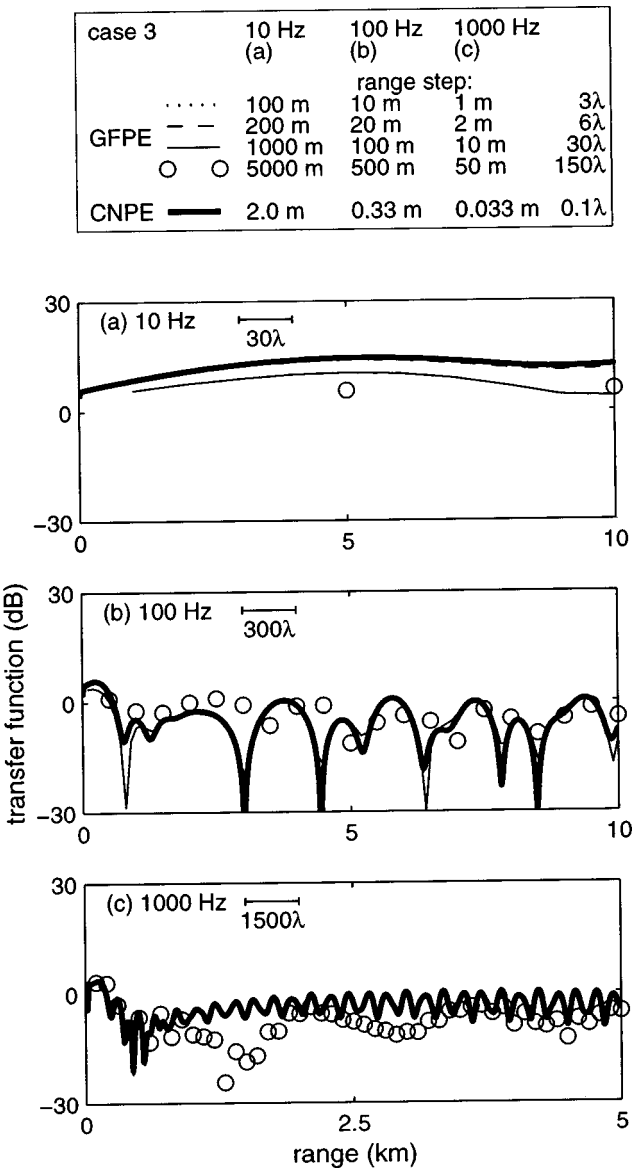

FIG. 5. The transfer function as a function of range, computed with different range steps, for test case 3, at three frequencies: 10 Hz (a), 100 Hz (b), and 1000 Hz (c). The dotted and dashed curves are indistinguishable from the CNPE curves (except at 10 Hz).

for these cases will be determined by comparison with CNPE results. Figure 4 demonstrates that the accuracy of GFPE results for case 3 is improved by using the refraction factor (10) instead of the factor given in Eq. (7). For case 4 we also found that the refraction factor (10) gives a better agreement with CNPE results. It should be noted that the CNPE method yields a solution of the wide-angle parabolic equation, which is more accurate than the low-angle parabolic equation solved by the GFPE method. Therefore, CNPE results may be considered as a reference for the refraction factor used in the GFPE method. Figure 4 shows that the interference pattern is slightly shifted when the refraction factor (A) given in Eq. (7) is used. It should be noted, however, that slight phase errors have no physical meaning at long range, as atmospheric fluctuations always cause additional phase shifts. Nevertheless, the refraction factor (10) is used in the following. It should also be noted that Gilbert and Di[4] obtained no improvement by using the refraction factor (10), for test cases with linear sound speed profiles with gradients of $0.1\ \mathrm{s}^{-1}$. Finally we mention that the phase errors shown in Fig. 4 can also be reduced by using a different reference wave number k_r. In the foregoing we used $k_r = k_0$, but if we use $k_r = \omega/c_{10}$ with c_{10} the sound speed at a height of ten meters, then the shift of the interference pattern observed in Fig. 4 is reduced by a factor of about 4 [using the refraction factor given in Eq. (7)].

Figures 5 and 6 demonstrate the errors caused by the split-step approximation. The split-step approximation assumes that the computation of the propagation over a single range step can be split into two steps:

(i) computation of the propagation in a nonrefracting atmosphere,
(ii) multiplication of the result of step (i) by an exponential refraction factor.

The error caused by this approximation increases with increasing range step. Figure 5 shows that in case 3 the errors are unacceptably large for a range step of 150λ at frequencies 100 and 1000 Hz, and at frequency 10 Hz already for a range step of 30λ. Figure 6 shows that in case 4 the errors are unacceptably large for a range step of 30λ for all three frequencies. From the figures we conclude that the maximum acceptable range step varies roughly between 5λ and 50λ, for the cases 3 and 4.

The maximum acceptable range step is larger for case 3

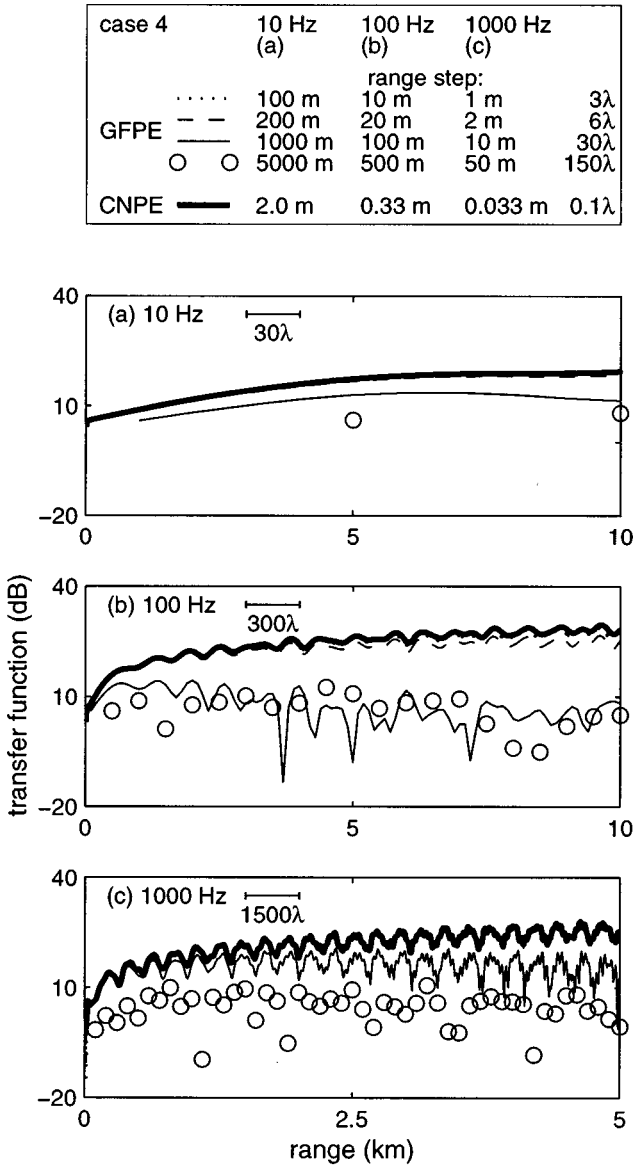

FIG. 6. The transfer function as a function of range, computed with different range steps, for test case 4, at three frequencies: 10 Hz (a), 100 Hz (b), and 1000 Hz (c). The dotted curves and the dashed curve for 1000 Hz are indistinguishable from the CNPE curves.

than for case 4. The reason for this difference is not clear. DiNapoli and Deavenport[2] give an analytic expression for the split-step error. This expression shows that the split-step error increases with increasing vertical sound speed gradient, as expected. This suggests that the large gradients of the logarithmic profile near the ground may be responsible for the split-step errors observed in the cases 3 and 4. The gradient of the logarithmic profile is $\alpha = dc/dz = b/(z+z_0)$, so that $\alpha = b/z_0 = 10\ \mathrm{s}^{-1}$ near the ground. To investigate whether the observed split-step errors originate from large gradients near the ground, we performed computations for a linearized profile for $z < 10$ m:

$$c(z) = \begin{cases} c_0 + \alpha z, & \text{for } z < z_1, \\ c_0 + b\ \ln(z/z_0 + 1), & \text{for } z \geqslant z_1, \end{cases} \tag{22}$$

with $z_1 = 10$ m and $\alpha = 0.46\ \mathrm{s}^{-1}$. We found no significant reduction of the split-step errors for frequency 100 Hz, but we found reduced errors for range step $\Delta r = 50$ m for frequency 1000 Hz. We also performed computations for a linearized profile for $z < 100$ m, given by Eq. (22) with $z_1 = 100$ m and $\alpha = 0.07\ \mathrm{s}^{-1}$. For this profile we found for test case 3 reduced errors for $\Delta r = 500$ m for frequency 100 Hz, and negligible errors for $\Delta r = 50$ m for frequency 1000 Hz. These results indicate that the split-step errors decrease with decreasing average gradient, as expected, and that the split-step errors observed for the cases 3 and 4 originate partly from the large gradients near the ground. It should be emphasized that large gradients do occur in practice. The logarithmic sound speed profile (16) with $b = 1$ m/s is a realistic profile.

V. OPTIMIZATION OF NUMERICAL PARAMETERS

As mentioned in the introduction of this paper, the GFPE method may be considerably faster than the CNPE method. To obtain a maximum computational speed of the GFPE method, numerical GFPE parameters should be optimized. The parameters that determine the computational speed of the GFPE method are the range step Δr and the system height (or the number M of grid points along the z axis).

The range step was considered in the preceding section. It was found that the maximum acceptable range step varies roughly between 5λ and 50λ, for cases 3 and 4. For cases 1 and 2, with a nonrefracting atmosphere, a larger range step can be used.

Next we consider the system height M. The analysis given below applies to the GFPE method, but it should be noted that the results are expected to apply to the CNPE method as well. We performed GFPE computations for $M = 4096$, 2048, and 1024 for frequencies 10 and 100 Hz, and $M = 8192$, 4096, and 2048 for frequency 1000 Hz. We used an absorption layer with a thickness of $M - m = 1000$, 500, and 500 for the three values of M, respectively. We used a range step of $\Delta r = 3\lambda$. The results are shown in Figs. 7–10 for cases 1–4, respectively.

For cases 1–3, the figures show that the maximum range where GFPE results are accurate decreases with decreasing system height, except at frequency 10 Hz where the results are accurate up to 10 km for all three system heights. In case 4, there is hardly any effect of the system height.

To analyze this, we define $\eta \equiv m\Delta z/\lambda = m/10$ as the system height expressed in wavelengths (not including the absorption layer at the top of the system), and $\rho \equiv r/\lambda$ as the range expressed in wavelengths. We define $\rho_{\max}$ as the minimum value of ρ where deviations occur, say, larger than 1 dB. For cases 1 and 3 (Figs. 7 and 9), we find that $\rho_{\max}$ is about equal to 20η to 25η (this holds also for frequency 10 Hz, where we found for $\eta = 50$ that deviations occur for $r \geqslant 30$ km, so that $\rho_{\max} \approx 1000$). For case 2 (Fig. 8) we also find $\rho_{\max} \approx 20\eta$ for frequency 100 Hz, but for frequency 1000 Hz we find $\rho_{\max} \approx 60\eta$ for $\eta = 150$. We conclude that for cases 1 to 3 $\rho_{\max}$ varies between 20η and 60η.

The effect of the system height can also be analyzed in a different way. In cases 3 and 4, with a downward refracting atmosphere, sound rays are curved toward the ground. The maximum height of the highest ray between a source and a

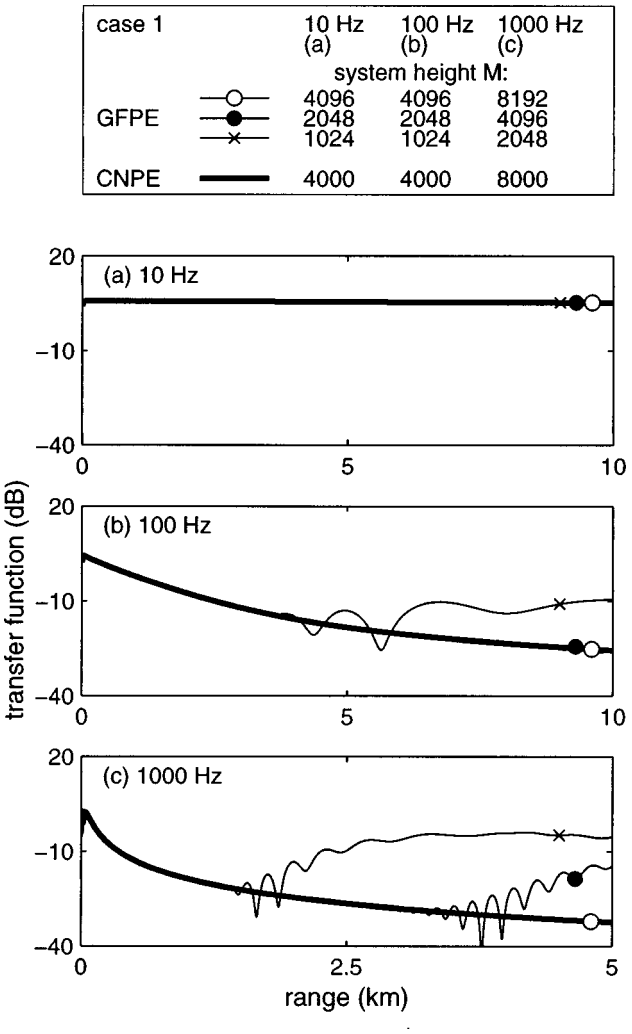

FIG. 7. The transfer function as a function of range, computed with different values of M (indicated in the legend), for test case 1, at three frequencies: 10 Hz (a), 100 Hz (b), and 1000 Hz (c).

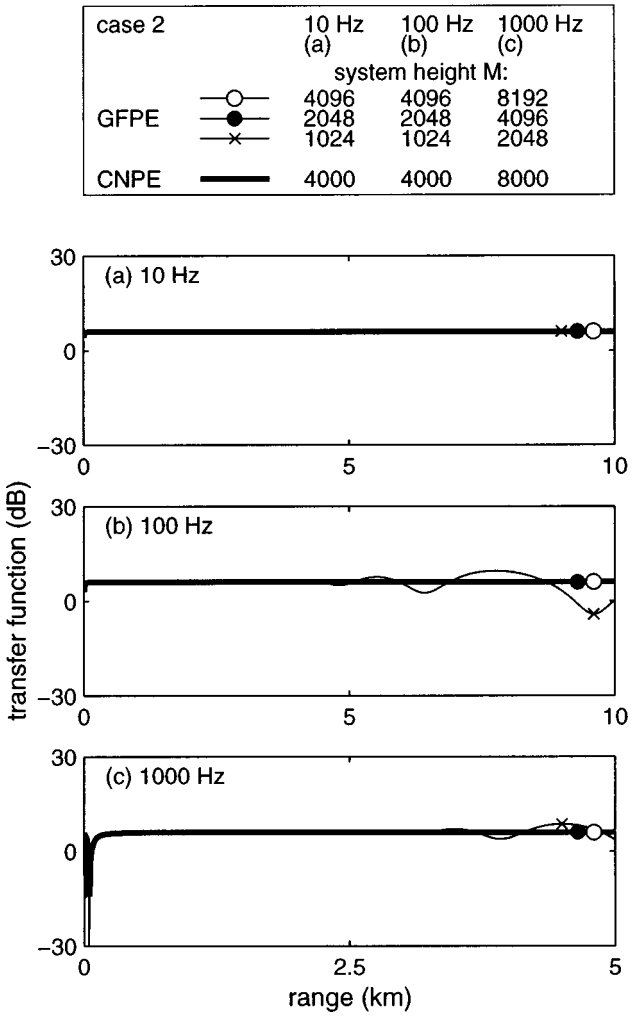

FIG. 8. The transfer function as a function of range, computed with different values of M (indicated in the legend), for test case 2, at three frequencies: 10 Hz (a), 100 Hz (b), and 1000 Hz (c).

receiver close to the ground is, for the logarithmic profile, given by:[18]

$$z_{\max} = r\sqrt{\frac{b}{2\pi c_0}}. \tag{23}$$

For $b=1$ m/s we get $z_{\max}\approx 0.02r$. For example, for frequency 1000 Hz and $m=1500$ the system height is $m\Delta z = 50$ m, so that the highest sound ray crosses the absorption layer for $r>2500$ m. Indeed, the transfer function shows a clear decrease at $r=2500$ m for test case 3 [see Fig. 9(c)]. For test case 4, however, no effect is visible at $r=2500$ m (see Fig. 10). This difference between case 3 and case 4 can be explained as follows. In case 3, with an absorbing ground surface, most of the acoustical energy is carried by the highest sound rays, as these rays have the smallest number of ground reflections (a ray loses energy at each ground reflection).[18] In this case, if the highest rays cross the absorption layer, the received sound pressure decreases. In case 4, however, with a reflecting ground surface, all rays between the source and the receiver carry an approximately equal amount of acoustical energy (neglecting focussing effects).[18] The number of rays that arrive at a distant receiver (at a height of 2 m) is of the order of 10^2 for ranges of the order of a few kilometers. In this case, if a few of the highest rays cross the absorption layer, there is only a small change in the received sound pressure.

The foregoing may be used as a guideline for the optimum choice of numerical GFPE parameters. The optimized values of the parameters were obtained from computations for the necessarily limited set of geometrical configurations and atmospheric and ground conditions considered here. The optimized values may be different for other geometries and conditions. For practical applications, it is therefore advisable to perform a few control computations. A simple method to check the accuracy of a GFPE computation performed with system height M and range step Δr, is to perform a second computation with system height $2M$ and range step $\Delta r/2$. Figure 11 shows an example of these control computations. Shown is a spectrum of the transfer function for test case 3, with a source–receiver distance of 1 km. The curve represents GFPE computations using $\Delta r = 6\lambda(1+f/f_0)$ with $f_0=500$ Hz, $M=1024$ for $10<f<100$ Hz, $M=2048$ for $100<f<1000$ Hz, $M=4096$ for $1000<f<3000$ Hz, and $M-m=500$. For the spectrum, 300 logarithmically spaced frequencies were used. The dots in the

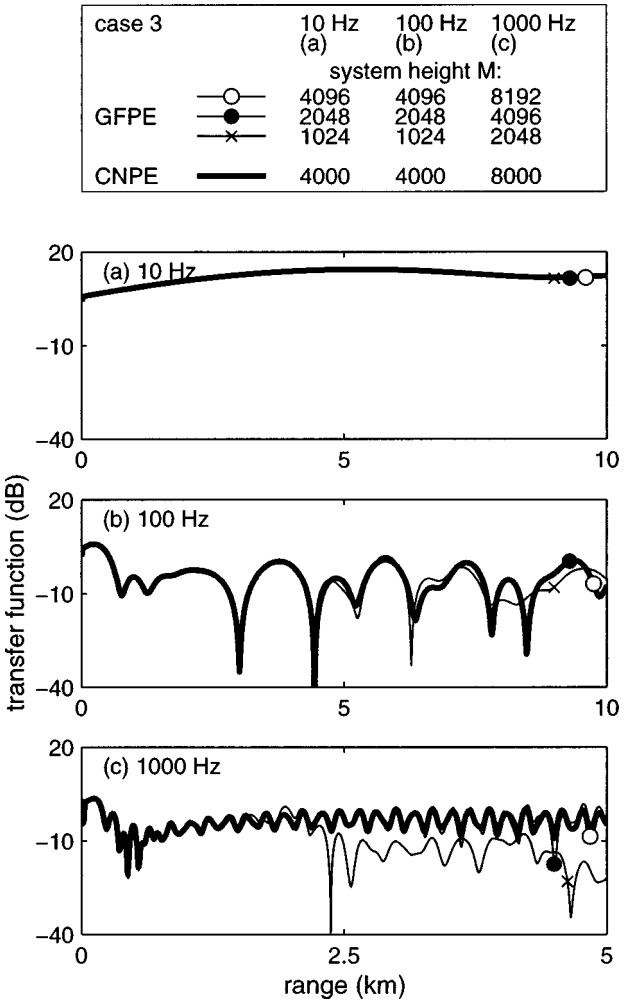

FIG. 9. The transfer function as a function of range, computed with different values of M (indicated in the legend), for test case 3, at three frequencies: 10 Hz (a), 100 Hz (b), and 1000 Hz (c).

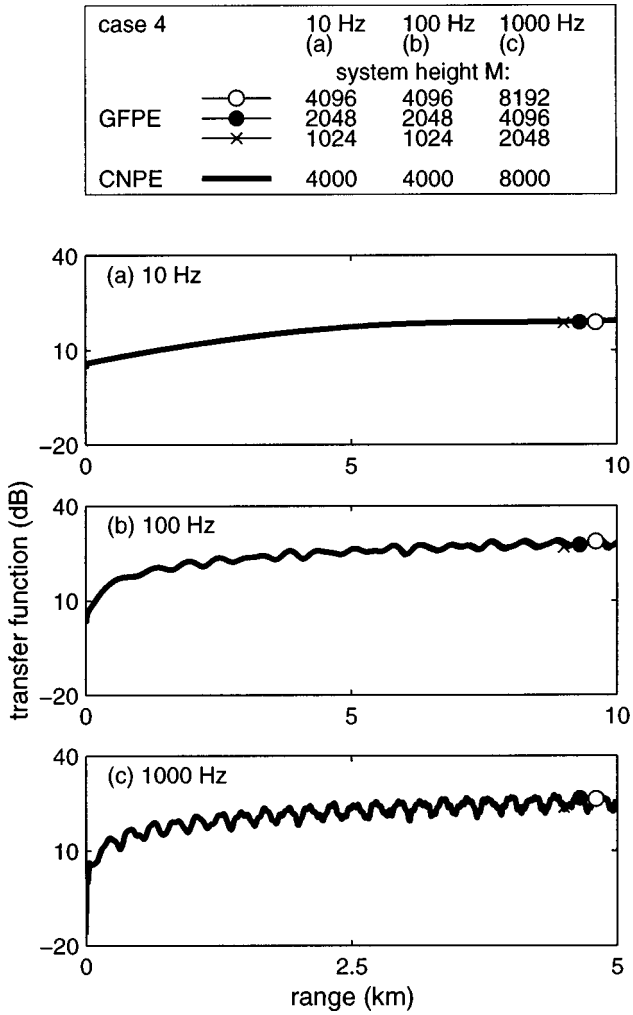

FIG. 10. The transfer function as a function of range, computed with different values of M (indicated in the legend), for test case 4, at three frequencies: 10 Hz (a), 100 Hz (b), and 1000 Hz (c).

figure represent control computations for system height $2M$ and range step $\Delta r/2$, at 50 logarithmically spaced frequencies. The dots are in good agreement with the curve, although above 1000 Hz some deviations occur near the interference dips.

VI. COMPUTING TIMES

The CPU time of a numerical computation is approximately proportional to the number of floating point operations (flop's). A complex addition requires two flop's, a complex multiplication requires six flop's, and a complex FFT of size N requires $5N \log_2 N$ flop's. A GFPE step requires two complex FFT's and about $10N$ complex multiplications, or $60N+10N \log_2 N$ flop's. A GFPE computation consists of $r/\Delta r$ steps, so that the computing time is, with $N=2M$:

$$t_{\mathrm{GFPE}}=\frac{r}{\Delta r}\,\tau[120M+20M\,\log_2(2M)], \tag{24}$$

where τ is the average CPU time per flop. If we use $\Delta r = 6\lambda = 6c_0/f$, the computing time is proportional to the frequency. For example, for $\tau=0.1$ μs, $r=1$ km, and $M=2048$, we get $t_{\mathrm{GFPE}}=\gamma f$, with $\gamma=4\times10^{-2}$ s^2. For a complete spectrum with n logarithmically spaced frequencies per

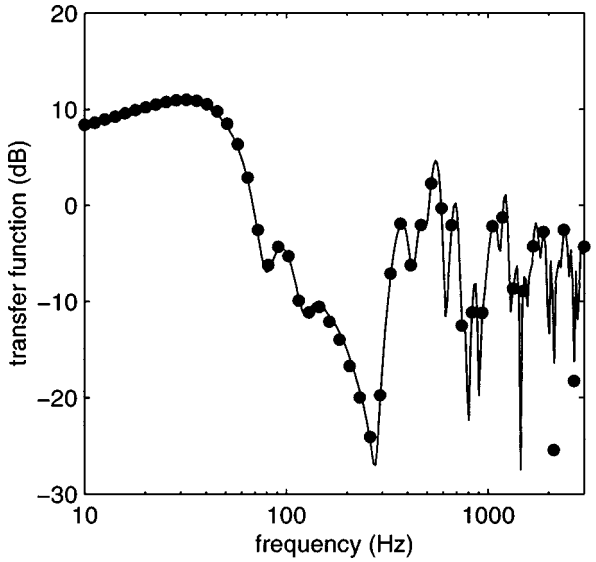

FIG. 11. Spectrum of the transfer function for test case 3 with range $r=1$ km. The curve represents GFPE computations with frequency-dependent system height M and range step Δr (see the text). The dots represent GFPE computations with system height $2M$ and range step $\Delta r/2$.

decade, between frequencies f_1 and f_2, we get a computing time

$$T_{\mathrm{GFPE}}=\gamma\int_{\lg f_1}^{\lg f_2} nfd(\lg f)=\gamma\,\lg(e)n(f_2-f_1). \tag{25}$$

For a spectrum with 300 frequencies between $f_1=10$ Hz, and $f_2=3000$ Hz, $r=1$ km, and $M=2048$, the computing time is about 2 h. The computing time is approximately proportional to the upper frequency f_2, so that the upper frequency should be chosen as low as possible. If one uses $\Delta r=6\lambda(1+f/f_0)$ instead of $\Delta r=6\lambda$, the computing time may be considerably reduced.

Finally we compare the GFPE computing time with the computing time of the CNPE method. A CNPE step requires the inversion of an $M\times M$ tridiagonal complex matrix. We use an efficient algorithm for this inversion (based on the algorithm given on page 40 of Ref. 14). With this algorithm, a CNPE step requires $5M$ complex multiplications and $4M$ complex additions, or $38M$ flop's. The CPU time of a CNPE computation is:

$$t_{\mathrm{CNPE}}=\frac{r}{\Delta r}\,\tau 38M, \tag{26}$$

where $\Delta r=\lambda/10$ is the CNPE range step. The ratio of the CPU times of the CNPE method and the GFPE method is then:

$$\frac{t_{\mathrm{CNPE}}}{t_{\mathrm{GFPE}}}=\frac{\Delta r_{\mathrm{GFPE}}}{\Delta r_{\mathrm{CNPE}}}\,\frac{38}{120+20\log_2(2M)}, \tag{27}$$

where Δr_{GFPE} is the GFPE range step and Δr_{CNPE} is the CNPE range step. We assumed here that the average CPU time per flop is equal for the two methods (in fact, we find that this time is two times larger for GFPE than for CNPE, on our computer). As M is in the range 1024 to 8192, we obtain $(t_{\mathrm{CNPE}}/t_{\mathrm{GFPE}})\approx(\Delta r_{\mathrm{GFPE}}/\Delta r_{\mathrm{CNPE}})/10$. For the test cases 3 and 4 we found that the maximum acceptable GFPE range step Δr_{GFPE} varies roughly between 5λ and 50λ, so that with $\Delta r_{\mathrm{CNPE}}=\lambda/10$ we find that the speed-up factor $(t_{\mathrm{CNPE}}/t_{\mathrm{GFPE}})$ varies roughly between 5 and 50. For atmospheres with smaller sound speed gradients than in the cases 3 and 4, larger speed-up factors are possible.

It should be noted that the speed-up factors of the order of 100 reported by Gilbert and Di[4] were relative to a finite-element CNPE method, whereas here we used a finite-difference CNPE method. The finite-difference CNPE method is a factor of 2 to 3 faster than the finite-element CNPE method.

VII. CONCLUSIONS

An improved implementation of the GFPE method for atmospheric sound propagation has been presented. The improvement is based on the use of the midpoint rule of numerical integration for evaluating the Fourier integrals in the GFPE method. For a few realistic test cases, the improved accuracy obtained with the midpoint rule has been demonstrated. In some cases, use of the midpoint rule reduced the errors from about 50 dB to less than 0.1 dB. In general, the error reduction and the errors themselves depend strongly on the sound speed profile and the ground impedance.

The errors in the standard GFPE method originate from phase errors introduced by the standard approximation of the Fourier integrals by discrete Fourier sums. The improvement of the GFPE method requires only a shift of the grid point heights and the inclusion of an exponential phase factor at each range step. This causes a negligible increase of computing times.

Further, optimized values have been presented for numerical GFPE parameters. Finally, computing times of the GFPE method and the CNPE method have been compared. It has been found that the GFPE method is faster than the CNPE method, by a factor that varies between 5 and 50 for the test cases considered in this paper.

ACKNOWLEDGMENTS

The author is grateful to K.E. Gilbert and X. Di for many helpful suggestions and valuable comments on this paper. The author is grateful to C.P.A. Wapenaar and N.A. Kinneging for interesting discussions.

[1] F. D. Tappert, ''The parabolic approximation method,'' in *Wave Propagation and Underwater Acoustics*, edited by J. B. Keller and J. S. Papadakis (Springer-Verlag, Berlin, 1977), Chap. V, pp. 224–287.
[2] F. R. DiNapoli and R. L. Deavenport, ''Numerical models of underwater acoustic propagation,'' in *Ocean Acoustics*, edited by J. A. DeSanto (Springer-Verlag, Berlin, 1979), Chap. 3, pp. 79–156.
[3] K. E. Gilbert and M. J. White, ''Application of the parabolic equation to sound propagation in a refracting atmosphere,'' J. Acoust. Soc. Am. **85**, 630–637 (1989).
[4] K. E. Gilbert and X. Di, ''A fast Green's function method for one-way sound propagation in the atmosphere,'' J. Acoust. Soc. Am. **94**, 2343–2352 (1993).
[5] X. Di and K. E. Gilbert, in *Proceedings of the Fifth International Symposium on Long Range Sound Propagation*, 24–26 May 1992, Milton Keynes, England, pp. 128–146.
[6] K. Attenborough *et al.*, ''Benchmark cases for outdoor sound propagation models,'' J. Acoust. Soc. Am. **97**, 173–191 (1995).
[7] K. E. Gilbert and M. J. White, in *Proceedings of the Third International Symposium on Long Range Sound Propagation and Coupling into the Ground*, 28–30 March 1988, Jackson, Mississippi, pp. 218–242.
[8] M. West, K. Gilbert, and R. A. Sack, ''A tutorial on the parabolic equation (PE) model used for long range sound propagation in the atmosphere,'' Appl. Acoust. **37**, 31–49 (1992).
[9] A. J. Berkhout, *Applied Seismic Wave Theory*, Advances in Exploration Geophysics, Vol. 1 (Elsevier, Amsterdam, 1987), pp. 231–277.
[10] C. P. A. Wapenaar and A. J. Berkhout, *Applied Seismic Wave Theory*, Advances in Exploration Geophysics, Vol. 2 (Elsevier, Amsterdam, 1989), pp. 159–199.
[11] A. D. Pierce, *Acoustics. An Introduction to its Physical Principles and Applications* (American Institute of Physics, New York, 1991).
[12] D. J. Thompson and N. R. Chapman, ''A wide-angle split-step algorithm for the parabolic equation,'' J. Acoust. Soc. Am. **74**, 1848–1854 (1983).
[13] D. C. Champeney, *Fourier Transforms in Physics* (Adam Hilger, Bristol, 1985).
[14] W. H. Press, B. P. Flannery, S. A. Teukolsky, and W. T. Vetterling, *Numerical Recipes. The Art of Scientific Computing* (Cambridge U.P., Cambridge, 1986).
[15] K. E. Gilbert and X. Di, private communication.
[16] K. Attenborough, ''Acoustical impedance models for outdoor ground surfaces,'' J. Sound Vib. **99**, 521–544 (1985). We use Eqs. (11) and (12) of this paper.
[17] K. Attenborough, S. I. Hayek, and J. M. Lawther, ''Propagation of sound above a porous half-space,'' J. Acoust. Soc. Am. **68**, 1493–1501 (1980). Some typographical errors in this paper were reported by K. B. Rasmussen, J. Sound Vib. **78**, 247–255 (1981).
[18] E. M. Salomons, ''Downwind propagation of sound in an atmosphere with a realistic sound speed profile: A semianalytical ray model,'' J. Acoust. Soc. Am. **95**, 2425–2436 (1994).

Controlled focused sonic booms from maneuvering aircraft

Micah Downing
Air Force Research Laboratory, Wright-Patterson AFB, Ohio 45433

Noel Zamot, Chris Moss, Daniel Morin, Ed Wolski, and Sukhwan Chung
USAF Test Pilot School, Edwards AFB, California 93524

Kenneth Plotkin
Wyle Laboratories, Arlington, Virginia 22202

Domenic Maglieri
Eagle Aeronatics, Inc., Newport News, Virginia 23606

(Received 4 March 1996; revised 8 March 1998; accepted 27 March 1998)

In April 1994, the USAF Armstrong Laboratory, in cooperation with USAF Test Pilot School, conducted an experimental study of controlled focus boom generated by supersonic maneuvers. The objective of this study was to collect focus and postfocus booms and to assess the ability of aircrews to control the placement of the focal region during basic maneuvers. Forty-nine supersonic passes were flown and included level linear acceleration, level turn, accelerating dives, and climbout-pushover maneuvers. These flights were flown under calm and turbulent atmospheric conditions. Turbulent conditions had a defocusing effect which caused distortions in the focus region and resulted in smaller maximum overpressures. Sonic booms were collected by up to 25 boom event analyzer recorders (BEARs) placed in a 13 000-ft linear array. The BEAR units were spaced 500–2000 ft apart with the denser spacing at the expected focal region. This spacing was chosen to evaluate the thickness of both the focal and postfocal regions. The target location varied from 2000–5000 from the uptrack end of the array. Of the 49 flights, a focus boom was placed within the array 37 times and within ± 3000 feet of the target point 27 times, demonstrating the ability to place controlled focus booms.
[S0001-4966(98)04507-X]

PACS numbers: 43.28.Mw, 43.50.Lj [LCS]

INTRODUCTION

Supersonic operations from military aircraft generate sonic booms that can affect people, animals and structures. A substantial experimental data base exists on sonic booms for aircraft in steady flight and confidence in the predictive techniques has been established. All the focus sonic boom data that are in existence today were collected during the 1960s and 1980s as part of the information base to the US Supersonic Transport program,[1–4] the French Jericho studies for the Concorde,[5] and the US Space Shuttle Program.[6–9] These experiments formed the data base to develop sonic boom propagation and prediction theories for focusing. There is a renewed interest in high-speed transports for civilian application.[10] Moreover, today's fighter aircraft have better performance capabilities, and supersonic flights are more common during air combat maneuvers. Most of the existing data on focus booms are related to high-speed civil operations such as transitional accelerations and mild turns. Military aircraft operating in training areas perform these types of maneuvers along with more drastic maneuvers such as dives and high-g turns (here and throughout the paper, g denotes the earth gravitational acceleration rate of 9.8 m/s^2). An update and confirmation of USAF prediction capabilities is required to demonstrate the ability to predict and control sonic boom impacts, especially those produced by air combat maneuvers.

In April 1994, the USAF Armstrong Laboratory, in cooperation with USAF Test Pilot School, conducted an experimental study of controlled focus booms generated by supersonic maneuvers.[11] This study had three main objectives: to test the ability of pilots to control the placement of the focus region, to validate prediction methods, and to evaluate the effects of atmospheric turbulence within the earth boundary layer on focusing. This paper describes the test procedures and summarizes the measurements obtained from the test.

I. TEST PROCEDURES

The four air combat-type maneuvers used in the study were level acceleration, diving acceleration, level steady-state turn, and a climbout-pushover. The test aircraft was the F-16B (Fig. 1). Test were conducted within the Black Mountain Supersonic Corridor at Edwards AFB (Fig. 2) where the ground elevation is 2900 ft above mean sea level (MSL). The maneuvers were flown at 10 000 ft MSL except for the dives which were started at 20 000 ft MSL. This altitude range is common for military operations and differs from previous focus sonic boom measurements, which involved higher altitudes and slower accelerations.[1–5] Also, the flights were flown under calm and turbulent atmospheric conditions since previous studies[3,5] have suggested that turbulent conditions may defocus and distort the booms within the focus region. A linear array of sonic boom monitors collected the sonic boom signatures along or parallel to the ground track. The

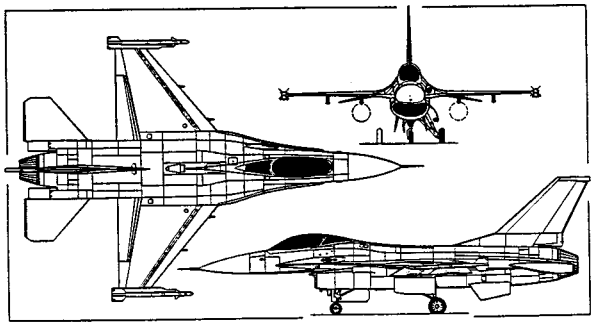

Aircraft:	F-16	Height:	16.4 ft
Name:	Fighting Falcon	Wing Span:	31.0 ft
Engines:	(1) F100-PW-200	Wing Area:	300 sq ft
Thrust Per Engine:	25,000 lbs	Empty Weight:	15,140 lbs
Length:	47.6 ft	Gross Weight:	23,360 lbs

FIG. 1. Planview drawing of F-16B aircraft.

length of the array varied during the test from 10 500–13 700 ft with 15–21 measurement sites. The target location varied from 2000–5000 ft from the uptrack end of the array. It should be noted that the measurement sites were restricted to existing roads to avoid any disturbance to the desert habitat. The boom event analyzer recorders (BEAR)[12] were used to measure the sonic boom waveforms. The BEAR systems digitally record the pressure waveform of the sonic boom and have a frequency range of 0.1–2500 Hz and a pressure range of 0.01–76 psf (0.5–3600 Pa). The spacing of the BEARs ranged from 500–2000 ft. The closer spacing was within the planned focus region with the wider spacing for the pre- and postfocus and carpet region of the sonic boom footprint.

To predict the flight profile, F-16B horizontal acceleration rates, sustained turn rates, and constant speed climb rates were calculated by using specific excess power curves

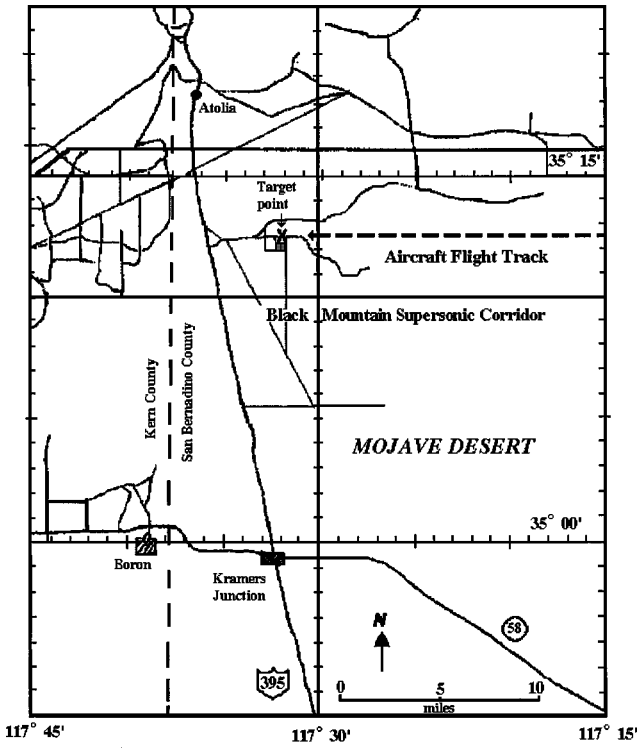

FIG. 2. Area planview of the test area including flight track.

from the F-16B flight manual.[13] Aircraft performance predictions for acceleration rates were made for standard day and standard day plus 10 °C conditions. With this information, acceleration rates, climb rates, and sustained turn rates were calculated, and the sonic boom footprint from this profile was predicted using a ray tracing sonic boom model, PCBoom3.[14] With the boom prediction, the flight profile for each pass was aligned with the array for proper placement of the focus region. The alignment provided the distance-to-target from the maneuver point. The aircrews programmed these distances into the on-board guidance system along with the appropriate initial inbound and steady-state cruise points. The steady-state point was established to ensure that the aircraft was not maneuvering before the desired maneuver point was reached.

Rawinsonde balloon launches were scheduled within one hour of each test sortie launch time to gather atmospheric profile data. Data included temperature, pressure altitude, wind speed and direction aloft, and relative humidity. As a backup to rawinsonde balloon data, the aircrew recorded inertial navigation system (INS) wind data from the heads-up display (HUD) via the aircraft video tape recording (VTR) system. During the climbout, the pilot qualitatively assessed turbulence. Prior to each run, inertial winds at altitude were recorded by aircrew by hand and on the VTR tape. Surface temperature, wind speed and direction, and relative humidity were measured at the test site and collected as 1-min averages with extremes.

The Black Mountain Supersonic Corridor was reserved from surface to 20 000 ft during all data runs to preclude noise interference from other aircraft activities. Ground personnel were stationed at specified locations throughout the array to provide real-time feedback to aid in determining the location of the sonic boom focus. Personnel uprange of the sonic boom focus should have heard no sonic boom. Personnel located in the vicinity of the focal region would hear a very loud ''double boom'' while those located downrange of the focus would hear a normal intensity ''double boom'' from the N wave followed by a ''pop'' or a rumbling sound of the U wave which indicated the trailing edge of the focal region as demonstrated in Fig. 3. Feedback from these observers gave rapid qualitative feedback on the location of the focus. From this feedback, adjustments could be made to the timing of the profile flown to best place the location of the focal region at the designated target point in the array.

For all testing, aircraft tracking data were gathered via the Airborne Range Data System (ARDS). The aircraft carried ARDS pods that supply differential GPS based time-space position information to ground stations for both tracking purposes and position data. For this test the ARDS time-space position data collection rate was 100 samples per second and included 14 different aircraft parameters such as time, position, Mach number, heading angle, dive angle, angle of attack, etc. This information was used in-flight along with normal air-traffic control radar to provide course corrections to the aircrew for all runs except the autonomous level accelerations. Figure 4 shows an example of the flight track data for one of the level acceleration passes where the dots denote 10-s intervals. The aircraft flew in the negative *x*

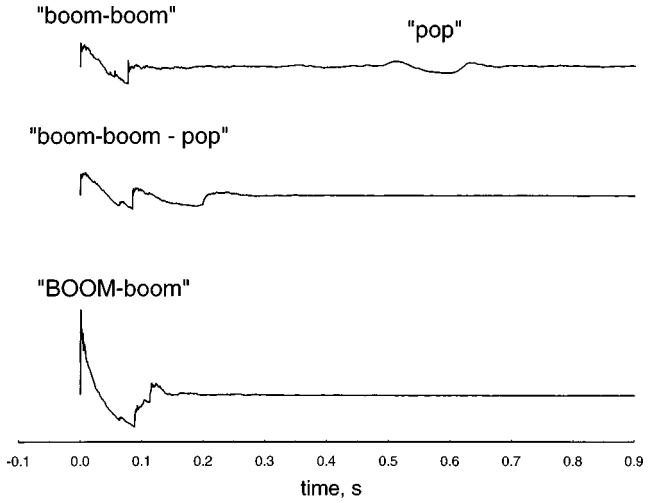

FIG. 3. Sonic boom waveforms: bottom signature is the focus boom; middle signature is an N wave directly followed by the U wave that occurs at downtrack end of the focus region; and the top signature is a carpet N wave followed by a postfocus U wave that occurs well downtrack of the focus boom.

direction (due west) and broke the level acceleration off after passing the target point (0,0) by climbing above 20 000 ft MSL to regain potential energy.

A. Description of the four maneuvers

Figure 5 provides a sketch of the flight profiles for the four maneuvers performed during this test. The sketch provides the main points of the profiles: initial, steady, maneuver, Mach 1 (level and diving accelerations), and break points. Also the sketches show the relationship between the maneuver point and the target point. For the level and diving accelerations the flight track was in line with the array, while the turn and climbout-pushover flight tracks were parallel to the array but offset to the south of the array.

The level acceleration profile [Fig. 5(a)] was the priority profile for data collection purposes since it was the easiest profile for the aircrews to become proficient at for the autonomous runs. Prior to initiation of the maneuver, the test aircraft was stabilized at 0.9 Mach number and 10 000 ft pressure altitude. At initiation of the maneuver, the pilot selected full afterburner and accelerated on course to 1.2 Mach number. Course corrections were provided up to the maneuver point by ground controllers based on real-time display of ARDS data. The course corrections were limited to five degrees of bank or less. The pilot would call the transition point when the aircraft speed reached Mach 1.0. The maneuver was terminated as the aircraft flew over the array, or reached 1.2 Mach number, whichever occurred first. Several autonomous flights were performed with the linear acceleration to test the feasibility of pilots placing the focus region at the target point without external real-time guidance. For the autonomous runs before each flight, distance-to-target data from the maneuver point for each pass were calculated. These data were used by the aircrews as an input to the on-board guidance. Minor corrections to the distance-to-target from the maneuver point, if required, were given only between passes. However, no other corrections were given to the aircrews during the autonomous runs.

For the diving accelerations [Fig. 5(b)], the aircraft was stabilized in level flight at 0.9 Mach number and 20 000 ft pressure altitude prior to maneuver initiation. At the maneuver point, the pilot accelerated the aircraft by selecting full afterburner while performing the dive initiation. At the start of the dive, the pilot rolled the aircraft to an inverted attitude while pushing the nose into a 30-degree dive relative to the horizon. Once the 30-degree dive was established, the pilot rolled the aircraft to an upright attitude while maintaining the dive. This entire dive initiation took about 4 s to establish the 30-degree dive from level flight. The roll maneuver was performed during the dive initiation since this is common for the initiation for a high-degree dive and it ensures a crisp dive profile. No course corrections were provided after initiation of the maneuver. The pilot called the Mach 1 point as

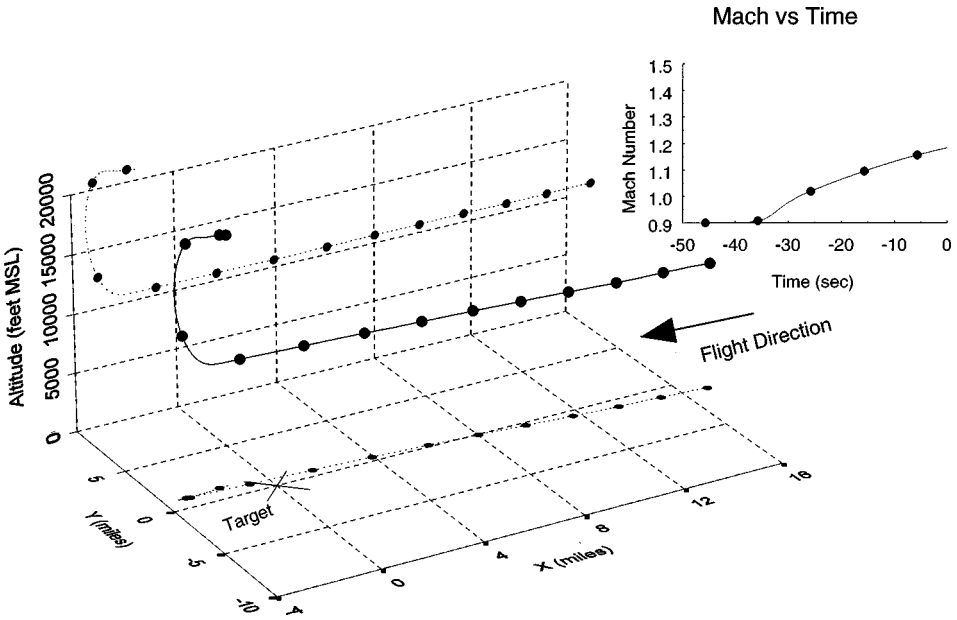

FIG. 4. Sample of the actual flight profile. Note, dots appear at 10-s intervals for reference. The data was collected at 100 samples per second.

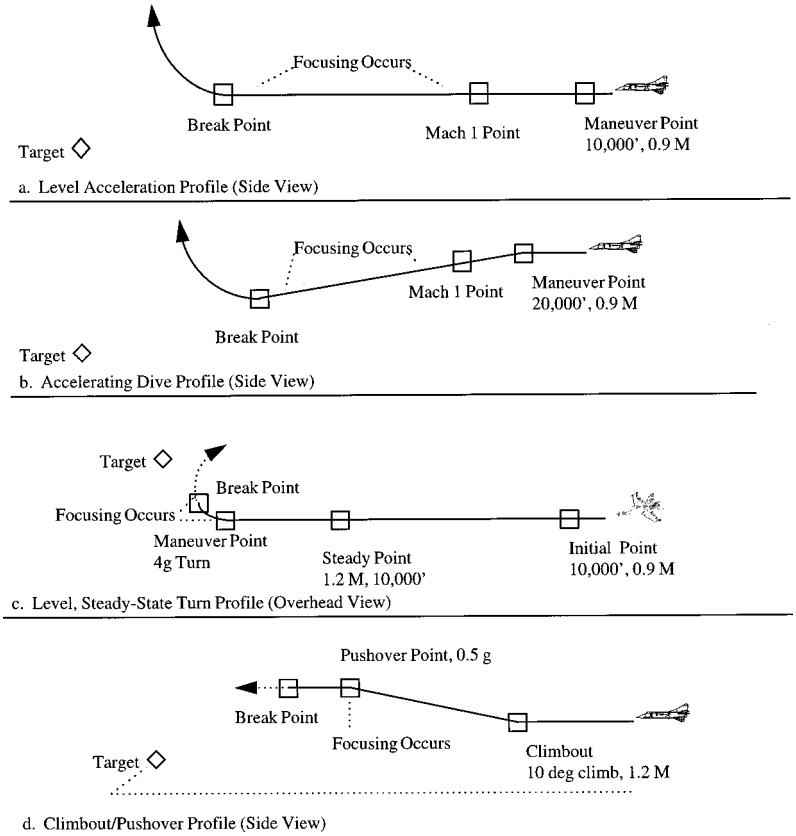

FIG. 5. Sketch of flight profiles with reference points: (a) level acceleration, (b) accelerating dive, (c) level steady-state turn, and (d) climbout-pushover.

the aircraft transitioned into supersonic flight. The maneuver was terminated as the aircraft reached 1.2 Mach number or descended below 13 000 ft pressure altitude.

For the level turn [Fig. 5(c)], a load factor of 4g was chosen as a maximum sustainable load factor for the turn maneuver while trying to maintain 1.2 Mach number. Before the maneuver, the aircraft was stabilized in level flight at 1.2 Mach number and 10 000 ft pressure altitude. At the start of

TABLE I. Level accelerations (guided) focus boom placements.

Pass no.	Date	Time (PDT)	Focus location from target (ft)	Comments	Atmospheric conditions
1	12 Apr 94	9:23:27	−2880		Sunny with high scattered
2		9:29:01		Focus in array, no boom data	clouds. 70 °F–71 °F at test site.
3		9:32:12	960		Winds at 1.0 knots gusting to
4		9:35:32	−5120		4 knots. 16% rel. hum.
5		9:39:06	3000	Focus up track of array	
6		9:43:55		Focus in array, no boom data	
7		12:10:20	−5690		Sunny with high scattered
8		12:16:43		Focus in array, no boom data	clouds. 68 °F–70 °F at site.
9		12:23:22	−1370		Winds at 5 knots gusting to
10		12:27:36	−2580		8 knots. 7% rel. hum.
11		12:53:17		Focus in array, no boom data	
12		12:59:39	1900		
13		13:05:26	−3050		
23	13 Apr 94	12:34:47	0		Sunny with high scattered
24		12:40:23	−7000	Distorted focus region	clouds. 63 °F–65°F at site.
25		12:45:16	−3000		Winds at 2.5 knots gusting
26		12:49:48	~2000/ −8390	Multiple focus regions	to 5 knots. 9% rel. hum.
27		12:52:09	−1120		
28		13:00:43	−6940		
29		13:05:42	~−7500		

TABLE II. Level accelerations (autonomous) focus boom placements.

Pass no.	Date	Time (PDT)	Focus location from target (ft)	Comments	Atmospheric conditions
39	20 Apr 94	15:19:32	+1520/ −6870	Multiple focus regions	Sunny, clear skies. 95 °F–97 °F at site. Winds at 4 knots gusting to 8 knots. 8% rel. hum.
40		15:25:09	0/−7390	Distorted focus regions	
41		15:30:05		Defocused	Thermal turbulence
42		15:35:33		Defocused	
43	21 Apr 94	7:40:58	+1940		Sunny, clear. 61 °F–63 °F at site. Winds at 2.5 knots gusting to 5 knots. 50%–46% rel. hum.
44		7:47:00	+80		
45		7:52:34	+1120		
46		7:58:06	+440		
47		16:51:50	+2860		Sunny clear, stiff winds at altitude. 81 °F at site. Winds at 11 knots gusting to 20 knots. 15% rel. hum. mech. turb.
48		16:58:59	+1440	Distorted focus regions	
49		17:06:09	+140		

the turn, the pilot selected full afterburner and initiated a 4g level turn. The maneuver was terminated after 50 degrees of turn, and the pilot called the break point.

The climbout-pushover maneuver [Fig. 5(d)] included two supersonic flight segments, a climbout followed by a pushover to level flight. Prior to the climbout, the aircraft stabilized in level flight at 1.2 M and 10 000 ft pressure altitude. At the climbout point, the aircraft would start a ten-degree climb while maintaining 1.2 M. Once the climbout angle and speed were stabilized, the pilot pushed the aircraft over with an acceleration load factor of 0.5g to the level flight attitude while maintaining constant Mach number. The maneuver was terminated as the aircraft reached the level flight attitude. During this profile the pilot called the climbout, pushover, and break points while receiving guidance. The focus boom created by this maneuver was generated at the pushover point and occurred lateral to the centerline of the flight track. Thus, the flight track was offset 13 700 ft south of the array.

II. RESULTS

For the overall study, 49 maneuvering passes were performed: 31 level accelerations (11 of which were autonomous passes), 9 diving accelerations, 7 turns, and 2 climbout-pushovers. The aircrews were successful in placing a focus boom within the array 37 times out of these 49 passes and within ±3000 ft of the target point 27 times. Tables I–V list the summary information for the individual passes. Of the 12 ''misses,'' the focus was produced in front of the array five times and behind the array only once. For five passes, turbulence distorted the sonic boom within the array so that a focus region could not be clearly defined. The separation time of the leading shocks between the N and the U waves was used to estimate the location of the onset of the focus region. Note, for the table and the following boom signature plots, the zero point is the target point, positive distance is uptrack of the target, and negative is downtrack.

A. Level acceleration

One objective of this test was to test the ability of pilots to control the placement of the focus region. Table I lists the focus boom placement data for all of the guided level acceleration passes, and Table II lists the data for all of the autonomous passes. In summarizing the statistics of the focus boom placement for the level acceleration profiles, the data are grouped into three different sets: total, calm atmospheric conditions, and autonomous run passes. The total group in-

TABLE III. The 30° diving acceleration focus boom placements.

Pass no.	Date	Time (PDT)	Focus location from target (ft)	Comments	Atmospheric conditions
14	13 Apr 94	9:42:11		Missed array to west	Sunny, high scattered clouds. 55 °F–58 °F at site. Winds at 3 knots gusting to 7 knots. 19% rel. hum.
15		9:47:41	~−8000	Estimated from observations	
16		9:52:53	−4450		
17		9:57:23	+2213	Focus up track of array	
18		10:10:00	+3950	Focus up track of array	
19		10:19:24	+2800	Focus up track of array	
20		10:25:56	+1450		
21		10:28:40	+2160		
22		10:35:50	+4930	Focus up track of array	

TABLE IV. Level turn focus boom placement.

Pass no.	Date	Time (PDT)	Focus location from target (ft)	Comments	Atmospheric conditions
30	15 Apr 94	12:18:28		Distorted	Sunny, clear. 65 °F–66 °F at site.
31		12:21:39		Distorted	Winds at 7 knots gusting to
32		12:24:45	+1500/ −6390	Multiple focus regions	14 knots. 8% rel. hum.
33		12:28:45		Distorted	
34	18 Apr 94	12:05:23		Aborted run	Sunny, high clouds. 91 °F at
35		12:11:15	−900		site. Winds at 3 knots gusting
36		12:17:05	−1920		to 8 knots. 39% rel. hum.

cludes 25 passes and excludes 2 passes, 41 and 42, where atmospheric turbulence in the earth boundary layer defocused the boom and 4 passes, 2, 6, 8, and 11, where insufficient boom data were collected by the monitoring array. For this group the focus boom had a mean placement of −1150 ft downtrack from the target point with a standard deviation of 3230 ft. The calm atmospheric conditions group that includes passes flown before 1200 local time includes eight passes, 1, 3, 4, 5, 43, 44, 45, and 46. The mean placement of the focus boom for this grouping was −60 ft downtrack from the target with a standard deviation of 2660 ft. The autonomous run group (Table II) includes nine passes and excludes two passes, 41 and 42, in which turbulence severely distorted the focusing of the boom. For this group the focus placement had a mean of +1060 ft uptrack from the target point with a standard deviation of 980 ft. In comparing these different sets, the placement precision for the autonomous passes demonstrates the ability of the aircrews to control the placement of the focus region and the ability of the current USAF sonic boom prediction program[14] to plan supersonic profiles. However, atmospheric turbulence greatly diminishes this ability since turbulent conditions defuse the focusing of the booms.

Three level accelerations passes are considered in detail to show some of the effects of atmospheric turbulence on sonic boom focusing. The first boom series was measured during calm atmospheric conditions, the second series during thermally turbulent conditions (low winds, high solar heating), and the third series during mechanical turbulence (gusting winds, low heating). The aircraft acceleration for these three atmospheric situations are given in Fig. 6 which shows the Mach number versus time for each of these flights. This plot shows that the accelerations were fairly consistent between the flights. For flight during thermal turbulence, the actual acceleration was less than the other cases which would result in the focus region occurring slightly further downstream. Figure 7 shows the boom signatures recorded along the array for pass 46 that was flown during calm atmospheric conditions. The time scales of the booms are adjusted to have the same leading shock time. The first boom recorded was 500 ft uptrack of the target point and had a peak overpressure of 10.8 psf. However, the maximum measured peak overpressure of 19 psf occurred at the target point. It should be noted that the spatial distances are set relative to the target point that corresponds to 0-ft distance downtrack and are aligned with the direction of flight. Figure 7 shows the increased separation between the N and U waves with distance downtrack from the focus region. The comparison between the amplitudes of the N and U waves, Fig. 8, shows the amplification of the peak overpressure within the focus region. For this case the amplification factor was 3.8 when compared to the predicted carpet boom overpressure of 5.0 psf for steady flight conditions of 1.2 M at 10 000 ft. It can be seen that the amplitude of the postfocus boom (open symbols) diminishes with distance downtrack of the focus region.[2–5]

Figure 9 shows the signature computed from PCBoom3,[14] using the actual flight profile of pass 46. Comparing these signatures to the measured signatures of Fig. 7, it appears that the predicted focus is slightly too far uptrack and the N–U separations are larger than measured. However, the focal zone methodology in PCBoom3 applies a numeric focus solution by Gill and Seebass[15] to the linear ray acoustic caustic location. The Gill–Seebass solution shows nonlinear distortion of the ray geometry, with the focus occurring slightly above the caustic. This displaces the focus down-

TABLE V. Climbout-pushover focus boom placement.

Pass no.	Date	Time (PDT)	Focus location from target (ft)	Comments	Atmospheric conditions
37	19 Apr 94	12:21:00	−170		Sunny, high scattered clouds.
38		12:28:00	+2440		90 °F–91 °F at site. Winds at 2 knots gusting to 7 knots. 21% rel. hum.

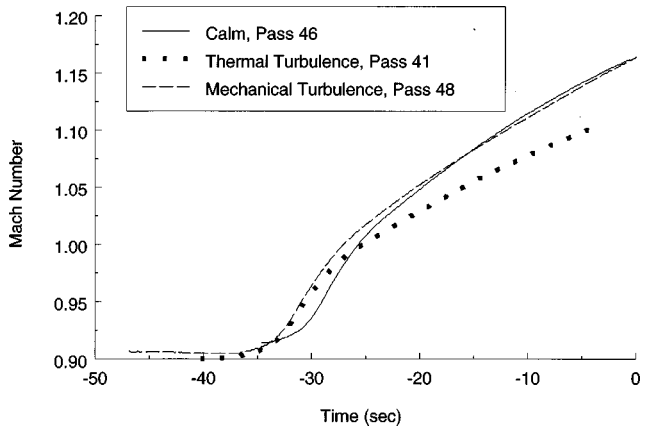

FIG. 6. Mach number versus time for the level accelerations during calm and turbulent atmospheric conditions. (Note time is relative to aircraft crossing target point.)

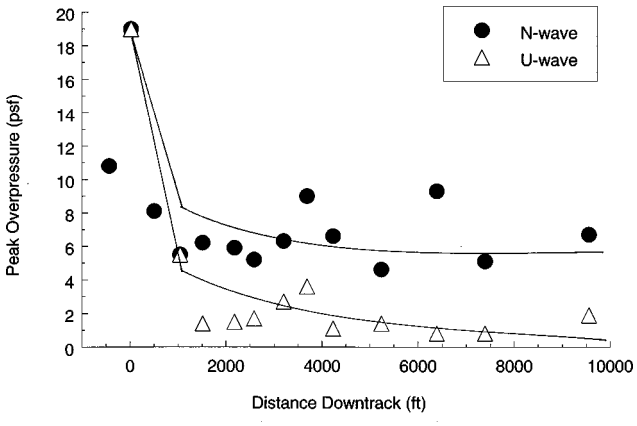

FIG. 8. The N- and U-wave peak overpressures versus distance down track of focal zone for a level acceleration flight during calm atmospheric conditions, pass 46.

track. For the conditions of the pass 46 focus, this displacement has been calculated to be 3500 ft. Applying this offset, the measured and predicted N–U separations are in very good agreement. The offset predicted focus location is then about 1500 ft downtrack of the measured focus, but this is associated with nonlinear displacement in the Gill–Seebass solution and is also a distance comparable to the focal zone dimension. The predicted overpressures also agree well with the measurements. Within the focus region the solution is very sensitive to small errors, so the estimation is reasonably good even though the maximum measured focused boom of 19.1 psf was greater than the estimated level of 12.1 psf.

The second boom series, as shown in Fig. 10, was measured during thermally turbulent conditions. The surface conditions were hot with a temperature of 97 °F with no sustained winds and a few minimal wind gusts to 1.0 knots. This series demonstrates no clear focus region although the acceleration profile is similar to the previous case, pass 46. The maximum peak overpressure was 10.0 psf and occurred 5250 ft downtrack from the target point which can be expected from the reduced acceleration rate indicated in Fig. 6. For this pass the amplification factor was reduced to 2.0.

The third boom series, shown in Fig. 11, was measured during mechanically turbulent conditions. The surface conditions were mild with a temperature of 81 °F with a sustained head wind of 14 knots with gusts to 18.5 knots. This series is drastically different since two focus regions occurred within the array. The first focus region was at 500 ft uptrack of the target point and had a peak overpressure of 20.9 psf, amplification factor of 4.2. The second region was at 7000 ft downtrack of the first and had a peak overpressure of 19.3 psf, amplification factor of 3.4. The last measured signature shows two postfocus U waves trailing the N wave. These two boom series signatures suggest that turbulent conditions can minimize and distort the focus region and its amplified peak overpressures.

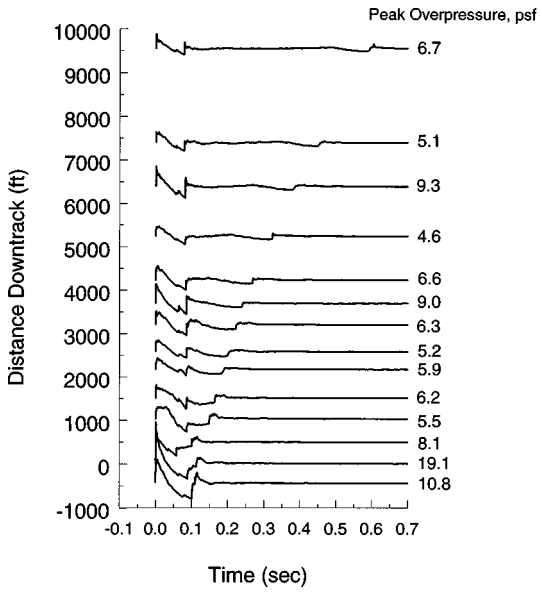

FIG. 7. Measured sonic boom waveforms produced by a level acceleration during calm atmospheric conditions, pass 46. (Signatures are aligned in time relative to the leading shock and in space relative to the target point.)

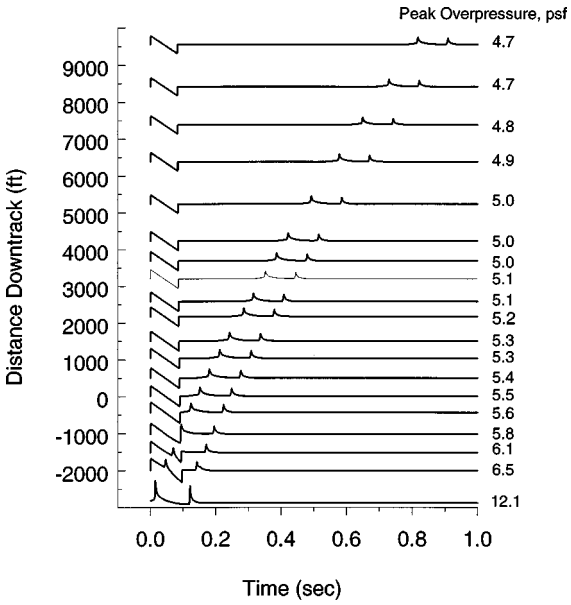

FIG. 9. Predicted sonic boom waveforms produced by a level acceleration during calm atmospheric conditions, pass 46. (Signatures are aligned in time relative to the leading shock and in space relative to the target point.)

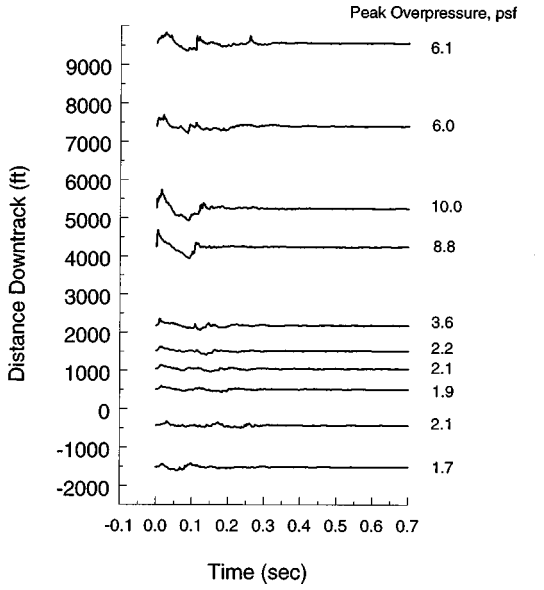

FIG. 10. Measured sonic boom waveforms produced by a level acceleration during thermally turbulent atmospheric conditions, pass 41. (Signatures are aligned in time relative to the leading shock and in space relative to the target point.)

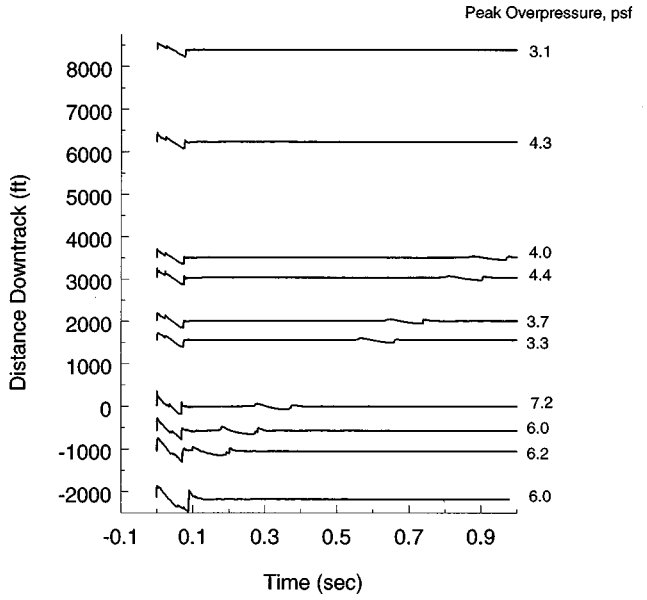

FIG. 12. Measured sonic boom waveforms produced by a 30-degree accelerating dive, pass 20. (Signatures are aligned in time relative to the leading shock and in space relative to the target point.)

B. Dive

The summary information on the nine diving acceleration passes is provided in Table III. The boom series for pass 20 is shown in Fig. 12 and is representative of the data collected for this maneuver. The maximum boom was 7.2 psf and measured 1380 ft uptrack from the target point (0 ft downtrack distance). This series shows that the postfocus region is narrower than the level acceleration maneuver since the postfocus U wave moves away from the N wave at a quicker rate. This narrowing of the focus region is demonstrated in Fig. 13 that shows the predicted footprints for both the level acceleration and the accelerating dive. This comparison shows that the thickness of the focal region of the dive is much narrower than for the level acceleration even though the overall focal region is wider. Figure 14 shows the peak overpressures of the N and U waves measured along the

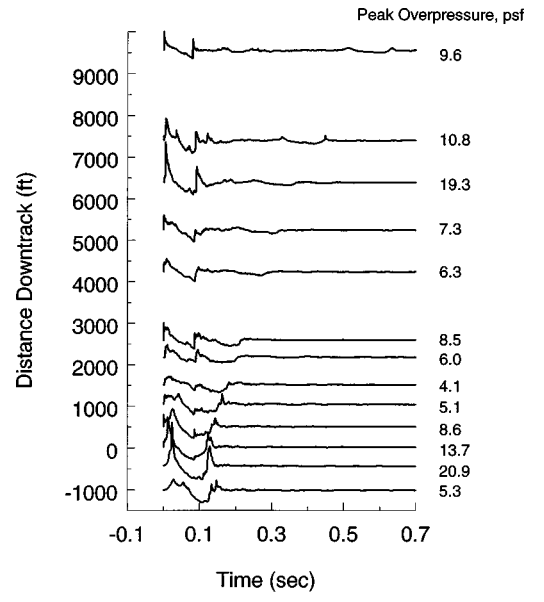

FIG. 11. Measured sonic boom waveforms produced by a level acceleration during mechanically turbulent atmospheric conditions, pass 48. (Signatures are aligned in time relative to the leading shock and in space relative to the target point.)

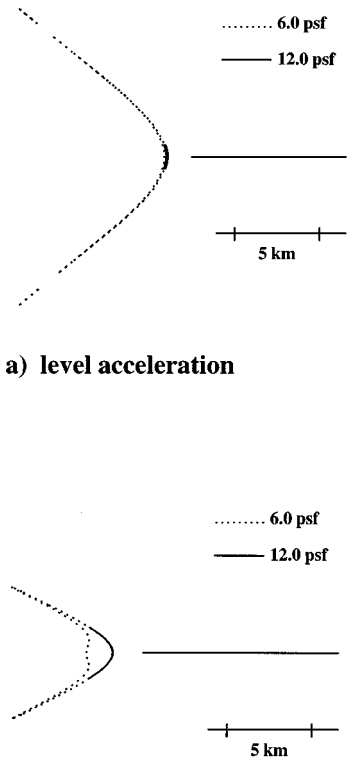

FIG. 13. Focal boom footprint contours: (a) level acceleration and (b) accelerating dive.

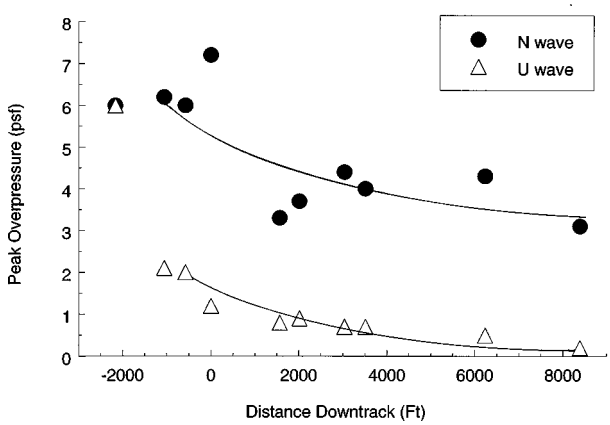

FIG. 14. The N- and U-wave peak overpressures versus distance down track of focal zone for a 30-degree accelerating dive, pass 20.

array. Within the focus region the peak overpressure was amplified by a factor of 2.3 when compared to the predicted carpet boom overpressure of 3.2 psf from a level flight at 1.2 M at 15 000 ft. This maneuver involved the most difficulty in placing the focus boom at the target point because of the narrowing of the focal region and the sensitivity of the focus location to the actual dive angle.

C. Turn

The next boom maneuver was a 4g turn at a Mach number of 1.2. The profile was aligned with the array so that the array would capture the focal line from the steady part of the turn and not the superfocus region generated by the initiation of the turn. Seven passes were performed with this maneuver and Table IV lists the summary information from these passes. The measured booms from pass 36 are shown in Fig. 15. At the first part of the array, the measured booms were from the steady portion prior to the maneuver point. Focusing was measured within a band of 2500 ft about the target

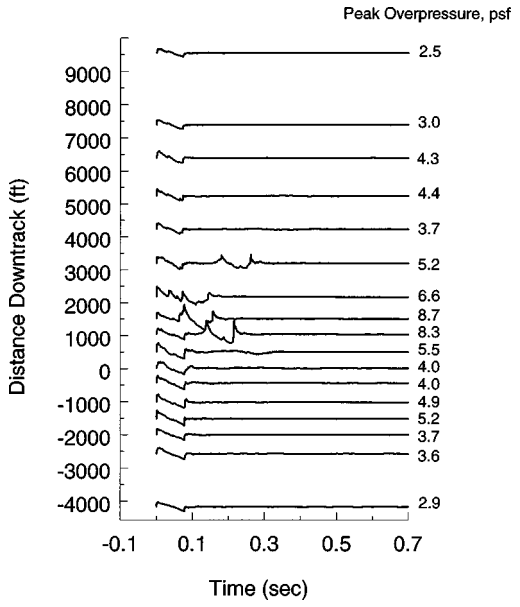

FIG. 15. Measured sonic boom waveforms produced by a 4g turn at 1.2 M, pass 36. (Signatures are aligned in time relative to the leading shock and in space relative to the target point.)

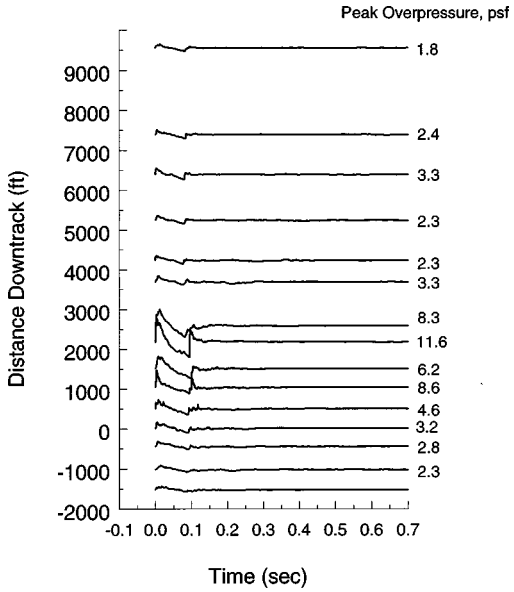

FIG. 16. Measured sonic boom waveforms produced by a 0.5g pushover maneuver, pass 37. (Signatures are aligned in time relative to the leading shock and in space relative to the target point.)

point with the maximum overpressure measured at −1500 ft from the target point (0 ft downtrack distance). This shows that the focal line is very narrow for this maneuver. Postfocus signatures or disturbances appear in both directions from the focus region. The maximum overpressure was 8.7 psf which gives an amplification factor of 1.7 when compared to the carpet boom overpressure from steady level flight at 1.2 M at 10 000 ft. However, by comparing the maximum overpressure to the carpet boom measured during this pass the amplification factor is around 4. This pass occurred during mild atmospheric turbulent conditions and had provided the best defined focus region compared to the other passes. Passes 30–33 had distorted focus regions while pass 35 created a similar series as pass 36.

D. Pushover

The final maneuver performed during the study involved a climbout-pushover type of profile as shown in Fig. 5(d). The ground track was set parallel to the measurement array by 13 700 ft based on predictions by PCBoom3.[14] Only two passes were performed for this maneuver with the data provided in Table V. The booms measured from pass 37 are shown in Fig. 16. The maximum peak overpressure was 11.6 psf and occurred 2000 ft downtrack of the target point (0 ft downtrack distance). This booms was amplified by a factor of 3.4 when compared to a 3.4 psf overpressure from steady level flight at 1.2 M at 14 000 ft. For this series only slight disturbances appear to trail behind the N wave in the postfocus region and the focus region is very narrow. Pass 38 did not have as well defined a focused region since the maximum peak overpressure was only 5.8 psf. The results demonstrate that the focus region occurs lateral to the flight track centerline for this maneuver which is important for supersonic civil transports to consider as the aircraft levels off during cruise.

III. CONCLUSIONS

This paper summarizes the basic data collected for a controlled focus boom study completed in April 1994 at Edwards AFB CA, USA. The objectives of this study were to test the ability of aircrews to control the placement of focus booms with preplanned supersonic maneuvers, to validate prediction methods, and to measure the effect of turbulent conditions on the focusing of the sonic booms produced by these maneuvers. Of the 49 flights, 37 focus booms were placed within the array. Predictions of focal zone geometry (accounting for both linear ray geometry and nonlinear displacement from the caustic) agree well with measurements. These results are consistent with previous focus sonic boom studies and show that the focus region produced by the four aircraft maneuvers have a width varying from 100 to 1000 ft. This study demonstrates the ability of aircrews to control the focal region of the sonic boom footprints with preplanning of the flight profile. This finding could help in minimizing adverse impacts from planned supersonic training flights. Also, the results of this study confirm that turbulent conditions can defocus the focal regions as suggested by previous studies. Examples of this effect show that the focus regions can be distorted and/or diminished. One flight under mechanical turbulent conditions displayed two focus regions with reduced amplification of the peak levels, while one flight under thermal turbulent conditions showed that the focus region is almost completely diminished. These two examples demonstrate that turbulence can have a strong defocusing effect on sonic boom propagation.

[1] D. J. Maglieri and D. L. Lansing, ''Sonic Booms from Aircraft in Maneuvers,'' NASA TN D-2370, Washington, DC, July 1964.

[2] D. L. Lansing and D. J. Maglieri, ''Comparison of Measured and Calculated Sonic-Boom Ground Patterns Due to Several Different Aircraft Maneuvers,'' NASA TN D-2730, Washington, DC, April 1965.

[3] D. J. Maglieri and D. A. Hilton, ''Experiments on the Effects of Atmospheric Refraction and Airplane Accelerations on Sonic-Boom Ground-Pressure Patterns,'' NASA TN D-3520, Washington, DC, July 1966.

[4] D. J. Maglieri, ''Sonic Boom Flight Research—Some Effects of Airplane Operations and the Atmosphere on Sonic Boom Signature,'' NASA SP 147, Washington, DC, 1967, pp. 25–48.

[5] J-C. L. Wanner, J. Vallee, C. Vivier, and C. Thery, ''Theoretical and experimental studies of the focus of sonic booms,'' J. Acoust. Soc. Am. **52**, 13–32 (1972).

[6] F. Garica, Jr., H. R. Henderson, and J. H. Jones, ''Preliminary Sonic Boom Correlation of Predicted and Measured Levels for STS-5 Launch,'' NASA TM-58253, Washington, DC, April 1983.

[7] E. G. Stansbery, J. L. Stanley, and A. E. Potter, ''Sonic Boom Levels Measured for STS-7 Launch,'' JSC-19237, NASA, Washington, DC, August 1983.

[8] E. G. Stansbery and J. L. Stanley, ''Sonic Boom Levels Measured for STS-41D Launch,'' JSC-200218, NASA, Washington, DC, December 1984.

[9] E. G. Stansbery and J. L. Stanley, ''Descent Sonic Boom Measurements for STS-26 Including a Mach 23 Measurement,'' JSC-23579, NASA, Washington, DC, April 1989.

[10] C. M. Darden, C. A. Powell, W. D. Hayes, A. R. George, and A. D. Pierce, ''Status of Sonic Boom Methodology and Understanding,'' NASA CP 3027, NASA—Langley Research Center, 19–20 January 1988.

[11] N. Zamot, C. Moss, D. Morin, E. Wolski, and S. Chung, ''Evaluation of Controlled Focus Sonic Booms Produced by Maneuvering Supersonic Aircraft,'' AFFTC-TLR-94-29, Edwards AFB, CA, May 1994.

[12] R. A. Lee and J. M. Downing, ''Boom Event Analyzer Recorder: Unmanned Sonic Boom Monitor,'' J. Aircr. **33**(1), 171–175 (1996).

[13] *USAF Series F-16A/B Aircraft Flight Manual*, Technical Order 1F-16A-1, Lockheed Fort Worth Division, Forth Worth, Texas, Change 8, 7 June 1993.

[14] K. J. Plotkin, J. M. Downing, and J. Page, ''USAF Single Event Sonic Boom Prediction Model: PCBoom,'' AL/OE-TR-1997-0003, Brooks AFB, TX, January 1997.

[15] P. M. Gill and A. R. Seebass, ''Non-Linear Acoustic Behavior at a Caustic: An Approximate Solution,'' in *AIAA Progress in Astronautics and Aeronautics*, edited by H. Nagamatsu (MIT, Cambridge, 1975).

Sound absorption by an orifice plate in a flow duct

J. C. Wendoloski

Department of Architectural and Design Science, Faculty of Architecture, University of Sydney, NSW 2006, Australia, and CSIRO, Telecommunications and Industrial Physics, P.O. Box 218 Lindfield, NSW 2070, Australia

(Received 4 April 1996; revised 6 October 1997; accepted 17 February 1998)

In this paper the acoustic absorption due to an orifice plate in a duct supporting a mean flow is studied theoretically. Absorption takes place as the acoustic field energizes a vortex field which is generated at the orifice rim. A linearized approximation is made to the absorption mechanism. This work presents an analytical extension of Howe [Proc. R. Soc. London, Ser. A **366**, 205–233 (1979)]. The latter deals with unsteady high Reynolds number flow through a circular aperture in a thin infinite screen. To the author's knowledge, such an extension has not been previously made. The problem is formulated analytically insofar as it is possible and numerical results are presented. A Green's function series expansion is used in the formulation. A difficulty arises with the convergence of this expansion. It is solved by a renormalization technique, which has been developed for this problem. The technique appears to be a novel method for dealing with convergence problems associated with term by term differentiation of Green's function series expansions. To provide a check on the solution, it is shown that when the radius of the duct tends to infinity the present expression for the Rayleigh conductivity of the orifice plate limits to the expression obtained by Howe for an aperture in a thin infinite screen. With respect to the numerical results, it appears that for orifice mean flow Mach numbers ≤ 0.2, an orifice to duct open area ratio of 0.3 provides near optimal average absorption, for the band of frequencies limited by the first symmetric mode cutoff frequency.
[S0001-4966(98)00806-6]

PACS numbers: 43.28.Py, 43.20.Mv, 43.50.Gf [LCS]

BACKGROUND

In this paper we will examine the acoustic behavior of a constricted duct when a mean flow is present. The constriction considered here is in the form of a concentrically placed orifice (or aperture) plate. The acoustic impedance is altered from the zero flow case via an interaction of the sound field with the steady flow in the vicinity of the orifice plate. This phenomenon in the said geometry has been known for some time, and has been described by authors dating back to Borth[1] in 1916. He noted the possibility of using the flow through a throttle to attenuate vibrations in the ducts of a piston compressor. More recent experimental investigations have been made by Ingard and Ising[2] and Ronneberger.[3] The investigations of the latter author included study of a variety of geometries with rapidly changing cross section. These investigations showed acoustic energy to be *absorbed* by apertures supporting a mean flow. A more complete listing of such studies is given by Bechert.[4]

Many areas of practical application for this type of work have been indicated in the literature. The design of reactive silencers in the exhaust systems of internal combustion engines, and sound absorption by orifice flow meters in gas pipelines are obvious examples (see Cummings and Chang[5] and Cummings[6]). More generally, Davies[7] lists a number of areas of application for acoustically reactive duct flow systems. These include flow duct systems in power generating plants, petrochemical and construction plants, prime movers, and fluid distribution systems. The latter paper gives a number of practical formulae for reflection and transmission coefficients of plane waves in flow ducts with obstacles, discontinuities, and side branches, etc. Lastly, a more detailed example of sound absorption by vorticity production in a cross flow heat exchanger is given in the introduction of Howe.[8] In this example thin perforated plates are aligned parallel to the flow in the heat exchanger cavity, damping being obtained as the sound field generates vorticity in the perforations. The kinetic energy of the vorticity is convected away by the mean flow and eventually dissipated into heat by viscous and thermal action. The geometry of this last example is somewhat different to the one under present consideration, however, the method of the sound absorption is identical.

As implied in the last example, the physical mechanism behind the absorption in the present case is an acoustically induced shedding of fluctuating vorticity at the rim of the aperture. The strength of this vorticity is determined by the condition that the fluctuating velocity remain finite at the sharp edge of the rim of the aperture. This latter condition is generally referred to as the Kutta condition (see *Encyclopaedic Dictionary of Physics*[9]).

A number of theoretical studies have been made concerning problems of this general nature. Papers by Munt,[10] Howe,[11,12] Rienstra,[13] Fukumoto and Takayama,[14] and Dowling and Hughes[15] have dealt explicitly with the shedding of vorticity as determined by the Kutta condition and its effect on the resultant sound field.

The paper by Munt[10] deals with the interaction of sound with a subsonic jet issuing from a semi-infinite cylindrical pipe. In this paper, he employs the Kutta condition as out-

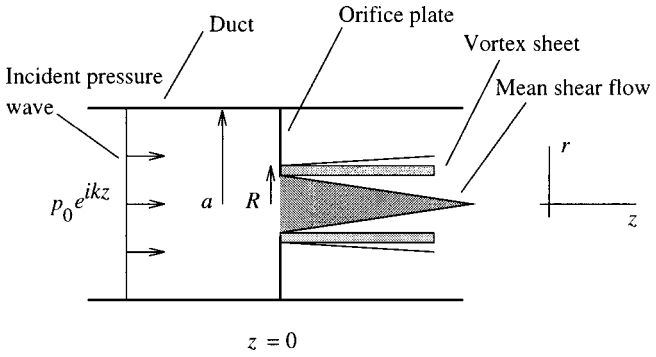

FIG. 1. Representation of an orifice plate in a duct supporting a mean flow, subject to an acoustic pressure perturbation.

lined above to formulate an integral equation for the problem which he then solves using a Wiener–Hopf technique. We note here that such techniques are substantially complicated by the existence of vertical structures such as that of an orifice plate and, hence, are not easily adaptable to the current geometry (see Levine and Schwinger[16]). Conversely, Howe,[11] whose method of solution we will adapt to the current problem, addresses the canonical geometry of an aperture in an infinite plane. He uses results from this canonical solution to develop a theory of sound transmission through a perforated screen. The paper by Fukumoto and Takayama,[14] and the more comprehensive study by Dowling and Hughes,[15] extend Howe's theory to deal with screens perforated by arrays of slits. We note, for completeness, the studies of Rienstra[13] and Howe.[12] The former is a study of acoustic radiation from a semi-infinite annular duct in a mean flow, and the latter is a study of sound attenuation by a splitter plate in a mean flow.

As mentioned above, we will be dealing in this paper with a flow duct in which an orifice plate has been embedded. In particular, we will be concerned with the effect of orifice geometry on the acoustic absorption and conductivity of the duct when an axial mean flow is present. This work is in essence an analytical extension of Howe.[11] To the author's knowledge, such an extension has not been previously made.

The problem is formulated analytically insofar as it is possible and numerical results are presented. A Green's function series expansion is used in the formulation. A difficulty arises with the convergence of this expansion. It is solved by a renormalization technique, which has been developed for this problem. The technique appears to be a novel method for dealing with convergence problems associated with term by term differentiation of Green's function series expansions.

I. THE ANALYTICAL SOLUTION

Consider a rigid cylindrical duct of radius a with a rigid concentrically placed orifice plate in its interior. This orifice plate has an inner radius R, and an axial mean flow is assumed to exist in the duct, as shown in Fig. 1. Now consider a nominally plain pressure wave (of amplitude p_0 and wave number k) emanating from $z=-\infty$ and incident on the leading face of the orifice plate at $z=0$.

Let the jet velocity in the center of the orifice be V and let ν be the kinematic viscosity. We will now assume that the Reynolds number (VR/ν) is sufficiently large so that the presence of viscosity in the fluid has the *sole effect* of leading to the shedding of fluctuating vorticity at the perimeter of the orifice (see Howe[11]). We will also neglect any dissipation of fluid energy due to heat conduction.

Under these conditions it has been shown by Howe[11] that, provided convection of sound by the mean flow is unimportant, the problem can be solved in terms of a compressible stagnation enthalpy equation:

$$(\nabla^2+k^2)B=-\mathrm{div}(\mathbf{w}\times\mathscr{U}), \tag{1}$$

where $\mathbf{w}$ is the vorticity perturbation due to the incident wave and $\mathscr{U}$ is the orifice mean flow velocity, the magnitude of the latter $(\mathscr{U})$ being the velocity at which the vorticity convects. The fluctuating stagnation enthalpy B has been shown by Howe[17] to be a convenient variable to use when considering sound generation by vorticity inhomogeneities. It is defined by

$$B=\frac{p}{\rho_0}+\frac{1}{2}\{v^2\}, \tag{2}$$

where p is the fluctuating pressure in the fluid, ρ_0 is the fluid density, and v is the magnitude of the fluid velocity. The brackets around v^2 signify that the steady parts of this term are omitted. In irrotational regions $B=-\partial\phi/\partial t$, where ϕ is the perturbation velocity potential. It will be assumed that the fluctuating flow is irrotational away from the vortex sheets, and therefore that homogeneous Neumann conditions in B are satisfied on all the rigid surfaces in the duct. (See Morse and Feshbach,[18] page 679, for background on Neumann boundary conditions.)

The fact that convection has been ignored in Eq. (1) implies that the only effect of the flow in the duct is to produce a convected fluctuating vorticity source. Hence, the ambient medium (i.e., the air outside of the vortex sheet) is assumed to be effectively stationary. This situation will approximate that in which the ambient medium is nonstationary when the *duct* mean flow Mach number is much less than unity. This restriction will be discussed further in Sec. III.

Equation (1) assumes a linearized approximation in which the radial component of the perturbation velocity is neglected. It leads us to a version of equation (2.10) of Howe,[11] modified for compressibility:

$$\frac{1}{r}\frac{\partial}{\partial r}\left(r\frac{\partial B}{\partial r}\right)+\frac{\partial^2 B}{\partial z^2}+k^2B = -\frac{\sigma\mathscr{U}R}{r}H(z)\delta'(r-R)e^{i\kappa z}, \tag{3}$$

where H is the Heaviside unit function, $\kappa=\omega/\mathscr{U}$, and σ represents the amplitude of the circulation of the shed vorticity per unit axial length of the jet. The symbols r and z are coordinate variables defined with respect to Fig. 1. Equation (3) is axisymmetric as required by the symmetry of the excitation.

To solve this inhomogeneous Helmholtz equation, we will make use of the relation:

$$B=\int\int\int_{V_0}\rho_s G\,dv_0-\frac{1}{4\pi}\int\int_{S_0}B\,\frac{\partial G}{\partial n_0}\,ds_0+\frac{1}{4\pi}\int\int_{S_0}G\,\frac{\partial B}{\partial n_0}\,ds_0, \tag{4}$$

where $\partial/\partial n_0$ is the outward normal derivative to the surface S_0, G is a Green's function depending on the boundary conditions at S_0, and the triple integral is taken over the volume of the duct. This is the formal solution of

$$\nabla^2 B+k^2 B=-4\pi\rho_s(\mathbf{r}). \tag{5}$$

In our case

$$\rho_s=\frac{1}{4\pi}\left(\frac{\sigma\mathscr{U}R}{r}\,H(z)\,\delta'(r-R)e^{i\kappa z}\right). \tag{6}$$

We will appeal to the Green's function expansion:

$$G_k(\mathbf{r}|\mathbf{r_0})=-\frac{8\pi}{ia^2}\sum_{n=0}^{\infty}\frac{J_0(j_n(r/a))J_0(j_n(r_0/a))}{k_n J_0^2(j_n)}\times\begin{cases}\cos k_n z e^{ik_n z_0}, & z_0>z>0,\\ \cos k_n z_0 e^{ik_n z}, & z>z_0>0,\\ \cos k_n z e^{-ik_n z_0}, & z_0<z<0,\\ \cos k_n z_0 e^{-ik_n z}, & z<z_0<0,\end{cases} \tag{7}$$

where $k_n=\sqrt{k^2-(j_n/a)^2}$, and j_n is the nth zero of the J_1 Bessel function. This expansion, which may be derived from methods in Morse and Feshbach,[18] has an explicit discontinuous axial derivative and is bilinear in the radial coordinates. It has a normal derivative equal to zero across both sides of the plane of the orifice plate and the cylindrical wall of the duct. These properties are of great advantage in the present calculation as they imply the second term in Eq. (4) will be identically zero.

We now turn to the other terms in Eq. (4), and divide the duct into two sections about the coordinates of the orifice plate at $z=0$. Considering first the region $z>0$ and evaluating the source term, we have

$$B_V(r,z)=\int\int\int_{V_0}\rho_s G\,dv_0=-\frac{2\sigma\mathscr{U}R}{ia^2}\sum_{n=1}^{\infty}\frac{J_0(j_n(r/a))J_1(j_n(R/a))j_n}{k_n a J_0^2(j_n)}\times\left(\frac{i\kappa e^{ik_n z}-ik_n e^{i\kappa z}}{\kappa^2-k_n^2}\right). \tag{8}$$

This term was evaluated assuming κ and k to have small positive imaginary parts to make the infinite z_0 integral converge (see Munt,[10] page 613). We have also employed term by term differentiation in the Green's function expansion. It should be noted that the $n=0$ term has been omitted as it evaluates to zero for all nonzero κ and k, and we assume the solution to be a continuous function of these variables. Next we evaluate the surface term in this region, which yields:

$$B_{S^+}(r,z)=\frac{1}{4\pi}\int\int_{S_0}\frac{\partial B}{\partial n_0}\,G\,ds_0=\frac{2}{ia^2}\sum_{n=0}^{\infty}\frac{J_0(j_n(r/a))e^{ik_n z}}{k_n J_0^2(j_n)}\,\Omega_n, \tag{9}$$

where Ω_n is defined by

$$\Omega_n=\int_0^R u(r_0)J_0\left(j_n\,\frac{r_0}{a}\right)r_0\,dr_0, \tag{10}$$

where

$$u(r_0)=\left(\frac{\partial B(r_0,z_0)}{\partial z_0}\right)_{(z_0=0)}\qquad 0\leqslant r_0<R. \tag{11}$$

In the region $z<0$, we have for the surface term:

$$B_{S^-}(r,z)=\frac{1}{4\pi}\int\int_{S_0}\frac{\partial B}{\partial n_0}\,G\,ds_0=-\frac{2}{ia^2}\sum_{n=0}^{\infty}\frac{J_0(j_n(r/a))e^{-ik_n z}}{k_n J_0^2(j_n)}\,\Omega_n. \tag{12}$$

The incident pressure wave described at the start of this section will define a corresponding enthalpy wave. We will group this incident wave and an ideal reflection from the orifice plate as a wave perturbation term:

$$(B_0 e^{ikz}+B_0 e^{-ikz}). \tag{13}$$

Hence, the fields for $z>0$ and $z<0$ are given by

$$B_+(r,z)=B_V(r,z)+B_{S^+}(r,z)\quad z>0 \tag{14}$$

and

$$B_-(r,z)=(B_0 e^{ikz}+B_0 e^{-ikz})+B_{S^-}(r,z)\quad z<0, \tag{15}$$

respectively. An examination of Eq. (5) reveals that there exist no sources of fluctuating enthalpy in the opening of the orifice for $r<R$. Hence we shall assume that the enthalpy and the axial enthalpy gradient are continuous across the orifice opening. We will, therefore, match the $z<0$ and $z>0$ expressions for these fields at $z=0$, for $r<R$. The continuity of the axial enthalpy gradient is enforced by the use of the same symbol for the latter (this is contained in Ω_n) in both of the field expressions (9) and (12). This procedure yields:

$$\frac{1}{2}\left(B_0-\frac{1}{2}\,B_V(r,0)\right)=\frac{1}{ia^2}\sum_{n=0}^{\infty}\frac{J_0(j_n(r/a))}{k_n J_0^2(j_n)}\,\Omega_n. \tag{16}$$

This equation needs now to be modified slightly to obtain our final form. We wish to group the $n=0$ term of the summation on the r.h.s. with the B_0 term on the l.h.s. This will produce the term

$$B_\Delta\overset{\text{def}}{=}B_0-\frac{2}{ika^2}\int_0^R u(r_0)r_0\,dr_0=\frac{1}{2}\Delta B \tag{17}$$

within the parentheses on the l.h.s. The term B_Δ, will be of use in Sec. III where it will be assumed that $ka<3.83$ so that only the fundamental mode (nominally a plane wave) propa-

gates (see Sec. III). In this case ΔB will represent the difference in enthalpy in the far field, away from the orifice plate.

Both B_Δ and ΔB must remain finite as $k \to 0$, in which case ΔB will limit to the applied enthalpy perturbation described by Howe[11] (again see Sec. III). Rewriting Eq. (16) in terms of B_Δ we have our central equation for this section:

$$\frac{1}{2}(B_\Delta + B_s) = \frac{1}{ia^2} \sum_{n=1}^{\infty} \frac{J_0(j_n(r/a))}{k_n J_0^2(j_n)} \Omega_n, \tag{18}$$

where

$$B_s = -\tfrac{1}{2} B_V(r,0)$$

$$= \frac{\sigma \mathscr{U} R \kappa}{a^2} \sum_{n=1}^{\infty} \frac{J_0(j_n(r/a)) J_1(j_n(R/a)) j_n}{k_n a J_0^2(j_n) \kappa(\kappa + k_n)}. \tag{19}$$

Equation (18) is an integral equation for the unknown enthalpy gradient $u(r_0)$, which depends on an unknown parameter σ (the amplitude of the circulation of the shed vorticity per unit axial length of the jet).

To solve Eq. (18) we begin by expanding the unknown enthalpy gradient $u(r_0)$ in terms of a series of even Legendre polynomials:

$$u(r_0)\sqrt{R^2 - r_0^2} = \sum\nolimits_{m=0}^{\infty} U_m P_{2m}\left(\sqrt{1 - \frac{r_0^2}{R^2}}\right). \tag{20}$$

(The Legendre polynomials produce a number of conveniences later in the analysis, such as the production of Gegenbauer type integrals which have simple representations in terms of Bessel functions. For background on these integrals, see Watson,[19] page 378.) This expansion will be very efficient if the form of the edge singularity in the enthalpy gradient (which we will later remove, and in the process determine σ) is $(R^2 - r_0^2)^{-1/2}$. This is the case for the solution of Laplace's equation for a circular hole in a thin infinite plane with homogeneous Neumann conditions (see Lamb[19]). The same form for the singularity will be valid for the Helmholtz equation very near the rim of the orifice plate, as the spatial coordinates here will vary on a scale much smaller than a wavelength. It should also be noted that only even polynomials have been used due to the axial symmetry of the enthalpy field.

What we wish to do now is to form a matrix equation from Eq. (18). The usual Galerkin type procedure for this would be to substitute expansion (20) into Eq. (18), and then multiply each side of the resulting equation by the set of factors (incorporating the Legendre polynomials):

$$P_{2m}\left(\sqrt{1 - \frac{r^2}{R^2}}\right) \frac{r}{\sqrt{R^2 - r^2}} \quad m \geqslant 0, \tag{21}$$

and integrate term by term from 0 to R. However, expression (8) for the source integral contains a derivative of the Green's function. This implies that there will be a discontinuity in the source integral with respect to the source points. (The derivative of the Green's function arises from the dipole nature of the source, which can be seen from integration by parts.) The discontinuity manifests itself in the series in Eq. (8). This series has been formed from term by term differentiation of the original Green's function series, and it is not uniformly convergent over the closed interval $[0,R]$. In particular, it is conditionally convergent at all points except $r = R$, where it is divergent. Integrating this series term by term over this region will produce a divergent sum later in the calculation.

In order to overcome this difficulty, we have developed a technique which we will describe presently. The value of this technique is that it enables the series in Eq. (19), as it stands, to be integrated term by term. [The series in Eq. (19) is the same as the one occurring in Eq. (8) with z set equal to zero.] We will verify the technique analytically in Sec. II, for the limiting case of the problem dealt with by Howe.[11] We add further that techniques of a similar genre to that which we will describe have been employed by authors in the field of statistical mechanics, where divergent perturbation series are often encountered (see McComb,[20] Chap. 5).

The procedure we have adopted is as follows. First we make the replacement $R \to R^-$, with $R^- < R$, in the factors of (21). Next we integrate both sides of Eq. (18) over a closed interval $[0,R^-]$.

We then *renormalize* expressions arising from the sum in (8) to make them differentiable in R^- at the point $R^- = R$. [The word ''renormalize'' is used here and throughout this paper in the sense described by McComb[20] (see Chap. 5).] This will be equivalent to making the definition:

$$R^- \overset{\text{def}}{=} \gamma R, \tag{22}$$

and then renormalizing expressions arising from the sum in (8) to make them differentiable in γ at the point $\gamma = 1$. We shall show later that if γ is considered to be a complex variable, the procedure we have outlined amounts to making an analytic continuation to the divergent series resulting from Eq. (8). We thus, in effect, keep the observation points r away from the source points r_0 until the source integral has been evaluated.

This procedure results in a set of simultaneous equations which may be represented as the matrix equation:

$$A\mathbf{U} = \mathbf{B}, \tag{23}$$

where the components of the vector $\mathbf{B}$ are given by

$$B_m = \frac{1}{2}\left(B_\Delta \frac{R}{a} \delta_{0m} + \frac{\sigma \mathscr{U} R \kappa}{a^2} S_m\right), \tag{24}$$

where

$$S_m = \widehat{\lim_{\gamma \to 1}} \sum_{n=1}^{\infty} \frac{J_1(j_n(R/a)) j_n I_{mn}(\gamma R)}{k_n a J_0^2(j_n) \kappa(\kappa + k_n)} \tag{25}$$

and

$$I_{mn}(\gamma R) = \frac{R}{a} \int_0^{\pi/2} P_{2m}(\cos\theta) J_0\left(j_n \frac{\gamma R}{a} \sin\theta\right) \sin\theta \, d\theta. \tag{26}$$

The components of the matrix A are given by

$$A_{mn}=\frac{1}{2i}\left(\frac{R}{a}\right)\sum_{n'=1}^{\infty}\frac{J_{2m+1/2}(j_{n'}(R/a))J_{2n+1/2}(j_{n'}(R/a))}{k_{n'}aJ_0^2(j_{n'})j_{n'}}\times\left\{\frac{\Gamma(m+\frac{1}{2})\Gamma(n+\frac{1}{2})}{\Gamma(m+1)\Gamma(n+1)}\right\}. \tag{27}$$

It can be seen that the infinite sum in Eq. (8) has been transformed, via the integration process, into the convergent sum S_m defined by Eq. (25). This sum will, however, alter its convergent status throughout the course of the calculation. The symbol $\widehat{\lim}_{\gamma\to 1}$ occurring in front of the sum in Eq. (25) means that we must take the limit as $\gamma\to 1$ of this sum, while renormalizing any expressions arising from it, to make them differentiable in γ at $\gamma=1$. We will find it necessary only to retain the factor γ in the *arguments* of functions occurring in the summand of Eq. (25). In other cases, the factor γ may be collected outside the infinite sum and will have no bearing on the renormalization procedure. Furthermore, we have already set $\gamma=1$ in the infinite sum on the r.h.s. of Eq. (18). [This has given rise to the A_{mn} terms of Eq. (27).] This is allowable, since the sum can be shown to be uniformly convergent on $[0,R]$ *before* term by term integration.

The integrals in Eq. (26) are similar to the Gegenbauer integrals except insofar as the integration range extends only to $\pi/2$ rather than π. Setting the integrals in this form requires the change of variable: $r_0=R\sin\theta$. Following our comments on the inclusion of γ, these integrals may be evaluated as

$$I_{mn}(\gamma R)=\frac{1}{2}\frac{R}{a}\left[\frac{2}{(j_n(R/a))}\right]^{1/2}\frac{\Gamma(m+\frac{1}{2})}{\Gamma(m+1)}J_{2m+1/2}\left(j_n\frac{\gamma R}{a}\right), \tag{28}$$

$$I_{00}=\frac{R}{a} \tag{29}$$

(see Watson,[21] page 379). Provided A is invertible (a fact which for the moment we will tacitly assume), Eq. (23) may be solved for **U**. We will find it necessary to write out an explicit expression for the components of **U**. This is given as

$$U_m=\frac{1}{2}\sum_{m'=0}^{\infty}\left(B_\Delta\frac{R}{a}\delta_{0m'}+\frac{\sigma\mathscr{C}R\kappa}{a^2}S_{m'}\right)A^{-1}_{m'm}, \tag{30}$$

where A^{-1} is the inverse of A. (Note that we have introduced the notation $A^{-1}_{m'm}$ for the components of A^{-1}.)

Now, to find the vortex strength σ we will employ the Kutta condition. This condition, as stated earlier, requires that the velocity field remain finite as $r\to R$. A trivial rearrangement of Eq. (20) yields

$$u(r_0)=\frac{1}{\sqrt{R^2-r_0^2}}\sum_{m=0}^{\infty}U_mP_{2m}\left(\sqrt{1-\frac{r_0^2}{R^2}}\right), \tag{31}$$

which implies that for the Kutta condition to be satisfied it is necessary that

$$\sum_{m=0}^{\infty}U_mP_{2m}(0)=0. \tag{32}$$

(It will be seen shortly that this assumption also provides a unique expression for σ.) Using the limiting form for the Legendre polynomials given by Abramowitz and Stegun[22] (page 777), Eq. (32) simplifies to

$$\sum_{m=0}^{\infty}(-1)^m\frac{\Gamma(m+\frac{1}{2})}{\Gamma(\frac{1}{2})\Gamma(m+1)}U_m=0. \tag{33}$$

Finally, by substituting Eq. (30) into Eq. (33) and rearranging the resultant expression, we have

$$\frac{\sigma}{B_\Delta}=-\left(\frac{a^2}{\mathscr{C}R\kappa}\right)\left(\frac{R}{a}\right)\frac{\Sigma_{m=0}^{\infty}G_mA^{-1}_{m0}}{\Sigma_{m'm=0}^{\infty}A^{-1}_{m'm}G_mS_{m'}}, \tag{34}$$

where

$$G_m=(-1)^m\frac{\Gamma(m+\frac{1}{2})}{\Gamma(\frac{1}{2})\Gamma(m+1)}. \tag{35}$$

This equation renders an expression for the ratio of the circulation density of the shed vorticity to B_Δ: the latter being proportional to the far-field enthalpy difference across the orifice plate ($B_\Delta=\Delta B/2$), when $ka<3.83$. Equation (34) is in essence a generalization of Eq. (2.35) of Howe.[11] Its form is substantially more complicated, however, due to the cylindrical geometry and the existence of compressibility in the fluid.

II. THE LIMITING CASE

We expect Eq. (34) to limit to Howe's Eq. (2.35) as $kR\to 0$ and $R/a\to 0$. We will examine this limit now to demonstrate the necessity for the renormalization procedure we have just outlined. Small R/a and kR approximations may be made to the functions occurring in Eq. (34) and the equations it depends on [i.e., Eqs. (24)–(27)]. These may be used to arrive at the following limiting expression for the strength of the shed vorticity:

$$\sigma_{\lim}=\frac{\Delta B}{i\kappa R\mathscr{C}}\left[\widehat{\lim_{\gamma\to 1}}\int_0^{\infty}\frac{J_1(\mu)\mu\cos\gamma\mu}{\kappa R(\kappa R+i\mu)}d\mu\right]^{-1} \tag{36}$$

(where the factor γ has been retained only in the argument of the cosine function following the comments in Sec. I). A proof of this is given in Wendoloski[23] (pages 34–35).

A preliminary inspection of the integral in this last expression shows that it has a real part which is identical to the real part of the integral in Eq. (2.35) of Howe.[11] The imaginary part, however, is not in the same form. We note now that if we let $\gamma\to 1$ before performing the integration, this integral will not converge.

We will demonstrate these facts as follows. Let $\gamma=1$, then

$$\int_0^{\infty}\frac{J_1(\mu)\mu\cos\mu}{\kappa R(\kappa R+i\mu)}d\mu=\int_0^{\infty}\frac{J_1(\mu)\mu\cos\mu}{\kappa R((\kappa R)^2+\mu^2)}\times(\kappa R-i\mu)d\mu.$$

The real part of this is

$$\mathscr{I}_{\text{real}}=\int_0^{\infty}\frac{J_1(\mu)\mu\cos\mu}{(\kappa R)^2+\mu^2}d\mu, \tag{37}$$

which is identical to the real part in Howe's integral. The imaginary part of the integral, however, is

$$\mathscr{I}_{\text{imag}} = -\frac{i}{\kappa R}\int_0^\infty \frac{J_1(\mu)\mu^2\cos\mu}{(\kappa R)^2+\mu^2}\,d\mu. \tag{38}$$

An examination of this integral reveals it to be of the form:

$$\sqrt{\frac{\pi}{2}}\int_0^\infty \frac{x^{\varrho-1}J_v(bx)}{x^2+\zeta^2}\left[J_\nu(ax)\cos\frac{1}{2}(\varrho+v-\nu)\pi + Y_\nu(ax)\sin\frac{1}{2}(\varrho+v-\nu)\pi\right]$$
$$= -\sqrt{\frac{\pi}{2}}\,I_v(b\zeta)K_\nu(a\zeta)\zeta^{\varrho-2}, \tag{39}$$

with $\varrho=7/2$, $v=-1/2$, $\nu=1$, $a=b=1$, and $\zeta=\kappa R$ [see Watson,[21] page 430, Eq. (6)]. The problem is that the condition $a=b=1$ causes a nonoscillatory term to occur in the asymptotic expansion of the integrand causing the integral to diverge. Now, let us retain the γ factor in the argument of the cosine. Our integral then remains as:

$$\mathscr{I} = \int_0^\infty \frac{J_1(\mu)\mu\cos\gamma\mu}{\kappa R(\kappa R+i\mu)}\,d\mu, \tag{40}$$

with $\gamma<1$. We may now use Eq. (39) to evaluate the imaginary part:

$$-\frac{i}{\kappa R}\int_0^\infty \frac{J_1(\mu)\mu^2\cos\gamma\mu}{(\kappa R)^2+\mu^2}\,d\mu$$
$$= -i\sqrt{\frac{\pi}{2}}\,I_{-1/2}(\gamma\kappa R)K_1(\kappa R)(\kappa R)^{1/2}$$
$$= -\frac{i}{\sqrt{\gamma}}\cosh(\gamma\kappa R)K_1(\kappa R). \tag{41}$$

As $\gamma\to 1$, the r.h.s. of the last result will tend to

$$-i\cosh(\kappa R)K_1(\kappa R), \tag{42}$$

which is identical to the imaginary part of Howe's integral. [See Eq. (3.13) of Howe.[11]] So, assuming ΔB describes Howe's static perturbation "B_0" (see Sec. III), we may write our limiting result as

$$\sigma_{\text{lim}} = \frac{\Delta B}{i\kappa R\mathscr{U}}\left[\int_0^\infty \frac{\mu\cos\mu H_1^{(1)}(\mu)}{(\kappa R)^2+\mu^2}\,d\mu\right]^{-1}, \tag{43}$$

which is then identical to Eq. (2.35) of Howe.[11]

The closed form expression on the r.h.s. of Eq. (41) is equal to the integral on the l.h.s. of this equation for $\gamma<1$. It is also a differentiable function of γ at $\gamma=1$. Hence, it can be seen that by replacing the integral in Eq. (41) with this expression, we have renormalized the integral to make it differentiable in γ at the point $\gamma=1$.

If γ is considered to be a complex variable, then the r.h.s. of Eq. (41) is an analytic continuation of the integral on the l.h.s. of this equation, from any real set $E=[\epsilon,1-\varepsilon]$ (with $0<\epsilon<1-\varepsilon<1$) into the whole complex plane. It is also clear that the complex plane contains at least one *limit point* of E, hence, the analytic continuation is unique (see Silverman,[24] page 341). (A point P is said to be a limit point of an arbitrary set S if every neighborhood of P contains infinitely many distinct points of S. See Silverman,[24] page 25.)

III. THE PHYSICAL QUANTITIES

Let us consider again the original physical problem. An axial mean flow has been established in a cylindrical duct containing an orifice plate. A fluctuating pressure wave is incident upon the leading face of this plate. The presence of this wave will establish a fluctuating pressure differential across the orifice plate. The pressure disturbances correspond to fluctuating disturbances in enthalpy and we shall continue to use enthalpy as our fundamental field variable.

Although the primary concern in this paper is with acoustic absorption, we shall also give an expression for the Rayleigh conductivity of the orifice plate. Our primary purpose for this is to show that this expression limits to that given in Howe.[11] However, in Sec. IV we shall also calculate results for the long wavelength limit of the Rayleigh conductivity as a function of Strouhal number, for several open area ratios (the open area ratio being the ratio of the area of the orifice opening to the cross-sectional area of the duct).

It was stated in Sec. I that Eq. (1) was derived with the assumption that convection of the *sound field* by the mean flow is unimportant. In practice this usually implies that the duct mean flow Mach number M_d is small, that is, $M_d\ll 1$. This type of assumption is relatively common; see Dowling and Hughes[15] for instance, as well as, of course, Howe.[11] It follows that the primary effect of the flow field on the plane wave absorption coefficient (which will be defined shortly) is that arising from the convection of the *vorticity* shed from the orifice. In addition to this, the above papers assume, as does this one, that the orifice flow is effectively irrotational, except in the shed vortex sheets, whereupon the vorticity acts to contribute inhomogenous source terms for fluctuating enthalpy, as shown on the r.h.s. of Eq. (1).

In situations where the orifice open area ratio is large we may often have the case that $M_d^2\ll 1$ in place of $M_d\ll 1$. Under these circumstances convection of the sound field may be significant, invalidating our assumption in writing Eq. (1). However, for the purpose of comparison with future work (theoretical or experimental) we have plotted the absorption coefficient results, in the following section up to $M_d^2\ll 1$ (i.e., $M_d\leqslant 0.3$). The results for which $M_d\ll 1$ (i.e., $M_d\leqslant 0.1$) are shown in a different shade to distinguish them from the results for which $M_d\not\ll 1$, where we expect the convectionless approximation to become less accurate.

Concerning the orifice flow, we assume that the orifice mean flow Mach number $M_0=\mathscr{U}/c$ (where c is the speed of sound) satisfies $M_0^2\ll 1$. In this case, variations in the nonacoustic component of the fluid density, and also the speed of sound, may be neglected in the vicinity of the orifice (see Howe[25]).

In addition to the above considerations, it will be assumed that ka will be restricted so as to allow only the propagation of the fundamental mode (nominally a plane wave). Limiting ka in the above manner implies that the Rayleigh conductivity (which again will be defined shortly)

can be defined in terms of plane wave pressure differentials across the orifice. Here M_d will be assumed to be small enough so that the pressure differentials can be approximated by enthalpy differentials. When addressing the limit to Howe's result our definition for the Rayleigh conductivity, in terms of plane wave pressure (or enthalpy) differentials, will agree with Howe's definition, independently of ka, since the latter is given in terms of a *uniform* pressure perturbation across the orifice. For the convectionless approximation used in this paper this implies $ka<3.83$, given that the problem is axisymmetric. If convection were taken into account in a uniform circular duct flow, a Prandtl–Glauert transformation such as that used in Howe[12] or Wu and Lee[26] may be used to show that the cutoff frequencies are given by

$$f_n^{(M_d)}=f_n^{(0)}\sqrt{1-M_d^2}, \tag{44}$$

which implies that changes in cutoff frequency are negligible for our purposes even when $M_d=0.3$. The symbol in the superscript in Eq. (44) denotes the value of the duct mean flow Mach number for which the cutoff frequency applies. Actually the modal axial wave numbers become complex at frequencies above cutoff when a uniform flow exists in the duct. Exponential attenuation is still present, however, and this is all we require to neglect the propagation of all but the fundamental mode.

Applying the above arguments, it may be seen that the source term in Eq. (8) contributes no acoustically propagating component of enthalpy. There is a convected hydrodynamic field associated with the shed vorticity, varying axially as $e^{i\kappa z}$. This field, however, exists independently from the acoustic field at large distances from the orifice (see Howe,[12] page 91), and therefore will be omitted from the acoustic absorption calculation.

Drawing upon the above discussion, we assume that in the far-field upstream of the orifice plate, the acoustic enthalpy field contains only fundamental mode radiation. However, even when the convectionless approximation is valid for the calculation of the reflection and transmission coefficients of the fundamental mode, it may still be more precise to assume the far field consists of uniformly convected plane wave potentials rather than unconvected ones. This is especially the case when the phase of the field is important. An obvious example is if one wished to use a two microphone correlation technique (see Seybert and Soenarko[27]) to determine the reflection coefficient of an orifice in a flow duct. (Of course a measurement of pressure rather than enthalpy would be made in this case, see Howe[25] for the appropriate relations.) For this reason we shall suggest a more accurate form for the far field is

$$B_{z<0}=B_0\left\{\exp\left[\frac{ikz}{1+M_d}\right]+\mathscr{R}\exp\left[\frac{ikz}{1-M_d}\right]\right\} \tag{45}$$

[as found in Howe,[25] Eq. (2.13)], where $\mathscr{R}$, defined as the reflection coefficient of the incident wave, is assumed to be approximately the same as its unconvected value (when $M_d \ll 1$). Here $k=\omega/c$. Similarly, we write the transmitted acoustic enthalpy wave in the far field as

$$B_{z>0}=B_0\mathscr{T}\exp\left[\frac{ikz}{1+M_d}\right], \tag{46}$$

where the symbol $\mathscr{T}$ is defined as the transmission coefficient of the incident wave, and is again assumed to be approximately the same as its unconvected value. To see that these approximations for $\mathscr{R}$ and $\mathscr{T}$ can be reasonable we refer to Howe.[12] In this paper the diffraction of sound by a splitter plate in a rectangular section duct carrying a steady uniform flow is considered. A Prandtl–Glauert transformation is used to calculate the reflection coefficient. In this case the reflection coefficient is frequency independent, and is not changed at all by the inverse Prandtl–Glauert transformation. This is actually equivalent to the assumption we made in writing Eqs. (45) and (46).

In point of fact, though, our case differs from that which Howe addressed. First, our reflection coefficient is frequency dependent. In particular it is dependent on the axial wave number k_z (the component of the wave number in the direction of the flow) and the Strouhal number κR. This does not seem like a particularly serious problem, however, since the Prandtl–Glauert transformation used by Howe shows that these quantities scale by a factor of $\sqrt{1-M_d^2}$ in the presence of uniform axial flow. That is, even at $M_d=0.3$, k_z and κ are only altered by $\sim 5\%$.

More serious limitations to this argument are caused by the presence of the orifice: both in causing a nonuniform flow region and in its capacity as a reflector. The first condition strictly invalidates the Prandtl–Glauert transformation, although it is possible to imagine it may be applicable in the sense of cross-sectionally averaged flow. The second condition alters the boundary condition which must be applied along the rigid part of the orifice plate, since Neumann boundary conditions in the direction of the flow must also be transformed under a Prandtl–Glauert transformation (see Wu and Lee[26]). We are, however, only positing Eqs. (45) and (46) for $M_d \ll 1$, not for all $M_d<1$ as in Howe.[12]

We shall now write down expressions for the reflection and transmission coefficients of the incident plane wave. This may be done by reference to Eqs. (14), (15), and (17):

$$\mathscr{R}=\frac{B_\Delta}{B_0} \tag{47}$$

and

$$\mathscr{T}=\frac{B_0-B_\Delta}{B_0}, \tag{48}$$

for reflection and transmission, respectively. From these equations it is evident that $\mathscr{T}=1-\mathscr{R}$.

The fraction of incident acoustic energy which is absorbed at the orifice may be inferred from Eq. (2.14) of Howe[11] as

$$\mathscr{A}=1-|\mathscr{R}|^2-|\mathscr{T}|^2=1-|1-\mathscr{T}|^2-|\mathscr{T}|^2. \tag{49}$$

The symbol $\mathscr{A}$ will be referred to as the absorption coefficient.

Since we will be considering the absorption coefficient as a function of orifice Mach number (M_0), and open area ratio ($\alpha = R^2/a^2$), it will be convenient to rewrite the transmission coefficient as

$$\mathscr{T} = \frac{2\alpha}{iM_0}\left(\frac{U_0}{B_\Delta}\right) \Bigg/ \left(\kappa R + \frac{2\alpha}{iM_0}\left(\frac{U_0}{B_\Delta}\right)\right). \tag{50}$$

Using Eq. (30) we may determine U_0/B_Δ as

$$\frac{U_0}{B_\Delta} = \frac{1}{2}\sum_{m'=0}^{\infty}\left(\frac{R}{a}\,\delta_{0m'} + \left(\frac{\sigma}{B_\Delta}\right)\frac{\mathscr{C}R\kappa}{a^2}\,S_{m'}\right)A^{-1}_{m'0}, \tag{51}$$

with (σ/B_Δ) defined in Eq. (34). Mathematical techniques required for the numerical evaluation of Eq. (34) are given in Wendoloski,[23] pages 41–44.

When $M_d \ll 1$ we may apply the concept of the Rayleigh conductivity to the orifice. Let $m_0 e^{-i\omega t}$ be the fluctuating volume flux through the orifice produced by the enthalpy perturbation ΔB. The duct Mach number M_d is assumed to be small enough so that this is equivalent to a pressure perturbation. In this case

$$K = m_0\omega/i\Delta B, \tag{52}$$

as in Eqs. (3.1) and (5.9) of Howe.[11] Now assuming $u(r)$ is the axial enthalpy gradient given by Eq. (11) we may use the expansion in Eq. (31) to calculate m_0 as follows:

$$\begin{aligned} m_0 &= \frac{2\pi}{i\omega}\int_0^R u(r)r\,dr \\ &= \frac{2\pi}{i\omega}\int_0^R \sum_{m=0}^{\infty} U_m P_{2m}\left(\sqrt{1-\frac{r^2}{R^2}}\right)\frac{r}{\sqrt{R^2-r^2}}\,dr \\ &= \frac{2\pi}{i\omega}RU_0. \end{aligned} \tag{53}$$

The last step follows from the orthogonality of the Legendre polynomials. Using Eq. (53) with Eq. (52), and remembering that $\Delta B = 2B_\Delta$ we have the following expression for K:

$$K = -2R\left(\frac{\pi}{2}\frac{U_0}{B_\Delta}\right). \tag{54}$$

We shall plot this quantity as a function of the Strouhal number for several open area ratios, and demonstrate the numerical limit to the result in Howe.[11]

The analytical limit of K as $kR \to 0$ and $R/a \to 0$ is derived in Wendoloski[23] (pages 34–35, 38–39). The results are as follows. The S'_m term in Eq. (51) limits as

$$(S_{m'})_{\lim} = \delta_{0,m'}\left(\frac{aR}{2i}\right)\widehat{\lim_{\gamma\to 1}}\int_0^\infty \frac{J_1(\mu)\sin\gamma\mu}{\kappa R(\kappa R + i\mu)}\,d\mu, \tag{55}$$

$$\begin{aligned} &= \delta_{0,m'}\left(\frac{aR}{2i}\right)\left\{\int_0^\infty \frac{J_1(\mu)\sin\mu}{(\kappa R)^2+\mu^2}\,d\mu\right. \\ &\quad \left. - \frac{i}{\kappa R}\int_0^\infty \frac{J_1(\mu)\mu\,\sin\mu}{(\kappa R)^2+\mu^2}\,d\mu\right\}. \end{aligned} \tag{56}$$

Note that in this case, we may set $\gamma = 1$ inside the integral without altering the result [see comments following Eq. (25) on the inclusion of γ]. The imaginary integral inside the braces of Eq. (56) may be evaluated using Eq. (39), with $\varrho = 5/2$, $v = 1/2$, $\nu = 1$, $a = b = 1$, and $\zeta = \kappa R$. This renders:

$$\begin{aligned} &-\frac{i}{\kappa R}\int_0^\infty \frac{J_1(\mu)\mu\,\sin\mu}{(\kappa R)^2+\mu^2}\,d\mu \\ &\quad = -\sqrt{\frac{\pi}{2}}\,I_{1/2}(\kappa R)K_1(\kappa R)(\kappa R)^{3/2} \\ &\quad = -\frac{i}{\kappa R}\sinh(\kappa R)K_1(\kappa R). \end{aligned} \tag{57}$$

From this result it can be seen that the integral described in Eq. (56) is identical to that described by Eq. (3.11) of Howe.[11] Using this limiting form for $S_{m'}$ it is then shown that

$$\lim_{\substack{kR\to 0\\ R/a\to 0}}\left(\frac{U_0}{B_\Delta}\right) = -\frac{2}{\pi}(\varphi - i\varpi), \tag{58}$$

where

$$\varphi - i\varpi = 1 - \frac{\displaystyle\int_0^\infty \frac{\sin z H_1^{(1)}(z)\,dz}{z^2+(\kappa R)^2}}{\displaystyle\int_0^\infty z\,\frac{\cos z H_1^{(1)}(z)\,dz}{z^2+(\kappa R)^2}} \tag{59}$$

as in Eq. (3.8) of Howe.[11] We note here that the sign of the r.h.s. of Eq. (58) is consistent with *positive* acoustic resistance. This can be seen by an examination of Fig. 3 of Howe[11] and Eq. (54) of this paper. In the following section we give numerical results for the conductivity K and the absorption coefficient $\mathscr{A}$.

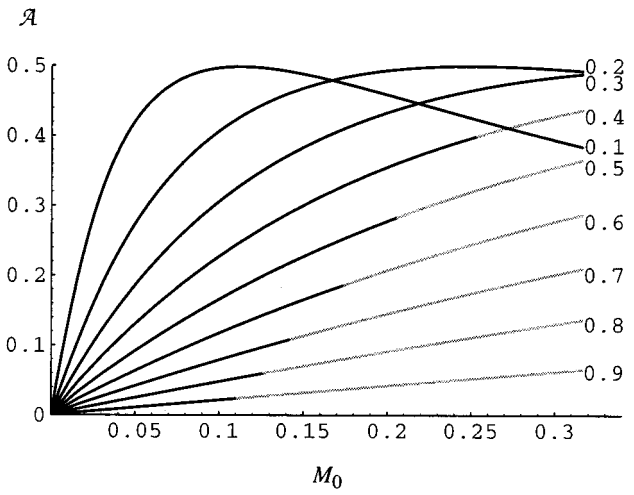

FIG. 2. The absorption coefficient $\mathscr{A}$ as a function of orifice mean flow Mach number M_0 for a range of open area ratios. The open area ratio is labeled to the right of the corresponding curve. Here $ka = 0.1$.

IV. RESULTS AND DISCUSSION

The acoustic absorption coefficient $\mathscr{A}$ as a function of orifice mean flow Mach number has been evaluated for a range of open area ratios and frequencies. These results are presented in Figs. 2, 3, and 4. The orifice Mach number has been limited so that $M_d^2 < M_0^2 \leqslant 0.1$, corresponding to our dis-

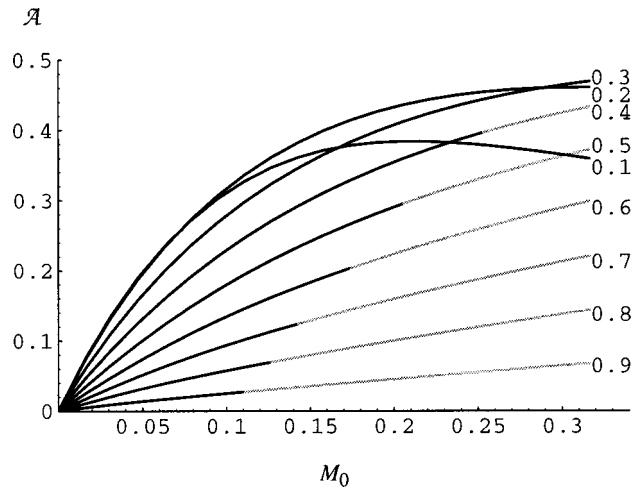

FIG. 3. The absorption coefficient $\mathscr{A}$ as a function of orifice mean flow Mach number M_0 for a range of open area ratios. The open area ratio is labeled to the right of the corresponding curve. Here $ka=1$.

cussion in Sec. III. Again, as discussed in this section, the results are in different shades depending on whether $M_d \ll 1$ (this was required for our convectionless approximation). That is, we have shown portions of the curves for which $M_d<0.1$ in black, and the portions of the curves for which $0.1\leqslant M_d<0.3$ in gray. As it is expected that the convectionless approximation will be more accurate when $M_d<0.1$, our comments in this section will be primarily directed at the black parts of the curves, but due to the regularity of the results they will usually also be true for the gray regions.

In Fig. 2, we see that for low frequencies ($ka=0.1$), an increase in open area corresponds to a decrease in absorption at Mach numbers lower than about 0.15. For higher frequencies the situation differs. In Fig. 3, for instance, we see that when $ka=1$, an open area ratio of 0.2 is as, or more, effective for absorption than that of 0.1 for the whole plotted range of Mach numbers. Figure 4 corresponds to a frequency just less than the cutoff for the first symmetric mode ($ka=3.83$). Here it appears as if there exists an optimal open area ratio for absorption. For the range of Mach numbers

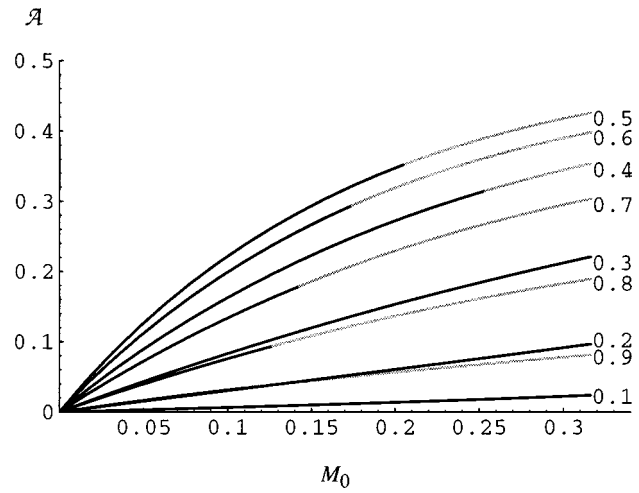

FIG. 4. The absorption coefficient $\mathscr{A}$ as a function of orifice mean flow Mach number M_0 for a range of open area ratios. The open area ratio is labeled to the right of the corresponding curve. Here $ka=3.83$.

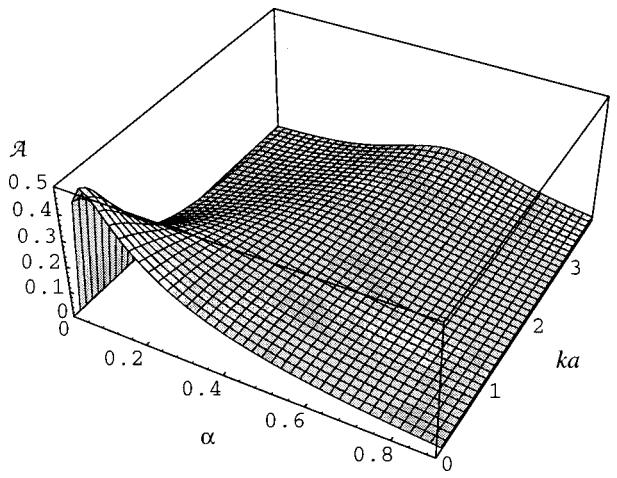

FIG. 5. The absorption coefficient $\mathscr{A}$ as a function of ka, and open area ratio (α) for an orifice mean flow Mach number of 0.05.

plotted, this optimal value would appear to be near 0.5.

A qualitative understanding of these results may be obtained if we consider that as the frequency is increased, a small open area ratio will lead increasingly toward acoustic reflection, which will reduce the amount of acoustic energy which can be absorbed. To demonstrate the dependence on frequency and open area ratio explicitly, a calculation has been made of the absorption coefficient as a function of frequency and open area ratio, for an orifice mean flow Mach number of 0.05. This is shown in Fig. 5. Calculations of the same nature were made for orifice mean flow Mach numbers of 0.1 and 0.2. The form of the results are of a similar nature, so the results are not shown here. Instead it will simply be commented here that the maximum value of absorption (with respect to the open area ratio) for a given frequency (i.e., ka value) decreases with increasing frequency. Furthermore, the value of the open area ratio required for maximum absorption for a given frequency increases with increasing frequency (as implied before in Figs. 2–4).

The average absorption levels with respect to frequency, however, are generally higher for the larger orifice mean flow Mach numbers. To demonstrate this, average values of $\mathscr{A}$, over the range $0\leqslant ka\leqslant 3.8$, versus open area ratio have been plotted in Fig. 6, for orifice mean flow Mach numbers of 0.05, 0.1, and 0.2. The averages referred to are described by

$$\mathscr{A}_{\mathrm{av}}=\frac{1}{ka_{\max}}\int_0^{ka_{\max}}\mathscr{A}(ka)\,dka, \tag{60}$$

where $ka_{\max}=3.8$. As for Figs. 2, 3, and 4, the portions of the curves for which $M_d<0.1$ are shown in black, while the remainder of the curve is shown in gray.

It can be seen from Fig. 6 that the open area ratio required for maximum average absorption varies considerably with Mach number. Nevertheless, it is also apparent that the sensitivity of $\mathscr{A}_{\mathrm{av}}$ to open area ratio decreases with decreasing Mach number. Correspondingly, it appears from Fig. 6 that an open area ratio of ~ 0.3 would render average absorptions within a few percent of maximum for all of the Mach numbers shown. As mentioned above, the average absorption

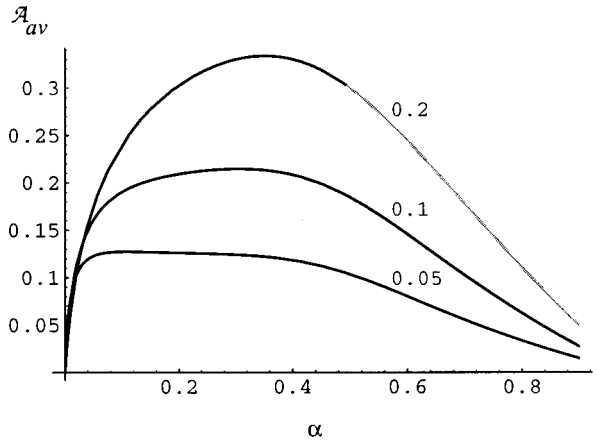

FIG. 6. The average absorption coefficient $\mathcal{A}_{\mathrm{av}}$ as a function of open area ratio (α) for orifice mean flow Mach numbers of 0.05, 0.10, and 0.20. The Mach number label is shown above the corresponding curve.

levels increase with increasing Mach number for essentially all values of the open area ratio. As a final comment on the absorption results, it should be noted that an upper bound on all the absorption coefficients we have calculated is 0.5. This is consistent with the results derived by Dowling and Hughes[15] for an isolated screen (i.e., not backed by a resonator) perforated with either slits or holes.

We will now give results on the long wavelength limit (i.e., $kR \ll 1$) of the Rayleigh conductivity K as a function of Strouhal number (κR). Evaluations were made for four values of α, for Strouhal numbers ranging from 0.1 to 10. The values of α chosen were 10^{-4}, 0.1, 0.5, and 0.9. The limiting value of $\alpha = 10^{-4}$ has been included for comparison with Howe.[11]

The conductivity as a function of Strouhal number is presented in the form of curves representing the modulus and phase of the complex ratio of the conductivity to its value as $\kappa R \to \infty$. This ratio will be referred to as the normalized conductivity (K_N). The value of the conductivity as $\kappa R \to \infty$ (i.e., as the mean flow tends to zero at finite frequency), may easily be obtained from Eq. (51) by setting the value of σ to zero.

Figure 7 illustrates the modulus of the normalized conductivity as a function of Strouhal number. It can be seen

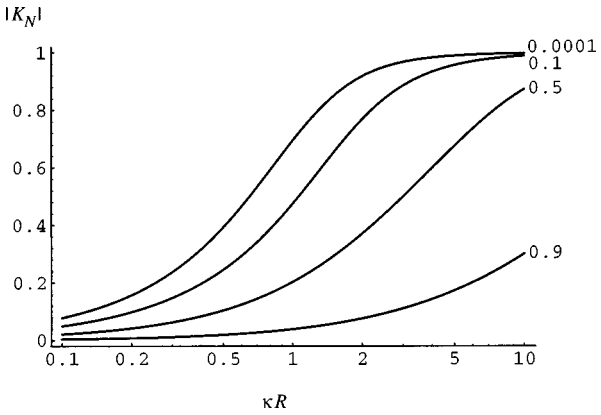

FIG. 7. The modulus of normalized Rayleigh conductivity $|K_N|$ as a function of the Strouhal number κR, for a variety of open area ratios (α). The open area ratio is labeled to the right of the corresponding curve.

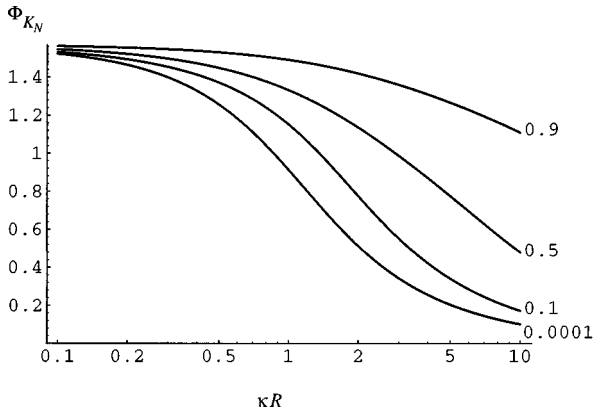

FIG. 8. The phase of normalized Rayleigh conductivity Φ_{K_N} as a function of the Strouhal number κR, for a variety of open area ratios (α). The open area ratio is labeled to the right of the corresponding curve.

that as the Strouhal number decreases (from infinity) there is a marked reduction in the modulus of the conductivity. In addition, it is evident that the effect is stronger for larger values of α. This is perhaps because, as the orifice's open area is increased, its zero flow conductivity will increase markedly so that additional impedance introduced by vortex shedding will be more significant. The assumption we make in saying this is that the impedance due to the vortex shedding is relatively insensitive to the presence of the duct walls.

Figure 8 illustrates the phase of the normalized conductivity as a function of Strouhal number (i.e., the phase difference between the conductivity at a finite value of κR and the conductivity as $\kappa R \to \infty$). It is evident from this figure that the phase of the conductivity changes by a factor of $\pi/2$ as the Strouhal number moves from zero to infinity. This implies that the nature of the associated acoustic impedance changes from resistive to reactive (through complex values) as the Strouhal number moves over the said range. It is further evident that this change in phase is effected more quickly (with respect to changes in the Strouhal number) for orifice plates with smaller open area ratios.

Finally, we illustrate the numerical limit of our calculation to the Rayleigh conductivity as calculated by Howe.[11] This is shown in Fig. 9.

V. CONCLUSIONS

The absorption coefficient and the Rayleigh conductivity of an orifice plate in a flow duct have been examined. The theory presented in this paper is asymptotic in nature, being strictly valid only when the duct mean flow Mach number is small compared with unity. Within the limits of this approximation, however, it appears that for orifice mean flow Mach numbers $\lesssim 0.2$, an orifice to duct open area ratio of 0.3 provides near optimal average absorption, for the band of frequencies bounded from above by the first symmetric mode cutoff frequency. The absorption curves and surfaces in general appear to take a simple form. This state of affairs is almost certainly due to the fact that an axisymmetric system has been assumed in which the frequency has been limited to be less than the first symmetric mode cutoff frequency. The

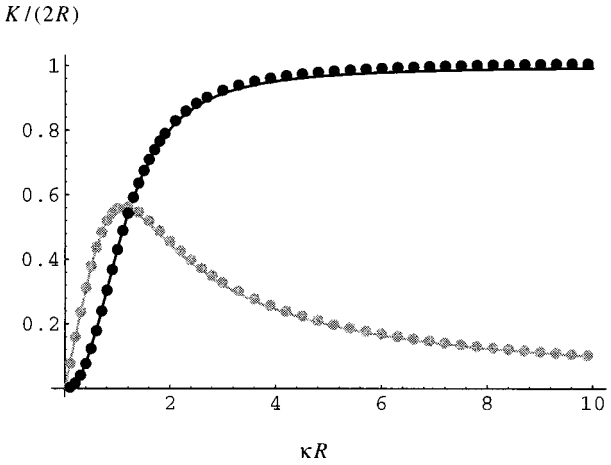

FIG. 9. A comparison of Howe's solution for the real and imaginary parts of the Rayleigh conductivity K of an infinite plane (solid line), with those for an open area ratio of 10^{-4} (points). The real part is shown in black (lines and points), and the imaginary part in gray.

work of Howe[12] shows that splitter plate absorption coefficients in flow ducts can develop complicated dependencies on frequency when modes other than the fundamental are allowed to propagate.

The analytical work in this paper reveals that Green's function series expansions can provide certain difficulties when cavities and dipole source terms are combined. In Howe's paper,[11] where no external cavity was present, a Fourier transform type solution could be used to represent the field due to the dipole source term. The solution to the resulting one-dimensional radial equation contained the gradient discontinuity explicitly. This was represented by the use of two solutions for the different regions in space. By choosing only one of these, one could manifestly satisfy the condition of keeping the source points away from the observer points until the relevant integrations were performed.

For the present problem, however, a solution has been developed by employing a renormalization procedure which, in effect, keeps the source and observer points of the Green's function apart until the source integral is evaluated. The method of solution depends to some extent on the availability of analytical results for the series and integrals one encounters. This does, however, appear to be a general property of renormalization techniques.

ACKNOWLEDGMENT

The author would like to thank Professor Ann Dowling for valuable discussions and suggestions made at the outset of this work.

[1] W. Borth, ''Schwingungs- und Resonanzerscheinungen in den Rohrleitungen von Kolbengebläsen (vibration and resonance phenomena in the ducts of piston compressors),'' Zeitschrift des Vereines Deutscher Ingenieure **60**, 565 (1916).
[2] K. U. Ingard and H. Ising, ''Acoustic nonlinearity of an orifice,'' J. Acoust. Soc. Am. **42**, 6–17 (1967).
[3] D. Ronneberger, ''Experimentelle Untersuchungen zum akustischen Reflexionsfaktor von unstetigen Querschnittsänderungen in einem luftdurschströmten Rohr (experimental investigations on the acoustic reflections coefficient of discontinuous changes of the cross-section in tubes with air flow),'' Acustica **19**, 222–235 (1967/68).
[4] D. W. Bechert, ''Sound absorption caused by vorticity shedding, demonstrated with a jet flow,'' J. Sound Vib. **70**, 389–405 (1980).
[5] A. Cummings and I. J. Chang, ''The transmission of intense transient and multiple frequency sound waves through an orifice plate with mean fluid flow,'' Rev. Phys. Appl. **21**, 151–161 (1986).
[6] A. Cummings, ''Transient and multiple frequency sound transmission through perforated plates at high amplitude,'' J. Acoust. Soc. Am. **79**, 942–951 (1986).
[7] P. O. A. L. Davies, ''Practical flow duct acoustics,'' J. Sound Vib. **124**, 91–115 (1988).
[8] M. S. Howe, ''On the absorption of sound by turbulence and other hydrodynamic flows,'' IMA J. Appl. Math. **32**, 187–209 (1984).
[9] *Encyclopaedic Dictionary of Physics*, edited by J. Thewlis (Macmillan, New York, 1962).
[10] R. M. Munt, ''The interaction of sound with a subsonic jet issuing from a semi-infinite cylindrical pipe,'' J. Fluid Mech. **83**, 609–640 (1977).
[11] M. S. Howe, ''On the theory of unsteady high Reynolds number flow through a circular aperture,'' Proc. R. Soc. London, Ser. A **366**, 205–223 (1979).
[12] M. S. Howe, ''Attenuation of sound due to vortex shedding from a splitter plate in a mean flow duct,'' J. Sound Vib. **105**, 385–396 (1986).
[13] S. W. Rienstra, ''Acoustic radiation from a semi-infinite annular duct in a uniform subsonic mean flow,'' J. Sound Vib. **94**, 267–288 (1984).
[14] Y. Fukumoto and M. Takayama, ''Vorticity production at the edge of a slit by sound waves in the presence of a low-Mach-number bias flow,'' Phys. Fluids A **3**, 3080–3082 (1991).
[15] A. P. Dowling and I. J. Hughes, ''Sound absorption by a screen with a regular array of slits,'' J. Sound Vib. **156**, 387–405 (1992).
[16] H. Levine and J. Schwinger, ''On the radiation of sound from an unflanged circular pipe,'' Phys. Rev. **73**, 383–406 (1948).
[17] M. S. Howe, ''Contributions to the theory of aerodynamic sound, with applications to excess jet noise and the theory of the flute,'' J. Fluid Mech. **71**, 625–673 (1975).
[18] P. M. Morse and H. Feshbach, *Methods of Theoretical Physics* (McGraw-Hill, New York, 1953).
[19] H. Lamb, *Hydrodynamics*, 6th ed. (Cambridge U.P., Cambridge, 1932).
[20] W. D. McComb, *The Physics of Fluid Turbulence* (Oxford U.P., New York, 1990).
[21] G. N. Watson, *A Treatise on the Theory of Bessel Functions*, 2nd ed. (Cambridge U.P., Cambridge, 1922).
[22] *Handbook of Mathematical Functions*, 9th ed., edited by M. Abramowitz and I. Stegun (Dover, New York, 1965).
[23] J. C. Wendoloski, ''Applications of Green's Functions to Acoustic Ducts and Cavities with Rigid Boundaries,'' Ph.D. thesis, Sydney University, 1995.
[24] R. A. Silverman, *Introductory Complex Analysis* (Dover, New York, 1972).
[25] M. S. Howe, ''Attenuation of sound in a low mach number nozzle flow,'' J. Fluid Mech. **91**, 209–229 (1979).
[26] T. W. Wu and L. Lee, ''A direct boundary integral formulation for acoustic radiation in a subsonic uniform flow,'' J. Sound Vib. **175**, 51–63 (1994).
[27] A. F. Seybert and B. Soenarko, ''Error analysis of spectral estimates with application to the measurement of acoustic properties using random sound fields in ducts,'' J. Acoust. Soc. Am. **69**, 1190–1199 (1981).

Environmental acoustic influences on array beam response

William Carey
79 Whippoorwill Road, Old Lyme, Connecticut 06371

James Reese
Applied Hydroacoustics, 4655 Cass Street, San Diego, California 92109

Homer Bucker
Spwar Systems Center, San Diego, California 92109

(Received 20 February 1997; revised 23 February 1998; accepted 17 April 1998)

Experimental data (environmental propagation loss and beam response) obtained in the Levantine Basin of the Mediterranean Sea are presented and compared to calculations performed with a multilayer, normal-mode computer model. The comparisons show good agreement between measured propagation loss and computer calculations. Beam response data show that the primary source of signal gain degradation is the bifurcated and broadened beam response. The degraded response pattern results from the combined effects of acoustic pressure field variations and motional array shape deformation. Calculations performed with the multilayer, normal-mode model show similar degraded response patterns caused by array tilting. These results indicate that system response and performance characteristics can be calculated for a specific sound channel as a function of the array shape and motion.
[S0001-4966(98)05607-0]

PACS numbers: 43.30.Es, 43.30.Pc, 43.20.Ye, 43.25.Yw [SAC-B]

INTRODUCTION

This paper presents transmission loss and array signal gain results obtained in the Levantine Basin of the Mediterranean Sea. A multilayer, normal-mode computer program model[1] was used to calculate transmission loss and array beam response patterns. These results demonstrate the importance of propagation effects that were present in the measurements and are consistent with previous work predicting array response using normal-mode and parabolic equation models.[1–3]

Array signal gain experiments have been performed with moderately long arrays, and the effects of multipath, shape, and motion have been reviewed and discussed elsewhere.[3,4] This paper presents calibrated acoustic transmission loss data, array beam response measurements, and array signal measurements that compare favorably with theoretical expectations of the response of a tilted array in a modal sound field. The comparison between calculations and theory is found to be good.

The measurements reported were collected during an experiment conducted in the eastern Levantine Basin of the Mediterranean Sea as shown in Fig. 1. A towed line array was used to receive acoustic signals transmitted by a source vessel. The source vessel towed a calibrated Honeywell HX-231F projector along a track while transmitting three tones simultaneously. The projector was towed at a nominal depth of 90 m at a speed of $\sim$5 kn. Depth variations of the source correspond to speed variations and in this experiment were not important. The array tow ship was steered to minimize motion effects and to keep the projector ship near broadside to the array. The array tow ship speed varied between 2.5 and 4.9 kn, which resulted in array depths between 130 and 200 m and array tilt at an average angle of $-2°$ (ranging between 0° and $-4°$). Nonacoustic data (heading, temperature, and depth) were continually monitored to ensure that the tilt and bow were minimal. The recorded variations in receiver shape, orientation, and motion enabled this analysis.

The measurement array consisted of 105 hydrophones with heading and depth sensors at the head and tail of the array. The array had 54 hydrophones spaced uniformly at 2.11 m, followed by 27 hydrophones spaced uniformly at 4.22 m, with the remaining 24 hydrophones spaced uniformly at 12.65 m. This provided a total physical aperture length of 533 m and total effective acoustic aperture of 530 m.

This system was a hard-wired geophysical array (8.9-cm diameter). Typical tow configurations consisted of 1000-m flag-faired armored tow cable, 350-m vibration isolation modules (VIMS) forward of the array 533 m in length, 305-m VIMS aft of the array and drogues. The tow platforms for these experiments were offshore supply vessels 48.8 m in length. Nonacoustic data (NAD) (temperature, heading, and depth) modules were located fore and aft of the acoustic sections. The hydrophone consisted of four series-connected ceramic elements. Each hydrophone group consisted of 4 (high-frequency) to 20 (low-frequency) series-parallel-connected hydrophones. The sensitivity of each hydrophone group at the input of its preamplifier was -186 dB *re:* (1 V/1 μPa), with a frequency response of -3 dB at 25 Hz.

The hydrophone groups were calibrated by use of a Lloyd Mirror[1] interference pattern. The results of this calibration showed that the absolute value of hydrophone sensitivity was 186 ± 1 dB *re:* 1 V μPa and are shown in Figs. 2 and 3. Figure 3 shows that, except for two ''bad'' hydrophone groups, the relative response was excellent. A noise calibration showed that the relative group sensitivities were ±0.9 dB at 57 Hz, ±1.3 dB at 67 Hz, and ±1 dB at 323 Hz.

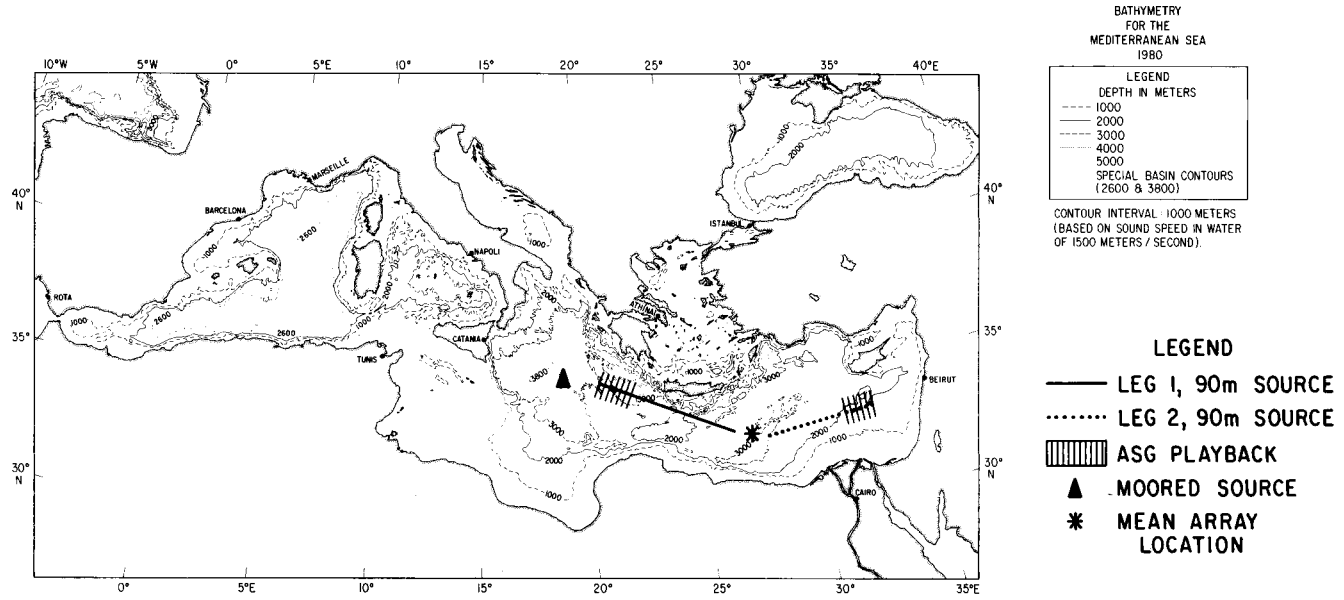

FIG. 1. The experiment in the Levantine Sea.

The directional response of the low-frequency hydrophone groups was observed.

Since the measurement array used twisted shielded-pair cable for transmission, equalizers were used to compensate for differences in transmission line lengths from the hydrophone groups in the array and in the two cable. The signals from each hydrophone group, after equalization, were amplified by a signal conditioning unit (SCU) that provided $+36$ dB of fixed amplification, and variable amplification from -12 to 42 dB in 6-dB steps. Analog SCU outputs were sampled at 2048 samples/s and converted to 8-bit digital words. The digitized signals, along with nonacoustic data, were routed via an input/output controller to a Bell and Howell Density Digital Recorder (HDDR). On-line beamforming was accomplished with a digital time domain beamformer (TDB) (64 beams) with computer-selectable beam steering, shading, and sector definition. The TDB could operate on the digitized signal or on the HDDR playback signal. Data quality and monitoring were accomplished with an HP-5420 spectrum analyzer on both hydrophones and beams.

The calibration of the beamformer was accomplished by the introduction of sinusoidal signals at the signal conditioning unit and digitized input. One of these calibrations showed that the beamformer was functioning properly. The electronic signals were also recorded on an HDDR and used to calibrate the 128 point-FFT analysis software that was used for postprocessing.

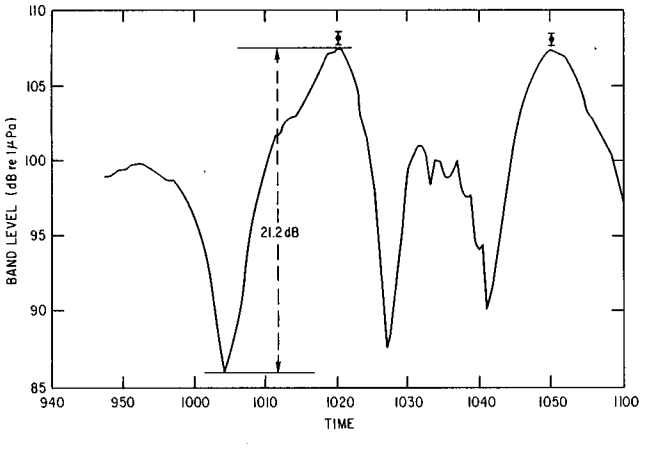

FIG. 2. The Lloyd Mirror interference pattern. The results of the mirror interference pattern measurement are shown as a function of time as the array moves by the moored source. Dots represent a mean hydrophone sensitivity of -186 dB *re:* 1 V/μ Pa. The closest point of approach is the region between the two highest peaks. The moored source was driven at 175 Hz with a level of 170 dB *re:* 1 μ Pa at 1 m.

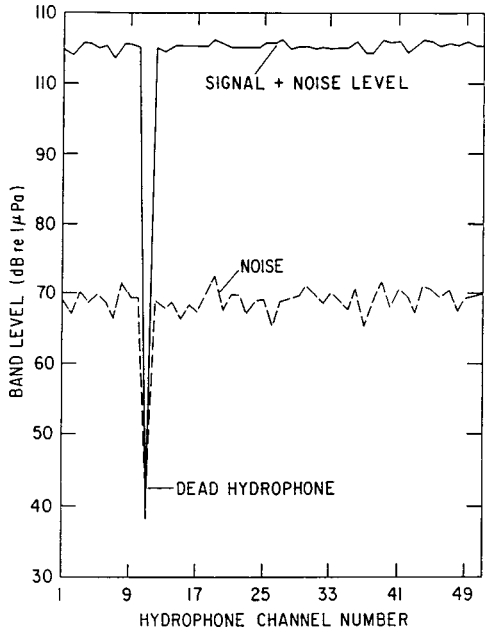

FIG. 3. Signal-plus-noise level and noise level versus hydrophone number. This figure shows the signal-plus-noise level versus hydrophone group number for the first 54 hydrophones during the Lloyd Mirror calibration. The corresponding noise level versus hydrophone number is also shown since both cures can be used to determine relative hydrophone calibrations.

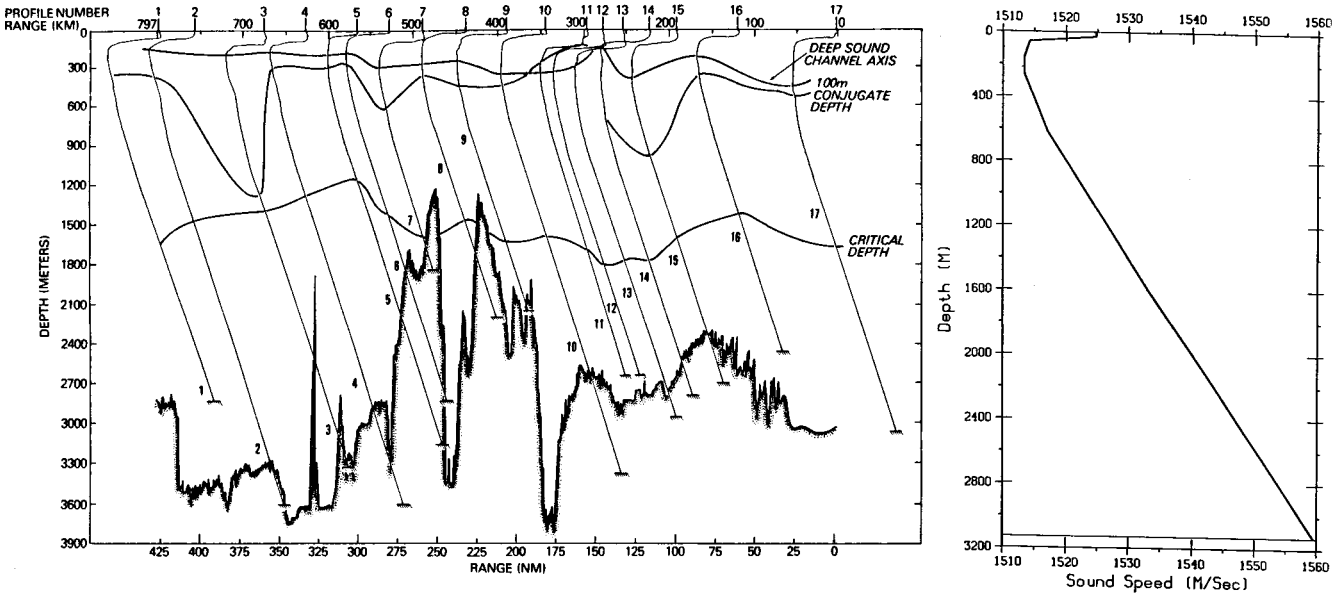

FIG. 4. Bathymetry and sound-speed profiles versus range along leg 1.

Batch processing was done at sea to determine the spectral characteristics of selected hydrophones and beams. The system processed 64 channels of information by digital filtering within the Floating Point systems (AP120B) array processor. The batch processing system used the Hewlett–Packard 21Mx series minicomputer with 20-megabyte disks, graphic line printers, and nine-track tape drives. Beam and single hydrophone power data, in selected 4- to 5-Hz bands, were recorded routinely on the nine-track tapes. These tapes were then replayed through the same batch processor to yield array gain and beam noise characteristics. This system, which operated with a resolution of 0.08 Hz, enabled the preliminary analysis of data to be performed on board the research vessel.

The batch processing system had a nonacoustic data system (NADS) that logged the nonacoustic data from the array subsystem and ships sensor systems on a minute-by-minute basis to provide a detailed summary of location, speed, heading, array heading, depths, tilt, and bow. This system allowed for the placing of selected sensor outputs that were used to monitor and to determine optimum tow condition.

The playback calibrations at the Naval Research Laboratory's (NRL) signal processing facility used the measured system's response calibration curve shown and phase compensation based on the phase corrected calibration signals for each hydrophone channel. Calibrated beamformer outputs were generated at 55, 169, and 323 Hz calibration frequencies from the HDDR tape. The NRL results were essentially the same as we had determined at sea.

Measurements of beam output power using fast Fourier transforms (FFT), which are discussed here, were based on a set of 54 beams equally spaced by wave number that correspond to an increment in cosine of 0.005, and steered to bracket the source bearing. These beam outputs and the output power of selected hydrophones were recorded as the source ship towed the projector along its track. These were used to determine transmission loss (TL), array signal gain degradation (ASGD), and array response patterns. In addition, extensive supporting environmental measurements of water temperature versus depth, bottom characteristics, and meteorology conditions were collected during the experiment.

Figure 4 shows the bathymetry and sound-speed structure along leg 1. A representative sound-speed profile for leg 1 is also shown and is the one used in the normal-mode model to calculate the propagation loss along leg 1. A nominal 90-m source for this composite profile would have a critical ray angle of 30.1° in waters of 3000-m depth.

I. MEASURED SOUND TRANSMISSION RESULTS

Transmission loss measurements were conducted to obtain data to validate transmission loss models used for predicting the performance of the array. The transmission loss data were partially processed and reduced at sea. FFTs were used to separate the acoustic signals that were digitized and recorded on the HDDR into 0.08-Hz frequency bins. The modulus of the complex Fourier coefficient was squared to determine the instantaneous intensity level in each frequency bin. These values were then averaged for 1 min to determine the average power level per frequency bin and recorded on tape and were used in the postanalysis for determining transmission loss. A requirement of the postanalysis determination of signal gain was that the estimate came from beam(s) that were steered in the direction of the source and sensor(s) with the frequency of the maximum signal response on the average hydrophone. The frequency of the maximum response was determined by examining neighboring FFT bins (zero filling was used to provide an interperlation and to minize scalloping loss) to the signal frequency (source frequency plus Doppler shift) for the maximum level FFT bins removed from this maximum provided an estimate of the noise power. For the most part, signal and noise data were

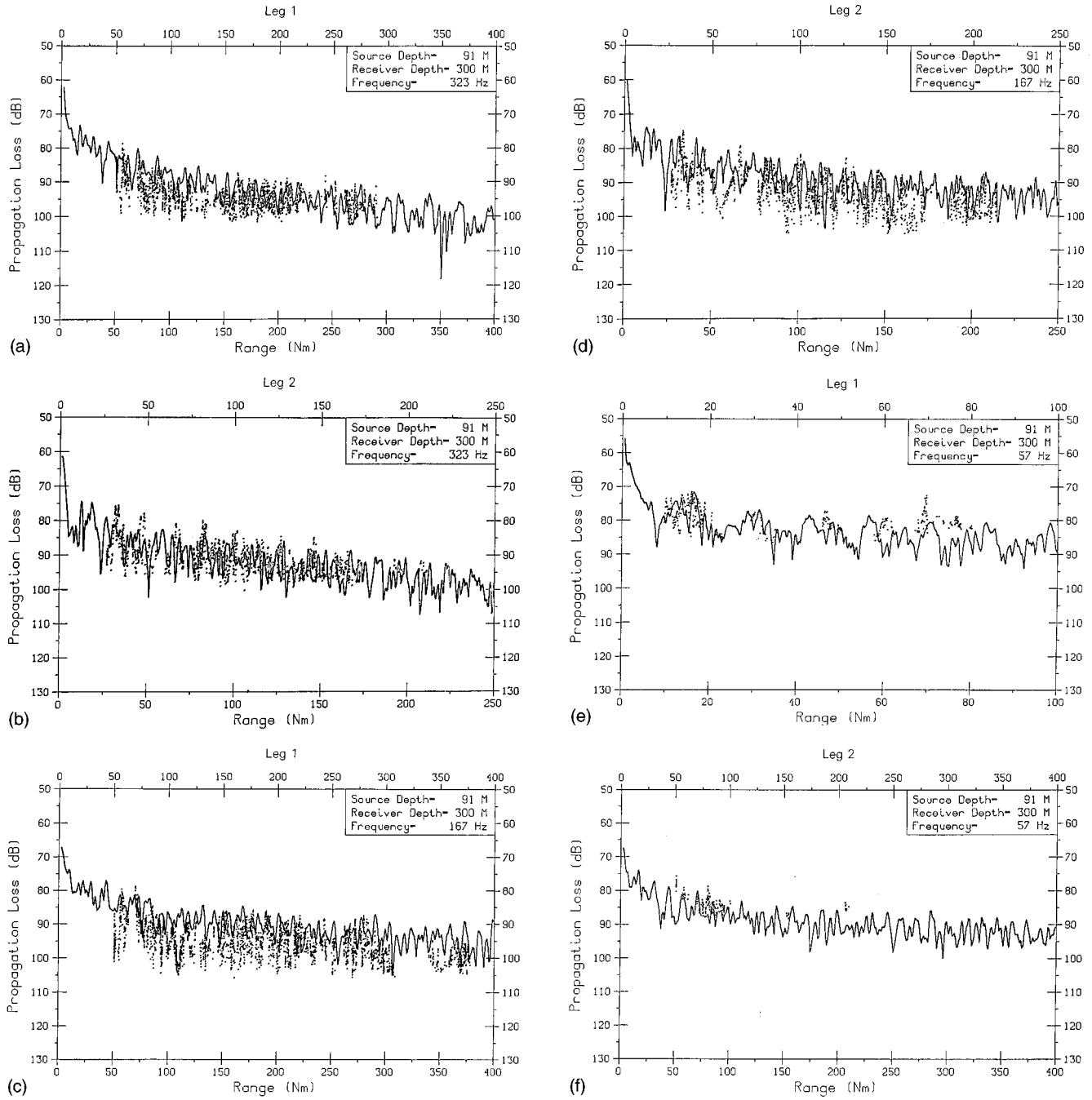

FIG. 5. Measured and computed propagation loss versus range for (small dots represent data and the solid line the calculated results): (a) leg 1 at 323 Hz, (b) leg 2 at 323 Hz, (c) leg 1 at 167 Hz, (d) leg 2 at 167 Hz, (e) leg 1 at 57 Hz, and (f) leg 2 at 57 Hz.

averaged over 28 hydrophone channels to obtain the average signal and noise level results that were to be plotted as a function of range.

Two tests were made on the signal intensity data points to ensure their validity. First, the signal-to-noise (S/N) ratio had to be at least 5 dB. Second, the frequency of the data point had to be close to the expected frequency. Figure 5 shows plots of propagation loss as 323, 167, and 57 Hz versus range for the two tow paths. The results for each tow leg are fairly consistent, as can be seen by the comparison of Fig. 2(a) and (b) at 323 Hz, Fig. 2(c) and (d) at 167 Hz, and Fig. 2(e) and (f) at 57 Hz. The paucity of data points on the 57-Hz plot is due to the high omnidirectional noise levels and the subsequent loss of data with S/N ratio's less than 3 dB.

II. THEORETICAL TRANSMISSION LOSS

A multilayer, normal-mode computer program model was used to generate theoretical transmission loss curves as a function of range for comparison with measured results obtained in the Levantine Basin. The model used can also calculate signal coherence between sensors. Propagation loss calculations were made for the three frequencies and the two tow run segments. Model inputs were source and receiver depths, the bottom depth, and a bottom loss curve (i.e., bot-

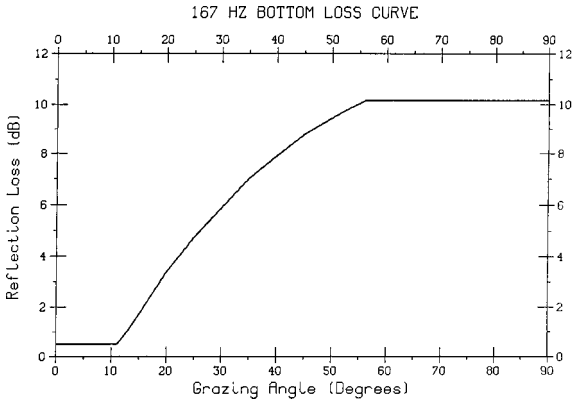

FIG. 6. 167-Hz bottom loss versus grazing angle (Ref. 5).

tom loss in dB versus grazing angle, Fig. 6[5]). Using the inputs provided, the model essentially provides an exact solution of the complex sound field (i.e., amplitude and phase) for a range-independent environment.

In situ sound-speed profiles collected during the two tow runs were used as inputs. Figure 4 shows a plot of the sound-speed profiles used in the leg 1 calculations. The profiles for leg 2 are similar in shape except for different sound speeds at the surface and the varying depth at each site (indicated by the line in the plot of Fig. 4). In most cases during the propagation measurements, the source and receiver were located such that there were several hundred meters of depth excess (the distance between the depth of the 0° ray and the sea bottom). Therefore one can say that there was no loss of sound energy due to bottom interactions during the measurements for most legs. (An exception to this is shown in Fig. 5, where the absence of received signals between the range of 310 and 340 nmi was due to sound interacting with a small seamount south of the Island of Crete.

The results of the measured propagation losses and the theoretical losses at the aforementioned legs were displayed on a composite plot for visual comparison. It should be mentioned that the theoretical losses were calculated at 1-nmi increments for leg 1, and 0.5-nmi increments for leg 2.

The overall comparison of the measured and theoretical curves at 167 Hz is very good. As a general rule, exact agreement between measured and theoretical sound levels is usually an exception. This is because the measured data will show more scattering of points as the result of interference from many different sound paths, the sensitivity of the receiving system to small changes in source and receiver depth, and the sound-speed profile. At this frequency and source receiver separation, volume scattering is not considered an important factor. In the theoretical curves shown, there is less scatter of data points because of the smoothing caused by 1-nmi and 0.5-nmi increments.

III. THE BEAMFORMING ALGORITHM

Let P'_{ij} be the complex field calculated by the normal-mode model at the lattice point jth depth ith range. The complex field of a wave incident at an angle θ is determined by the rotation about the vertical axis through a relative bearing angle θ where $\theta=0$ corresponding to direction of the source and receiver.

$$P_{ij}=R\cdot P'_{ij},$$

where R is the rotation matrix

$$R=\begin{Vmatrix}\cos\theta & \sin\theta\\ -\sin\theta & \cos\theta\end{Vmatrix}.$$

Since the field is determined at lattice point i,j; an interpolation must be performed to determine the hydrophone pressure field at positions between lattice points. The x_n, y_n component of the nth hydrophone location corresponding to a spacing within the lattice referred to the 0,0 element of the lattice is

$$x_n=(n-1)d\cos\theta\cos\phi,$$

$$y_n=(n-1)d\sin\theta\sin\phi,$$

where ϕ is the tilt angle and θ is the horizontal relative-bearing angle.

The complex acoustic field at the point (x_n,y_n) can be written

$$p_n=F^n_{ji}p^n_{ji},$$

where F is a bicubic-spline two-dimensional interpolator between adjacent lattice points.

The p_n is the interpolated complex acoustic field for the nth hydrophone and can be written as

$$p_n=A_n\exp(i\theta_n).$$

A_n is the real amplitude and θ_n is the phase of the field.

The voltage response of a plane-wave beamformer steered to the relative bearing θ_s is

$$Q(\theta,\theta_s)=\sum_{l=1}^{n} W_lA_l\exp(i(\theta_l-\theta_{sl})),$$

where

$$\theta_{sl}=2\pi(l-1)(d/\lambda)\sin\theta_s,\quad \lambda=C_0/f.$$

W_l is the weighting coefficient of the lth hydrophone, d is the distance between hydrophones, N is the total number of hydrophones, C_0 is the sound speed, and f is the frequency in Hz. The signal power of the beamformer is

$$IP_s(\theta_s=\theta)=Q(\theta,\theta_s)\cdot Q(\theta,\theta_s)^*|_{\theta_s=\theta}=\left|\sum_{l=1}^{n} W_lA_l\right|^2\rightarrow cN^2.$$

The mean hydrophone signal power is

$$\langle IP_{hs}\rangle=\sum_{l=1}^{n} W_l^2\cdot A_l^2/N\rightarrow c.$$

Then the signal gain may be written as

$$\text{signal gain (sg)}=IP_s(\theta_s=\theta)/\langle IP_{hs}\rangle$$

$$=\left|\sum_{l=1}^{n} W_lA_l\right|^2\Big/\sum_{l=1}^{n} W_l^2\cdot A_l^2/N\rightarrow N^2.$$

The differential array signal gain is then

TABLE I. Array results.

Frequency (Hz)	Leg No.	ASGD (dB)	σ	NOBS	Aperture (m)	Acoustical Aperture (m)
			At-sea results			
323	1	0.4	3.1	1163	114	112
323	2	0.2	2.0	1587		
175	1	1.0	2.3	547		
167	1	0.3	1.8	2351	228	224
167	2	0.2	1.5	1724		
57	1	2.9	2.0	144	533	519
57	2	2.3	2.0	435		
323		1.2		47		
		1.1				
57		1.1		49		
			FFT results			
323	2	0.6	0.8	59	533	530
	2	0.9	1.2	77		
167	1	0.8	1.6	234	533	530
	1	0.8	1.2	349		
	2	0.3	0.4	673		
	2	0.6	0.7	754		

Differential signal gain$=N^2/\mathrm{sg}=$(signal gain degradation)$^{-1}$, sgd (ASGD$=10\log[\mathrm{sgd}]$).

IV. SIGNAL GAIN AND BEAM RESPONSE RESULTS

Array signal gain (ASG) was determined for signals from the nominal 90-m towed source for frequencies of 323, 167, and 57 Hz.[6] The ASG was calculated when the S/N ratio on the average hydrophone was greater than or equal to 3 dB. Data were processed at sea in (0.08 Hz) Hann shaded bands and covered more than four (12.5 s) time samples. Peak-FFT bins and peak-beam, signal-plus-noise levels were used to estimate beam signal levels. The mean hydrophone level was estimated from four hydrophones over the first 114 m (effective HF acoustic aperture 112 m), 6 hydrophones over 228 m (effective MF acoustic aperture 224 m), and nine hydrophones spaced over the 533-m (effective LF acoustic aperture 519 m) aperture. Data were processed separately for legs 1 and 2 of the Levantine tow; comparable results were obtained during both tow legs as shown in Table I.[6]

The 112-m aperture and 224-m aperture ASG results at 323 and 167 Hz, respectively, yielded an average value within 2 dB of theoretical signal gain. The convention employed here is to designate the difference between theoretical signal gain and measured signal gain as the signal gain degradation (ASGD). The computer standard deviations (σ) were found to be 2 to 3 dB. These data were examined on a case-by-case basis, and three causes for the large σ's were identified: undersampling of the hydrophones; pronounced multipath and array shape effects; and contaminated data (that is, a tonal near the signal frequency caused by high and erroneous level to be measured by the omnidirectional hydrophone groups).

Only a few data points were obtained at 57 Hz that had a mean hydrophone S/N ratio greater than 3 dB. For this reason, the performance of the 530-m array was examined by use of the higher S/N ratio data at 323 and 167 Hz. Short

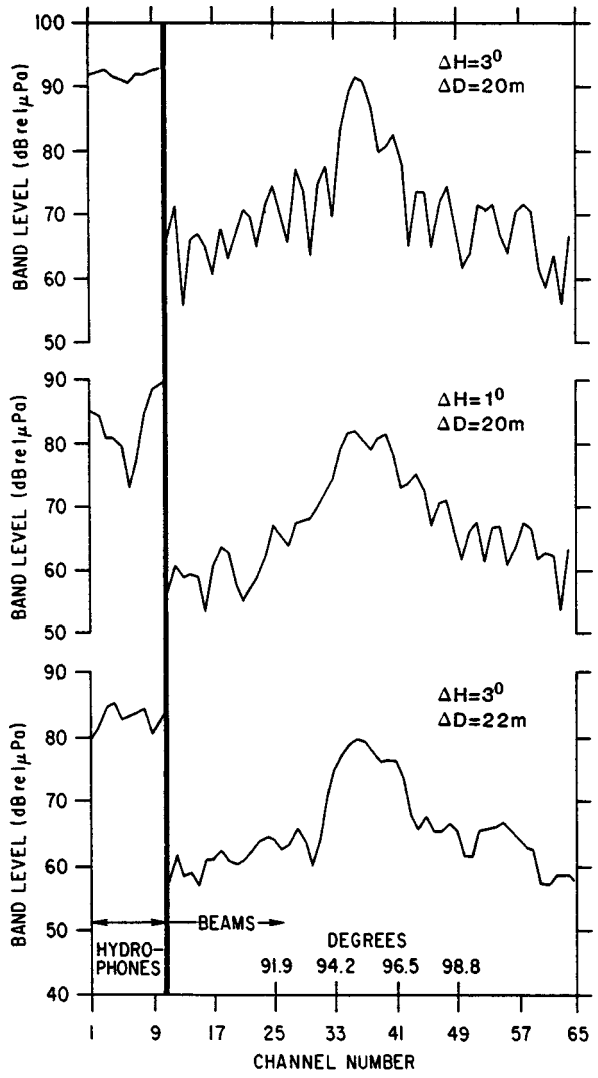

FIG. 7. The 533-m array response at 167 Hz illustrating: (a) nearly ideal response, ASGD $\approx$0.16 dB, (b) degraded-bifurcated response, ASGD $\approx$2.16 dB, and (c) degraded broadened response, ASGD $\approx$2.8 dB.

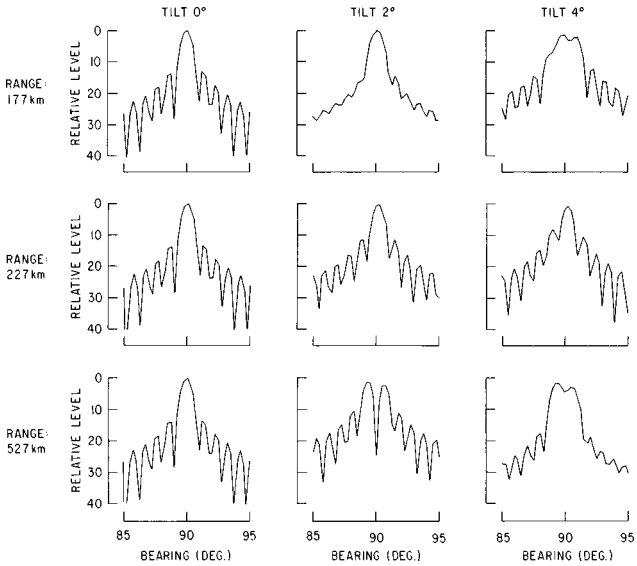

FIG. 8. Computed response of the 533-m aperture at 167 Hz for a broadband field.

TABLE II. Calculated signal gain.

Tilt (deg)	Frequency (Hz)	Median ASGD (dB)	Maximum ASGD (dB)	10% ASGD (dB)	90% ASGD (dB)	$*_{N_{OBS}}$	Aperture (m)
0	167	0.1	1.4	0.9	0.0	20	546
2	167	1.1	2.3	2.1	0.2	20	546
4	167	1.2	3.3	2.8	0.3	20	546

averaging times (50 s) were used on selected data sets, and the results showed that ASGD=1 dB when array motion was not dominant.

The at-sea results were verified by postprocessing the high-frequency data at NRL. The processing involved the analysis of high-density digital recordings of the hydrophone data obtained at the extremes of leg 1 and leg 2. The analysis consisted of a Hann-weighted temporal FFT (0.125 Hz) and a uniformly weighted spatial FFT. The mean hydrophone level was determined from the sum of all functional hydrophones. The subsequent ASGD values were less than 1 dB, and the standard deviations were reduced to $\leqslant$1.6 dB for leg 1 and $\leqslant$1.2 dB for leg 2.

Examination of the time history of the received beam-signal level for the 167-Hz signal at a source receiver range of 648 km (350 nmi) and a fairly constant relative bearing shows bifurcation of the mainlobe response. There appear to be specific periods of pronounced bifurcation and good mainlobe reception. Array tilts were on average $<2°$, and the array was observed to be well behaved.

Figure 7 illustrates three examples of array performance at 167 Hz for the 533-m aperture. Figure 7(a) shows a uniform illumination (received signal versus aperture length) and near-ideal response. Figure 7(b) shows an illumination with a deep null and a bifurcated response. Figure 7(c) shows a variable illumination and a broadened deformed beam response. Also shown are the differences in depth (ΔD) and heading (ΔH) between the fore and aft of the array. The heading sensor difference ΔH was found to have a bias, and care must be taken not to interpret the value of 3° as absolute. The array tilts were $\sim 2°$ (20 m/533 m). The degradations in signal performance were 0.2, 2.2, and 2.8 dB, respectively, and are the types of signal performance degradations to be expected for the 533-m array when the averaging time is short, 4×12.5 s=50 s. Observe the variation in the band signal-plus-noise level along the aperture and the arrival of energy over several beams at 167 Hz. Examination of successive 50-s averages revealed that the signal performance of the large aperture varied between cases of small and large DASG (-ASGD) as shown. This represents the second class of degradations (previously mentioned) caused by the combined effects of multipath arrival and array shape deformation.

V. MODELED RESPONSE PATTERNS

To calculate the response pattern of the array, the multilayer, normal-mode model validated earlier in the discussion of propagation loss was used to calculate the acoustic field over a rectangular lattice of points extending 546 m in range and 40 m in depth. The real and imaginary components of the field were calculated at a 2-m grid interval over the rectangular lattice. Since the resulting field represented an end-fire source, the lattice was mathematically rotated to either 45° or to broadside. The response of an array with 128 elements spaced at 4.3 m was calculated with the resulting lattice at tilts of 0°, 2°, and 4°. A two-dimensional cubic spline was used to interpolate the acoustic field from the lattice points to hydrophone positions; the resulting acoustic field points were beamformed to determine the array response pattern. Figure 8 shows several of the calculated patterns.

The mainlobe responses were also used to determine ASGD for each of the three tilts. Table II presents the median ASGD and the parameters used in developing these statistics. Little loss is observed at 0° tilt; however, as the tilt is increased, both the median and the maximum observed ASGD increases. The change in structure of the mainlobe response pattern with range is shown in Fig. 9. The results are from calculated response patterns of an array with 2° of down tilt. Also the array encounters a null in the acoustic field, the mainlobe splits, the array being able to resolve different multipaths. There is also a slight shifting of the mainlobe with range. The comparison of the response patterns of Figs. 6 and 7 shows a great deal of similarity between the calculated and the measured results. The degraded performance observed is believed to be caused by the combined effect of the multipath field and array shape. The measured ASGD cumulative distribution functions (CDFs) are compared in Fig. 10 with calculated CDF results. The calculated median CDF, or tail, of the calculated results exhibited

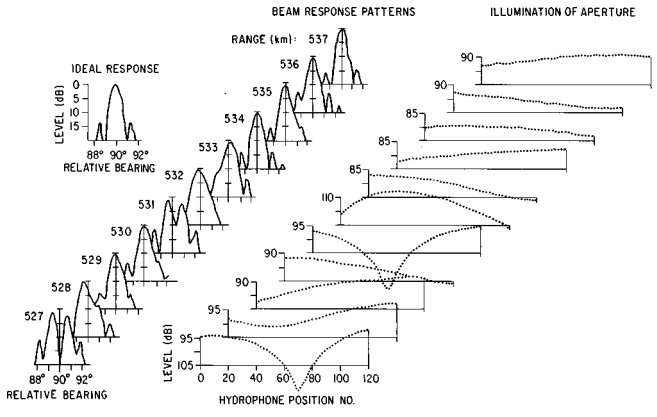

FIG. 9. Calculated mainlobe response versus range at 167 Hz with an array tilt of 2°.

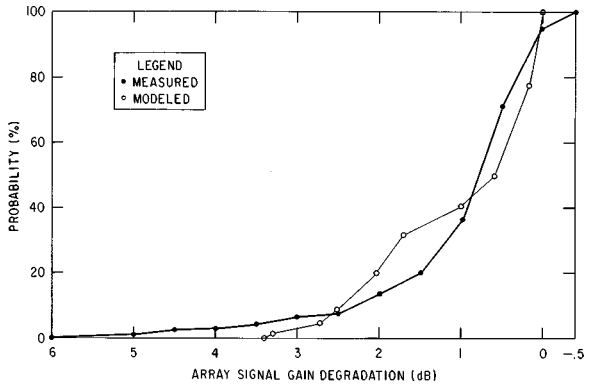

FIG. 10. Comparison of measured and computed ASGD cumulative distribution function (CDF) at 167 Hz.

less loss than observed in the measured results. The calculations do not include effects of array disturbances induced by tow point motion. These differences are believed explainable by array distortions. Since these distortions can result in horizontal and vertical displacement and consequently a dynamic bowing of the array, the experimental results may be expected to exhibit more loss than the theoretical calculations, and thus these results.

VI. SUMMARY AND CONCLUSIONS

Acoustic data have been analyzed for extended propagation loss tows in the Levantine Basin at frequencies of 57, 167, and 323 Hz. Sound propagation was good because of the shallow sound axis channel ($\sim$200 m) and the large depth excess that existed during the experiment. Comparisons of the measured and theoretical values of propagation loss as a function of range showed good agreement at 167 and 323 Hz, and fair agreement at 57 Hz. It is reasonable to conclude that a normal-mode propagation loss model, such as the one used in this analysis, can be used to accurately calculate sound levels in any part of the Levantine Basin that is not bottom limited. In addition, it should be possible to predict array signal gain by using a normal-mode model since the model includes multipath interference in its formulation.

An assessment of array signal performance is presented in this paper. The measure of performance is taken to be the array signal gain degradation. The three apertures examined in this experiment were found to perform on average within 1 dB of the theoretical signal gain. The observed signal gain degradation and standard deviations (as seen on the CDF shown in Fig. 10) is found to be greater than predicted by coherent multipath effects and are believed to be the result of array shape and array motion not included in the calculation. Examples of the degraded performance are shown and compared to calculations performed with the normal-mode model and showed qualitative agreement. By inference, these comparisons allow us to conclude that the primary causes of array degradations in this frequency range are the combined deformation and propagation effects.

Finally, the multilayer, normal-mode code used in performing these calculations can serve as the basis for prediction. Comparisons of the measured and computed ASGD distribution function showed that we underestimated the true effect of tilt, bow, and motion. It is our opinion that with better estimates of motional effects, these distributions would closely agree and that system simulation is entirely possible.

[1] H. P. Bucker, ''Sound propagation in a channel with lossy boundaries,'' J. Acoust. Soc. Am. **48**, 1187–1194 (1970).
[2] J. F. Lynch, ''On the use of focused horizontal arrays as mode separation and source location devices in ocean acoustics. Part I: Theory,'' J. Acoust. Soc. Am. **74**, 1406–1417 (1983).
[3] W. Carey, I. Gereben, and B. Brunson, ''Measurements of sound propagation downslope to a bottom limited sound channel,'' J. Acoust. Soc. Am. **81**, 244–257 (1987).
[4] W. Carey, J. Reese, and C. Stuart, ''Mid-frequency measurements of array signal and noise characteristics,'' IEEE J. Oceanic Eng. **22**(3), 548–565 (1997).
[5] C. Bassett and P. Wolf, ''Fleet numerical weather central bottom loss values,'' T.N.58, FNWC, Montery, CA, 1970.
[6] W. Carey, ''Sonar array characterization, experimental results,'' IEEE J. Oceanic Eng. **23**(3) (July 1998).

Dependence of scattered acoustical signal intensity on the form of distribution of plankton concentration

Natalia Gorska and Zygmunt Klusek
Institute of Oceanology, Polish Academy of Sciences, ul. Powstańców Warszawy 55, PL81 712, Sopot, Poland

(Received 3 June 1993; accepted for publication 14 April 1998)

Sounding of the plankton aggregation which consists of identical statistically uncorrelated particles by a plane monochromatic wave has been studied. Analytical formulas for scattered signal intensity and interference coefficient have been obtained for an arbitrary plankton spatial distribution form. The role of interference of waves scattered by individual plankton targets has been under investigation. The influence of the plankton probability density function form on the sounding signal mean intensity has also been considered. © *1998 Acoustical Society of America.*
[S0001-4966(98)05007-3]

PACS numbers: 43.30.Gv, 43.30.Sf [JHM–DLB]

INTRODUCTION

Sounding vertically down in the Baltic Sea, we could observe at night in the summer period strong sound scattering biological layers with clearly defined sharp boundaries. The process of scatterers condensation started after sunset. Close to sunrise the layers were dispersed and registered echointensity integrated over the entire water column decreased.

The typical results of the sound backscattering measurements are presented on the echogram in Fig. 1. The echosounding was carried out at the Gdańsk Deep station (φ=54°40′N, λ=19°20′E) using echosounder ELAC 4700 working at the frequency 30 kHz, in September 1991.[1]

It is interesting to explain the observed phenomena of echointensity decreasing. Plankton spatial changes may be one of the reasons. The space transformations of plankton aggregation influence the phase relationship among individual target echoes and so the coherent part of the backscattering sound intensity depends on these transformations. To get a better understanding of the observed changes of echointensity, an investigation of the significance of the echoes coherent superposition has to be conducted.

Such analysis was carried out by Bruno and Novarini[2] for linear arrays of scattering objects and by Sun and Gimenez[3] for a planar distribution of spherical targets. For the three-dimensional case the investigation has been made by Glotov[4] (in the case of plane horizontal scattering layers with distinct even boundary) and by Kurianov[5] (in the case of a lack of sharp aggregation borders). All investigations indicated that the interference can be important and that the value of the coherent component of intensity depends on the scatterer concentration, on the wavelength of the sounding signal, on the position of the transducer, respectively, to the aggregation of targets, and on the character of the probability density function, describing spatial distribution of scatterers.

The main goal of the paper is studying the significance of the individual echo interference and the influence of spatial structure of the aggregation on the sounding signal intensity. So the analytical model of plane monochromatic sound wave scattering at plankton aggregation is developed for an arbitrary sufficiently smooth probability density function determined in domain with arbitrary sufficiently smooth boundary.

The developed model considers only the aggregations with identical isotropic scattering targets. However, some features of the influence of plankton spatial distribution on the sounding signal intensity can be also applied in a more general situation.

I. PROBLEM DESCRIPTION

We consider scattering of a monochromatic plane acoustic wave with a frequency ω (Fig. 2). The expression for the pressure in the incident wave is given in the form:

$$P_{\text{inc}} = P_0 \exp(i\mathbf{k}_{\text{inc}}\mathbf{r} + i\omega t), \tag{1}$$

where $\mathbf{k}_{\text{inc}}$ is the wave number (parallel to the z axis), $|\mathbf{k}_{\text{inc}}| = k$ and i is the imaginary unit. Here $\mathbf{r}=(x,y,z)$ is a vector in space with coordinates x, y, z.

The plankton is modeled as a group of identical immobile particles.

We also use the uncorrelation assumption for the particles. According to Ref. 6 the assumption is acceptable when the fractional volume number of scatterers n_f (the relative volume of individuals) is not very high: $n_f < 0.065$. Let us also neglect the multiple scattering.

Our aim is to obtain the analytical formula for the mean intensity, I, of a wave scattered from a plankton aggregation, evaluate the role of the coherent part of the intensity, and study its dependence upon the internal structure of the aggregation.

II. MAIN FORMULA FOR MEAN SCATTERED WAVE INTENSITY

In further considerations we use an approach which is similar to the one presented in Refs. 3, 5, and 6.

We denote the positions of N plankton particles by the vectors $\mathbf{r}_m$ $(m=1,2,...,N)$. At great distances from the receiver $(k|\mathbf{r}-\mathbf{r}_m| \gg 1)$, the acoustic field scattered from each target is given as:[7]

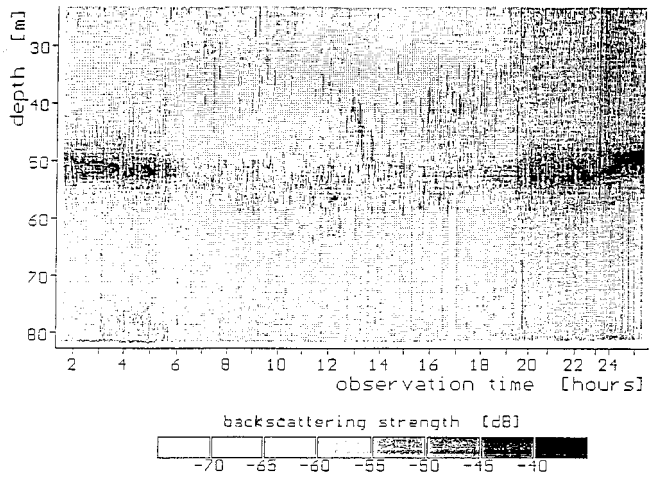

FIG. 1. The echogram. Day and night observation of Baltic plankton.

$$P_{\mathrm{sc}}^{m}=\frac{P_0\ \exp(i\mathbf{k}_{\mathrm{inc}}\mathbf{r}_m+ik|\mathbf{r}-\mathbf{r}_m|+i\omega t)}{|\mathbf{r}-\mathbf{r}_m|}\ \phi(\mathbf{n}_{\mathrm{inc}},\mathbf{n}_m), \quad (2)$$

where $\mathbf{r}$ represents the position of the receiver, $\mathbf{n}_{\mathrm{inc}}=\mathbf{k}_{\mathrm{inc}}/\mathbf{k}$, $\mathbf{n}_m=(\mathbf{r}-\mathbf{r}_m)/|\mathbf{r}-\mathbf{r}_m|$, and ϕ denotes here the scattering amplitude, $|\phi|=\sigma^{1/2}$, σ is the scattering cross section of the target.

The pressure of the signal scattered by all targets has the form:

$$P_{\mathrm{sc}}=P_0\sum_{m=1}^{N}\ \frac{\exp(i\mathbf{k}_{\mathrm{inc}}\mathbf{r}_m+ik|\mathbf{r}-\mathbf{r}_m|+i\omega t)}{|\mathbf{r}-\mathbf{r}_m|}\ \phi(\mathbf{n}_{\mathrm{inc}},\mathbf{n}_m) \quad (3)$$

and intensity averaged over an ensemble of realizations of the particular spatial target distributions, $I=(\rho c)^{-1}\langle|P_{\mathrm{sc}}|^2\rangle$, is expressed by

$$I=|P_0|^2(\rho c)^{-1}\sum_{l,m=1}^{N}\left\langle\frac{\phi(\mathbf{n}_{\mathrm{inc}},\mathbf{n}_l)\,\phi^*(\mathbf{n}_{\mathrm{inc}},\mathbf{n}_m)}{|\mathbf{r}-\mathbf{r}_l||\mathbf{r}-\mathbf{r}_m|}\right.$$
$$\left.\times\exp(i\mathbf{k}_{\mathrm{inc}}(\mathbf{r}_m-\mathbf{r}_l)+ik(|\mathbf{r}-\mathbf{r}_m|-|\mathbf{r}-\mathbf{r}_l|))\right\rangle. \quad (4)$$

According to Refs. 3, 5, and 6 we extract two parts of the formula. The first part includes N terms with $m=1$ from the double sum and the second includes the remaining N^2-N terms with $m\neq 1$. We also carry out the averaging of (4) by the integration over the random parameters $\mathbf{r}_1$, $\mathbf{r}_2$, $\mathbf{r}_3,\ldots,\mathbf{r}_N$ with the probability density function $w(\mathbf{r}_1,\mathbf{r}_2,\mathbf{r}_3,\ldots,\mathbf{r}_N)$. The result of the transformations is

$$I=|P_0|^2(\rho c)^{-1}\left\{N\int_V\frac{|\phi(\mathbf{n}_{\mathrm{inc}},\mathbf{n})|^2 w_1(\mathbf{r}_1)}{|\mathbf{r}-\mathbf{r}_1|^2}\,d\mathbf{r}_1\right.$$
$$+(N^2-N)\left|\int_V\frac{\phi(\mathbf{n}_{\mathrm{inc}},\mathbf{n})w_1(\mathbf{r}_1)}{|\mathbf{r}-\mathbf{r}_1|}\right.$$
$$\left.\left.\times\exp(i\mathbf{k}_{\mathrm{inc}}\mathbf{r}_1+ik|\mathbf{r}-\mathbf{r}_1|)d\mathbf{r}_1\right|^2\right\}, \quad (5)$$

where $w_1(\mathbf{r}_n)$ denotes the probability density function for the individual nth target to be at position $\mathbf{r}_n$: $w(\mathbf{r}_n)=\int d\mathbf{r}_1\,d\mathbf{r}_2,\ldots,d\mathbf{r}_{n-1},\quad d\mathbf{r}_{n+1},\ldots,d\mathbf{r}_N w(\mathbf{r}_1,\ldots,\mathbf{r}_{n-1},\mathbf{r}_n,\mathbf{r}_{n+1},\ldots,\mathbf{r}_N)$. Here V denotes the domain, where the function $w_1(\mathbf{r})$ is determined, $\mathbf{n}=(\mathbf{r}-\mathbf{r}_1)/|\mathbf{r}-\mathbf{r}_1|$. The uncorrelation assumption among targets is applied. The independence of $w_1(\mathbf{r}_i)$ on a scatterer number ''i'' is also supposed. Next we assume the isotropic angular dependence of the target scattering cross section σ. Hence we have

$$I=I_{\mathrm{nonc}}+I_{\mathrm{coh}},$$
$$I_{\mathrm{nonc}}=|P_0|^2(\rho c)^{-1}\sigma N\int_V\frac{w_1(\mathbf{r}')}{|\mathbf{r}-\mathbf{r}'|^2}\,d\mathbf{r}', \quad (6)$$
$$I_{\mathrm{coh}}=|P_0|^2(\rho c)^{-1}\sigma N(N-1)$$
$$\times\left|\int_V\frac{w_1(\mathbf{r}')\exp(i\mathbf{k}_{\mathrm{inc}}\mathbf{r}'+i\mathbf{k}|\mathbf{r}-\mathbf{r}'|)}{|\mathbf{r}-\mathbf{r}'|}\,d\mathbf{r}'\right|^2. \quad (7)$$

The coherent part of the intensity I_{coh} describes the interference of elementary signals scattered by different targets. In the integral (7) the phase $\psi=\mathbf{k}_{\mathrm{inc}}\mathbf{r}_1$ of the incident plane wave and the phases $\psi_{\mathrm{sc}}=\mathbf{k}|\mathbf{r}-\mathbf{r}_1|$ of the echoes are affected by the target positions $\mathbf{r}_1$. As a result the form of the probability density function $w_1(\mathbf{r})$ influences the I_{coh}.

The dependence of the scattered field intensity on frequency is determined by the following two factors. The frequency dependence of the target scattering cross section[7,8] and of the integral in I_{coh} are important. Since the integral is affected by the form of the function $w_1(\mathbf{r})$, the last one influences the frequency changes of the intensity I.

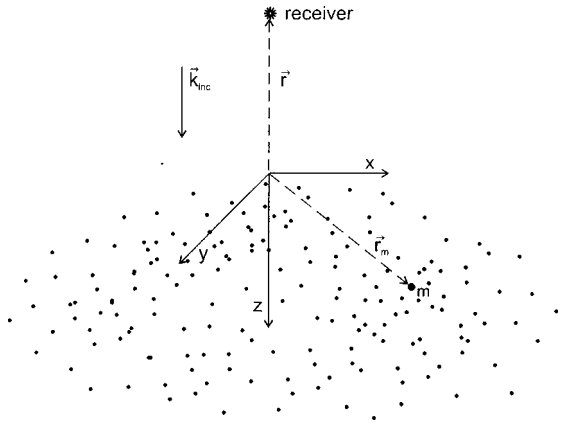

FIG. 2. Scattering geometry.

III. SOME ANALYTICAL RESULTS AND DISCUSSION

We shall further transform the formulas (6) and (7) to study the influence of the plankton probability density function form on the mean scattered wave intensity.

The coordinate system is chosen so that the z axis passes through the receiver, and the origin of coordinates is at the point of intersection of the z axis with the upper boundary of the space V (cf. Fig. 2). We assume that

$$\frac{\sqrt{x_1^2+y_1^2}}{z_1-z_r}\ll 1, \quad (8)$$

where z_r is the coordinate of the receiver. Here, x_1 and y_1 are coordinates of the positions of scatterers in the horizontal plane $z=z_1$, which are significant in calculating the integral

in Eq. (7). The phase ψ is expanded in a series relative to the small parameter [Eq. (8)]:

$$\psi \cong 2kz_1 - kz_r + k\,\frac{x_1^2+y_1^2}{2(z_1-z_r)} + \cdots . \tag{9}$$

We consider the case of the Fresnel approximation,[9,10] when the condition

$$\frac{k(x_1^2+y_1^2)^2}{(z_1-z_r)^3} \ll 1 \tag{10}$$

is satisfied. The expansion of the phase [Eq. (9)] may be limited to the presented terms due to the condition [Eq. (10)]. We assume additionally that $L_z \ll |z_r|$ (where L_z is the characteristic thickness of a plankton aggregation). Then the expression for the mean intensity has the form:

$$I = |P_0|^2\,\frac{\sigma_{bs}N}{\rho c z_r^2}\left\{1+(N-1)\left|\int_{z_{\min}}^{z_{\max}} dz_1\,\exp(2ikz_1)\right.\right.$$
$$\times \int_{y_{\min}(z_1)}^{y_{\max}(z_1)} dy_1\,\exp\left(\frac{iky_1^2}{2(z_1-z_r)}\right)$$
$$\left.\left.\times \int_{x_{\min}(z_1,y_1)}^{x_{\max}(z_1,y_1)} dx_1\,\exp\left(\frac{ikx_1^2}{2(z_1-z_r)}\right) w_1(x_1,y_1,z_1)\right|^2\right\}, \tag{11}$$

where $z_{\min}$ is the minimum vertical coordinate of the upper boundary and $z_{\max}$ denotes the maximum vertical coordinate of the lower boundary of the aggregation. Here each of the horizontal sections of the space contains several Fresnel zones.

Next we discuss in more detail the case of sufficiently large transverse dimensions L of the assembly, when the following condition is true:

$$z_{\max} - z_r \ll kL^2 \tag{12}$$

and a considerable number of the Fresnel zones is contained in an arbitrary transverse horizontal section. We assume that the plankton probability density function $w_1(\mathbf{r})$ is sufficiently smooth in the horizontal plane:

$$L_w \gg L_{\mathrm{Fr}}, \tag{13}$$

where L_w is the characteristic space scale of $w_1(x,y,z)$, changes in horizontal plane—L_{Fr} denotes the characteristic difference of the radii of adjacent Fresnel zones, and also the condition

$$L_b \gg L_{\mathrm{Fr}} \tag{14}$$

is applied for the rough boundary of the aggregation. Here L_b denotes the characteristic correlation length of the surface.

On these assumptions the position of scatterer inside the first Fresnel zone is most significant in intensity calculations.[9,10] The stationary phase method is employed in evaluation of the integral over x and y. Then, transformations yield

$$I = |P_0|^2\,\frac{\sigma_{bs}N}{\rho c z_r^2}\left\{1+(N-1)\left(\frac{2\pi z_r}{k}\right)^2\right.$$
$$\left.\times\left|\int_{z_{\min}}^{z_{\max}} dz_1\,\exp(ikz_1)\,w_1(0,0,z_1)\right|^2\right\}. \tag{15}$$

On the basis of the above expression it can be demonstrated that the scattered field mean intensity is affected by the depth dependence of the function $w_1(0,0,z)$ immediately underneath the receiver. Changing the receiver position over the plankton layer and measuring the mean intensity, we collect the information about the distribution $w_1(x,y,z)$ in the entire layer. Analysis of Eq. (15) also indicates that the form of the probability density function influences the intensity for the significant interference of the echoes only.

Next we consider the effect of the form of the function $w_1(0,0,z_1)$ on the scattered signal mean intensity and its frequency dependence. Two depth profiles of the probability function are considered:

$$w_1(x,y,z) = \begin{cases} w_1(x,y), & z \in [z_{\min}(x,y); z_{\max}(x,y)] \\ 0, & z \notin [z_{\min}(x,y);\ z_{\max}(x,y)] \end{cases} \tag{16}$$

and

$$w_1(x,y,z) = \begin{cases} \tilde{w}_1(x,y)\displaystyle\sum_{n=0}^{M-1} \delta(z - z_{\min}(x,y) - nd(x,y)), \\ \quad z \in [z_{\min}(x,y); z_{\max}(x,y)] \\ 0, \quad z \notin [z_{\min}(x,y); z_{\max}(x,y)], \end{cases} \tag{17}$$

where M is the number of layers and δ denotes the Dirac function. Here, $d(x,y)$ is the distance between the adjacent layers and $z_{\min}(x,y)$ and $z_{\max}(x,y)$ are the minimum and maximum vertical coordinates of the aggregation for fixed (x,y), The first case relates to the uniform vertical distribution $w_1(x,y,z)$ for each (x,y) and the second one to the layered structure distribution. We would like to underline here that only condition (14) limits the shape of the aggregation rough boundary.

After substitution of the expressions for the $w_1(0,0,z)$ to Eq. (15) we have

$$I = |P_0|^2\,\frac{\sigma_{bs}N}{\rho c z_r^2}$$
$$\times\left\{1+(N-1)w_1^2(0,0)\left(\frac{2\pi z_r}{k}\right)^2\frac{\sin^2(kL_z(0,0))}{k^2}\right\} \tag{18}$$

for the first case [Eq. (16)] and

$$I = |P_0|^2\,\frac{\sigma_{bs}N}{\rho c z_r^2}$$
$$\times\left\{1+(N-1)\tilde{w}_1^2(0,0)\left(\frac{2\pi z_r}{k}\right)^2\frac{\sin^2(kMd(0,0))}{\sin^2(kd(0,0))}\right\} \tag{19}$$

for the second one [Eq. (17)]. Here, $L_z(x,y) = z_{\max}(x,y) - z_{\min}(x,y)$.

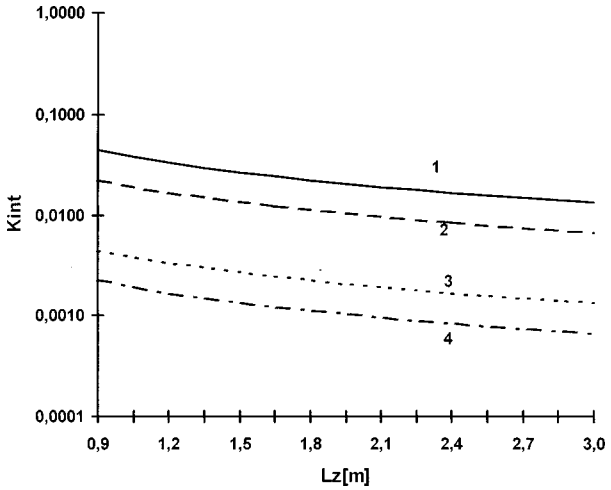

FIG. 3. The interference coefficient dependence on the layer vertical thickness for different plankton concentration value.

The comparison of Eqs. (18) and (19) indicates the different character of the dependence of the coherent part upon wave number k. For the first case the coherent component decreases much more rapidly when the sound frequency increases.

IV. COMPUTATIONS

We evaluate the influence of the interference effects on the scattered wave intensity and so introduce the following parameter:

$$K_{\text{int}} = I_{\text{coh}} / I_{\text{nonc}}. \tag{20}$$

Based on the above equations (18) and (19) the expressions for the interference coefficients are obtained:

$$K_{\text{int}} \cong (N-1)\left(\frac{2\pi z_r}{kS}\right)^2 \frac{\sin^2(kL_z)}{(kL_z)^2} \tag{21}$$

for the distribution given by Eq. (16) and

$$K_{\text{int}} \cong (N-1)\left(\frac{2\pi z_r}{kS}\right)^2 \frac{\sin^2(kMd)}{M^2 \sin^2(kd)} \tag{22}$$

for the second one [Eq. (17)]. Here we suppose that in the largest part of the aggregation, excluding relatively small space near the border, the horizontal cross section area of the aggregation $S(z)$ does not depend on the z coordinates and the functions $\tilde{w}_1(x,y)$ and $w_1(x,y)$ are uniform over x,y. We also assume that the characteristic height ξ of the boundary roughness is smaller than the thickness $L_z(x,y)$:

$$\xi \ll L_z(x,y). \tag{23}$$

The results of the interference coefficient calculations are presented in Fig. 3 in the first case and in Fig. 4 in the second one. The results (Fig. 3) are obtained for the different mean densities ρ ($\rho = N/V_a$, V_a is the volume of the aggregation) of scatterers: $\rho = 1000$ ind./m^3 (curve 1), $\rho = 500$ ind./m^3 (curve 2), $\rho = 100$ ind./m^3 (curve 3), $\rho = 50$ ind./m^3 (curve 4) and for the aggregation cross section area $S = 6$ m^2. However, calculations in the second case [Fig. 4(a) and (b)] are conducted for the $S = 200$ m^2, $\rho = 100$ ind./m^3 and for a different number of assembly layers,

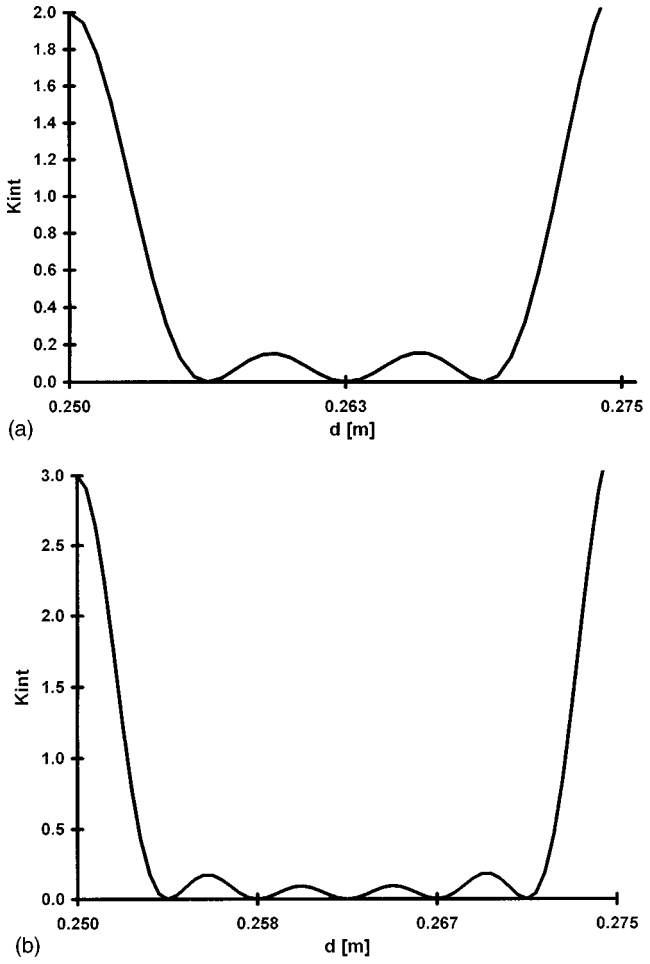

FIG. 4. (a) and (b) Variation of the interference coefficients versus layer distance d. Stratified spatial distribution of plankton.

$M = 4$ [Fig. 4(a)], $M = 6$ [Fig. 4(b)]. In this case the coefficient K_{int} is quasiperiodic in the layer distance d. It is a result of the relevant phase dependence on the value d for waves scattered at the separate layers. Only one ''period'' of the coefficient changes is presented in Fig. 4. All evaluations are carried out at the frequency of 30 kHz and the distance between the receiver and the upper layer boundary $z_r = 40$ m.

The numerical investigation proves that in the first case the coherent sum of echoes is significant only for very dense plankton layers (Fig. 3): $K_{\text{int}} > 0.1$ for the considered range of L_z in case of $\rho > 10\,000$ ind./m^3 and in the second one for less plankton densities.

The calculations also show that in the case of the distribution, given by the Eq. (16), for large plankton densities $\rho = 50\,000$ ind./m^3 and for the parameters, presented above, the intensity decreases 3 dB when L_z increases from 1 to 3 m. However, for the distribution, given by Eq. (17), with $M = 6$ (other parameters are as above) the small changes of d near $d = 0.25$ m can decrease the intensity by 6 dB. In both cases the interference is significant. These calculations give the basis to state that the changes of the form of probability density function and of its determination domain can be one of the reasons of echogram changes, described above in the Introduction.

V. SUMMARY

The analytical model of the scattering of plane monochromatic acoustic waves in plankton aggregation is developed. Analytical formulas for the scattered signal mean intensity and interference coefficient are obtained for an arbitrary sufficiently smooth probability density function $w_1(\mathbf{r})$ and an arbitrary sufficiently smooth surface bounding its determination domain [conditions, Eqs. (13) and (14)].

Despite the model limitations (the isotropic character of scattering by individual targets and the identical length of the scattering objects) the model was able to characterize some features of mean intensity dependence on plankton spatial distribution $w_1(\mathbf{r})$. This analysis showed:

(i) In the case of a receiver operating in a nearzone, the scattered sound mean intensity is affected by the vertical dependence of the probability density function, describing the position of individual plankton, directly underneath the receiver $(w_1(0,0,z))$.

(ii) The spatial structure of the plankton probability density function can influence the mean intensity value and its frequency dependence.

(iii) The interference effects can be significant for high plankton densities.

(iv) Plankton spatial changes can be one of the reasons for the changes between day and night of backscattering signal intensity.

These results prove the importance of the subsequent investigation of the echo interference effect influence, in view of the specific features of the actual plankton aggregations.

[1] A. Sliwiński, Z. Klusek, M. Ostrowski, J. Szczucka, and K. Groza, ''Ultrasonic signals backscattered from inhomogeneities of water column in the Southern Baltic Sea,'' in *Ultrasonics International 93 Conference Proceedings*, 1993 (Butterworth-Heinemann, Oxford), pp. 595–598.

[2] D. R. Bruno and J. C. Novarini, ''Coherence and multiple scattering effects on acoustic backscattering from linear arrays of gas-filled bubbles,'' J. Acoust. Soc. Am. **71**, 1359–1361 (1982).

[3] Z. Sun and G. Gimenez, ''Evaluation of interference effect in the energy investigation of echoes scattered by an uncorrelated planar distribution of spherical targets,'' J. Acoust. Soc. Am. **92**, 3259–3270 (1992).

[4] V. P. Glotov, ''Coherent scattering of plane and spherical waves in deep-sea layers containing discrete inhomogeneities,'' Sov. Phys. Dokl. **7**, 211–213 (1962).

[5] B. F. Kurianov, ''On coherent and incoherent scattering of waves by point scatterers randomly distributed in space,'' Akust. Zh. **10**, 195–201 (1964).

[6] Z. Sun and G. Gimenez, ''Influence of target composition on the relationship between echo energy and target quantity,'' J. Acoust. Soc. Am. **96**, 3080–3087 (1994).

[7] T. K. Stanton, ''Sound scattering by spherical and elongated shelled bodies,'' J. Acoust. Soc. Am. **88**, 1619–1633 (1990).

[8] M. C. Macaulay, ''A generalised target strength model for euphausiids, with applications to other zooplankton,'' J. Acoust. Soc. Am. **95**, 2452–2466 (1994).

[9] E. Skudrzyk, *The foundation of Acoustics. Basic Mathematics and Basic Acoustics* (Springer-Verlag, Wien, 1971).

[10] M. Born and E. Wolf, *Principles of Optics. Electromagnetic Theory of Propagation, Interference and Diffraction of Light* (Pergamon, Oxford, 1968).

Determining an ocean internal wave model using acoustic log-amplitude and phase: A Rytov inverse

Terry E. Ewart, Stephen A. Reynolds, and Daniel Rouseff
Applied Physics Laboratory, College of Ocean and Fishery Sciences, University of Washington, Seattle, Washington 98105

(Received 25 November 1997; accepted for publication 20 March 1998)

The feasibility of inverting acoustic field statistics to obtain the parameters of a stochastic internal wave model is demonstrated using numerical simulations. For weak scattering satisfying the Rytov approximation, the parameters of a generalized form of the Garrett–Munk internal wave model can be obtained. A hierarchy of experiment scenarios has been studied. Scenarios range from a densely populated vertical receiving array to single-point measurements. In each case, the intrinsic range-averaging of acoustic measurements provides integral constraints on the environmental model. The success of the inversion improves with increasing experimental complexity. With a vertical array, up to four parameters of the internal wave model can be recovered. For the simplest situation, two parameters can be fit with reasonable accuracy. The implications of these results for understanding oceanographic processes are discussed. © *1998 Acoustical Society of America.* [S0001-4966(98)01907-9]

PACS numbers: 43.30.Pc, 43.30.Re [DLB]

INTRODUCTION

During the 1970s, Garrett and Munk proposed a universal spectral model for ocean internal waves.[1] The model was based on a large number of deep sea measurements and has found wide application. In the intervening years, oceanographers have looked for cases that deviate from this ''universal'' norm. Some variations have indeed been found[2] and the possibility of developing a shallow-water internal wave model remains an open research question. Improved understanding of this ubiquitous ocean phenomenon will depend upon new ways of measuring internal wave variability and its influences.

A natural measurement approach for characterizing an internal wave field is to use propagating sound. Acoustic propagation in the ocean offers the flexibility of sampling the region probed by the sound paths over a range of temporal and spatial scales not easily monitored by conventional dropped, towed, or moored oceanographic instrumentation. Because internal waves cause fluctuations in the sound speed, a propagating acoustic wave will acquire fluctuations in both its phase and amplitude. The statistical moments of these acoustic fluctuations can be estimated and compared to calculations produced by well-established wave propagation in random media theories. The deep water Mid-ocean Acoustic Transmission Experiment (MATE)[3] is a case where acoustic predictions and observed statistics are in good agreement.[4] This agreement in the forward problem suggests acoustics can be used to solve the inverse problem: from the observed statistics of the acoustics, determine the parameters of an ocean internal wave model. Such an approach was proposed by Uscinski[5] and implemented using the MATE acoustic phase data by Ewart.[6]

Considerations, both theoretical and practical, go into the design of an acoustic experiment specifically intended to invert for the parameters of an internal wave spectral model. Ideally, the frequencies and ranges selected would be such that the weak-scattering Rytov approximation[7,8] would be valid. For the strong-scattering situations where Rytov fails, it can be shown that the moments of the acoustic field are relatively insensitive to the details of the internal wave spectrum; the field then has little ''memory'' of the medium.[5] It is precisely these details of the internal wave field, however, that are of interest to oceanographers and are, in fact, the objective of the inversion. Rytov theory yields predictions for the statistical moments of both the acoustic phase and log-amplitude. The phase and log-amplitude are sensitive to different portions of the internal wave spectrum, a potentially advantageous feature for doing an inversion, especially when several acoustic frequencies are used.

A basic consideration is the type of acoustic measurement required to accomplish a satisfactory inversion. This will have a direct bearing on the cost and complexity of a field experiment. At one extreme, one could imagine an experiment featuring a rigid vertical receiving array. If the positions of the individual array elements were known with sufficient precision (millimeters, e.g., in the case of the MATE phase inversion), both the acoustic amplitude and phase could be accurately tracked. Temporal spectra for both the amplitude and the phase could be estimated at each element. In a vertical array sparsely populated by receivers, correlations as a function of vertical separation could be estimated. If the array were densely populated, it might also be possible to estimate the vertical wave-number spectra. Combining depth and time statistics would offer a rich data set upon which to base an inverse. At the other extreme, consider a single moored receiver. In this case, there is no vertical aperture and it would be difficult to separate sensor motion from phase fluctuations; perhaps the only quantity that could be estimated from the measurement is the temporal amplitude spectrum. Compared to the first, this latter scenario offers a reduced data set but it presumably could be implemented at a much reduced cost. Consequently, there is

not a single inversion strategy, but rather a hierarchy of possible methods. Rational trade-offs can be envisioned between the type of data available for the inversion and the cost required to acquire it. Numerical simulations are necessary to make intelligent design decisions.

The present work is an initial numerical study evaluating a hierarchy of inversion strategies. The goal of each inversion is to determine the parameters of a generalized Garrett–Munk (GM) internal wave model. The simulations are arranged to assure weak scattering so that the Rytov approximation may be used to predict both acoustic log-amplitude and phase fluctuation statistics. Three-dimensional realizations of internal wave displacement fields are obtained using direct numerical simulation. These fields are evolved in time and converted to sound-speed fluctuations using standard methods. Time series of acoustic signals at depth-separated distant receivers are obtained using the parabolic equation (PE) method to propagate energy through the internal wave fields. Statistical moments of the acoustic fields are then estimated for various proposed experimental configurations. These are compared with theoretical predictions. Free parameters in the theory are adjusted to optimize the fit between theory and experiment using a modified least-squares routine.

We begin by demonstrating the forward problem in Sec. I. Techniques for simulating both the internal wave field and the acoustic propagation are outlined. Acoustic statistics are compared with predictions obtained using the input model parameters. Section II presents theory used in the inversion along with a description of the optimization method. Section III presents the inversion results for a hierarchy of possible experimental situations. Discussion follows in Sec. IV where implications for future work are considered.

I. FORWARD PROBLEM

If the forward problem is not sufficiently understood, a successful inversion is unlikely. In this section, the modeling is described and the forward problem summarized. We consider the statistics of acoustic log-amplitude and phase obtained from numerical simulations and compare them with theory developed using the Rytov approximation.

A. Numerical ocean model for internal waves

The numerical technique used to simulate the ocean utilizes the initialization method described in detail in Sec. 2.b of Winters and D'Asaro[9] (hereafter referred to as WD97). We provide enough of a description to convey the modeling. Sound-speed fluctuations arise from internal wave displacements, $\zeta(x,y,z,t)$, where x is in the range direction, y is transverse, and z is positive-up. Time, t, is essentially a parameter in the linear modeling used here. For convenience the formulation is developed using the horizontal Fourier transform of the displacement field. Letting a tilde denote the transform and (k_x,k_y) be the transform wave-number pairs of (x,y) then the transformed displacement field, at time t is given by Eq. (18) from WD97

$$\tilde{\zeta}(k_x,k_y,z,t)=e^{i(k_x x+k_y y)}\sum_{j=1}^{j\max}\{G_- e^{-i\omega t} + G_+ e^{i\omega t}\}\hat{\zeta}_{jk_xk_y}(z). \tag{1}$$

The vertical modes, $\hat{\zeta}_{jk_xk_y}(z)$, are explicit functions of k_x and k_y. These modes as well as the eigenfrequencies, ω, are obtained by solving a well-known eigenvalue problem. The shapes of the vertical modes are functions of the buoyancy frequency, $N(z)$, where

$$N^2(z)=-\frac{g}{\rho_0}\frac{\partial\rho(z)}{\partial z}, \tag{2}$$

$\rho(z)$ is the potential density, ρ_0 is a reference density, and g is the acceleration of gravity.

For the numerical problem, a length, width, and depth (L_x,L_y,L_z) are prescribed along with discretization (N_x,N_y,N_z). This defines the range of horizontal wave numbers produced by the simulation: $k_x=2\pi/L_x\{0,1,...,N_x/2\}$ and $k_y=2\pi/L_y\{-N_y/2+1,-N_y/2,...,-1,0,1,...,N_y/2\}$. Because the displacement field is real, negative values of k_x are given by symmetry. The numerical solution of the eigenvalue problem results in eigenfunctions, $\hat{\zeta}_{jk_xk_y}(z)$, and eigenfrequencies, $\omega_{jk_xk_y}$, for discrete sets of modes, j, and horizontal wave numbers, k_x and k_y.

There is a normality condition associated with the vertical modes so that the vertical structure is determined to an arbitrary amplitude. This overall amplitude along with the phase of the displacement field is given by complex spectral coefficients, G_+ and G_- obtained from the GM spectrum. G_+ and G_- are generated as random deviates with expected values

$$\langle|G_-(k_x,k_y,j)|\rangle=\langle|G_+(k_x,k_y,j)|\rangle = \frac{1}{2\sqrt{2\pi\kappa}}\langle|G(\kappa,j)|\rangle. \tag{3}$$

Horizontal isotropy has been assumed: $\kappa^2=k_x^2+k_y^2$. WD97 use the form of the spectrum given by Flatté *et al.*[10] with energy density

$$G^2(\kappa,j)=EH(j)B(\kappa,j), \tag{4}$$

where

$$H(j)=\frac{2j_*}{\pi(j^2+j_*^2)}, \tag{5}$$

$$B(\kappa,j)=\frac{4}{\pi}\kappa_j\frac{\kappa^2}{(\kappa^2+\kappa_j^2)^2}, \quad \text{with} \quad \kappa_j=\frac{\pi f}{N_0 b}j. \tag{6}$$

In (4)–(6), E is the internal wave energy, j_* is the characteristic mode number, and f is the inertial frequency. The reference depth is taken equal to the computational depth L_z and

$$N_0 b=\int_{-L_z}^{0} dz\ N(z). \tag{7}$$

The ocean fluctuation model is now defined. Given G_+, G_-, $\omega_{jk_xk_y}$, and the modes $\hat{\zeta}_{jk_xk_y}(z)$, Eq. (1) can be evalu-

ated for any time, t. A two-dimensional inverse Fourier transform at each z produces $\zeta(x,y,z,t)$.

It should be emphasized that the ocean simulator produces three-dimensional realizations that evolve in time. Several recent articles studying acoustic propagation through internal waves have used two-dimensional numerical simulations of the displacement fields.[11,12] If only uncorrelated realizations are needed, two-dimensional simulations are adequate. In our case, we seek to generate acoustic time series. Using the method of WD97 assures that all horizontal wave numbers are properly included as the internal waves advance in time. The resulting correct temporal evolution of internal waves allows a proper acoustic time series to be simulated. Even though the acoustic propagation is inherently two dimensional because of the vastly differing vertical and horizontal scales, the internal wave field must be simulated in three dimensions to obtain proper evolution in time.

B. Obtaining the sound-speed field

It remains to convert internal wave displacements into changes in sound speed. Let

$$c(x,y,z,t)=\overline{c}(z)+\delta c(x,y,z,t), \tag{8}$$

where $\overline{c}(z)$ is the average, depth-dependent background sound-speed profile and δc is a mean zero fluctuating part. Following Flatté *et al.*,[10] we relate the sound-speed changes to the internal wave displacements using the approximate relationship

$$\frac{\delta c(x,y,z,t)}{c_0}=-\frac{gG}{\rho_0}\frac{\partial \rho}{\partial z}\,\zeta(x,y,z,t), \tag{9}$$

where c_0 is a reference sound speed. G is of order unity and relates the relative potential sound-speed gradient to the buoyancy profile

$$\frac{1}{c_0}\frac{\partial c_p}{\partial z}=GN^2(z). \tag{10}$$

C. Model parameters

The above discussion is quite general. Before a simulation can be conducted, specific choices must be made for the numerical values of several of the quantities.

The first choice is to set the buoyancy profile $N(z)$ to the constant N_0. This makes the internal wave modes into simple sinusoids. It is also assumed that temperature and salinity compensate in such a way that the average sound speed is a constant. The unperturbed acoustic rays then travel along straight paths. In shallow water, the straight ray approximation may be reasonable for certain isolated acoustic paths.[13] In deep water, it is usually a poor approximation. We justify it on several grounds. Our interest in the present context is in examining a hierarchy of inversion strategies. We want to consider cases where there are multiple vertically separated receivers. When there is no background profile, standard Rytov theory can handle two point statistics for the acoustic fluctuations. Munk and Zachariasen[14] extended the theory to include a profile, but considered only the variance of the field at a single point, not the vertical correlation.

TABLE I. Internal wave simulation parameters.

Parameter	Value	Description
E	40 J/m^2	IW spectral energy density
j_*	15	modal bandwidth
f	1.396×10^{-4} s^{-1}	inertial frequency (1/12.5 cph)
N_0b	5.672 m s^{-1}	reference buoyancy frequency
j max	200	maximum mode number
L_z	1 km	total depth ($=b$ in this case)
L_x, L_y	25 km, 6.25 km	horizontal dimensions
N_x, N_y, N_z	128, 32, 256	volume discretization

In this, an initial testing of the inversion methodology, it seemed best to consider a case where the theory was mature. A discussion of how the inversion strategy might be extended to consider the general case with a profile is deferred to Sec. IV.

For the remaining parameters, values were selected based on oceanographic measurements at the Arctic Internal Waves Experiment (AIWEX).[15] AIWEX featured the investigation by several researchers of internal wave and mixing dynamics under arctic ice. The primary reason for choosing to simulate this experiment is that associated with it was the AIWEX Acoustic Transmission Experiment (AATE).[16] AATE featured a long vertical receiving array. A long-term goal of our work is to apply the inversion methodology to the AATE data and confirm its consistency with the direct oceanographic measurements. The numerical values for the parameters in the simulation are given in Table I. Note that the energy density in the simulation is half of that observed at AATE. This was done to assure that the acoustic propagation always satisfied Rytov even at the 8-kHz maximum frequency used here. Typical for under ice conditions, internal wave energy was low during AATE and the modal bandwidth was quite high. The E in Table I is 1/100th the open ocean GM value; j_* is five times GM.

Because of limits in computer memory, the numerical algorithm cannot produce variability at very low or very high wave numbers and will not reproduce completely the statistics prescribed by the internal wave model. This fact is apparent in the comparison shown in Fig. 1 between spectra for the numerically generated internal wave displacements and a prediction obtained using a continuous form of the model spectrum. Conversion to vertical wave number, k_z, utilizes the WKB derived expression

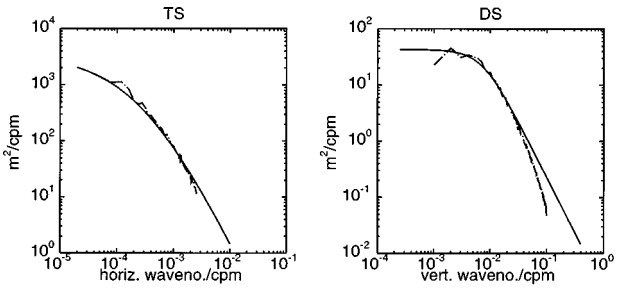

FIG. 1. Average horizontal (TS) and vertical (DS) spectra obtained from a numerically generated 3-D displacement field (dashed). Predictions obtained from Levine *et al.* (Ref. 17) are overplotted solid. Spectra are one-sided (variance equals the area under the displayed curves).

TABLE II. Sound-speed perturbation parameters: AATE situation.

Parameter	Value	Description
c_0	1450 m/s	reference sound speed
ρ_0	1027 kg/m^3	reference density
G	0.96 s^2/m	gradient constant

$$k_z = \frac{\pi j}{N_0 b} N. \tag{11}$$

The simulation spectra tail-off below the model at both low and high k_z and have a narrower bandwidth. There is, however, reasonable agreement with the model over a factor of about 50 in bandwidth. For constant N, the smallest vertical scale in the simulation is $2L_z/j\max = 10$ m; while the largest scale in the vertical equals $L_z = 1$ km. In the horizontal, it will be the reciprocal of the horizontal unit wave number or about 25 km. These scales are apparent in Fig. 1. The variance of the process is 0.42 m^2, very near the desired level of 0.5 m^2. In converting displacements to sound speed using Eq. (9), the index-of-refraction variance $\langle \mu_0^2 \rangle = 0.5 \times 10^{-9}$.

Time steps of 250 s are used, with a run consisting of 1024 steps. For each time step, we obtain a three-dimensional field of sound-speed fluctuations in a domain 1-km deep by 25-km long and 6.25-km wide (Table I). Displacements are converted to sound speed using Eqs. (8) and (9) with parameter values listed in Table II.

D. Acoustic field propagation using a PE solver

The volume domain from the internal wave simulation is subsampled into sixteen 1-by-6.25-km slices. A narrow-angle parabolic equation (PE) solver is used to propagate the acoustic field through these two-dimensional depth/range slices. Each slice is interpolated in depth and range to assure accuracy in the simulation. We extend slices to a depth of 2 km by zero padding. Absorption is used to reduce spurious edge effects and for further analysis we limit the output field to the middle 0.5-km depth range.

It is desirable to initialize the acoustic simulation using a point source that fills the depth region of interest while minimizing energy leakage back into the computational domain through wraparound. This is accomplished with a Gaussian point source having a half-width of 2.0°. Series of log-amplitude (χ) and phase (ϕ) as a function of depth are obtained from each time step by normalizing received fields by the deterministic field obtained from a constant sound-speed run. Specifically,

$$\chi(z,t) = \log(a'(z,t)/a'_{\rm det}(z)), \tag{12}$$

and

$$\phi(z,t) = (\phi'(z,t) - \phi'_{\rm det}(z)). \tag{13}$$

$a'(z,t)$ and $\phi'(z,t)$ are the amplitude and phase output with sound-speed fluctuations; $a'_{\rm det}(z)$ and $\phi'_{\rm det}(z)$ are the solutions using a constant sound speed. Last, any 2π-discontinuities in $\phi(z,t)$ are removed.

Results are obtained at a range of 6.25 km for three acoustic frequencies (2, 4, and 8 kHz, these frequencies were used in AATE). The same sound-speed field is used for all the frequencies. Theory shows that phase fluctuations in depth are dominated by longer scales (lower wave numbers) than is χ. This sensitivity is apparent in the depth and time series; examples for the 4-kHz case are shown in the waterfall plots of Fig. 2. Note how the acoustic field exhibits significant temporal correlations at time scales of 1 h or more. This emphasizes the importance of doing fully three-dimensional oceanographic simulations. Two-dimensional simulations, with uncorrelated realizations of the internal waves, would not produce the proper temporally correlated acoustic fields.

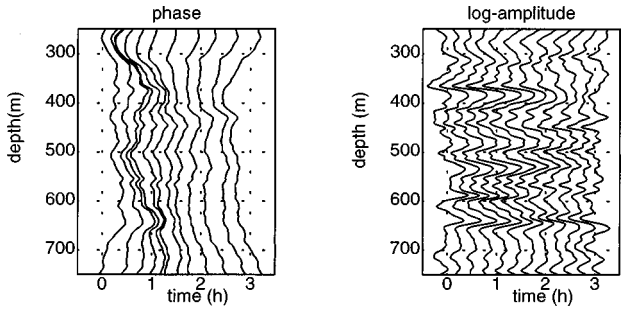

FIG. 2. Example 4-kHz phase and log-amplitude for three simulated hours of depth segments are plotted at the 6.25-km range. The phase and log-amplitude are defined by Eqs. (12) and (13).

The success of the forward problem is demonstrated in Fig. 3. The spectrum in vertical wave number of acoustic phase and log-amplitude for the 8-kHz numerical sets are shown along with theory. Both the theory and the simulated spectra coalesce at high wave number, with the simulated spectra having lower levels than theory at high wave number. The data falloff sharply at wave numbers above 0.1 cpm as expected. The comparison between theory and the simulation is excellent.

From Fig. 2 one might expect that the phase spectrum would not extend to low enough wave numbers to fully capture the phase variance because of the vertical aperture used in the simulation. However, in Fig. 3 data and theory spectra

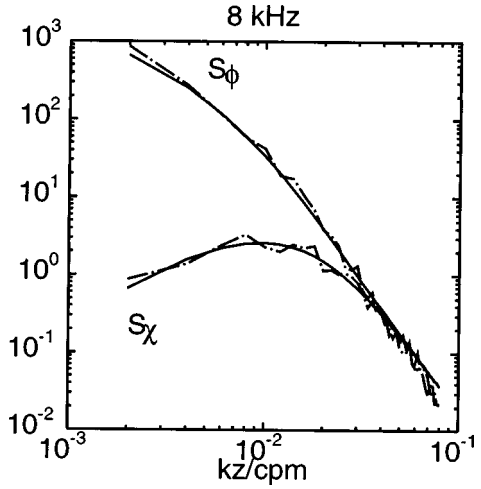

FIG. 3. Spectra in vertical wave number of acoustic phase (S_ϕ) and log-amplitude (S_χ) for 8 kHz. Simulation results are plotted as dot-dashed. Theory [Eq. (A5)] is plotted solid, with $\langle \mu_0^2 \rangle = 0.5 \times 10^{-9}$, $j_* = 15$, and $p = q = 2$.

compare well over a wide range in vertical wave number, even for phase. Frequency spectra, similarly, compare well; they are presented in the next section.

II. INVERSE PROBLEM: FORMULATION

In the Appendix, expressions for the acoustic spectra are derived as filtered versions of the internal wave spectrum. These expressions were used to calculate the theoretical results used for comparison in Fig. 3. The same theoretical expressions can be used to solve an inverse problem. In this context, the acoustic spectra are estimated from the observed acoustic data while the internal wave spectrum is treated as an unknown. The goal of the inversion is to determine the parameters of an internal wave model that predict acoustic spectra consistent with experimental estimates. In this section, the inversion is cast as a problem in parameter estimation.

A. Spectral model for internal waves

The first step in the inversion is to define a suitable model for the internal wave spectrum. Note that the spectrum used in the inversion differs from that used to synthesize data; we deliberately avoid the ''inverse crime,'' [18] common in numerical studies, of using exactly the same model both to generate data and perform an inversion. Several constraints on the model spectrum should be considered. It should include the assumed dispersion relationship relating the spatial and temporal properties of internal waves. When integrated over wave number and frequency, it must yield the variance of the process. Finally, the number of free parameters in the model must be adequate to represent the process, yet not so numerous as to cause instability in the inversion. Let $\mathbf{k}=(k_x,k_y,k_z)$ be the wave number and τ the time separation. A mixed spectral representation that is adequate for our purposes is

$$\Phi(\mathbf{k};\tau)=F(\mathbf{k})\cos(\omega_0\tau), \tag{14}$$

where

$$\omega_0^2=\frac{\kappa^2N^2+k_z^2f^2}{\kappa^2+k_z^2}, \tag{15}$$

$$F(\mathbf{k})=\frac{\phi_g\kappa|k_z|}{(\kappa^2+(f/N)^2k_z^2)^q(k_z^2+k_g^2)^{p/2}}, \tag{16}$$

where $\kappa^2=k_x^2+k_y^2$, ϕ_g is the spectral strength, and $F(\mathbf{k})$ rolls off at the wave number $k_g=j_*(\pi/b)(N/N_0)$.

The spectral model (14)–(16) shows the desired properties. The cosine in (14) forces the local dispersion relationship (15) to be satisfied. Being only a function of κ, the model is horizontally isotropic. Since $(f/N)\ll 1$, the model has the desired scale separation; there is more small scale variability in the vertical than in the horizontal. The exponents p and q are parameters of the model. In the standard representation of the GM model, $q=2$ but p is treated as a free parameter.[10] Although $q=2$ is typically used, other, usually smaller values have been observed. For example, both temperature and acoustic phase temporal statistics observed during MATE.[17,19] correspond to $q=1.85$.

Integration of the spectral model (14)–(16) must yield the internal wave variance. This permits ϕ_g to be written in terms of the other model parameters. Typically, the variance is a function of depth[10] and scales approximately like N^3. For completeness, we consider this typical scaling and only later set N to a constant. Letting $\langle\mu_0^2\rangle$ be the variance at the reference depth where $N=N_0$, define

$$\langle\mu_0^2\rangle(N/N_0)^3=\int d\mathbf{k}\Phi(\mathbf{k};0). \tag{17}$$

The integrations over first κ and then k_z can be evaluated analytically[20] when $\frac{3}{2}<q<\frac{5}{2}$, $p>5-2q$. Solving for ϕ_g yields

$$\phi_g=\frac{2}{\pi^{5/2}}\langle\mu_0^2\rangle\beta\left(\frac{N}{N_0}\right)^{1+p}\left(\frac{f}{N_0}\right)^{2q-3}\left(\frac{\pi j_*}{b}\right)^{p+2q-5}, \tag{18}$$

where

$$\beta=\sin(\pi(q-3/2))\,\frac{\Gamma(p/2)\Gamma(q)}{\Gamma((p+2q-5)/2)} \tag{19}$$

and Γ is the gamma function. For $p=q=2$, (18) reduces to the standard result.[10]

B. Rytov model for acoustic spectra

Theoretical expressions for the acoustic spectra are derived in the Appendix. The log-amplitude and phase spectra as a function of vertical wave number are given by (A5). This equation is used for inversion scenarios where there is a vertical receiving array. The log-amplitude and phase spectra as a function of temporal frequency are given by (A10). This equation is used for all inversion scenarios where an acoustic time series is measured at a receiver.

As appropriate for a particular inversion scenario, the ocean spectral model (14)–(16) is substituted into (A5) or (A10). The resulting multidimensional integrals are evaluated numerically using adaptive quadrature. The integrals are evaluated repeatedly for candidate values of the free parameters in the ocean model. The final values for the parameters are found by optimization using the numerical algorithm outlined in the following section.

C. Numerical optimizer

There are up to four free parameters in the ocean spectral model: the variance $\langle\mu_0^2\rangle$, the mode bandwidth, j_*, and the exponents p and q. We assume that the constant N_0b would be known from other methods (e.g., CTD-profiles); for our case, $N_0b=N_0L$. The inversion routine explicitly estimates p, q, j_*, and ϕ_g with $\langle\mu_0^2\rangle$ inferred from (18).

Given the acoustic field statistics from the numerical simulations and a defined model framework, the method described in Bell *et al.*[21] is utilized to determine the model parameters. An important feature of this weighted nonlinear least-squares method is that it is designed to work on multiple data sets. These data may have disparate values and errors. In the present context, the type of data sets included depend on the measurement geometry employed in the experiment. In a complicated scenario, the data might include

TABLE III. Rytov inversion results from four experimental configurations: (1) a rigid vertical array of receivers, (2) a single fixed receiver, (3) a less rigid vertical mooring of receivers, and (4) a single, moored receiver. The phase spectra inversions use $\log(S_\phi)$ data and theory; S_χ comparison is linear.

	Data used in the inversion	$\langle\mu_0^2\rangle/10^{-9}$	j_*	q	p
Model values	⋯	0.5	15	2	2
Configuration 1	$\phi(t,z),\chi(t,z)$	0.47 ± 0.03	23.4 ± 0.8	1.89 ± 0.02	2.64 ± 0.05
Configuration 1	$\phi(t,z),\chi(t,z)$	0.47 ± 0.01	16.4 ± 0.8	1.96 ± 0.01	2 (fixed)
Configuration 2	$\phi(t),\chi(t)$	0.43 ± 0.03	16.6 ± 1.1	1.91 ± 0.03	2 (fixed)
Configuration 3	$\chi(t,z)$	0.52 ± 0.04	15.3 ± 1.7	1.87 ± 0.02	2 (fixed)
Configuration 4	$\chi(t)$	$j_*\langle\mu_0^2\rangle/10^{-9}=8.1\pm0.2$		1.87 ± 0.01	2 (fixed)

the log-amplitude and phase spectra as functions of both temporal frequency and vertical wave number. In a simple case, only the log-amplitude frequency spectra might be available. Another useful feature of the method is that it estimates the covariance between parameters. In some cases, model parameters may be highly correlated requiring a reformulation of the optimization problem.

The optimization problem is to minimize a reduced objective function $R(x)$ that can be written, following Bell *et al.*:[21]

$$R(x)=\frac{1}{N}\sum_{i=1}^{M} N_i \log[V_i(x)], \tag{20}$$

where the parameter vector x is $x=(\phi_g, j_*, q, p)$, M is the number of data sets and, $N=\Sigma_{i=1}^{M}N_i$ is the total number of data points. Denoting the ith model and data spectral density as $\hat{S}_j^i$ and S_j^i, respectively, each having $j=1,...,N_i$ data points,

$$V_i(x)=\frac{1}{N_i}\sum_{j=1}^{N_i}(\hat{S}_j^i-S_j^i)^2. \tag{21}$$

For our problem, the goal is to fit the level and shape of the model spectra to the data spectra. Consequently a log-fit is done with acoustic phase; i.e., $\log(S_j^i)$ is used in place of S_j^i in (21). Log-amplitude is fit linearly to emphasize the knee in the vertical wave-number spectrum. See the Bell *et al.*[21] paper for further details.

Numerical optimization can be sensitive to initial values for parameters as well as step size for the function derivatives. We have explored a wide range of conditions and attempted to minimize these factors. For initial values, it seemed natural to use parameters typical of an open ocean experiment[17] and so we have initialized $\langle\mu_0^2\rangle$, j_*, q, and p to 1×10^{-9}, 6, 2, and 2, respectively.

III. INVERSE PROBLEM: PARAMETER DETERMINATION FOR A HIERARCHY OF EXPERIMENTS

The complete simulated data set includes the acoustic field at 2, 4, and 8 kHz recorded in both time and depth at a range of 6.25 km. Not all of these data, however, would necessarily be available in a field experiment. We now consider a hierarchy of inversion strategies. Members of the hierarchy correspond to different physically realizable experimental configurations. Four possible configurations, using different subsets of the complete data set, are now outlined.

Configuration 1. This configuration uses the full data set of phase $\phi(t,z)$ and log-amplitude $\chi(t,z)$. This would be the most complicated experiment to implement. It would require a long vertical array where the position of each receiver is known with sufficient precision to determine phase variations.

Configuration 2. A single accurately positioned receiver is simulated in this case and is similar to the configuration used at MATE. Provided the experiment was in the Rytov regime for both phase and log-amplitude, the resulting data sets that could be used in the inversion are $\phi(t)$ and $\chi(t)$.

Configuration 3. This case features a moored vertical receiving array. In this configuration, it may be difficult to separate sensor motion from changes in travel time rendering phase measurements unreliable. The remaining usable data are $\chi(t,z)$. This was the situation at AATE.

Configuration 4. Here a single moored receiver measures $\chi(t)$. Clearly, this would be the least expensive experiment to implement.

Table III presents a concise summary of our inversion studies. The model input parameter set is listed at the top followed by the values determined from each configuration. All four parameters were obtained only for configuration 1. As smaller data sets were used, the parameter set needed to be reduced to avoid parameter–parameter correlations. Parameter rms errors for p, q, and j_* derive directly from the diagonals of the covariance matrix produced by the optimization routine. Since, from Eqs. (18) and (19), $\langle\mu_0^2\rangle$ is a derived quantity, its mean value depends on the fit for ϕ_g and the other three parameters. The error in $\langle\mu_0^2\rangle$ is calculated using cross terms in the covariance matrix.

Consider the results for configuration 1. First, a full four parameter inversion was attempted. The inversion result $p=2.64$ differs significantly from the input value. Other terms also deviate. This can be understood by realizing that the high vertical wave number behavior of the spectra is largely

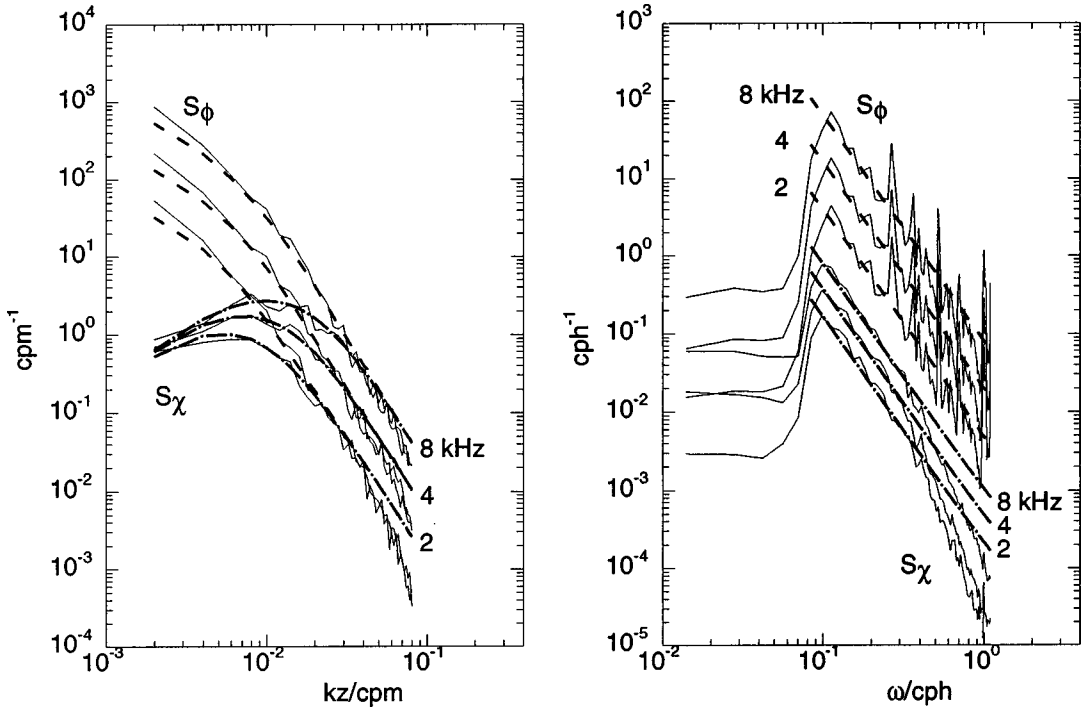

FIG. 4. Results from simultaneous optimization of average vertical wave number and frequency spectra of log-amplitude, S_χ, and phase, S_ϕ, at three acoustic frequencies. Fitted predictions are shown overplotted as dashed for S_ϕ and dot-dashed for S_χ. The S_ϕ levels are everywhere higher than for S_χ except at high k_z where $S_\chi = S_\phi$. Log-amplitude variance is proportional to the acoustic frequency; phase variance is proportional to frequency squared.

determined by the value of p; see Eq. (16). Returning to the environmental spectrum in Fig. 1, we see that inability to simulate the full model bandwidth results in spectra that fall-off too rapidly at high k_z, resulting in a higher value for p. This in turn affects the determination of the other parameters. A three parameter inversion was then attempted with fixed $p=2$. The inversion is very close to the input. Calculated and data spectra for this case are shown in Fig. 4. At high k_z, the data spectral levels are clearly below the model. So the difficulty lies not in our ability to do the inversion, but rather in simulating the forward problem.

For configuration 2, the case of a single fixed receiver, temporal spectra of log-amplitude and phase for the three acoustic frequencies were obtained from a single middepth receiver (and averaged over the 16 range/slice ''realizations''). The inversion uses a data set similar to that shown in the right of Fig. 4. The optimization gives values very close to those for configuration 1 (with $p=2$). Note, however, that the error levels are greater. Also, the value obtained for $\langle \mu_0^2 \rangle$ is somewhat smaller.

How successful is the inversion using only log-amplitude? Use of log-amplitude would be appropriate in any weakly scattering environment, as simulated here to make use of the Rytov approximation. The vertical array case, configuration 3, where $\chi(t,z)$ is measured, gives remarkably good results with inverted values only slightly less accurate than for a fixed receiver. Note once again that the rms error is larger. For the single moored receiver, configuration 4, an inversion could be made for only two parameters: the product $j_* \langle \mu_0^2 \rangle$ and q. The optimization gives a value within 5%–10% of the model value of $j_* \langle \mu_0^2 \rangle = 7.5 \times 10^{-9}$.

Most oceanographic studies consider determining the strength of the internal waves to within a factor of 2 to be sufficient. That is, use of the GM model is not expected to be appropriate within a factor of 2. For this numerical study, we expect to do significantly better. Indeed, for all configurations we see that $\langle \mu_0^2 \rangle$ is determined within 10%. For other parameters, notably q and p, because of the limitations to the numerical domain, one cannot expect to fit the input model parameters. The simulations demonstrate that the acoustic statistics are in fact determining the properties of the numerical internal wave field. For example, the high vertical wavenumber dependence ''observed'' in the internal wave spectra shown in Fig. 1 are reproduced in the inversion. Lines in the temporal spectra in Fig. 4 occur at frequencies corresponding to the lowest horizontal modes for the 6-by-25-km size of the numerical box.

IV. DISCUSSION

There are important implications for oceanographic research in these results. When standard Rytov theory is applicable, we have shown how acoustic measurements can be used to invert for the parameters of an internal wave model. The parameters are determined over a horizontal scale equal to the transmission range and thus are an integral measurement. Acoustics offers the flexibility to probe the medium over horizontal scales not easily accessible with conventional oceanographic measurements. For time-varying internal waves, the method potentially could be used to determine model parameters for weakly nonstationary, possibly intermittent, shallow-water internal wave processes.

A hierarchy of inversion strategies has been considered. In terms of the number of internal wave parameters that can be recovered and the associated uncertainty, the inversion improves with experimental complexity; see Table III for a summary. Configurations 1–3 each yielded good estimates for the internal wave variance $\langle \mu_0^2 \rangle$. Configuration 4 could recover the product of $\langle \mu_0^2 \rangle$ and the modal bandwidth j_*. A particularly significant result is that a satisfactory inversion could be obtained simply by measuring the log-amplitude of the acoustic field. Because precise tracking of the source and receiver positions is not required for measuring the log-amplitude, it would be relatively straightforward to implement; in fact, it could be included on standard ocean moorings.[15] Consequently, the method has the potential to be an important and inexpensive adjunct to oceanographic experiments.

Other inversion strategies beyond those considered in this paper could be investigated. For configuration 2, where the phase and log-amplitude spectra are obtained at a single point, it might prove useful to look at the product and quotient of the two spectra.[22] This should better separate the contributions from $\langle \mu_0^2 \rangle$ and j_*. For the moored array in configuration 3, it might be desirable to examine the difference in acoustic phase for elements along the array. For any of the configurations, adding temperature sensors would give additional information easily incorporated in the inversion.

The chief constraint on the proposed inversion is that the forward-scattering problem must be adequately described by Rytov theory. This means that an experiment must be carefully designed; frequencies and ranges must be selected that are adequate for sampling the medium yet still satisfy the assumptions of Rytov scattering. For the cases considered in this study, Rytov was well satisfied since the internal wave energy level was 1/100th of the standard open ocean value. Stronger ocean fluctuations would still satisfy Rytov if the frequencies and ranges were chosen appropriately. The standard criterion for the validity of Rytov is that the variance of the log amplitude be less than 0.3.[7] It is well known, however, that the Rytov approximation for the phase remains valid in a much larger range/frequency domain than the log amplitude. Thus it is still possible to do an inversion in moderately strong scattering situations using the acoustic phase. This has been done for the case of GM level internal waves using phase data from the MATE experiment.[6,19] It does mean, though, that the simpler experimental geometries (configurations 3 and 4 in the present study) would not be appropriate.

In this study of possible approaches to obtaining the parameters of a proposed stochastic model, we have focused on internal wave processes only. Other stochastic ocean processes one might include are baroclinic tides, finestructure, and turbulence. One need only provide a three-dimensional (3-D) plus time model for each process. The parameters for these additional processes are then found as part of the inversion. The addition of these processes was considered in an earlier paper that examined phase data from transmission experiments.[19] Inclusion of these processes in simulation studies such as these is straightforward, and may need to be done when simulating a realistic ocean.

In future work, we expect to extend this formalism to situations where there is a background sound-speed profile. This is essential before the AATE and most shallow-water inversions can be attempted. There are potential complications for inversions using the log-amplitude, in that log-amplitude is sensitive to small-scale variability in the medium.[23] In an inversion, it could prove difficult to distinguish uncertainty in the background ray path from variability in the medium. Having a vertical array of receivers would likely lessen this uncertainty; this remains a research issue. Another potential complication arises in shallow water and where a ray turns near the surface, i.e., where j_* is small. In practical situations, the acoustic range may not be large relative to the integral scale of the medium or a ray may turn within this scale, invalidating the Markov approximation in conventional Rytov theory. Some work has been done on this problem,[24] but this remains a subject of active research.[25]

ACKNOWLEDGMENTS

The authors would like to thank Dr. Frank Henyey and Dr. Bradley Bell for helpful discussions on this topic. This research was sponsored by the Department of the Navy, Office of the Chief of Naval Research, under Grant No. N00014-94-1-0569.

APPENDIX: RYTOV APPROXIMATION FOR THE ACOUSTIC SPECTRA

The Rytov approximation yields useful expressions for the statistics of a wave propagating through a weakly fluctuating random medium.[7] In this Appendix, certain essential results from Rytov theory are summarized for acoustic propagation through ocean internal waves. The results are specialized to the case of an ocean with a constant background sound speed. Both the log-amplitude χ and phase ϕ of the acoustic field are considered. The acoustic spectra as a function of vertical wave number are first presented. The temporal spectra are then derived using a consistent representation of the medium. Finally, the full two-dimensional acoustic spectrum is given for completeness.

The index of refraction fluctuations caused by internal waves are described by the spectrum $F(k_x, k_y, k_z)$ and the associated dispersion relationship. A time-harmonic point source generates an acoustic field measured along a distant vertical array at range $x = L$ as a function of time and depth. Within the Rytov approximation, the autocorrelation of the log-amplitude, χ, and phase, ϕ, is

$$B_{\chi/\phi}(z_d, \tau) = 2\pi k^2 L \int_0^1 ds \int_{-\infty}^{\infty} dk_y \int_{-\infty}^{\infty} dk_z \, F(0, k_y, k_z) \times \cos(\omega_0 \tau) g_{\chi/\phi}(k_y, k_z) e^{ik_z s z_d}, \quad \text{(A1)}$$

where τ and z_d are the separations in time and depth, respectively, and k is the wave number. The integrations are over the transverse spectral components and the normalized range $s = x/L$. The filter functions $g_{\chi/\phi}(k_y, k_z)$ are

$$g_{\chi/\phi}(k_y, k_z) = \frac{1}{2}\left[1 \mp \cos\left(\frac{sL(1-s)}{k}(k_y^2 + k_z^2)\right)\right] \quad \text{(A2)}$$

with + corresponding to ϕ, and − to χ.

The filter functions for the phase and log-amplitude emphasize different portions of the internal wave spectrum. Because g_ϕ is at a maximum at $k_y=k_z=0$, the acoustic phase is highly sensitive to the large scale (low spatial frequency) fluctuations in the medium. The filter g_x is zero at $k_y=k_z=0$ and the log-amplitude is most sensitive to fluctuations in the medium at the Fresnel scale or smaller.

When $\tau=0$, (A1) reduces to the standard textbook version of Rytov theory.[7] The generalized form in (A1) is useful in the context of solving an inverse problem since it permits possible alternative experimental configurations to be studied within a uniform mathematical framework. For this generalized form, the dispersion relationship fixes ω_0. An approximate expression in terms of the local buoyancy frequency, N, and the inertial frequency, f, is

$$\omega_0^2=\frac{k_y^2N^2+k_z^2f^2}{k_y^2+k_z^2}. \tag{A3}$$

Equation (A1) can be used to derive various acoustic spectra. Consider first the vertical wave-number spectra defined by

$$S(k_z)=\frac{1}{2\pi}\int_{-\infty}^{\infty}B(z_d,\tau=0)e^{-ik_zz_d}\,dz_d, \tag{A4}$$

where the χ/ϕ subscript is suppressed. It follows from (A1)

$$S(k_z)=2\pi k^2L\int_0^1\frac{ds}{s}\int_{-\infty}^{\infty}dk_y \times F(0,k_y,k_z/s)g(k_y,k_z/s). \tag{A5}$$

In doing a forward calculation, the internal wave spectrum F would be treated as a given with S_χ or S_ϕ then calculated via (A5). In solving the inverse problem, estimates of the acoustic spectra are derived from the measured data. The goal is to invert (A5) and determine the properties of the internal wave spectrum.

Consider next the temporal spectra. Usually the forward calculation is done by using an alternative form for F, typically in terms of the internal wave frequency and mode number.[10] This is not satisfactory in the present application. Because we are ultimately solving an inverse problem, it is desirable to have all of the observable acoustic spectra written in terms of the same internal wave spectra; an inversion would then estimate the parameters of a single common model. Define the two-sided temporal spectrum

$$\hat{S}(\omega)=\frac{1}{2\pi}\int_{-\infty}^{\infty}B(z_d=0,\tau)e^{+i\omega\tau}\,d\tau. \tag{A6}$$

It follows that for $\omega>0$,

$$\hat{S}(\omega)=2\pi k^2L\int_0^1ds\int_{-\infty}^{\infty}dk_y\int_{-\infty}^{\infty}dk_z\,F(0,k_y,k_z) \times\delta(\omega-\omega_0)g(k_y,k_z). \tag{A7}$$

Let $w(k_y)=\omega-\omega_0$. The delta function in (A7) can be used to evaluate the k_y integral by using the property[26]

$$\delta[w(k_y)]=\sum_n\frac{\delta(k_y-k_{y0}^{(n)})}{|w'(k_{y0}^{(n)})|}, \tag{A8}$$

where $k_{y0}^{(n)}$ are the values of k_y that are zeros of w. From (A2), there are zeros at

$$k_{y0}^2=\frac{\omega^2-f^2}{N^2-\omega^2}\,k_z^2. \tag{A9}$$

Note that k_{y0} is real only when $f<|\omega|<N$. Outside of the range, the acoustic spectra are zero. Inside this range,

$$\hat{S}(\omega)=4\pi k^2L\int_0^1ds\int_{-\infty}^{\infty}dk_z\,F(0,k_{y0},k_z) \times|w'(k_{y0})|^{-1}g(k_{y0},k_z), \tag{A10}$$

where

$$w'(k_{y0})=\frac{(N^2-\omega^2)^2}{N^2-f^2}\,\frac{1}{\omega}\,\frac{k_{y0}}{k_z^2}. \tag{A11}$$

Finally, for completeness, the full two-dimensional acoustic spectra can be considered. Transforming (A1) with respect to both time and depth yields

$$S(k_z,\omega)=4\pi k^2L\int_0^1\frac{ds}{s}\,F(0,k_{y0}/s,k_z/s) \times|w'(k_{y0}/s)|^{-1}g(k_{y0}/s,k_z/s). \tag{A12}$$

[1] W. H. Munk, ''Internal waves and small-scale processes,'' in *Evolution of Physical Oceanography*, edited by B. A. Warren and C. Wunsch (MIT, Cambridge, MA, 1981), pp. 264–291.

[2] M. D. Levine, C. A. Paulson, and J. H. Morison, ''Internal waves in the Arctic Ocean: Comparison with lower-latitude observations,'' J. Phys. Oceanogr. **15**, 800–809 (1985).

[3] T. E. Ewart and S. A. Reynolds, ''The Mid-ocean Acoustic Transmission Experiment, MATE,'' J. Acoust. Soc. Am. **75**, 785–802 (1984).

[4] C. Macaskill and T. E. Ewart, ''Numerical solution of the fourth moment equation for acoustic intensity correlations and comparison with the mid-ocean acoustic transmission experiment,'' J. Acoust. Soc. Am. **99**, 1419–1429 (1996).

[5] B. J. Uscinski, ''Acoustic scattering by ocean irregularities: Aspects of the inverse problem,'' J. Acoust. Soc. Am. **79**, 347–355 (1986).

[6] T. E. Ewart, ''Acoustic propagation, internal waves and finestructure,'' Proc. Inst. Acoust. **8**, 106–122 (1986).

[7] A. Ishimaru, *Wave Propagation and Scattering in Random Media* (Academic, New York, 1978), Vol. 2, Chap. 18.

[8] T. F. Duda, ''Modeling weak fluctuations of undersea telemetry signals,'' IEEE J. Ocean Eng. **16**, 3–11 (1991).

[9] K. B. Winters and E. D'Asaro, ''Direct simulation of internal wave energy transfer,'' J. Phys. Oceanogr. **27**, 1937–1945 (1997).

[10] S. M. Flatté, R. Dashen, W. Munk, K. Watson, and F. Zachariasen, *Sound Transmission Through a Fluctuating Ocean* (Cambridge U.P., London, 1979).

[11] D. Tielbürger, S. Finette, and S. Wolf, ''Acoustic propagation through an internal wave field in a shallow water waveguide,'' J. Acoust. Soc. Am. **101**, 789–808 (1997).

[12] X. Tang and F. D. Tappert, ''Effects of internal waves in sound pulse propagation in the Straits of Florida,'' IEEE J. Ocean Eng. **22**, 245–255 (1997).

[13] F. S. Henyey, D. Rouseff, J. M. Grochocinski, S. A. Reynolds, K. W. Williams, and T. E. Ewart, ''Effects of internal waves and turbulence on horizontal aperture sonar,'' IEEE J. Ocean Eng. **22**, 270–280 (1997).

[14] W. H. Munk and F. Zachariasen, ''Sound propagation through a fluctuating, stratified ocean: Theory and observation,'' J. Acoust. Soc. Am. **59**, 818–838 (1976).

[15] M. D. Levine, ''Internal waves under the arctic pack ice during the Arctic

Internal Wave Experiment: the coherence structure,'' J. Geophys. Res. **95**(C5), 7347–7357 (1990).
[16] T. E. Ewart and S. A. Reynolds, ''Instrumentation to measure the depth/time fluctuations in acoustic pulses propagated through arctic internal waves,'' J. Atmos. Ocean. Tech. **7**, 129–139 (1990).
[17] M. D. Levine, J. D. Irish, T. E. Ewart, and S. A. Reynolds, ''Simultaneous spatial and temporal measurements of the internal wave field during MATE,'' J. Geophys. Res. **91**(C8), 9709–9719 (1986).
[18] P. M. van den Berg, M. G. Coté, and R. E. Kleinman, '''Blind' shape reconstruction from experimental data,'' IEEE Trans. Antennas Propag. **43**, 1389–1396 (1995).
[19] T. E. Ewart and S. A. Reynolds, ''Ocean acoustic propagation measurements and wave propagation in random media'' in *Wave Propagation in Random Media (Scintillation)*, edited by V. I. Tatarski, A. Ishimaru, and V. U. Zavorotny (SPIE, Bellingham, 1993), pp. 100–123.
[20] I. S. Gradshteyn and I. M. Ryzhik, *Tables of Integrals, Series and Products* (Academic, New York, 1980), Eq. 3.251.2.
[21] B. M. Bell, J. V. Burke, and A. Schumitzky, ''A relative weighting method for estimating parameters and variances in multiple data sets,'' Comput. Stat. Data Anal. **22**, 119–135 (1996).
[22] D. Rouseff, T. E. Ewart, and S. A. Reynolds, ''Obtaining the ocean index of refraction spectrum from the acoustic amplitude fluctuations'' in *High Frequency Acoustics in Shallow Water*, edited by N. G. Pace, E. Pouliquen, O. Bergen, and A. P. Lyons (NATO SACLANT Undersea Research Centre, La Spezia, Italy, 1997), pp. 467–474.
[23] Y. J. F. Desaubies, ''On the scattering of sound by internal waves,'' J. Acoust. Soc. Am. **64**, 1460–1469 (1978).
[24] S. Frankenthal, ''Close range scintillations in anisotropic scattering media,'' J. Acoust. Soc. Am. **77**, 1395–1402 (1985).
[25] F. S. Henyey, ''Sound through internal waves: difficult cases,'' in *Proceedings 'Aha Huliko'a Hawaiian Winter Workshop*, edited by P. Müller and D. Henderson (SOEST Special Publication, Honolulu, 1997), pp. 175–180.
[26] R. N. Bracewell, *The Fourier Transform and its Applications* (McGraw-Hill, New York, 1986).

Extracting modal wave numbers from data collected in range-dependent environments

Ronald T. Kessel
School of Earth and Ocean Sciences, E-Hut 132A, University of Victoria, P.O. Box 3055, Victoria, British Columbia V8W 3P6, Canada

(Received 22 August 1997; accepted for publication 25 March 1998)

Properties of the seafloor affecting sound propagation can be inferred from the horizontal wave numbers of bottom-interacting modes of sound propagation. To this end, the modal wave numbers can be extracted from the harmonic sound field recorded by a single hydrophone, when either the source or hydrophone are towed at constant depth, giving in effect a well-sampled synthetic aperture array. This method has been used to determine the bottom properties in a range-independent environment, by first applying a Hankel transform to get a representative wave-number spectrum in which the wave numbers of the dominant modes feature prominantly [S. D. Rajan *et al.*, J. Acoust. Soc. Am. **82**, 998–1017 (1987)]. In range-dependent environments, however, the modes vary owing to changes in bathymetry and seafloor properties, making it impossible to speak of a single set of range-independent modal wave numbers as the Hankel transform method requires. In this paper, a phase demodulation technique is derived from the adiabatic mode model of sound propagation whereby range-dependent wave numbers can be extracted from data collected in range-dependent environments using the same experimental setup as in range-independent environments. [S0001-4966(98)02307-8]

PACS numbers: 43.30.Pc, 43.30.Ma [DLB]

INTRODUCTION

Harmonic resonances can be used to determine the salient properties of mechanical systems: the force constant for a spring, the length of a pendulum, or the speed of sound in a pipe, for example. Likewise, in ocean acoustics, the properties of the seafloor affecting sound propagation—the sediment compressional-and shear-wave speeds, density, depth, or thickness, for example—can be inferred from resonances in the sound field, which are the normal modes of sound propagation in the sea.

This is the approach followed in the Hankel-transform plus perturbative-inversion scheme proposed by Rajan *et al.*[1] for range-independent environments. Their acoustic measurement procedure is perhaps simpler than most. A stationary hydrophone continuously records the pressure field due to a cw source towed radially outwards at roughly constant depth. The magnitude and phase of the received tone $p(r_s)$ is recorded as a function of the horizontal source–receiver separation r_s, to which a cylindrical wave spectrum $G(k)$ can be ascribed using a numerical Hankel transform. The dominant modes of sound propagation appear as distinct peaks in the discrete spectrum $|G(k)|$; the peaks occurring at a series of modal wave numbers k_m, which, for bottom-interacting modes, are determined in part by the sediment properties. The sediment properties can then be inferred from k_m using an inversion computer algorithm that matches them to a geoacoustic model of the overall environment including both the water column and sediment properties.

One advantage of this method for estimating seafloor properties is its relatively simple experimental setup, requiring just one receiver, while not bothering about the particular source and receiver depths provided both remain fairly constant and the receiver is sufficiently insonified for the depths used. Another advantage is that a mode-based inversion scheme can be linearized, as Rajan *et al.* have done for the sediment compressional speed, for example, or could be done more generally for any geoacoustic parameter using derivatives of the modal wave number with respect to any geoacoustic property,[2] as opposed to the nonlinear schemes generally required when matching the pressure field itself.[3–5] Linear schemes are usually faster and more tractable than nonlinear, which is particularly important for range-dependent media, where we must in effect solve many range-independent problems to assemble the overall range-dependent domain.

But as Rajan *et al.* point out, the Hankel-transform method assumes that the geoacoustic properties of the seafloor, including bathymetry, are constant over the path traversed by the source. In practice, the variation of the modal wave numbers resulting from environmental variations along the tow path smears and broadens what would have been the discrete spectrum in the range-independent case.[6] Large variations may ruin the discrete spectrum entirely, leaving no clearly identifiable peaks because there is no discrete spectrum representative of the entire tow path.

The need to assume range invariance is perhaps more restrictive for inverse problems than for forward modeling. In the present case at least, the source tow path must be fairly long to resolve the discrete spectrum using the Hankel transform, typically on the order of several kilometers to resolve a few modes in shallow water, and considerably longer to resolve many modes in deep water. Range invariance over such distances is rarely found in practice. What is worse, modes responding most sensitively to the seafloor—typically the high-order modes representing steep angle propagation which undergo more bottom reflections and penetrate deeper

into the sediments than low-order modes do, and which therefore carry more information about seafloor properties—, will by virtue of their sensitivity be most affected by range variation, making them ineligible for the inversion processes when range variation is ignored.

A workable trade-off can sometimes be reached in which the Hankel transform is applied to a segment of the source tow path that is at once short enough that range variation can safely be ignored, but long enough to resolve individual mode peaks in the spectrum (though the peaks may now be considerably broadened). Ohta and Frisk[7] have done this using a shortened ''sliding'' aperture that is advanced step-by-step over the entire tow path. Using computer simulations, they show that the modes extracted at each step will, if the range dependence is not too great, closely approximate the local modes at the aperture's center range. They then applied the sliding-aperture method to extract the modal wave numbers from data collected at two different sites from which the corresponding geoacoustic properties were inferred by inversion.

The goal of this paper is to show how the wave-number extraction method can be applied for the same type of experiments when range-dependence cannot be ignored. To this end it will be shown how a steadily towed cw source ''broadcasts'' the wave numbers of the local modes in the form of a phase-modulated carrier signal, and then how the range-dependent wave numbers can be retrieved directly from that signal using *phase demodulation* from communication theory.[8] The result is a signal-processing tool for mode-based inversion schemes in range-dependent environments for which the adiabatic-mode approximation applies. This is a brief demonstration of principle only, outlining first the theoretical basis of phase demodulation for wave-number extraction, and then demonstrating its use by numerical simulations. Techniques for inverting the retrieved modal wave numbers for geoacoustic parameters are not considered, but can be found in the references.

I. ADIABATIC MODES

Under the usual adiabatic mode approximation,[9] it is assumed that (1) the sound field is dominated by the normal modes of vibration excited by the source, (2) the environmental variation with range is gradual enough that energy transfer between modes due to scattering can be neglected, and (3) there is no horizontal refraction of the sound out of the vertical r-z plane through the source at $\mathbf{x}_s=(r_s,z_s)$ and receiver at $\mathbf{x}=(r,z)$. Each mode is then characterized by a local horizontal wave number $k_m(r)$ and vertical mode function $\Psi_m(\mathbf{x})$, both of which can be computed using a range-independent mode model as if the environment were locally range independent. The far-field acoustic pressure $p(\mathbf{x},\mathbf{x}_s)$ due to a cw source with harmonic time dependence $e^{-i\omega t}$ can then be written as the superposition of M propagating modes

$$p(\mathbf{x},\mathbf{x}_s)=\sum_{m=1}^{M} p_m(\mathbf{x},\mathbf{x}_s), \tag{1}$$

where $p_m(\mathbf{x},\mathbf{x}_s)$ is the contribution of the mth mode

$$p_m(\mathbf{x},\mathbf{x}_s)=A_m(\mathbf{x},\mathbf{x}_s)e^{i\phi_m(r,r_s)}, \tag{2}$$

$\phi_m(r,r_s)$ being the horizontal phase accumulated as the mode propagates from the source to receiver

$$\phi_m(r,r_s)=\int_{r_s}^{r} k_m(r)\,dr, \tag{3}$$

and $A_m(\mathbf{x},\mathbf{x}_s)$ representing the combined depth z dependence of the mode, the (monopole) source excitation, and cylindrical spreading

$$A_m(\mathbf{x},\mathbf{x}_s)=\Psi_m(\mathbf{x}_s)\Psi_m(\mathbf{x})/\sqrt{\phi_m(r,r_s)}. \tag{4}$$

If the receiver is stationary and the source is towed at constant depth, then the pressure varies with source range r_s alone. Hence $p(\mathbf{x},\mathbf{x}_s)\equiv p(r_s)$, and (1) can be viewed as the sum of M signals $p_m(\mathbf{x},\mathbf{x}_s)\equiv p_m(r_s)$ in r_s; each signal consisting of a carrier $e^{i\phi_m(r_s)}$ whose amplitude is modulated through the range dependence of $A_m(\mathbf{x},\mathbf{x}_s)$, and whose phase is modulated through the range dependence of $k_m(r)$ in $\phi_m(r_s)$. Our object is to isolate the signal of a mode $p_m(r_s)$ from the total signal $p(r_s)$, and then apply phase demodulation to extract its range-dependent local wave number $k_m(r_s)$.

II. ISOLATING INDIVIDUAL MODES

A. Range-independent environments

In range-independent environments, the field due to a monopole source is related to its plane-wave spectrum $G(k)$ (vertical Green's function) through a Hankel transform pair[10]

$$p(r_s)=\int_0^\infty G(k)J_0(kr_s)k\,dk, \tag{5}$$

$$G(k)=\int_0^\infty p(r_s)J_0(kr_s)r_s\,dr_s. \tag{6}$$

(The depth z dependence of p and G is usually stated explicitly in their arguments, but is omitted here as mentioned above. The source, moreover, is assumed to lie on the vertical axis of a cylindrical coordinate system, and the range coordinate of the receiver r is used rather than r_s, but the transform is invariant with respect to the interchange of r and r_s in range-independent media.)

The contribution of dominant modes appears as sharp maxima in $|G(k)|$ when plotted as a function of (real) k; the maxima occurring where the contour of integration in (5) crosses over the shoulder of nearby poles (from complex variable theory), which are located at the complex wave numbers k_m of the modes. The contribution of a mode can be isolated by bandpass filtering $G(k)$ in the wave-number domain over a narrow band $k_1<k_m<k_2$. That is,

$$p_m(r_s)\approx\int_0^\infty w_m(k)G(k)J_0(kr_s)k dk, \tag{7}$$

where $w_m(k)$ is a bandpass windowing function, a Hanning window perhaps

$$w_m(k) = \begin{cases} 0, & \text{for } k<k_1, \\ \frac{1}{2}\left(\cos\frac{2\pi[k-(k_2+k_1)/2]}{(k_2-k_1)}+1\right), & \text{for } k_1\leqslant k\leqslant k_2, \\ 0, & \text{for } k>k_2, \end{cases} \tag{8}$$

for a narrow band k_1 to k_2. Contour-integration models of sound propagation based on (5) usually have the option of isolating the field due to one or more modes by selectively filtering $G(k)$ in much the same way.[11]

B. Range-dependent environments

Turning now to range-dependent media, the Hankel transform pair (5) and (6) can still be applied to the measured pressure field $p(r_s)$, if only as a numerical exercise, where $G(k)$ is simply the Hankel transform of $p(r_s)$ and cannot justifiably be called the vertical Green's function. If the range dependence is slight, however, then the wave-number spectrum should closely resemble the range-independent case: individual modes should still be identifiable, but now their peaks in the spectrum will be broadened by the range variation of $k_m(r_s)$. The contribution of a single mode may nevertheless be isolated by bandpass filtering in the wave-number domain, even when the spectral spreading is considerable, provided that the wave-number spectrum of one mode does not significantly overlap that of neighboring modes. Spectral overlap is more likely as (1) the frequency f is increased, when there are many propagating modes close together along the real k axis; and (2) as the range dependence becomes more extreme, forcing each mode to occupy a larger bandwidth. Overlap is like cross talk between bands in a communication system and calls for additional signal processing to distinguish between signals. This might be done using a vertical receiver array together with beamforming to spatially filter the modes, rather than using a single receiver.[7,12]

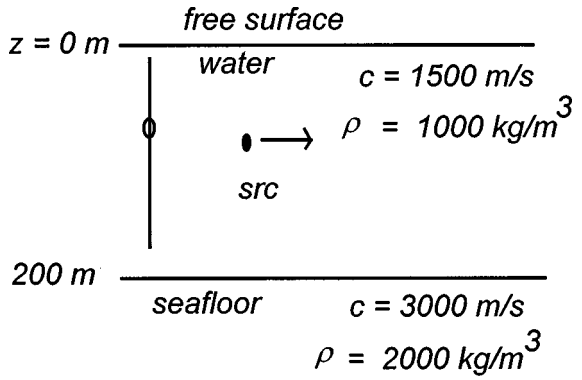

FIG. 1. A simple two-layer range-independent environment. The receiver is stationary at $(r,z)=(0,90\text{ m})$, and the source is towed from $r=1$ to 10 km at constant depth $z=60$ m. The compressional speed is denoted c, and the density ρ.

III. PHASE DEMODULATION

Assuming that the spectrum of one mode can be isolated by selective bandpass filtering in the wave-number domain, its contribution $p_m(r_s)$ to the total pressure can be found by transforming back to the r_s domain using (7), and we can apply phase demodulation by differentiating with respect to source range r_s:

$$\frac{dp_m}{dr_s} = i\,\frac{d\phi_m}{dr_s}\,p_m + \frac{dA_m}{dr_s}\,e^{i\phi_m}, \tag{9}$$

where

$$\frac{d\phi_m}{dr_s} = -k_m(r_s) \tag{10}$$

by (3), and

$$\frac{dA_m}{dr_s} = \frac{\Psi_m(\mathbf{x})}{\sqrt{\phi_m}}\,\frac{d\Psi_m(\mathbf{x}_s)}{dr_s} - \frac{1}{2}\,\frac{\Psi_m(\mathbf{x})\Psi_m(\mathbf{x}_s)}{\phi_m^{3/2}}\,\frac{d\phi_m}{dr_s} \tag{11}$$

by (4). We assume that the derivative of the amplitude modulation dA_m/dr_s can be neglected because $d\Psi_m/dr$ is small for weakly range-dependent media, and because $\phi_m^{-3/2}$ decays quickly for large source–receiver separation. Hence (9) is approximately

$$\frac{dp_m}{dr_s} \approx \frac{d\phi_m}{dr_s}\,p_m = -ik_m(r_s)p_m, \tag{12}$$

whereby

$$|k_m(r_s)| \approx \left|\frac{dp_m(r_s,z)/dr_s}{p_m(r_s,z)}\right| \approx k_m(r_s) \tag{13}$$

for dominant propagating modes whose wave numbers are predominantly real. In other words, the range-dependent

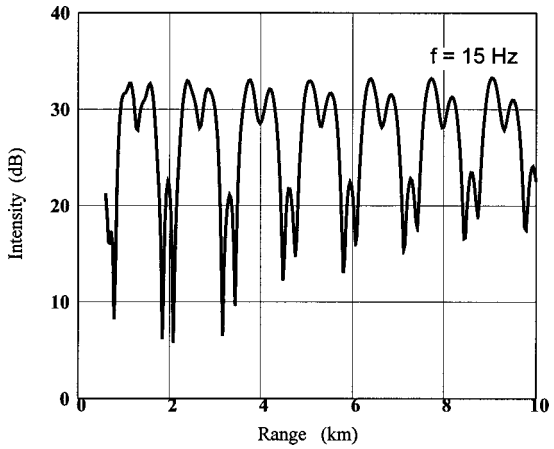

FIG. 2. The received intensity as a function of source range, computed using the PE model RAM for the range-independent environment shown in Fig. 1.

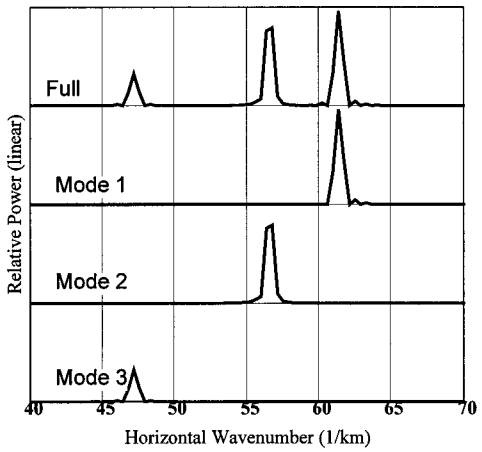

FIG. 3. The wave-number spectrum for the entire 9-km towpath (full) and for each mode (1, 2, and 3) after selective bandpass filtering for the range-independent environment shown in Fig. 1.

modal wave number is approximately equal to the magnitude of the derivative of the mode's contribution divided by the contribution itself.

IV. USING THE FOURIER TRANSFORM

Phase demodulation does not require the Hankel transform. Indeed, if the receiver remains in the far field of the source over the entire tow path, then its two-dimensional plane-wave equivalent, the Fourier transform,

$$p(r_s)=\int_{-\infty}^{\infty} G'(k)e^{ikr_s}\,dk, \tag{14}$$

$$G'(k)=\frac{1}{2\pi}\int_{-\infty}^{\infty} p(r_s)e^{-ikr_s}\,dr_s, \tag{15}$$

may serve better. For not only is the Fourier transform more familiar for numerical work with real-time series by way of the fast Fourier transform (FFT), but differentiation with respect to the source range r_s can be performed in the wave-number domain simply by multiplication by ik. As with the

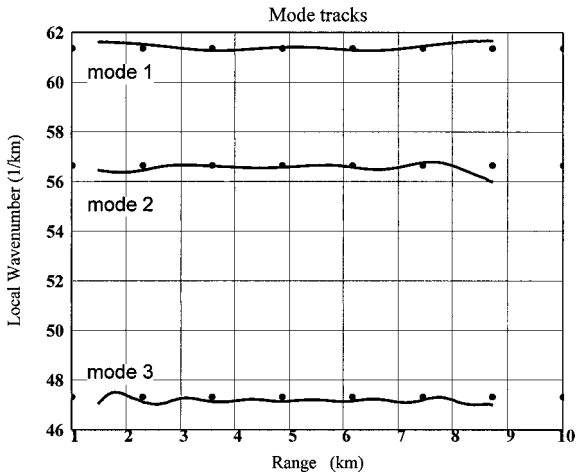

FIG. 4. The local wave numbers (solid lines) extracted using phase demodulation in the range-independent environment shown in Fig. 1 and the local wave numbers (points) computed independently using the mode model ORCA.

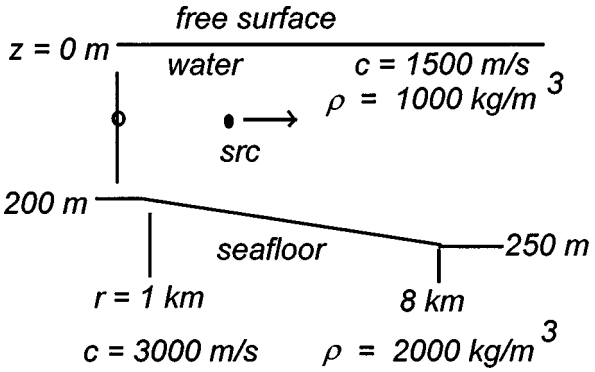

FIG. 5. A simple two-layer environment with a linearly sloped bottom. The source, receiver, and geoacoustic properties are the same as in Fig. 1.

Hankel transform, we only require that the wave-number spectrum of at least one mode can be isolated from all others by selectively bandpass filtering the wave-number spectrum from k_1 and k_2 in the wave number k domain; that is

$$p_m(r_s)\approx\int_{-\infty}^{\infty} w_m(k)G'(k)e^{ikr_s}\,dk, \tag{16}$$

$$\frac{dp_m(r_s)}{dr_s}\approx\int_{-\infty}^{\infty} ikw_m(k)G'(k)e^{ikr_s}\,dk, \tag{17}$$

where $w_m(k)$ is a suitable windowing function.

V. EXAMPLES

For a preliminary assessment, the principle of phase demodulation is demonstrated here using computer simulations, thereby avoiding the complications real data invariably entail, such as noise, uncertainties in source ranging, time-dependent fluctuations of the environment, and so forth, all of which have been neglected above. Computer simulations are at any rate advisable before applying the phase-demodulation method, if only using a rough estimate of the bathymetry and sediment properties expected at a site, in order to determine by numerical experiments (1) the frequencies at which the spectra of a few dominant modes can be separated from all others by filtering in the wave-number domain, (2) the width of the spectral bands associated with

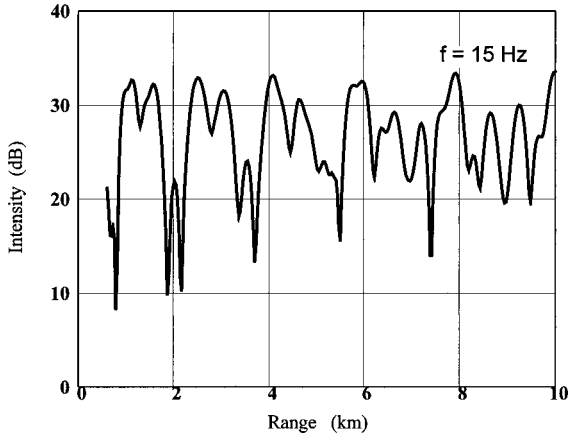

FIG. 6. The received intensity as a function of source range, computed using the PE model RAM for the sloped environment shown in Fig. 5.

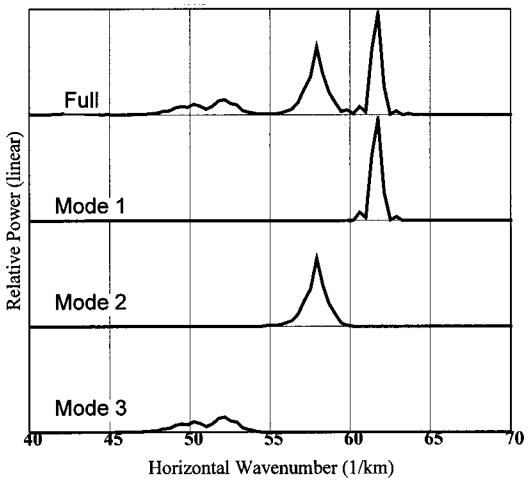

FIG. 7. The wave-number spectrum for the entire 9-km towpath (full) and for each mode (1, 2, and 3) after selective bandpass filtering for the sloped environment shown in Fig. 5.

each of those modes, and (3) a reasonable length for the source towpath: being at once long enough to resolve modes in the wave-number domain without becoming prohibitively long, and short enough that progressive range variation will not cause overlap between mode spectra.

In the examples below, the ''measured'' pressure field $p(r_s)$ has therefore been synthesized using the parabolic equation (PE) model RAM,[13] a model that permits range dependence, but, unlike the adiabatic mode model, includes both the continuous and discrete wave-number spectrum without making adiabatic approximations, though making different approximations characteristic of PE models generally.[9] As in real data, the modes therefore appear indirectly, as dominant resonances produced by the constructive interference of multiple reflections from the surface and seafloor, quite apart from the theory of modes.

Using RAM, then, essentially the same experiment was simulated in four different shallow-water environments: one range independent, and three range dependent. In each case a 15-Hz cw source was towed slowly (velocity$\rightarrow$0) at constant depth $z_s = 60$ m along a 9-km towpath from $r_s = 1$ to 10 km; the path being directed radially outwards from a stationary receiver placed at depth $z = 90$ m. The modal wave numbers for the first three dominant modes were extracted from the simulated pressure field $p(r_s)$ by applying numerical equivalents (FFT) of (15), (16), and (17), giving $G'(k)$, $p_m(r_s)$, and $dp_m(r_s)/dr_s$, respectively; and then by applying (13) to get $k_m(r_s)$. The extracted wave numbers were then verified against the ''exact'' local wave numbers computed independently for each environment using the mode propagation model ORCA.[14]

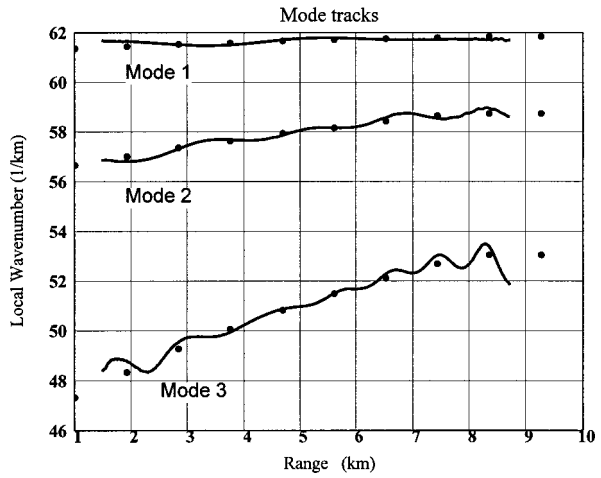

FIG. 8. The local wave numbers (solid lines) extracted using phase demodulation in the sloped environment in Fig. 5 and the local wave numbers (points) computed independently using the mode model ORCA.

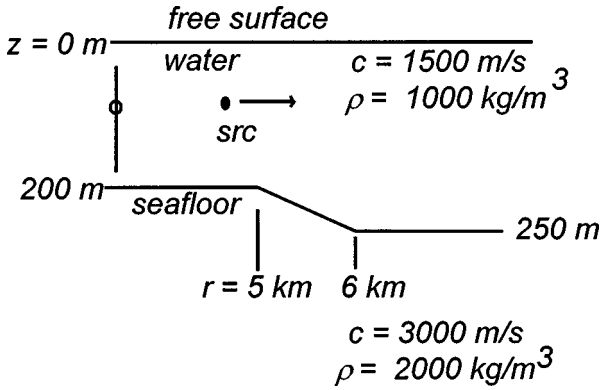

FIG. 9. A simple two-layer environment with a steep sloped bottom. The source, receiver, and geoacoustic properties are the same as in Fig. 1.

A. Range-independent example

Figure 1 illustrates the environment used in the first trial, which to begin is range independent. The magnitude of the received intensity $|p(r_s)|^2$ computed using RAM is plotted as a function of source range r_s in Fig. 2, and Fig. 3 shows the spectrum $|G'(k)|^2$ derived from it using (15) for the entire source towpath. The discrete spectra associated with the first three modes are clearly evident and can be isolated using bandpass filters as shown.

The local mode wave numbers $k_m(r_s)$, extracted from the isolated mode spectra using phase demodulation, are plotted as a function of range r_s in Fig. 4. For this range-independent problem the mode tracks should be horizontal

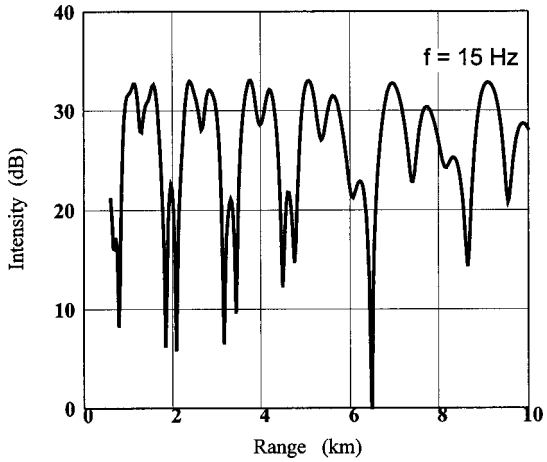

FIG. 10. The received intensity as a function of source range, computed using the PE model RAM for the sloped environment shown in Fig. 9.

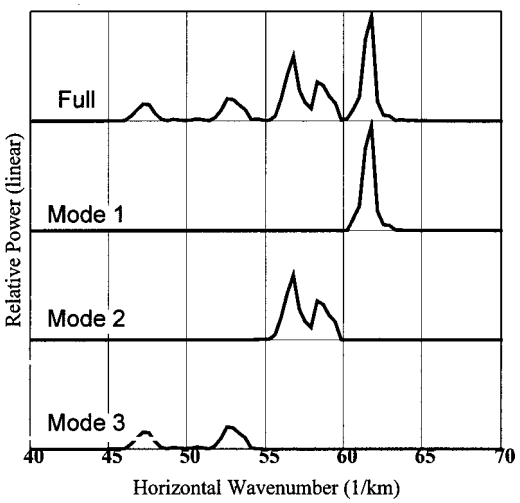

FIG. 11. The wave-number spectrum for the entire 9-km towpath (full) and for each mode (1, 2, and 3) after selective bandpass filtering for the sloped environment shown in Fig. 9.

straight lines passing through the points computed using ORCA, also plotted in Fig. 4. Slight oscillations about the exact points are due primarily to windowing effects, when a finite length data window (9 km) was used in the FFT to approximate the infinite limits of the Fourier integral, and when a bandpass filter was applied to the wave-number spectrum. This has been proven by experiments (omitted here) with different window lengths and windowing functions $w_m(k)$.

Notice that the modal wave numbers could have been read directly (and more simply) from the location of the peaks in the full spectrum in Fig. 3. This peak-extraction method works for range-independent environments, but not for range-dependent environments as shown below.

B. Gentle slope

Bathymetry is perhaps the single most important factor affecting the modal wave numbers in shallow water. This next example considers sloped (linear) bathymetry as shown

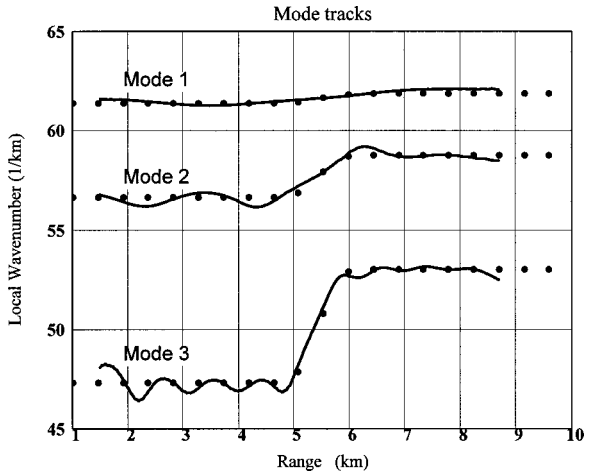

FIG. 12. The local wave numbers (solid lines) extracted using phase demodulation in the sloped environment shown in Fig. 9 and the local wave numbers (points) computed independently using the mode model ORCA.

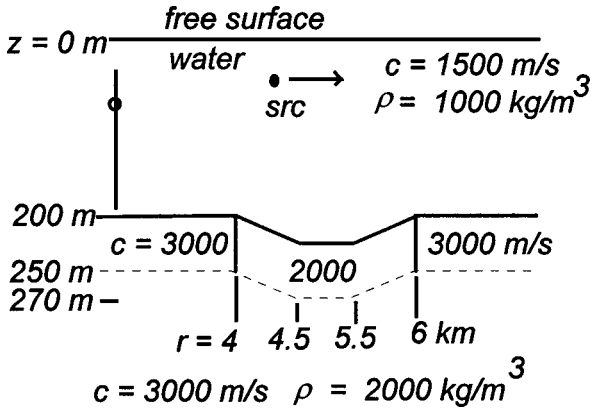

FIG. 13. A sediment pond. The sediment compressional wave speed c decreases linearly with a range from 3000 m/s at 4 km to 2000 m/s at 4.5 km, remains constant at 2000 m/s from 4.5 to 5.5 km, then increases from 2000 m/s at 5.5 km back to 3000 m/s at 6.0 km. The source and receiver are the same as in Fig. 1.

in Fig. 5. Figure 6 shows the received intensity over the same 9-km source towpath, and Fig. 7 the corresponding wave-number spectrum. The peaks of the discrete spectra associated with the first three modes are now broader than in the range-independent case, but the contributions from each adiabatic mode can nevertheless be isolated one from another by filtering in the wave-number domain as shown. The range-dependent mode tracks extracted using phase demodulation in Fig. 8 agree well with exact local modes aside from small oscillations as before.

This example demonstrates (as the remaining examples likewise do), that (1) higher-order modes are more sensitive to bathymetry because they interact more strongly with the bottom, and (2) that the range-dependent wave numbers can be extracted using the same experimental setup used for range-independent environments, only the processing of the received signal is changed.

C. "Steep" slope

An equal but more sudden change in bathymetry is shown in Fig. 9. Figure 10 shows the received intensity, and

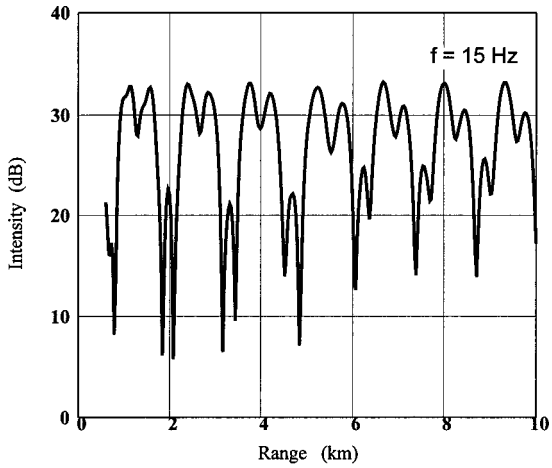

FIG. 14. The received intensity as a function of source range, computed using the PE model RAM for the sediment pond shown in Fig. 13.

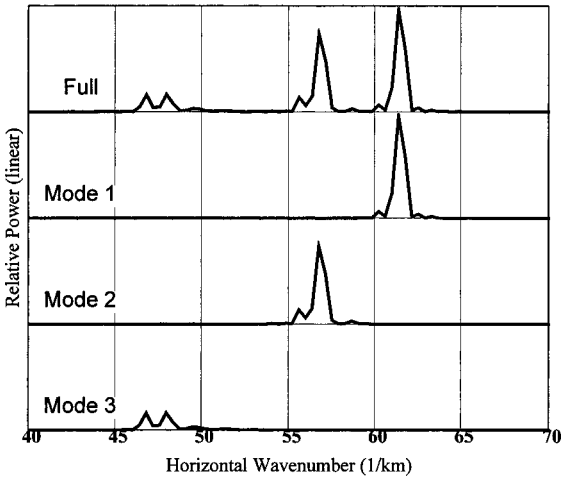

FIG. 15. The wave-number spectrum for the entire 9-km towpath (full) and for each mode (1, 2, and 3) after selective bandpass filtering for the sediment pond shown in Fig. 13.

Fig. 11 the corresponding spectrum. This environment is like two range-independent models joined abruptly together, so the spectra look like the superposition of the spectra expected for each range-independent section. This is most evident in the double peaks in the spectrum for mode three. Figure 12 shows the modal tracks extracted by phase demodulation, which agree well with the exact local modes.

D. Sediment pond

The final example includes variation in both the sediments and bathymetry as shown in Fig. 13. Figure 14 shows the received intensity and Fig. 15 the corresponding spectrum. Figure 16 shows the modal wave numbers extracted by phase demodulation which agree well with the exact local modes. The variation of the modal wave numbers is now due to the combined influence of the changing sediment phase speed and bathymetry.

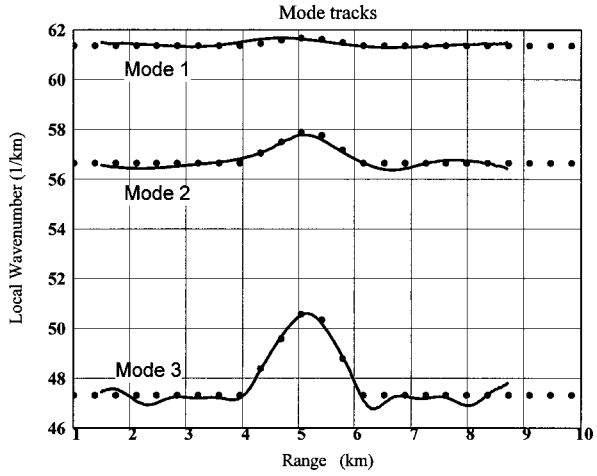

FIG. 16. The local wave numbers (solid lines) extracted using phase demodulation in the sediment pond shown in Fig. 13 and the local wave numbers (points) computed independently using the mode model ORCA.

VI. CONCLUSIONS

It has been shown how phase demodulation can in principle be used to extract the modal wave numbers from the field due to a cw source towed at constant depth in a range-dependent environment. Essentially the same method can be applied to the reverse scenario, extracting the local wave numbers of modes in the vicinity of a receiver towed at constant depth when the source is kept stationary. The greatest limitation to the method is that imposed by overlap between modes in the wave-number spectrum, either when the modes are too close together along the real axis because the frequency is too high, or when the mode variation with range is too large over the towpath. Overlap might be suppressed using a receiver array together with spatial filtering, rather than a single receiver.

The next step is to apply phase demodulation to extract the modal wave-numbers from real data, and to infer from them the range-dependent geoacoustic properties using a suitable inversion scheme. One significant advantage of this mode-based approach to geoacoustic inversion over other matched-field inversion schemes (those matching the pressure field itself) is that a forward model for generating the replica pressure field in a range-dependent environment is not required because a range-independent mode model suffices for matching local wave numbers to local sediment properties, much as ORCA was used to verify the range-dependent examples given here.

[1] S. D. Rajan, J. F. Lynch, and G. V. Frisk, ''Perturbative inversion methods for obtaining bottom geoacoustic parameters in shallow water,'' J. Acoust. Soc. Am. **82**, 998–1017 (1987).
[2] R. T. Kessel, ''The variation of modal wave numbers with geoacoustic parameters in layered media,'' J. Acoust. Soc. Am. **102**, 2690–2696 (1997).
[3] M. D. Collins and W. A. Kuperman, ''Non-linear inversion for ocean bottom properties,'' J. Acoust. Soc. Am. **92**, 2770–2783 (1992).
[4] S. E. Dosso, M. L. Yeremy, J. M. Ozard, and N. R. Chapman, ''Estimation of ocean-bottom properties by matched field inversion of acoustic field data,'' IEEE J. Ocean Eng. **18**, 232–239 (1993).
[5] P. Gerstoft, ''Inversion of seismoacoustic data using genetic algorithms and *a posteriori* probability distributions,'' J. Acoust. Soc. Am. **95**, 770–782 (1994).
[6] G. V. Frisk, J. F. Lynch, and S. D. Rajan, ''Determination of compressional wave speed profiles using inverse techniques in a range-dependent environment in Nantucket Sound,'' J. Acoust. Soc. Am. **86**, 1928–1939 (1989).
[7] K. Ohta and G. Frisk, ''Modal evolution and inversion for seabed geoacoustic properties in weakly range-dependent shallow-water waveguides,'' IEEE J. Ocean Eng. **22**, 501–521 (1997).
[8] F. G. Stremler, *Introduction to Communication Systems* (Addison-Wesley, Reading, MA, 1982).
[9] F. B. Jensen, W. A. Kuperman, M. B. Porter, and H. Schmidt, *Computational Ocean Acoustics* (American Institute of Physics, New York, 1994).
[10] F. R. Di Napoli and R. L. Deavenport, ''Theoretical and numerical Green's function field solution in a plane multilayered medium,'' J. Acoust. Soc. Am. **67**, 92–105 (1980).
[11] H. Schmidt, *SAFARI: Seismo-acoustic Fast Field Algorithm For Range Independent Environments* (SR 113, SACLANT ASW Research Center, La Spezia, Italy, 1987).
[12] W. M. Carey, J. Doutt, R. B. Evans, and L. M. Dillman, ''Shallow water sound transmission measurements on the New Jersey continental shelf,'' IEEE J. Ocean Eng. **20**, 321–336 (1995).
[13] M. D. Collins, ''A split-step Padé solution for the parabolic equation method,'' J. Acoust. Soc. Am. **93**, 1736–1742 (1993).
[14] E. K. Westwood, C. T. Tindle, and N. R. Chapman, ''A normal mode model for acousto-elastic ocean environments,'' J. Acoust. Soc. Am. **100**, 3631–3645 (1996).

Robust multi-tonal matched-field inversion: A coherent approach

Zoi-Heleni Michalopoulou
Department of Mathematical Sciences and Center for Applied Mathematics and Statistics, New Jersey Institute of Technology, Newark, New Jersey 07102

(Received 15 May 1997; accepted for publication 18 March 1998)

Matched-field processing is a method for inversion of the acoustic field utilizing its spatial coherence. In this work, a matched-field processor is introduced that incorporates the spatial coherence of the acoustic field not only at a single frequency but across frequencies as well. The new processor is suitable for multitonal sources and does not require knowledge of the source spectrum which is typically unavailable in passive estimation problems. A performance evaluation on source localization under low signal-to-noise ratios shows that the new processor is significantly superior, under certain circumstances, to the conventional incoherent Bartlett processor especially in cases involving receiver arrays with a small number of phones. © *1998 Acoustical Society of America.* [S0001-4966(98)00407-X]

PACS numbers: 43.30.Pc, 43.30.Wi, 43.60.Gk [DLB]

INTRODUCTION

This work introduces a processor suitable for inversion with matched-field processing (MFP) when the source signal consists of multiple tonals. The new processor exploits hitherto ignored spatial coherence without requiring prior knowledge of the source spectrum and is, under certain conditions, significantly superior to conventional, broadband MFP.

MFP is a technique applied to acoustic measurements to extract information on parameters that determine sound propagation in the ocean. Mostly implemented in a passive framework, MFP is based on the evaluation of a measure of similarity between the true acoustic field recorded at an array of hydrophones and theoretically predicted fields calculated using sound propagation models.

A key factor in MFP is the exploitation of the spatial coherence of the acoustic field. For this reason, the acoustic field is both measured and evaluated at different sensors that are spatially separated.

MFP has traditionally been applied in a narrow-band fashion to deep water problems. The interest of the underwater acoustics community, however, has recently shifted towards shallow-water situations, where environments present additional challenges arising from the complex interaction patterns of the sound with the sea bottom boundary, which is frequently inaccurately known. To overcome the difficulties generated by shallow-water propagation, broadband MFP has been employed in an effort to increase robustness by making use of multiple frequency information.

Recent work has shown that broadband MFP is indeed more robust and accurate than its narrow-band counterpart.[1] Several broadband variants of MFP have been described in the literature, the most prominent being incoherent broadband MFP: incoherent averaging of narrow-band MFP ambiguity surfaces in a linear or logarithmic fashion.[2]

This paper proposes a broadband MFP scheme that is *coherent* in contrast to the majority of broadband matched-field processors. The new processor, the basis for which was first described in Refs. 1 and 3, explores the spatial coherence of the acoustic field not only at a single frequency but across frequencies as well. This processor has been designed to handle sources that are multitonal instead of sources with a continuous spectrum over frequency. Multiple tones can be present in the spectrum of a mechanical source[4,5] and also in the spectra of sounds generated by vocalizing marine mammals.[6,7]

A coherent approach for broadband MFP was first introduced by Tolstoy.[8] A method similar to the one proposed by Tolstoy, but using only parts of the cross-spectral density matrix, was presented by Westwood;[9] and a coherent realization of the minimum variance processor with environmental perturbation constraints (MV-EPC) designed for broadband random sources was developed by Czenszak and Krolik.[5] Also, the term ''coherent broadband processing'' has been used to describe time-domain MFP.[10–12]

The proposed approach builds on work introduced in Refs. 1 and 3, which extended Tolstoy's spatially coherent broadband processor.[8] In addition to improved estimation performance, the new processor has the advantage of a simple implementation. The coherent processor is presented here as a straightforward extension of the Bartlett estimator; however, the proposed methodology can be used to extend other narrow-band MFP schemes that make use of a cross-spectral density matrix (the minimum variance, MV, processor, for example).

The paper is organized as follows: Sec. I presents the conventional incoherent Bartlett processor frequently used in broadband MFP. Section II discusses the spatial coherence of the acoustic field across frequencies, presents the original coherent matched-field processor, and introduces an improved variant. Section III compares and contrasts the results from the application of the incoherent broadband Bartlett processor and the new coherent processor to simulated data for source localization; the focus is on localization performance under low signal-to-noise ratios (SNR). Section IV discusses the problem of temporal uncertainty and how this affects the proposed coherent processor. Finally, Sec. V sum-

marizes the results and benefits obtained using the new coherent processor.

I. INCOHERENT BROADBAND MATCHED-FIELD PROCESSING

Narrow-band MFP can be performed using the Bartlett (linear) processor, which calculates the inner product between the true, measured acoustic field and replica fields calculated for likely values of the unknown parameters. The processor leads to the formulation of an ambiguity/correlation surface (which is a function of the unknown parameters) expressed as follows:

$$P_{\text{bart}}(\mathbf{q},f\ )=\mathbf{w}^*(\mathbf{q})\mathbf{d}\mathbf{d}^*\mathbf{w}(\mathbf{q}), \tag{1}$$

where $\mathbf{w}(\mathbf{q})$ is the replica field generated for the vector of unknown parameters $\mathbf{q}$, normalized to have unit length, $\mathbf{d}$ is a vector of acoustic field measurements, and $(\cdot)^*$ indicates conjugate transpose. The replicas $\mathbf{w}$ and data $\mathbf{d}$ correspond to a specific frequency f.

The inner product of Eq. (1) is essentially a *coherent* summation of the *weighted* received acoustic field at spatially separated hydrophones for a single frequency. It therefore captures the spatial coherence of the acoustic field in the ocean, a fundamental element of MFP.[13]

Usually more than one data vector is available, in which case Eq. (1) becomes

$$P_{\text{bart}}(\mathbf{q},f\ )=\mathbf{w}^*(\mathbf{q})\left(\frac{1}{M}\sum_{m=1}^{M}\mathbf{d_m}\mathbf{d_m^*}\right)\mathbf{w}(\mathbf{q})$$

$$=\mathbf{w}^*(\mathbf{q})C\mathbf{w}(\mathbf{q}), \tag{2}$$

where M is the number of data observations and C is an estimate of the cross-spectral density matrix of the data for frequency f.

In shallow water the conditions for source localization (and/or environmental inversion) are more challenging than in deep water because of the heavy interaction of the acoustic signals with the often poorly known ocean bottom. To overcome these difficulties, broadband matched-field implementations have been investigated and have been shown to lead to more robust estimation than narrow-band techniques.[1]

The term ''broadband MFP'' is currently being used both for processing information obtained for a number of tones (the Hudson Canyon experiment[1]) and for processing data resulting from a source with a continuous broad spectrum (the Gulf of Mexico experiment[11]). Both cases require extension of typical narrow-band MFP techniques. A simple way to implement the extension is to average over ambiguity surfaces obtained for single frequencies. Averaging can be done linearly or logarithmically.[2] Other techniques have been proposed that handle in different ways the information at multiple frequencies.

II. COHERENT MULTITONAL MATCHED-FIELD PROCESSING

A. Spatial coherence of the acoustic field

The conventional broadband Bartlett processor described in Sec. I makes use of the spatial coherence of the acoustic field by exploring cross-covariance structure along an array of hydrophones. This spatial coherence is strictly monochromatic since it is evaluated for the acoustic field received at a specific frequency f: the summation across frequency is performed *incoherently*. However, spatial coherence exists across frequencies as well. Figure 1 shows an example of a cross-spectral density matrix across hydrophone and frequency. This matrix was obtained through simulations run for a 110-m-deep waveguide and ten vertically separated equidistant hydrophones with the shallowest hydrophone being at 10 m and the deepest one at 100 m. The source transmitted tones at frequencies 50, 100, 150, and 200 Hz.

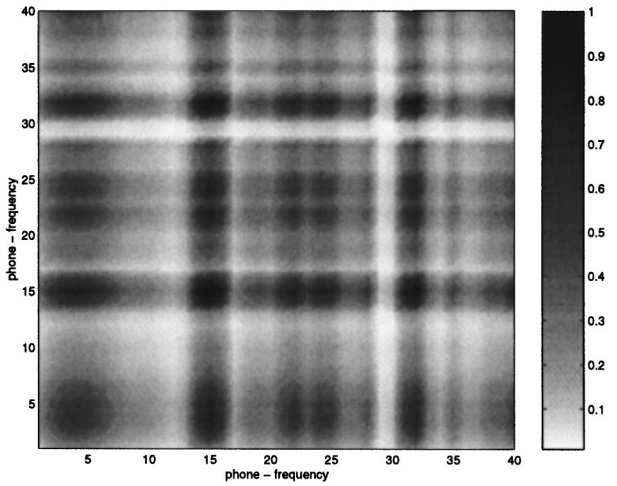

FIG. 1. The augmented cross-spectral density matrix for ten hydrophones and four frequencies.

The cross-spectral matrix of Fig. 1 was calculated as follows: the data vectors were generated for a source location of 50 m and 3 km in depth and range using KRAKEN[14] for the four different frequencies. The four field vectors were then concatenated creating a data vector consisting of $10\times4=40$ entries (ten hydrophones by four frequencies). No noise was assumed present and the cross-spectral density matrix was based on a single (augmented) vector [M of Eq. (2) was 1]. Figure 1 illustrates that the spectral matrix is not zero in the off-diagonal regions. Nonzero values in these regions show the existence of covariance structure between data at different frequencies and different hydrophones. For example, high values in the covariance structure appear between phone-frequency observations 15 and 3. Phone-frequency observation 15 corresponds to the fifth receiver and the second frequency, and the phone-frequency observation 3 corresponds to the third receiver and first frequency.

Since spatial coherence contributes significantly to the utility of MFP in underwater communications, it is reasonable to expect greater utility from exploiting the additional spatial coherence structure between fields at different frequencies.

B. Coherent Bartlett processing for an unknown source spectrum

The matched-field technique proposed in this paper differs from most other broadband MFP methods suggested so

far in that it exploits information across frequency and across space; moreover, it exploits the extra information without requiring knowledge of the source spectrum.

Taking into account the interfrequency spatial coherence can be realized by using the ''concatenated'' data vectors discussed previously to form the cross-spectral density matrix required in the Bartlett processor [Eq. (2)]. Naturally, the concatenation procedure should be applied to the replica vectors as well.

The concatenation procedure was originally suggested by Tolstoy,[8] who also pointed out that this implementation requires knowledge of the source spectrum. In the passive case, source spectrum information is unavailable, prohibiting the successful application of coherent MFP. A solution to this problem is proposed here.

Assume that the source transmits sound at four frequencies f_1, f_2, f_3, and f_4. Usually data are received in different frames corresponding to times t_1, $t_2=t_1+\delta t_2$, $t_3=t_1+\delta t_3,\ldots,t_M=t_1+\delta t_M$. The tones at the source have phases $\phi_{f_1,t_m}=2\pi f_1 t_m+\phi_{0,1}$, $\phi_{f_2,t_m}=2\pi f_2 t_m+\phi_{0,2}$, $\phi_{f_3,t_m}=2\pi f_3 t_m+\phi_{0,3}$, and $\phi_{f_4,t_m}=2\pi f_4 t_m+\phi_{0,4}$ for the four different frequencies and the M different frames ($m=1,\ldots,M$). Phases $\phi_{0,k}$, $k=1,\ldots,4$, are the starting phases corresponding to the four different frequencies.

The acoustic field is received at L vertically separated hydrophones. The phase of the received field at the L hydrophones is a function of the phase at the source and that of the transfer function corresponding to the path between the source and the specific hydrophone. Furthermore, in the presence of noise, the phase at the receiver will be contaminated by a noise term.

For the assumed initial phases, the phase of the acoustic field at the L hydrophones will be

$$\phi_{r,lkm}=\phi_{f_k,t_m}+\phi_{lk}+\phi_{n,lkm}, \tag{3}$$

where index l indicates the hydrophone, index k indicates the frequency, and index m indicates the time frame ($l=1,\ldots,L$, $k=1,\ldots,4$, $m=1,\ldots,M$); subscript r indicates that the calculated phase is the phase at the receiver. Terms ϕ_{lk} and $\phi_{n,lkm}$ correspond to the phase of the transfer function between the source and receiver l at frequency k and the phase component introduced by the existing noise, respectively.

We are interested in the coherence of the acoustic field at different frequencies and locations, which is captured in the difference between phase component ϕ_{lk} for different l's and k's (hydrophones and frequencies, respectively). However, we cannot separate the three terms of the sum that form the phase at each receiving phone, because all three phase components ϕ_{f_k,t_m}, ϕ_{lk}, and $\phi_{n,lkm}$ are unknown. Replica calculation attempts to reproduce phases ϕ_{lk}. Ignoring noise effects for a moment, if the unknown phases ϕ_{f_k,t_m} are not added to the phases of the field vectors obtained from the replica field computation, a mismatch (low correlation) between true and replica fields will be observed even when the parameters used for the replica calculation are the true parameters that generated the observed acoustic field.

A normalization scheme has been proposed to address the problem of the unknown source phases that appear in the received field.[1,3] Specifically, before the concatenation of the acoustic field vectors for the generation of the ''long'' data vectors (that contain information across all hydrophones and frequencies), all data vectors at individual frequencies were normalized with respect to the phase at the first (shallowest) hydrophone. The phase term ϕ_{f_k,t_m} is carried in the phase at all hydrophones for the measurements corresponding to frame m. By normalizing the individual phases at the different hydrophones with respect to the phase at the first one at each frame, this phase term is cleared away.

This scheme should in theory remove the unwanted phase components from the received acoustic observations, at least as far as the unknown starting phases are concerned. However, the proposed normalization is very dependent on the quality of the measurement at the first hydrophone. When the SNR is low at that hydrophone, the measurement is likely to be corrupted by large $\phi_{n,lkm}$ terms leading to problems when used in the normalization process. At first glance one way to obviate this problem appears to be to choose the phase at the hydrophone with the highest SNR for normalization; even this SNR, however, might not be adequately high, leading eventually to poor estimation results.

Ideally, instead of normalizing over the phase at a single hydrophone, one could set the four source phases as unknown parameters and scan over them in the same way that MFP handles other unknown parameters. However, that would substantially increase the dimensionality of the search procedure, a side effect that is not desirable.

A new phase normalization–estimation scheme is proposed in this paper to overcome the unknown source spectrum difficulty: the normalization procedure just described is now applied in a way that reduces noise contamination. As reference for the normalization we now use an estimate of the phase for the first hydrophone obtained from a number of different measurements (the SNR is the same across hydrophones). Specifically, the exponentiated phases of the received vector measurements are averaged, and the phase corresponding to the average (complex) value at the first hydrophone is extracted and used to normalize the individual observations at the other hydrophones. The addition is performed as follows:

$$\begin{aligned}
A\ \exp(j\theta_{r,1}) &= \frac{1}{M}\,\Sigma_{m=1}^{M}\,\exp(j\phi_{r,1km}) \\
&= \frac{1}{M}\,[\exp(j(2\pi f_k t_1+\phi_{0,k}+\phi_{1k}+\phi_{n,1k1})) \\
&\quad +\exp(j(2\pi f_k(t_1+\delta t_2) \\
&\quad +\phi_{0,k}+\phi_{1k}+\phi_{n,1k2})) \\
&\quad +\cdots+\exp(j(2\pi f_k(t_1+\delta t_M) \\
&\quad +\phi_{0,k}+\phi_{1k}+\phi_{n,1kM}))] \\
&= \frac{1}{M}\,\exp(j(\phi_{0,k}+\phi_{1k}+2\pi f_k t_1)) \\
&\quad \times[\exp(j\phi_{n,1k1})+\exp(j(2\pi f_k\delta t_2+\phi_{n,1k2})) \\
&\quad +\cdots+\exp(j(2\pi f_k\delta t_M+\phi_{n,1kM}))].
\end{aligned} \tag{4}$$

In a noise-free scenario, Eq. (4) becomes

$$A\exp(j\theta_{r,1}) = \frac{1}{M}\exp(j(\phi_{0,k}+\phi_{1k}+2\pi f_k t_1)) \times (1+\exp(j2\pi f_k \delta t_2) + \cdots + \exp(j2\pi f_k \delta t_M)). \quad (5)$$

Since there is control over the times when measurements are obtained, time differences δt_m, $m=2,...,M$ are known. Setting, then, $\alpha = 1+\exp(j2\pi f_k \delta t_2)+\cdots+\exp(j2\pi f_k \delta t_M) = |\alpha|\exp(j\phi_\alpha)$, Eq. (5) becomes

$$A\exp(j\theta_{r,1}) = \frac{1}{M}\exp(j(\phi_{0,k}+\phi_{1k}+2\pi f_k t_1+\phi_\alpha))|\alpha|, \quad (6)$$

from which we find the phase $(\phi_{0,k}+\phi_{1k}+2\pi f_k t_1)$ to be equal to $\theta_{r,1}-\phi_\alpha$. In the presence of noise, this phase cannot be found exactly; instead, an estimate of $(\phi_{0,k}+\phi_{1k}+2\pi f_k t_1)$, $(\phi_{0,k}+\widehat{\phi_{1k}+2\pi f_k t_1})$, can be found using the above analysis:

$$(\phi_{0,k}+\widehat{\phi_{1k}+2\pi f_k t_1}) = \theta_{r,1}-\phi_\alpha. \quad (7)$$

According to the Central Limit theorem, a larger number M of observations leads to a better estimate of the true phase because of variance reduction. (Recall that the original normalization scheme[1,3] used a *single* measurement for the phase estimation.)

Phase $(\phi_{0,k}+\widehat{\phi_{1k}+2\pi f_k t_1})+2\pi f_k \delta t_m$ is then used for the phase normalization of the data for frame m: For every frequency f_k the data vector is normalized with respect to that phase before the vector concatenation. [The amplitude A in Eqs. (4)–(6) is not used in the normalization process.]

After normalization, the coherent Bartlett ambiguity surface is calculated as follows:

$$P_{\text{bart,coh}}(\mathbf{q}) = \mathbf{w}^*_{\text{coh}}(\mathbf{q})\left(\frac{1}{M}\sum_{m=1}^{M}\mathbf{d_{m,coh}}\mathbf{d^*_{m,coh}}\right)\mathbf{w}_{\text{coh}}(\mathbf{q}) = \mathbf{w}^*_{\text{coh}}(\mathbf{q})C_{\text{coh}}\mathbf{w}_{\text{coh}}(\mathbf{q}), \quad (8)$$

where $\mathbf{w}_{\text{coh}}$ and $\mathbf{d_{m,coh}}$ are the concatenated replica and data vectors, respectively, and C_{coh} is the new coherent cross-spectral density matrix.

III. PERFORMANCE TESTING OF THE COHERENT PROCESSOR

This section presents the results of simulations showing the comparative performance of the coherent and incoherent Bartlett processors in source localization. Performance is examined as a function of SNR and also as a function of the number of available data observations.

A. Performance evaluation of the coherent and incoherent Bartlett processors versus SNR

The original coherent broadband processor has been tested with respect to mismatch with both synthetic and real data.[1] Tests were performed for mismatch in the sound-speed profile using empirical orthogonal functions to express perturbations. Comparison of broadband coherent and incoherent implementations of the Bartlett and MV processors showed that (i) the incoherent MV processor had the poorest performance of all, being very sensitive to mismatch, and (ii) the performance of the coherent Bartlett and MV and incoherent Bartlett processors was very similar. Regarding conclusion (ii), it was noticed that for certain degrees of mismatch the coherent processors were superior to the incoherent Bartlett processor, whereas for other values of the mismatch coefficient the reverse was true.

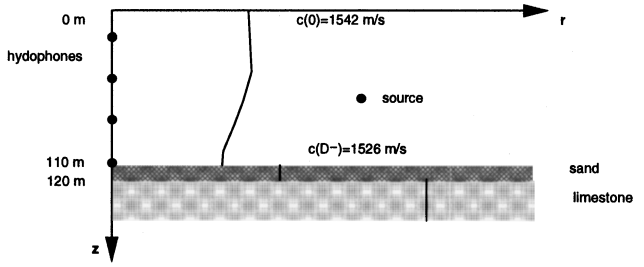

FIG. 2. The simulation environment.

Those mismatch simulations were performed for a relatively high SNR (10 dB).[1] Here we wish to examine the coherent and incoherent broadband processors under low SNRs, since the real challenge in passive matched-field estimation lies in cases where the sound signals are weak. We are also focusing on the Bartlett processor in its conventional incoherent and interfrequency coherent implementations.

To overcome the drawback of the original coherent processor in the presence of a strong noise field, the new variant introduced in Sec. II B was implemented. Initially, it was assumed that 100 vector observations of the acoustic field were available at every frequency. The phase estimate used for normalization was then obtained by averaging the observations at the first hydrophone and extracting the phase of the average. Simulations were run for arrays of the same aperture but for different numbers of hydrophones and two sets of frequencies: 450, 500, 550, and 600 Hz and 50, 100, 150, and 200 Hz; 200 simulations were run for every case, and 100 data observations were assumed available for every simulation. The environment selected was similar to that in Ref. 11 with a bottom depth of 110 m and a 10-m-thick sandy sediment on top of limestone, shown in Fig. 2. The source was at a depth of 50 m and a range of 3 km. The search grid for the source location was between 0 and 5 km and 0 and 100 m for range and depth, with resolution of 10 and 2 m, respectively (501×51 points).

Figure 3 summarizes the results of the incoherent Bartlett and the coherent Bartlett processors by demonstrating the probability of correct localization for SNRs ranging between -30 and -5 dB for the four hydrophone experiment for the two sets of tones. The probability of correct localization is here defined as the probability of finding the correct source range and depth within 300 and 5 m, respectively. In both cases the coherent Bartlett processor has a much better performance than the incoherent processor for most of the SNR range [the coherent performance is insignificantly lower for SNRs between -17 and -25 dB in (a) and between -25 and -30 dB in (b) where localization performance in both cases is negligible].

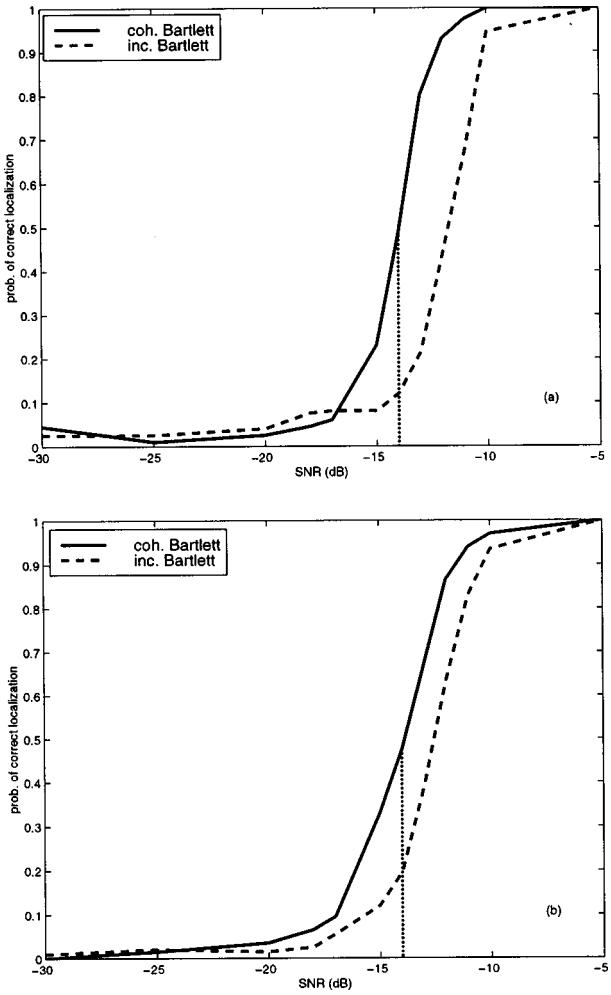

FIG. 3. Probability of correct localization for the coherent and incoherent Bartlett processors for a four receiver array for frequencies (a) 450, 500, 550, and 600 Hz and (b) 50, 100, 150, and 200 Hz.

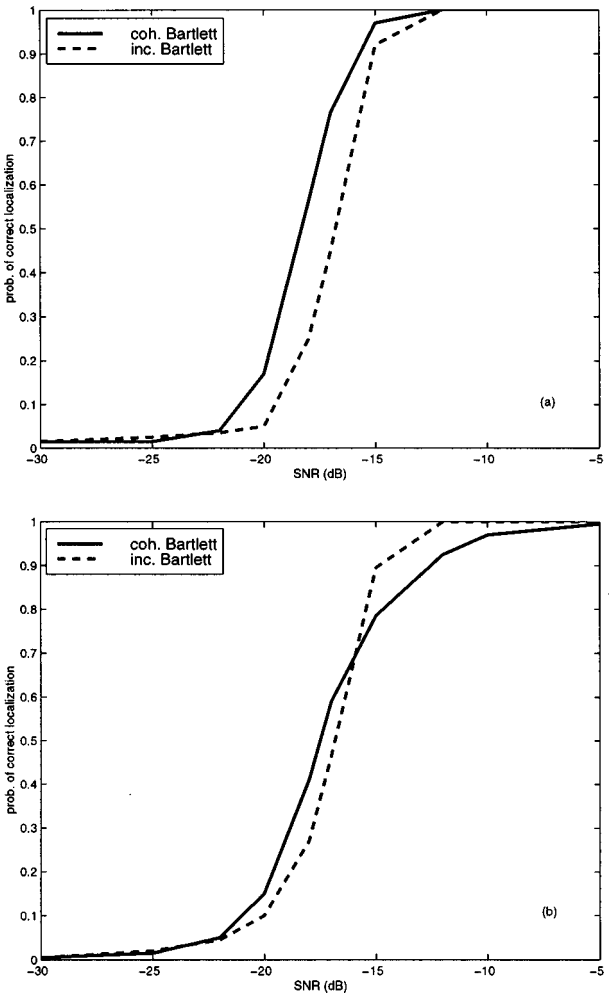

FIG. 4. Probability of correct localization for the coherent and incoherent Bartlett processors for a ten receiver array for frequencies (a) 450, 500, 550, and 600 Hz and (b) 50, 100, 150, and 200 Hz.

The performance difference is more pronounced for the set of higher frequencies; for some SNRs the probability of correct localization of the coherent processor appears to be two to almost three times greater than that of the incoherent processor.

Results for a ten hydrophone array in the same environment are summarized in Fig. 4. Figure 4(a) shows again the superiority of the coherent Bartlett processor over the incoherent Bartlett. However, the difference in the performances is reduced in comparison to the results of Fig. 3. When the frequencies are lower, Fig. 4(b) shows that the coherent processor outperforms the incoherent processor only when the SNR drops below -15 dB. For higher SNR values, the incoherent Bartlett performs best. It appears that the degraded performance of the coherent processor when the number of hydrophones increases is because of problems in the estimation of the coherent cross-spectral density matrix. Figure 5(a) and (b) shows the noise-free 40×40 matrix and the estimate of the matrix in the presence of noise when the SNR is -15 dB, illustrating the poor quality of the estimate. The cross-spectral density matrix estimation becomes more problematic in the coherent case than in the incoherent one because of the increased dimension of the matrix.

Summarizing the results, it is observed that the benefit from using the coherent Bartlett processor is more substantial when few hydrophones are available for measuring the acoustic field. Qualitatively, it appears that the coherent processor ''spatially interpolates'' the array and obtains more spatial samples than the incoherent processor. When undersampling is a substantial problem, this ''spatial interpolation'' improves the localization performance of the Bartlett processor significantly. When, however, the receiving array has several hydrophones, the estimation process becomes more complex and potentially erroneous when the coherent processor is employed because of the large dimension of the cross-spectral density matrix.

B. Performance evaluation of the coherent and incoherent Bartlett processors versus number of data observations

The results presented in Sec. III A illustrate the performance of the two Bartlett processors, coherent and incoherent, for different SNRs. All simulations in that section were run assuming 100 data vectors were available for each case. In practice, the number of data measurements varies from problem to problem. A single measurement might be all that is available (shot data), or several measurements might be

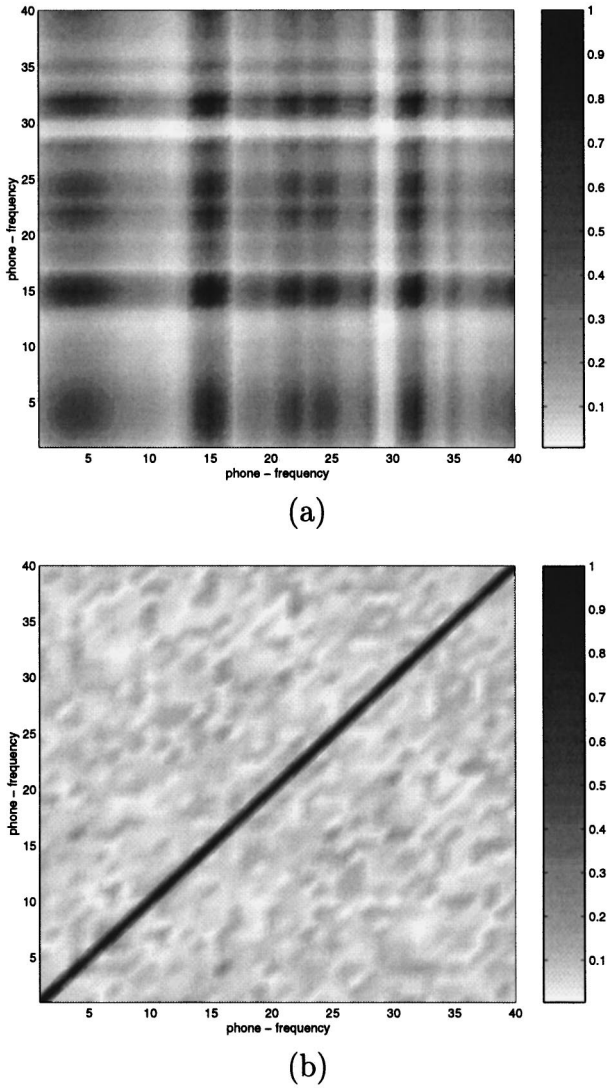

FIG. 5. Problems in the estimation of the augmented cross-spectral density matrix: (a) correct matrix, (b) estimate.

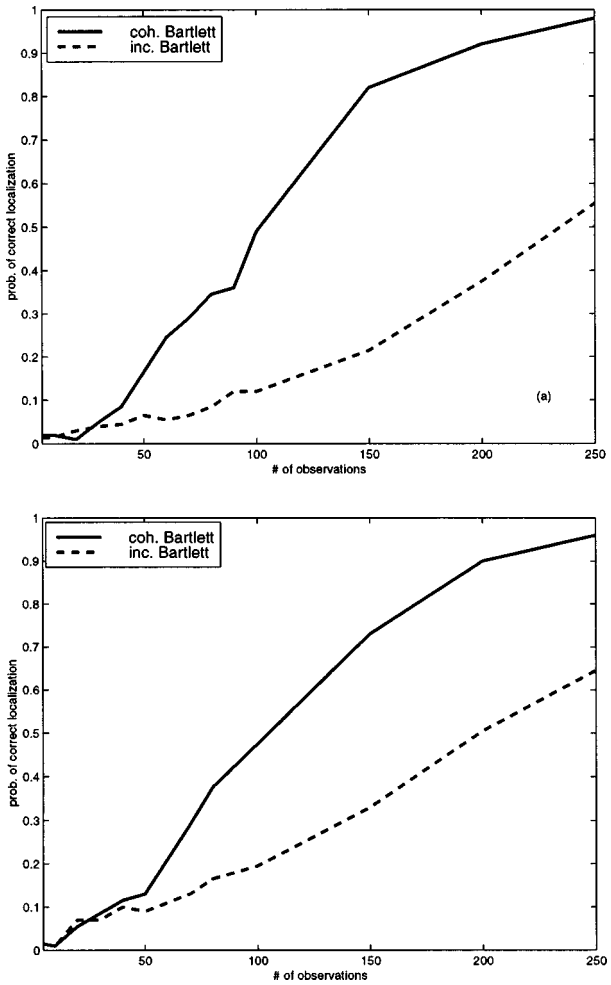

FIG. 6. Probability of correct localization for the coherent and incoherent Bartlett processors for a four receiver array for frequencies (a) 450, 500, 550, and 600 Hz, (b) 50, 100, 150, and 200 Hz, SNR of −14 dB, and for a varying number of data observations.

given. The actual number M of observations in Eq. (2) depends on the nature of the data, how the received data can be segmented depending on stationarity constraints,[15] and computational limitations.[9] MFP performance evaluation studies have employed observation numbers that vary greatly: for example, 200 observations were used by Czenszak and Krolik,[5] and ten by Michalopoulou and Porter,[1] whereas 100 observations were used in Sec. III A.

Figure 6 presents the probability of correct localization versus the number of data observations for the coherent and incoherent processors. The results were obtained from 200 runs of the four receiver case of Sec. III A for frequencies of 450, 500, 550, and 600 Hz and 50, 100, 150, and 200 Hz for an SNR of −14 dB [a dotted line in Fig. 3(a) and (b) indicates the −14-dB level for the 100 observation case for these frequencies].

As expected, Fig. 6 shows that both processors perform better for a larger number of observations for both sets of frequencies. It is also observed that for most of the range of observation numbers (5–250) the coherent processor outperforms the incoherent processor, the difference in the performance mostly increasing with an increasing number of observations. This was also expected, since the estimate of the phase obtained in Sec. II B is more accurate with a large number of observations, improving the performance of the coherent processor. For 250 observations, the largest sample size considered in this study, the coherent processor achieved an almost perfect score, whereas the incoherent processor barely passed the 50% success rate for the high-frequency case and approached the 70% rate for the low-frequency case.

Finally, Fig. 7 presents ambiguity surfaces obtained from the coherent and incoherent processor for the set of low frequencies and an SNR of −14 dB for the same set of 100 observations. The source is correctly estimated with both processors (2.98 km and 50 m are the coherent processor estimates and 3.01 km and 50 m are the incoherent processor estimates of a true location of 3 km in range and 50 m in depth). Comparison of the two ambiguity surfaces shows that the sidelobe level is considerably decreased in the coherent processing case giving a much more certain result.

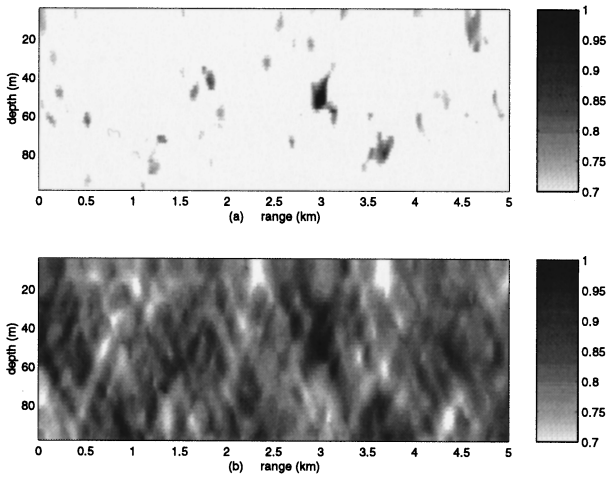

FIG. 7. Ambiguity surfaces generated with the (a) coherent and (b) incoherent Bartlett processors for a four receiver array for frequencies 50, 100, 150, and 200 Hz and SNR of −14 dB for 100 data observations.

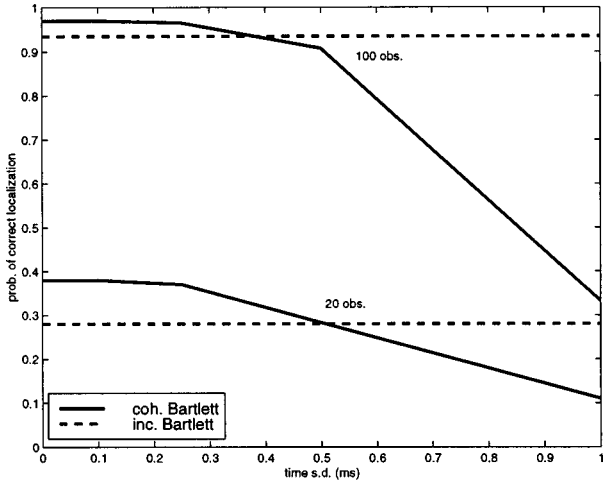

FIG. 9. Probability of correct localization for the coherent and incoherent Bartlett processors for a four receiver array for frequencies 50, 100, 150, and 200 Hz for an SNR of −10 dB for 100 and 20 observations versus temporal uncertainty.

IV. PERFORMANCE EVALUATION OF THE COHERENT PROCESSOR FOR UNCERTAIN TIME

The coherent processor has been evaluated under the assumption that the times at which the data measurements are collected are exactly known. As with other parameters, however, there is uncertainty involved in the times at which measurements are made, typically less than a few milliseconds.

This section investigates the performance of the coherent Bartlett processor as a function of temporal uncertainty, where time is assumed to be a zero mean Gaussian random variable with a standard deviation ranging from 0 (perfect knowledge) to 1 ms.

Figure 8 shows the performance of the coherent processor for two cases, the first corresponding to 100 observations for an SNR of −14 dB and the second one corresponding to 100 observations for an SNR of −10 dB for the set of low frequencies (50, 100, 150, and 200 Hz). The figure includes the performance of the incoherent Bartlett processor for the two cases as a point of reference. Naturally, the performance of the incoherent Bartlett processor is not affected by time uncertainty. The solid curves, illustrating the performance of the coherent Bartlett processor, show the median probability of correct localization obtained from 50 runs of different realizations of the temporal uncertainty. (For each of the 50 runs, 200 data plus noise realizations were generated; a single probability of correct localization was calculated from each set of 200 realizations, resulting in 50 values, in total, of the probability of correct localization.) The median was preferred over the mean because of the lack of symmetry in the distribution of the probability of correct localization.

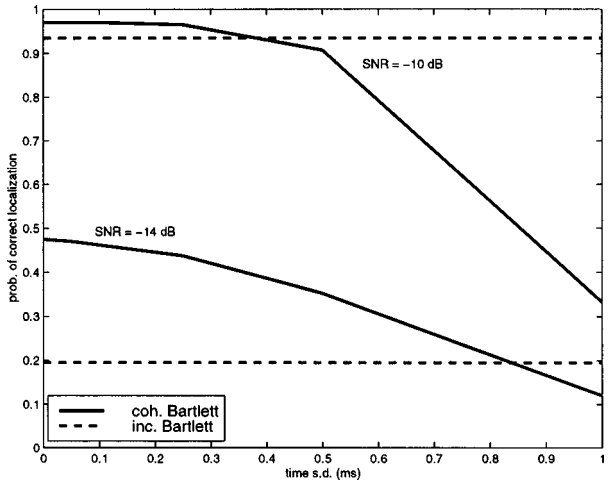

FIG. 8. Probability of correct localization for the coherent and incoherent Bartlett processors for a four receiver array for frequencies 50, 100, 150, and 200 Hz for 100 observations and SNR of −10 and −14 dB versus temporal uncertainty.

As expected the performance of the coherent processor degrades as the temporal uncertainty increases, illustrated by the drop of the probability of correct localization with larger values of the time standard deviation. Although the performance of the processor for an SNR of −10 dB is superior to that for the −14 dB case, the coherent processor tolerates uncertainty better in the lower SNR (−14 dB) case (in terms of a comparison to the incoherent Bartlett processor). That is, the coherent processor is on average preferable to the incoherent processor for temporal standard deviations up to 0.85 ms in the −14 dB case but only up to 0.4 ms in the −10-dB case.

Similar observations can be made from Fig. 9 showing the (median) probability of correct localization of the coherent processor and its degradation with temporal uncertainty for 100 and 20 data observations for the same SNR (−10 dB) and the same frequencies. The coherent processor is more tolerant of temporal uncertainty for the 20 observation case than for the 100 observation case, being superior to the incoherent processor for temporal standard deviation up to 0.52 ms.

Figure 10 focuses on the curves of Fig. 8 for the −14-dB results. In order to demonstrate the variation in the probability of correct localization values obtained for the different samples of temporal uncertainty, Fig. 10 includes, in addition to the median, the 10th percentile for the probability of correct localization of the coherent Bartlett processor. It

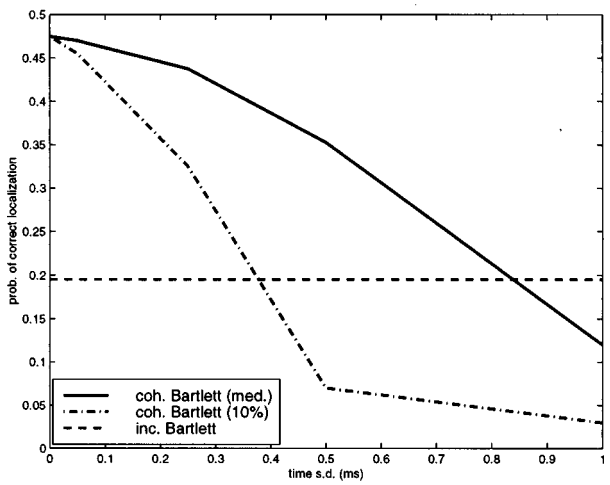

FIG. 10. Probability of correct localization for the coherent and incoherent Bartlett processors for a four receiver array for frequencies 50, 100, 150, and 200 Hz for 100 observations and SNR of -14 dB versus temporal uncertainty: median and 10th percentile for the coherent probability of correct localization.

can be observed that in this case 90% of the time the coherent processor is preferable to the incoherent processor for temporal uncertainty characterized by a standard deviation smaller than 0.4 ms, whereas in a median (average) sense, the coherent processor is preferable to the incoherent processor up to a temporal standard deviation of 0.85 ms.

Finally, it should be noted that the degradation in the performance of the coherent Bartlett processor with temporal uncertainty is frequency dependent. Because the sources considered here are tonal, the introduced phase error (which manifests itself as a form of mismatch between replicas and true field) consists of the time error multiplied by the frequency (and 2π) and it is therefore more pronounced for higher frequencies.

V. CONCLUSIONS

This paper explores spatial coherence of the acoustic field across multiple frequencies. It shows that incorporation of this coherence in MFP algorithms improves correct localization statistics. The effect of the new processor is most pronounced when the array consists of only a few hydrophones severely undersampling the spatial domain. When spatial sampling becomes more adequate by increasing the number of phones, however, the simple incoherent Bartlett processor might be preferable because estimation of the increased-dimension cross-spectral density matrix required for the coherent implementation might be unstable. Additionally, the new scheme requires knowledge of the measurement times of the signals. The processor's behavior and robustness with respect to temporal uncertainty varies with the number of available observations, the source frequencies, and SNR.

Because of its superior performance when a small hydrophone array is used, the new processor is an attractive inversion estimation scheme. Since it can improve the results obtained by using only a few hydrophones, it is clearly more cost-effective than the incoherent Bartlett processor.

The new processor does not require knowledge of the source spectrum, a key difference from, and a significant advantage over, other coherent processors recently discussed in the MFP literature.

Future work will assess the sensitivity of the coherent Bartlett to mismatch (extending the work presented in Ref. 1) and the benefit in optimization techniques from using the additional coherence factor.

ACKNOWLEDGMENTS

This work was supported by the Office of Naval Research, Ocean Acoustics, through Grants No. N00014-95-1-0558 and No. N00014-97-1-0600 and NJIT through SBR.

[1] Z.-H. Michalopoulou and M. B. Porter, ''Matched-field processing for broadband source localization,'' IEEE J. Ocean Eng. **21**, 384–392 (1996).
[2] A. Baggeroer, W. Kuperman, and H. Schmidt, ''Matched-field processing: Source localization in correlated noise as an optimum parameters estimation problem,'' J. Acoust. Soc. Am. **83**, 571–587 (1988).
[3] Z.-H. Michalopoulou and M. B. Porter, ''Source tracking in the Hudson Canyon experiment,'' J. Comput. Acoust. **4**, 371–383 (1996).
[4] R. Urick, *Principles of Underwater Sound* (McGraw-Hill, New York, 1983).
[5] S. P. Czenszak and J. L. Krolik, ''Robust wideband matched-field processing with a short vertical array,'' J. Acoust. Soc. Am. **101**, 749–759 (1997).
[6] G. L. D'Spain, W. A. Kuperman, and W. S. Hodgkiss, ''3-d localization of a blue whale,'' technical report, MPL, Scripps, Technical Memorandum 447, 1995.
[7] Z.-H. Michalopoulou, ''Underwater transient signal processing: marine mammal identification, localization, and source signal deconvolution,'' in ICASSP-97, Vol. 1, pp. 503–506, 1997.
[8] A. Tolstoy, ''Computational aspects of matched field processing in underwater acoustics,'' in *Computational Acoustics*, edited by D. Lee, A. Cakmak, and R. Vichnevetsky (North-Holland, Amsterdam, 1990), Vol. 3, pp. 303–310.
[9] E. K. Westwood, ''Broadband matched-field source localization,'' J. Acoust. Soc. Am. **91**, 2777–2789 (1992).
[10] R. Brienzo and W. S. Hodgkiss, ''Broadband matched-field processing,'' J. Acoust. Soc. Am. **94**, 2821–2831 (1993).
[11] Z.-H. Michalopoulou, M. B. Porter, and J. P. Ianniello, ''Broadband source localization in the Gulf of Mexico,'' J. Comput. Acoust. **4**, 361–370 (1996).
[12] Z. H. Michalopoulou and M. B. Porter, ''Focalization in the Gulf of Mexico,'' in ICASSP-96, Vol. 6 (Atlanta), pp. 3086–3089, May 1996.
[13] A. Baggeroer, W. Kuperman, and P. N. Michalevsky, ''An overview of matched field processing in ocean acoustics,'' IEEE J. Ocean Eng. **18**, 401–424 (1993).
[14] M. B. Porter and E. L. Reiss, ''A numerical method for ocean acoustic normal modes,'' J. Acoust. Soc. Am. **76**, 244–252 (1984).
[15] A. Tolstoy, *Matched Field Processing for Underwater Acoustics* (World Scientific, Singapore, 1993).

A least-squares approximation for the delays used in focused beamforming

Andrea Trucco[a)]
Department of Biophysical and Electronic Engineering (DIBE), University of Genoa, Via all'Opera Pia 11A, I-16145 Genova, Italy

(Received 10 June 1997; accepted for publication 16 March 1998)

A novel approximation for the delays used in focused beamforming is presented that is based on weighting the terms of the conventional Fresnel approximation. The objective is to enlarge the validity region of the Fresnel approximation in order to investigate wider scanning regions. A least-squares solution provides the exact weight values by the minimization of the mean-square error computed over the desired scanning region and on the basis of the array geometry. The attractive results obtained by applying the proposed approximation to a linear array are presented. [S0001-4966(98)06506-0]

PACS numbers: 43.30.Vh, 43.30.Pc [DLB]

INTRODUCTION

Beamforming is a linear technique aimed at processing array signals in order to enhance incoming signals from a selected steering direction and to abate incoming signals from any other direction.[1] Thanks to its flexibility, beamforming can be successfully employed in many application fields with different objectives. If the array works under far-field conditions, the delays required by the beamforming operation can be easily computed exactly, whereas, if it works under near-field conditions, the focusing is required to take into account the curvature of waves. In the latter case, a fast computation of the exact delays is often prohibitive, so an approximate version is preferred: generally, the Fresnel approximation (obtained by the expansion of the time-independent free-space Green's function[2,3]) is adopted.[1] Moreover, the Fresnel approximation makes it possible to apply the fast Fourier transform (FFT) in the implementation of beamforming even when focusing is necessary.[4,5] Not always is the FFT implementation the best choice as the computational advantage strongly depends on the computer architecture. However, by using a conventional (not parallel) computer architecture, one can show that the FFT implementation assures a great computational advantage, as compared with the direct implementation of the beamforming definition.[5] Moreover, this profit considerably increases when a planar array is involved.[6] Despite its simplicity and advantages, the Fresnel approximation has a well-defined region of validity[2] that forces potential steering directions to be contained inside a narrow scanning region. This constraint is inconvenient in applications (e.g., acoustic imaging) that require a wide region of view, for both medical and underwater investigations. To avoid this drawback, some imaging techniques that do not need the Fresnel approximation have been devised[7,8] but, unfortunately, they increase the computational load and/or the system complexity.

This paper presents a novel approximation (not too different from the Fresnel one) that is based on the minimization of the mean-square error, thus resulting in an acceptable precision inside wide scanning regions. The same terms as used for the Fresnel expansion are weighted by coefficients whose values are fixed, given the array geometry, by a least-squares procedure on the basis of the desired scanning region. Thus the new approximation keeps the low computational load and the low system complexity that characterize the Fresnel expansion and maintains the opportunity to be implemented in an FFT focused beamformer, too.

This paper is organized as follows. Section I briefly defines the problem and the Fresnel approximation with its validity region. In Sec. II, the least-squares approximation is presented, and its application to a linear array with related error measures is described in Sec. III. Results are discussed in Sec. IV and some conclusions are drawn in Sec. V.

I. FOCUSED BEAMFORMING AND THE FRESNEL APPROXIMATION

A beam signal (generated by a conventional delay and sum beamformer[1]) steered in the direction of the unit vector $\mathbf{u}$ is defined as

$$bs_{\mathbf{u}}(t)=\sum_{i=1}^{M} w_i \cdot x_i(t-\tau(\mathbf{u},i)), \tag{1}$$

where $x_i(t)$ is the temporal signal received by the ith sensor, $\tau(\mathbf{u},i)$ and w_i are the delay and the weight applied to such a signal, respectively, and M is the number of array elements.

Under the far-field hypothesis, the exact delay can be written as

$$\tau_{ff}(\mathbf{u},i)=\frac{(\mathbf{u}\mathbf{v}_i^{+})}{c}, \tag{2}$$

where $\mathbf{v}_i=[x_i,y_i,z_i]$ is the position vector of the ith sensor, the superscript plus indicates the transposition operator (both $\mathbf{u}$ and $\mathbf{v}_i$ are row vectors), and c is the carrier speed. This delay formulation is compatible with the FFT implementation of beamforming. If focusing is necessary, as the far-field hypothesis does not hold any more, then the exact delay is

a)Electronic mail: fragola@dibe.unige.it

$$\tau_{\mathrm{ex}}(\mathbf{u},i)=\frac{R-\sqrt{R^2+\|\mathbf{v}_i\|^2-2R\mathbf{u}\mathbf{v}_i^+}}{c}, \tag{3}$$

where R is the focal distance in the steering direction $\mathbf{u}$ and $\|\cdot\|^2$ is the Euclidean norm. These delays are difficult to compute on line (mainly due to the presence of a square root) and inhibit the implementation of focused beamforming by the FFT.

For these reasons, one tries to approximate the exact delay by a formulation that allows an easy on line computation and the FFT implementation. This goal is generally achieved thanks to the Fresnel expansion, which results in the following approximation[1] to the exact delay:

$$\tau_{\mathrm{Fr}}(\mathbf{u},i)=\frac{(\mathbf{u}\mathbf{v}_i^+)}{c}-\frac{\|\mathbf{v}_i\|^2}{2Rc}. \tag{4}$$

The first term of the addition depends on both $\mathbf{v}_i$ and $\mathbf{u}$, and represents the distance-independent delay equal to that defined in Eq. (2). The second term (called ''curvature term'') takes into account the wave curvature, depends on $\mathbf{v}_i$, and does not depend on $\mathbf{u}$. Thanks to the last observation, received signals can be phase-shifted according to the curvature term before the beamforming operation.[4,6] After this preliminary correction, phase-shifted signals can be considered as signals received under a far-field hypothesis, and a conventional (not focused) FFT beamforming scheme can be applied.[4,5]

According to Ziomek,[2] there are three necessary conditions that define the validity region of the Fresnel approximation. In the numerator of the second term that appears on the right-hand side of Eq. (4) the term $(\mathbf{u}\mathbf{v}_i^+)^2$ has been neglected. In order to justify this neglect, it is necessary that $\|\mathbf{v}_i\|^2 \gg (\mathbf{u}\mathbf{v}_i^+)^2$. If one uses a factor of 10 to represent ''much greater than,'' one obtains the first necessary condition that imposes a small steering sector; if one denotes by ϕ the angle between $\mathbf{u}$ and $\mathbf{v}_i$, one can write this condition as

$$72° \leqslant \phi \leqslant 108°. \tag{5}$$

As the Fresnel approximation uses a binomial expansion of the square root in Eq. (2), it is mandatory[2] that $|(\|\mathbf{v}_i\|/R)^2 - 2(\mathbf{u}\mathbf{v}_i^+)/R| < 1$. When ϕ is bound to be in the range shown in Eq. (5), the last relation turns out to be the second necessary condition that stipulates the minimum focal distance:

$$R > 1.356V \tag{6}$$

where V is the maximum value of $\|\mathbf{v}_i\|$. The third necessary condition establishes the boundary between near-field and far-field regions and has been obtained by requiring that the curvature term in the Fresnel expansion of the Green's function[2] (i.e., $\pi\|\mathbf{v}_i\|^2/\lambda R$, λ being the wavelength of the carrier frequency) be a non-negligible function of $\mathbf{v}_i$ and R:

$$R < \pi V^2/\lambda. \tag{7}$$

These restrictive conditions (in particular, the one that limits the angular extension) are often not satisfied in imaging systems, with potential low performances in the lateral regions of images.

II. THE LEAST-SQUARES APPROXIMATION

In order to relax the constraint of Eq. (5), a possible solution is to weight the terms of the Fresnel approximation by two constants, k_1 and k_2, computed on the basis of the desired steering region and of a fixed focal distance. The importance of keeping unchanged the two terms of the Fresnel approximation lies in their computational simplicity and in the possibility of implementing focused beamforming by the FFT. One can write the new delay approximation as follows:

$$\tau_{ls}(\mathbf{u},i)=k_1\frac{(\mathbf{u}\mathbf{v}_i^+)}{c}+k_2\frac{\|\mathbf{v}_i\|^2}{Rc} \tag{8}$$

and try to fix the values of the two constants by minimizing the sum of the square differences between the delays provided by the approximation and the exact delays. Square errors can be measured over a two-dimensional grid containing all the possible pairs $(\mathbf{u},i)$. Denoting by $e(\mathbf{u},i)$ the error between the approximate and exact delays, and by $\mathbf{u}_1,\mathbf{u}_2,\ldots,\mathbf{u}_N$ the steering directions of interest, one can write an overdetermined system of equations by using a matrix formulation:

$$\begin{bmatrix} \tau_{\mathrm{ex}}(\mathbf{u}_1,1) \\ \vdots \\ \tau_{\mathrm{ex}}(\mathbf{u}_1,M) \\ \tau_{\mathrm{ex}}(\mathbf{u}_2,1) \\ \vdots \\ \tau_{\mathrm{ex}}(\mathbf{u}_2,M) \\ \vdots \\ \tau_{\mathrm{ex}}(\mathbf{u}_N,M) \end{bmatrix} = \begin{bmatrix} (\mathbf{u}_1\mathbf{v}_1^+)/c & \|\mathbf{v}_1\|^2/(Rc) \\ \vdots & \vdots \\ (\mathbf{u}_1\mathbf{v}_M^+)/c & \|\mathbf{v}_M\|^2/(Rc) \\ (\mathbf{u}_2\mathbf{v}_1^+)/c & \|\mathbf{v}_1\|^2/(Rc) \\ \vdots & \vdots \\ (\mathbf{u}_2\mathbf{v}_M^+)/c & \|\mathbf{v}_M\|^2/(Rc) \\ \vdots & \vdots \\ (\mathbf{u}_N\mathbf{v}_M^+)/c & \|\mathbf{v}_M\|^2/(Rc) \end{bmatrix} \begin{bmatrix} k_1 \\ k_2 \end{bmatrix} + \begin{bmatrix} e(\mathbf{u}_1,1) \\ \vdots \\ e(\mathbf{u}_1,M) \\ e(\mathbf{u}_2,1) \\ \vdots \\ e(\mathbf{u}_2,M) \\ \vdots \\ e(\mathbf{u}_N,M) \end{bmatrix}. \tag{9}$$

The system in Eq. (9) can be written in a shortened form as

$$\mathbf{d}=\mathbf{A}\mathbf{k}+\mathbf{e}, \tag{10}$$

where $\mathbf{d}$ is the column vector (NM by 1) of the exact delays, $\mathbf{k}$ is the column vector (2 by 1) of the unknowns, $\mathbf{e}$ is the column vector (NM by 1) of the errors, and $\mathbf{A}$ is the matrix (NM by 2) containing the two terms of the approximation.

By using a least-squares inverse,[9] $\mathbf{A}^{\mathrm{ls}}$ (2 by NM), of the matrix $\mathbf{A}$, one can compute a system solution $\mathbf{k}^*$ that minimizes the mean-square error (i.e., $\mathbf{k}^*$ is a solution of the problem $\min_{\mathbf{k}}\{\|\mathbf{e}\|^2\}$):

$$\mathbf{k}^*=(\mathbf{A}^{\mathrm{ls}})\mathbf{d}=[(\mathbf{A}^+\mathbf{A})^{-1}\mathbf{A}^+]\mathbf{d}. \tag{11}$$

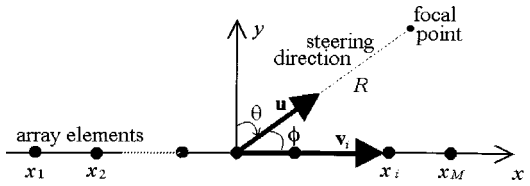

FIG. 1. Geometry of a linear array and related notation.

Once the solution, $\mathbf{k}^*$, has been computed off line, one can begin the focused beamforming operation under the guarantee that the approximate delays τ_{ls} are optimum in the least-squares sense. It is not necessary to recompute the values of k_1 and k_2 every time the beamforming has to be performed; this means that exact delays are used only off line and do not affect the computational load of the beamforming process.

One can verify that, if one fixes a steering region perfectly overlapped with the validity region of the Fresnel approximation, the differences between the least-squares and Fresnel approximations are negligible, i.e., $k_1 \approx 1$ and $k_2 \approx -0.5$.

III. RESULTS FOR A LINEAR ARRAY

The effectiveness of the proposed method has been assessed in the case of an equispaced linear array. In this case, the steering faculty is restricted to a plane containing the antenna.[1] Therefore supposing the array to be placed on the x axis, without loss of generality, one can consider the plane $z=0$ (see Fig. 1) and rewrite the unit vector $\mathbf{u}$, the vector $\mathbf{v}_i$, and the least-squares delay τ_{ls} as follows:

$$\mathbf{u}=[\sin\theta,\cos\theta,0], \tag{12}$$

$$\mathbf{v}_i=[x_i,0,0]=\left[\left(i-\frac{M+1}{2}\right)d,0,0\right], \tag{13}$$

$$\tau_{\mathrm{ls}}(\theta,i)=k_1\frac{(x_i\sin\theta)}{c}+k_2\frac{x_i^2}{Rc}, \tag{14}$$

where θ is the steering angle measured between $\mathbf{u}$ and the y axis (i.e., $\theta=90°-\phi$) and i is an integer included between 1 and M.

To test the accuracy of the delay approximation, one can use the total mean-square error (i.e., $\mathrm{MSE}=\|\mathbf{e}\|^2/MN$) plotted versus the focal distance, the MSE as a function of the steering angle (computed at a fixed focal distance):

$$\mathrm{MSE}(\theta)=\frac{1}{M}\sum_{i=1}^{M}e(\theta,i)^2, \tag{15}$$

and the MSE as a function of the array element position (computed at a fixed focal distance):

$$\mathrm{MSE}(i)=\frac{1}{N}\sum_{l=1}^{N}e(\theta_l,i)^2, \tag{16}$$

where θ_l is one of the N steering angles. This error distribution is important as array elements with large errors give greater contributions to the beam-pattern deformation.[1] The beam pattern is very important as it allows (like the point spread function) an objective evaluation of an imaging system's performances in terms of resolution and dynamic range. When low MSE values are obtained for all the array elements, one can be confident that, on average, the deformations of the beam patterns related to the N steering angles considered in Eq. (16) will be limited. The beam pattern deformation is really another way to test the accuracy of a delay approximation. After fixing the steering angle θ, one can compute the normalized beam power pattern (BPP) as a function of the arrival angle α, $\mathrm{BPP}_\theta(\alpha)$, as follows:

$$\mathrm{BPP}_\theta(\alpha)=10\log\left\{\frac{1}{M^2}\left|\sum_{i=1}^{M}\exp\left\{-j\frac{2\pi c[\tau_{\mathrm{ex}}(\alpha,i)-\tau(\theta,i)]}{\lambda}\right\}\right|^2\right\}, \tag{17}$$

where $\tau(\theta,i)$ can be the exact delay (to obtain the not deformed BPP), the Fresnel approximation, or the proposed approximation (to evaluate the deformations of the related BPPs).

As an example, one can consider an array composed of 120 $\lambda/2$-spaced elements, working at 500 kHz, with a sound speed $c=1500$ m/s (i.e., $M=120$, $\lambda=3$ mm, and $d=1.5$ mm). A forward-looking sonar system is a potential imaging application of this kind of array. A region defined by $|\theta|\leq 32°$ is considered for the computation of (k_1,k_2) and a range domain $0.5\ \mathrm{m}\leq R\leq 10\ \mathrm{m}$ is required. The angular extent of this region is larger than that of the validity region of the Fresnel approximation [i.e., from Eq. (5), $|\theta|<18°$], whereas the range extension is similar (i.e., the Fresnel approximation is valid for $0.12\ \mathrm{m}<R<8.34\ \mathrm{m}$). The scanning region is covered by $N=65$ beams in equispaced steering directions θ_l, from $-32°$ to $32°$. Figure 2 shows the computed values of k_1 (panel a) and k_2 (panel b) versus the focal distance R, and the total MSE (panel c), measured in $\mu\mathrm{s}^2$, for the least-squares approximation τ_{ls}, the Fresnel approximation τ_{Fr}, and the far-field delay τ_{ff}. Figure 3(a) compares the $\mathrm{MSE}(\theta)$ of the least-squares approximation with that of the Fresnel approximation, and Fig. 3(b) shows the same comparison for the $\mathrm{MSE}(i)$. Both errors were computed after fixing $R=1$ m and measured in $\mu\mathrm{s}^2$. Finally, Fig. 4 shows the not deformed BPP together with BPPs obtained by the Fresnel and least-squares approximations, when the steering angle θ was equal to 0° (panel a) and 26° (panel b).

IV. DISCUSSION

One can notice that, for every delay approximation, the total MSE decreases as the focal distance increases, and that, for a distance out of the near-field region (i.e., $R>8.34$ m), the far-field hypothesis can be adopted with negligible error differences. Within the near-field region, the proposed approximation has a total MSE lower than that of the Fresnel approximation. Moreover, the weights k_1 and k_2 tend to assume constant values for a focal distance larger than a few meters, so excluding the strict necessity for computing them for each R (in particular, k_1 tends to be equal to 1, as in the Fresnel approximation).

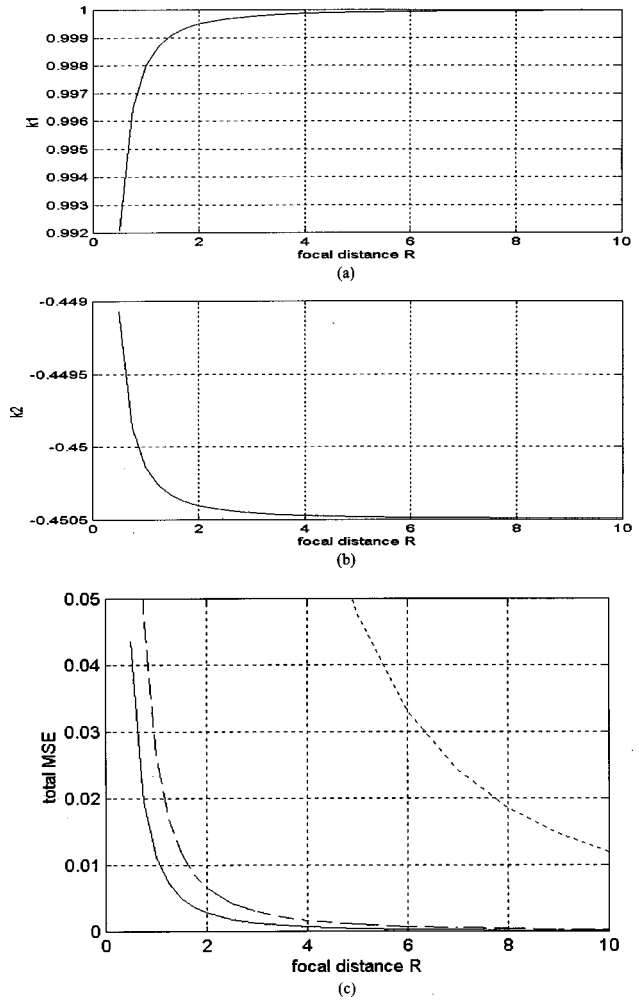

FIG. 2. Behaviors of the weights k_1 (a) and k_2 (b) of the least-squares approximation versus the focal distance R in m. (c) Total MSE in μs^2 versus R for the least-squares approximation (solid line), the Fresnel approximation (dashed line), and the far-field hypothesis (dotted line).

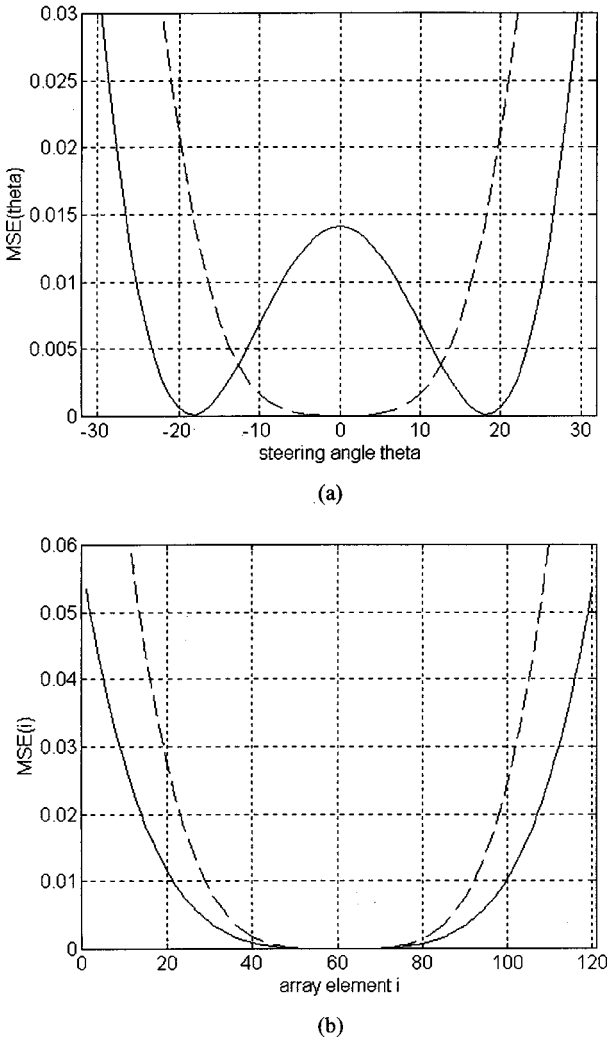

FIG. 3. Behaviors of MSE(θ) (a) and MSE(i) (b), computed at $R=1$ m and measured in μs^2, for the least-squares approximation (solid line) and the Fresnel approximation (dashed line).

Concerning the MSE versus the steering angle, one can notice that the error of the Fresnel approximation increases with $|\theta|$ and its value at the border of the validity region is MSE(18°)$=0.014\ \mu s^2$ (at $R=1$ m). Despite the fact that the error of the least-squares approximation is not zero for $\theta=0°$, its value does not exceed $0.014\ \mu s^2$ over the domain $|\theta|<26.5°$. Therefore as within the validity region of the Fresnel approximation the loss of image quality is generally negligible, one can deduce that, moving from the Fresnel approximation to the least-squares approximation, the safe scanning region can be enlarged from $\pm 18°$ to $\pm 26.5°$, with a gain factor of about 1.5.

Concerning the MSE versus the array element, one can notice that the proposed approximation has the lowest error for whatever array element. Therefore the deformations of the beam patterns computed over the considered set of steering angles will be, on average, lower. This fact does not exclude that, for a given steering angle, the beam pattern obtained by the least-squares approximation may be more distorted than that obtained by the Fresnel approximation. Examination of Fig. 4(a) reveals that the BPP obtained by the Fresnel approximation is perfectly overlapped with the not distorted BPP, whereas the first side lobes of the BPP obtained by the proposed approximation are slightly higher than those of the not distorted BPP. However, the advantages of the proposed approximation are evident in Fig. 4(b): The obtained BPP has two side lobes (to the right of the main lobe) that are slightly higher than the not distorted ones, whereas the BPP obtained by the Fresnel approximation has a lower main lobe together with sharply increased side lobes to both the right and the left of the main lobe. Therefore one can affirm that the BPP deformation produced by the least-squares approximation is weak and about constant over the fixed steering sector. Instead, the BPP deformation produced by the Fresnel approximation increases with the steering angle and is very significant for $\theta=26°$ [see Fig. 4(b)].

By repeating the same reasoning on the errors computed for $R\neq 1$ m, the same conclusion (about the potential enlargement of the scanning region) will be reached. Moreover, if a change of the desired scanning sector is performed, one can verify that the least-squares approximation provides a sort of compromise between the approximation precision and the extension of the desired scanning region. For instance, if a region $|\theta|\leqslant 44°$ is considered for the computation of (k_1,k_2), then the MSE(0°) of the least-squares approxima-

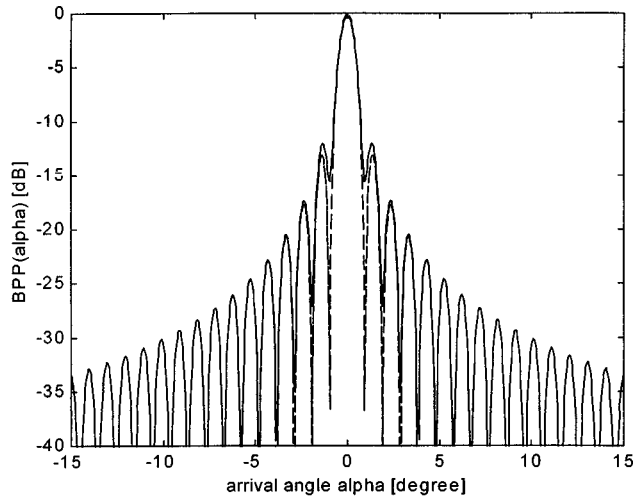

FIG. 4. Not deformed BPP obtained by perfect focusing (dashed line) and BPPs obtained by the Fresnel (dotted line) and least-squares (solid line) approximations, when the steering angle was (a) $\theta=0°$ and (b) $\theta=26°$.

tion exceeds the previous limit of 0.014 μs^2. However, if the limit is expanded up to the MSE(θ) of the Fresnel approximation at $\theta=25°$ (as can often be tolerated), then the error of the least-squares approximation does not exceed the new limit (i.e., 0.047 μs^2) within the sector $|\theta|\leqslant 37°$ (the gain is still equal to 1.5).

As shown in Fig. 3(a), the proposed approximation is worse than the Fresnel one for small values of θ. Consequently, it is reasonable to use the Fresnel approximation to compute beam signals for small θ values, whereas the least-squares scheme should be used for beam signals steered for larger θ values. However, when the FFT implementation is exploited, this procedure is not possible any more as the beam signals are computed all together by a preliminary phase shifting of the received signals[4,6] followed by an M-point FFT (one for each time instant) that transforms the sensor index i into the spatial frequency index m. The relation[5,6] between the index m and the corresponding steering angle θ_m is

$$\theta_m=\sin^{-1}(m\lambda/dM), \quad -M/2\leqslant m\leqslant M/2. \tag{18}$$

Therefore one has to fix a given delay approximation and to use it to compute all the beam signals. Finally, one can verify that for a large set of focal distances, the value of k_1 can be set equal to 1, without a notable loss of precision. When $k_1 \neq 1$ is essential, Eq. (18) should be slightly updated as follows:

$$\theta_m=\sin^{-1}(m\lambda/k_1dM), \quad -M/2\leqslant m\leqslant M/2. \tag{19}$$

V. CONCLUSIONS

In conclusion, an approximation for the delays required by focused beamforming has been proposed that minimizes the MSE computed over the scanning region of interest. The minimization has been obtained by weighting the terms of the conventional Fresnel approximation through a least-squares solution of an overdetermined equation system. In general, one can observe that, if the desired scanning region is not too extended, the least-squares approximation yields an acceptable precision for many practical operations. At the same time, thanks to the similarity of the proposed approximation to the Fresnel one, the computational load and the system complexity do not notably increase, and the opportunity of implementing focused beamforming via the FFT can be easily kept.

Future work will be mainly aimed at the application of the proposed approximation to planar arrays and at the discussion of its performance. The computational advantage of the FFT beamforming implementation is especially great when a planar array (which is mandatory in three-dimensional imaging) is involved.[6] Therefore the least-squares approximation may result in a widening of the scanning region of every 3-D imaging system that has a high frame rate[4] owing to the FFT implementation.

[1] R. O. Nielsen, *Sonar Signal Processing* (Artech House, Boston, 1991).
[2] L. J. Ziomek, ''Three necessary conditions for the validity of the Fresnel phase approximation for the near-field beam pattern of an aperture,'' IEEE J. Ocean Eng. **18**, 73–75 (1993).
[3] J. W. Goodman, *Introduction to Fourier Optics* (McGraw-Hill, New York, 1968).
[4] V. Murino and A. Trucco, ''Dynamic focusing by FFT beamforming for underwater 3D imaging,'' Acoust. Lett. **17**, 169–172 (1994).
[5] B. Maranda, ''Efficient digital beamforming in the frequency domain,'' J. Acoust. Soc. Am. **86**, 1813–1819 (1989).
[6] V. Murino and A. Trucco, ''Underwater 3D imaging by FFT dynamic focused beamforming,'' *1st IEEE International Conference on Image Processing, Austin, Texas* (IEEE, New York, 1994), Vol. I, pp. 890–894.
[7] M. Soumekh, ''Array imaging with beam-steered data,'' IEEE Trans. Image Process. **1**, 379–390 (1992).
[8] R. K. Hansen and P. A. Andersen, ''3D acoustic camera for underwater imaging,'' Acoust. Imaging **20**, 723–727 (1993).
[9] C. R. Rao and S. K. Mitra, *Generalized Inverse of Matrices and its Applications* (Wiley, New York, 1971).

Estimation of the elastic constants of a cylinder with a length equal to its diameter

F. J. Nieves and F. Gascón
Departamento de Física Aplicada, Universidad de Sevilla, E.T.S. Arquitectura, Reina Mercedes 2, 41012-Sevilla, Spain

A. Bayón
Departamento de Física Aplicada a los Recursos Naturales, Universidad Politécnica de Madrid, E.T.S.I. Minas, Ríos Rosas 21, 28003 Madrid, Spain

(Received 13 October 1997; accepted for publication 23 March 1998)

A simple and noncomputational intensive method is proposed for elastically characterizing an isotropic material. The Poisson's ratio and the shear modulus are determined from the axisymmetric vibrations of a cylinder with a length equal to its diameter. These vibrations are excited by means of a wide spectrum impact. The optical system used allows the simultaneous detection of several vibration modes. The out-of-plane displacement is detected by speckle interferometry. From the resulting vibration displacement spectrum, the two lowest frequencies are obtained, both corresponding to axisymmetric modes—specifically, the first symmetric mode and the first antisymmetric mode. The values of both dynamic elastic constants are obtained by comparing previously computed nondimensional natural frequencies and the measured frequencies. The method requires only one experiment and needs no electronic computation. The results obtained for an aluminum cylinder are coherent and confirm the appropriateness of the method. The relative difference between the Young's modulus values calculated by the proposed method and applying the elementary theory to a long rod of the same material is 0.27%. Comparing the shear modulus value obtained by this method and the calculated one from the lower frequency in torsion, a relative difference of 4.6% is found. [S0001-4966(98)01007-8]

PACS numbers: 43.35.Cg [HEB]

INTRODUCTION

The elementary theory of elastic wave propagation in rods of infinite length states that the velocity of propagation of an elastic longitudinal wave is $v_e=(E/\rho)^{1/2}$, where E is the corresponding Young's modulus and ρ is the density. In the case of slender rods of finite length and free edges, the free vibration frequencies are expressed by $f_N=(N/2L)\times(E/\rho)^{1/2}$, where L is the rod length and N is an integer. The mode is in turn termed symmetric if N is odd, and antisymmetric if N is even. Figure 1 illustrates the first symmetric mode and the first antisymmetric mode. The elementary theory is based on two hypotheses: (1) the rod length is much longer than its diameter D, and (2) the wavelength λ of the propagating harmonic wave is much longer than D. If the elementary theory is applicable, it allows the estimation of the elastic constant E of the material of a rod. A further experiment is required to determine the second elastic constant. Due to the lack of concordance between actual experience and the elementary theory, some standards[1–4] require specific geometrical shapes of the sample.

The study of elastic wave propagation in circular cylindrical rods of non-negligible diameter remains of interest. In this sense, it has been concluded that the velocity of propagation is dependent upon λ and D, among other variables. For wavelengths that are long, though not much longer than the diameter of the cylinder, Pochhammer's formula—which states how the velocity of propagation decreases when the ratio D/λ increases—is appropriate for relating phase velocity to the elastic constants of the cylinder and to the wavelength. A theoretical and quantitative interpretation is inferred from Zemanek's study[5] of wave propagation. This author calculated the dispersion curves for symmetric propagation modes of a longitudinal wave traveling along a cylinder of infinite length. These curves give the nondimensional frequency $\pi fD/v_s$ versus the nondimensional wave number $kD/2$, where v_s is the shear wave velocity and k is the wave number.

For finite cylinders of length L, the elastic wave equation and boundary conditions must be considered. Love[6] proposed a solution obtained from a time harmonic function, multiplied by another harmonic in the longitudinal coordinate. This solution satisfies the condition for the longitudinal component of forces in the bases, but fails to satisfy the boundary condition of the shear component in these surfaces. Love added that the shear component should be low when $L \gg D$. Brancroft[7] asserts that the error implied when neglecting these stresses is lower than 0.05%, provided the length-to-diameter ratio is greater than 2.5.

An accurate theory of mode shapes and free vibration frequencies of finite circular cylinders has been developed by a number of authors. The elasticity equations are applied with the appropriate boundary conditions to compute the modes and natural frequencies by numerical methods. A very useful technique is the Ritz–Rayleigh method, based upon the fact that the difference between the maximum kinetic energy and maximum potential energy is minimum when the cylinder is vibrating in a natural mode. Tables dependent

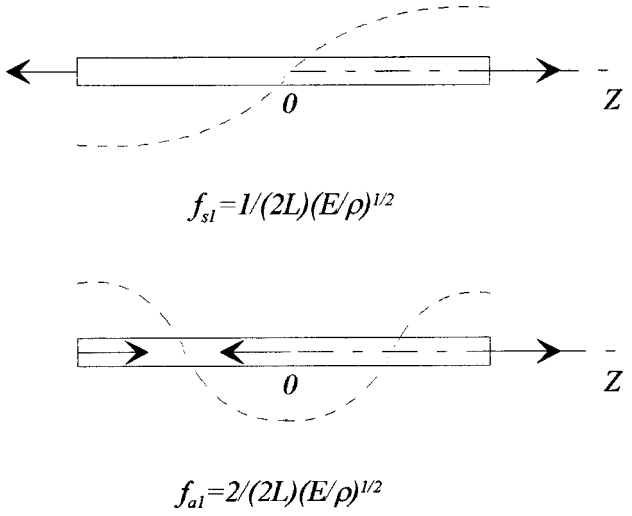

FIG. 1. Rod showing the first longitudinal symmetric mode and the first longitudinal antisymmetric mode according to the elemental theory of vibration.

upon the cylinder properties are made with the obtained frequencies. An ''accurate'' theory implies that the frequency can be obtained as accurately as desired—computer performance being the only limiting factor.

Some papers[8,9] have studied a tridimensional solution in series; such studies have managed to calculate the natural frequencies for both axisymmetric and nonaxisymmetric modes, for length-to-diameter ratios in the range of 0–2. In these papers trigonometric and Bessel's functions are used as admissible functions. In other papers,[10,11] Legendre's polynomials are used along the cylinder axis, and a finite element method is applied to concentric cylinders. More recently,[12–14] algebraic polynomials have been used as displacement functions. Correspondence between results of these studies have been widely commented on by their authors.[15–18] The frequency obtained by these calculations is the nondimensional frequency $\Omega \equiv \pi f D(\rho/G)^{1/2}$, where f is an eigenvalue of the frequency and G is the shear modulus. Specifically, Tables III and IV in Ref. 14 refer to a cylinder with an L/D ratio of 1 and free lateral surfaces and bases, i.e., a free–free case. The results reported by these authors show the effect of the Poisson's ratio ν upon the frequencies of different modes. It is seen that all the frequencies increase as ν increases, except those corresponding to the torsion modes, which are independent of ν.

In general, resonance methods for calculating the elastic constants employ the spectra of natural vibration frequencies obtained from several experiments, in which resonance of a specific type is provoked. Each spectrum allows the estimation of only one elastic constant. Two spectra, either longitudinal or flexural and torsional, allow the calculation of both constants.

The present paper proposes a method for the elastic characterization of an isotropic material, based on the simultaneous detection of several vibration axisymmetric modes. A laser interferometer is used to detect vibration at a point. This coherent light-based detection system adds no mass to the cylinder, and applies no force, i.e., the vibration is free, detection is without contact, and the frequency detection spectrum offers a large bandwidth.[19–21] The theoretical results obtained from the three-dimensional analysis of vibration in cylinders are used.[12,14] Based on the data corresponding to the experimental frequencies and using the abovementioned theoretical results, we are able to quickly and easily determine the two elastic constants of an isotropic material by means of a single experiment.

TABLE I. Effects of Poisson's ratio ν upon the nondimensional frequencies $\Omega=\pi f D\sqrt{\rho/G}$ for symmetric (s) and antisymmetric (a) axisymmetric modes of a free cylinder with $L/D=1$.

ν	Ω_{s1}	Ω_{a1}	Ω_{s2}	Ω_{a2}	Ω_{s3}	Ω_{a3}
0	2.221	2.306	2.454	3.235	2.604	4.288
0.1	2.290	2.496	2.636	3.365	2.917	4.407
0.2	2.315	2.686	2.843	3.467	3.377	4.545
0.3	2.326	2.872	3.067	3.541	3.989	4.707
0.4	2.333	3.045	3.304	3.596	4.439	4.896
0.499	2.337	3.198	3.547	3.637	4.609	5.103

I. FIRST AXISYMMETRIC MODES

Let us use cylindrical coordinates r, θ, and z, with the origin at the center of the cylinder and the Z axis joined with the cylinder revolution axis. When the displacement of the cylinder points does not depend upon θ, the vibration is axisymmetric. This kind of vibration is the unique one that we study in this paper. It is named symmetric axisymmetric vibration, if the longitudinal displacement is an odd function of z.

Table I in the present paper reproduces in its second column some values from Table III in Ref. 14, specifically those referring to the first symmetric axisymmetric mode, for $L/D=1$, corresponding to the basic mode or first harmonic of the elementary theory, associated to the longitudinal vibrations, as it is drawn at the top of Fig. 1 ($N=1$). In turn, some values from Table IV[14] in reference to the first antisymmetric axisymmetric mode are reproduced in the third column of our Table I, corresponding to the second harmonic of the elementary theory. The fourth and sixth columns in Table I refer to the second and third symmetric axisymmetric modes, while the fifth and seventh columns refer to the same antisymmetric modes. Thus, Table I, corresponding to free–free cylinders, $L/D=1$, axisymmetric modes, gives, for each value of Poisson's ratio ν (column 1), values of the frequencies Ω_{s1} for the first symmetric mode, and of Ω_{a1} for the first antisymmetric mode (columns 2 and 3, respectively). Both columns in Table I show an increasing order of frequencies as ν increases.

The data in Table I, which reproduces values of $\Omega=\pi f D(\rho/G)^{1/2}$ and Poisson's ratio ν, in turn suggest calculation of the elastic constants ν and G of the material of which the cylinder is composed. In effect, based on a cylindrical rod of measured diameter D, we cut a sample of length $L=D$. This mass is weighed and its volume and density calculated. The sample is then simultaneously set into vibration in its first symmetric and first antisymmetric modes, followed by measurement of the respective resonant frequencies f_{s1} and f_{a1}.

The values obtained for the parameter $\Omega = \pi f D(\rho/G)^{1/2}$, presented in Table I for ν from 0 to 0.5 in steps of 0.1, show that Ω_{a1} is always greater than Ω_{s1} for the same value ν. In addition, the values of Ω_{s2}, Ω_{a2} and higher are always greater than Ω_{s1} and Ω_{a1} for a same ν. Moreover, these frequencies Ω exhibit an increasing order with ν, as do the corresponding frequencies f. Thus, both first frequencies of the longitudinal vibration spectrum f_1 and f_2 correspond to the above-mentioned modes f_{s1} and f_{a1}, i.e., the first symmetric and first antisymmetric modes. In the event that the analytical functions $\Omega_{s1}(\nu)$ and $\Omega_{a1}(\nu)$ are available, the problem of calculating the sample elastic constants, ν and G, is reduced to the resolution of a system of two equations with two unknown quantities: $\Omega_{s1}(\nu) = \pi f_{s1} D(\rho/G)^{1/2}$ and $\Omega_{a1}(\nu) = \pi f_{a1} D(\rho/G)^{1/2}$.

Let us solve the proposed problem by trial. Suppose ν is given a value ν_e, where $0 < \nu_e < 0.5$. For this ν_e Table I provides $\Omega_{s1,e}$. A first value for the shear modulus $G_e = \pi^2 f_{s1}^2 D^2 \rho / \Omega_{s1,e}^2$ is deduced from the definition of Ω. With this G_e and f_{a1} we in turn obtain $\Omega_{a1,e} = \pi f_{a1} D(\rho/G_e)^{1/2}$. This value $\Omega_{a1,e}$ will be between two values of the Ω_{a1} column in Table I. With the simple assumption that a linear interpolation is valid, we obtain a new value for Poisson's ratio. A new linear interpolation gives a second value for Ω_{s1}. In this same manner successively, we obtain correct values for ν and G. The other elastic constants are in turn functions of ν and G, for instance $E = 2(1+\nu)G$.

II. MEASUREMENT OF THE NATURAL FREQUENCIES BY SPECKLE INTERFEROMETRY

The studied sample is a commercial aluminum cylinder with a diameter D equal to its length L; $L = D = 40.30$ mm and mass $m = 143.5$ g, therefore its density is $\rho = 2791$ kg/m^3. In order to secure free vibration of the rod, the latter is placed with its axis horizontally and supported at its center on a small rubber block. Vibration is induced by using a simple steel sphere pendulum. Longitudinal oscillations are excited by a brief impact of the steel sphere perpendicular to the base of the cylinder at its center. This type of excitation allows the rod to vibrate over a wide range of frequencies, though only its natural frequencies remain. The sample vibrates freely, as no further forces act upon the sample following the impact.

The steel ball used to produce the vibration has a radius $R_b = 1.60$ mm. The travel time of the sound across the ball is much shorter than the period of the longest natural frequency under study. In order to estimate the bandwidth caused by the ball used to excite the vibration, we apply the theory of impact of two solid spheres.[22] To simplify, we assume that both the cylinder and ball are made of steel, $E = 200$ GPa, $\nu = 0.3$, $\rho = 7.9 \times 10^3$ kg/m^3, and the velocity of the ball before the impact is $v = 0.6$ m/s. The ball has a very small size and mass with respect to the length and mass of the vibrating cylinder. When neglecting both the ball radius and mass m_b, impact duration time is calculated as $t = 3.78(m_b^2(1-\nu^2)^2/(R_b E^2 v))^{1/5} = 10^{-5}$ s, as a result of which the maximal excited frequency to be expected is 0.1 MHz. This frequency adequately covers the frequencies of interest in the present study, as demonstrated further on.

A laser interferometer is used to measure sample vibration at a point. The system employed is an OP-35 I/O interferometer (Ultra Optec, Inc.)[23,24] with a detection bandwidth of 1 kHz to 35 MHz, and a resolution of about 1 nm. By using this system, both displacement components—the normal to the free surface (i.e., out-of-plane) and the tangential (in-plane)—can be detected at the same point, though not simultaneously. The detection principle is based on speckle interferometry. The speckle phenomenon is produced when a diffusing surface is illuminated by coherent light.[25,26] Interference from the wavelets diffused by the surface yields an intensity distribution consisting of bright and dark spots. In our experiments, the diameter of the illuminated area on the surface is about 20 μm, and the sample was scratched with 320 sandpaper to diffract light in the plane where the optical components are located.

Taking into account the waves generated, the displacement component to be measured will be the normal to the free surface (i.e., the out-of-plane component), which should be detected at the center of the rod base opposite to the base where the impact was applied.

The detection system includes a 5-mW He–Ne laser, whose beam is split into two by a Bragg cell; one of the split beams is deflected and the frequency shifted by 40 MHz. In the out-of-plane configuration the angle θ between the incident light beam and the normal to the surface at the point of detection is equal to the angle between that normal and the direction of observation. The unshifted frequency beam is directed to the surface of the sample. The scattered light is led to the beam mixer, where it interferes with the frequency-shifted beam used as reference beam. The resulting interference is then focused onto a photodiode. A displacement out-of-plane δz at the detection point produces a variation in the path length of the optical beams and, consequently, a phase change equal to $4\pi \cos\theta \delta z/\lambda$, where λ is the wavelength.

The intensity on the detector resulting from the interference is a 40-MHz signal, which is phase modulated by the displacement of the detection point. The signal is processed by a demodulating unit to yield a signal proportional to the instantaneous displacements of the surface.

Finally, the signal is digitized using a 400-MHz HP54504A oscilloscope. The sampling frequency is always greater than twice the maximum frequency expected. The signal is subsequently computer processed to calculate the fast Fourier transform (FFT). The obtained spectrum includes the natural vibration frequencies, which coincide with the maximum amplitudes in the FFT. In accordance to the excitation applied, the peak amplitudes will be associated to the longitudinal natural vibration frequencies of the specimen.

III. EXPERIMENTAL RESULTS

The experimentally obtained graph in Fig. 2 shows the out-of-plane vibration frequency spectrum, according to the method described above. The lowest frequencies, e.g., the first six, are: $f_0 = 1708$ Hz, $f_1 = 58\,349$ Hz, $f_2 = 73\,242$ Hz, $f_3 = 78\,857$ Hz, $f_4 = 88\,867$ Hz, and $f_5 = 104\,736$ Hz. In principle, we are unaware of the frequencies f_{s1} and f_{a1} of interest to us. However, f_0 may be excluded as a candidate,

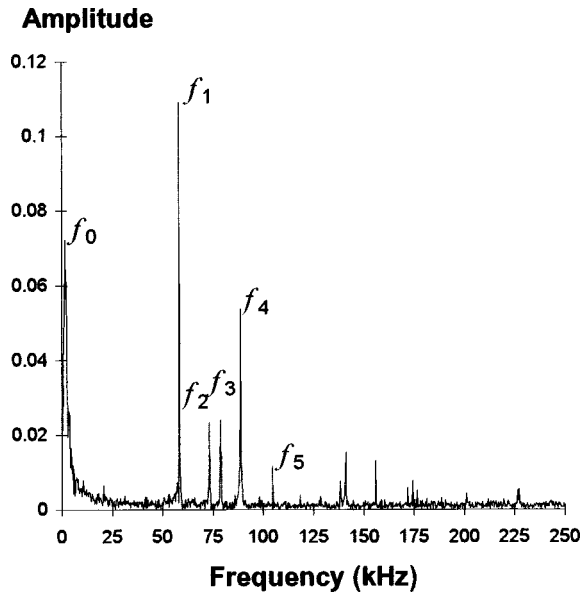

FIG. 2. Frequency spectrum of longitudinal vibration corresponding to a rod with a length equal to its diameter. The vibration was originated by an axial percussion.

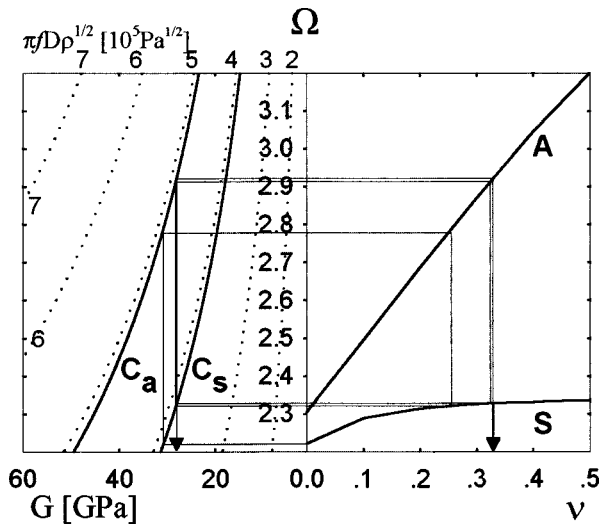

FIG. 3. Nondimensional frequencies Ω_{s1} and Ω_{a1} of the first axisymmetric symmetric and antisymmetric modes in a cylinder with $L=D$ versus Poisson's ratio ν and shear modulus G. This allows us to graphically estimate ν and G. The estimation for our experimental data is shown.

for at least three reasons: (1) the corresponding peak lacks sharpness in the spectrum, (2) f_0 is about 38 times lower than the first harmonic frequency obtained from the elementary theory, and (3) the quotient f_1/f_0 is about 34, i.e., 17 times bigger than the quotient between the two first harmonic from the elementary theory. The frequencies f_1 and f_2 are the preferred frequencies. The first two sharp peaks must correspond to the natural frequencies of the two first axisymmetric modes. We thus accept as starting hypothesis that $f_{s1}=58\,349$ Hz and $f_{a1}=73\,242$ Hz.

The above method involving successive approximations for estimating ν and G is applied. As first value of ν we propose the absurd condition $\nu_1=0$. In this case, Table I attributes ν_1 a frequency $\Omega_{s1,1}=2.221$. From the definition of Ω we obtain a first estimation for the shear modulus $G_1=4\pi m f_{s1}^2/(L\Omega_{s1,1}^2)=30.883$ GPa. With G_1 and f_{a1} we derive a nondimensional frequency corresponding to the first antisymmetric mode, where $\Omega_{a1,1}=2.788$. For this $\Omega_{a1,1}$, Table I gives a Poisson ratio of $\nu_2=0.255$. For this ν_2, Table I provides $\Omega_{s1,2}=2.321$; hence, $G_2=28.280$ GPa, and $\Omega_{a1,2}=2.9134$. In turn, $\nu_3=0.324$ and therefore $\Omega_{s1,3}=2.328$; as a result, $\Omega_{a1,3}=2.922$ — from which we obtain $\nu_4=0.329$ and finally $\Omega_{s1,4}=2.328$. Thus, the elastic constants are $\nu=0.329$ and $G=28.1$ GPa. From both values we can calculate the other elastic constants, for instance, Young's modulus $E=2(1+\nu)G=74.6$ GPa.

If our hypothesis that f_1 and f_2 are the correct respective values of f_{s1} and f_{a1} is true, then we may in turn predict the values $f_3, f_4, \ldots$. In effect, from the definition of Ω we deduce that for one same sample $\Omega_{s2}/\Omega_{s1}=f_{s2}/f_{s1}$, and so $f_{s2}=\Omega_{s2}f_{s1}/\Omega_{s1}$. Based on the fourth column in Table I, we find that $f_{s2}=78\,568$ Hz; the concordance with f_3 is evident (relative difference 0.37%). The same occurs with $f_{a2}=89\,145$ and f_4 (0.31%), and also with $f_{s3}=103\,203$ and f_5 (1.46%). Therefore, when using the first two detected frequencies and following the established theoretical methodology, we obtain the frequencies corresponding to higher modes, and these are seen to coincide with those detected experimentally. That shows the goodness of f_1 and f_2, and the coherence with other frequencies.

The resonances have different amplitudes, as it appears in Fig. 2. The percussion applied for exciting the cylinder vibration has a complicated frequency spectrum. The set of natural frequencies forms a complicated sequence. The amplitude of vibration for a frequency depends on the excitation amplitude for that frequency. Therefore, the vibration FFT modulus must be necessarily complicated. Furthermore, the amplitudes also depend on attenuation. In order to study the influence of the support, the one mentioned in Sec. II was replaced by others (e.g., another consisting of two rubber's simple supports at the edges), and the results of the frequencies $f_1, f_2, \ldots$, did not change, but f_0 did. That is, the elastic rubber support produces low frequency vibrations that might be, together with the lower limit of the interferometer detection bandwidth, a source of the apparition of the peak f_0. And so, it can be assumed that the rod vibrates freely, with that kind of support, for the aim of this work.

IV. GRAPHICAL METHOD

The resolution of the problem may be easily illustrated by a double graphic representation of Ω vs ν and Ω vs G (Fig. 3). To the right of the figure are represented the values of Ω_{s1} vs ν, obtained from the first two columns of Table I, along with the values of Ω_{a1} vs ν, obtained from the first and third columns of the same table. The resulting points have been joined by straight lines (linear interpolation), to respectively yield polygons S and A.

To the left of Fig. 3 are represented the values of Ω versus G, based on the definition of $\Omega=\pi D\rho^{1/2}f/G^{1/2}$. The variation range of Ω is (2.221, 3.198) for the two first modes, and the range of G is estimated as (0, 60 GPa); hence, the existence interval of $\pi D\rho^{1/2}f$ is estimated as (0, 10^6 Pa$^{1/2}$).

Curves $\Omega=\Omega(G)$ are then traced for different values of $\pi D\rho^{1/2}f$.

Based on a sample with $L/D=1$, we proceed to measure D and calculate ρ. We measure f_{s1} and calculate $\pi D\rho^{1/2}f_{s1}$. The curve C_s corresponding to that value (for our specimen 3.9×10^5 $\mathrm{Pa}^{1/2}$) is indicated. We also calculate $\pi D\rho^{1/2}f_{a1}$ (4.9×10^5 $\mathrm{Pa}^{1/2}$) and indicate the corresponding curve C_a. On considering a value ν_1 of ν (for instance, $\nu_1=0$ in Fig. 3), the vertical through ν_1 intersects the polygon S at a point. From this point, we trace a horizontal line to the left, which intercepts the curve C_s at a point. In turn, from this point, an ascendant vertical trace intersects the curve C_a. From this crossing point, a horizontal line to the right intercepts polygon A at a certain point. A downward vertical line from this point in turn intersects S at another point. The method is then repeated from this last point. The line consisting of straight segments is seen to converge onto a rectangle with vertical edges at the correct values of ν and G, and with horizontal edges at the correct values of Ω_{s1} and Ω_{a1}.

V. OTHER EXPERIMENTS

As verification, the above experiment has been repeated with a rod of the same material, but with $L=400$ mm and $D=40.30$ mm. Since $L/D>2.5$, the elementary theory is applicable in principle; thus, $E_{el}=4L^2f_{s1}^2\rho=74.8$ GPa. The relative difference with respect to the previous value is $(E_{el}-E)/E=0.27\%$.

A further experimental test has been conducted by exciting the torsional modes of the long rod.[21] A horizontal grazing impact at a point on the lateral surface produces torsional oscillations (as well as bending oscillations). This vibration is detected by recording the tangential component of the displacement at a point on the opposite base and near the edge.[21] In our experiment we obtained for the first torsional mode $f_t=3857$ Hz. The nonzero lower frequency in torsion is $f_t=(G_t/\rho)^{1/2}/(2L)$; consequently, in our experiment it is $G_t=4\rho L^2f_t^2=26.8$ GPa. The relative difference with respect to our proposed method is approximately 4.6%.

The value of the elastic modulus determined by an adiabatic process is usually larger than the one determined by an isothermal process (e.g., static uniaxial tension test).[27] Dynamic testing is neither adiabatic nor isotherm. The larger the frequency is, the more the adiabatic conditions are fulfilled. The frequencies f_1 and f_2 are very different; then, the motion of the corresponding waves is different, from a thermodynamic point of view. Fortunately, the difference between adiabatic and isothermal elastic constants is usually on the order of 1% or lower (see Ref. 22, p. 24). Therefore, the uncertainty associated with the shear modulus must be originated by other experimental errors.

[1] ASTM C 747-74, ''Standard test method for moduli of elasticity and fundamental frequencies of carbon and graphite materials by sonic resonance'' (American Society for Testing Materials, Philadelphia, 1974).

[2] ASTM C 848-88, ''Standard test method for Young's modulus, shear modulus, and Poisson's ratio for ceramic whitewares by resonance'' (American Society for Testing Materials, Philadelphia, 1988).

[3] ASTM C 623-71, ''Standard method of test for Young's modulus, shear modulus, and Poisson's ratio for glass and glass ceramics by resonance'' (American Society for Testing Materials, Philadelphia, 1971).

[4] ASTM C 215-85, ''Standard test method for fundamental transverse, longitudinal and torsional frequencies of concrete specimens'' (American Society for Testing Materials, Philadelphia, 1985).

[5] J. Zemanek, ''An experimental and theoretical investigation of elastic wave propagation in a cylinder,'' J. Acoust. Soc. Am. **52**, 265–283 (1971).

[6] A. E. H. Love, *Mathematical Theory of Elasticity* (Dover, New York, 1944), p. 287.

[7] D. Bancroft, ''The velocity of longitudinal waves in cylindrical bars,'' Phys. Rev. **59**, 588–593 (1941).

[8] J. R. Hutchinson, ''Axisymmetric vibrations of a free finite-length rod,'' J. Acoust. Soc. Am. **51**, 233–240 (1972).

[9] J. R. Hutchinson, ''Vibration of solid cylinders,'' J. Appl. Mech. **47**, 901–907 (1980).

[10] M. Senoo, T. Nishimura, and M. Hirano, ''Measurement of elastic constants of polycrystals by the resonance method in a cylindrical specimen,'' Bull. JSME **27**, 2339–2346 (1984).

[11] M. Senoo, T. Nishimura, A. Matsumuro, and S. Ishigai, ''Measurement of elastic constants of polycrystals in a cylindrical specimen by the resonance method,'' JSME Int. J. **30**, 747–753 (1987).

[12] J. So, ''Three dimensional vibration analysis of elastic bodies of revolution,'' Ph.D. dissertation, The Ohio State University, 1993.

[13] A. W. Leissa and J. So, ''Comparisons of vibration frequencies for rods and beams from one-dimensional and three-dimensional analyses,'' J. Acoust. Soc. Am. **98**, 2122–2135 (1995).

[14] A. W. Leissa and J. So, ''Accurate vibration frequencies of circular cylinders from three-dimensional analysis,'' J. Acoust. Soc. Am. **98**, 2136–2141 (1995).

[15] J. R. Hutchinson, ''Comments on 'Comparisons of vibration frequencies for rods and beams from one-dimensional and three-dimensional analyses' [J. Acoust. Soc. Am. **98**, 2122–2135 (1995)],'' J. Acoust. Soc. Am. **100**, 1890–1892 (1996).

[16] A. W. Leissa and J. So, ''Response to ''Comments on 'Comparisons of vibration frequencies for rods and beams from one-dimensional and three-dimensional analyses' [J. Acoust. Soc. Am. **100**, 1890–1892 (1996)],'' '' J. Acoust. Soc. Am. **100**, 1893 (1996).

[17] J. R. Hutchinson, ''Comments on 'Accurate vibration frequencies of circular cylinders from three-dimensional analysis' [J. Acoust. Soc. Am. **98**, 2136–2141 (1995)],'' J. Acoust. Soc. Am. **100**, 1894–1895 (1996).

[18] A. W. Leissa and J. So, ''Response to ''Comments on 'Accurate vibration frequencies of circular cylinders from three-dimensional analysis' [J. Acoust. Soc. Am **100**, 1894–1895 (1996)],'' J. Acoust. Soc. Am. **100**, 1896 (1996).

[19] A. Bayón, F. Gascón, and A. Varadé, ''Measurement of the longitudinal and transverse vibration frequencies of a rod by speckle interferometry,'' IEEE Trans. Ultrason. Ferroelectr. Freq. Control **40**, 265–269 (1993).

[20] A. Bayón, A. Varadé, and F. Gascón, ''On the acoustical longitudinal vibration modes of finite cylinders,'' J. Acoust. Soc. Am. **96**, 1539–1548 (1994).

[21] A. Bayón, A. Varadé, and F. Gascón, ''Determination of the elastic constants of isotropic solids by optical speckle interferometry,'' J. Acoust. Soc. Am. **96**, 2589–2592 (1994).

[22] L. D. Landau and E. M. Lifshitz, *Theory of Elasticity* (Pergamon, Oxford, 1975), p. 36.

[23] J. P. Monchalin, ''Optical detection of ultrasound,'' IEEE Trans. Ultrason. Ferroelectr. Freq. Control **33**, 485–499 (1986).

[24] J. P. Monchalin, J. D. Aussel, R. Heon, C. K. Jen, A. Boundreault, and R. Bernier, ''Measurement of in-plane and out-of-plane ultrasonic displacements by optical heterodyne interferometry,'' J. Nondestruct. Eval. **8**, 121–132 (1989).

[25] J. W. Goodman, ''Statistical properties of laser speckle patterns,'' in *Laser Speckle and Related Phenomena*, edited by J. C. Dainty (Springer-Verlag, Berlin, 1984), Chap. 2, pp. 9–75.

[26] A. E. Ennos, ''Speckle interferometry,'' in *Laser Speckle and Related Phenomena*, edited by J. C. Dainty (Springer-Verlag, Berlin, 1984), Chap. 6, pp. 203–253.

[27] H. B. Callen, *Thermodynamics* (Wiley, New York, 1960), p. 235.

Examination of the two-dimensional pupil function in coherent scanning microscopes using spherical particles

Wieland Weise
Physics Department, University of Bremen, 28334 Bremen, Germany

Pavel Zinin and Andrew Briggs
Department of Materials, University of Oxford, Oxford OX1 3PH, United Kingdom

Tony Wilson
Department of Engineering Science, University of Oxford, Oxford OX1 3PH, United Kingdom

Siegfried Boseck
Physics Department, University of Bremen, 28334 Bremen, Germany

(Received 2 May 1997; accepted for publication 16 March 1998)

The determination of the modulus of the pupil function in reflection acoustic and optical microscopy with the help of spherical particles is demonstrated. The theoretical examination shows that this method can give good results if the pupil function drops smoothly towards the edge. For a pupil with a sharp edge this technique can give the accurate pupil function only by imaging large spheres. The dependence of the accuracy of the method on the size of the spherical particle is analyzed. Numerical and experimental results obtained for the confocal scanning optical microscope and the scanning acoustic microscope are examined. © *1998 Acoustical Society of America.*
[S0001-4966(98)00307-5]

PACS numbers: 43.35.Sx [HEB]

INTRODUCTION

If the confocal scanning optical or the acoustic microscope are used for accurate quantitative analysis, their emission and detection characteristic must be taken into account. The emission and detection properties of the imaging system can be described by the pupil function of the lens. The available methods of pupil function determination are based on the axial response or $V(z)$ curve measurement (acoustic microscope,[1] confocal interference microscope[2]). Hereby the fact is used that the inverse Fourier transform of the $V(z)$ curve gives the product of the pupil function and the reflection coefficient. However, the results are only good if the accurate phase of the output signal is available[3,4] (see also Ref. 5). To extract the pupil function from the obtained data it is then, in the case of the acoustic microscope, necessary to know the reflection coefficient. But the technique contains a crucial disadvantage. The obtained pupil function is averaged over the azimuthal angle. Especially in acoustic microscopy strong asymmetry might occur, for example, if the transducer and lens are not aligned coaxially. Another method proposed by Ref. 6, which is based on the measurement of the signal generated by a second planar transducer, involves considerable experimental effort. In Ref. 7 a method is described to measure aberrations of optical instruments (telescopes) by transforming intensity data, but this method would require a second measuring device, when applying it to confocal microscopes.

In Ref. 8 it has been proposed to investigate the two-dimensional pupil function or sensitivity characteristic from images of rigid spherical particles without a data transformation being involved. Using a geometrical optics approach, it has been shown that this method would give the absolute value of the squared pupil function when the phase of the output signal is not detected, which is the normal case for high-frequency acoustic microscopes. In Ref. 9 it has been found that in order to estimate the limitations and accuracy of the method a theoretical analysis based on the solution of the diffraction problem is required. In this paper a theoretical analysis of the accuracy of the method is presented. Numerical and experimental results obtained for the reflection scanning acoustic microscope and the confocal reflection optical microscope are examined. The limitations of the method are discussed.

I. THEORETICAL DEVELOPMENT

The importance of the sensitivity characteristic in confocal microscopy is clarified by considering the expression for the output signal V of the acoustic microscope under time harmonic conditions, given by[10]

$$V=\int_{-\infty}^{\infty}\int U^{-}(k_x,k_y)U^{+}(-k_x,-k_y) \times\sqrt{k^2-k_x^2-k_y^2}\,dk_x\,dk_y. \tag{1}$$

U^{-} is the angular spectrum of the sound velocity potential field, which is returning to the microscope. U^{+} is the angular spectrum of the potential field Ψ^{+} emitted by the microscope. We will use Eq. (1) equally to describe the confocal optical microscope, in this case the fields denote the scalar potential. For our purpose, both spectra are taken in the focal plane. k is the wave number; the harmonic time dependence and a proportionality constant are omitted. The formula was derived originally for a transducer that is directly radiating into the coupling medium. However, it was demonstrated,[11]

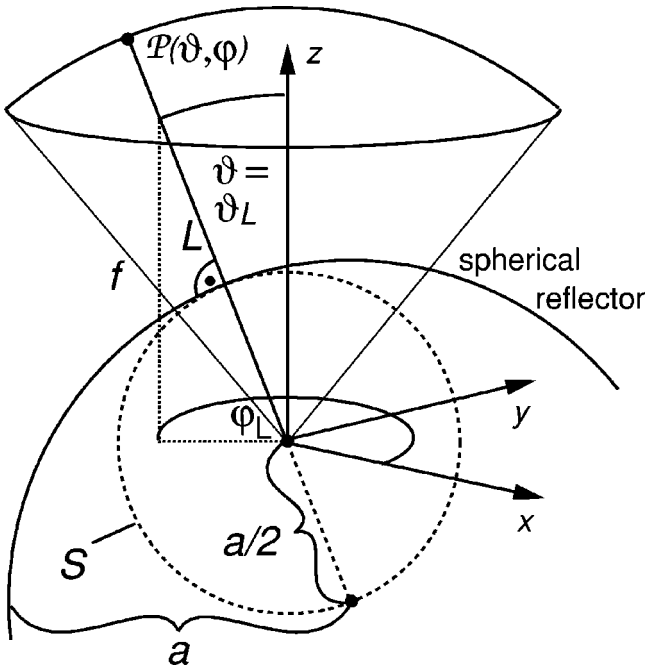

FIG. 1. Model of the setup for measuring the pupil function.

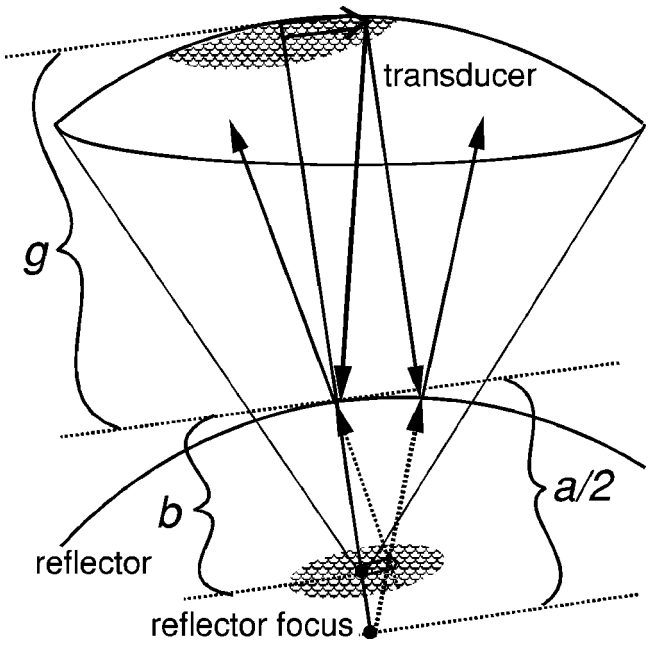

FIG. 2. The reflecting spherical surface as ''thin lens.''

that also a general type of microscope, consisting of a planar transducer, buffer rod, and spherical lens, is described with the same accuracy by it in the continuous wave regime.

By reciprocity $U^+(-k_x,-k_y)\sqrt{k^2-k_x^2-k_y^2}$ in Eq. (1) represents the sensitivity characteristic to the angular components of the returning wave field, and consequently is important for interpreting the output signal. In Eq. (1) the integration extends to infinity, and therefore evanescent waves are involved. However, in the Debye approximation the angular spectrum is restricted to $\sqrt{k_x^2+k_y^2}<k$.[12,13] This fact will give us the possibility to replace the Cartesian components of the wave vector by spherical coordinates. The sensitivity characteristic may then be connected to a pupil function defined in the space domain, which we will introduce in the following.

Let us define a spherical coordinate system that is centered in the focal point of the microscope. The polar axis is directed upwards and lying along the optical axis, polar and azimuthal angle are denoted (ϑ,φ), respectively (see Fig. 1). The pupil function $\mathcal{P}$ is now introduced with the help of the radial component $v_\perp$ of gradient of the emitted potential field Ψ^+ at distance f (focal length) from the focal point:

$$\mathcal{P}(\vartheta,\varphi)=\frac{v_\perp(\vartheta,\varphi)}{k}. \tag{2}$$

The pupil function here is obviously defined on a spherical surface. Let us consider, for example, an acoustic microscope buildup from a spherical transducer, whose radius of curvature defines the focal length f. Then $v_\perp$ is the radial component of the velocity distribution on the transducer surface, which equals the one in the adjacent coupling fluid. If $v_\perp(\vartheta,\varphi)$ is slowly varying on the scale of the wavelength, the emitted potential field can be calculated from it with the Rayleigh integral.[14] By applying the Debye approximation,[12] the above pupil function can then be shown to be related to U^+ by:[15]

$$\mathcal{P}(\vartheta,\varphi)=\frac{k}{2\pi f}\,U^+(-k\,\sin\vartheta\,\cos\varphi,\; -k\,\sin\vartheta\,\sin\varphi)\cos\vartheta. \tag{3}$$

Hence in the Debye approximation, which becomes exact for $f\to\infty$, $\mathcal{P}$ is given (up to a constant factor) by the sensitivity characteristic in spherical coordinates. In this approximation $\mathcal{P}(\vartheta,\varphi)$ gains an additional meaning: It directly equals the far-field angular distribution of the potential Ψ^+.[16] Due to the choice of the constants, $\mathcal{P}$ is normalized to the potential value at distance f from the focal point.

To derive the method for measuring the sensitivity characteristic or pupil function of the microscope we assume that the focal length f is large in comparison with the wavelength, and the pupil function is slowly varying on the scale of the wavelength. This calculation has been briefly discussed in Ref. 9. The setup for measuring the pupil function is depicted in Fig. 1. The focal point of the microscope is positioned at half-radius $a/2$ in the upper half of a perfectly reflecting spherical particle with radius times wave number $ka\gg 2\pi$ $(ka>100)$. The straight line L, that connects the center of sphere and focal point, subtends as viewed in direction of the transducer angles (ϑ_L,φ_L). In the vicinity of the straight line L the surface of the spherical particle can be considered to reflect like a paraboloid. The paraboloidal focus of the sphere in our situation coincides with the focus of the incident wave field.

Let us describe the method at first ray-optically: Consider the potential field Ψ^+ emitted by the microscope. It is easy to derive a thin lens law for the reflection of the field incident on the sphere from the directions around L, as sketched in Fig. 2:

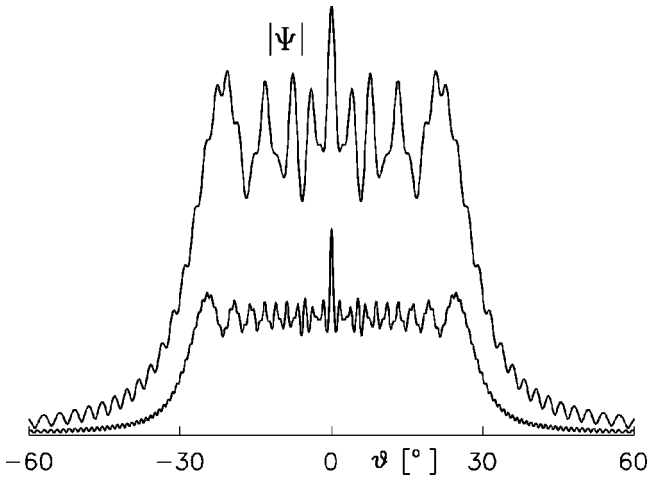

FIG. 3. Absolute value of the virtually incident wave field ψ^+ in Debye approximation on the spherical surface S around the focal point. The radius of S is $200/k$ (upper curve) and $500/k$ (lower curve), $\alpha=30°$.

$$\frac{1}{b}-\frac{1}{g}=\frac{1}{a/2}, \tag{4}$$

with b being the distance below the reflector from where the field incident from distance g above the reflector and then reflected seems to originate. Therefore the far-field value of $\Psi^+(\vartheta_L,\varphi_L)$, which is in the Debye approximation equal to $\mathscr{P}(\vartheta_L,\varphi_L)$, virtually originates from the paraboloidal focus at $a/2$ and propagates back along L. This is also the position of the focal point of the microscope. Because the microscope detects the field that occurs (virtually) at the position of the focal point,[17–19] it will measure its own pupil function. Additionally, the detection is weighted with the value of the pupil function in the direction of propagation of the measured field. Therefore we expect to observe the squared pupil function when scanning the half-radius surface of the spherical particle.

Let us investigate this more thoroughly. The potential field Ψ^+, that is virtually incident at a spherical surface S of radius $a/2$ around the paraboloidal focus, is depicted as a dashed circle in Fig. 1. This field is given in the Debye approximation by[15]

$$\Psi^+(\vartheta,\varphi)=\frac{kf}{2\pi}\int_0^{2\pi}\int_0^{\pi/2}\exp(-i\mathbf{qr}) \times\mathscr{P}(\vartheta_q,\varphi_q)\sin\vartheta_q\,d\vartheta_q\,d\varphi_q. \tag{5}$$

(ϑ_q,φ_q) are the angles of $\mathbf{q}=-\mathbf{k}$, which is the backwards prolongation of the wave vector of the emitted wave field $\mathbf{k}=(k_x,k_y,-\sqrt{k^2-k_x^2-k_y^2})$. For the emission case the wave vector $\mathbf{k}$ is pointing in the negative z direction. The vector $\mathbf{r}$ has angles (ϑ,φ) and length $a/2$. From the assumption that a is large, the surface S has a wide separation from the focal point. For a constant pupil function

$$\mathscr{P}(\vartheta)=\begin{cases}1, & \vartheta\leqslant\alpha,\\ 0, & \vartheta>\alpha,\end{cases} \tag{6}$$

with semiaperture angle $\alpha=30°$ the potential field integral (5) at distances $200/k$ and $500/k$ is depicted in Fig. 3. If the pupil function is sufficiently smooth, the integral (5) can be evaluated by the method of stationary phase.[8,20] Taking into account only inner stationary points we find up to a constant phase factor for the virtual field Ψ^+ above the focal point on S:

$$\Psi^+(\vartheta,\varphi)=\frac{2f}{a}\mathscr{P}(\vartheta,\varphi). \tag{7}$$

Hence if the pupil function is sufficiently smooth, the virtual potential field on S is, up to a constant factor, approximately equal to it. Considering the reflection in combination of the physical optics and a ''thin lens'' approximation, this field distribution arrises at a plane A, which cuts line L orthogonally at distance $a/2$ from the focal point. This is depicted in Fig. 4. To describe the reflection, we introduce a second coordinate system. It is also centered on the focal point, but its polar axis lies along line L, polar and azimuthal angles within this system are denoted (θ,ϕ), respectively (see Fig. 4). The azimuthal angle is oriented such that for the acoustical axis $\phi=0$ is valid. To describe the reflected field within this system, we use cylindrical coordinates (ρ,ϕ,Z). For example, A is given by the plane with $Z=a/2$. If the pupil function and accordingly the incident field is rotationally symmetric around the acoustical axis, $\Psi^+=\Psi^+(\vartheta)$, we can express it within the second system as

$$\Psi^+(\vartheta(\theta,\phi))=\Psi^+(\arccos(\sin\theta\cos\phi\sin\vartheta_L +\cos\theta\cos\vartheta_L)). \tag{8}$$

The field virtually incident on S at the point under (θ,ϕ) is reflected in a good approximation to the point on A with $\rho=\theta a/2$, unchanged azimuthal angle ϕ, and $Z=a/2$. Corresponding points are obtained by ''rolling'' S on A. This ''thin lens'' approximation is valid for small ρ. But this area

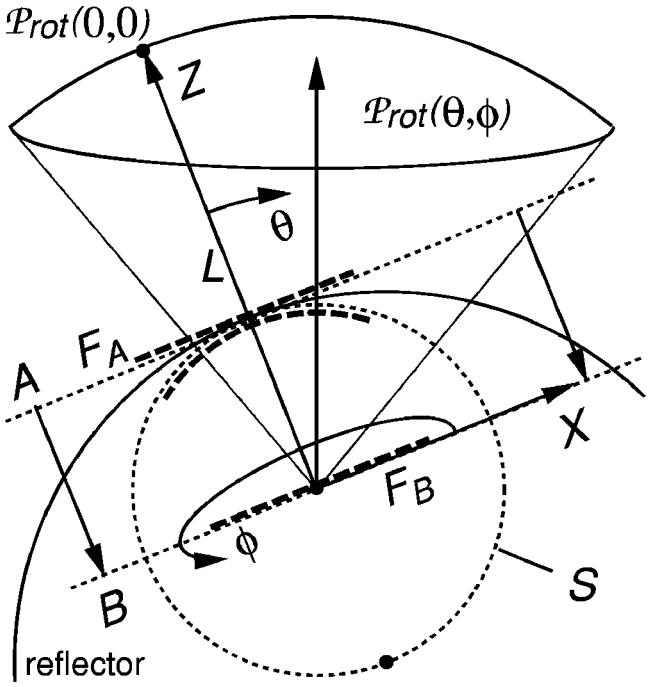

FIG. 4. Coordinate systems used for the description of the reflected wave fields.

will determine the output signal. So the reflected field F_A^- on A for Ψ^+ given by Eq. (8) is

$$F_A^-(\rho,\phi)=\Psi^+\left(\arccos\left(\sin\left(\rho\,\frac{2}{a}\right)\cos\,\phi\,\sin\,\vartheta_L+\cos\left(\rho\,\frac{2}{a}\right)\cos(\vartheta_L)\right)\right). \tag{9}$$

To calculate the output signal with Eq. (1), we need the angular spectrum in the focal plane. The spectrum of the backpropagated field $F_B^-(\rho,\phi)$ in plane B, which runs parallel to A through the focal point, is given by[21]

$$U_B^-(k_X,k_Y)=\mathscr{F}(F_A^-)\exp\left(-i\,\frac{2}{a}\,\sqrt{k^2-k_X^2-k_Y^2}\right). \tag{10}$$

$\mathscr{F}$ stands for two-dimensional Fourier transformation. According to Eq. (1), Cartesian coordinates X,Y have been introduced, the capital letters indicate orientation along B.

When propagating F_A^- backwards (towards plane B) by $a/2$, it will approximately keep its shape. The reason is that it exhibits only slight phase variations within plane A. In fact, numerical calculations show that it becomes even more similar to the pupil function (as the incident field, propagated backwards to the transducer, tends more and more towards the pupil function). This is expected from the thin lens law Eq. (4): in plane B is the image of the pupil function. The field distribution moves orthogonally to plane A, again because F_A^- exhibits only slight phase variations. So the field at the position of the focal point $F_B^-(0,0)$ corresponds by propagation to the field incident on S under (ϑ_L,φ_L), and hence is approximately equal to the value of the pupil function under this angle.

To determine the output signal of the microscope, Eq. (1) is used. Both spectra are calculated in the rotated focal plane B, which is equivalent to the assumption that the whole microscope is rotated by the angle ϑ_L:

$$V(\vartheta_L,\varphi_L)=\int_{-\infty}^{\infty}\int U_B^-(k_X,k_Y)U_{\mathrm{rot}}^+(-k_X,-k_Y)\times\sqrt{k^2-k_X^2-k_Y^2}\,dk_X\,dk_Y. \tag{11}$$

The subscript ''rot'' indicates that the emitted angular spectrum is calculated for the rotated microscope. Now we introduce the pupil function in the Debye approximation, according to Eq. (3), into Eq. (11):

$$V(\vartheta_L,\varphi_L)=2\pi f\int_{-\infty}^{\infty}\int U_B^-(k_X,k_Y)\times\mathscr{P}_{\mathrm{rot}}(\theta,\phi)dk_X\,dk_Y. \tag{12}$$

The relation between θ, ϕ and k_X,k_Y is

$$k_X=k\,\sin\,\theta\,\cos\,\phi,\quad k_Y=k\,\sin\,\theta\,\sin\,\phi. \tag{13}$$

In the case of a rotationally symmetric pupil we see from Eq. (8):

$$\mathscr{P}_{\mathrm{rot}}(\theta,\phi)=\mathscr{P}(\vartheta)=\mathscr{P}(\arccos(\sin\,\theta\,\cos\,\phi\,\sin\,\vartheta_L+\cos\,\theta\,\cos\,\vartheta_L)). \tag{14}$$

Because the phase of F_B^- varies only slightly, the angular spectrum $U_B^-(k_X,k_Y)$ for very large ka is concentrated around $k_X=k_Y=0$. So $\mathscr{P}$ can be taken out of the integral in Eq. (12) (for sufficiently slowly varying $\mathscr{P}$) and we obtain:

$$V(\vartheta_L,\varphi_L)=2\pi f\mathscr{P}_{\mathrm{rot}}(0,0)\int_{-\infty}^{\infty}\int U_B^-(k_X,k_Y)dk_X\,dk_Y. \tag{15}$$

The integral over the Fourier transform of a function results in the value of the function at the origin; $\mathscr{P}_{\mathrm{rot}}$ can be expressed by $\mathscr{P}$. So Eq. (15) leads to

$$V(\vartheta_L,\varphi_L)=(2\pi)^3 f\mathscr{P}(\vartheta_L,\varphi_L)F_B^-(0,0). \tag{16}$$

As seen above, $F_B^-(0,0)$ is approximately equal to the pupil function at (ϑ_L,φ_L) and we finally find

$$V(\vartheta_L,\varphi_L)=\frac{(2\pi)^3 f^2 2}{a}\,\mathscr{P}^2(\vartheta_L,\varphi_L). \tag{17}$$

The output signal is proportional to the pupil function squared when scanning along the half radius of the sphere. The signal strength is fairly small. The maximum output voltage, which is, for example, obtained from Eq. (1) by focusing to a perfectly reflecting plane, is approximately a factor $(1-\cos\,\alpha)ka/2$ greater.

Let us once more consider Eq. (12). The width of the function $U_B^-(k_X,k_Y)$ is due to the properties of the Fourier transformation inversely proportional to the radius of the sphere. For example, if a variation of $\mathscr{P}(\vartheta,\varphi)$ is spread over an area that reaches to $\vartheta=0.1$, the area of the variation (e.g., step function) of $F_B^-(\rho,\phi)$ for a sphere with radius a has the radius $0.1a/2$. The Fourier transformed $U_B^-(k_X,k_Y)$ covers in this case an area (main lobe) that is roughly restricted by $\sqrt{k_X^2+k_Y^2}=2\pi/(0.1a)=20\pi/a$. For drawing the pupil function out of integral (12) the width of its above-described variation must be greater than the width of U_B^-. Therefore the condition $ka>200\pi\approx 630$ must be fulfilled. At this size we can expect that the image will approximate the square of the pupil function quantitatively. But for obtaining a qualitative expression of the variation from the image, the demands are much weaker. The lens must only be able to *resolve* the variation of $F_B^-(\rho,\phi)$; with $\alpha=30°$ this is already the case for $ka>40\pi\approx 130$.

Aberrations of the wavefront emitted by the microscope will also result in a considerable change of the image amplitude. To investigate this we will at first assume that near (ϑ_L,φ_L) the emitted wavefront is locally tilted with respect to ϑ from the perfectly focused wave. This deviation is to be modest, so that the particle can still be considered to reflect the wave like a paraboloid. The derivative with respect to ϑ of the phase deviation of $\mathscr{P}$ will be denoted by δ. By geometrical considerations based on the thin lens model of the spherical particle, the consequent derivative of the phase of F_B^- with respect to ρ is $2\delta/a$. Due to the shift theorem of Fourier transforms U_B^- therefore suffers a shift with absolute value $2\delta/a$. When drawing $\mathscr{P}_{\mathrm{rot}}$ out of integral (12) we obtain its value shifted in θ by $2\delta/ka$. On the other hand the phase of $\mathscr{P}_{\mathrm{rot}}$ will cause the result of integral (15) $F_B^-(\rho,\phi)$

to be shifted in ρ by δ/k. So eventually both pupil functions in Eq. (17) determining $V(\vartheta_L,\varphi_L)$ are shifted from ϑ_L by $2\delta/ka$.

Next we want to discuss the effect of a local deviation in wavefront curvature near (ϑ_L,φ_L). If the two Gaussian radii of the curvature are equal, the local focus of the part of the wave emitted near $\mathscr{P}(\vartheta_L,\varphi_L)$ is simply shifted along L. A second derivative (with respect to ϑ) of the phase deviation of magnitude δ will result in a local focus shift of δ/k. Because the microscope detects the virtual value of the reflected wave at the focus, we are interested in the change of amplitude of the wave there in comparison to the case when no aberration is present. In terms of Fig. 2 the distance of the local focus from the reflector surface is $b=a/2-\delta/k$. The amplitude of the potential incident at the reflector surface is changed by a factor of $a/(2b)$. Additionally, the reflected wave will now be focused. The position of this focus is given by g in the thin lens law Eq. (4) (g might be positive or negative). When propagating the reflected wave from plane A to the position of the local focus of the microscope it will therefore suffer a change in amplitude by a factor of $g/(g+b)$. Hence the value of the potential at the focus of the microscope and consequently the output voltage will be increased by a factor $(ka/2)^2/[(ka/2-\delta)(ka/2+\delta)]$. For example, in case of a microscope with semiaperture angle $\alpha=30°$ having a balanced coma of peak-to-valley aberration of 2/10 of a wavelength, the maximal second derivative of the phase is $\delta=45$ at the edge of the pupil. We will assume that for deviation of the wavefront curvature only in one direction the change in output voltage will not be greater. Then we find that for $ka=400$ the output voltage will be increased by less than 5.4%. Although spherical aberration is small for a acoustic microscope which is constructed of a piston transducer and a sapphire rod with a lens, the wave field generated by the transducer might exhibit phase variations. Such phase variations are inhibited if the lens is positioned at the Fresnel distance from the transducer,[22] but in the case of the lenses treated below this distance is, by far, not reached.

A. Image calculations

To analyze the validity of the model leading to Eq. (12) we compare the absolute value of the output signal calculated with Eq. (12) to a rigorous calculation for images of perfect reflecting spheres (Neumann boundary conditions, corresponding to rigid particles in acoustics) according to Refs. 8 and 23. This rigorous solution involves only the Debye approximation, so it is exact for $f\to\infty$. To calculate U_B in Eq. (12), the emitted field in the Debye approximation on the surface S, as it is given by Eq. (5), is taken (see Fig. 3). In Fig. 5 we see the output signal for a line scan along the half radius of a rigid sphere with normalized radius $ka=200$. The semiaperture angle is $\alpha=30°$. The solid line is calculated with Eq. (12), the dotted line is calculated rigorously.[8] Obviously the coincidence between the above model and the rigorous solution is very good even in the fine oscillations. On the other hand Fig. 5 reveals deviations between the line scan and the pupil function, which is shown dashed. The main reason for these deviations is that the potential field Ψ^+ exhibits oscillations, which are due to the discontinuous edge of the pupil. With increasing $|\mathbf{r}|$, Ψ^+ converges towards $\mathscr{P}$ except at $\vartheta=0$. For a sphere with $ka=400$ the rigorously calculated line scan is depicted on the left-hand side of Fig. 6 as a solid line. As expected, it is more similar to the pupil function.

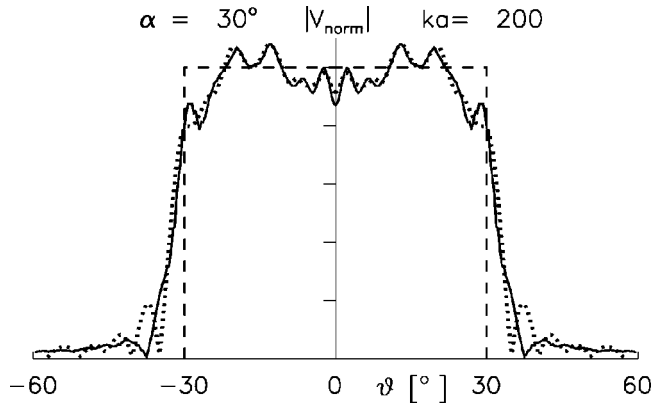

FIG. 5. Output signal at $a/2$, $ka=200$. Approximation (solid line), rigorous calculation (dotted line), and corresponding pupil function (dashed line).

For a smooth pupil function we expect greater similarity between pupil and scan. To clarify this, a pupil function which is continuously differentiable at the edge as suggested by Ref. 24 is taken:

$$\mathscr{P}(\vartheta)=\begin{cases}\dfrac{1}{2}\left[1+\cos\left(\pi\,\dfrac{\cos\vartheta-1}{\cos\alpha-1}\right)\right], & \vartheta\leqslant\alpha,\\ 0, & \vartheta>\alpha.\end{cases}\tag{18}$$

The semiaperture angle again is $\alpha=30°$, the square of the pupil function is depicted as a dashed line on the right-hand side of Fig. 6. The rigorously calculated line scan along the half radius of a sphere with $ka=400$ is depicted as a solid line. Here the deviations between pupil function and line scan are quite small.

B. Acoustically penetrable particles

In acoustic microscopy the fact that real particles are not acoustically rigid affects the considerations in several ways. First, reflections from the back side of the particle will occur. Their influence can be excluded by time gating emission and

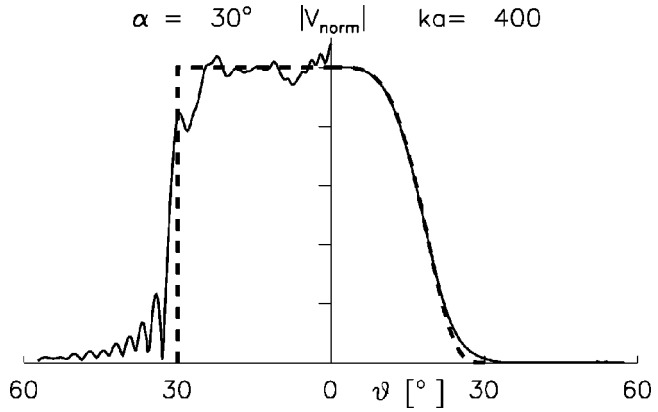

FIG. 6. Calculated output signals at $a/2$, $ka=400$ (solid lines), and square of the corresponding pupil functions (dashed lines).

detection. Second, the reflection function might exhibit rapid variations at the critical angles. As the angle of incidence of the field on the particle surface is increasing with the distance from (ϑ_L, φ_L), the singularities in the reflection function are transferred to F_A^- (see Fig. 4). Especially if Rayleigh surface waves are generated, a considerable contribution to the output signal might occur. But at angles of incidence on the sphere slightly beyond the longitudinal critical angle, longitudinal waves, which are propagating near to the surface, can also be generated (Ref. 25, p. 51). (Waves not propagating near the surface will not be detected by the microscope after leaving the sphere unless they are reflected from the back side.) We want to analyze in more detail the condition for detection of these waves. Consider the part of the spherical wave, incident at angle θ to line L as seen from the focal point. Its angle of incidence on the surface of the spherical particle is in paraxial geometrical optics equal to $\theta/2$, as the focal point coincides with the paraboloidal focus of the particle. Analogous to the detection of Rayleigh waves on a planar surface, the ray exciting a Rayleigh or longitudinal wave and the ray leaving the sphere must lie symmetrically with respect to the axis L in order to contribute significantly to the output signal. Because of the factor 1/2 the semiaperture angle must for inclusion of a Rayleigh or near surface wave be at least double the Rayleigh or longitudinal angle on the surface of the sphere.

To consider the effect of the reflection function in acoustic microscope images, the output signal for solid penetrable particles is calculated rigorously. Time gating is introduced by superposing several harmonic solutions V_n calculated at frequencies $\omega_0 + n\Delta\omega$, with ω_0 the centered frequency of the transducer. The used pulse train is to have a Gaussian-shaped envelope. The Fourier coefficients, which are the weighting factors of the V_n, then follow a shifted Gaussian. The time-dependent output signal $V(t)$ can now be written

$$V(t) = \sum_{n=-g}^{g} V_n \exp(-i(\omega_0 + n\Delta\omega)t) \times \exp\left(-\frac{(\sigma n \Delta\omega)^2}{2}\right), \tag{19}$$

σ determines the pulse width and the signal period is $2\pi/\Delta\omega$. The pupil function in this section is given by Eq. (6). Damping losses inside the particle are neglected and the coupling fluid is water with a wave velocity of 1480 m/s.

In Fig. 7 the incident pulse (dashed) and the returning signal for the focal position $\vartheta_L = 0$ are depicted for a lead particle ($ka = 200$). The unit on the time axis is the oscillation period of the longitudinal mode inside the sphere.

In Fig. 8 the half-radius line scans for $\alpha = 60°$ and $ka = 200$ are depicted: the solid line is calculated for a lead sphere (density: $\rho_i = 11.3$ g/cm^3, sound velocities: longitudinal 2160 m/s, transversal 700 m/s), the dashed line for an aluminum sphere (density: $\rho_i = 2.7$ g/cm^3, sound velocities: longitudinal 6420 m/s, transversal 3040 m/s).[26,27] The time position is adjusted to the earliest returning pulse. For the lead particle this is the zero time position in Fig. 7. As the reflection function for lead is nearly constant,[3] the pupil function is well approximated. The same is true for Teflon

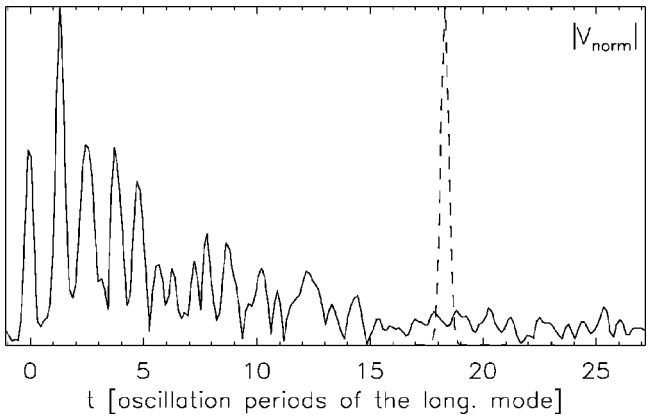

FIG. 7. Time-dependent amplitude envelope of the pulse train incident (dashed line) and reflected by a lead sphere (solid line); focal position: $\vartheta_L = 0$; $\alpha = 60°$.

spheres or air bubbles. In the case of aluminum we expect distortion due to the influence of Rayleigh waves, because α is slightly bigger than twice the Rayleigh angle. But they can only play a role in the innermost area of the pupil. Mainly the appearance is influenced by the longitudinal angle, which is slightly smaller than 14° and which is also relevant for small aperture angles. This can be seen as a dashed line in Fig. 9, where $\alpha = 45°$ and $ka = 200$.

Additionally, in Fig. 9 the output signal for a steel sphere (density: $\rho_i = 7.9$ g/cm^3, sound velocities: longitudinal 5900 m/s, transversal 3200 m/s)[27] of the same size is depicted as a solid curve. The influence of the longitudinal angle is weaker here. Therefore steel seems to be appropriate to achieve at least qualitative results. This is confirmed by the calculations with a bigger steel sphere ($ka = 400$), shown as a dotted line.

C. Finite focal length

Next the situation in the case of a spherical transducer, which has finite focal length, is discussed. Here we will not apply the Debye approximation. Following,[19] the output voltage V of the finite transducer is obtained by integrating the returning field Ψ^- over the transducer surface, weighted with a pupil function:

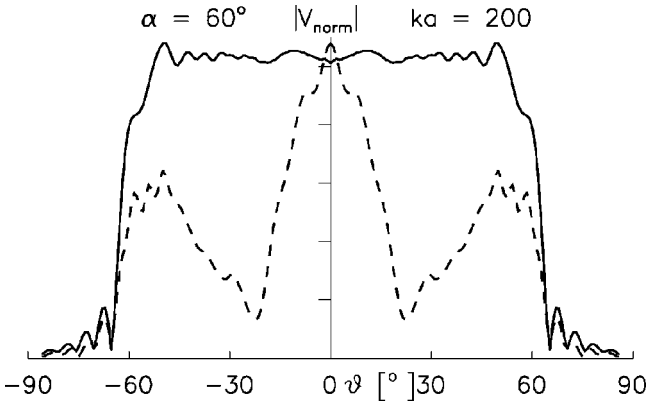

FIG. 8. Output signal of the pulse train reflected at the surface of an elastic sphere, $\alpha = 60°$. Solid line: lead sphere, $ka = 200$; dashed line: aluminum sphere, $ka = 200$.

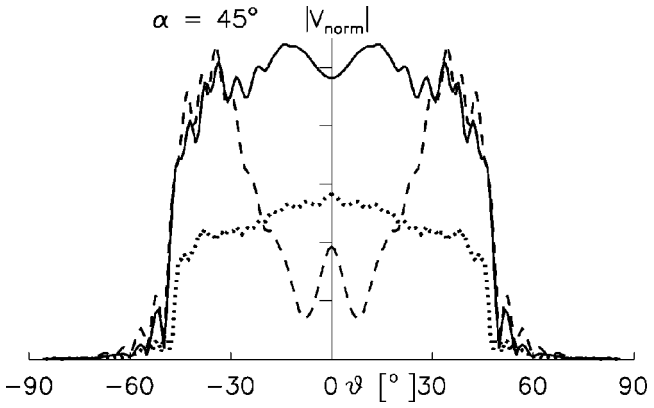

FIG. 9. Output signal of the pulse train reflected at the surface of an elastic sphere, $\alpha=45°$. Solid line: steel sphere, $ka=200$; dotted line: steel sphere, $ka=400$; dashed line: aluminum sphere, $ka=200$.

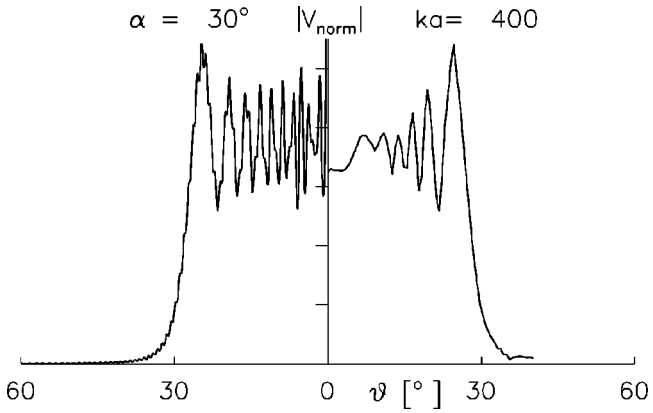

FIG. 10. Calculated output signal at $a/2(ka=400)$ for the finite transducer $(kf=500)$ emitting the angular spectrum U^+ (right), and $(U^+k_z)^2$ (left).

$$V=-i(2\pi)^2k\int_0^{2\pi}\int_0^{\pi/2}\Psi^-(\mathbf{f})\mathscr{P}(\vartheta,\varphi)f^2\sin\vartheta\,d\vartheta\,d\varphi. \tag{20}$$

The vector $\mathbf{f}$ has direction (ϑ,φ) and length f. A constant factor is omitted. The pupil function falls to zero at the aperture edge. After substituting Cartesian integration variables, Ψ^- is expressed by its angular spectrum $U^-(k_x,k_y)$ in the focal plane:

$$\Psi^-(x,y,z)=\frac{1}{(2\pi)^2}\int_{-\infty}^{\infty}\int U^-(k_x,k_y)\times\exp(ik_zz)\exp\left(i(k_xx+k_yy)\right)dk_x\,dk_y \tag{21}$$

with $k_z=\sqrt{k^2-k_x^2-k_y^2}$. Changing the order of integration, Eq. (20) can be rewritten:

$$V=-ik\int_{-\infty}^{\infty}\int U^-(k_x,k_y)\int_0^{2\pi}\int_0^{\pi/2}\exp(i\mathbf{kf})\times\mathscr{P}(\vartheta,\varphi)f^2\sin\vartheta\,d\vartheta\,d\varphi\,dk_x\,dk_y. \tag{22}$$

By comparing Eq. (22) with Eq. (1) the sensitivity characteristic U^+k_z is recognized to be

$$U^+(-k_x,-k_y)k_z=-ikf^2\int_0^{2\pi}\int_0^{\pi/2}\exp(i\mathbf{kf})\mathscr{P}(\vartheta,\varphi)\sin\vartheta\,d\vartheta\,d\varphi. \tag{23}$$

As $\mathbf{k}$ is the wave vector of the returning wave field, it is pointing in the positive z hemisphere. Note that the integral in Eq. (23) is for a real-valued pupil function equal to the complex conjugate of the integral in Eq. (5), that describes the field structure for a spherical transducer with infinite focal length, when simply exchanging the variables. The curves in Fig. 3 can therefore alternatively be interpreted as the angular spectrum (multiplied by k_z) of the potential emitted by a spherical transducer with finite focal length $kf=200$, $kf=500$, $\alpha=30°$. Obviously this spectrum exhibits oscillations if the pupil function is discontinuous. For bigger f the depth of these oscillations and the scale decreases. However, as $U_B^-(k_X,k_Y)$ has finite width, the oscillations of the emitted angular spectrum in Eq. (11) are smoothed. With increasing particle size the width of $U_B^-(k_X,k_Y)$ decreases, and therefore the smoothing process will be diminished.

U^+ from Eq. (23) is used for the rigorous calculation of the output signal to simulate the measurement of the pupil function of a finite spherical transducer. The radius of curvature of the transducer is taken to be $kf=500$, its constant pupil function has a semiaperture angle $\alpha=30°$. The result for scanning along $a/2$ of a rigid sphere with $ka=400$ is shown in the right-hand side of Fig. 10. On the left-hand side $(U^+k_z)^2$ is depicted. The oscillations of the sensitivity characteristic in the outer area are accurately reproduced, because the emitted spectrum is continuous. For small angles ϑ the period of the oscillations is very short and the measurement cannot resolve them using the above sphere size.

II. EXPERIMENTAL RESULTS AND DISCUSSION

A. Acoustic microscope

Now let us discuss the experimental results in the case of the acoustic microscope. If the pupil function is not known *a priori*, it is not possible to estimate the quality of the measurement results immediately from the images. However, a well-controlled structure can be generated on the pupil function by partly covering the microscope lens with a sound-absorbing rubber coating. Then the potential distribution on the level of the lens will exhibit well-defined depletion areas with the shape of the rubber stains. Because in this case the potential distribution along the lens fluctuates considerably on the scale of a wavelength, it is expected to differ from the backpropagated distribution at infinity. Sharp reproduction of the stains can be expected when scanning along a radius larger than $a/2$. This can be understood from the thin lens law Eq. (4). As discussed before the best reproduction of the field distribution at infinity is obtained when scanning with radius $a/2$. To obtain a sharp reproduction of the structure of the field distribution that occurs at the finite distance f from the focus of the microscope, this field must virtually come from the position of the focus of the microscope (see Fig. 2). Hence we must introduce $g=f-b$ in Eq. (4) with b becoming the scanning distance from the surface of the sphere:

$$b = a/2 + f/2 - \sqrt{(a/2)^2 + (f/2)^2}. \tag{24}$$

For the experimental scans to reproduce the rubber stains, b in Eq. (24) is calculated with f approximately the distance between the focus of the microscope and the lens surface. In this case the reflected signal will be focused to the lens surface.

From the thin lens considerations it also becomes obvious that by scanning inside of a concave cavity in general the pupil function cannot be reproduced with the same accuracy. The reason is that in that case the detected field is the image of the field occurring virtually below the focus which deviates from the field confocally above. In the experiment the spherical scan is extracted from a three-dimensional data array which is composed from a series of two-dimensional, lateral scans. For small aperture angles the deviation between planar and spherical scan is slight. Therefore a qualitative impression of the pupil function can be obtained from a single take. But in the case of the acoustic microscope with planar scanning, strong water ripples might occur, due to the varying signal phase. They lead to a disturbing ring structure. On the other hand, when scanning along $a/2$, the signal phase is simply twice the phase of the pupil function. Consequently by slight deviation from the spherical scan it can always be ensured that the phase is constant and internal lens echoes lead only to a constant offset. In the case of the depicted images, the maximum of the oscillations around $a/2$ is searched in the z direction. If it is possible to perform an exact spherical scan, principally also aberrations of the pupil can be determined.

For the scanning path given by Eq. (24) a very strong signal can be obtained experimentally when shifting the time gate for detection. This signal might be mistaken as the pupil function. It is due to double reflection of the wave at the sphere, the lens surface, and once more at the sphere. Because the once reflected wave is focused on the lens surface, the signal is similar to the signal detected from an inclined plane.[15] If this focus does not hit the lens but the rubber stains or a point outside of the aperture, it is not reflected appropriately, and this signal disappears. In this way the rubber distribution can be imaged very accurately for the purpose of comparison. As this signal appears only within a small range of defocus, it might be used to find the defocus for imaging the rubber stains.

For the first lens the results obtained with a steel bearing ball are depicted in Figs. 11 and 12. The transducer is oriented orthogonally to the c axis of the sapphire and the longitudinal wave velocity in this direction is 11 150 m/s.[26] The radius of the curvature of the lens is 2 mm. Consequently for the geometrical aperture angle of 30° the distance between the paraxial focus and the lens edge is $f = 2276\ \mu$m. For Figs. 11 and 12 the size of the sphere is $a = 750\ \mu$m ($ka = 334$). The focus is scanned at distance $b = 315\ \mu$m from the surface of the sphere, as calculated with Eq. (24). Depicted is the projection of the spherical scan on the paper plane. The coordinate axes are k_x/k and k_y/k. The lens is partly covered with rubber coating. Figure 11 exhibits the once reflected signal. The ''woodlike'' appearance is due to the coarse stepping in axial direction of 1 μm. Around the

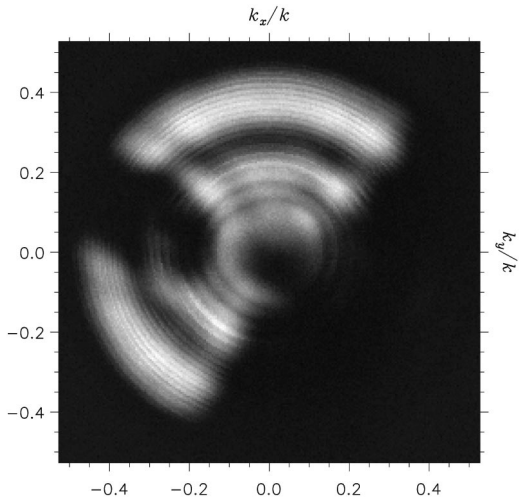

FIG. 11. Experimental image of the pupil function of the first lens, $ka = 334$, $kb = 140$, cavity with rubber coating.

depletion areas an oscillation can be observed. A similar artifact structure also occurs in the calculated Fig. 6 (left). With increasing radius of sphere this oscillation becomes narrower. Its appearance can be partly explained with the help of Eq. (12): The function U_B has side maxima, as it is the Fourier transform of a restricted function (by the aperture), which are convolved with $\mathscr{P}_{\mathrm{rot}}(\theta, \phi)$. The corresponding image based on the double reflection Fig. 12 shows that the shape of the coating is well reproduced by Fig. 11.

Figure 11 exhibits a striking structure consisting of three concentric rings. Fully this structure may be observed in Fig. 13, where the scan is performed at half radius of the same sphere and no rubber coating is present. The radius of the rings appears to be invariant against an increase in the size of the sphere used, which could be tested up to $ka \approx 1000$. Therefore the rings cannot be compared with the oscillations in Figs. 5 and 6 (left), that arise from the measuring method. Similarly they could be observed in measurements with an air bubble and therefore are not due to the reflection function of steel. While the previously discussed image is influenced by the field distribution along the lens cavity, Fig. 13 depicts

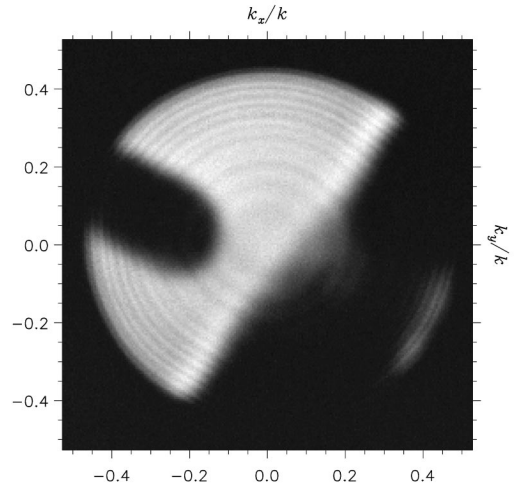

FIG. 12. Double reflection signal of the first lens, $ka = 334$, $kb = 140$, cavity with rubber coating.

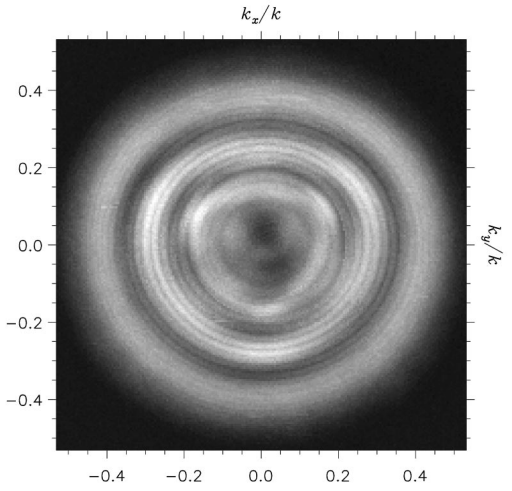

FIG. 13. Experimental image of the pupil function of the first lens, $ka = 334$, focus at half radius of the sphere.

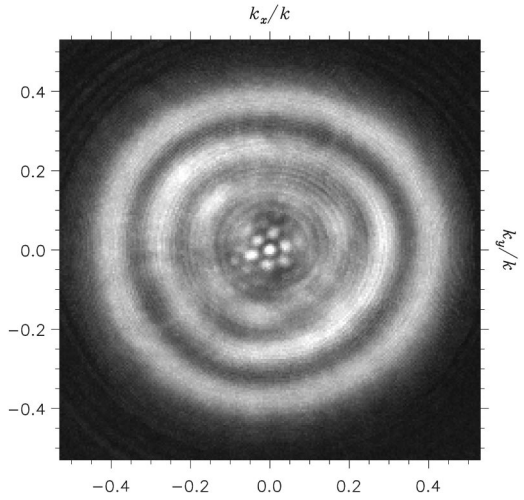

FIG. 15. Experimental image of the pupil function of the first lens, $ka = 713$, focus at half radius of the sphere.

the field distribution backpropagated to infinity. Here the inner rings have a slightly larger radius. The figure exhibits a threefold symmetry. It arises from the trigonal structure of the sapphire, which leads to a threefold symmetry of the transmission coefficient into the coupling fluid.

To investigate the origin of the ring structure we calculate the field distribution generated by the transducer along the surface of the lens. The Rayleigh integral providing the potential field generated by a piston transducer can be found in Ref. 28. As the buffer rod consists of sapphire, this calculation model permits some simplifications: The neglecting of transversal waves and of the anisotropy of sapphire. Because the size of the transducer and the length of the buffer rod are not exactly known, these values are varied deliberately to approximate the experimentally observed structure.

The obtained field amplitude is squared and multiplied by a factor $\cos(\vartheta)$ according to Ref. 29, for comparison with the experimental data. The exact angular dependence of the transmission through the lens is not known, as the lens is covered with an antireflection coating. With a centered frequency of 105 MHz, a transducer radius of 1200 μm, and a distance of 1411 μm between the transducer and the middle of the lens cavity we obtain Fig. 14. The coincidence with Fig. 13 is very good. So with plausible assumptions concerning the geometry of the microscope the above ring structure indeed occurs. Figure 15 is obtained with the same lens, but with a bigger steel ball ($a = 1.6$ mm, $ka = 713$). The scanning distance is $a/2$, the stepping in axial direction is 1 μm. The deviations from the previous image are slight, but in the center of the image a dot pattern becomes visible. It arises from the interference between the middle of the pupil and the edge of the aperture. It exhibits the threefold symmetry of the sapphire. When defocusing, its appearance changes like the picture in a kaleidoscope. When excluding the edge wave, whose return time is slightly longer, the pattern disappears.

Next we examine a second lens, which has asymmetrical imaging properties. The radius of the curvature of the lens is 500 μm, the geometrical aperture angle is again about 30°. The distance between the paraxial focus and the lens edge consequently is $f = 569$ μm. The radius of the steel sphere

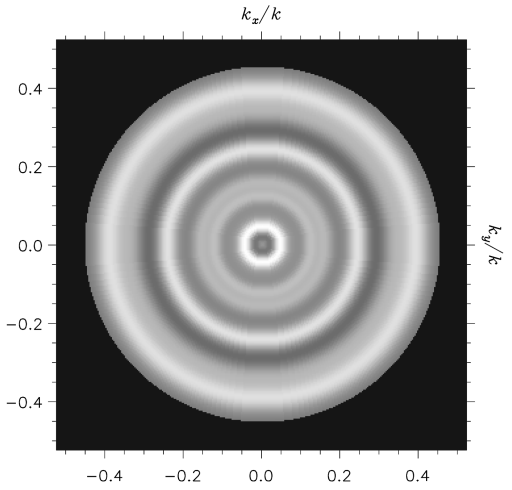

FIG. 14. Simulation of the field distribution generated by the piston transducer on the cavity of the first lens.

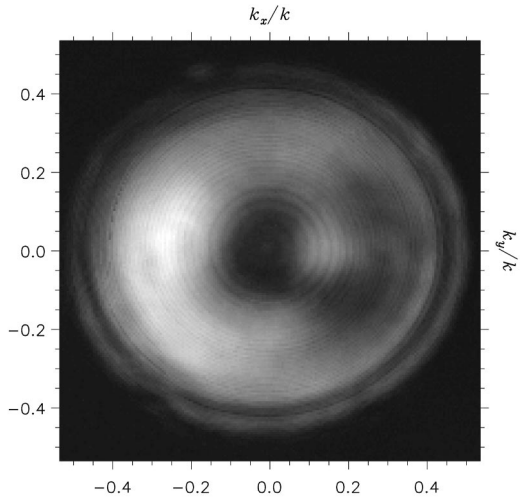

FIG. 16. Experimental image of the pupil function of the second lens, $ka = 384$, $kb = 120$.

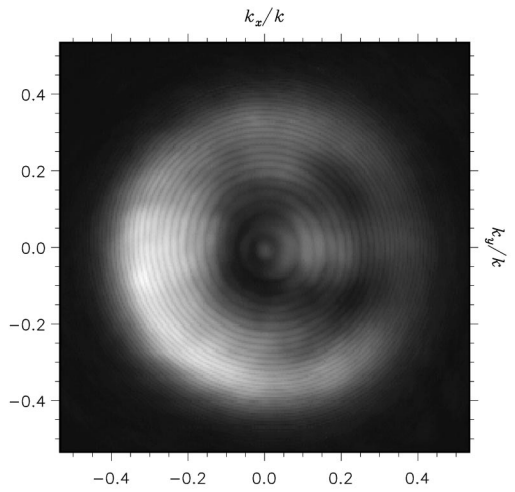

FIG. 17. Experimental image of the pupil function of the second lens, $ka = 384$, focus at half radius of the sphere.

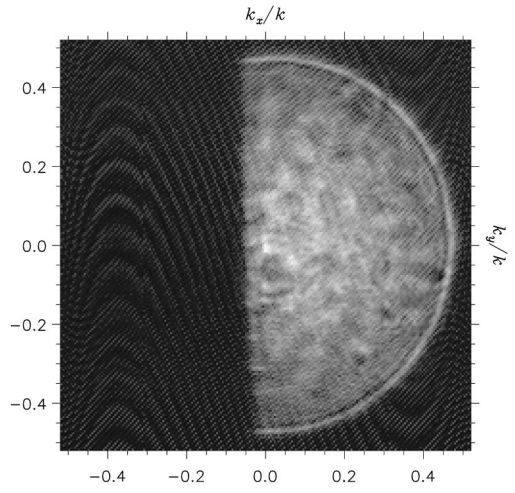

FIG. 19. Experimental image of the pupil function of the confocal light microscope with a sheet of cardboard in the ray tube, $ka = 1172$, plane scan at $z = a/2$.

used is 500 μm ($ka = 384$). For Fig. 16 the focus is scanned at distance $b = 156$ μm from the surface of the sphere, for Fig. 17 at half radius of the sphere. Both figures are asymmetrical. Figure 16 exhibits clear oscillation artifacts at the edge. In Fig. 17 these oscillations are not present, and the contrast decreases slowly towards the edge. This indicates that the pupil function decreases towards the edge.

Again we try to understand the appearance on the base of the field generated by the piston transducer on the lens cavity. For a transducer with radius 500 μm and centered frequency 180 MHz, whose distance from the middle of the lens is 250 μm, we obtain in the case of a lateral displacement of the transducer of 80 μm the simulation shown in Fig. 18. The similarity to the experiment is high. Differences might stem from phase variations of the wave field generated by the transducer.

B. The confocal optical microscope

The applied method is especially suited for the confocal optical microscope in several ways. First, the focal length is in general very large on the scale of the wavelength, and consequently large spheres can be used. Second, inner reflections do not cause any disturbance, so that for the usual aperture angles, one lateral image is sufficient. For test purposes, the pupil function can be easily manipulated by introducing filters into the collimated beam.[30] The images are obtained using a single-mode fiber-based confocal microscope together with a 670-nm semiconductor laser source. The numerical aperture of the microscope objective was 0.5 ($\alpha = 30°$). The images display the square root of the measured intensity values.

At first a steel ball bearing with a radius of 125 μm ($ka = 1172$) is used and a single lateral image is taken at $z = a/2$ between the top and center of the sphere. Figure 19 shows the resultant pupil function when additionally a sheet of cardboard is put into the collimated beam. The right side of the image shows that the microscope objective is illuminated nearly homogeneously, the pupil function is only slightly depleted towards the edge. The ringing structures

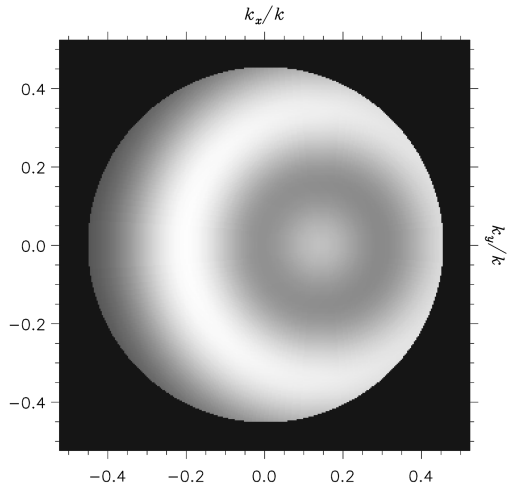

FIG. 18. Simulation of the field distribution generated by the piston transducer on the cavity of the second lens.

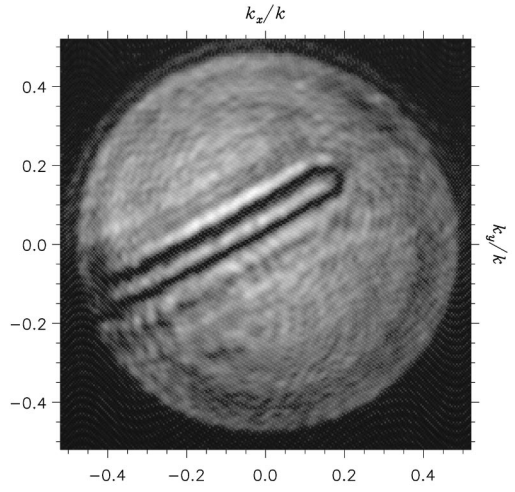

FIG. 20. Experimental image of the pupil function with a pencil lead in the ray tube, $ka = 375$, plane scan at $z = a/2$.

originate in defects of the ball bearing or simply dust grains. The moiré structure evolves from disturbances from external light sources reaching the detecting photomultiplier. For Fig. 20 a glass sphere with a radius of 40 μm ($ka=375$) is used. A pencil with a 0.5-mm lead was put into the collimated beam. At the edges of the illuminated areas, wide oscillation artifacts occur, as the size of the sphere is small. Because of these artifacts here maximal intensity arises within the area, where the pupil is covered by the pencil lead.

III. CONCLUSIONS

In this paper a method is described which makes it possible to investigate the pupil function of a confocal reflection microscope from images of spherical objects, without invoking a data transformation. The focus of the microscope is scanned along the half radius of the sphere. For high-frequency acoustic microscopes as well as for optical microscopes the phase of the output signal is often not detected. In this case the absolute value of the squared pupil function is obtained if the size of the sphere is sufficiently large. If this condition cannot be fulfilled, qualitative impressions of the pupil function may be obtained. The method makes it possible to measure the dependence of the pupil function on the azimutal angle φ. Because the output signal is determined by the ray reflected from the surface of the sphere orthogonally, the knowledge of the exact angular dependence of the reflection coefficient is not required.

[1] J. A. Hildebrand and L. K. Lam, ''Directional acoustic microscopy for observation of elastic anisotropy,'' Appl. Phys. Lett. **42**, 413–415 (1983).

[2] C. J. R. Sheppard, ''Confocal interference microscopy,'' in *Confocal Microscopy*, edited by T. Wilson (Academic, London, 1990), pp. 389–411.

[3] K. K. Liang, G. S. Kino, and B. T. Khuri-Yakub, ''Material characterization by the inversion of $V(z)$,'' IEEE Trans. Sonics Ultrason. **32**, 213–224 (1985).

[4] K. Liang, S. D. Bennet, B. T. Khuri-Yakub, and G. S. Kino, ''Precise phase measurements with the acoustic microscope,'' IEEE Trans. Sonics Ultrason. **32**, 286–273 (1985).

[5] W. R. Fright, R. H. T. Bates, J. M. Rowe, D. S. Spencer, M. G. Somekh, and G. A. D. Briggs, ''Reconstruction of the complex reflectance function in acoustic microscopy,'' J. Microsc. **153**, 103–107 (1989).

[6] L. D. Bakhrakh and S. A. Titov, ''Generalized aperture function of an acoustic microscope,'' Sov. Tech. Phys. Lett. **15**, 543–544 (1989).

[7] C. Roddier and F. Roddier, ''Wave-front reconstruction from defocused images and the testing of ground-based optical telescopes,'' J. Opt. Soc. Am. A **10**, 2277–2287 (1993).

[8] P. Zinin, W. Weise, O. Lobkis, O. Kolosov, and S. Boseck, ''Fourier optics analysis of spherical particles image formation in reflection acoustic microscopy,'' Optik (Stuttgart) **98**, 45–60 (1994).

[9] W. Weise, P. Zinin, and S. Boseck, ''The accuracy of Pupil Function measurement in reflection acoustic microscope by imaging spherical particles,'' in *Proceeding of 1994 IEEE Ultrasonic Symposium* (IEEE, New York, 1994), Vol. 3, pp. 1409–1412.

[10] A. Atalar, ''A backscattering formula for acoustic transducers,'' J. Appl. Phys. **51**, 3093–3098 (1980).

[11] W. Weise, *Konfokale Rastermikroskopie zur Abbildung kugelförmiger Objekte*, Ph.D. thesis, Universität Bremen (Shaker Verlag, Aachen, 1996), Chap. 3.

[12] M. Born and E. Wolf, *Prinziples of Optics* (Pergamon, Oxford, 1980), p. 436.

[13] P. Zinin, W. Weise, O. Lobkis, and S. Boseck, ''The theory of three dimensional imaging of strong scatterers in scanning acoustic microscopy,'' Wave Motion **25**, 213–236 (1997).

[14] H. T. O'Neil, ''Theory of focusing radiators,'' J. Acoust. Soc. Am. **21**, 516–526 (1949).

[15] W. Weise, P. Zinin, and S. Boseck, ''Modeling of inclined and curved surfaces in the reflection scanning acoustic microscope,'' J. Microsc. **176**, 87–98 (1994).

[16] W. Weise, P. Zinin, T. Wilson, A. Briggs, and S. Boseck, ''Imaging of spheres with the confocal scanning optical microscope,'' Opt. Lett. **21**, 1800–1802 (1996).

[17] L. R. Gavrilov, V. N. Dmitriev, and L. V. Solontsova, ''Noncontacting method for investigating the sound fields of focusing ultrasonic transducers,'' Sov. Phys. Acoust. **32**, 416–419 (1986).

[18] L. R. Gavrilov, V. N. Dmitriev, and L. V. Solontsova, ''Use of focused ultrasonic receiver for remote measurements in biological tissue,'' J. Acoust. Soc. Am. **83**, 1167–1179 (1988).

[19] V. M. Levin, O. I. Lobkis, and R. G. Maev, ''Investigation of the spatial structure of acoustic fields by a spherical focusing transducer,'' Sov. Phys. Acoust. **36**, 391–395 (1990).

[20] J. J. Stamnes, *Waves in Focal Regions* (Hilger, Bristol, 1986), Chap. 9.

[21] A. Atalar, ''An angular-spectrum approach to contrast in reflection acoustic microscopy,'' J. Appl. Phys. **49**, 5130–5139 (1978).

[22] J. E. Heisermann and C. F. Quate, ''The scanning Acoustic Microscope,'' in *Frontiers in Physical Acoustics, Course XCIII*, edited by D. Sette (North-Holland, Amsterdam, 1984), pp. 343–394.

[23] O. I. Lobkis and P. V. Zinin, ''Acoustic microscopy of spherical objects. Theoretical approach,'' Acoust. Lett. **14**, 168–172 (1990).

[24] Y. Sasaki, T. Endo, T. Yamagishi, and M. Sakai, ''Thickness measurement of a thin-film layer on an anisotropic substrate by phase-sensitive acoustic microscope,'' IEEE Trans. Ultrason. Ferroelectr. Freq. Control **39**, 638–642 (1992).

[25] H. Überall, ''Surface waves in acoustics,'' in *Physical Acoustics*, edited by W. P. Mason and R. N. Thurston (Academic, New York, 1973), Vol. X, pp. 1–60.

[26] A. Briggs, *Acoustic Microscopy* (Clarendon, Oxford, 1992), p. 103.

[27] G. S. Kino, *Acoustic Waves: Devices, Imaging and Analog Signal Processing* (Prentice-Hall, Englewood Cliffs, NJ, 1987).

[28] J. Zemanek, ''Beam behavior within the nearfield of a vibrating piston,'' J. Acoust. Soc. Am. **49**, 181–191 (1971).

[29] C. J. R. Sheppard and T. Wilson, ''Effects of high angles of convergence on $V(z)$ in the scanning acoustic microscope,'' Appl. Phys. Lett. **38**, 858–859 (1981).

[30] Z. S. Hegedus,''Pupil filters in confocal imaging,'' in *Confocal Microscopy*, edited by T. Wilson (Academic, London, 1990), pp. 171–183.

Determination of acoustic center correction values for type LS2aP microphones at normal incidence[a)]

Randall P. Wagner and Victor Nedzelnitsky
National Institute of Standards and Technology, Sound Building, Room A147, Gaithersburg, Maryland 20899

(Received 8 May 1997; accepted for publication 26 March 1998)

Frequency-dependent acoustic center correction values are required to obtain accurate microphone calibrations in the free-field by the reciprocity technique. These values were determined for IEC type LS2aP microphones at normal incidence by utilizing the theoretical inverse relationship between the sound pressure amplitude at the acoustic center of a receiver and the distance between acoustic centers of source and receiver. A dynamic signal analyzer was used to measure the gain factor between the amplified output voltage of the receiver and the source input voltage at 500-Hz intervals in the extended frequency range 2–50 kHz. This procedure allowed all the data for a microphone pair to be gathered within several hours for microphone diaphragm separations from 101–311 mm at 10-mm intervals. At each frequency, the reciprocal of this gain factor as a function of microphone diaphragm separation was fit to a straight line after correction for atmospheric effects, including attenuation of sound caused by atmospheric absorption. Mean acoustic center correction values (from four microphones combined in six pairs) were calculated using the parameters obtained from the fit and found to be in good agreement with published values calculated by the boundary element method, as well as with values predicted by scaling published values of the acoustic center correction for microphones with a geometrical configuration similar to that of IEC type LS1P microphones. [S0001-4966(98)01407-6]

PACS numbers: 43.38.Kb, 43.58.Vb [SLE]

INTRODUCTION

A microphone's acoustic center, which serves as the location of an equivalent point-transducer, is generally not at the microphone diaphragm. In the International Electrotechnical Commission (IEC) international standard 61094-3 (1094-3 in the previous IEC numbering scheme) (p. 9), which addresses primary free-field calibration of standard condenser microphones by the reciprocity technique, the acoustic center of a microphone is defined as: ''For a sound-emitting transducer, for a sinusoidal signal of given frequency and for a specified direction and distance, the point from which the approximately spherical wavefronts, as observed in a small region around the observation point, appear to diverge.'' [1] Two notes that apply to this definition are included in the standard. First, if the transducer is a reciprocal one, as are laboratory standard microphones, the location of the acoustic center is independent of whether the transducer is being used as a receiver or a source. Second, the definition is valid only for those regions of the sound field where spherical, or approximately spherical wavefronts are observed.

The reciprocity technique utilizes basic electroacoustic reciprocity relations to obtain the sensitivities of (i.e., calibrate) microphones. A microphone's free-field sensitivity expresses, at a given frequency in the sinusoidal state, the ratio of the microphone's output voltage to the sound pressure that existed at its acoustic center prior to the introduction of the microphone into the sound field. At least two microphones are calibrated together in the free-field by the reciprocity technique. Reciprocity relations yield an expression for the product of the two microphones' free-field sensitivities in terms of measurable quantities. One microphone serves as the source, with the second as a receiver, to obtain the product of the sensitivities. An auxiliary source, which often is another microphone of similar size but higher sensitivity, is used to obtain the ratio of sensitivities. The sensitivity of each microphone in the pair being calibrated is then determined using the ratio and product of the two microphone sensitivities.

For microphone calibration in the free-field by the reciprocity technique, the location of the acoustic center of each microphone to be calibrated must be known. This information is used to derive the distance r_{ab} between the acoustic centers of the source (microphone a) and the receiver (microphone b) when measuring the magnitude of the product of the source's free-field sensitivity M_{fa} and the receiver's free-field sensitivity M_{fb}. The expression for this product is

$$|M_{fa}M_{fb}| = \frac{2r_{ab}}{\rho_0 f}\,\frac{e_{ocb}}{i_a}\,\exp(\alpha r_{ab}), \tag{1}$$

where ρ_0 is the ambient static density of the acoustic medium, f is the excitation frequency, e_{ocb} is the open circuit voltage of microphone b, i_a is the source drive current, and α is the sound attenuation coefficient due to atmospheric absorption (also called the air attenuation coefficient). Using Eq. (1) along with the quantity β_f, which denotes the ratio of M_{fa} to M_{fb} that is readily determined during a free-field reciprocity calibration using the auxiliary source, the dependence of the microphones' free-field sensitivities on r_{ab} is displayed in the equations:

[a)]Portions of this paper were presented at the 130th meeting of the Acoustical Society of America, 27 November–1 December 1995, St. Louis, Missouri [J. Acoust. Soc. Am. **98**, 2917(A) (1995)].

$$|M_{fa}| = \left[\beta_f \frac{2r_{ab}}{\rho_0 f} \frac{e_{ocb}}{i_a} \exp(\alpha r_{ab}) \right]^{1/2}, \quad (2)$$

$$|M_{fb}| = \left[\frac{1}{\beta_f} \frac{2r_{ab}}{\rho_0 f} \frac{e_{ocb}}{i_a} \exp(\alpha r_{ab}) \right]^{1/2}. \quad (3)$$

Free-field calibrations are usually carried out for sound waves at normal incidence. Source and receiver are arranged facing each other, and the same principal axis passes through the center of, and is perpendicular to, the diaphragms of both microphones. For this arrangement, the acoustic center of each microphone is located at a certain distance from its diaphragm along the principal axis. If both microphones are identical, this distance is the same for each microphone and is equal to the value of the acoustic center correction. To obtain an acceptable signal-to-noise ratio over the entire frequency range of calibration, the separation between source and receiver diaphragms used at the National Institute of Standards and Technology (NIST) is typically about 200 mm. At this working distance, the uncertainty in r_{ab} and the free-field sensitivities derived from the calibration are strongly dependent on how well the acoustic center correction is known. A 0.09-dB error in the free-field sensitivity levels of both microphones would result from an error of 2.0 mm in the value of an acoustic center correction of each microphone nominally equal to 2.0 mm. For many microphone types, an uncertainty component of this magnitude can be the dominant component of the overall uncertainty of the measured free-field sensitivity at many frequencies.

Recently, an IEC standard[2] that gives specifications for laboratory standard microphones and describes a mnemonic system for classifying these microphones, including type LS2aP, has been developed. This emphasizes the need to have a readily available and reliable acoustic center correction for this microphone type to carry out accurate free-field calibrations. Type LS2aP microphones, meeting the specifications of this standard, must be suitable for highly accurate calibrations via a primary method, such as the reciprocity technique, and be highly stable with respect to both time and environmental conditions. In addition, specifications for both the mechanical and electroacoustical characteristics must be met within the strict tolerances defined by the standard. Type LS2aP microphones have a 12.7-mm ($\frac{1}{2}$-in.) base diameter. They have a flatter pressure response to higher frequencies, but are less sensitive, than the nominal 1-in.- (actually about 23.8 mm, 0.936 in.)-diam laboratory standard LS1P microphones. Type LS2bP microphones have different specifications for their diaphragm and center pin recess depths, and outer and inner rim diameters, but conform to the same essential electroacoustical specifications as LS2aP.

A comparison of free-field microphone calibrations was recently done among several European laboratories.[3] In this comparison, the first measurements of normal incidence acoustic center correction values for LS2aP microphones were obtained at two laboratories, the National Physical Laboratory (NPL) in the United Kingdom, and the Technical University of Denmark (DTH). Figure 1 shows that, particularly at the higher frequencies, there are unexpectedly large differences between the values of the corrections measured at these laboratories. Furthermore, there is significant disagreement between the measured values and two sets of predicted values calculated using two different methods. One set of predicted values was calculated by applying the boundary element method.[3,4] The second set was calculated at NIST by scaling the acoustic center correction values for microphones with a geometrical configuration[5] similar to that of LS1P microphones by the ratio of the diameter of LS2aP to that of LS1P microphones, and by scaling frequencies by the inverse of this ratio so that the ratio of the microphone diameter to the wavelength of the incident sound remained constant. The need for better agreement motivated performing acoustic center correction measurements for LS2aP microphones at NIST.

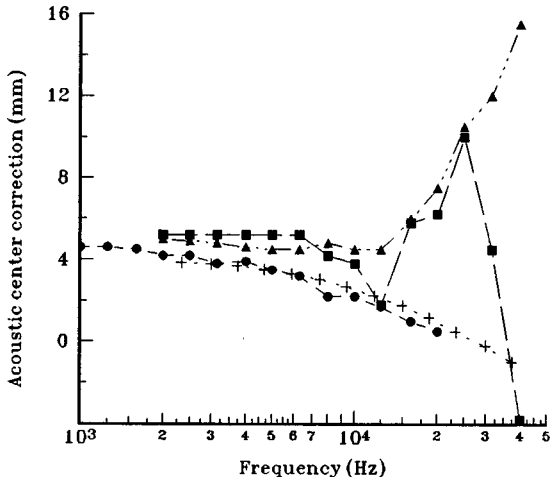

FIG. 1. Comparison of acoustic center correction values for type LS2aP microphones determined by the National Physical Laboratory (NPL), United Kingdom (—■—) and the Technical University of Denmark (DTH) (– - - ▲ - - –) with those theoretically predicted using the boundary element method (BEM) (--●--) and by scaling IEC published values for microphones with a geometrical configuration similar to that of type LSIP microphones (---+---). [NPL, DTH, and BEM values from Ref. 3 and IEC values from IEC Publication 486 (Ref. 5).]

I. THEORY AND CALCULATION OF THE ACOUSTIC CENTER CORRECTION

For a receiver in the far field of a source generating a spherically diverging progressive wave that closely approximates a plane wave in the spatial region of interest, in a free sound field, and with ideal environmental conditions (including those that would result in negligible attenuation of sound caused by atmospheric absorption), the sound pressure amplitude at the acoustic center of the receiver is inversely proportional to r_{ab}. This relationship can be utilized to determine the sum of the acoustic center corrections for a pair of microphones where one is used as the sound source and the second as a receiver. For these ideal conditions, the theoretical inverse relationship between the sound pressure amplitude p_i at the acoustic center of the receiver and r_{ab} is given by the general expression

$$p_i = \frac{A}{r_{ab}} = \frac{A}{(x_{ab} - 2d)}, \quad (4)$$

where A is a linear proportionality constant, x_{ab} is the distance between the diaphragms of the source and receiver, and it is assumed that the microphones are of the same type so that the acoustic center correction d is effectively the same for both microphones. Positive values of d indicate that the acoustic center is in front of the microphone diaphragm.

At a given frequency, the sound pressure produced by the source is directly proportional to the voltage at its input, and the voltage at the output of the receiver is directly proportional to the sound pressure at its acoustic center. These relationships allow the acoustic center correction calculation to be developed in terms of a gain factor, defined as the result of dividing the rms voltage of the filtered and amplified receiver output by the rms voltage across the source input. The equation

$$|H(f)|_i = \frac{C}{x_{ab} - 2d} \tag{5}$$

can be written for the ideal gain factor $|H(f)|_i$ that would be obtained under ideal conditions, where C is another linear proportionality constant (different from A). Inverting Eq. (5) yields an expression for $|H(f)|_i^{-1}$ that shows its linear dependence on x_{ab} and is written as

$$|H(f)|_i^{-1} = \frac{1}{C} x_{ab} - \frac{1}{C} 2d. \tag{6}$$

Equation (6) describes a straight line with slope

$$m = \frac{1}{C}, \tag{7}$$

and y-axis intercept

$$b = \frac{-1}{C} 2d. \tag{8}$$

From these equations, the acoustic center correction can be expressed as

$$d = \frac{-b}{2m}, \tag{9}$$

is independent of C, and can be extracted from a set of experimentally determined values of $|H(f)|_i^{-1}$ for a set of values of x_{ab}.

Because, under practical circumstances, sound is attenuated by atmospheric absorption, it is necessary to compensate the measured gain factor $|H(f)|_m$ for this attenuation when determining values of $|H(f)|_i^{-1}$ via experiment. It is also necessary to compensate for the effects of variations in the static density of the air that occur during the course of the measurements. The formula used is

$$|H(f)|_i^{-1} = \frac{(T_R/T)(P/P_R)}{|H(f)|_m \exp(\alpha x_{ab})}, \tag{10}$$

where T is the ambient absolute temperature and P is the ambient absolute static pressure. The numerator refers all values of $|H(f)|_i^{-1}$ to a single reference static density with reference absolute temperature T_R and reference absolute static pressure P_R. Values of α are calculated by using a standard method,[6] which takes into account frequency, relative humidity, temperature, and static pressure. Although attenuation of sound caused by atmospheric absorption is strictly determined with r_{ab} in the exponential term, x_{ab} was used instead because it is a directly controlled experimental parameter that is a good approximation to r_{ab}. If r_{ab} had been used, the multiplicative factor $\exp(2\alpha d)$ would have been included implicitly in Eq. (10). If α were constant, this factor would not affect the determination of d. Because the changes that occurred in the value of α during the acquisition of an entire data set were indeed small, the approximation $x_{ab} \cong r_{ab}$ changes the maximum uncertainty in d by no more than about 0.1%.

II. EXPERIMENTAL SETUP AND PROCEDURE

In 1994, data were gathered at NIST with a single pair of LS2aP microphones using an experimental setup and procedure that are almost identical to those described in a previous NIST publication.[7] It was found that these data showed better agreement with the predicted acoustic center correction values than the data reported from the European interlaboratory comparison.[3] The IEC working group on calibration of microphones used these 1994 NIST data, data from the European comparison, and predicted values to develop a table, included in an annex of IEC standard 1094-3, that contains acoustic center correction values for LS2aP microphones at frequencies up to 20 kHz. For the current study, a modified experimental setup and procedure were developed which make it possible for data to be taken much more rapidly at more frequencies. Both setups allow for the data to be gathered with sound waves at normal incidence to the microphones. They also both use the same anechoic chamber, preamplifier, switch box, microphone ground shield, and mounting arrangements described in the reference.[7] Results showed good agreement between the two sets of data taken with the two different NIST setups. This agreement validates the use of the modified setup in the current study.

A block diagram of the modified setup is shown in Fig. 2. The sinusoidal electrical drive signal is taken from a dynamic signal analyzer (DSA). After this signal is amplified, it is applied to channel one of the DSA. At the same time, the amplified signal is also applied via a switch box to either the source or a precision attenuator. If the signal is applied to the source, this microphone operates as an electrostatic loudspeaker, generating a sound pressure that in turn produces an electrical output at the receiver. When the amplified electrical drive signal is switched to the attenuator, the output of the attenuator functions as a voltage source in series with the electrical output terminals of the receiver. In either case, the signal path through the detection system following the output terminals of the receiver remains the same. These terminals are connected to the preamplifier from which the signal is sent to the input stage of a measuring amplifier. The amplified signal from this stage is then routed to a high-pass filter with a cutoff frequency of 1.5 kHz. Finally, the filter output signal is applied to channel two of the DSA where it is further filtered by the DSA itself. The DSA, used in its swept-sine mode, measures $|H(f)|_m$.

Instruments for monitoring the ambient environmental conditions are also part of the experimental setup. Tempera-

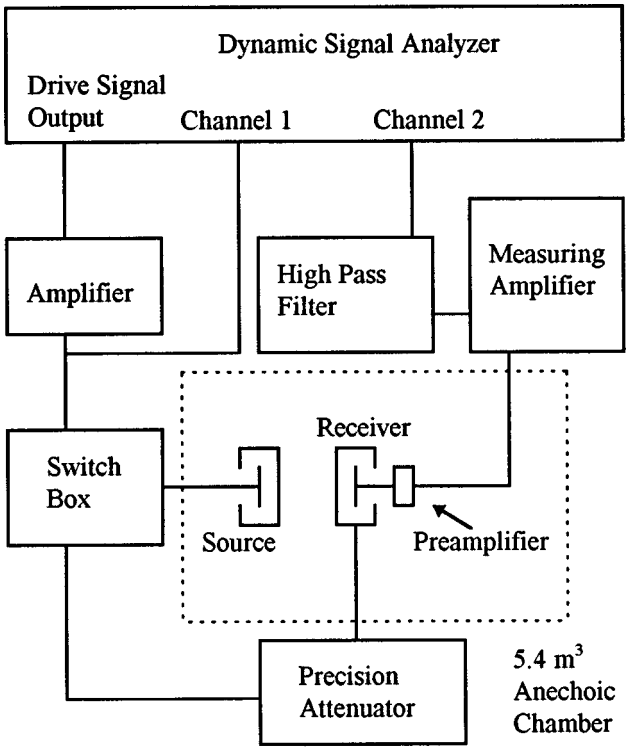

FIG. 2. Simplified block diagram of the modified experimental setup used at NIST to measure the acoustic center correction.

ture measurements are made with a thermistor probe near the perforated open end of a 1.0-m-long Bakelite tube with a 0.79-cm outer diameter. The tube serves to support the probe and its cables when all are slid through a small hole into the chamber. This arrangement allows for the air temperature to be measured about 0.4 m from the center of the gap between the two microphones. The tube is removed and the hole is plugged during sound measurements in order to prevent the tube from perturbing the sound field around the microphones. A hygroscopic film coated sensor, located in a corner of the anechoic chamber between fiberglass wedges, is used in conjunction with a humidity indicator placed outside the chamber to measure the relative humidity. Values of the relative humidity are calculated from the humidity indicator readings and the ambient temperature via calibration charts. Barometric pressure readings are taken with an aneroid barometer positioned near the chamber.

Data were gathered for six different pairs of Brüel & Kjaer type 4180 microphones created by combining a total of four different microphones.[8] Microphones of this type were chosen because they are designed to meet IEC LS2aP specifications. Six different microphone pairs were used to check the reproducibility of the measured acoustic center correction values. This check helps to ensure that the acoustic center correction for these microphones is not unduly sensitive to relatively small differences in their geometry or sensitivity. Also, the acoustic center correction values obtained for different microphone pairs were used to calculate mean acoustic center correction values. These mean values are better estimates of the values intended to be used for any given pair of type LS2aP microphones. Table I lists the microphone pair reference numbers assigned to each pair along with the serial

TABLE I. Microphone pair reference numbers which indicate the serial numbers of the microphones used in each pair.

Microphone pair reference no.	Serial number of microphone used as source	Serial number of microphone used as receiver
00	1746847	1698183
01	1698181	1698200
02	1698183	1698181
03	1698200	1746847
04	1698200	1698183
05	1698181	1746847

numbers of the individual microphones in each pair. Both the source and receiver from a given microphone pair were installed, and left overnight in the anechoic chamber with the chamber doors closed. For a given setting of x_{ab}, gain factor data were obtained during a frequency sweep, which was performed by driving the source with a nominal 10-V rms sinusoid stepped down in frequency from 50 to 2 kHz at 0.5-kHz intervals. Furthermore, the DSA calculated seven interpolated points at 62.5-Hz intervals between each measured point. An entire set of data for a given microphone pair was taken by repeating this sweep at values of x_{ab} equal to 101–311 mm in 10-mm steps. In order to check that this 10-mm resolution was adequate, a second set of data was gathered with microphone pair 02 at values of x_{ab} equal to 101–311 mm in 2-mm steps. A screw-driven mechanical slide with a line-scale positioning indicator located outside the chamber allowed the receiver to be moved in order to set the spacing between the diaphragms of the microphones without opening the chamber doors. At each frequency, the DSA used ten averages and an integration time of 250 ms in both channels. With this integration time and number of averages, an entire set of data for a given microphone pair could be obtained within a single day, and only about 6 min were required for a single sweep.

Checking for drift in the gain of the detection system while taking data for a given pair of microphones over the entire range of x_{ab} was important. Therefore, the gain factor of the detection system was measured periodically by applying the amplified electrical drive signal to the attenuator (set to 86.36 dB) rather than the source. This was done with the DSA before, after, and three times during the accumulation of a data set for a given microphone pair. Each measurement was compared with the first one taken by using a division operation internal to the DSA. It was found that the gain of the detection system drifted by no more than 0.014 dB at any frequency while gathering any complete data set. Although checking for drift in the gain of the detection system was necessary, the magnitude of the gain itself as a function of frequency was not needed to evaluate the acoustic center correction. This gain was approximately 57 dB, of which 50 dB was due to the measuring amplifier and 7 dB from the amplifier in the high-pass filter.

All of the ambient environmental conditions were measured immediately before an entire set of data was gathered with a new microphone pair. At the same time, the polarizing voltages of both microphones were set to 199.96 V by using

an electrometer. Each time a new microphone separation distance was set, both the static pressure and humidity indicator readings were taken before the frequency sweep. However, due to the amount of time required for the thermistor probe to stabilize after it was put in place within the chamber, the temperature was only measured when the detection system gain was checked (before, after, and three times during the accumulation of a data set for a given microphone pair). During these periods when the temperature was being measured, the polarizing voltages were also checked and reset to 199.96 V if necessary.

III. DATA REDUCTION, RESULTS, AND DISCUSSION

Measured values of $|H(f)|_m$ were compensated for the attenuation of sound caused by atmospheric absorption and referenced to a single reference ambient static density by applying Eq. (10). All of the data obtained from any single frequency sweep were compensated with values, which apply specifically to that sweep, of the static pressure, temperature, relative humidity, and the distance between the diaphragms of the source and receiver. Values of the static pressure and humidity indicator reading used were recorded at the start of the sweep. The value of the temperature was interpolated from the most recent temperature measurement before the sweep and the first one made after the sweep was completed. It was assumed that the temperature changed linearly with respect to time between the two measurements. This interpolated temperature value was also used with the humidity indicator reading and calibration charts to determine the relative humidity value used to calculate the sound attenuation coefficient due to atmospheric absorption.

Data obtained from all frequency sweeps performed for a given microphone pair were sorted so that a new data set was created for every frequency point in the sweeps. Each new data set contained the values of $|H(f)|_i^{-1}$ calculated at a single frequency over the entire range of x_{ab} for a given microphone pair. A straight line was fit to each new data set by the method of ordinary least squares (OLS).

After the slope and y-axis intercept for a new data set were determined via OLS, these parameters were used, as in Eq. (9), to calculate acoustic center correction values. These values, determined using all values of $|H(f)|_i^{-1}$ gathered over the entire range of x_{ab}, are plotted as a function of frequency for each microphone pair in Fig. 3. By averaging these values found for each of the six different microphone pairs, mean acoustic center correction values were also calculated at each frequency. These mean values are plotted in Fig. 4, and given in Table II at intervals of 0.5 kHz from 2–50 kHz. Overall, these mean values are largest at the lower measured frequencies. They gradually decrease with increasing frequency until they become negative (corresponding to an acoustic center position behind the diaphragm). This behavior agrees with prediction. Between approximately 35 and 40 kHz, the negative slope observed at lower frequencies reverses sign. While this slope reversal has not yet been predicted for LS2aP microphones, it is not unprecedented.[9] A quantitative comparison between the predicted and measured values is presented in Sec. V.

Besides measurement noise, certain physical phenomena cause relatively small deviations from the linear model for $|H(f)|_i^{-1}$ used here to fit the data. The magnitudes of these deviations vary with both frequency and microphone spacing. Burnett and Nedzelnitsky[7] discuss in detail how these phenomena can influence the data. Standing waves created by reflections from the interior surfaces of the anechoic chamber produce relative maxima and minima of sound pressure throughout the chamber. These standing waves are more significant at lower frequencies where the sound-absorbing wedges are typically less effective, since the ratio of their dimensions to the wavelength of sound is smaller than at higher frequencies. Reflections from the interior surfaces of the chamber behind the receiver have a greater effect at larger microphone spacings, where the ratio of the amplitude of the reflected sound wave to that of the direct sound wave is larger than at smaller spacings. Additional standing waves exist due to reflections between the microphones themselves. Standing waves of this type produce larger deviations from the linear model at smaller microphone separations. This effect is more pronounced at higher frequencies, since the acoustic radiation pattern from the source and the reflected radiation pattern from the receiver are more directional than at lower frequencies. Electrical crosstalk between the signal driving the source and the signal from the receiver is another factor that can produce deviations from the linear model. Both standing waves and crosstalk produce distinctive deviations that oscillate in magnitude as a function of microphone separation. Bias effects may result if the traverse length does not include enough periods of these oscillations. It is also possible that far-field conditions did not exist for all the data gathered at the smallest microphone separations. In the event near-field conditions did influence the data, a significantly nonzero slope should be observed in the residuals from the fits at the smaller microphone spacings. However, the effects of standing waves and crosstalk make it difficult to view this influence clearly.

Effects due to at least some of the phenomena discussed were observed in the residuals obtained from the fit, which are expressed here logarithmically as levels, in dB. Each logarithmically expressed residual is equal to 20 times the logarithm to the base 10 of the ratio of the value of $|H(f)|_i^{-1}$ determined from measured data to the value of $|H(f)|_i^{-1}$ calculated from the parameters obtained via an OLS fit to the data. In Fig. 5, residuals obtained from the data gathered at 40 kHz are shown. They display an oscillatory pattern that becomes smaller in amplitude as x_{ab} increases. This trend agrees with the expected behavior due to standing waves caused by reflections between the microphones themselves at this relatively high frequency. Residuals from the data gathered at a much lower frequency, 6 kHz, are shown for comparison in Fig. 6. In this instance, the larger residuals are found at larger microphone spacings. The dominant standing waves are more likely due to reflections from the chamber surfaces rather than reflections between microphones. At both frequencies, the residuals exhibit a periodic structure that is similar for all microphone pairs. However, the systematic periodicity in the residual structure, which is observed at many of the frequencies examined, could not be readily cor-

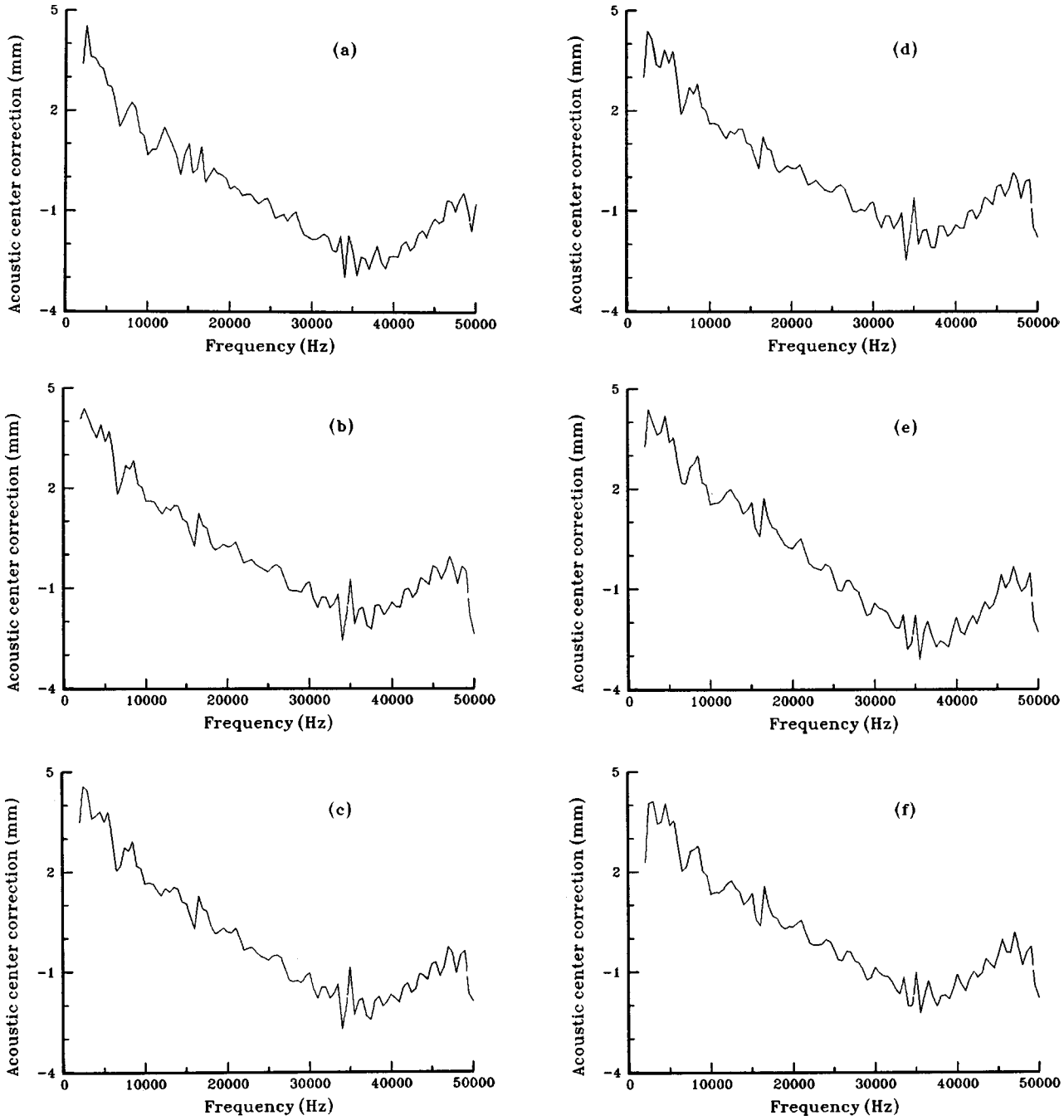

FIG. 3. Plot of acoustic center correction values calculated using data gathered with (a) microphone pair 00, (b) microphone pair 01, (c) microphone pair 02, (d) microphone pair 03, (e) microphone pair 04, and (f) microphone pair 05. Serial numbers of both the source and receiver microphones are given along with their corresponding microphone pair reference number in Table I.

related with the acoustic wavelength. This was generally true for all of the frequencies examined and is most likely due to the effects of nonaxial standing wave modes within the chamber and spatial aliasing at higher frequencies, for which the 10-mm spacing between data points is too large to resolve the relative maxima and minima of individual standing waves.

Additional OLS fits were done with spatially truncated data sets to determine the extent to which spatially dependent factors biased the results of the linear fitting. Noisier data at larger microphone separations may also have adversely affected these results at frequencies where the signal-to-noise ratio was relatively low. In addition, since the acoustic center correction is dependent on the distance between the microphone and the observation point, it conceivably could change in value within the 101–311-mm range of x_{ab} used. Acoustic center correction values determined from data sets truncated in the same manner were averaged using data from all the microphone pairs. Figure 7 includes two curves that show the mean acoustic center correction values calculated by using data sets truncated in two different spatial regions. Both are regions where the physical phenomena discussed are expected to have their largest influence. One curve shows results for data gathered at values of x_{ab} ranging from 101–261 mm, while the other displays results of measurements made from 151–311 mm. Results obtained using the com-

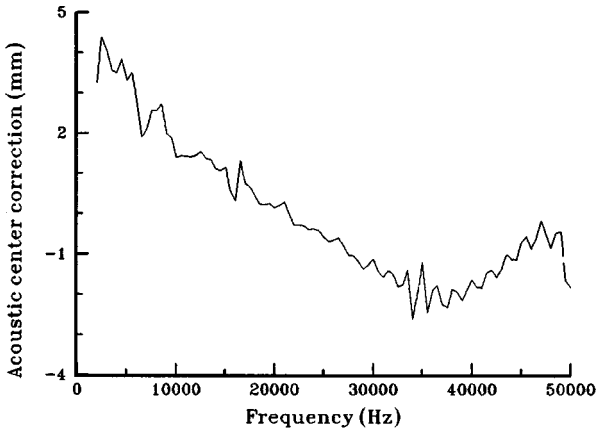

FIG. 4. Plot of the mean acoustic center correction values for type LS2aP microphones determined at NIST. Values shown were calculated by averaging the results for the six microphone pairs.

plete data sets are included for comparison. Both curves developed from the truncated data sets have the same general shape as the one resulting from the complete data sets. In all three, mean acoustic center correction values decrease with increasing frequency, become negative, and then increase with frequency above approximately 35 kHz. Plots that show the difference between each curve developed from the complete data set and the truncated data sets are presented in Fig. 8. With the results from data taken over the range in x_{ab} from 101–261 mm, displayed in Fig. 8(a), the largest absolute value of this difference is 1.0 mm. Results for the other truncation scheme used are presented in Fig. 8(b), where the maximum absolute value of this difference is 1.2 mm.

IV. UNCERTAINTY OF MEASUREMENT RESULTS

To develop an overall standard uncertainty for the mean acoustic center correction values, general rules for evaluating and expressing uncertainties applicable to a broad range of measurements were followed.[10,11] Two different types of uncertainties, defined according to the methods used to evaluate them, are given. Type A evaluations are carried out on the measured data using statistical analysis, while type B evaluations invoke scientific judgment and information about the measurements to obtain standard uncertainties. A combined standard uncertainty is calculated by combining all the individual standard uncertainties using the ''root-sum-of-squares'' (RSS) method. Finally, an expanded uncertainty is determined by multiplying the combined standard uncertainty by an appropriate coverage factor. By convention, the coverage factor is usually 2.

For each frequency, a type A standard uncertainty, equal to the standard deviation of the mean acoustic center correction values for all microphone pairs, was calculated in the conventional manner. A plot of this type A standard uncertainty between 2 and 50 kHz is presented in Fig. 9. Its largest value is 0.26 mm at 35 kHz. Bootstrap operations[12] were also performed, using data from only a single microphone pair at a time. This was done to estimate the standard deviation in the acoustic center correction value determined for each mi-

TABLE II. The NIST mean acoustic center correction values for the type LS2aP microphone. A positive value represents an acoustic center position in front of the diaphragm.

Frequency (kHz)	Mean acoustic center correction value (mm)	Frequency (kHz)	Mean acoustic center correction value (mm)	Frequency (kHz)	Mean acoustic center correction value (mm)	Frequency (kHz)	Mean acoustic center correction value (mm)
2.0	3.3	14.5	1.1	27.0	−0.8	39.5	−1.9
2.5	4.4	15.0	1.2	27.5	−1.0	40.0	−1.6
3.0	4.1	15.5	0.6	28.0	−1.0	40.5	−1.8
3.5	3.6	16.0	0.3	28.5	−1.2	41.0	−1.8
4.0	3.5	16.5	1.3	29.0	−1.4	41.5	−1.5
4.5	3.8	17.0	0.8	29.5	−1.3	42.0	−1.4
5.0	3.3	17.5	0.7	30.0	−1.1	42.5	−1.6
5.5	3.5	18.0	0.4	30.5	−1.4	43.0	−1.4
6.0	2.8	18.5	0.2	31.0	−1.6	43.5	−1.0
6.5	1.9	19.0	0.2	31.5	−1.4	44.0	−1.1
7.0	2.1	19.5	0.3	32.0	−1.5	44.5	−1.1
7.5	2.6	20.0	0.2	32.5	−1.8	45.0	−0.7
8.0	2.6	20.5	0.2	33.0	−1.8	45.5	−0.6
8.5	2.7	21.0	0.3	33.5	−1.4	46.0	−0.9
9.0	2.0	21.5	0.0	34.0	−2.6	46.5	−0.6
9.5	1.9	22.0	−0.3	34.5	−2.0	47.0	−0.2
10.0	1.4	22.5	−0.3	35.0	−1.2	47.5	−0.5
10.5	1.4	23.0	−0.3	35.5	−2.4	48.0	−0.9
11.0	1.4	23.5	−0.4	36.0	−1.9	48.5	−0.5
11.5	1.4	24.0	−0.4	36.5	−1.8	49.0	−0.5
12.0	1.4	24.5	−0.4	37.0	−2.3	49.5	−1.7
12.5	1.5	25.0	−0.6	37.5	−2.3	50.0	−1.8
13.0	1.4	25.5	−0.7	38.0	−1.9		
13.5	1.3	26.0	−0.7	38.5	−1.9		
14.0	1.1	26.5	−0.6	39.0	−2.2		

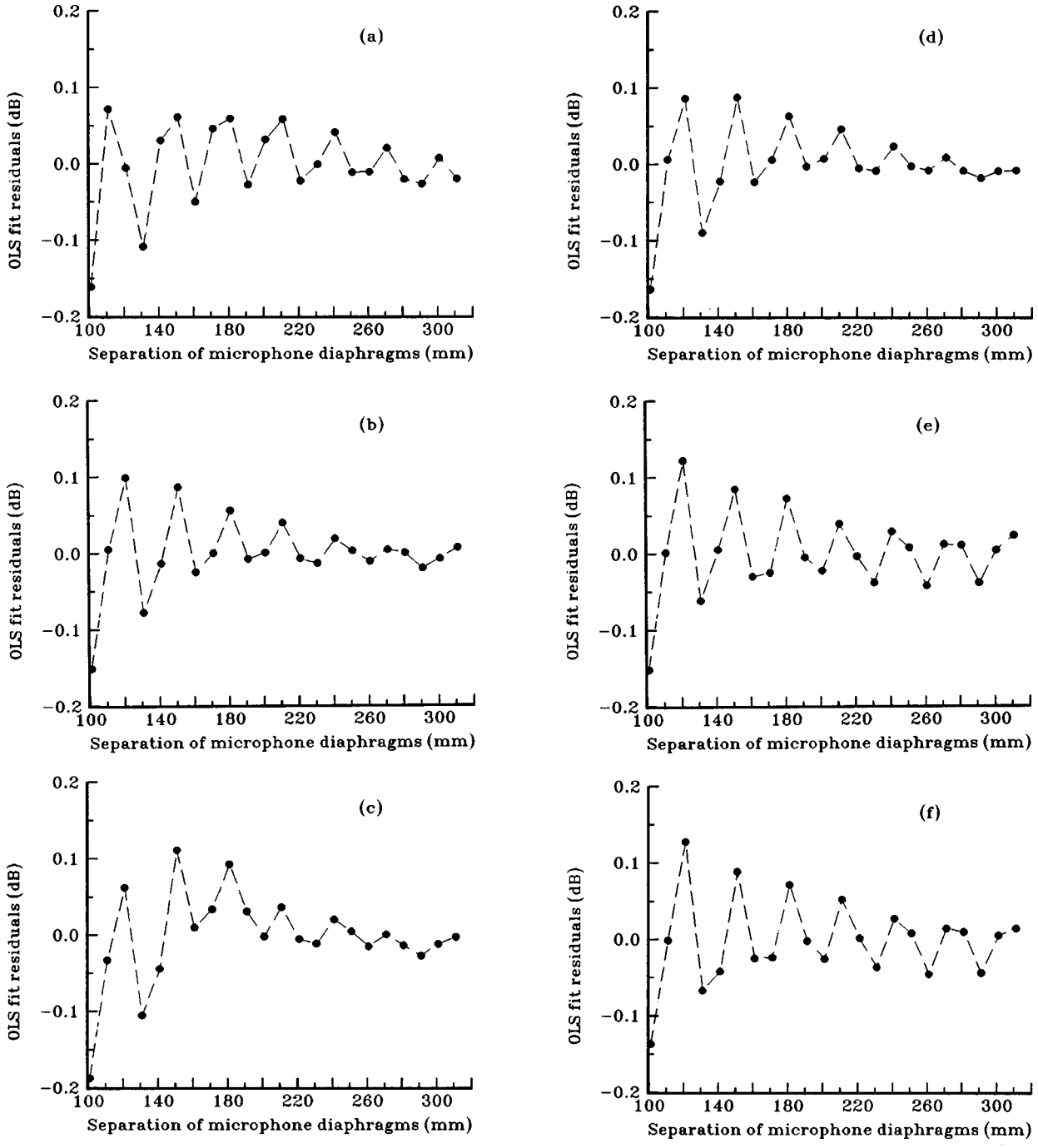

FIG. 5. Residuals, expressed logarithmically, from OLS fits to the data obtained at 40 kHz for (a) microphone pair 00, (b) microphone pair 01, (c) microphone pair 02, (d) microphone pair 03, (e) microphone pair 04, and (f) microphone pair 05. Each logarithmically expressed residual is equal to 20 times the logarithm to the base 10 of the ratio of the value of $|H(f)|_i^{-1}$ determined from measured data to the value of $|H(f)|_i^{-1}$ calculated from the parameters obtained via an OLS fit to the data.

crophone pair at each frequency. All of these estimates were found to be comparable, validating the use of data from all microphone pairs.

A type B standard uncertainty was derived via a sensitivity analysis done by varying the measured parameters in Eq. (10) and refitting the results using OLS. Perturbed values for each parameter in Eq. (10) were obtained by adding and subtracting an amount equal to the standard uncertainty of that parameter. Except where otherwise noted, the same perturbations were applied to each data point contained within the entire range of x_{ab}. Effects of varying the parameters both individually and in all possible combinations were examined for ten selected frequencies ranging from 2–50 kHz. At each frequency, this type B standard uncertainty is taken to be the largest absolute value of the difference between the acoustic center correction derived from the fit using the measured values of the parameters and the acoustic center correction derived from the fits using the parameters perturbed by their standard uncertainties.

The standard uncertainty for each parameter in Eq. (10) was calculated by assuming a symmetric rectangular probability distribution and using instrument specifications and

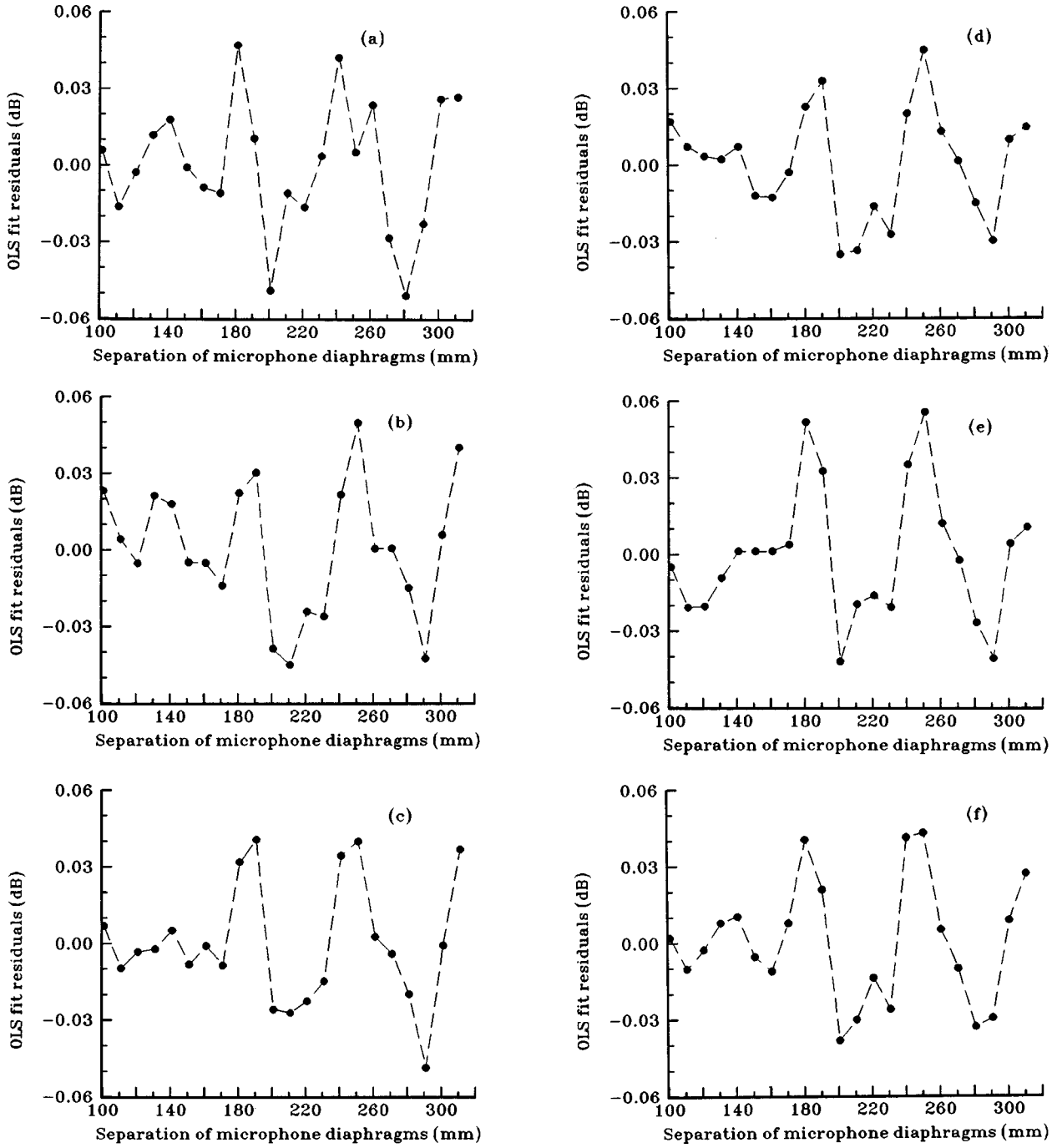

FIG. 6. Residuals, expressed logarithmically, from OLS fits to the data obtained at 6 kHz for (a) microphone pair 00, (b) microphone pair 01, (c) microphone pair 02, (d) microphone pair 03, (e) microphone pair 04, and (f) microphone pair 05. Each logarithmically expressed residual is equal to 20 times the logarithm to the base 10 of the ratio of the value of $|H(f)|_i^{-1}$ determined from measured data to the value of $|H(f)|_i^{-1}$ calculated from the parameters obtained via an OLS fit to the data.

measurement experience acquired at NIST to obtain values for the upper and lower bounds of this distribution. Given this assumption, the resulting standard uncertainty is equal to half the width of the distribution multiplied by a factor of 0.58. Using this method, for example, a standard uncertainty of 0.81 mbar was assigned to the barometric pressure. Upper and lower distribution bounds were based on experience gained with the aneroid barometer during microphone calibrations and related work conducted at NIST.

A standard uncertainty of 0.058 K was assigned to the measured temperature. Bounds on the rectangular distribution were chosen based on the accuracy specification of the temperature measurement system, the degree to which the probe approached thermal equilibrium after insertion into the chamber, and uncertainties due to linear interpolation of temperatures between actual measurements.

For the distance between the diaphragms of the source and receiver, the standard uncertainty is 0.09 mm. Upper and lower distribution bounds were determined by allowing for uncertainties arising from both systematic and random effects that occurred while measuring the lengths of the microphones, the distance between the fittings that held the micro-

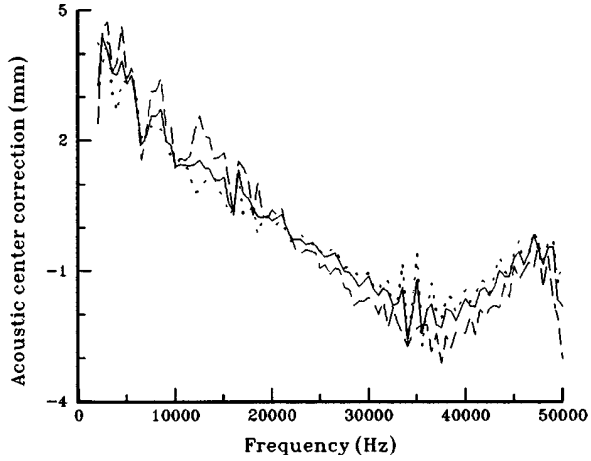

FIG. 7. Mean acoustic center correction values calculated using truncated data sets which only included measurements from 101–261 mm (···), and 151–311 mm (- - -). Results calculated from the complete data set (———) are shown for comparison. In all cases, mean values were calculated by averaging the results for the six microphone pairs.

phones, and the uncertainty in the depths of the diaphragm recesses of the microphones used.

The relative standard uncertainty for the parameter α is 8.7%. The accuracy of the theoretical model for attenuation of sound due to atmospheric absorption, the manufacturer's

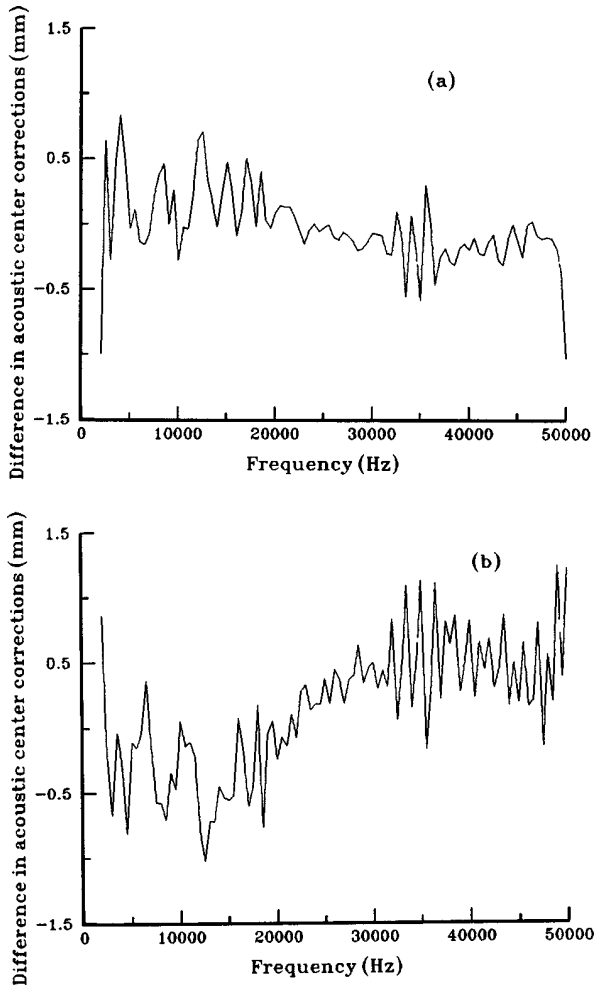

FIG. 8. Differences between the mean acoustic center correction values calculated using the complete data set and the data sets truncated by only including data points from (a) 101–261 mm or (b) 151–311 mm.

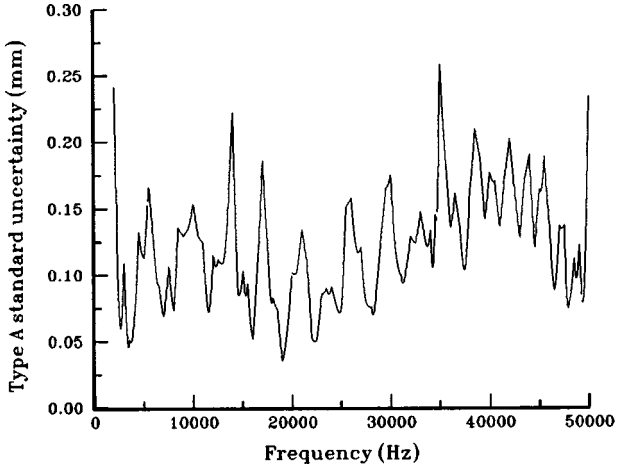

FIG. 9. Plot of the type A standard uncertainty of the mean acoustic center correction values, determined at NIST, for the frequency range 2–50 kHz.

accuracy specification for the humidity sensors, and experience with sensors of this type contributed to the distribution bounds selected. Effects due to standard uncertainties in the temperature and barometric pressure measurements were also examined, but these effects on the calculated values of α were insignificant compared with those resulting from the standard uncertainty in the relative humidity.

Drift and nonlinearities in the gain of the detection system affect the measured values of $|H(f)|_m$. For the sensitivity analysis, the values of $|H(f)|_m$ were varied in a way that allowed for larger changes in the value of $|H(f)|_m$ as the value of x_{ab} was incremented. A standard uncertainty of 0.026 dB was used for the difference between the change applied to the values of $|H(f)|_m$ at the two extreme values of x_{ab}. Between these points, the percentage change applied was incremented in linear steps. Bounds on the rectangular distribution were determined by accounting for uncertainties in the gain of the measuring amplifier and different DSA ranges, and the drift over time in the gain of the detection system measured with the amplified electrical drive signal switched to the precision attenuator.

In addition to the effects noted, it was assumed that the measured value of $|H(f)|_m$ consisted of the RSS combination of noise and the true (noiseless) value of $|H(f)|_m$. An allowance was determined for a frequency-dependent noise level influencing the value of $|H(f)|_m$ by performing the measurement sweep with the amplified electrical drive signal disconnected from the source. The gain factor measured during this sweep was recorded for frequencies at which type B uncertainties were calculated. This gain factor was then utilized to calculate the theoretical true (noiseless) value of $|H(f)|_m$ that was used at each of these frequencies in the sensitivity analysis.

For the ten selected frequencies of calculation, the largest absolute value of the type B standard uncertainty derived via the sensitivity analysis for the mean acoustic center correction is 0.65 mm at 50 kHz. At any frequency between 2 and 50 kHz, this is considered to be the largest absolute value of this uncertainty, due to its strong dependence on the magnitude of α. Within this frequency range, the magnitude of α is greatest at 50 kHz for the range of ambient environ-

TABLE III. Uncertainties in the NIST mean acoustic center correction values for type LS2aP microphones at ten selected frequencies. Type A standard uncertainties are equal to the standard deviation of the mean value of the acoustic center correction calculated at a given frequency. The first set of type B standard uncertainties was derived from a sensitivity analysis that involved varying each measured parameter in Eq. (10) by an amount equal to its own standard uncertainty and refitting the results. The second set of type B standard uncertainties was derived using the differences between the mean acoustic center correction values calculated using the complete data set and the truncated data sets.

Frequency (kHz)	2	4	8	10	16	20	25	31.5	40	50
Type A standard uncertainty (mm)	0.24	0.07	0.07	0.16	0.05	0.10	0.07	0.10	0.18	0.23
Type B standard uncertainty derived from sensitivity analysis (mm)	0.38	0.36	0.39	0.41	0.46	0.49	0.53	0.56	0.61	0.65
Type B standard uncertainty derived using results from fits of truncated data (mm)	0.58	0.48	0.34	0.16	0.05	0.14	0.21	0.18	0.47	0.70
Combined standard uncertainty (mm)	0.73	0.60	0.52	0.47	0.47	0.52	0.57	0.60	0.79	0.98
Expanded uncertainty (mm) (using a coverage factor of 2)	1.5	1.2	1.0	0.9	0.9	1.0	1.1	1.2	1.6	2.0

mental conditions measured in the anechoic chamber.

The physical phenomena discussed in Sec. III, including standing waves that result because the sound field inside the anechoic chamber is not a perfectly free sound field, may have had a slight influence on the calculation of the mean acoustic center correction values. To account for this possible influence, a second type B uncertainty was determined using the differences between the mean acoustic center correction values calculated using the complete data set and the truncated data sets (see Fig. 8). For each of the ten selected frequencies at which the other type B uncertainty was calculated, the largest absolute value of the difference obtained at a given frequency using either truncation scheme was considered to represent half the width of a symmetric rectangular probability distribution. Therefore, the type B standard uncertainty attributed to the phenomena discussed in Sec. III is equal to half the width of this distribution multiplied by 0.58. This method is considered to provide a conservative estimate of this uncertainty.

Type A and B standard uncertainties are combined using the RSS method to determine the combined standard uncertainty. Its maximum value calculated is equal to 0.98 mm at 50 kHz. When multiplied by a coverage factor of 2, this combined standard uncertainty yields an expanded uncertainty of the mean acoustic center correction values for LS2aP microphones no greater than 2.0 mm in the frequency range 2–50 kHz. Table III summarizes the type A, type B, combined standard, and expanded uncertainties for the ten selected frequencies.

V. CONCLUSIONS

To achieve accurate calibrations of microphones in the free-field by the reciprocity method, frequency-dependent acoustic center corrections must be applied to calculate the exact effective distances between microphones, that is, the distance between acoustic centers. For LS2aP microphones used at normal incidence, relatively large discrepancies had existed between measured values of the acoustic center correction and those values that had been theoretically predicted. More acoustic center correction data were required, especially since this microphone type had been defined as a laboratory standard microphone in an international standard. Therefore, LS2aP microphone acoustic center correction values were determined at NIST. Measurements were done using a dynamic signal analyzer and a procedure that permitted a large amount of data to be taken in a relatively short amount of time. Microphone diaphragm separations from 101–311 mm with a 10-mm resolution were used to collect data at frequencies between 2 and 50 kHz. The differences in the acoustic center correction values determined from a fit of data obtained using microphone pair 02 with a 2-mm resolution and a fit of a subset developed from the same data to obtain a 10-mm resolution are well within the expanded uncertainty of the acoustic center correction values reported here, indicating that there was no significant spatial subsampling problem with the 10-mm resolution. Figure 10 displays the mean acoustic center correction values obtained in this work, values predicted by using the boundary element method,[3,4] and values obtained by scaling standardized values for microphones with a geometrical configuration[5] similar to that of LS1P microphones. Overall, the mean acoustic

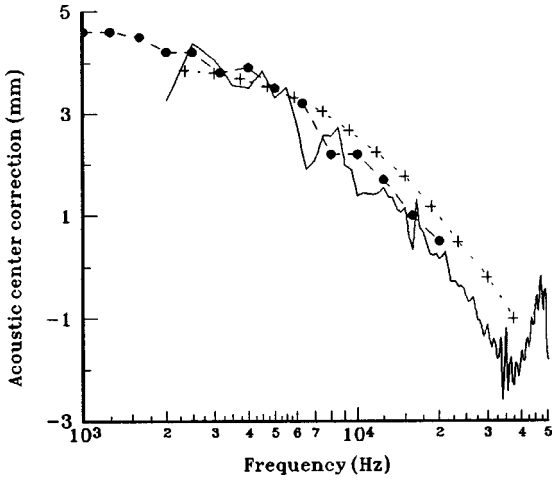

FIG. 10. Comparison of the mean acoustic center correction values for type LS2aP microphones determined at NIST (———), with values theoretically predicted using the boundary element method (BEM) (--●--) and values obtained by scaling IEC published values for microphones with a geometrical configuration similar to that of type LS1P microphones (---+---). [BEM values from Ref. 3 and IEC values from IEC Publication 486 (Ref. 5).]

center correction values determined at NIST, which have an expanded uncertainty no greater than 2.0 mm in the frequency range 2–50 kHz, are in good agreement with the predicted values within the frequency range of the predicted values (2–37.44 kHz). At frequencies common to the set of values determined at NIST and those predicted using the boundary element method, the largest absolute value of the difference in the acoustic center correction is 0.9 mm at 2 and 10 kHz. Each acoustic center correction value scaled from one used for microphones with a geometrical configuration[5] similar to that of LSIP microphones was compared with the value determined by NIST for the frequency nearest to the scaled frequency. The maximum absolute value of the difference between the two sets of values is 1.3 mm at 37.44 kHz.

The sharply frequency-dependent local ''spikes'' seen in the acoustic center correction data are generally small in amplitude, are within the expanded measurement uncertainty, and are not the same in repeated measurements. Consequently, a smoothed version of the NIST measured data reported in Fig. 10 will be developed and used for the acoustic center correction values applied to primary calibrations of LS2aP microphones in the free-field by the reciprocity method at NIST. This is consistent with current and past NIST practice (described in Ref. 7) for calibrations of other types of measurement microphones by this method.

Acoustic center correction values obtained from the smoothed version of the NIST measured data will be applied to free-field calibrations of LS2aP microphones done at NIST at normal incidence with microphone diaphragm separations of about 200 mm (the measurement range used here was chosen based on this microphone separation distance), and probably would also be applicable to such calibrations performed in other anechoic chambers with different geometries (but of comparable quality), provided the microphone diaphragm separation used is at or near this distance. Microphone diaphragm separations significantly smaller than 200 mm are not recommended for these calibrations, and the acoustic center correction values may be different at much larger separations.

ACKNOWLEDGMENTS

The authors thank D. J. Evans of the NIST Automated Production Technology Division for writing the computer program used to fit the data and carry out the bootstrap calculations, and S. D. Leigh of the NIST Statistical Engineering Division for providing statistical guidance and assistance in determining the uncertainty of the measurement results.

[1] IEC 61094-3 (1094-3 in the previous IEC numbering scheme), ''Measurement microphones-Part 3: Primary method for pressure calibration of laboratory standard microphones by the reciprocity technique'' (International Electrotechnical Commission, Geneva, Switzerland, 1995), p. 9.

[2] IEC 61094-1 (1094-1 in the previous IEC numbering scheme), ''Measurement microphones-Part 1: Specifications for laboratory standard microphones'' (International Electrotechnical Commission, Geneva, Switzerland, 1992).

[3] K. Rasmussen and E. Sandermann Olsen, ''Intercomparison on free-field calibration of microphones,'' The Acoustics Laboratory, Report PL-07, Technical University of Denmark, Lyngby, Denmark (1993).

[4] P. Juhl, ''A numerical investigation of standard condenser microphones,'' J. Sound Vib. **177**(4), 433–446 (1994).

[5] IEC Publication 486, ''Precision method for free-field calibration of one-inch standard condenser microphones by the reciprocity technique'' (International Electrotechnical Commission, Geneva, Switzerland, 1974) (Figure 5, microphone configuration 2, p. 33).

[6] ANSI S1.26-1978, R1988 (ASA 23-1978, R1989), ''Method for the calculation of the absorption of sound by the atmosphere'' (American Institute of Physics for the Acoustical Society of America, New York, 1988).

[7] E. D. Burnett and V. Nedzelnitsky, ''Free-field reciprocity calibration of microphones,'' J. Res. Natl. Bur. Stand. **92**(2), 129–151 (1987).

[8] The mention of a commercial product by manufacturer's name and/or model number is intended only to adequately specify the apparatus, and in no way implies an endorsement by the National Institute of Standards and Technology.

[9] IEC Publication 486, ''Precision method for free-field calibration of one-inch standard condenser microphones by the reciprocity technique'' (International Electrotechnical Commission, Geneva, Switzerland, 1974) (Figure 4, microphone configuration 1, p. 31).

[10] B. N. Taylor and C. E. Kuyatt, ''Guidelines for evaluating and expressing the uncertainty of NIST measurement results,'' NIST Technical Note 1297-1994 edition (U.S. Government Printing Office, Washington DC, 1994).

[11] BIPM, IEC, IFCC, ISO, IUPAC, IUPAP, OIML, ''Guide to the expression of uncertainty in measurement'' (International Organization for Standardization, Geneva, Switzerland, 1993).

[12] B. Efron and R. J. Tibshirani, *An Introduction to the Bootstrap* (Chapman & Hall, New York, 1993).

On the free and forced vibration of single and coupled rectangular plates

N. H. Farag and J. Pan
Department of Mechanical and Materials Engineering, University of Western Australia, Nedlands, Western Australia 6907, Australia

(Received 20 August 1997; revised 2 February 1998; accepted 19 March 1998)

A mathematical model is developed for the coupling of two finite plates at an arbitrary angle for the prediction of the dynamic response and power flow at the coupling edge and at any cross section. The coupling at the joint edge considers bending, out-of-plane shear, and in-plane longitudinal (perpendicular to the joint edge) vibration. No constraint is imposed on the in-plane displacement perpendicular to the coupling edge. The exact solution for flexural mode shapes and resonance frequencies of rectangular plates with one edge free and the other edges simply supported is considered. This exact solution satisfies both the displacement and force boundary conditions, consequently it is used in the coupling of plate panels. An approximate relation is derived for prediction of the flexural resonance frequencies of higher-order modes with a reasonable accuracy. An approximate solution is presented for the in-plane response of the same plate panels when excited by in-plane forces perpendicular to the free edge. A simple expression is given for an approximate estimation of the cut-off frequencies for the different in-plane modes. The frequency response of the individual plate panels is presented as receptance functions for both flexural and in-plane vibration which are used in the plate coupling. The vibrational power injected into a plate by out-of-plane concentrated force and moment is computationally investigated. The importance of power input by a small moment excitation in some resonant bands even at low frequencies is highlighted. The spatial distribution of the components of flexural power transmitted by shear and moment across a section of the plate are investigated and the reason for the circulatory patterns of active power flow in plates is illustrated. The power flow characteristics in two plates coupled at an arbitrary angle is examined by a computational example. The effect of the coupling angle on the components of input power and power flow across the coupling edge is investigated. It is shown that the coupling of the two plates is mainly due to moment at frequencies up to the cut-off frequency of the first in-plane mode. Above this frequency, the coupling is due to out-of-plane shear and in-plane vibration with a diminishing participation of the moment in transmitting vibrational power through the coupling edge. [S0001-4966(98)00607-9]

PACS numbers: 43.40.Dx [CBB]

LIST OF SYMBOLS

a, b, h	plate dimensions along X, Y, Z directions
ρ	material density (mass per unit volume)
ν	Poisson's ratio
η	structural (hysteretic) damping coefficient
E	Young's modulus of elasticity of the plate material
$\{X_e, Y_e, Z_e, M_e\}$	excitation force vector, the components are, respectively, the linear forces in X, Y, and Z directions and the moment about X axis
Q_x, Q_y	components of transverse shear force (force per unit length) in the directions shown in Fig. 1
V_x, V_y	transverse shear forces including the effect of the twisting moment
M_{xx}, M_{yy}, M_{xy}	moment components (moment per unit length) in the directions shown in Fig. 1
(x_e, y_e)	excitation position on the middle plane of the plate
u, v, w	components of the response displacement in the directions of the coordinate axes
$\ddot{u}$, $\ddot{v}$, $\ddot{w}$	corresponding components of the acceleration response
ω	angular frequency (radian per second)
m, n	number of half-wave lengths for flexural vibration in X direction
$D = Eh^3/12(1-\nu^2)$	flexural stiffness of the plate
$C_L^2 = E/\rho(1-\nu^2)$	square of the longitudinal wave speed in the plate
$C_T^2 = E/2\rho(1+\nu)$	square of the transverse (in-plane) shear wave speed in the plate

INTRODUCTION

The dynamic response and vibrational power flow characteristics of single and coupled thin finite plates are the concern of this paper. Two specific cases are mathematically modeled and computationally investigated by examples. The first is the case of simultaneous excitation of a flat rectangular plate by out-of-plane point moment and out-of-plane force. The aims of considering this case are to highlight the importance of the moment excitation in injecting vibrational power in some resonant frequency bands even at low frequencies and to investigate the nature of the spatial distribution of power flow and the participation of moment and shear in transmitting the flexural vibrational power. The second case is that of two rectangular plates coupled at an arbitrary angle. In addition to the two components of flexural response, namely; moment and out-of-plane shear, the coupling also considers in-plane response in the direction perpendicular to the coupling edge. The model is used to examine the nature of coupling at low and high frequencies.

A modal receptance approach is used all through the work. Hence natural frequencies and mode shapes are obtained first. The mode shapes satisfy both the geometric and force boundary conditions and consequently can be used in the plate coupling formulation. The frequency response is expressed in the form of receptance functions for both flexural and in-plane vibration. The receptance functions are then used in the coupling of two plates at an arbitrary angle.

Plate edge conditions used in this work are referred to as simply supported conditions for flexural vibration and clamped conditions for in-plane vibration. These conditions are representative of the practical case of flat plate panels fixed to frames from two parallel edges and to stiffening beams along the other two sides so that linear displacements along the boundaries can be considered negligible while rotational displacements are permissible. Plate panels having one edge free are considered because plates are coupled at the free edges. The coupling is achieved mathematically by satisfying force equilibrium and displacement compatibility at the common edge.

In Ref. 1, the equation governing free flexural vibration of thin plates is derived and the assumptions of thin plate theory are discussed in detail. A solution for the resonance frequencies and mode shapes of rectangular plates with different boundary conditions adopting beam deflection functions in two perpendicular directions is presented by Warburton.[2] However, such solutions are not suitable for force predictions because the assumed deflection functions do not satisfy the force conditions at the plate edges. In his paper, Leissa[3] presents exact characteristic equations for rectangular plates for six cases of two parallel sides simply supported. He also used the Rayleigh–Ritz solution adopting beam functions for the mode shapes for other cases.

The equation governing the forced flexural response of thin plates can be found in Refs. 4 and 5. This equation is solved for forced response in finite plates by Langley[6] using a particular integral. Hansen *et al.*[7] solved it considering the excitation forces as boundary conditions at the free edges of separate plate panels. Modal receptance solutions are presented in Refs. 4 and 8 and are adopted in this work.

The interest in the response of thin plates to moment excitation goes back to 1960 when this case was investigated by Dyer.[9] He shows that the classical (thin) plate theory is adequate in determination of moment impedance when the application of the moment occurs at an area of dimensions greater than the thickness. Although the mathematical modeling of the moment implies zero area of application, in practice there is a finite area. The mathematical solution is usually not valid in a limited area around the point of application of the moment. This is because the application of moment on a small area (as compared to plate thickness) means that the power is transmitted mainly due to shear deformation in the vicinity of the point of application of the moment. Excessive shear deformation violates a basic assumption of the thin plate theory which considers shear stresses and neglects shear deformations.

The response to point moment excitation was also examined for infinite plates in Ref. 5 and for finite plates in Ref. 4. Reference 5 gives an expression for the input power due to point moment excitation in an infinite plate. Petersson[10] investigated the significance of point moment excitation near corner boundaries in semi-infinite plates. This case is arising in the practical applications when the force transmitted to the plate panel which is designed to be perpendicular to the middle plane of the plate is practically inclined and has in-plane components as well as moment component due to imperfections in manufacturing, assembly, or alignment of the supporting mounts. A modal receptance function is presented here for the flexural response to point moment excitation in finite flat plate panels. The resonant behavior of finite plates excited simultaneously by flexural force and moment is examined.

According to the thin plate theory, the assumptions of small deflections and small slopes of the deflected shapes lead to an equation governing the flexural vibration which is uncoupled to the in-plane vibration.[1] However, the two components of in-plane vibration remain coupled even for small oscillations. The causes and the physical meaning of this coupling are demonstrated in this paper. A solution of the two coupled equations for in-plane forced vibration is presented in Ref. 11. This solution considers the coupling between the in-plane longitudinal and in-plane shear waves and can predict the in-plane resonance frequencies in rectangular plate panels with clamped edges. A simplified solution is used in the plate coupling model in the present work.

Over the last few decades, researchers developed different models to predict the dynamic response of coupled plates. Nilsson[12] considered the bending and in-plane longitudinal power transmission through the T and L junctions of semi-infinite plates adopting a wave approach. Guyader *et al.*[13] used a modal approach to examine the coupling of finite plates forming L, T, or cross junctions. Shen *et al.*[14] gave a solution for the bending vibration of T and L combinations of rectangular plates using beam functions. Shear and bending at the coupling edges are considered in that model. Langley[15] considered bending, out-of-plane shear and two perpendicular components of in-plane vibration in his model for the coupling of curved panels.

References 15–17 report some of the present efforts to

include the in-plane response into the predictions and measurements of the response to simultaneous flexural and in-plane excitations. They emphasize the importance of the in-plane response at high frequencies and in large coupled platelike structures. Cuschieri and McCollum[18] presented a model for the coupling of two perpendicular plates considering flexural and in-plane vibration. They adopted Mindlin plate theory which considers the effect of rotary inertia and shear deformation. Their solution for in-plane response considers the coupling between in-plane longitudinal and in-plane shear. Modal decomposition is used in the direction parallel to the coupling edge and wave solution in the direction perpendicular to the coupling edge. They presented results up to 100 KHz.

In this paper, the equations of motion used for flexural and in-plane vibration are based on the assumptions of the thin plate theory. The assumptions leading to these equations, the introduction of damping and the delta function representation of the concentrated excitation forces and moments are briefly discussed. In the first section, the flexural response of plate panels having one edge free and the other edges simply supported is considered. The exact characteristic equation is considered for this case of boundary conditions. An approximate equation is given which may be used for quick prediction of the resonance frequencies with a reasonable accuracy. The flexural response to harmonic point force and point moment excitations is developed in terms of receptance functions. The second section presents an approximate receptance function for the prediction of the in-plane response of finite plates excited by in-plane forces perpendicular to one free edge when all other edges are constrained against in-plane vibration (corresponding to the case of simply supported edges for flexural vibration).

The receptance functions developed in the first two sections for flexural and in-plane response are employed in the subsequent analysis to develop a model for prediction of the response of two finite plates coupled at an arbitrary angle. This coupling model considers in-plane response of the coupled plates perpendicular to the coupling edge in addition to bending and out-of-plane shear.

Computational examples are given which illustrate the capability of the moment excitation to input a large amount of power, as compared to the force excitation, in some resonant bands even at low frequencies. The spatial distribution of the flexural power transmitted by the shear and moment components is presented. The participation of both components in transmitting the vibrational power and the reason for the circulatory patterns of power flow in plates (see, for example, Ref. 19) are illustrated. Predictions of the power flow components transmitted by moment, out-of-plane shear and in-plane waves suggest that the coupling is mainly due to bending at frequencies up to the cut-off frequency of the first in-plane mode. Above this frequency the participation of moment diminishes rapidly and the coupling is due to shear and in-plane vibration.

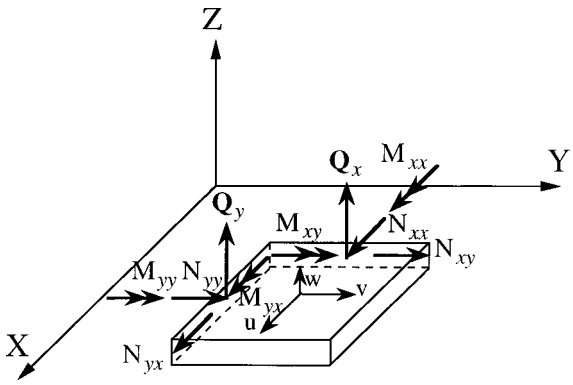

FIG. 1. Positive directions of force and displacement components on a plate element.

I. FLEXURAL VIBRATION OF THIN RECTANGULAR PLATES

In this section, the equation of forced flexural vibration will be presented. The assumptions leading to this equation will be briefly discussed together with the introduction of damping and the delta function representation of point force and moment excitations. The exact characteristic equation will be presented for rectangular plates having one edge free and the other edges simply supported. An approximate equation is derived to predict the resonance frequencies to a good accuracy specially for higher-order modes.

A. Equations of motion for flexural vibration

The equation governing the forced vibrational response of thin plates to point excitation force vector $[Z_e, M_{xe}, M_{ye}]^T$ at (x_e, y_e) may be written in the form:[5]

$$D\nabla^2\nabla^2 w + \rho h\ddot{w} = Z_e\delta(x-x_e)\,\delta(y-y_e) - M_{xe}\delta(x-x_e)\,\frac{\partial}{\partial \mathbf{y}}\,\delta(y-y_e) + M_{ye}\delta(y-y_e)\,\frac{\partial}{\partial x}\,\delta(x-x_e). \qquad (1)$$

The terms in the right-hand side are the equivalent distributed forces corresponding to the concentrated force components using Dirac delta functions. The positive directions of force and displacement components are illustrated in Fig. 1. They are such that positive force components when combined with the corresponding velocity components in the positive directions will produce power flowing in the positive directions of the coordinate axes. For harmonic vibrations of the form $e^{-j\omega t}$, the flexural acceleration $\ddot{w}$ in the above equation is replaced by $-\omega^2 W$ and the components of the excitation and response are represented by their complex amplitudes.

The above equation is based on the assumptions of thin plate theory for isotropic materials which are discussed in detail in Ref. 1. The basic assumption of small deflections and small slopes of the deformed shape leads to the flexural response represented by Eq. (1) and uncoupled from the in-plane response. The thin plate assumption also implies neglecting of shear deformation and rotary inertia and consequently puts a high-frequency limit to the solution.

For the case of two simply supported edges parallel to the Y axis, it is possible to separate the variables and satisfy the boundary conditions along the simply supported edges by assuming a solution in the form:

$$w(x,y)=\sum_{m=1}^{\infty} W_m(y)\sin\frac{m\pi x}{a}. \tag{2}$$

Substituting (2) into (1), multiplying by $\sin(m'\pi x/a)$, and integrating with respect to x from $x=0$ to $x=a$ gives rise to the equation of vibration in the Y direction governing the mth mode (in the X direction):

$$W_m^{(4)}(y)-2\left(\frac{m\pi}{a}\right)^2 W_m''(y)+\left[\left(\frac{m\pi}{a}\right)^4-\frac{\omega^2\rho h}{D}\right]W_m(y)$$
$$=\frac{2}{aD}\left[Z_e\sin\frac{m\pi x_e}{a}\,\delta(y-y_e)-M_{xe}\sin\frac{m\pi x_e}{a}\frac{\partial}{\partial y}\right.$$
$$\left.\times\delta(y-y_e)-M_{ye}\frac{m\pi}{a}\cos\frac{m\pi x_e}{a}\,\delta(y-y_e)\right]. \tag{3}$$

B. Natural frequencies and mode shapes

The aim of the present study is to find the resonance frequencies and the exact mode shapes for rectangular plates with one edge free and the other edges simply supported so that the solution can be employed in the plate coupling procedure as explained in a subsequent section. The exact mode shapes which must satisfy both the geometric and force boundary conditions are the ones to be used in plate coupling formulation.

The equation governing the free vibrational modes in the Y direction is obtained from Eq. (3) by setting the right-hand side equal to zero. The response along the Y direction may be written in the form:

$$W_m(y)=\sum_{n=1}^{\infty}\overline{W}_{mn}f_n(y), \tag{4}$$

where $f_n(y)$ is the mode shape of the nth mode along the Y direction. It may be expressed as $f_n(y)=Ce^{K_n y}$ which when substituted into the equation of free vibration in the Y direction gives:

$$K_{1n}^2=\left(\frac{m\pi}{a}\right)^2[K_m+1],\quad K_{2n}^2=\left(\frac{m\pi}{a}\right)^2[-K_m+1],$$

$$K_m=\frac{\omega}{(m\pi/a)^2\sqrt{D/\rho h}}. \tag{5}$$

While K_{1n}^2 is always positive, K_{2n}^2 may be positive, zero, or negative depending upon the value of K_m. The cut-off frequency of the mth mode is given by

$$\omega_{\rm co}^{(m)}=\left(\frac{m\pi}{a}\right)^2\sqrt{\frac{D}{\rho h}}. \tag{6}$$

At frequencies below $\omega_{\rm co}^{(m)}$, K_{2n}^2 of the mth mode is positive and the two parts of the response represent a very rapidly decaying response. At frequencies above $\omega_{\rm co}^{(m)}$, K_{2n}^2 is negative and the second part of the response represents a propagating wave.

1. All edges simply supported

In this case, the mode shape in the Y direction takes the form: $f_n(y)=\sin(n\pi y/b)$ and the eigenfrequencies are given by the simple equation: $\omega_{m,n}=[(m\pi/a)^2+(n\pi/b)^2]\times\sqrt{D/\rho h}$.

2. One edge free and the other edges simply supported

Consider a rectangular plate simply supported at the edges $x=0$, $x=a$, and $y=0$ with a free edge at $y=b$. The boundary conditions are[4] $w=M_{yx}=0$ along $y=0$ and $Q_y=M_{yx}=0$ along the free edge $y=b$. The characteristic equation may be written in the form:

$$\tan\left(\frac{m\pi\sqrt{K_m-1}}{r}\right)=\frac{\sqrt{K_m-1}}{\sqrt{K_m+1}}\frac{[K_m+(1-\nu)]^2}{[K_m-(1-\nu)]^2}$$
$$\times\tanh\left(\frac{m\pi\sqrt{K_m+1}}{r}\right),$$

where $r=a/b$ is the aspect ratio and K_m is the nondimensional frequency parameter defined by Eq. (5). The above equation is reported in Ref. 3. Substituting $\alpha_m=\sqrt{K_m-1}$ and $\beta_m=\sqrt{K_m+1}$, the characteristic equation becomes

$$\tan(m\pi\alpha_m/r)=\frac{\alpha_m}{\beta_m}\frac{[\beta_m^2-\nu]^2}{[\alpha_m^2+\nu]^2}\tanh(m\pi\beta_m/r). \tag{7}$$

For each mode m in the X direction, the characteristic equation, Eq. (7), has an infinite number of solutions $K_{m,n}$ ($n=1,2,...,\infty$) representing vibrational modes in the Y direction associated with the mth mode. The resonance frequencies are given by

$$\omega_{m,n}=K_{m,n}\left(\frac{m\pi}{a}\right)^2\sqrt{\frac{D}{\rho h}}. \tag{8}$$

Approximate values of the nondimensional frequency parameter $K_{m,n}$ for $n>1$ may be obtained from the equation:

$$K_{m,n}\cong 1+\left(n-\frac{3}{4}\right)^2\left(\frac{r}{m}\right)^2. \tag{9}$$

For example, for aspect ratios r in the range 0.25–4, this approximate equation gives the resonance frequencies within $\pm 14\%$, 7.5%, 6%, and 2% for modes $(m, 2)$, $(m, 3)$, $(m, 4)$, and $(m, 7)$, respectively. The accuracy increases for higher modes. The approximate values of $K_{m,n}$ may be used for quick estimations or as a start value in the iterative solution of Eq. (7).

The response in the Y direction is expressed as a modal summation:

$$W_m(y)=\sum_{n=1}^{\infty}\overline{W}_{m,n}\left[\sin\left(\frac{m\pi}{a}\alpha_{m,n}y\right)\right.$$
$$\left.+A_{m,n}\sinh\left(\frac{m\pi}{a}\beta_{m,n}y\right)\right], \tag{10}$$

where $A_{m,n}$ is given by

$$A_{m,n}=\frac{(\alpha_{m,n}^2+\nu)}{(\beta_{m,n}^2-\nu)}\,\frac{\sin(m\pi\alpha_{m,n}/r)}{\sinh(m\pi\beta_{m,n}/r)}. \tag{11}$$

The value of $A_{m,n}$ decreases rapidly for higher modes and the mode shape becomes sinusoidal. Reference 3 examined the cases where a solution can exist for the characteristic equation in the attenuation region ($K_{m,n}<1$). This case is not considered here due to the little contribution to the response by a mode below its cut-off frequency.

C. Receptance functions for forced response of flexural vibration

Flexural response to point force and point moment excitations will be written in terms of receptance functions.

In the predictions of forced response of structures, damping has to be introduced to represent the practical damping in the structure and to prevent numerical instability at resonances. The structural (hysteretic) damping model is employed in this work via using the complex modulus $E=E(1-j\eta)$ for harmonic time dependence of the form $e^{-j\omega t}$ (see Ref. 4).

In general, the response of a flat plate with two parallel edges simply supported and the other two edges assume any arbitrary boundary conditions is obtained by applying Galerkin's method[4] to Eq. (3) and employing the natural frequencies, mode shapes, and the orthogonality properties of the normal modes. The forced response at point $p(x,y)$ to harmonic excitation vector $[Z_e,M_{xe},M_{ye}]^T$ at point $p_e(x_e,y_e)$ can be shown to be given by

$$\begin{aligned} w(p,p_e)=&\frac{2}{\rho a h}\sum_m\sum_n\frac{\sin(m\pi x/a)f_{m,n}(y)}{(\bar{\omega}_{m,n}^2-\omega^2)S_{m,n}}\\ &\times\Bigg[Z_e\sin\frac{m\pi x_e}{a}f_{m,n}(y_e)\\ &+M_{ex}\sin\frac{m\pi x_e}{a}f'_{m,n}(y_e)\\ &-M_{ey}\frac{m\pi}{a}\cos\frac{m\pi x_e}{a}f_{m,n}(y_e)\Bigg]\\ =&\,r_{wZ}Z_e+r_{wM_x}M_{ex}+r_{wM_y}M_{ey}. \end{aligned} \tag{12}$$

The part of the response in the above equation which is due to force excitation Z_e has already been reported.[4] The part of the response due to point moment excitations M_{ex} and M_{ey} is developed for the present investigations of the effect of moment excitations in finite plates. It has to be mentioned that damping is introduced in Eq. (12) through the complex eigenfrequency $\bar{\omega}_{mn}^2=\omega_{mn}^2(1-i\eta)$. The out-of-plane response displacement w to excitations Z_e, M_{ex}, and M_{ey} can be expressed as receptance functions r_{wZ}, r_{wM_x}, and r_{wM_y}, respectively, as shown by the last line of Eq. (12). Receptance functions for the out-of-plane rotation θ_x are defined as r_{θ_xZ}, $r_{\theta_xM_x}$, and $r_{\theta_xM_y}$. They are obtained from Eq. (12) by direct differentiation.

D. Structural intensity

The solution of the equation of flexural vibration Eq. (1) gives the response vector at any point (x,y):

$$\mathbf{S}(x,y)=\left[w,\frac{\partial w}{\partial x},\frac{\partial w}{\partial y}\right]^T, \tag{13}$$

where T denotes the transpose of the matrix.

For harmonic vibration and time variation of the form $e^{-j\omega t}$, the velocity vector is given by the relation:

$$\dot{\mathbf{S}}(x,y)=-j\omega\mathbf{S}(x,y). \tag{14}$$

A diagonal force matrix at point (x,y) is defined as

$$\mathbf{F}_d(x,y)=\begin{bmatrix} V_x & 0 & 0 & 0\\ 0 & V_y & 0 & 0\\ 0 & 0 & M_{xy} & 0\\ 0 & 0 & 0 & M_{yx}\end{bmatrix}. \tag{15}$$

The input power is given by

$$\begin{aligned} P_{\text{in}}(x_e,y_e)=&\frac{1}{2}\,\text{Re}\Bigg[Z_e\overset{*}{\dot{w}}(x_e,y_e)+M_{ex}\frac{\partial}{\partial y}\overset{*}{\dot{w}}(x_e,y_e)\\ &-M_{ey}\frac{\partial}{\partial x}\overset{*}{\dot{w}}(x_e,y_e)\Bigg], \end{aligned} \tag{16}$$

where the asterisk denotes the complex conjugate.

Structural intensity components in the x and y directions at any point (x,y) are given by

$$\begin{aligned} I_x(x,y)=&\frac{1}{2}\,\text{Re}\Bigg[Q_x(x,y)\overset{*}{\dot{w}}(x,y)-M_{xy}(x,y)\frac{\partial}{\partial x}\overset{*}{\dot{w}}(x,y)\\ &+M_{xx}(x,y)\frac{\partial}{\partial y}\overset{*}{\dot{w}}(x,y)\Bigg], \end{aligned} \tag{17}$$

$$\begin{aligned} I_y(x,y)=&\frac{1}{2}\,\text{Re}\Bigg[Q_y(x,y)\overset{*}{\dot{w}}(x,y)+M_{yx}(x,y)\frac{\partial}{\partial y}\overset{*}{\dot{w}}(x,y)\\ &-M_{yy}(x,y)\frac{\partial}{\partial x}\overset{*}{\dot{w}}(x,y)\Bigg]. \end{aligned} \tag{18}$$

Following the relations of the Appendix, the above equations become:

$$\begin{aligned} I_x(x,y)=&\frac{1}{2}\,\text{Re}\Bigg[V_x(x,y)\overset{*}{\dot{w}}(x,y)\\ &-M_{xy}(x,y)\frac{\partial}{\partial x}\overset{*}{\dot{w}}(x,y)\Bigg], \end{aligned} \tag{19}$$

$$\begin{aligned} I_y(x,y)=&\frac{1}{2}\,\text{Re}\Bigg[V_y(x,y)\overset{*}{\dot{w}}(x,y)\\ &+M_{yx}(x,y)\frac{\partial}{\partial y}\overset{*}{\dot{w}}(x,y)\Bigg]. \end{aligned} \tag{20}$$

The prediction of power flow at any cross section requires the determination of the internal force vector at that position before applying Eqs. (19) and (20). Two methods may be used to predict the internal force vector at any arbitrary cross

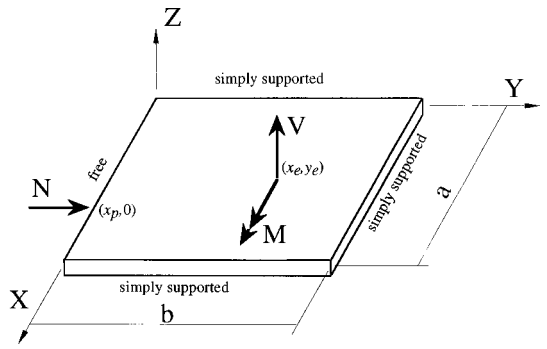

FIG. 2. Flexural and in-plane loading of the plate panels investigated in this work.

section. The first method is to use the force displacement relations[1] which relate the internal stress resultants to the spatial derivatives of response displacements. Reference 20 presents a matrix formulation for this method for coupled beam structures which can also be adapted to plates. The second method is to virtually cut the plate into two at the position of interest, mathematically connect it, and to determine the internal force vector from the displacement compatibility and force equilibrium conditions at that cut edge.

In Eq. (20), V_y is the transverse shear including the effect of the twisting moment M_{yy} according to the Kelvin–Kirchhoff's relation for edge reactions.[1] The Appendix gives a mathematical proof that V_y can replace both Q_y and M_{yy} in the calculation of the transmitted power in the y direction across any cross section perpendicular to the Y direction. A similar approach may be used for V_x in Eq. (19).

II. IN-PLANE VIBRATION OF FLAT RECTANGULAR PLATES

In a previous work of the authors,[11] the two coupled equations governing the in-plane vibration of flat plates are presented and the assumptions are discussed. These two equations are presented here for completion:

$$C_L^2\frac{\partial^2 u}{\partial x^2}+C_T^2\frac{\partial^2 u}{\partial y^2}+(\nu C_L^2+C_T^2)\frac{\partial^2 v}{\partial x\partial y}-\ddot{u}=-\frac{X_e}{\rho h}\delta(x-x_e)\delta(y-y_e), \tag{21}$$

$$C_L^2\frac{\partial^2 v}{\partial y^2}+C_T^2\frac{\partial^2 v}{\partial x^2}+(\nu C_L^2+C_T^2)\frac{\partial^2 u}{\partial x\partial y}-\ddot{v}=-\frac{Y_e}{\rho h}\delta(x-x_e)\delta(y-y_e). \tag{22}$$

The aim of the present section is to examine the in-plane response of a flat plate panel at a free edge to an in-plane excitation perpendicular to the same edge as shown in Fig. 2. The interest in this specific case evolves from the need to consider the in-plane response at the coupling edge of two plates even when the excitation is due to out-of-plane forces and moments. The boundary conditions at the other edges of the plate panel are such that they can be idealized as clamped boundaries for in-plane vibration.

In view of the above discussion, it seems reasonable to consider only the components of in-plane excitation and response at the coupling edge which are perpendicular to that edge. This means neglecting the coupling between the longitudinal response $v(y)$ (perpendicular to the coupling edge) and the transverse response $u(y)$ (parallel to the coupling edge). In Eqs. (21) and (22), the coupling term is the third one in the left-hand side. It shows that the coupling is due to Poisson's effect and to the shear waves accompanying the longitudinal waves. This coupling term is usually small and may be neglected in some cases as shown in Ref. 21. Because the coupling with flexural vibration is the main interest, only Eq. (22) will be considered (after neglecting the coupling term). A solution to this equation, which satisfies the boundary conditions, may be assumed in the form:

$$v(x,y,t)=\sum_{s=1}^{\infty}\sin\frac{s\pi x}{a}\,V_s(y)e^{-j\omega t}. \tag{23}$$

Substituting this solution into Eq. (22) and neglecting the coupling term give rise to the following equation governing the in-plane response due to in-plane excitation perpendicular to the edge (for a single mode s):

$$V_s''+\left[\frac{\omega^2}{C_L^2}-\frac{C_T^2}{C_L^2}\left(\frac{s\pi}{a}\right)^2\right]V_s=-\frac{2F_y}{\rho h a C_L^2}\sin\frac{s\pi x_e}{a}\,\delta(y-y_e). \tag{24}$$

In the above equation, s is the number of half-wavelengths of the response in the X direction and $V_s(y)$ is the accompanying mode shape of the response in the Y direction. The solution to the above equation may be written in the form:

$$V_s(y)=V_s^+e^{\lambda_s y}+v_s^-e^{-\lambda_s y}. \tag{25}$$

The free-vibrational characteristics are obtained from Eq. (24) when the left-hand side is set equal to zero. It can be shown that the characteristic frequency for mode s and the corresponding wave number are given, respectively, by

$$\omega_s=\left(\frac{s\pi}{a}\right)C_T,\quad \lambda_s=\sqrt{\frac{\omega_s^2-\omega^2}{C_L^2}}. \tag{26}$$

ω_s is the cut-off frequency for mode s. From Eqs. (25) and (26) it is evident that the in-plane response of the sth mode is attenuated in the frequency range below ω_s and is propagating at all frequencies above ω_s. This result is true for a plate with infinite extension in the Y direction since no boundary conditions have been introduced yet at $y=0$ and $y=b$ (note that the two parallel edges along the y direction are clamped).

The in-plane forces vanish at the free edge $y=0$. The component of the in-plane force perpendicular to the free edge (see Fig. 1) is given by[1] $N_{yy}=[-Eh/(1-\nu^2)][\partial v/\partial y+v(\partial u/\partial x)]$.

For the special case considered here, the component of the in-plane response along the free edge is neglected $[u(x,0,t)=0]$ and the boundary condition at $y=0$ is simplified to $N_{yy}(x,0)=-Eh/(1-\nu^2)[\partial v/\partial y]_{y=0}=0$. The condition of zero displacement at $y=b$ is expressed as $V_s(b)=0$.

The in-plane vibrational response is obtained by substituting Eqs. (23) and (25) into the above relations for the boundary conditions at $y=0$ and $y=b$. The result is written in the form:

$$v(x,y)=\frac{2(1-\nu^2)F_y(x_g,0)}{Eha}\times\sum_{s=1}^{\infty}\frac{\sin(s\pi x_g/a)\sin(s\pi x/a)}{\lambda_s(1+e^{2\lambda_s b})}\times\left[\frac{e^{2\lambda_s b}}{e^{\lambda_s y}}-e^{\lambda_s y}\right]. \tag{27}$$

The response may be expressed in the form of receptance functions as follows:

$$r_{vY}^{P\text{-}P}(p,p_g)=\frac{v(x,y)}{F_y(x_g,0)}=\frac{2(1-\nu^2)}{Eha}\sum_{s=1}^{\infty}\frac{\sin(s\pi x_g/a)\sin(s\pi x/a)}{\lambda_s(1+e^{2\lambda_s b})}\times\left[\frac{e^{2\lambda_s b}}{e^{\lambda_s y}}-e^{\lambda_s y}\right], \tag{28}$$

$$r_{vY}^{L\text{-}P}(y_r,p_g)_s=\frac{\overline{v}(y_r)}{F_y(x_g,0)}=\frac{2(1-\nu^2)}{Eha}\frac{\sin(s\pi x_g/a)}{\lambda_s(1+e^{2\lambda_s b})}\left[\frac{e^{2\lambda_s b}}{e^{\lambda_s y_r}}-e^{\lambda_s y_r}\right], \tag{29}$$

$$r_{vY}^{L\text{-}L}(y_r,y=0)_s=\frac{\overline{v}(y_r)}{\overline{F}_y(x,0)_s}=\frac{2(1-\nu^2)}{Eha}\frac{1}{\lambda_s(1+e^{2\lambda_s b})}\times\left[\frac{e^{2\lambda_s b}}{e^{\lambda_s y_r}}-e^{\lambda_s y_r}\right]. \tag{30}$$

In the above equations, the subscript g indicates that the position of excitation or response is on the free edge of the plate panel. r_{vY} is the receptance function of the response in-plane displacement component v to the in-plane edge excitation $F_y(x_g,0)$. Both the response and excitation are in the y direction. The superscript P-P in Eq. (28) denotes response at point $p(x,y)$ to excitation at the edge point $p_g(x_g,0)$, i.e., ''point response to point excitation.'' The P-P type receptance is the summation of contributions of all the modes. The L-P receptance of Eq. (29) is the amplitude of the sinusoidal distribution of the response at the cross section $y=y_r$ (a line response) to the excitation at the edge point $p_g(x_g,0)$, i.e., ''line response to point excitation.''

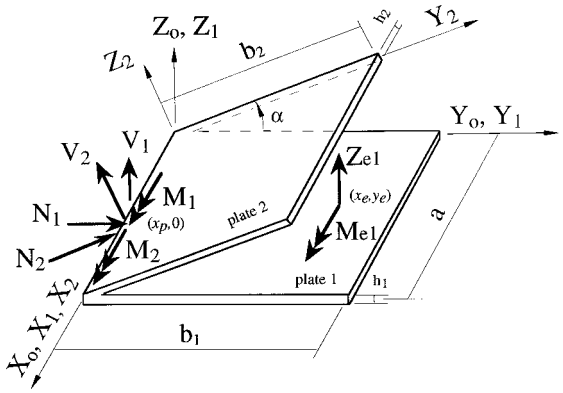

FIG. 3. Two plates coupled at an angle α, all uncoupled edges are simply supported.

Equation (30) is the line response to a sinusoidal excitation of amplitude $F_y(x,0)_s$ along the edge $y=0$, i.e., ''line response to line excitation.'' The L-P and L-L type receptance functions of Eqs. (29) and (30) are relating response and excitations for one specific mode ''s.''

The special case of interest is the response at the coupling edge to in-plane excitation at the coupling edge. The response and the receptance functions are obtained in this special case by substituting $y=0$ (or $y_r=0$) in Eqs. (27)–(30). The special case of Eq. (30) for $y_r=0$ is the one which will be used in the plate coupling formulation in the next section.

III. TWO COUPLED PLATES

In this section, a modal receptance formulation is presented for the prediction of the dynamic response and power flow in two plates coupled at an arbitrary angle. The mathematical model considers the coupling between the two components of flexural vibration, namely; bending and shear, and the component of in-plane vibration perpendicular to the coupling edge.

A. Forces, displacements, and transformation

Figure 1 shows the internal forces acting upon and the displacement components at the center of an infinitesimal element of a thin flat plate. The force vector at any cross section perpendicular to the y axis is $\mathbf{F}=[N_{yy}\ V_{yz}\ M_{yx}]^T$ and the displacement vector is $\mathbf{S}=[v\ w\ \theta_x]^T$.

It can be seen from Fig. 3 that the force and displacement vectors in the global system of axes (X_o,Y_o,Z_o) are related to those in the local system (X_l,Y_l,Z_l) via a transformation matrix $\mathbf{T}$ by the relations:

$$\mathbf{F_o}=\mathbf{T}\mathbf{F}_l,\quad \mathbf{S_o}=\mathbf{T}\mathbf{S}_l, \tag{31}$$

where the subscripts o and l refer to global and local coordinates, respectively. The subscript l is 1 or 2 for plate 1 or plate 2, respectively.

The transformation matrix is an orthogonal matrix satisfying the relation: $\mathbf{T}^{-1}=\mathbf{T}^T$. It is given, in this case, by

$$\mathbf{T}=\begin{bmatrix}\cos\alpha & -\sin\alpha & 0\\ \sin\alpha & \cos\alpha & 0\\ 0 & 0 & 1\end{bmatrix}.$$

B. Force-displacement relations

Employing the concept of receptance functions presented in the previous sections, the general relation between forces and displacements is written in the following matrix form:

$$\begin{bmatrix} v \\ w \\ \theta_x \end{bmatrix} = \begin{bmatrix} rij_{vY} & 0 & 0 \\ 0 & rij_{wZ} & rij_{wM} \\ 0 & rij_{\theta Z} & rij_{\theta M} \end{bmatrix} \begin{bmatrix} N \\ V \\ M \end{bmatrix}. \tag{32}$$

A more compact form is $[\mathbf{S}]=[\mathbf{rm}ij][\mathbf{F}]$, where $[\mathbf{rm}ij]$ is the receptance matrix. The components of the receptance matrix are the receptance functions relating response to excitations at the specified positions and directions. For example, rij_{vY} is the in-plane response v at position i to an excitation N_{yy} of unit quantity at position j. The subscripts are removed from the force components of Eq. (32).

In the following analysis $[\mathbf{rm}ii_1]$ and $[\mathbf{rm}ii_2]$ are receptance matrixes for response at the coupling edge to excitation force vectors $[\mathbf{F}i_1]$ and $[\mathbf{F}i_2]$ at the coupling edge for plate 1 and plate 2, respectively. $[\mathbf{rm}ie_1]$ is the receptance matrix for response at the coupling edge to an excitation force vector $[\mathbf{F}e_1]$ at position $p_e(x_e,y_e)$ in the middle plane of plate 1.

C. Coupling relations

For the two coupled plates shown in Fig. 3, the global axes (X_o,Y_o,Z_o) coincide with the local axes (X_1,Y_1,Z_1) of plate 1. The transformation matrix of plate 1 ($\alpha=0$) is a 3×3 unit matrix. The equilibrium of forces and compatibility of displacements at the coupling edge are given, respectively, by

$$[\mathbf{F}i_1]+[\mathbf{T_2}][\mathbf{F}i_2]=\mathbf{0}_{3\times1}, \tag{33}$$

$$[\mathbf{S_1}]=[\mathbf{T_2}][\mathbf{S}_2]. \tag{34}$$

The force-displacement relations for plate 1 and plate 2 are, respectively,

$$[\mathbf{S_1}]=[\mathbf{rm}ii_1][\mathbf{F}i_1]+[\mathbf{rm}ie_1][\mathbf{F}e_1], \tag{35}$$

$$[\mathbf{S_2}]=[\mathbf{rm}ii_2][\mathbf{F}i_2]. \tag{36}$$

Equations (33)–(36) can be solved for the internal force vector $[\mathbf{F}i_1]$ at the coupling edge in plate 1. This is carried out by substituting Eqs. (35) and (36) into Eq. (34) and solving the resulting equation and Eq. (33) for $[\mathbf{F}i_1]$ and $[\mathbf{F}i_2]$. The orthogonality property of the transformation matrix is also employed to get the following relation in $[\mathbf{F}i_1]$:

$$[\mathbf{F}i_1]=(-1)\{[\mathbf{rm}ii_1]+[\mathbf{T_2}][\mathbf{rm}ii_2][\mathbf{T_2}]^T\}^{-1}[\mathbf{rm}ie_1] \times[\mathbf{F}e_1]. \tag{37}$$

Employing the concept of the line-line and line-point modal receptances as discussed before, substitution of the elements of the transformation and the receptance matrices into Eq. (37) and performing some mathematical manipulation, the following equation is obtained:

$$\begin{bmatrix} \overline{Y}_{s,m} \\ \overline{Z}_{s,m} \\ \overline{M}_{s,m} \end{bmatrix}_{\text{plate 1}} = (-1) \begin{bmatrix} r11 & r12 & r13 \\ r21 & r22 & r23 \\ r31 & r32 & r33 \end{bmatrix}^{-1}_{L\text{-}L} \times \begin{bmatrix} 0 \\ rie1_{wZ}Ze_1+rie1_{wM}Me_1 \\ rie1_{\theta Z}Ze_1+rie1_{\theta M}Me_1 \end{bmatrix}_{L\text{-}P}, \tag{38}$$

where the elements $r11-r33$ are given by

$$r11=rii1_{vY}+C^2rii2_{vY}+S^2rii2_{wZ},$$

$$r12=r21=SC(rii2_{vY}-rii2_{wZ}),$$

$$r13=r31=-Srii2_{wM},$$

$$r22=rii1_{wZ}+S^2rii2_{vY}+C^2rii2_{wZ},$$

$$r23=r32=rii1_{wM}+Crii2_{wM},$$

$$r33=rii1_{\theta M}+rii2_{\theta M},$$

$$S\equiv\sin\alpha, \quad C\equiv\cos\alpha.$$

Equation (38) gives directly the amplitudes of the modal forces acting on plate 1 at the coupling edge with plate 2. These modal forces are for mode s of in-plane vibration which simultaneously occur with mode m of flexural vibration. The total response is the summation of the response for all combinations of modes s and m. The equation calculates the modal response to an excitation vector $\mathbf{F}e_1=[0\ Ze_1\ Me_1]^T$ at position (x_e,y_e) of plate 1 as shown in Fig. 3. The subscript L-L of the first matrix in the right-hand side of Eq. (38) indicates that the matrix includes line-line receptance functions which relate the amplitude of the modal response along the coupling edge to a modal force of unit amplitude applied along the same edge. The subscript L-P of the second matrix indicates that it includes line-point receptance functions which relate the amplitude of the modal response along the coupling edge to one force component of unit amplitude applied at the excitation point (x_e,y_e).

IV. COMPUTATIONAL EXAMPLES

A. Flexural response to simultaneous point force and moment excitation

The resonant behavior of a rectangular plate excited simultaneously by point force and point moment is computationally investigated. A steel plate of dimensions $0.5\times1.0\times0.0016$ m is simultaneously excited at point (0.19, 0.17) by 1.0 N force and 0.01 Nm moment about an axis parallel to the X axis as shown schematically in the left-bottom corner of Fig. 4. The material properties used are $E=205\times10^9$ N/m^2, $\rho=7800$ kg/m^3, $\nu=0.28$, and $\eta=0.001$. This example is representative of the practical case where the excitation of a plate through machine isolators is mainly by a force in the direction perpendicular to the plate. The small moment excitation is a result of practical imperfections and tolerances.

The resonance frequencies can be identified from the peaks of the input power spectrum in Fig. 4(a). If more than one resonant mode has the same frequency, the power spec-

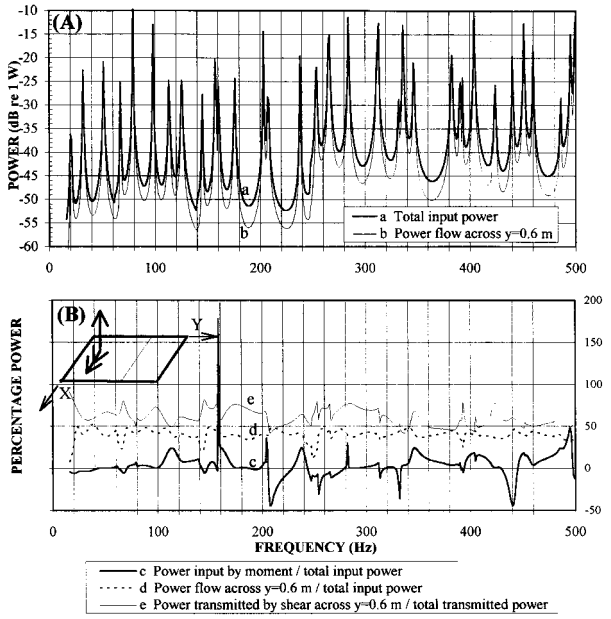

FIG. 4. Input and transmitted power in a rectangular plate simultaneously excited by point force and point moment.

trum will show them as one mode. The power input by the moment component is 10–20 dB below that due to the force in the nonresonance bands. In the resonance bands, the power input by this very small moment component is not very small and may be positive or negative as shown by plot ''c'' of Fig. 4(b). For example, 25% of the input power at 113 Hz is due to the moment excitation. The behavior at 158 Hz is worth noting. The input power is mainly by moment because the line of action of the moment is very close to a nodal line where the rotational response is maximum. Negative power is done by the force component which means that the plate is vibrating in such a way that it is moving against the force and doing work on the force. This very narrow resonance band is a clear example of the importance of moment excitation at some low-frequency resonant bands.

Reference 10 shows that in a semi-infinite plate excited by a point moment, the input power is directly proportional to frequency and inversely proportional to the bending stiffness of the plate, leading to a general conclusion that the input power in this case is important at high frequencies. However, the present example and Fig. 4 shows that moment excitation of thin finite plates can inject a considerable amount of power, compared to force excitation, at some resonant bands at low frequencies as can be seen in the resonance band at 158 Hz. More computational examples show that the thinner the plate the more power is input by moment excitation. In Fig. 4, plot ''d'' presents the frequency dependence of the total power flowing through the cross section $y=0.6$ m and plot ''e'' shows that the power flowing across this section is shared by shear and moment at a ratio which is also frequency dependent.

Figure 5 presents the spatial distribution of the total and the shear and moment components of power flow along cross-section $y=0.6$ m. As the plate is simply supported at $x=0$ and $x=a$, the solution represented by Eq. (12) and the force-displacement relations (see Ref. 1) suggest that the

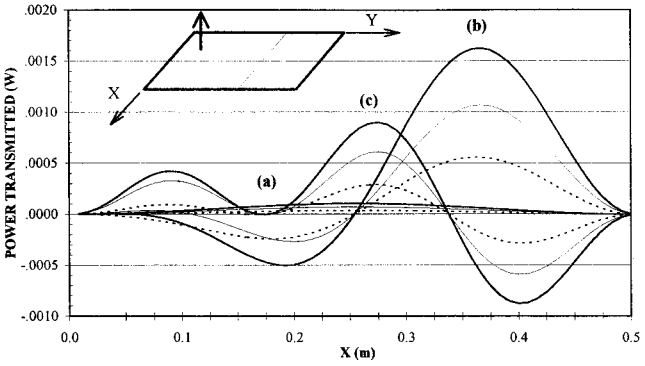

FIG. 5. Spatial distribution of power transmitted through the cross section $y=0.6$ m in a rectangular plate at (a) 51 Hz, (b) 98 Hz, (c) 157 Hz. ———— total power, ------ shear component, - - - - moment component.

modal components of force and displacement response along any cross section parallel to the X axis have a sinusoidal distribution. The contribution to plate response from a specific mode below its cut-off frequency is very small and is highly attenuated as explained in Sec. I B. This leads to the conclusion that below the cut-off frequency of the second mode, the plate response is mainly due to the first mode and the spatial distribution of the response in the X direction is approximately a half-sine-wave as illustrated in Fig. 5 at 51 Hz. Below the cut-off frequency of the third mode and above the cut-off frequency of the second mode, the response is mainly due to contributions of both the first and the second modes. This explains the reason for the distributions presented in Fig. 5 at 98 Hz. This result also highlights the reason for the circulatory patterns of active structural intensity in plates as presented, for example, in Ref. 19. It can be seen from Fig. 5(a) that the total vibrational power at 51 Hz flows away from the excitation point (the source) along the whole cross section $y=0.6$ m. At 98 Hz, the vibrational power flows towards the excitation point along the part of this cross section between $x=0$ and 0.26 m and flows away from the excitation point between $x=0.26$ and 0.5 m. The net power flow is always directed away from the source. It is also clear now why this circulatory pattern changes with frequency. The participation of both shear and moment in transmitting power across any cross section is also evident in Fig. 5. The spatial distribution of power flow, as presented by Fig. 5, was verified experimentally. The results are reported in Ref. 22.

B. Two coupled plates at arbitrary angle

Two coupled plates are shown schematically in Fig. 3. The dimensions used in the computations are $h_1=h_2=0.012$ m, $a=1.2$ m, $b_1=1.3$ m, and $b_2=1.0$ m. The two plates are assumed to be made of steel with the same material and damping properties as in the first example. Plate 1 is excited at point (0.455, 0.79, 0.0) by 1.0 N force in the Z direction and 0.01 Nm moment about an axis parallel to the X axis.

The in-plane response of plate 1 to an in-plane force of 1.0 N amplitude and distribution of the form $\sin(s\pi x/a)$ along the coupling edge is presented in Fig. 6. The peaks of the response correspond to the in-plane resonance frequen-

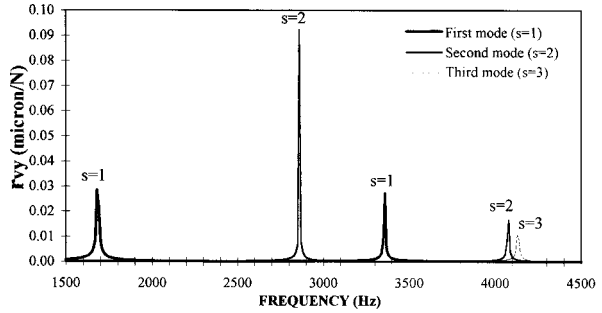

FIG. 6. In-plane resonances of plate 1 of the coupled plates of Fig. 3.

cies for $s=1$, 2, and 3 in the frequency range up to 4500 Hz. Guided with the results of Fig. 6, the dynamic response and power flow characteristics of the coupled plates are examined in two frequency ranges, namely, 0–500 Hz and 1500–2000 Hz. The total input power, total power flow through the coupling edge, and the components of power flow transmitted across the coupling edge by moment, transverse shear, and inplane longitudinal (perpendicular to the coupling edge) waves are presented in Fig. 7(a) for the lower frequency range and in Fig. 7(b) for the higher frequency range. The coupled plates are at a right angle in this part of the investigation.

In the frequency range 0–500 Hz, the power transmission across the coupling edge is mainly due to moment. It can be easily seen that the two plots for total transmitted power and the power carried by moment coincide. Meanwhile, the power transmitted by transverse shear and in-plane longitudinal waves is some 30 dB below the input power at both resonance and nonresonance frequencies. This result agrees with the previously reported work that the coupling is due to bending moment and the coupling edge may be assumed as pinned.[23] However, the situation is different in the frequency range 1500–2000 Hz. In this frequency range the

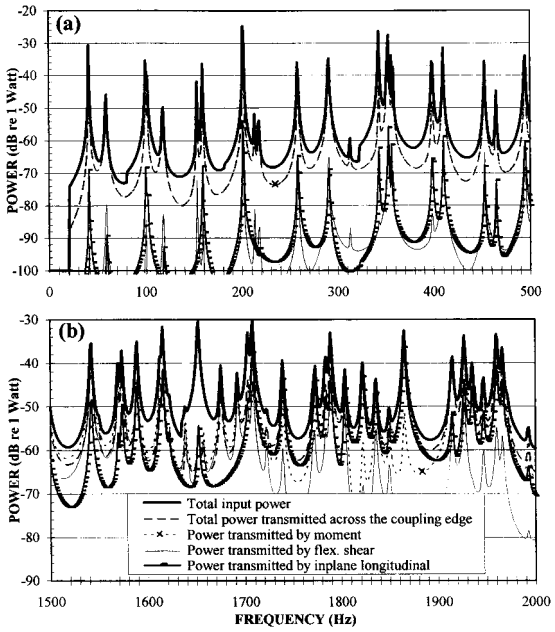

FIG. 7. Input power and components of power flow across the common edge of two perpendicular plates.

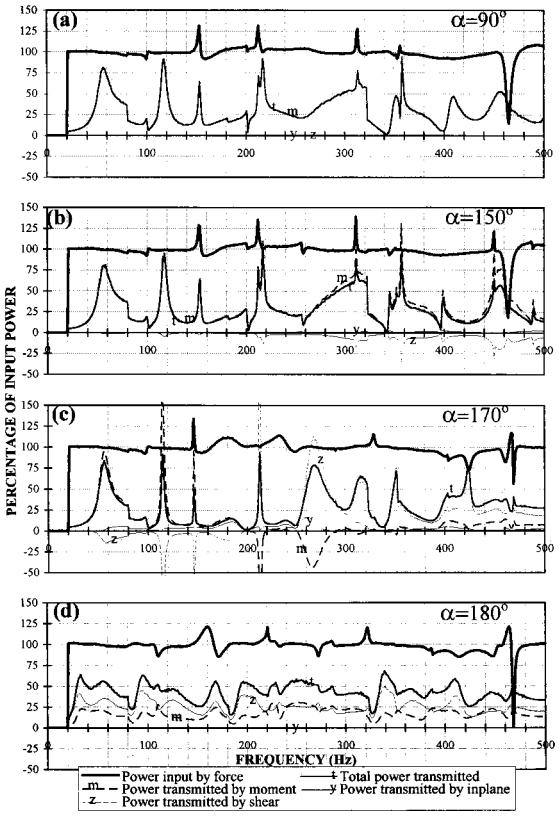

FIG. 8. Components of input power and of power flow across the coupling edge (expressed as percentage of total input power) for different plate angles in the frequency range 0–500 Hz.

first in-plane resonances of the uncoupled plate panels occur as illustrated by Fig. 6 (for plate 1). Consequently, an increased role of the in-plane waves in transmitting vibrational power across the coupling edge is expected. In Fig. 7(b), it is clear that the power transmitted by the in-plane wave increases as the frequency band of the first in-plane resonance is approached. This is obvious in Fig. 7(b) above 1700 Hz. Power transmitted by the in-plane wave is only 1 dB lower than the total transmitted power at the resonance frequency 1773 Hz. The participation of the moment in transmitting power across the coupling edge decreases as the in-plane resonance is approached. It becomes lower than the participation of the in-plane longitudinal wave in the frequency range 1715–1890 Hz. The coupling is no longer dominated by bending and it is not justified to use an assumption of pinned joint at the coupling edge. In this frequency range, the in-plane vibration cannot be neglected. The outset of the increasing role of in-plane vibration can be quantified using the approximate and simple relation given by the first of Eqs. (26) to estimate the cut-off frequency of the first in-plane mode.

The effect of increasing the coupling angle α from 90° to 180° on the input and transmitted power flow components is illustrated in Fig. 8 for the frequency range up to 500 Hz and in Fig. 9 for the frequency range 1500–2000 Hz. The following observations are worth noting:

(1) The first cut-off frequency for the flexural vibration of the coupled plate is 20 Hz. This is the reason for the

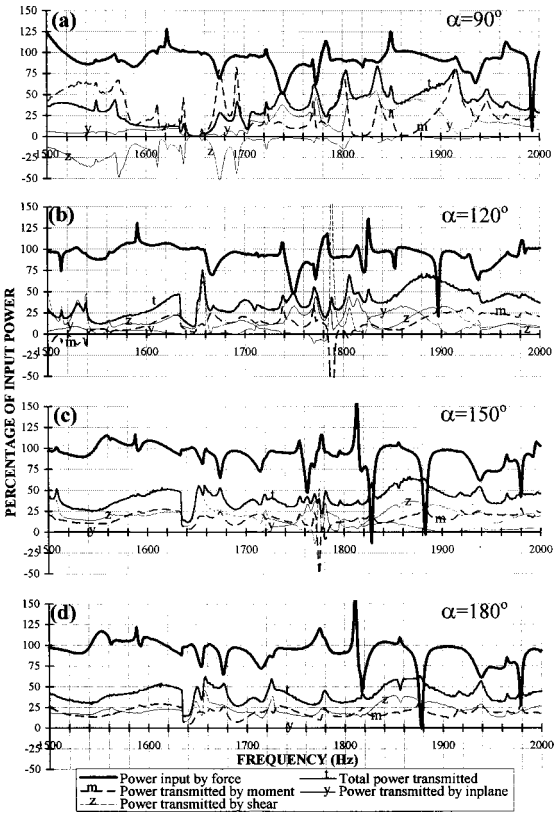

FIG. 9. Components of input power and of power flow across the coupling edge (expressed as percentage of total input power) for different plate angles in the frequency range 1500–2000 Hz.

nearly nil values of power flow below this frequency in Fig. 8.

(2) Up to 500 Hz, at 90° coupling angle, the power flow through the coupling edge is due to moment. The participation of shear (flexural shear) and in-plane waves is practically zero. This feature of power flow does not change up to 150° as shown in Fig. 8(b) where the participation of shear is small and limited in narrow bands.

(3) Up to 500 Hz, most of the changes of the contributions of power flow components happen as the plate angle changes between 170° and 180°. This is evident from Fig. 8(c) and (d). The role of the in-plane response in transporting power is still very small if not negligible.

(4) In the frequency range 1500–2000 Hz (see Fig. 9), power flow through the coupling edge is participated by moment and shear at frequencies up to the first cut-off frequency of in-plane vibration. This is the case for all plate angles from 90° to 180°. Meanwhile, above the cut-off frequency of in-plane vibration, power is transmitted mainly by bending and in-plane for $\alpha=90°$, by bending and shear for $\alpha=180°$, and by moment, shear, and in-plane for plate angles between 90° and 180°.

(5) The diminishing role of in-plane vibration in carrying power across the coupling edge at low and high frequencies when the plate angle is close to or equal 180° may be understood in view of the mostly symmetric configuration of the two coupled plates. The two coupled plates have a common edge, the same thickness and material properties. No external in-plane excitation applies to any of them (other than coupling forces at the common edge). The only difference is in the dimensions perpendicular to the coupling edge which is 1.3 m for the first plate and 1.0 m for the second one. As a consequence of such configuration, little difference is to be expected between the in-plane response of the two component plates perpendicular to the coupling edge. The power transmitted by in-plane waves across the coupling edge, as a result, is expected to be very small.

Experimental investigations are presented in Ref. 22 which further highlight the nature of coupling between two coupled plates, the role of in-plane response at the coupling edge, and the in-plane vibrational modes in the frequency range up to 5000 Hz.

V. CONCLUSIONS

Flexural mode shapes and resonance frequencies for rectangular plate panels with one edge free and the other edges simply supported are derived. The mode shapes satisfy both geometric and force boundary conditions. Using the computational capabilities available now, these predictions are accurate enough that it can be used in solving plate coupling problems taking the effect of transverse shear into consideration. Wave propagation characteristics are discussed. A closed-form simple expression is derived for the approximate estimation of resonance frequencies of higher flexural modes. The forced flexural response to point force and point moment excitations is expressed in the form of modal receptance functions.

An approximate solution is presented for the in-plane response of the same plate panels when excited by in-plane forces perpendicular to the free edge. A simple expression is given for an approximate estimation of the cut-off frequencies for the different in-plane modes. The in-plane frequency response is also presented as a receptance function.

A mathematical model is developed employing these receptance functions for the coupling of two finite plates at an arbitrary angle for the prediction of dynamic response and power flow at the coupling edge and at any cross section. The coupling at the joint edge considers bending, out-of-plane shear, and in-plane longitudinal (perpendicular to the joint edge) waves. No constraint is imposed on the in-plane displacement perpendicular to the coupling edge. The in-plane response parallel to the coupling edge is not considered because it is not coupled to the flexural response in the planes perpendicular to the coupling edge.

The flexural response of flat plates to simultaneous excitation by out-of-plane concentrated force and moment is investigated by a computational example adopting the modal receptance solution. The spectrums of the components of input power due to point force and point moment excitations are compared to illustrate their resonant characteristics and the importance of the moment excitation in some resonance bands even at low frequencies. The spatial distributions of the components of the flexural power transmitted by shear and moment across a section of the plate are investigated and the reason for the circulatory patterns of active power flow in plates is illustrated.

The power flow characteristics of two plates coupled at an arbitrary angle is examined by a computational example.

The effect of the coupling angle on the components of input power and power flow across the coupling edge is investigated. It is found that the coupling of the two plates is mainly due to moment at frequencies up to the cut-off frequency of the first in-plane mode. As the frequency goes through and exceeds this first cut-off frequency, the coupling becomes due to out-of-plane shear and in-plane vibration with a diminishing participation of the moment in transmitting vibrational power.

ACKNOWLEDGMENT

Support for this work from the Australian Research Council, the Engineering Foundation of Western Australia, and Transfield (Australian Shipbuilding Industries W.A.) is gratefully acknowledged.

APPENDIX: POWER TRANSMITTED BY TRANSVERSE SHEAR AND TWISTING MOMENT

Figure A1 shows a plate cross section perpendicular to the Y axis. The middle plane of the plate is lying in the xy plane. The internal transverse shear force intensities and twisting moment intensities (per unit length of the cross section) acting at positions $(x-\Delta x)$, x, $(x+\Delta x)$ are shown. A twisting moment $M_{yy}(x)$ at x may be replaced by two equal and opposite forces of magnitude $M_{yy}(x)/\Delta x$ acting at points $(x-\Delta x/2)$ and $(x+\Delta x/2)$. Each of the twisting moments at $(x-\Delta x)$ and $(x+\Delta x)$ is similarly replaced by two forces as shown in Fig. A1. It follows that the transverse shear at x considering the effect of the twisting moment is

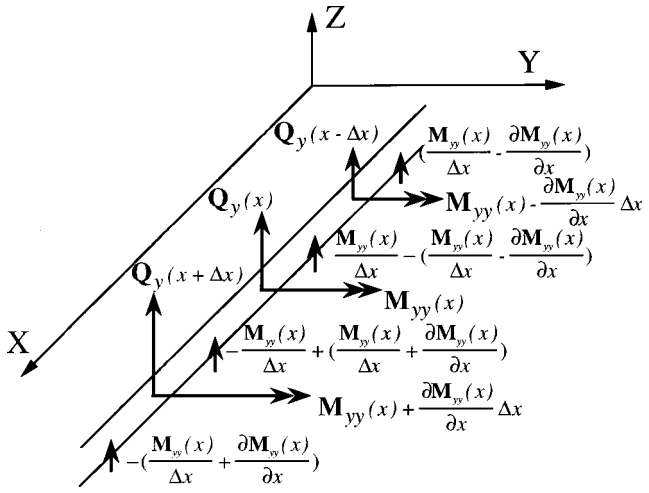

FIG. A1. Reactions due to twisting moments in thin plates.

$$V_y(x)=Q_y(x)+\frac{\partial M_{yy}}{\partial x}. \tag{A1}$$

Equation (A1) is the well-known ''Kelvin–Kirchhoff'' equation for edge reaction which can also be applied at any cross section to combine the effect of the transverse shear and the twisting moment.

Total transmitted power by the shear and twisting across Δx

$$=\text{Power transmitted by } Q_y(x)+\frac{1}{2}\text{ power transmitted by }\frac{\partial M_{yy}(x)}{\partial x}\text{ at }(x-\Delta x/2)$$

$$+\frac{1}{2}\text{ power transmitted by }\frac{\partial M_{yy}(x)}{\partial x}\text{ at }(x+\Delta x)$$

$$=Q_y(x)\dot{w}(x)\Delta x+\frac{\partial M_{yy}}{\partial x}\left[\frac{\dot{w}(x)+\dot{w}(x-\Delta x)}{2}\right]\frac{\Delta x}{2}+\frac{\partial M_{yy}}{\partial x}\left[\frac{\dot{w}(x)+\dot{w}(x+\Delta x)}{2}\right]\frac{\Delta x}{2}.$$

Substituting for $\dot{w}(x-\Delta x)=\dot{w}(x)-(\partial\dot{w}/\partial\mathbf{x})\Delta\mathbf{x}$ and $\dot{w}(x+\Delta x)=\dot{w}(x)+(\partial\dot{w}/\partial\mathbf{x})\Delta\mathbf{x}$ in the above equation, the following relation is obtained:

Power transmitted by shear and twisting

$$=\left[Q_y(x)+\frac{\partial M_{yy}(x)}{\partial x}\right]\dot{w}(x)\Delta x=V_y(x)\dot{w}(x)\Delta x. \tag{A2}$$

This leads to the conclusion that the resultant reaction V_y may replace both the transverse shear Q_y and the twisting moment M_{yy} in the calculation of transmitted power.

[1] A. Leissa, *Vibration of Plates* (Acoustical Society of America, Woodbury, NY, 1993).

[2] G. B. Warburton, ''The vibration of rectangular plates,'' Proc. Inst. Mech. Eng. **168**, 371–384 (1954).

[3] A. Leissa, ''The free vibration of rectangular plates,'' J. Sound Vib. **31**, 257–295 (1973).

[4] W. Soedel, *Vibrations of Shells and Plates* (Marcel Dekker, New York, 1981).

[5] H. G. D. Goyder and R. G. White, ''Vibrational power flow from machines into built-up structures, Part 1: Introduction and approximate analyses of beam and plate-like foundations,'' J. Sound Vib. **86**, 59–75 (1980).

[6] R. S. Langley, ''Application of the dynamic stiffness method to the free and forced vibrations of aircraft panels,'' J. Sound Vib. **135**, 319–331 (1989).

[7] C. H. Hansen and A. J. Young, ''Active control of vibration transmission in a stiffened semi-infinite plate,'' Proceedings of 3rd International Congress on Air- and Structure-Borne Sound and Vibration, Montreal, Canada, 1994 (International Scientific Publications, Auburn, GA), pp. 1485–1494.

[8] S. Azimi, J. F. Hamilton, and W. Soedel, ''The receptance method applied to the free vibration of continuous rectangular plates,'' J. Sound Vib. **93**, 9–29 (1984).

[9] I. Dyer, ''Moment impedance of plates,'' J. Acoust. Soc. Am. **32**, 1290–1297 (1960).

[10] B. A. T. Petersson, ''Structural acoustic power transmission by point mo-

ment and force excitation, Part II: Plate-like structures,'' J. Sound Vib. **160**, 67–91 (1993).
[11] N. H. Farag and J. Pan, ''Free and forced inplane vibration of rectangular plates,'' J. Acoust. Soc. Am. **103**, 408–413 (1998).
[12] A. C. Nilsson, ''Attenuation of structure-borne sound in superstructures on ships,'' J. Sound Vib. **55**, 71–91 (1977).
[13] J. L. Guyader, C. Boisson, and C. Lesueur, ''Energy transmission in finite coupled plates, Part 1: Theory,'' J. Sound Vib. **81**, 81–92 (1982).
[14] Y. Shen and B. M. Gibbs, ''An approximate solution for the bending vibrations of a combination of rectangular thin plates,'' J. Sound Vib. **105**, 73–90 (1986).
[15] R. S. Langley, ''Elastic wave transmission coefficients and coupling loss factors for structural junctions between curved panels,'' J. Sound Vib. **169**, 297–317 (1994).
[16] R. H. Lyon, ''Inplane contribution to structural noise transmission,'' Noise Control Eng. J. **26** (1), 22–27 (1986).
[17] J. S. Kim, H. S. Kim, H. J. Kang, and S. R. Kim, ''Effect of inplane modes in SEA on structure-borne noise transmission in ship structures,'' Proceedings of 4th International Congress on Sound and Vibration, 1996 (International Scientific Publications, St. Petersburg, Russia), pp. 217–222.
[18] J. M. Cuschieri and M. D. McCollum, ''In-plane and out-of-plane waves' power transmission through L-plate junctions using the mobility power flow approach,'' J. Acoust. Soc. Am. **100**, 857–870 (1996).
[19] D. U. Noiseux, ''Measurement of power flow in uniform beams and plates,'' J. Acoust. Soc. Am. **47**, 238–247 (1970).
[20] N. H. Farag and J. Pan, ''Dynamic response and power flow in 3-dimensional coupled beam structures. Part 1. Analytical modeling,'' J. Acoust. Soc. Am. **102**, 315–325 (1997).
[21] N. H. Farag and J. Pan, ''Modal characteristics of inplane vibration of rectangular plates,'' J. Acoust. Soc. Am. (submitted).
[22] N. H. Farag, ''Dynamic response and power flow characteristics of coupled structures—A modal receptance approach,'' Ph.D. thesis (submitted to The Department of Mechanical and Materials Engineering, University of Western Australia, 1998).
[23] J. M. Cuschieri and B. Cimmerman, ''Mobility power flow analysis of an L-shaped plate structure subjected to distributed loading,'' CETIM, Selis (France), 431–440 (1990).

One-dimensional distributed modal sensors and the active modal control for planar structures

Nobuo Tanaka,[a] Yoshihiro Kikushima, and Neil J. Fergusson
Sound and Vibration Division, Mechanical Engineering Laboratory, 1-2 Namiki, Tsukuba Science City, Ibaraki 305, Japan

(Received 29 August 1997; accepted for publication 16 March 1998)

This paper discusses distributed parameter sensors designed to extract vibration modes of a structure, as well as its active modal control. Compared to conventional point sensors such as accelerometers or displacement sensors, the distributed parameter sensors are superior to point sensors provided that they are properly designed. First, this paper overviews a conventional modal filter method using point sensors, and enumerates the problems they possess. To overcome the drawbacks of the point sensor-based modal filtering, a novel modal filtering technique based upon distributed parameter PVDF film sensors is proposed. This paper begins by discussing a design methodology for modal filtering using two-dimensional distributed sensors. Then, taking into consideration the applicability of the sensors, a design procedure for modal filtering using one-dimensional sensors is presented, the number, location, and shaping functions for the one-dimensional modal sensors being clarified. Furthermore, the modal filtering using the one-dimensional sensors is found to be applicable for two-dimensional structures subject to any ''classical'' boundary condition. Experimental results verify the capability of the desired modal filtering for both isolated and degenerate structural modes. Finally, using the modal sensors, experiments on active modal control are conducted, showing a significant suppression of the targeted mode without causing instability of the control system. [S0001-4966(98)00107-6]

PACS numbers: 43.40.Vn [PJR]

INTRODUCTION

Over the last decade interest in active vibration control has increased dramatically in response to the rapid advances in microprocessor technology that make the physical realization of such control systems possible. A large number of studies on active vibration control have been reported using classical control,[1] feedforward control, modern control,[2] and robust control.[3] Regardless of what control theory is employed, however, the essential conception of active vibration control relies upon modal control,[4–6] which is defined as control that changes the modes of a targeted structure to achieve the desired control objectives. Rosenbrock[4] appears to have been the first to propose modal control of a process, the concept being extended by Murray-Lasso,[5] Gould,[6] and Schlaefer[7] to include linear distributed-parameter systems.

Difficulty in modal control lies in the tremendous number of sensors required to construct a modal filter (or modal analyzer termed by Takahashi[8]), which is indispensable for modal control. When reviewing the reports on modal filtering, most papers would be dependent on the utilization of point sensors for implementing a modal filter, mainly due to the availability of only point-type sensors at that time. For instance, theoretical development has been used several times in the past for computer simulation studies of various aspects of active modal control using point sensors (see, for example, Morgan[9]). There are, however, practical difficulties in implementing such a point measurement-based modal sensing system for real problems. These problems arise from the number of measurements which are required to resolve modes with adequate fidelity. For example, if there are (a modest) 20 modes in the frequency band of interest to be resolved, then 40–60 transducers may be required. The signals from these transducers must be sampled by the control system, and each signal multiplied by the appropriate modal filtering coefficient. Constructing an electronic system with as many inputs is neither a trivial nor inexpensive task, and the need to perform an even larger number of multiple and accumulate operations (the computational part of modal filtering) in real time can be a significant burden even for high-speed digital signal processors.

The other way to reduce the burden is to exchange point sensors for distributed parameter sensors[10–13] such as PVDF film sensors. The distributed parameter sensor can be viewed as the limit of an infinite number of point sensors, thereby reducing a large number of point sensors. If it is possible to use distributed parameter sensors, the control information of a vibration field can be obtained not from points, but from lines or areas. Thus enhanced observability results in global vibration attenuation, free from the ill effects of observation spillover.[14]

The application of PVDF film sensors can be traced back to Lee and Moon[15] for measuring modal amplitudes. The applications, thereafter, have been limited to one-dimensional structures and cantilever plates for modal filtering. Although there have been some attempts[16] to apply the distributed sensors to a two-dimensional structure, the sys-

[a]Current address: Department of Production, Information and Systems Engineering, Tokyo Metropolitan Institute of Technology, 6-6 Asahigaoka, Hino-shi, Tokyo 191-0065, Japan.

tematic design procedure for modal filtering of a two-dimensional structure using the distributed parameter sensors has yet to be clarified.

It is the purpose of this paper to present the design methodology of a PVDF film sensor in view of filtering out a modal parameter of a two-dimensional planar structure. First, this paper overviews a conventional modal filter method using point sensors, and points out the problems they have. To overcome the drawbacks of the point sensor-based modal filter, a novel modal filtering technique based upon a distributed parameter PVDF film sensor is proposed. This paper begins by discussing a design methodology for modal filtering using two-dimensional distributed sensors. Then by considering the applicability of the sensors, a design procedure for one-dimensional sensors for modal filtering is presented, the number, location, and shaping function of the one-dimensional modal sensors clarified. Furthermore, modal filtering using the one-dimensional shaped sensors is found to be applicable for two-dimensional structures with any ''classical'' boundary conditions. Experimental results show the capability of modal filtering not only for an isolated mode but also a degenerate mode.

Finally, using one-dimensional modal sensors, experiments on active modal control are conducted, showing a significant reduction of the targeted modal amplitude without causing instability of the control system.

I. MODAL FILTERING USING POINT SENSORS

There are two common approaches to the problem of modal filtering. The first relies on modal orthogonality, where the complex modal amplitude of displacement w_i of the ith mode can be extracted from a known structural displacement distribution through the relationship

$$w_i = \int_D \varphi_i(\mathbf{r}) w(\mathbf{r}) dx\ dy, \tag{1}$$

where $w(\mathbf{r})$ is the displacement of the structure at location $\mathbf{r}=(x,y)$, and $\varphi_i(\mathbf{r})$ is the ith eigenfunction. Modal filtering can be constructed by implementing Eq. (1) numerically using measurements of the structural displacement at discrete locations (described by Meirovitch and Buruh[17]).

The second approach to modal filtering uses a least-squares, rather than numerical integration, problem format. To develop this, note that the output amplitude from a set of n sensors can be expressed in matrix form as

$$\tilde{\mathbf{y}} = \mathbf{\Psi}\mathbf{w}, \tag{2}$$

where $\tilde{\mathbf{y}}$ is the $(n\times 1)$ vector of sensor output amplitudes, $\mathbf{w}$ is the modal displacement vector, and $\mathbf{\Psi}$ is a sensitivity matrix, the i-, jth term of which describes the output of the ith sensor in response to a unit amplitude of mode j. For the most common discrete displacement or velocity sensors (accelerometers), the i-, jth term of $\mathbf{\Psi}$ is equal to the value of the jth mode shape function at the location of the ith sensor.

Since the purpose of the modal filtering operation is to estimate the modal coefficient w_i in the vector $\mathbf{w}$, a problem can be resolved directly by multiplying the inverse matrix of $\mathbf{\Psi}$ in Eq. (2) from the left-hand side, provided that the matrix $\mathbf{\Psi}$ is nonsingular. However, in general, the total number of modes excited in a structure is greater than that of sensors, and so the modal amplitude vector $\mathbf{w}$ cannot be obtained by solving a set of simultaneous equations.

One approach to overcome this problem is to use the pseudoinverse[9] of the matrix $\mathbf{\Psi}$, and the modal vector can be obtained as

$$\mathbf{w} = \mathbf{\Psi}^T(\mathbf{\Psi}\mathbf{\Psi}^T)^{-1}\tilde{\mathbf{y}}. \tag{3}$$

The pseudoinverse (sometimes called the minimum left-inverse[8]) provides the ''best'' estimate for $\mathbf{w}$ ''in the least-squares sense.'' Such an estimate, however, may be far from exact.

II. MODAL FILTERING USING DISTRIBUTED PARAMETER SENSORS

A. Two-dimensional distributed parameter modal sensors

The equation of motion for a self-adjoint linear distributed-parameter system can be written in the form

$$\mathbf{L}[w(\mathbf{r},t)] + m(\mathbf{r})\ddot{w}(\mathbf{r},t) = f(\mathbf{r},t), \tag{4}$$

where $w(\mathbf{r},t)$ is the displacement of the system at $\mathbf{r}=(x,y)$, $\mathbf{L}$ a linear self-adjoint differential operator, $m(\mathbf{r})$ the distributed mass, and $f(\mathbf{r},t)$ distributed force. Suppose the eigenpairs of the distributed-parameter system are (φ_i,λ_i). Because $\mathbf{L}$ is self-adjoint, the eigenfunctions possess the orthogonality property, and can be normalized so as to satisfy

$$\int_D m(\mathbf{r})\varphi_r(\mathbf{r})\varphi_s(\mathbf{r})d\mathbf{r} = \delta_{\mathrm{rs}} \tag{5}$$

and

$$\int_D \varphi_r(\mathbf{r})\mathbf{L}\varphi_s(\mathbf{r})d\mathbf{r} = \lambda_r\delta_{\mathrm{rs}} \quad (r,s=1,2,...), \tag{6}$$

where δ_{rs} is the Kronecker delta. Using the expansion theorem, the steady-state displacement of the system is given by

$$w(\mathbf{r},t) = e^{j\omega t}w(\mathbf{r}) = e^{j\omega t}\sum_{i=1}^{\infty} w_i\varphi_i(\mathbf{r}), \tag{7}$$

where ω is the driving frequency and where

$$w(\mathbf{r}) = \sum_{i=1}^{\infty} w_i\varphi_i(\mathbf{r}). \tag{8}$$

Consider the case when the PVDF film sensor is attached over the whole of a harmonically vibrating rectangular uniform plate of dimensions L_x and L_y in the x and y directions, respectively. Then the output $\tilde{q}$ of the sensor is given by (Lee and Moon[15]),

$$\tilde{q} = \int_0^{L_x}\int_0^{L_y}\Gamma(\mathbf{r})\left(e_{31}\frac{\partial^2 w(\mathbf{r})}{\partial x^2} + e_{32}\frac{\partial^2 w(\mathbf{r})}{\partial y^2} + e_{36}\frac{\partial^2 w(\mathbf{r})}{\partial x\ \partial y}\right) dx\ dy, \tag{9}$$

where e_{31}, e_{32}, and e_{36} are the directional piezoelectric field intensity constants. When the laminar is placed on the plate with no skew angle, then $e_{36}=0$, as is the case in this paper, and $\Gamma(\mathbf{r})$ is the spatial function describing the shape of the sensor.

Furthermore, assume the following relationships between the eigenfunction and its second derivative with respect to x and y,

$$\frac{\partial^2 \varphi_i(\mathbf{r})}{\partial x^2} = -\alpha_i^2 \varphi_i(\mathbf{r}) \tag{10}$$

and

$$\frac{\partial^2 \varphi_i(\mathbf{r})}{\partial y^2} = -\beta_i^2 \varphi_i(\mathbf{r}). \tag{11}$$

Substituting Eqs. (8), (10), and (11) into Eq. (9), the amplitude of the sensor output is given by

$$\begin{aligned}\tilde{q} &= \int_0^{L_x}\int_0^{L_y} \Gamma(\mathbf{r}) \\ &\quad \times \left(e_{31} \frac{\partial^2 \Sigma_{i=1}^{\infty} w_i \varphi_i(\mathbf{r})}{\partial x^2} + e_{32} \frac{\partial^2 \Sigma_{i=1}^{\infty} w_i \varphi_i(\mathbf{r})}{\partial y^2} \right) dx\, dy \\ &= \int_0^{L_x}\int_0^{L_y} \Gamma(\mathbf{r}) \sum_{i=1}^{\infty} b_i w_i \varphi_i(\mathbf{r}) dx\, dy, \end{aligned} \tag{12}$$

where

$$b_i = -(e_{31}\alpha_i^2 + e_{32}\beta_i^2). \tag{13}$$

With the aim of filtering out the sth modal amplitude, define the shaping function of the PVDF film sensor as

$$\Gamma(\mathbf{r}) = \varphi_s(\mathbf{r}). \tag{14}$$

Inserting Eq. (14) into Eq. (12) and introducing the modal orthogonality denoted by Eq. (5) leads to the output of the sensor,

$$\tilde{q} = b_s w_s. \tag{15}$$

Modal filtering is thus accomplished regardless of the number of participating modes. Two-dimensional distributed sensors are ideal in this sense.

B. One-dimensional distributed parameter modal sensors

1. General case

If a sensor is constructed with the charge generating capacity varying in accordance with Eq. (14), then the sensor will resolve a single two-dimensional mode. This variation could be achieved by varying the thickness of the sensor through lamination, however, a PVDF film is usually very thin, e.g., 25 μm, so that such a shaping technique is not practical. What is practically achievable is the use of strips of PVDF film, the type of sensor used to extract modal measurements in one-dimensional structures (such as described by Lee and Moon[15]).

In the interest of filtering out a particular modal amplitude, consider the one-dimensional PVDF film sensor of constant thickness shown in Fig. 1, which is attached to a rectangular plate at $x=x_0$ along the y direction with its width varying according to a shaping function $s(y)$. Therefore $\Gamma(\mathbf{r})$ may be described by

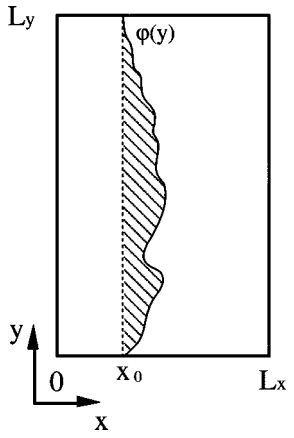

FIG. 1. One-dimensional modal sensor shaped with a shaping function $\varphi(y)$.

$$\Gamma(\mathbf{r}) = \begin{cases} 1, & x_0 \leqslant x \leqslant s(y) \\ 0, & \text{otherwise} \end{cases} \tag{16}$$

and Eq. (12) becomes

$$\tilde{q} = \int_0^{L_y}\int_{x_0}^{x_0+s(y)} \sum_{i=1}^{\infty} b_i w_i \varphi_i(\mathbf{r}) dx\, dy. \tag{17}$$

Consider the extraction of the sth modal amplitude, w_s. For this purpose, the shaping function is written as

$$s(y) = a_s \varphi_s(x_0, y), \quad a_s \ll 1. \tag{18}$$

As was introduced for the case of a two-dimensional modal sensor, the property of eigenfunctions shown in Eq. (10) is used in this case, too. Upon substituting Eq. (18) into Eq. (17) and using continuity, the sensor output amplitude $\tilde{q}$ becomes

$$\begin{aligned}\tilde{q} &= \int_0^{L_y}\int_{x_0}^{x_0+a_s\varphi_s(x_0,y)} \sum_{i=1}^{\infty} b_i w_i \varphi_i(\mathbf{r}) dx\, dy \\ &\doteq \int_0^{L_y} a_s \varphi_s(x_0,y) \sum_{i=1}^{\infty} b_i w_i \varphi_i(x_0,y) dy \\ &= a_s \sum_{i=1}^{\infty} b_i w_i \int_0^{L_y} \varphi_s(x_0,y)\varphi_i(x_0,y) dy. \end{aligned} \tag{19}$$

To proceed with the further expansion of Eq. (19), consider the integral

$$\hat{q} = \int_0^{L_y} \varphi_s(x_0,y)\varphi_i(x_0,y) dy. \tag{20}$$

Multiplying Eq. (20) by $-\beta_i^2$ and applying the properties of the eigenfunctions given by Eq. (11), Eq. (20) expands to

$$
\begin{aligned}
-\beta_i^2 \int_0^{L_y} \varphi_s(x_0,y)\varphi_i(x_0,y)dy
&= \int_0^{L_y} \varphi_s(x_0,y)\,\frac{\partial^2 \varphi_i(x_0,y)}{\partial y^2}\,dy \\
&= \varphi_s(x_0,y)\,\frac{\partial \varphi_i(x_0,y)}{\partial y}\bigg|_0^{L_y} - \frac{\partial \varphi_s(x_0,y)}{\partial y}\,\varphi_i(x_0,y)\bigg|_0^{L_y} \\
&\quad + \int_0^{L_y} \frac{\partial \varphi_s^2(x_0,y)}{\partial y^2}\,\varphi_i(x_0,y)dy. \qquad (21)
\end{aligned}
$$

Similarly, multiplying Eq. (20) by $-\beta_s^2$ leads to

$$
\begin{aligned}
-\beta_s^2 \int_0^{L_y} \varphi_s(x_0,y)\varphi_i(x_0,y)dy
&= \int_0^{L_y} \varphi_i(x_0,y)\,\frac{\partial^2 \varphi_s(x_0,y)}{\partial y^2}\,dy \\
&= \varphi_i(x_0,y)\,\frac{\partial \varphi_s(x_0,y)}{\partial y}\bigg|_0^{L_y} - \frac{\partial \varphi_i(x_0,y)}{\partial y}\,\varphi_s(x_0,y)\bigg|_0^{L_y} \\
&\quad + \int_0^{L_y} \frac{\partial \varphi_i^2(x_0,y)}{\partial y^2}\,\varphi_s(x_0,y)dy. \qquad (22)
\end{aligned}
$$

When applying the ''classical'' boundary conditions, the boundary terms in Eqs. (21) and (22) vanish at $y=0$ and L_y. To explain the reason, it is worthwhile summarizing the ''classical'' boundary conditions.

(a) Simply supported boundary conditions,

$$
\varphi(x_0,y) = \frac{\partial^2 \varphi(x_0,y)}{\partial y^2} = 0; \qquad (23)
$$

(b) clamped boundary conditions,

$$
\varphi(x_0,y) = \frac{\partial \varphi(x_0,y)}{\partial y} = 0; \qquad (24)
$$

(c) free boundary conditions,

$$
\frac{\partial^2 \varphi(x_0,y)}{\partial y^2} = \frac{\partial^3 \varphi(x_0,y)}{\partial y^3} = 0; \qquad (25)
$$

(d) slide boundary conditions,

$$
\frac{\partial \varphi(x_0,y)}{\partial y} = \frac{\partial^3 \varphi(x_0,y)}{\partial y^3} = 0. \qquad (26)
$$

In light of the assumption given by Eq. (10), the boundary terms in Eqs. (21) and (22) become zero as a result of applying any boundary condition as given by Eqs. (23)–(26). The clamped boundary conditions directly nullify the boundary terms in Eqs. (21) and (22), as do the free boundary conditions because of the relations

$$
\begin{aligned}
\frac{\partial^2 \varphi_i(x_0,y)}{\partial y^2} &= -\beta_i^2 \varphi_i(x_0,y), \\
\frac{\partial^3 \varphi_i(x_0,y)}{\partial y^3} &= -\beta_i^2 \frac{\partial \varphi_i(x_0,y)}{\partial y}.
\end{aligned} \qquad (27)
$$

Therefore Eqs. (21) and (22) simplify into

$$
\begin{aligned}
-\beta_i^2 \int_0^{L_y} \varphi_s(x_0,y)\varphi_i(x_0,y)dy
&= \int_0^{L_y} \varphi_s(x_0,y)\,\frac{\partial^2 \varphi_i(x_0,y)}{\partial y^2}\,dy \\
&= \int_0^{L_y} \frac{\partial \varphi_s^2(x_0,y)}{\partial y^2}\,\varphi_i(x_0,y)dy \qquad (28)
\end{aligned}
$$

and

$$
\begin{aligned}
-\beta_s^2 \int_0^{L_y} \varphi_s(x_0,y)\varphi_i(x_0,y)dy
&= \int_0^{L_y} \varphi_i(x_0,y)\,\frac{\partial^2 \varphi_s(x_0,y)}{\partial y^2}\,dy \\
&= \int_0^{L_y} \frac{\partial \varphi_i^2(x_0,y)}{\partial y^2}\,\varphi_s(x_0,y)dy. \qquad (29)
\end{aligned}
$$

Note that the right-hand sides of Eqs. (28) and (29) are equal, so that subtraction of Eq. (29) from Eq. (28) gives

$$
(\beta_s^2 - \beta_i^2) \int_0^{L_y} \varphi_s(x_0,y)\varphi_i(x_0,y)dy = 0. \qquad (30)
$$

For $\beta_s^2 \neq \beta_i^2$,

$$
\int_0^{L_y} \varphi_s(x_0,y)\varphi_i(x_0,y)dy = 0. \qquad (31)
$$

Note again that under the assumptions given in Eqs. (10) and (11), the modal orthogonality along $x=x_0$ on a planar structure is valid not only for a simply supported boundary condition but also other ''classical'' boundary conditions. Then one may ask, ''under what conditions do Eqs. (10) and (11) hold true?'' A discussion of this problem now follows.

The plate eigenproblem does not have a closed-form solution for general boundary conditions, however, a general form for the eigenfunctions[18] of a rectangular plate may be written in the form

$$
\begin{aligned}
\varphi(x,y) = {} & C_1 \sin \alpha_1 x \sin \beta_1 y + C_2 \sin \alpha_1 x \cos \beta_1 y \\
& + C_3 \cos \alpha_1 x \sin \beta_1 y + C_4 \cos \alpha_1 x \cos \beta_1 y \\
& + C_5 \sinh \alpha_2 x \sinh \beta_2 y + C_6 \sinh \alpha_2 x \cosh \beta_2 y \\
& + C_7 \cosh \alpha_2 x \sinh \beta_2 y \\
& + C_8 \cosh \alpha_2 x \cosh \beta_2 y, \qquad (32)
\end{aligned}
$$

where

$$
\alpha_1^2 + \beta_1^2 = \alpha_2^2 + \beta_2^2, \qquad (33)
$$

and C_i are coefficients specified by the boundary conditions. The first four terms in Eq. (32) denote the wave propagating terms, while the last four express the nonpropagating terms referring to the near fields (or evanescent waves). In light of this, if an eigenfunction can be expressed as a combination of the first four terms in Eq. (32), the eigenfunction satisfies the conditions of Eqs. (10) and (11). In the case of a simply supported boundary condition, for example, the eigenfunction consists of only the first term in Eq. (32), thereby satis-

TABLE I. Modal frequencies and modal indices of a simply supported rectangular plate of 180 cm ×88 cm×9 mm.

Mode number	Mode	Modal frequency Hz	Mode number	Mode	Modal frequency Hz
1	(1,1)	35.292	12	(3,2)	283.588
2	(1,2)	55.716	13	(2,5)	284.136
3	(1,3)	89.756	14	(3,3)	317.628
4	(2,1)	120.744	15	(2,6)	359.024
5	(1,4)	137.412	16	(1,7)	362.077
6	(2,2)	141.168	17	(3,4)	365.284
7	(2,3)	175.208	18	(3,5)	426.556
8	(1,5)	198.684	19	(2,7)	447.529
9	(2,4)	222.864	20	(4,1)	462.551
10	(3,1)	263.164	21	(1,8)	464.197
11	(1,6)	273.573	22	(4,2)	482.975

fying those conditions. Note that the nonpropagating terms decay exponentially with distance, this being especially noticeable at high frequencies. Therefore even in the case where the nonpropagating terms contribute to the eigenfunction, this phenomenon enables one to introduce the assumptions of Eqs. (10) and (11) within the interior of a plate especially for the higher eigenfunctions.

For $\beta_s^2=\beta_i^2$, Eq. (20) becomes

$$\hat{q}=c_s(x_0), \tag{34}$$

where c_s denotes a constant, depending only on x_0.

2. Simply supported plate

Consider the extraction of the sth modal amplitude of a simply supported, uniform, undamped, rectangular plate using one-dimensional PVDF sensors. The targeted eigenfunction, $\varphi_s(x,y)$, is written as

$$\varphi_s(x,y)=\sin\ \alpha_s x\ \sin\ \beta_s y, \tag{35}$$

where

$$\alpha_s=\frac{m_s\pi}{L_x},\quad \beta_s=\frac{n_s\pi}{L_y}, \tag{36}$$

and where m_s and n_s denote the modal indices of a plate. The output of the sensor with the shaping function given by

$$s(y)=a_s\ \sin\ \beta_s y \tag{37}$$

can be written as

$$q=\sum_{m=1}^{M} b_s(m,n_s)c_s(m)w_s(m,n_s), \tag{38}$$

where M denotes a total number of structural modes whose modal index in the y component is n_s (note that there are multiple cases satisfying the condition, $\beta_s^2=\beta_i^2$); $w_s(m,n_s)$ denotes the sth modal amplitude with the modal index of m and n_s in the x and y direction, respectively; and the coefficients b_s and c_s are defined as

$$b_s(m,n_s)=\left[e_{31}\left(\frac{m\pi}{L_x}\right)^2+e_{32}\left(\frac{n_s\pi}{L_y}\right)^2\right] \tag{39}$$

and

$$c_s(m)=\sin\frac{m\pi}{L_x}x_0. \tag{40}$$

As opposed to two-dimensional sensors, one-dimensional sensors utilize the modal orthogonality only in the direction of the sensor placement (y direction in this case). Therefore in addition to the ith modal amplitude of interest, all modal amplitudes with the modal index, n_i, are extracted with the weighting factor, $b_i(m,n_i)c_i(m)$. As a result, M one-dimensional sensors are needed to perform a modal filtering (As will be stated later, by making use of the nodal lines of a structure, the necessary number of the sensors could be reduced). Thus the modal amplitudes of interest may be obtained by the following formula

$$\begin{pmatrix}\tilde{q}_1\\ \tilde{q}_2\\ \vdots\\ \tilde{q}_M\end{pmatrix}=\begin{pmatrix} b_1c_1^1 & b_2c_2^1 & \cdots & b_Mc_M^1\\ b_1c_1^2 & b_2c_2^2 & \cdots & b_1c_M^2\\ \vdots & \vdots & & \vdots\\ b_1c_1^M & b_2c_2^M & \cdots & b_1c_M^M\end{pmatrix}\begin{pmatrix}w_1\\ w_2\\ \vdots\\ w_M\end{pmatrix}, \tag{41}$$

where $\tilde{q}_m$ ($m=1,2,3,...$) denotes the sensor outputs; c_m^j is defined by the following equation:

$$c_m^j=\sin\frac{m\pi}{L_x}x_j. \tag{42}$$

III. NUMERICAL EXAMPLE DEMONSTRATING ONE-DIMENSIONAL SENSORS

Consider a simply supported, thin, undamped, rectangular plate of the length L_x ($=0.88$ m) and L_y ($=1.8$ m) in the x and y directions, respectively, and of the thickness h ($=9$ mm). Note that the design methodology presented can also be applicable to a rectangular plate with other ''classical'' boundary conditions. Table I lists the modal indices and frequencies of the panel, for which the (1,3) modal amplitude will be numerically extracted using the one-dimensional modal sensors.

A. Direction of the prospective one-dimensional sensor

As seen in Table I, there are 22 structural modes spanning a frequency range up to 500 Hz, of which the (1,3)

modal amplitude shall be extracted. Eight of the 22 modes have a modal index of 1 in the x direction, e.g., (1,1), (1,2), (1,3), etc., while three modes possess that of 3 in the y direction. Therefore it is obviously advantageous to use the y direction for sensor placement, as the number of vibration modes extracted by a one-dimensional sensor determines the necessary number of the sensors.

B. Shaping function

The shaping function described in Eq. (37) is written as

$$s(y)=a_3 \sin \frac{3\pi}{L_y} y. \tag{43}$$

A sensor shaped using the shaping function of Eq. (43) permits extraction of three modes, with modal numbers of 3, 7, and 14, respectively. By employing these numbers, the sensor output is described as

$$\tilde{q}_1 = w_3 b_3 c_3^1 + w_7 b_7 c_7^1 + w_{14} b_{14} c_{14}^1. \tag{44}$$

C. Number of the necessary sensors

Among the three extracted structural modes given by Eq. (44), the (3,3) mode with the modal number of 14 has two nodal lines in the y direction. Moreover, considering the fact that three modes are filtered out at this stage, the necessary number of the sensors can be reduced to two by placing the sensors along the nodal lines of the (3,3) mode.

D. Extraction of modal amplitude

The amplitudes of the two sensor outputs are given by

$$\tilde{q}_1 = w_3 b_3 c_3^1 + w_7 b_7 c_7^1 \tag{45}$$

and

$$\tilde{q}_2 = w_3 b_3 c_3^2 + w_7 b_7 c_7^2. \tag{46}$$

Because of the symmetric location of the two sensors with regard to the central line of the plate, the following relations hold;

$$c_3^1 = c_3^2 \tag{47}$$

and

$$c_7^1 = -c_7^2. \tag{48}$$

By inserting Eqs. (47) and (48) into Eqs. (45) and (46), and further expanding the resulting equations, the modal amplitude of the (1,3) mode, w_3, is found to be

$$w_3 = \frac{1}{2 b_3 c_3^1} (\tilde{q}_1 + \tilde{q}_2)$$

$$= \frac{\sqrt{2}}{2\{e_{31}(\pi/L_x)^2 + e_{32}(3\pi/L_y)^2\}} (\tilde{q}_1 + \tilde{q}_2). \tag{49}$$

By adding the two sensor outputs with opposite polarity, the (2,3) modal amplitude, w_7, can also be obtained as

$$w_7 = \frac{1}{2 b_3 c_3^1} (\tilde{q}_1 - \tilde{q}_2)$$

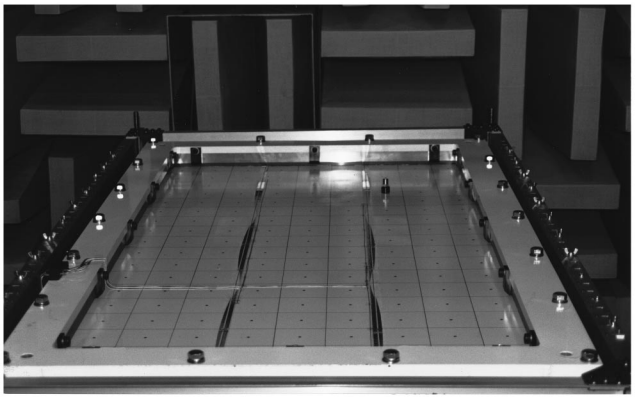

FIG. 2. Test rig with one-dimensional PVDF modal sensors attached to a rectangular plate.

$$= \frac{\sqrt{2}}{2\{e_{31}(\pi/L_x)^2 + e_{32}(3\pi/L_y)^2\}} (\tilde{q}_1 - \tilde{q}_2). \tag{50}$$

IV. MODAL FILTERING/CONTROL OF A RECTANGULAR PLATE

A. Experimental setup

The thickness of the PVDF film used in the experiment is 25 μm, and on both sides of the film are attached an aluminum electrode of thickness 60 nm. The directional piezoconstants are as follows; $e_{31}=0.0105$ C/m^2 and $e_{32}=3.5\times10^{-4}$ C/m^2. Figure 2 shows a test rig consisting of an enclosure and a steel panel ($L_x=88$ cm, $L_y=1.8$ m, $h=9$ mm). The perimeter of the panel is simply supported on the edge of the 10-cm-thick enclosure wall made of iron-reinforced concrete. Inside the enclosure are installed two electrodynamic shakers located at $\mathbf{r}=(0.645\text{ m}, 1.451\text{ m})$ and $\mathbf{r}_a=(0.44\text{ m}, 1.575\text{ m})$; one serves to provide an impact disturbance force, and the other as a control actuator. The impact force is measured by a force transducer installed between the shaker and panel.

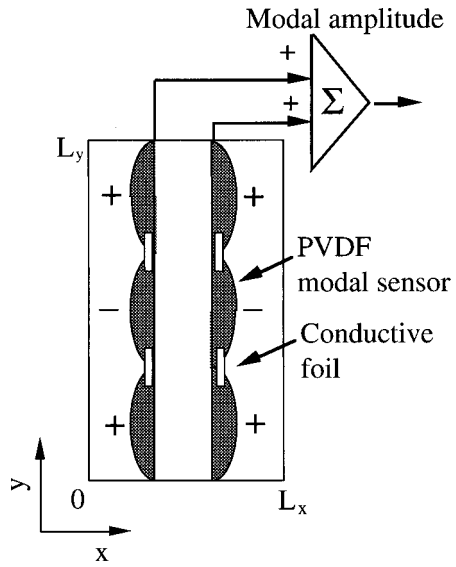

FIG. 3. Schematic diagram for measuring modal amplitude using PVDF modal sensors.

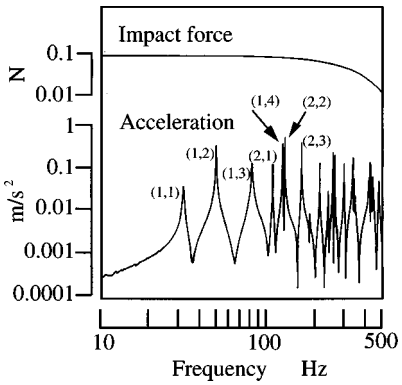

FIG. 4. Frequency spectrum; diagram of an impact force and acceleration response at a driving point.

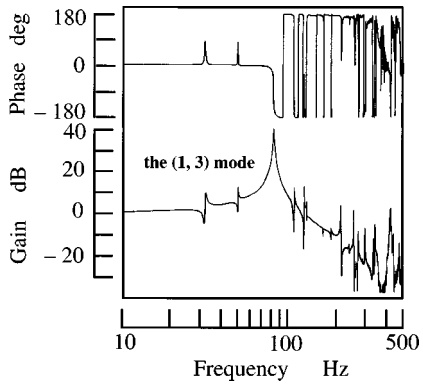

FIG. 6. Modal amplitude characteristics of the (1,3) mode.

A schematic diagram for extracting the (1,3) modal amplitude using PVDF film sensors is shown in Fig. 3. The polarity of the film sensor is changed by swapping the top and bottom surface of a sensor, each segment of the sensor connected by a conductive foil. Figure 4 shows the spectrums of the impact disturbance, together with the acceleration response at the driving point; the corresponding force and acceleration waveforms are depicted in Fig. 5(a) and (b), respectively. As is seen from the frequency characteristics, the impact force rolls off at 500 Hz, thereby determining the maximum frequency range of interest as 500 Hz.

B. Modal filtering/control of isolated structural mode; the (1,3) structural mode

In accordance with the design procedure presented in Sec. IV, the modal filtering of the (1,3) mode with a resonance frequency of 89 Hz has been conducted experimentally. The adjacent modes are the (1,2) and (2,1) modes with resonance frequencies of 55 and 120 Hz, respectively, thereby identifying the (1,3) mode as an isolated mode.

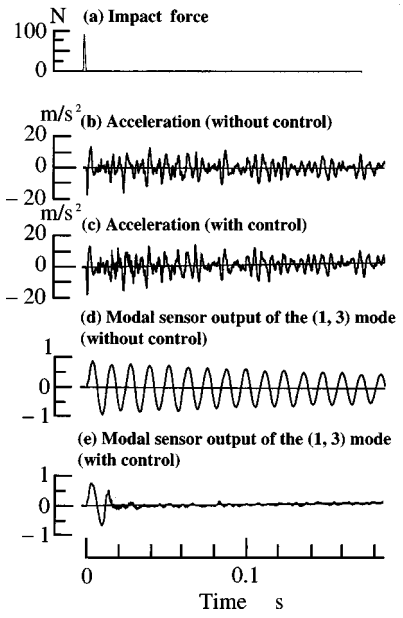

FIG. 5. Time history of an impact force, acceleration waves, and modal filter output of the (1,3) mode.

As shown in Fig. 3, a pair of PVDF film sensors shaped with the function described by Eq. (43) are attached along the two nodal lines of the (3,3) mode in the *y* direction. Each one-dimensional modal sensor consists of three segments with a half period of the sine function, these segments being connected by conductive foils. Combining these two sensor outputs with the same polarity enables one to filter out the (1,3) modal amplitude, while summing with the opposite polarity allows extraction of the (2,3) modal amplitude. Note that the combined sensor output *per se* is the desired modal signal, hence no further signal processing is required.

The waveform of the impact response of the extracted (1,3) modal amplitude is shown in Fig. 5(d), and the corresponding frequency characteristics are given in Fig. 6. As is seen in Fig. 5(d), a lightly damped sinusoidal signal appears which is filtered out from the ''turbulent'' acceleration waveform illustrated in Fig. 5(b). It should be noted that even with a narrow bandpass filter tuned to the targeted natural frequency [the (1,3) modal frequency], a similar waveform results. The two otherwise similar waveforms, however, substantially differ in the modal characteristics. In other words, as is found in Fig. 6, the signal obtained by the modal filter carries the dynamic characteristics of the (1,3) mode in the whole range of frequency (which can be viewed as a single-degree-of-freedom vibratory system), while the signal obtained by the narrow bandpass filter does not.

If one attempts to extract the (1,3) modal amplitude by using point sensors, at least 50 to 60 sensors, a few times the modal number of interest, should be necessary to ensure fidelity. In addition, the digital signal processing necessary to calculate the inverse matrix, multiplication, and addition of signals, makes it almost impossible to use in control systems, as the computation time to produce a control signal cannot be allowed. Thus a heavy burden is imposed on the use of the conventional modal filtering technique employing point sensors. In contrast to this, the modal filtering method using distributed sensors permits the extraction of a targeted mode by merely shaping its width with an appropriate shaping function, which is equivalent to spatial integration, reading, addition, and multiplication in digital signal processing, thereby completely eliminating the otherwise prohibitive calculation time.

The characteristics of the modal amplitude shown in Fig. 6 are now investigated. In the frequency range below that of

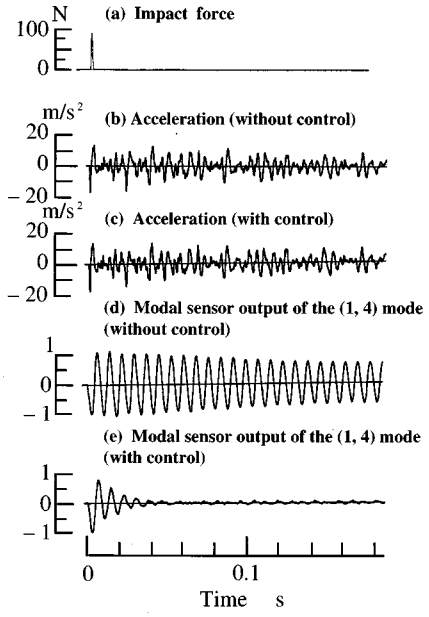

FIG. 7. Time history of an impact force, acceleration waves, and modal filter output of the (1,4) mode.

the (1,3) modal resonance frequency, there exist two structural modes [the (1,1) mode and (1,2) mode], these modes being easily eliminated due to the modal orthogonality in the y direction. Note that the modal indices in the y direction of these modes are 1 and 2, respectively, while the modal index of the (1,3) mode is 3, thereby modal orthogonality given by Eq. (31) holds. At frequencies higher than that of the (1,3) modal resonance frequency, the combination of the two sensors with opposite polarities permits the elimination of, for instance, the (2,3) mode, while the utilization of the (3,3) nodal lines for the sensor placement enables the exclusion of the (3,3) mode itself.

For the actual experiment, PVDF film sensors were shaped by hand using a utility cutter, and this handiwork seems to have caused some deterioration in modal filtering. In fact this effect can be identified in Fig. 6 as spikes in the gain characteristics; however, the maximum amplitude of the targeted (1,3) mode is still large enough compared to the spikes due to the inaccuracy in shaping. Improving the shaping technology of film sensors would lead to more accurate extraction of modal amplitudes.

To dampen a resonance peak, velocity feedback is necessary; however, the sensor output is proportional to the modal amplitude of displacement, and therefore an approximate differential circuit is required. Figure 5(e) shows the waveforms of the (1,3) mode suppressed by the active modal control using the distributed modal sensors. The optimal velocity feedback gain was determined experimentally by monitoring the waveforms being suppressed. Because of the control system comprised of distributed sensors and a point actuator, the observation spillover leading to a destabilization of the control system is avoided. Throughout the experiment, it was possible to increase the velocity feedback gain to a significantly high level, although the excess amount of feedback gain caused instability of the system due to the saturation of a power amplifier. Regarding the waveforms of

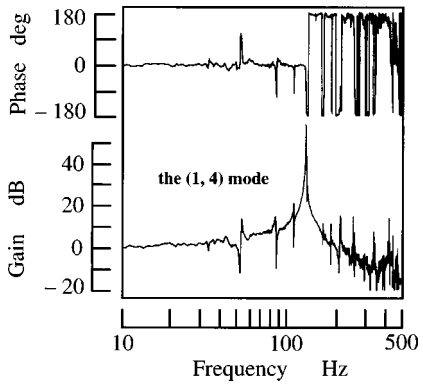

FIG. 8. Modal amplitude characteristics of the (1,4) mode.

the acceleration response before and after the active modal control as shown in Fig. 5(b) and (c), it is hard to recognize the difference in those waveforms, although the (1,3) modal signal was thoroughly eliminated from the uncontrolled acceleration waveform. This demonstrates the achievement of the active modal control without causing any effect on other structural modes.

C. Modal filtering/control of degenerate structural mode; the (1,4) mode

With a view to verifying the capability of modal filtering of a degenerate mode, the (1,4) mode was chosen as the target. The natural frequency of the (1,4) mode is 137 Hz, with the closest mode, the (2,2) mode with a natural frequency of 141 Hz, the difference between these modal frequencies being only 4 Hz, thereby identifying the (1,4) mode as an almost degenerate mode.

The procedure is identical to that performed for the (1,3) mode, and will not be detailed. By making use of the (3,4) nodal lines for sensor locations, the number of the necessary modal sensors is reduced to two. Hence two modal sensors with the shaping function given by Eq. (51) are attached along the nodal lines in the y direction,

$$s(y)=a_5 \sin \frac{4\pi}{L_x} y. \tag{51}$$

Figure 7(d) shows the waveform of the impact response of the (1,4) modal amplitude, the corresponding frequency spectrum is illustrated in Fig. 8. These figures indicate an extremely low damping ratio of 0.000 706 for the (1,4) mode. If the decomposition of the neighboring modes was not successful, the effect could have been observed as a beat due to two sinusoidal signals in close proximity of frequency. Thus it is found that the modal filtering presented is effective even on the (almost) degenerate mode.

By feeding back the signal of the targeted modal amplitude through a differential circuit, the active modal control was conducted. Figure 7(e) shows the waveform of the (1,4) modal amplitude suppressed by the active modal control. Comparison of the waveforms before and after control as shown in Fig. 7(d) and (e) indicates a significant control effect of 48 dB in attenuation. The feedback gain was again determined by a trial method.

V. CONCLUSIONS

The design of one-dimensional-shaped PVDF film sensors to provide the modal amplitude of interest has been considered. It was shown that the modal orthogonality of one-dimensional distributed sensors is applicable for a two-dimensional planar structure with any ''classical'' boundary condition. The design procedure for the one-dimensional modal sensor has been presented, the number, location, and shaping function of the one-dimensional sensor having been clarified. Experimental results showed that one-dimensional sensors accomplish the modal filtering for both the isolated and (almost) degenerate modes with significant accuracy. The active modal control as performed on both cases demonstrated the noticeable control effect for suppressing targeted modal resonances without causing instability of the control system.

[1] J. G. Truxal, *Automatic Feedback Control System Synthesis* (McGraw-Hill, New York, 1955).
[2] R. E. Kalman, ''When is a linear control system optimal,'' ASME Ser. D. Basic Eng. **86**, 1–10 (1964).
[3] J. C. Doyle, ''Analysis of feedback systems with structured uncertainties,'' IEEE Proc. Pt. D **129**, 242–250 (1982).
[4] H. H. Rosenbrock, ''Distinctive problems of process control,'' Chem. Eng. Prog. **58**, 43–550 (1962).
[5] M. A. Murray-Lasso, ''The modal analysis and synthesis of linear distributed control system,'' Sc.D. thesis, MIT, 1965.
[6] L. A. Gould and M. A. Murray-Lasso, ''On the modal control of distributed systems with distributed feedback,'' IEEE Trans. Autom. Control. **AC-11**, 729–737 (1966).
[7] F. M. Schlaefer, ''Modal control of ammonia reactor,'' Report No. ESL-R-293, MIT Project DSR-74994, 1966.
[8] Y. Takahashi, *Control and Dynamic System* (Addison-Wesley, Reading, MA, 1972), pp. 412–466.
[9] D. R. Morgan, ''An adaptive modal based active control systems,'' J. Acoust. Soc. Am. **89**, 248–256 (1992).
[10] N. Tanaka, S. D. Snyder, and C. H. Hansen, ''Distributed parameter modal filtering using smart sensors,'' ASME, J. Vib. Acoust. **118**, 630–640 (1996).
[11] S. D. Snyder, N. Tanaka, and Y. Kikushima, ''The use of optimally shaped piezo-electric film sensors in the active control of free field structural radiation, Part I: Feedforward control,'' ASME J. Vib. Acoust. **117**, 311–322 (1995).
[12] S. D. Snyder, N. Tanaka, and Y. Kikushima, ''The use of optimally shaped piezo-electric film sensors in the active control of free field structural radiation, Part 2: Feedback control,'' ASME, J. Vib. Acoust. **118**, 112–121 (1996).
[13] R. L. Clark and S. E. Burke, ''Practical limitations in achieving shaped modal sensors with induced strain materials,'' ASME J. Vib. Acoust. **118**, 668–675 (1996).
[14] M. J. Balas, ''Direct velocity feedback control of large space structures,'' J. Guid. Control. Dyn. **2**, 157–180 (1979).
[15] C. K. Lee and F. C. Moon, ''Modal sensors/actuators,'' ASME J. Appl. Mech. **57**, 434–441 (1990).
[16] Y. Gu, R. L. Clark, C. R. Fuller, and A. C. Zander, ''Experiments on active control of plated vibration using piezoelectric actuators and polyvinylidene fluoride modal sensors,'' ASME, J. Vib. Acoust. **116**, 303–308 (1994).
[17] L. Meirovitch and H. Baruh, ''On the problem of observation spillover in self-adjoint distributed-parameter systems,'' J. Optim. Theory Appl. **39**, 269–291 (1983).
[18] L. Meirovitch, *Analytical Methods in Vibration* (Macmillan, New York, 1971), p. 184.

Adaptive feedforward and feedback methods for active/passive sound radiation control using smart foam

C. Guigou[a] and C. R. Fuller
Vibration and Acoustics Laboratories, Virginia Polytechnic Institute and State University, Mechanical Engineering Department, Blacksburg, Virginia 24061-0238

(Received 10 November 1997; accepted for publication 16 March 1998)

This work investigates and compares the potential of adaptive feedforward and feedback methods for a hybrid active/passive radiation control using smart foam. The radiating structure is a vibrating plate mounted in a rigid baffle in an anechoic chamber. The smart foam, designed to reduce sound by the action of the passive absorption of the foam (which is effective at higher frequencies) and the active input of an embedded PVDF element driven by an oscillating electrical input (which is effective at lower frequencies), is positioned on the plate. The first test consists of using a single-input single-output (SISO) adaptive feedforward LMS controller to minimize the error sensor signal provided by a microphone in the close proximity of the active element under narrow-band excitation and broadband random excitation. For feedforward control, two different reference signals are considered: the voltage sent to the piezoceramic actuator driving the plate (disturbance) and the signal from an accelerometer directly mounted on the plate (more realistic in practice). In the latter case, the effect of the smart foam on the reference signal (or acceleration level) can be taken into account (feedback removal). An adaptive feedback controller is also implemented to avoid the use of a reference signal. In this case, a reference signal is obtained from the error signal using the internal model approach. The results from these three different control methods are compared in terms of the sound attenuation achieved. For broadband excitation, a feedforward adaptive control with an external reference is shown to be more efficient for this arrangement than a feedback adaptive control. © *1998 Acoustical Society of America.* [S0001-4966(98)00207-0]

PACS numbers: 43.50.Gf, 43.40.Vn [PJR]

INTRODUCTION

In the last few years, there has been an increased interest in the reduction of sound and/or vibrations by use of hybrid active–passive control techniques.[1] The passive device usually carries the primary noise attenuation function, while the active component is used to enhance the passive system performance or overcome the limitations of the passive system. The smart foam design integrates a lightweight distributed piezoelectric actuator (the active component) between individual layers of sound-absorbing foam (the passive component) such that the control can efficiently operate over a broad range of frequencies. Porous sound-absorbing materials are commonly implemented for a large range of applications (such as buildings, machinery enclosures and aircrafts) to reduce sound propagation. The use of a polyimide foam layer has been investigated for reducing sound transmission.[2] The oscillations of the air molecules in the interstices of the porous material at the frequency of the exciting sound wave result in frictional losses. Changes in flow direction and expansions and contractions of the flow throughout irregular pores result in a loss of momentum in the direction of wave propagation. These two phenomena account for most of the energy losses in the high-frequency range.[3] The piezoelectric PVDF element serves as the active input to contribute to the low-frequency sound attenuation. It is cylindrically curved to couple the in-plane strain associated with the piezoelectric effect with the vertical motion needed to radiate sound from the foam surface. The PVDF active layer is bonded between the two foam halves forming a very thin, compact arrangement. The smart foam can be bonded directly to a vibrating structure and acts as an active surface coating that provides reduction of structural sound radiation. The goal of implementing the smart foam is to modify the acoustic impedance seen by the structure in order to yield a net decrease in the far-field sound power radiated by the vibrating noise source. The potential of the smart foam to simultaneously control low- and high- frequency sound was demonstrated on a simple radiating source (piston).[4] Global cancellation of harmonic and broadband noise induced by a vibrating piston was successfully achieved by the smart foam. The passive–active device was able to modify the radiation impedance observed by the piston over a wide range of frequencies. The potential of smart foam to globally reduce low and high frequency sound radiating from a simple acoustic source was demonstrated. Recently, multiple smart foam modules [with a multiple-input multiple-output (MIMO) control system] were also successfully implemented to reduce the sound radiation from a complex radiating source (plate).[5] Such smart foam systems were also mounted on several fuselage crown panels of a mid-size business jet Cessna Citation III to reduce interior noise at the pilot's ear level.[6] Its potential for reducing aircraft interior noise was demonstrated under band-limited random excitation.

These works, providing the basis of the present study,

[a]Currently working at C.S.T.B., 24 Rue Joseph Fourier, 38400 St. Martin d'Hère, France.

 0001-4966/98/104(1)/226/6/$15.00

have been concerned with an adaptive feedforward controller based on the filtered- x LMS (FXLMS) algorithm.[7,8] Such a controller requires the use of a coherent reference signal in order to generate the control signal. A nonadaptive feedback usually consists of a large gain controller over the frequency band of interest. The advantages are the relative simplicity of the control algorithm and the lack of a reference signal. However, this approach suffers from potential instability when the phase shift of the secondary path approaches 180°; to ensure stability at these frequencies, the open-loop gain then has to be less than unity (''rolloff''). Therefore, it is commonly reported that it provides only limited cancellation over limited frequency bandwidth.[8] To overcome the limitations of a nonadaptive feedback controller and to avoid the use of a reference sensor required by a feedforward controller, an adaptive feedback controller is investigated in this work. An adaptive feedback controller can be viewed as an adaptive feedforward controller that generates its own reference signal based on the adaptive filter output (control signal) and the error sensor signal.[8] This type of control architecture is also known as internal model control (IMC) and has been previously studied by Elliott *et al.*[9] and Morari and Zafiriou.[10]

In this paper, the performance of the smart foam to reduce sound radiation from a vibrating plate is investigated with the use of adaptive feedforward and feedback controllers for different disturbance frequency bandwidths. An error microphone located in close proximity (for reason of compactness) of the smart foam provides the error signal, which has to be minimized by both adaptive controllers. For the feedforward controller, two different reference signals are implemented. First, the signal sent to the piezoceramic actuator exciting the plate (i.e., disturbance) is used as reference signal. The second reference signal is provided by an accelerometer located on the plate, which is more realistic in practice. The results of these three different control systems are compared in terms of the sound power attenuation achieved.

I. CONTROL ALGORITHMS

For the sake of completeness, the control algorithms and their corresponding block diagram for a single-input single-output (SISO) configuration are briefly presented in this section. More detailed discussion can be found in Refs. 7–10 The real-time implementation of these two SISO adaptive feedforward and feedback algorithms was performed on the TMS320 C30 DSP board resident in a personal computer.

A. Adaptive feedforward FXLMS algorithm

The block diagram of the feedforward FXLMS algorithm is shown in Fig. 1(a). The secondary path transfer function $S(z)$ (i.e., the transfer function between the error sensor and the control actuator) is assumed to be modeled off-line and its estimate is denoted $\hat{S}(z)$. As shown in Fig. 1(a), such a controller requires the use of a coherent reference signal $x(n)$ in order to generate the control signal $y(n)$. The undesired noise from the primary disturbance is measured by a reference sensor, which is filtered through an

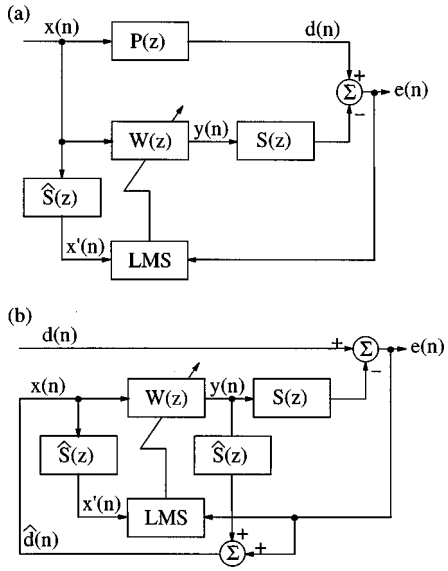

FIG. 1. Block diagram of an adaptive (a) feedforward and (b) feedback control system.

adaptive filter $W(z)$, and used to drive the secondary or control source to minimize the error sensor signal $e(n)$. The reference signal is also filtered by the estimate of the secondary path $\hat{S}(z)$ to obtain the filtered reference used to update the coefficients of the adaptive filter $W(z)$. The reference sensor signal should be highly correlated with the primary disturbance. For broadband random disturbances, the reference sensor should provide advance information about the primary disturbance before it reaches the secondary control source, which is the requirement for a causal controller. The signal from the error sensor is used to update the coefficients of the adaptive filter $W(z)$ in order to minimize the error sensor signal. The adaptive filter $W(z)$ as well as the estimate of the secondary plant transfer function $\hat{S}(z)$ are realized as finite impulse response (FIR) filters. The error signal $e(n)$ at time n is expressed as

$$e(n)=d(n)-\sum_{m=0}^{M-1}\hat{s}_m y(n-m), \tag{1}$$

where $\hat{s}_m$, for $m=0$ to $M-1$, are the coefficients of the Mth order FIR filter $\hat{S}(z)$ used to estimate the secondary path transfer function. The secondary or control signal is generated as

$$y(n)=\sum_{l=0}^{L-1} w_l(n)x(n-l), \tag{2}$$

where $w_l(n)$, for $l=0$ to $L-1$, are the coefficients of the Lth order adaptive FIR filter $W(z)$ at time n. These coefficients $w_l(n)$ are updated by the FXLMS algorithm as

$$w_l(n+1)=w_l(n)+\mu x'(n-l)e(n), \quad \text{for } l=0,\ldots,L-1, \tag{3}$$

where μ is the convergence parameter (or step size). In Eq. (3), the filtered reference signal $x'(n)$ at time n is defined as

$$x'(n)=\sum_{m=0}^{M-1}\hat{s}_m x(n-m), \tag{4}$$

and corresponds to the reference signal $x(n)$ filtered through the estimate of the secondary path $\hat{S}(z)$.

B. Adaptive feedback FXLMS algorithm

Feedback systems are required for applications in which it is not possible or not practical to sense a coherent reference signal. Such applications could include spatially incoherent noise generated by turbulence. A single-channel adaptive feedback algorithm that uses a reference signal synthesis technique is described in this section. Figure 1(b) depicts the block diagram of such a feedback system. This technique can be viewed as an adaptive feedforward system that synthesizes or generates its own reference signal based only on the adaptive filter output and the error signal. Therefore, the basic idea of the adaptive feedback system used in this work is to estimate the primary disturbance and use it as a reference signal. The reference signal $x(n)$ at time n is synthesized as an estimate of $\hat{d}(n)$, which is expressed as

$$x(n)\equiv\hat{d}(n)=e(n)+\sum_{m=1}^{M}\hat{s}_m(n)y(n-m). \tag{5}$$

This type of control architecture transforms a feedback control problem to a feedforward control. It is also known as internal model control (IMC) and is equivalent to a Youla parametrization since the internal model or estimate of the secondary path $\hat{S}(z)$ is used to give an estimate of the disturbance prior to control.[9,10] Note that IMC or Youla parametrization is originally used to find the set of all closed loop stabilizing controllers. The coefficient of the adaptive filter $W(z)$ are updated by the FXLMS in the same way as described in the previous section [see Eq. (3)]. The adaptive filter $W(z)$ of the feedback system acts as an adaptive predictor of the primary disturbance $d(n)$ to minimize the residual signal $e(n)$. Therefore, the performance of such an adaptive feedback system depends on the predictability of the primary disturbance $d(n)$.

II. EXPERIMENTAL SETUP

The experimental setup is depicted in Fig. 2. A rectangular aluminum plate ($6.75\times6\times1/64$ in.^{3}) with fixed boundary conditions is treated with the smart foam [Fig. 2(a)]. Note that the size of this plate is about half that of the Cessna Citation III fuselage crown panels on which the smart foam was previously tested.[6] The plate is mounted in a rigid baffle in an anechoic chamber. A piezoceramic actuator was bonded to the plate and provided the primary disturbance.

A sound-absorbing material, consisting of partially reticulated polyurethane foam, provides the passive element of ''smart foam'' (2 in. thick). Such material dissipates incident acoustic wave energy through friction associated with the coupling of the liquid and solid phases of the foam. Partially reticulated polyurethane foam is an acoustical grade, open cell, flexible ester-based urethane foam designed to give maximum sound absorption per given thickness.[11] Since passive sound control is only significant at high frequencies, a 28-μm Ag metallized PVDF film is embedded in the foam to implement the active control, which is most effective at low frequencies. A silver-electroded PVDF was chosen as it can sustain high-voltage amplitudes required for actuator applications. The main physical characteristic of the PVDF actuator is that it is intentionally curved to couple the predominantly in-plain strain associated with the piezoelectric effect and the vertical motion that is required to accelerate fluid particles and hence radiate sound away from the surface of the foam. The PVDF film is curved into a half-cylinder of 1.5-in. diameter and 2.5-in. length and is embedded in two foam halves with spray glue. This leads an ''active cell'' which is 3 in. long, 2 in. wide and 2 in. thick as depicted in Fig. 2(b). Note that the active cell is encased in a balsa wood frame for improved radiation efficiency.[5] The ''smart foam'' consists of the active cell tightly embedded in the center of a piece of passive foam [see Fig. 2(b)]. It is then mounted on the plate. An error microphone, whose signal has to be minimized in the active control process, is located at 3 in. away from the center of the active cell in the direction normal to the plate [see Fig. 2(a)].

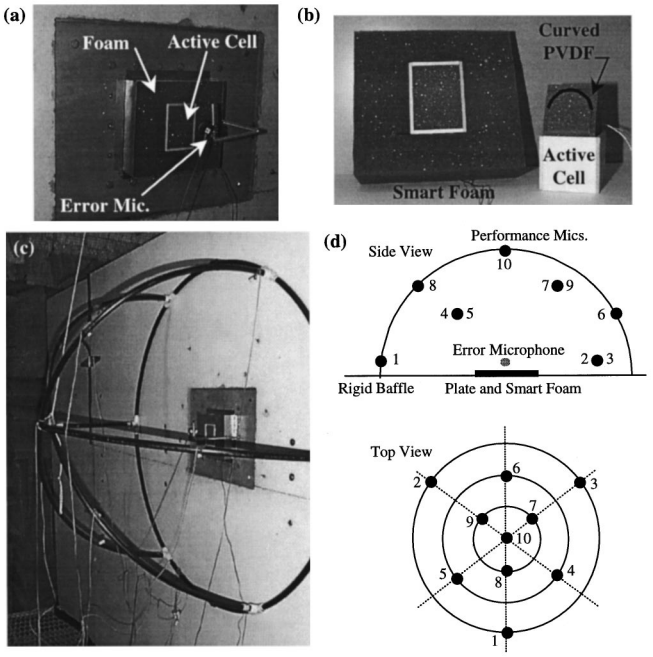

FIG. 2. Experimental setup.

The effect of minimizing the error microphone signal was monitored at ten microphones located on a hemispherical structure of 2-ft. radius. [see Fig. 2(c) and (d)]. The positions of these microphones are such that they measure equal areas on the hemisphere and therefore the acoustic power radiated in free space by the system can be deduced using the expression

$$\Pi=\frac{(S/10)}{2\rho_0 c_0}\sum_{i=1}^{10}|p_i|^2, \tag{6}$$

where S is the surface of the hemisphere and p_i is the sound

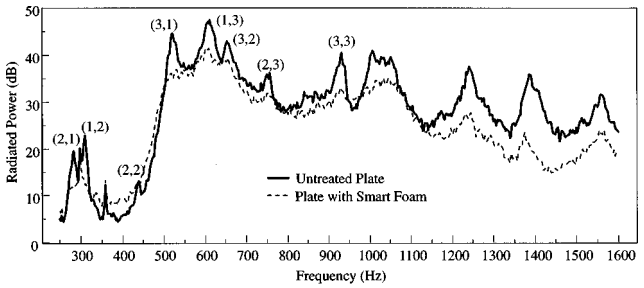

FIG. 3. Passive effect of the smart skin on the acoustic power radiated from the plate.

pressure measured at the ith microphone located on the hemisphere as shown in Fig. 2(d).

The passive effect of the smart foam on the radiated power is presented in Fig. 3. The smart skin provides good passive attenuation at the plate resonance frequencies mainly in the form of additional vibration damping. Its effect off-resonance is negligible, except in the high frequency range, i.e., above 1 kHz. It should also be mentioned that the resonance frequencies of the plate are slightly lowered by the presence of the smart foam, implying a slight added mass effect in addition to damping.

III. CONTROL RESULTS

The following results present a comparison of the effect on the radiated power achieved with the adaptive feedforward and feedback controllers for harmonic and band-limited disturbances. For the feedforward controller, two different reference signals were implemented. First, the signal sent to the piezoceramic actuator exciting the plate (i.e., disturbance) is used as reference signal; this case will be referred to as ''generator as reference.'' The second reference signal is provided by an accelerometer located on the plate; this case will be referred to as ''accelerometer as reference'' and corresponds to a more realistic system in practice. The effect of the active cell on the accelerometer signal was found to be negligible. Indeed, control results compensating for this feedback path on the reference signal (feedback removal) showed no improvement compared to those neglecting this

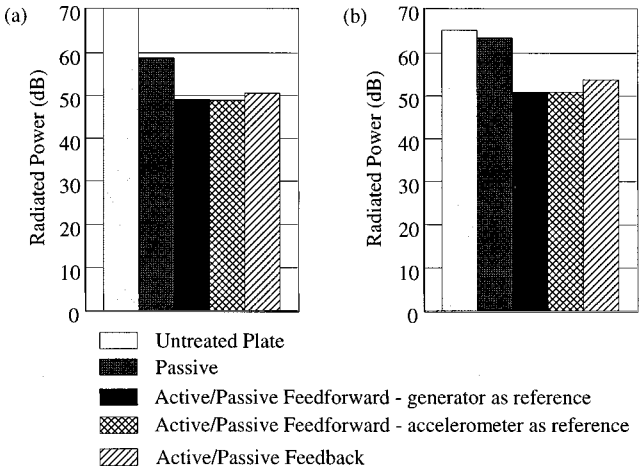

FIG. 4. Harmonic control at (a) 610 Hz (on-resonance) and (b) 560 Hz (off-resonance).

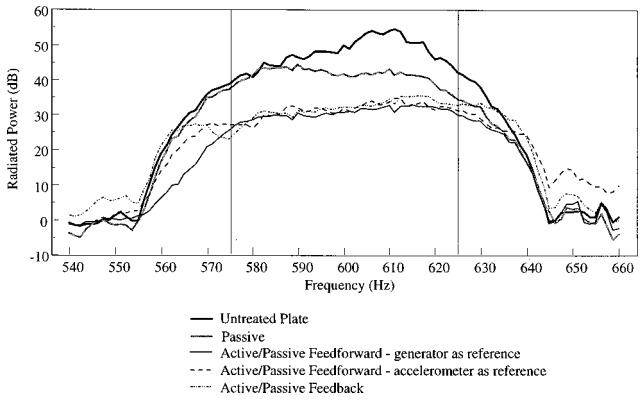

FIG. 5. Narrow-band control 600±25 Hz (50-Hz bandwidth).

feedback path. Therefore, the results are presented only for the accelerometer as a reference signal without feedback removal taken into account. The error microphone was located at 3 in. in front of the active cell (which corresponds to the main dimension of the active cell). Increasing the distance of the error microphone from the foam (up to 9 in.) yielded comparable control results in the frequency range of interest.

A. Harmonic disturbances

The plate was first excited via a piezoceramic actuator with a single frequency disturbance. The first harmonic frequency studied is 610 Hz, which corresponds to the resonance frequency of the (1,3) mode for the plate treated with smart foam (see Fig. 3). The second harmonic disturbance was chosen to be 560 Hz, corresponding to an off-resonance frequency of plate–foam system [between resonance frequencies of modes (3,1) and (1,3) as seen in Fig. 3] at which the passive effect of the smart foam is very limited. The radiated power for the different control cases is shown in Fig. 4. For the harmonic disturbance at 610 Hz, the smart foam provides about 11 dB of passive attenuation; while implementing active control, an extra 10 dB attenuation is achieved [see Fig. 4(a)]. When the plate is excited off-resonance at 560 Hz, the passive effect of the foam is very limited (less than 2 dB). Active control is seen to provide more than 10 dB power attenuation with respect to the untreated plate. For both frequencies, the adaptive feedback system performs as well as the adaptive control system since the disturbance is harmonic, i.e., perfectly predictable.

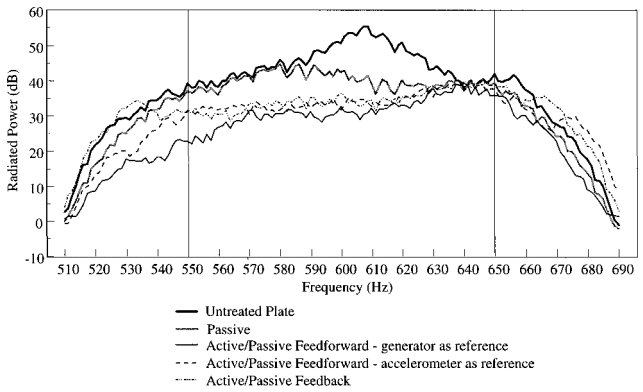

FIG. 6. Narrow-band control 600±50 Hz (100-Hz bandwidth).

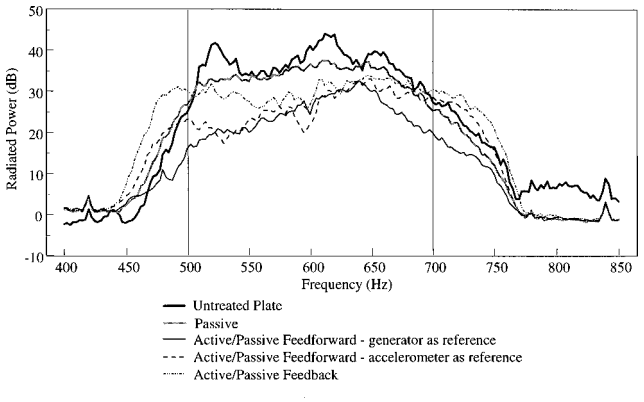

FIG. 7. Narrow-band control 600±100 Hz (200-Hz bandwidth).

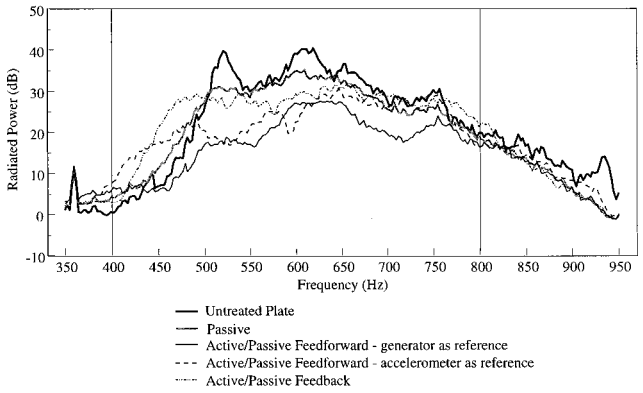

FIG. 8. Narrow-band control 600±200 Hz (400-Hz bandwidth).

B. Band-limited disturbances

The plate was then excited with band-limited random disturbances of increasing bandwidth around the center frequency 600 Hz [close to resonance frequency of (1,3) mode]. The radiated power for the different control cases investigated are presented in Figs. 5–8 for 50-, 100-, 200-, and 400-Hz frequency bandwidth, respectively. The achieved total power attenuation for the different frequency bandwidths and control systems is summarized in Table I. Note that for the different cases presented in this section, the sampling frequency associated with the DSP was fixed at 3.2 kHz and the FIR filters [estimated secondary path $\hat{S}(z)$ and adaptive filter $W(z)$] had 128 coefficients (i.e., $L=M=128$).

The control results obtained when the disturbance is limited to 50- and 100-Hz bandwidth with a center frequency of 600 Hz (see Figs. 5 and 6) are first investigated. The performance of the feedforward system with the disturbance signal as reference is slightly better than that when the reference signal is obtained from the accelerometer directly mounted on the plate. The adaptive feedback control system performs as well as the feedforward control system with the accelerometer signal as reference. The averaged power attenuation associated with these two control systems is similar. An active/passive power reduction of about 16 and 10.5 dB for the 50- and 100-Hz frequency bandwidths, respectively, is obtained with a realistic control system as seen in Table I. For these two frequency bandwidths, the plate response is associated with a single mode corresponding to a resonance frequency of 610 Hz. Due to the presence of this plate resonance frequency in the control bandwidth, the reference signal is more predictable, leading to good control results associated with the adaptive feedback control system.

The frequency bandwidth of the disturbance was then increased to 200 and 400 Hz (with a center frequency of 600 Hz). In this case, several modes of vibration are associated with the plate response [mainly modes (3,1), (1,3) and (3,2) are present in the control bandwidth]. The feedforward control with the disturbance generator signal as reference performs best, as expected. When the accelerometer is used to provide the reference signal to the controller, the control performance is decreased (see Table I). The difference in control performance between the two different reference signals for the feedforward control system is essentially related to the fact that the optimal compensating filters are acausal since the propagation time through the control path is longer than the propagation time through the disturbance path. The controller must be able to receive the reference signal and produce the appropriate control signal to the active cell of the smart skin before the structural disturbance from the piezoceramic on the plate propagates through the foam. In this situation, the time delay for the controller to react is shorter when the reference signal is from the accelerometer directly mounted on the plate than when it is the disturbance signal driving the piezoceramic actuator. This effect is increased when the disturbance frequency bandwidth is increased (see Table I). The adaptive feedback control results in even lower performance than the feedforward control with the accelerometer signal as reference. This could be expected; as for the adaptive feedback control, the reference signal has to be synthesized, i.e., predicted. Since the disturbance is random and

TABLE I. Total radiated power attenuation.

	Radiated power attenuation			
		Active passive feedforward		
Frequency bandwidth (Hz) (center frequency 600 Hz)	Passive (dB)	Ref. gener. (dB)	Ref. accel. (dB)	Active passive feedback (dB)
50	7.5	19.2	17.9	17.6
100	7.5	15.8	13.7	13.4
200	4.0	11.8	10.3	7.5
400	4.0	11.2	8.0	5.2

of increasing frequency bandwidth, it becomes more difficult to predict. These results demonstrate that, for broadband excitation of this particular test arrangement, an adaptive feedforward controller (with reference signal obtained from an accelerometer on the vibrating structure) is more efficient in reducing the radiated power than an adaptive feedback controller. However, the adaptive feedback controller provides similar power attenuation between 550 and 750 Hz as the feedforward controller with structural reference sensor. This is probably due to the presence of the resonance frequency of the dominant (1,3) mode in this frequency range; this indeed makes the reference signal more predictable. The major drawback of the adaptive feedback controller is the important increase in radiated power (control spillover) below 500 Hz, where no structural modes are present (off-resonance).

IV. CONCLUSIONS

The performance of SISO adaptive feedback and feedforward controllers to reduce the radiated power from a plate (similar to a small fuselage panel) treated with smart foam was discussed. The adaptive feedback controller was found to be as efficient as the feedforward controller with a structural reference sensor (accelerometer on the plate) when the disturbance was either harmonic or limited up to 100 Hz in bandwidth. This is related to the fact that the adaptive feedback controller generates its own reference signal based on the adaptive filter output (control signal) and the error sensor signal; therefore, it can be viewed as a predictor. When the frequency bandwidth was increased to 400 Hz, the adaptive feedback system was associated with control spillover in the low-frequency range where no structural mode resonance frequency is present. However, close to the system resonance frequencies (i.e., where reference signal is then more predictable), the efficiency of the adaptive feedback controller was found to be similar to that of the feedforward controller with a structural reference sensor (accelerometer).

Further work will involve the investigation of a multiple input multiple output (MIMO) feedback and feedforward control system on a plate located in a wind tunnel (excitation simulating turbulent boundary layer noise).

ACKNOWLEDGMENTS

The authors gratefully acknowledge the support of this work by the Army Research Office under the Grant No. DAA H04-95-10037.

[1] K. W. Ng, ''Applications of active control,'' in *Proceedings of the 1995 International Symposium on Active Control of Sound and Vibration, Active 95*, Newport Beach, California, Supplemental paper, July 1995.
[2] Y. J. Kang, W. Tsoi, and J. S. Bolton, ''The effect of mounting on the acoustical properties of finite-depth polyimide foam layers,'' in *Proceedings of Noise-Con 93*, pp. 285–290, Williamsburg, Virginia, 1993.
[3] L. Beranek and L. Ver, *Noise and Vibration Control Engineering: Principles and Applications* (Wiley, New York, 1992).
[4] C. A. Gentry, C. Guigou, and C. R. Fuller, ''Smart foam for applications in passive–active noise radiation control,'' J. Acoust. Soc. Am. **101**, 1771–1778 (1997).
[5] C. A. Gentry, C. Guigou, and C. R. Fuller, ''Plate radiation control with smart foam,'' to be submitted to J. Acoust. Soc. Am., 1998.
[6] C. Guigou and C. R. Fuller, ''Foam-PVDF smart skin for aircraft interior sound control,'' in *Proceedings of SPIE's 4th Symposium on Smart Structures and Materials*, San Diego, California, March 1997.
[7] P. A. Nelson and S. J. Elliott, *Active Control of Sound* (Academic, London, 1992).
[8] S. M. Kuo and D. R. Dennis, *Active Noise Control Systems: Algorithms and DSP Implementations* (Wiley, New York, 1996).
[9] S. J. Elliott, T. J. Sutton, B. Rafaely, and M. Johnson, ''Design of feedback controllers using a feedforward approach,'' in *Proceedings of the 1995 International Symposium on Active Control of Sound and Vibration, Active 95*, Newport Beach, California, pp. 863–874, July 1995.
[10] M. Morari and E. Zafiriou, *Robust Process Control* (Prentice–Hall, Englewood Cliffs, NJ, 1989).
[11] Polymer Technology, Inc., *Technical Data Sheet: ''Acoustical Products—An Overview,''* Polymer Technology, Inc., Newark, DE.

Ground influence on the definition of single rating index for noise barrier protection

F. Simón, J. Pfretzschner, C. de la Colina, and A. Moreno
Instituto de Acústica (CSIC), C. Serrano, 144 28006 Madrid, Spain

(Received 19 May 1997; revised 29 October 1997; accepted 20 March 1998)

A single number rating index to qualify the acoustical protection of a noise barrier that accounts for the influence of the ground is developed. This is an extension of a previous index for semi-infinite barrier developed by Pfretzschner [Pfretzschner *et al.*, Acust. Acta Acust. **82**, 504–508 (1996)]. This index is based on the asymptotic value found for the insertion loss or the acoustic attenuation as physical magnitude, and it is uniquely dependent on the barrier, noise source, and acoustic characteristics of the ground in the source semi-space. The new index agrees well with measured data on a scale model under laboratory conditions, and a direct experimental measuring procedure could be envisaged. In this way the proposed index, which accounts for extrinsic properties (acoustical protection) of barriers, would complete the two previous indices dealing with intrinsic properties (transmission loss and acoustical absorption). © *1998 Acoustical Society of America.* [S0001-4966(98)01807-4]

PACS numbers: 43.50.Gf, 43.20.Fn [GAD]

INTRODUCTION

For many years noise barriers have been erected alongside roads and highways to protect inhabited areas from high levels of traffic noise. Technical studies of the performance of noise barriers show that for a single barrier, a great deal of frequency and spatially dependent data are needed. These sets of data from different barrier configurations are very difficult to handle and compare. In order to overcome this problem and to get concise and meaningful descriptions, single number rating indexes are most convenient. These indices, resulting from elaborated procedures that account for the influence of the parameters involved, are intended to facilitate the arrangement of noise barriers in classes. Nevertheless these procedures obviously lead to some loss of accuracy. Procedures intended for metric indexes associated with intrinsic characteristics of noise barriers have been developed and have given birth to standards[1] in the European Union which define single rating indices for acoustic isolation and absorption. The present work is focused on characterizing the acoustical protection features of such noise reduction devices by a single number rating index. Taking into account the number of parameters involved, and keeping in mind the frequency and spatial dependence of most of them, this objective is not easy to accomplish since the protection will change according to the circumstances for each situation.

The acoustical protection of a noise barrier can be described by its insertion loss IL. A comparative study of the different solutions which describes this quantity showed that the asymptotic behavior of IL in relation to the horizontal barrier–receiver distance, r, is very useful to the purpose of this work. Based on this quantity, Pfretzschner *et al.*[2] were able to define a single number rating index to characterize the acoustical protection for the classical case of a semi-infinite barrier. They have shown that, from the Kurze–Anderson[3] algorithm, the asymptote insertion loss il_∞, when r tends to infinity, is

$$\mathrm{il}_\infty = 5 + 20 \log \frac{\sqrt{2\pi N_\infty}}{\tanh\sqrt{2\pi N_\infty}}, \tag{1}$$

where

$$N_\infty = \frac{2}{\lambda}\{\sqrt{(h-h_s)^2+s^2}-s\} \tag{2}$$

is the value of the Fresnel number at infinity, λ is the wavelength of the signal, and h, h_s, and s are defined in Fig. 1 (for this special case the ground is just a reference plane without physical meaning). Equation (1) is independent of the receiver height h_r, so the group of curves $\mathrm{il}(h_r, r)$, corresponding to the Kurze–Anderson algorithm, takes the same asymptote, when r tends to infinite. This theoretical result has been experimentally confirmed by means of scale model measurements under free field conditions.[4] Figure 2 shows the results obtained in an anechoic chamber with a barrier made of plywood covered by a layer of melamine. The receiver was a microphone that moved along a perpendicular to the barrier, comprising distances between 0.1 and 5.5 m. The receiver height ranged from 0–0.5 m, from a reference plane located at 0.4 m down the upper barrier edge. The emitting signal was pink noise filtered in the $\frac{1}{3}$-oct band centered at 4 kHz (for a 1:6 scale factor, corresponds to the $\frac{1}{3}$-oct band of 630 Hz, representative of normalized traffic noise spectrum[2]).

The asymptotic behavior of the il as a function of the reception parameters (h_r, r) and the correlation between experimental and theoretical results, calculated by the Kurze–Anderson algorithm, can be observed in Fig. 2. The existence of a receiver height $[h_r = (h_s - h)/2]$ for which $\mathrm{IL}(r)$ is approximately constant, according to the experimental method to measure il_∞ indicated in a previous paper[2] (thick curves in Fig. 2), can also be seen.

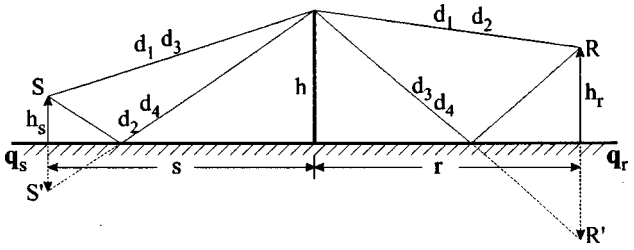

FIG. 1. Geometry of the problem. When the ground is present, four paths are possible. Without ground, only the first path (d_1) exists; q_s and q_r are the complex spherical reflection coefficients of the ground in source and receiver semi-spaces, respectively.

I. GROUND INFLUENCE ON THE ACOUSTICAL PROTECTION OF THE BARRIER

In practice ground is always present at any barrier location. Then a single number rating index cannot ignore this fact and should account for it. To calculate the diffracted field of a noise barrier, the Helmholtz equation must be used. The analytical solution is not always obtainable, so a number of numerical solutions have been proposed.[5–8] If the ground can be described by a finite impedance, the problem simplifies somehow, nevertheless, methods are still troublesome.[9] The Geometrical Theory of Diffraction of Keller[10] allows us to see the diffracted field as a superposition of single fields associated to different ray paths. This approximation makes the problem easier to understand and many authors have extended the idea[3,11–13] to obtain more and more accurate solutions and it is well adapted to an increasing number of situations.

The presence of a ground plane is a very important issue for the ground characteristics rule the behavior of the acoustic field above the ground. Models of soil impedance and the concept of spherical reflection coefficient play a significant role. In particular the so-called ground effect has been successfully explained by this way. In this work the one-parameter model of Delaney and Bazley[14] has been used, but more accurate and complicated models can be employed.[15–19] The frequency range over which destructive interference occurs is mainly dependent on the flow resistivity of the ground which causes phase change on reflection.

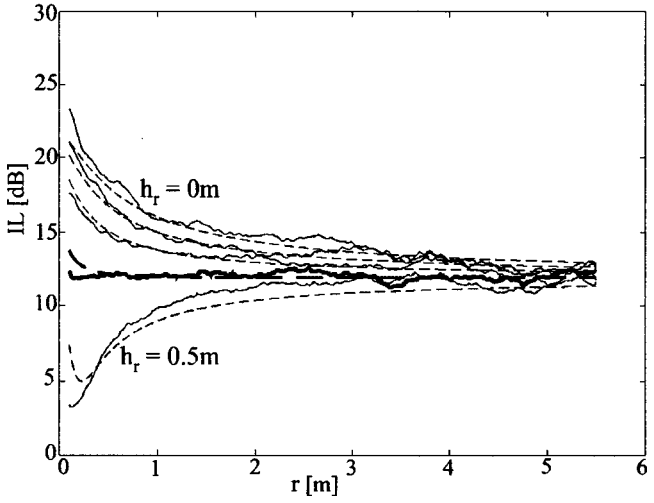

FIG. 2. Insertion loss for semi-infinite barrier. Source–barrier distance: 0.3 m. Source height: 0.25 m. Barrier height: 40 cm. Receiver heights: 0, 0.1, 0.2, 0.32, and 0.5 m. Frequency: $\frac{1}{3}$-oct band centered at 4 kHz. Heights measured from a reference plane (there is no ground): ——— measured, - - - - calculated.

In the following, we will apply these ideas in order to analyze the extension of the previous single rating index to cases where the contribution of the ground could influence actual performances of the barrier. The geometrical situation is sketched in Fig. 1 where it can be seen that there are four possible paths along which the sound field can get the receiver from the source.[20] In this figure, d_1 is the direct path from the source to the receiver diffracted over the barrier, d_2 is the corresponding path reflected on the source half-space then diffracted over the barrier, d_3 is the path of the ray reflected on the receiver half-space after being diffracted by the barrier, and d_4 is the diffracted path reflected in both half-spaces. The pressure for each diffracted path is

$$p_i = A_i Q_i e^{-jkd_i}, \tag{3}$$

where Q_i is the effective spherical reflection coefficient of the ground undergone by the ith path, that is, $Q_1=1$, $Q_2=q_s$, $Q_3=q_r$, and $Q_4=q_r q_s$ (q_s and q_r being the spherical reflection coefficients of the ground in the source and receiver half-spaces, respectively). Here A_i is the amplitude of the ith diffracted pressure ray (it includes the distance attenuation and the diffraction over the edge) and can be calculated by one of well-established methods[12,20] through

$$A_i = A_0 10^{\mathrm{il}_i/20}, \tag{4}$$

il_i being the insertion loss assuming there only exists the ith path. So the acoustic diffracted field p_d at the receiver position can be written

$$p_d = \sum_{i=1}^{4} A_i Q_i e^{-jkd_i}. \tag{5}$$

In Eqs. (3) and (5) the phase changes due to the diffraction at the barrier have been omitted for we assume that these phase changes are approximately the same for every ray path in the shadow zone and for long distances.[21] The incident sound field p_0 in the absence of the barrier is given by

$$p_0 = A_0 e^{-jkd_0} + A_0 Q e^{-jkd_{r0}}, \tag{6}$$

where Q is the spherical reflection coefficient of the ground without barrier, and d_0 and d_{r0} are the distances for the directed and reflected rays, respectively. The insertion loss is then given by

$$\mathrm{IL} = -10\log\left\{\sum_{i=1}^{4}\left|\frac{A_i}{A_0}Q_i\right|^2 + \sum_{\substack{i<1\\ t=2}}^{4} 2\,\mathrm{Re}\left(\frac{A_i}{A_0}\frac{A_t}{A_0}Q_i Q_t\right)\right\} + 10\log\left|1+Qe^{-jk(d_{r0}-d_0)}\right|^2. \tag{7}$$

The argument of the first logarithm has two terms. The first takes into account the energy of each ray, and the second has to do with the interference between every pair of rays. For random broadband signals (as it is for our case) this second term tends to be negligible[22] and Eq. (7) can be rewritten as

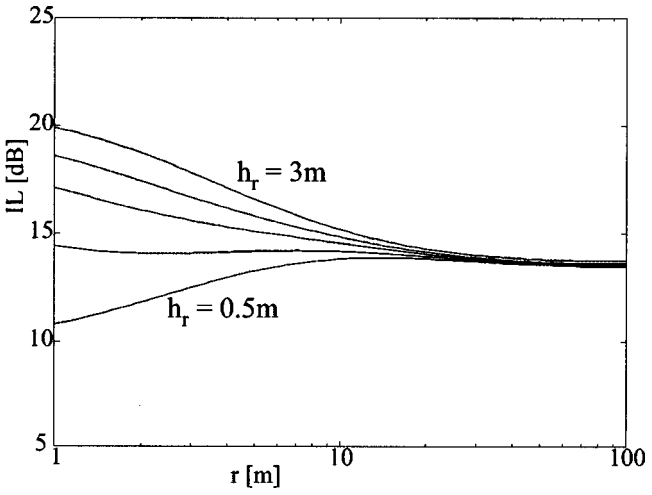

FIG. 3. Insertion loss of a barrier placed on a hard ground ($\sigma = 3 \times 10^7$ Pa·s·m^{-2}) for wideband noise at different receiving heights. It can be observed how all the curves tend to the same asymptote. Source height: 0.5 m. Distance between source and barrier: 7 m. Barrier height: 3 m. Receiver heights: 0.5, 1.5, 2, 2.5, and 3 m. Frequency: 630 Hz.

$$\mathrm{IL} = -10 \log\left\{ \sum_{i=1}^{4} |10^{\mathrm{il}_1/20} Q_i|^2 \right\} + 10 \log\{1 + |Q|^2\}. \quad (8)$$

This expression gives rise to sets of IL curves as functions of r as those in Fig. 3, where h_r is the parameter associated to each curve. It can be seen that, for a given barrier, the whole group of curves has the same asymptote. This provides a way to account for the ground effect at the receiver side by a single value. This asymptotic value will depend on the characteristics related to the barrier and to the source half-space. Therefore its ability to account for the global protection of the barrier should be analyzed.

In the former example, r has been taken as the variable of the problem. If we would have taken s as the variable, the curves would have been the same as that of Fig. 3 due to the reciprocity principle (if source and receiver positions are interchanged, the field must be the same in the new receiving position).

Then the problem can be focused on the calculation of the asymptote IL_∞ of Eq. (8). This asymptote can be calculated through the asymptotic values of its different terms, i.e., through the insertion loss of a semi-infinite barrier $\mathrm{il}_{i\infty}$ and the reflection coefficient of the ground. The former corresponds to Eq. (1) for every ray path, and the latter is calculated in the Appendix, obtaining that

$$\lim_{r \to \infty} q_r = -1. \quad (9)$$

This means that for r big enough it is possible to use a plane wave reflection coefficient for spherical waves as well.[20] Therefore the asymptotic value of the insertion loss is given by

$$\mathrm{IL}_\infty = \lim_{r \to \infty} \mathrm{IL} = -10 \log\{10^{-0.1 \mathrm{il}_{1\infty}} + |q_s|^2 10^{-0.1 \mathrm{il}_{2\infty}}\}, \quad (10)$$

which can also be expressed as

$$\mathrm{IL}_\infty = \lim_{r \to \infty} \mathrm{IL} = \mathrm{il}_{1\infty} - 10 \log\{1 + |q_s|^2 10^{0.1(\mathrm{il}_{1\infty} - \mathrm{il}_{2\infty})}\}, \quad (11)$$

where $\mathrm{il}_{1\infty}$ and $\mathrm{il}_{2\infty}$ are the asymptotic insertion losses in the absence of the ground for paths 1 and 2. The second term of the argument of the logarithm is the product of two factors; the first one is the square of the modulus of a reflection coefficient so it must be less or equal to one. The second is the exponential of a difference that is always less than zero. Therefore this second term will be lower than one and the logarithm can be expanded as a power series, resulting in

$$\mathrm{IL}_\infty \cong \mathrm{il}_{1\infty} - 4.3 |q_s|^2 10^{0.1(\mathrm{il}_{1\infty} - \mathrm{il}_{2\infty})}. \quad (12)$$

The IL_∞ value obtained is always lower to that of the semi-infinite barrier, and, furthermore, the decrease protection will never be higher than 4.3 dB. In Eq. (11), $\mathrm{il}_{i\infty}$ can be calculated by means of any of the well-established methods.[3,11,23] We must keep in mind that what we are looking for is not a better approximation for the noise barrier acoustical protection but an overall value by which the protection can be estimated for a given barrier. The formalism is independent of the computing algorithm used to determine the insertion loss.

In order to get a single number rating index the frequency dependence must be rated. To do that, the index is defined as the energy contained in the frequency bands of analysis, assuming that the spectrum of the source corresponds to that of normalized traffic noise, as used by European standards[1] on insulation and absorption of noise barriers. A-weighting is additionally involved to include subjective characteristics that have been proved to account for loudness reduction in related problems.[24] This process is expressed by

$$\mathrm{IP}_{\mathrm{IL}} = \mathrm{IL}_{w,\infty} = -10 \log \sum_{i=1}^{6} 10^{0.1(L_i - \mathrm{IL}_{1,\infty})} \quad (\text{A-weighted dB}). \quad (13)$$

where $\mathrm{IL}_{i\infty}$ is given by Eq. (9) or (10) for the ith octave band, and L_i is the A-weighted normalized traffic noise. The analysis is carried out in octave bands to assure that the approximation that leads to Eq. (8) is fulfilled, which, on the other hand, matches well with common methods used to check the noise performances of actual noise barriers. This rating index, IP, depends on the height of the barrier, source position, and on the acoustical properties of the ground in source half-space. If the last ones are normalized as it is done in ISO Standards related to the measurement of noise emitted by vehicles, then Eq. (13) can be useful to determinate the noise performance of any barrier.

II. ATTENUATION

Sometimes to study the protection of a barrier the concept of attenuation is useful.[25] The difference between attenuation and insertion loss is that the SPL in the absence of the barrier is calculated for free field propagation conditions,

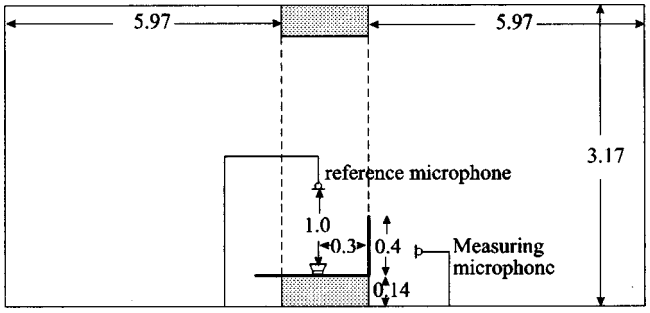

FIG. 4. Experimental setup. Distances are expressed in meters.

i.e., for attenuation only the geometrical spreading of the field is taken into account (assuming free field propagation conditions). Therefore Eq. (6) becomes

$$p_0 = A_0 e^{-jkd_0}, \tag{14}$$

and attenuation is given by

$$\mathrm{At} = -10 \log\left\{ \sum_{i=1}^{4} |Q_i|^2 10^{-0.1 \mathrm{il}_i} \right\}, \tag{15}$$

where the same approximation as that in Eq. (8) (neglecting the interference terms) has been made. The asymptotic value of Eq. (15) is then

$$\mathrm{At}_\infty = \mathrm{il}_{1\infty} - 10 \log\{1 + |q_s|^2 10^{0.1(\mathrm{il}_{1\infty} - \mathrm{il}_{2\infty})}\} - 3, \tag{16}$$

which can be related to Eq. (11) by

$$\mathrm{At}_\infty = \mathrm{IL}_\infty - 3. \tag{17}$$

This expression shows that all the arguments developed for the insertion loss can be applied for the attenuation; so a protection index for the attenuation can be defined as

$$\mathrm{IP}_{\mathrm{At}} = -10 \log \sum_{i=1}^{6} 10^{0.1(L_i - \mathrm{At}_{i,\infty})} \quad \text{(A-weighted dB)}. \tag{18}$$

Substituting Eq. (17) into Eq. (18),

$$\mathrm{IP}_{\mathrm{At}} = \mathrm{IP}_{\mathrm{IL}} - 3 \quad \text{(A-weighted dB)}. \tag{19}$$

III. SCALE MODEL EXPERIMENTS

Scale model experiments were carried out in a 200-m^3 two-room facility for airborne sound insulation tests with a hard concrete floor with a very high acoustic impedance. Band-limited pulsed noise (white noise filtered in the octave band centered at 8 kHz) was used as test signal. The pulse had a sufficiently short duration to allow the signal to be distinguished from the reflections from the wall and ceiling, and a sufficiently long duration to allow interference with the ground reflected sound. The barrier made of plywood, covered with melamine for a low absorption coefficient, was placed at the room discontinuity (see Fig. 4).

The sound source was a loudspeaker with a diaphragm diameter of 25 mm. The receiver was a $\frac{1}{2}$-in. condenser microphone. The receiving height ranged from 0.14–0.75 m. The receiver–barrier distance was from 0.1–5 m. Sound pressure level measurements were made with the barrier, and, in this way, the attenuation was calculated.

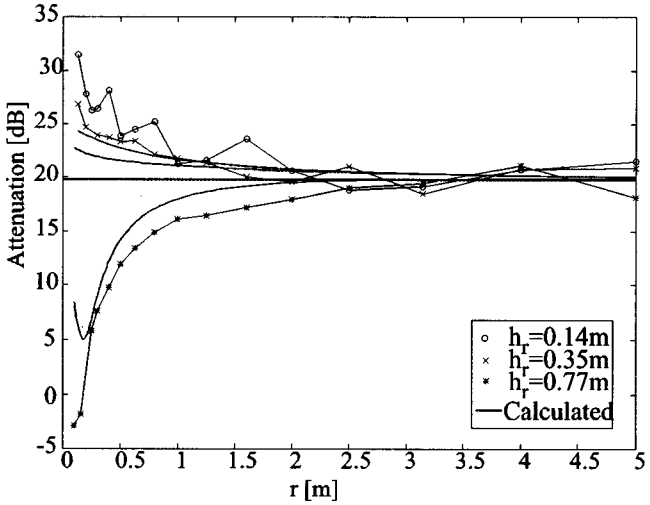

FIG. 5. Measured attenuation for different receiver heights, according to the Fig. 4 experimental setup. Its asymptotic value is represented by a horizontal line, at 19.7 dB.

Figure 5 shows the results for three different heights and their comparison with theoretical predictions. The ground impedance was calculated by the Delany and Bazley[13] approximation using an acoustic resistivity of 3×10^7 Pa·s·m^{-2} for the concrete floor. The horizontal line corresponds to the value of the proposed index. The result supports the approximation of neglecting the interference terms.

Thus the single number rating index defined could be used to describe the overall protection of a noise barrier, since traffic noise has a wideband spectrum. This index can be worked out from experimental data at points located not far away from the barrier.

IV. CONCLUSIONS

An asymptote for the IL of noise barriers has been shown to exist, even when the influence of the ground is taken into account. A model of rating index is developed and shown to be adequate to describe the overall acoustical protection produced by a noise barrier. The predictions from the model agree well with experimental results even at short barrier–receiver distances. The single number rating index has been developed for wideband signals, so it is adequate to octave bands. In addition frequency dependence can be evaluated, including subjective aspects, by means of A weighting a representative spectrum of the noise source (traffic noise, usually).

This index depends on the source position as well as on the reflection coefficient of the source half-space. So, it can be useful in practice if both properties are fixed by means of suitable standardization.

A relation has been found between this index, involving the ground, and the previous one defined for a semi-infinite barrier. In addition an easy relationship between insertion loss and attenuation global indices has been found so that, in cases where the configuration is complex, the latter can be used.

ACKNOWLEDGMENT

This work was supported by the Dirección General de Investigación Cientifica y Técnica (DGICYT), Project No. AMB 95-0101.

APPENDIX: ASYMPTOTIC VALUE OF THE GROUND REFLECTION COEFFICIENT

The reflection coefficient in the receiver half-space is

$$q_r = R_p + (1 - R_p)F(w), \tag{A1}$$

where

$$R_p = \frac{z_r \sin\theta - 1}{z_r \sin\theta + 1} \tag{A2}$$

is the plane wave reflection coefficient. It is well known that for grazing angles (that is our case) its value is -1. On the other hand,

$$F(w) = 1 + j\sqrt{\pi} w e^{-w^2} \operatorname{erfc}(-jw) \tag{A3}$$

is the so-called boundary loss factor, where the variable

$$\begin{aligned} w &= \sqrt{\tfrac{1}{2} jkd_{ro}}\beta \\ &= \tfrac{1}{2}\sqrt{kd_{ro}}\{(\beta_1 - \beta_2) + j(\beta_1 + \beta_2)\} \\ &= w_1 + jw_2 \end{aligned} \tag{A4}$$

is the numerical distance ($\beta = \beta_1 + j\beta_2$ is the ground admittance). For great values of w, Eq. (A3) can be expressed as[26]

$$F(w) = 1 + j\sqrt{\pi} w \sum_{i=1}^{3} j \frac{w a_i}{w^2 - b_i} = 1 - \sqrt{\pi} \sum_{i=1}^{3} \frac{w^2 a_i}{w^2 - b_i}, \tag{A5}$$

where

$$\begin{aligned} &a_1 = 0.4\,613\,135, \quad b_1 = 0.1\,901\,635, \\ &a_2 = 0.09\,999\,216, \quad b_2 = 1.7\,844\,927, \\ &a_3 = 0.002\,883\,894, \quad b_3 = 5.52\,553\,437. \end{aligned} \tag{A6}$$

Thus we have to find

$$\lim_{r\to\infty} S_i = \lim_{r\to\infty} \frac{|w|^4 a_i - w^2 a_i b_i}{|w^2 - b_i|^2}. \tag{A7}$$

By introducing real and imaginary parts of w as a function of real and imaginary parts of β it can be obtained that

$$\lim_{r\to\infty} S_i = \frac{(\beta_1^2 + \beta_2^2)^2 a_i}{4\beta_1^2\beta_2^2 + (\beta_1^2 - \beta_2^2)^2} = a_i, \tag{A8}$$

and the value of Eq. (A5) at infinity is

$$\lim_{r\to\infty} F(w) = 1 - \sqrt{\pi} \sum_{i=1}^{3} a_i \approx 1 - \sqrt{\pi}\,\frac{1}{\sqrt{\pi}} = 0. \tag{A9}$$

So from Eqs. (A2) and (A9) it is easy to verify that

$$\lim_{r\to\infty} q_r = -1. \tag{A10}$$

At first sight this result can be surprising, because if the receiver is moved a long distance from the barrier, then the resulting q_r should tend to the ground effect for a receiver at the height of the barrier. Nevertheless, at infinity the spherical wave becomes plane and because of that the ground effect beyond the barrier vanishes, as Jonasson[20] pointed out in 1972.

[1] European Standard prEN 1973, ''Road traffic noise reducing devices—test method for determining the acoustic performance'' (1995).
[2] J. Pfretzschner, F. Simón, C. de la Colina, and A. Moreno, ''A rating index for estimating insertion loss of noise barriers under traffic noise conditions,'' Acust. Acta Acust. **82**, 504–508 (1996).
[3] U. J. Kurze and G. S. Anderson, ''Sound attenuation by barriers,'' Appl. Acoust. **4**, 35–53 (1971).
[4] F. Simón, ''Acoustical characterization of noise barriers by means of a single number rating index'' (in Spanish), Doctoral thesis, Universidad Complutense de Madrid, Spain, January 23, 1997.
[5] T. Terai, ''On calculation of sound fields around three dimensional objects by integral equation methods,'' J. Sound Vib. **69**(1), 44–54 (1983).
[6] S. Thomasson, ''Diffraction by a screen above an impedance boundary,'' J. Acoust. Soc. Am. **63**, 1768–1781 (1978).
[7] W. J. Hadden and A. D. Pierce, ''Sound diffraction around screens and wedges for arbitrary point source locations,'' J. Acoust. Soc. Am. **69**, 1266–1276 (1981).
[8] A. L'Espérance, J. Nicolas, and G. A. Daigle, ''Insertion loss of absorbent barriers on ground,'' J. Acoust. Soc. Am. **86**, 1060–1064 (1989).
[9] T. Isei, T. F. W. Embleton, and J. E. Piercy, ''Noise reduction by barriers on finite impedance ground,'' J. Acoust. Soc. Am. **67**, 46–58 (1980).
[10] J. B. Keller, ''Geometrical theory of diffraction,'' J. Opt. Soc. Am. **52**, 116–130 (1962).
[11] Z. Maekawa, ''Noise reduction by screens,'' Appl. Acoust. **1**, 157–173 (1968).
[12] R. B. Tatge, ''Barrier-wall attenuation with a finite-sized source,'' J. Acoust. Soc. Am. **53**, 1317–1319 (1973).
[13] Y. W. Lam and S. C. Roberts, ''A simple method for accurate prediction of finite barrier insertion loss,'' J. Acoust. Soc. Am. **93**, 1445–1452 (1993).
[14] M. E. Delaney and E. N. Bazley, ''Acoustical properties of fibrous absorbent materials,'' Appl. Acoust. **3**, 105–116 (1970).
[15] K. Atenborough, ''Ground parameter information for propagation modeling,'' J. Acoust. Soc. Am. **92**, 418–427 (1992).
[16] D. L. Johnson, J. Koplik, and R. Dashen, ''Theory of dynamic permeability and tortuosity in fluid saturated porous media,'' J. Fluid Mech. **176**, 379–402 (1987).
[17] Y. Champoux and M. R. Stinson, ''On acoustical models for sound propagation in rigid frame porous materials and the influence of shape factors,'' J. Acoust. Soc. Am. **92**, 1120–1131 (1992).
[18] M. A. Biot, ''Theory of propagation of elastic waves in a fluid-saturated porous solid,'' J. Acoust. Soc. Am. **28**, 179–191 (1956).
[19] C. Zwikker and C. W. Kosten, *Sound Absorbing Materials* (Elsevier, New York, 1949).
[20] H. G. J. Jonasson, ''Sound reduction by barriers on the ground,'' J. Sound Vib. **22**, 113–126 (1972).
[21] A. D. Pierce, ''Diffraction of sound around corners and over wide barriers,'' J. Acoust. Soc. Am. **55**, 941–955 (1974).
[22] U. J. Kurze, ''Noise reduction by barriers,'' J. Acoust. Soc. Am. **55**, 504–518 (1974).
[23] A. L'Espérance, ''The insertion loss of finite length barriers on the ground,'' J. Acoust. Soc. Am. **86**, 179–183 (1986).
[24] A. Moreno and C. de la Colina, ''Single number ratings for airborne sound insulation. Psychoacoustic foundations, analysis and new definitions,'' Current Topics in Acoust. Res. **1**, 591–600 (1994).
[25] Y. W. Lam, ''On the modeling of the effect of ground terrain profile in environmental noise calculations,'' Appl. Acoust. **42**, 99–123 (1994).
[26] C. F. Chien and W. W. Soroka, ''A note on the calculation of sound propagation along an impedance surface,'' J. Sound Vib. **69**(2), 340–343 (1980).

Plant uncertainty analysis in a duct active noise control problem by using the H_∞ theory

Mingsian R. Bai and Hsinhong Lin
Department of Mechanical Engineering, Chiao-Tung University, 1001 Ta-Hsueh Road, Hsin-Chu 30050, Taiwan, Republic of China

(Received 2 June 1997; accepted for publication 25 March 1998)

Plant uncertainty is one of the major contributing factors that could affect the performance as well as stability of active noise control (ANC) systems. Plant uncertainty may be caused by either the errors in modeling, computation, and measurement, or the perturbations in physical conditions. These factors lead to deviations of the plant from the nominal model, which will in turn affect the robustness of the control system. In this paper, the effects due to changes in physical conditions on the ANC system are investigated. The analysis is carried out in terms of performance and robustness by using a general framework of the H_∞ robust control theory. The *size* of plant uncertainty is estimated according to the infinity norm of the perturbations to physical conditions, which provides useful information for subsequent controller design that accommodates both performance and stability in an optimal and robust manner. The guidelines for designing the ANC systems with reference to plant uncertainties are also addressed.
[S0001-4966(98)02007-4]

PACS numbers: 43.50.Ki [GAD]

INTRODUCTION

Active noise control (ANC) has received persistent research attention since Lueg filed his patent.[1] Advances in fundamental theories, control algorithms, and practical applications of the ANC field have been achieved and can be found in much literature, e.g., Refs. 2 and 3. The potential of this emerging technology masks somewhat the limitations that prevent the technology from full commercial use. One of the limitations of the ANC techniques is the robustness problem of the control systems in the face of plant uncertainties. Plant uncertainties influence the performance and even the stability of closed-loop feedback control systems so severe that ANC methods are sometimes viewed as unreliable approaches in comparison with conventional passive means.

Plant uncertainties generally arise because of the errors in modeling, computation, and measurement. In addition, plant uncertainties may be caused by the change of environmental factors. For example, modeling errors are inevitable prior to an ANC design of a low-frequency duct silencer, where high-frequency modes are usually truncated so that a controller of reasonable order can be implemented. Aside from the modeling error, perturbations of the duct system may also occur due to variations of physical conditions, e.g., temperature, viscosity, boundary conditions, and so forth. In this sense, plant uncertainties are referred to as the *plant variations* due to changes in physical conditions. These factors result in deviations of the plant from the nominal model, which in turn affects the robustness of the closed-loop system. A good feedback ANC system needs a reasonably accurate nominal model for the acoustic plant, which is is assumed to be linear time-invariant (LTI). In many control problems encountered in ANC applications, plant uncertainties can be so severe that any attempt to employ stable feedback controllers results in unacceptable performance.

In this paper, the effects due to changes in physical conditions on the ANC duct silencer are investigated. With the change of various physical conditions taken into account, the mathematical model of a low-frequency duct is established. Performance and robustness analysis is then carried out by using a general framework of the H_∞ robust control theory.[4–9] The *size* of plant uncertainty is first estimated according to the infinity norm of the perturbations to various physical conditions. This provides useful information in choosing appropriate weighting functions for designing an optimal feedback controller that accommodates both performance and stability in a robust manner. The guidelines for designing the ANC systems with reference to plant uncertainties are also addressed. It should also be remarked that the discussions of this paper are limited to fixed, feedback systems only. The results do not always apply to other ANC methods such as feedforward structures.

I. MATHEMATICAL MODELING OF THE LOW-FREQUENCY DUCT

In this section, the mathematical models of the sound fields in a rectangular duct subject to various physical conditions are derived. A duct of length l is schematically shown in Fig. 1(a). It is assumed that the duct is open at one end and terminated at the other. Below the cutoff frequency, the sound field in the duct can be treated as one dimensional with spatial coordinate x, $0 \leqslant x \leqslant l$. A monopole source is located at $x = x_s$, while the sensor is located at $x = x_m$.

To begin with, we consider the joint effects due to lining, viscosity, temperature, and flow. Knowing that, similar to the loss mechanism due to viscosity of the medium, the effect of duct lining is to dissipate acoustic energy at the boundaries. As shown in pp. 26–30 of Ref. 12, lining duct walls results in attenuations in the axial direction and the

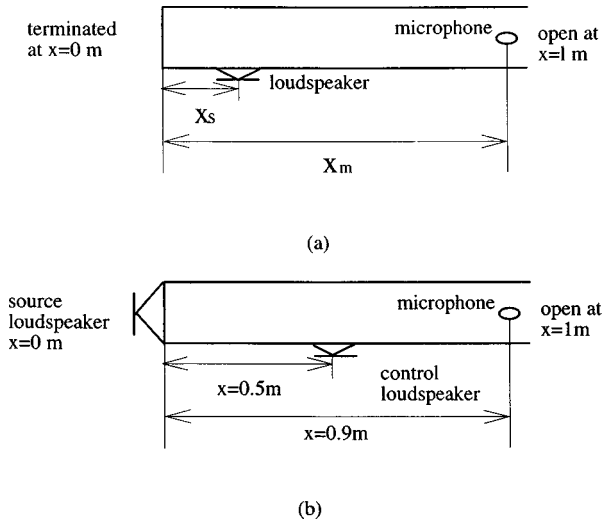

FIG. 1. (a) Modeling configuration of the low-frequency duct; (b) the experimental configuration of the low-frequency duct.

plane-wave number becomes complex. By the same token, rather than modeling the duct lining precisely as a boundary condition, we take a simpler approach to model this attenuation effect by an *ad hoc* relaxation constant τ, which corresponds to the complex wave number

$$k=\frac{\omega}{c}\frac{1}{\sqrt{1+j\omega\tau}}, \tag{1}$$

where ω is angular frequency and c is sound speed.[10] By substituting the definition

$$k\equiv\beta-j\alpha \tag{2}$$

into Eq. (1) and by collecting real and imaginary parts, the attenuation constant α is obtained

$$\alpha=\frac{k}{\sqrt{2}}\left[\sqrt{1+(\omega\tau)^2}-1\right]^{1/2}. \tag{3}$$

In the following simulation, the attenuation constant α, or equivalently the relaxation constant τ, for each case can be obtained from the method described in p. 510 of Ref. 11. Following the procedure described in pp. 503–510 of Ref. 11, we further assume the normal acoustical impedance of the lining to be $Z=f\times(0.471-j0.392)$, where f is the frequency in Hz.

Next the temperature is assumed for simplicity to be uniformly distributed inside the duct. Therefore the effect of temperature variation would be to alter the speed of sound.[10] That is,

$$c=C_0\sqrt{1+\frac{T}{273}}, \tag{4}$$

where C_0 is sound speed at 0 °C and T is Celsius temperature.

It can be shown that the dynamic equation that incorporates the effects due to lining, viscosity, temperature, and flow for the sound field in the duct is[12]

$$\left(1+\tau\frac{\partial}{\partial t}\right)\nabla^2 p(x,t)=\frac{1}{c}\frac{D^2}{Dt^2}p(x,t)+d(x,t) \tag{5}$$

with the *material derivative*

$$\frac{D}{Dt}\equiv\frac{\partial}{\partial t}+u\frac{\partial}{\partial x},$$

where u is mean flow velocity, p is the sound pressure, and ρ_0 is the density of acoustic medium. It is assumed that a monopole source[13] is located at $x=x_s$.

$$d(x,t)=v_s(t)\,\delta(x-x_s), \tag{6}$$

where v_s is the volume velocity. Assume further that the boundary conditions of the duct are

$$\frac{\partial}{\partial x}p(0,t)=0 \quad \text{at } x=0 \tag{7}$$

and

$$p(l,t)=0 \quad \text{at } x=l. \tag{8}$$

By separation of variables

$$p(x,t)=q(t)v(x), \tag{9}$$

Eq. (5) can be written into a modal form

$$\ddot{q}(t)+\Omega_i\dot{q}_i(t)+\sum_{\substack{j=1\\ j\neq i}}^{\infty}\omega_{ij}\dot{q}_j(t)+\psi_i\dot{q}_i(t)+\lambda_i q_i(t)=b_i u_s(t), \tag{10}$$

where

$$b_i\equiv\nu_i(x_s),\quad u(t)\equiv\rho_0 v(t),$$

$$\Omega_i=\frac{u}{l}\left[(-1)^i-1\right],$$

$$\omega_{ij}=\frac{(2j-1)\pi}{l}\left[\frac{\cos[(i+j-1)\pi]-1}{i+j-1}+\frac{\cos[(j-i)\pi]-1}{j-i}\right], \tag{11}$$

$$\psi_i=c(T)^2\tau_i\left[\frac{(2i-1)\pi}{l}\right]^2,$$

$$\lambda_i=(c^2-u^2)\left[\frac{(2i-1)\pi}{l}\right]^2,$$

with

$$\nu_i(x)=c(T)\sqrt{\frac{2}{l}}\cos\frac{(2i-1)\pi}{2l}x. \tag{12}$$

Hence the sound pressure y_m measured by a microphone located at $x=x_m$ is

$$y_m(t)=p(x_m,t)=\sum_{j=1}^{\infty}q_j(t)v_j(x_m). \tag{13}$$

To obtain the state-space model, we retain only r modes and let

$$x(t)=[q_1 \quad q_1 \quad \cdots \quad q_r \quad q_r],$$

$$y(t)=y_m(t)$$

so that

$$\dot{x}(t)=Ax(t)+Bu_s(t), \quad y(t)=Cx(t), \tag{14}$$

where

$$A_{ij}=\begin{cases} i \text{ is odd:} & \begin{cases} j=i+1: \ A_{ij}=1 \\ \text{others:} \ A_{ij}=0 \end{cases} \\ i \text{ is even:} & \begin{cases} j=i: \ A_{ij}=\Omega_{i/2} \\ j=i-1: \ A_{ij}=\lambda_{i/2} \\ \text{others:} & \begin{cases} j \text{ is odd:} \ A_{ij}=0 \\ j \text{ is even:} \ A_{ij}=\omega_{i/2j/2} \end{cases} \end{cases} \end{cases},$$

$$B=[0 \quad b_1 \quad \cdots \quad 0 \quad b_r]^T,$$

$$C=[V_1(x_m) \quad 0 \quad \cdots \quad V_r(x_m) \quad 0].$$

The second half of the section is focused on the modeling of the sound field in the duct subject to the radiation impedance at the open end. This boundary condition can be described by an impedance function[14]

$$Z_l(s)=\frac{p(l,s)}{u(l,s)}, \quad x=l, \tag{15}$$

where $Z_l(s)$ is the Laplace transform of the specific acoustic impedance. The relationship between the sound pressure and the particle velocity satisfies the momentum equation

$$\frac{\partial p(x,s)}{\partial x}=-\rho_0 s u(l,s). \tag{16}$$

Thus the problem is formulated as the following modified wave equation and boundary conditions:

$$\frac{1}{c(T)^2}\left(s^2+2us\frac{\partial}{\partial x}+u^2\frac{\partial^2}{\partial x^2}\right)p(x,s)$$

$$=(1+\tau s)\frac{\partial^2}{\partial x^2}p(x,s)+\rho_0 s v_s(s)\delta(x-x_s)$$

such that

$$\frac{\partial p(0,s)}{\partial x}=0,$$

$$p(l,s)=-\frac{1}{s\rho_0}Z_l(s)\frac{\partial p(l,s)}{\partial x}, \tag{17}$$

where $c(T)$ is the speed of sound as a function of temperature T. It can be shown by some manipulations that the transfer function between any source point and field point is[15]

$$G(x,\xi,s)=\begin{cases} x<\xi \\ \dfrac{c(T)^2(\lambda_2 e^{\lambda_2 x}-\lambda_1 e^{\lambda_1 x})[e^{\lambda_2(1-\xi)}-e^{\lambda_1(1-\xi)}+(Z_l/s\rho_0)(\lambda_2 e^{\lambda_2(1-\xi)}-\lambda_1 e^{\lambda_1(1-\xi)})]}{e^{(\lambda_1+\lambda_2)x}(\lambda_2-\lambda_1)[u^2-(1+\tau s)c(T)^2][\lambda_2 e^{\lambda_1}-\lambda_1 e^{\lambda_2}+(Z_l/s\rho_0)\lambda_1\lambda_2(e^{\lambda_1}-e^{\lambda_2})]} \\ x>\xi \\ \dfrac{c(T)^2(\lambda_2 e^{\lambda_1\xi}-\lambda_1 e^{\lambda_2\xi})[e^{\lambda_1+\lambda_2 x}-e^{\lambda_2+\lambda_1 x}+(Z_l/s\rho_0)(\lambda_1 e^{\lambda_1+\lambda_2 x}-\lambda_2 e^{\lambda_2+\lambda_1 x})]}{e^{(\lambda_1+\lambda_2)\xi}(\lambda_2-\lambda_1)[u^2-(1+\tau s)c(T)^2][\lambda_2 e^{\lambda_1}-\lambda_1 e^{\lambda_2}+(Z_l/s\rho_0)\lambda_1\lambda_2(e^{\lambda_1}-e^{\lambda_2})]} \end{cases},$$

where $\lambda_1(s)$ and $\lambda_2(s)$ are two roofs of

$$\lambda^2-\frac{2us}{u^2-(1+\tau s)c(T)^2}\lambda-\frac{s^2}{u^2-(1+\tau s)c(T)^2}=0. \tag{18}$$

In terms of $G(x,\xi,s)$, the Laplace transform of sound pressure at any location x in the duct can be expressed as

$$p(x,s)=G(x,\xi,s)|_{\xi=x_s}Q(x_s,s), \tag{19}$$

where $Q(x_s,s)$ is the Laplace transform of $\rho_0\dot{v}_s(t)$. It should be noted that the above solution gives an exact description of the system without truncating any high-order terms. Thus Eq. (18) can be used to calculate the frequency response and provides complete information about plant uncertainties. However, it is generally difficult to produce dynamic responses, as required in a numerical simulation, based on Eq. (18) that are not a rational transfer function. To obviate the problem, we simply curve-fit the frequency response of Eq. (18) and convert it into a more tractable rational transfer function by using a MATLAB routine INVFREQS.[16]

II. H_∞ ROBUST CONTROL ANALYSIS AND SYNTHESIS

A brief review of the H_∞ robust control theory is given in this section. Because the H_∞ theories can be found in much control literature,[4–9] we present only the key ones needed in the analysis of our problem. The rest are mentioned without proof.

In modern control theory, all control structures can be described by using a generalized control framework, as depicted in Fig. 2. The framework contains a controller $C(s)$ and an *augmented plant* $P_\gamma(s)$. The controlled variable $\nu(t)$ corresponds to various control objectives $z_1(t)$, $z_2(t)$, and $z_3(t)$, and the extraneous input $w(t)$ consists of the reference $r(t)$, the disturbance $d(t)$, and the noise $n(t)$. The signals $u(t)$ and $e(t)$ are the control inputs to the plant and the measured output from the plant, respectively. The general input–output relation can be expressed as

$$P_\gamma(s)=\begin{bmatrix} P_{11}(s) & P_{12}(s) \\ P_{21}(s) & P_{22}(s) \end{bmatrix}, \tag{20}$$

where the submatrices $P_{ij}(s)$, $i,j=1,2$ are compatible par-

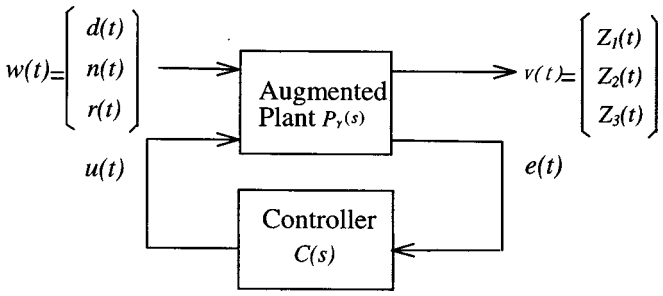

FIG. 2. Generalized control framework. $P_\gamma(s)$ is the augmented plant and $C(s)$ is the controller.

titions of the augmented plant $P_\gamma(s)$ and the symbols are capitalized to represent the Laplace transform variables. The main idea of the H_∞ control is to minimize the infinity norm of the transfer function $T_{\nu w}(s)$ between $\nu(t)$ and $w(t)$ that can be expressed by the *linear fraction transformation* (LFT)

$$T_{\nu w}(s)=\mathrm{LFT}(P_\gamma(s),C(s)) =P_{11}(s)+P_{12}(s)C(s)[1-P_{22}(s)C(s)]^{-1}P_{21}(s). \tag{21}$$

Hence the optimal H_∞ problem can be stated as

$$\min_{C(s)}\|T_{\nu w}(s)\|_\infty=\min_{C(s)}\sup_{-\infty\leqslant\omega\leqslant\infty}\|T_{\nu w}(j\omega)\|. \tag{22}$$

However, instead of finding the optimal solution, which is generally very difficult, one is content with the suboptimal solution that can be analytically obtained. This becomes the so-called *standard* H_∞ *problem*: finding $C(s)$ such that $\|T_{\nu w}(s)\|_\infty<1$.

Insofar as the solution of the suboptimal problem is concerned, we would like to remark that the H_∞ algorithms are by large divided into two classes: the model matching algorithms (the 1984 approach) and the two Riccati equation algorithms (the 1988 approach). The details are omitted for brevity. The interested reader may consult Refs. 4 and 7.

In the sequel, an analysis is carried out for the feedback structure (Fig. 3) on the basis of the generalized control framework. The symbols $P_1(s)$ and $P_2(s)$ correspond to the primary (disturbance) path and the secondary (control) path, respectively. To find an H_∞ controller, we weight the sensitivity function $\tilde{S}(s)$ by $W_1(s)$, the control input $u(t)$ by $W_2(s)$, and the complementary sensitivity function $\tilde{T}(s)$ by $W_1(s)$, where the sensitivity function and the complementary sensitivity function are defined, respectively, as[17]

$$\tilde{S}(s)=\frac{1}{1+P_2(s)C(s)} \tag{23}$$

and

$$\tilde{T}(s)=\frac{P_2(s)C(s)}{1+P_2(s)C(s)}. \tag{24}$$

Note that $\tilde{S}(s)+\tilde{T}(s)=1$. To achieve disturbance rejection and tracking performance, the following nominal performance condition must be satisfied

$$\|\tilde{S}(s)W_1(s)\|_\infty<1. \tag{25}$$

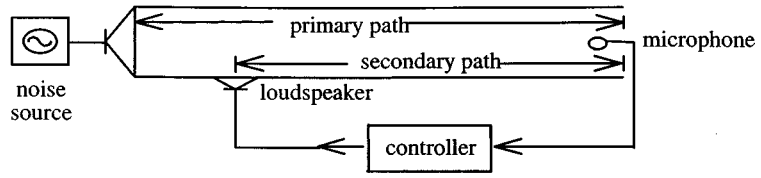

(a)

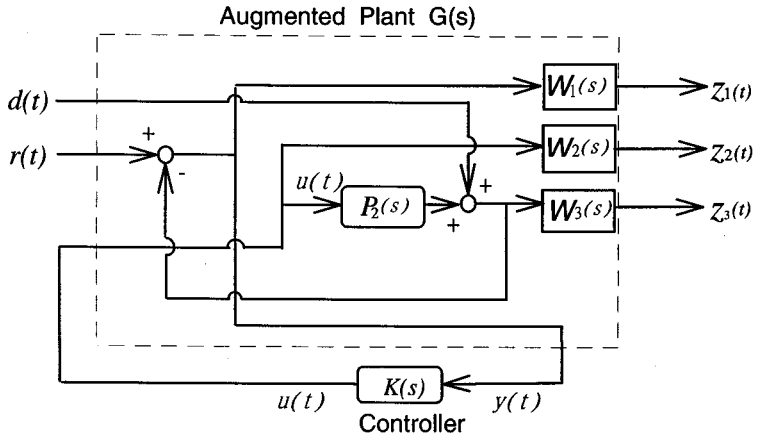

FIG. 3. System diagrams of the active silencer diagrams. (a) Duct arrangement; (b) block diagram of the feedback control.

TABLE I. The mathematical models of the sound field in the duct subject to different physical conditions.

Model	Flow	Temperature	Radiation impedance	Lining
1				
2				X
3	X			
4	X			X
5		X		
6		X		X
7			X	
8			X	X

On the other hand, for system stability against plant perturbations and model uncertainties, the robustness condition derived from the *small-gain theorem*[7] must also be satisfied

$$\|\tilde{T}(s)W_3(s)\|_\infty < 1. \tag{26}$$

The choice of $W_3(s)$ is determined by the size of uncertainty Δ that is defined in

$$\tilde{P}_2 = (1+\Delta)P_2, \tag{27}$$

where P_2 and $\tilde{P}_2$ are the nominal and the perturbed plants, respectively. The idea behind this definition of uncertainty is that Δ is the plant perturbation away from the nominal one and so $|\Delta(j\omega)|$ provides the uncertainty profile and the peak of which (evaluated by the infinity norm) renders the size of uncertainty.

In the common practice of loop shaping, $W_1(s)$ is chosen as a low-pass function and $W_3(s)$ is chosen as a high-pass function. The guidelines for choosing weight functions can be found in pp. 255–268 of Ref. 8. It is well known that the trade-off between $\tilde{S}(s)$ and $\tilde{T}(s)$ in conjunction with the *waterbed effect* dictate the performance and robustness of the feedback design. This classical trade-off renders the so-called *mixed sensitivity problem*:[8]

$$\| |\tilde{S}(s)W_1(s)| + |\tilde{T}(s)W_3(s)| \|_\infty < 1 \tag{28}$$

which is also a necessary and sufficient condition for the controller to achieve robust performance.

In terms of the generalized control framework, the input–output relation of the augmented plant corresponding to the feedback structure is

$$\begin{bmatrix} Z_1(s) \\ Z_2(s) \\ Z_3(s) \\ E(s) \end{bmatrix} = \begin{bmatrix} W_1(s) & -W_1(s)P_2(s) \\ 0 & W_2(s) \\ 0 & W_3(s)P_2(s) \\ 1 & -P_2(s) \end{bmatrix} \begin{bmatrix} D(s) \\ U(s) \end{bmatrix}. \tag{29}$$

Hence it can be shown by LFT that the suboptimal condition of the feedback controller is

$$\left\| \begin{bmatrix} W_1(s)\tilde{S}(s) \\ W_2(s)\tilde{S}(s)C(s) \\ W_3(s)\tilde{T}(s) \end{bmatrix} \right\|_\infty < 1. \tag{30}$$

III. NUMERICAL SIMULATION

Numerical investigations were carried out to explore the characteristics of the forgoing H_∞-based active controller subject to various plant perturbations. In the simulation, a rectangular duct with 0.25×0.25-m cross section (cutoff frequency=690 Hz) and of length 1 m is selected. A monopole source is located at one end of the duct, while the duct is left open at the other end [Fig. 1(b)]. Another loudspeaker located at $x=0.5$ m is used as the actuator. The sensor is

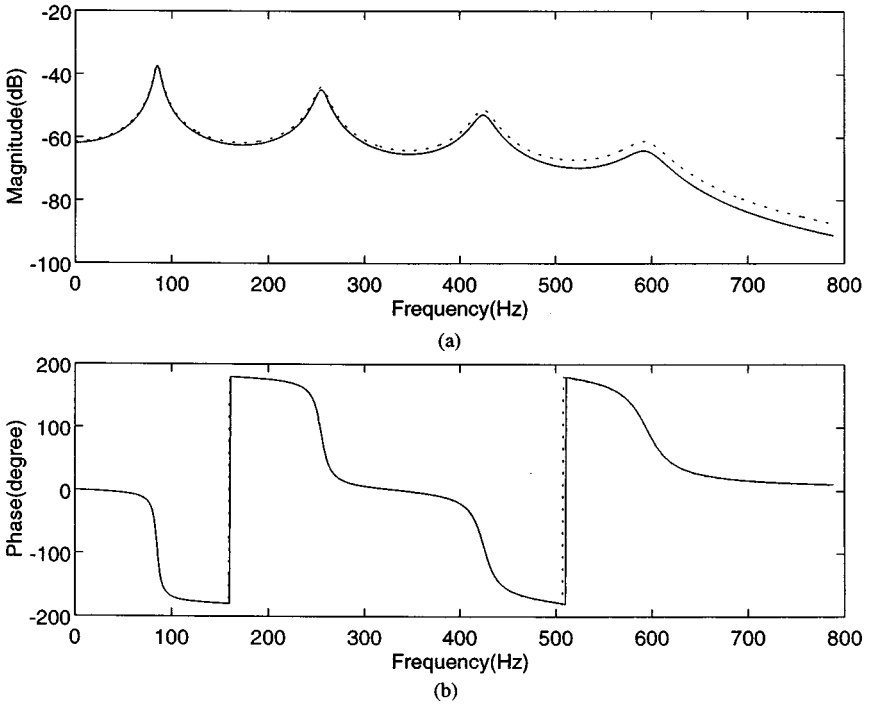

FIG. 4. Frequency response of the derived model and a real muffler (derived model: ———; real muffler: ---). (a) Magnitude (dB); (b) Phase (degree).

TABLE II. The system poles and zeros of model 1. The asterisk denotes nonminimal phase zeros.

Primary path		Secondary path	
Zeros ($\times 10^3$)	Poles ($\times 10^3$)	Zeros ($\times 10^3$)	Poles ($\times 10^3$)
$*2.2725 \pm 1.5081i$	$-0.0005 \pm 0.5341i$	$*1.8564 \pm 1.3748i$	$-0.0005 \pm 0.5341i$
$-0.0004 \pm 3.5118i$	$-0.0005 \pm 1.6022i$	$-0.0005 \pm 3.4732i$	$-0.0005 \pm 1.6022i$
$-2.2731 \pm 1.5076i$	$-0.0005 \pm 2.6703i$	$-1.8573 \pm 1.3742i$	$-0.0005 \pm 2.6703i$
	$-0.0005 \pm 3.7384i$		$-0.0005 \pm 3.7384i$
gain $= -2.7876$		gain $= 5.5771$	

TABLE III. The system poles and zeros of model 2. The asterisk denotes nonminimal phase zeros.

Primary path		Secondary path	
Zeros ($\times 10^3$)	Poles ($\times 10^3$)	Zeros ($\times 10^3$)	Poles ($\times 10^3$)
$*2.2599 \pm 1.5705i$	$-0.0202 \pm 0.5336i$	$*1.8403 \pm 1.4189i$	$-0.0202 \pm 0.5336i$
$-0.1094 \pm 3.5101i$	$-0.0412 \pm 1.6017i$	$-0.1074 \pm 3.4716i$	$-0.0412 \pm 1.6017i$
$-2.2848 \pm 1.4459i$	$-0.0675 \pm 2.6695i$	$-1.8726 \pm 1.3305i$	$-0.0675 \pm 2.6695i$
	$-0.1253 \pm 3.7364i$		$-0.1253 \pm 3.7364I$
gain $= -2.7876$		gain $= 5.5771$	

TABLE IV. The system poles and zeros of model 3. The asterisk denotes nonminimal phase zeros.

Primary path		Secondary path	
Zeros ($\times 10^3$)	Poles ($\times 10^3$)	Zeros ($\times 10^3$)	Poles ($\times 10^3$)
$*1.4423 \pm 2.5471i$	$-0.0216 \pm 0.5332i$	$*1.3320 \pm 2.1803i$	$-0.0242 \pm 0.5299i$
$*1.5192$	$-0.0276 \pm 1.6020i$	$-0.4164 \pm 3.0452i$	$-0.0276 \pm 1.5902i$
-1.9499	$-0.0321 \pm 2.6678i$	$-1.7659 \pm 2.6509i$	$-0.0321 \pm 2.6510i$
$-2.7569 \pm 2.7680i$	$-0.0463 \pm 3.7372i$		$-0.0463 \pm 3.7577i$
gain $= -2.7876$		gain $= 5.5771$	

TABLE V. The system poles and zeros of model 4. The asterisk denotes nonminimal phase zeros.

Primary path		Secondary path	
Zeros ($\times 10^3$)	Poles ($\times 10^3$)	Zeros ($\times 10^3$)	Poles ($\times 10^3$)
$*1.3320 \pm 2.1803i$	$-0.0242 \pm 0.5321i$	$*1.4560 \pm 2.2013i$	$-0.0242 \pm 0.5321i$
$*1.5192$	$-0.0469 \pm 1.6004i$	$-1.2504 \pm 1.9087i$	$-0.0469 \pm 1.6004I$
-1.9499	$-0.0714 \pm 2.6413i$	$-1.8106 \pm 2.6430i$	$-0.0714 \pm 2.6413I$
$-1.7659 \pm 2.6509I$	$-0.1329 \pm 3.7331I$		$-0.1329 \pm 3.7331I$
gain $= -2.7876$		gain $= 5.5771$	

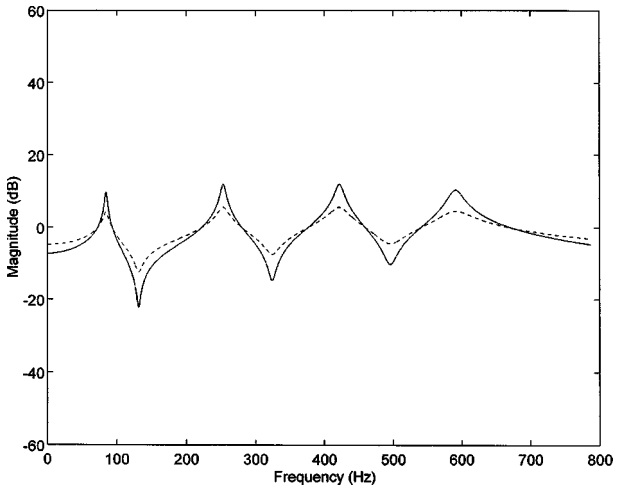

FIG. 5. Plant uncertainty due to moving medium (mean-flow velocity=30 m/s). Without lining: ———; with lining: ---.

located at $x=0.9$ m. In what follows, a series of numerical experiments will be conducted to explore the effects of flow, temperature, and radiation impedance on the system. To aid the comparison, the models used in the simulation under various physical conditions are summarized in Table I.

To show how well the derived model matches a real duct silencer, the frequency response magnitude and phase of model 2 is compared with a real silencer with lining in p. 27 of Ref. 12. The comparison shown in Fig. 4 indicates that the derived model agrees reasonably well with a real silencer.

In the first experiment, the effect of flow on the duct silencer is examined. In addition, it is demonstrated in this experiment that the size of uncertainty due to flow relies on whether the duct is lined or not. In the lined duct, the walls of the duct are lined with absorbing material. The lining thickness and the flow resistance of the absorptive lining material are 0.025 m and 4000 mks rayls, respectively. The cross section of the lined duct is intentionally chosen to be the cross section of a duct in p. 503 of Ref. 11. Using the mathematical model derived in the last sections, the system poles and zeros of the unlined duct and the lined duct for the stationary medium (models 1 and 2 in Table I) are listed in Tables II and III, respectively. The system poles and zeros of the unlined duct and the lined duct for the moving medium (mean flow velocity=30 m/s; models 3 and 4 in Table I) are listed in Tables IV and V, respectively. Before showing the result, a brief note regarding duct lining is in order. The importance of passive lining that has often been overlooked in ANC design lies in not only high-frequency attenuation but also the robustness of active control with respect to plant uncertainties.[18] With proper damping treatment, the plant can be gain-stabilized even when the flexible modes are poorly modeled. Another benefit of passive lining is that a lower order of plant model can usually be obtained than the lightly damped plants so that numerical error is reduced. The importance of passive treatment can be seen by noting the effect of flow subject to different lining conditions. By comparing the nominal model 1 and the perturbed model 3, the plant uncertainty due to flow calculated for the unlined duct is shown by a solid line in Fig. 5. Similarly, by comparing the nominal model 2 and the perturbed model 4, the plant uncertainty due to flow calculated for the lined duct is shown by a dashed line in the same figure. The peaks of uncertainty appear at the resonances and antiresonances of the nominal perturbed plants. However, as seen in Fig. 5, the peaks of the lined duct are lower than those of the unlined duct. This implies that the passive lining indeed has the desirable effect of neutralizing system perturbation. The smaller the size of uncertainty is, the less the requirement of robust stability and the more room for achieving performance in the control design. On the basis of the plant uncertainty due to flow, optimal controllers can be obtained for both the unlined duct and the lined duct by using the aforementioned H_∞ design procedure (Fig. 6). The resulting loop shaping of sensitivity functions versus weight functions for the unlined duct and the lined duct are shown in Figs. 7 and 8. The active control results in terms of the power spectrum of sound pressure at the sensor position are shown in Fig. 9. It can be observed that the performance of the lined duct is better than the unlined duct (12 dB versus 7 dB at the peak of 85 Hz) and also the effective control band of the lined duct is wider than the

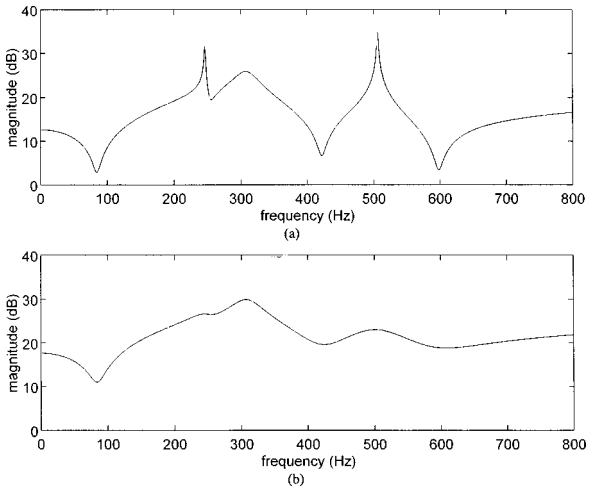

FIG. 6. Magnitude (dB) of frequency responses of the H_∞ controllers (mean-flow velocity=30 m/s). (a) Unlined duct; (b) lined duct.

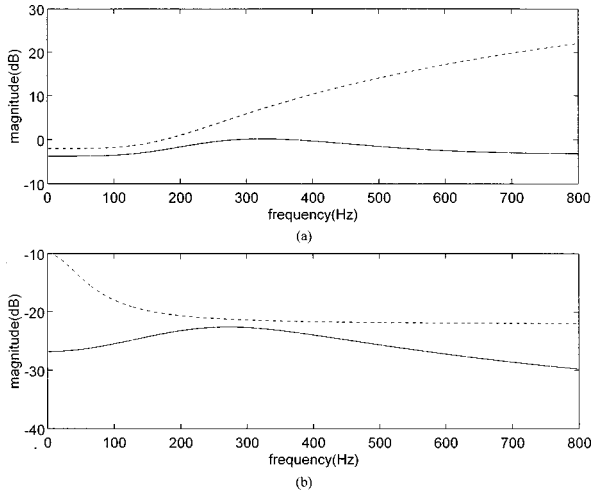

FIG. 7. Loop shaping for the unlined duct (mean-flow velocity=30 m/s). (a) $W_1^{-1}(s)$: ⋯ versus $\tilde{S}(s)$: ———; (b) $W_3^{-1}(s)$: ⋯ versus $\tilde{T}(s)$: ———.

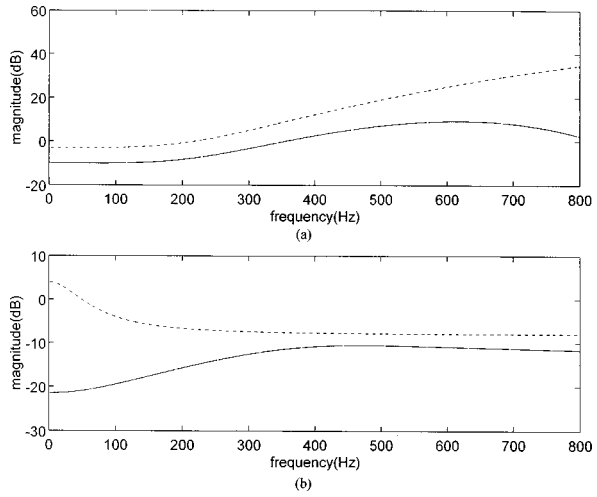

FIG. 8. Loop shaping for the lined duct (mean-flow velocity=30 m/s). (a) $W_1^{-1}(s)$: ⋯ versus $\tilde{S}(s)$: ———; (b) $W_3^{-1}(s)$: ⋯ versus $\tilde{T}(s)$: ———.

control band of the unlined duct. It is noteworthy that Fig. 9 shows good control at low frequency down to 0 Hz because the acoustic sources used in the simulation are ideal point sources. Practical acoustic actuators should have poor response at the very low-frequency range.

In the second experiment, the effect of temperature variation on the silencer is examined. It is assumed that the temperature is changed from 25 to 90 °C for both the unlined duct and the lined duct. By comparing the nominal model 1 and the perturbed model 5, the plant uncertainty due to temperature variation calculated for the unlined duct is shown by a solid line in Fig. 10. Similarly, by comparing the nominal model 2 and the perturbed model 6, the plant uncertainty due to flow calculated for the lined duct is shown by a dashed line in the same figure. The plant uncertainty shows strong peaks (maximum 45 dB) for the unlined duct, while the plant uncertainty of the lined duct shows only moderate variations. This sharp contrast (which is even more pronounced than the forgoing case of flow effect) indicates again the need of passive lining, insofar as the system robustness against system

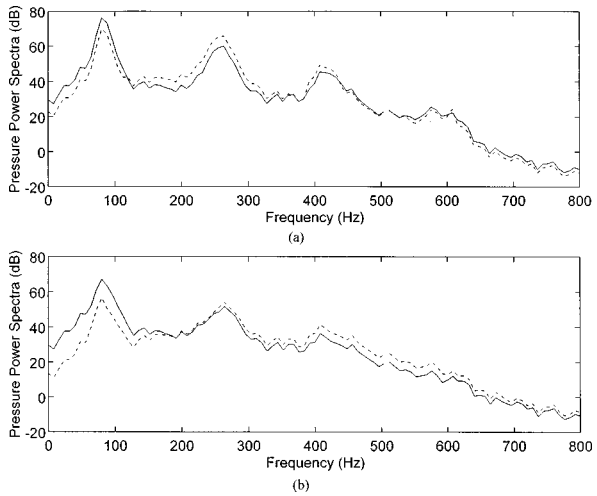

FIG. 9. The active control results for the duct subject to flow effect in terms of the power spectrum of sound pressure at the sensor position (control off: ———; control on: ---). (a) Without lining; (b) with lining.

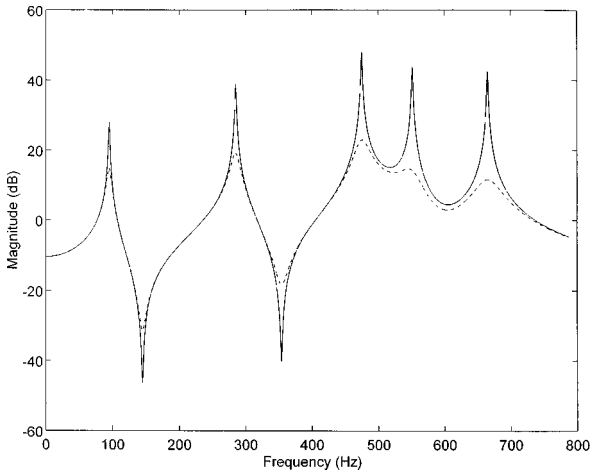

FIG. 10. Plant uncertainty due to temperature variation (25–90 °C). Without lining: ———; with lining: ---.

perturbation is concerned. In fact, for the unlined duct, the plant uncertainty is so severe that virtually no controller can meet the requirements of the H_∞ design. Hence only the controller for the lined duct is calculated on the basis of the plant uncertainty. For brevity, we omit the frequency response of the controller and show only the result of active control in Fig. 11. Noise attenuation is achieved by using the lined duct in the band 0–150 Hz. Nevertheless, noise amplification around the second peak at 280 Hz indicates the difficulty in designing the controller to accommodate the perturbation due to temperature variation.

In the third experiment, the effect of radiation impedance at the open end of the duct is examined. The Laplace transform of radiation impedance is assumed to be $Z_t = -0.01s^2 + 100s$ that is intentionally made larger than that of an open end. This situation may happen, for example, when the open end of the silencer is near a wall. Because the importance of passive lining against plant uncertainty has been manifested in the previous cases, we now explore the effect of radiation impedance on only the lined duct. Taking model 2 as the nominal case and model 8 as the perturbed case, the corresponding plant uncertainty is shown in Fig. 12.

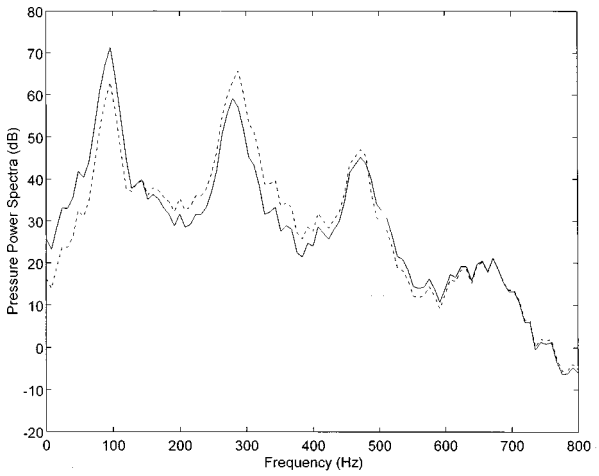

FIG. 11. The active control results for the lined duct subject to temperature variation in terms of the power spectrum of sound pressure at the sensor position (control off: ———; control on: ---).

TABLE VI. The system poles and zeros of model 5. The asterisk denotes nonminimal phase zeros.

Primary path		Secondary path	
Zeros ($\times 10^3$)	Poles ($\times 10^3$)	Zeros ($\times 10^3$)	Poles ($\times 10^3$)
*1.5114±2.4650*i*	−0.0005±0.5950*i*	1.4876±2.5214*i*	0.0005±0.5950*i*
*1.7214	−0.0005±0.7851*i*	1.2390±3.7165*i*	0.0005±1.7851*i*
−2.1520	−0.0005±2.9752*i*	1.9416±2.9247*i*	0.0005±2.9752*i*
−1.9453±2.9362*i*	−0.0005±4.1653*i*		0.0005±4.1653*i*
gain=−2.7876		gain=5.5771	

TABLE VII. The system poles and zeros of model 6. The asterisk denotes nonminimal phase zeros.

Primary path		Secondary path	
Zeros ($\times 10^3$)	Poles ($\times 10^3$)	Zeros ($\times 10^3$)	Poles ($\times 10^3$)
*1.5114±2.4650*i*	−0.0202±0.5950*i*	*1.4892±2.4319*i*	−0.0202±0.5950*i*
−1.7214±2.1520*i*	−0.0412±1.7851*i*	−1.6754±2.2347*i*	−0.0412±1.7851*i*
−1.9453±2.9362*i*	−0.0675±2.9752*i*	−1.8892±2.8764*i*	−0.0675±2.9752*i*
	−0.1253±4.1653*i*		−0.1253±4.1653*i*
gain=−2.7876		gain=5.5771	

TABLE VIII. The system poles and zeros of model 7. The asterisk denotes nonminimal phase zeros.

Primary path		Secondary path	
Zeros ($\times 10^3$)	Poles ($\times 10^3$)	Zeros ($\times 10^3$)	Poles ($\times 10^3$)
*1.6763±2.5082*i*	−0.0005±0.5162*i*	*1.6043±2.5732*i*	−0.0005±0.5162*i*
*1.4182	−0.0005±1.5486*i*	−1.1432±2.1746*i*	−0.0005±1.5486*i*
−1.8490	−0.0005±2.5811*i*	−1.2226±2.0457*i*	−0.0005±2.5811*i*
−1.2425±2.0380*i*	−0.0005±3.6135*i*		−0.0005±3.6135*i*
gain=−2.7876		gain=5.5771	

TABLE IX. The system poles and zeros of model 8. The asterisk denotes nonminimal phase zeros.

Primary path		Secondary path	
Zeros ($\times 10^3$)	Poles ($\times 10^3$)	Zeros ($\times 10^3$)	Poles ($\times 10^3$)
*1.2113±1.9981*i*	−0.0202±0.5158*i*	*1.2145±1.9972*i*	−0.0202±0.5158*i*
*1.3855	−0.0412±1.5451*i*	*1.4255	−0.0412±1.5451*i*
−1.8884	−0.0675±2.5784*i*	−1.8912	−0.0675±2.5784*i*
−1.2113±1.9981*I*	−0.1253±3.6012*i*	−1.2318±1.9847*I*	−0.1253±3.6012*i*
gain=−2.7876		gain=5.5771	

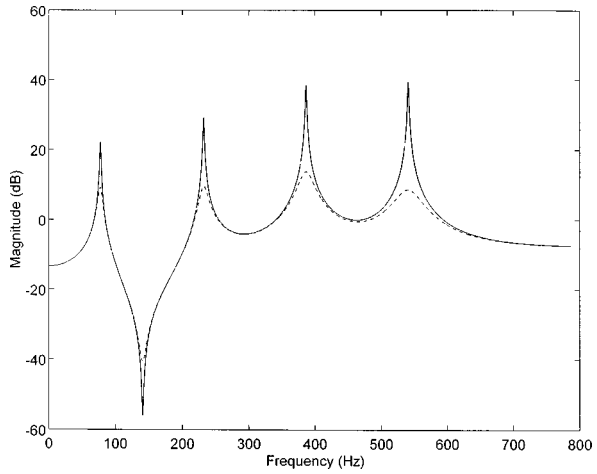

FIG. 12. Plant uncertainty due to radiation impedance at open end. Without lining: ———; with lining: ---.

The plant uncertainty due to radiation impedance appears less drastic than the temperature effect. On the basis of the plant uncertainty, optimal controllers are obtained for the lined duct by using the H_∞ design procedure. The resulting loop shaping of sensitivity functions versus weight functions is shown in Fig. 13. The active control results in terms of the power spectrum of sound pressure at the sensor position are shown in Fig. 14. It can be observed that the effective control bandwidth is approximately 140 Hz and the first peak of sound pressure at 82 Hz is attenuated by approximately 15 dB. The poles and zeros of models 5–8 are shown in Table VI–IX.

In the last experiment, the effect of time delay is investigated. The microphone is originally located at $x=0.9$ m and the control source is located at $x=0.5$ m, which gives a time delay of 0.0167 s. Then, the control source is moved to $x=0.9$ m. This corresponds to the so-called *collocated control*. In doing so, the waterbed effect[8] in conjunction with nonminimal phase zeros and time delay can be alleviated.[7,17] Except the delay, all physical conditions in the duct are similar to those in model 1. The Pade's approximation[17] is em-

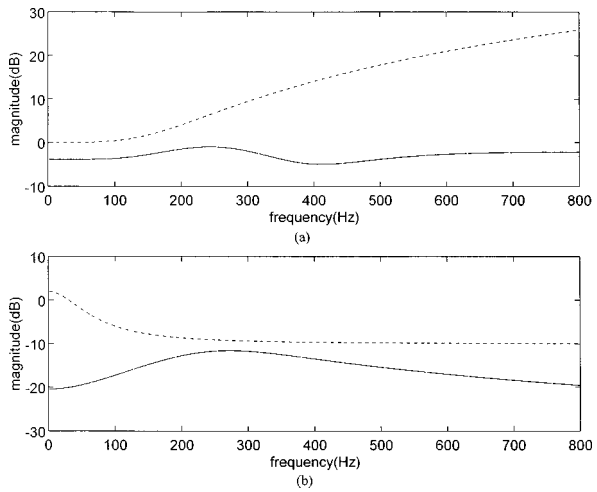

FIG. 13. Loop shaping for the lined duct (radiation impedance $=-0.01s^2+100$ s). (a) $W_1^{-1}(s)$: ⋯ versus $\tilde{S}(s)$: ———; (b) $W_3^{-1}(s)$: ⋯ versus $\tilde{T}(s)$: ———.

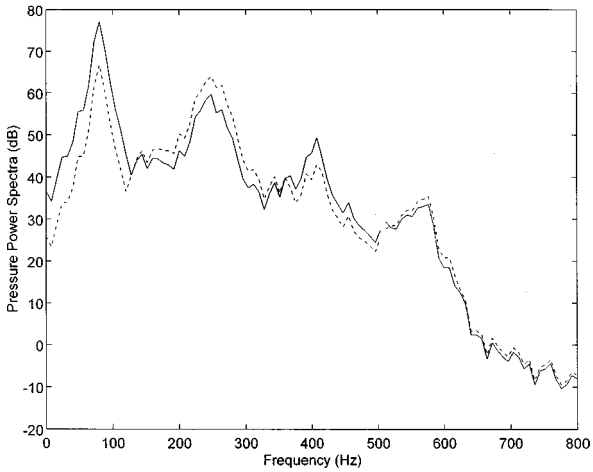

FIG. 14. The active control results for the lined duct subject to the effect of radiation impedance in terms of the power spectrum of sound pressure at the sensor position (control off: ———; control on: ---).

ployed to approximate the delay with a rational function $e^{-0.0167s}\cong[1-(0.0167s/2)]/[1+(0.0167s/2)]$. The active control results in terms of the power spectrum of sound pressure at the sensor position are shown in Fig. 15. It can be seen that the performance of the system without delay is better than the system with delay (10 versus 2 dB at the peak of 87 Hz). The effective control band of the former system is also wider than that of the latter system.

IV. CONCLUSIONS

The effects on stability and performance due to perturbations in physical conditions on ANC systems are investigated. The analysis is carried out by using a general framework of the H_∞ robust control theory. The size of plant uncertainty is assessed according to the perturbations in physical conditions. Optimal controllers that accommodate both performance and stability are designed via a H_∞ synthesis procedure. The term optimal controller means that the controller is optimally comprised to achieve maximum noise reduction under the constraint of robust stability.

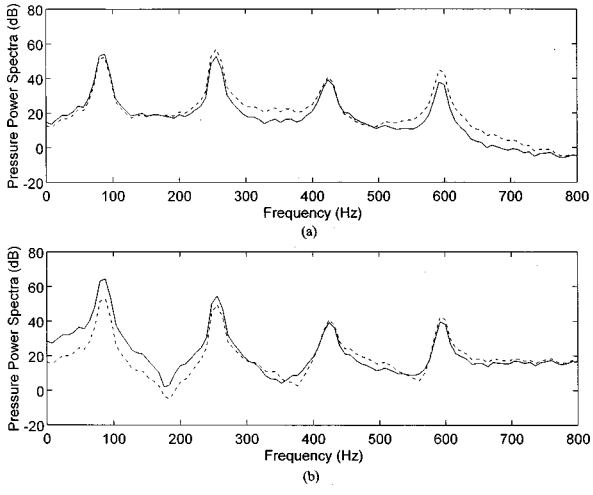

FIG. 15. The active control results for the duct subject to acoustic delay in terms of the power spectrum of sound pressure at the sensor position (control off: ———; control on: ---). (a) System with delay; (b) system without delay.

A low-frequency duct is chosen as the test example to explore the effects of plant uncertainties on the ANC systems. The physical conditions investigated in the paper fall into two categories. One category behaves like damping, e.g., flow, viscosity, and lining, while the other category alters both the resonance frequencies and the damping of the system, e.g., temperature and radiation impedance. In general, the latter factors have more pronounced impact on the plant uncertainties than the former. To cope with plant uncertainties, passive lining plays an important role in improving the robustness of the system. With appropriate lining, fixed controllers suffice to accommodate the damping type of perturbations. However, it was also found in the results that the plant uncertainties can become so severe, e.g., due to temperature variation, that virtually no fixed controller meets the design requirements. In this regard, adaptive algorithms may become necessary in these types of ANC applications. The effect of time delay is also investigated in this paper. It is found in the results that time delay indeed has detrimental effects on the performance of the system. Hence to avoid the effect of time delay, the distance between the microphone and actuator should be made as small as possible.

The structures of plant uncertainties are not considered in this paper. The H_∞ controllers synthesized to meet the requirement of the standard H_∞ problem, $\|T_{vw}(S)\|_\infty < 1$, tend to result in conservative designs in practice. When the plant uncertainty is non-disklike, better performance may be achieved by using design methods such as the μ-synthesis technique[7] that is capable of handling structured uncertainties.

This paper discusses only the feedback structure that has been the mainstream of control theories. More investigations on the feedforward structure, acoustic, feedback, low-frequency response of actuators, and structured uncertainties in ANC problems are currently on the way.

ACKNOWLEDGMENTS

This paper is written in memory of the late Professor Anna Pate, Iowa State University. Special thanks also go to Professor F. B. Yeh and Professor M. C. Tsai for the helpful discussions on the H_∞ control theory. The work was supported by the National Science Council in Taiwan, Republic of China, under the project number NSC 83-0401-E-009-024.

[1] P. Lueg, ''Process of silencing sound oscillations,'' US Patent No. 2,043,416 (1936).
[2] S. J. Elliott and P. A. Nelson, ''Active noise control,'' Noise/New Int. **2**, 75–98 (1994).
[3] C. R. Fuller and A. H. Flotow, ''Active control of sound and vibration,'' IEEE Control Syst. Mag. **2**, 9–19 (1995).
[4] J. C. Doyle, K. Glover, P. Khargonekar, and B. A. Francis, ''State space solution to standard H_2 and H_∞ control problems,'' IEEE Trans. Autom. Control. **34**(8), 832–847 (1989).
[5] P. A. Iglesias and K. Glover, ''State space solution to standard H_2 and H_∞ control problems,'' Int. J. Control **54**, 1031–1073 (1991).
[6] I. Yaesh and U. Shaked, ''Transfer function approach to the problems on discrete-time systems: H_∞-optimal linear control and filtering,'' IEEE Trans. Autom. Control **36**, 1264–1271 (1991).
[7] J. C. Doyle, B. A. Francis, and A. R. Tannenbaum, *Feedback Control Theory* (Macmillan, New York, 1992).
[8] F. B. Yeh and C. D. Yang, *Post Modern Control Theory And Design* (Eurasia, Taiwan, 1992).
[9] M. C. Tsai and C. S. Tsai, ''A transfer matrix framework approach to the synthesis of H_∞ controllers,'' Int. J. Control **5**, 155–173 (1995).
[10] L. E. Kinsler, A. R. Frey, A. B. Coppens, and J. V. Sanders, *Fundamentals of Acoustics* (Wiley, New York, 1982).
[11] L. L. Beranek, *Noise and Vibration Control* (McGraw-Hill, New York, 1988).
[12] M. L. Munjal, *Acoustics of Ducts and Mufflers* (Wiley, New York, 1982).
[13] J. Hong, J. C. Akers, R. Venugopal, M. N. Lee, A. G. Sparks, P. D. Washabaugh, and D. S. Bernstein, ''Modeling, identification and feedback control of noise in an acoustic duct,'' *Proceedings of The American Control Conference*, Seattle, 1995, pp. 3669–3673.
[14] J. S. Hu, ''Active sound cancellation in finite-length ducts using close form transfer function models,'' ASME J. Dynamic Syst. Measurement Control **117**, 143–154 (1995).
[15] B. Yang and C. A. Tan, ''Transfer function of one dimensional distributed parameter systems,'' J. Appl. Mech. **59**, 1009–1014 (1992).
[16] A. Grace, A. J. Laub, J. N. Little, and C. M. A. Thompson, *Control System Toolbox User's Guide* (The Math Works, Natick, 1992).
[17] G. F. Franklin, J. D. Powell, and A. Emami-Naeini, *Feedback Control of Dynamic Systems* (Addison-Wesley, New York, 1994).
[18] R. Gueler, A. H. von Flotow, and D. W. Vos, ''Passive damping for robust feedback control of flexible structures,'' J. Guid. Control. Dyn. **16**, 662–667 (1992).

An active noise control algorithm for controlling multiple sinusoids

Seung Man Lee, Hyuck Jae Lee, Cha Hee Yoo, Dae Hee Youn, and Il Whan Cha
Department of Electronic Engineering, Yonsei University, 134 Schinchon-dong, Sudaemun-gu, Seoul, 120-749 Korea

(Received 27 November 1995; revised 12 November 1997; accepted 25 March 1998)

The filtered-*x* LMS algorithm and its modified versions have been successfully applied in suppressing acoustic noise such as single and multiple tones and broadband random noise. This paper presents an adaptive algorithm based on the filtered-*x* LMS algorithm which may be applied in attenuating tonal acoustic noise. In the proposed method, the weights of the adaptive filter and estimation of the phase shift due to the acoustic path from a loudspeaker to a microphone are computed simultaneously for optimal control. The algorithm possesses advantages over other filtered-*x* LMS approaches in three aspects: (1) each frequency component is processed separately using an adaptive filter with two coefficients, (2) the convergence parameter for each sinusoid can be selected independently, and (3) the computational load can be reduced by eliminating the convolution process required to obtain the filtered reference signal. Simulation results for a single-input/single-output (SISO) environment demonstrate that the proposed method is robust to the changes of the acoustic path between the actuator and the microphone and outperforms the filtered-*x* LMS algorithm in simplicity and convergence speed. © *1998 Acoustical Society of America.* [S0001-4966(98)02107-9]

PACS numbers: 43.50.Ki [GAD]

INTRODUCTION

Active noise control (ANC) has been widely studied as an effort to cancel noise by superposing a sound with the opposite phase of the noise.[1] The ANC approach is very effective especially against low-frequency noise below 500 Hz which is hard to reduce by passive methods.[1] The schematic diagram in Fig. 1 explains the ANC problem with a loudspeaker generating antiphase noise and a microphone monitoring the controlled noise level. The adaptive digital filter processes the reference signal such that the superposed noise level at the output of the error microphone is minimized.

The LMS algorithm has been most widely used to compute the coefficients of the adaptive digital filter for electrical noise cancellation.[2] However, applying the LMS algorithm to the ANC problem may result in an unstable system due to the presence of the secondary path between the loudspeaker and the microphone.[3] As a solution to this problem, it was proposed to pass the reference signal through a filter modeling the secondary path and to update the coefficients of the controller using the filtered reference signal and the error. The resulting update equation is called the ''filtered-*x* LMS'' algorithm.[3] The performance of the filtered-*x* LMS algorithm is significantly affected by the difference between the estimated and the true transfer functions representing the acoustic path from the loudspeaker to the error microphone.[4,5] Since this transfer function is unknown and continuously changing in a real situation, it is desirable to perform an on-line estimation of the secondary path.

The use of auxiliary random noise for on-line modeling of the secondary path has been studied.[6] However, the random noise used to identify the secondary path may become the source of the residual noise of the system. Therefore the level of the noise should be kept very low so that the final effect on the residual noise is negligible.[7] Also, it has been suggested[8] to use two additional adaptive filters for on-line identification. However, since these solutions are signal dependent, a remodeling process will take place whenever the frequency of the input signal changes.[7]

In many ANC applications, the noise of interest is composed of several harmonic components with the fundamental frequency related to rotational speed.[9] For example, transformer noise is composed of an unchanging 60-Hz fundamental frequency component and its harmonic components and engine noise is composed of a time-varying fundamental frequency component and its harmonic components. When multiple sinusoids are to be controlled, it is known[10] that processing each sinusoid independently enhances the convergence speed. However, processing harmonic components separately increases computational complexity,[10] for convolution operations are required to generate multiple filtered sinusoids.

In this paper, a new ANC algorithm to control multiple sinusoids composed of a reference fundamental frequency component and its harmonic components is proposed. The adaptive filters are implemented independently for each frequency component and the multiple filtered reference signal is obtained by shifting the phase of each harmonic component generated from the fundamental frequency component. Thus the algorithm can reduce the computational complexity by eliminating the convolution operation required to generate the filtered reference signal. In the proposed method, both the coefficients of the adaptive filter and the phase shift due to the secondary path are computed simultaneously and recursively to continuously minimize the power of the error signal monitored by the microphone.

 0001-4966/98/104(1)/248/7/$15.00

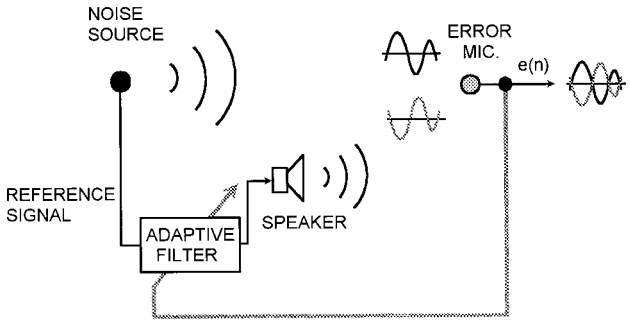

FIG. 1. Schematic diagram explaining the ANC system.

I. PROPOSED ALGORITHM

Figure 2 shows the block diagram explaining the ANC system using the filtered-x LMS algorithm.[3] In Fig. 2, $P(z)$ represents the acoustic path from the noise source to the microphone and $C(z)$ denotes the secondary path from the controller output to the microphone. The filtered-x LMS algorithm requires an estimate $\hat{C}(z)$ of the secondary path to generate the filtered reference signal $r(n)$ which is multiplied by the error $e(n)$ to form the gradient estimate.

Now, let us assume that the noise source is given by a single sinusoid. That is,

$$x(n)=A\ \cos\ (2\pi f_0 n+\xi), \tag{1}$$

where f_0 is the normalized frequency of the noise source and ξ is a random phase. The results for a single tone can be easily extended to the case of multiple sinusoids since the tonal components with different frequencies are uncorrelated and can then be processed separately.[10] For a single tone, $C(z)$ and $P(z)$ can be modeled by their gains and phase shifts at f_0:

$$C(z)=ae^{-j\theta}, \tag{2a}$$

$$P(z)=e^{-i\delta}. \tag{2b}$$

In Eq. (2b), a unit gain of $P(z)$ is assumed for simplicity.

The ANC system for a single sinusoid can be explained by the schematic diagram in Fig. 3 where the phase shift $\pi/2$ can be realized using a differentiator or Hilbert transformation.[11] From Eqs. (1) and (2b) the noise at the microphone can be expressed as

$$d(n)=A\ \cos(2\pi f_0 n+\xi-\delta). \tag{3}$$

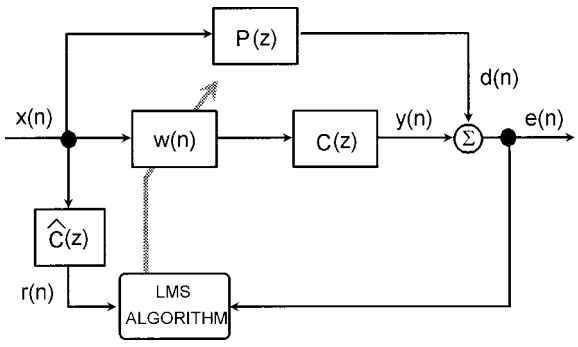

FIG. 2. Block diagram of the filtered-x LMS algorithm.

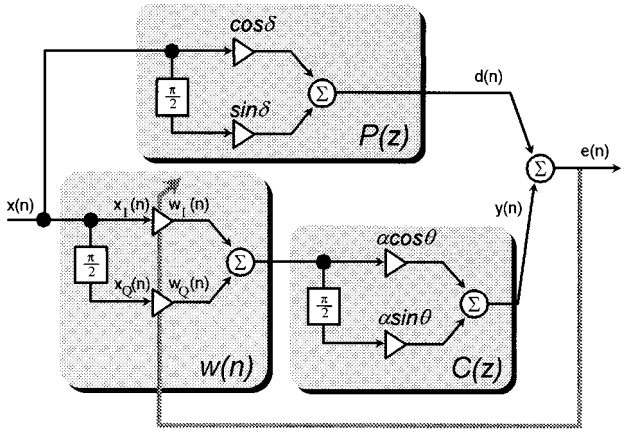

FIG. 3. Schematic diagram of the ANC system for a single sinusoid.

From Fig. 3 the microphone output can be obtained by superposing the secondary noise on the primary one. That is,

$$e(n)=d(n)+y(n), \tag{4a}$$

where

$$y(n)=a\{\cos\ \theta x_1(n)+\sin\ \theta x_Q(n)\}w_I(n) + \alpha\{-\sin\ \theta x_I(n)+\cos\ \theta x_Q(n)\}w_Q(n). \tag{4b}$$

In Eq. (4b), $x_I(n)$ and $x_Q(n)$ represent the in-phase and the quadrature phase components of the reference signal, respectively,

$$x_I(n)=A\ \cos(2\pi f_0 n+\xi), \tag{5a}$$

$$x_Q(n)=A\ \sin(2\pi f_0 n+\xi). \tag{5b}$$

A. Controller coefficient update equation

Now, applying the LMS approach[3] to minimize the average power of the error signal yields the following recursive weight update equation:

$$w_I(n+1)=w_1(n)-\mu\ \frac{\partial e_2(n)}{\partial w_I(n)} =w_I(n)-2\mu a\{\cos\ \theta x_I(n)+\sin\ \theta x_Q(n)\}e(n), \tag{6a}$$

$$w_Q(n+1)=w_Q(n)-\mu\ \frac{\partial e^e(n)}{\partial w_Q(n)} =w_Q(n)-2\mu a\{-\sin\ \theta x_I(n)+\cos\ \theta x_Q(n)\}e(n). \tag{6b}$$

In Eqs. (6a) and (6b), μ is the convergence parameter which controls convergence speed and stability. From Eqs. (6a) and (6b), we can see that it is necessary to know the gain α and the phase θ of the secondary path to use the weight update equation.

B. Phase shift update equation

Rewriting Eqs. (6a) and (6b) using the estimated phase shift $\hat{\theta}(n)$, we obtain

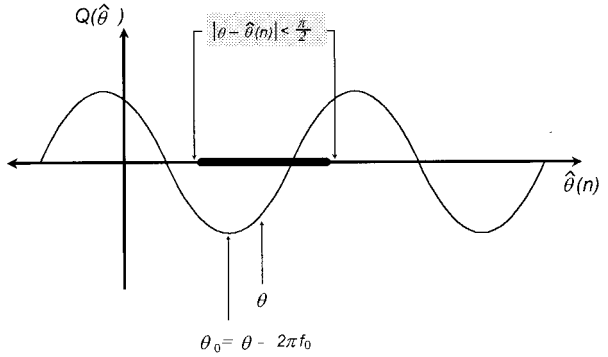

FIG. 4. Error signal as a function of the phase shift estimate.

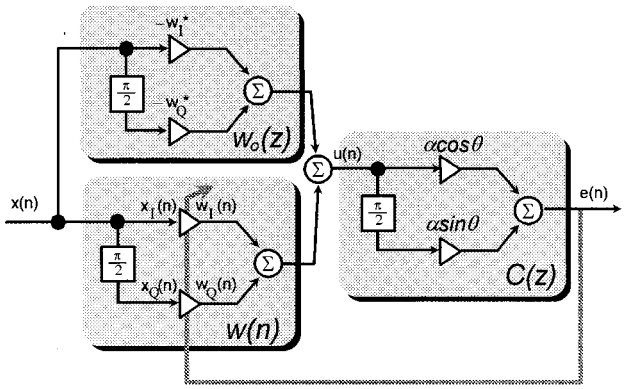

FIG. 5. Rearranged form of the ANC system.

$$\widehat{w_I}(n+1)=\widehat{w_I}(n)-\rho\cos\hat{\theta}(n)e(n)x_I(n)-\rho\sin\hat{\theta}(n)e(n)x_Q(n), \tag{7a}$$

$$\widehat{w_Q}(n+1)=\widehat{w_Q}(n)+\rho\sin\hat{\theta}(n)e(n)x_I(n)-\rho\cos\hat{\theta}(n)e(n)x_Q(n), \tag{7b}$$

where $\rho=2\alpha\mu$.

Substituting Eqs. (7a) and (7b) into Eq. (4b), the error signal in Eq. (4a) can be expressed as (see the Appendix)

$$e(n)=d(n)+\alpha\{\cos\theta x_I(n)+\sin\theta x_Q(n)\}w_I(n-1)+a\{-\sin\theta x_I(n)+\cos\theta x_Q(n)\}w_Q(n-1)-\alpha\rho A^2e(n-1)\cos\{\hat{\theta}(n-1)-\theta+2\pi f_0\}. \tag{8}$$

The above equation can be rearranged as

$$Q(\hat{\theta})\triangleq-\alpha\rho A^2\cos\{\hat{\theta}(n-1)-\theta+2\pi f_0\}=\frac{e(n)}{e(n-1)}-f\{\hat{\theta}(n-2)\}, \tag{9a}$$

where

$$f\{\hat{\theta}(n-2)\}=\frac{d(n)}{e(n-1)}+\frac{\alpha\{\cos\theta x_I(n)+\sin\theta x_Q(n)\}w_I(n-1)}{e(n-1)}+\frac{\alpha\{\sin\theta x_I(n)+\cos\theta x_Q(n)\}w_Q(n-1)}{e(n-1)}. \tag{9b}$$

As shown in Fig. 4, the cosine term on the left side of Eq. (9a) has a single minimum value in $[0,2\pi)$ and the relevant phase shift is given by

$$\theta_0=\theta-2\pi f_0. \tag{10}$$

From Fig. 4 the difference between θ_0 and the phase shift θ due to the secondary path is $2\pi f_0$. Thus as the sampling frequency increases (i.e., the normalized frequency decreases), the estimated phase shift $\hat{\theta}(n)$ estimated to minimize $Q(\hat{\theta})$ becomes close to the phase shift of the secondary path. It has been shown[10,11] that the adaptive control system converges to the optimum solution if the phase estimation error $|\hat{\theta}(n)|$ is less than $\pi/2$. Thus if the sampling rate is faster than four times the frequency of the tonal noise (i.e., $f_0<0.25$), the difference between θ_0 and θ becomes less than $\pi/2$. This suggests that the use of $\hat{\theta}(n)$ estimated to minimize $Q(\hat{\theta})$ in Eq. (9a) results in a stable controller. Now, since $Q(\hat{\theta})$ has a single minimum value in $[0,2\pi)$, the gradient descent method is applied to estimate θ_0:

$$\hat{\theta}(n)=\hat{\theta}(n-1)-\nu\frac{\partial Q(\hat{\theta})}{\partial\hat{\theta}(n-1)}, \tag{11a}$$

where

$$\frac{\partial Q(\hat{\theta})}{\partial\hat{\theta}(n-1)}=\frac{\partial\{e(n)/e(n-1)\}}{\partial\hat{\theta}(n-1)}-\frac{\partial[f\{\hat{\theta}(n-2)\}]}{\partial\hat{\theta}(n-1)}. \tag{11b}$$

The gradient in Eq. (11b) cannot be evaluated. Thus it is suggested to disregard the second term of Eq. (11b) since a function $f(\cdot)$ with the variable $\hat{\theta}(n-2)$ is differentiated with respect to $\hat{\theta}(n-1)$.[12–15] The resulting approximation of the first term of Eq. (11b) can be expressed as

$$\frac{\partial\{e(n)/e(n-1)\}}{\partial\hat{\theta}(n-1)}\approx\frac{[e(n)/e(n-1)]-[e(n-1)/e(n-2)]}{\hat{\theta}(n-1)-\hat{\theta}(n-2)}. \tag{12}$$

Now, substituting Eq. (12) for the gradient in Eq. (11a) yields the following phase update equation:

$$\hat{\theta}(n)=\hat{\theta}(n-1)-\nu\frac{[e(n)/e(n-1)]-[e(n-1)/e(n-2)]}{\hat{\theta}(n-1)-\hat{\theta}(n-2)}. \tag{13}$$

II. CONVERGENCE CONDITION

A. Convergence condition for the mean of the coefficients

To investigate the condition for the mean of the coefficient to converge to the optimum solution, the expected value of the weight estimation error is evaluated. The ANC system in Fig. 3 can be rearranged as in the block diagram in Fig. 5 by modeling $P(z)$ as the product of $W_0(z)$ and $C(z)$.

In Fig. 5, w_I^* and w_Q^* represent the optimum weight of the controller in the sense of zero error output.

From Fig. 5, the error signal can be expressed as

$$e(n)=av_I(n)\{\cos\ \theta x_I(n)+\sin\ \theta x_Q(n)\} + av_Q(n)\{-\sin\ \theta x_I(n)+\cos\ \theta x_Q(n)\}, \tag{14a}$$

where

$$v_I(n)=\widehat{w_I}(n)-w_I^*, \tag{14b}$$

$$v_Q(n)=\widehat{w_Q}(n)-w_Q^*. \tag{14c}$$

Substituting Eq. (14a) into Eqs. (7a) and (7b) yields

$$v_I(n+1)=\gamma_I(n)v_I(n)-\beta_I(n)v_Q(n), \tag{15a}$$

$$v_Q(n+1)=\beta_Q(n)v_I(n)+\gamma_Q(n)v_Q(n). \tag{15b}$$

In Eqs. (15a) and (15b), $\gamma_I(n)$, $\beta_I(n)$, $\gamma_Q(n)$, and $\beta_Q(n)$ are given by

$$\gamma_I(n)=1-\alpha\rho\{\cos\ \hat{\theta}(n)x_I(n)+\sin\ \hat{\theta}(n)x_Q(n)\} \times\{\cos\ \theta x_I(n)+\sin\ \theta x_Q(n)\}, \tag{16a}$$

$$\beta_1(n)=\alpha\rho\{\cos\ \hat{\theta}(n)x_I(n)+\sin\ \hat{\theta}(n)x_Q(n)\} \times\{-\sin\ \theta x_I(n)+\cos\ \theta x_Q(n)\}, \tag{16b}$$

$$\gamma_Q(n)=1+\alpha\rho\{\sin\ \hat{\theta}(n)x_I(n)-\cos\ \hat{\theta}(n)x_Q(n)\} \times\{-\sin\ \theta x_I(n)+\cos\ \theta x_Q(n)\}, \tag{16c}$$

$$\beta_Q(n)=\alpha\rho\{\sin\ \hat{\theta}(n)x_I(n)-\cos\ \hat{\theta}(n)x_Q(n)\} \times\{\cos\ \theta x_I(n)+\sin\ \theta x_Q(n)\}. \tag{16d}$$

Taking the expectation of both sides of Eqs. (15a) and (15b) and assuming the coefficients at time n are independent of the reference signal, we obtain a set of difference equations which can be expressed in matrix form as

$$\begin{pmatrix} E\{v_I(n+1)\} \\ E\{v_Q(n+1)\} \end{pmatrix}=G\begin{pmatrix} E\{v_I(n)\} \\ E\{v_Q(n)\} \end{pmatrix}, \tag{17a}$$

where

$$G=\begin{pmatrix} 1-\dfrac{\alpha\rho A^2}{2}\cos(\hat{\theta}(n)-\theta) & -\dfrac{\alpha\rho A^2}{2}\sin(\hat{\theta}(n)-\theta) \\ \dfrac{\alpha\rho A^2}{2}\sin(\hat{\theta}(n)-\theta) & 1-\dfrac{\alpha\rho A^2}{2}\cos(\hat{\theta}(n)-\theta) \end{pmatrix}. \tag{17b}$$

Transforming Eq. (17a) to the principal coordinate system,[3] we obtain

$$\begin{pmatrix} E\{v_I'(n+1)\} \\ E\{v_Q'(n+1)\} \end{pmatrix}\triangleq C^T\begin{pmatrix} E\{v_I(n+1)\} \\ E\{v_Q(n+1)\} \end{pmatrix} =\begin{pmatrix} \lambda_1 & 0 \\ 0 & \lambda_2 \end{pmatrix}\begin{pmatrix} E\{v_I'(n)\} \\ E\{v_Q'(n)\} \end{pmatrix}. \tag{18}$$

In Eq. (18), C represents the eigenmatrix of G and λ_1 and λ_2 are the relevant eigenvalues given by

$$\lambda_1,\ \lambda_2=1-\frac{\alpha\rho A^2}{2}\{\cos(\hat{\theta}(n)-\theta)\pm j\ \sin(\hat{\theta}(n)-\theta)\}. \tag{19}$$

Since the eigenvalues are complex, modifying Eq. (18) in terms of magnitude yields

$$\begin{pmatrix} |E\{v_I'(n)\}| \\ |E\{v_Q'(n)\}| \end{pmatrix}=\begin{pmatrix} |\lambda_1|^n & 0 \\ 0 & |\lambda_2|^n \end{pmatrix}\begin{pmatrix} |E\{v_I'(0)\}| \\ |E\{v_Q'(0)\}| \end{pmatrix}. \tag{20}$$

From Eq. (20) we can see that the mean of the coefficients converges to the optimum value if $|\lambda_1|<1$ and $|\lambda_2|<1$. This condition results in the range of the convergence parameter given by

$$0<\mu<\frac{2\cos\{\hat{\theta}(n)-\theta\}}{\alpha^2A^2}. \tag{21}$$

It is necessary that the sampling frequency should be at least four times the signal frequency to be controlled to ensure convergence of the total algorithm. To enhance the convergence speed of the algorithm, we used a sampling frequency ten times that of the signal in the simulation. In this case, the difference between the estimated phase shift and the actual phase shift becomes less than $\pi/4$ and the convergence parameter of the adaptive filter can be set to a large value.

B. Convergence condition for the second moment of the coefficients

The stability condition for the mean of the coefficients does not imply finite variances of the weights and the mean-square error in the steady state.

Taking the expectation of the squares of Eqs. (15a) and (15b) and adding the two results yields

$$E\{v_I^2(n+1)\}+E\{v_Q^2(n+1)\} =\left\{1+\frac{\alpha^2\rho^2A^4}{2}-\alpha\rho A^2\cos(\hat{\theta}(n)-\theta)\right\} \times\{E\{v_I^2(n)\}+E\{v_Q^2(n)\}\}. \tag{22}$$

The solution of the above difference equation is

$$E\{v_I^2(n)\}+E\{v_Q^2(n)\} =\left\{1+\frac{\alpha^2\rho^2A^4}{2}-\alpha\rho A^2\cos(\hat{\theta}(n)-\theta)\right\}^n \times\{E\{v_I^2(0)\}+E\{v_Q^2(0)\}\}. \tag{23}$$

From Eq. (23) we can see that the second moment of the coefficients converges to zero if

$$\left|1+\frac{\alpha^2\rho^2A^4}{2}-\alpha\rho A^2\cos\{\hat{\theta}(n)-\theta\}\right|<1. \tag{24}$$

This condition results in the range of the convergence parameter given by

$$0<\mu<\frac{\cos\{\hat{\theta}(n)-\theta\}}{\alpha^2A^2}. \tag{25}$$

From the conditions in Eqs. (21) and (25), we can see that the inequality in Eq. (25) always satisfies the inequality in Eq. (21).

C. Convergence condition for the phase shift estimate

The phase shift due to the secondary path is estimated using the recursive equation in Eq. (13) which can be approximated and rearranged as

$$\hat{\theta}(n) \cong \hat{\theta}(n-1) + \nu\alpha\rho A^2 \frac{G[\hat{\theta}(n-1), \hat{\theta}(n-2)]}{\hat{\theta}(n-1) - \hat{\theta}(n-2)}, \quad (26a)$$

where

$$G[\hat{\theta}(n-1), \hat{\theta}(n-2)] = \cos\{\hat{\theta}(n-1) - \theta + 2\pi f_0\} - \cos\{\hat{\theta}(n-2) - \theta + 2\pi f_0\}. \quad (26b)$$

To obtain Eq. (26b) it is assumed that the variations of the coefficients $\widehat{w_I}(n)$ and $\widehat{w_Q}(n)$ are relatively small compared to that of $\hat{\theta}(n)$. Approximating the cosine terms of Eq. (26b) as the sum of the first two terms of a Taylor series, Eq. (26a) can be expressed as

$$\hat{\theta}(n) = (1-M)\hat{\theta}(n-1) - M\hat{\theta}(n-2) + N, \quad (27a)$$

where

$$M = \frac{\nu\alpha\rho A^2}{2} \quad \text{and} \quad N = \nu\alpha\rho A^2(\theta - 2\pi f_0). \quad (27b)$$

Solving the difference equation in Eq. (27a) yields

$$\hat{\theta}(n) = \frac{N}{(1-a_1)(1-a_2)} + \frac{Na_1^{n+2}}{(a_1-a_2)(a_1-1)} + \frac{Na_2^{n+2}}{(a_2-a_1)(a_2-1)}, \quad (28a)$$

where

$$a_1, \quad a_2 = \frac{(1-M) \pm \sqrt{M^2-6M+1}}{2}. \quad (28b)$$

From Eq. (28a) we can see that the recursive equation is stable if

$$|a_1|, \quad |a_2| = \left| \frac{1-M \pm \sqrt{M^2-6M+1}}{2} \right| < 1. \quad (29)$$

The inequality in Eq. (29) can be rewritten in terms of M as

$$0 < M < 1. \quad (30)$$

From Eqs. (27b) and (30), we can obtain the following condition for the convergence parameter ν:

$$0 < \nu < \frac{1}{\mu\alpha^2 A^2}. \quad (31)$$

The condition in Eq. (30) shows that the maximum allowable value of the convergence parameter ν is inversely proportional to μ, the convergence parameter used in the recursive equation to compute the controller coefficients.

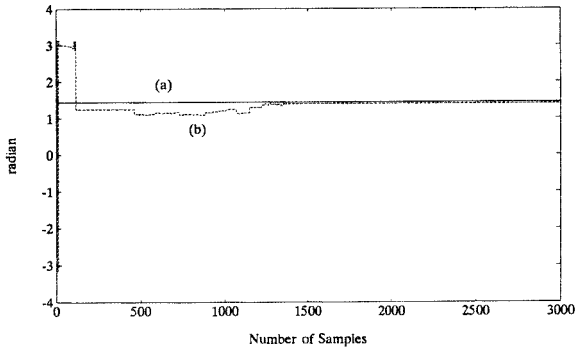

FIG. 6. Behaviors of the estimated phase shift $\hat{\theta}(n)$ when the measured phase shift of the secondary path is 0.66π. (a) $\hat{\theta}_0 = \theta - 2\pi f_0$. (b) $\hat{\theta}(n)$.

III. SIMULATIONS

In order to evaluate the proposed algorithm, we performed a simulation. The transfer function measured in a car was used as the secondary transfer function in the simulation and sinusoid noise signals generated in a car were controlled. Also, we added zero mean white Gaussian noise whose power is 30 dB below that of the noise signal.

A. Convergence of the phase shift estimates

The first simulation tests the recursive equation estimating the phase shift due to the secondary path. The noise signal to be controlled is a sinusoid of 100 Hz and the sampling frequency is 1 KHz. A relatively small value of μ is used to simulate a slowly time varying controller. Such an assumption was made in deriving the estimated phase shift in the steady state.

In Fig. 6, the solid line (a) indicates the steady-state phase shift estimate θ_0 analytically predicted using Eq. (10), while the dotted line (b) is $\hat{\theta}(n)$ which is recursively estimated using Eq. (13).

The phase shift θ for the simulation is $\theta = 0.66\pi > \pi/2$. A large convergence parameter ν is used such that the phase shift estimate $\hat{\theta}(n)$ reaches the value less than $\pi/2$ before the weight update equation diverges. From Fig. 6 we can see that

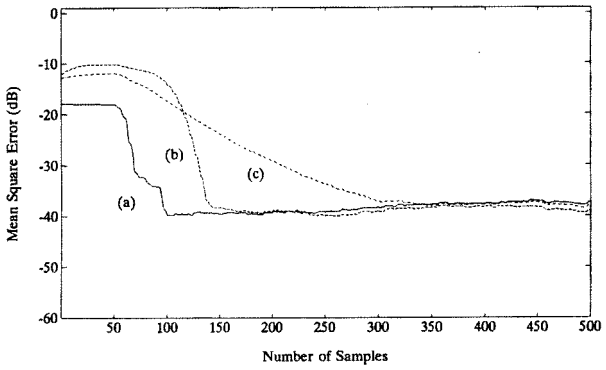

FIG. 7. Mean-squared values of the error signal when the phase shift of the secondary path is -0.34π. (a) The proposed algorithm. (b) The algorithm using auxiliary random noise. (c) The algorithm using two additional adaptive filters.

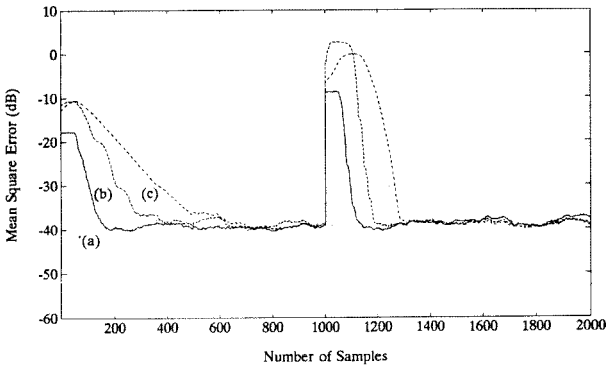

FIG. 8. Mean-squared values of the error signal when the phase shift of the secondary path is changing. (a) The proposed algorithm. (b) The algorithm using auxiliary random noise. (c) The algorithm using two additional adaptive filters.

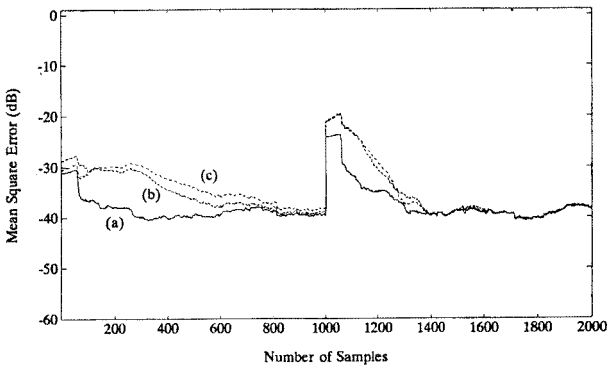

FIG. 9. Mean-squared values of the error signal when the frequency of the input signal is changing. (a) The proposed algorithm. (b) The algorithm using auxiliary random noise. (c) The algorithm using two additional adaptive filters.

the estimated phase shift converges to the analytically predicted value $\theta_0 = 0.66\pi - 2\pi f_0$. In this simulation, the initial values of $e(n-1) = 0.0001$, $e(n-2) = 0.0002$ are used. Other experiments also verify the analytical results.

B. Comparisons of the proposed algorithm and others

Simulations are performed to compare the convergence properties of the proposed algorithm and other filtered-x LMS algorithms.[6,8] One of the filtered-x LMS algorithms uses an auxiliary noise,[6] and another uses an additional adaptive filter to estimate the impulse response function of the secondary path.[8] The convergence parameters are experimentally chosen so that the three methods yield the same level of mean-square errors in the steady state.

Figures 7 and 8 show the mean-square errors obtained using the three methods when $\theta = -0.34\pi$ and the phase shift changes from $\theta = 0.66\pi$ to $\theta = -0.34\pi$ at $n = 1000$, respectively. The results demonstrate that simultaneous computation of the phase shift and the coefficient of the controller using the proposed algorithm yields the fastest convergence both at the beginning and in the period of phase shift change. Other results not included in this paper show that the proposed method gives slightly faster convergence speed than others for $|\theta| > \pi/2$. However, the differences are negligible.

Figure 9 shows the mean-square errors when the frequency of the tonal noise changes from 100 to 200 Hz at $n = 1000$. The sampling frequency for the simulation is 2 kHz. As in the case of the previous simulation, this result also demonstrates the fastest convergence of the proposed algorithm both at the beginning and at the transient.

In Table I we compared computational load of the two on-line secondary path estimations and the proposed algorithm in the simulations.

C. On controlling multiple sinusoids

The proposed algorithm is applied to controlling tonal noise which consists of multiple sinusoids of 100, 300, and 500 Hz at which the phase shifts due to the secondary path are given by $\pi/4$, $5\pi/6$, and $4\pi/3$, respectively. The sampling rate for the simulation is 3 kHz. In this simulation, the reference signal and the error signal are processed by a bank of bandpass filters to separate each total component. The output signal of the three controllers are added before being processed by the secondary path. Figure 10 shows the power density spectra of the error signals (a) before and (b) after applying the proposed ANC algorithm.

IV. CONCLUSIONS

This paper presents an adaptive algorithm based on the filtered-x LMS which is applicable to attenuate sinusoidal acoustic noise. The algorithm consists of two recursive equations. The first recursive equation derived by rearranging the filtered-x LMS algorithm updates the coefficients of the controller. Since the algorithm processes each tonal component independently of others, fast convergence becomes possible. The second recursive formula updates the phase shift due to

TABLE I. Comparison of computational load, where N_h is the length of secondary path, N_w is the length of adaptive filter, N_p is the length of estimated primary path, N_q is computation load for generating quadrature signal, N_s is the number of sine waves.

	Filtered-x	Adaptive filtering	Updating adaptive filter	Estimating secondary path	Total (single sinusoid)	Total (multiple sinusoid)
Using additive noise	N_h	N_w	$4*N_w$	$5*N_h$	$6*N_h+5*N_w$	$6*N_h+5*N_w*N_s$
Using additional adaptive filter	N_h	N_w	$4*N_w$	$5*(N_h+N_p)$	$6*N_h+5*(N_w+N_p)$	$6*N_h+5*N_p+5*N_w+N_s$
Proposed algorithm	$\cdots$	N_q+2	10	8	N_q+20	$(N_q+20)*N_s$

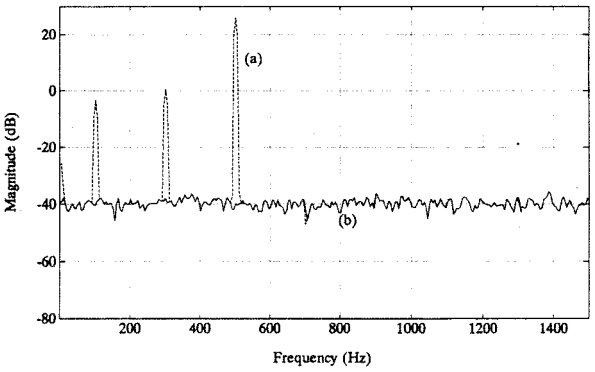

FIG. 10. Power spectrum of the error signal. (a) ANC off. (b) ANC on.

the secondary path. The resulting phase shift estimate is biased by the amount of $2\pi f_0$ which can be made less than $\pi/2$ by choosing the sampling rate to be faster than four times the frequency of the tonal component. When the frequencies of the sinusoids are known, the bias can be removed by adding $2\pi f_0$. Experimental results indicate that such an approach improves convergence speed when the phase shift is larger than $\pi/2$. The estimated phase shift is used to generate the filtered reference signal required to estimate the weights of the controller. Since the phase shift of the reference signal is estimated for each frequency component, computational complexity can be reduced by omitting the convolution operation. Also, the recursive estimate of the phase shift makes it possible to adapt to a time-varying environment.

Convergence conditions for the recursive equations are also derived. Analytical results indicate that the algorithm yields unbiased estimates of the controller coefficients and that the maximum allowable value of the convergence parameter for the phase shift estimate is inversely proportional to the one for updating controller weights.

Simulations demonstrate that the proposed method is robust to change in environment and outperforms other filtered-x LMS based approaches.

APPENDIX

Substituting Eqs. (7a) and (7b) into Eq. (4b), the error signal in Eq. (4a) can be expressed as

$$\begin{aligned} e(n) &= d(n) + \alpha\{\cos\ \theta x_1(n) + \sin\ \theta x_Q(n)\} w_I(n-1) \\ &\quad + \alpha\{-\sin\ \theta x_I(n) + \cos\ \theta x_Q(n)\} w_Q(n-1) \\ &\quad + p(n). \end{aligned} \tag{A1}$$

Substituting Eq. (2) into Eq. (4) and rearranging, $p(n)$ in Eq. (A1) yields

$$\begin{aligned} p(n) &= -\alpha\rho e(n-1) S(\theta,n) S(\hat{\theta}(n-1),n-1) \\ &\quad - \alpha\rho e(n-1) T(\theta,n) T(\hat{\theta}(n-1),n-1) \\ &= -\alpha\rho A^2 e(n-1) \cos\{\hat{\theta}(n-1) - \theta + 2\pi f_0\}, \end{aligned} \tag{A2}$$

where

$$\begin{aligned} S(\theta,n) &= \cos\ \theta x_I(n) + \sin\ \theta x_Q(n), \\ S(\hat{\theta}(n-1),n-1) &= \cos\ \hat{\theta}(n-1) x_I(n-1) \\ &\quad + \sin\ \hat{\theta}(n-1) x_Q(n-1), \\ T(\theta,n) &= -\sin\ \theta x_I(n) + \cos\ \theta x_Q(n), \\ T(\hat{\theta}(n-1),n-1) &= -\sin\ \hat{\theta}(n-1) x_I(n-1) \\ &\quad + \cos\ \hat{\theta}(n-1) x_Q(n-1). \end{aligned} \tag{A3}$$

Substituting Eq. (A2) into Eq. (A1), the error signal in Eq. (4a) can be expressed as

$$\begin{aligned} e(n) &= d(n) + \alpha\{\cos\ \theta x_I(n) + \sin\ \theta x_Q(n)\} w_I(n-1) \\ &\quad + \alpha\{-\sin\ \theta x_I(n) + \cos\ \theta x_Q(n)\} w_Q(n-1) \\ &\quad - \alpha\rho A^2 e(n-1) \cos\{\hat{\theta}(n-1) - \theta + 2\pi f_0\}. \end{aligned} \tag{A4}$$

[1] S. J. Elliott and P. A. Nelson, ''Active noise control,'' IEEE Signal Process. Mag. October, 12–35 (1993).

[2] B. Widrow, J. R. Glover, J. M. McCool, J. Kaunitz, C. S. Williams, R. H. Hearn, J. R. Zeidler, E. Dong, and R. C. Goodlin, ''Adaptive noise cancelling principles and applications,'' Proc. IEEE **63**, 1692–1716 (1975).

[3] B. Widrow and S. D. Stearns, *Adaptive Signal Processing* (Prentice-Hall, Englewood Cliffs, NJ, 1985).

[4] C. C. Boucher, S. J. Elliott, and P. A. Nelson, ''Effect of errors in the plant model on the performance of algorithms for adaptive feedforward control,'' Proc. Inst. Electr. Eng. **138**, 313–319 (1991).

[5] S. D. Snyder and C. H. Hansen, ''The effect of transfer function estimation errors on the filtered-x LMS algorithm,'' IEEE Trans. Signal Process. **42**, 950–953 (1994).

[6] L. J. Eriksson and M. C. Allie, ''Use of random noise for on-line transducer modeling in an adaptive active attenuation system,'' J. Acoust. Soc. Am. **88**, 797–802 (1989).

[7] C. Bao, P. Sas, and H. Van Brussel, ''Comparison of two on-line identification algorithms for active noise control,'' Second Conference on Recent Advances in Active Control of Sound and Vibration, 1993 (unpublished), pp. 38–51.

[8] S. D. Sommerfeldt and J. Tichy, ''Adaptive control of a two-stage vibration isolation mount,'' J. Acoust. Soc. Am. **88**, 938–944 (1990).

[9] Xu Dian and R. J. Bernhard, ''Spatial extent of active noise control in an automotive vehicle,'' Proc. Noise-Con 91, 1991 (unpublished), pp. 245–252.

[10] R. L. Clark and G. P. Gibbs, ''A novel approach to feedforward higher harmonic control,'' J. Acoust. Soc. Am. **96**, 926–936 (1994).

[11] Alan V. Oppenheim, *Discrete-Time Signal Processing* (Prentice-Hall, Englewood Cliffs, NJ).

[12] P. L. Feintuch, ''An adaptive recursive LMS filter,'' Proc. IEEE **64**, 1622–1624 (1976).

[13] C. R. Johnson, Jr., M. G. Larimore, P. L. Feintuch, and N. J. Bershad, ''Comments and addition to an adaptive recursive LMS filter,'' Proc. IEEE **65**, 1399–1402 (1977).

[14] L. J. Eriksson, ''Development of the filtered-U algorithm for active noise control,'' J. Acoust. Soc. Am. **89**, 257–265 (1991).

[15] J. J. Shynk, ''Adaptive IIR filtering,'' IEEE Trans. Acoust., Speech, Signal Process. **6**(2), 4–21 (1989).

Relations among interaural cross-correlation coefficient ($IACC_E$), lateral fraction (LF_E), and apparent source width (ASW) in concert halls

Toshiyuki Okano
Takenaka Research and Development Institute, 1-5-1, Ohtsuka, Inzai, Chiba, 270-1395, Japan

Leo L. Beranek
975 Memorial Drive, Suite 804, Cambridge, Massachusetts 02138

Takayuki Hidaka
Takenaka Research and Development Institute, 1-5-1, Ohtsuka, Inzai, Chiba, 270-1395, Japan

(Received 25 September 1997; revised 6 March 1998; accepted 15 April 1998)

Relations are determined between one of the important subjective attributes of concert hall acoustics, the apparent source width, ASW, and three acoustical measures, interaural cross-correlation coefficient $IACC_E$, LF_E, and strength factor G. Although these measures previously have been found to correlate with ASW, their relations with it have not been examined sufficiently, especially in respect to their frequency characteristics. Herein, ASW's are directly determined for electronically reproduced musical sound fields with extensive ranges of values for $IACC_E$ and LF_E. Investigated as parameters are angles of incidence, the time delay difference between a pair of symmetric early lateral reflections, and the number of early lateral reflections. These studies indicate the relative efficacy of $IACC_E$ and LF_E for determining ASW under conditions that are realistically encountered in concert halls. The results were compared with measured $IACC_E$'s, LF_E's, and also the strength factor G's in existing concert halls. It is concluded that the arithmetic average of $[1-IACC_E]$'s at 500, 1 k and 2 k Hz combined with the strength factor G_{low} of the sound field at frequencies below 250 Hz are physical measures highly correlated with the subjective rank ordering of concert halls and that they cover the effects on ASW of the entire octave-band frequency range from 125 to 4 k Hz. [S0001-4966(98)05907-4]

PACS numbers: 43.55.Fw, 43.55.Gx, 43.55.Hy [JDQ]

INTRODUCTION

The objective of this paper is to find measures of the acoustical fields that aid in the engineering design of concert halls. Most important, these engineering measures must correlate highly with the subjective rank ordering of halls as determined from interviews (Beranek, 1996, Chap. 5) and written questionnaires (Fricke in same reference, Appendix 3).

Following, in part, the suggestion of Potter *et al.* (1995b) we use the term ''spatial impression'' as a generic term that has three subcomponents: ''spaciousness,'' ''size impression,'' and ''reverberance.'' The term ''spaciousness'' has two subcomponents: ''apparent source width (ASW)'' and ''listener envelopment (LEV).'' ASW is primarily related to early lateral reflections and low-frequency sound level, while LEV is related mostly to subsequent reverberation (Kuhl, 1978; Morimoto *et al.*, 1989; Beranek, 1994, 1996; Bradley *et al.*, 1995a). We define:

> Apparent source width (ASW) is the apparent auditory width of the sound field created by a performing entity as perceived by a listener in the audience area of a concert hall. It is generally accepted that ASW can be determined from the sound field reaching the ears of a listener in a concert hall or opera house in the first 80 ms after (and including) the arrival of the direct sound from the source on stage. It is measured in degrees.

Listener envelopment (LEV) is the subjective impression by a listener that (s)he is enveloped by the sound field, a condition that is primarily related to the reverberant sound field. The reverberant sound field is generally said to begin 80 ms after arrival of the direct sound. There is no standard measurement of LEV at this writing. Bradley *et al.* (1995a, b) have suggested a measure that appears to correlate with LEV. They determine a quantity LG (80 ms to 3 s) that is the ratio of the sound pressure level of the late arriving sound at a position in a hall as measured by a figure-8 microphone, with its null pointed to the sound source, to that measured in an anechoic chamber at 10 m from the same omnidirectional sound source operating with the same power level.

In the physical measures that follow, the subscript ''E'' indicates the 80-ms interval named above.

$IACC_{E3}$ is obtained by averaging the values of the early interaural cross-correlation coefficient $IACC_E$ in the three octave bands with mid-frequencies 500, 1 k, and 2 k Hz (Beranek, 1996, Appendix 2). This measure favors the frequency region where the

wavelengths are comparable or smaller than the acoustical distance between the two sides of a head.

LF_{E4} is obtained by averaging the values of the early lateral fraction LF_E in the four octave bands with mid-frequencies 125, 250, 500, and 1 k Hz (Beranek, 1996, Appendix 2). This measure favors the frequency region where the wavelengths are mostly longer than the acoustical distance between the two sides of a head.

The strength factor G the sound pressure level at a point in a hall, with an omni-directional source on the stage, minus the sound pressure level that would be measured at a distance of 10 m from the same sound source operating at the same power level located in an anechoic chamber. The measurements include the direct sound. G_{low} is the average of the early strength factors measured in the 125- and 250-Hz octave bands.

Several measures have been found to relate to ASW, including: (a) the interaural cross-correlation coefficient $IACC_E$; (b) the lateral fraction LF_E; (c) the overall sound pressure level SPL; and (d) the strength factor of lower-frequency components, measured by G_{low}. References include Keet (1968), Barron (1971), Barron *et al.* (1981), Blauert (1986a, b), Morimoto *et al.* (1988), Bradley *et al.* (1995a), Potter *et al.* (1995b), Hidaka *et al.* (1995), and Beranek (1996).

Because the subjective rank orderings obtained from the interviews and written questionnaires apply to the acoustics of a hall overall, values of $IACC_E$ and LF_E as reported here are the averages at many positions (seats) throughout the halls. No attempt is made to correlate measurements at particular seats with the sound quality at those seats. Further, it is not pretended that the measurement of either $IACC_E$ or LF_E is a measure of how a listener actually perceives the effect of acoustics on music, e.g., both quantities vary greatly with rotation of the measuring head or the figure-8 microphone, while no such variation is observed as a person's head is rotated during a concert. Notwithstanding, it is believed that lateral reflections of sound in a hall as measured by these quantities at the listeners' positions are directly related to the subjective impression of spaciousness and that ASW is one of six or so subjective attributes that lend quality to a hall's acoustics (Beranek, 1996).

In the present study, a series of psychoacoustic experiments were conducted in order to examine the efficacy and limitations for $[1-IACC_E]$ and LF_E as measures for spaciousness, and to determine ASW's for extensive conditions of early reflections using octave-band filtered music as a source. From the literature, it would appear that lower-frequency components are as great or of greater importance in determining ASW than middle- and high-frequency components, (Morimoto *et al.*, 1988; Okano *et al.*, 1994; Potter *et al.*, 1995a; Beranek, 1996). At frequencies below 355 Hz the sound fields are nearly the same at both ears, making one inquire whether it is the sound pressure level that contributes to acoustical quality and not LF_{E4}, whose basis is at low frequencies.

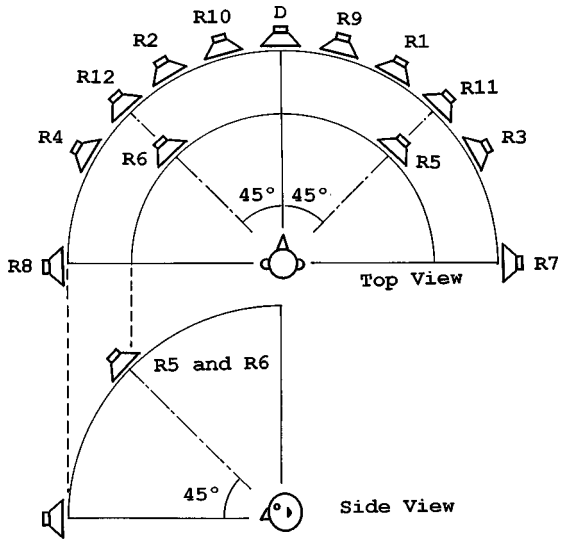

FIG. 1. Experimental arrangement used for determining ASW. Loudspeaker D always radiates the direct sound and the listener always faces it. The other 12 loudspeakers radiate ''reflected'' sound waves with different time delays and angles of incidence.

I. DESCRIPTIONS OF THE EXPERIMENTS

A. Procedure

Musical signals were presented to a subject with a multiple loudspeaker system in an anechoic room (Fig. 1). Each signal was a musical composition recorded in an anechoic room convolved with the impulse response of a test sound field and fed through an octave-band filter. The center frequencies of the filters ranged from 125 to 4 k Hz for each test sound field. All of the signals were presented at the same averaged level of 67 dB regardless of the frequency band and the nature of the test sound field. The subject evaluated perceived ASW for each test as follows: A scale graduated in 2.5° steps was placed along the circular loudspeaker arrangement. The subject judged which graduation of the scale corresponded to the edge of the perceived sound image. The average of all the subjects' judgments for the left and right edges was defined as ASW for the signal. *The angles listed are half the total width from left to right.*

The $IACC_E$'s and LF_E's for the sound fields were measured in six octave bands with center frequencies ranging from 125 to 4000 Hz. An impulse sound was used for $IACC_E$ and a pink noise for LF_E. A musical signal was not used in the physical measurements in order to eliminate the fluctuations and spectral changes of music.

B. Test sound field

Fourteen types of test sound fields were studied. Each was composed of direct sound and 2 to 12 early reflections within 80 ms after arrival of the direct sound. The best halls generally have a large number of early reflections, particularly in the part of the balcony at the rear facing the stage, and the poorer halls have only a few, particularly on the front main floor.

The test fields, as listed in Table I, cover the range generally found in a concert hall. Seven of the signals were designed to represent sound fields near the center line of a

TABLE I. Composition of test sound fields.

Name of test sound field			A1	A2	A3	A4	A5	A6	A7	B1	B2	B3	B4	B5	B6	B7
Number of reflections			2	2	2	4	6	8	12	2	2	2	4	4	6	8
Attributes of the direct sound and reflections																
	Angle of incidence (°)					Delay							Delay			
Amplitude	horizontal	vertical				(ms)							(ms)			
1.00	0	0	0	0	0	0	0	0	0	0	0	0	0	0	0	0
0.64	15	0						33	33							60
0.72	−15	0						23	23							49
0.79	30	0	20			20	20	20	20	36			32		32	24
0.75	−30	0	16			16	16	16	16	16			16		16	16
0.56	45	0					46	46	46						65	68
0.48	−45	0					64	64	64						78	78
0.66	60	0				30	30	30	30				55	32	55	41
0.69	−60	0				27	27	27	27				75	16	75	32
0.72	60	0		20							36					
0.79	−60	0		16							16					
0.43	90	0							78					78		
0.44	−90	0							75					55		
0.72	90	0			20							36				
0.79	−90	0			16							16				
0.50	45	45							60							
0.52	−45	45							55							

hall, comprising pairs of early reflections with symmetrical angles of incidence and relative time delay mostly with differences of 3–5 ms, A1–A7. The other seven were designed to represent sound fields off the center line, comprising pairs of symmetrical reflections all with delay differences larger than 8 ms, B1–B7. All had initial time-delay gaps of 16 ms. Three variations of angle of incidence were included for the condition of two early reflections. Two variations of angle of incidence were included for the conditions of four early reflections. For conditions with more than four reflections, the variation of angle of incidence was not included because the sound field does not change much when there are a large number of reflections.

In addition, seven test sound fields were added to examine in detail the effect of delay differences between a pair of early reflections. An angle of incidence of 90° was selected because it is the angle most affected by relative time-delay differences. The range of delay differences were 0–2 ms and 2–8 ms. The levels of these two reflections were made equal for the 0–2 ms range of delay differences because symmetrical reflections would have the same level considering the center line position in a symmetrical room.

TABLE II. Eight music compositions compared.

No.	Composer	Composition
1	Mozart:	Overture, ''Le Nozze di Figaro''
2	Menderssohn:	4th movement, Symphony No. 3 in A minor, Op. 56 ''Scottish,'' bars 396–490.
3	Bizet:	L'Arlesienne'' Suite No. 2.
4	Johan and Josef Strauss:	Pizzicate-Polka.
5	Glinka:	Overture, ''Ruslan and Lyudmila''
6	Verdi:	Prelude to Act 1, ''La Traviata''
7	Bruckner:	1st movenent, Symphony No. 4 in E-flat major ''Romantic,'' bars 517–573.
8	Debussy:	Prelude a 1'Apres-Midi d'un Faune, bars 1–20.

C. Musical source signal

In a preliminary study, the power spectrum of eight anechoically recorded orchestral musical compositions were compared (see Table II). They cover a range of compositions that are often played at classical symphony concerts. All were recorded in a temporally constructed anechoic room, having enough floor area for a full-sized orchestra (Hidaka *et al.*, 1988). The characteristics of the room satisfied the requirements for a semi-anechoic room defined by ISO 3745. The power spectra are shown in Fig. 2. The ordinate gives the relative sound pressure level compared to the overall SPL. Except for the 63-Hz band, the variation of the levels in the frequency bands is not more than approximately 10 dB, excluding a few extreme tones. The average level in 4-kHz

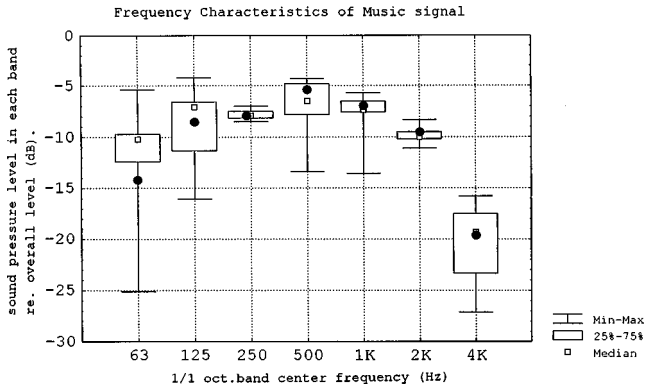

FIG. 2. Comparison of power spectrum of eight musical compositions. Vertical bar shows the variance of maximum to minimum. Box shows the range from 25% to 75% cumulative point. Open square shows median. The filled circle shows the spectrum of the musical composition used, namely, the first movement of Bruckner's Symphony No. 4.

band is more than 10 dB lower than that for the bands from 125 to 2 k Hz. The division in power between the lower- and higher-frequency components is somewhere between 250 and 500 Hz, approximately the fundamental of middle C on the piano keyboard. The cutoff frequency between these two bands is 355 Hz, roughly the middle point of the musical frequency range.

The source signal chosen for the experiment was Bar 560 to 561 of the First Movement of Bruckner's Symphony No. 4. As indicated by the filled circles, its frequency characteristic is near the average of those of the compositions and the levels in the bands were nearly stationary over the total frequency range so that the subjects could judge ASW relatively easily.

D. The subjects

Four subjects took part in the experiments. Three were acoustical engineers and the fourth a singer. All had sufficient experience as subjects in this kind of hearing test. The hearing level of each was measured and all had normal thresholds of hearing as defined by ISO 7029.

II. EFFECT OF ANGLE OF INCIDENCE ON SUBJECTIVE ASW, $[1-\mathrm{IACC}_E]$, AND LF_E FOR SOUND FIELDS WITH A PAIR OF REFLECTIONS

Figure 3 shows a portion of the experimental results described in Sec. I, indicating relations between the subjectively determined ASW (circles) and the angle of incidence of a pair of symmetrical reflections at each frequency band. The vertical bars indicate the standard deviation of the responses of the subjects. The angles of incidence were $\pm 30°$, $\pm 60°$, and $\pm 90°$ and at each angle the delay difference was either 4 ms (open markers) or 20 ms (solid markers). Relations between $[1-\mathrm{IACC}_E]$ (squares) and LF_E (triangles) versus angle of incidence are plotted in the same figures.

A large change of ASW with angle of incidence is clearly observed in the frequency range below 500 Hz but not for the range above 500 Hz. For most of the cases at the 500-Hz band and below, the differences among perceived ASW's with different angles of incidence were found statistically significant by means of *t*-test. On the other hand, the differences were not statistically significant for most of the cases at the bands above 500 Hz. The same but smaller tendency is observed for $[1-\mathrm{IACC}_E]$, except that for 30° incidence at 2 k Hz it was relatively larger. Ando (1985) has found that 30° is the angle that most effectively decreases IACC at this frequency. LF_E depends on the angle of incidence in all of the frequency bands, which means that LF_E does not correspond to ASW above 500 Hz, at least in regard to the change of angle of incidence.

It is seen that for the frequency bands above 500 Hz, an increase in delay difference from 4 ms to 20 ms makes no difference on ASW. For the 500-Hz band and below, the delay difference is significant and the effect on ASW is more pronounced for $\theta = 90°$ than for lesser angles. For the 125- and 250-Hz bands both $[1-\mathrm{IACC}_E]$ and LF_E are influenced by the delay difference—the effect is especially pronounced for LF_E at 125 Hz.

III. EFFECT OF THE TIME DELAY DIFFERENCE BETWEEN TWO 90° LATERAL REFLECTIONS ON SUBJECTIVE ASW, $[1-\mathrm{IACC}_E]$, AND LF_E

Because the delay difference between two reflections is more pronounced at 90° than at other angles, its effects on ASW, IACC_E, and LF_E were explored as described in Sec. I B. The practical purpose of this examination was to determine how near the centerline of a symmetrical hall measurements can be made without obtaining incorrect data. Figure 4 shows the dependence of ASW, $[1-\mathrm{IACC}_E]$, and LF_E on the delay difference. As before, the vertical bars indicate the standard deviation of the responses of the subjects.

It is seen that, in general, the subjective ASW (solid circles) grows from a small value at $\Delta t = 0$ ms, makes a rounded peak at about $1/(2f)$ s and generally stabilizes at about $4/f$ s. LF_E (open triangles) reaches an enormous peak at $1/(2f)$ s and also stabilizes at about $4/f$ s. $[1-\mathrm{IACC}_E]$ (open circles) also tends to stabilize at somewhere between $2/f$ and $4/f$ s, which corresponds to about 5 ms or so in the frequency range of 500–2000 Hz bands, where it is usually determined. LF_E, measured with two microphones, i.e., an omni-directional type and a figure-8 type, can take on values from 0 to infinity, contrary to some statements that it cannot exceed 1.0. This happens with this method of measuring LF_E especially for a symmetrical sound field.

This examination shows that ASW, as well as $[1-\mathrm{IACC}_E]$ and LF_E are unstable near the center line of a symmetrical hall especially so in the frequency range below 500 Hz. These results, admittedly taken with only two reflections compared to larger numbers in real halls, indicate that when determining $[1-\mathrm{IACC}_{E3}]$, the measuring positions should be no less than 1 m off the center line. For LF_{E4} values to be correct in the lowest (125-Hz) band, the measurements must be not less than 5 m off the center line. With many more reflections and averaging of four bands, one surmizes that this minimum distance for LF_{E4} could probably be halved.

IV. THE EFFECT OF THE NUMBER OF EARLY REFLECTIONS ON SUBJECTIVE ASW, $[1-\mathrm{IACC}_E]$, AND LF_E

Plots of ASW (circles), $[1-\mathrm{IACC}_E]$ (squares), and LF_E (triangles) against the number of early reflections are shown in Fig. 5. As before, the vertical bars indicate the standard deviation of the responses of the subjects. All of these ten test sound fields have approximately the same value of L_f, which is defined as the cos θ of the incident energy, the range being 0.44–0.51, as calculated from Table I. This difference is less than 0.07 which is the difference limen for L_f defined by Barron and Marshall (1981). The test sound field with two reflections ($\theta = 60°$) and with 12 reflections have L_f values of 0.47 and 0.48, respectively, which is in the middle of that range. Thus all of these test sound fields correspond to the same class of lateral efficiency.

It is seen that for a large number of lateral reflections, subjective ASW is almost independent of frequency (60°–70°). For few reflections, ASW decreases from a large value in the lowest-frequency band (ca. 60°) to smaller values in

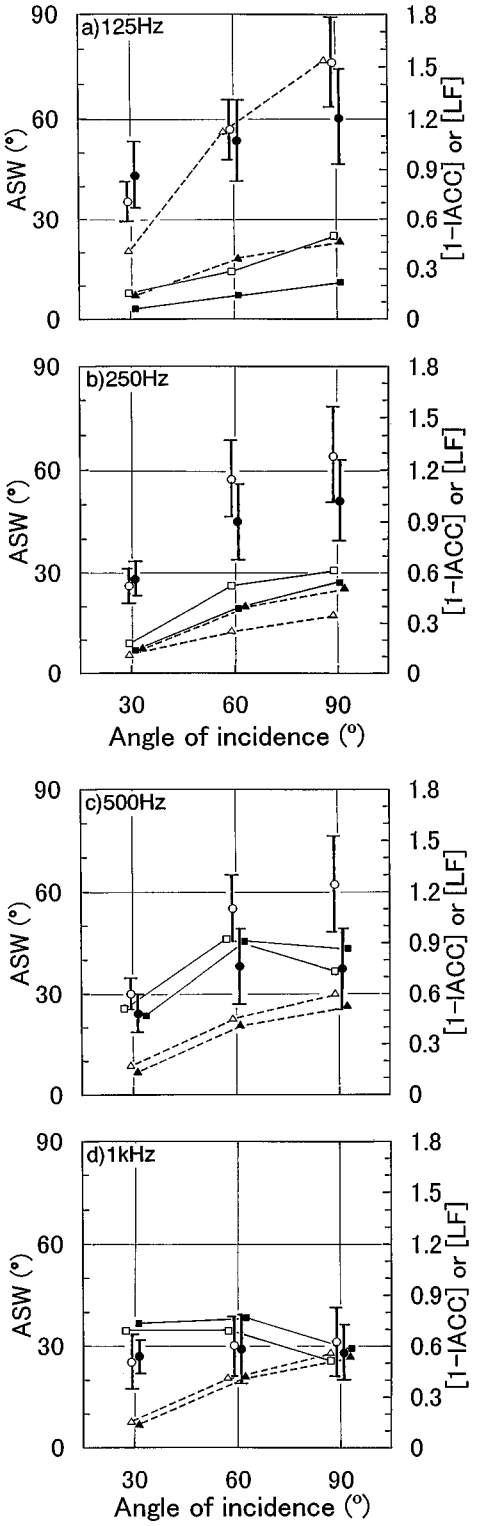

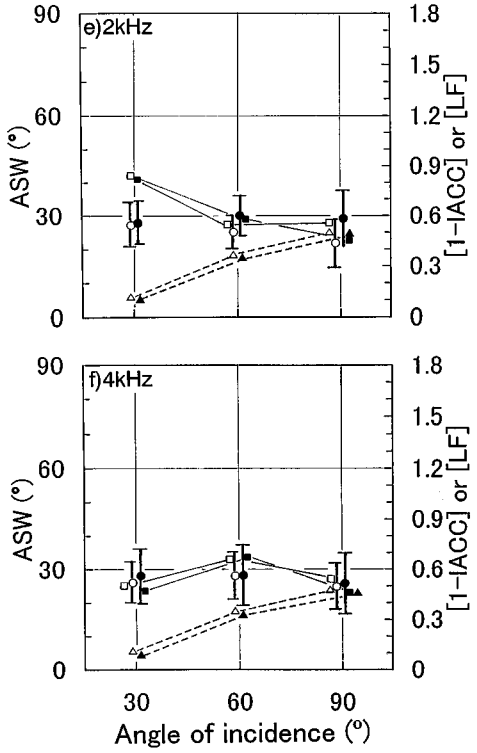

FIG. 3. Subjective determination of ASW as a function of angle of incidence of a pair of symmetrical reflections. The measured values of $[1-\mathrm{IACC}_E]$ (squares) and LF_E (triangles) are shown for each ASW (circles). The standard deviations of ASW are shown by the vertical bars. Open markers indicate 4-ms delay between the two reflections and solid markers indicate 20 ms.

the higher-frequency bands (ca. 40°). For the higher-frequency bands, ASW increases with the number of lateral reflections until they become ten or more. For the lower-frequency bands, ASW constantly keeps a large value regardless of the number of reflections. $[1-\mathrm{IACC}_E]$ shows the same kind of dependence on number of early reflections, especially for 500 Hz and higher-frequency bands. On the other hand, LF_E is independent of the number of reflections in any octave band and, thus does not represent ASW well at least when the sound field, at higher frequencies, contains a number of reflections.

V. EFFECT OF CHANGE IN LOW- AND HIGH-FREQUENCY STRENGTH FACTORS ON SUBJECTIVE ASW

In Hidaka *et al.* (1995) the authors investigated the change in subjective ASW for incremental changes in the strength factors at low (below 355 Hz) frequencies (GL) and

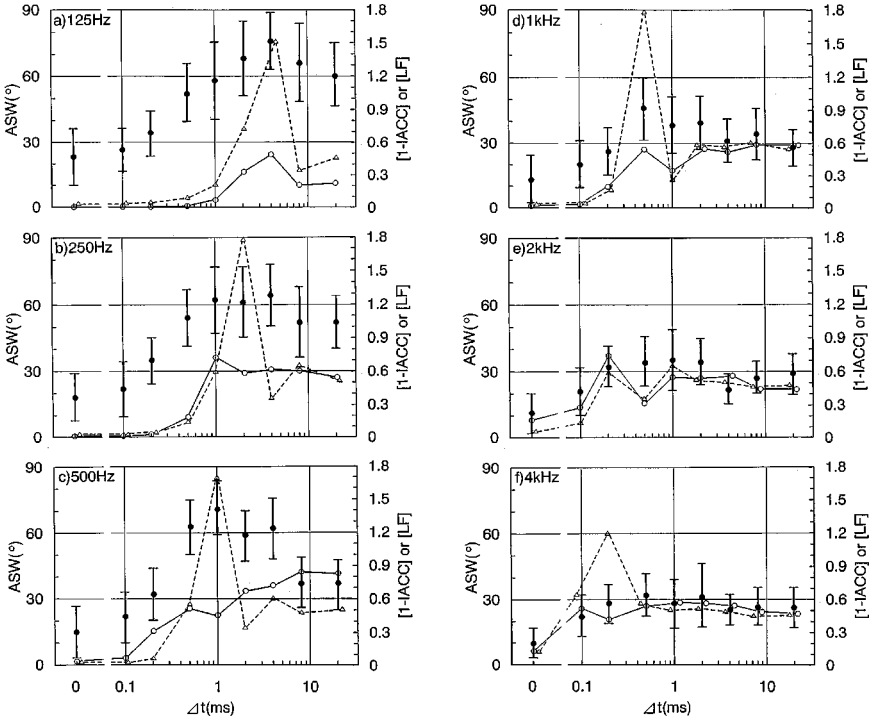

FIG. 4. ASW (solid circles), $[1-\mathrm{IACC}_E]$ (open circles), and LF_E (open triangles) versus the delay difference between two 90° lateral reflections.

at high (above 355 Hz) frequencies (GH) with the music of Sec. I C as the source. In concert halls, the incremental difference between the levels in the high- and low-frequency regions ranges from about -2.4 to $+1.0$ dB, averaging about -0.9 dB (Beranek, 1996, p. 431). In the 1995 subjective experiment, ASW was plotted against $\Delta\mathrm{GL}=\mathrm{GL}-\mathrm{GH}$, where GH was held constant or $\Delta\mathrm{GH}=\mathrm{GH}-\mathrm{GL}$ where GL was held constant. The range in ΔGH and ΔGL

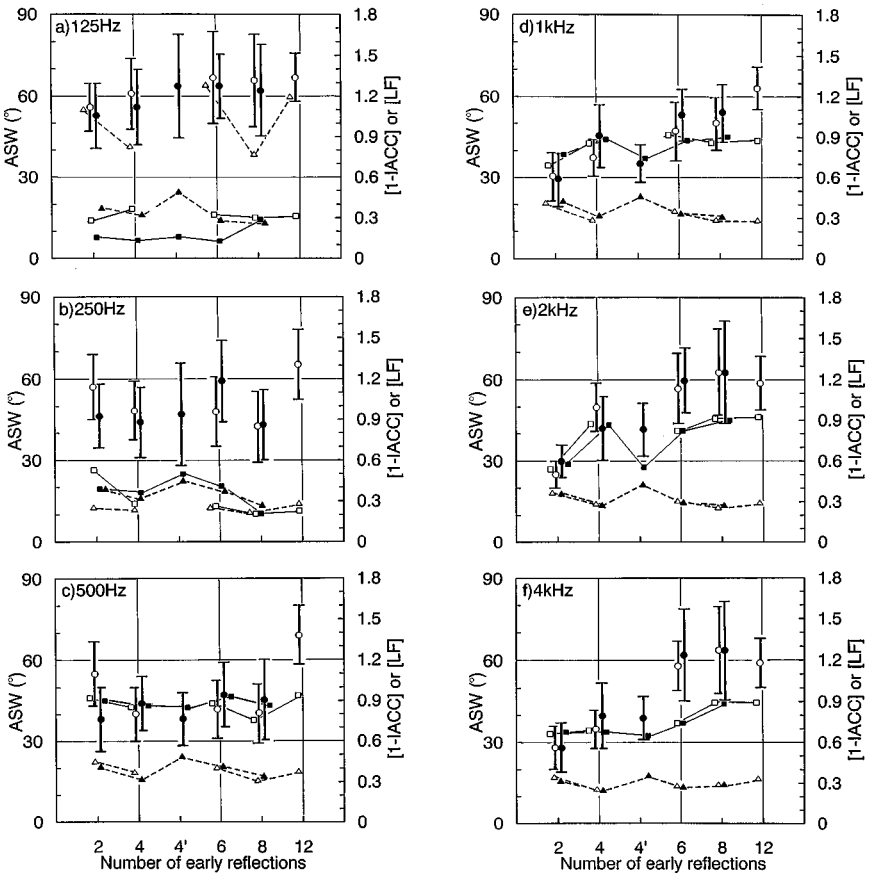

FIG. 5. ASW (circles), $[1-\mathrm{IACC}_E]$ (squares), and LF_E (triangles) as a function of the number of early (less than 80 ms) reflections. Solid markers indicate delay differences between the two reflections equal to or greater than 8 ms, while open markers indicate differences of 3 ms.

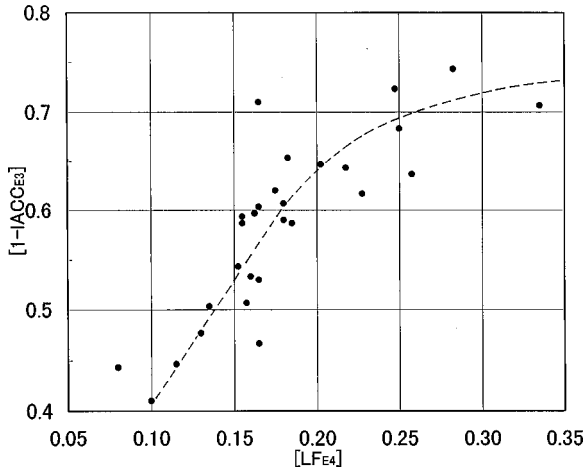

FIG. 6. Hall-averaged values of $[1-\mathrm{IACC}_{E3}]$ versus LF_{E4} as determined in 28 existing concert halls.

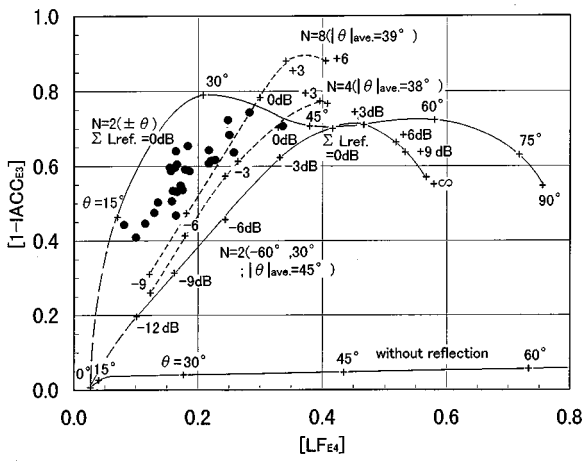

FIG. 7. Plots of $[1-\mathrm{IACC}_{E3}]$ versus LF_{E4}, for the experimental sound fields described in the text. The solid circles show the hall-averaged values determined in 28 concert halls, as in Fig. 6.

was -5 to $+10$ dB. The experiment showed that ΔASW/ΔGL was about 2 degrees for each decibel change in GL. The change in ΔASW/ΔGH was less than half as much.

VI. HALL DATA AND THE RANKING OF HALLS

The authors now have available both the physical data IACC_{E3} and LF_{E4} measured in 28 concert halls. As shown in Fig. 6, there is relatively high correlation between $[1-\mathrm{IACC}_{E3}]$ and LF_{E4} for these halls. However, Hidaka *et al.* (1995) showed that IACC_{E3} *taken alone* is more accurate in separating the halls according to their subjective ratings. Intuitively, one feels that the former is more basic, because it measures the difference in the sound fields at the two ears of a head as compared to measurements of the field at a point in space.

Contrary to the high correlation shown in Fig. 6, no proper relation can be derived between the formulations for the two measures without introducing an unrealistic assumption. A study was made to learn under what conditions the relation of Fig. 6 is to be expected.

Using the experimental setup of Fig. 1, IACC_{E3}'s and LF_{E4}'s were first measured with only a direct sound whose angle of incidence was varied from 0° (front) to 90° (lateral). One expects LF to vary from zero at frontal incidence to unity at lateral incidence in any of the four frequency bands. Contrawise, as shown by the lowest curve in Fig. 7, $[1-\mathrm{IACC}_{E3}]$ remains near zero for all angles of incidence.

In the next experiment, the sound field was comprised of a direct sound wave and two symmetrical early reflections, with sufficient time delay between the two. The angle of incidence was varied from 15° to 90° and the total level of the reflections equaled that of the direct sound. We see from the left-hand (and uppermost) curve of Fig. 7 that $[1-\mathrm{IACC}_{E3}]$ reaches a maximum value as high as 0.8 at 30°, remaining at about 0.7 from 40° to 70° and decreasing to 0.5 at 90°. LF_{E4} increases from zero at frontal incidence to 0.75 at lateral incidence, approximately according to $\cos^2\theta$. It is obvious that $[1-\mathrm{IACC}_{E3}]$ is not much influenced by the angle of incidence between $\theta=30°$ and 75°, while LF_{E4} changes greatly.

In a second test, the sound field was comprised of a direct sound and two early lateral reflections whose angles of incidence were $-60°$ and 30°. The total sound level of the reflections minus the direct sound level was varied from -12 dB to $+\infty$ (see right-hand lowest curve of Fig. 7). For the range of levels that are lower than 0 dB, $[1-\mathrm{IACC}_{E3}]$ and LF_{E4} are linearly related. For levels above 0 dB, $[1-\mathrm{IACC}_{E3}]$ flattens out and LF_{E4} continues to increase.

In a third test, the sound field was comprised of four to eight reflections with $|\theta|_{\mathrm{avg}}\cong 38°$. The dashed lines of Fig. 7 also reveal that the two quantities are linearly related for levels below 0 dB, and that $[1-\mathrm{IACC}_{E3}]$ flattens off at levels above about $+3$ dB.

The dots in Fig. 7 represent *hall-averaged* data measured in 28 concert halls. These dots fall in a confined region. For comparison, *individual-seat* data from four halls are shown by the dots in Fig. 8. These data scatter widely. It appears that the process of hall-averaging yields a more explicit relation between $[1-\mathrm{IACC}_{E3}]$ and LF_{E4} as shown to larger scale in Fig. 6. The correlation in Fig. 6 is high for $\mathrm{LF}_{E4}\leqslant 0.2$, but for $\mathrm{LF}_{E4}\geqslant 0.2$, $[1-\mathrm{IACC}_{E3}]$ approaches as-

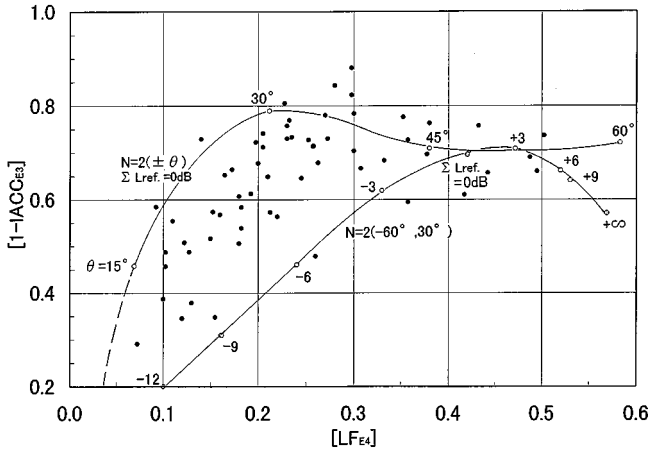

FIG. 8. Same as Fig. 7, except that the dots indicate the values measured at individual seats in four concert halls.

TABLE III. Acoustical attributes and rank ordering of concert halls. Hall average with unoccupied condition.

		G								G_E							
Rank	Name of hall	125	250	500	1000	2000	4000	low	high	125	250	500	1000	2000	4000	low	high
A+	Amsterdam, Concertgebouw	5.3	5.4	6.0	6.0	5.9	4.6	5.3	6.0	−2.1	−0.9	0.3	1.6	1.3	1.0	−1.5	1.1
	Boston, Symphony Hall	2.2	3.1	4.4	5.0	5.1	4.4	2.6	4.8	−1.8	−1.1	−0.5	0.6	0.9	1.2	−1.5	0.3
	Vienna, Gr. Musikvereinssaal	7.1	6.7	6.9	7.2	6.4	5.3	6.9	6.9	1.5	−0.1	0.9	2.1	1.5	1.8	0.7	1.5
A	Basel, Stadt-Casino	8.5	8.3	7.3	7.7	7.1	6.6	8.4	7.4	2.7	2.6	2.7	3.7	3.4	3.4	2.7	3.3
	Berlin, Konzerthaus (Schauspiel)	7.7	6.5	6.1	6.4	5.3	4.8	7.1	5.9	2.5	0.6	0.8	2.3	1.9	1.8	1.6	1.7
	Cardiff, St. David's Hall	2.2	1.2	3.4	3.4	2.7		1.7	3.2								
	Detroit, Orchestra Hall	4.8	3.9	4.0	4.3	3.0	1.7	4.4	3.7								
	Zurich, Gr. Tonhallesaal	8.4	8.3	8.3	7.6	7.7	7.3	8.4	7.9	2.1	0.8	2.4	2.4	3.0	3.3	1.5	2.6
B+	Baltimore, Joseph Meyerhoff	3.5	3.2	4.2	4.0	3.2	1.9	3.4	3.8	−2.5	−3.0	−0.5	0.2	0.9	1.1	−2.8	0.2
	Berlin, Philharmony Hall	3.6	2.8	4.3	4.3	3.5	3.1	3.2	4.0	−0.4	−0.1	1.5	1.6	0.7	0.3	−0.3	1.3
	Cleveland, Severance Hall	1.8	3.7	3.5	2.6	2.4	0.8	2.8	2.8								
	Costa Mesa, Segerstrom Hall	2.0	3.3	4.3	4.6	4.3	3.5	2.7	4.4	−3.5	−1.7	−0.1	0.4	0.2	0.9	−2.6	0.2
	Munich, Philharmonie	1.2	1.6	2.6	2.4	3.1	1.7	1.4	2.7								
	Paris, Salle Pleyel[b]	6.1	3.8	4.4	4.6	4.3	3.9	4.9	4.4								
	Salt Lake, Symphony Hall	1.3	−0.3	1.8	2.1	1.9	1.0	0.5	1.9	−5.0	−5.9	−2.4	−1.8	−1.8	−2.5	−5.5	−2.0
	Tokyo, Bunkakaikan	2.7	2.8	3.6	3.7	3.8	4.9	2.8	3.7								
	Tokyo, Suntory Hall	2.7	3.2	4.0	4.7	4.8	5.0	3.0	4.5								
	Washington, Kennedy Center	2.7	3.0	3.5	2.8	2.9	0.6	2.9	3.0								
B	Akron, E. J. Thomas Performing	0.2	1.4	2.9	2.5	−0.1	−2.0	0.8	1.8								
	Brandon, W. Manitoba Centennial	3.8	3.5	3.1	1.5	0.0	−1.2	3.6	1.5								
	Buffaro, Kleinhaus Music Hall	4.7	3.5	3.2	2.9	2.1	−0.1	4.1	2.7								
	Edmonton, N. Alberta Jubilee	−2.0	−1.5	0.4	0.4	−1.1	−3.3	−1.7	−0.1								
	London, Barbican L. Concert Hall	1.5	1.0	3.6	4.0	3.3		1.2	3.6								
	London, Royal Albert Hall	−1.1	−1.3	0.1	−0.3	−0.2		−1.2	−0.1								
	Montreal, Salle Wilfrid-Pelletier	0.2	−0.3	0.2	1.1	0.1	−2.6	−0.1	0.5								
	Philadelphia, Academy of Music	−1.3	0.5	2.4	1.7	0.1	−1.8	−0.4	1.4								
	San Francisco, Davies Hall[b]	1.9	2.4	2.7	2.8	2.3	2.3	2.2	2.6	−4.5	−2.4	−1.4	−0.4	−0.6	0.0	−3.5	−0.8
	average	3.0	2.9	3.7	3.7	3.1	2.2	3.0	3.5	−1.0	−1.0	0.3	1.2	1.0	1.1	−1.0	0.8
	standard deviation	2.8	2.6	2.0	2.1	2.3	3.0	2.7	2.1	2.8	2.3	1.5	1.5	1.5	1.6	2.5	1.5
	Max	8.5	8.3	8.3	7.7	7.7	7.3	8.4	7.9	2.7	2.6	2.7	3.7	3.4	3.4	2.7	3.3
	Min	−2.0	−1.5	0.1	−0.3	−1.1	−3.3	−1.7	−0.1	−5.0	−5.9	−2.4	−1.8	−1.8	−2.5	−5.5	−2.0
	Max-Min	10.5	9.8	8.2	8.0	8.8	10.6	10.1	8.0	7.7	8.5	5.1	5.5	5.2	5.9	8.1	5.3

ymptotically a level of about 0.75 while LF_{E4} continues to increase from 0.2 to 0.35.

Shown in Table III are measured hall-averaged G's, $[1-IACC]$'s, and LF's along with the subjective rank ordering from Beranek (1996). The G's are the values after compensating the difference between measurement organizations (Beranek, 1996, Chap. 9). Because ASW is determined primarily by the early arriving sounds, $G_{E\text{low}}$ ought to be the best form for correlation with ASW. Unfortunately, there are very few halls in which $G_{E\text{low}}$'s were measured. For the other halls we can only presume $G_{E\text{low}}$'s from G_{low}'s and C_{80}'s because correct values can only be obtained by averaging calculations made from G_{low}'s and C_{80}'s for individual seats. So, we sought whether the G_{low}'s integrated from 0 to several seconds, measured without audience, are surrogates for evaluating the effects of low-frequency SPL on ASW. The correlation between the $G_{E\text{low}}$'s and G_{low}'s for the 14 halls for which they are available is as high as 0.91. Hence, we feel justified in using G_{low} to investigate whether the low-frequency level is an important factor in the determination of ASW.

Figure 9 shows plots of $[1-IACC_{E3}]$'s vs G_{low}'s for 20 concert halls for which the physical data and subjective rank orderings are available (see Table III). The values of the $[1-IACC_{E3}]$'s for Amsterdam, Vienna, Zurich, and Berlin (Konzerthaus) have been adjusted upward to make their unupholstered seat data comparable to the upholstered seat data of the other halls (Hidaka *et al.*, 1995). The highest A, A+ ranking category is on the upper right and the lowest B ranking is on the lower left.

A similar graph for 21 halls for which LF_{E4} and subjective ratings are available is shown in Fig. 10 (see Table III). The addition of G_{low} to LF_{E4} permits separation of the halls into only two categories, (1) A+, A, B+, and (2) B. Hidaka *et al.* (1995) found that LF_{E4} alone was able only to separate clearly the A+, A halls from the B halls.

It is apparent that $[1-IACC_{E3}]$ and G_{low} more closely separate the halls into three categories that correlate with the subjective judgments than LF_{E4} and G_{low}. It might be argued that if, in Fig. 10, the points for Cardiff and Costa Mesa were eliminated, the separation would be improved. However, the subjective interviews and professional judgments for these two halls indicate that they are properly ranked. Further, the data for those halls were obtained under the best controls and are not suspect. Pending comparable data on many more halls, it is concluded that $[1-IACC_{E3}]$ and G_{low} are successful in estimating the subjective judgments of the acoustical quality of concert halls. This state-

TABLE III. (*Continued*.)

Rank	Name of hall	1-IACC$_E$ 125	250	500	1000	2000	4000	3*B*	3*B*[a]	LF$_E$ 125	250	500	1000	2000	4000	4*B*
A+	Amsterdam, Concertgebouw	0.06	0.22	0.54	0.58	0.49	0.56	0.54	0.62	0.19	0.15	0.19	0.17	0.14	0.23	0.18
	Boston, Symphony Hall	0.05	0.18	0.51	0.70	0.73	0.77	0.65		0.23	0.19	0.17	0.22	0.25	0.18	0.20
	Vienna, Gr. Musikvereinssaal	0.08	0.24	0.58	0.68	0.66	0.60	0.64	0.71	0.13	0.17	0.19	0.17			0.17
A	Basel, Stadt-Casino	0.11	0.22	0.54	0.66	0.67	0.71	0.62	0.64							
	Berlin, Konzerthaus (Schauspiel)	0.08	0.20	0.63	0.71	0.58	0.64	0.64	0.66							
	Cardiff, St. David's Hall									0.16	0.17	0.19	0.16			0.17
	Detroit, Orchestra Hall	0.06	0.18	0.52	0.58	0.69	0.71	0.60		0.18	0.16	0.14	0.17	0.21	0.14	0.16
	Zurich, Gr. Tonhallesaal	0.07	0.21	0.52	0.73	0.67	0.72	0.64	0.71							
B+	Baltimore, Joseph Meyerhoff	0.05	0.16	0.47	0.56	0.60	0.74	0.54		0.18	0.15	0.13	0.15	0.18	0.13	0.15
	Berlin, Philharmony Hall	0.04	0.12	0.40	0.50	0.47	0.55	0.46								
	Cleveland, Severance Hall	0.05	0.13	0.49	0.59	0.70	0.68	0.59		0.20	0.14	0.13	0.15	0.18	0.13	0.16
	Costa Mesa, Segerstrom Hall	0.08	0.20	0.53	0.63	0.69	0.70	0.62		0.27	0.19	0.23	0.22			0.23
	Munich, Philharmonie									0.13	0.13	0.14	0.12	0.10	0.18	0.13
	Paris, Salle Pleyel[b]									0.10	0.15	0.19	0.15	0.11	0.18	0.15
	Salt Lake, Symphony Hall	0.07	0.19	0.52	0.60	0.65	0.74	0.59								
	Tokyo, Bunkakaikan			0.49	0.62	0.66	0.70	0.59		0.17	0.17	0.19	0.19	0.22	0.25	0.18
	Tokyo, Suntory Hall			0.47	0.55	0.58	0.61	0.53		0.16	0.15	0.17	0.16	0.18	0.19	0.16
	Washington, Kennedy Center	0.06	0.26	0.58	0.60	0.64	0.70	0.61		0.18	0.17	0.17	0.20	0.24	0.17	0.18
B	Akron, E. J. Thomas Performing	0.04	0.09	0.33	0.38	0.62	0.62	0.44		0.09	0.07	0.07	0.09	0.13	0.08	0.08
	Brandon, W. Manitoba Centennial	0.05	0.12	0.41	0.38	0.55	0.61	0.45		0.19	0.12	0.08	0.07	0.06	0.06	0.12
	Buffaro, Kleinhaus Music Hall	0.03	0.10	0.21	0.39	0.63	0.62	0.41		0.11	0.10	0.09	0.10	0.11	0.08	0.10
	Edmonton, N. Alberta Jubilee									0.14	0.10	0.13	0.16	0.17	0.14	0.13
	London, Barbican L. Concert Hall									0.11	0.10	0.14	0.13			0.12
	London, Royal Albert Hall									0.13	0.16	0.14	0.13	0.14		0.14
	Montreal, Salle Wilfrid-Pelletier									0.09	0.12	0.15	0.12	0.09	0.16	0.12
	Philadelphia, Academy of Music	0.06	0.19	0.42	0.46	0.52	0.59	0.47		0.19	0.16	0.14	0.17	0.19	0.12	0.17
	San Francisco, Davies Hall	0.05	0.13	0.35	0.46	0.50	0.60	0.44								
	average	0.06	0.17	0.48	0.57	0.62	0.66	0.55		0.16	0.14	0.15	0.15	0.16	0.15	0.15
	standard deviation	0.02	0.05	0.10	0.11	0.08	0.07	0.08		0.05	0.03	0.04	0.04	0.05	0.05	0.03
	Max	0.11	0.26	0.63	0.73	0.73	0.77	0.65		0.27	0.19	0.23	0.22	0.25	0.25	0.23
	Min	0.03	0.09	0.21	0.38	0.47	0.55	0.41		0.09	0.07	0.07	0.07	0.06	0.06	0.08
	Max-Min	0.08	0.17	0.42	0.35	0.26	0.22	0.24		0.18	0.12	0.16	0.15	0.19	0.19	0.15

[a]Corrected data for nonupholstered seat [Hidaka *et al.* (1995)].
[b]Before reconstruction.

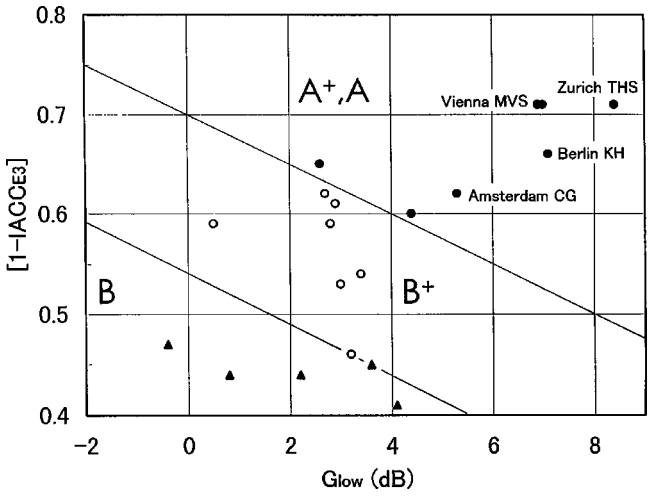

FIG. 9. Hall-averaged values of $[1-\mathrm{IACC}_{E3}]$ versus G_{low} compared to the three subjective quality ratings, (A+,A) (solid circles), B+ (open circles), and B (triangles) for which measurements of the two physical quantities and subjective ratings were available.

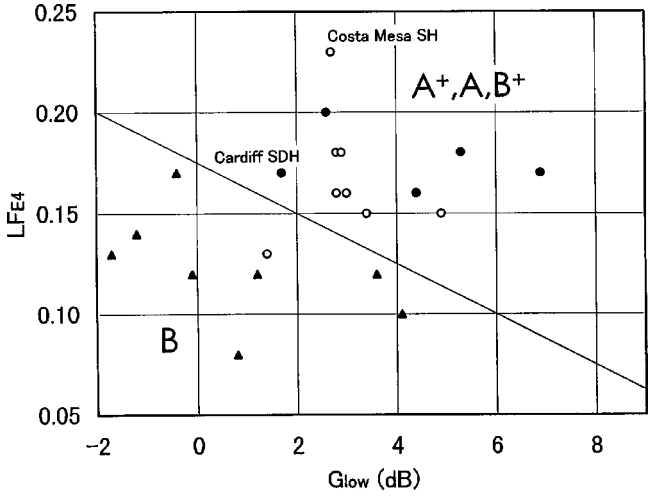

FIG. 10. Hall-averaged values of LF_{E4} versus G_{low} compared to the three subjective quality ratings, (A+,A) (solid circles), B+ (open circles), and B (triangles) for which measurements of the two physical quantities and subjective ratings were available.

ment assumes that the reverberation times, initial time-delay gaps, sound diffusion, and G_{mid}'s fall within acceptable ranges.

VII. PRINCIPAL FINDINGS

From the above experiments, the following points are emphasized:

(1) *Addition of* G_{low}: When G_{low} (or $G_{E\mathrm{low}}$) is combined with $[1-\mathrm{IACC}_{E3}]$ or with LF_{E4}, all measured in usual concert halls (Figs. 9 and 10), it is found that the G_{low} and $[1-\mathrm{IACC}_{E3}]$ combination is more accurate in rank ordering the halls according to the ratings derived from interviews of conductors and music critics than is $\mathrm{LF}_{E4}/G_{\mathrm{low}}$.

(2) *Dependence of ASW on number of early lateral reflections*: (Fig. 5) At octave-band frequencies above 500 Hz, the subjective values of ASW increase as the number of early lateral reflections increases, until the number reaches 10 or so. $[1-\mathrm{IACC}_{E3}]$ behaves the same way. Contrawise, LF_E is independent of the number of reflections in any of the octave bands. Hence, one must use $[1-\mathrm{IACC}_{E3}]$ to evaluate the effect on ASW of the number of reflections. Early reflections in a well-designed concert hall seldom come from a specific direction because at any seat there are more, and often many more, than two early reflections. With a large number, say 10 or more, early reflections in a concert hall, a fused continuous smooth image is achieved. $[1-\mathrm{IACC}_E]$ is better able to evaluate such a level of complexity than LF_E.

(3) *Dependence of ASW on angle of incidence*: (Fig. 3) At octave-band frequencies below 500 Hz, values of ASW are dependent on the angle of incidence. At 500 Hz, the ASW's for $\phi=60°$ and 90° are the same for both measures, although ASW is lower for $\theta=30°$. From Fig. 5 it is seen that with four or more reflections, subjective ASW is not significantly changed by the angles of incidence among the reflections.

(4) *Variability of physical measures among seats in halls*: From Figs. 7 and 8 it is apparent that there is a wider variation of LF_{E4} for *individual seats* in a hall (0.05–0.57) than for *hall-average values* among halls of LF_{E4} (0.1–0.4). The variations in $[1-\mathrm{IACC}_{E3}]$ among *individual seats* in a hall (0.3–0.85) are about the same as the variations in *hall-average values* among halls (0.4–0.75).

(5) *Location of microphones relative to the center-line axis for a source located on the stage of a symmetrical hall*: For the 500-Hz band, the microphone should be no less than 1 m away from the center line. For the 125-Hz band, the microphone distance should be no less than 5 m from the center line. With multiple reflections in real halls and four-band averaging, this figure for LF_{E4} can probably be halved. For all the data of Table III, the IACC_{E3}'s were measured at least 1 m, off the center line. However, because the LF_{E4}'s contain the 125-Hz band, that average is likely inaccurate for a considerable number of the customary measuring points in the audience areas of a typical hall.

(6) *Influence of angle of incidence and time delays on physical measures*: Not to its advantage, LF_{E4} is more influenced by the angle of incidence and the time delay between symmetrical reflections than is $[1-\mathrm{IACC}_{E3}]$. This difference in influence is more pronounced in the 500 Hz and lower octave bands.

VIII. CONCLUSION

$[1-\mathrm{IACC}_{E3}]$ together with G_{low}, the surrogate for $G_{E\mathrm{low}}$, were found to be the best measure of ASW. The effect of low-frequency reflections on ASW is covered by G_{low}, and the effect of high-frequency reflections on ASW is covered by $[1-\mathrm{IACC}_{E3}]$. Together they rank-order concert halls in correspondence with subjective ratings. This assumes, of course, that the reverberation times, initial time-delay gaps, diffusion and G_{mid}'s fall within acceptable ranges.

Although LF_{E4} seems to be a substitute measure for $[1-\mathrm{IACC}_{E3}]$, it appeared from earlier studies to be unable to distinguish the best halls from medium-ranked halls in regard to their subjective rankings (Hidaka *et al.*, 1995; Beranek, 1996, p. 468). The use of G_{low} and LF_{E4} together does not improve their ability to rank order the halls as shown in this paper.

The authors feel that these conclusions are well founded from this and earlier studies, but they welcome the results of further research on the strengths and weaknesses of LF's as an acoustical measure of real halls.

Ando, Y. (**1985**). *Concert Hall Acoustics* (Springer-Verlag, Berlin).

Barron, M. (**1971**). ''The subjective effect of first reflections in concert halls—The need for lateral reflections,'' J. Sound Vib. **15**, 475–494.

Barron, M., and Marshall, A. H. (**1981**). ''Spatial impression due to early lateral reflections in concert halls: The derivation of a physical measure,'' J. Sound Vib. **77**, 211–232.

Beranek, L. (**1994**). ''Comparison between subjective judgments of concert hall quality and objective measurements of acoustical attributes,'' Symposium for the 25th Anniversary of the Foundation of Acoustical Society of Spain, Madrid, Spain.

Beranek, L. (**1996**). *Concert and Opera Halls: How They Sound* (Acoustical Society of America, New York).

Blauert, J., and Lindemann, W. (**1986a**). ''Auditory spaciousness: some further psychoacoustic analysis,'' J. Acoust. Soc. Am. **80**, 533–542.

Blauert, J., Moebius, U., and Lindemann, W. (**1986b**). ''Supplementary psychoacoustical results on auditory spaciousness,'' Acustica **59**, 292–293.

Bradley, J., and Soulodre, G. (**1995a**). ''The influence of late arriving energy on spatial impression,'' J. Acoust. Soc. Am. **97**, 2263–2271.

Bradley, J., and Soulodre, G. (**1995b**). ''Objective measures of listener envelopment,'' J. Acoust. Soc. Am. **98**, 2590–2597.

Hidaka, T., Kageyama, K., and Masuda, S. (**1988**). ''Recording of anechoic orchestral music and measurement of its physical characteristics based on the auto-correlation function,'' Acustica **67**, 68–70.

Hidaka, T., Beranek, L., and Okano, T. (**1995**). ''Interaural cross-correlation, lateral fraction, and low- and high-frequency sound levels as measures of acoustical quality in concert halls,'' J. Acoust. Soc. Am. **98**, 988–1007.

Keet, W. (**1968**). ''The influence of early lateral reflections on the spatial impression,'' in Proceedings of the 6th ICA, Tokyo, Japan, E53–E56.

Kuhl, W. (**1978**). ''Räumlichkeit als Komponente des Raumeindrucks,'' Acustica **40**, 167–181.

Morimoto, M., and Maekawa, Z. (**1988**). ''Effects of low frequency components on auditory spaciousness,'' Acustica **66**, 190–196.

Morimoto, M., and Maekawa, Z. (**1989**). ''Auditory spaciousness and envelopment,'' Proceedings of the 13th ICA, Belgrade, Yugoslavia, pp. 215–218.

Okano, T., Hidaka, T., and Beranek, L. (**1994**). ''Relations between the apparent source width (ASW) of the sound field in a concert hall and its sound pressure level at low frequencies (GL), and its inter-aural cross correlation coefficient (IACC),'' J. Acoust. Soc. Am. **96**, 3268.

Potter, J., Bilsen, F., and Raatgever, J. (**1995a**). ''Frequency dependence of spaciousness,'' Acta Acust. (China) **3**, 417–427.

Potter, J., Raatgever, F., and Bilsen, J. (**1995b**). ''Measures for spaciousness in room acoustics based on a binaural strategy,'' Acta Acust. (China) **3**, 429–443.

Effect of electrical outlet boxes on sound insulation of a cavity wall

T. R. T. Nightingale and J. D. Quirt
Acoustics Laboratory, Institute for Research in Construction, National Research Council Canada, Ottawa, Ontario K1A 0R6, Canada

(Received 2 January 1998; revised 26 February 1998; accepted 6 April 1998)

The results of a systematic study investigating the effect on the sound insulation of wood stud walls having penetrations made by electrical outlet boxes are presented. The effect on sound insulation is shown to be almost negligible, regardless of box separation, if the boxes are themselves airtight and form an airtight seal with the gypsum board surfaces. However, if the boxes are not airtight, then the degradation to the sound insulation is strongly dependent on the separation between the boxes. Other significant factors include the presence of cavity absorption, and its method of installation. A series of retrofits for poorly installed boxes is examined and show that commonly available devices for reducing airflow (and sound insulation) through electrical boxes can be very effective but are highly dependent on installation. [S0001-4966(98)03607-8]

PACS numbers: 43.55.Rg [DWM]

INTRODUCTION

Many authors have studied the effect of penetrations in walls in the form of slits or cylinders both experimentally and analytically. In previous studies of penetrations through walls, two simplifications were common:

(a) The penetration can be treated as a cylinder[1,2] or slit[3,4] (in the case of the slit a further restriction is usually added requiring the length to be much greater than the width);

(b) The wall is monolithic such that the slit or cylinder is continuous and vented only to the source and receive side of the wall. Mechel[5,6] provided a theoretical description which included addition of a fibrous absorbing material of variable airflow resistance in the penetration. But again, the penetration did not vent into a cavity. Most of the work on slits originated from investigations of door and window seals.

These previous studies have indicated that penetrations through walls in the form of slits or cylinders can be very detrimental to the sound insulation especially for frequencies above the quarter wavelength frequency corresponding to the depth of the slit or cylinder. This may have helped the growth of the generally accepted feeling that the presence of closely spaced electrical outlet boxes in a party walls can degrade the sound insulation.

In a limited set of double leaf walls containing cavity absorption, Royle[7] investigated the effect of slits around a wall's perimeter, as well as penetrations by a cylinder and by back-to-back electrical boxes. It was shown experimentally that the type of wall penetration or ''leak'' affects the sound insulation in different ways, indicating that work for slits and cylinders might not be applicable to outlet boxes. Royle concluded from the work done with walls containing cavity absorption that penetrations by back-to-back electrical boxes did not present a serious problem if the wall cavity contained glass fiber insulation, 80 mm thick.

In this paper, which presents a systematic study of the factors affecting the sound insulation of gypsum board cavity walls having penetrations in the form of electrical boxes (see Figs. 1 and 2), it is shown that the offset distance between penetrations is only one factor and is often of secondary importance. Royle's conclusion regarding offset distance is shown to be correct for a subset of the cases considered in his study, but in general the conclusion is not valid.

I. TEST SPECIMENS

The study examined the reduction in sound insulation caused by installing electrical outlet boxes in two types of load-bearing wood framed party walls that nominally (i.e., without penetrations) provide a sound insulation greater than STC 50. The wall details, the box locations, and the nomenclature to identify box locations are given in Figs. 1 and 2 for the double- and single-stud framing types considered, respectively.

All the walls had gypsum board surfaces and 38×89 mm wood studs separated 400 mm o.c. The wall specimens were 3.05 m wide and 2.44 m high and were installed in the specimen frame between the reverberation chambers of the Institute for Research in Construction (IRC) at the National Research Council of Canada (NRCC). The electrical boxes were positioned with the bottom of each box approximately 300 mm from the bottom of the wall. All wiring needed to simulate normal field installation was installed.

These specimens allowed for a systematic investigation of the following factors:

- Box type (standard metal box or plastic box with a built-in air barrier, see Fig. 3);
- Box placement (back-to-back, same cavity or adjacent stud cavity; Figs. 1 and 2) for the two wall constructions;
- Box treatment including gaskets to seal the opening and inserts or other materials for lining the boxes;
- Baffles in the wall cavity to block line-of-sight between boxes;

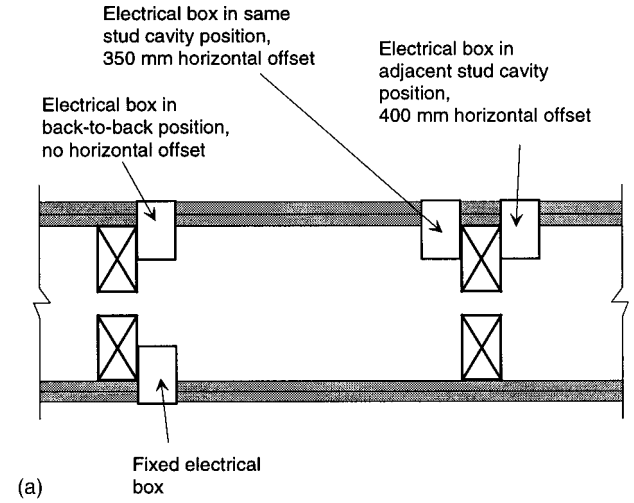

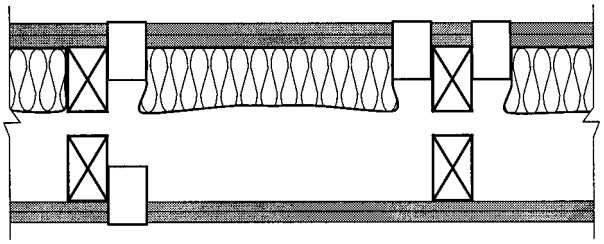

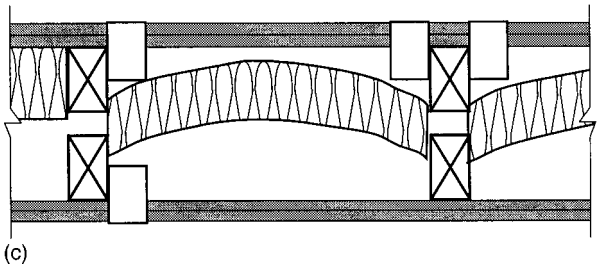

FIG. 1. Positions of the electrical boxes in the double-stud wall. The double wood stud wall was constructed in the following manner: two layers 12.7-mm regular gypsum board, 38×89 mm wood studs 400 mm o.c., 25-mm air space, 38×89 mm wood studs, 400 mm o.c., two layers 12.7-mm regular gypsum board. (a) No cavity absorption. (b) Cavity absorption 90 mm thick displaced around boxes allowing an unimpeded path between boxes in the back-to-back configuration. (c) Cavity absorption 90 mm thick covering backs of the boxes. In all three cases there was no connection or contact between sets of framing.

- Possible structural vibration transmission through the electrical boxes when the gypsum board is mounted on resilient channels;
- Frequency dependence of the sound insulation degradation due to boxes of various dimensions.

II. TEST METHOD AND PROCEDURE

The tests to assess the sound insulation of each assembly were conducted in accordance with the requirements of ASTM E90-1990,[8] Standard Method for Laboratory Measurement of Airborne Sound Transmission Loss of Building

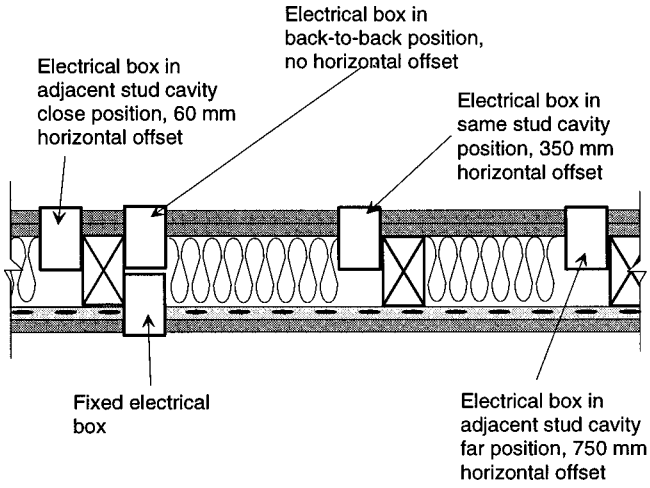

FIG. 2. Positions of electrical boxes in the single-stud wall. The single-stud wall was constructed as follows: two layers 15.9-mm type-X gypsum board, 38×89 mm wood studs, 400 mm o.c., 90-mm glass fiber batts displaced around electrical boxes, 13-mm resilient metal channel spaced 600 mm o.c., single layer 15.9 mm type-X gypsum board.

Partitions. The Sound Transmission Class (STC) was determined in accordance with ASTM Standard Classification E413-1990.[9]

The test procedure was designed to optimize the accurate comparison between the different electrical outlet positions for the same wall specimen. For the two types of framing considered, a base wall specimen was constructed with no penetrations and the sound insulation was measured. The gypsum board was removed and saved for later reinstallation.

The four or five electrical outlet boxes, complete with duplex outlets, face plates, and associated wiring were installed in accordance with the Canadian Electrical Code[10] (which is essentially equivalent to the National Electrical Code[11] used in the USA). Holes were cut in the gypsum board to accommodate the boxes and the gypsum board was reinstalled. The openings in the gypsum board for each outlet were masked with covers made from a double layer of 12.7-mm-thick gypsum board that overlapped about 25 mm beyond the edges of the opening. A 3-mm neoprene gasket formed an airtight seal between the masks and the gypsum board. The masks were held in place by screws into the threaded tabs of the electrical box. With the masks installed, the wall was retested.

In all cases considered in this study, the difference between the result with all the outlets masked and the original result (with no penetrations) was less than the known reproducibility uncertainty associated with removing and replacing a layer or layers of gypsum board in the IRC laboratory, r_{95} 2 dB or 2 STC points for lightweight walls. (This value not only contained any effect due to fabrication anomalies but also uncertainties associated with the test method which are laboratory dependent.) This small uncertainty justified using the case with no penetrations as the reference case relative to which the results with various outlet configurations were assessed.

Duplex electrical outlet fittings and cover plates were then installed and tested for each outlet configuration in turn,

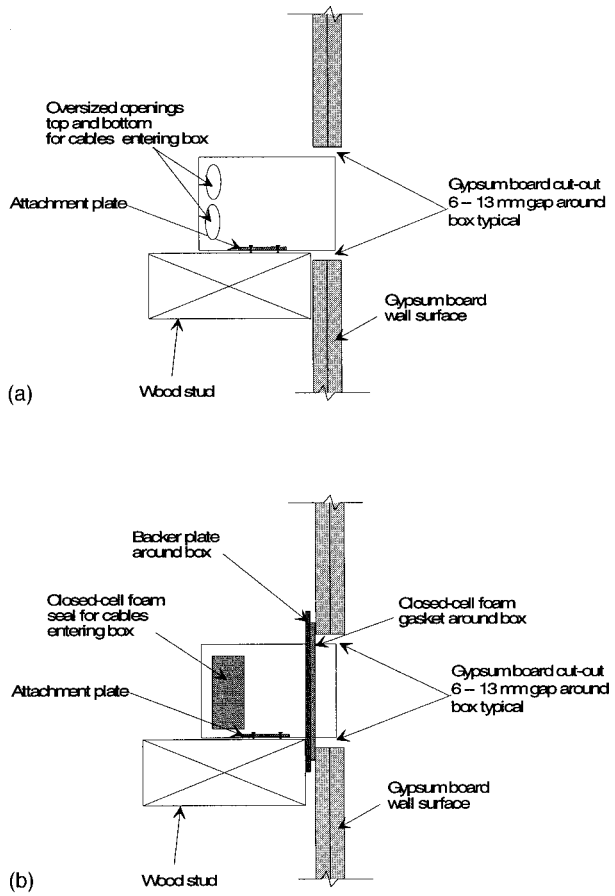

FIG. 3. Plan view sketches showing typical installation details for a metal electrical box (a) and a plastic vapor barrier box (b). (Note that in both sketches the electrical fittings and face plates are not shown.) The metal box had in addition to the unsealed cable openings, two on the top and bottom, several 3-mm-diam penetrations on the rear of the box that are used for surface mount applications. The plastic vapor barrier box had no unsealed penetrations. The box height and width are the dimensions in the plane of the box mouth, while the box depth refers to the dimension in the direction normal to box mouth.

with the other outlet positions masked. This masking technique allows the examination of many different box locations without reconstructing the wall specimen, thus enabling accurate measurement of changes in sound insulation resulting from small changes to the location and/or treatment(s) of the electrical outlet.

III. FACTORS AFFECTING SOUND INSULATION

The key factors affecting the sound insulation of wood stud walls with electrical outlets were systematically investigated. Unless otherwise noted the electrical boxes under test were fitted with duplex electrical outlet fittings and face plates.

A. Effect of box type

Two types of boxes were investigated: standard metal boxes, and plastic vapor barrier boxes. Typical installation details are shown in Fig. 3. Standard metal boxes (nominal dimensions: height, 75 mm; width, 47 mm; depth, 63 mm) were used in all specimens, unless specifically noted. (Later the frequency dependence of the degradation will be related to the dimensions of the box.) The metal boxes had oversized

TABLE I. Measured sound insulation expressed in STC, for untreated metal boxes and plastic vapor barrier boxes with built-in air barrier, when installed in the double wood stud wall without cavity absorption [Fig. 1(a)]. Reference case data, without penetrations, are included for comparison.

Comparison of box type		Electrical box location	
Box type	Reference case	Back-to-back no offset	Adjacent cavity 400-mm offset
Metal (untreated)	55	51	53
Plastic vapor barrier (untreated)	55	55	55

cable penetrations and mounting holes on the back side of the box which permitted free movement of air in and out of the box. These penetrations represent about 370 mm^2 or about an 11% open area when normalized to the area of the face of the box in the plane of the wall.

Plastic vapor barrier (PVB) boxes are designed to be placed in walls where maintaining the integrity of the air/vapor barrier is important (e.g., exterior walls). The boxes tested had total dimensions of 140 mm height, 105 mm width, 75 mm depth. Like the metal boxes, they were mounted to the studs using nails and were able to accept four NMD-type cables. In the case of the PVB boxes, a closed-cell foam membrane provided an airtight seal around cable(s) inserted into the box.

The greatest difference in overall airtightness arises from the method of sealing the box to the gypsum board wall surface. In the case of the metal boxes, the nominal 6–12 mm gap between the gypsum board cutout and the box remains unsealed; this represents an open area of 1000–2200 mm^2. The PVB boxes utilize a backer plate that is 25 mm larger than the outside box dimensions, with closed-cell foam to form an airtight seal with the gypsum board. If the cutout in the gypsum board is sized properly, then the opening will be completely covered when the face-

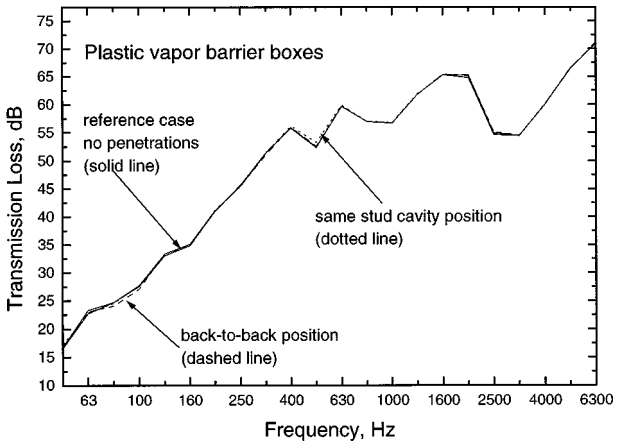

FIG. 4. Measured sound insulation for a double wood stud wall without cavity absorption [Fig. 1(a)], with plastic electrical boxes installed for the following conditions: no wall penetrations (reference case), boxes in the back-to-back, and same stud cavity positions. The performance with the plastic boxes is almost indistinguishable from that of the reference case without penetrations. All achieved STC 55.

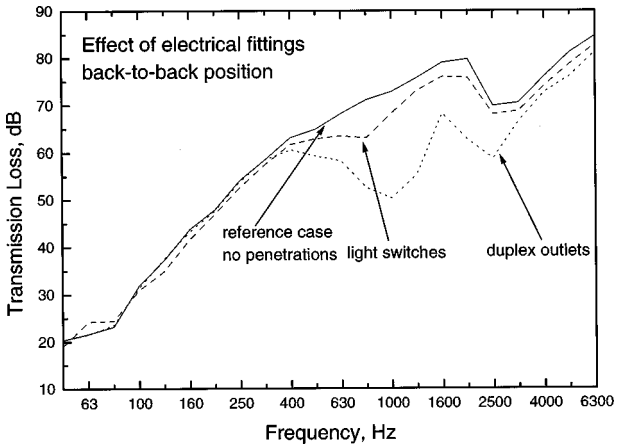

FIG. 5. Measured transmission of a double wood stud wall with cavity absorption displaced around the back-to-back metal boxes [Fig. 1(b)] with two types of electrical fittings; standard duplex electrical outlet (STC 55), and a standard single light switch (STC 59). The reference case with no penetrations is shown for comparison (STC 61).

plate is installed. However, this may not always be the case and will be shown later to cause some variability in the effectiveness of retrofit techniques for poorly placed boxes.

The sound insulation for standard metal boxes without any treatment was compared to that with the PVB boxes, when installed in the double wood stud wall without cavity absorption (a sensitive case). The results are shown in Table I. The plastic boxes provided consistently better sound insulation than the untreated metal boxes, especially in the back-to-back configuration. The transmission loss data shown in Fig. 4 indicate that the sound insulation of a party wall with plastic boxes installed in any position, even back-to-back, was nearly identical to that without any penetrations.

The correlation between airtightness and sound insulation has been employed by several authors[12,13] as a method of estimating the degree of airtightness of the separating building element(s).

To establish the effect of different types of electrical fittings, single toggle light switch fittings were installed in the same metal boxes of the double wood stud wall. Figure 5 shows that the transmission loss of the wall assembly for the two types of fittings is similar in the ranges 50–500 Hz and 3.15–6.3 kHz. However, there is a marked difference in the range 800–1250 Hz; the wall containing the light switches offers up to 15 dB better performance. This may be attributed to the fact that the light switch assembly does not have penetrations, quite unlike the duplex outlet which has six holes to accept the prongs of two electrical plugs.

Thus if electrical boxes can be made relatively airtight, there is negligible effect. This should not be surprising, as Mechel[5] has previously shown numerically that even a very lightweight impervious material at either end of a penetration can improve the sound reduction significantly. However, when the installed boxes are not airtight and allow the unimpeded passage of air (i.e., the metal boxes with the duplex outlets) the effect on the sound insulation can be significant.

B. Box placement and cavity absorption

The degradation of sound insulation that was observed when electrical boxes were placed in the back-to-back configuration in a double wood stud wall is shown in Fig. 5. The effect is strongest in the frequency range around 1 kHz, where an 18-dB degradation was observed. This is much greater than the six point reduction in STC would suggest. The change in the sound insulation in the 1–2 kHz frequency range will be shown to be a function of the box dimension and is discussed later.

Table II shows the change in sound insulation relative to the reference case, without penetrations, for various locations of the untreated metal boxes. From the table it can be seen that the effect of electrical boxes on the sound insulation of a wall can be large and the reduction in the sound insulation depends on several factors: the separation (horizontal offset) of the electrical boxes, the construction of the wall, and the location of wall cavity absorption. Within the scope of this study, these cannot be fully separated, but general trends can be identified.

The greatest reduction of the STC occurred when there was a short unimpeded path between boxes—that is, the sound did not have to travel through the cavity absorption (or in the case of the double wood stud wall through the 25-mm gap between studs into the next cavity). This is shown by the reduced sound insulation for walls with boxes in the back-to-back and same cavity positions without cavity absorption, and the back-to-back position with the batts displaced around

TABLE II. Wall sound insulation expressed in STC for walls with untreated metal boxes at various locations. The sound insulation of the reference case wall without penetrations is given for comparison.

Untreated metal boxes			Electrical box location		
Wood stud framing	Cavity absorption	Reference case	Back-to-back no offset	Same cavity offset 350 mm	Adjacent cavity offset >400 mm
Double stud	None	55	51	49	53
	90 mm displaced	61	55	60	61
	90 mm	62	61	61	61
Single stud	90 mm displaced	55	50	54	54

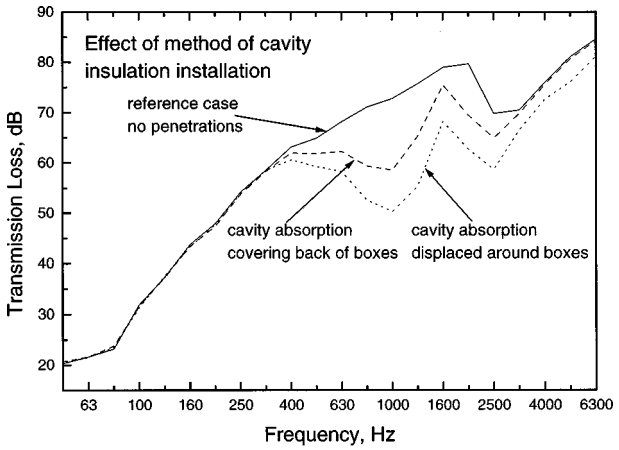

FIG. 6. Comparison of the sound transmission loss of a double-stud wall with and without the cavity absorption displaced around the boxes (STC 55 and 61, respectively). The reference case wall without any penetrations is given for comparison (STC 61). The electrical boxes are in the back-to-back configuration [Fig. 1(b)].

the boxes as shown in Fig. 1(b). Conversely, when the sound energy must travel through, or at grazing incidence to, the cavity absorption (i.e., all other absorption cases), the effect is greatly reduced.

Table II and Fig. 6 show the change in sound insulation for the double stud wall with cavity absorption installed in two ways: displaced around the side of the box or placed completely over the back of the box. The table shows that having the layer of cavity absorption between back-to-back electrical boxes greatly minimizes the reduction in the STC rating. This is not surprising since for each 90 mm thickness of glass fiber building insulation that the sound energy passes through the sound energy may be attenuated by as much as 10 dB at 1000 Hz.

It is evident from Table II that when the boxes are offset by 350 mm or more there is very little degradation when compared to the wall without penetrations except when no cavity insulation is present. For the single-stud wall, this may be explained by the fact that the sound energy propagating between the boxes will be highly attenuated in the fibrous medium. Unlike the single-stud wall, the double-stud constructions of Fig. 1(a) and (b) have a nominal 25-mm cavity between the frame and the layers of insulation that might allow a relatively short and unimpeded path. Yet there is also very little degradation when the boxes are separated by 350 mm or more. This may be explained by the work of Mechel[6] where it was shown in a series of numerical simulations that the amount of energy transmitted through a narrow cavity or slit could be significantly reduced if the cavity walls were lined with a fibrous porous absorber. Similar grazing incidence propagation over an absorbing surface occurs in transmission between the offset boxes of the double-stud walls having cavity absorption in Table II.

For walls having cavity absorption the effect of boxes separated by 350 mm or more is very small, typically one STC point. However, results from the double-stud wall with no cavity absorption indicate that introducing a 350-mm separation between the boxes by moving them from the back-to-back position reduces the sound insulation. This may be attributed to directional radiation from the boxes or standing waves in the cavity. To determine the cause an examination of the sound pressure field in the cavity would be required which was beyond the scope of this study. Moving the box an additional 40 mm from the same stud cavity position so that it is in the adjacent cavity position caused the line-of-sight to be broken by a stud which resulted in a 4 STC improvement.

Cavity absorption reduces the effect that poorly placed electrical boxes have on the sound insulation of a party wall. The batt insulation should not be displaced around the electrical boxes as shown in Fig. 1(b) as this will reduce the effectiveness of cavity absorption. The combination of absorptive material and a horizontal offset greater than the stud separation ensure transmission through the electrical boxes does not significantly reduce the sound insulation of the wall assembly.

C. Retrofit box treatments

The section that considered box type has shown that as the airtightness of the box is increased, so too is the sound insulation of the wall assembly increased. With this in mind several metal box retrofit techniques were investigated that would improve the airtightness of the wall assembly when the boxes were poorly located. The methods investigated are described and measured sound insulation improvements given.

Draft stopper: This is a gasket of closed-cell foam that is placed between the gypsum board of the wall and the face plate of the electrical outlet and has cutouts designed to form a tight fit with the electrical fitting (duplex outlet or light switch).

Electrical box inserts: Also designed to reduce airflow through the electrical box, inserts are placed inside the box. These are made from a rubber or plastic material. A hole or slit must be cut in the insert to allow the wires to pass through to the electrical fitting. (The penetration to the insert was sealed with a latex caulk.) The insert tested had a flange designed to provide a seal with the gypsum board.

Caulking: Filling the gap between the electrical box and the cutout in the gypsum board with a bead of caulk may help to increase the airflow resistance and hence increase the sound insulation of the wall. However, this method still allows air to flow through the electrical fitting (outlet or switch) into the electrical box then into the cavity via the penetrations in the box.

Mass-loaded materials: Lining the interior of an electrical box with a pliable material impervious to air will help to increase the airflow resistance and hence the acoustic performance. The gap between the box and the gypsum board was also filled. In this series, a mastic-type material designed to fill cracks was used.

Table III shows the change in sound insulation of the wall with various box treatments which are listed in order of their effectiveness. The increase in sound insulation due to a treatment is somewhat variable. This may be partly attributed to the fact that the effectiveness of treatments is largely determined by the ability of the treatment to form an airtight

TABLE III. Wall sound insulation expressed in STC for the same wall subject to the various treatments. The sound insulation of the reference case wall without penetrations is given for comparison.

Treatments	Double stud back-to-back (no absorption)	Single stud back-to-back
None	51	50
Gap caulked	52	···
Draftstopper under face plate	52	54
Gap caulked and insert in box	54	53
Mass-loaded material	···	55
No penetrations	55	55

seal with the gypsum board. Poorly cut holes and poorly installed boxes will reduce the ability of the treatment to be airtight and hence limit the sound insulation improvement. The best and most consistent improvement was obtained for retrofit treatments that both provided a seal between the box and the gypsum board and also blocked the passage of air through the penetrations at the back of the box.

D. Baffles and fire resistance

Electrical outlets are also of potential concern where fire resistance is required. Unfortunately, no data were found on the effect of such penetrations on fire resistance of full-scale wall assemblies.

Two small-scale tests were performed in the NRCC Fire Laboratory, to examine the effect of electrical boxes in a gypsum board wall assembly. Each specimen was a 0.91 m×0.91 m wall section with 12.7-mm type X gypsum board directly applied to both faces of 38 mm×89 mm wood studs and no insulation in the interstud cavities. The studs were spaced approximately 400 mm o.c., dividing the specimen into two cavities. The first specimen, a reference assembly, had no penetrations. The other specimen had a single metal box installed in the first stud cavity and a single PVB box installed in the other. Both boxes were installed on the side of the wall exposed to the flames. The times for failure were: 142 min for the reference assembly, 121 min for the single metal box, and 130 min for the PVB box. These results cannot be applied directly to full-scale assemblies or to cases where boxes are more widely separated but suggest that the presence of electrical outlets may be a serious concern for fire resistance of party walls.

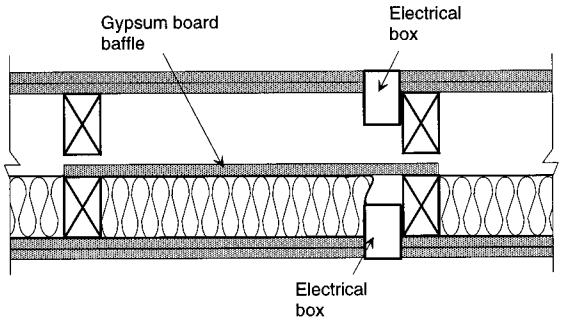

FIG. 7. Sketch of a baffle for a double-stud wall (note that the structural isolation between the two faces is preserved).

Some better building practice guides suggest the use of baffles in walls having electrical boxes. Figure 7 shows a sketch of a baffle that might be used in a double-stud wall. The baffle constructed from 13-mm gypsum board extended from the sole plate to a height 300 mm above the top of the electrical boxes. Table IV shows the measured effect of adding this baffle, for two box locations.

The effectiveness of a partial-height baffle depends on the presence of cavity absorption. This is to be expected since the absorption controls the reverberant field in the cavity and a baffle will only be effective if the reverberant energy is much less than that traveling directly between the two boxes. Consequently, reducing the direct component with the use of a baffle will only provide marginal improvement without cavity absorption as shown in Fig. 8.

However, when there is significant cavity absorption the amount of reverberant energy is very low and reducing the direct energy with the use of a baffle will be most effective. This is demonstrated in Fig. 9.

Baffles that are designed correctly (so that structural isolation between the two faces of the wall is maintained) can improve the acoustical performance, and may improve the fire-resistance performance, especially if there is cavity absorption.

E. Resilient channels

A specimen with a single row of wood studs was used to establish whether the effectiveness of resilient channels

TABLE IV. Comparison of the effectiveness of a gypsum board baffle in a double-stud wall with and without absorption to reduce the effect of poorly located electrical boxes. The sound insulation is expressed in terms of the STC.

Metal electrical boxes		Electrical box location			
		Back-to-back (no offset)		Same stud cavity (350-mm offset)	
Cavity absorption	Reference case	No treatment	Baffle	No treatment	Baffle
None	55	51	52	49	52
90-mm displaced	61	55	62	60	61

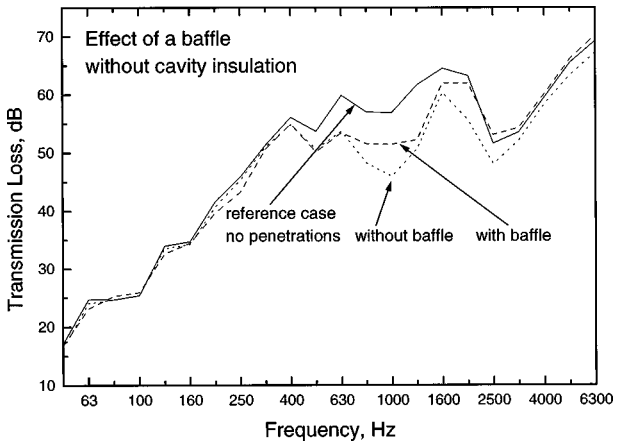

FIG. 8. Effect of a baffle separating back-to-back electrical boxes in a double wood stud wall that does not have cavity absorption [Fig. 1(a)]. The data show that there was only a marginal improvement as a result of adding the baffle (STC 51 to STC 52). The reference case without any penetrations (STC 55) is given for comparison.

would be limited by electrical boxes, which might provide an effective alternate path for vibration energy to travel from the gypsum board surfaces to wood stud framing.

Figure 10 shows the measured sound insulation (with and without electrical boxes) of a wall with one gypsum board surface mounted on resilient channels (as shown in Fig 2). The duplex electrical outlet fitting and the face plate were screwed firmly against the gypsum board.

The figure shows that placement of the electrical boxes in a wall having resilient channels did not affect the wall's sound insulation significantly.

F. Transmission through open penetrations to a cavity wall

Figure 11 shows that there is very little effect on the sound insulation for frequencies below 315 Hz as a result of having back-to-back 47×75 mm holes in the double wood stud wall of Fig. 1(b). The cavity absorption was displaced so that there was an unimpeded passage across the wall cavity from one hole to the other. For frequencies above 315 Hz (frequency at which the wall depth 257 mm represents a quarter wavelength) the degradation due to the hole is pronounced. The onset of the degradation at the quarter wavelength frequency has been observed for slits in monolithic walls, i.e., walls without cavities.[3] Typically, for slits and cylinders in monolithic walls the sound reduction begins to drop for frequencies greater than the quarter wavelength frequency and has a local minimum at the half-wavelength frequency. This is not exhibited by the double leaf wall of this study. Presumably, the monotonic reduction in the sound insulation with increasing frequency above the quarter wavelength frequency is due to the fact that the wall cavity is not a one-dimensional system and will allow propagation in all three orthogonal directions many of which will satisfy the boundary conditions necessary for strong transmission, which differs from the problem of the hard-walled cylinder or slit.

Also shown in Fig. 11 is a simple prediction of the total sound insulation based on the commonly used worst-case assumption that the transmission coefficient through an open penetration is unity and is independent of frequency. Using

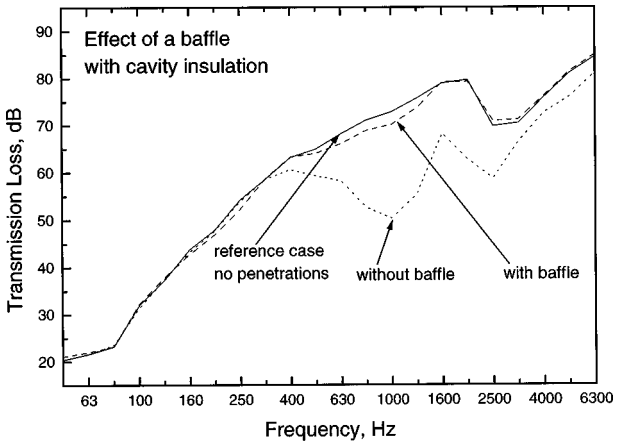

FIG. 9. Effect of a baffle separating back-to-back electrical boxes in a double wood stud wall that has 90-mm glass fiber cavity absorption (Fig. 7). The data show that there is a significant improvement as a result of adding the baffle (STC 55 to STC 62) when there is cavity absorption. The reference case without any penetrations (STC 61) is given for comparison.

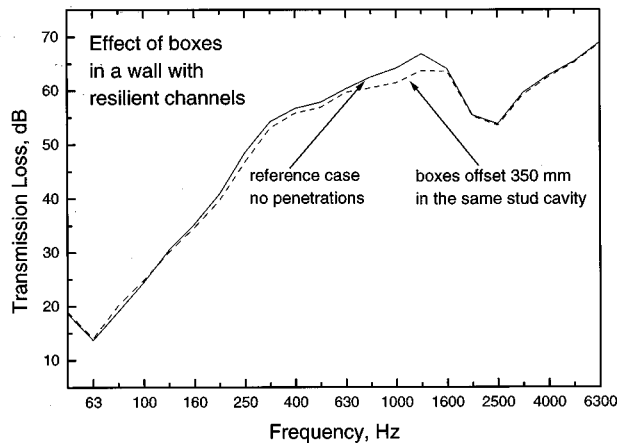

FIG. 10. Comparison of the sound insulation for a single-stud wall having resilient channels with (STC 54) and without (STC 55) electrical boxes installed in the same cavity position (a 350-mm offset as shown in Fig. 2).

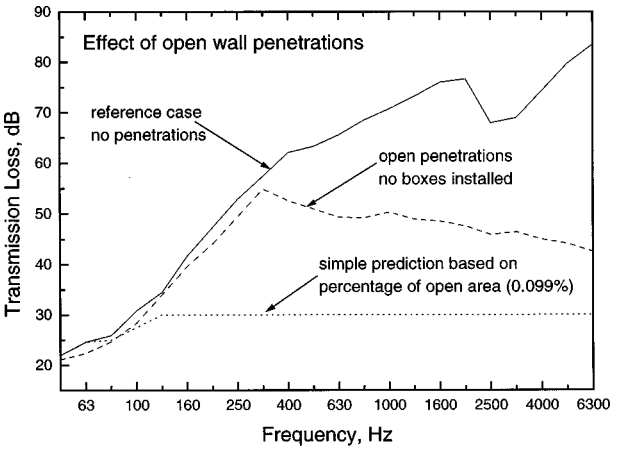

FIG. 11. Measured transmission loss for a double wood stud wall [Fig. 1(b)] with back-to-back open penetrations representing 0.099% open area. Cavity absorption was displaced so that there was an unobstructed path from one opening to the other.

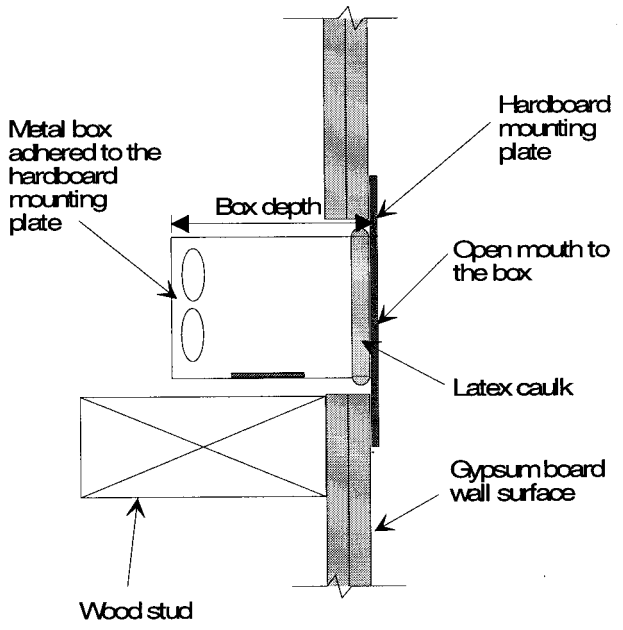

FIG. 12. Plan view sketch showing the method of mounting the electrical box to a hardboard plate. This was done to allow the boxes of various depths to be removed and replaced without removing the gypsum board of the wall. The mounting was used when investigating effect of sealing the holes in the back of the box. The hardboard mounting plate was sealed to the gypsum board with aluminum tape. As shown in the figure the depth of the box is measured in the direction normal to the plane containing the mouth of the box.

this simple assumption the 0.099% open area would reduce the sound insulation of the wall assembly to about 30 dB across the frequency range 125–6300 Hz. The figure indicates that this assumption is far too conservative for estimates of room-to-room sound transmission through open penetrations in a thick double leaf wall.

G. Transmission characteristics of an electrical box

In this section electrical box insertion loss values are presented (relative to the case with empty holes in the wall) to evaluate the effect of systematic changes to box dimension and hole treatment. The method of mounting the electrical boxes was changed to allow boxes of varying depth and interior treatment to be examined without removing the gypsum board of the wall. This was done by placing each electrical box in a thin hardboard mounting plate. As shown in Fig. 12, the mounting assembly formed an airtight seal to both the mouth of the box and the gypsum board of the wall.

From Fig. 13, which shows the measured insertion loss for a series of different box conditions, it can be seen that the 63-mm-deep box offers virtually no insertion loss in the 1250-Hz third-octave band when penetrations to the box for electrical cables and mounting fasteners were open [see Fig. 3(a)] However, when an aluminum tape covers the penetrations, the insertion loss minimum at 1250 Hz becomes an insertion loss maximum. If it is assumed that the system can be considered one dimensional and that only one set of boundary conditions are changing as a result of taping the holes, then by inspection it can be seen that the quarter

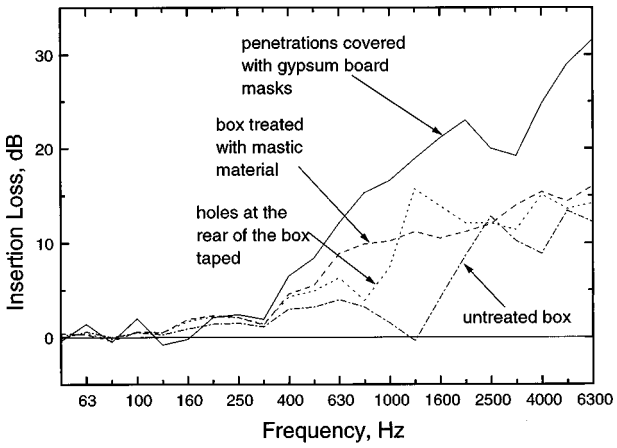

FIG. 13. Measured insertion loss of a single electrical outlet box when placed in a double-stud wall assembly having open back-to-back penetrations. The electrical box was 63 mm deep without faceplate and electrical fitting and the cavity absorption was displaced around the box and open penetration(s). The data indicate that the insertion loss of an electrical box is highly dependent on the presence of penetrations on the backside of the box.

wavelength frequency of the system is about 1250 Hz. This corresponds to an actual length of about 69 mm which is very close to the box depth of 61 mm. With the holes sealed and the box volume open, the insertion loss value at 1250 Hz is greater than if the box and gaps to the gypsum board had been completely filled with a mastic-like material. Again, this behavior strongly suggests the presence of a coupled resonant system with the holes at the back of the box coupling the wall cavity and the electrical box.

Electrical boxes designed to accommodate only a single fitting tend to have a standard opening dimension (47 mm width, 75 mm height) while the depth of the box can vary from 51 mm to 78 mm depending on the intended application. To show the effect of box depth on the frequency at which local minima in the sound insulation would occur, boxes of three different depths were examined; 51, 62, and 78 mm. Figure 14 shows that for all three cases the local minimum transmission loss occurred at different frequencies with the deepest box having the lowest frequency for this

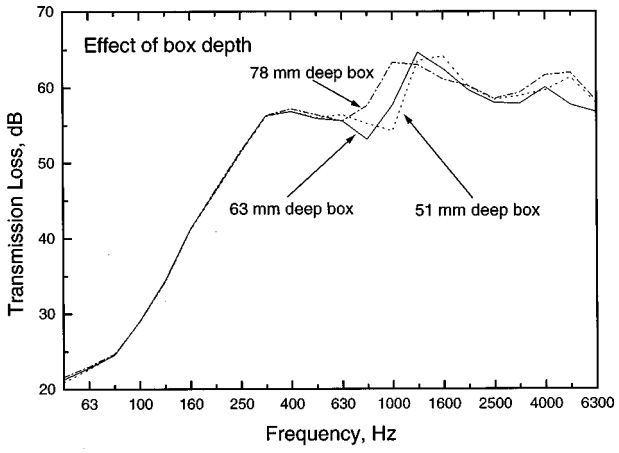

FIG. 14. Measured transmission loss for the double wood stud wall assembly with back-to-back penetrations and a series of different box depths; 51, 63, and 78 mm. Cavity absorption was displaced around the box, and a box was installed on one side only, with no face plate.

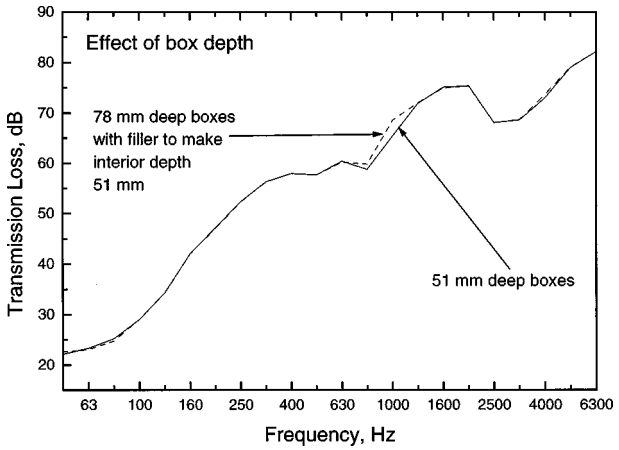

FIG. 15. Measured transmission loss for the double wood stud wall assembly with back-to-back boxes of similar interior dimension, but different exterior dimension. A filler was placed in a box of 78 mm depth to create an interior depth of 51 mm. The wall had cavity absorption displaced around the box.

minimum, further supporting that the depth of the box is a factor in the transmission characteristic.

Figure 15 shows that a 78-mm-deep box can be made to perform almost identically to a 51-mm box (with the holes at the back of the box filled) if a hardboard filler is glued in the larger box so that the nominal interior depth as measured from the mouth is identical. This illustrates the fact that it is the interior depth, or the volume, of the box that is important and not the exterior dimensions.

It should be noted that due to the strong dependence on the depth of box and nature of box penetrations, the data presented in this paper may not be applicable to all types of electrical boxes which also includes boxes used for data and telecommunication receptacles.

IV. CONCLUSIONS

Penetrations to a cavity wall, in the form of electrical boxes, can severely reduce the sound insulation. The magnitude and frequency dependence of the degradation is a complex function involving, the wall thickness, the presence of cavity absorption and method of its installation, the box location and airtightness, as well as the type of electrical fitting installed in the boxes.

To minimize the degradation, locate the boxes as far apart as possible and use cavity absorption that is placed so that the backs of the boxes are covered.

It was shown that if the boxes are airtight (i.e., plastic vapor barrier type) then the STC rating of a wall is not affected as a result of poor box location. Similarly, if existing poorly placed boxes can be made airtight through retrofits then the sound insulation of the wall assembly can be greatly improved. Sealing the inside of the box with a mastic-type material and caulking the gap between the box and the gypsum board cutout proved to be the most effective. Baffles placed in the cavity were shown to be effective only if cavity absorption was present.

Penetrations to the double-stud assemblies considered in this study had virtually no effect for frequencies below 315 Hz, (the quarter wavelength frequency for the thickness of the wall). This result was consistent with previous studies of penetrations to monolithic walls. Above the quarter wavelength frequency the wall with open penetrations and no boxes exhibited a monotonic reduction in sound insulation with increasing frequency. This differed from previous studies of penetrations to monolithic walls. An examination of the insertion loss associated with placing a single box on one side of the wall indicated that resonance effects associated with the interior dimension of the box play a significant role in determining the magnitude of the degradation. Sealing the holes in the back of the box as found to change the frequency at which the electrical box offers minimum insertion loss.

[1] M. C. Gomperts and T. Kihlman, ''The sound transmission loss of circular and slit-shaped apertures in walls,'' Acustica **18**, 144–150 (1964).
[2] M. C. Gomperts, ''The influence of viscosity on sound transmission through small circular apertures in walls of finite thickness,'' Acustica **15**, 191–198 (1965).
[3] Ljudtransmission genom sprigor, Tor Kihlman, Byggforskiningen Repport 93, 1963.
[4] D. J. Oldham and X. Zhao, ''Measurement of the sound transmission loss of circular and slit-shaped apertures in rigid walls of finite thickness by intensimetry,'' J. Sound Vib. **161**, 119–135 (1993).
[5] F. P. von Mechel, ''Schalldurchgang durch Löcher un Schlitze mit Absorberfülling und Versiegelung,'' Acustica **61**, 87–104 (1986).
[6] F. P. von Mechel, ''Die Schalldämmung von Schalldämpfer-Fugen,'' Acustica **62**, 177–193 (1987).
[7] P. Royle, ''The effect of leakage on the sound insulation of plasterboard constructions,'' Proceedings of the Institute of Acoustics **84**, 184–188 (1986).
[8] ASTM E90, Standard Test Method for Laboratory Measurement of Airborne Sound Transmission of Building Partitions.
[9] ASTM E413, Classification for Rating Sound Insulation.
[10] Canadian Electrical Code.
[11] National Fire Protection Agency, National Electrical Code, Section 70, Article 370, 1996 Edition.
[12] M. Ringger and P. Hartmann, ''Evaluation of an acoustical method for detecting air leaks,'' Air Infiltration Review **11**, 6–9 (1989).
[13] T. Sonoda and F. Peterson, ''A sonic method for building air-leakage measurements,'' Appl. Energy **22**, 205–224 (1986).

Broadband model-based processing for shallow ocean environments

J. V. Candy
University of California, Lawrence Livermore National Laboratory, P.O. Box 808, L-156, Livermore, California 94550

E. J. Sullivan
Naval Undersea Warfare Center, NUWC Code 82101, Bldg. 679, Newport, Rhode Island 02841

(Received 16 December 1996; accepted for publication 6 April 1998)

Most acoustic sources found in the ocean environment are spatially complex and broadband. In the case of shallow water propagation, these source characteristics complicate the analysis of received acoustic data considerably. A common approach to the broadband problem is to decompose the received signal into a set of narrow-band lines. This then allows the problem to be treated as a multiplicity of narrow-band problems. Here a model-based approach is developed for the processing of data received on a vertical array from a broadband source where it is assumed that the propagation is governed by the normal-mode model. The goal of the processor is to provide an enhanced (filtered) version of the pressure at the array and the modal functions. Thus a pre-processor is actually developed, since one could think of several applications for these enhanced quantities such as localization, modal estimation, etc. It is well-known that in normal-mode theory a different modal structure evolves for each temporal frequency; thus it is not surprising that the model-based solution to this problem results in a scheme that requires a ''bank'' of narrow-band model-based processors—each with its own underlying modal structure for the narrow frequency band it operates over. The ''optimal'' Bayesian solution to the broadband pressure field enhancement and modal function extraction problem is developed. It is shown how this broadband processor can be implemented (using a suboptimal scheme) in pseudo real time due to its inherent parallel structure. A set of noisy broadband data is synthesized to demonstrate how to construct the processor and achieve a minimum variance (optimal Bayesian) design. It is shown that both broadband pressure-field and modal function estimates can be extracted illustrating the feasibility of this approach. [S0001-4966(98)04907-8]

PACS numbers: 43.60.Gk, 43.30.Zk [JLK]

INTRODUCTION

The treatment of continuous and transient broadband sources has long been a problem of interest in the ocean acoustic community. Initially, the work of Parvulescu[1] and Clay[2] began with a temporal matched-filter approach to the localization problem, which was validated through a series of experiments.[3] Here the assumed source location was used to provide a replica employed to match to the measured data. Brienzo and Hodgkiss[4] successfully applied this same approach to the localization of transient sources in deep ocean experiments. Model-based matched filtering was achieved by Hermand and Roderick[5] where a ray-type channel model was used to develop a replica capable of localizing a broadband source. An alternative to the temporal matched-filter evolved as a natural extension to matched-field/matched-mode processing which entails the ''matching'' of a predicted to a measured pressure field under the assumed source location. After an exhaustive search the location selected was that which provided a maximum value of the so-called ambiguity surface. Baggeroer[6] solved the broadband problem by decomposing it into a set of narrow-band lines and incoherently averaging to produce improved source localization, while Westwood[7] used a ray propagation model and coherent averaging to achieve notable results. Matched-mode processing of broadband source signals also offers a computational improvement over the matched-field approach as well as the improved enhancement offered in the modal space. Yang[8] developed a coherent matched-mode processor capable of not only localizing the transient target, but also capable of estimating its broadband temporal spectrum. The works of Lu *et al.*[9] and Chen and Lu[10] employed both coherent and incoherent techniques to localize a broadband source using matched-mode processing and time-frequency techniques. In these papers as well as the work of Mignerey,[11] a Green's function approach using normal modes was developed to deconvolve the source function and localize its position using a matched-mode or matched-field processor. We shall also use the normal-mode model in this work, wherein we develop a model-based processor for the enhancement of the pressure field at the array, in this case a vertical array, and the extraction of the modal functions. Thus we actually are describing a form of *pre-processor* that provides an enhanced or filtered form of the pressure field and modal functions that could be applied to many different broadband acoustic signal processing problems, such as localization, detection, modal estimation, etc.

The uncertainty of the ocean medium motivates the use of stochastic models to capture the random and often nonstationary nature of the phenomena ranging from ambient noise

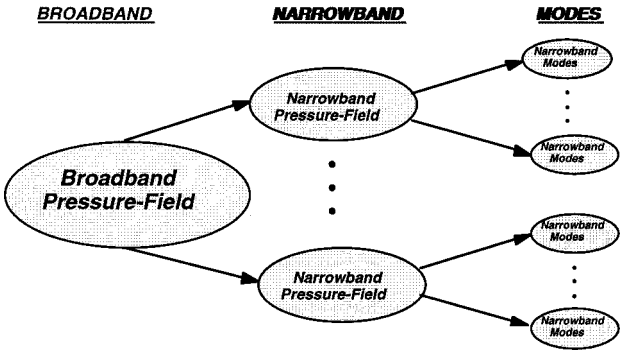

FIG. 1. Broadband normal-mode problem decomposition into narrow frequency bands.

and scattering to distant shipping noise. Therefore, processors that do not take these effects into account are susceptible to large estimation errors. This uncertainty was discussed by Tolstoy,[12] in the work of Carey[13] when investigating space–time processing, and in the overview by Sullivan and Middleton.[14] When contemplating the broadband problem, it is quite natural to develop temporal techniques, especially if the underlying model is the time-dependent wave equation; however, since the normal-mode propagation model is based on the time-independent (Hemholtz) equation, it seems more natural to: (1) filter the broadband receiver outputs into narrow bands in the frequency domain; (2) process each band with a devoted processor; and then (3) combine the narrowband results in a manner that is consistent with the goal of the final processor to create a broadband solution. This is the approach we take in this paper in the construction of our broadband model-based processor (MBP). That is, we first decompose the problem into a multiplicity of narrow-band problems and construct a bank of narrow-band model-based processors as depicted in Fig. 1.

The manner in which the outputs are recombined depends upon the particular goal of the processing. As will be seen later, this determines the particular form of the so-called *measurement equation* in a Kalman-based estimator. Thus we wish to reemphasize that the model-based processor presented here should be considered to be a *pre-processor* that can provide *enhancements* of the measurements and *estimates* of desired model parameters or states, where the *final* operations on these quantities depend upon the goal of the user. In this work, we employ a vertical array of hydrophone sensors and treat the problem of enhancing the noisy broadband acoustic pressure-field measurements and modal functions by applying a multichannel model-based technique based on a normal-mode propagation model.

Propagation theory predicts that a different *modal* structure evolves for each spectral frequency; therefore, it is not surprising that the multichannel model-based solution to this problem results in a scheme that requires a ''bank'' of processors, each employing its *own underlying modal structure* for the narrow frequency band that it operates over. The model-based solution using state-space forward propagators is developed using first principles, where it is shown that each processor is decoupled in modal space and recombined in the measurement space to provide enhanced estimates. It is also shown that the underlying model is decoupled in modal space leading to an inherent parallel structure (suboptimal) that is amenable to pseudo-real-time implementation.

The methodology employed is based on a state-space representation of the normal-mode propagation model. When state-space representations can be accomplished, a Kalman-type recursive processor can be used to provide estimates of any desired (observable) parameters. A major advantage of this approach is that uncertainties in the model can be dealt with via the additive process or system noise and noisy pressure field data can be modeled by the measurement equation and its additive measurement noise. Furthermore, the performance of the model can be monitored by the innovations sequence. Many of the current ocean acoustic processing problems can be treated using this more revealing and intuitive framework, which is based on firm statistical and system theoretic grounds. In this application, we seek techniques to incorporate the: (1) ocean acoustic propagation model; (2) sensor array measurement model; and (3) noise models (ambient, shipping, surface, and measurement) into the processor to solve the associated signal enhancement problem.

It has already been shown that the state-space representation can be utilized for signal enhancement to spatially propagate both modal and range functions as discussed in Candy and Sullivan.[15] Specifically, using the normal-mode model of the acoustic field, and a known source location, the modal functions and the pressure field can be estimated from noisy array measurements. In the stochastic case, a Gauss–Markov model evolves allowing the inclusion of stochastic phenomena such as noise and modeling errors in a consistent manner. The Gauss–Markov representation includes the second order statistics of the measurement noise and the modal uncertainty. In our case, the measurement noise can be ''lumped'' to represent the near-field acoustic noise field, flow noise on the hydrophones, and electronic noise, whereas the modal/range uncertainty can also be lumped to represent sound-speed profile (SSP) errors, noise from distant shipping, errors in the boundary conditions, sea state effects, and ocean inhomogeneities. It should also be noted that ''adaptive'' forms of the MBP are also available to provide a realizable solution to the so-called *mismatch problem* where the model and it underlying parameters do not faithfully represent the measured pressure-field data.[16,17] Reference 18 addresses the mismatch problem and its corresponding solution using MBPs. In this paper we concentrate on the extension of the processor to the broadband problem. It is possible to extend the resulting broadband MBP to an adaptive form by ''augmenting'' the model parameters providing a solution to the mismatch problem.[18] The results will show that the processor has an inherent parallel structure evolving directly from the normal-mode solutions. This structure, coupled with the sequential nature of the proposed algorithms, makes the MBP a potentially efficient solution for the broadband source problem. We provide a brief discussion of the related broadband problem in Sec. I and develop the underlying state-space model structures. In Sec. II we develop the broadband model-based processor showing that it is in fact the ''optimal'' Bayesian solution to the signal enhancement problem. A shallow ocean simulation is developed in Sec. III

illustrating the application of the model-based processor developed in Sec. II as well as its performance when applied to noisy broadband pressure-field data. We summarize our results in the final section and discuss future work.

I. BROADBAND STATE-SPACE PROPAGATORS

In this section we discuss the development of the broadband propagator to be employed in a model-based scheme, where the data are the noisy pressure-field measurements from a vertical array of hydrophone sensors.

We begin with the homogeneous, time-dependent, wave equation, which is given by

$$\frac{\partial^2}{\partial r^2}\,p(r,z,t)+\frac{1}{r}\,\frac{\partial}{\partial r}\,p(r,z,t)+\frac{\partial^2}{\partial z^2}\,p(r,z,t) - \frac{1}{c^2}\,\frac{\partial^2}{\partial t^2}\,p(r,z,t)=0. \tag{1}$$

In the case of range independence, the solution is separable. That is, the pressure-field solution can be written as

$$p(r,z,t)=R(r)Z(z)s(t). \tag{2}$$

The temporal Fourier transform of Eq. (1) yields

$$\frac{\partial^2}{\partial r^2}\,R(r)Z(z)S(\omega)+\frac{1}{r}\,\frac{\partial}{\partial r}\,R(r)Z(z)S(\omega) + \frac{\partial^2}{\partial z^2}\,R(r)Z(z)S(\omega)+\frac{\omega^2}{c^2}\,R(r)Z(z)S(\omega)=0, \tag{3}$$

where we see that, upon division by $S(\omega)$, we obtain the Hemholtz equation. For our shallow water acoustic waveguide, we then obtain the well-known normal mode-solution for a given value of ω:[19,20]

$$\mathcal{G}(r,z,\omega)=\sum_{m=1}^{M}\,\mathscr{H}_o(\kappa_r(m)r)\,\phi_m(z_s,\omega)\,\phi_m(z,\omega). \tag{4}$$

Here r and z_s are the source range and depth coordinates, respectively and $\phi_m(z,\omega)$ is the mth eigensolution for $Z(z)$, satisfying the so-called *vertical* or *depth* equation given by

$$\frac{d^2}{dz^2}\,\phi_m(z,\omega)+\kappa_z^2(m,\omega)\,\phi_m(z,\omega)=0. \tag{5}$$

$\mathcal{G}(r,z,\omega)$ is, in fact, the *Green's* function or impulse response. $\mathscr{H}_0$, the solution for $R(r)$, is the zeroth order Hankel function, $\kappa_r(m)$ is the horizontal wave number associated with the mth mode, and r is the horizontal range. The wave numbers satisfy the corresponding *dispersion relation*

$$\frac{\omega^2}{c^2(z)}=\kappa_r^2(m,\omega)+\kappa_z^2(m,\omega),\quad m=1,...,M, \tag{6}$$

where κ_z is the vertical wave number and $c(z)$ the depth-dependent sound-speed profile. Therefore, the resulting pressure field in the temporal frequency domain is given by

$$p(r,z,\omega)=\mathcal{G}(r,z,\omega)S(\omega), \tag{7}$$

which is equivalent to a convolution of $\mathcal{G}(r,z,t)$ and $s(t)$ in the time domain.

In the discrete Fourier case, with N temporal samples and sample interval Δt, the nth time sample of $s(t)$ becomes

$$s(n\Delta t)=\frac{1}{N}\sum_{q=0}^{N-1}\,S(\omega_q)e^{i\omega_q n\Delta t}, \tag{8}$$

with

$$S(\omega_q)=\sum_{n=0}^{N-1}\,s(n\Delta t)e^{-i\omega_q n\Delta t}, \tag{9}$$

so that from Eq. (8), the spectral amplitude at ω_q is given by

$$a_q=\frac{1}{N}\,S(\omega_q). \tag{10}$$

Thus from Eq. (7), we have a set of narrow-band solutions given by

$$p(r,z,\omega_q)=\sum_{m=1}^{M_q}\,a_q\mathscr{H}_o(\kappa_r(m)r)\,\phi_m(z_s,\omega_q)\,\phi_m(z,\omega_q), \tag{11}$$

where M_q is the number of modes supported at frequency ω_q. The dispersion relation now satisfies

$$\frac{\omega_q^2}{c^2(z)}=\kappa_r^2(m,q)+\kappa_z^2(m,q),\quad q=1,...,Q\leqslant N;\quad m=1,...,M_q, \tag{12}$$

with Q being the number of spectral lines to be processed. The reason for using the condition $Q\leqslant N$ is to allow the processor the option of including only significant spectral peaks.

We are now in a position to construct the model-based propagator. Following the development in Ref. 15, we define the modal state vector for the mth mode, at frequency ω_q, as

$$\Phi_m(z,\omega_q)=\begin{bmatrix}\phi_m(z,\omega_q)\\ \dfrac{d}{dz}\,\phi_m(z,\omega_q)\end{bmatrix},\quad m=1,...,M_q. \tag{13}$$

Equation (5) can now be written in state-space form as

$$\frac{d}{dz}\,\Phi_m(z,\omega_q)=\mathbf{A}_m(z,\omega_q)\Phi_m(z,\omega_q), \tag{14}$$

where

$$\mathbf{A}_m(z,\omega_q)=\begin{bmatrix}0 & 1\\ -\kappa_z^2(m,q) & 0\end{bmatrix},\quad m=1,...,M_q. \tag{15}$$

Expanding over the M_q modes for frequency ω_q, we have that

$$\frac{d}{dz}\,\mathbf{\Phi}(z,\omega_q)=\mathbf{A}(z,\omega_q)\mathbf{\Phi}(z,\omega_q) =\begin{bmatrix}\mathbf{A}_1(z,\omega_q) & \cdots & O\\ \vdots & \ddots & \vdots\\ O & \cdots & \mathbf{A}_{M_q}(z,\omega_q)\end{bmatrix}\mathbf{\Phi}(z,\omega_q), \tag{16}$$

with the single frequency state vector given by

$$\mathbf{\Phi}^T(z,\omega_q)\equiv[\Phi_1^T(z,\omega_q)\cdots\Phi_{M_q}^T(z,\omega_q)],$$
$$\Phi^T(z,\omega_q)\in R^{2M_q\times 1}. \tag{17}$$

If we now sample the spatial pressure field with a vertical line array of hydrophones, then at the lth hydrophone we have

$$p(z_l,\omega_q)=\mathbf{C}_q^T(r_s,z_s,\omega_q)\mathbf{\Phi}(z_l,\omega_q), \tag{18}$$

with the *measurement matrix* given by

$$\mathbf{C}_q^T(r_s,z_s,\omega_q)=[\beta_1(r_s,z_s,\omega_q)0|\ldots|\beta_{M_q}(r_s,z_s,\omega_q)0] \tag{19}$$

where, from Eq. (4),

$$\beta_m(r_s,z_s,\omega_q)\equiv\mathscr{H}_o(\kappa_r(m,q)r_s)\,\phi_m(z_s,\omega_q). \tag{20}$$

Equations (16) and (18) constitute the *state equation* and *measurement equation*, respectively, to be used in our model-based processor for frequency ω_q.

This model is only valid for a single temporal frequency, ω_q. We would now like to extend it to the broadband case. From the normal-mode pressure-field solution carried out previously, we see from Eqs. (11) and (12) that as the temporal frequency (ω_q) changes, the corresponding number of modes (M_q) and horizontal wave numbers [$\kappa_r(m,q)$] at each frequency also change. Thus the state-space propagator for the broadband case must allow for this frequency dependence.

Bearing this issue in mind, we now define the overall *broadband state-space propagator* as

$$\frac{d}{dz}\mathbf{\Phi}(z,\omega)=\mathbf{A}(z,\omega)\mathbf{\Phi}(z,\omega), \tag{21}$$

with

$$\mathbf{A}(z,\omega)=\mathrm{diag}[\mathbf{A}(z,\omega_1)\ldots\mathbf{A}(z,\omega_Q)],$$
$$\mathbf{A}(z,\omega)\in\mathbf{R}^{2M\times 2M}, \tag{22}$$

and

$$\mathbf{\Phi}^T(z_l,\omega)\equiv[\mathbf{\Phi}^T(z_l,\omega_1)\ldots\mathbf{\Phi}^T(z_l,\omega_Q)],$$
$$\mathbf{\Phi}^T(z_l,\omega)\in\mathbf{R}^{2M\times 1}, \tag{23}$$

and as before,

$$\mathbf{A}_m(z,\omega_q)=\begin{bmatrix}0 & 1\\ -\kappa_z^2(m,q) & 0\end{bmatrix},$$
$$q=1,\ldots,Q\leqslant N;\quad m=1,\ldots,M_q. \tag{24}$$

The parameter M, the total number of single frequency modes, is given by $M=\Sigma_1^Q M_q$. Note that we use the parameter ''ω'' to signify the entire set of discrete temporal frequencies, $\{\omega_q\}$, $q=1,\ldots,Q$.

At this point a discussion of the measurement equation is in order. We see from Eq. (19) that the form of the measurement matrix is determined by Eq. (4) for the single frequency case. However, in the broadband case the form of the measurement matrix is determined by the processing task itself. For example, we may choose to make a *coherent average* over frequency. In this case, the measurement equation takes the form

$$p(z_l,\omega)=\mathbf{C}(r_s,z_s,\omega)\mathbf{\Phi}(z_l,\omega), \tag{25}$$

with

$$\mathbf{C}(r_s,z_s,\omega)\equiv\frac{1}{Q}\,[\mathbf{C}_1^T(r_s,z_s,\omega_1)\cdots\mathbf{C}_Q^T(r_s,z_s,\omega_Q)]. \tag{26}$$

On the other hand, we may choose to recast the measurement model into that of a broadband system obtained by ''stacking'' all of the narrow-band pressure-field measurements, thus producing a spectral representation of the pressure field. This then would create the stacked or *spectral* version of the measurement matrix $\mathbf{C}(r_s,z_s,\omega)$ with the resulting measurement model at the lth sensor now given by

$$\mathbf{p}(z_l,\omega)=\mathbf{C}(r_s,z_s,\omega)\mathbf{\Phi}(z_l,\omega), \tag{27}$$

where

$$\mathbf{p}(z_l,\omega)=\begin{bmatrix}p(z_l,\omega_1)\\ p(z_l,\omega_2)\\ \vdots\\ p(z_l,\omega_Q)\end{bmatrix}, \tag{28}$$

and

$$\mathbf{C}(r_s,z_s,\omega)=\begin{bmatrix}\mathbf{C}_1^T(r_s,z_s,\omega_1) & O & \ldots & O\\ O & \mathbf{C}_2^T(r_s,z_s,\omega_2) & \ldots & O\\ & & \ddots & \\ O & O & \ldots & \mathbf{C}_Q^T(r_s,z_s,\omega_Q)\end{bmatrix}. \tag{29}$$

Here, $\mathbf{p}\in\mathbf{C}^{Q\times 1}$, $\mathbf{C}\in\mathbf{R}^{Q\times 2M}$, and $\mathbf{\Phi}(z_l,\omega)\in R^{2M\times 1}$ is defined in Eq. (23).

This is the form we shall use in the next section in the development of our model-based processor. As discussed earlier, the purpose of this processor will be to provide enhanced (filtered) versions of the pressure field and modal functions in a normal-mode shallow-water propagation problem.

II. BROADBAND MODEL-BASED PROCESSING

Since we assume that the field is measured by a vertical array, then at each sensor the acquired time series is given by

$p(z_l,t)$. Clearly, this sensor measurement contains all of the information about the source, both temporally and spatially, but due to the complexity of this received data coupled with the noise, the required signal processing is quite a challenging problem. If we take the Fourier transform in the temporal domain, then the broadband source can be thought of as being viewed through a bank of narrow-band filters, that is, the broadband pressure-field surface or image is then given by: $p(z_l,\omega_q)$; $l=1,...,L$, and $q=1,...,Q$. Once this surface is constructed, it is possible to infer other useful information about the dynamics of the ocean as well as the source. In the case of a shallow-water environment characterized by trapped wave propagation, we may represent the underlying Green's function or channel impulse response in terms of a normal-mode model. In this case it may also be of interest to observe the surface created by the various broadband modal functions, that is, as a function of temporal frequency, $\phi_m(z_l,\omega_q)$; for $m=1,...,M_q$. It is clear that as we decompose this complex temporal pressure-field measurement into these narrow frequency bands, each band will contain useful oceanographic and source information.

We begin by defining the underlying Gauss–Markov model. As shown in previous work[15] the deterministic model described by Eqs. (21) and (27) can be extended to the stochastic Gauss–Markov representation given by

$$\begin{aligned}\frac{d}{dz}\,\mathbf{\Phi}(z,\omega)&=\mathbf{A}(z,\omega)\mathbf{\Phi}(z,\omega)+\mathbf{w}(z,\omega),\\ \mathbf{p}(z_l,\omega)&=\mathbf{C}(r_s,z_s,\omega)\mathbf{\Phi}(z_l,\omega)+\mathbf{v}(z_l,\omega).\end{aligned}\tag{30}$$

Assuming the source is temporally correlated, especially since it is broadband, then the process noise spectral covariance, $\mathbf{R}_{ww}(z,\omega)$ is not diagonal and, in fact, it probably should be modeled by a temporal coloring filter (see Ref. 18 for details) assuming its stationarity and the possibility that its statistics can be estimated from any of the sensor time series. The measurement noise at each sensor is reasonably modeled by a white sequence; however, the underlying spectral covariance matrix, $\mathbf{R}_{vv}(z_l,\omega)$ is probably not diagonal. In the subsequent development of the model-based scheme, we will assume that the spectral covariance matrices are *diagonal*, since any sequence in which the cross-frequency terms are correlated can be transformed using a UD factorization to a sequence that is uncorrelated *prior* to the processing.[21] That is, we assume that the corresponding measurement spectral covariance is given by

$$\mathbf{R}_{vv}(z_l,\omega)=\mathrm{diag}[R_{vv}(z_l,\omega_1)\cdots R_{vv}(z_l,\omega_Q)].\tag{31}$$

In order to obtain the optimal (minimum error variance) estimator, we cast our problem into a probabilistic framework under the Gauss–Markov assumptions; therefore, the time series of pressure-field measurements at each sensor is Fourier transformed to yield a discrete set of frequencies $\{\omega_q\}$, $q=1,...,Q$ and the set of broadband sensor measurements, $\{\mathbf{p}(z_l,\omega)\}$, $l=1,...,L$; $p\in C^{Q\times 1}$. Note that the window length of the Fourier transform is determined by the temporal correlation time of the measurement (source) to assure the independence of the frequency samples. For our pressure-field/modal function estimation problem, we define the underlying *broadband pressure-field/modal function enhancement problem as*:

GIVEN a set of noisy broadband pressure-field measurements, $\{\mathbf{p}(z_l,\omega)\}$, $l=1,...,L$ and the underlying Gauss–Markov model, FIND the best (minimum error variance) estimate of the broadband modal functions, $\hat{\mathbf{\Phi}}(z_l,\omega)$, and pressure field, $\hat{\mathbf{p}}(z_l,\omega)$.

The minimum variance solution to this problem can be obtained by the maximizing the *a posteriori* density as follows. Defining the set of broadband pressure-field measurements as: $P_L\equiv\{\mathbf{p}(z_1,\omega),\ldots,\mathbf{p}(z_L,\omega)\}$; $\mathbf{p}\in C^{Q\times 1}$, the probability of obtaining the measurement vector P_l, with the help of Bayes' rule, can be written as

$$\begin{aligned}\Pr(P_l)&=\Pr(\mathbf{p}(z_l,\omega),P_{l-1})\\ &=\Pr(\mathbf{p}(z_l,\omega)|P_{l-1})\times\Pr(P_{l-1}).\end{aligned}\tag{32}$$

Here, $\Pr(\mathbf{p}(z_l,\omega)|P_{l-1})$ is the probability of obtaining the hydrophone measurement $\mathbf{p}(z_l,\omega)$ based on (conditioned on) all of the hydrophone measurements up to and including $\mathbf{p}(z_{l-1},\omega)$, i.e., P_{l-1}.

Now the maximum *a posteriori* (MAP) estimator of the modal functions must maximize the posterior density given by

$$\begin{aligned}\Pr(\mathbf{\Phi}(z_l,\omega)|P_l)&=\frac{\Pr(\mathbf{\Phi}(z_l,\omega),P_l)}{\Pr(P_l)}\\ &=\frac{\Pr(\mathbf{\Phi}(z_l,\omega),\mathbf{p}(z_l,\omega),P_{l-1})}{\Pr(P_l)}.\end{aligned}\tag{33}$$

Substituting Eq. (32) in the denominator and applying Bayes' rule to the numerator, Eq. (33) becomes

$$\Pr(\mathbf{\Phi}(z_l,\omega)|P_l)=\frac{\Pr(\mathbf{p}(z_l,\omega)|\mathbf{\Phi}(z_l,\omega),P_{l-1})\times\Pr(\mathbf{\Phi}(z_l,\omega),P_{l-1})}{\Pr(\mathbf{p}(z_l,\omega)|P_{l-1})\times\Pr(P_{l-1})}.\tag{34}$$

Again using Bayes' rule, we expand the second term in the numerator yielding

$$\Pr(\mathbf{\Phi}(z_l,\omega),P_{l-1})=\Pr(\mathbf{\Phi}(z_l,\omega)|P_{l-1})\Pr(P_{l-1}).\tag{35}$$

Substituting this relation in the previous equation and canceling like terms, we obtain the required expression for the posterior density, which is

$$\Pr(\mathbf{\Phi}(z_l,\omega)|P_l)=\frac{\Pr(\mathbf{p}(z_l,\omega)|\mathbf{\Phi}(z_l,\omega),P_{l-1})\times\Pr(\mathbf{\Phi}(z_l,\omega)|P_{l-1})}{\Pr(\mathbf{p}(z_l,\omega)|P_{l-1})}.\tag{36}$$

That is, we have obtained the posterior density, which is conditioned on the set of l measurements, in terms of densities conditioned on the set of $l-1$ measurements. This leads in a natural way to the recursive form of the the processor that we seek.

Introducing the explicit Gaussian forms of these densities, we have

$$\Pr(\mathbf{p}(z_l,\omega)|P_{l-1})\sim\mathcal{N}(\mathbf{C}(r_s,z_s,\omega)\hat{\mathbf{\Phi}}(z_{l|l-1},\omega),$$

TABLE I. Continuous-discrete broadband linear Kalman filter algorithm: predictor/corrector form.

Prediction	
$\frac{d}{dz}\hat{\Phi}(z,\omega)=\mathbf{A}(z,\omega)\hat{\Phi}(z,w)$	(*state prediction*)
$\frac{d}{dz}\tilde{\mathbf{P}}(z,\omega)=\mathbf{A}(z,\omega)\tilde{\mathbf{P}}(z,\omega)+\mathbf{A}^T(z,\omega)\tilde{\mathbf{P}}(z,\omega)+\mathbf{R}_{ww}(z,\omega)$	(*covariance prediction*)
Innovation	
$\boldsymbol{\epsilon}(z_l,\omega)=\mathbf{p}(z_l,\omega)-\hat{\mathbf{p}}(z_{l\|l-1},\omega)=\mathbf{p}(z_l,\omega)-\mathbf{C}(r_s,z_s,\omega)\hat{\Phi}(z_{l\|l-1},\omega)$	(*innovation*)
$\mathbf{R}_{ee}(z_l,\omega)=\mathbf{C}(z_l,\omega)\tilde{\mathbf{P}}(z_{l\|l-1},\omega)\mathbf{C}^T(r_s,z_s,\omega)+\mathbf{R}_{vv}(z_l,\omega)$	(*innovation covariance*)
Gain	
$\mathbf{K}(z_l,\omega)=\tilde{\mathbf{P}}(z_{l\|l-1},\omega)\mathbf{C}^T(r_s,z_s,\omega)\mathbf{R}_{\epsilon\epsilon}^{-1}(z_{l-1},\omega)$	(*Kalman gain or weight*)
Correction	
$\hat{\Phi}(z_{l\|l},\omega)=\hat{\Phi}(z_{l\|l-1},\omega)+\mathbf{K}(z_l,\omega)\boldsymbol{\epsilon}(z_l,\omega)$	(*state correction*)
$\tilde{\mathbf{P}}(z_{l\|l},\omega)=[I-\mathbf{K}(z_l,\omega)\mathbf{C}(r_s,z_s,\omega)]\tilde{\mathbf{P}}(z_{l\|l-1},\omega)$	(*covariance correction*)
Initial conditions	
$\hat{\Phi}(0\|0,\omega)\quad\tilde{\mathbf{P}}(0\|0,\omega)$	

$$\mathbf{C}(r_s,z_s,\omega)\tilde{\mathbf{P}}(z_{l|l-1},\omega)\mathbf{C}^T(r_s,z_s,\omega)+\mathbf{R}_{vv}(z_{l-1},\omega)); \quad (37)$$

$$\Pr(\mathbf{p}(z_l,\omega)|\boldsymbol{\Phi}(z_l,\omega),P_{l-1}) \sim\mathcal{N}(\mathbf{C}(r_s,z_s,\omega)\boldsymbol{\Phi}(z_l,\omega),\mathbf{R}_{vv}(z_{l-1},\omega)); \quad (38)$$

and

$$\Pr(\boldsymbol{\Phi}(z_l,\omega)|P_{l-1})\sim\mathcal{N}(\boldsymbol{\Phi}(z_{l|l-1},\omega),\tilde{\mathbf{P}}(z_{l|l-1},\omega)), \quad (39)$$

where

$$\tilde{\mathbf{P}}(z_{l|l-1},\omega)=\mathbf{A}(z_{l-1},\omega)\tilde{\mathbf{P}}(z_{l-1|l-1},\omega)\mathbf{A}^T(z_{l-1},\omega)+\mathbf{R}_{ww}(z_{l-1},\omega). \quad (40)$$

Here the notation $\hat{\Phi}(z_{l|l-1},\omega)\equiv E\{\boldsymbol{\Phi}(z_l,\omega)|P_{l-1}\}$ is the conditional mean, that is, the ''best'' (minimum variance) estimate at depth z_l based on the previous sensor measurements up to the depth z_{l-1}. The symbol $\sim$ means ''distributed as'' and $\mathcal{N}(m,v)$ is a Gaussian distribution of mean m and variance v.

Now substituting these into the *a posteriori* density and performing the necessary manipulations (see the Appendix for details), we obtain

$$\Pr(\boldsymbol{\Phi}(z_l,\omega)|P_l) = \mathscr{C}_l \exp\{-\tfrac{1}{2}(\mathbf{v}(z_l,\omega)\mathbf{R}_{vv}^{-1}(z_l,\omega)\mathbf{v}^T(z_l,\omega) + \tilde{\Phi}^T(z_{l|l-1},\omega)\tilde{\mathbf{P}}^{-1}(z_{l|l-1},\omega)\tilde{\Phi}(z_{l|l-1},\omega) - \boldsymbol{\epsilon}^T(z_l,\omega)\mathbf{R}_{\epsilon\epsilon}^{-1}(z_l,\omega)\boldsymbol{\epsilon}(z_l,\omega))\}, \quad (41)$$

where the broadband *modal estimation error* is defined by

$$\tilde{\Phi}(z_{l|l-1},\omega)\equiv\boldsymbol{\Phi}(z_l,\omega)-\hat{\Phi}(z_{l|l-1},\omega), \quad (42)$$

and the broadband *innovation* is

$$\boldsymbol{\epsilon}(z_l,\omega)\equiv\mathbf{p}(z_l,\omega)-\hat{\mathbf{p}}(z_{l|l-1},\omega), \quad (43)$$

with the enhanced (MAP estimated) broadband measurement defined by

$$\hat{\mathbf{p}}(z_l,\omega)\equiv\mathbf{C}(r_s,z_s,\omega)\hat{\Phi}(z_{l|l-1},\omega), \quad (44)$$

and the constant C_l with respective spectral covariance matrices, $\tilde{\mathbf{P}}(z_{l-1|l-1},\omega)$ and $\mathbf{R}_{\epsilon\epsilon}(z_l,\omega)$. By maximizing the *a posteriori* density or equivalently, minimizing its its logarithm,[21] we have the *MAP equation*,

$$\boldsymbol{\nabla}_\phi \ln \Pr(\boldsymbol{\Phi}(z_l,\omega)|P_{l-1})|_{\boldsymbol{\Phi}=\hat{\boldsymbol{\Phi}}_{\mathrm{MAP}}}=\mathbf{O}. \quad (45)$$

Differentiating the posterior density and noting that $\hat{\Phi}(z_{l|l-1},\omega)$ and $\boldsymbol{\epsilon}(z_l,\omega)$ are both functions of the data set, P_{l-1}, we obtain

$$\boldsymbol{\nabla}_\phi \ln \Pr(\boldsymbol{\Phi}(z_l,\omega)|P_{l-1}) = \mathbf{C}(r_s,z_s,\omega)\mathbf{R}_{vv}^{-1}(z_l,\omega)\mathbf{v}(z_l,\omega) - \tilde{\mathbf{P}}^{-1}(z_{l|l-1},\omega)\tilde{\Phi}(z_{l|l-1},\omega)=\mathbf{O}. \quad (46)$$

Solving the MAP equation for $\boldsymbol{\Phi}=\hat{\Phi}_{\mathrm{MAP}}$ yields

$$\hat{\Phi}_{\mathrm{MAP}}(z_l,\omega)=\tilde{\mathbf{P}}(z_{l|l},\omega)[\tilde{\mathbf{P}}^{-1}(z_{l|l-1},\omega)\hat{\Phi}(z_{l|l-1},\omega) + \mathbf{C}^T(r_s,z_s,\omega)\mathbf{R}_{vv}^{-1}(z_l,\omega)p(z_l,\omega)], \quad (47)$$

where we have used the fact that

$$\tilde{\mathbf{P}}(z_{l|l},\omega)=[\mathbf{C}(r_s,z_s,\omega)\mathbf{R}_{vv}^{-1}(z_l,\omega)\mathbf{C}^T(r_s,z_s,\omega) + \tilde{\mathbf{P}}^{-1}(z_{l|l-1},\omega)]^{-1}, \quad (48)$$

from the matrix inversion lemma.[21] As shown in the Appendix, the optimal broadband MAP processor $\hat{\Phi}_{\mathrm{MAP}}(z_l,\omega)=\hat{\Phi}(z_{l|l},\omega)$ evolves from Eq. (47) as

$$\hat{\Phi}(z_{l|l},\omega)=\hat{\Phi}(z_{l|l-1},\omega)+\mathbf{K}(z_l,\omega)\boldsymbol{\epsilon}(z_l,\omega), \quad (49)$$

where $\hat{\Phi}(z,\omega_q)\in R^{2M\times 1}$, $\mathbf{K}(z_l,\omega)\in\mathbf{C}^{2M\times Q}$, and $\boldsymbol{\epsilon}(z_l,\omega)\in\mathbf{C}^{Q\times 1}$. The form of $\mathbf{K}(z_l,\omega)$, the *Kalman gain* is given in Table I.

Equation (49) is the recursive (in depth) processor we have been seeking. $\hat{\Phi}(z_{l|l-1},\omega)$, is the *predicted* modal estimate and $\hat{\Phi}(z_{l|l},\omega)$ is the *corrected* or *filtered* modal estimate. The *enhanced* or filtered measurement is then obtained

by substituting the corrected estimate into the measurement equation. The complete linear space-varying broadband Kalman filter algorithm is given in Table I.

The overall structure of the estimator can now be seen by expanding the Kalman gain matrix over the set of discrete frequencies for $\omega \rightarrow \omega_q$, one for each of the Q columns to give

$$\hat{\Phi}(z_{l|l},\omega)=\hat{\Phi}(z_{l|l-1},\omega)+[\mathbf{K}(z_l,\omega_1)\cdots\mathbf{K}(z_l,\omega_Q)] \times\begin{bmatrix}\boldsymbol{\epsilon}(z_l,\omega_1)\\ \vdots\\ \boldsymbol{\epsilon}(z_l,\omega_Q)\end{bmatrix}, \tag{50}$$

or

$$\hat{\Phi}(z_{l|l},\omega)=\hat{\Phi}(z_{l|l-1},\omega)+\sum_{q=1}^{Q}\mathbf{K}(z_l,\omega_q)\boldsymbol{\epsilon}(z_l,\omega_q), \tag{51}$$

where $\hat{\Phi}(z,\omega)\in R^{2M\times 1}$, $\mathbf{K}(z_l,\omega_q)\in\mathbf{C}^{2M\times 1}$, and $\boldsymbol{\epsilon}(z_l,\omega_q)\in\mathbf{C}^{1\times 1}$. Now let us rewrite this equation in a slightly different manner by expanding over the set of discrete frequencies and expressing the gain in terms of $2M_q\times Q$ block rows

$$\begin{bmatrix}\hat{\Phi}(z_{l|l},\omega_1)\\ \vdots\\ \hat{\Phi}(z_{l|l},\omega_Q)\end{bmatrix}=\begin{bmatrix}\hat{\Phi}(z_{l|l-1},\omega_1)\\ \vdots\\ \hat{\Phi}(z_{l|l-1},\omega_Q)\end{bmatrix} +\begin{bmatrix}\mathbf{K}_1^T(z_l,\omega)\\ \vdots\\ \mathbf{K}_Q^T(z_l,\omega)\end{bmatrix}\boldsymbol{\epsilon}(z_l,\omega). \tag{52}$$

If we further decompose each block row $\mathbf{K}_q^T(z_l,\omega)$ into its individual column vectors defined by $\mathbf{K}_{qn}(z_l,\omega_n)\in C^{2M_q\times 1}$, that is,

$$\mathbf{K}_q^T(z_l,\omega)\equiv[\mathbf{K}_{q1}(z_l,\omega_1)\cdots\mathbf{K}_{qQ}(z_l,\omega_Q)], \tag{53}$$

then we can obtain the *narrow-band recursion* for the corrected estimate as

$$\hat{\Phi}(z_{l|l},\omega_q)=\hat{\Phi}(z_{l|l-1},\omega_q)+\sum_{n=1}^{Q}\mathbf{K}_{qn}(z_l,\omega_n)\boldsymbol{\epsilon}(z_l,\omega_n), \tag{54}$$

with $\hat{\Phi}(z_{l|l},\omega_q)\in\mathbf{C}^{2M_q\times 1}$ the gain $\mathbf{K}_{qn}(z_l,\omega_n)\in\mathbf{C}^{2M_q\times 1}$, and $\boldsymbol{\epsilon}(z_l,\omega_n)\in\mathbf{C}^{1\times 1}$ showing how each narrow-band frequency line ω_q is combined to form the *optimal* MAP estimate. Note that the entire broadband pressure-field measurement is required at each sensor, since

$$\boldsymbol{\epsilon}(z_l,\omega)=\begin{bmatrix}p(z_l,\omega_1)\\ \vdots\\ p(z_l,\omega_Q)\end{bmatrix}-\hat{p}(z_{l|l-1},\omega). \tag{55}$$

However, this relation suggests an efficient parallel, but *suboptimal* approach to implementing this broadband estimator might be achieved by constructing a ''local'' narrow-band processor for each ω_q and then combining their outputs to obtain the final broadband estimate, that is,

$$\hat{\Phi}(z_{l|l},\omega_q)=\hat{\Phi}(z_{l|l-1},\omega_q)+\mathbf{K}_{qq}(z_l,\omega_q)\boldsymbol{\epsilon}(z_l,\omega_q), \tag{56}$$

where we have discarded the other $2M_q\times 1$ submatrices, i.e., $\mathbf{K}_{qn}(z_l,\omega_n)=\mathbf{0}$, $n\neq q$. To see this recall (see Table I) that

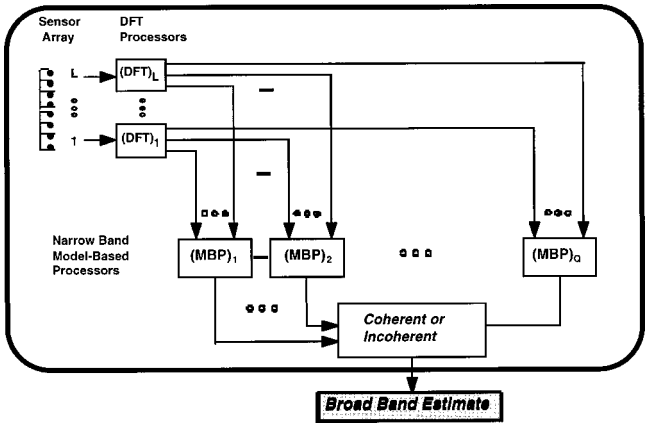

FIG. 2. Structure of the suboptimal model-based broadband processor.

the broadband Kalman gain is calculated from

$$\mathbf{K}(z_l,\omega)=\tilde{\mathbf{P}}(z_{l|l-1},\omega)\mathbf{C}^T(r_s,z_s,\omega)\mathbf{R}_{\boldsymbol{\epsilon}\boldsymbol{\epsilon}}^{-1}(z_l,\omega), \tag{57}$$

and if we now assume the parallel (suboptimal) form, then the covariance is block diagonal

$$\tilde{\mathbf{P}}(z_{l|l-1},\omega)=\mathrm{diag}[\tilde{\mathbf{P}}(z_{l|l-1},\omega_1)\cdots\tilde{\mathbf{P}}(z_{l|l-1},\omega_Q)], \tag{58}$$

and thus performing the implied partitions and multiplying gives

$$\mathbf{K}(z_l,\omega)=\begin{bmatrix}\mathbf{K}_{11}(z_l,\omega_1) & & \mathbf{O}\\ & \ddots & \\ \mathbf{O} & & \mathbf{K}_{QQ}(z_l,\omega_Q)\end{bmatrix}, \tag{59}$$

where

$$\mathbf{K}_{qq}(z_l,\omega_q)=\tilde{\mathbf{P}}(z_{l|l-1},\omega_q)\mathbf{C}^T(r_s,z_s,\omega_q)\mathbf{R}_{\boldsymbol{\epsilon}\boldsymbol{\epsilon}}^{-1}(z_l,\omega_q) \tag{60}$$

We depict the structure of the suboptimal broadband implementation of the MBP structure in Fig. 2.

It is interesting to return to the *optimal* solution and note some of its features. First from the physics of the normal-mode model (narrow-band temporal frequency), it is necessary to develop a bank of optimal narrow-band estimators at each bin, ω_q so that the broadband estimate can be reconstructed from the optimal set, $\{\hat{p}(z_l,\omega_q)\}$, $q=1,\ldots,Q$ over the array. Note also that the broadband modal estimates are also constructed in a similar manner as $\{\hat{\Phi}(z_l,\omega_q)\}$, $q=1,\ldots,Q$.

Thus our implementation of the optimal algorithm will be processed as a bank of narrow-band model-based predictors combined during the correction phase of the algorithm to create the optimal broadband MAP estimator. The estimation algorithm then proceeds for each $\{\omega_q\}$, $q=1,\ldots,Q$ as:

Prediction:

$$\frac{d}{dz}\hat{\Phi}(z,\omega_q)=\mathbf{A}(z,\omega_q)\hat{\Phi}(z,\omega_q). \tag{61}$$

Innovation:

$$\boldsymbol{\epsilon}(z_l,\omega_q)=p(z_l,\omega_q)-\mathbf{C}_q^T(r_s,z_s,\omega_q)\hat{\Phi}(z_{l|l-1},\omega_q). \tag{62}$$

Correction:

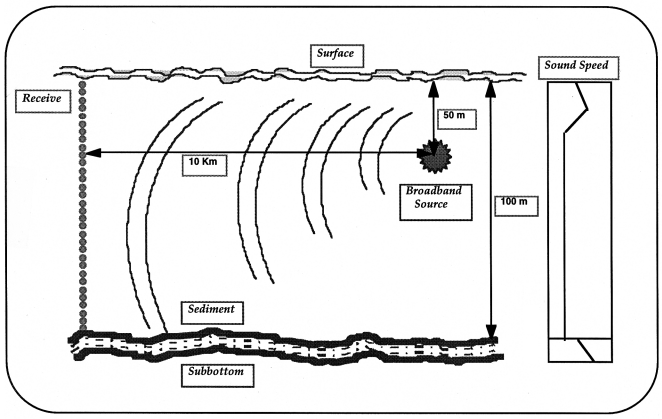

FIG. 3. Shallow ocean environment problem: Channel (100 m) with broadband (50–100 Hz) source located at range, $r_s = 10$ Km and depth, $z_s = 50$ m.

$$\hat{\Phi}(z_{l|l},\omega_q) = \hat{\Phi}(z_{l|l-1},\omega_q) + \sum_{n=1}^{Q} \mathbf{K}_{qn}(z_l,\omega_n)\boldsymbol{\epsilon}(z_l,\omega_n). \tag{63}$$

Gain:

$$\mathbf{K}(z_l,\omega) = \tilde{\mathbf{P}}(z_{l|l-1},\omega)\mathbf{C}^T(r_s,z_s,\omega)\mathbf{R}_{\epsilon\epsilon}^{-1}(z_l,\omega). \tag{64}$$

Here the respective predicted and corrected spectral covariances are also found from Table I.

This completes the theoretical discussion of the development of the broadband model-based processor; next we consider its application to simulated data.

III. BROADBAND MBP DESIGN FOR A SHALLOW OCEAN SIMULATION

In this section we discuss the application of the optimal model-based processor to data synthesized by a broadband normal-mode model using the state-space forward propagator and the underlying Gauss–Markov representation of Sec. II. In order to develop the propagator we *first* must define the shallow-water boundary value problem and solve it to obtain the parameters required for the processor.

Consider the shallow-water channel depicted in Fig. 3. We assume a flat bottom, a range independent three layer environment with a channel depth of 100 m, a sediment depth of 2.5 m, and a subbottom. A vertical line array of 100 sensors with spacing of $\Delta z = 1$ m spans the entire water column and a broadband source of unit amplitude and 50-Hz bandwidth ranging from 50 to 100 Hz in 10-Hz increments is located at a depth of 50 m and a range of 10 km from the array. The sound speed profile in the water column and the sediment are sketched in the figure and specified along with the other problem parameters in Table II. SNAP, a normal-mode propagation simulator,[22] is used to find solutions for each of the set of discrete temporal source frequencies. The results are shown in Table III below. We note from the table (as expected) that as the temporal frequency increases, the number of modes increases.

Next we design the state-space propagator. The parameters obtained from SNAP are now used to construct the broadband state-space and measurement models of Eqs. (21) and (27). Here we use the set of horizontal wave numbers, $\{\kappa_r(m,q)\}$, $m = 1,...,M_q$; $q = 1,...,Q$, and sound speed, $\{c(z_l)\}$, to implement the state models along with the corresponding modal function values at source depth, $\{\phi_{m1}(z_s,\omega_q)\}$, as well as the Hankel functions at source range, $\{\mathscr{H}_0(\kappa(m,q)r_s)\}$ to construct the measurement models.

The final set of parameters for our simulation are the modal and measurement noise covariance matrices required by the Gauss–Markov model. Both are specified by the input (modal) and output (measurement) signal-to-noise ratios (SNR) defined by:

TABLE II. Shallow-ocean simulation parameters.

Problem parameters			
Parameter	Water	Sediment	Bottom
Depth (m)	100	2.5	-
Density (G/cm^3)	1	1.8	1.84
Attenuation (dB/NL)	0.13	0.15	0.0
Source			
Frequency (Hz)	50–100		
Range (km)	10		
Depth (m)	50		
Sound speed			
0.0	1503.0	1597.95	1597.95
0.1		1597.95	
0.2		1522.58	
1.6		1537.65	
2.5		1552.73	
5.0	1503.1		
10.0	1503.2		
15.0	1503.3		
20.0	1503.4		
100.0	1504.7		

TABLE III. Shallow ocean boundary solutions.

SNAP parameters				
Frequency (Hz)	No. modes	Mode No.	Modal coeff.	Wave No.
50	2	1	0.122	0.207386
		2	−0.070	0.202489
60	3	1	0.125	0.249339
		2	−0.063	0.245106
		3	−0.097	0.237639
70	3	1	0.127	0.291255
		2	−0.057	0.287522
		3	−0.108	0.280907
80	4	1	0.129	0.333144
		2	−0.052	0.329802
		3	−0.113	0.323913
		4	0.087	0.315526
90	4	1	0.130	0.375015
		2	−0.047	0.371985
		3	−0.117	0.366685
		4	0.084	0.358997
100	5	1	0.131	0.416871
		2	−0.043	0.414098
		3	−0.119	0.409278
		4	0.079	0.402279
		5	0.081	0.393399

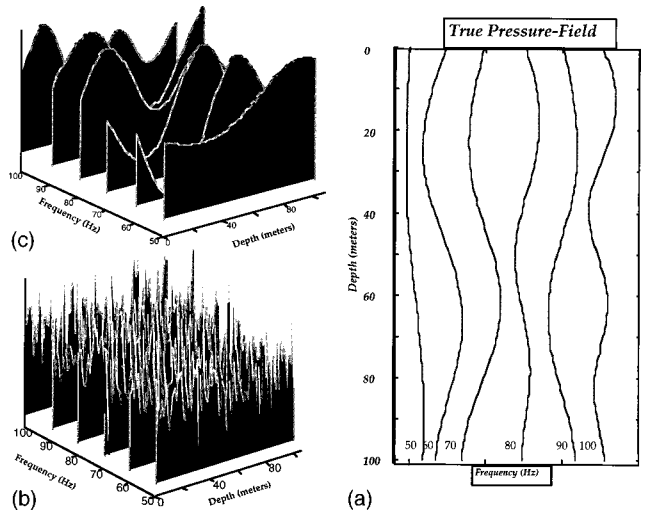

FIG. 4. Synthesized broadband pressure-field surface: (a) true pressure field; (b) Noisy (-30 dB) pressure field; (c) narrow-band DFT filter outputs of true field.

$$\begin{aligned} \mathrm{SNR}_{\mathrm{in}} &:= \frac{[\mathbf{P}(z_l,\omega_q)]_{m,m}}{R_{ww}(m,m)}, \quad m=1,...,2M_q; \\ \mathrm{SNR}_{\mathrm{out}} &:= \frac{\mathbf{C}_q^T \mathbf{P}(z_l,\omega_q)\mathbf{C}_q}{R_{vv}(q,q)}, \quad q=1,...,Q; \end{aligned} \tag{65}$$

with $\mathbf{P}(z_l,\omega_q) \equiv \mathrm{Cov}\,[\mathbf{\Phi}_m(z_l,\omega_q)]$, i.e., it is the $2M_q \times 2M_q$ submatrix of $\mathbf{P}(z,\omega)$ and $\mathbf{C}_q$ is defined in Eq. (19). We use the ''stacked'' measurement model of Eq. (27) for our simulations, but the model based on a coherent sum [Eq. (25)] could just as easily been employed.

It is important to realize that the state-space ''forward'' propagators do *not* offer an alternative solution to the Helmholtz equation (and are not to be confused with a marching method), but rather use the parameters *from* the boundary value solution to obtain a set of initial conditions/parameters for the propagator construction. Even the adaptive model-based processors still utilize the boundary value solutions to ''initialize'' the processing.[18]

With this information in hand, the Gauss–Markov simulation was performed at $\mathrm{SNR}_{\mathrm{in}}=25$ dB (noise free) and $\mathrm{SNR}_{\mathrm{out}}=-30$ dB. The ''true'' pressure-field surface is shown in Fig. 4 along with the corresponding noisy surface—both produced as outputs of a set of narrow-band DFT filters. We also show the true pressure-field functions which are expected to be extracted by the optimal processor along with the modal function estimates.

The optimal Bayesian or minimum variance MBP was designed using the identical set of parameters used in the Gauss–Markov simulation thereby eliminating any ''mismatch'' between model and environment.[16,17,23–27] We can consider this simulation as a bound on the best one could hope to achieve, since it is in fact the minimum variance estimates satisfying the Cramer–Rao lower bound.[28] In minimum variance estimation it is important to realize the overall design philosophy. First, the key issue is that a necessary and sufficient condition for optimality is that the innovation sequences (difference between measured and predicted pressure-fields) of Eq. (62) are zero mean and uncorrelated (white). Thus actual minimum variance designs are *not* considered ''tuned'' unless this condition is satisfied; therefore, the free parameters in the MBP (usually initial conditions and process/measurement noise vectors/matrices) are adjusted (if possible) until this condition is achieved. Once satisfied, then and only then can the state (modal function) and measurement (pressure-field) estimates along with their associated covariances be considered viable.

For the zero-mean test, recall that a sample mean, $\hat{m}$, based on N samples taken from a population with variance σ^2 has a variance given by σ^2/N. Thus if the population mean is zero, since $\mathrm{erf}(1.96)=0.95$, the sample innovations mean $\hat{m}$ will satisfy the inequality

$$|\hat{m}_{\epsilon}| < 1.96\sqrt{\frac{\sigma_{\epsilon}^2}{N}} \tag{66}$$

95% of the time. Here we use the sample innovations variance σ_{ϵ}^2 as an estimate of the population variance. It is given by

$$\sigma_{\epsilon}^2 = \frac{1}{N}\sum_{j=1}^{N} \epsilon_j^2. \tag{67}$$

Similarly, to test that the innovation sequence is white, we use the sample innovations covariance bounds predicted by the MBP. That is, whiteness requires that at least 95% of the sample (normalized) innovation correlations lie within the bounds specified by

$$\left[\hat{c}_{\epsilon\epsilon}(k) \pm \frac{1.96}{\sqrt{N}}\right], \quad \hat{c}_{\epsilon\epsilon}(k) = \frac{\hat{R}_{\epsilon\epsilon}(k)}{\hat{R}_{\epsilon\epsilon}(0)}, \tag{68}$$

where k is the lag.

Care must be taken when using these statistical tests. First, if the system is multi-channel, the innovations sequence is a vector, and these tests must be performed on each channel individually. Second, these zero-mean and whiteness tests rely on quasi-stationary assumptions and sample statistics to estimate the required correlations. If the models are nonlinear or nonstationary, other tests may be more reliable. However, it usually is argued heuristically that when the estimator is tuned, the nonstationarities are being tracked by the MBP even in the nonlinear case and therefore, the innovations should be covariance stationary.

In the case of nonstationarity, a more reliable statistic to use is the *weighted sum squared residual (WSSR)*, which is a measure of the overall global estimation performance for the MBP processor, determining the ''whiteness'' of the innovations sequence.[21] It is particularly useful in the multi-channel case. It essentially aggregates all of the information available in the innovation vector and tests whiteness by requiring that the underlying decision function lies *below* the specified threshold. If the WSSR statistic does lie beneath the calculated threshold, then theoretically, the estimator is tuned and said to converge. The WSSR statistic aggregates all of the information available in the innovation vector over some finite window of N samples, that is, the WSSR defined by $\rho(k)$ is

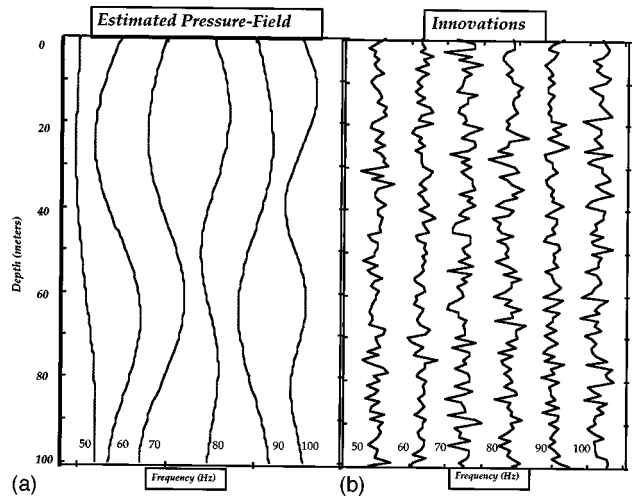

FIG. 5. Broadband model-based processor design: (a) enhanced pressure-field estimates; (b) innovation sequences.

$$\rho(k) \equiv \sum_{i=n-N+1}^{n} \boldsymbol{\epsilon}^T(i)\mathbf{R}_{\boldsymbol{\epsilon}\boldsymbol{\epsilon}}^{-1}(i)\boldsymbol{\epsilon}(i), \quad l \geq N. \tag{69}$$

Under the hypothesis that there is no model ''mismatch'' (white innovations), it can be shown that $\rho(k)$ is distributed $\chi^2(NK)$. Here, K is the number of channels. In our case, $K=Q$, i.e., the number of frequencies. For $NK>30$, $\rho(k)$ can be considered to be Gaussian distributed with mean NK and variance $2NK$. Thus we test $\rho(k)$ against the threshold

$$\tau = NK + 1.96\sqrt{2NK}. \tag{70}$$

That is, for the whiteness test, the inequality given by

$$\rho(k) < \tau, \tag{71}$$

must be satisfied 95% of the time. Here the window is designed to slide through the innovations data and estimate its whiteness. Even in the worst case where these estimators may not prove to be completely consistent, the MBP (when tuned) predicts the nonstationary innovations covariance, $R_{\epsilon\epsilon}(i)$, enabling a simple confidence interval to be constructed and used for testing as well, that is,

$$[\boldsymbol{\epsilon}(i) \pm 1.96\sqrt{R_{\epsilon\epsilon}(i)}], \quad i=1,...,K, \tag{72}$$

where $R_{\epsilon\epsilon}(i)$ is the ith element of the the innovations covariance.

Thus overall performance of the processor can be assessed by analyzing the statistical properties of the innovations, which is essentially the approach we take in this feasibility test for the broadband processor design on synthesized data. There are other tests that can be used with real data to check the consistency of the processor and we refer the interested reader to Ref. 18, Chapter 5 for more details.

We use SSPACK_PC,[29] a model-based processing toolbox available in MATLAB[30] to design our broadband MBP. The results of the minimum variance design are shown in Fig. 5 where we see the enhanced pressure field and the corresponding innovations sequences at each discrete temporal frequency as a function of depth. Again each of the sequences test zero mean and white as demonstrated by the

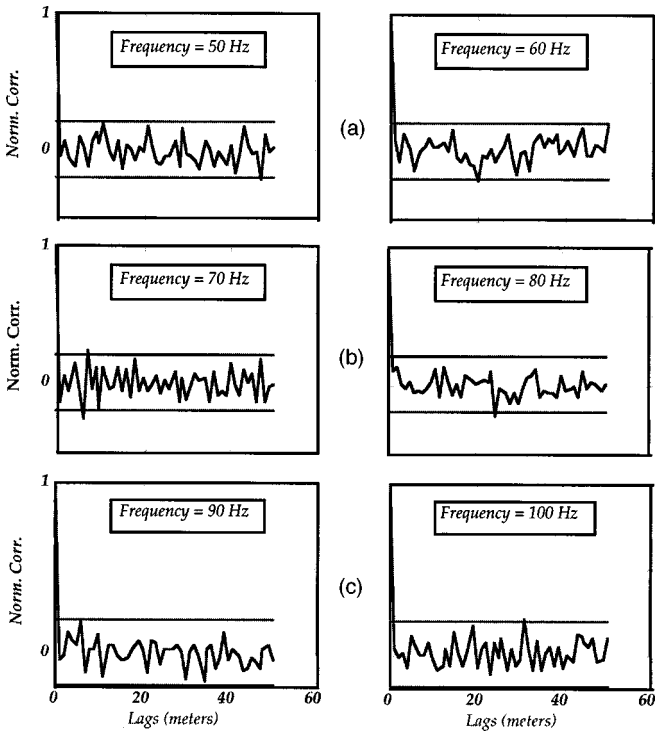

FIG. 6. Broadband model-based processor innovation sequence zero-mean/whiteness testing: (a) 50 Hz (2% out; $0.08<7.5$), 60 Hz (2% out; $0.98<2.5$) innovations whiteness; (b) 70 Hz (3.9% out; $0.66<2.6$), 80 Hz (2% out; $0.70<3.8$) innovations whiteness; (c) 90 Hz (0% out; $0.70<1.9$), 100 Hz (2% out; $1.90<3.4$) innovations whiteness.

whiteness tests in Fig. 6 and the corresponding WSSR statistic lying below the threshold in Fig. 7. Thus we have (as expected) achieved a minimum variance ''broadband'' design. Note that the enhanced pressure-field estimate at each temporal frequency, $\omega_q=\{50,60,70,80,90,100\}$, is governed by the measurement model of Eq. (27) and indicates what the array samples at the particular frequency. The corresponding modal functions extracted from the noisy pressure field are viable estimates and shown in Figs. 7–9 bounding to the ''best'' (minimum error variance) we could hope to achieve for this type of data. In Fig. 8 we observe the ''optimal''

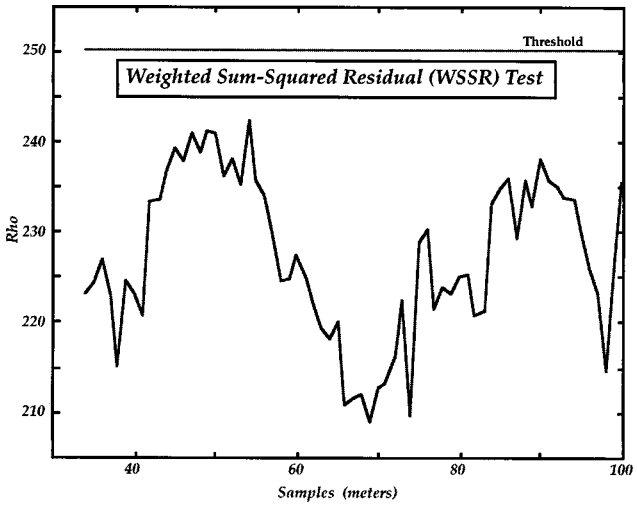

FIG. 7. Innovation sequence whiteness testing: WSSR statistic (window $=35$ samples; threshold$=250$.

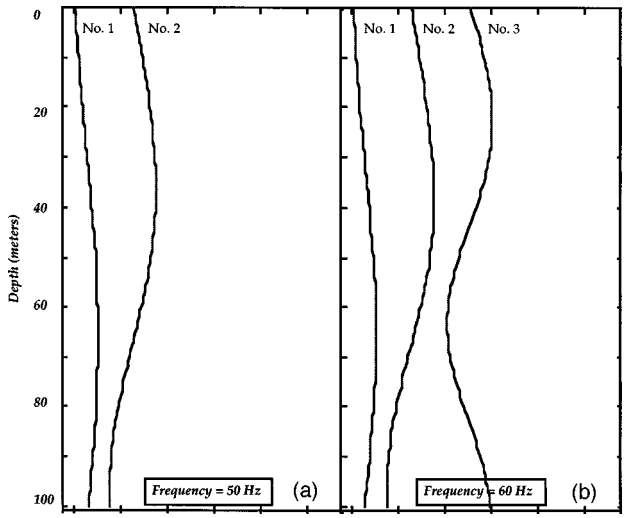

FIG. 8. Broadband MBP modal function estimates: (a) 50-Hz frequency estimate (2 modes); (b) 60-Hz frequency estimate (3 modes).

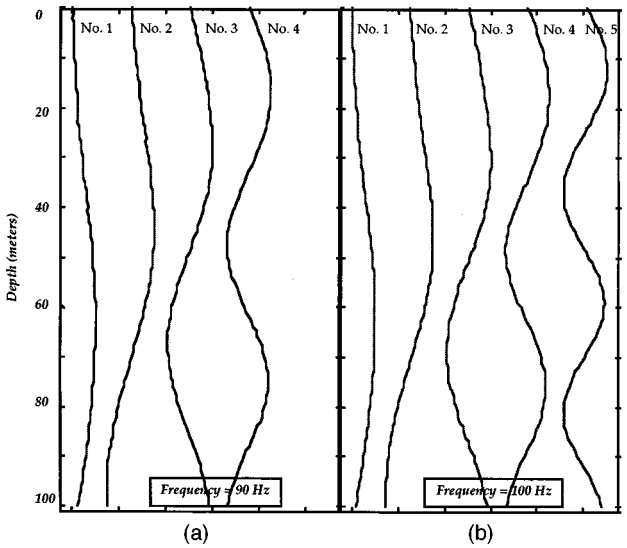

FIG. 10. Broadband MBP modal function estimates: (a) 90-Hz frequency estimate (4 modes); (b) 100-Hz frequency estimate (5 modes).

enhanced modal functions corresponding to the two (2) modes at 50 Hz and three (3) at 60 Hz. The other estimated modes (from the noisy data) at 70 Hz (3 modes), 80 Hz (4 modes), 90 Hz (4 modes), and 100 Hz (5 modes) are also shown in Figs. 9 and 10, respectively. Again note from Eq. (27) that the modal estimates $\hat{\Phi}(z_l,\omega_q)$ along with the measurement model at each temporal frequency, $\mathbf{C}_q^T(r_s,z_s,\omega_q)$ are used to construct the filtered pressure field, $\hat{\mathbf{p}}(z_l,\omega_q)$, at each temporal frequency along with the corresponding innovation of Eq. (62).

The suboptimal (diagonal Kalman gain) processor was also constructed using this same synthesized data set and executed. The results of this run show almost identical estimates (modes), etc. with the individual innovations sequence whiteness slightly less than 95% (greater than 5% outside bounds) indicating its suboptimal but clearly acceptable (in this case) performance. It should also be noted that a MBP based on the *coherent* measurement model of Eq. (25) was constructed and applied to synthesized pressure-field data from SNAP. A minimum variance design was also achieved at the same SNRs discussed in this paper. This completes the application of the broadband model-based processor designed to enhance the pressure-field surface and extract the corresponding modal functions. We summarize our results and discuss future work.

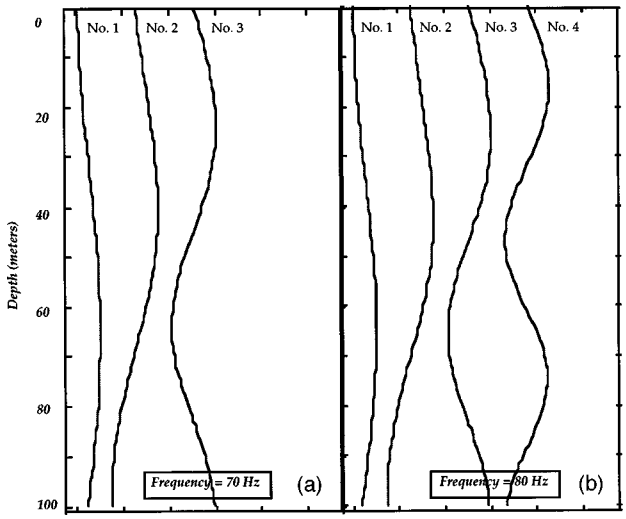

FIG. 9. Broadband MBP modal function estimates: (a) 70-Hz frequency estimate (3 modes); (b) 80-Hz frequency estimate (4 modes).

IV. DISCUSSION

In this paper we have developed both the optimal Bayesian and suboptimal (diagonal gain) solutions to the broadband pressure-field enhancement and modal function extraction (enhancement) problem. Modeling a shallow ocean environment by a normal-mode propagator, we developed the broadband model-based solution. We showed how each of the corresponding temporal frequency bands lead to an underlying state-space structure which is eventually used in the development of a forward propagator for simulation and the optimal processor for enhancement, when the underlying processes are modeled as Gauss–Markov. We developed a shallow ocean simulation using SNAP[19] to solve the associated boundary value problem first and supplied these parameters to implement the MBP. We showed the results of the minimum variance design demonstrating the feasibility of such an approach.

It was also shown how a suboptimal MBP could be constructed by ignoring matrix terms in the corresponding optimal error covariance matrix [Eq. (58)] leading to a block diagonal gain matrix [Eq. (59)] and an inherent parallel processor. Applying this processor to the synthesized data indicates little deterioration in overall MBP performance. We found that the form of the measurement model could only be uniquely defined in terms of the application.

It is of interest to note that the formalism should lead directly to an optimal broadband ''localizer.'' It was shown in Ref. 20 that an adaptive form of the MBP, the model-based identifier (MBID) could be designed to estimate the so-called range-depth functions modal coefficients or modal amplitudes defined by [see Eq. (20)]

$$\beta_m(r_s,z_s,\omega_q)\equiv\mathscr{H}_0(\kappa_r r_s)\phi_m(z_s,\omega_q), \tag{73}$$

along with the modal function estimates, $\{\hat{\phi}_m(z_s,\omega_q)\}$ leading to a nonlinear least-squares localizer. It seems clear that using this same framework, a broadband model-based localizer (MBL) would use an adaptive form of the processor developed in this paper to estimate broadband range-depth functions[31] defined by

$$\beta(r_s,z_s,\omega)=\{\beta_m(r_s,z_s,\omega_q)\},$$
$$m=1,...,M_q:\quad q=1,...,Q, \tag{74}$$

where the position estimates, $(\hat{r}_s,\hat{z}_s)$, are obtained by minimizing a nonlinear least-squares cost function. But this is the subject of future work.

ACKNOWLEDGMENTS

We especially would like to thank Dr. R. Doolittle for motivating this effort and Commander M. Shipley and Dr. J. Tague of the Office of Naval Research (ONR) for their support as well as the continued support of Dr. T. Goldsbury also of ONR.

APPENDIX

In the interest of clarity, we simplify the notation by suppressing the dependence on z and ω and carrying the dependence on the index l in the subscript. Thus $\mathbf{\Phi}(z_l,\omega)\rightarrow\hat{\mathbf{\Phi}}_l$, $\hat{\mathbf{\Phi}}(z_{l|l-1},\omega)\rightarrow\hat{\mathbf{\Phi}}_{l|l-1}$, etc. Also, since the dependence upon l of $\mathbf{R}_{\epsilon\epsilon}(z_l,\omega)$ and $\mathbf{R}_{vv}(z_l,\omega)$ does not play a role in the following derivation, we shall simply designate them as $\mathbf{R}_{\epsilon\epsilon}$ and $\mathbf{R}_{vv}$, respectively.

We begin by with Eq. (41), which we rewrite in our new notation as

$$\Pr(\mathbf{\Phi}_l|\mathbf{P}_l)=\mathscr{C}_l\exp\{-\tfrac{1}{2}[(\mathbf{p}_l-\mathbf{C}^T\mathbf{\Phi}_l)^T\mathbf{R}_{vv}^{-1}(\mathbf{p}_l-\mathbf{C}^T\mathbf{\Phi}_l)$$
$$+(\mathbf{\Phi}_l-\hat{\Phi}_{l|l-1})^T\tilde{\mathbf{P}}_{l|l-1}^{-1}(\mathbf{\Phi}_l-\hat{\Phi}_{l|l-1})$$
$$-(\mathbf{p}_l-\mathbf{C}^T\hat{\Phi}_{l|l-1})^T\mathbf{R}_{\epsilon\epsilon}^{-1}(\mathbf{p}_l-\mathbf{C}^T\hat{\Phi}_{l|l-1})]\}. \tag{A1}$$

Here, $\mathbf{p}_l-\mathbf{C}^T\mathbf{\Phi}_l=\mathbf{v}_l$, the measurement noise, $\mathbf{\Phi}_l-\hat{\Phi}_{l|l-1}=\tilde{\Phi}_l$, the state estimation error, and $\mathbf{p}_l-\mathbf{C}^T\hat{\Phi}_{l|l-1}=\boldsymbol{\epsilon}_l$, the innovation. $\mathbf{R}_{vv}$, $\tilde{\mathbf{P}}$, and $\mathbf{R}_{\epsilon\epsilon}$ are the measurement noise covariance, the state error covariance and the innovations covariance, respectively.

The MAP equation requires the zero gradient condition given by

$$\nabla_\phi\ln\Pr(\mathbf{\Phi}_l|\mathbf{P}_l)\big|_{\mathbf{\Phi}_l=\mathbf{\Phi}_{\mathrm{MAP}}}=0, \tag{A2}$$

where

$$\ln\Pr(\mathbf{\Phi}_l|\mathbf{P}_l)=(\mathbf{p}_l-\mathbf{C}^T\mathbf{\Phi}_l)^T\mathbf{R}_{vv}^{-1}(\mathbf{p}_l-\mathbf{C}^T\mathbf{\Phi}_l)$$
$$+(\mathbf{\Phi}_l-\hat{\Phi}_{l|l-1})^T\tilde{\mathbf{P}}_{l|l-1}^{-1}(\mathbf{\Phi}_l-\hat{\Phi}_{l|l-1})$$
$$-(\mathbf{p}_l-\mathbf{C}^T\hat{\Phi}_{l|l-1})^T\tilde{\mathbf{P}}_{l|l-1}^{-1}(\mathbf{\Phi}_l-\hat{\Phi}_{l|l-1}). \tag{A3}$$

Note that the zero condition of Eq. (A2) allows us to ignore the $\frac{1}{2}$ and $\ln\mathscr{C}_l$ terms. Starting with the first term on the RHS of Eq. (A3), we define $\mathbf{a}\equiv\mathbf{p}_l-\mathbf{C}^T\mathbf{\Phi}_l$, $\mathbf{b}\equiv\mathbf{R}_{vv}^{-1}(\mathbf{p}_l-\mathbf{C}^T\mathbf{\Phi}_l)$, and apply the *chain rule*[18] given by

$$\nabla_\phi(\mathbf{a}^T\mathbf{b})=(\nabla_\phi\mathbf{a}^T)\mathbf{b}+(\nabla_\phi\mathbf{b}^T)\mathbf{a}, \tag{A4}$$

which results in

$$\nabla_\phi(\mathbf{a}^T\mathbf{b})=-2\mathbf{C}\mathbf{R}_{vv}^{-1}(\mathbf{p}_l-\mathbf{C}^T\mathbf{\Phi}_l). \tag{A5}$$

Since the second term of Eq. (A2) is of the same form, we find that

$$\nabla_\phi[(\mathbf{\Phi}_l-\hat{\Phi}_{l|l-1})^T\tilde{\mathbf{P}}_{l|l-1}^{-1}(\mathbf{\Phi}_l-\hat{\Phi}_{l|l-1})]$$
$$=2\tilde{\mathbf{P}}_{l|l-1}^{-1}(\mathbf{\Phi}_l-\hat{\Phi}_{l|l-1}). \tag{A6}$$

The third term of Eq. (A2) is zero, since it does not depend upon $\mathbf{\Phi}$. Substituting these results into Eq. (A2) results in the condition

$$\mathbf{C}\mathbf{R}_{vv}^{-1}(\mathbf{p}_l-\mathbf{C}^T\mathbf{\Phi}_l)-\tilde{\mathbf{P}}_{l|l-1}^{-1}(\mathbf{\Phi}_l-\hat{\Phi}_{l|l-1})=0 \tag{A7}$$

which, upon solving for $\mathbf{\Phi}_l$ results in

$$\mathbf{\Phi}_{\mathrm{MAP}}=\mathbf{\Phi}_l=[\tilde{\mathbf{P}}_{l|l-1}^{-1}+\mathbf{C}\mathbf{R}_{vv}^{-1}\mathbf{C}^T]^{-1}$$
$$\times(\tilde{\mathbf{P}}_{l|l-1}^{-1}\hat{\Phi}_{l|l-1}+\mathbf{C}\mathbf{R}_{vv}^{-1}\mathbf{p}). \tag{A8}$$

Equation (A8) can be simplified with the help of the matrix inversion lemma,[18] which is given by

$$(A+BD^T)^{-1}=A^{-1}-A^{-1}B(I+D^TA^{-1}B)^{-1}D^TA^{-1}. \tag{A9}$$

Defining $A\equiv\tilde{\mathbf{P}}_{l|l-1}^{-1}$, $B\equiv\mathbf{C}\mathbf{R}_{vv}^{-1}$, and setting $D=C$, we find

$$(\tilde{\mathbf{P}}_{l|l-1}^{-1}+\mathbf{C}\mathbf{R}_{vv}^{-1}\mathbf{C}^T)^{-1}=\tilde{\mathbf{P}}_{l|l-1}-\tilde{\mathbf{P}}_{l|l-1}\mathbf{C}\mathbf{R}_{vv}^{-1}(I$$
$$+\mathbf{C}^T\tilde{\mathbf{P}}_{l|l-1}\mathbf{C}\mathbf{R}_{vv}^{-1})^{-1}\mathbf{C}^T\tilde{\mathbf{P}}_{l|l-1}. \tag{A10}$$

By making the observation that the bracketed term on the RHS of Eq. (A10) can be rewritten as

$$(I+\mathbf{C}^T\tilde{\mathbf{P}}_{l|l-1}\mathbf{C}\mathbf{R}_{vv}^{-1})^{-1}=\mathbf{R}_{vv}(\mathbf{R}_{vv}+\mathbf{C}^T\tilde{\mathbf{P}}_{l|l-1}\mathbf{C})^{-1}, \tag{A11}$$

then Eq. (A10) can also be rewritten as

$$(\tilde{\mathbf{P}}_{l|l-1}^{-1}+\mathbf{C}\mathbf{R}_{vv}^{-1}\mathbf{C}^T)^{-1}=\tilde{\mathbf{P}}_{l|l-1}-\tilde{\mathbf{P}}_{l|l-1}\mathbf{C}(\mathbf{R}_{vv}$$
$$+\mathbf{C}^T\tilde{\mathbf{P}}_{l|l-1}\mathbf{C})^{-1}\mathbf{C}^T\tilde{\mathbf{P}}_{l|l-1}, \tag{A12}$$

and from Table I we see that

$$\mathbf{R}_{\epsilon\epsilon}=\mathbf{R}_{vv}+\mathbf{C}^T\tilde{\mathbf{P}}_{l|l-1}\mathbf{C}. \tag{A13}$$

Thus Eq. (A12) becomes

$$(\tilde{\mathbf{P}}_{l|l-1}^{-1}+\mathbf{C}\mathbf{R}_{vv}^{-1}\mathbf{C}^T)^{-1}=\tilde{\mathbf{P}}_{l|l-1}-\tilde{\mathbf{P}}_{l|l-1}\mathbf{C}\mathbf{R}_{\epsilon\epsilon}^{-1}\mathbf{C}^T\tilde{\mathbf{P}}_{l|l-1}$$
$$=(I-\mathbf{K}_l\mathbf{C}^T)\tilde{\mathbf{P}}_{l|l-1}, \tag{A14}$$

where

$$\mathbf{K}_l=\tilde{\mathbf{P}}_{l|l-1}\mathbf{C}\mathbf{R}_{\epsilon\epsilon}^{-1} \tag{A15}$$

is the Kalman gain. Referring again to Table I, we see that the RHS of Eq. (A14) is the corrected error covariance $\tilde{\mathbf{P}}_{l|l}$, so that Eq. (A14) can be written as

$$\tilde{\mathbf{P}}_{l|l}=(\tilde{\mathbf{P}}_{l|l-1}^{-1}+\mathbf{C}\mathbf{R}_{vv}^{-1}\mathbf{C}^T)^{-1}. \tag{A16}$$

Using this to eliminate, the first bracketed term on the RHS of Eq. (A8) gives us

$$\mathbf{\Phi}_{\mathrm{MAP}}=\tilde{\mathbf{P}}_{l|l}(\tilde{\mathbf{P}}_{l|l-1}^{-1}\hat{\Phi}_{l|l-1}+\mathbf{C}\mathbf{R}_{vv}^{-1}\mathbf{p}). \tag{A17}$$

Using Eq. (A16) again to eliminate $\tilde{\mathbf{P}}_{l|l-1}$ from Eq. (A17) results in

$$\mathbf{\Phi}_{\mathrm{MAP}}=\tilde{\mathbf{P}}_{l|l}[(\tilde{\mathbf{P}}_{l|l}^{-1}-\mathbf{C}\mathbf{R}_{vv}^{-1}\mathbf{C}^{T})\hat{\Phi}_{l|l-1}+\mathbf{C}\mathbf{R}_{vv}^{-1}\mathbf{p}], \tag{A18}$$

which after some manipulation, becomes

$$\mathbf{\Phi}_{\mathrm{MAP}}=\hat{\Phi}_{l|l-1}+(\tilde{\mathbf{P}}_{l|l}\mathbf{C}\mathbf{R}_{vv}^{-1})[\mathbf{p}-\mathbf{C}^{T}\hat{\Phi}_{l|l-1}], \tag{A19}$$

or finally,

$$\mathbf{\Phi}_{\mathrm{MAP}}\equiv\hat{\Phi}_{l|l}=\hat{\Phi}_{l|l-1}+\mathbf{K}_{l}\boldsymbol{\epsilon}_{l}. \tag{A20}$$

Here, we have used the fact that $\mathbf{p}-\mathbf{C}^{T}\hat{\Phi}_{l|l-1}=\boldsymbol{\epsilon}_{l}$.

Note that we have identified $\mathbf{K}_{l}$ with $\tilde{\mathbf{P}}_{l|l}\mathbf{C}\mathbf{R}_{vv}^{-1}$ whereas in Eq. (A15), it is given by $\tilde{\mathbf{P}}_{l|l-1}\mathbf{C}\mathbf{R}_{\boldsymbol{\epsilon}\boldsymbol{\epsilon}}^{-1}$, which is its standard definition. The equivalence between the two expressions can be seen as follows. From the usual expression for $\mathbf{K}_{l}$ have

$$\mathbf{K}_{l}=\tilde{\mathbf{P}}_{l|l-1}\mathbf{C}\mathbf{R}_{\boldsymbol{\epsilon}\boldsymbol{\epsilon}}^{-1}=(\tilde{\mathbf{P}}_{l|l})(\tilde{\mathbf{P}}_{l|l}^{-1})\tilde{\mathbf{P}}_{l|l-1}\mathbf{C}\mathbf{R}_{\boldsymbol{\epsilon}\boldsymbol{\epsilon}}^{-1}. \tag{A21}$$

Using Eq. (A6), this expression can be rewritten as

$$\mathbf{K}_{l}=\tilde{\mathbf{P}}_{l|l-1}\mathbf{C}\mathbf{R}_{\boldsymbol{\epsilon}\boldsymbol{\epsilon}}^{-1}=(\tilde{\mathbf{P}}_{l|l})[\mathbf{C}\mathbf{R}_{vv}^{-1}\mathbf{C}^{T}+\tilde{\mathbf{P}}_{l|l-1}^{-1}]\tilde{\mathbf{P}}_{l|l-1}\mathbf{C}\mathbf{R}_{\boldsymbol{\epsilon}\boldsymbol{\epsilon}}^{-1}. \tag{A22}$$

After some straightforward manipulation, we have

$$\mathbf{K}_{l}=\tilde{\mathbf{P}}_{l|l}\mathbf{C}\mathbf{R}_{vv}^{-1}[\mathbf{C}^{T}\tilde{\mathbf{P}}_{l|l-1}\mathbf{C}+\mathbf{R}_{vv}]\mathbf{R}_{\boldsymbol{\epsilon}\boldsymbol{\epsilon}}^{-1}. \tag{A23}$$

But from Table I, we see that

$$\mathbf{C}^{T}\tilde{\mathbf{P}}_{l|l-1}\mathbf{C}+\mathbf{R}_{vv}=\mathbf{R}_{\boldsymbol{\epsilon}\boldsymbol{\epsilon}}, \tag{A24}$$

so that

$$\mathbf{K}_{l}=\tilde{\mathbf{P}}_{l|l}\mathbf{C}\mathbf{R}_{vv}^{-1}. \tag{A25}$$

This completes the derivation.

[1] A. Parvulescu, ''Signal detection in a multipath medium by MESS processing,'' J. Acoust. Soc. Am. **29**, 223–228 (1965).

[2] C. S. Clay, ''Optimum time domain signal transmission and source localization in a waveguide,'' J. Acoust. Soc. Am. **81**, 660–664 (1987).

[3] S. Li and C. S. Clay, ''Optimum time domain signal transmission and source localization in a waveguide: Experiments in an ideal wedge waveguide,'' J. Acoust. Soc. Am. **82**, 1409–1417 (1987).

[4] R. K. Brienzo and W. Hodgkiss, ''Broadband matched-field processing,'' J. Acoust. Soc. Am. **94**, 1409–1417 (1994).

[5] J. P. Hermand and W. I. Roderick, ''Acoustic model-based matched filter processing for fading time dispersive ocean channels: Theory and experiment,'' IEEE J. Ocean Eng. **18**, 447–465 (1993).

[6] A. B. Baggeroer, W. A. Kuperman, and H. Schmidt, ''Matched-field processing: source localization in correlated noise as an optimum parameter estimation problem,'' J. Acoust. Soc. Am. **83**, 571–587 (1988).

[7] E. K. Westwood, ''Broadband matched-field source localization,'' J. Acoust. Soc. Am. **91**, 2777–2789 (1992).

[8] T. C. Yang, ''Broadband source localization and signature estimation,'' J. Acoust. Soc. Am. **93**, 1797–1806 (1993).

[9] I. T. Lu, H. Y. Chen, and P. Voltz, ''A matched-mode processing technique for localizing a transient source in the time domain,'' J. Acoust. Soc. Am. **93**, 1365–1373 (1993).

[10] H. Y. Chen and I. T. Lu, ''Localization of a broadband source using a matched-mode procedure in the time-frequency domain,'' IEEE J. Ocean Eng. **19**, 166–174 (1994).

[11] P. C. Mignerey and S. Finette, ''Multichannel deconvolution of an acoustic transient in an ocean waveguide,'' J. Acoust. Soc. Am. **92**, 351–364 (1992).

[12] A. Tolstoy, *Matched Field Processing for Ocean Acoustics* (World Scientific, Singapore, 1993).

[13] W. M. Carey and W. B. Moseley, ''Space-time processing, environmental-acoustic effects.'' IEEE J. Ocean Eng. **16**, 285–301 (1991).

[14] E. J. Sullivan and D. Middleton, ''Estimation and detection issues in matched-field processing,'' IEEE J. Ocean Eng. **18**, 156–167 (1993).

[15] J. V. Candy and E. J. Sullivan, ''Ocean acoustic signal processing: a model-based approach,'' J. Acoust. Soc. Am. **92**, 3185–3201 (1992).

[16] C. Feuillade, D. Del Balzo, and M. Rowe, ''Environmental mismatch in shallow-water matched-field processing: Geoacoustic parameter variability,'' J. Acoust. Soc. Am. **85**, 2354–2364 (1989).

[17] R. Hamson and R. Heitmeyer, ''Environmental and system effects on source localization in shallow water by the matched-field processing of a vertical array,'' J. Acoust. Soc. Am. **86**, 1950–1959 (1989).

[18] J. V. Candy and E. J. Sullivan, ''Model-based identification an adaptive approach to ocean acoustic signal processing,'' IEEE J. Ocean Eng. **21**, 240–252 (1996).

[19] F. B. Jensen, W. A. Kuperman, M. B. Porter, and H. Schmidt, *Computational Ocean Acoustics* (AIP Press, New York, 1994).

[20] A. R. Robinson and D. Lee, *Oceanography and Acoustics* (AIP Press, New York, 1994).

[21] J. V. Candy, *Signal Processing: The Model-Based Approach* (McGraw-Hill, New York, 1986).

[22] F. B. Jensen and M. C. Ferla, ''SNAP: the SACLANTCEN normal-mode acoustic propagation model,'' SACLANTCEN Report, **SM-121**, SACLANT Undersea Research Centre, La Spezia, Italy (1982).

[23] E. J. Sullivan and K. Rameau, ''Passive ranging as an inverse problem: a sensitivity study,'' SACLANTCEN Report, **SR-118**, SACLANT Undersea Research Centre, La Spezia, Italy (1987).

[24] R. D. Doolittle, A. Tolstoy, and E. J. Sullivan (Eds.), ''Special issue on detection and estimation in matched-field processing,'' IEEE J. Ocean Eng. **18**, 153–357 (1993).

[25] A. M. Richardson and L. W. Nolte, ''A posteriori probability source localization in an uncertain sound speed, deep ocean environment,'' J. Acoust. Soc. Am. **89**, 2280–2284 (1991).

[26] W. A. Kuperman, M. D. Collins, J. S. Perkins, and N. R. Davis, ''Optimum time domain beam-forming with simulated annealing including application of *a priori* information,'' J. Acoust. Soc. Am. **88**, 1802–1810 (1990).

[27] J. L. Krolik, ''Matched-field minimum variance beamforming in a random ocean channel,'' J. Acoust. Soc. Am. **92**, 1408–1419 (1992).

[28] A. Jazwinski, *Stochastic Processes and Filtering Theory* (Academic, New York, 1970).

[29] J. V. Candy and P. M. Candy, ''SSPACK_PC: A model-based signal processing package on personal computers,'' DSP Applications **2**, 33–42 (1993).

[30] MATLAB, *MATLAB Reference Manual* (MathWorks, Boston, 1993).

[31] J. V. Candy and E. J. Sullivan, ''Passive localization in ocean acoustics: A model-based approach,'' J. Acoust. Soc. Am. **98**, 1455–1471 (1995).

A high-resolution algorithm for complex spectrum search

I-Tai Lu,[a] Robert C. Qiu,[b] and Jaeyoung Kwak
Weber Research Institute/Department of Electrical Engineering, Polytechnic University, Route 110, Farmingdale, New York 11735

(Received 14 August 1996; revised 8 December 1997; accepted 15 February 1998)

The principal aim of this work is to estimate, or to approximate, the complex k-space spectrum of the wave field arriving on a linear array. First, using linear approximation, the location-dependent effect of the wave field magnitudes is modeled as an extra ''loss'' factor in the complex spectral variable. This complex spectrum model may provide a better description of the physical process and require less sensor elements than the real spectrum model because of the additional degree of freedom provided by the ''loss'' factor. A high-resolution algorithm combining the singular value decomposition method and the eigen-matrix pencil method is then employed to find the complex spectra representing the incoming real spectrum and the location dependent factors of multipath and multimode arrivals. Five key features (noise immunity, robustness, resolution, accuracy, and physical insight) of the proposed algorithm are studied using numerical examples. © *1998 Acoustical Society of America.* [S0001-4966(98)00907-2]

PACS numbers: 43.60.Gk [JLK]

INTRODUCTION

A linear receiving array is commonly employed to discern and to evaluate the arriving angles of multi-path or multi-mode arrivals. In conventional approaches, the total field p received by the linear array is expressed as a sum of noiseless incident waves plus the additive noise w:

$$p(x)=p'(x)+w(x), \quad p'(x)\equiv\sum_{m=1}^{M} c_m \exp(i\eta_m x), \quad (1)$$

where x denotes the coordinates of receivers along the linear array, p' is expressed in terms of a sum of M exponentials, and M is the total number of arrivals. For the mth arrival, η_m is phase constant along the x coordinate and c_m is the amplitude. Various spectrum resolving methods can be used to estimate η_m and c_m of relevant arrivals while the arriving spectra will be derived from the estimated η_m.

However, there are two deficiencies in those conventional approaches for applications in underwater environments. First, the amplitude c_m is assumed to be x independent. This assumption is usually not very practical because the gains or locations of different receivers may not be well calibrated,[1] the incoming waves may be beam-like fields,[2] the incoming wavefronts may not be on plane surfaces,[1,2] there may be more than two waves arriving with very close incoming directions but not totally in phase,[3] etc. All these practical factors can cause c_m to be dependent on x. Second, the spectrum η_m is assumed to be real which is not always true. For example, consider the case of a horizontal array in an underwater waveguide where p denotes the total acoustic pressure, x is the range coordinate, and η_m and c_m are the modal eigenvalues and amplitudes, respectively. If the waveguide is lossy, the modal eigenvalue η_m will be complex. To remedy these two deficiencies, we first extend the conventional model to incorporate the x-dependent effects and the loss mechanism into the model. Let $c_m=f_m(x)$ and $\eta_m=-i\alpha_{1m}+\beta_m$, where α_{1m} accounts for the loss mechanisms and $f_m(x)$ accounts for the x dependency of c_m. Noting that $f_m=\exp[\ln(f_m(x))]$ and $\ln(1+\epsilon)\approx\epsilon$ if $|\epsilon|\ll 1$, the received field p can still be expressed in the same form as the above equation. Choosing a reference coordinate x_0,

$$p(x)\approx\sum_{m=1}^{M} b_m \exp(ik_m x)+w(x),$$

$$k_m\equiv\beta_m-i\alpha_m, \quad b_m=f_m(x_0)\exp(-\alpha_{2m}x_0), \quad (2)$$

$$\alpha_m=\alpha_{1m}+\alpha_{2m}, \quad \alpha_{2m}\equiv[\partial f_m(x_0)/\partial x_0]/f_m(x_0).$$

Here, $f_m(x)$ is approximated by a linear function $f_m(x_0)+[\partial f_m(x_0)/\partial x_0](x-x_0)$ which, in turn, is approximated by the exponential function $f_m(x_0)\exp[\alpha_{2m}(x-x_0)]$. The linear approximation implicitly assumed that the signal (on location dependent variations) is narrow band. In the real-spectrum model in (1), each arriving field strength is approximated by a constant. If there are many arrivals, the *total sum* of complex-spectrum arrivals in (2) may not necessarily match the measured data better than the *total sum* of real-spectrum arrivals in (1). However, if any of the incoming arrivals does not have a constant amplitude along the receiving array, the model in (2) can definitely provide better *insight* of the physical mechanism. Moreover, the variable α_m in (2) depicts an additional degree of freedom which is absent in (1). This feature implies that the model in (2) may have the advantage of reducing the the required number of sensors in a detection system.

Based on (2), the problem of estimating the complex spectrum reduces to estimation of the complex poles in a linear system. In fact the work on linear antenna arrays is equivalent to existing techniques of pole estimation for discrete-time systems perturbed by noise, with discrete time increment replaced by the uniform spatial separation on a linear array. Having set up the model, we can then use a

[a]Electronic mail: itailu@rama.poly.edu
[b]Robert C. Qiu is currently with Bell Laboratories, Lucent Technologies, Room 2B3F, 450 Clark Drive, Mt. Olive, NJ 07828.

spectral estimation algorithm to evaluate the complex amplitudes b_m and the complex exponents ik_m. Although there exist many conventional approaches,[4–9] none can work satisfactorily. The spectral resolution of the fast Fourier transform (FFT)-based approaches is limited by the array length which is relatively fixed by the experimental setup. Periodogram, Black-Tukey, and MUltiple SIgnal Classification methods cannot provide the real parts α_m of the complex exponents ik_m. Prony-based algorithms can only work in conditions with high signal-to-noise ratios. The AutoRegressive and AutoRegressive Moving Average series usually have trouble in relating their estimated results directly to the physical unknowns b_m and k_m. To remedy these difficulties, we apply a newly developed modified eigen-matrix pencil which is originally developed for identifying scattering centers for target identification[9,10] and is used for the wireless channel modeling more recently.[11,12] This new algorithm consists of three steps. First, the singular value decomposition (SVD) method[13] is employed to filter out the white noise. Secondly the eigen-matrix pencil method is used to identify the complex damped exponents. Finally, the complex amplitudes can be obtained by a least-square approach. The eigen-matrix pencil method is similar to the matrix pencil by Hua and Sarkar,[14] due to the fact that both methods use a matrix pencil to find the system poles in the transformed domain. However, the matrix pencil of the former is based on the principal eigenvectors of the Hermitian data matrix, while the matrix pencil of the latter is directly based on the data to be processed.

The Cramer–Rao lower bounds[15] are used as a benchmark to study the algorithm performance. It is found that unlike its conventional counterpart, our approach, the SVD eigen-matrix pencil method, is statistically efficient and almost ''optimal'' in the sense of the smallest variance. The underlying idea is to establish a rank properly satisfied by the noise-free signal matrices and use it to approximate noisy data via rank reduction. This approach is well known.[5] For the real signals the SVD is equivalent to the conventional eigen value decomposition and thus the role of SVD is negligible. However for complex signals SVD improves considerably the accuracy and statistical properties of the eigen-matrix method. The fundamental reason to explain why this prefitering step works is that the signal space spanned by the M principal singular vectors obtained using the singular value decoposition (SVD) is different (for complex signals) from that spanned by the M principal singular vectors obtained from the eigen value decoposition. For real signals, it can be proven that these two signal spaces are identical.

I. METHODOLOGY

Let $p[n]$ denote the acoustic pressure measured by the nth receiver located at $x=nd+x_0$, where x_0 is the reference location and d is the distance between two adjacent receivers and $n=1,2,...,2N+1$. Equation (2) becomes

$$p[n]=\sum_{m=1}^{M} a_m z_m^n + w[n],$$
$$a_m=b_m e^{ik_m x_0}, \quad z_m=e^{ik_m d}, \quad m=1,2,...,M. \quad (3)$$

A. Hankel data matrix decomposition

Now form a square Hankel data matrix $\mathbf{P}$ of size $(N+1)\times(N+1)$ with $N\geqslant M$, and $\mathbf{P}$ is defined as

$$\mathbf{P}=\begin{bmatrix} p[0] & p[1] & p[2] & \cdots & p[N] \\ p[1] & p[2] & p[3] & \cdots & p[N+1] \\ \cdots & \cdots & \cdots & & \cdots \\ \cdots & \cdots & \cdots & & \cdots \\ \cdots & \cdots & \cdots & & \cdots \\ p[N] & p[N+1] & p[N+2] & \cdots & p[2N] \end{bmatrix} \quad (4)$$

where the $2N+1$ data samples are used. The Hankel matrix $\mathbf{P}$ has equal elements along lines perpendicular to the principal diagonal.[16] We also know that a square Hankel matrix is a special case of a Hermitian matrix.[16]

Define $\mathbf{W}$ as the Hankel noise matrix constructed from $w[n]$ in the same way as in (4). The Hankel data matrix $\mathbf{P}$ can then be decomposed as

$$\mathbf{P}=\mathbf{S}_N\mathbf{A}\mathbf{S}_N^T+\mathbf{W}, \quad (5)$$

where the Vandermonde matrix $\mathbf{S}_N$ has the structure

$$\mathbf{S}_N=\begin{bmatrix} 1 & 1 & \cdots & 1 \\ z_1 & z_2 & \cdots & z_M \\ \cdots & \cdots & & \cdots \\ \cdots & \cdots & & \cdots \\ \cdots & \cdots & & \cdots \\ z_1^N & z_2^N & \cdots & z_M^N \end{bmatrix} \quad (6)$$

and $\mathbf{A}$ is a $M\times M$ diagonal matrix with the mth diagonal element given by a_m, $m=1,2,...,M$. Here superscript T in (5) represents the matrix transpose. Both matrices $\mathbf{S}_N$ and $\mathbf{A}$ are of rank M. Thus, for the noiseless case, the $N\times N$ matrix $\mathbf{P}$ is also of rank M and has $N-M$ zero eigenvalues among the total N eigenvalues.

B. Rank-reducing filtering through singular value decomposition

With noise, the matrix $\mathbf{P}$ is of rank N and the task of spectrum estimation becomes very difficult. Fortunately, we can employ the singular value decomposition algorithm to reduce noise strength in many practical occasions. Write the matrix $\mathbf{P}$ as

$$\mathbf{P}=\sum_{n=1}^{N+1} \sigma_n \mathbf{u}_n \mathbf{v}_n^H, \quad (7)$$

where the superscript H denotes matrix Hermitian. Here, σ_n, $\mathbf{u}_n$, and $\mathbf{v}_n$ are the nth singular value, left singular vector, and the right singular vector of the matrix $\mathbf{P}$, respectively.[12] In other words,

$$\mathbf{P}^H\mathbf{P}\mathbf{v}_n=\sigma_n^2\mathbf{v}_n, \quad \mathbf{P}\mathbf{P}^H\mathbf{u}_n=\sigma_n^2\mathbf{u}_n, \quad n=1,2,...,N+1. \quad (8)$$

TABLE I. Estimation of the three fundamental waves and the first leaky bending wave of an infinite circular cylindrical thin shell.

Parameters	Given	Noiseless	SNR=30	SNR=15
α_1	−5.807*E*-4	−5.807*E*-4	−0.283 848	−2.56 197
α_2	0.0	−4*E*-14	1.924 702	−0.23 045
α_3	0.0	−1.36-13	−1.029 932	−6.49 755
α_4	−8.6 959 203	−8.6 959 203	−9.356 470	−1.491 432
β_1	1.1 586 599	1.1 586 599	2.01 696	4.61 486
β_2	1.9 744 053	1.9 744 053	10.845 679	23.730
β_3	9.1 418 616	9.1 418 616	−12.20 365	2.37 801
β_4	0.4 750 813	0.4 750 813	1.04 364	−20.6571
$\lvert b_1\rvert$	1.0	1.0	1.98 222	1.97 286
$\lvert b_2\rvert$	0.8	0.8	0.43 009	1.48 426
$\lvert b_3\rvert$	0.6	0.6	0.18 922	0.88 410
$\lvert b_4\rvert$	0.2	0.2	0.13 845	0.38 338
$\angle b_1$	0.0	1.9363*E*-12	−4.91567*E*-4	−0.31 048
$\angle b_2$	0.0	−2.4128*E*-12	−0.12 538	−0.53 887
$\angle b_3$	0.0	−1.2123*E*-14	0.55 829	1.21 599
$\angle b_4$	0.0	−1.6936*E*-14	0.362 381	1.47 979

Arrange the positive singular values σ_n $(n=1,2...,N+1)$ with decreasing order. Assume the signal strength is sufficiently strong. Then, among the $N+1$ pairs of left and right eigenvectors, there are only M pairs (with M largest singular values) primarily spanning the M signal space.[12,16] The other $N-M+1$ pairs primarily span the noise space. Thus, we can replace the matrix $\mathbf{P}$ through SVD with its rank-M approximation matrix $\mathbf{P}_0$:

$$\mathbf{P}_0 \equiv \sum_{m=1}^{M} \sigma_m \mathbf{u}_m \mathbf{v}_m^H \approx \mathbf{S}_N \mathbf{A} \mathbf{S}_N^T. \tag{9}$$

The rank-M approximation reduces the noise and therefore enhances the SNR. The noise energy is given by the Frobenius norm of the difference matrix $\mathbf{P}-\mathbf{P}_0$ defined as $\|\mathbf{P}-\mathbf{P}_0\|_F=\Sigma\sigma_m^2$, where $m=M+1$, $M+2$,...,$N+1$.

C. Principal eigenvectors

Let λ_n be the nth eigenvalue and e_n be the nth eigenvector of $\mathbf{P}_0$ where $n=1,2,...,N+1$. Since $\mathbf{P}_0$ is a $N+1$ by $N+1$ matrix but is with rank M, λ_n is 0 for $n=M+1$, $M+2$,...,$N+1$ and $\mathbf{e}_n$ is a $(N+1)$ by 1 column vector. Construct a M by $(N+1)$ matrix $\mathbf{E}=[\mathbf{e}_1,\mathbf{e}_2,\ldots,\mathbf{e}_M]$ from the M principle eigenvectors. Then

$$\mathbf{P}_0\mathbf{E}=\mathbf{E}\mathbf{\Lambda}\approx\mathbf{S}_N\mathbf{A}\mathbf{S}_N^T\mathbf{E}, \tag{10}$$

where $\mathbf{\Lambda}$ is a M by M diagonal matrix with λ_n as its nth diagonal element. Therefore, we can express $\mathbf{E}$ as

$$\mathbf{E}\equiv\mathbf{S}_N\mathbf{D}, \quad \mathbf{D}\approx\mathbf{A}\mathbf{S}_N^T\mathbf{E}\mathbf{\Lambda}^{-1}, \tag{11}$$

where $\mathbf{D}$ is $\mathbf{M}$ by M matrix with rank M.

D. Generalized eigenvalues of the matrix pencil

Next, we form matrix $\mathbf{F}_1$ using the first L rows of $\mathbf{E}$ ranging from the first row to the Lth row, and $\mathbf{F}_2$ using the next L rows of $\mathbf{E}$ ranging from the second row to the $(L+1)$th row. Here L is chosen to be larger than M. Then, $\mathbf{F}_1=\mathbf{S}_L\mathbf{D}$ and $\mathbf{F}_2=\mathbf{S}_L\mathbf{Z}\mathbf{D}$, where $\mathbf{S}_L$ is defined in (6) and $\mathbf{Z}$ is a M by M diagonal matrix with z_m as its mth element, $m=1,2,...,M$. The generalized eigenvalue of the matrix pencil $\{\mathbf{F}_1^H\mathbf{F}_1,\mathbf{F}_1^H\mathbf{F}_2\}$ is defined by the complex roots of the characteristic polynomial:

$$\det\{(\lambda\mathbf{F}_1^H\mathbf{F}_1)-(\mathbf{F}_1^H\mathbf{F}_2)\}=\det\{(\mathbf{F}_1^H\mathbf{S}_L)(\lambda\mathbf{I}_M-\mathbf{Z})\mathbf{D}\}$$
$$=\prod_{m=1}^{M}(\lambda-z_m)=0, \tag{12}$$

where I_M is a M-dimensional identity matrix and ''det'' denotes the determinant of the matrix. Equation (12) is valid when the eigenvalues z_m are distinct. By solving (12), the desired complex spectra $k_m=(-i\ln z_m)/d$ where $m=1,2,...,M$.

E. Complex amplitudes

By defining vectors $\mathbf{a}=[a_1,a_2,\ldots,a_M]^T$, $\mathbf{p}=[p[0],p[1],\ldots,p[2N]]^T$, and $\mathbf{w}=[w[0],w[1],...,w[2N]]^T$, Eq. (3) can be expressed in matrix form

$$\mathbf{p}=\mathbf{S}_{2N}\mathbf{a}+\mathbf{w}, \tag{13}$$

where Vandermonde matrix $\mathbf{S}_{2N}$ is defined in (6). The least-square solution of (13) leads to the complex amplitudes $\mathbf{a}$ as

$$\mathbf{a}=(\mathbf{S}_{2N}^H\mathbf{S}_{2N})^{-1}\mathbf{S}_{2N}^H\mathbf{p}. \tag{14}$$

II. EXAMPLES OF COMPLEX SPECTRUM

Let $\mathbf{r}_n=(x_n,z_n)$ be the coordinate of the nth element of a linear receiving array where $z_n=0$, and $x_n=(n-N-1)d$ for $n=1,2,...,2N+1$. Here, d is the distance between two adjacent array elements and $2N+1$ is the total number of the array elements. The reference x_0 in Eq. (2) is chosen to be zero. The complex spectrum formulation is first applied to a waveguide supporting both trapped and leaky modes. Consider a fluid-loaded infinite circular cylindrical shell which supports three fundamental waves: compressional, torsional, and bending. In our calculation, we also include the first leaky bending wave which is relevant for near zone testing. The complex wave numbers $(\beta-i\alpha)$ and the complex excitations $(|b|\exp I\angle b)$ of these four waves are shown in the

second column of Table I. Here, no azimuthal variation has been assumed. One can refer to Table V of Ref. 17 for detailed structure parameters which are used for deriving these numerical values. Note that the bending wave has a zero α and a very large β (9.1418616) which is much larger than the wave number of the surrounding fluid. Thus, the energy of the bending wave is primarily confined in the shell. The torsional wave has a zero α and a nonzero β (1.9744053) which is smaller than the wavenumber of the surrounding fluid. However, the energy of the torsional wave is solely confined in the shell because the shear motion does not interact with the fluid when the azimuthal variation is zero. The compressional wave is a leaky mode because of the nonzero α ($-5.807E$-4) and the small value β (1.1586599). The first leaky bending wave is a very strong leaky wave because it has an α with very large negative value (-8.6959203). In our numerical simulation, we substitute these parameters into (2) to generate the received field $p(x)$ and then use the SVD eigen-matrix pencil method to perform the spectral estimation. The estimated results using $d=0.11$ and $N=5$, shown in the third column of Table I, are very accurate. When the noise is present, the spectral estimation becomes very difficult because of the co-existence of both large β and negative large α.

The second example of complex spectrum formulation is when the wavefront is not plane. Consider the field excited by a point source located at $\mathbf{r}_s=(x_s,z_s)$ with unit strength. Thus, the field received at the nth receiver is

$$p(x_n)=\frac{e^{ikr}}{kr}, \quad r=[(x_s-x_n)^2+z_s^2]^{1/2}, \tag{15}$$

where k is the wave number in the medium. Equation (15) can be formally written as

$$p(x_n)\equiv f(x_n)e^{i\beta(x_s-x_n)}, \quad f(x_n)\equiv p(x_n)e^{-i\beta(x_s-x_n)}, \tag{16}$$

where the phase constant β is chosen such that $f(x_n)$ is a slowly varying function with respect to the exponential term. For the two special cases,

$$\begin{aligned} &\beta\approx k, \quad r\approx|x_s x_s|+\frac{z_s^2}{2(x_s-x_n)}, \quad \text{if } |x_s-x_n|\gg|z_s|, \\ &\beta\approx k/2|z_s|, \quad r\approx z_s+\frac{|x_s-x_n|^2}{2z_s}, \quad \text{if } |x_s-x_n|\ll|z_s|. \end{aligned} \tag{17}$$

From (16), the complex phase constant k_m and amplitude b_m in Eq. (2) can be obtained approximately following the procedure shown in (2). In numerical simulations, we consider two source locations $\mathbf{r}_{s1}=(50d,5d)$ and $\mathbf{r}_{s2}=(2d,30d)$, where $d=\lambda/4$ and $k=2\pi/\lambda$. We use $N=5$ and $d=0.11$. For the case with $\mathbf{r}_{s1}$ (see Fig. 1), $|x_s-x_n|\gg|z_s|$. But for the case with $\mathbf{r}_{s2}$ (see Fig. 2), $|x_s-x_n|\ll|z_s|$. In Figs. 1 and 2, the top, middle, and bottom figures represent SNR$=\infty$, 30 dB and 15 dB, respectively. The curves denoted by *, ○, and + represent the noise-free incident field $p'(x)$ in (1), the noise contaminated incident field $p(x)$ in (1), and the reproduced in-

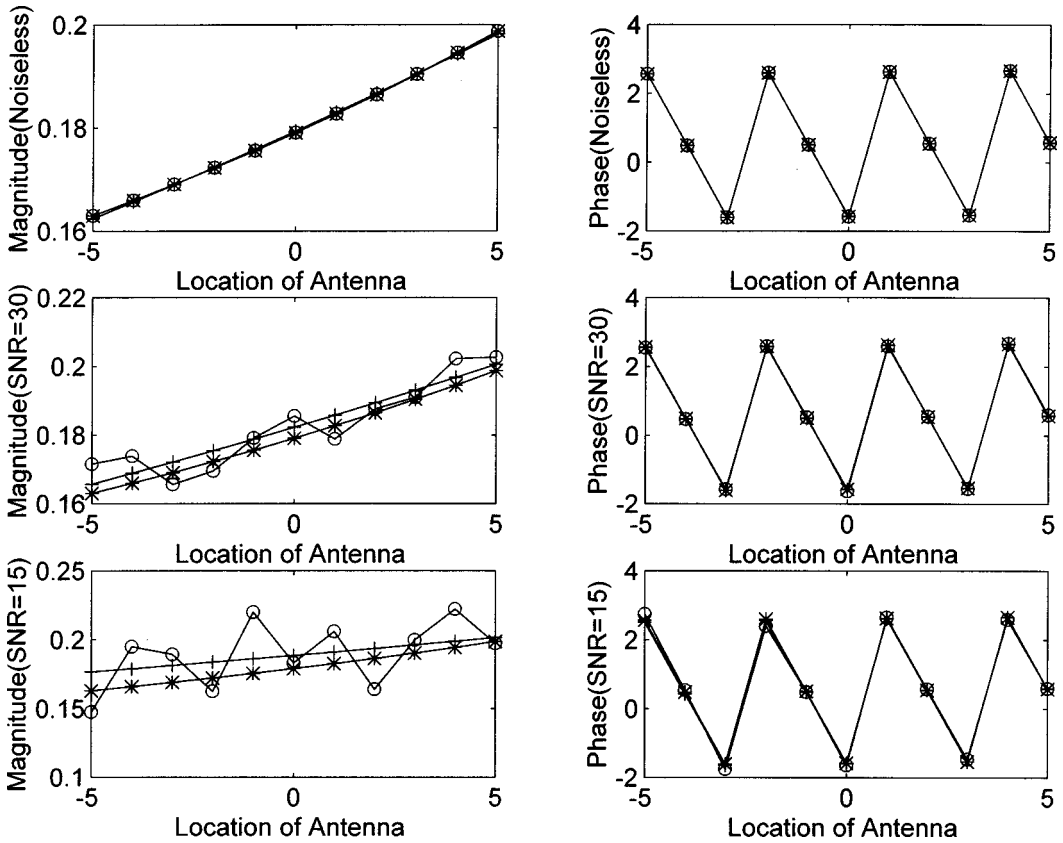

FIG. 1. A point source located at $(50d,5d)$. $N=5$ and $d=0.11$. Curves with *, ○, and + denote the noiseless incident field, noisy incident field, and simulated results.

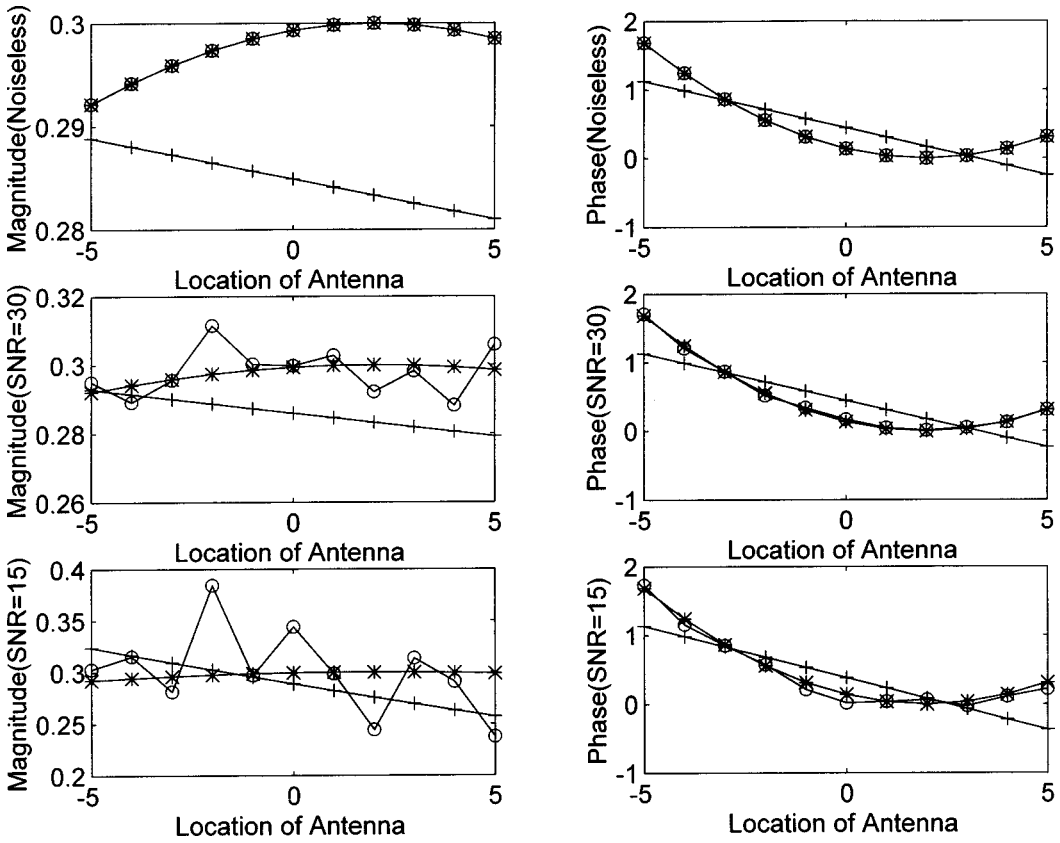

FIG. 2. A point source located at $(2d,30d)$. $N=5$ and $d=0.11$. Curves with *, ○, and + denote the noiseless incident field, noisy incident field, and simulated results.

cident field using estimated complex wave numbers and amplitudes in (12)–(14), respectively. In Fig. 1, the phase and the amplitude of the noiseless incident field are almost linear (see the two top figures). Thus, the incident field can be conveniently described by the complex spectrum model. When the noise increases, the complex spectrum model still gives very good linear approximations to the fluctuated magnitudes and phases. The estimated results tend to ignore the random fluctuation due to noise and stay close to the mean value. In Fig. 2, the phase and the amplitude of the noiseless incident field are not linear. Thus, it is not very convenient to use the complex spectrum model. Nevertheless, the complex spectrum model gives a good linear approximation to the phase. The maximum error in the magnitude is less than 7%. When the noise increases, the complex spectrum model still gives very good linear approximations to phases. It is interesting to see that the error of magnitudes remains controllable even when noise increases.

The third example of complex spectrum formulation is for beam incidence where the incident field strength along the wavefront is not constant. Here, we use a complex source point technique to generate a Gaussian beam. Consider a complex source location $r_s'=(x_s+i\eta\cos\xi, z_s+i\eta\sin\xi)$ where $\mathbf{r}_s=(x_s,z_s)$ is the center of beam waist, η is the beamwidth parameter, and ξ is the beam propagation angle (see Ref. 18). The field received at the sensor becomes

$$p(x_n)=\frac{e^{ik\hat{r}-k\eta}}{k\hat{r}},$$
$$\hat{r}\equiv[(x_s+i\eta\cos\xi-x_n)^2+(z_s+i\eta\sin\xi)^2]^{1/2}, \tag{18}$$

where $\exp(-k\eta)$ is a normalization constant and

$$\hat{r}\approx(r+i\eta)+\frac{2i\eta r[1-\cos(\zeta-\xi)]}{r+i\eta},$$
$$\zeta\equiv\cos^{-1}\frac{x_s-x_n}{r},\quad \text{if } r>0,\ \eta>0,\ \text{and } \zeta\approx\xi, \tag{19}$$

where the real distance r is defined in (15). Here, the condition $\zeta\approx\xi$ denotes that the receiver is in the paraxial region of the beam, i.e., the receiver is near the beam axis. The complex spectrum model of a beam incident field can be obtained by substituting (18) into (16) and by employing (2). The numerical simulation is shown in Figs. 3 and 4 with beam waist location $\mathbf{r}_{s1}=(0,50d)$ and $\mathbf{r}_{s2}=(50d,50d)$, respectively. Note that $N=11$, $d=\lambda/4=0.11$, and $k=2\pi/\lambda$. In both cases, the beam width parameter $\eta=100d$. The beam incident angle ξ is $\pi/2$ and $\pi/4$ for the cases with $\mathbf{r}_{s1}$ and $\mathbf{r}_{s2}$, respectively. The arrangement of numerical results is similar to those in Figs. 1 and 2 where the top, middle, and bottom figures represent SNR=∞, 30 dB, and 15 dB, respectively. The curves denoted by *, ○, and + represent the noise-free incident field $p'(x)$ in (1), the noise contaminated incident

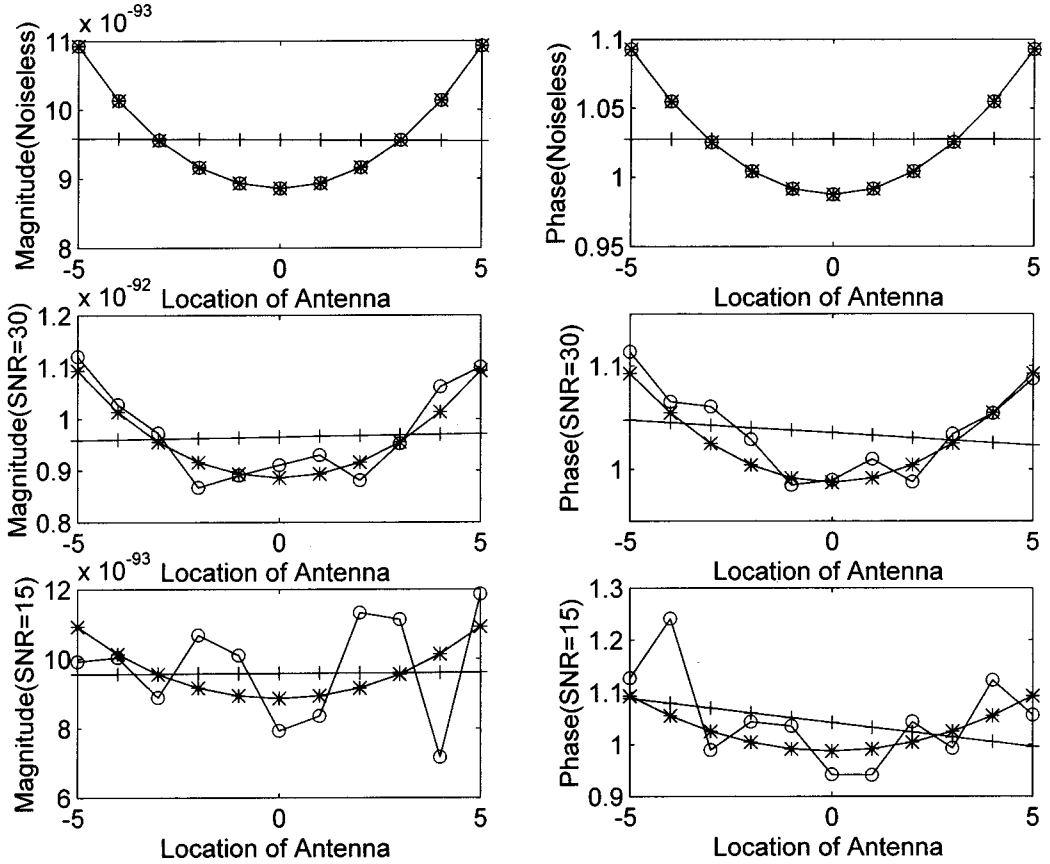

FIG. 3. The beam waist center is located at $(0,50d)$. The beam angle $\theta=\pi/2$. The beamwidth parameter $\eta=100d$. Curves with *, ○, and + denote the noiseless incident field, noisy incident field, and simulated results.

field $p(x)$ in (1), and the reproduced results using estimated complex wave numbers and amplitudes in (12)–(14), respectively. The noiseless incident field in Fig. 3 is symmetric with respect to the z axis. The simulated results using estimated complex spectra and amplitudes remains symmetric. When the noise increases, the simulated results are no longer symmetric but provide the best linear approximations to the noise contaminated field. In Fig. 4, the phase of the received fields are almost linear and, therefore, the simulated results give very good approximations for both noiseless and noisy situations. Examples in Figs. 1–4 show that the complex spectrum model provides the best linear approximation for the magnitude of an incoming ray with either zero or nonzero slope where the conventional real spectrum model can only provide the approximation result with a constant magnitude (i.e., a linear approximation with zero slope).

In the fourth example, we consider two plane waves with close incident angles:

$$p(x_n)=b_1e^{i\beta_1x_n}+b_2^{i\beta_2x_n}\equiv f(x_n)e^{i\beta_1x_n},$$
$$f(x_n)\approx b_1\left(1+\frac{b_2}{b_1}\,e^{i(\beta_2-\beta_1)x_n}\right). \tag{20}$$

If β_1 is close to β_2, we can use a plane wave with complex spectrum to represent these two plane waves. The estimated complex spectra and amplitudes are shown in Table II using $N=5$ and $d=0.11$. The second column gives the exact values of the two incoming plane waves with real spectrums (i.e., the two α's are equal to zero). Note that the difference of the two β's is very small. The third column shows the estimated results under the noise free condition. The numerical error is extremely small. The fourth and fifth columns show the estimated results of two noisy situations when the SNR are equal to 30 dB and 15 dB, respectively. In both situations, the results indicate only one dominant complex spectrum ray because $|b_1|\gg|b_2|$ and α_1 is nonzero. The estimated β_1 is quite accurate. The resulting complex spectrum ray is a combination of the two incident real spectrum rays. We conclude that rays with close incident angles are not resolvable in noisy environments. Figure 5 shows the exact incident fields and the simulated data using estimated spectra and amplitudes. Legends and arrangements of the graphs are the same as those in Figs. 1–4. In all situations, it is demonstrated again that the complex spectrum model tends to ignore the random fluctuation of the noise and provides the best linear approximation to the incident results. We consider the other case of two incident plane waves with a larger separation of the two incident angles. However, we purposely assume only one incident wave during the spectral estimation where $N=5$ and $d=0.11$. The exact input parameters and the estimated results are shown in Table III. The resulting complex spectrum ray is a combination of the two incident real spectrum rays. It is remarkable that the estimated results are insensitive to the increase of noise. The simulated results using the estimated parameters are shown in Fig. 6. Again, the complex spectrum model ignores the random fluctuation of the noise and provides the best linear

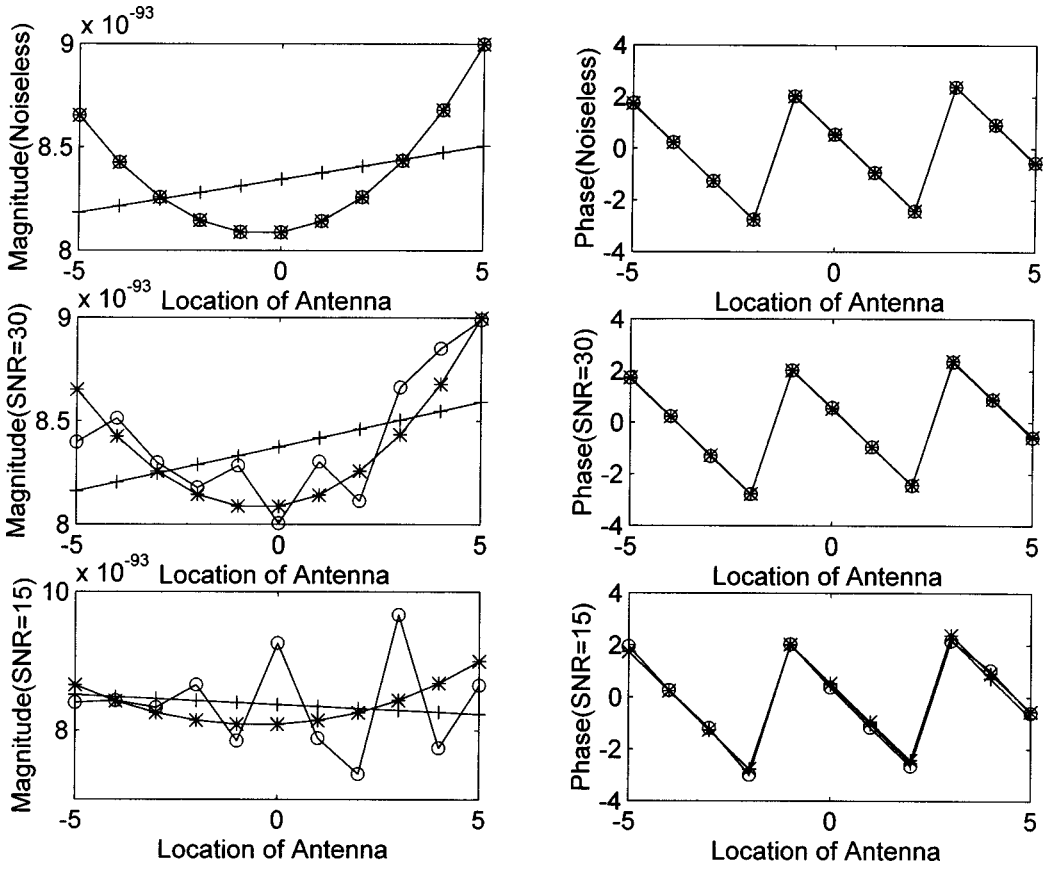

FIG. 4. The beam waist center is located at $(50d,50d)$. The beam angle $\theta=\pi/4$. The beamwidth parameter $\eta=100d$. Curves with *, ○, and + denote the noiseless incident field, noisy incident field, and simulated results.

approximation. From these two examples, we conclude that the complex spectrum model is more robust than the real spectrum model when two plane waves arriving at the receiving array with close incident angles. Next, we will consider multiple incident waves.

In Table IV and Fig. 7, we consider seven incident plane waves where the incident angles of three of them are close to one another. The true input parameters and the estimated results obtained by using $N=5$ and $d=0.11$ are shown in Table IV. Since the degree of freedom is 5 when $N=5$ of the receiver array, we can estimate at most five rays. The contributions due to the three rays with close incident angles are combined and reduced into a complex spectrum ray in the estimated results. It is remarkable that the estimated results are accurate and also insensitive to the increase of noise. The simulated results using the estimated parameters are shown in Fig. 7. It is not surprising to see that the complex spectrum model ignores the random fluctuation of the noise and provides very good approximation. This example confirms again that the complex spectrum model is more robust with respect to noise than the conventional real spectrum model when many plane waves arrive with close incident angles. Moreover, the complex model may be employed in systems with fewer degree of freedom than the number of incoming waves where the conventional real spectrum model breaks down.

TABLE II. Estimation of two incident plane waves with very close incident angles. Two incident waves are assumed.

Parameters	Given	Noiseless	SNR=30	SNR=15
α_1	0.0	2.776*E*-11	−0.02191	−0.161 547
α_2	0.0	−2.852*E*-11	−4.60023	−1.394 746
β_1	16.32 419	16.32 419	16.351 767	16.28 072
β_2	16.35 372	16.35 372	−20.838 676	−11.42 969
$\lvert b_1\rvert$	1.0	0.9999	1.37 358	1.416 186
$\lvert b_2\rvert$	0.95	0.95	2.6231*E*-3	0.080 047
$\angle b_1$	0.0	−1.8807*E*-9	0.75 838	0.763 279
$\angle b_2$	1.57 079	1.57 079	−0.25 147	2.031 808

From Tables II–IV and Figs. 6 and 7, it seems that the complex model is not able to resolve rays with close incident angles under noisy conditions. A question may be raised concerning about the resolution of the complex spectrum model. To address this issue, consider a shallow waveguide with a very lossy bottom and a horizontal receiving array with a constant depth z_0. In the numerical calculation, we use the shallow water waveguide in Ref. 3, which supports three propagating modes. The three complex modal eigenvalues $(k_m=-1\alpha_m+\beta_m)$ and modal excitation strengths (b_m) for $m=1,2,3$ are shown in the second column of Tables V–VII. The results in Table V are obtained using $N=5$ and $d=5$. The estimated results are very accurate in the noiseless situation. When noise increases, only one modal eigenvalue can be obtained. Since $|b_1|\gg|b_2|$ and $|b_1|\gg|b_3|$, the contributions from the two inaccurate modes are negligible. Thus, contributions due to the three modes are accounted by only one mode with a larger α. This result is similar to what we have obtained from the previous examples. The results in

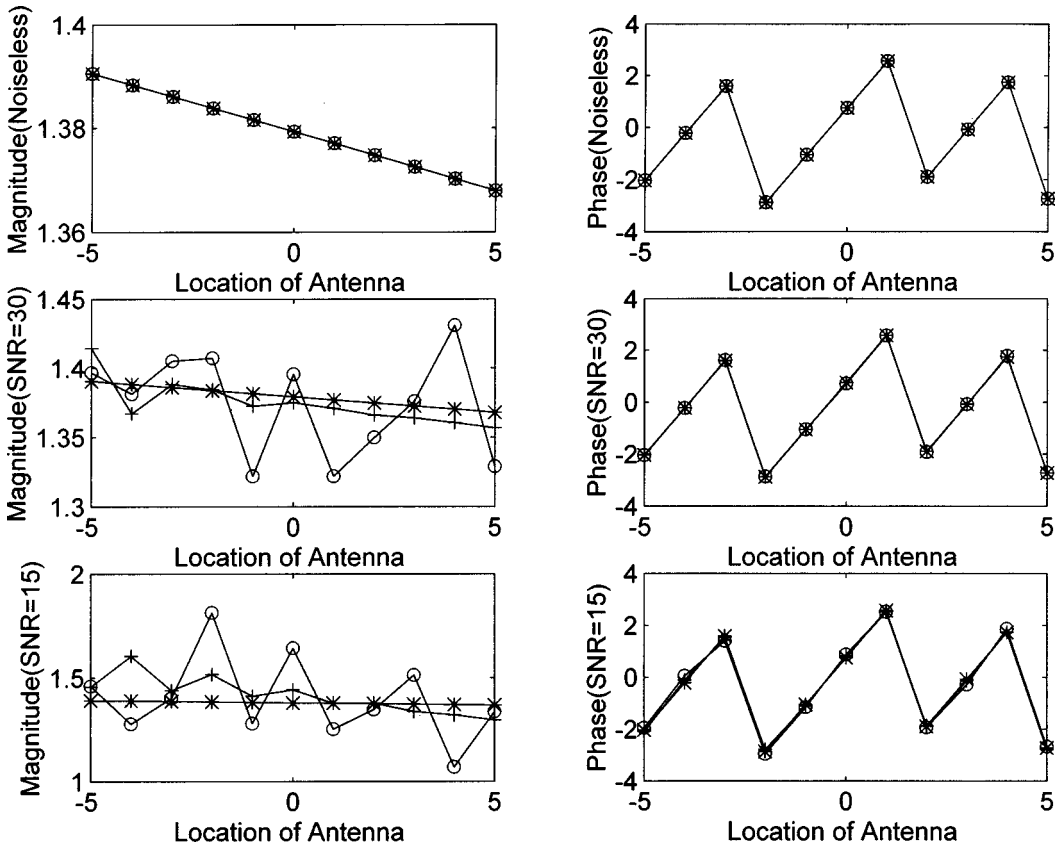

FIG. 5. Simulated results using parameters in Table II. Curves with *, ○, and + denote the noiseless incident field, noisy incident field, and simulated results.

Table VI are obtained using $N=5$ and $d=50$. Here, we keep the same number of antenna elements but increase the antenna spacing. Although the estimation of the spectra is not accurate, the estimation of the magnitude of excitation strengths of the three modes is quite accurate even in the situations with noise. The results in Table VII are obtained using $N=50$ and $d=5$. Here, we keep the small antenna spacing but increase the aperture of the array by increasing the number of the antenna elements. The estimated results are very accurate even in situations with noise. Again, the reproduced incident field using the estimated parameters from Tables V–VII give good approximations to the received filed $p(x)$ even in noisy situations. The corresponding figures look very similar to the previous figures and are therefore omitted. We conclude that there is no fundamental limitation on the resolution of the complex spectrum approach.

TABLE III. Estimation of two incident plane waves with close incident angles. Only one incident wave is assumed.

Parameters	Given	Noiseless	SNR=30	SNR=15
α_1	0.0	−0.9360	−0.93 248	−1.08 209
α_2	0.0			
β_1	16.324 194	17.326	17.32 865	17.13 931
β_2	18.437 648			
$\lvert b_1\rvert$	1.0	1.25 033	1.246 197	1.27 451
$\lvert b_2\rvert$	0.95			
$\angle b_1$	0.0	0.75 041	0.74 461	0.70 211
$\angle b_2$	1.57 079			

From the above numerical studies, the combination of the real spectral number β_n and the location dependence α_n seems to provide better physical insights into the multipath or multimode arrivals than using the real spectral number β_n alone. The complex spectrum model has also been shown to provide good resolution and accuracy even in noisy situations. To further characterize the noise performance of this approach statistically, we consider a two-ray model with additive white noise. In Fig. 8, we made 50 independent Monte Carlo runs to obtain 50 independent shots of each pole on the complex Z plane, where an independent Gaussian noise series is generated in each run. There are no spurious poles in our method when the SNR is sufficiently large. (This is called ''robust.'') Moreover, we can see from Fig. 8 that the mean estimated value is close to the ''true'' values and the standard deviation or variance of the estimated values is small. This means that our algorithm is very accurate and robust, since for almost every shot the estimated poles hit the right positions on the Z plane. Note that the absence of spurious pole is one of the most important features of our approach. All the estimated poles using our method are true system poles due to our rank reducing procedure in (9) when the SNR is sufficiently high. Other approaches will give spurious poles because the order M in (1) is unknown.

The variance of any unbiased algorithm is bounded by the Cramer–Rao (CR) lower bound. Such a bound is very useful because it predicts the best possible performance (smallest variances) for an unbiased estimator. Estimators or algorithms whose variances are close to or equals this bound

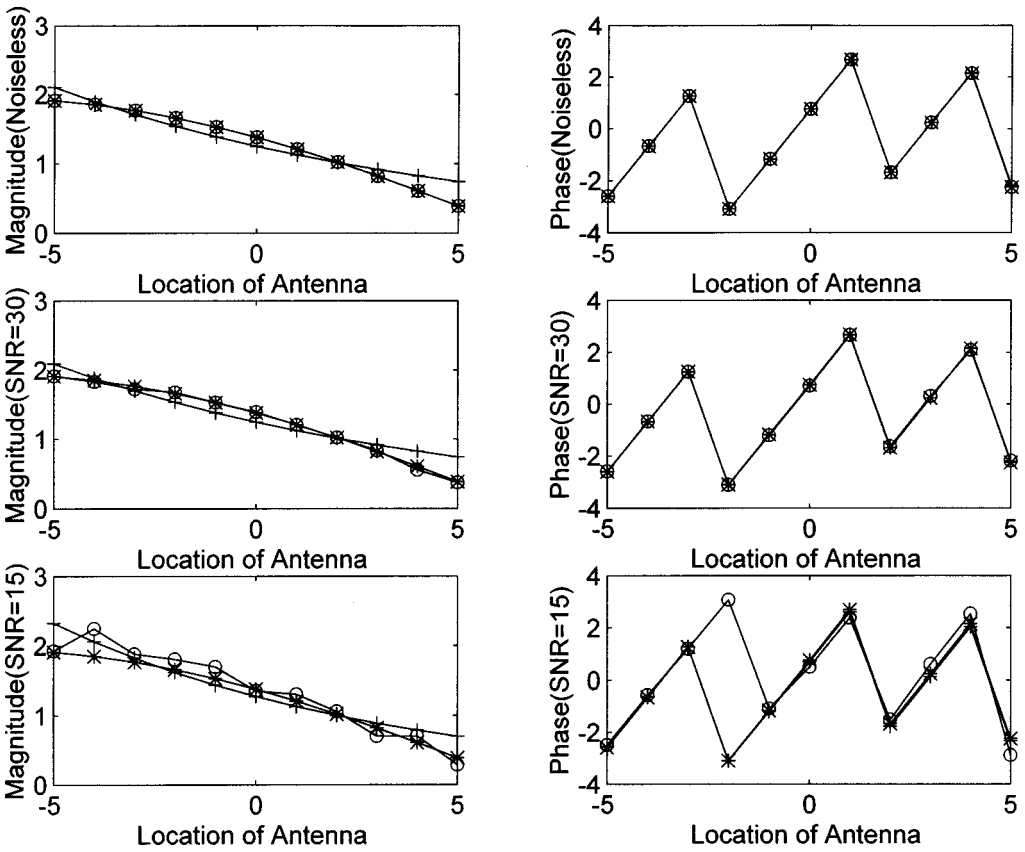

FIG. 6. Simulated results using parameters in Table III. Curves with *, ○, and + denote the noiseless incident field, noisy incident field, and simulated results.

TABLE IV. Estimation of seven incident plane waves where three incident angles are close to one another.

Parameters	Given	Noiseless	SNR=30	SNR=15
α_1	0.0			
α_2	0.0	−3.18 434E-3	−1.71758E-2	−0.15 148
α_3	0.0			
α_4	0.0	−6.65 515E-3	−3.86876E-2	−0.67 417
α_5	0.0	−2.08 838E-3	−3.30605E-2	0.24 145
α_6	0.0	5.73 600E-2	0.3 180 148	−0.37 215
α_7	0.0	5.34 340E-2	0.5 408 533	−1.31 188
β_1	9.424 778			
β_2	8.557 519	9.376 967	9.420 899	9.19 658
β_3	10.26 620			
β_4	18.20 727	18.20 492	18.23 419	18.01 627
β_5	−17.41 472	−17.41 192	−17.39 740	−18.15 382
β_6	0.0	4.623 663E-3	0.238 573	−0.38 012
β_7	−6.446 928	−6.449 813	−6.059 761	−6.66 379
$\lvert b_1\rvert$	1.0			
$\lvert b_2\rvert$	0.11	1.143 404	1.133 494	1.179 322
$\lvert b_3\rvert$	0.04			
$\lvert b_4\rvert$	0.7	0.700 412	0.705 496	0.701 919
$\lvert b_5\rvert$	0.5	0.500 107	0.474 610	0.487 003
$\lvert b_6$	0.4	0.399 946	0.392 962	0.478 977
$\lvert b_7\rvert$	0.2	0.199 832	0.217 816	0.200 976
$\angle b_1$	0.78 539			
$\angle b_2$	0.62 832	0.761 990	0.778 379	0.813 909
$\angle b_3$	0.52 359			
$\angle b_4$	1.83 259	1.830 899	1.840 839	1.718 489
$\angle b_5$	1.25 663	1.256 477	1.287 125	1.363 654
$\angle b_6$	2.09 439	2.095 081	2.144 097	1.808 495
$\angle b_7$	2.24 399	2.229 879	2.123 066	2.132 728

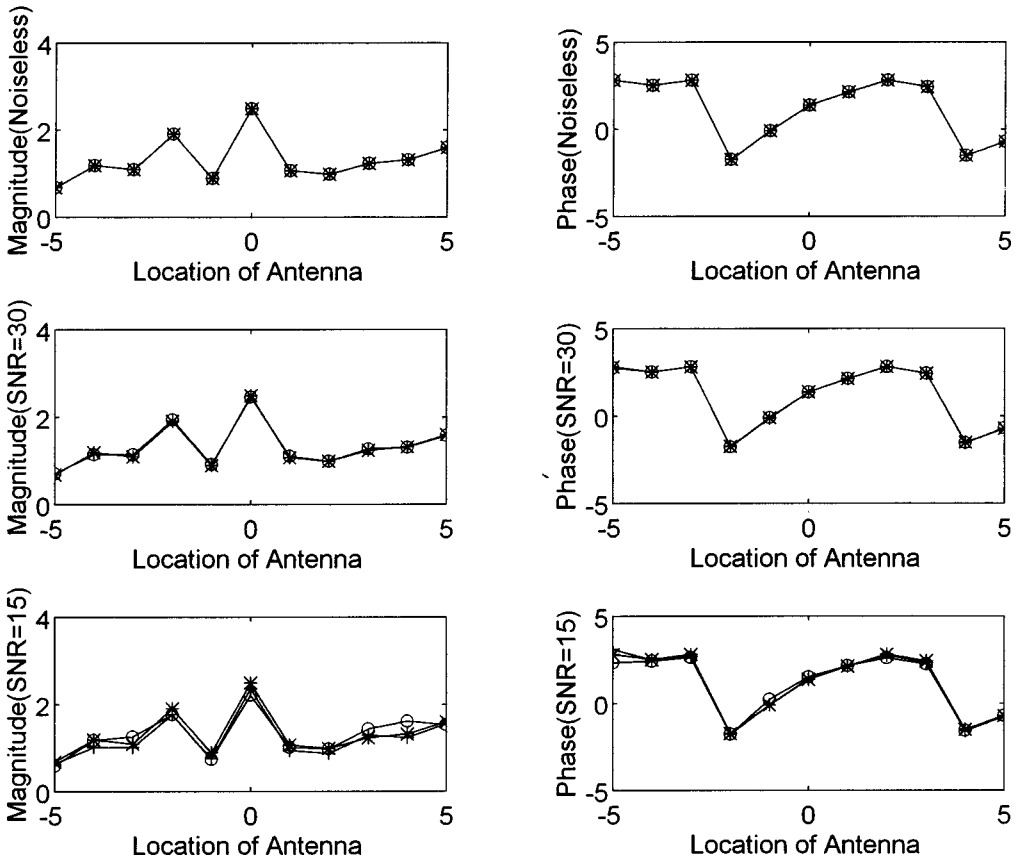

FIG. 7. Simulated results using parameters in Table IV. Curves with *, ○, and + denote the noiseless incident field, noisy incident field, and simulated results.

can then be said to be ''optimal.'' In Figs. 9 and 10, we made 500 independent Monte Carlo runs to obtain the mean and the variance where an independent Gaussian noise is generated in each run. Figure 9 shows the mean values and Fig. 10 shows the variance. Parts (a) and (b) of both figures report the outcomes of β_n and α_n, respectively. The daggered curve and the dotted curve represent the estimated values of the first ray and second ray, respectively. Solid lines in Fig. 9 are the true values and solid lines in Fig. 10 represent the Cramer–Rao (CR) lower bounds. The closed-form expressions of CR bounds for the complex exponents of two damped exponentials are given in Ref. 15. Figure 9 shows that our algorithm yields good results for SNR>10 dB. (Without using the SVD to filter out the noise, the algorithm only works when SNR>30 dB.) Since the variance in Fig. 10 is so close to the CR bound, our algorithm is almost ''optimal'' in the sense of the smallest variance for SNR>10 dB. But it is unbiased only up to SNR=22 dB. Strictly speaking, the CR bound applies only to an unbiased estimator. However, it is still a good reference for our algorithm which is with small bias. It is shown from this example that the proposed method has good noise immunity features.

III. CONCLUSIONS

Complex spectra can be used to model the location-dependent features of a linear array for the spectrum search

TABLE V. Estimation of the three guided modes of a shallow water waveguide using $N=5$ and $d=5$.

Parameters	Given	Noiseless	SNR=30	SNR=15
α_1	−8*E*-5	−8.0*E*-5	1.04269*E*-3	3.7409*E*-3
α_2	−2.2*E*-4	−2.1999*E*-4	3.89797*E*-2	−7.2812*E*-4
α_3	−6.5*E*-5	−6.4999*E*-5	−9.20704*E*-3	4.6107*E*-3
β_1	0.4145	0.4145	0.40 359	0.39 660
β_2	0.3998	0.3998	0.24 889	−0.38 613
β_3	0.3737	0.3737	−0.34 502	−0.04 784
$\lvert b_1\rvert$	1.0	0.9999	1.49 575	1.58 732
$\lvert b_2\rvert$	0.13	0.1299	0.03 073	0.05 436
$\lvert b_3\rvert$	0.42	0.4200	0.03 424	0.12 438
$\angle b_1$	0.0	1.1706*E*-11	0.01 096	0.014 149
$\angle b_2$	0.0	−6.9373*E*-11	0.54 749	−2.965 347
$\angle b_3$	0.0	−6.3998*E*-12	−2.55 906	1.138 659

TABLE VI. Estimation of the three guided modes of a shallow water waveguide using $N=5$ and $d=50$.

Parameters	Given	Noiseless	SNR=30	SNR=15
α_1	−8*E*-5	−8.0*E*-5	−6.82898*E*-5	2.68396*E*-4
α_2	−2.2*E*-4	−2.1999*E*-4	−9.46313*E*-4	3.95316*E*-4
α_3	−6.5*E*-5	−6.4999*E*-5	2.93974*E*-5	2.55697*E*-3
β_1	0.4145	0.03 756	0.037 564	0.03 701
β_2	0.3998	0.02 281	0.023 381	0.02 190
β_3	0.3737	−0.00 329	−0.003 317	−2.26356*E*-3
$\lvert b_1\rvert$	1.0	0.9999	0.99 925	1.07 232
$\lvert b_2\rvert$	0.13	0.1299	0.12 671	0.15 093
$\lvert b_3\rvert$	0.42	0.4200	0.43 147	0.43 446
$\angle b_1$	0.0	1.1914*E*-16	0.00 136	2.4493*E*-3
$\angle b_2$	0.0	4.2761*E*-16	−0.05 947	−0.035 113
$\angle b_3$	0.0	1.7894*E*-16	−0.01 435	0.048 951

TABLE VII. Estimation of the three guided modes of a shallow water waveguide using $N=50$ and $d=5$.

Parameters	Given	Noiseless	SNR=30	SNR=15
α_1	$-8E$-5	$-8.0E$-5	$-6.3045E$-5	$-5.5827E$-5
α_2	$-2.2E$-4	$-2.2E$-4	$-1.3634E$-4	$-1.5151E$-4
α_3	$-6.5E$-5	$-6.4999E$-5	$-5.8499E$-5	$-8.9995E$-3
β_1	0.4145	0.4145	0.41 452	0.41 465
β_2	0.3998	0.39979	0.40 008	0.40 071
β_3	0.3737	0.3737	0.37 368	0.37 342
$\lvert b_1\rvert$	1.0	1.0	0.99 949	1.00 269
$\lvert b_2\rvert$	0.13	0.13	0.13 207	0.11 847
$\lvert b_3\rvert$	0.42	0.42	0.41 847	0.42 185
$\angle b_1$	0.0	$-1.2986E$-14	$-2.8739E$-3	$-6.47401E$-5
$\angle b_2$	0.0	$-1.2038E$-13	$6.8624E$-4	$-6.35475E$-2
$\angle b_3$	0.0	$-2.4143E$-14	$7.0565E$-5	$-6.64745E$-3

of multiple arrivals. The real part of the complex phase constant represents the phase vector along the linear array, and the imaginary part of the complex phase constant models a linear variation of the incident field strength along the antenna array. We have shown that the complex spectrum model is more effective in modeling nonplanar or nonuniform waves than the real spectrum model. In these situations, the complex spectrum model also provide a better description of the physical process. It is remarkable that the complex spectrum model can also be used in systems with ''fewer degrees of freedom'' than the number of incoming waves because of the additional degree of freedom provided by the ''loss'' factor in the complex phase. This feature is very important for practical applications where sufficient number of sensors are not always feasible.

A combination of the singular value decomposition method and the eigen-matrix pencil method is proven to be very useful for finding the complex spectra. The algorithm consists of five steps: (1) Form a Hankel matrix using the noisy data sequence. (2) Filter the noisy data matrix through the rank-reducing approximation with the aid of SVD. (3) Find the complex eigenvalues and associated eigenvectors of the re-formed Hankel matrix. (4) Form an eigen-matrix pencil using principal eigenvectors and find the complex generalized eigenvalues associated with this eigen-matrix pencil. (5) Obtain the complex amplitude by employing a least square approach. The eigen-matrix pencil method has been

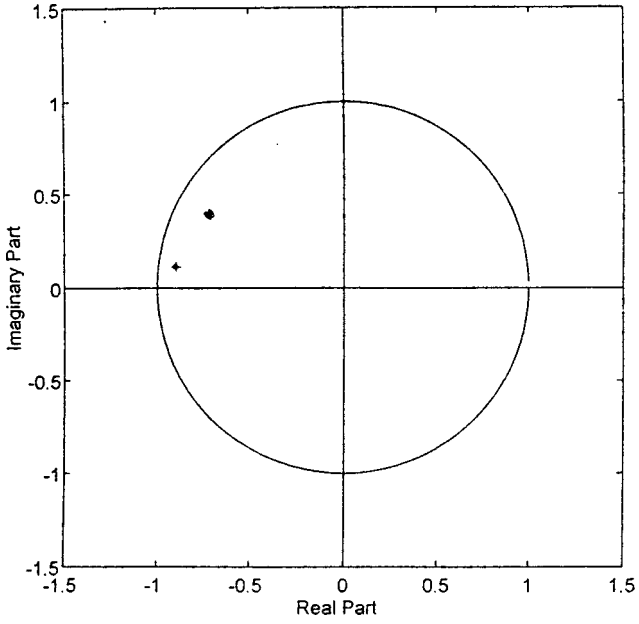

FIG. 8. Estimation of the complex spectra of a two-ray model in the complex Z plane.

improved by using a rank-reducing approximation based on the SVD to reduce the noise and to estimate the order of the system. It is found that the rank-reducing approximation considerably improves the performance of the eigen-matrix pencil method for the noisy data. The Cramer–Rao lower bound have been used as a benchmark for the variance and the mean. For a two-ray model, the variance of the location dependence factor is approximately 15 dB larger than that of phase constant. The variance for phase constant and location dependence is very close to the CR bound.

In our numerical simulations, modes in a cylindrical shell, modes in a lossy shallow water, nonplanar wavefronts, beams, and plane waves with close incident angles are modeled with complex spectra. The SVD eigen-matrix pencil method works satisfactorily when SNR is greater than 10 dB if the incident waves can be well approximated by the complex spectrum model. It has the following five key advantages: noise immunity, robustness, resolution, accuracy, and physical insight. And we conclude that it has the best performance for our purpose of complex spectrum finding. An im-

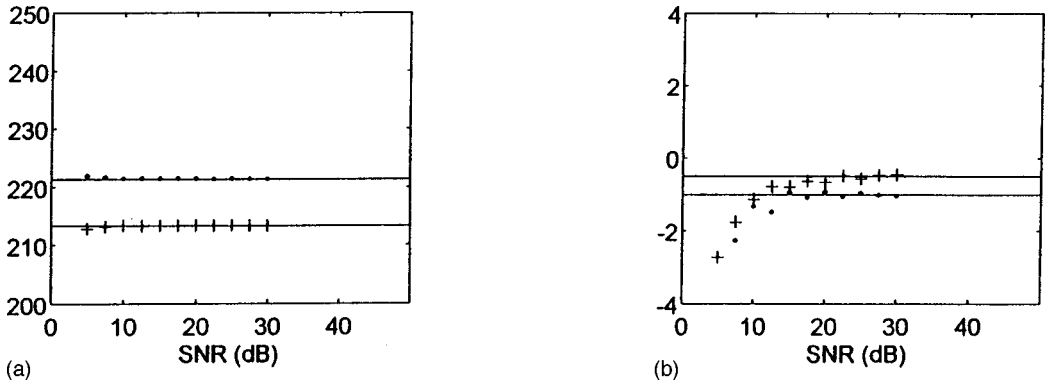

FIG. 9. (a) Mean values of β_n. The daggered curve and the dotted curve represent the estimated values of the first ray and second ray, respectively. Solid lines are the true values. (b) Mean values of α_n. The daggered curve and the dotted curve represent the estimated values of the first ray and second ray, respectively. Solid lines are the true values.

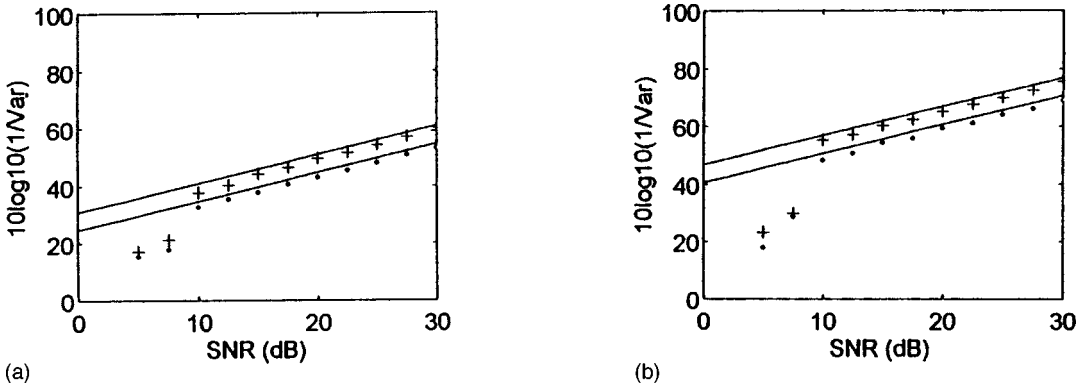

FIG. 10. (a) Variance of β_n. The daggered curve and the dotted curve represent the estimated values of the first ray and second ray, respectively. Solid lines represent the Cramer–Rao (CR) lower bounds. (b) Variance of α_n. The daggered curve and the dotted curve represent the estimated values of the first ray and second ray, respectively. Solid lines in represent the Cramer–Rao (CR) lower bound.

portant point to make is that the method can be applied to array data, in the absence of an assumed number M of arrivals, to extract a model of the complex plane-wave arrival structure. This permits, for example, identification of dominant propagation and scattering paths and therefore provides physical insight of the wave propagation and scattering processes. This approach has been employed to evaluate the travel times and resonances of scattering returns from submerged targets using experimental data provided by Naval Undersea Warfare Center.[19] It has also been employed to simultaneously estimate the environment and multiple-source locations in shallow waters.[20] Applicability to large vertical apertures in a waveguide with strong vertical variations in sound speed is more problematic and will be discussed in future publications.

ACKNOWLEDGMENT

The work is supported by ONR.

[1] I. T. Lu, ''Simultaneous characterization of source and environment using a ray travel-time inversion approach,'' J. Comput. Acoust. **5**(2), 193–218 (1997).
[2] I. T. Lu, ''Forward modeling and data inversion for beam propagation in a stratified medium: I. Theory,'' J. Acoust. Soc. Am. **91**, 1228–1238 (1992).
[3] H. Y. Chen and I. T. Lu, ''Matched mode processing schemes of a moving point source,'' J. Acoust. Soc. Am. **92**, 2039–2050 (1992).
[4] S. M. Kay, *Modern Spectral Estimation: Theory and Applications* (Prentice-Hall, Englewood Cliffs, NJ, 1988).
[5] S. L. Marple, *Digital Spectral Analysis with Applications* (Prentice-Hall, Englewood Cliffs, NJ, 1987).
[6] R. Roy, A. Paulraj, and T. Kailath, ''ESPRIT—A subspace rotation approach to estimation of parameters of cisoids in noise,'' IEEE Trans. Acoust., Speech, Signal Process. **34**(10), 1340–1342 (1986).
[7] R. Kumaresan and D. W. Tufts, ''Estimating the Parameters of Exponentially Damped Sinusoids and Pole-Zero Modeling in Noise,'' IEEE Trans. Acoust., Speech, Signal Process. **30**(6), 833–840 (1982).
[8] B. Porat and B. Friedlander, ''On the Accuracy of the Kumeresan–Tufts Method for Estimating Complex Damped Exponentials,'' IEEE Trans. Acoust., Speech, Signal Process. **35**(2), 231–235 (1987).
[9] S. U. Pillai and H. S. Oh, ''Extraction of resonant modes from scattering noisy data,'' in *Ultra-Wideband Short-Pulse Electromagnetics II*, edited by L. Carin and L. B. Felsen (Plenum, New York, 1995), pp. 585–594.
[10] M. McClure, R. C. Qiu, and L. Carin, ''On the superresolution identification of observables from swept-frequency scattering data,'' submitted to IEEE Trans. Antennas Propagat.
[11] C. M. Qiu and I. T. Lu, ''Multipath resolving with frequency dependence for broadband wireless channel modeling,'' to appear in IEEE Trans. Veh. Technol., R. C. Qiu and I-Tai Lu, ''High-resolution algorithms for multipath resolving and indoor channel modeling,'' Proceedings of the 1995 sixth IEEE International Symposium on Personal, Indoor and Mobile Radio Communications, Vol. 1, pp. 148–152.
[12] R. C. Qiu, ''Time/Frequency Dispersion of Digital Transmission Media: Wideband Wireless Channel Model, Chiral Optical Fiber, and Superconducting MMIC,'' Ph.D. dissertation, Polytechnic University, Jan. 1996.
[13] G. H. Golub and C. F. Van Loan, *Matrix Computations* (Johns Hopkins U.P., Baltimore, 1993), pp. 1340–1342.
[14] Y. Hua and T. K. Sarkar, ''Matrix pencil method for estimating parameters of exponentially damped/undamped sinusoids in noise,'' IEEE Trans. Acoust., Speech, Signal Process. **38**(5), 814–824 (1990); Y. Hua and T. K. Sarkar, ''On SVD for Estimating Generalized eigenvalues of singular matrix pencil in noise,'' IEEE Trans. Signal Process. **39**(4), 892–900 (1991).
[15] R. Kumaresan and D. W. Tufts, ''Estimating the Parameters of Exponentially Damped Sinusoids and Pole-Zero Modeling in Noise,'' IEEE Trans. Acoust., Speech, Signal Process. **30**(6), 833–840 (1982).
[16] A. K. Jain, *Fundamentals of Digital Image Processing* (Prentice-Hall, Englewood Cliffs, NJ, 1989)
[17] I. T. Lu and Y. Q. Yao, ''Ray shooting, eigenray search, and complex resonances of submerged structures of revolution,'' submitted to J. Acoust. Soc. Am.
[18] I. T. Lu, L. B. Felsen, and Y. Z. Ruan, ''Spectral aspects of the Gaussian beam method: reflection from an isovelocity half space,'' Geophys. J. R. Astron. Soc. **89**, 915–932 (1987).
[19] I. T. Lu and F. P. Wu, ''A High-Resolution Spectral Estimation Approach for Evaluating the Traveltimes and Resonances of Scattering Returns from Submerged Targets,'' Third International Conference on Theoretical & Computational Acoustics, Newark, NJ, 14–18 July 1997.
[20] I. T. Lu and H. L. Wu, ''Range Estimation of Multiple Sources in Shallow Waters Without Knowing the Sound Speed Profile,'' Third International Conference on Theoretical & Computational Acoustics, Newark, NJ, 14–18 July 1997.

Linking auto- and cross-correlation functions with correlation equations: Application to estimating the relative travel times and amplitudes of multipath

John L. Spiesberger
Department of Meteorology and the Applied Research Laboratory, 512 Walker Building, Pennsylvania State University, University Park, Pennsylvania 16802

(Received 28 February 1997; accepted for publication 6 April 1998)

A location problem is considered where the sound which propagates along multipath are impractical to model because the environment is poorly known. The acoustic bandwidth is assumed to be large enough so that the cross-correlation functions between pairs of receivers contain multiple peaks from multipath. The highest peak may not correspond to the difference in path lengths between the source and the receivers. Using similarities in the patterns of peaks in auto- and cross-correlation functions, an algorithm is developed to identify which cross-correlation peak corresponds to the difference in first arrivals, which can be used for locating the source if these arrivals are straight. The similarities are expressed with new ''correlation equations.'' The number of lag-type correlation equations is $O(\mathscr{R}^2N^2)$, where N is the typical number of multipath at each of $\mathscr{R}$ receivers. The correlation equations may be impractical to solve exactly. Accurate solutions are found in simulations for the numbers, relative travel times, and amplitudes of all the multipath with the aid of a new ''augmented-template correlation function'' which is a cross-correlation of nonnegative lags of an auto-correlation function with lags from a cross-correlation function. The technique relies on time series which are filtered to yield one dominant source. [S0001-4966(98)04407-5]

PACS numbers: 43.60.Gk [JLK]

LIST OF SYMBOLS

$a_j[n]$	The amplitude of the nth multipath at receiver j
$B_{ij}(T)$	The ''B-Augmented-Template Correlation Function'' (B-ATCF) is the cross-correlation between nonnegative lags in $\check{R}_{jj}$ and $\check{R}_{ji}$
C	An objective function based on the sum of F-augmented-template correlation functions
$e_j(t)$	The noise at receiver j as a function of time t
f	A fraction between 0 and 1 used to pass candidates for lag equations
$F_{ij}(T)$	The ''F-Augmented-Template Correlation Function'' (F-ATCF) is the cross-correlation between nonnegative lags in $\check{R}_{ii}$ and $\check{R}_{ij}$
F_0	A lower bound for choosing candidates for reference-lags from F-ATCFs or B-ATCFs
F_1	A lower bound for selecting candidates for reference-lags from combinations of $\mathscr{R}-1$ intersected ATCFs
M_{jk}	The maximum number of peaks in the cross-correlation function
M'_{jk}	The number of peaks in the cross-correlation function
N_j	The number of multipath at receiver j arriving at intervals exceeding the inverse bandwidth of the signal
$\tilde{N}_j$	The estimated number of multipath at receiver j arriving at intervals exceeding the inverse bandwidth of the signal
P_{data}	The number of selected peaks from a cross-correlation function
P_j	The maximum number of positively lagged peaks in the auto-correlation function at receiver j
P'_j	The number of positively lagged peaks in the auto-correlation function from receiver j
$r_j(t)$	The waveform at receiver j
$\mathbf{r}$	The residual between the modeled and measured amplitudes of nondegenerate peaks in correlation functions
r	The length of the residual vector between the modeled and measured amplitudes of nondegenerate peaks in correlation functions
$\check{R}_{ij}(\tau)$	The peak selection function from correlation pair $i-j$ as a function of lag τ
$\mathscr{R}$	The number of receivers
$R_{jk}(\tau)$	The cross-correlation function from receivers j and k as a function of lag
$R'_{jk}(\tau)$	The amplitude of the Hilbert transform of the correlation between receivers j and k
$\check{R}_{jk}(\tau)$	The occurrence counter for the presence of a peak in a correlation function between receivers j and k
$\mathscr{R}$	The number of receivers
$s(t)$	The signal emitted from the animal as a function of time
S_i	The number of multipath satisfying the lag equations at receiver i

S	The number of multipath satisfying the lag equations at all receivers
$t_j[n]$	The travel time of the nth multipath at receiver j
Δf	The bandwidth of the signal
$\tau_{jk}[n,m]$	The lag in the correlation between receivers j and k corresponding to the travel time of multipath n at receiver j minus the travel time of multipath m at receiver k

INTRODUCTION

Cross-correlation[1] is a standard method for estimating the travel-time difference of a signal at two locations. This difference may be used to estimate the location of the source using hyperbolic techniques if the paths are approximately straight.[2,3] When attempting to locate birds from a set of widely separated microphones, there are typically many paths, called multipath, reaching each receiver.[4] If there are four multipath at one receiver and three at another, the cross-correlation function contains up to $3\times4=12$ peaks (Fig. 1). The largest of these does not always correspond to the difference in travel time between the first arrivals.[4] Without some further means of identifying the peak corresponding to the differences in distances from the bird to each receiver, the cross-correlation method may not be useful for locating sounds. In practice, it is difficult to produce a reliable model for the received signal because some paths reflect from boundaries, such as rough terrain or trees, whose locations are typically not measured. Having said this, one cannot use matched field processing to locate the source.

Using time-domain information in auto-correlation functions, a solution is presented for identifying the cross-correlation peak corresponding to the difference in the first arrivals. When this peak corresponds to the difference in distance from the source to each receiver, the animal can be located.

There are three benefits in using auto-correlation functions to identify peaks in cross-correlation functions. First, like cross-correlation functions, auto-correlation functions provide a gain in the received signal-to-noise ratio if the time-bandwidth product of the signal is larger than $O(1)$.[3] Second, the temporal resolution of the signal is compressed to its inverse bandwidth in both the auto- and cross-correlation functions, thus allowing for a temporal discrimination that may not be evident at the receiver.[1] Third, all the required data are at hand to compute auto-correlation functions when computing cross-correlation functions. Thus, the methods given here do not compromise the well-known benefits associated with cross-correlating signals.

Estimating the arrival times of multipath at a receiver has been investigated by many.[5–13] To the best of my knowledge, there is no general method for estimating the relative arrival times when all of the following five conditions are true: (1) the number of multipath is unknown; (2) the received signal-to-noise ratio is so low that the multipath cannot be discerned above the noise in the received waveforms; (3) the transmission time is unknown; (4) the transmitted waveform is unknown; (5) it is impractical to obtain *a priori* information concerning the coordinates and travel times of the multipath. The arrival times can be estimated under these five conditions when: (6) the signal-related peaks in the auto- and cross-correlation functions have large signal-to-noise ratios; (7) the differential Doppler between multipath at each receiver is sufficiently small so as to not reduce an otherwise significant peak in an auto-correlation function to a level indistinguishable from noise; and (8) the received time series are filtered to suppress all but one dominant signal.[14] This paper introduces a solution for the relative arrival times and

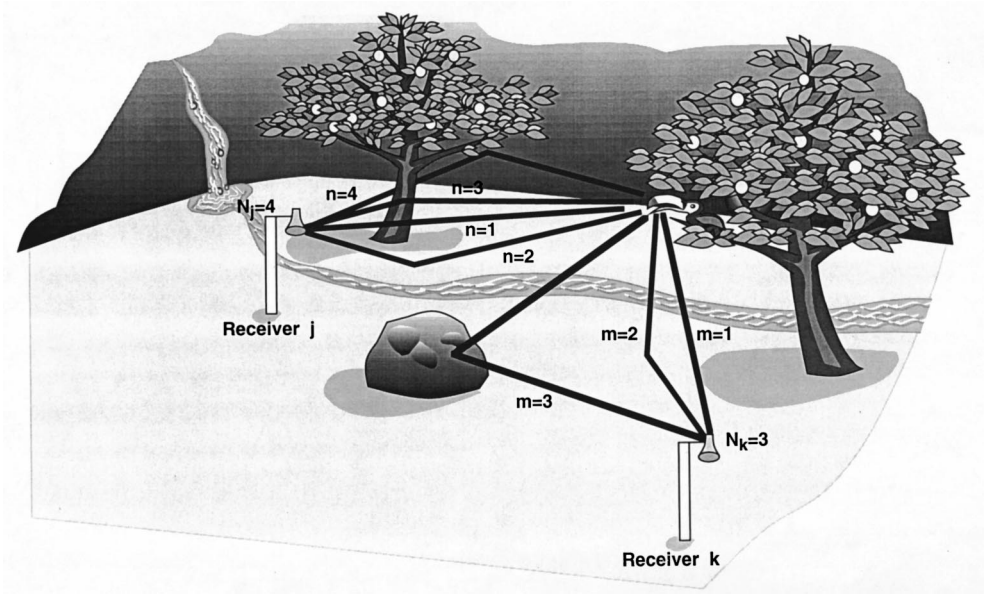

FIG. 1. View of $N_j=4$ and $N_k=3$ acoustic paths between a Toucan and receivers j and k, respectively. The direct paths are $n=1$ and $m=1$. The other paths reflect from the ground, a rock, and a cliff. Adapted from Ref. 14.

amplitudes of the multipath when constrains (6) and (7) are relaxed. In particular, it is unnecessary that the signal-related peaks in the correlation functions have large signal-to-noise ratios. In fact some, but not all, of the peaks may have negative signal-to-noise ratios. The relaxation of conditions (6) and (7) is more realistic and allows for the further step of locating the source if one has *a priori* knowledge that the first arrival at each receiver is a straight path.

I. PRELIMINARIES

Following Ref. 14, a signal, $s(t)$, is emitted at time $t=0$. There are N_j multipath reaching receiver j at time intervals exceeding Δf^{-1}, where the bandwidth of the signal is Δf. Multipath arriving at intervals less than Δf^{-1} are counted as one arrival. The signal arriving at receiver j is assumed to have the form,

$$r_j(t)=\sum_{n=1}^{N_j} a_j[n]s(t-t_j[n])+e_j(t), \tag{1}$$

where the amplitude and travel time of the nth multipath are $a_j[n]$ and $t_j[n]$, respectively. The noise is $e_j(t)$. Although the received waveform is assumed to consist of attenuated and delayed replicas of the signal, the methods which follow allow for a solution when there is some distortion of the phase and amplitude of Fourier components of the signal. We mainly need the multipath to lead to peaks in auto- and cross-correlation functions.

The auto- and cross-correlations are defined as

$$R_{ij}(\tau)\equiv\int r_i(t)r_j(t-\tau)dt, \tag{2}$$

where $i=j$ for auto-correlations and $i\neq j$ for cross-correlations.

II. COUNTING MULTIPATH

Let there be $\mathscr{R}$ receivers numbered from 1 to $\mathscr{R}$. Let the number of positively lagged peaks in the auto-correlation function from receiver i be denoted P_i'. When all the signal-related peaks in an auto-correlation function are guaranteed to have large signal-to-noise ratios, there are no ambiguities in choosing P_i'. Otherwise, there are ambiguities, and a method for selecting peaks must be specified. In this paper, I choose peaks which exceed a specified signal-to-noise ratio. Some of these peaks may be due to noise. If all the peaks are due to signal, then given P_i', an estimate for the lower bound of the number of multipath at receiver i is

$$\tilde{N}_i\geqslant\left\lceil\frac{1+\sqrt{1+8P_i'}}{2}\right\rceil;\quad i=1,2,\ldots,\mathscr{R}, \tag{3}$$

where $\tilde{N}_i$ is the estimated number of multipath and $\lceil x\rceil$ is the ceiling function denoting the least integer greater than or equal to x [Eq. (30) in Ref. 14]. Cross-correlation functions provide further constraints on the number of multipath at each receiver. If M_{ij}' denotes the number of resolved peaks in the cross-correlation function, the additional constraint is

$$\tilde{N}_i\tilde{N}_j\geqslant M_{ij}',\quad i\neq j, \tag{4}$$

[Eq. (31) in Ref. 14]. A solution for the number of multipath may be obtained by minimizing the total number of multipath,

$$Y\equiv\sum_{i=1}^{\mathscr{R}}\tilde{N}_i, \tag{5}$$

subject to Eqs. (3) and (4).

III. CORRELATION EQUATIONS: LAGS

A. Lags in auto- and cross-correlation functions

Let

$$\tau_{ij}[m,n]\equiv t_i[m]-t_j[n],\ \ i\leqslant j,\quad i\ \text{ and }\ j=1,2,3,\ldots,\mathscr{R} \tag{6}$$

denote the lags at which peaks occur in the auto- and cross-correlation functions of receivers i with j. The ''reference lag'' is defined to be the difference in travel time between the first arrivals at two receivers. Equations (25)–(26) in Ref. 14 provide two independent estimates for the reference lags given by

$$\tau_{ij}[1,1]=\tau_{ij}[1,N_j]+\tau_{jj}[N_j,1], \tag{7}$$

$$\tau_{ij}[1,1]=\tau_{ij}[N_i,1]-\tau_{ii}[N_i,1]. \tag{8}$$

The data required to solve these equations may be found by inspecting four peaks in the correlation functions. The peaks must have large signal-to-noise ratios so that they can be unambiguously identified. The most negatively and positively lagged peaks in the cross-correlation function are $\tau_{ij}[1,N_j]$ and $\tau_{ij}[N_i,1]$, respectively. $\tau_{ii}[N_i,1]$ and $\tau_{jj}[N_j,1]$ are the most positively lagged peaks in the auto-correlation functions from receivers i and j, respectively. The two equations provide independent estimates of the reference lag, $\tau_{ij}[1,1]$. However, if the signal-to-noise ratios of the peaks at these four lags cannot be unambiguously identified from the noise, this method may fail.

A new set of lag equations that can be formed from auto- and cross-correlation functions is

$$\tau_{ii}[q,1]=\tau_{ij}[q,n]-\tau_{ij}[1,n];\quad i\neq j, \tag{9}$$

where

$$i=1,2,3,\ldots,\mathscr{R},$$

$$j=1,2,3,\ldots,\mathscr{R},$$

$$n=1,2,3,\ldots,N_j,\quad \text{for } i<j$$

$$n=1,\quad \text{for } i>j$$

$$q=2,3,\ldots,N_i.$$

This set is exact if there is (1) no noise, (2) no interference between multipath leading to a correlation peak being shifted in lag space, and (3) no lack of coherence between multipath in the auto- and cross-correlation functions. To the best of my knowledge, these lag equations have not previously been considered, except for the subset expressed by Eqs. (7) and (8).

1. Interpretation

For receivers i and j, the peaks in the cross-correlation function occur at lags

$$\tau_{ij}[m,n]=t_i[m]-t_j[n].$$

The pattern of relative travel times,

$$t_i[m]-t_i[1], \quad m=2,3,4,\ldots,N_i, \tag{10}$$

appears N_j times in $R_{ij}(\tau)$, once for each $t_j[n]$. These are the patterns expressed by Eq. (9). For each i on the left side of Eq. (9), there are $\mathscr{R}-1$ different j's with attendant $\mathscr{R}-1$ different cross-correlation functions which yield the pattern of relative travel times in Eq. (10).

Similarly, the pattern of relative travel times,

$$t_j[n]-t_j[1], \quad n=2,3,4,\ldots,N_j,$$

appears in $R_{ji}(\tau)$ N_i times, once for each $t_i[m]$.

2. Number of lag equations

The number of lag equations in (9) equals

$$I=\sum_{j=2}^{\mathscr{R}} N_j \sum_{i=1}^{j-1} N_i - \frac{1}{2}(\mathscr{R}^2-\mathscr{R}). \tag{11}$$

When the numbers of multipath at each receiver are the same,

$$I=\tfrac{1}{2}(\mathscr{R}^2N^2-\mathscr{R}N^2-\mathscr{R}^2+\mathscr{R}), \quad N_i=N, \quad \forall i, \tag{12}$$

where the symbol, $\forall$, means ''for all.'' At highest order, the number of lag equations is proportional to the square of the number of multipath times the square of the number of receivers.

IV. CORRELATION EQUATIONS: AMPLITUDES

The amplitudes of some peaks in the correlation functions contain information that may be used for identification purposes. To avoid interference effects, peaks are only utilized if they are derived from a single pair of paths. For example, if there is a peak at lag τ_{ij}, then its amplitude information is only used if there is only one m and n satisfying $\tau_{ij}=\tau_{ij}[m,n]$. Such peaks will be called nondegenerate. Otherwise, they are called degenerate. As will be seen in Sec. V, the lag equations introduced in Sec. III may be used to identify the nondegenerate peaks.

The amplitude of the nondegenerate peak at lag $\tau_{ij}[m,n]$ is obtained by substituting Eq. (1) into Eq. (2),

$$R_{ij}(\tau_{ij}[m,n])=a_i[m]a_j[n]\int s^2(t)dt+\mathscr{N}_{ij}(\tau_{ij}[m,n]), \tag{13}$$

where $\mathscr{N}_{ij}(\tau_{ij}[m,n])$ denotes that component of the peak due to noise. For simplicity, we assume the noise component to be negligible, but this assumption is not necessary to make in general. Define

$$b_j[n]\equiv a_j[n]E^{1/2}, \tag{14}$$

where

$$E\equiv\int s^2(t)dt. \tag{15}$$

Equation (13) reduces to

$$R_{ij}(\tau_{ij}[m,n])\cong b_i[m]b_j[n]. \tag{16}$$

The goal is to estimate the amplitudes, $b_i[m]$ and $b_j[n]$, given measured amplitudes of the peaks, $R_{ij}(\tau_{ij}[m,n])$. Equation (16) may be transformed into a linear set of equations by taking the logarithm of both sides. This leaves

$$\rho_{ij}[m,n]=\beta_i[m]+\beta_j[n], \tag{17}$$

where

$$\rho_{ij}[m,n]\equiv\ln R_{ij}[m,n], \tag{18}$$

$$\beta_i[m]\equiv\ln b_i[m]. \tag{19}$$

These equations may be underdetermined, determined, or overdetermined, and standard least-squares procedures may be used to find solutions.

One can use amplitude information to identify peaks in correlation functions by selecting a set of multipath travel times and amplitudes that yield a best fit to the measurements. That is, one forms the residual vector,

$$\mathbf{r}_{D\times 1}\equiv\frac{1}{D}\begin{pmatrix}(R_{ij}[m,n]-\tilde{b}_i[m]\tilde{b}_j[n])/R_{ij}[m,n]\\(R_{ik}[m,p]-\tilde{b}_i[m]\tilde{b}_k[p])/R_{ik}[m,p]\\\vdots\\\vdots\end{pmatrix}, \tag{20}$$

where there are D nondegenerate peaks in the correlation functions. The least-squares solutions to Eq. (17) are denoted $\tilde{b}_i[m]$. One finds the peaks in correlation functions such that the length of $\mathbf{r}$ is minimum. A practical means for doing this is given in Sec. V. Note that this residual vector places equal weight on the model's fit to large and small peaks since the misfit for each peak is normalized by the amplitude of the peak.

V. IMPLEMENTING THE CORRELATION EQUATIONS

A. The difficulty of a global search

For two receivers, it may be impractical to find the global solution of the lag equations (Table III in Ref. 14). The simulations in Sec. VI have ten multipath at each of five receivers because these numbers are similar to experimental conditions.[4] With $\mathscr{R}=5$ and $N_j=10$ for all j, Eq. (12) yields 990 lag equations. A global search for the best solution of relative travel times requires about 3×10^{33} trials (Appendix A).

Suboptimal but efficient techniques are used to find solutions to the lag equations in lieu of a global search. The process of finding a solution is one in which one winnows down the number of trials that must be examined by any means that can be thought of. I will also explain how to estimate the peaks that are nondegenerate so that their amplitudes may be used to identify reference lags.

B. Estimating reference lags and relative travel times with lag equations

In order to find solutions of the lag equations, it is necessary to define how peaks are selected from correlation functions (Sec. II) and to define some misfit criterion for the equations. The misfit criterion should account for the amount that a peak could be shifted due to noise and interference with unresolved peaks in correlation functions.

There are nine principal steps used to estimate the reference lags and the relative travel times of the multipath from the lag equations.

1. Estimating N_i

Peaks are selected from each correlation function. For $\mathscr{R}$ receivers, there are $\mathscr{R}$ different auto-correlations and $[\mathscr{R}(\mathscr{R}-1)]/2$ different cross-correlations. For example, for $\mathscr{R}=3$, the three auto-correlations are R_{11}, R_{22}, and R_{33}. The three cross-correlations are R_{12}, R_{13}, and R_{23}. After the peaks are selected, the numbers of multipath at each receiver are estimated (Sec. II).

2. Definition: Reference-lag sets

Subtraction of certain equations in (9) from one another yields the following relationships between the reference lags in the cross-correlation functions:

$$\tau_{ij}[1,1]=\tau_{ik}[1,1]+\tau_{kj}[1,1], \quad i=1, \quad \text{and } j<k. \tag{21}$$

Letting $i>1$ yields redundant equations. As we will see later, there may be more than one set of peaks satisfying this equation. Each set of lags satisfying Eq. (21) is called a ''reference-lag set.'' For example, if there are five receivers, each reference-lag set contains values for,

$$\begin{pmatrix} \tau_{12}[1,1] & \tau_{13}[1,1] & \tau_{14}[1,1] & \tau_{15}[1,1] \\ & \tau_{23}[1,1] & \tau_{24}[1,1] & \tau_{25}[1,1] \\ & & \tau_{34}[1,1] & \tau_{35}[1,1] \\ & & & \tau_{45}[1,1] \end{pmatrix}. \tag{22}$$

The upper and lower bounds for each reference lag are given by

$$|\tau_{ij}[1,1]| \leqslant \frac{d_{ij}}{c_{\text{slowest}}}, \tag{23}$$

where the distance between the receivers is d_{ij} and the slowest speed that sound can propagate between the receivers is c_{slowest}. This means that the absolute value of the difference in travel time between the first arrivals at each receiver is bounded by the distance between the receivers divided by the slowest speed that sound can travel.

A global search for reference-lag sets may be impractical to implement. For example, if there are 100 peaks in each cross-correlation function between the lags specified in Eq. (23), and if there are five receivers, then there are $100^4=10^8$ candidate reference-lag sets to try in Eq. (21).

3. Definition: Augmented-Template Correlation Functions (ATCFs)

Instead of using a global search for reference-lag sets, a function is introduced that may facilitate a practical solution to the problem. Consider the travel times of three multipath at receivers i and j (Fig. 2, panels A and B), and suppose initially that the multipath have high signal-to-noise ratios. The relative travel times of the paths at receivers i and j also appear in their respective auto-correlation functions at nonnegative lags (Fig. 2, panels C and D). This follows because the auto-correlation function for receiver i (or j) has lags at $\tau_{ii}[m,1]=t_i[m]-t_i[1]$ (or $\tau_{jj}[m,1]=t_j[m]-t_j[1]$). Note, however, that the auto-correlation functions have an additional peak at a lag which does not match the relative arrival times of the multipath. This nonmatching lag for receiver i occurs at $\tau_{ii}=t_i[3]-t_i[2]$, which equal 1.5 s (Fig. 2, panel C). The nonmatching lag for receiver j occurs at 0.8 s (Fig. 2, panel D). The auto-correlation functions thus contain augmented templates for the relative arrival times of multipath.

In contrast, the cross-correlation function, R_{ij}, contains lags at the relative arrival times of multipath at receiver i without additional nonmatching lags. These arrival times are repeated three times (Fig. 2, panel E). In general, if there were N_i multipath at receiver i and N_j multipath at receiver j, the relative arrival times at receiver i would appear N_j times,

$$t_i[m]-t_j[N_j], \quad m=1,2,3,\ldots,N_i,$$

$$t_i[m]-t_j[N_j-1], \quad m=1,2,3,\ldots,N_i,$$

$$t_i[m]-t_j[N_j-2], \quad m=1,2,3,\ldots,N_i,$$

etc.

$$t_i[m]-t_j[1], \quad m=1,2,3,\ldots,N_i.$$

Because the auto- and cross-correlation functions, R_{ii} and R_{ij}, both contain lags at the relative arrival times of multipath at receiver i, it may be useful to identify the relative arrival times by cross-correlating nonnegative lags of the auto-correlation function with the cross-correlation function. This operation is referred to as an ''Augmented-Template Correlation Function'' (ATCF). The word ''augmented'' appears because the auto-correlation function may contain a lag (or lags) not matching the relative arrival times of multipath at receiver i. The forward ATCF, (F-ATCF), is defined as

$$F_{ij}(T) \equiv \int_0^{\tau_{\max}} \breve{R}_{ii}(\tau)\breve{R}_{ij}(\tau-T)\,d\tau, \tag{24}$$

where the peak-selection function,

$$\breve{R}_{ij}(\tau) \equiv \begin{cases} 0, & \text{if there is no peak at lag } \tau \text{ in } R_{ij}(\tau), \\ 1, & \text{if there is a peak at lag } \tau \text{ in } R_{ij}(\tau), \end{cases} \tag{25}$$

is used so that $F_{ij}(T)$ yields the number of occurrences of matching peaks between the auto- and cross-correlation functions as a function of the lag T. The maximum lag considered in an auto-correlation is $\tau_{\max}$.

In the example from Fig. 2, the F-ATCF has a maximum value of N_i equal to three, the number of multipath at receiver i (Fig. 2, panel F). This is expected because when the auto- and cross-correlation functions are properly aligned, they share the same number of multipath in their common patterns, i.e., three in this case. $F_{ij}(T)$ attains this value exactly N_j times, where N_j equals three in this example. These N_j occurrences occur at intervals equal to the relative travel times at receiver j. The most negative lag of these N_j occurrences equals $-\tau_{ij}[1,1]$ (e.g., 0.6 s), the opposite of a desired reference lag (Fig. 2, panel F). We thus see it may be possible to use the F-ATCF to both identify the relative arrival times of multipath at receiver i and to estimate the difference in travel times of the first multipath at receivers i and j.

In less idealistic cases, the F-ATCF may have large values at lags not associated with reference lags either because not all the peaks in auto- and cross-correlations are selected or because the augmented templates in auto-correlations have peaks at lags that are not equal to the relative travel times at a receiver and those peaks line up with other peaks in the cross-correlation function under the ATCF operation.

In the idealistic case, $F_{ij}(T)$ has a maximum value of N_i exactly N_j times. The most negatively lagged occurrence of N_i occurs at $-\tau_{ij}[1,1]$.

There is a complimentary ATCF which picks up the relative arrival times from receiver j called a B-ATCF. The B stands for ''backwards'' since the lags in the cross-correlation function, R_{ij}, are reversed prior to correlating them with the nonnegative lags of the auto-correlation function from receiver j. It is defined as

$$B_{ij}(T) \equiv \int_0^{\tau_{\max}} \breve{R}_{jj}(\tau)\breve{R}_{ji}(\tau - T)\,d\tau. \tag{26}$$

Again, the peaks in the auto-correlation function not corresponding to relative travel times may add undesirable counts in the B-ATCF, but when this does not occur, the B-ATCF reaches a value of N_j, the number of multipath at receiver j (Fig. 2, panel G). Then, $B_{ij}(T)$ will reach a value of N_j exactly N_i times. In Fig. 2, $B_{ij}(T)$ has a value of 3 exactly 3 times. These N_i occurrences occur at intervals equal to the relative travel times at receiver i. The most negative lag of these N_i occurrences equals $\tau_{ij}[1,1]$ (e.g., -0.6 s), the desired reference lag (Fig. 2, panel G).

4. Using ATCFs to narrow down candidates for reference lags

Steps 4, 5, and 6 are included to narrow down the possibly exorbitant number of candidate reference lags that could be used to form candidate reference-lag sets (Sec. V B 2).

Recall that $F_{ij}(T)$ and $B_{ij}(T)$ tend to have large values at lags, $-\tau_{ij}[1,1]$ and $\tau_{ij}[1,1]$, respectively (Sec. V B 3). The idea here is to choose candidate reference lags from sufficiently large values of these ATCF's to aid in the search for the true reference lags.

Preliminary candidates for the reference lags, $\tau_{ij}[1,1]$, are chosen at lags, $-T = T_{F_{ij}}(p)$, $p = 1,2,3,\ldots,P_{F_{ij}}$ and $T = T_{B_{ij}}(p)$, $p = 1,2,3,\ldots,P_{B_{ij}}$, from the forward and backwards ATCFs, respectively. These candidates are restricted to

$$F_{ij}(-T) \geq F_0, \quad |-T| \leq \frac{d_{ij}}{c_{\text{slowest}}}, \tag{27}$$

$$B_{ij}(T) \geq F_0, \quad |T| \leq \frac{d_{ij}}{c_{\text{slowest}}}, \tag{28}$$

where F_0 is a threshold value above which preliminary candidates are chosen. More candidates are selected as F_0 decreases. In general, the most thorough examinations of the lag equations are found by choosing F_0 to be zero. In this case, there is no point in using ATCF's no help narrow down the number of reference-lag candidates. With sufficient computer resources, one would choose F_0 to be zero, and then do a global search for all the reference-lag sets, as mentioned at the bottom of Sec. V B 2. In practice, one may have to choose a positive value for F_0 which yields few enough reference-lag candidates so that further computations are practical.

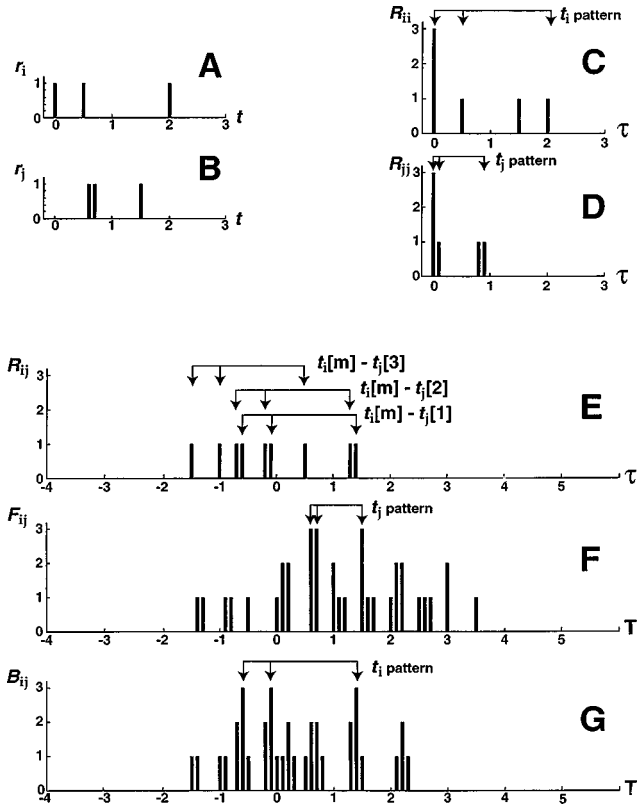

FIG. 2. **(A) and (B)** Time series from receivers i and j, respectively. The travel times of the multipath are $t_i[1]$, $t_i[2]$, and $t_i[3]=0$, 0.5, and 2 s and $t_j[1]$, $t_j[2]$, and $t_j[3]=0.6$, 0.7, and 1.5 s, respectively. **(C)** The nonnegative lags of the auto-correlation function from A. **(D)** The nonnegative lags of the auto-correlation function from B. **(E)** The cross-correlation function from A and B. It has peaks whose lags have patterns which replicate the relative travel times at receiver i. The number of replicates equals the number of multipath at receiver j. **(F) and (G)** The $F_{ij}(T)$ and $B_{ij}(T)$-Augmented Template Correlation Functions, defined by Eqs. (24) and (26), respectively. The largest values of these functions occur at the relative arrival times of multipath at receivers j and i respectively. The most negative lags of the largest three peaks in each of $F_{ij}(T)$ and $B_{ij}(T)$ occur at $-\tau_{ij}[1,1]$ and $\tau_{ij}[1,1]$, respectively. Note that $\tau_{ij}[1,1]=t_i[1]-t_j[1]=0-0.6=-0.6$ s (panels A and B).

Only preliminary candidates obeying the intersections, $\cap$, of the three sets,

$$T_{FB_{ij}} \in \{T_{F_{ij}}(1), T_{F_{ij}}(2), \ldots, T_{F_{ij}}(P_{F_{ij}})\} \cap \{T_{B_{ij}}(1), T_{B_{ij}}(2), \ldots, T_{B_{ij}}(P_{B_{ij}})\} \cap \{\tau_{ij}(1), \tau_{ij}(2), \ldots, \tau_{ij}(P_{\text{data}})\}, \quad (29)$$

are taken under further consideration. The lags at which the P_{data} peaks occur in the cross-correlation function $i-j$ are in the third set. The intersection with the third set is used to eliminate values from the ATCF's that are due to extraneous occurrences rather than from the relative arrival times of the multipath. In other words, if there is not a peak in the cross-correlation function at a candidate reference lag from the ATCF's, then that candidate lag is discarded.

5. Using Eq. (21) to narrow down candidates for reference lags

Candidate reference lags from step 4 are further considered only if they satisfy one of the equations in Eq. (21) within a specified tolerance. This step yield triples of consistent reference lags which can be used for further consideration. Reference-lag candidates that do not satisfy any of the equations from Eq. (21) are discarded.[15]

6. Using $\mathscr{R}-1$ combinations of ATCFs to narrow down candidates for reference lags

There may still be large numbers of reference-lag candidates from each cross-correlation function, and it may be efficient to decrease their numbers prior to forming reference-lag sets. This can be done by using ATCFs again, but now using them in combinations of $\mathscr{R}-1$ at a time.

First consider $\mathscr{R}-1$ ATCFs, namely, $F_{ir}(T)$, $i \neq r$. If $i < r$, $F_{ir}(T)$ has the pattern of relative lags, $t_r[n]$ starting at lag $T=-\tau_{ir}[1,1]$ (Sec. V B 3). If $i>r$, $F_{ir}(T)$ has the same pattern of relative lags starting at $T=\tau_{ri}[1,1]=-\tau_{ir}[1,1]$ (Sec. V B 3). The last sentence is true because $F_{ir}(T) = B_{ri}(T)$ when $i>r$. If we knew the correct reference lags, then we could correctly align each of these $\mathscr{R}-1$ ATCF's by adjusting their starting lags to occur at $T=-\tau_{ir}[1,1]$. Then if we intersect the pattern of occurrences in these aligned ATCF's, we would expect to get a larger number of intersections if the correct reference lags are used as the alignment lags.

The intersection function is such that if all aligned $\mathscr{R}-1$ ATCF's have a nonzero occurrence count at a lag, then the intersection function at that lag has a value of unity. Otherwise, that lag has a value of zero. For a large enough number of receivers, the expected number of intersections among the correctly aligned $\mathscr{R}-1$ ATCF's is just the number of multipath at receiver r, namely N_r. This follows because each of these ATCF's has the same pattern of relative arrival times, $t_r[n]$, $n=1,2,3,\ldots,N_r$. The extraneous occurrences in each ATCF, i.e., those not associated with the relative arrival times of multipath, will tend to be intersected to zero because they do not have the same pattern among the different ATCFs (Sec. V B 3).

When computing resources are a constraint, one can choose to only consider reference lags which yield a sufficient number of occurrence counts, F_1, following the intersections of the $\mathscr{R}-1$ ATCF's. If F_1 is zero, then there is no point in intersecting the ATCF's at this stage, as all the reference lags from the previous step would pass this criterion.

The remaining candidates for reference lags hopefully form a small enough set so that they can be sorted into reference-lag sets using an exhaustive technique which is truncated if a particular branch cannot be fitted to the equations.[15] Afterward, there may be more than one reference-lag set.

7. Using Eq. (9) with n=1

The seventh and eighth steps require peaks in correlation functions to obey all equations Eqs. (9) for $n=1$. For each reference-lag set, we find the number of different q at receiver i which satisfy all the equations,

$$\tau_{ii}[q,1]=\tau_{ij}[q,1]-\tau_{ij}[1,1], \quad i \neq j, \quad (30)$$

where $q \geqslant 2$. One hopes that the correct reference-lag set, which comes into play with the $\tau_{ij}[1,1]$ term, yields a greater number of q's satisfying Eq. (30) than incorrect reference-lag sets. Note that Eq. (30) yields estimates of the relative travel times at each receiver. One chooses the ith receiver, and goes through each positively lagged peak in its auto-correlation function. If the lag of that peak is the same as the difference of lags given on the right-hand side of Eq. (30) for all j's not equal to i, then we have found an acceptable value of q, and we have an estimate as to whether it is the second, third, or nth arrival at receiver i.

8. Using Eq. (9) with n>1

The eighth step checks if accepted values of $\tau_{ii}[q,1]$ from step seven obey the remaining equations in (9) for n greater than one. Equation (9) is written as

$$\tau_{ij}[q,n]=\tau_{ii}[q,1]-\tau_{ji}[n,1], \quad i \neq j \quad (31)$$

for $q=2,3,4,\ldots$. Although Eq. (9) limits $n=1$ for $i>j$, valid, but redundant, equations are also produced when $n>1$. In my implementation of the lag equations, n is allowed to exceed one when $i>j$.

In practice, I find that some of the $\tau_{ij}[q,n]$ above are not selected from the cross-correlation functions because they are below the signal-to-noise threshold used to select peaks. A missing $\tau_{ij}[q,n]$ can have catastrophic effects if it is required that every $\tau_{ii}[q,1]$ and $\tau_{ji}[n,1]$ be matched to its $\tau_{ij}[q,n]$. For example, if $\tau_{ij}[q,n]$ is missing, then it would be necessary to discard $\tau_{ji}[n,1]$ and then every other $\tau_{ii}[q,1]$ ($q=2,3,4,\ldots$) would have to be discarded because there would be no companion $\tau_{ji}[n,1]$ to match them up with.

A more forgiving criterion is chosen for accepting values of $\tau_{ii}[q,1]$. The criterion accepts a candidate for $\tau_{ii}[q,1]$ if a sufficient number of the equations from (31) are satisfied. The sufficient number is specified as follows.

Step seven identifies candidates for the right-hand side of Eq. (31). Consider a particular value for i and q in Eq. (31). There are

$$\text{maxfind}(i)=\sum_{j=1,\,j\neq i}^{\mathscr{R}}\text{ncand}(j) \tag{32}$$

different equations involving the candidate lag $\tau_{ii}[q,1]$ where the number of candidates for $\tau_{ji}[n,1]$ is ncand(j). The number of times that $\tau_{ii}[q,1]$ obeys Eq. (31) is denoted by ''nmatchup.'' This candidate, $\tau_{ii}[q,1]$, is accepted if a fraction, $0\leqslant f\leqslant 1$, of the maximum number of matches is found from the data, e.g., when

$$\text{nmatchup}>=f\cdot\text{maxfind}(i). \tag{33}$$

Otherwise, it is discarded.

9. Objective functions

Two objective functions are used to identify the correct reference-lag set. These functions depend on the numbers of peaks in the correlation functions which satisfy the lag equations. They do not depend on the amplitudes of the correlation peaks.

For the first function, step 8 yields $q=2,3,4,\ldots,S_i-1$ multipath at the ith receiver which satisfy Eq. (30). S_i is the total number of multipath at receiver i satisfying the lag equations, including the first arrival. We expect that the correct reference-lag set will yield better fits to the data which will tend to yield greater values of S_i. An objective function for goodness of fit is thus defined as

$$S\equiv\sum_{i=1}^{\mathscr{R}}S_i, \tag{34}$$

which is a function of the reference-lag set. This measure does not depend on the amplitudes of peaks in the auto- and cross-correlations as long as peaks are detected in the output of a correlator.

The second objective function is based on the F-ATCFs. $F_{ij}(T)$ tends to have large values at times corresponding to the pattern of relative arrival times of multipath at receiver j (Fig. 2). In fact, $t_j[1]$ occurs at lag $T=-\tau_{ij}[1,1]$, where $\tau_{ij}[1,1]$ is an element of a candidate reference-lag set. There are $\mathscr{R}-1$ different F-ATCFs yielding the relative arrival times, $\tau_{ij}[n,1]$, namely $F_{ij}(T)$, $i=1,2,3,\ldots,\mathscr{R}$; $i\neq j$. If each $F_{ij}(T)$ is shifted to place $t_j[1]$ at the same lag, then the sum of the $\mathscr{R}-1$ shifted F-ATCFs tends to have large values at the relative arrival times, $t_j[n]-t_j[1]$. The advantage in summing the F-ATCFs is that the sum tends to suppress extraneous values in each F-ATCF at lags that do not correspond to the relative arrival times of multipath at receiver j (Sec. V B 3). These extraneous peaks tend to occur at different lags in each of the $\mathscr{R}-1$ different F-ATCFs that are summed, but the relative arrival times at receiver j always occur at the same relative arrival times in each F-ATCF. The sum is defined as

$$\mathscr{F}_j(\mathscr{T})\equiv\sum_{i=1,i\neq j}^{\mathscr{R}}F_{ij}(T+\tau_{ij}[1,1]),\quad -\tau_{ij}[1,1]\leqslant T. \tag{35}$$

For each reference-lag set, an objective function may be formed by summing the values of $\mathscr{F}_j(\mathscr{T})$ at the lags which correspond to the relative arrival times of multipath, $\tau_{jj}[q,1]$, found from step 8. An objective function that accounts for all the $\mathscr{F}_j(\mathscr{T})$, $j=1,2,3,\ldots,\mathscr{R}$ is

$$C\equiv\sum_{j=1}^{\mathscr{R}}\sum_{q=1}^{S_j}\mathscr{F}_j(\mathscr{T}=\tau_{jj}[q,1]). \tag{36}$$

This objective function should be greatest for the correct reference-lag set.

C. Evaluating reference-lags sets with amplitude information

All correlation functions are constructed for each reference-lag set using the relative travel times, $\tau_{ii}[q,1]$; $q=2,3,4,\ldots,S_i-1$, found above. The amplitude of a peak in a correlation function is used only if that peak is nondegenerate. The length of the residual vector given by Eq. (20),

$$r\equiv|\mathbf{r}|, \tag{37}$$

is used as an objective function for each particular set of reference lags. Smaller residuals indicate that the candidate reference-lag set is more consistent with the amplitude equations.

VI. SIMULATIONS

Twelve simulations are carried out to demonstrate that the correlation equations can be used to estimate the correct reference lags and the amplitudes and relative arrival times of many multipath. The examples are similar to an experiment conducted by the author.[4] In that experiment, there were $O(10)$ multipath arriving at each of five receivers.

The simulated signal from the source is frequency modulated from 2500 to 3500 Hz over a period of 0.3 s. The frequency changes linearly with time and the envelope of the energy is constant throughout the 0.3 s interval. The waveform is output at a sample frequency of 16 000 Hz. The center frequency and bandwidth are similar to the calls of Red-Winged Blackbirds, *Agelaius phoeniceus*.[4]

In the first two simulations, the source is located at Cartesian coordinate (10,10,2), given in meters. The locations of the five receivers are given in Table I. The speed of sound is assumed to be 340 m s^{-1}. The wind speed is set to zero. The resulting differences in travel times between the first arrivals are,

$$\begin{aligned}&\tau_{12}[1,1]=+0.0004\ \text{s},\quad \tau_{13}[1,1]=-0.0458\ \text{s},\\ &\tau_{14}[1,1]=-0.0771\ \text{s},\quad \tau_{15}[1,1]=-0.0546\ \text{s}.\end{aligned} \tag{38}$$

Nine other multipath arrive at each receiver. All ten multipath are modeled according to Eq. (1) with values given in Table II. White Gaussian noise is added at each receiver so that the first arrival has a signal-to-noise ratio of 4 dB (Fig. 3).

The correlation functions have a ringing component near 3000 Hz; the center frequency of the synthesized signal (Fig. 4). If there is one multipath, then the correlation functions have a main peak with nearby peaks of lesser magnitude at $\frac{1}{3000}$ s intervals. The envelope of this energy is confined within a millisecond, which is the inverse bandwidth of the signal. To suppress the selection of these peaks of lesser magnitude, peaks are selected from an envelope which is the

TABLE I. The Cartesian coordinates of the five receivers used for the simulation in Sec. VI.

Receiver	x (m)	y (m)	z (m)
R1	0	0	0
R2	19.787	0	0
R3	17.739	−18.770	0
R4	2.023	−29.690	1.216
R5	−12.489	−13.923	2.182

amplitude of the Hilbert transform[16] of the auto- or cross-correlation function (Fig. 4). The envelope of a correlation function is denoted by R'_{ij}.

In these simulations, the lag equations are satisfied if the right- and left-hand sides of Eq. (9) are within $\pm 0.000\,562\,3$ s of each other. This misfit corresponds to about one-half of the pulse resolution, allowing for peaks to be displaced by noise and interference with other signals. Results for simulations 1 and 2 below are not sensitive to this misfit criterion. For example, the correct reference-lag sets are still found when the misfit is reduced to $\pm 0.000\,125$ s, but fewer multipath are found which satisfy the lag equations. For simulations 3 through 13, the correct reference-lag sets are sometimes not found without using the larger misfit threshold, i.e., $0.000\,562\,3$ s because the effects of noise and interference are sufficient to displace a sufficient number of correlation peaks by about one-half their resolution.

The threshold, f is set to 0.6 in Eq. (33). Identical results are obtained when $f=0.8$. All simulations set the threshold, F_1, to zero, because the available computational resources are sufficient to compute all possible intersections of the ATCFs (Sec. V B 6).

Simulations 1 and 2 below are designed to investigate whether the estimated reference lags are sensitive to the numbers of peaks selected from each correlation.

A. Simulation 1

The auto-correlation functions from receivers one through five had $O(100)$ peaks at positive lag. Peaks at lags less than 0.5 s are shown in Fig. 5. Peaks exceeding a threshold signal-to-noise ratio were picked from each correlation function. The thresholds were selected by looking at the correlation functions and choosing a level which appeared to pick up many peaks. These thresholds varied from 2.5 to 10 dB. Forty to one hundred percent of the selected peaks were due to multipath, depending on the correlation pair (Table III). Thus, sixty to zero percent of the selected peaks were due to noise. Between sixty and one hundred percent of all the resolved multipath peaks were selected (Table III).

Even though most of the peaks due to multipath were selected, I could not identify the reference lags using the algorithm which assumes that the signal-related peaks have high signal-to-noise ratios.[14] In particular, it proved impossible to determine the most positively lagged peak in the auto-correlation functions and the most positively and negatively lagged peaks in each cross-correlation function (Sec. III A). The algorithm in Ref. 14 also failed for simulation 2 in this section for the same reasons.

The numbers of multipath at each receiver, N_i, are estimated using the criterion given in Eq. (5). The results yield $\tilde{N}_i$ equal to 17, 22, 10, 14, and 12 for i equal to one through five respectively. The estimated values are generally larger than the correct value of ten because most of the peaks corresponding to signal are selected and many additional peaks due to noise are selected (Table III).

The threshold parameter, F_0 from Eq. (27), is set to a different value for each correlation function according to the following procedure. If the ATCF's do not contain occurrences due to coincidental matches of noisy peaks and augmented signal-related lags in auto-correlation functions with noise related peaks in cross-correlation functions, then F_0 should be set to the number of multipath, N_i and N_j respectively for $F_{ij}(T)$ and $B_{ij}(T)$, respectively (Sec. V B 4). The efficacy of the ATCF's in pulling out the reference lags is thus measured by F_0. The greatest value of F_0 which yielded any candidate reference-lag sets was three less than each of the $\tilde{N}_i$ given in the previous paragraph. Two reference-lag sets were found, and neither were correct.

Consequently, it was necessary to find more candidate reference lags by decreasing F_0. When F_0 was set to a value of ten less than each of the $\tilde{N}_i$, 28 reference-lag sets were found. Finding these sets required an hour of computer time. The two incorrect reference-lag sets mentioned in the last paragraph appeared in these 28 sets. The correct reference-lag set also appeared, yielding the values listed in Eq. (38). The arrows in Fig. 6 point to the peaks having these lags in

TABLE II. Travel times, t_i (s), and amplitudes, a_i, of the ten multipath at each of five receivers.

Receiver No.									
R1		R2		R3		R4		R5	
$t_1[n]$	$a_1[n]$	$t_2[n]$	$a_2[n]$	$t_3[n]$	$a_3[n]$	$t_4[n]$	$a_4[n]$	$t_5[n]$	$a_5[n]$
0.0420	0.8	0.0416	1.0	0.0878	0.7	0.1191	1.0	0.0966	1.0
0.0470	1.0	0.0446	0.4	0.0958	0.3	0.1291	0.9	0.2966	0.9
0.0510	0.3	0.1416	0.6	0.2078	1.0	0.1361	0.8	0.3096	0.7
0.0570	0.5	0.2416	0.3	0.2878	0.5	0.3491	0.7	0.4416	0.7
0.1020	0.2	0.2506	0.3	0.2958	0.5	0.3691	0.6	0.5966	0.7
0.1420	0.4	0.2716	0.3	0.3878	0.4	0.4191	0.5	0.6366	0.5
0.1510	0.7	0.2726	0.3	0.5878	0.4	0.4281	0.4	0.6766	0.5
0.1620	0.3	0.5416	0.3	0.6878	0.4	0.5191	0.3	0.6966	0.3
0.2320	0.5	0.5425	0.2	0.7878	0.4	0.6191	0.3	0.7966	0.3
0.5420	0.6	0.7416	0.1	0.7948	0.3	0.6331	0.3	0.9966	0.1

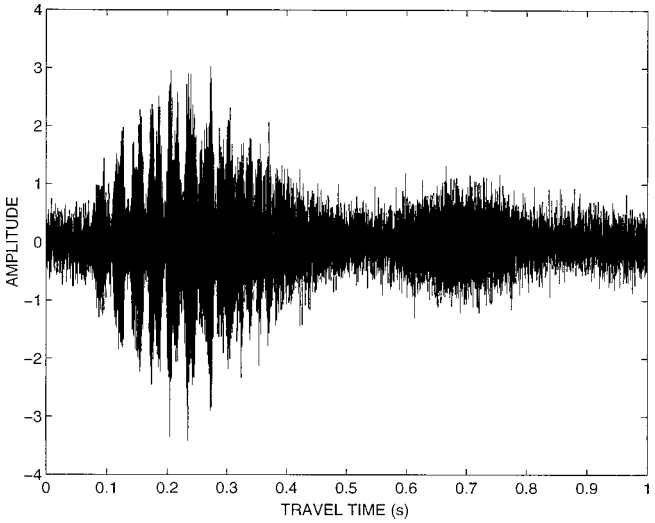

FIG. 3. The simulated signal at receiver one consists of ten multipath whose travel times and amplitudes are indicated in Table II. The peak signal-to-noise ratio for the first multipath is 4 dB. See Sec. VI.

R'_{1i} for $i=2,3,4,5$. Note that the peak having the correct reference lag in R'_{14} is not the largest peak.

The correct set had the largest values, among all 28 sets, for both objective functions for the number of occurrences, namely S and C, having values of 69 and 2314, respectively [Eqs. (34), (36)]. Of the 69 estimated multipath, 54 corresponded to correct travel times, and 15 did not. Some of these 54 multipath corresponded to more than one actual correct travel time, within the error tolerence, since there were only 50 correct travel times (10 multipath at each of five receivers). Of all the ten correct multipath at each receiver, the estimates only missed one multipath at each of receivers two and five.

Because there was a unique solution for the best reference-lag set based on the objective functions S and C, it was unnecessary to utilize amplitudes to estimate the correct reference-lag set. However, it is instructive to see if the amplitude-equations point to the correct answer. The length of the residual vector, r, in Eq. (37) for the correct reference-lag set was 0.006. In other words, modeled amplitudes fit the amplitudes of the nondegenerate peaks in the correlation functions to better than one percent. Of the 28 reference-lag sets, the residual, r, was smallest for the correct reference-lag set. The mean fractional error of the estimated amplitudes of multipath was 0.4 with a standard deviation of 0.4.

Errors for the modeled travel times were estimated from Eq. (B4) in Appendix B. The typical magnitude of the error was 0.0001 s.

B. Simulation 2

This simulation is identical to the first except fewer peaks were chosen (Table III). A greater fraction of the picked peaks were due to signal than in the first simulation, although fewer signal-related peaks were picked. From these selections, the estimated numbers of multipath, $\tilde{N}_i$, at receivers one through five were 10, 9, 11, 12, and 12, respectively. These are closer to the correct answer of ten than in the first simulation because there are fewer selections of noisy peaks.

The greatest value of F_0 which yielded any reference-lag sets was three less than the $\tilde{N}_i$. This set was the correct one. When F_0 was decreased to be ten less than the $\tilde{N}_i$, there were 40 reference-lag sets, and the correct one had the greatest values for both objective functions, S and C, namely 60 and 1747, respectively. Thus the objective functions based on occurrence counts both pointed to the correct reference-lag set. The amplitude objective function, r, for the correct reference-lag set was 0.0055. It was the next to the smallest residual, which was 0.0049. Thus, the amplitude objective function pointed to the wrong reference-lag set.

Of the 60 estimated travel times of multipath ($S=60$), 53 corresponded to correct travel times and 7 did not. Of all the ten correct multipath at each receiver, the estimates only

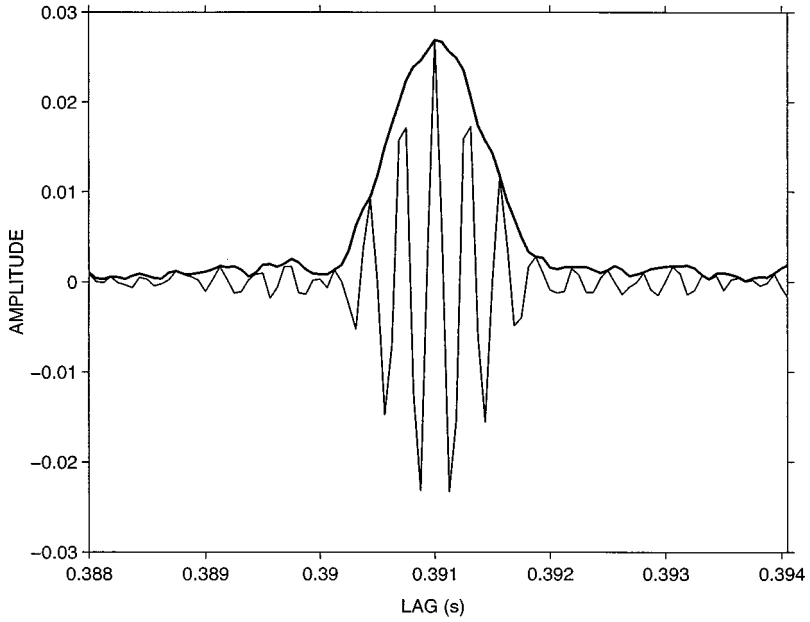

FIG. 4. The thin line is the auto-correlation function from receiver one near a peak. The thick line is the amplitude of the Hilbert transform.

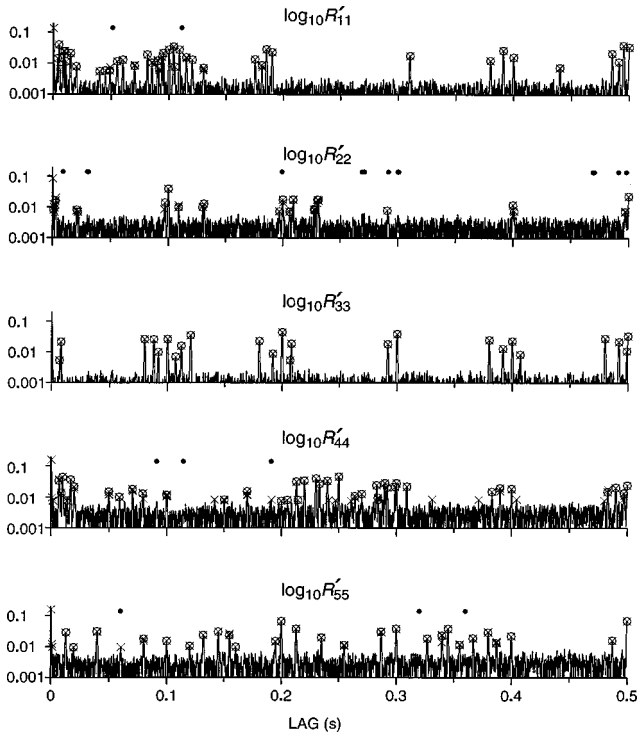

FIG. 5. The logarithms of the envelopes of the auto-correlation functions (ACF) at the five receivers up to a lag of 0.5 s. R'_{11} is the amplitude of the Hilbert transform of the ACF of the signal shown in Fig. 3. The peaks selected for implementing the equations given in (9) are marked with an ''x.'' Without noise, the auto-correlation functions would have peaks at lags where the circles and dots are placed. If the peaks in the noiseless ACF are within 0.000 25 s of a selected peak, the selected peak is also circled. Otherwise, a dot is placed at the lag where the noiseless auto-correlation function has a peak. The peaks of the noise-less auto-correlation function are computed from the parameters in Table II.

missed one multipath at each of receivers one, two, and five.

C. Ten more simulations

Ten more simulations were carried out with the same type of signal and with the same receivers but with the source at a new Cartesian coordinate, (5,8,2) (m). The resulting differences in travel times between the first arrivals were,

$$\tau_{12}[1,1] = -0.0214 \text{ s}, \quad \tau_{13}[1,1] = -0.0590 \text{ s},$$

$$\tau_{14}[1,1] = -0.0829 \text{ s}, \quad \tau_{15}[1,1] = -0.0541 \text{ s}.$$

As before, there were ten multipath at each receiver, and the multipath travel times were chosen using a uniform random number generator for each simulation. The difference in travel time between the first and tenth path was set to 0.8 s. For simplicity, all multipath had the same amplitude.

Peaks were selected from the correlation functions when their signal-to-noise ratios exceeded 12 dB. With this choice, the mean number of peaks selected from a correlation function was about 120. For a simulation, typical values for the minimum and maximum numbers of peaks selected among the correlation functions were 50 and 200, respectively.

For each simulation, the mean fraction of selected peaks due to signal among all ten auto- and cross-correlation functions was 0.7. Thus, about one-third of the selected peaks were due to noise overall. Some of these functions had signal fractions as little as 0.3 and some as large as 0.9.

The mean fraction of resolved signal-related peaks selected from all ten correlation functions was 0.8, with some correlation functions having fractions as little as 0.5 and some as large as 1.0.

In all cases, the threshold value, F_0 was set to equal 25 less than the estimated number of multipath from each receiver. This threshold typically resulted in a computer run of about an hour for each simulation. The numbers of reference-lag sets found for each simulation varied from 1 to 13 (Table IV).

In all ten cases, the objective functions based on occurrence counts, i.e., S and C, were largest for the correct reference-lag sets. Almost all of the travel times estimated from the algorithm corresponded to correct values (Table IV).

TABLE III. The row and column in each block indicate the correlation pair, e.g., there are 212 peaks selected from R'_{23} in simulation 1. The fraction of all picked peaks due to multipath are given in the middle blocks. The fraction of the total number of resolved multipath picked from the correlation functions is indicated in the bottom blocks. Matches between picked peaks and actual multipath travel times are affirmed when their travel times differ by about one-half the pulse resolution, i.e., 0.000 562 5 s.

	Simulation 1					Simulation 2				
	52	358	123	147	116	45	63	107	89	69
# Peaks		56	212	190	137		20	95	89	72
picked			38	133	101			36	102	89
				83	160				52	137
					53					43
	1.00	0.41	0.89	0.88	0.95	1.00	1.00	1.00	1.00	1.00
Fraction		0.89	0.57	0.73	0.82		1.00	1.00	1.00	1.00
due to			0.95	0.89	0.89			1.00	1.00	0.99
signal				0.89	0.91				1.00	0.95
					1.00					1.00
Fraction of	0.95	0.89	0.99	0.96	0.88	0.88	0.51	0.98	0.79	0.67
resolved		0.60	0.94	0.83	0.72		0.30	0.84	0.61	0.60
signal peaks			1.00	0.99	0.92			1.00	0.94	0.92
picked				0.95	0.90				0.77	0.85
					0.86					0.73

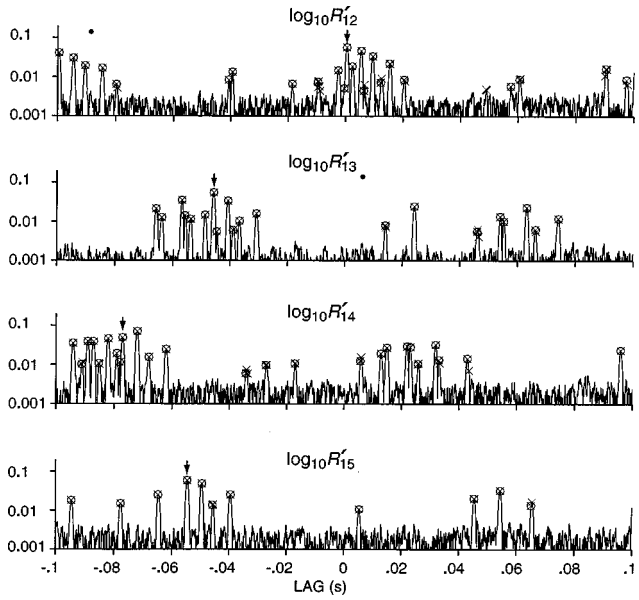

FIG. 6. The logarithms of the envelopes of the indicated cross-correlation functions (CCF) between the lags of -0.1 and $+0.1$ s for the simulation discussed in Sec. VI A. The x's, circles, and dots indicate the same things as in Fig. 5. The arrows identify the reference lags, $\tau_{12}[1,1]$, $\tau_{13}[1,1]$, $\tau_{14}[1,1]$, and $\tau_{15}[1,1]$, which best satisfy the lag and amplitude equations discussed in Secs. III and IV. Those reference lags are $+0.0004$, -0.0459, -0.0771, and -0.0546 s, respectively. These are consistent with the travel-time differences computed from the first-arrivals in Table II within 0.000 25 s.

Values of the objective function, r, for the correct reference-lag sets were the smallest found for 7 of the 10 simulations. In the other three cases, this amplitude-based objective function had the next to the smallest value among all the reference-lag sets. Typical values for r were 0.01 for the correct reference-lag sets.

D. Simulation summary

Both objective functions, S and C, identified the correct reference-lag set in 100% of the simulations. These objective functions are based on the numbers of multipath which fit the selected peaks in the correlation functions.

The r objective function, based on the residual between the measured and modeled amplitudes of correlation peaks, pointed to the correct reference-lag set in 8 of the 12 simulations. In the four other simulations, it had a value which was next to the smallest among all reference-lag sets. If error bars were computed for r, then the difference between the smallest and next to the smallest residual might not be statistically significant, because they differ by only 12%, 2.4%, 1.1%, and 7.8% for these four simulations.

VII. DISCUSSION

Correlation equations were derived which related the lags and amplitudes of peaks in the auto- and cross-correlation functions to one another. The global solution for the relative travel times and amplitudes of multipath was impractical to estimate because of the large number of cases to check. The sub-optimal solution of the equations yielded correct answers for the differences in travel time between the first signals that arrived at each receiver pair. The implementation also yielded information for the relative travel times and amplitudes of other multipath. The results were not sensitive to the numbers of peaks picked from the correlation functions, even when a substantial fraction, e.g., 30%, were due to noise.

Other implementations of the equations may yield solutions whose objective functions have greater variations between the correct and incorrect reference-lag sets. For example, a global search can yield a variation of two orders of magnitude (Fig. 5 in Ref. 14). Another variation might involve a rating of selected peaks based on their signal-to-noise ratios. Then values for the peak-selection function, i.e., $\check{R}_{ij}(\tau)$ from Eq. (25), would take on values in the interval 0 to 1 based on the probability that a peak was due to signal.

The utility of the techniques presented here can only be appreciated after testing them with many different kinds of data. I successfully located calling birds in my yard in Pennsylvania using these techniques.[4] The techniques may have application for locating acoustic sources such as whales when the geometry of only some of the multipath may be estimated.[17]

ACKNOWLEDGMENTS

I thank Roy Greenfield, Vince Premus, Andrew Watson, and the reviewers (one of which was Kurt Fristrop, who revealed his name) for their comments. I thank Mary, Ari, Maia, and Cleo for making these ideas more enjoyable to contemplate. I thank my colleagues in the Department of Meteorology at Penn State for providing a warm and intellectually open and exciting environment in which to think.

APPENDIX A: GLOBAL SOLUTION FOR LAG EQUATIONS

Generalizing the method in Ref. 14, a decision is made for the number of peaks in each auto-correlation function at positive lag, P_i', and the number of peaks in each cross-correlation function at all lags, M_{ij}'. An estimate is made for the number of multipath at each receiver, $\tilde{N}_i$ (Sec. II). For each auto-correlation function, the number of ways to choose $\tilde{N}_i-1$ candidate lags for $\tau_{ii}[n,1]$ $(n=2,3,4,\ldots,\tilde{N}_i)$ from P_i' lags without replacement is

$$\binom{P_i'}{\tilde{N}_i-1} \equiv \frac{(P_i')!}{(P_i'-(\tilde{N}_i-1))!(\tilde{N}_i-1)!}. \tag{A1}$$

For cross-correlation between receivers i and j, there are M_{ij}' candidates for the reference lag, $\tau_{ij}[1,1]$. For each candidate, the candidates for $\tau_{ij}[m,n]$ are determined from the $\tilde{N}_i-1$ and $\tilde{N}_j-1$ candidates for $\tau_{ii}[n,1]$ and $\tau_{jj}[m,1]$, respectively. Then, the residual for each identity in Eq. (9) can be calculated. So for each $i-j$ pairing there are

$$\binom{P_i'}{\tilde{N}_i-1}\binom{P_j'}{\tilde{N}_j-1} M_{ij}',$$

realizations. For $\mathscr{R}$ receivers, there are

$$\sum_{j=2}^{\mathscr{R}} \sum_{i=1}^{j-1} \binom{P_i'}{\tilde{N}_i-1}\binom{P_j'}{\tilde{N}_j-1} M_{ij}',$$

TABLE IV. Results from ten simulations in Sec. VI C. The second column is the number of reference-lag sets found. Column three is the number of estimated multipath among all five receivers, which is the same as the objective function in Eq. (34). The number of those estimated paths whose travel times are correct is given in the right column.

Simulation #	# Reference-lag sets found	Correct reference-lag set # Multipath (S)	Correct reference-lag set # That correspond to correct travel time
3	1	29	29
4	2	27	26
5	8	29	29
6	1	29	29
7	1	28	28
8	2	32	32
9	13	38	38
10	1	29	28
11	4	29	28
12	4	33	30

realizations of the lag equations. Because the estimated number of multipath is uncertain, an additional sum over realizations of the multipath is necessary, say from $\check{N}_i \leqslant \tilde{N}_i \leqslant \hat{N}_i$. The global search thus requires,

$$Z = \sum_{\tilde{N}_1=\check{N}_1}^{\hat{N}_1} \sum_{\tilde{N}_2=\check{N}_2}^{\hat{N}_2} \sum_{\tilde{N}_3=\check{N}_3}^{\hat{N}_3} \cdots \sum_{\tilde{N}_{\mathscr{R}}=\check{N}_{\mathscr{R}}}^{\hat{N}_{\mathscr{R}}} \sum_{j=2}^{\mathscr{R}} \sum_{i=1}^{j-1} \binom{P_i'}{\tilde{N}_i - 1} \times \binom{P_j'}{\tilde{N}_j - 1} M_{ij}', \tag{A2}$$

realizations of the lag equations. For $\mathscr{R}=5$, $P_i'=M_{ij}'=100$, $\forall i$ and j, and $8 \leqslant \tilde{N}_i \leqslant 12$, $\forall i$, $Z \cong 3\times 10^{33}$.

APPENDIX B: ESTIMATING ERRORS IN MEASURED LAGS

Let the measured lag of a correlation peak be

$$\tilde{\tau}_{ij}[m,n] = \tau_{ij}[m,n] + \epsilon_{ij}[m,n], \tag{B1}$$

where $\tau_{ij}[m,n]$ is the lag without error $\epsilon_{ij}[m,n]$. Substituting this in Eqs. (21) and (30) yields

$$\epsilon_{ij}[1,1] - \epsilon_{ik}[1,1] + \epsilon_{jk}[1,1] = \tilde{\tau}_{ij}[1,1] - \tilde{\tau}_{ik}[1,1] + \tilde{\tau}_{jk}[1,1], \quad i=1, \quad j<k, \tag{B2}$$

and,

$$\epsilon_{ii}[q,1] - \epsilon_{ij}[1,1] + \epsilon_{ij}[1,1] = \tilde{\tau}_{ij}[q,1] - \tilde{\tau}_{ij}[q,1] + \tilde{\tau}_{ij}[1,1], \quad i \neq j, \quad q \geqslant 2, \tag{B3}$$

respectively. Equations (B2) and (B3) can be combined into a linear system of equations as

$$W_{L\times U}\boldsymbol{\epsilon}_{U\times 1} = \mathbf{d}_{L\times 1}, \tag{B4}$$

which may be solved using least squares. The vector, $\boldsymbol{\epsilon}$, contains all the epsilons in Eqs. (B2) and (B3). The vector, $\mathbf{d}$, contains the right-hand sides of Eqs. (B2) and (B3), which are measured quantities.

[1] C. W. Hellstrom, *Statistical Theory of Signal Detection* (Pergamon, New York, 1968).
[2] W. A. Watkins and W. E. Schevill, ''Four hydrophone array for acoustic three-dimensional location,'' Woods Hole Oceanogr. Inst. Tech. Rep., 71–60, Woods Hole, MA (1971).
[3] J. L. Spiesberger and K. M. Fristrup, ''Passive localization of calling animals and sensing of their acoustic environment using acoustic tomography,'' Am. Nat. **135**, 107–153 (1990).
[4] J. L. Spiesberger, ''Locating animals from their sounds and tomography of the atmosphere: Experimental demonstration,'' J. Acoust. Soc. Am. (submitted).
[5] B. M. Bell and T. E. Ewart, ''Separating multipaths by global optimization of a multidimensional matched filter,'' IEEE Trans. Acoust., Speech, Signal Process. **34**, 1029–1037 (1986).
[6] R. J. Vaccaro and T. Manickam, ''Time-delay estimation for deterministic transient signals in a multipath environment,'' in *IEEE International Conference on Acoustics, Speech and Signal Processing, ICASSP-92* (IEEE, New York, 1992), Vol. 2, pp. 549–552.
[7] T. G. Manickam, R. J. Vaccaro, and D. W. Tufts, ''A least-squares algorithm for multipath time-delay estimation,'' IEEE Trans. Signal Process. **42**, 3229–3233 (1994).
[8] A. B. Baggeroer, ''Matched field processing: source localization in waveguides,'' in *Conference Record of the Twenty-Sixth Asilomar Conference on Signals, Systems and Computers*, Pacific Grove, CA, edited by A. Singh (IEEE Comput. Soc. Press, New York, 1992), Vol. 2, pp. 1122–1126.
[9] L. Ju. Fradkin, ''Identification of the acoustic ocean transfer function in the Tyrrhenian Sea. I. Statistical considerations,'' J. Acoust. Soc. Am. **87**, 1569–1576 (1990).
[10] R. J. Vaccaro, E. Maragakis, and R. L. Field, ''Time delay estimation for ocean acoustic transient signal extraction in a multipath environment,'' International Conference on Acoustics, Speech and Signal Processing **5**, 2923–2926 (1990).
[11] J. L. Spiesberger, R. C. Spindel, and K. Metzger, ''Stability and identification of ocean acoustic multipaths,'' J. Acoust. Soc. Am. **67**, 2011–2027 (1980).
[12] C. Carter, *Coherence and Time Delay Estimation: An Applied Tutorial for Research, Development, Test, and Evaluation Engineers*, edited by G. Clifford Carter (IEEE, Piscataway, NJ, 1993), p. 506.
[13] R. J. Vaccaro, C. S. Ramalingam, and D. W. Tufts, ''Least-squares time-delay estimation for transient signals in a multipath environment,'' J. Acoust. Soc. Am. **92**, 210–218 (1992).
[14] J. L. Spiesberger, ''Identifying cross-correlation peaks in the presence of echoes with application to optimal passive localization of calling animals and tomographic mapping of the environment,'' J. Acoust. Soc. Am. **100**, 910–917 (1996).
[15] V. Premus, personal communication (1996).
[16] J. F. Claerbout, *Fundamentals of Geophysical Data Processing* (McGraw-Hill, New York, 1976), pp. 59–62.
[17] V. Premus and J. L. Spiesberger, ''Can acoustic multipath explain finback (*B. physalus*) 20-Hz doublets in shallow water?,'' J. Acoust. Soc. Am. **101**, 1127–1138 (1997).

Ultrasonic focusing through inhomogeneous media by application of the inverse scattering problem

Osama S. Haddadin[a] and Emad S. Ebbini
Department of Electrical Engineering and Computer Science, University of Michigan, Ann Arbor, Michigan 48109

(Received 19 July 1996; accepted for publication 6 April 1998)

A new approach is introduced for self-focusing phased arrays through inhomogeneous media for therapeutic and imaging applications. This algorithm utilizes solutions to the inverse scattering problem to estimate the impulse response (Green's function) of the desired focal point(s) at the elements of the array. This approach is a two-stage procedure, where in the first stage the Green's functions is estimated from measurements of the scattered field taken outside the region of interest. In the second stage, these estimates are used in the pseudoinverse method to compute excitation weights satisfying predefined set of constraints on the structure of the field at the focus points. These scalar, complex valued excitation weights are used to modulate the incident field for retransmission. The pseudoinverse pattern synthesis method requires knowing the Green's function between the focus points and the array, which is difficult to attain for an unknown inhomogeneous medium. However, the solution to the inverse scattering problem, the scattering function, can be used directly to compute the required inhomogeneous Green's function. This inverse scattering based self-focusing is noninvasive and does not require a strong point scatterer at or near the desired focus point. It simply requires measurements of the scattered field outside the region of interest. It can be used for high resolution imaging and enhanced therapeutic effects through inhomogeneous media without making any assumptions on the shape, size, or location of the inhomogeneity. This technique is outlined and numerical simulations are shown which validate this technique for single and multiple focusing using a circular array.
[S0001-4966(98)04107-1]

PACS numbers: 43.60.Pt, 43.35.Wa [JLK]

INTRODUCTION

Ultrasound in the range of 500 kHz–13 MHz is gaining wider acceptance for a range of diagnostic and therapeutic applications.[1–3] Phased arrays have become the standard in most diagnostic imaging systems since the mid 1980's. Recently, therapeutic systems that utilize phased arrays in hyperthermia[4–7] and other high intensity applications have been introduced.[8–10] One of the main advantages of phased arrays is their ability to scan at electronic speed thus eliminating the need for mechanical scanning. Coupled with advanced VLSI-based digital beamforming architectures, phased arrays promise to increase the utility of diagnostic systems by improving image quality, improving reliability, and increasing functionality. Similar improvements can be expected for therapeutic systems utilizing phased arrays.

A major promise of phased arrays that has not yet been fulfilled is their ability to noninvasively compensate for tissue inhomogeneity and, therefore, focus in the presence of such inhomogeneity.[11–15] The successful implementation of such self-focusing arrays will have a major impact on ultrasonic imaging systems by allowing the use of large-aperture arrays which could help improve both spatial and contrast resolution in the next generation. Similarly, self-focusing arrays will provide essential components of a completely noninvasive therapeutic system capable of producing precise therapeutic dose at deep-seated tissue targets (for example, tumors) with a high degree of spatial localization.

Focusing is achieved by adjusting the phases of the ultrasound waves incident from each of the array elements so that they add constructively at the focus point of interest. In conventional (or geometrical) focusing, the phase associated with each transducer is computed from the known constant background speed of sound and the distance between that transducer and the desired focus point.[16] This type of focusing is purely geometrical. In other words, it ignores the effects of tissue inhomogeneity on the speed of propagation of the ultrasonic waves. The phase distortions introduced by using the conventional focusing mechanism could be severe and may not be ignored. Phase aberrations can cause the energy at the focus to be dispersed and shifted from the intended location.[15] Different invasive and noninvasive aberration correction mechanisms have been introduced and are being used for imaging[13–15,17] and hyperthermia.[5,7,18,19] Time delay estimation techniques, such as by cross-correlating signals from neighboring array elements, only correct for the effects of a thin aberrating layer near the phased array.[13] Effectively, such techniques correct phase errors only. Recent extensions of this work attempt to correct for amplitude distortions as well as phase distortions.[20]

Optimal pattern synthesis through homogeneous or inhomogeneous media can be attained using the pseudoinverse method.[18,21–23] Using this technique, we solve for a scalar, complex valued excitation weight for each array transducer

[a]Current address: Schlumberger-Doll Research, Old Quarry Road, Ridgefield, CT 06877.

from the wave propagation matrix of that medium. This method was demonstrated to provide powerful results for field pattern synthesis within the region of interest (ROI) according to a predetermined collection of constraints on the structure of the total field at a set of points in the ROI (control points). The idea behind this method is to relate the excitation weights to the set of control points using a matrix operator for wave propagation in the homogeneous or inhomogeneous media. One can solve for the minimum-norm least-squares solution of the excitation weights using the pseudoinverse of the propagation matrix. A major advantage of this method is the ability to deliver precise power deposition levels to multiple points in space. Another advantage is the ability to optimize the solution procedure for increased array excitation efficiency and intensity gain, without introducing undesired hot spots.[23] The pseudoinverse pattern synthesis method requires knowing the Green's function of the desired focus point at the array.[5,7,18] This cannot be easily achieved for the inhomogeneous case (in the presence of an aberrating medium).

The Green's function can be measured using a needle hydrophone implanted in the region at the point of interest.[5,7,18,19] This measurement can also be used to compute the Green's function at other desired locations near the hydrophone. This method has been used successfully for hyperthermia, however, it has some limitations. First, it is invasive, requiring a hydrophone near the desired focus point. Second, it expects the desired point to be within the homogeneous medium surrounding the hydrophone. In other words, the region where focusing is to take place must be reasonably far from any aberrating medium (or inhomogeneity).

A time reversal mirror approach was demonstrated with several phased arrays and was shown to provide effective method of focusing in the presence of strong tissue inhomogeneities.[12] It was also shown that the iterative time reversal method converges to an estimate of the Green's function of the location of the dominant scatterer in the ROI to the array surface.[24,25] This method has been extended to allow focusing near the dominant scatterer by estimating the Green's function to a desired point using the Green's function of the dominant scatterer.[26] Although these approaches are not limited to a thin aberrating layer near the transducer array, they do require a distinct dominant scatterer surrounded with a homogeneous medium.[26] Another extension of the time reversal mirror is the transfer matrix approach which allows for selective focusing.[24,25] A time reversal operator is computed whose eigenvectors provide the amplitudes and delays required to focus on selected scatterers. This approach requires that the scatterers be distinct (well resolved), and are distant from the aberrating medium. In fact, most approaches to aberration correction assume that the aberrating medium is a layer situated far from the desired focus point. In many cases, such as in breast tissue, this assumption is invalid.

We present a new self-focusing strategy which can prove successful in focusing through inhomogeneous media. In this strategy, we make use of the scattered field measured by the phased array to estimate the Green's function needed

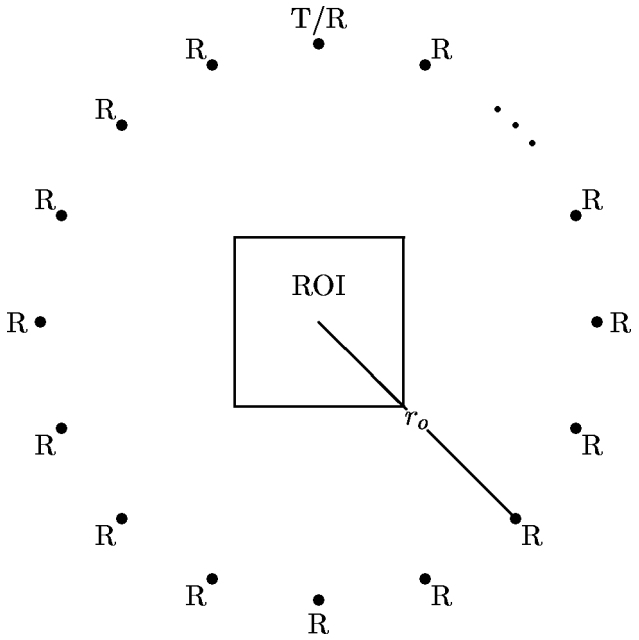

FIG. 1. The circular receive/transmit array and region of interest.

by the pseudoinverse pattern synthesis method. In particular, we use the distorted Born iterative (DBI) method to solve the nonlinear inverse scattering problem. The main idea behind the DBI method is that it alternates between (1) updating an estimate of the spatial structure of the inhomogeneity (the scattering function) given a current best estimate of the inhomogeneous Green's function and the total acoustic field in the ROI (i.e., solving an inverse scattering problem) and (2) updating the total field and Green's function given the previously generated estimate of the inhomogeneity (i.e., solving a forward scattering problem). The initial step of the algorithm corresponds to the zeroth order Born approximation, and the algorithm terminates when the Green's function is deemed to have converged. The convergence criterion is a percentage change in the estimated Green's function. Since the algorithm improves on the estimate of the kernel (the Green's function) at every iteration, it is referred to as the distorted Born iterative method (as opposed to the Born iterative method which updates only the total field at every iteration).[27–30] Once convergence is achieved, we use the estimated Green's function of the desired focus pixel to construct the propagation matrix required by the pseudoinverse pattern synthesis method.[21,23] This self-focusing approach is noninvasive and it does not make any assumptions about the background medium, about the shape and location of the aberrator, and about the distribution of the scatterers. It simply requires measurements of the scattered field outside the region of interest.

We present numerical simulations using a circular array with 128 line transducers which surround the region of interest as shown in Fig. 1. Only a subset, 32 transducers, is used for transmission in solving the inverse scattering problem. The results show the accuracy of the DBI method in estimating the Green's function as compared with the Green's function computed using the true spatial speed of sound. We use the pseudoinverse pattern synthesis method as the means of

obtaining optimized (in the minimum-norm least-squares sense) excitation weights for retransmission using the 128 array transducers. We present simulation results of field patterns, which show the quality of focus as compared with geometrical focusing. We also compare the obtained field patterns with field patterns obtained using the true Green's function (computed from the true speed of sound). In addition, we present results of multiple focusing which show the additional advantage of this combined inverse scattering-based focusing and the pseudoinverse pattern synthesis methods.

In Sec. I, we present the theory and solution of the forward and inverse scattering problems. We also discuss the solution of the general Green's function in terms of the forward scattering problem, and present a numerical method for solving such a problem for an unknown ROI. In Sec. II, we discuss the pseudoinverse pattern synthesis method and focusing through inhomogeneous media using estimates of the Green's function. The quality of focus is discussed in relation with the geometrical focusing technique and with the optimal focusing technique obtained using the true Green's function. We show simulation results and discuss the advantages of inverse scattering-based self-focusing in Sec. III. Finally, in Sec. IV, we conclude with a summary and planned future work.

I. MATHEMATICAL FORMULATION

Consider an infinite space containing a homogeneous loss-free acoustic medium with a constant background speed of sound, c_0. Embedded inside this space is a lossy, inhomogeneous medium with associated space-varying speed of sound, and constant density. Then the total field at a point, $\mathbf{r}$, due to a time-harmonic radiating source with $e^{-j\omega t}$ time dependence, can be described by the Helmholtz equation,

$$(\nabla^2 + k^2(\mathbf{r}))\Phi(\mathbf{r}) = 0, \tag{1}$$

and

$$\Phi(\mathbf{r}) = \Phi_i(\mathbf{r}) + \Phi_s(\mathbf{r}), \tag{2}$$

for $\mathbf{r} \in \Re^2$, where Φ is the total acoustic field for the longitudinal motion, Φ_i is the incident field, and Φ_s is the scattered field which satisfies the Sommerfeld radiation condition uniformly in all directions. The spatial function $k^2(\mathbf{r}) = [\omega^2/c^2(\mathbf{r})] + j[2\omega\alpha(\mathbf{r})/c(\mathbf{r})]$ is the wave number at frequency ω, speed of sound $c(\mathbf{r})$, and attenuation factor $\alpha(\mathbf{r})$.

An integral form representation of the scattering problem, equivalent to Eqs. (1) and (2) is the Lippmann–Schwinger equation, defined as

$$\Phi(\mathbf{r}) = \Phi_i(\mathbf{r}) + \int_{\Re^2} G_0(\mathbf{r},\mathbf{r}') f(\mathbf{r}') \Phi(\mathbf{r}') d\mathbf{r}', \tag{3}$$

where $f(\mathbf{r}) = \omega^2[1/c^2(\mathbf{r}) - 1/c_0^2] + j[2\omega\alpha(\mathbf{r})/c(\mathbf{r})]$ is the unknown scattering function, and G_0 is the scalar homogeneous Green's function.[28,31] The second term on the right hand side of Eq. (3) is the scattered field, $\Phi_s(\mathbf{r})$, which is measured at discrete points outside the ROI.

The scalar free-space (homogeneous) Green's function satisfies the wave equation,

$$(\nabla^2 + k_0^2) G_0(\mathbf{r},\mathbf{r}') = -\delta(\mathbf{r}-\mathbf{r}'), \tag{4}$$

where $k_0 = \omega/c_0$, and $\delta(\mathbf{r})$ is a two-dimensional unit impulse function which could represent a line source, or a line inhomogeneity. In other words, Green's function, $G_0(\mathbf{r},\mathbf{r}')$ models the field at a point $\mathbf{r}$ resulting from a single line source at $\mathbf{r}'$, in the absence of any boundaries. The two dimensional free-space Green's function in cylindrical coordinates has a closed form solution in terms of the zeroth order cylindrical Hankel function of the first kind,[28,32]

$$G_0(\mathbf{r},\mathbf{r}') = \frac{j}{4} H_0^{(1)}(k_0|\mathbf{r}-\mathbf{r}'|). \tag{5}$$

In general, the Green's function for inhomogeneous media is unknown and must be computed numerically as shown below.

A. The forward scattering problem

We define the forward scattering problem as that of solving the scattering problem defined by Eq. (3) for the total field, $\Phi(\mathbf{r})$, at any point $\mathbf{r} \in \Re^2$. We follow the method of moments to construct a matrix system representing Eq. (3),[28,33] which is then solved by matrix inversion.

First, the unknown field $\Phi(\mathbf{r})$ is expanded as follows:

$$\Phi(\mathbf{r}) = \sum_{n=1}^{N} \phi_n g_n(\mathbf{r}), \tag{6}$$

where ϕ_n are the expansion coefficients, the integer parameter N is the number of pixels covering the region of interest, and the function $g_n(\mathbf{r})$ is an appropriate basis function. In this paper, $g_n(\mathbf{r})$ is simply a two-dimensional rectangular pulse centered at the nth pixel. The region of interest is large enough so that it completely contains the scattering object. It must be noted that for an accurate recovery of the field from ϕ_n, N (for a given region of interest) must be selected to satisfy the sampling theorem.

Replacing $\Phi(\mathbf{r})$ from both sides of Eq. (3) by its expansion, and after some algebraic manipulations, gives

$$\sum_{n=1}^{N} \phi_n \left[g_n(\mathbf{r}) - \int_{S_n} G_0(\mathbf{r},\mathbf{r}') f(\mathbf{r}') g_n(\mathbf{r}') d\mathbf{r}' \right] = \Phi_i(\mathbf{r}), \tag{7}$$

where S_n is the region of support of the nth basis function, in this case, the square area of the nth pixel.

Upon multiplying both sides of Eq. (7) with a point matching function, $w_m = \delta_m$, $m = 1,...,N$, and integrating the result, we obtain

$$\sum_{n=1}^{N} \phi_n \left[\delta_{mn} - \int_{S_n} G_0(\mathbf{r}_m,\mathbf{r}') f(\mathbf{r}') g_n(\mathbf{r}') d\mathbf{r}' \right] = \Phi_i(\mathbf{r}_m). \tag{8}$$

The two-dimensional impulse step function δ_m is unity at $\mathbf{r} = \mathbf{r}_m$, and is zero everywhere else. Similarly, the function δ_{mn} is unity at $\mathbf{r} = \mathbf{r}_n = \mathbf{r}_m$ (or when $m = n$), and is zero everywhere else.

Equation (8) can be written in matrix form as

$$\mathbf{P}\boldsymbol{\phi} = \boldsymbol{\phi}_i, \tag{9}$$

where $\mathbf{P}$ is an $N \times N$ nonsingular matrix, $\boldsymbol{\phi}$ is an $N \times 1$ vector containing the unknown total field coefficients, and $\boldsymbol{\phi}_i$ is an

$N\times 1$ vector of elements from the incident field evaluated at $\mathbf{r}_m$ for $m=1,...,N$. Once the matrix $\mathbf{P}$ is computed, it may be inverted to solve for the coefficients of the total field. Normally, a solution of this forward scattering problem is obtained for each transmit position, using the scattering function, $f(\mathbf{r})$, or its estimate.

B. The inverse scattering problem

The inverse scattering problem is that of solving Eq. (3) for the scattering function, $f(\mathbf{r})$, from measurements of the scattered field outside a ROI. As in the forward scattering problem, we use the method of moments to obtain a matrix representation of the inverse scattering problem. In this case, however, the unknown parameter is $f(\mathbf{r})$. Hence, we use the expansion $f(\mathbf{r})=\Sigma_{n=1}^{N} f_n g_n(\mathbf{r})$ in the integral formula of the scattered field $\Phi_s(\mathbf{r})$,

$$\Phi_s(\mathbf{r})=\int_{\Re^2} G_0(\mathbf{r},\mathbf{r}')f(\mathbf{r}')\Phi(\mathbf{r}')d\mathbf{r}', \tag{10}$$

to produce

$$\sum_{n=1}^{N} f_n\left[\int_{S_n} G_0(\mathbf{r}_m,\mathbf{r}')g_n(\mathbf{r}')\Phi(\mathbf{r}')d\mathbf{r}'\right]=\Phi_s(\mathbf{r}_m), \tag{11}$$

for $m=1,...,M$ and $n=1,...,N$, where M is the number of array elements used for reception, and N is the number of pixels in the ROI. In matrix form, we have

$$\mathbf{Qf}=\boldsymbol{\phi}_s, \tag{12}$$

where $\mathbf{Q}$ is an $M\times N$ matrix, $\mathbf{f}$ is an $N\times 1$ vector containing the unknown scattering function coefficients, and $\boldsymbol{\phi}_s$ is an $M\times 1$ vector containing measurements of the scattered field as observed at all M points.

We note, by observing Eq. (11), that Eq. (12) is dependent on the total field inside the ROI which is normally unknown. This requires approximating the wave equation using either the Born or Rytov methodologies. Both have certain advantages and disadvantages.[34] The Rytov approximation is potentially useful at high operating frequencies. Whereas, the Born approximation is more appropriate at low operating frequencies[34,35] and is, therefore, the method of choice throughout our current work. The zeroth order Born approximation assumes that the total field in the ROI is equal to the incident field, which is acceptable only for weak scattering. In other words, it assumes that $\Phi_s(\mathbf{r})$ is small compared to the incident field, $\Phi_i(\mathbf{r})$.[28,34] In applications of interest, such as image-guided therapy in the breast, the regions are characterized as highly scattering,[36] thus corrections are usually needed to obtain reasonable inverse solutions.[27–30,35] Also, the kernel matrix of the inverse scattering problem is underdetermined and ill-posed.[37] We resolve these problems by using the singular value decomposition to obtain a regularized minimum-norm least-squares solution.[37–40] The inverse solution obtained from Eq. (12) is due to one transmit position. Normally, the inverse scattering problem is solved for multiple transmit position, where the individual inverse solution vectors are vector-averaged to produce a reasonable final solution vector.

C. Estimation of the Green's function

We utilize the distorted Born iterative method for solving the nonlinear inverse scattering problem. This method, unlike the Born iterative method, attempts to correct for the integral equation kernel (Green's function) as well as the total field. At every iteration, the algorithm uses the latest estimate of the scattering function to compute the Green's function and the total field at every pixel in the ROI. These estimates are used in the inverse scattering problem to update the scattering function incrementally. The advantages of the DBI method are that it is not limited to a simple homogeneous background and that it has a larger range (in scattering strength) of applicability.[29,35] Although this algorithm has a faster convergence rate relative to the simpler Born iterative method, it is computationally intensive and, at this stage, cannot be used for real time applications. Also, the algorithm is sensitive to measurement noise, therefore careful treatment of updating and inverting the inverse problem kernel matrix is essential.[39–41] Finally, in the case of strongly scattering media, the DBI method could diverge or converge to an erroneous inverse solution, thus producing wrong estimates of the inhomogeneous Green's function. This is caused by a misleading initial Born approximation. Another aspect of our research deals with improving the DBI method for solving the inverse scattering problem of large, strongly scattering regions. These techniques can still be used in place of the DBI method for self-focusing.[41] The DBI method was developed and used extensively for electromagnetic inverse scattering applications.[27–29] Its applicability and utility in ultrasound is obvious and appears to be promising.[41]

In estimating the inhomogeneous Green's function, we make use of the fact that this general (inhomogeneous) Green's function is the impulse response of the inhomogeneous wave equation. Consequently, we can write the Green's function at any point $\mathbf{r}$ due to some fictitious source at $\mathbf{r}_s$ as the solution to the forward scattering problem,

$$G(\mathbf{r},\mathbf{r}_s)=\Phi_i(\mathbf{r})+\int_{\Re^2} G_0(\mathbf{r},\mathbf{r}')f(\mathbf{r}')G(\mathbf{r}',\mathbf{r}_s)d\mathbf{r}'. \tag{13}$$

Equation (13) is a forward scattering problem which, upon discretization using the method of moments, translates into a matrix system equivalent to Eq. (9),

$$\mathbf{P}\underbrace{\begin{bmatrix} G(\mathbf{r}_1,\mathbf{s}_1) & G(\mathbf{r}_1,\mathbf{s}_2) & \cdots & G(\mathbf{r}_1,\mathbf{s}_M) \\ \vdots & \vdots & \vdots & \\ G(\mathbf{r}_N,\mathbf{s}_1) & G(\mathbf{r}_N,\mathbf{s}_2) & \cdots & G(\mathbf{r}_N,\mathbf{s}_M) \end{bmatrix}}_{\mathbf{G}}$$
$$=\underbrace{\begin{bmatrix} G_0(\mathbf{r}_1,\mathbf{s}_1) & G_0(\mathbf{r}_1,\mathbf{s}_2) & \cdots & G_0(\mathbf{r}_1,\mathbf{s}_M) \\ \vdots & \vdots & \vdots & \vdots \\ G_0(\mathbf{r}_N,\mathbf{s}_1) & G_0(\mathbf{r}_N,\mathbf{s}_2) & \cdots & G_0(\mathbf{r}_N,\mathbf{s}_M) \end{bmatrix}}_{\mathbf{G}_0}, \tag{14}$$

where $\mathbf{P}$ is as defined in Eq. (9), $G(\mathbf{r}_n,\mathbf{s}_m)$ and $G_0(\mathbf{r}_n,\mathbf{s}_m)$ for $n=1,...,N$ and $m=1,...,M$ are the expansion coefficients of the true inhomogeneous Green's function and the homo-

geneous Green's function, respectively, M is the number of scattered field measurements, and N is the total number of pixels covering the ROI. The expansion coefficients, which are similar to those defined for the total field in Eq. (6), reduce to samples of the Green's functions when using the simple rectangular pulse expansion function.[41]

Figure 2 shows a flowchart description of the DBI method for estimating the Green's function. At every iteration we solve the inverse scattering problem for an average incremental correction vector, $\mathbf{\Delta f}$, which is added to the scattering function vector. This correction vector is a function of the kernel matrix, $\mathbf{Q}(\boldsymbol{\phi}^{k,l-1},\mathbf{G}^{l-1})$, and the difference between the measured scattered field, $\boldsymbol{\phi}_s^k$, and the $(l-1)$th estimate of the scattered field, $\hat{\boldsymbol{\phi}}_s^{k,l-1}$, averaged over K transmit positions. Effectively, we solve K inverse problems whose average solution comprise the incremental correction vector, where K is a subset of the array transducers used for transmission. Initially, $\hat{\boldsymbol{\phi}}_s^{k,0}=0$ for $k=1,...,K$, thus the incremental change in the first step is the zeroth order Born inverse solution which is added to an initial scattering function solution of zero.

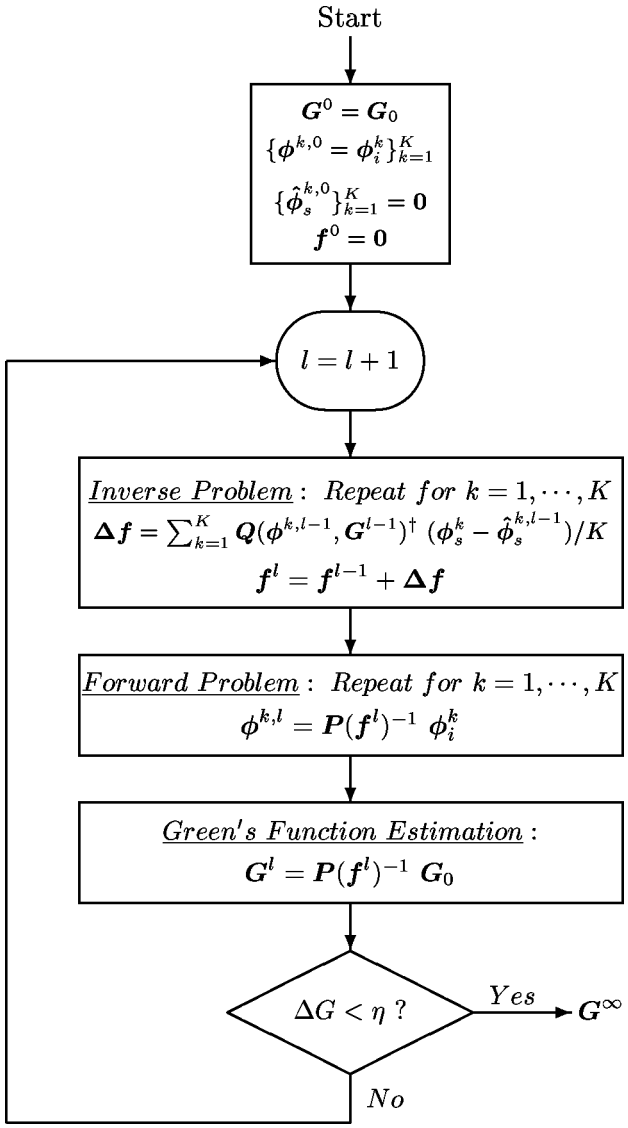

FIG. 2. A flow chart description of the DBI estimation of the Green's function. The $(\cdot)^\dagger$ denotes the generalized inverse.

Each incremental inverse scattering problem is of the form:

$$\Phi_s(\mathbf{r})-\hat{\Phi}_s^{k,l-1}(\mathbf{r})=\int_{\Re^2} G^{l-1}(\mathbf{r},\mathbf{r}')\Delta f^{k,l}(\mathbf{r}')\Phi^{k,l-1}(\mathbf{r}')d\mathbf{r}', \tag{15}$$

which is discretized using the method of moments to produce

$$\mathbf{Q}(\phi^{k,l-1},\mathbf{G}^{l-1})\mathbf{\Delta}\,\mathbf{f}^{k,l}=(\boldsymbol{\phi}_s^k-\hat{\boldsymbol{\phi}}_s^{k,l-1}). \tag{16}$$

Also, at every iteration we compute the total field in the ROI due to the incident field from each of the K transmitters independently. The incident field vectors, $\{\boldsymbol{\phi}_i^k\}_{k=1}^K$, and the total field vectors, $\{\boldsymbol{\phi}^k\}_{k=1}^K$, are of size $N\times 1$, where N is the total number of pixels in the ROI. This solution uses the latest estimate of the scattering function, $\mathbf{f}^{\,l}$, in forming the $N\times N$ matrix $\mathbf{P}(\mathbf{f}^{\,l})$. Finally, the inhomogeneous Green's function is computed at every iteration using $\mathbf{P}(\mathbf{f}^{\,l})$ in Eq. (14). That is, $\mathbf{P}(\mathbf{f}^{\,l})$ is computed once per iteration and is used to solve for the total field and the inhomogeneous Green's function.

The algorithm terminates when ΔG falls below a preset threshold parameter, η, where ΔG is a normalized distance measure between the current estimate and previous estimate of the Green's function averaged over the N pixels and the M measurements. Currently, we use

$$\Delta G=\frac{\Sigma_{n=1}^N\Sigma_{m=1}^M|G(\mathbf{r}_n,\mathbf{s}_m)^l-G(\mathbf{r}_n,\mathbf{s}_m)^{l-1}|^2}{\Sigma_{n=1}^N\Sigma_{m=1}^M|G(\mathbf{r}_n,\mathbf{s}_m)^l|^2}. \tag{17}$$

This measure can be easily modified to account for the Green's function due to specific focus points in the ROI or due to the pixel with the largest change, for example,

$$\Delta G=\max_{n=1,...,N}\left\{\frac{\Sigma_{m=1}^M|G(\mathbf{r}_n,\mathbf{s}_m)^l-G(\mathbf{r}_n,\mathbf{s}_m)^{l-1}|^2}{\Sigma_{m=1}^M|G(\mathbf{r}_n,\mathbf{s}_m)^l|^2}\right\}. \tag{18}$$

II. PATTERN SYNTHESIS METHOD

The incident field pattern delivered by the M time-harmonic array elements can be written as

$$\Phi_i^f(\mathbf{r})=\sum_{m=1}^M G_0(\mathbf{r},\mathbf{r}_m)u_m, \tag{19}$$

where it is assumed that the incident field is generated using infinite line sources modeled by the homogeneous Green's function, which has been defined by Eq. (5), Φ_i^f is the focused incident field pattern, and u_m is a scalar, complex valued excitation weight associated with the mth array element.

In geometric focusing, the excitation weights are determined using the known background speed of sound and the distance between the single focus point and the transducers.[16] Mathematically,

$$\Phi_i^f(\mathbf{r})=\sum_{m=1}^M G_0(\mathbf{r},\mathbf{r}_m)e^{-j(\omega/c_0)d_m}, \tag{20}$$

where d_m is the distance between the focus point and the mth transducer, ω is the operating frequency, and c_0 is the known

speed of sound in the homogeneous medium. Equivalently, we can use the homogeneous Green's function for geometrical focusing, which, in the far field assumption, reduces to Eq. (20).

Following the theoretical development of the pseudoinverse pattern synthesis method,[21,23] we write Eq. (19) in matrix form,

$$\begin{bmatrix} \Phi_i^f(\mathbf{r}_1) \\ \vdots \\ \Phi_i^f(\mathbf{r}_N) \end{bmatrix} = \begin{bmatrix} G_0(\mathbf{r}_1,\mathbf{s}_1) & G_0(\mathbf{r}_1,\mathbf{s}_2) & \cdots & G_0(\mathbf{r}_1,\mathbf{s}_M) \\ \vdots & \vdots & & \vdots \\ G_0(\mathbf{r}_N,\mathbf{s}_1) & G_0(\mathbf{r}_N,\mathbf{s}_2) & \cdots & G_0(\mathbf{r}_N,\mathbf{s}_M) \end{bmatrix} \times \begin{bmatrix} u_1 \\ \vdots \\ u_M \end{bmatrix}, \tag{21}$$

where the $N\times 1$ vector $\boldsymbol{\phi}_i^f=[\Phi_i^f(\mathbf{r}_1)\cdots\Phi_i^f(\mathbf{r}_N)]^T$ contains samples of the focused incident field, $G_0(\mathbf{r}_n,\mathbf{s}_m)$ for $n=1,...,N$ and $m=1,...,M$ are samples of the homogeneous Green's function, and $\mathbf{u}=[u_1\cdots u_M]^T$ is an $M\times 1$ excitation-weight vector.

The homogeneous media does not change the focused incident field pattern, ϕ_i^f, equivalently, the P matrix of the forward scattering problem is equal to the identity matrix. In this case, the actual total field pattern delivered to the ROI is the focused incident field pattern, ϕ_i^f. On the other hand, when the medium is inhomogeneous, this field pattern goes through a distortion operation which can be defined in terms of the forward scattering problem. Therefore, by application of the forward scattering problem, Eq. (21) becomes

$$\mathbf{P}^{-1}\boldsymbol{\phi}_i^f=\mathbf{P}^{-1}\mathbf{G}_0\mathbf{u}, \tag{22}$$

where $\mathbf{P}$ is the $N\times N$ forward scattering problem matrix, and $\mathbf{G}_0$ is the $N\times M$ homogeneous Green's function matrix encountered in Eqs. (14) and (21). Note that $\boldsymbol{\phi}=\mathbf{P}^{-1}\boldsymbol{\phi}_i^f$ is the total field vector due to the focused (modulated) incident field, $\boldsymbol{\phi}_i^f$, and $\mathbf{G}=\mathbf{P}^{-1}\mathbf{G}_0$ is the inhomogeneous Green's function matrix defined by Eq. (14). The $\mathbf{P}$ matrix distorts the focused incident field due to the presence of inhomogeneities in the media. This could result in shifting the focus point and in widening the main lobe. Such distortions could be dramatic and must be accounted for when computing the excitation weights.

For a given $n\leqslant M$ predetermined set of control points on the field pattern at some pixels in the ROI defined by the control pattern vector $\mathbf{p}$, we can write Eq. (22) as

$$\mathbf{p}=\mathbf{H}\mathbf{u}, \tag{23}$$

where the $n\times M$ matrix, $\mathbf{H}$ is the propagation matrix, and $\mathbf{u}$ is the excitation-weight vector. For simplicity and without loss of generality, the $n\times 1$ control pattern vector, $\mathbf{p}$, is set to $[1\cdots 1]^T$ throughout our simulations presented in Sec. III. It should be clear from Eq. (22) that using an estimate of $\mathbf{P}$, or equivalently $\mathbf{G}$, in constructing the propagation matrix, $\mathbf{H}$, compensates for the inhomogeneities in the media. Therefore, the rows of the $n\times M$ matrix $\mathbf{H}$ are the n rows of the estimated Green's function matrix, $\mathbf{G}$, corresponding to the pixels referenced by the control pattern vector. In other words,

$$\mathbf{H}=\begin{bmatrix} G(\mathbf{r}_{i_1},\mathbf{s}_1)^\infty & G(\mathbf{r}_{i_1},\mathbf{s}_2)^\infty & \cdots & G(\mathbf{r}_{i_1},\mathbf{s}_M)^\infty \\ \vdots & \vdots & & \vdots \\ G(\mathbf{r}_{i_n},\mathbf{s}_i)^\infty & G(\mathbf{r}_{i_n},\mathbf{s}_2)^\infty & \cdots & G(\mathbf{r}_{i_n},\mathbf{s}_M)^\infty \end{bmatrix}, \tag{24}$$

where $i_1\cdots i_n$ are the pixels corresponding to the focus locations of interest, and $G(\mathbf{r}_i,\mathbf{s}_m)^\infty$ for $m=1,...,M$ is the ith row from the best estimate (after convergence of the estimation algorithm as indicated by the $(\cdot)^\infty$) of the $N\times M$ matrix $\mathbf{G}$.

Minimum-norm least-squares optimized excitation weights, which can be used for synthesizing the field patterns of inhomogeneous wave propagation, are obtained by taking the pseudoinverse of $\mathbf{H}$,[21,23]

$$\hat{\mathbf{u}}=\mathbf{H}^{*T}(\mathbf{H}\mathbf{H}^{*T})^{-1}\mathbf{p}, \tag{25}$$

where the $(\cdot)^{*T}$ denotes the conjugate transpose, and the operator $\mathbf{H}^\dagger=\mathbf{H}^{*T}(\mathbf{H}\mathbf{H}^{*T})^{-1}$ is the pseudoinverse of $\mathbf{H}$. For example, in the single focus case with a unity control point, the propagation matrix becomes a row vector equal to $\mathbf{h}=[G(\mathbf{r}_f,\mathbf{s}_1)\ G(\mathbf{r}_f,\mathbf{s}_2)\cdots G(\mathbf{r}_f,\mathbf{s}_M)]$ for the M-element phased array, where $\mathbf{r}_f$ is the focus point of interest. The excitation solution vector reduces to

$$\hat{\mathbf{u}}=\frac{\mathbf{h}^{*T}}{(\mathbf{h}\mathbf{h}^{*T})}. \tag{26}$$

The advantages of the pseudoinverse pattern synthesis method include the ability to produce optimal field patterns for multiple focusing through homogeneous and inhomogeneous media.[5,19] This scheme also has the capability of optimizing the solution for increased gain and array excitation efficiency, without introducing undesired hot spots.[17,21–23]

This inverse scattering-based focusing incorporates information about the true nature of the ROI in the pseudoinverse pattern synthesis method. We estimate the inhomogeneous Green's function from the scattered field measured outside the ROI. Unlike geometrical focusing, this approach does account for the spatial variation in the speed of sound throughout the ROI. Also, this technique is noninvasive; it does not make any assumption about the location of the inhomogeneity (or aberrating medium) relative to the transducer array; and it does not rely on the existence of distinct dominant or pointlike scatterers near the focus point. Finally, we benefit from the advantages of the pseudoinverse pattern synthesis method such as producing optimal multiple focus field patterns through the inhomogeneous media, and optimizing solutions for increased array excitation efficiency and intensity gain.

III. SIMULATION RESULTS AND DISCUSSION

We simulated the DBI algorithm for the circular array shown in Fig. 1. It consists of 128 receive elements which are equally distributed over a circle of radius $10\lambda_0$. Only 32 equally spaced elements are used, one at a time, to transmit a continuous wave at a frequency of 500 kHz. The background medium is assumed loss-free with a known constant speed of sound equal to 1.484 mm/μs, thus $\lambda_0=2.968$ mm. We consider two cases for the region of interest. In the first case, a two-dimensional region of interest of size $6\lambda_0\times 6\lambda_0$, cen-

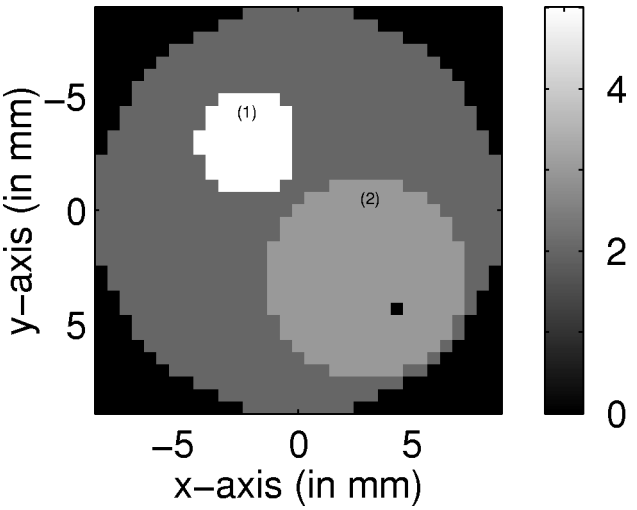

FIG. 3. The true speed of sound in the ROI shown as a percentage increase over the background speed of sound.

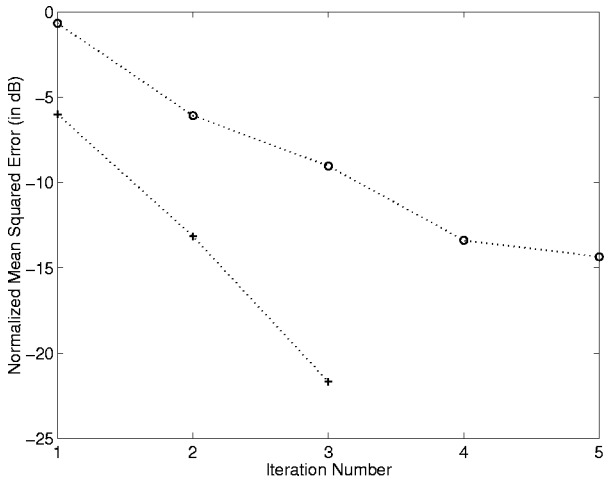

FIG. 5. The mean squared error of the Green's function estimates versus iteration number for the low contrast case (+) and the high contrast case (○), where the reference is the true Green's function.

tered at the center of the circular array, is discretized at pixel width of $\lambda_0/5.5 \times \lambda_0/5.5$. Hence, the dimension of the **Q** matrix computed in the inverse scattering problem is 128×1089, and the dimension of the **P** matrix computed in the forward scattering problem is 1089×1089. In the second case, the two-dimensional region of interest (shown in Fig. 12) is of size $12\lambda_0 \times 12\lambda_0$, discretized at pixel width of $\lambda_0/6 \times \lambda_0/6$. This produces a **Q** matrix of size 128×5184 and a **P** matrix of size 5184×5184. This intensive memory requirement is the limiting factor of the method of moments for solving the forward scattering problem. Other techniques, such as finite element methods, produce symmetric and sparse matrices of which we can take advantage. The rank reduction strategy is used to obtain a regularized pseudoinverse operator[37–41] for solving the inverse scattering problem at every iteration of the DBI algorithm.

Figure 3 shows a gray scale image of a true region of interest, which displays the contrast as a percentage increase in the speed of sound inside the scattering objects relative to the speed of sound in the background medium. Although this figure shows percentage contrasts of 2%, 3%, and 5%, we vary the contrast on the two smaller object [marked (1) and (2)] in the simulation results. Figure 4 shows the squared error between the estimated Green's function and the true Green's function (computed using the true scattering function) averaged over all pixels in the ROI versus transducer index for low contrast case (using contrasts 2%, 3%, and 5%), and high contrast case (object contrasts increased to 2%, 13%, and 15%, respectively). Figure 5 shows the squared error of these estimates, averaged over all pixels in the ROI and over all transducers, versus the iteration number of the DBI algorithm for both, the low and the high contrast cases. Note that the true Green's function is computed via the forward scattering problem using the true spatial speed of sound in the ROI. The simulations show excellent estimation of the true Green's function even for the stronger inhomogeneous media. The algorithm can be permitted to iterate further for better estimate of the Green's function. However, at signal-to-noise ratios (SNR) lower than 30 dB, the DBI method could show increasing mean squared error after

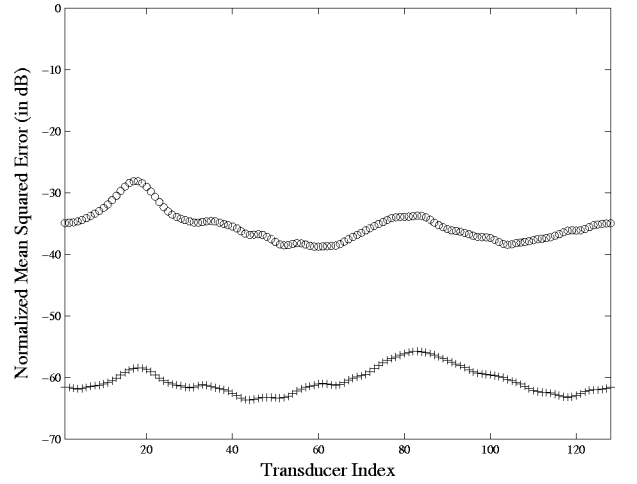

FIG. 4. The squared error in estimating the Green's function averaged over all pixels in the region of interest for the low contrast case (+) and the high contrast case (○), where the reference is the true Green's function.

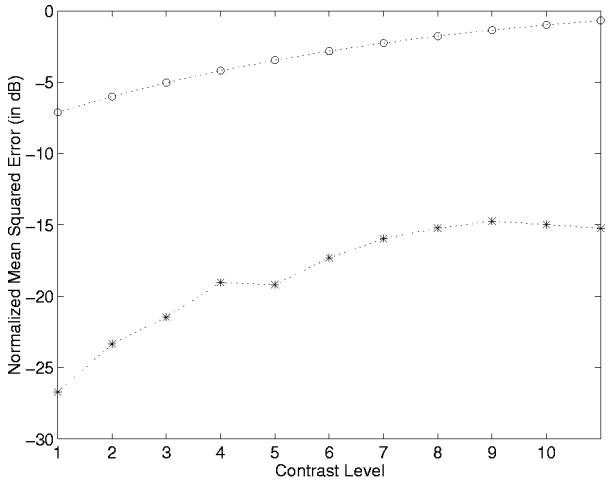

FIG. 6. The mean squared error of the estimated Green's function (∗) and the homogeneous Green's (○) function versus average contrast level percentage, where the reference is the true Green's function.

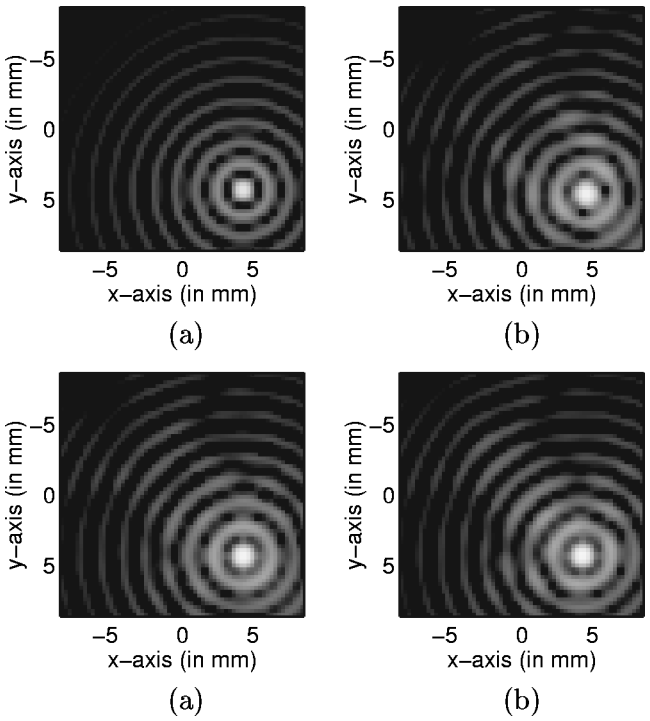

FIG. 7. The magnitude of the total field intensity in the region for (a) geometrical focusing through homogeneous media, (b) geometrical focusing through inhomogeneous media, (c) true Green's function focusing through inhomogeneous media, and (d) estimated Green's function focusing through inhomogeneous media.

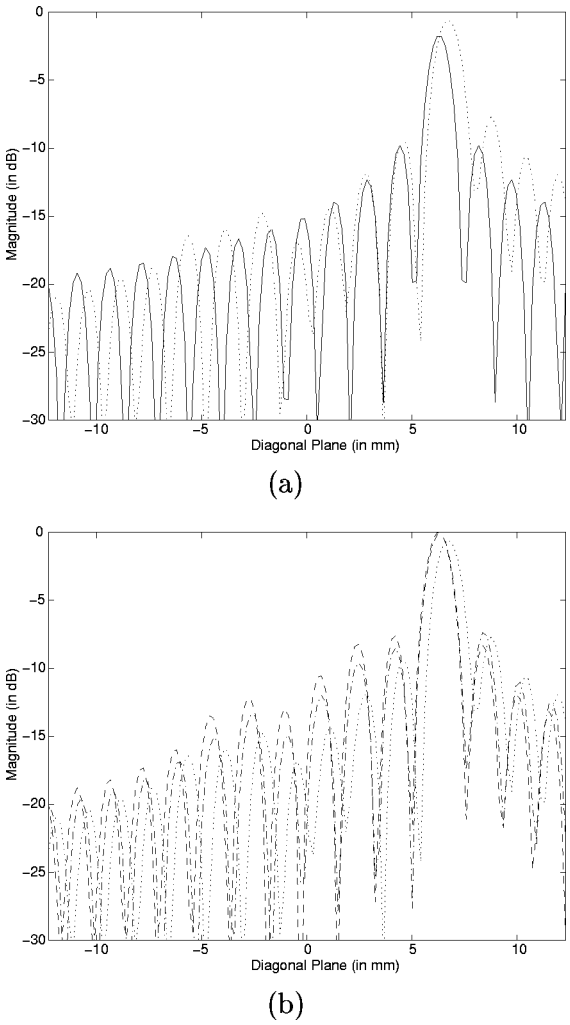

FIG. 8. A slice at the diagonal of the total field pattern for geometrical focusing through homogeneous media (solid), geometrical focusing through inhomogeneous media (dotted), true Green's function focusing through inhomogeneous media (dashed), and estimated Green's function focusing through inhomogeneous media (dash-dotted).

many iterations due to the accumulation of error. A modified DBI method has been investigated for use with low SNR measurements.[40,41]

It is expected the quality of Green's function estimate to degrade for increased scattering media (either due to increase in the size of the scatterers, or due to the increase in contrast levels). Figure 6 shows a plot of the average squared error of the estimated Green's function versus contrast level, where the true Green's function is used as the reference. The contrast level cases (x-axis in Fig. 6) correspond to the contrasts of objects (1) and (2) in Fig. 3 increased from 5% and 3% to 15% and 13%, respectively, in increments of 1%. Although the error measure increases as a function of contrast, we can allow the algorithm to iterate further so as to provide the needed accuracy for the Green's function estimate. The results discussed so far show that the DBI provide excellent estimates for the Green's function, and therefore, can be used as the tool for focusing the ultrasonic waves through inhomogeneous media.

We simulate the Green's function focusing for the same circular array shown in Fig. 1. In the estimation of the Green's function, we use 128 receive elements, of which only 32 elements are used for transmission. As for the focusing procedure, we retransmit the continuous ultrasound wave from all 128 elements. The focused incident beam is computed as given by Eq. (19), and the excitation weights are computed as described in Sec. II. As a reference, we compute the focused incident field using excitation weights derived from the true Green's function (computed from the true speed of sound), and excitation weights derived from the homogeneous Green's function to simulate geometrical focusing through inhomogeneous media. We operate on the focused incident field with the true **P** matrix (computed using the true scattering function) to compute the total field in the ROI. Also, we show results of the total field in the ROI obtained for geometrical focusing through homogeneous media. In this case, the **P** matrix is replaced with identity matrix, operating on the geometrically focused incident field. These results show the effects of the true inhomogeneity on each of the focusing schemes relative to the homogeneous case.

In the first simulation study, we use the true ROI shown in Fig. 3 with contrast level equal to 15% for object (1), and contrast level equal to 13% for object (2). The focus point of interest is the pixel marked in black in Fig. 3. In Fig. 7, we display intensity images with 16-dB dynamic range for the total field in the ROI. These results are computed for the geometrical focusing through homogeneous media, the geometrical focusing through inhomogeneous media, the true Green's function focusing through inhomogeneous media, and the estimated Green's function focusing through inhomogeneous media. We show a cross-section line plot of the

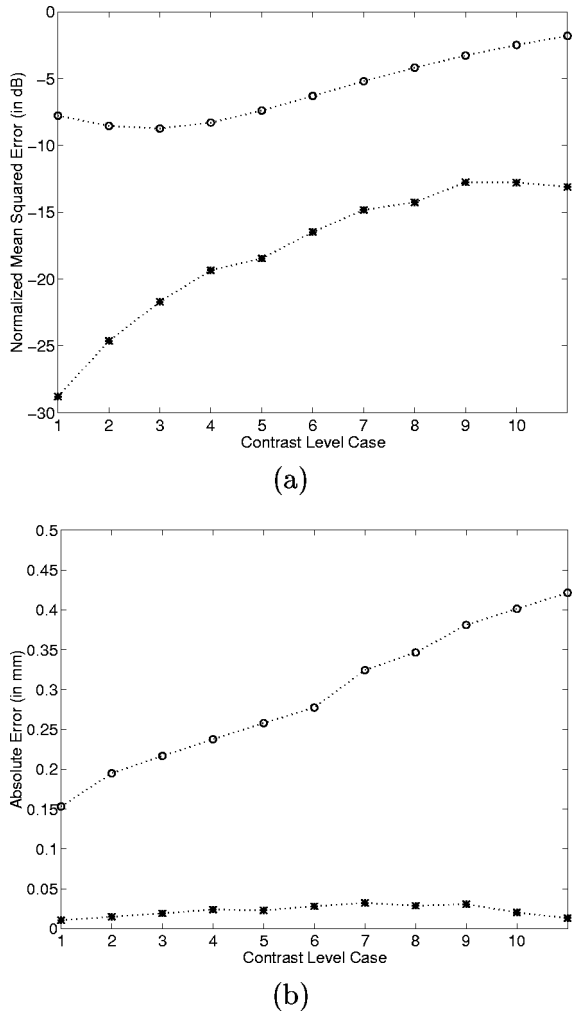

FIG. 9. (a) The mean squared error of the total field in the region of interest, and (b) the error shift of the focus point for the geometrical focusing through inhomogeneous media (○) and for the estimated Green's function focusing (∗) as a function of contrast.

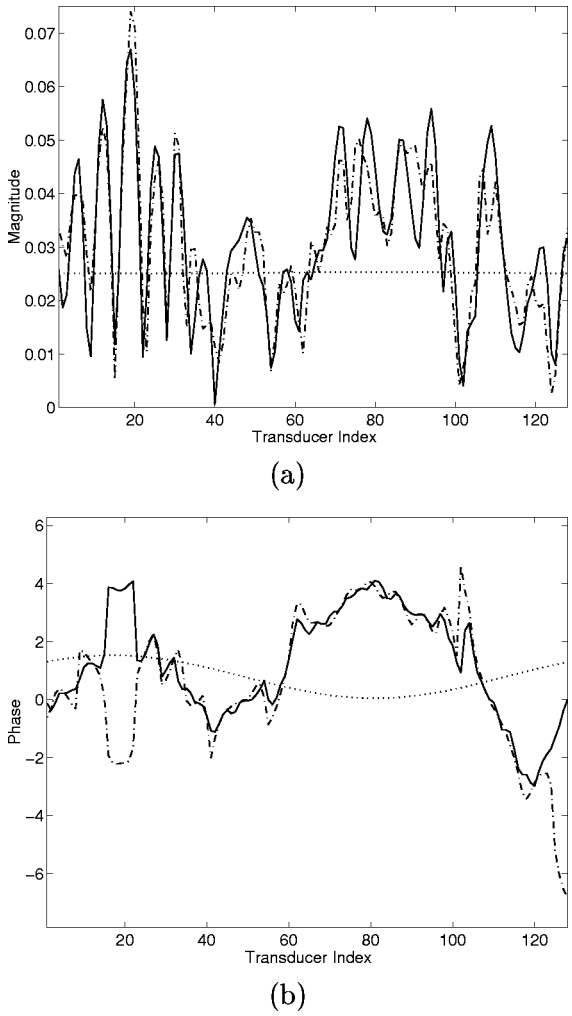

FIG. 11. (a) Magnitude and (b) phase of the true Green's function (solid), the estimated Green's function (dash-dotted), and the homogeneous Green's function (dotted) for the center pixel.

total fields of Fig. 7 in Fig. 8. These results show the effects of the inhomogeneity on the total field, which are particularly visible in the geometrically focused field pattern. These results also show that the geometrically focused pattern has a slightly wider main lobe and a shift in the focal point, which are somewhat corrected for in the Green's function focusing. Finally, the energy outside the main lobe is apparently larger, and is unevenly distributed in the field patterns obtained from the geometrical focusing scheme. This uneven distribution of energy and focal point shift are dependent on the scattering properties of inhomogeneous media in the ROI. Therefore, for increased size inhomogeneities, as in breast tissue, the distortions in the field pattern are expected to increase. On the other hand, the estimation of the Green's function is independent of the strength of the inhomogeneity as long as it is within the applicability of the algorithm used for solving the inverse scattering problem.

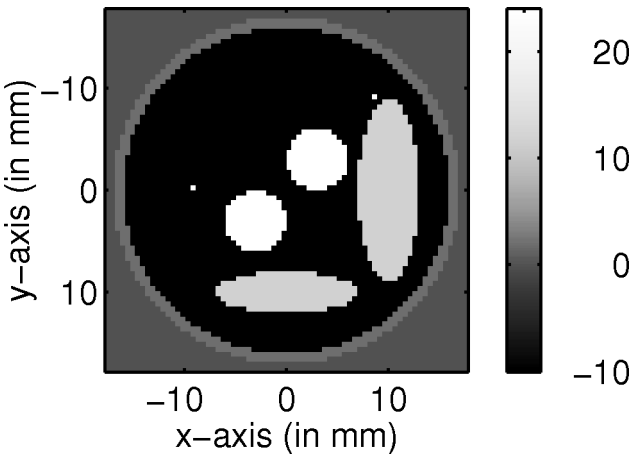

FIG. 10. The true speed of sound in the ROI shown as a percentage increase over the background speed of sound.

We compute the mean squared error for the total fields resulting from geometrical focusing and from the inverse scattering-based focusing. The total field distribution computed using the true Green's function focusing is used as the reference field. Figure 9(a) shows such results as a function of contrast for the same focus point, where the contrast level for objects (1) and (2), respectively, is increased from 5% and 3% to 15% and 13% in steps of 1%. Figure 9(b) presents

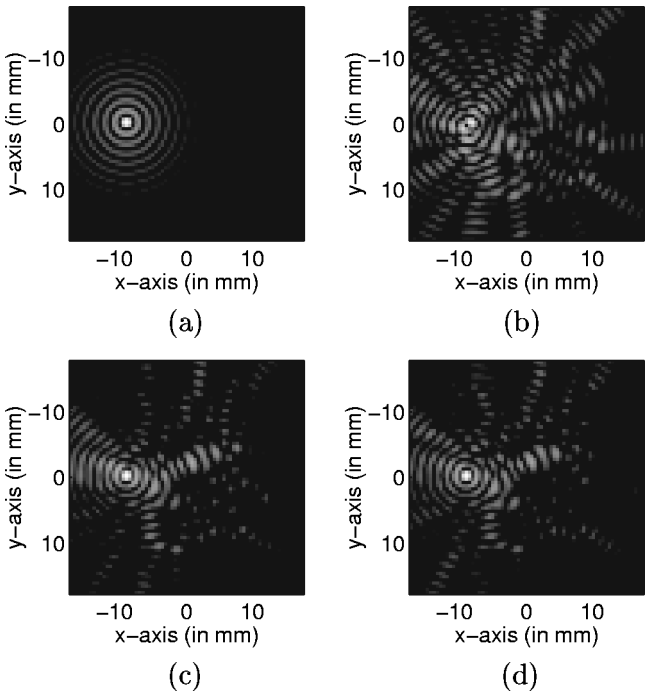

FIG. 12. The magnitude of the total field intensity in the region for (a) geometrical focusing through homogeneous media, (b) geometrical focusing through inhomogeneous media, (c) true Green's function focusing through inhomogeneous media, and (d) estimated Green's function focusing through inhomogeneous media.

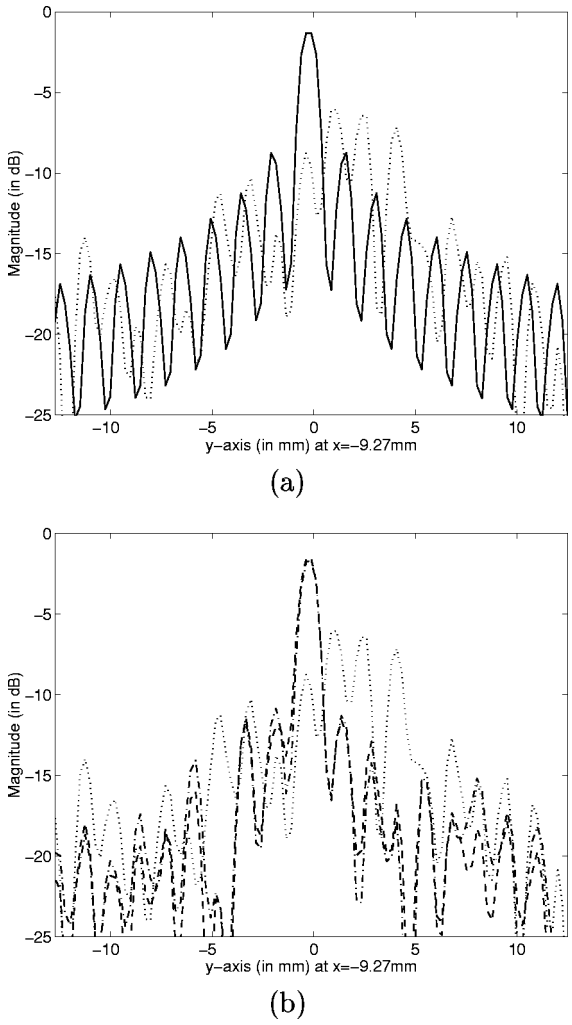

FIG. 13. A slice at $x=-9.27$ mm of the total field pattern (a) for geometrical focusing through homogeneous media (solid) and geometrical focusing through inhomogeneous media (dotted), and (b) for true Green's function focusing (dashed), estimated Green's function focusing (dash-dotted) and geometrical focusing (dotted) through inhomogeneous media.

the absolute error in focal point shift (in mm) at each contrast level for the geometrical focusing and the inverse scattering based focusing. The results presented in this simulation show the field pattern produced using the inverse scattering-based focusing has at least a 10-dB error improvement over the geometrically focused pattern. Also, it is apparent that the technique does not suffer from problems of shifting the focal point even at high contrast levels.

Figure 10 shows the gray scale image of the spatial distribution for the second case. This region is larger with higher contrast than the previously simulated case. Also, the SNR level is 30 dB, which is well within the capabilities of our measurement systems. Figure 11 shows the magnitude and phase of the true Green's function (solid), the estimated Green's function (dash-dotted), and the homogeneous Green's function (dotted) versus transducer index for the pixel at the center of the array. The apparent large phase difference between the estimated Green's function and the true Green's function around the 20-th transducer index is approximately 2π, which is a negligible phase error. Figure 12 displays the field pattern intensity in the region of interest on a 16-dB scale using the geometrical focusing in (a) and (b) and the Green's function focusing in (c) and (d). The pixel location of the focal point of interest is shown, in white, on the region in Fig. 10. We also show cross-section line plots through the field patterns at $x=-0.25$ mm in Fig. 13, and at $y=-9.27$ mm in Fig. 14. This simulation result, once again, demonstrates the accuracy of estimating the Green's function for highly scattering media, and in the presence of noise. It is apparent from the field pattern of the geometrical focusing through inhomogeneous media [Fig. 12(b)] that geometrical focusing is inappropriate in this more realistic situation. As for focusing using the estimated Green's function, the focused field pattern in preserved and the field pattern is almost exactly the same as that produced using the true Green's function. With the use of the pseudoinverse pattern synthesis method, we can further constrain the solution to produce better distributed interference patterns outside the focal spots.

In the second simulation result using the region shown in Fig. 10, we make use of the capability of the pseudoinverse method to synthesize multiple focus field patterns. One advantage of this inverse scattering based focusing is the ability of incorporating it in the pseudoinverse pattern synthesis method. The pixel locations of the points of interest are marked in white on Fig. 10. In Fig. 15, we display an intensity image of the resulting field pattern with 16-dB dynamic range for the multiple focusing. Figures 16 and 17 shows cross-sectional plots for the y-axis planes through the two focus points. This simulation study demonstrates the capability to produce multiple focus through highly scattering

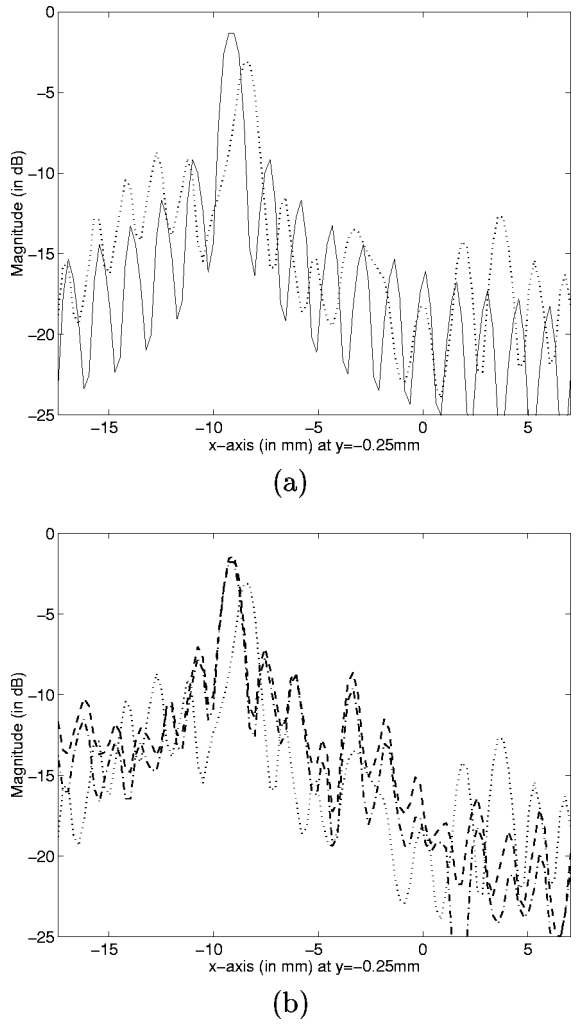

FIG. 14. A slice at $y=-0.25$ mm of the total field pattern (a) for geometrical focusing through homogeneous media (solid) and geometrical focusing through inhomogeneous media (dotted), and (b) for true Green's function focusing (dashed), estimated Green's function focusing (dash-dotted), and geometrical focusing (dotted) through inhomogeneous media.

media. It also shows that the field patterns produced using the estimated Green's function are almost identical to the patterns produced using the true Green's function. This simulation shows the superiority of this inverse scattering-based focusing approach over geometrical focusing. In fact, the field pattern produced using geometrical focusing is not acceptable since it is almost impossible to locate both foci. Finally, Fig. 15 shows relatively high intensity levels outside the focus points even for the Green's function focusing. The estimated Green's function and the spatial structure of the inhomogeneous media, also obtained by solving the same inverse scattering problem, can be exploited in the pseudo-inverse pattern synthesis method to solve a constrained optimization problem for better distribution of the energy outside the focal spots.[23]

The simulation results presented in this section are for loss-free acoustic media. However, additional simulations we carried out for lossy media show that there is not a major difference from the results presented in this section. The advantages of the Green's function focusing still hold under such circumstances.

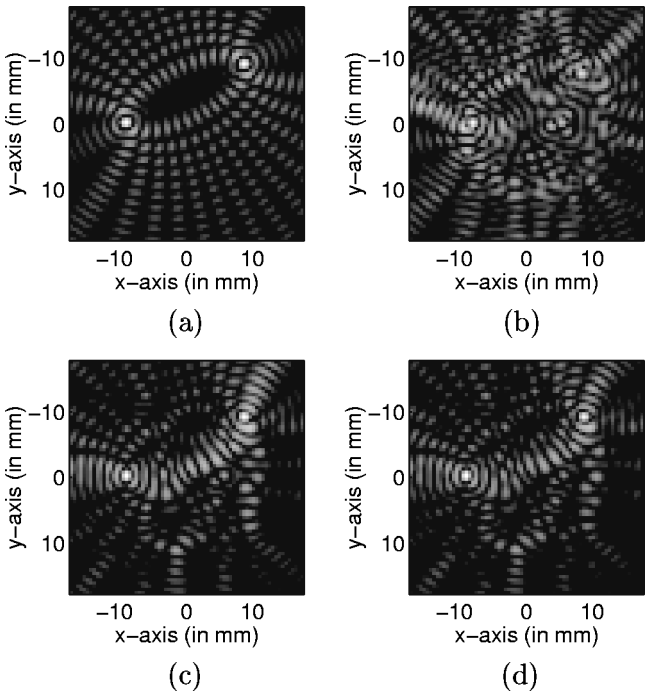

FIG. 15. The magnitude of the total field intensity in the region for (a) geometrical focusing through homogeneous media, (b) geometrical focusing through inhomogeneous media, (c) true Green's function focusing through inhomogeneous media, and (d) estimated Green's function focusing through inhomogeneous media.

IV. CONCLUSION

We introduced a self-focusing approach which uses the scattered field, measured by the array outside a region of interest, to estimate the Green's function from the desired focal point(s) to the array. We use these estimates in constructing the propagation matrix of the pseudoinverse pattern synthesis method to compute the excitation weights required for retransmission with the same array. We formulate the Green's function estimation problem in terms of the ultrasound inverse scattering problem, which is solved using the distorted Born iterative method. In this DBI method we iteratively solve the inverse scattering problem for the scattering function and the forward scattering problem for the total field and the Green's function. Convergence criterion is specified in terms of the normalized mean squared change in the Green's function of the focus point between one iteration and the next. This technique results in an excellent estimation of the true Green's function as shown in the simulation results provided in Sec. III. We also show simulation results for self-focusing through inhomogeneous media. These results indicate improved quality focusing compared to the geometrical focusing. Also, the quality of field patterns obtained using geometrical focusing is expected to degrade with increased size and contrast of the inhomogeneities.

Although, we presented the DBI algorithm as the method of choice, other approaches to solving the nonlinear

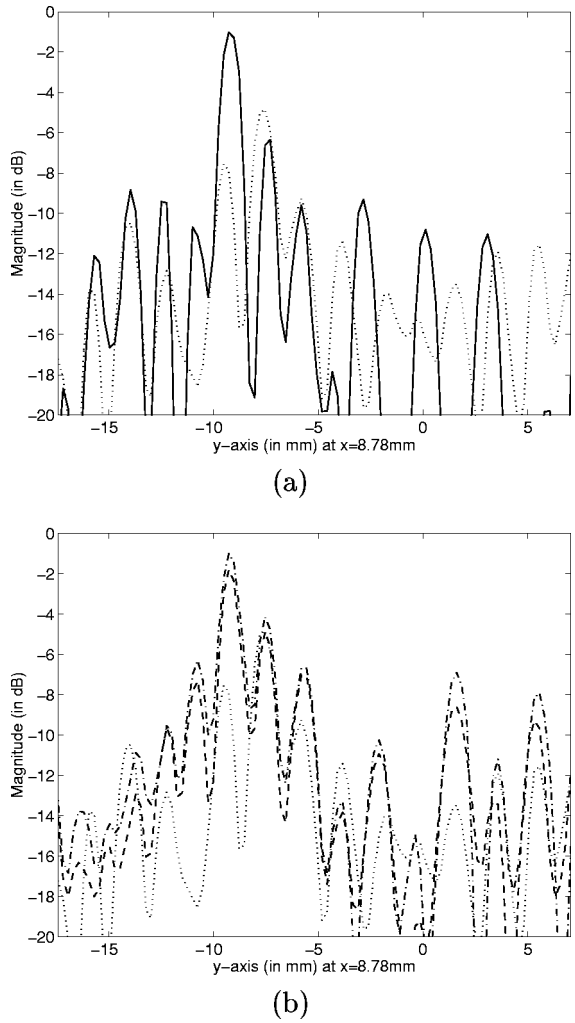

FIG. 16. A slice at $x=8.78$ mm of the total field pattern (a) for geometrical focusing through homogeneous media (solid) and geometrical focusing through inhomogeneous media (dotted), and (b) for true Green's function focusing (dashed), estimated Green's function focusing (dash-dotted), and geometrical focusing (dotted) through inhomogeneous media.

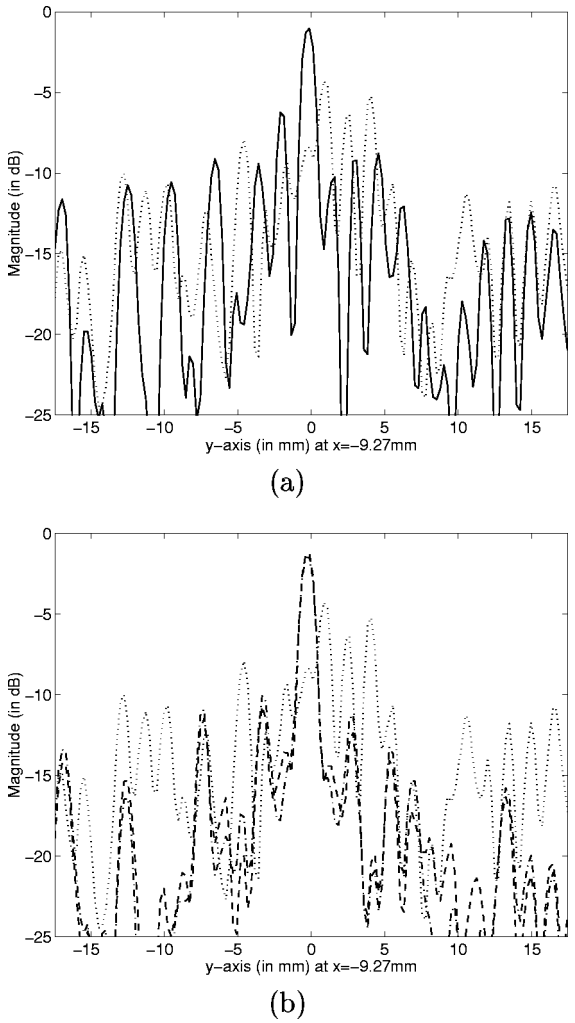

FIG. 17. A slice at $x=-9.27$ mm of the total field pattern (a) for geometrical focusing through homogeneous media (solid) and geometrical focusing through inhomogeneous media (dotted), and (b) for true Green's function focusing (dashed), estimated Green's function focusing (dash-dotted), and geometrical focusing (dotted) through inhomogeneous media.

inverse scattering problem can be used instead. Our recent research efforts are directed toward developing DBI-based robust algorithms for large size, high contrast inhomogeneities. Also, the use of finite element methods (FEM) will make the computational complexity and memory requirements of the DBI method reasonable for image-guided therapy systems for breast tissue, which is characterized as strongly scattering. In our simulations, we only consider circular arrays suitable for breast imaging and therapy. We plan to extend this strategy to work with limited angle (circular section) arrays for applications with limited access regions. We also plan to extend this approach using time-domain inverse scattering for real-time applications with pulse-mode phased arrays.

ACKNOWLEDGMENTS

This work is partially supported by Grant No. NIH CA 66602. Computing services were provided by the University of Michigan Center for Parallel Computing, which is partially funded by NSF Grant No. CDA 9214296.

[1] J. Driller and F. L. Lizzi, ''Therapeutic applications of ultrasound: A review,'' IEEE Engineering in Medicine and Biology Magazine **6**, 33–40 (1987).
[2] A. Macovski, ''Ultrasonic imaging using arrays,'' Proc. IEEE **67**, 484–495 (1979).
[3] N. T. Sanghvi, F. J. Fry, R. Foster, R. Chua, and G. Chua, ''System design considerations for high intensity focused ultrasound device for the treatment of tissue *in vivo*,'' Med. Biol. Eng. Comput. **29**, 748 (1991).
[4] M. T. Buchanan and K. Hynynen, ''Design and experimental evaluation of an intracavitary ultrasound phased array system for hyperthermia,'' IEEE Trans. Biomed. Eng. **41**, 1178–1187 (1994).
[5] R. Seip, P. D. VanBaren, and E. S. Ebbini, ''Dynamic focusing in ultrasound hyperthermia treatments using implantable hydrophone arrays,'' IEEE Trans. Ultrason. Ferroelectr. Freq. Control **41**, 706–713 (1994).
[6] R. Seip and E. S. Ebbini, ''Invasive and noninvasive feedback for ultrasound phased array thermometry,'' in *IEEE Ultrasonics Symposium Proceedings*, Seattle, WA, edited by M. Levy, S. C. Schneider, and B. R. McAvoy (IEEE, New York, 1995).
[7] P. D. VanBaren, R. Seip, and E. S. Ebbini, ''Real-time dynamic focusing through tissue inhomogeneities during hyperthermia treatments with phased arrays,'' in *IEEE Ultrasonics Symposium Proceedings*, Cannes, France, edited by M. Levy, S. C. Schneider, and B. R. McAvoy (IEEE, New York, 1994), pp. 1815–1819.

[8] E. B. Hutchinson, M. T. Buchanan, and K. Hynenen, ''Evaluation of an aperiodic phased array for prostate thermal therapies,'' in *IEEE Ultrasonics Symposium Proceedings*, Seattle, WA, edited by M. Levy, S. C. Schneider, and B. R. McAvoy (IEEE, New York, 1995), pp. 1601–1604.
[9] E. S. Ebbini, R. Seip, P. D. VanBaren, C. Simon, and C. Cain, ''Noninvasive temperature measurement for feedback control of thermal therapy using ultrasound phased arrays,'' in *Proceedings of the 9th International Symposium on Acoustical Imaging*, Bochum, Germany, edited by H. Ermert (Plenum, New York, 1992).
[10] P. D. VanBaren, C. Simon, R. Seip, T. Solf, C. Cain, and E. S. Ebbini, ''Image-guided phased array system for ultrasound thermotherapy,'' in *IEEE Ultrasonics Symposium Proceedings*, edited by M. Levy, S. C. Schneider, and B. R. McAvoy (IEEE, New York, 1996).
[11] M. A. Fink, C. Prada, F. Wu, and D. Cassereau, ''Self-focusing in inhomogeneous media with time reversal acoustic mirrors,'' in *IEEE Ultrasonics Symposium Proceedings*, Montreal, edited by B. R. McAvoy (IEEE, New York, 1989), pp. 681–686.
[12] M. A. Fink, ''Time reversal of ultrasonic fields—Part I: Basic principles,'' IEEE Trans. Ultrason. Ferroelectr. Freq. Control **39**, 555–566 (1992).
[13] S. W. Flax and M. O'Donnell, ''Phase-aberration correction using signals from point reflectors and diffuse scatterers: Basic principles,'' IEEE Trans. Ultrason. Ferroelectr. Freq. Control **35**, 758–767 (1988).
[14] R. Mallart and M. A. Fink, ''Sound speed fluctuations in medical ultrasound imaging: Comparison between different correction algorithms,'' in *Proceedings of the 19th International Symposium on Acoustical Imaging*, edited by C. Franconi, G. Arcangeli, and R. Cavaliere (Tor Vergata, Rome, Italy, 1991).
[15] G. E. Trahey, D. Zhao, J. A. Miglin, and S. W. Smith, ''Experimental results with a real-time adaptive ultrasonic-imaging system for viewing through distorting media,'' IEEE Trans. Ultrason. Ferroelectr. Freq. Control **37**, 418–427 (1990).
[16] E. S. Ebbini, S. Umemura, M. S. Ibbini, and C. Cain, ''A cylindrical-section ultrasound phased-array applicator for hyperthermia cancer therapy,'' IEEE Trans. Ultrason. Ferroelectr. Freq. Control **35**, 561–572 (1988).
[17] L. Nock, G. E. Trahey, and S. W. Smith, ''Phase aberration correction in medical ultrasound using speckle brightness as a quality factor,'' J. Acoust. Soc. Am. **85**, 1819–1833 (1989).
[18] E. S. Ebbini, H. Wang, M. O'Donnell, and C. A. Cain, ''Acoustic feedback for hyperthermia phased-array applicators: Aberration correction, motion compensation and multiple focusing in the presence of tissue inhomogeneities,'' in *IEEE Ultrasonics Symposium Proceedings*, edited by B. R. McAvoy (IEEE, New York, 1991), pp. 1343–1346.
[19] H. Wang, E. S. Ebbini, M. O'Donnell, and C. A. Cain, ''Phase aberration correction and motion compensation for ultrasonic hyperthermia phased arrays: Experimental results,'' IEEE Trans. Ultrason. Ferroelectr. Freq. Control **41**, 34–43 (1994).
[20] S. Krishnan, P-C. Li, and M. O'Donnell, ''Adaptive compensation of phase and magnitude aberrations,'' IEEE Trans. Ultrason. Ferroelectr. Freq. Control **43**, 44–55 (1996).
[21] E. S. Ebbini and C. Cain, ''Multiple-focus ultrasound phased-array pattern synthesis: optimal driving signal distribution for hyperthermia,'' IEEE Trans. Ultrason. Ferroelectr. Freq. Control **36**, 540–548 (1989).
[22] E. S. Ebbini, F. Ngo, and C. Cain, ''The pseudoinverse pattern synthesis method: Experimental verification using a prototype cylindrical-section ultrasound hyperthermia phased-array applicator,'' in *IEEE Ultrasonics Symposium Proceedings*, Montreal, edited by B. R. McAvoy (IEEE, New York, 1989).
[23] E. S. Ebbini, ''Deep localized hyperthermia with ultrasound phased arrays using the pseudoinverse pattern synthesis method,'' Ph.D. dissertation, University of Illinois at Urbana–Champaign, 1990.
[24] C. Prada, N. Lartillot, and M. A. Fink, ''Selective focusing in multiple-target media: The transfer matrix method,'' in *IEEE Ultrasonics Symposium Proceedings*, edited by M. Levy and B. M. McAvoy (IEEE, New York, 1993), pp. 1139–1142.
[25] C. Prada and M. A. Fink, ''Eigenmodes of the time reversal operator: A solution to selective focusing in multiple-target media,'' Wave Motion **20**, 151–163 (1994).
[26] C. Dorme and M. A. Fink, ''Ultrasonic beam steering through inhomogeneous layers with a time reversal mirror,'' IEEE Trans. Ultrason. Ferroelectr. Freq. Control **43**, 167–175 (1996).
[27] W. C. Chew and Y. M. Wang, ''Reconstruction of two-dimensional permittivity distribution the using distorted Born iterative method,'' IEEE Trans. Med. Imaging **9**, 218–225 (1990).
[28] W. C. Chew, *Waves and Fields in Inhomogeneous Media* (Van Nostrand Reinhold, New York, 1992).
[29] T. M. Habashy and R. Mittra, ''On some inverse methods in electromagnetics,'' J. Electromagn. Waves Appl. **1**, 25–58 (1987).
[30] Y. M. Wang and W. C. Chew, ''An iterative solution of two-dimensional electromagnetic inverse scattering problem,'' Int. J. Imaging Syst. Technol. **1**, 100–108 (1989).
[31] D. Colton and R. Kress, *Inverse Acoustic and Electromagnetic Scattering Theory* (Springer-Verlag, New York, 1992).
[32] V. V. Vardan and A. Lakhtakia and V. K. Vardan, Eds., *Field Representations and Introduction to Scattering* (Elsevier Science, New York, 1991).
[33] R. F. Harrington, *Field Computation by Moment Methods* (IEEE with Oxford U.P., New York, 1993).
[34] A. C. Kak and M. Slaney, *Principles of Computed Tomographic Imaging* (IEEE, New York, 1988).
[35] T. M. Habashy, R. W. Groom, and B. R. Spies, ''Beyond the Born and Rytov approximations: A nonlinear approach to electromagnetic scattering,'' J. Geophys. Res. **98**, 1759–1775 (1993).
[36] Q. Zhu and B. D. Steinberg, ''Large-transducer measurements of wavefront distortion in the female breast,'' Ultrason. Imaging **14**, 276–299 (1992).
[37] H. W. Engl and C. W. Groetsch, Eds., *Inverse and Ill-posed Problems* (Academic, New York, 1987).
[38] G. Demoment, ''Image reconstruction and restoration: Overview of common estimation structures and problems,'' IEEE Trans. Acoust., Speech, Signal Process. **37**, 2024–2036 (1989).
[39] G. H. Golub and C. F. VanLoan, *Matrix Computations* (Johns Hopkins U.P., Baltimore, MD, 1983).
[40] O. S. Haddadin and E. S. Ebbini, ''Adaptive regularization of a distorted Born iterative algorithm for diffraction tomography,'' in *IEEE Proceedings of the International Conference on Image Processing*, edited by P. Delogne (IEEE, New York, 1996), pp. 725–728.
[41] O. S. Haddadin, ''Ultrasonic inverse scattering for tomographic imaging and self-focusing arrays,'' Ph.D. Dissertation, University of Michigan at Ann Arbor, 1997.

Acoustic distortion products from the ear of a grasshopper

M. Kössl[a] and G. S. Boyan
Zoologisches Institut, Universität München, Luisenstrasse 14, 80333 München, Germany

(Received 5 January 1998; accepted for publication 26 March 1998)

Distortion-product otoacoustic emissions were recorded from the tympanum of the grasshopper, *Locusta migratoria*. The hearing organ of this insect is in direct contact with the tympanum and does not contain sensory hair cells. $2f1-f2$ distortions were measured for stimulus frequencies between 2–70 kHz. For frequencies between 3–9 kHz, the level of $2f1-f2$ was 30–50 dB below the stimulus level. $2f1-f2$ threshold curves calculated from distortion growth functions at different $f2$ frequencies are most sensitive between 3–9 kHz. These thresholds match the auditory sensitivity of low frequency receptor neurons in the ear [Römer, J. Comp. Physiol. **109**, 101–122 (1976)]. In contrast to vertebrates, the dependence of the $2f1-f2$ level on the frequency ratio $f2/f1$ did not show distinct maxima for most $f2$ frequencies. The distortion levels were largest for small ratios close to 1. The behavior of $2f1-f2$ was significantly different for stimulus frequencies below and above 10 kHz. Below 10 kHz, the thresholds were more sensitive, the slope of distortion growth curves was shallower by a factor of at least 2, and the distortion levels reversibly decreased during CO_2-induced hypoxia. Nonlinear mechanical processing may therefore be a general feature of sensitive hearing organs, even if these involve very different morphologies. Our results suggest that the the ciliated dendrites of the receptor cells of the insect may play a role in distortion generation.
 [S0001-4966(98)01207-7]

PACS numbers: 43.64.Jb, 43.80.Lb [BLM]

INTRODUCTION

Distortion-product otoacoustic emissions (DPOAEs) have become a valuable tool in assessing the functional properties of vertebrate ears. They are used to measure relative hearing sensitivity (Gaskill and Brown, 1990; Kössl, 1992; Manley and Köppl, 1993; Faulstich *et al.*, 1996) or hearing deficits (Whitehead *et al.*, 1996; Janssen *et al.*, 1996), to gain information about mechanical frequency tuning (Brown and Kemp, 1984), and to describe the action of the so-called ''cochlear amplifier'' in mammals (Mills *et al.*, 1993; Mills and Rubel, 1996; Frank and Kössl, 1996). In the mammalian cochlea, the acoustic distortions are known to depend on intact and functioning outer hair cells. If these are absent (Horner *et al.*, 1985), damaged (Brown *et al.*, 1989), or if their electro-motility is blocked by salicylate (Kujawa *et al.*, 1992), the distortion levels deteriorate markedly. There is ample evidence that force generation by outer hair cells is the basis for nonlinear mechanical amplification of low-level sound stimuli, and consequently of distortion-product otoacoustic emissions in mammals (e.g., Dallos, 1992; Ruggero, 1993).

In nonmammalian vertebrates there is no known hair cell motility in respect to movement of the cell body (Köppl, 1995; Manley, 1995). Nonetheless, auditory sensitivity, tuning, and the properties of distortion-product otoacoustic emissions are in most respects similar to those in mammals. In these animals, the mechanics of the sensory hair bundle of the hair cells most likely generates the ear's nonlinearity and mechanical distortions (Howard and Hudspeth, 1988; Jaramillo *et al.*, 1993). Indeed, it is worth noting that nonlinear mechanical properties are also found in mammalian hair bundles (Russell *et al.*, 1992).

Thus far, otoacoustic emissions have not been investigated in invertebrates, a group whose hearing organs are very different to those of vertebrates. To explore if sensitive hearing may also involve mechanical nonlinearities in the ear of insects, we attempted to measure distortion-product otoacoustic emissions in the grasshopper. Grasshoppers are known to have well-developed hearing capabilities, particularly for frequencies between 3–8 kHz where auditory nerve thresholds are close to 20 dB SPL (Römer, 1976). This range coincides with the frequencies of maximum sound energy in the animals' communication signals (Meyer and Elsner, 1996).

In grasshoppers, a large tympanum is situated on each side of the first abdominal body segment, and a receptor organ, the Müller's organ, contacts the inner surface of the tympanum (Gray, 1960) [Fig. 1(a)]. The tympanum is divided into two regions based on membrane thickness. In the center of the tympanum, where the thin and the thick membranes merge, the receptor organ is in contact with sclerites that protrude from the tympanum [Fig. 1(b)]. Within the receptor organ, ciliated dendrites of primary receptor neurons [Fig. 1(c)] are in contact with attachment cells coupled to the tympanal hypodermis. The receptor cells are surrounded by supporting cells known as scolopale cells, which also contribute to the linkage between dendrite and attachment cell (Gray, 1960).

There are four groups of receptor cells [Fig. 1(a): a, b, c, d] whose dendrites are in contact with different sclerites and hence receive mechanical drive from different regions of the tympanum. As shown for the closely related species *Schistocerca gregaria* (Michelsen, 1971), the a, b, and c cells

[a]Electronic mail: koessl@zi.biologie.uni-muenchen.de

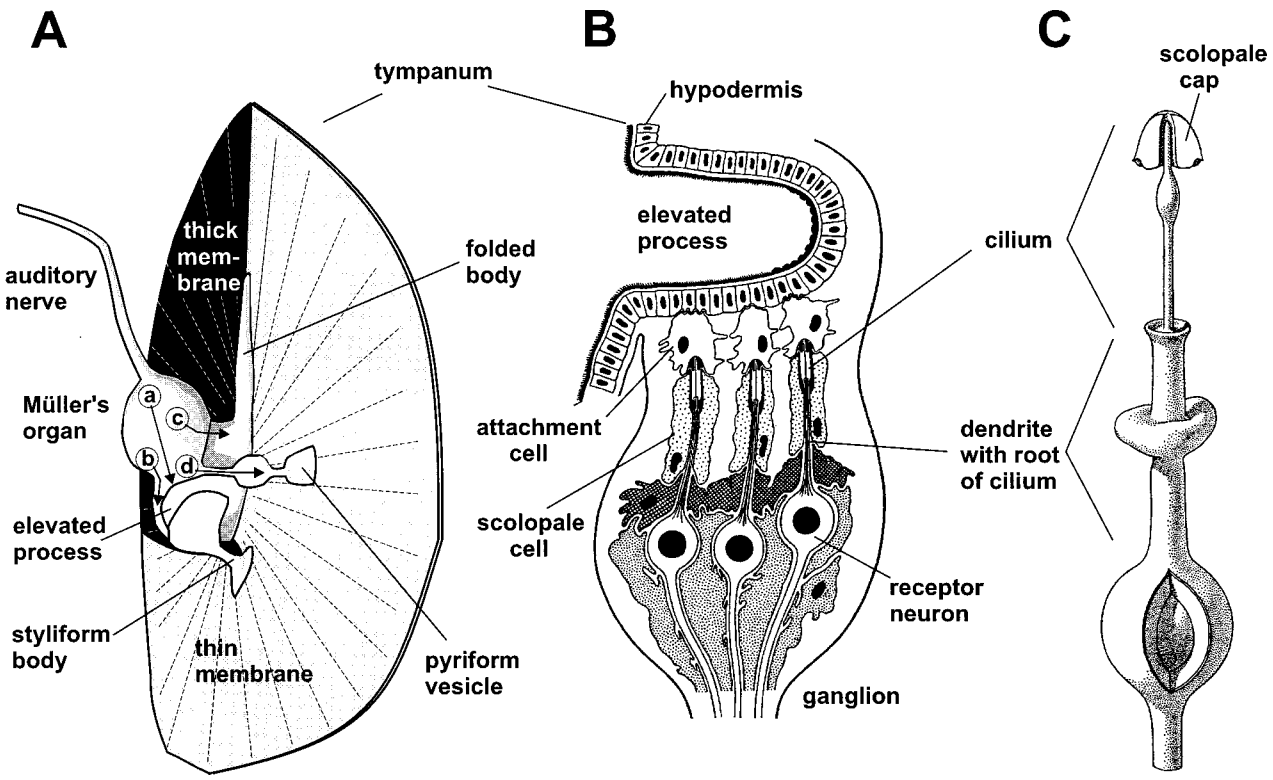

FIG. 1. Schematic of the hearing organ of *Locusta migratoria*. (a) View of the inner surface of the tympanum. A receptor organ, the Müller's organ, is attached via sclerites (elevated process, sytyliform body, pyriform vesicle, folded body) to the center region of the tympanal membrane where the thick and the thin membrane regions merge. (b) Schematic of a crossection through the receptor organ showing receptor neurons and their supporting cells. (c) Ciliated dendrite of a receptor neuron, adapted from Gray (1960).

mainly receive input from the thick membrane, or the interaction between thick and thin membranes, and respond best to frequencies below about 10 kHz, with the b cells being most sensitive. The d cells receive input from the thin membrane, are less sensitive than the low-frequency cells, and are tuned to frequencies above 10 kHz (Michelsen, 1971). The mechanical displacement of the tympanum is governed by different vibration modes, by a resonance with a fundamental frequency at about 3.84 kHz (Michelsen, 1971), and by independent movement of the sclerites against each other (Stephen and Bennet-Clark, 1982; Breckow and Sippel, 1985). In summary, while the grasshopper hearing organ contains fewer receptor cells (about 80) than in vertebrates, its mechanics are highly sophisticated. Preliminary results from this study were presented in the form of short communications (Kössl and Boyan, 1997, 1998).

I. MATERIALS AND METHODS

Twelve grasshoppers (*Locusta migratoria*), of both sexes and raised in crowded laboratory cultures at 30 °C, were used in the experiments. The animals were treated in strict accordance with the guidelines for animal experimentation laid down by the Deutsche Forschungsgemeinschaft. Each grasshopper was lightly anaesthetized by cooling before wings and legs were removed. Following recovery from anaesthesia the animals were pinned dorsal side up to a cork platform. Nine of the grasshoppers were alert (as indicated by antennal movement) and sensitive distortions could be measured from these animals; three animals were discarded because their distortion thresholds in the range 3–8 kHz were more than 30 dB higher than in the other animals. These three animals were also not as alert as the others and also did not show significant antennal movement.

The acoustic measurements took place in a soundproof chamber that was heated to 28 °C. An acoustic coupler, initially designed for otoacoustic emission measurement in small mammals (Kössl, 1994), consisted of two adjacent

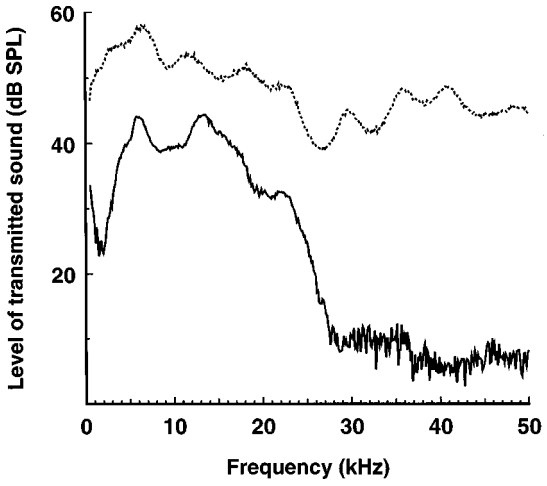

FIG. 2. Measurement of sound transduction through the body of the grasshopper. A microphone connected to the right tympanum measured the response to white noise generated by a speaker connected to the left tympanum. The solid curve gives the measured response. Note the sharp cutoff for frequencies above about 15 kHz. The dotted curve gives the measured response with the microphone and speaker directly coupled.

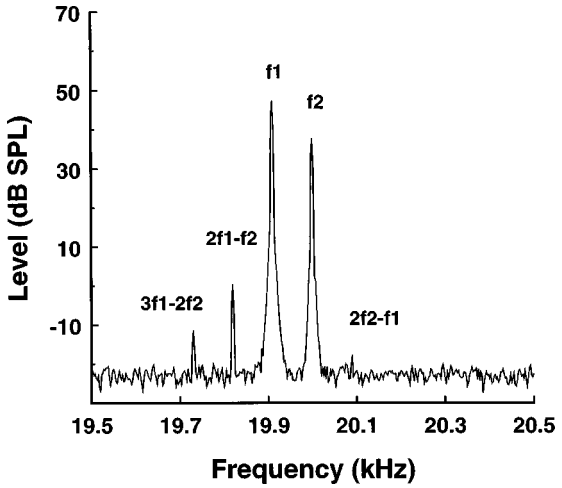

FIG. 3. Example of acoustic two-tone distortions measured at the tympanum of *Locusta migratoria*.

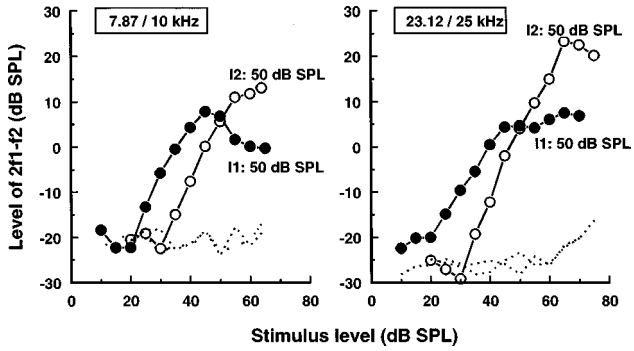

FIG. 4. Growth of the level of the $2f1-f2$ distortion with increasing level of $f1$ (open circles) and $f2$ (filled circles). The other stimulus was held constant at 50 dB SPL. Two cases are shown with the frequency of $f2$ either at 10 kHz (left) or at 25 kHz (right). Dotted lines give the noise level. For a constant level of $f1$ of 50 dB SPL, the distortion is at a maximum at a level of $f2$ of 45 (left) or 40–70 dB SPL (right). For a constant level of $f2$ of 50 dB SPL, maximum distortion is elicited by levels of $f1$ of 55–65 dB SPL.

conical tubes for stimulation and recording. The coupler had an overall tip diameter equal to the size of the tympanum of the insect and was positioned within a distance of about 0.3–1 mm from the tympanum. Sensitive distortion measurements at frequencies below 10 kHz require a tightly closed acoustic system. The connection between the body surface of the locust and the walls of the coupler tip was therefore sealed with toothpaste. One coupler channel was connected to a Brüel & Kjaer 4133 microphone to measure responses up to 40 kHz, or to a Brüel & Kjaer 4135 microphone for frequencies above 40 kHz. Two additional 4133 Brüel & Kjaer microphone capsules served as loudspeakers and fed signals into the other coupler channel. Continuous pure tone stimuli were generated with a dual Hewlett-Packard 8904A synthetizer and fed into two GPIB (general purpose interface bus) controlled attenuators. The sound system was calibrated *in situ* using white noise, and sound pressure levels used in the experiments are expressed in dB SPL (dB *re*: 2×10^{-5} Pa). Stimulation and data acquisition were controlled by a Pentium PC using ASYST (Keithley) software. The microphone response was fed via a B&K 2610 measuring amplifier into a Hewlett Packard 3651A spectrum analyzer for FFT (fast Fourier transform) analysis using Hanning windows. Four FFT recordings were averaged for each data point and a resolution between 75 and 0.94 Hz was used. In the latter case, and using the 4133 microphone, the average noise level for frequencies above 2 kHz ranged between -18 and -25 dB SPL. Within the analyzed frequency range of 2–70 kHz, distortions produced by the setup were detectable just above the baseline noise floor for high primary levels above 83–91 dB SPL. To exclude any setup distortion in the present experiments, we therefore only applied stimuli of up to 80 dB SPL $f1$ level and 70 dB SPL $f2$ level. For a detailed description of the setup, see Kössl (1994).

Stimulation and recording of DPOAEs was performed unilaterally. In the grasshopper there is an acoustic connection between the two ears via tracheae inside the body. To test for crosstalk between the ears, we applied white noise at the left ear of one animal and recorded the response at the right ear. For this purpose a B&K 4133 microphone was connected via a conical coupler to the right tympanum. Another B&K 4133 microphone capsule serving as a speaker was connected to the left tympanum. Both tympana were left intact and stimulation and recording took place in a closed sound system. We found that the body of the insect basically acts as a low-pass filter with a cutoff frequency at about 15 kHz and additional slight transmission loss for frequencies below 4 kHz (Fig. 2). Comparable results were obtained by Miller (1977) and Michelsen and Rohrseitz (1995) for *Schistocerca gregaria*, however, the cutoff frequency in their experiments was distinctly lower and there was nearly no loss at the lowest frequencies. These differences could depend on the body fat content of the animals used, or on a difference between closed versus open sound systems. Our data on *Locusta migratoria* resemble more the transmission characteristics of the small grasshopper *Chorthippus biguttulus* used in the study of Michelsen and Rohrseitz (1995).

To test if the ipsilaterally recorded DPOAEs are influenced by the contralateral ear, we destroyed the contralateral tympanum and either closed the ear with resin or left it open. In both cases the ipsilaterally recorded DPOAEs did not change within the accuracy of the measurements (±2 dB). The grasshopper auditory pathway may therefore be viewed as being unilateral with respect to measurements of acoustic distortion products.

For the experiments involving ventilation with CO_2, a grasshopper was mounted on its side to the cork platform described above after first removing the wings and legs. The assembly containing the grasshopper was placed vertically inside a plastic container into which CO_2 was passed. In order to keep the air humidity constant, the plastic container was partly filled with warm water. The temperature of the CO_2 delivered to the preparation was maintained at 28 °C. An experiment began with control measurements performed with the animal exposed to normal air in the recording environment described above. The CO_2 was then applied for 10 min or until the antennae of the animals assumed the depressed attitude typical for hypoxia. The experimental measurements were then carried out and lasted approximately 15 min. Subsequently a plug was removed from the container,

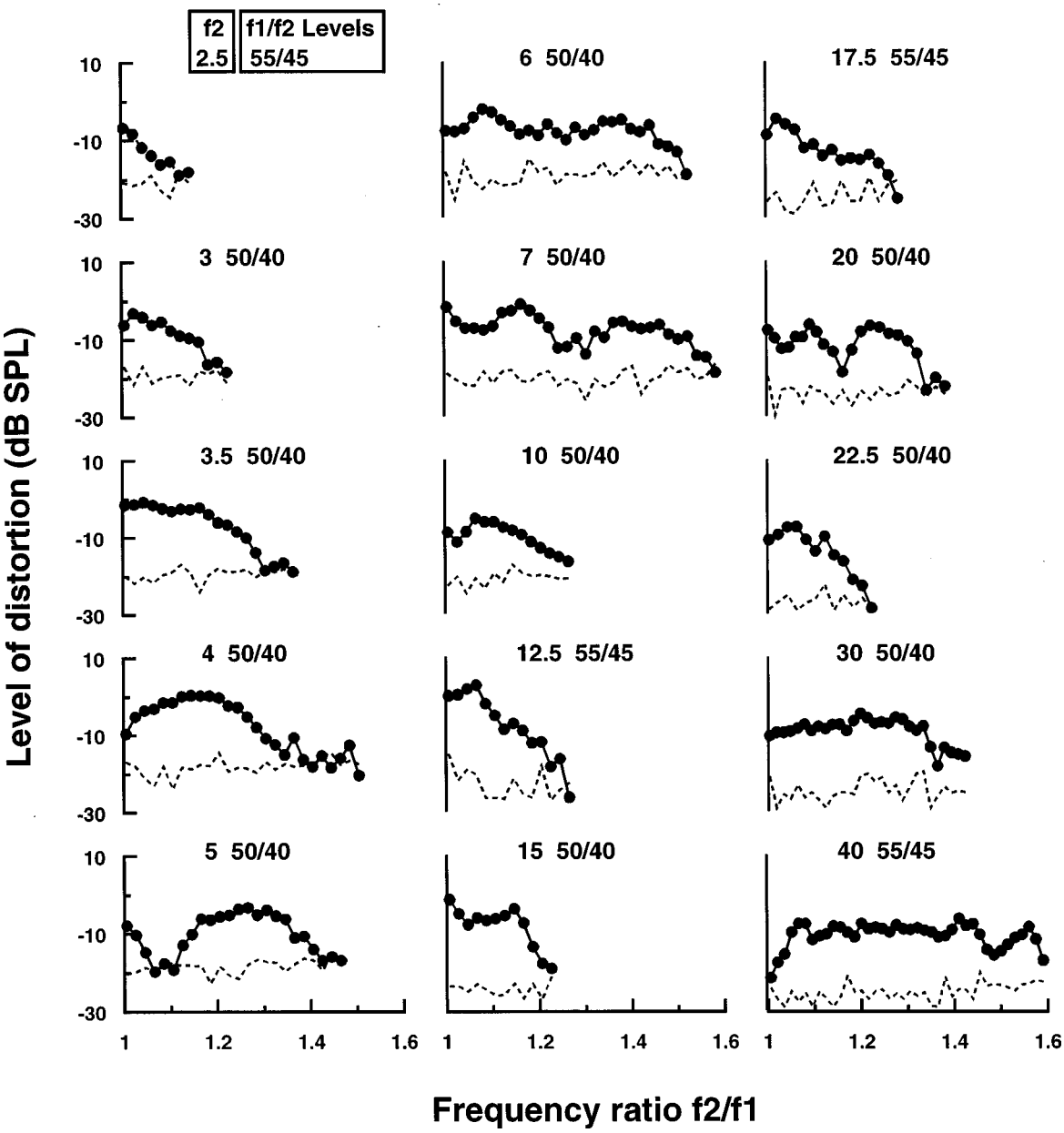

FIG. 5. Level of the $2f1-f2$ distortion as a function of frequency ratio $f2/f1$. Shown are measurements for different $f2$ frequencies between 2.5–40 kHz in a single animal. The numbers above the traces give the $f2$ frequency and the levels of both stimuli. The noise level is given by the dotted lines. For most cases, the distortion level grows with decreasing frequency ratio.

allowing the CO_2 to escape. Recovery of the grasshopper from hypoxia was signalled by the antennae again assuming their normal elevated position and beginning to move freely. The identical series of control measurements was then repeated. This complete experimental procedure, including CO_2 application, could be repeated up to three times with the same results (described below).

II. RESULTS

Acoustic distortion products proved to be relatively easy to measure in the grasshoppers due to their large exposed tympanum. It was, however, critical to have a completely sealed sound system (see above) and important that the coupler tip was as perpendicular as possible to the surface of the tympanum. Before each measurement we routinely tested for the appearance of spontaneous otoacoustic emissions but were not able to detect any. Further, acoustic distortions could only be measured from the tympanum itself. When the coupler was directed towards any other cuticular body surface of the locust, distortions could not be recorded. The acoustic distortions also immediately disappeared when the tracheal space behind the tympanum was filled with ringer solution. Figure 3 shows an acoustic spectrum near 20 kHz with the level of $f2$ adjusted 10 dB below that of $f1$. As in vertebrates, the $2f1-f2$ distortion is dominant. With higher primary levels, $3f1-2f2$, $4f1-3f2$, and $2f2-f1$ distortions also appear. Figure 4 shows the dependence of the $2f1-f2$ level on the level difference between the two primaries. For this purpose, the level of either $f1$ or $f2$ was kept constant at 50 dB SPL and the level of the other stimulus, given by the x axis, was changed stepwise. Maximum

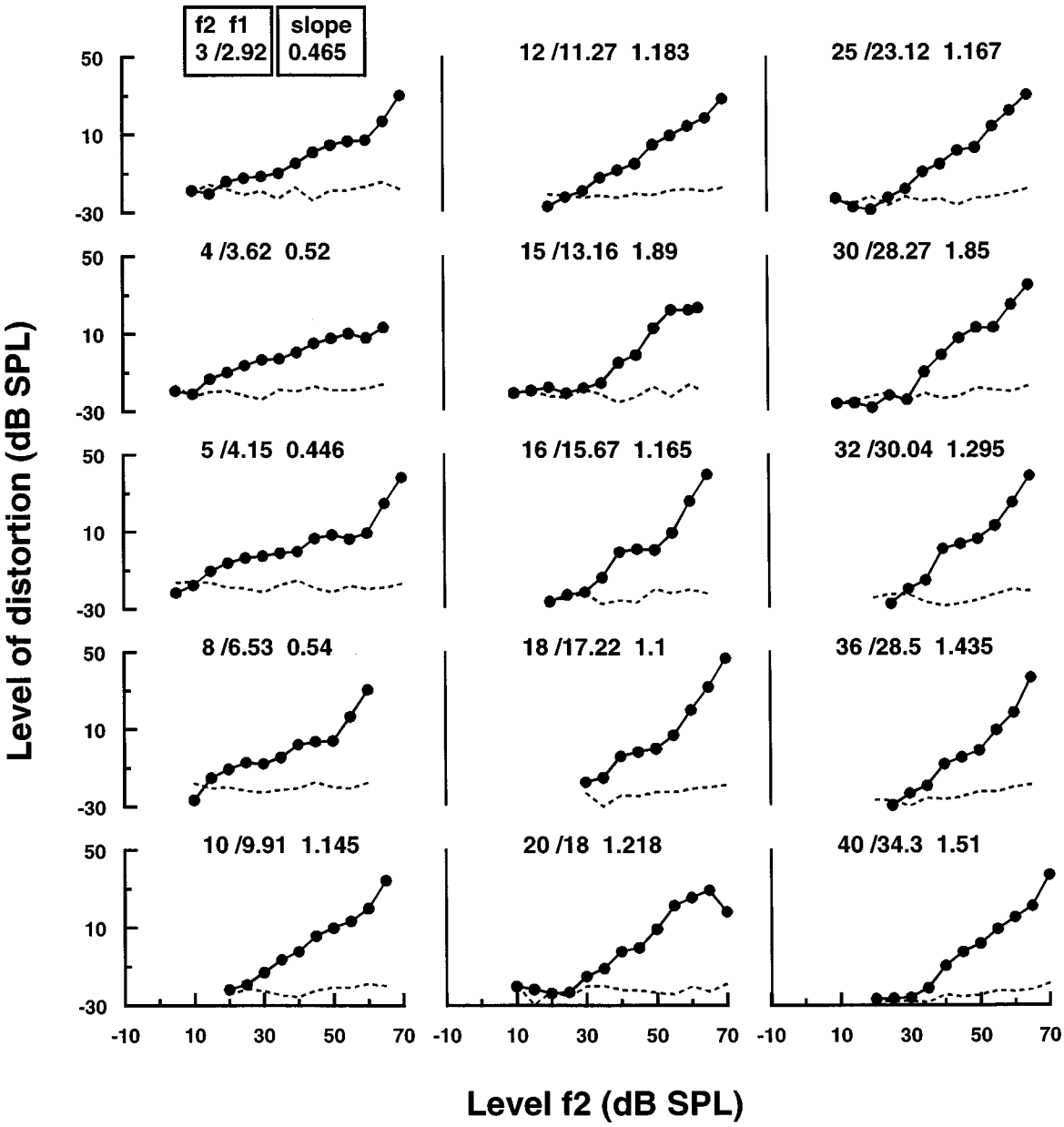

FIG. 6. Growth of the level of the $2f1-f2$ distortion with increasing stimulus levels for different $f2$ frequencies in a single animal. The level of $f1$ was always 10 dB above that of $f2$. The numbers above the traces indicate the stimulus frequencies and the initial slope of the growth functions.

$2f1-f2$ distortion is elicited when the level of $f1$ is 5–15 dB above that of $f2$. In the following measurements, the $f1$ level was therefore always chosen to be 10 dB above that of the $f2$ stimulus, similar to measurements in mammals (Kössl, 1992, 1994).

A. Dependence of distortion product amplitude on the frequency ratio *f2/f1*

In vertebrates, the frequency ratio $f2/f1$ is an important parameter in the measurement of distortion products. Depending on the species and the frequency range, the $2f1-f2$ distortion product is maximal at a so-called optimum ratio ($f2/f1$) whose value lies between about 1.1 and 1.4. This optimum ratio is considered to be due either to a secondary mechanical filtering process in the cochlea (Brown *et al.*, 1992) or to phase-dependent reflections and cancellations on the basilar membrane itself (Neely and Stover, 1997).

The standard procedure for measuring the optimum ratio is to keep one stimulus frequency, normally $f2$, constant, and to vary the other stimulus frequency ($f1$). Figure 5 shows that an optimum ratio could not easily be defined for most $f2$ frequencies in the insect. The $2f1-f2$ distortion either has nearly equal levels over a large range of ratios up to about 1.6 (Fig. 5: $f2$ at 6, 7, and 40 kHz), or there is a steady increase in distortion level with decreasing ratio (Fig. 5: $f2$ at 2.5, 3, 3.5, 10, 12.5, 15, and 17.5 kHz). In nearly all of these cases, very small ratios close to 1 are sufficient in inducing large distortions. At $f2$ frequencies of 4 and 5 kHz the distortion level maxima and minima for certain ratios are better defined.

B. Distortion growth functions

In order to study the growth of the $2f1-f2$ distortion product with increasing stimulus levels over different $f2$ fre-

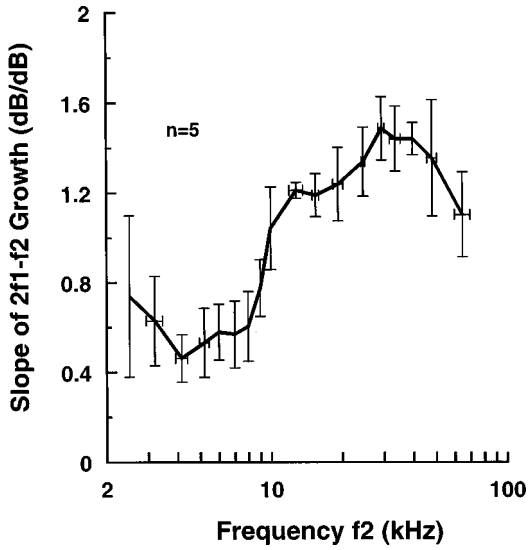

FIG. 7. Initial slope of the $2f1-f2$ growth function in five animals. Standard deviations are given by vertical bars. The horizontal bars give the respective standard deviations of $f2$ in cases where slightly differing $f2$ values from different animals were grouped together.

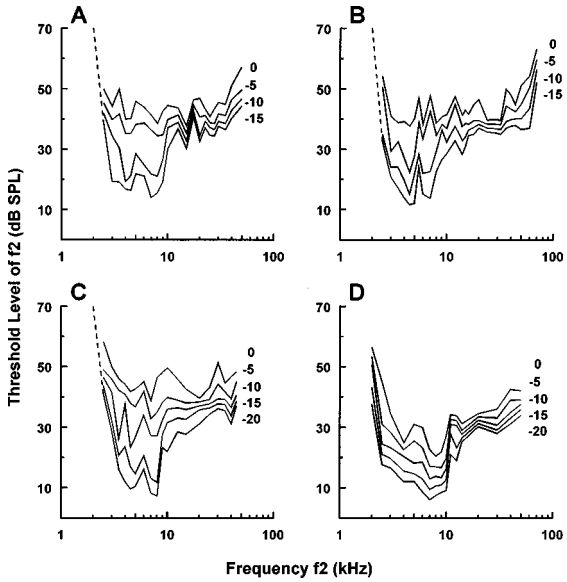

FIG. 8. Distortion threshold curves in four grasshoppers. The individual traces give the level of the $f2$ stimulus (the $f1$ level always was 10 dB higher than that of $f2$) which was sufficient to induce a $2f1-f2$ distortion of -20, -15, -10, -5, and 0 dB SPL (numbers given on the right side of the isothreshold curves).

quencies, the frequency of $f1$ was adjusted to a value that produced maximum distortion levels in the ratio curves (see Fig. 5). This was performed for each measurement at a given $f2$ frequency. Then the levels of both stimuli were increased in equal size steps with the level of $f1$ always being 10 dB above that of $f2$.

There is a clear difference in distortion growth for $f2$ frequencies below and above 10 kHz (Figs. 6 and 7). For $f2$ frequencies below 10 kHz, the distortion growth functions (Fig. 6) are characterized by an initial slow growth for stimulus levels up to about 50–60 dB SPL, followed by steeper growth for higher stimulus levels. The initial slope was determined by linear regression of the growth function data points over a stimulus range of 20 dB, starting with the first appearance of the $2f1-f2$ distortion at more than 3 dB above the average noise level. This slope lies between 0.46 and 0.78 (Fig. 7: average values) for $f2$ frequencies below 10 kHz. Above 10 kHz, the initial distortion growth is steeper, ranging between 1.1 and 1.48 (Fig. 7: average values). A minimum slope of 0.46 was obtained for $f2$ close to 4 kHz, and a maximum slope of 1.48 appears close to 30 kHz. In some cases, the slope values were averaged for a range of $f2$ values used in measurements from different animals (see figure legend).

C. Distortion thresholds

Threshold curves for the nonlinear mechanics can be derived from $2f1-f2$ growth functions obtained at the frequency ratios where maximum distortion is found. The $2f1-f2$ threshold curves from four grasshoppers are shown in Fig. 8. Displayed is the $f2$ level that for a given $f2/f1$ stimulus combination is sufficient to induce a small distortion of -20, -15, -10, -5, and 0 dB SPL. These iso-level thresholds were interpolated from the growth functions described above. Similar to measurements in mammals (e.g., Faulstich *et al.*, 1996), the data are referenced to the frequency of $f2$, since in mammals there is strong evidence that the $2f1-f2$ distortion is generated close to the $f2$ frequency place in the cochlea. Of course, this same assumption cannot apply to the insect. We kept the reference to $f2$ to allow for a better comparison with mammalian data.

The threshold curves are most sensitive for $f2$ frequencies between about 3–9 kHz, at least for threshold criteria of -10 dB SPL or lower. For higher threshold criteria, the minimum is smaller or absent. This difference reflects the different slopes of distortion growth (see above). In three of the four animals tested, and for low threshold criteria, the overall threshold minimum can be divided into two most sensitive regions, one at 3–5 kHz and the other at 7–9 kHz. In the fourth animal [Fig. 8(d)] a trend toward two minima is not seen for low threshold criteria but is present for high threshold criteria. There is a steep threshold increase for frequencies between 2–2.5 kHz and 8–12 kHz. Above 12 kHz, the thresholds remain fairly constant up to about 60 kHz [see Fig. 8(b)], and are about 20 dB higher than those at the threshold minimum.

D. Effects of manipulations of the physiological state of the grasshoppers

We first tested if it is possible to influence the distortion products in the grasshopper in any way, or if they are a completely passive and invulnerable characteristic of the hearing organ. For this purpose we decapitated one animal. This procedure of course does not allow us to determine the possible metabolic changes we thereby induced. It is known that ventral cord neurons in decapitated insects remain functional for a period of time (Kutsch and Otto, 1972). Immediately after decapitation there was no change in the sensitivity of distortion thresholds, which indicates that the hearing organ together with its tracheal tubes remained basically intact. Changes in the distortions became apparent

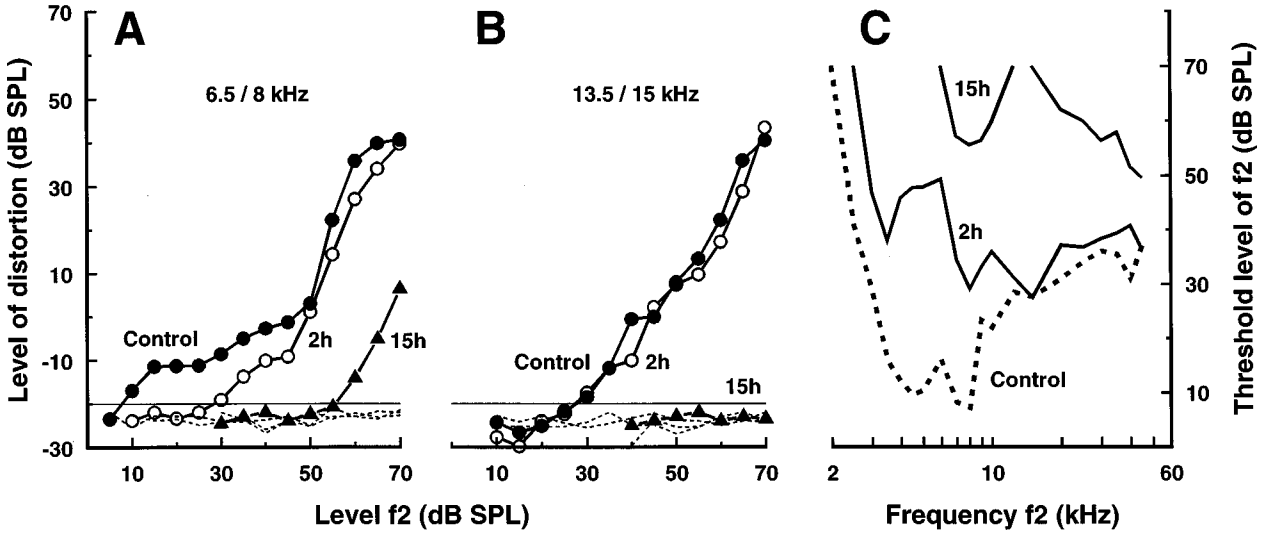

FIG. 9. The $2f1-f2$ growth functions [(a) and (b)] and threshold curves (c), measured before (control), 2 h, and 15 h after decapitation of the animal. A threshold criterion of -20 dB SPL [horizontal line in (a) and (b)] was used to calculate the thresholds. The frequencies of the primary stimuli are given above the curves in (a) and (b).

about 90 min after decapitation. Figure 9 shows changes in the slope of distortion growth functions and upward shifts of the distortion threshold curves. About 2 h after decapitation there was a pronounced loss of distortion level at the threshold minimum between 3–9 kHz. The corresponding growth functions became steeper [Fig. 9(a)]. A maximum threshold loss of 37 dB occurred at an $f2$ frequency of 4.5 kHz. Fifteen hours after decapitation there was another large overall upward shift of the threshold, but distortions were still measurable at around 8 kHz and above 15 kHz. Taken together these data indicate that the mechanical processing of low frequencies is clearly more vulnerable than that of high frequencies above 10 kHz.

In order to influence the animals's metabolism in a more controlled way, we introduced hypoxia by ventilation with CO_2. In insects, CO_2 application is known to halt the movement of legs or antennae and it is used to introduce a state similar to anaesthesia in vertebrates. Insects are not killed by short-term CO_2-induced hypoxia, they recover quickly after they are supplied with oxygen again. In our experiments we measured distortion growth functions before, during a 10–25-min period of CO_2 ventilation, and after the CO_2 was replaced with oxygen (see methods). During CO_2 ventilation the distortion growth functions became insensitive and shifted towards higher stimulus levels (Fig. 10). In most cases the distortion level was affected equally at both low and at high stimulus levels [examples in Fig. 10(a), (c), and (e)]. In some cases (not shown in Fig. 10) the decrease in distortion level was most pronounced at low stimulus levels. This decrease only occurred for $f2$ frequencies below 10 kHz. At higher frequencies the distortion growth functions remained unchanged [Fig. 10(b) and (d)]. Figure 10(f) shows the corresponding shift in the distortion thresholds for three animals measured at a threshold criterion of -10 dB SPL. It is obvious that in the grasshopper the sensitive low-frequency distortions are much more vulnerable to hypoxia than the high-frequency distortions elicited by stimuli above 10 kHz.

III. DISCUSSION

The properties of DPOAEs in the grasshopper are in many respects similar to those from the verebrate ear. The

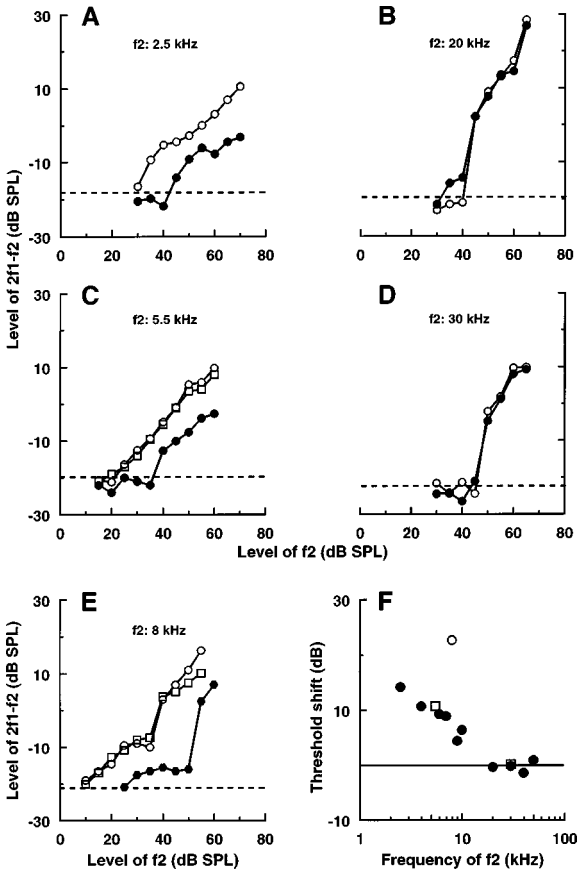

FIG. 10. (a)–(e) The $2f1-f2$ growth functions before (open circles), during (filled circles), and after ventilation with CO_2 (open squares). Dashed lines give the average noise level. The $f2$ frequencies are indicated above the individual traces; for $f2$ at 20 and 30 kHz there was no change in the growth functions. (f) Shift of the distortion threshold during CO_2 application in three animals (different symbols) for a threshold criterion of -10 dB SPL.

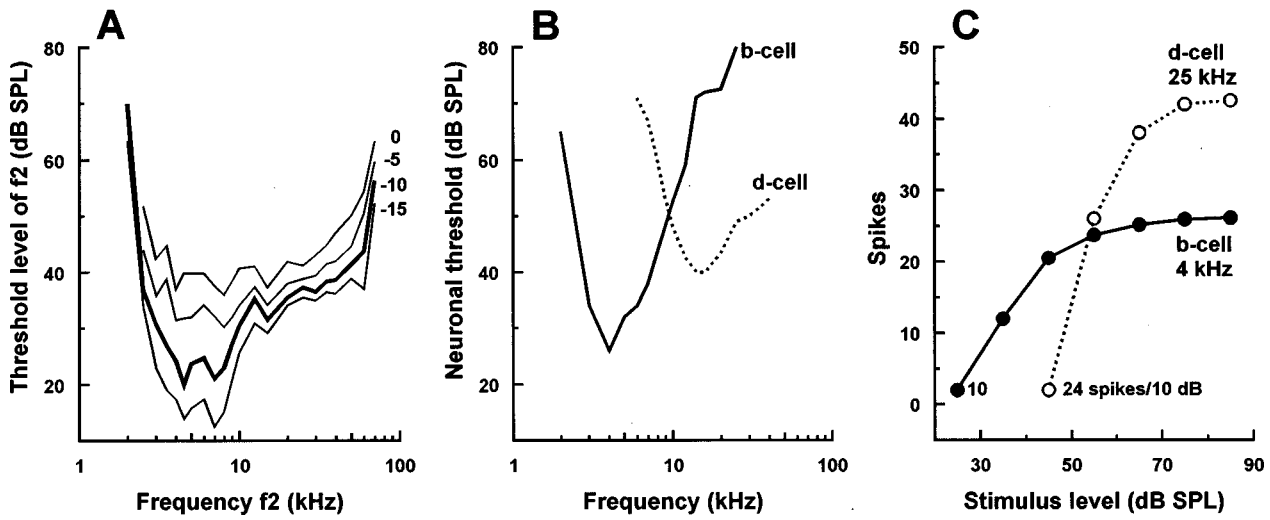

FIG. 11. Comparison between acoustic distortions and neuronal data. (a) Average isothreshold curve from the four animals in Fig. 8 for a threshold criterion of −15, −10, −5, and 0 dB SPL. (b) Neuronal threshold tuning curves from a b cell and a d cell (Römer, 1976) (c) Neuronal intensity/response functions in a d cell stimulated with 25 kHz and a b cell stimulated with 4 kHz (from Römer, 1976). The difference in the slope of intensity response function between the two cells is also evident in distortion slopes (Fig. 7) and in the spacing of the threshold curves obtained for different threshold criteria in (a).

$2f1-f2$ distortion is most prominent and can be elicited at maximum levels when the $f1$ stimulus level is higher than that of $f2$. This is comparable to the situation in the mammalian ear (Probst *et al.*, 1991). The difference between the $2f1-f2$ distortion level and that of the $f1$ stimulus (with the level of $f2$ being 10 dB lower) was between 30–50 dB in the most sensitive frequency region. This difference range is larger than values obtained with the same setup and paradigm in small laboratory mammals (Faulstich *et al.*, 1996; Frank and Kössl, 1996) where the minimum difference is between 10–30 dB. This indicates that in the grasshopper the DPOAEs are less pronounced than in mammals by factor of about 20 dB. In terms of distortion level, the grasshopper DPOAEs are more comparable to those found in birds and lizards (Manley and Köppl, 1993; Kettembeil *et al.*, 1995). In humans, the $2f1-f2$ levels are also lower than those measured in most laboratory mammals (see, e.g., Whitehead *et al.*, 1996). This, however, could be due to the fact that in humans the microphone coupler tube cannot be positioned as close to the tympanum as in small mammals.

A. Stimulus frequency ratio

In mammals, the dependence of the distortion level on the frequency ratio may reflect secondary cochlear filtering processes in the tectorial membrane (Brown *et al.*, 1992; Allen and Fahey, 1993) and/or reflections and phase-dependent cancellations in the cochlea (Neely and Stover, 1997). Contrasting with DPOAE measurements in mammals, the level of the $2f1-f2$ DPOAE in grasshoppers is largest for the smallest ratios and an optimum ratio is hard to define. This implies that the distortion level is at a maximum when the distortion frequency is close to the stimulus frequencies, as is typical of simple nonlinear resonators. For mammals, there is one exception known where the smallest ratios also induce maximum distortion, namely in bats which use pure tone echolocation calls. Here extremely small optimum ratios are found close to the call frequencies. Pronounced anatomical specializations of the basilar and tectorial membrane in the cochlea of these animals suggest that in this case the small optimum ratios are a consequence of a complex double-resonator system that enhances frequency tuning (Kössl and Vater, 1996; Vater and Kössl, 1996).

As far as the best ratios are concerned, the mechanical processes that are responsible for a specific tuning of distortion frequencies in the grasshopper are not present for the $f2$ frequencies tested. Since mechanical frequency tuning in this species is observed in the vibration patterns of specific tympanal areas (Michelsen, 1971), and we always measured the response from the whole tympanum, we could have missed more localized tuning phenomena. Only in the range of 4–5 kHz were there larger irregularities in the dependence of the distortion levels on the frequency ratio $f2/f1$ (Fig. 5). This frequency roughly corresponds to that of a tympanal resonance (Michelsen, 1971).

B. Distortion threshold curves

Iso-distortion thresholds are an efficient means with which to noninvasively determine the frequency dependence of cochlear sensitivity, at least with respect to nonlinear mechanical processing. In a number of vertebrate species, distortion thresholds were found to run parallel to neuronal or behavioral threshold measurements and there is a good correlation between the minima of distortion thresholds and the most sensitively perceived auditory frequencies (e.g., Kössl, 1992; Manley and Köppl, 1993; Faulstich *et al.*, 1996).

In the grasshopper, the distortion threshold minimum between 3–9 kHz correlates with the most sensitive threshold tuning of the b cells [Römer (1976), compare Fig. 11(a) and (b)]. The same applies to a and c cells which have higher thresholds but similar tuning to the b cells. The d cells are tuned to frequencies above 10 kHz and are less sensitive than the low-frequency receptors, a physiology which agrees with our distortion threshold data. The distortion threshold minimum also coincides with the absolute sensitivity minimum in gross auditory nerve recordings (see Michelsen, 1971), and

with maximum motion of the thick membrane measured at the tympanal insertion point for the a cells (Meyer and Elsner, 1996), which are tuned to the same low-frequency range as the b cells. The slow growth of distortion levels within the frequency region of maximum sensitivity versus the steep growth for frequencies above 10 kHz corresponds to a comparable change in the slopes of neuronal intensity-response functions of b versus d cells [Römer (1976); Fig. 11(c)]. The initial slope of the d cell intensity-response function stimulated with 25 kHz is a factor 2.4 steeper than that of the b cell responding to 4 kHz. A comparable difference (factor 2.8) is seen in the distortion growth between $f2$ frequencies of 4 and 24 kHz (see Fig. 7). The b and d cells are associated with the thick and thin membranes of the tympanum, respectively (see the Introduction). Therefore, our data indicate that the sensitive low-frequency distortions may be produced by the mechanics of the thick membrane, and/or the interaction between thick and thin membrane, whereas the high-frequency distortions are probably due to vibration of the thin membrane alone.

C. Possible nonlinear mechanisms

Nonlinear neural activity in receptor cells and higher-order neurons of the grasshopper was studied in detail by Sippel and Breckow (1983, 1984). They show that this nonlinearity is related to adaptation phenomena and suggest that it is largely due to electrochemical processes intrinsic to the nerve cells. One reason for this suggestion is that these authors assume from mechanical measurements at high sound pressure levels that the mechanics of the hearing organ are basically linear (Breckow and Sippel, 1985). Even if the non-monotonicity of neuronal intensity-response functions is related to intrinsic neuronal properties acting at higher sound pressure levels, the present study clearly shows that the mechanics of the tympanum of the grasshopper are nonlinear at low sound pressure levels close to the threshold of hearing.

The vulnerability of the DPOAEs to hypoxia implies that they may involve a stage of the electromechanical transduction process which is metabolically dependent. As in the grasshopper, reversible hypoxia effects in vertebrates are induced within a few minutes and deterioration of the DPOAE levels of up to 20–30 dB has been observed (Rebillard and Lavigne-Rebillard, 1992; Manley and Köppl, 1993). In mammals, hypoxia leads to a decrease of the endocochlear potential (EP) which is the driving voltage for forward and reverse transduction. The time courses of changes in the DPOAEs and the EP, however, are significantly different, and it is likely that the DPOAEs are affected both by the changed EP and by a direct influence of hypoxia on the properties of the outer hair cells (Rebillard and Lavigne-Rebillard, 1992). In contrast to mammals, the hypoxia effects in the grasshopper are more pronounced at low stimulus frequencies than at high frequencies. The most sensitive frequency region between 3–9 kHz is clearly also the most vulnerable. We know of no other report which shows that hypoxia can influence the functional properties of insect receptor organs. However, it is known that hypoxia affects spike generation and propagation in receptor neurons (Hamon *et al.*, 1988). In addition, there is evidence that the mechanoelectrical transduction process in locusts is strongly dependent on temperature (Oldfield, 1988). The characteristic frequency of low-frequency neurons shifts up to 0.2 octaves depending on the ambient temperature. Temperature does not affect the properties of high-frequency receptor neurons, as is the case with the hypoxia effects on DPOAEs in the present study.

The most likely candidate responsible for the metabolically dependent nonlinear transduction in the grasshopper is Müller's organ itself. The sclerites by which it is attached to the tympanum are known to exhibit frequency-dependent strain and rotation movements which seem to be crucial for the stimulation of the sensory dendrites (Stephen and Bennet-Clark, 1982). Due to its mass and compliance, Müller's organ exhibits its own properties of oscillation and can act as a resistive load for the tympanum (Stephen and Benett-Clark, 1982). In addition, there are in-phase and antiphase movements within Müller's organ (Breckow and Sippel, 1985). The mechanics of Müller's organ change profoundly during development (Breckow and Sippel, 1985), and its complex characteristics led several authors to suggest that it really is an ''active observer'' which influences tympanal motion (Michelsen, 1973; Stephen and Bennet-Clark, 1982; Breckow and Sippel, 1985).

Within Müller's organ, metabolic vulnerability can occur at the level of the attachment cells, the scolopale cells, and the receptor neurons themselves (see Fig. 1). Scolopale cells are known to contain actin and tropomyosin and it was suggested that the elasticity or stiffness of these cells depends on the extent of tropomyosin binding (Wolfrum, 1991). The receptor cell dendrite contains a single large cilium with a long process that extends towards the cell body. An active role of the cilia in sensory transduction is described for the chordotonal organ of the grasshopper *Melanoplus bivittatus* (Moran *et al.*, 1977). Moran *et al.* suggest that an active sliding movement between adjacent doublets of the axoneme leads to a local bending in the cilium and to an enhancement of displacement at the base of the cilium. The cilium and transduction apparatus in the insect receptors might therefore be well involved in the creation of mechanical nonlinearity. As far as the hair bundles of vertebrate hair cells are concerned, it is known that their mechanics are nonlinear (Howard and Hudspeth, 1988; Russell *et al.*, 1992) and able to produce strong frequency distortions (Jaramillo *et al.*, 1993). If the same were true for the insect cilium, then the underlying mechanisms probably depend on different structures, since the insect has a true cilium, whereas the vertebrate hair bundle mainly consists of stereovilli with an actin core.

ACKNOWLEDGMENTS

For discussion of the presented data we are grateful to F. Huber, G. Manley, A. Michelsen, G. Neuweiler, U. Thurm, and M. Vater. This study was supported by the Deutsche Forschungsgemeinschaft.

Allen, J. B., and Fahey, P. F. (**1993**). ''A second cochlear frequency map that correlates distortion product and neural tuning measurements,'' J. Acoust. Soc. Am. **94**, 809–816.

Breckow, J., and Sippel, M. (**1985**). ''Mechanics of the transduction of sound in the tympanal organ of adult and larvae of locusts,'' J. Comp. Physiol. A **157**, 619–629.
Brown, A. M., and Kemp, D. T. (**1984**). ''Suppressibility of the $2f1-f2$ stimulated acoustic emission in gerbil and man,'' Hearing Res. **13**, 29–37.
Brown, A. M., Gaskill, S. A., and Williams, D. M. (**1992**). ''Mechanical filtering of sound in the inner ear,'' Proc. R. Soc. London, Ser. B **250**, 26–34.
Brown, A. M., McDowell, B., and Forge, A. (**1989**). ''Acoustic distortion products can be used to monitor the effects of chronic gentamicin treatment,'' Hearing Res. **42**, 143–156.
Dallos, P. (**1992**). ''The active cochlea,'' J. Neurosci. **12**, 4575–4585.
Faulstich, M., Kössl, M., and Reimer, K. (**1996**). ''Analysis of non-linear cochlear mechanics in the marsupial *Monodelphis domestica*: ancestral and modern mammalian features,'' Hearing Res. **94**, 47–53.
Frank, G., and Kössl, M. (**1996**). ''The acoustic two-tone distortions $2f1-f2$ and $f2-f1$ and their possible relation to changes in the operating point of the cochlear amplifier,'' Hearing Res. **98**, 104–115.
Gaskill, S. A., and Brown, A. M. (**1990**). ''The behavior of the acoustic distortion product, $2f1-f2$, from the human ear and its relation to auditory sensitivity,'' J. Acoust. Soc. Am. **88**, 821–839.
Gray, E. G. (**1960**). ''The fine structure of the insect ear,'' Philos. Trans. R. Soc. London, Ser. B **243**, 75–94.
Hamon, A., Guillet, J. C., and Callec, J. J. (**1988**). ''Initiation and conduction of impulses in mechanosensory neurons: effects of hypoxia,'' Comp. Biochem. Physiol. **91A**, 797–805.
Horner, K. C., Lenoir, M., and Bock, G. R. (**1985**). ''Distortion product otoacoustic emissions in hearing-impaired mutant mice,'' J. Acoust. Soc. Am. **78**, 1603–1611.
Howard, J., and Hudspeth, A. J. (**1988**). ''Compliance of the hair bundle associated with gating of mechanoelectrical transduction channels in the bullfrog's saccular hair cell,'' Neuron **1**, 189–199.
Janssen T., Kummer, P., and Arnold, W. (**1996**). ''Growth of the $2f1-f2$ distortion product otoacoustic emission in tinnitus,'' in Abstracts of the 19th midwinter research meeting of the Assoc. for Research in Otolaryngology, St. Petersburg Beach, p. 96.
Jaramillo, F., Markin, V. S., and Hudspeth, A. J. (**1993**). ''Auditory illusions and the single hair cell,'' Nature (London) **364**, 527–529.
Kettembeil, S., Manley, G. A., and Siegl, E. (**1995**). ''Distortion-product otoacoustic emissions and their anaesthesia sensitivity in the starling and the European chicken,'' Hearing Res. **86**, 47–62.
Köppl, C. (**1995**). ''Otoacoustic emissions as an indicator for active cochlear mechanics: a primitive property of vertebrate hearing organs,'' in *Advances in Hearing Research*, edited by G. A. Manley, G. M. Klump, C. Köppl, H. Fastl, and H. Oeckinghaus (World Scientific, Singapore), pp. 207–218.
Kössl, M. (**1992**). ''High frequency distortion products from the ears of two bat species, *Megaderma lyra* and *Carollia perspicillata*,'' Hearing Res. **60**, 156–164.
Kössl, M. (**1994**). ''Otoacoustic emissions from the cochlea of the 'constant frequency' bats, *Pteronotus parnellii* and *Rhinolophus rouxi*,'' Hearing Res. **72**, 59–72.
Kössl, M., and Boyan, G. S. (**1997**). ''Distortion-product otoacoustic emissions from the ear of the grasshopper, *Locusta migratoria*,'' in Abstracts of the 20th Midwinter Research Meeting of the ARO, St. Petersburg Beach, Florida, Abstract #238.
Kössl, M., and Boyan, G. S. (**1998**). ''Otoacoustic emissions from a non-vertebrate ear,'' Naturwissenschaften **85**, 124–126.
Kössl, M., and Vater, M. (**1996**). ''Further studies on the mechanics of the cochlear partition in the mustached bat. II. A second cochlear frequency map derived from acoustic distortion products,'' Hearing Res. **94**, 78–86.
Kujawa, S. G., Fallon, M., and Bobbin, R. P. (**1992**). ''Intracochlear Salicylate reduces low-intensity acoustic and cochlear microphonic distortion products,'' Hearing Res. **64**, 73–80.
Kutsch, W., and Otto, D. (**1972**). ''Evidence for spontaneous song production independent of head ganglia in *Gryllus campestris L.*,'' J. Comp. Physiol. **81**, 115–119.
Manley, G. A. (**1995**). ''The avian hearing organ: a status report,'' in *Advances in Hearing Research*, edited by G. A. Manley, G. M. Klump, C. Köppl, H. Fastl, and H. Oeckinghaus (World Scientific, Singapore), pp. 219–229.
Manley, G. A., and Köppl, C. (**1993**). ''Distortion-product otoacoustic emissions in the bobtail lizard. I. General characteristics,'' J. Acoust. Soc. Am. **93**, 2820–2844.
Meyer, J., and Elsner, N. (**1996**). ''How well are frequency sensitivities of grasshopper ears tuned to species-specific song spectra,'' J. Exp. Biol. **199**, 1631–1642.
Michelsen, A. (**1971**). ''The physiology of the locust ear. I. Frequency sensitivity of single cells in the isolated ear,'' ''II. Frequency discrimination based upon resonances in the tympanum,'' and ''III. Acoustical properties of the intact ear,'' Z. Vergl. Physiologie **71**, 49–128.
Michelsen, A. (**1973**). ''The mechanics of the locust ear: an invertebrate frequency analyzer,'' in Basic Mechanisms in Hearing, edited by A. R. Moller (Academic, New York), pp. 911–934.
Michelsen, A., and Rohrseitz, K. (**1995**). ''Directional sound processing and interaural sound transmission in a small and a large grasshopper,'' J. Exp. Biol. **198**, 1817–1827.
Miller, L. A. (**1977**). ''Directional hearing in the locust *Schistocerca gregaria* Forskal (Acrididae, Orthoptera),'' J. Comp. Physiol. **119**, 85–98.
Mills, D. M., and Rubel, E. W. (**1996**). ''Development of the cochlear amplifier,'' J. Acoust. Soc. Am. **100**, 428–441.
Mills, D. M., Norton, S. J., and Rubel, E. W. (**1993**). ''Vulnerability and adaptation of distortion-product otoacoustic emissions to endocochlear potential variation,'' J. Acoust. Soc. Am. **94**, 2108–2122.
Moran, D. T., Varela, F. J., and Rowley III, J. C. (**1977**). ''Evidence for active role of cilia in sensory transduction,'' Proc. Natl. Acad. Sci. USA **74**, 793–797.
Neely, S. T., and Stover, L. J. (**1997**). ''A generation of distortion products in a model of cochlear mechanics,'' in *Diversity in Auditory Mechanics*, edited by E. R. Lewis, G. R. Long, R. F. Lyon, P. M. Narins, C. R. Steele, and E. Hecht-Poinar (World Scientific, Singapore), pp. 434–440.
Oldfield, B. P. (**1988**). ''The effect of temperature on tuning and physiology of insect auditory receptors,'' Hearing Res. **35**, 151–158.
Probst, R., Lonsbury-Martin, B. L., and Martin, G. K. (**1991**). ''A review of otoacoustic emissions,'' J. Acoust. Soc. Am. **89**, 2027–2067.
Rebillard, G., and Lavigne-Rebillard, M. (**1992**). ''Effect of reversible hypoxia on compared time courses of endocochlear potential and $2f1-f2$ distortion products,'' Hearing Res. **62**, 142–148.
Römer, H. (**1976**). ''Die Informationsverarbeitung tympanaler Rezeptorelemente von *Locusta migratoria* (Acrididae, Orthoptera),'' J. Comp. Physiol. **109**, 101–122.
Ruggero, M. A. (**1993**). ''Distortion in those good vibrations,'' Curr. Biol. **3**, 755–758.
Russell, I. J., Kössl, M., and Richardson, G. P. (**1992**). ''Nonlinear mechanical responses of mouse cochlear hair bundles,'' Proc. R. Soc. London, Ser. B **250**, 217–227.
Sippel, M., and Breckow, J. (**1983**). ''Non-linear analysis of the transmission of signals in the auditory system of the migratory locust *Locusta migratoria*,'' Biol. Cybern. **46**, 197–205.
Sippel, M., and Breckow, J. (**1984**). ''Non-monotonic response-intensity characteristic of auditory receptor cells in *Locusta migratoria*,'' J. Comp. Physiol. A **155**, 633–638.
Stephen, R. O., and Bennet-Clark, C. (**1982**). ''The anatomical and mechanical basis of stimulation and frequency analysis in the locust ear,'' J. Exp. Biol. **99**, 279–314.
Vater, M., and Kössl, M. (**1996**). ''Further studies on the mechanics of the cochlear partition in the mustached bat. II. Ultrastructural observations on the tectorial membrane and its attachments,'' Hearing Res. **94**, 63–77.
Whitehead, M. L., Lonsbury-Martin, B. L., Martin, G. K., and McCoy, M. J. (**1996**). ''Otoacoustic emissions: Animal Models and Clinical Observations,'' in *Clinical Aspects of Hearing*, edited by T. R. Van de Water, A. N. Popper, and R. F. Fay (Springer-Verlag, New York), pp. 199–258.
Wolfrum, U. (**1991**). ''Tropomyosin is colocalized with actin filaments of the scolopale in insect sensilla,'' Cell Tissue Res. **265**, 11–17.

Correlated amplitude fluctuations of spontaneous otoacoustic emissions

Pim van Dijk[a] and Hero P. Wit
Department of Otorhinolaryngology, University Hospital Groningen, P.O. Box 30.001, 9700 RB Groningen, The Netherlands

(Received 6 November 1997; accepted for publication 30 March 1998)

The frequency spectrum of a spontaneous otoacoustic emission (SOAE) recording may contain multiple narrow peaks. These peaks correspond to multiple SOAEs emitted by the inner ear. The individual SOAEs exhibit small amplitude fluctuations. The correlation between the amplitude fluctuations of multiple SOAEs in an individual ear was studied in 19 SOAE recordings from humans. For 424 pairs of SOAEs, the normalized amplitude cross-correlation function was computed. Significant correlation was found in 63 pairs (15%): 34 pairs showed positive and 29 pairs showed negative correlation. Some SOAE pairs were part of an equally spaced triplet of emission peaks, with one SOAE apparently generated as a distortion product of the other two ''primary'' SOAEs. The occurrence of correlation between a distortion product SOAE and a ''primary'' SOAE was 56%. This is significantly higher than the occurrence of correlation for the entire set of SOAE pairs. In addition, the spectral width of the distortion product SOAE was correlated with the spectral width of the ''primary'' SOAEs ($R=0.87$, $p<10^{-6}$). For 79% of the correlated SOAE pairs, the cross-correlation function peaked at positive time delay. This indicates that for these pairs the fluctuation of the lower frequency emission lagged the fluctuation of the higher frequency emission. The average peak delay was 11.0 ms (s.d. 22.1 ms). The results demonstrate that interactions between SOAEs in an individual ear frequently occur and are asymmetrical. © *1998 Acoustical Society of America.* [S0001-4966(98)03307-4]

PACS numbers: 43.64.Jb, 43.64.Kc [BLM]

INTRODUCTION

The inner ear of a normal hearing subject may emit acoustic signals in the absence of any external acoustic stimulation. These spontaneous otoacoustic emissions [SOAEs, reviewed in Probst *et al.* (1991)] can be detected with a sensitive microphone connected to the ear canal. Several characteristics of individual SOAE peaks may be described by a simple limit-cycle oscillator model [reviewed in Van Dijk *et al.* (1994)]. In particular, SOAE suppression (Long *et al.*, 1991; Murphy *et al.*, 1995a) and synchronization (Van Dijk and Wit, 1990b; Long *et al.*, 1991) by external tones have been modeled with limit-cycle oscillator models.

Although several properties of individual SOAEs can be described by a model system including a single limit-cycle oscillator, there are clear indications that a SOAE peak is not an isolated phenomenon.

First of all, neighboring SOAEs have a preferred spectral spacing (0.4 Bark; Dallmayr, 1985), which shows that the presence of a SOAE at a particular frequency is correlated with other SOAEs in the same ear.

Second, the suppression of a SOAE by an external stimulus may enhance the amplitude of another SOAE in the same ear (Burns *et al.*, 1984; Long, 1993). Apparently, in this case the two emission peaks mutually suppress each other. Mutual suppression of spontaneous otoacoustic emissions may also lead to quasistable emission modes, in which individual SOAE peaks switch on and off in an apparently random sequence (Burns *et al.*, 1984). In one subject, these SOAE interactions were shown to be present during two measurements separated by approximately two years (Burns *et al.*, 1994). The dynamics of mutual suppression of a SOAE pair has also been analyzed by Murphy *et al.* (1995a), who could describe their data in a model with two coupled limit-cycle oscillators.

Finally, Burns *et al.* (1984) and Jones *et al.* (1986) described triplets of equally spaced SOAE peaks, where one of the peaks appeared to be a distortion product of the other two peaks. Clearly, a distortion product SOAE cannot be considered an isolated phenomenon.

In the absence of an external stimulation, SOAEs also exhibit random amplitude fluctuations (Bialek and Wit, 1984; Van Dijk and Wit, 1990a). If multiple SOAEs in a single ear may mutually suppress each other (Burns *et al.*, 1984; Long, 1993; Murphy *et al.*, 1995a), it is expected that their random envelope[1] fluctuations are correlated. Such correlated fluctuations have been described in human (Burns *et al.*, 1984; Wit, 1990), and for one pair of barn owl spontaneous emissions (Van Dijk *et al.*, 1996). In the current study, we systematically searched for envelope cross correlation. Indeed, we found a number of correlated SOAE pairs. For the majority of correlated pairs, the fluctuation of the lower frequency emission lagged fluctuation of the higher frequency emission. Our data provide additional evidence for the frequent interactions between SOAEs.

I. MATERIAL AND METHODS

Recordings of SOAEs from 19 human ears were analyzed, 16 female and three male. All these recordings have

[a]Electronic mail: P.van.Dijk@med.rug.nl

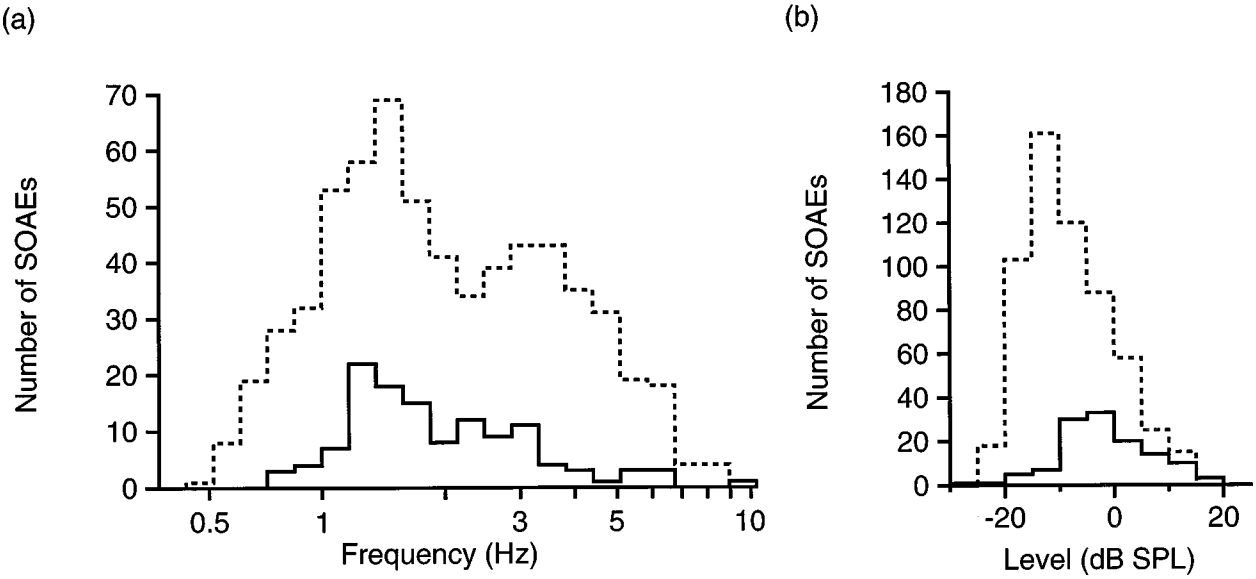

FIG. 1. Distribution of SOAE frequencies (panel a) and levels (panel b). The solid curves in both panels show results for the SOAEs included in this study. For comparison, the dashed curves show data for a general population of SOAEs (Talmadge *et al.*, 1993). As follows from panel (b), this study included mostly SOAEs with a relatively large level.

been described in earlier studies, and were reanalyzed here. Seven recordings have been described by Van Dijk and Wit (1990a) while the remaining 12 recordings were included in a study by Talmadge *et al.* (1993). The SOAEs of one of the Talmadge *et al.* subjects were also described by Murphy *et al.* (1995b, see Discussion). The 19 recordings were selected on the basis of their spectral properties: To be included in the present study, the spectrum had to contain at least two peaks with full width at half maximum (FWHM) smaller than 10 Hz (see below).

The nine recordings from the Van Dijk and Wit (1990a) study were digitized with a Digital Ears 16-bit A/D converter attached to the DSP-port of a NeXT computer, at a sampling rate of 44.1 kHz. The 12 remaining recordings were digitized by Talmadge *et al.* (1993) using a Singular Solution A/D64x, at 16-bit resolution and 44.1- or 48-kHz sampling rate. All further analysis was performed on the digital signals. The sampling rate of each recording was brought to 22.05 or 24 kHz after anti-aliasing filtering.

For each SOAE recording, a spectrum was computed, in which the SOAE peaks were identified. For the amplitude correlation analysis described below, individual SOAEs were isolated using a narrow bandpass filter. An SOAE peak was included in our study, if its FWHM$<$10 Hz, because then the SOAE fell well within the 50-Hz filter width typically used. In addition, if two SOAEs were separated by less than twice the filter width, the envelope cross correlation for this pair was discarded, in order to omit the artifacts introduced by overlap of the respective bandpass filters.

The 19 SOAE recordings we analyzed contained a total of 293 SOAE peaks. Among these 293 SOAE peaks, 124 had a FWHM smaller than 10 Hz and were included in the amplitude correlation analysis. The frequencies of these SOAEs ranged from 727 to 9219 Hz, while their levels ranged from -26 to 19 dB SPL. Figure 1 displays the distribution of the frequencies (panel a) and levels (panel b) of the SOAEs included in our analysis, along with similar distributions for a general population of SOAEs (Talmadge *et al.*, 1993).

For each pair of SOAEs, which could be formed from the included SOAEs in a recording, the envelope cross correlation was computed as follows.

The digitized emission recording was divided into 75% overlapping 32 768-point sections. In each section, the two SOAEs of interest were singled out by bandpass filtering with a fourth-order butterworth filter with the amplitude response

$$A(f)=\frac{1}{\sqrt{1+[(f-f_{\text{center}})/(1/2\Delta f)]^8}}, \tag{1}$$

and the (acausal) zero phase response

$$\phi=0. \tag{2}$$

The filter's center frequency f_{center} in Eq. (1) was set at the SOAE frequencies f_1 and f_2, respectively, in order to produce two filtered signals $x_1(t)$ and $x_2(t)$. The filter width Δf in Eq. (1) was usually set to 50 Hz. For one recording we used a 30-Hz filter width, while in another case of 40 Hz was used. In these two cases, the widths of the emissions permitted the use of the narrower filter.

For both filtered signals $x_1(t)$ and $x_2(t)$, each of which contained a single emission, we computed the Hilbert transforms $\tilde{x}_1(x)$ and $\tilde{x}_2(t)$, respectively (Bendat and Piersol, 1971). The signals $x_1(t)$ and $x_2(t)$, and their Hilbert transforms $\tilde{x}_1(t)$ and $\tilde{x}_2(t)$, were used to compute the envelopes $A_1(t)=[x_1^2(t)+\tilde{x}_1^2(t)]^{1/2}$ and $A_2(t)=[x_2^2(t)+\tilde{x}_2^2(t)]^{1/2}$, respectively. Both the filtering described above and the computation of the Hilbert transforms were performed in the frequency domain.

The analysis so far yields two 32 768-point envelope signals: $A_1(t)$ and $A_2(t)$. For further analysis only the

middle 16 384 data points of each 32 768-point section were used in order to prevent wraparound effects introduced by the digital filtering procedure (Press *et al.*, 1992). For each envelope signal we extracted the fluctuation components, e.g., $\delta A_1(t)=A_1(t)-A_{1,\mathrm{avg}}$ and $\delta A_2(t)=A_2(t)-A_{2,\mathrm{avg}}$.

The 16 384-point envelope fluctuation signals $\delta A_1(t)$ and $\delta A_2(t)$ were padded with 16 384 zeros, to prevent wraparound effects contaminating cross-correlation computation (Press *et al.*, 1992). From the fast Fourier transform $F[\delta A_1]$ and $F[\delta A_2]$ of the padded signals we computed the cross-correlation spectrum $F[\delta A_1]F^*[\delta A_2]$ and its inverse Fourier transform, the cross-correlation function $r(\tau)$. Here the asterisk refers to complex conjugate. The cross-correlation function $r(\tau)$ was used to obtain the *normalized* cross-correlation function $R_k(\tau)=r(\tau)/[\mathrm{s.d.}(\delta A_1)\times\mathrm{s.d.}(\delta A_2)]$. Recall that this correlation function was computed for a particular section of the full emission recording. The subscript k was added to represent the fact that R_k is a result for the kth section in the SOAE recording.

Finally, the results R_k from all 32 768-point sections in the recordings were averaged to yield the average envelope cross correlation $R(\tau)=N^{-1}\Sigma_k^N R_k(\tau)$. In order to determine the significance of the envelope correlation, a probability p was computed with the method described in the Appendix. We considered $p<0.01$ as evidence for a significant correlation.

We separately considered triplets of spontaneous emissions peaks, equally spaced in the frequency spectrum. For these triplets, one of the peaks is at a cubic distortion frequency of the other two SOAEs. For each SOAE peak we systematically searched the spectrum for two possible ''primary'' SOAEs. An emission triplet was classified ''equally spaced'' if the frequency separation between (a) the low- and midfrequency peak, and (b) the mid- and high-frequency peak, differed less than 1 Hz. We assumed the broadest emission to be the distortion frequency one (see Discussion). In addition to the amplitude correlation analysis described above, we investigated the relation between the spectral width (FWHM) of the primary and the distortion product SOAEs.

II. RESULTS

Figure 2(a) shows the envelope cross-correlation function between the SOAEs at 1529 and 1923 Hz in the spontaneous emission signal recorded from the left ear of subject ML. The corresponding amplitude and phase spectrum are displayed in Fig. 2(b) and (c). The shape of the correlation function, with a single peak slightly shifted away from time $\tau=0$ ms, is typical for all cross-correlation functions we observed. The cross-correlation function can be described by three parameters: (1) the peak correlation R_{peak} [see Fig. 2(a)], (2) the spectral width Δf_{peak} [see Fig. 2(b)], and (3) the peak delay τ_{peak} [see Fig. 2(c)]. The width Δf_{peak} follows from a Lorenz curve fitted to the amplitude spectrum. The peak delay τ_{peak} is the slope of a straight line fitted to the phase spectrum.

For the SOAE pair in Fig. 2, the peak correlation $R_{\mathrm{peak}}=-0.24$ occurs at a slightly positive time delay $\tau_{\mathrm{peak}}=9.6$ (± 0.2) ms. The negative sign of the peak correlation indicates that an amplitude increase of one of the SOAEs was associated with an amplitude decrease of the other SOAE. The positive sign of time delay, e.g., a shift of the peak correlation to a positive delay time, indicates that amplitude fluctuation of the lower frequency SOAE tends to lag the associated fluctuation of the higher frequency SOAE.

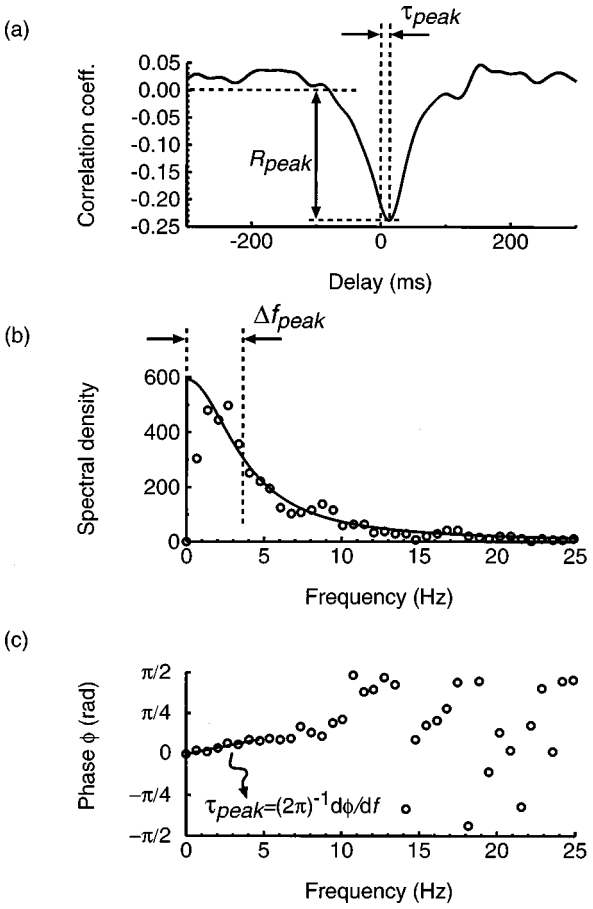

FIG. 2. (a) Cross-correlation function between the envelopes of two spontaneous otoacoustic emissions in the left ear of subject ML. The emission levels and frequencies were 11.0 dB SPL at 1529 Hz and −3.3 dB SPL at 1923 Hz, respectively. (b) Amplitude and (c) phase spectrum of the function in panel (a). $R_{\mathrm{peak}}=-0.24$ ($p<10^{-6}$), $\Delta f_{\mathrm{peak}}=3.8(\pm 0.3)$ Hz, and $\tau_{\mathrm{peak}}=9.6(\pm 0.2)$ ms.

Figure 3 displays the spectrum of the SOAE signal recorded from the same ear of subject ML. The figure summarizes the correlations which were found between the various emission peaks in the spectrum.

From the 124 narrow SOAEs included in this study, 424 pairs could be formed. For all these 424 pairs the envelope cross correlation was computed. For 63 pairs (15% of 424) we found a significant correlation between the envelopes of both SOAEs. For 34 pairs, the cross correlation was positive ($R_{\mathrm{peak}}>0$). For the remaining pairs correlation was negative. Across SOAE pairs, the peak correlations ranged from $R_{\mathrm{peak}}=-0.40$ to 0.16. Figure 4 is a histogram as a function of the frequency ratio f_2/f_1 of all emission pairs investigated, with the subgroup of correlated pairs displayed in grey. Here f_1 and f_2 are the frequency of the lower and higher frequency SOAE, respectively. With two exceptions, the frequency ratio f_2/f_1 was smaller than 1.7 for the corre-

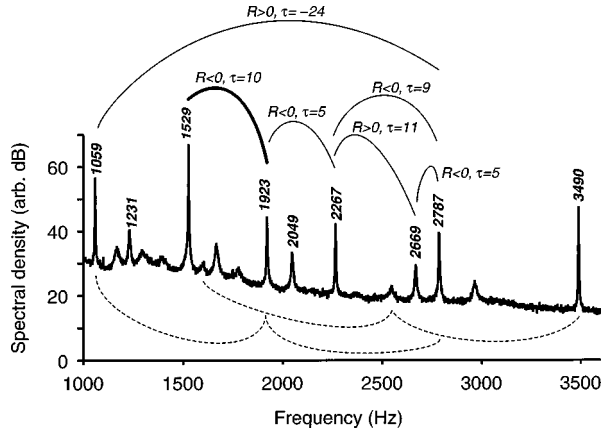

FIG. 3. Spectral density of the spontaneous otoacoustic emission signal in the left ear canal of subject ML. For the emission peaks labeled by a center frequency: FWHM<10 Hz. These peaks were included in the cross-correlation analysis. Solid arches point to emission pairs for which the peak envelope correlation R_{peak} was statistically significant. For each correlated pair, the sign of R_{peak} is indicated (i.e., $R<0$), along with the lag time τ_{peak} in milliseconds of the lower frequency peak relative to the higher frequency peak (i.e., $\tau=10$). The correlation between the emission pair connected by the heavy solid arch is also illustrated in Fig. 2. The dashed arches connect the equally spaced emission triplets, present in the spectrum [e.g., either a $(2f_1-f_2,f_1,f_2)$ or a $(f_1,f_2,2f_2-f_1)$ combination].

lated pairs. The average ratio was 1.27 with standard deviation 0.27.

The delay τ_{peak} of the correlation peak, as obtained from the phase spectra, ranged from -40.2 to 108.8 ms with average 11.0 ms and standard deviation 22.1 ms. The delay was not correlated with the levels of the spontaneous emission peaks in a pair, nor with the level difference. Figure 5 shows a histogram of the measured delay values. The delay was positive for 79% of the emissions pairs, e.g., for these pairs a fluctuation of the lower frequency SOAE lagged fluctuation of the higher frequency SOAE.

The width Δf_{peak} of the correlation amplitude spectrum ranged from 1.2 to 26.7 Hz across the correlated SOAE pairs, and was not correlated with SOAE level. The average width was 5.6 Hz with standard deviation 4.9 Hz. For three pairs, the width was larger than 15 Hz. Note that for these

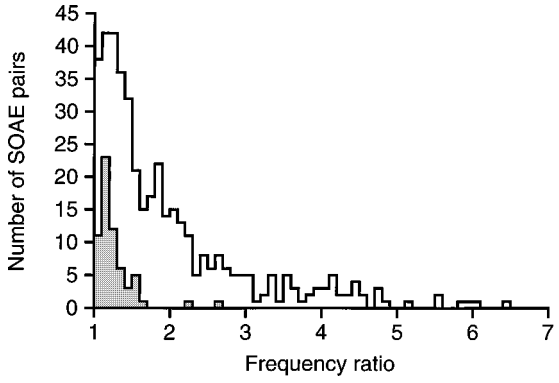

FIG. 4. Distribution of SOAE frequency ratios. Open curve: distribution of the frequency ratios of all SOAE pairs included in the amplitude correlation analysis. Grey filled curve: histogram of the subgroup of SOAE pairs with significantly correlated amplitude fluctuations. For six pairs, the frequency ratio exceeded the horizontal axis. None of these pairs were significantly correlated.

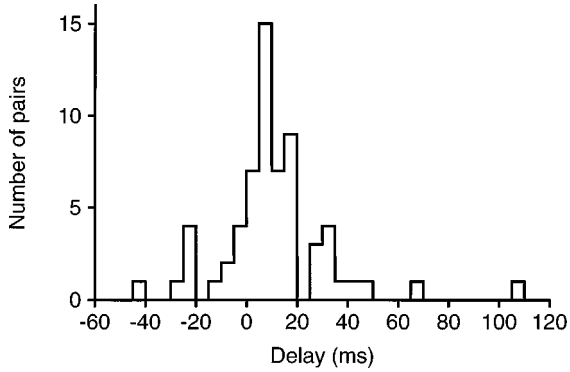

FIG. 5. Histogram of the delay τ_{peak} for all significantly correlated SOAE pairs.

broader spectra, the width was limited by the 50 Hz analysis filter, which caused correlation spectra to be cut off at about 25 Hz.

Figure 6 illustrates the relation between delay τ_{peak} and the ratio f_2/f_1 $(f_2>f_1)$. Each data point in the figure corresponds to one of the 63 SOAE pairs for which a significant amplitude correlation was observed. In panel (a) all pairs are illustrated, except those for which one of the SOAEs was identified as a distortion product of two other SOAEs. These cubic distortion SOAE pairs are shown separately in panel (b). Pairs with a positive peak correlation R_{peak} are represented by open symbols in Fig. 6, while closed symbols correspond to a negative peak correlation. The different symbols in Fig. 6(b) reflect the different relations a distortion product SOAE may have to its respective primary SOAEs (see below).

For frequency ratios up to 1.15, the delay typically varies between -10 and 20 ms (see Fig. 6). For larger ratios the scatter is considerably larger, between -40 and 70 ms. As far as the peak delay τ_{peak} is concerned, there is no conspicuous difference between positively and negatively correlated SOAE pairs illustrated in Fig. 6(a) (e.g., open and closed symbols are evenly distributed).

Across the 19 SOAE recordings, 22 equally spaced emission triplets were observed. Assuming the broadest emission peak in a triplet to be a distortion SOAE, 14 triplets were a $(2f_1-f_2,f_1,f_2)$ combination, five were a $(f_1,f_2,2f_2-f_1)$ combination, and for three triplets the mid-frequency peak was broadest, which would imply a $[f_1,\frac{1}{2}(f_1+f_2),f_2]$ combination (see Discussion).

Seven $2f_1-f_2$ and two $2f_2-f_1$ distortion product SOAEs were included in the amplitude correlation analysis. For these nine distortion peaks we investigated the envelope cross correlation with both primary SOAEs (e.g., 18 pairs).

Among the total of 18 SOAE pairs, which included a cubic distortion product, ten (56%) showed a significant correlation. This occurrence of correlation is significantly larger $(p=0.0004)$ than the 15% occurrence found in the entire group of emission pairs.

The correlation between a $2f_1-f_2$ SOAE and the corresponding f_1 primary SOAE was significant for six out of the seven pairs investigated. For all six pairs the correlation R_{peak} was positive, and the delay ranged from $\tau_{\text{peak}}=-4.7$ to 34.9 ms [see open squares in Fig. 6(b)].

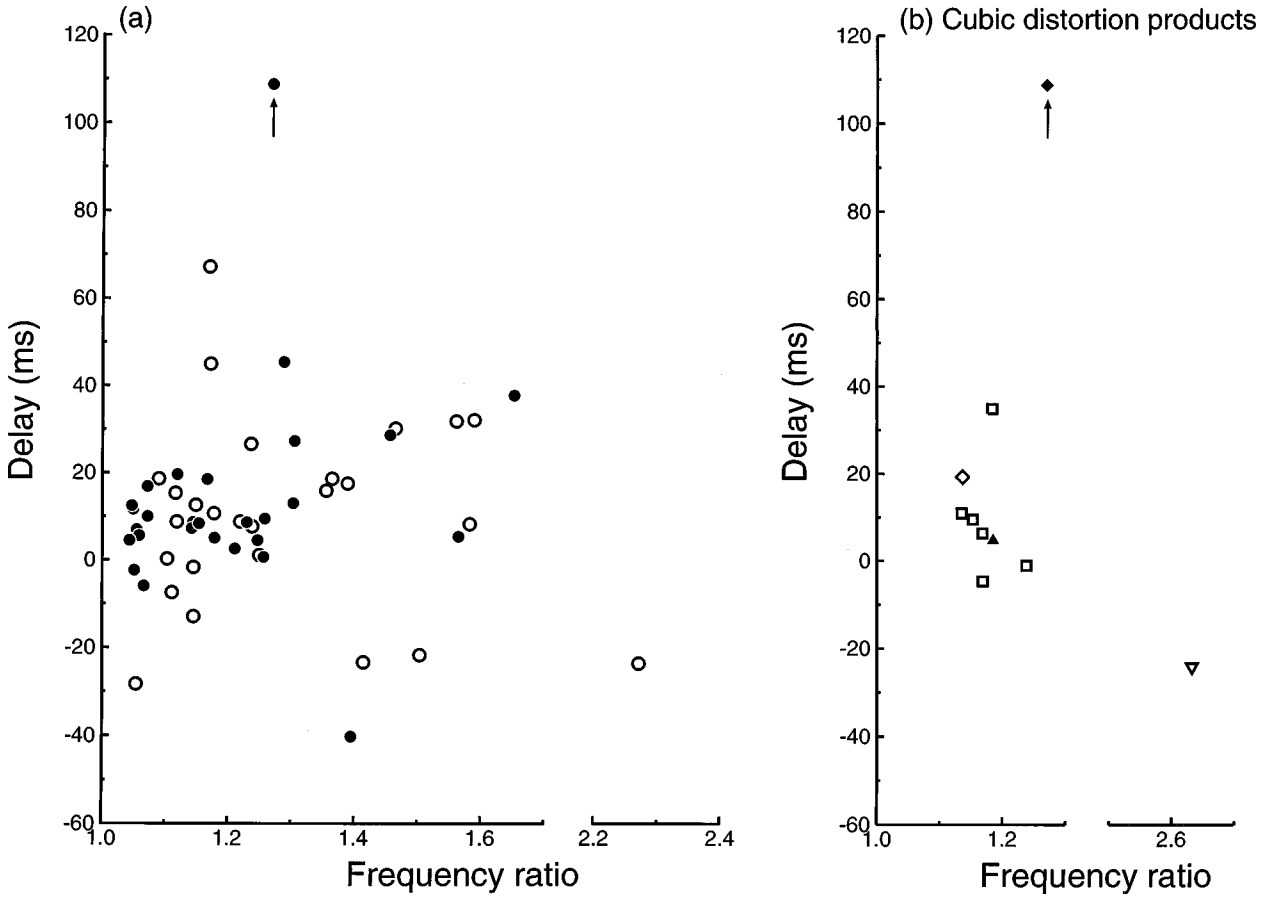

FIG. 6. Scatter plot of the peak delay τ_{peak} versus the frequency ratio (f_2/f_1). Each data point corresponds to a pair of spontaneous emission (frequencies f_2 and f_1, respectively) with a statistically significant peak correlation R_{peak}. Emission pairs for which one emission peak was at the cubic distortion frequency of two other emission peaks are displayed separately in panel (b). Data for all other pairs are shown in panel (a). Open symbols: positive cross correlation $R_{peak}>0$; closed symbols negative cross correlation $R_{peak}<0$. In panel (b), various symbols are used to identify the relation of the cubic distortion product to the primary to which it is correlated: squares: ($2f_1-f_2 \leftrightarrow f_1$); diamonds: ($2f_1-f_2 \leftrightarrow f_2$); down triangle: ($f_1 \leftrightarrow 2f_2-f_1$); up triangle: ($f_2 \leftrightarrow 2f_2-f_1$). One data point appears in both panels: see arrow. This point appears in panel (a) because it corresponds to a pair of emissions which formed the primaries of another cubic distortion emission. Also it is shown in panel (b), since the lower frequency SOAE also was the cubic distortion product of the higher frequency emission and yet another SOAE.

A correlation between a $2f_1-f_2$ SOAE and the second primary SOAE at f_2 was found for only two of the seven pairs investigated. In one case, the peak correlation was negative [see the closed diamond in Fig. 6(b)], while for the other pair it was positive [open diamond in Fig. 6(b)]. The negatively correlated ($2f_1-f_2, f_2$) pair also formed the primary components of another cubic distortion SOAE triplet. Therefore it is displayed in both panels of Fig. 6 (arrows). The peak correlation for this ''complicated'' pair was delayed by 108.8 ms, which is the largest delay encountered in this study.

Among the two $2f_2-f_1$ SOAE distortion products, one was positively correlated with the primary SOAE at f_1, while fluctuation of the primary preceded fluctuation of the distortion product [e.g., $\tau_{peak}=-24.1$ ms; see the open down-triangle in Fig. 6(b)]. For the other distortion SOAE, we found a negative correlation with the primary at f_2, while the envelope fluctuation of the primary lagged fluctuation of the distortion emission's envelope by $\tau_{peak}=4.8$ ms [see the closed up-triangle in Fig. 6(b)].

The rms-frequency fluctuation of a distortion product SOAE was predicted from the frequency fluctuation of the respective primary SOAEs. For example, if two primaries at f_1 and f_2 exhibit rms frequency fluctuations of σ_1 and σ_2, respectively, the frequency fluctuation of the distortion product $2f_1-f_2$ was predicted to be $\sqrt{(2\sigma_1^2+\sigma_2^2)}$. Figure 7 shows the relation between the measured spectral width of a distortion product and the width predicted from the widths of the primary emissions. Predicted and measured widths were significantly correlated ($R=0.87$, $p<10^{-6}$), but the measured width was usually larger than the predicted width (see Fig. 7).

III. DISCUSSION

We have analyzed the linear cross correlation between the envelopes of SOAE pairs measured in the same ear. The envelope cross-correlation function $R(\tau)$, which we computed, is simply the linear cross-correlation coefficient or Pearson correlation coefficient of the envelope of one SOAE and the envelope of a second SOAE, with a delay of τ seconds later.

A significant envelope cross correlation was revealed for 15% of all analyzed emission pairs. Due to the presence of microphone noise in the analysis filters, correlation may be obscured for some of the emission pairs. Thus (1) the num-

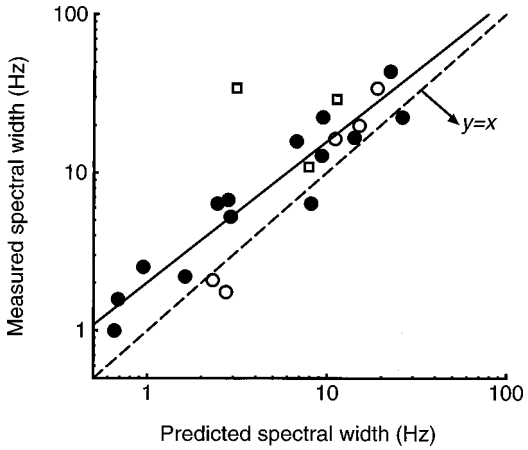

FIG. 7. Predicted versus measured spectral width Δf_{dp} of distortion product SOAEs. For each equally spaced triplet of emissions, the broadest spectral peak was assumed to be the distortion SOAE, while the other peaks were considered ''primary'' SOAEs (see main text). The width Δf_{dp} is predicted from the widths Δf_1 and Δf_2 of the primary emissions. Closed circles: $[2f_1-f_2, f_1, f_2]$ triplets: $\Delta f_{dp,predicted}=\sqrt{2\Delta f_1^2+\Delta f_2^2}$. Open circles: $[f_1, f_2, 2f_2-f_1]$ triplets: $\Delta f_{dp,predicted}=\sqrt{2\Delta f_2^2+\Delta f_1^2}$. Squares: $[f_1, \frac{1}{2}(f_1+f_2), f_2]$ triplets (see Discussion): $\Delta f_{dp,predicted}=\sqrt{\frac{1}{2}\Delta f_2^2+\frac{1}{2}\Delta f_1^2}$. The solid line is a linear regression line fitted to the data points ($R=0.87$, $p<10^{-6}$).

ber of correlated emission pairs is probably larger than 15%, and (2) the range of peak correlations we found (-0.40 to 0.16) is probably reduced by the effect of the microphone noise.

The SOAE recordings included in the present study were selected on the basis of their spectral characteristics. All included recordings contained at least two SOAEs with a spectral width smaller than 10 Hz. The frequency distribution of the SOAEs in our study is similar to that in a general population of emitting ears [see Fig. 1(a); Talmadge *et al.*, 1993], except that our inclusion criteria discarded all SOAEs below 700 Hz. In contrast, the SOAE levels were relatively large, compared to the general population [see Fig. 1(b)]. Also the mean number of SOAEs per ear was 15.4, while Talmadge *et al.* found 6.9 SOAEs per ear. Thus with respect to level and number of SOAEs per ear, the recordings included in this study do not represent a general population of emitting ears. We do not know whether this biases the data presented.

Interestingly, for emission pairs which included a cubic distortion product SOAE, the occurrence of cross correlation was higher: 56%. One might expect that the envelope of all cubic distortion emissions is tightly linked to the envelope of the respective primary emissions. That would imply that 100% of these emission pairs have correlated envelopes. Assuming this to be the case, we might conclude that our analysis reveals about 56% of the existing correlations.

If our analysis indeed reveals only 56% of the existing correlations, the actual number of correlated emission pairs is 27% ($=15\%/0.56$) rather than 15%. Thus a large number of pairs (73%) is expected to be uncorrelated, even after correction for the effect of the microphone noise. In particular, emission pairs with a frequency ratio larger than 1.7 will still be uncorrelated. The virtual absence of correlation for these larger ratios (see Fig. 4) cannot be accounted for by the presence of microphone noise, and must therefore be considered a property of the SOAEs.

We separately described correlation in equally spaced triplets of SOAEs, where one of the SOAEs is at a distortion frequency of the other SOAEs. For an equally spaced triplet of SOAEs, it is not clear (a) whether one of the emission peaks is actually generated by distortion of the other two peaks, and (b) if so, which of the three peaks should be considered the ''primaries'' and which peak should be considered the distortion product. Since the frequency fluctuation of both primaries will contribute to spectral broadening of the distortion product, we assumed that the broadest emission peak in a triplet is the cubic distortion product of the two remaining peaks.

With this criterion 19 of the 22 emission triplets in this study appeared to involve cubic distortion. In contrast, the remaining three pairs seemed to include a $\frac{1}{2}(f_1+f_2)$ distortion product. This distortion product corresponds to a subharmonic of the summation frequency of the ''primaries.'' Since it has not been described in the distortion emission literature, it seems unlikely that the three $\frac{1}{2}(f_1+f_2)$ emissions we identified were indeed generated by distortion of their respective ''primary'' SOAEs. Possibly, (1) the observed relation between the emission frequencies of each of these triplets is coincidental, or (2) our criterion failed to identify the distortion emission.

The spectral width of the distortion SOAE was positively correlated with the width of the primary SOAEs (see Fig. 7). In addition to the correlated amplitude fluctuation, which we found for several of the peaks, this strongly suggests that the emission triplets we identified are indeed related to each other. The observed width of the distortion product SOAE was typically larger than the width predicted from the primary SOAEs (see Fig. 7). In fact, the prediction is based on the assumption that the distortion emission is generated by some static nonlinearity. The discrepancy between measured and predicted width may indicate that this assumption is not correct. Alternatively, the distortion emission may be a spontaneous emission, which is synchronized by a weak cubic distortion product generated by the two ''primary'' emissions (Jones *et al.*, 1986; Van Dijk and Wit, 1990b). Then, frequency fluctuation of both the synchronized SOAE and the ''primary'' SOAEs contribute to the spectral width of the distortion emission. Possibly, this may account for the observed spectral width.

For the majority of emission pairs, the envelope fluctuation of the lower frequency SOAE lagged the envelope fluctuation of the higher frequency SOAE. Similarly, for click-evoked otoacoustic emissions, low-frequency emission components lag high-frequency emission components. These findings are presumably related to the more basal generation site of higher frequencies in the cochlea. Also, our result may indicate that the coupling between emission generators is asymmetric: higher frequency emissions may affect low-frequency emissions more strongly than visa versa.

Murphy *et al.* (1995b) described the dynamics of suppression of a SOAE by an external tone, along with simultaneous release from suppression of a second lower fre-

quency SOAE. Apparently, in absence of the external tone, the higher frequency emission suppresses the lower frequency emission. They modeled their results with two Van der Pol oscillators. By introducing a unidirectional coupling, they could describe suppression of the lower frequency emission by the higher frequency emission. The same subject described by Murphy *et al.* was also incorporated in the present study. In agreement with the Murphy *et al.* study we found negative envelope correlation, indicative of mutual suppression. Also, we found a positive peak delay $\tau_{\text{peak}} = 6.3$ ms, which implies an asymmetric coupling. However, since the envelope cross-correlation function is not entirely causal [e.g., $R(\tau) \neq 0$ for all $\tau < 0$], we conclude that the coupling cannot be entirely unidirectional, as was assumed by Murphy *et al.* (1995b).

It is likely that the data presented in this work can be described with coupled pairs of oscillators. The large number of parameters which determine the characteristic of such a coupled system are likely to be adequate to describe both negative and positive correlation, along with both negative and positive delay times. However, a description in a more comprehensive model of cochlear mechanics will provide a better understanding of the mechanisms involved. The data presented here provide a straightforward test of cochlear models which describe SOAEs. Of course, such models need to include active components to yield spontaneous emissions, in line with the notion of Talmadge *et al.* (1991) that SOAEs are generated by cochlear amplifiers. In addition, the models need to include internal noise in the cochlea, in order to account for the random amplitude and frequency fluctuation of SOAEs.

ACKNOWLEDGMENTS

We thank Carrick Talmadge, Glenis Long, and Arnold Tubis at Purdue University for providing some of their emission recordings for analysis. Also, we thank Glenis Long and Arnold Tubis for their comments on an earlier version of this paper. This study was supported by a Royal Netherlands Academy of Sciences and Arts fellowship (to P.vD.) and the Heinsius Houbolt Fund. The study is part of the research program of our Department, Communication through Hearing and Speech, which is incorporated in the Sensory Systems Group of the Groningen Graduate School for Behavioral and Cognitive Neurosciences (BCN).

APPENDIX: SIGNIFICANCE OF THE PEAK CORRELATION

Consider the data pairs (x_i, y_i), with $i = 1,...,N$. The linear correlation coefficient or Pearson correlation coefficient for the variables x and y is given by

$$R_{xy} = \frac{\Sigma_i^N (x_i - \overline{x}) \times (y_i - \overline{y})}{(\text{s.d.}x) \times (\text{s.d.}y)}, \tag{A1}$$

where $\overline{x}$ and $\overline{y}$ indicate average value.

The (double-sided) significance q of a particular value R is defined as the probability that $|R|$ is larger than or equal to the observed value, assuming uncorrelated data sets x and y. This probability can be computed from the probability distribution function of R for uncorrelated data. If the number N of data pairs is large, and x and y are uncorrelated, the probability distribution of R is approximately Gaussian. If neither x nor y are autocorrelated, the standard deviation of this distribution is (i.e., Press *et al.*, 1992)

$$\sigma = \frac{1}{\sqrt{N}}. \tag{A2}$$

Given this standard deviation, the significance can be computed using the error function (i.e., Press *et al.*, 1992):

$$q = \text{erfc}\left(\frac{|R| \sqrt{N}}{\sqrt{2}} \right). \tag{A3}$$

A small value of q indicates significant cross correlation.

Next, consider two uncorrelated times series $x_i = x(t_i)$ and $y_i = y(t_i)$, where $t_i = i/f_s$ is a discrete time variable, with $i = 1,...,N$, and sampling rate f_s. We will describe the case where the data sets x and y are autocorrelated. The autocorrelation of the time series $x(t)$ $[y(t)]$ can be expressed by the autocorrelation function $R_{xx}(\tau)$ $[R_{yy}(\tau)]$. This function represents the linear correlation coefficient for $x(t)$ $[y(t)]$ and $x(t+\tau)$ $[y(t+\tau)]$. If $R_{xx}(\tau) \neq 0$ for any $\tau \neq 0$, the data set x is said to be autocorrelated.

For autocorrelated data sets $x(t_i)$ and $y(t_i)$, the probability density of R is approximately Gaussian, as is the case for data without autocorrelation. However, the standard deviation of the probability distribution is no longer given by Eq. (A2), and consequently the significance of an observed value R cannot be computed with Eq. (A3).

The autocorrelation functions of the envelope fluctuation signals studied in this work resembled a Gaussian curve. Therefore we will consider two autocorrelated time series with

$$R_{xx} = e^{-(1/4)\tau^2/\tau_{xx}^2} \tag{A4}$$

and

$$R_{yy} = e^{-(1/4)\tau^2/\tau_{yy}^2}. \tag{A5}$$

where τ_{xx} and τ_{yy} are autocorrelation time constants. Via Monte Carlo simulation, in which 1000 data sets were generated, each of which contained 8192 uncorrelated data pairs, we found that the cross-correlation coefficient R is a Gaussian variable with standard deviation approximately given by the phenomenological relation (adapted from Ostrom, 1990)

$$\sigma = \frac{1}{\sqrt{N}} \times \left(\frac{1 + e^{-1/(f_s \tau_{xx})} e^{-1/(f_s \tau_{yy})}}{1 - e^{-1/(f_s \tau_{xx})} e^{-1/(f_s \tau_{yy})}} \right)^{1/2}. \tag{A6}$$

Various combinations of τ_{xx} and τ_{yy} were used in order to verify this result.

We may define an effective number of data points

$$N_{\text{eff}} = N \times \frac{1 - e^{-1/(f_s \tau_{xx})} e^{-1/(f_s \tau_{yy})}}{1 + e^{-1/(f_s \tau_{xx})} e^{-1/(f_s \tau_{yy})}} \tag{A7}$$

and use the error function Eq. (A3), with N replaced by N_{eff}, to compute the significance of the cross-correlation coefficient R. Note that autocorrelation (e.g., $N_{\text{eff}} < N$), enlarges the variance σ of the distribution of R. This will increase the

probability q in Eq. (A3), and thus reduce the significance of an observed cross-correlation coefficient R.

As described in Sec. I, we used a probability p in order to describe the significance of the peak correlation R_{peak} of the envelope cross-correlation function. The peak is extracted from the $n=16\,386$ data points which comprise the computed cross-correlation function. Again, due to autocorrelation of each of the envelope signals, an effective number of data points in the computed correlation function is given by $n_{\text{eff}}=(N/N_{\text{eff}})\times n$, where N_{eff} is given by Eq. (A7). The probability that, for uncorrelated envelopes, (a) one or more correlation values $|R(\tau)|$ are larger than the observed peak value $|R_{\text{peak}}|$, and (b) the remaining correlation values $|R(\tau)|$ are smaller, is given by the cumulative binomial distribution

$$p=\sum_{i=1}^{n_{\text{eff}}}\binom{n_{\text{eff}}}{i}q^i(1-q)^{n_{\text{eff}}-i}. \tag{A8}$$

This probability was used to rate the significance of the peak correlation in the envelope cross-correlation function.

In summary, from the autocorrelation function of each of the envelope signals in an emission pair, the autocorrelation time constants τ_{xx}, respectively τ_{yy}, were calculated. Next, Eq. (A7) was used to compute the effective number of data points N_{neff} in the emission recording. This number was substituted in the error function Eq. (A3). The resulting probability q was used in Eq. (A8) in order to obtain the significance p of the peak correlation R_{peak}. A $p<0.01$ was considered evidence for significant envelope cross correlation.

[1]The terms ''amplitude'' and ''envelope'' are used as synonyms.

Bendat, J., and Piersol, A. (**1971**). *Random Data: Analysis and Measurement Procedures* (Wiley–Interscience, New York).

Bialek, W., and Wit, H. P. (**1984**). ''Quantum limits to oscillator stability: theory and experiments on acoustic emissions from the human ear,'' Phys. Lett. **104A**, 173–178.

Burns, E. M., Campbell, S. L., and Arehart, K. H. (**1994**). ''Longitudinal measurement of spontaneous otoacoustic emissions in infants,'' J. Acoust. Soc. Am. **95**, 385–394.

Burns, E. M., Strickland, E. A., Tubis, A., and Jones, K. (**1984**). ''Interactions among spontaneous otoacoustic emissions. I. Distortion products and linked emissions,'' Hearing Res. **16**, 271–278.

Dallmayr, C. (**1985**). ''Spontane oto-akustische Emissionen: Statistik und Reaktion auf akustische Störtöne,'' Acustica **59**, 67–75.

Jones, K., Tubis, A., Long, G. R., Burns, E. M., and Strickland, E. A. (**1986**). ''Interactions among multiple spontaneous otoacoustic emissions,'' in *Peripheral Auditory Mechanisms*, edited by J. B. Allen, J. L. Hall, A. Hubbard, S. T. Neely, and A. Tubis (Springer-Verlag, Berlin), pp. 266–273.

Long, G. R. (**1993**). ''Interactions between spontaneous emissions and external tones: suppression, frequency shifting and distortion product generation,'' in *Biophysics of Hair Cell Sensory Systems*, edited by H. Duifhuis, J. W. Horst, P. van Dijk, and S. M. van Netten (World Scientific, Singapore), pp. 40–46.

Long, G. R., Tubis, A., and Jones, K. L. (**1991**). ''Modelling synchronization and suppression of spontaneous otoacoustic emissions using Van der Pol oscillators: Effects of aspirin administration,'' J. Acoust. Soc. Am. **89**, 1200–1212.

Murphy, W. J., Talmadge, C. L., Tubis, A., and Long, G. R. (**1995a**). ''Relaxation dynamics of spontaneous otoacoustic emissions perturbed by external tones. I. Response to pulsed single-tone suppressors,'' J. Acoust. Soc. Am. **97**, 3702–3710.

Murphy, W. J., Talmadge, C. L., Tubis, A., and Long, G. R. (**1995b**). ''Relaxation dynamics of spontaneous otoacoustic emissions perturbed by external tones. II. Suppression of interacting emissions,'' J. Acoust. Soc. Am. **97**, 3711–3720.

Ostrom, Jr., C. W. (**1990**). *Time Series Analysis: Regression Techniques* (Sage, Newbury Park, CA).

Press, W. H., Teukolsky, S. A. Vetterling, W. T., and Flannery, B. P. (**1992**). *Numerical Recipes in C* (Cambridge U.P., Cambridge, England), 2nd ed.

Probst, R., Lonsbury-Martin, B. L., and Martin, G. K. (**1991**). ''A review of otoacoustic emissions,'' J. Acoust. Soc. Am. **89**, 2027–2067.

Talmadge, C., Long, G., Murphy, W., and Tubis, A. (**1993**). ''New off-line method for detecting spontaneous otoacoustic emissions in human subjects,'' Hearing Res. **71**, 170–182.

Talmadge, C. L., Tubis, A., Wit, H. P., and Long, G. R. (**1991**). ''Are spontaneous otoacoustic emissions generated by self-sustained cochlear oscillators?,'' J. Acoust. Soc. Am. **89**, 2391–2399.

Van Dijk, P., and Wit, H. P. (**1990a**). ''Amplitude and frequency fluctuations of spontaneous otoacoustic emissions,'' J. Acoust. Soc. Am. **88**, 1779–1793.

Van Dijk, P., and Wit, H. P. (**1990b**). ''Synchronization of spontaneous otoacoustic emissions to a $2f_1-f_2$ distortion product,'' J. Acoust. Soc. Am. **88**, 850–856.

Van Dijk, P., Manley, G. A., Gallo, L., and Pavusa, A. (**1996**). ''Statistical properties of spontaneous otoacoustic emissions in one bird and three lizard species,'' J. Acoust. Soc. Am. **100**, 2220–2227.

Van Dijk, P., Wit, H. P., Tubis, A., Talmadge, C. L., and Long, G. R. (**1994**). ''Correlation between amplitude and frequency fluctuations of spontaneous otoacoustic emissions,'' J. Acoust. Soc. Am. **96**, 163–169.

Wit, H. P. (**1990**). ''Spontaneous otoacoustic emission generators behave like coupled oscillators,'' in *The Mechanics and Biophysics of Hearing*, edited by P. Dallos, C. Geisler, J. Matthews, M. Ruggero, and C. Steele (Springer-Verlag, Berlin), pp. 259–266.

Enhancement of the transient-evoked otoacoustic emission produced by the addition of a pure tone in the guinea pig

Robert H. Withnell[a] and Graeme K. Yates[b]
The Auditory Laboratory, Department of Physiology, University of Western Australia, Nedlands 6907, Western Australia, Australia

(Received 9 December 1997; accepted for publication 13 April 1998)

This study examined the transient-evoked otoacoustic emission obtained in response to a click stimulus presented in combination with a pure tone in the guinea pig. Low-pass filtered click waveforms were digitally generated using a $\sin(t)/t$ function windowed over 3 ms with an elevated cosine envelope. Transient-evoked otoacoustic emissions were obtained using the nonlinear derived response technique. Phase locked pure tones of various frequencies at ~70 dB SPL were electrically mixed with electrical clicks, with the pure tone present only for the three lower level stimuli in the train of four stimuli. Enhancement in the amplitude of the response spectrum at frequencies which corresponded to regions of the basilar membrane apical to the tone was observed with the addition of the tone. This finding is inconsistent with the transient-evoked otoacoustic emission being the result of independent generators. It suggests that intermodulation distortion energy may contribute to the transient-evoked otoacoustic emission, the enhancement in the emission response spectrum at frequencies below the pure tone being a result of a complex interaction on the basilar membrane of intermodulation distortion products. © *1998 Acoustical Society of America.* [S0001-4966(98)06107-4]

PACS numbers: 43.64.Jb, 43.64.Kc [BLM]

INTRODUCTION

Otoacoustic emissions are evidence of an active process or mechanical injection of energy in the cochlea (Patuzzi *et al.*, 1989; Dallos, 1992). The active process is a positive feedback mechanism which enhances the vibration of the basilar membrane with negative damping or mechanical amplification (Patuzzi and Rajan, 1992; Dallos, 1992; Davis, 1983). An understanding of the physiological origin of the various types of otoacoustic emission is essential if otoacoustic emissions are to be meaningfully applied as an investigative tool of auditory function. Of the two most commonly measured types of emission, distortion product otoacoustic emissions are now felt to be reasonably well understood, being due to a nonlinearity inherent in the mechano-electrical transduction process (Jaramillo *et al.*, 1993; Howard and Hudspeth, 1988). The origin of the transient-evoked otoacoustic emission (TEOAE), it has been suggested, involves reflections from impedance discontinuities, either anatomical or as a result of a wave related mechanical interaction (Kemp, 1978, 1986; Guelke and Bunn, 1985; Strube, 1989).

A transient acoustical stimulus has a broad spectral profile which stimulates a wide region of the cochlear partition and produces an otoacoustic emission with a similarly broad power spectrum. TEOAEs have been presumed to involve a linear correspondence between the stimulus spectrum and the response spectrum (Wit *et al.*, 1981; Kemp *et al.*, 1990; Xu *et al.*, 1994), the frequency spectrum of the TEOAE being correlated with the presence or absence of auditory dysfunction at the corresponding cochleotopic location on the basilar membrane (Kemp *et al.*, 1990; Prieve *et al.*, 1993, 1996; Ueda *et al.*, 1997). However, this simple relationship may not be valid, since the assumption of a cochleotopic correlation between the acoustic stimulating energy and the resultant emission for TEOAEs does not satisfactorily explain certain experimental and histopathological findings (Wit and Ritsma, 1983; Avan *et al.*, 1993, 1995, 1997; Hilger *et al.*, 1995).

Sutton (1985) examined suppression of a TEOAE by pure tones, considering the spectral energy of the emission in the 1–3 kHz region with suppressor tones at 1010, 1290, 1760, and 2000 Hz on one human ear. He reported that the emission spectrum was reduced by a pure-tone suppressor, but in a complex manner and not confined to the region of the suppressor frequency. Sutton suggested that ''the emission generator does not behave as a simple localized source at the place for that frequency, but rather that the activity is distributed over a considerable length of the basilar membrane.'' Kemp and Chum (1980) and Tarvartkiladze *et al.* (1994) have also examined suppression of a TEOAE by pure tones. In contrast to Sutton (1985), Kemp and Chum (1980) reported suppression of a TEOAE in the human to be confined to the region of the suppressor tone frequency; however, for the example given in that paper the frequency of the suppressor tone was the ''particular frequency [that] resulted in the greatest and most tuned suppression'' (Kemp and Chum, 1980). Tarvartkiladze *et al.* (1994) reported iso-suppression tuning curves and also found a degree of ''tuning,'' but this tuning was associated with the spectrum of the response.

To explore further the question of origin of the TEOAE, we have extended the work of Sutton to consider the effect

[a]Electronic mail: rwithnel@cygnus.uwa.edu.au
[b]Electronic mail: gyates@cyllene.uwa.edu.au

of a pure-tone suppressor on the TEOAE with a variety of stimulus spectra and pure-tone suppressors, but in this case in the guinea pig. Pure tones of ~70 dB SPL were used in this study: a 70 dB SPL pure tone presumably suppresses a region on the basilar membrane that roughly matches the suppressor excitation pattern on the basilar membrane with maximum suppression occurring in the region of the frequency of the pure tone. If TEOAE generators act independently, then with the addition of a 70 dB SPL tone we expect a reduction in the amplitude of the TEOAE power spectrum over a range of frequencies but with the predominant effect being a maximal reduction of the emission near the frequency of the tone. Enhancement of the emission is not to be expected at any frequency.

I. METHOD

Pigmented guinea pigs approximately 600 grams in weight were anaesthetized with Nembutal (30–35 mg/kg i.p.) and Atropine (0.06 mg i.p.), followed approximately 15 min later by Leptan or Hypnorm (0.15–0.2 ml i.m.). Neuroleptanaesthesia (Evans, 1979) was maintained using supplementary doses of Nembutal and Leptan or Hypnorm. The guinea pigs were tracheostomised and artificially respired on Carbogen (5% CO_2 in O_2), with body (rectal) temperature maintained at 37 °C. The head was positioned using a headholder which could then be rotated for access to the ear canal. Alloferin or Pancuronium (0.15 ml i.m.) was administered to reduce stapedius muscle contractions. During paralysis potentially noxious stimuli produced no change in heart rate. The bulla was opened post-auricularly and a silver wire electrode placed on the round window niche for recording of the compound action potential to monitor the condition of the cochlea. A plastic tube was positioned in the bulla opening to ensure that the bulla was always adequately ventilated, although no attempt was made to seal the bulla. This could have resulted in some variation in bulla resonance from animal to animal (in the range 300–1000 Hz), but OAEs were only examined above 1000 Hz.

This experiment was computer controlled with custom software and a sound-card (Crystal Semiconductor Corporation CS4231A). Electrical mono-polar click stimuli were acoustically delivered open-field by a Foster dynamic earphone type T016H01A0000. Ear canal sound pressures were measured with a Sennheiser MKE 2–5 electrostatic microphone coupled to a metal probe tube 9 mm in length and 1.3-mm internal diameter. A 1500-Ω acoustic filter was used as an acoustic damper in the probe tube. The probe tube was placed approximately 2 mm into the external auditory meatus and the earphone positioned near the pinna with the position of the earphone adjusted to obtain a relatively flat ear canal sound pressure spectrum. This arrangement provides a viable alternative to conventional acoustic probe systems for the measurement of otoacoustic emissions, the position of the earphone close to the pinna but not coupled to the meatus providing a much wider stimulus spectrum than that typically obtained with conventional acoustic probe designs (Withnell *et al.*, 1998).

The output from the probe tube microphone was amplified 20 dB, bandpass filtered (0.3–100 kHz) using two-pole Butterworth filters, and then digitized in 26-ms epochs at a rate of 44.1 kHz. Stimulus repetition rate was approximately 38.5 Hz. A cosine-ended window was applied to the first and last 2 ms of the averaged response *post hoc* to avoid frequency splatter associated with the Fourier transform calculation; no windowing of the TEOAE was performed though as stimulus onset in each epoch occurred at 2 ms. Corrections for the probe tube response have been made.

Low-pass filtered click waveforms were digitally generated using a $\sin(t)/t$ function windowed over 3 ms with an elevated-cosine envelope. TEOAEs were obtained using the nonlinear derived response technique (Kemp *et al.,* 1990). The stimulus train consisted of three click stimuli followed by a single similar click stimulus at three times the intensity. The three ear canal sound pressure measurements to the lower level click were added together, and the fourth ear canal measurement to the higher level click subtracted. The result was then divided by three to form the derived response. Each stimulus train was repeated 250 or 1000 times and the responses averaged. Pure tones of various frequencies at ~70 dB SPL and phase locked to the click repetition were electrically mixed with electrical clicks, with the pure tone present only for the three lower level stimuli in the train of four stimuli but not for the higher level reference stimulus. The phase of the tone was inverted on each alternate stimulus train so as to cancel it in the averaging process. Thus we were able to examine the effect of the pure tones on the response to the lower level click stimulus only. The choice of pure-tone frequency was restricted by the requirement of the tone having a phase relationship with respect to the signal averaging process such that the tone was cancelled from the averaged response. Fourier transforms for TEOAEs were calculated with 1024 data points. Data analysis was performed using Microsoft Excel.

The care and use of animals reported on in this study were approved by the Animal Experimentation Ethics Committee of the University of Western Australia and all procedures conformed with the Code of Practice of the National Health and Medical Research Council of Australia.

II. RESULTS

Figure 1 shows examples of the effect of a pure tone presented in combination with a click stimulus when the frequency of the pure tone was within the passband of the stimulus. TEOAEs are shown in response to an 80 dB pSPL (peak sound pressure level) click stimulus with the addition of a 66–72 dB SPL pure tone with a frequency of 3, 4, 5, or 6 kHz, the click stimulus having a relatively flat spectrum from 0 to 7 kHz. The 3-kHz tone enhanced the emission from 1 to 2 kHz and caused some reduction in the emission spectrum centered around 2.5 kHz. A 4-kHz tone produced enhancement of the TEOAE from 1.5 to 3 kHz, a 5-kHz tone from 2.5 to 5 kHz, and a 6-kHz tone from 4 to 6 kHz. Some reduction in the emission is seen around 2 and 5 kHz for the 5-kHz tone and from 2 to 4 kHz and from 6 to 7 kHz for the 6-kHz tone. In complete contrast to our expectation, but consistent with the findings of Sutton (1985) in a human ear, there was effectively no suppression centered on the suppressor frequency. Furthermore, there was evidence of enhance-

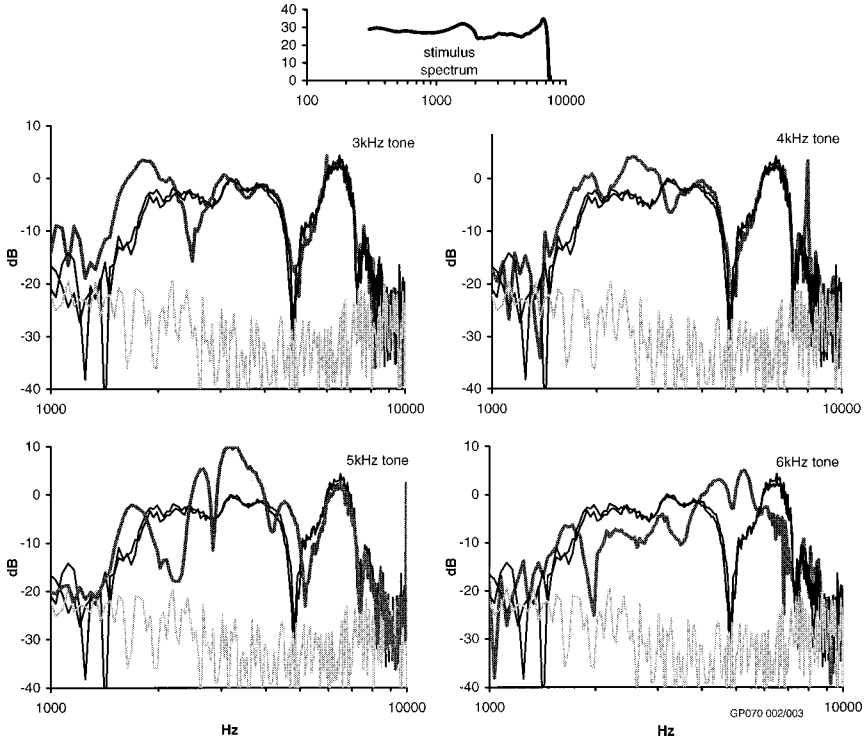

FIG. 1. TEOAEs in response to a 0–7 kHz bandwidth transient acoustic stimulus demonstrating enhancement and suppression of the emission spectrum when combined with an ~70 dB SPL 3-, 4-, 5-, or 6-kHz pure tone. Response repeatability is illustrated by two separate measures of the response without a pure tone added (dark curves). The lighter shading curve represents the TEOAE with the addition of a pure tone. A low level second harmonic of the pure tone that has not been cancelled is evident. Also shown is the noise floor. Decibels on ordinate scale is calculated *re*: 0.000 01 Pa/$\sqrt{\text{Hz}}$.

ment in all cases at frequencies corresponding to regions on the basilar membrane apical to the tone. Only for the case of the 6-kHz tone is there evidence of suppression in the region of the tone frequency.

We extended Sutton's work by considering the effect of a tone above the stimulus frequency range. Figure 2 shows power density spectra for TEOAEs obtained from a 75 dB pSPL click stimulus with a relatively flat signal spectrum from 0 to 5 kHz. The addition of a 66–70 dB SPL tone with a frequency of 10, 12, or 15 kHz clearly enhances the amplitude of the response spectrum below 5 kHz, the degree of enhancement being related to the frequency of the tone. The higher the frequency of the tone, the smaller the effect on the amplitude of the response spectrum. For the 10-kHz tone there is enhancement of the response spectrum from 1 to 5 kHz; the 12-kHz tone produces enhancement from 1.5 to 5 kHz; the 15-kHz tone enhancement is predominantly from 3.5 to 5 kHz. In all three cases the frequency of the tone is above the uppermost frequency of the stimulus spectrum.

Figures 1 and 2 provide results obtained from different animals. In Figs. 3 and 4, the effect on the TEOAE with the addition of a 68–69 dB SPL pure tone with a frequency both within and above the stimulus passband is shown for the one animal. Figure 3 is for an 80 dB pSPL click stimulus with a

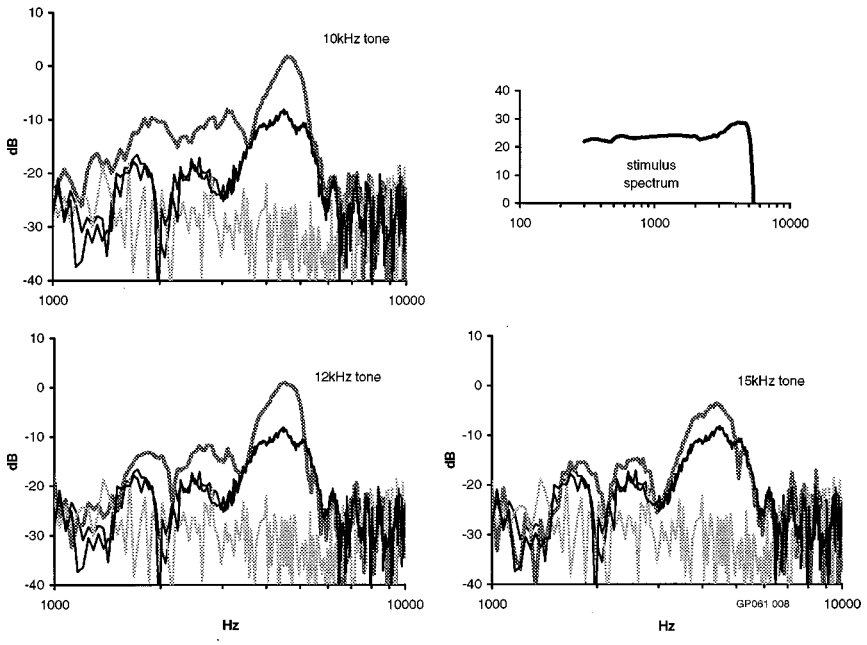

FIG. 2. TEOAEs in response to a 0–5 kHz bandwidth transient acoustic stimulus showing predominantly enhancement of the emission when combined with an ~70 dB SPL 10-, 12-, or 15-kHz pure tone. The lighter shading curve represents the TEOAE with the addition of a pure tone, the dark curves without a pure tone. Also shown is the noise floor.

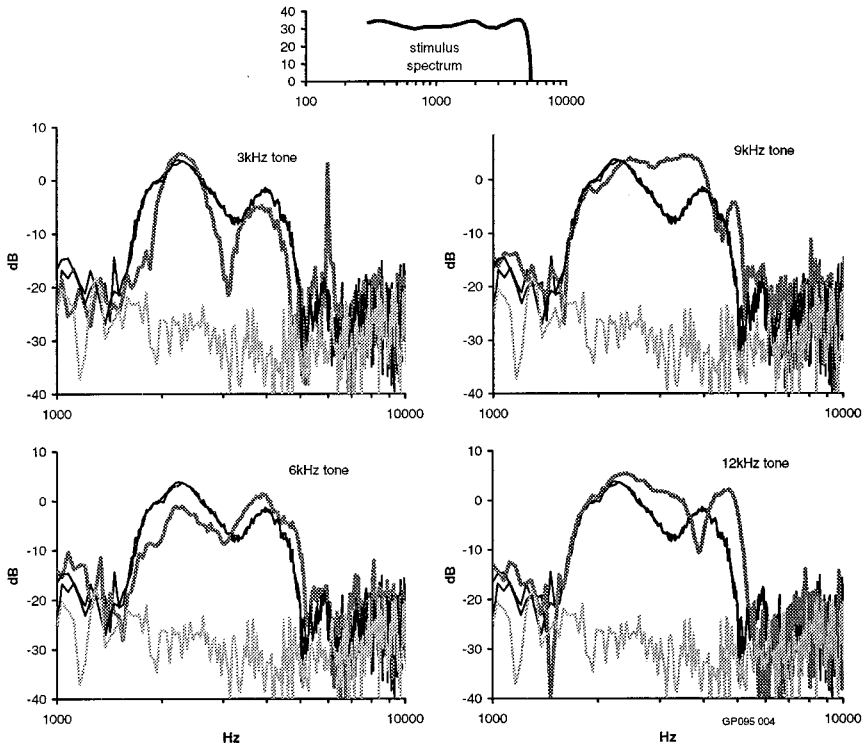

FIG. 3. TEOAEs in response to a 0–5 kHz bandwidth stimulus demonstrating the effect on the emission of adding an ~70 dB SPL 3-, 6-, 9-, or 12-kHz pure tone. The lighter shading curve represents the TEOAE with the addition of a pure tone, the dark curves without a pure tone. A low level second harmonic of the pure tone that has not been cancelled is evident. Also shown is the noise floor.

5-kHz bandwidth; Fig. 4 for an 89 dB pSPL stimulus with a 10-kHz bandwidth. In Fig. 3, enhancement of the TEOAE is evident from 3 to 5-kHz with the addition of the 6-kHz tone, from 2.5 to 5 kHz with a 9-kHz tone, and from 2.5 to 5.5 kHz with a 12-kHz tone. The TEOAE is reduced essentially from 1.5 to 5 kHz with the addition of a 3-kHz tone, from 1.5 to 3 kHz for a 6-kHz tone, from 2 to 2.5 kHz for a 9-kHz tone, and centered around 4 kHz with a 12-kHz tone.

Figure 4 shows changes to the TEOAE in response to a 10-kHz click stimulus with the addition of a 6-, 9-, 12-, or 15-kHz tone. Enhancement of the TEOAE is seen essentially from 3 to 6 kHz with the addition of a 6-kHz tone, and around 7 kHz for a 15-kHz tone. Note that in all cases there is TEOAE evident above the stimulus passband. The TEOAE is reduced from 2 to 3 kHz for a 6-kHz tone, from 6 to 8 kHz for a 12-kHz tone, and from 10 to 13 kHz and possibly around 3 and 5 kHz with a 15-kHz tone. The changes to the TEOAE in all cases are not as pronounced as

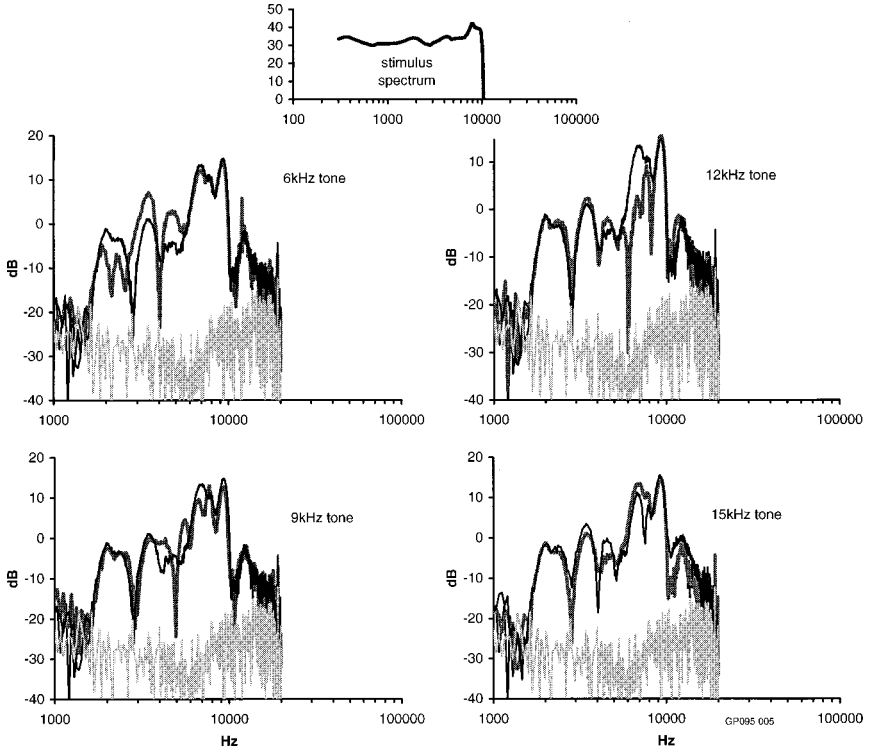

FIG. 4. TEOAEs in response to a 0–10 kHz stimulus demonstrating the effect on the emission of adding an ~70 dB SPL 6-, 9-, 12-, or 15-kHz pure tone. The lighter shading curve represents the TEOAE with the addition of a pure tone, the dark curves without a pure tone. Also shown is the noise floor.

for Figs. 1–3, with indeed very little change to the TEOAE with the addition of a 9-kHz tone.

Thus as seen in Figs. 1 and 2, changes to the TEOAE in Figs. 3 and 4 are seen at frequencies remote from the pure-tone suppressor, with enhancement of the TEOAE present in a number of cases for some part of the emission spectrum.

In these experiments, the contralateral ear was not occluded; measurement of the sound pressure level in the contralateral ear of animal GP061 revealed the level to be 20–60 dB less than the ipsilateral ear in the range 0.3–20 kHz. Destruction of the ossicular chain in the contralateral ear of animal GP061 did not alter the emission measured. The physiological nature of the results presented in this study have been verified with post mortem measurements: the magnitude of the response measured post mortem was significantly reduced, the responses post mortem with and without the suppressor tone being similar.

III. DISCUSSION

If the TEOAE truly represents a one-to-one frequency response to component frequencies of the stimulus, then simultaneous presentation of a pure tone with a click should suppress those TEOAE components which are close to the pure-tone frequency. We therefore expected the TEOAE spectra to be attenuated in amplitude close to the tone frequency. Instead, we found enhancement of the TEOAE spectra at frequencies below the pure tone, with suppression predominantly occurring in the case of tones within the passband of the stimulus, and usually not at the frequency of the tone. Thus the observed pattern of interference does not agree with the simple concept of local suppression of the TEOAE and is therefore at odds with existing theories of TEOAE production (Kemp and Chum, 1980; Kemp, 1986; Probst *et al.*, 1986; Prieve *et al.*, 1996).

There is other evidence that the existing model of TEOAE production may be incomplete. While Prieve *et al.* (1996) found that basal cochlear pathology in humans did not affect TEOAEs evoked from apical regions of the cochlea, Avan *et al.* (1993, 1995, 1997) have reported changes in low-frequency components of the TEOAE when basal-region damage was produced in guinea pigs or had been acquired in humans. Our results are more consistent with those of Avan *et al.* in that we observed changes in low-frequency components of the emission when the basal region of the cochlea was stimulated by high-frequency tones.

We considered two possible explanations for these results. First, the pure tone could have ''phase entrained'' certain components of the response, leading to enhancement of the spectrum due to phase locking (Neumann *et al.*, 1997). This is unlikely, however, because the tone was cancelled by phase inversion on alternate presentations of the click stimulus and so any component of the TEOAE which phase locked to the tone would also have been removed. Second, the tone may have modified the efficacy of transmission of the response from the site of generation back to the middle ear. There is some evidence of an enhancement effect in electrically evoked emissions, but only for acoustic frequencies below or close to the characteristic frequency of the stimulation site (Kirk and Yates, 1996; Mountain and Hubbard, 1989). We are left with no reasonable explanation in terms of existing models of emissions.

We can think of only one explanation for the unexpected effects of an interfering tone on the TEOAE. If a tone which stimulates only the basal region of the cochlea produces enhancement of the low-frequency energy in the emission, then it follows that at least a part of that low-frequency energy must have had its origin in the basal region. But the amplitude of vibration of the basilar membrane due to low-frequency components of the click stimulus will be small in the basal turn, so it seems likely that the modified emission is not a result of stimulation by those low-frequency components. On the other hand, it is well established that two high-frequency tones stimulating the basal region of the cochlea can produce significant amounts of intermodulation energy at much lower frequencies, so it is plausible that a broadband stimulus might also produce, in such a nonlinear system, quantities of intermodulation distortion. Thus we postulate that the TEOAE is actually comprised of significant quantities of intermodulation energy generated all along the cochlea, and that the introduction of an interferring tone suppresses local production of intermodulation energy over a range of frequencies.

We propose that each component frequency of the click stimulus interacts with every other component frequency to produce a range of intermodulation products. Thus each frequency in the emission may be the weighted vector sum of intermodulation products generated all along the basilar membrane; however, the predominant contribution to each frequency component would arise from more basal regions of the cochlea as emissions arising at sites below their own characteristic frequency do not propagate well back to the middle ear (Kirk and Yates, 1994) due to the low-pass filtering characteristics of the basilar membrane.[1] A pure tone will reduce the basilar membrane vibration at and basal of its characteristic place, thereby reducing the amplitude of intermodulation energy produced at that place. Significant amounts of intermodulation energy at similar frequencies will still be present due to activity at other, more apical, unsuppressed sites on the basilar membrane. The net result would depend on the precise way in which the remaining intermodulation products sum, but any outcome presumably is possible from suppression to enhancement. Furthermore, our proposal also provides a satisfactory explanation for the results of Avan *et al.* in that a reduction in mechanical vibration of the basilar membrane in basal regions of the cochlea will reduce the amount of intermodulation energy generated there and so influence the spectrum of the TEOAE, even at low emission frequencies.

The TEOAE being a composite of intermodulation distortion products with each frequency component having its origin in more basal regions of the cochlea provides a satisfactory explanation for the results seen in Figs. 1–4. Only in Fig. 1 with the addition of a 5- or 6-kHz tone and in Fig. 3 with the addition of a 3-kHz tone is there reduction in the amplitude of the TEOAE in the region of the tone frequency. In Fig. 1, the 6-kHz tone frequency is near the upper limit of the stimulus spectrum and so the energy present in the

TEOAE in this region might be dominated by more local contributions, since there is no stimulus energy at higher frequencies to contribute to the emission energy in this region. For the 5-kHz tone in Fig. 1, the dip in the emission spectrum near 5 kHz would appear to be a shifting of the dip present in the TEOAE without the addition of a suppressor tone rather than a localized suppressive effect. In Fig. 3 there is widespread reduction of the TEOAE subsequent to the addition of a 3-kHz tone. In Figs. 2 and 3, enhancement of the TEOAE is present over much of the response spectrum for tone frequencies significantly above the frequency range of the click stimulus. At face value this may appear to suggest a different mechanism for the enhancement of the TEOAE in comparison to that observed in Fig. 1. However, neural suppression tuning curves have been found to be much broader than threshold tuning curves (Schmiedt, 1982; Prijs, 1989; Delgutte, 1990) and so tones with frequencies considerably above the frequency range of the click stimulus presumably suppress some part of the basilar membrane response to the click. Figure 4 shows evidence for TEOAE present outside of the stimulus passband (above 10 kHz), this being consistent with intermodulation distortion energy contributing to the TEOAE.

It remains that there exists evidence to suggest that TEOAE energy at specific frequencies is not produced over a large extent of the cochlea (Prieve *et al.*, 1996), and so resolution of this question must await further studies.

ACKNOWLEDGMENTS

We wish to thank Foster Electric Company of Japan for generously supplying the earphones used in this study. Our thanks also to Greg Nancarrow for technical advice and to Dr. Des Kirk for valuable comments. This work was supported by the National Health and Medical Research Council of Australia and the Department of Physiology, University of Western Australia. R.H.W. is the recipient of a postgraduate scholarship from the Department of Physiology.

[1]Electrically evoked otoacoustic emissions show a low-pass filtering effect above the electrode location characteristic frequency (Mountain and Hubbard, 1989; Kirk and Yates, 1994, 1996), demonstrating that emissions that arise at a place with a characteristic frequency below the emission frequency do not propagate well back to the stapes.

Avan, P., Elbez, M., and Bonfils, P. (**1997**). ''Click-evoked otoacoustic emissions and the influence of high-frequency hearing losses in humans,'' J. Acoust. Soc. Am. **101**, 2771–2777.

Avan, P., Bonfils, P., Loth, D., and Wit, H. (**1993**). ''Temporal patterns of transient-evoked otoacoustic emissions in normal and impaired cochleae,'' Hearing Res. **70**, 109–120.

Avan, P., Bonfils, P., Loth, D., Elbez, M., and Erminy, M. (**1995**). ''Transient-evoked otoacoustic emissions and high-frequency acoustic trauma in the guinea pig,'' J. Acoust. Soc. Am. **97**, 1–9.

Dallos, P. (**1992**). ''The active cochlea,'' J. Neurosci. **12**, 4575–4585.

Davis, H. (**1983**). ''An active process in cochlear mechanics,'' Hearing Res. **9**, 79–90.

Delgutte, B. (**1990**). ''Two-tone rate suppression in auditory-nerve fibers: Dependence on suppressor frequency and level,'' Hearing Res. **49**, 225–246.

Evans, E. F. (**1979**). ''Neuroleptanaesthesia: an ideal anaesthetic procedure for long-term physiological studies of the guinea pig cochlea,'' Acta Oto-Laryngol. **105**, 185–186.

Guelke, R. W., and Bunn, A. E. (**1985**). ''A mechanism for stimulated acoustic emissions in the cochlea,'' Hearing Res. **19**, 185–189.

Hilger, A. W., Furness, D. N., and Wilson, J. P. (**1995**). ''The possible relationship between transient evoked otoacoustic emissions and organ of Corti irregularities in the guinea pig,'' Hearing Res. **84**, 1–11.

Howard, J., and Hudspeth, A. J. (**1988**). ''Compliance of the hair bundle with gating of the mechanoelectrical transduction channels in the bullfrog's saccular hair cell,'' Neuron **1**, 189–199.

Jaramillo, F., Markin, V. S., and Hudspeth, A. J. (**1993**). ''Auditory illusions and the single hair cell,'' Nature (London) **364**, 527–529.

Kemp, D. T. (**1978**). ''Stimulated acoustic emissions from within the human auditory system,'' J. Acoust. Soc. Am. **64**, 1386–1391.

Kemp, D. T. (**1986**). ''Otoacoustic emissions, travelling waves and cochlear mechanisms,'' Hearing Res. **22**, 95–104.

Kemp, D. T., and Chum, R. (**1980**). ''Properties of the generator of stimulated acoustic emissions,'' Hearing Res. **2**, 213–232.

Kemp, D., Ryan, S., and Bray, P. (**1990**). ''A guide to the effective use of otoacoustic emissions,'' Ear Hear. **11**, 93–105.

Kirk, D. L., and Yates, G. K. (**1994**). ''Evidence for electrically evoked travelling waves in the guinea pig cochlea,'' Hearing Res. **74**, 38–50.

Kirk, D. L., and Yates, G. K. (**1996**). ''Frequency tuning and acoustic enhancement of electrically evoked otoacoustic emissions in the guinea pig cochlea,'' J. Acoust. Soc. Am. **100**, 3714–3725.

Mountain, D. C., and Hubbard, A. E. (**1989**). ''Rapid force production in the cochlea,'' Hearing Res. **42**, 195–202.

Neumann, J., Uppenkamp, S., and Kollmeier, B. (**1997**). ''Interaction of otoacoustic emissions with additional tones: Suppression or synchronization?,'' Hearing Res. **103**, 19–27.

Patuzzi, R., and Rajan, R. (**1992**). ''Additivity of threshold elevations produced by disruption of outer hair cell function,'' Hearing Res. **60**, 165–177.

Patuzzi, R. B., Yates, G. K., and Johnstone, B. M. (**1989**). ''Outer hair cell receptor current and sensorineural hearing loss,'' Hearing Res. **42**, 47–72.

Prieve, B., Gorga, M., and Neely, S. (**1996**). ''Click and tone burst evoked otoacoustic emissions in normal hearing and hearing impaired ears,'' J. Acoust. Soc. Am. **99**, 3077–3086.

Prieve, B., Gorga, M., Schmidt, A., Neely, S., Peters, J., Schultes, L., and Jesteadt, W. (**1993**). ''Analysis of transient evoked otoacoustic emissions in normal hearing and hearing impaired ears,'' J. Acoust. Soc. Am. **93**, 3308–3319.

Prijs, V. P. (**1989**). ''Lower boundaries of two-tone suppression regions in the guinea pig,'' Hearing Res. **42**, 73–82.

Probst, R., Coats, A. C., Martin, G. K., and Lonsbury-Martin, B. L. (**1986**). ''Spontaneous, click- and toneburst-evoked otoacoustic emissions from normal ears,'' Hearing Res. **21**, 261–275.

Schmiedt, R. A. (**1982**). ''Boundaries of two-tone rate suppression of cochlear-nerve activity,'' Hearing Res. **7**, 335–351.

Strube, H. W. (**1989**). ''Evoked otoacoustic emissions as cochlear Bragg reflections,'' Hearing Res. **38**, 35–46.

Sutton, G. J. (**1985**). ''Suppression effects in the spectrum of evoked otoacoustic emissions,'' Acustica **58**, 57–63.

Tarvartkiladze, G. A., Frolenkov, G. I., Kruglov, A. V., and Artamasov, S. V. (**1994**). ''Ipsilateral suppression effects on transient evoked otoacoustic emissions,'' Br. J. Audiology **28**, 193–204.

Ueda, H., Tsuge, H., and Hattori, T. (**1997**). ''Changes in evoked otoacoustic emissions in the guinea pig after pure-tone acoustic overstimulation,'' J. Acoust. Soc. Am. **101**, 3577–3582.

Wit, H. P., Langevoort, J. C., and Ritsma, R. J. (**1981**). ''Frequency spectra of cochlear acoustic emissions (''Kemp-echoes''),'' J. Acoust. Soc. Am. **70**, 437–445.

Wit, H. P., and Ritsma, R. J. (**1983**). ''Two aspects of cochlear acoustic emissions: Response latency and minimum stimulus energy,'' in *Mechanics of Hearing*, edited by E. de Boer and M. A. Viergever (Martinus Nijhoff Publishers, Delft University Press, The Hague), pp. 101–107.

Xu, L., Probst, R., Harris, F. P., and Roede, J. (**1994**). ''Peripheral analysis of frequency in human ears revealed by tone burst evoked otoacoustic emissions,'' Hearing Res. **74**, 173–180.

Withnell, R. H., Kirk, D. L., and Yates, G. K. (**1998**). ''Otoacoustic emissions measured with a physically open recording system,'' J. Acoust. Soc. Am. **104**, 350–355.

Otoacoustic emissions measured with a physically open recording system

Robert H. Withnell, Desmond L. Kirk, and Graeme K. Yates[a)]
The Auditory Laboratory, Department of Physiology, The University of Western Australia, Nedlands 6907, Western Australia, Australia

(Received 1 January 1998; accepted for publication 27 March 1998)

Otoacoustic emissions have historically been measured with an acoustical probe assembly hermetically sealed in the ear canal, imposing in most cases a limited stimulus bandwidth. A physically open recording system should afford the possibility of a greater stimulus bandwidth but the change in acoustical load may affect the magnitude of otoacoustic emissions obtained. Here it is reported that the authors have measured in the guinea pig transient-evoked otoacoustic emissions extending in frequency to 20 kHz and cubic distortion tone otoacoustic emissions for $f_2 = 4737$ and 8096 Hz with a physically open sound system. To address the effect of acoustical load provided by a physically open versus hermetically sealed system, the authors compared the amplitude of electrically evoked otoacoustic emissions recorded from a guinea pig in each case. The change in acoustical load in the ear canal introduced by the change in recording setup did not appear to make a substantial difference to the magnitude of otoacoustic emissions measured. A physically open recording system provides a good alternative to traditional acoustical probe assemblies sealed in the ear canal for the laboratory measurement of acoustically evoked otoacoustic emissions, with the advantage of permitting a greater stimulus bandwidth. [S0001-4966(98)03207-X]

PACS numbers: 43.64.Jb, 43.64.Kc, 43.64.Yp [BLM]

INTRODUCTION

Power spectra for transient-evoked otoacoustic emissions (TEOAEs) reported in the literature are commonly restricted to frequencies between approximately 1 and 6 kHz. A lower frequency limit for the TEOAE would not be surprising, given the probable stiffening of the middle ear and the reduced activity of the active process at low frequencies (Kirk and Yates, 1996), but an upper frequency limit, if present, would be unexpected. The middle ear appears quite capable of transmitting pressure from scala vestibuli to the external ear canal for frequencies up to at least 8 kHz (Magnan *et al.*, 1997), and the cochlear amplifier is strongly active up to tens of kilohertz in mammals, so otoacoustic emissions to wideband stimuli might be expected well above 6 kHz. Indeed, distortion product otoacoustic emissions have been recorded at frequencies well above 10 kHz (Fahey and Allen, 1985; Mills and Rubel, 1996). The apparent absence of the TEOAE above 6 kHz may be due to unknown factors internal to the cochlea, but it is more probable that technical limitations in the frequency response of the stimulus have contributed to their absence from recordings to date.

Kemp (1978) first measured otoacoustic emissions (OAEs) with an acoustical probe assembly that housed both microphone and speaker, the assembly being acoustically sealed to the ear canal entrance to minimize the enclosed volume of air. This original configuration was reported to have a stimulus spectrum that was flat to within ± 6 dB up to 3.5 kHz (Kemp, 1978). Subsequent sound delivery systems have also employed acoustical probe assemblies that house both the microphone and speaker/s (e.g., Kim *et al.*, 1980; Anderson, 1980; Wilson, 1980; Kemp *et al.*, 1990), but one shortcoming of such assemblies is that in most cases they have a limited stimulus bandwidth. Consequently, power spectra for TEOAEs reported in the literature seldom extend past 6 kHz, although this is partly a product of windowing of the response, low-pass filtering of the stimulus, and/or limited recording sample rate (Bray and Kemp, 1987; Prieve *et al.*, 1996).

Typically, sound-generating sources for evoking OAEs have taken the form of dynamic earphone transducers in sealed enclosures, typified by the hearing aid receiver. These have inherently limited frequency responses, the reasons for which are unclear but probably are connected with the following two effects: (i) Typical dynamic transducers such as those used in audio equipment have resonance frequencies in the range 30–250 Hz, resulting in constant displacement of the radiating diaphragm below the resonance frequency and constant acceleration (or -12 dB/oct displacement response) above. In free-field use this is countered by the radiation efficiency of the diaphragm which rises at a rate of 12 dB/oct. The result is a rising, 12 dB/oct response below resonance and a flat response above. But when such a transducer is coupled into a small cavity, the expected pressure response will be the reverse: flat up to the resonance frequency and an attenuation at the rate of -12 dB/oct above. (ii) Even if a flat frequency response can be generated in the enclosed cavity in front of the speaker, that sound must be communicated to the ear canal by a small tube or hole and the mass of air enclosed in the tube or hole will typically form a Helmholtz resonator with the series connections of the cavity volumes of the transducer and the ear canal. Such a resonantor will

[a)]Electronic mail: gyates@cyllene.uwa.edu.au

function as a low-pass filter between the transducer and the ear canal, further attenuating the sound in the canal at high frequencies.

Additional to the effect of an enclosed volume on the stimulus source, the acoustical load presented by the probe system may also influence the emissions themselves. Kemp (1978, pp. 1386 and 1387) stated that acoustically closing the ear canal had the effect of ''greatly intensifying... sound pressure fluctuations created by movement of the eardrum,'' or in other words, the amplitude of the otoacoustic emission was directly dependent upon the acoustical probe assembly being acoustically sealed to the ear canal. Consistent with this, later authors have observed that acoustical probe impedance affects the ear canal OAE sound pressures generated by the cochlea (Matthews, 1983; Zwicker, 1990; Jurzitza and Hemmert, 1992; Thornton *et al.*, 1994; Nakajima *et al.*, 1994; Puria and Rosowski, 1997).

Thornton *et al.* (1994) considered two types of OAE apparatus and suggested that differences in measured TEOAEs were the product of differences in acoustical loading of the ear canal by the acoustical probes. The authors assumed, however, that the nonlinear derived TEOAE is not influenced by the frequency response of the recording system, arguing that the frequency dependence of the system is removed by the subtraction in the response recovery process. This is not the case, however, and it is likely that the differences in the TEOAEs they recorded using the two systems were a consequence of the different frequency responses of the loudspeakers and/or microphones.

Zwicker (1990) reported that the spectral structure of OAEs could be altered by different acoustical probe impedances, but this was based only on the 900–1100-Hz region in one human subject. Matthews (1983) and Jurzitza and Hemmert (1992) considered that acoustical probe impedance could significantly affect OAEs recorded, but in both cases this was based on a theoretical treatment. Puria and Rosowski (1997) examined forward and reverse transmission in a human temporal bone preparation over the frequency range 0.1–4.2 kHz. They reported a significant effect on reverse transmission by comparing two different acoustical probe assemblies sealed in the ear canal with differing acoustical impedances, while the drive source in the cochlea was kept constant. It is unclear, however, how these measurements relate to the living human.

Clearly our current understanding of the effects of acoustical load on the ear canal OAE sound pressures generated by the cochlea is incomplete. In attempting to address this problem using acoustically delivered stimuli, one inevitably finds that changing the acoustical load in the ear canal alters the intensity of the stimulus at the eardrum. However, the problem can be successfully addressed by using electrical stimuli which generate OAEs but are themselves independent of external acoustical conditions, with two recording conditions that produce different acoustical loads in the ear canal (e.g., Nakajima *et al.*, 1994). Stimulation of the cochlear partition with an electrical current appears to generate a motile response of the outer hair cells which is then detected in the ear canal as an OAE (Hubbard and Mountain, 1983; Mountain and Hubbard, 1989; Kirk and Yates, 1996). If the stimulus conditions are maintained constant, then, without precluding the possibility that external acoustical impedance might influence the emission mechanism, any difference measured in the amplitude of emissions under different recording conditions can be attributed solely to the difference in acoustical load in the ear canal. Nakajima *et al.* (1994) have measured the magnitude of electrically evoked otoacoustic emissions using an acoustical probe assembly that was hermetically sealed within the ear canal, and altered the acoustical load of the probe assembly by increasing the volume from 0.03 to 0.75 cm^3 with a 7-cm-long plastic tube. For the larger volume probe assembly, they found marked dips in emission level, at $\sim$1.5, 3, and 4.5 kHz. The arithmetic relationship between these frequencies suggests a standing wave effect in the 7-cm-long tube, indicating that the authors may not have corrected for this effect. If this is so, then it would seem that any difference between these acoustic loads may have been confined to $<$500 Hz, that is the smaller probe volume and consequently higher acoustic impedance produced larger sound pressures for frequencies $<$500 Hz.

An alternative to an hermetically sealed acoustical probe assembly is a physically open recording system. Such a system has been considered previously, recognizing the potential for greater stimulus bandwidth (Kemp *et al.*, 1986). However, a physically open system might be expected to reduce greatly the magnitude of the otoacoustic emissions measured (Kemp, 1978; Kemp *et al.*, 1986) if the cochlea is a high-impedance drive source and scala vestibuli pressure-induced movement of the eardrum does not alter with changes in acoustical load, i.e., the measured pressure may be load dependent.

In this paper, we consider a physically open recording system and the effect of acoustical load by addressing the following two questions:

(1) *Is it possible to measure OAEs without having the acoustical probe assembly hermetically sealed in the ear canal?*
(2) *What effect does changing the acoustical load have on the amplitude of OAEs measured in the ear canal?*

I. METHODS

Pigmented guinea pigs (500–800 g) were anesthetized with Nembutal (30–35 mg/kg i.p.) and Atropine (0.06 mg i.p.), followed approximately 15 min later by Leptan (0.15–0.2 ml i.m.). Neuroleptanaesthesia (Evans, 1979) was maintained using supplementary doses of Nembutal and Leptan. The guinea pigs were tracheostomized and artificially respired on Carbogen (5% CO_2 in O_2), with body (rectal) temperature maintained at 37 to 38 °C. The head was positioned using a head-holder which could be rotated for access to the ear canal. Alloferin (0.15 ml i.m.) was administered to reduce stapedius muscle contractions. During paralysis potentially noxious stimuli produced no change in heart rate.

A. Surgical procedure for the measurement of acoustically evoked otoacoustic emissions (AEOAEs)

The bulla was opened postauricularly and a silver wire electrode placed on the round window niche for recording of

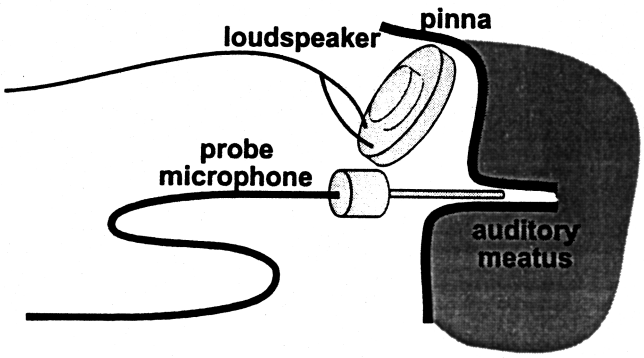

FIG. 1. Schematic of measurement setup for a physically open recording system.

the compound action potential to monitor the condition of the cochlea. A plastic tube was positioned in the bulla opening to ensure that the bulla was always adequately ventilated, although no attempt was made to seal the bulla. This could have resulted in some variation in bulla resonance from animal to animal (in the range 300–1000 Hz), but OAEs were only examined above 1000 Hz.

B. Surgical procedure for the measurement of electrically evoked otoacoustic emissions (EEOAEs)

Surgical procedure for insertion of a micropipette electrode in scala media and the method of electrical stimulation has been described previously (Kirk and Yates, 1996). The cochlea was exposed by a ventro-medial approach and an opening shaved over scala media in the first turn. A micropipette electrode filled with 160-mM KCl and with Ag/AgCl wire leads was placed in the basal turn of scala media.

C. Recording of otoacoustic emissions

We measured TEOAEs, cubic distortion tones (CDTs), and EEOAEs with stimulus delivery and response acquisition computer controlled with custom software and a sound card (Crystal Semiconductor Corporation CS4231A). Ear canal sound pressures were measured with a Sennheiser MKE 2-5 electrostatic microphone coupled to a metal probe tube (1.8-mm outer diameter) placed approximately 2 mm into the external auditory meatus. The probe tube microphone was estimated to obstruct the area of the ear canal by 40%. The output from the probe tube microphone was amplified by either 20 or 40 dB, then digitized at a rate of 44.1 or 48 kHz. Corrections for probe tube response and microphone response have been made.

D. Measurement of AEOAEs

Acoustical stimuli were delivered open-field by a Foster dynamic earphone (type T016H01A0000), positioned so as to obtain a relatively flat ear canal sound-pressure spectrum, as shown in the schematic in Fig. 1. Ear canal sound pressures were recorded in response to transient and two-tone acoustical stimuli. Responses were bandpass filtered using two-pole Butterworth filters prior to digitization of the signal. TEOAEs were extracted using the nonlinear derived response technique (Kemp *et al.*, 1990). The two-tone stimuli for the generation of CDTs had a frequency ratio of 1.2 with $f_2 = 4.737$ or 8.096 kHz.

E. Measurement of EEOAEs

EEOAEs were recorded under two conditions: (i) with the probe tube sealed in the ear canal, or (ii) with the probe tube inserted into the ear canal but not sealed. In the first condition, the seal was effected by placing a sleeve [either a metal tube (3 mm o.d.×9.5 mm) or silicone tube (3.5 mm o.d.×8.5 mm)] over the probe tube and then placing the probe tube in the meatus with the end of the sleeve abutting the entrance to the meatus. Visual inspection confirmed that the end of the sleeve, in abutting the entrance to the meatus, created an acoustical seal. In the case of GP079, petroleum jelly was additionally placed on the end of the sleeve to ensure a seal.

The EEOAE frequency response was measured from 100–20 000 Hz in 250-Hz steps using custom software. Voltage to the micropipette electrode was kept constant over the frequency range of measurement, resulting in a 10 ± 2 μA current. At each frequency, data was acquired over 0.2–0.5 s. Measurement of the EEOAE frequency response was repeated to obtain a series of measurements at each frequency.

The care and use of animals reported on in this study were approved by the Animal Experimentation Ethics Committee of The University of Western Australia and all procedures conformed with the Code of Practice of the National Health and Medical Research Council of Australia.

II. RESULTS

A. AEOAEs

The open system which we use here to deliver the acoustical stimulus results in a much wider frequency response than we have been able to achieve by any other method. Figure 2 shows three examples from different animals of the spectrum typically recorded in the guinea pig ear canal (curve a), together with the TEOAE spectrum obtained with those stimuli (b). The noise level (c) is also shown in each case. The stimulus spectra are flat to within approximately ± 5 dB from 1 to 20 kHz in the top two cases, 1 to 18 kHz in the third. The TEOAEs extend over approximately the same frequency range as the stimuli, far wider than has previously been recorded (e.g., Hilger *et al.*, 1995).

Acoustical spectra demonstrating the presence of the $2f_1 - f_2$ intermodulation distortion product is shown in Fig. 3 for $f_2 = 4737$ and 8096 Hz and $f_2/f_1 = 1.2$. The CDT ($2f_1 - f_2$) is approximately 45 and 35 dB below the primary tones, respectively, comparable with closed system measurements (e.g., Brown and Gaskill, 1990; Avan *et al.*, 1996).

It is apparent from Figs. 2 and 3 that OAEs are indeed measurable with a physically open recording system. The remaining question is to what degree have the emissions been altered by the open sound system?

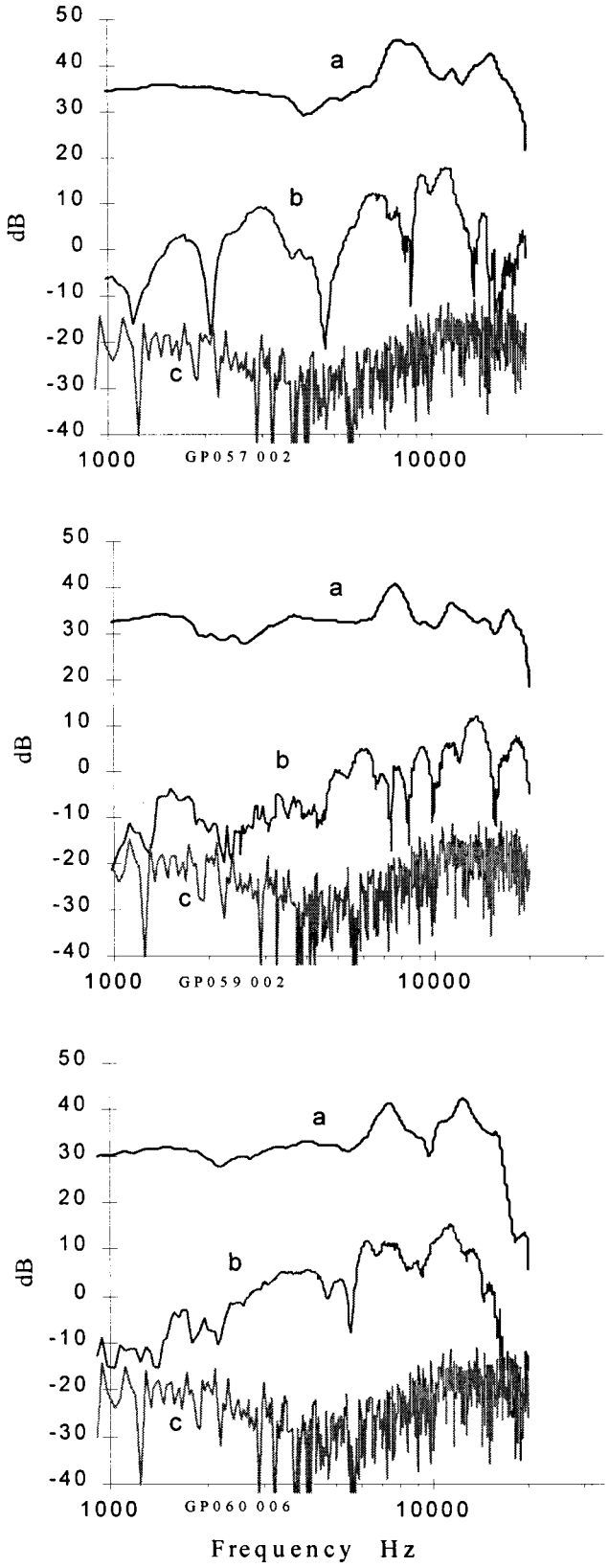

FIG. 2. Three examples from different animals using a physically open recording system of (a) spectrum of acoustical stimulus recorded in the ear canal of a guinea pig, (b) TEOAE obtained with that stimulus, and (c) noise level. Corrected for probe tube characteristics.

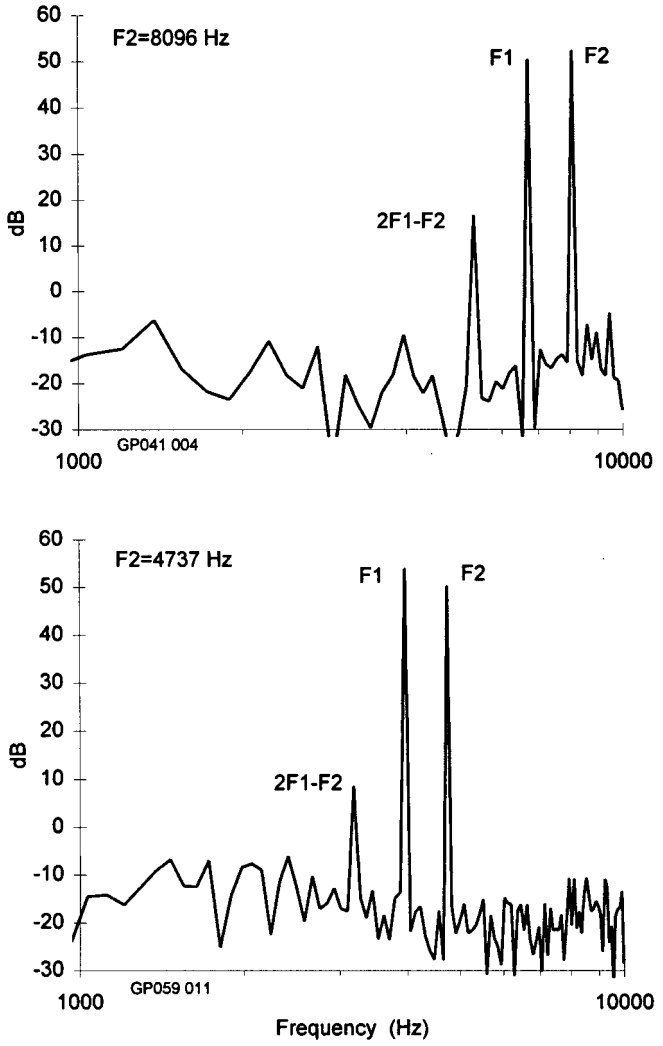

FIG. 3. Two examples of the sound spectrum recorded in the guinea pig meatus in response to two pure tones. The primary tones, at 8096/6747 and 4737/3947 Hz, are accompanied by a strong peak at the difference tone (5398 and 3157 Hz).

B. EEOAEs

Figure 4 shows a representative frequency response function of EEOAEs from electrical stimulation in scala media in the first turn in both the sealed and open conditions. The curve for the open condition represents the average of 15 measurements made at each frequency, each measurement acquired over 0.2 s, while the curve for the sealed condition represents the average of ten measurements made at each frequency, each measurement acquired over 0.2 s. The error bars represent one standard deviation. Above 5 kHz there is effectively no difference in the amplitude of the emissions measured under the sealed and open conditions. Below 5 kHz the functions increasingly separate with decreasing frequency to a mean difference of 7 to 8 dB at 1 kHz between the sealed and open conditions.

Figure 5 shows the mean of the differences between the sealed and open condition versus frequency from data pooled from four animals. Five measurements made at each frequency for the sealed and the open conditions were paired and the difference for each pair calculated. However, to reduce the variance in the data due to noise, data was included only if the standard deviation of each set of five measure-

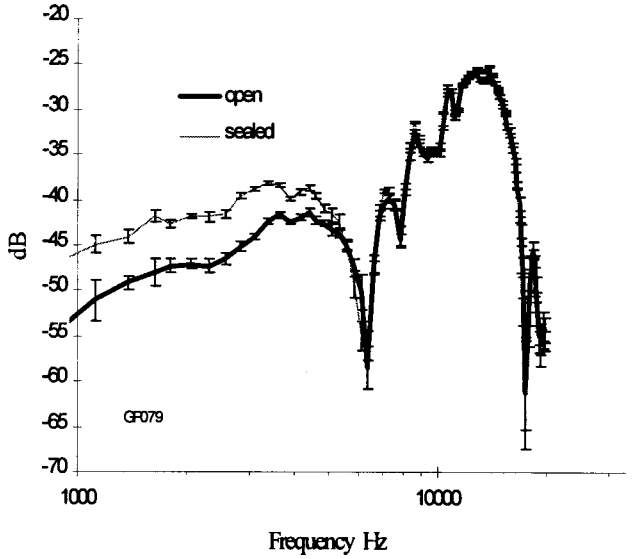

FIG. 4. Sealed and open otoacoustic emission sound-pressure levels measured in response to a 10 μA current injected into the first turn of scala media. Error bars are also shown.

ments for both the sealed and open conditions was less than 1 dB. This resulted in 0–20 difference values from all four animals being used to calculate the overall mean and standard deviation of the differences at any one frequency. For approximately 50% of frequencies, the mean of the differences was derived from the maximum number of difference values, i.e., 20. From Fig. 5 it can be seen that below 4 kHz, the means of the differences range from 2 to 7 dB while from 4 to 20 kHz it is essentially $\leqslant 2$ dB. Error bars in Fig. 5 represent one standard deviation.

To examine the reliability of the technique of placing a probe tube in the meatus in the open condition, the effect of position of the probe tube in the x-y plane (± 1 mm from central position) was examined in one animal as was the effect of depth of the probe tube (from 1 to 3-mm depth in 1-mm steps). This is illustrated in Fig. 6(i) and (ii) with the maximum recorded value minus the mean and minimum recorded value minus the mean for each frequency plotted versus frequency. The variation from the mean value is predominantly less than 2 dB which would suggest that the technique would have reasonable intersubject reproducibility.

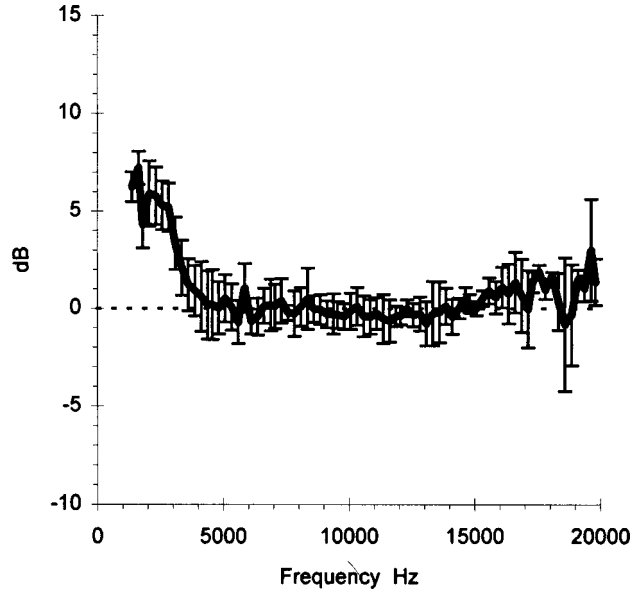

FIG. 5. The mean of the differences between the sealed and open condition versus frequency from data pooled from four animals. Error bars represent one standard deviation.

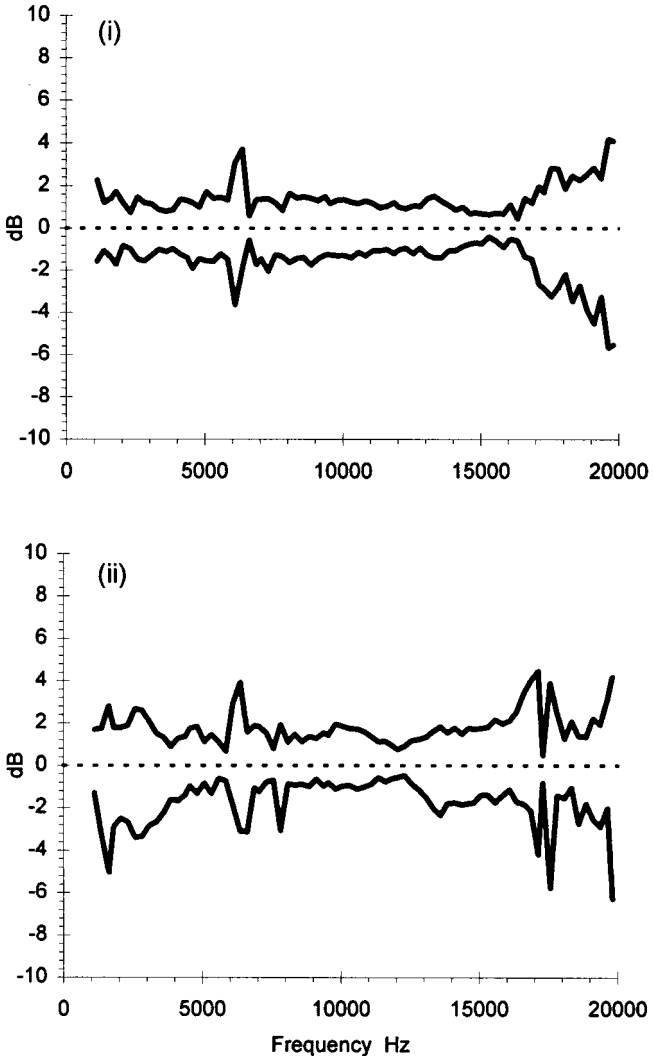

FIG. 6. Maximum variation from the mean sound-pressure level with changes in the position of the probe tube in (i) x-y plane, (ii) depth, in one animal.

III. DISCUSSION

This paper compares the amplitude of EEOAEs measured with a physically open system versus a sealed system in the ear canal. EEOAEs rather than AEOAEs were compared to avoid the confounding effect of different acoustical probe assemblies on the acoustical stimulus level. We have demonstrated that OAEs are largely unaltered by changing the acoustical load in the ear canal. One could infer from this finding that, in the guinea pig, the generation mechanism of OAEs is largely unaffected by changes in ear canal impedance.

In the past it has been assumed that a small-volume, well-sealed enclosure is necessary to record otoacoustic emissions (Matthews, 1983; Kemp *et al.*, 1990). Evidently this is not the case in guinea pigs. In this paper, distortion product, transient-evoked, and electrically evoked emissions have all been demonstrated for a system in which the external ear canal is only partially (perhaps 40%) obstructed by the microphone probe tube. The largest difference in emissions for an open system relative to a sealed system was about 7 dB at 1 kHz, reducing progressively to effectively no difference above 5 kHz. An open-field stimulus system permits the use of much wider-band stimuli and we have been able to show that this, in turn, results in wide-band emissions. A probe microphone placed in the ear canal of a guinea pig with a sound source placed near the entrance provides a superior alternative to the traditional acoustical probe assembly for the laboratory measurement of evoked OAEs in the guinea pig.

Recordings of OAEs to date have utilized a small volume, well-sealed enclosure. Perhaps the most commonly used system in this regard is the ILO88 and later versions. The ILO88 shows a greatly reduced OAE if the acoustical probe is not well sealed in the ear canal (Kemp *et al.*, 1990), but this may be due more to the reduction in the strength of the stimulus than to a direct effect on the emission. Also, a good acoustical probe seal is important in the clinical setting to reduce environmental noise which would otherwise confound recording of OAEs (Kemp *et al.*, 1990).

The significant advantage of a physically open recording system is the greater stimulus bandwidth obtainable when combined with an appropriate loudspeaker; we have recorded TEOAEs up to 20 kHz in the guinea pig, providing what we believe is the first published evidence of TEOAEs obtained as a result of stimulating the 10–20 kHz region of the basilar membrane in a mammalian species.

ACKNOWLEDGMENTS

This work was supported by the Australian National Health and Medical Research Council, Project Grant No. 960566, and by the University of Western Australia. R.H.W. is the recipient of a postgraduate scholarship from the Department of Physiology.

Anderson, S. D. (**1980**). ''Some ECMR properties in relation to other signals from the auditory periphery,'' Hearing Res. **2**, 273–296.

Avan, P., Erre, J., da Costa, D. L., Aran, J., and Popelar, J. (**1996**). ''The efferent-mediated suppression of otoacoustic emissions in awake guinea pigs and its reversible blockage by gentamicin,'' Exp. Brain Res. **109**, 9–16.

Bray, P., and Kemp, D. (**1987**). ''An advanced cochlear echo technique suitable for infant screening,'' Br. J. Audiology **21**, 191–204.

Brown, A. M., and Gaskill, S. A. (**1990**). ''Measurement of acoustic distortion levels reveals underlying similarities between human and rodent mechanical responses,'' J. Acoust. Soc. Am. **88**, 840–849.

Evans, E. F. (**1979**). ''Neuroleptanaesthesia: an ideal anaesthetic procedure for long-term physiological studies of the guinea pig cochlea,'' Acta Oto-Laryngol. **105**, 185–186.

Fahey, P. F., and Allen, J. B. (**1985**). ''Nonlinear phenomena as observed in the ear canal and at the auditory nerve,'' J. Acoust. Soc. Am. **77**, 599–612.

Hilger, A. W., Furness, D. N., and Wilson, J. P. (**1995**). ''The possible relationship between transient evoked otoacoustic emissions and organ of Corti irregularities in the guinea pig,'' Hearing Res. **84**, 1–11.

Hubbard, A. E., and Mountain, D. C. (**1983**). ''Alternating current delivered into the scala media alters sound pressure at the eardrum,'' Science **222**, 510–512.

Jurzitza, D., and Hemmert, W. (**1992**). ''Quantitative measurements of simultaneous evoked otoacoustic emissions,'' Acustica **77**, 93–99.

Kemp, D. T. (**1978**). ''Stimulated acoustic emissions from within the human auditory system,'' J. Acoust. Soc. Am. **64**, 1386–1391.

Kemp, D. T., Bray, P., Alexander, L., and Brown, A. M. (**1986**). ''Acoustic emission cochleography—practical aspects,'' Scand. Audiol. Suppl. **25**, 71–95.

Kemp, D. T., Ryan, S., and Bray, P. (**1990**). ''A guide to the effective use of otoacoustic emissions,'' Ear Hear. **11**, 93–105.

Kim, D. O., Molnar, C. E., and Matthews, J. W. (**1980**). ''Cochlear mechanics: Nonlinear behavior in two-tone responses as reflected in cochlear-nerve-fiber responses and in ear canal sound pressure,'' J. Acoust. Soc. Am. **67**, 1704–1721.

Kirk, D. L., and Yates, G. K. (**1996**). ''Frequency tuning and acoustic enhancement of electrically evoked otoacoustic emissions in the guinea pig cochlea,'' J. Acoust. Soc. Am. **100**, 3714–3725.

Magnan, P., Avan, P., Dancer, A., Smurzynski, J., and Probst, R. (**1997**). ''Reverse middle-ear transfer function in the guinea pig measured with cubic difference tones,'' Hearing Res. **107**, 41–45.

Matthews, J. W. (**1983**). ''Modelling reverse middle ear transmission of acoustic distortion signals,'' in *Mechanics of Hearing*, edited by E. de Boer and M. Viergever (Delft U.P., Delft, The Netherlands), pp. 11–18.

Mills, D. M., and Rubel, E. W. (**1996**). ''Development of the cochlear amplifier,'' J. Acoust. Soc. Am. **100**, 428–441.

Mountain, D. C., and Hubbard, A. E. (**1989**). ''Rapid force production in the cochlea,'' Hearing Res. **42**, 195–202.

Nakajima, H. H., Olsen, E. S., Mountain, D. C., and Hubbard, A. E. (**1994**). ''Electrically evoked otoacoustic emissions from the apical turns of the gerbil cochlea,'' J. Acoust. Soc. Am. **96**, 786–794.

Prieve, B. A., Gorga, M. P., and Neely, S. T. (**1996**). ''Click- and tone-burst-evoked otoacoustic emissions in normal-hearing and hearing-impaired ears,'' J. Acoust. Soc. Am. **99**, 3077–3086.

Puria, S., and Rosowski, J. J. (**1997**). ''Measurement of reverse transmission in the human middle ear: Preliminary results,'' in *Diversity in Auditory Mechanics*, edited by E. R. Lewis, G. R. Long, R. F. Lyon, P. M. Narins, C. R. Steele, and E. Hecht-Poinar (World Scientific, Singapore), pp. 151–157.

Thornton, A. R. D., Kimm, L., Kennedy, C. R., and Cafarelli-Dees, D. (**1994**). ''A comparison of neonatal evoked otoacoustic emissions obtained using two types of apparatus,'' Br. J. Audiology **28**, 99–109.

Wilson, J. P. (**1980**). ''Evidence for a cochlear origin for acoustic re-emissions, threshold fine structure and tonal tinnitus,'' Hearing Res. **2**, 233–252.

Zwicker, E. (**1990**). ''On the influence of acoustical probe impedance on evoked otoacoustic emissions,'' Hearing Res. **47**, 185–190.

The level dependence of response phase: Observations from cochlear hair cells

M. A. Cheatham[a] and P. Dallos
Communication Sciences and Disorders, Audiology and Hearing Sciences, Hugh Knowles Center, Frances Searle Building, Northwestern University, Evanston, Illinois 60208-3550

(Received 29 December 1997; revised 23 March 1998; accepted 23 March 1998)

Hair cell responses are recorded from third turn of the guinea pig cochlea in order to define the relationship between hair cell depolarization and position of the basilar membrane. Because the latter is determined locally, using the cochlear microphonic recorded in the organ of Corti (OC) fluid space, no corrections are required to compensate traveling wave and/or synaptic delays. At low levels, inner hair cells (IHC) depolarize near basilar membrane velocity to scala vestibuli reflecting the free standing nature of their stereocilia. At high levels, the time of depolarization changes rapidly from velocity to scala vestibuli to the scala tympani phase of the basilar membrane response. This change in response phase, recorded in the fundamental component of the IHC response, is associated with a decrease in response magnitude. The absence of this behavior in OC and outer hair cell responses implies that basilar membrane mechanics may not be responsible for these response patterns. Because these features are reminiscent of the magnitude notches and the large phase shifts observed in single unit responses at high stimulus levels, they provide the IHC correlates of these phenomena. [S0001-4966(98)01607-5]

PACS numbers: 43.64.Ld, 43.64.Nf, 43.64.Tk [RDF]

INTRODUCTION

The single unit literature states that response phase depends on stimulus level and that this level dependence is expressed in several different variations (Kiang *et al.*, 1969; Kiang and Moxon, 1972; Allen, 1983; Liberman and Kiang, 1984; Kiang *et al.*, 1986; Ruggero and Rich, 1983, 1987, 1989; Kiang, 1990; Ruggero *et al.*, 1996; Cai and Geisler, 1996). For example, phase lags are exhibited as stimulus level increases for inputs below best frequency (BF); phase leads, for inputs above BF (Anderson *et al.*, 1971). This behavior is also observed in cochlear hair cell responses (Dallos, 1986) and is thought to depend on preceding mechanical events (Rhode, 1971; Rhode and Robles, 1974; Sellick *et al.*, 1982; Geisler and Rhode, 1982; Nuttall and Dolan, 1996; Ruggero *et al.*, 1997). In contrast to this relatively well characterized aspect of response phase which is expressed around BF, other phase behaviors have been documented for low-frequency inputs below ~1000 Hz. In fact, auditory nerve fibers tend to fire more than once per cycle as stimulus level increases from low to moderate levels (Kiang and Moxon, 1972; Johnson, 1974; McGee *et al.*, 1982; Ruggero and Rich, 1983). This phenomenon, known as peak splitting, has its counterpart at the IHC level and is thought to relate to harmonic distortion (Dallos *et al.*, 1986; Cody and Mountain, 1989; Dallos and Cheatham, 1989a,b). In other words, when IHC responses at harmonic frequencies are comparable to those at the fundamental, additional peaks occur during a single period of a low-frequency sinusoid.

A third nonlinearity is observed at high stimulus levels where abrupt changes in response phase of nearly one half-cycle are exhibited in single unit responses (Kiang *et al.*, 1969). This feature, which is sometimes coupled with a notch in the rate-intensity function, is so obvious that two response components are identified, with component I dominating below, and component II dominating above, a transition region where the rapid changes in rate and phase occur. Because a null can be observed at high intensities and because these features were originally reported by Nelson Kiang and his colleagues at the Eaton–Peabody Laboratory, this behavior is often referred to as Nelson's Notch. In spite of the fact that these observations have been replicated, the physiological precursors of this phenomenon are not yet known. Consequently, measurements from cochlear hair cells and from the OC fluid space may further our understanding of the ways in which intensity is processed over a range of some 120 dB (Viemeister, 1988).

I. METHODS

Because previous publications (Dallos *et al.*, 1982; Dallos, 1985) provide detailed accounts of the procedures required for hair cell recording in the apical half of the cochlea, only a few issues are considered here. In the present experiments, the cochlea is exposed in anesthetized guinea pigs using the traditional ventrolateral approach. A window is made over scala media in turn 3 which allows outputs to be sampled from hair cells with best frequencies of approximately 1000 Hz. After traversing the spiral ligament and the endolymphatic fluid space, Hensen cells are encountered at the boundary of the organ of Corti. Ideally, the recording electrode follows a track roughly parallel to but below the reticular lamina, thereby optimizing the chances for hair cell recordings. All animal care procedures were approved by the National Institutes of Health and by Northwestern University's Institutional Review Committee.

[a]Electronic mail: m-cheatham@nwu.edu

Electrical measures from the OC fluid space are always collected and used to determine the instantaneous position of the basilar membrane. In other words, the motion pattern of the basilar membrane is estimated locally in the same general area as the hair cell recordings and no corrections are required to compensate for traveling wave and/or synaptic delays. The OC measure is also preferable to that at the round window for at least two reasons. First, there is usually a disparity between the round window location where basilar membrane motion is estimated and the place along the cochlear partition where a nerve fiber innervates its hair cell target. Thus traveling wave delays must be estimated and compensated. Second, the anatomy in the hook region is complex, with the result that recordings on opposite sides of the OC are not 180° out-of-phase (Weiss *et al.*, 1969; Dallos *et al.*, 1971). This is important because it is only when the cochlear microphonic (CM) measured across the cochlear partition is out-of-phase that one can be assured that measured responses are generated locally. Consequently, this electrical complication makes estimation of basilar membrane position from round window recordings less accurate when compared to measures from the OC fluid space because the latter are made in the same region as the hair cell recordings. Organ of Corti potentials are also preferable to those from perilymphatic scalae because the length constant within the organ may be significantly shorter (Geisler *et al.*, 1990).

Responses recorded by the microelectrode are preamplified (Dagan model 8700) and low-pass filtered at 3000 Hz to remove the effect of aliasing. An automatic gain control system optimizes amplification in order to maximize the signal without saturating the analog-to-digital converter. A laboratory computer (Digital Equipment Corp., PDP 11/73) is used to average responses on line with the number of averages decreasing with increasing level. Consequently, the use of short duration tone bursts and the averaging of only a few samples, minimizes the possibility of acoustic trauma at the highest input levels. Magnitude and phase data are obtained off line from fast Fourier transforms (FFT) of stored, averaged response waveforms. Waveform segments, 35–40 ms in duration, are windowed before transformation using a Hanning function. Although response magnitudes are usually reported as millivolts peak, the average voltage is sometimes obtained in order to estimate the signal driving transmitter release (Cheatham and Dallos, 1993). In this case, the average voltage is computed over a ten cycle segment after the averaged response waveform has been half-wave rectified. In other words, deflections of the waveform below the baseline in quiet are not included in the average value.

In order to assay the magnitudes of individual components from distorted responses, averaged response waveforms are digitally filtered off-line. These manipulations are performed using Igor Pro® (WaveMetrics, Lake Oswego, OR 97035) equipped with the Igor Filter Design Laboratory. In this program, filter outputs appear in phase with the input because the large linear phase component associated with the filter's response is removed so that small phase variations are not obscured. Design macros are used to implement either low-pass or band-pass filters by using the McClellan–Parks–Rabiner technique. Attenuations in the stop band are at least 75 dB down from the pass band where rippling is less than ± 0.02 dB.

Sound pressure levels (SPL) generated by a single driver (Beyer DT-48) are measured in the ear canal utilizing a subminiature microphone (Knowles BT-1751) equipped with a probe tube. The latter is placed inside the sound tube in a concentric arrangement and cemented into the external auditory meatus forming a closed system. Because the Knowles microphone is sensitive, measurements of sound pressure level are made using 60 dB of attenuation. In addition, high-level distortion in the sound is determined in a coupler using a 1/2-in. Brüel & Kjær condenser microphone (type 4134). This is required because the output of the Knowles microphone is distorted at high levels. At the highest levels used in these experiments, the second harmonic is $\sim$40 dB down for fundamentals at 140 and 200 Hz. At 700 Hz and above, the second harmonic is at least 60 dB down. In all cases, odd harmonics are less prominent than evens.

II. RESULTS

Response phase at the single unit level is defined as the time when discharge rate increases, during a single period of a low-frequency sinusoid. This is thought to correspond to the time when the hair cell depolarizes, thereby inducing transmitter release (Flock, 1971). Consequently, hair cell data are evaluated to determine when the voltage gradient across the cell's basolateral membrane becomes more positive relative to that in quiet and to relate this to the instantaneous position of the basilar membrane. It should be emphasized that the results are based on limited data because high-level inputs are not routinely presented. This makes it impossible to estimate the percentages of IHCs showing the rapid phase changes and the magnitude notches associated with Nelson's Notch.

Figure 1 displays IHC and OC waveforms for 200 Hz presented at 50 and 90 dB. In this, and in several other figures, two cycles of the low-frequency input are displayed in order to demonstrate temporal aspects of the responses. Although the stimulus onset is not included, adaptation was not observed and played no part in the hair cell responses documented here. Because the 200-Hz input produces a larger intracellular voltage than that recorded extracellularly in the OC fluid space, each individual response is plotted using its own ordinate. A line at 0 mV represents the hair cell's membrane potential in quiet and is included for reference. Shading is also included under the positive segments of the IHC curves to emphasize that these deviations are associated with transmitter release (Flock, 1971).

In order to determine the timing of hair cell depolarizations relative to the position of the basilar membrane, the OC response is interpreted in the following way. The positive phase of the CM response is associated with basilar membrane displacement to SV; the negative phase with displacement to ST. This relationship is based upon evidence which suggests that the CM reflects outer hair cell (OHC) receptor currents (Dallos and Cheatham, 1976) and that OHCs respond to basilar membrane displacement at least for low-frequency inputs (Dallos *et al.*, 1972). Hence, the local CM

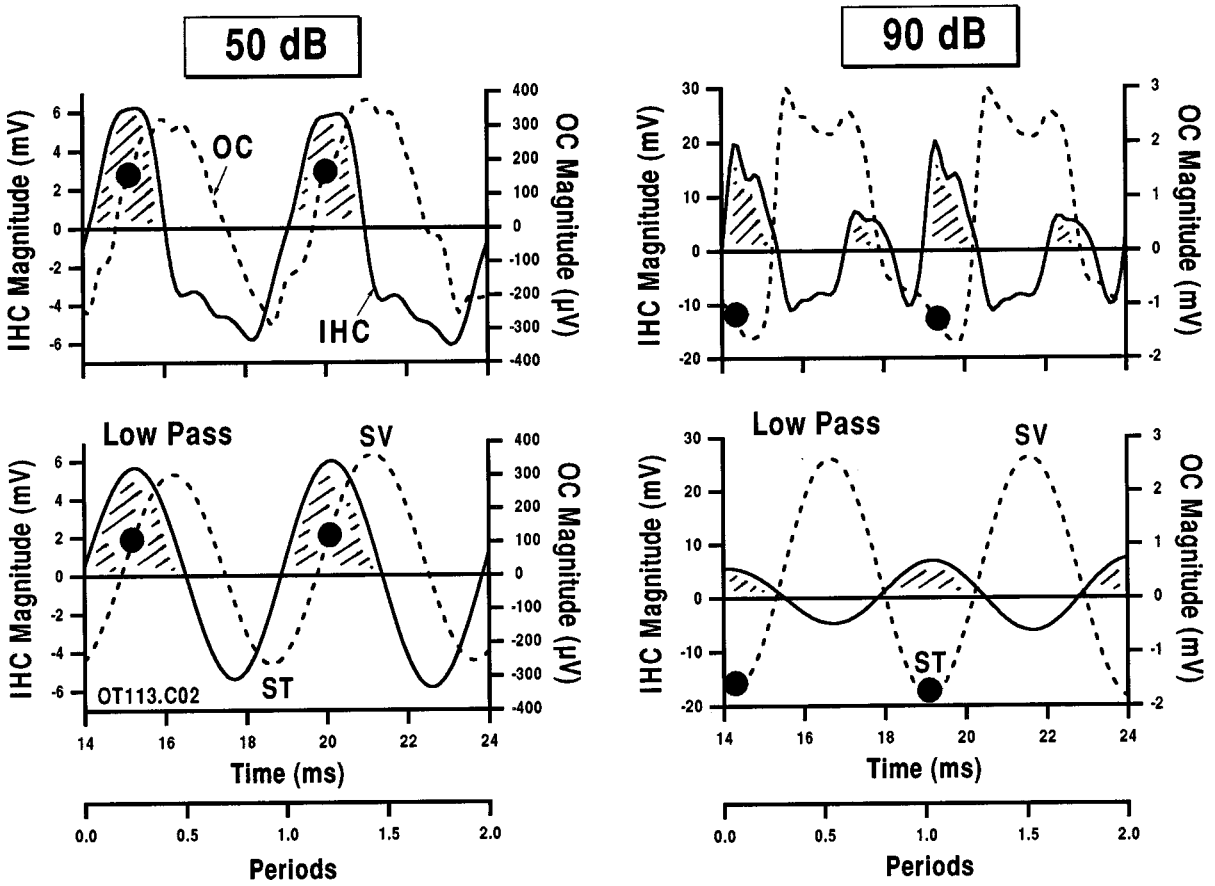

FIG. 1. Inner hair cell (solid lines) and organ of Corti (dotted lines) waveforms recorded under identical conditions are plotted for a 200-Hz input at 50 dB, on the left and 90 dB, on the right. In each panel, the abscissa is plotted in msec relative to the beginning of the analog-to-digital window used for averaging the responses. A second abscissa is also included at the bottom to indicate two periods of the low-frequency sinusoid. Because of disparities is magnitude, each individual response is plotted on its own ordinate. Symbols are placed on the OC waveform at the time that the IHC is maximally depolarized, i.e., positive. Responses on the lower panels have been low-pass filtered at 210 Hz to remove energy at higher harmonic frequencies. In these experiments, the sound pressure levels are measured in dB *re*: 20 μPa.

reflects basilar membrane displacement. Based on this association, one concludes that the IHC plotted at the top of Fig. 1 depolarizes near basilar membrane velocity to SV. This is more clearly demonstrated at the bottom where low-pass filtered versions of the averaged response waveforms are plotted. Solid symbols are placed on the OC waveform at the time that the IHC potential is maximally positive. This observation that the IHC response leads the OC potential (Sellick and Russell, 1980; Nuttall *et al.*, 1981; Dallos and Santos-Sacchi, 1983; Patuzzi and Yates, 1987) implies differentiation. From this it follows that IHC dc receptor potentials result from asymmetries in the hair cell transducer and not from a direct, dc mechanical input (Russell and Ashmore, 1983; Le Page, 1987).

Because the single unit literature (Kiang *et al.*, 1969; Kiang and Moxon, 1972; Allen, 1983; Liberman and Kiang, 1984; Kiang *et al.*, 1986; Ruggero and Rich, 1989; Kiang, 1990; Ruggero *et al.*, 1996; Cai and Geisler, 1996) demonstrates that the timing of discharges changes at high levels, response phase is also documented at 90 dB. These results are plotted on the right in Fig. 1. At this higher level, the IHC depolarizes to the largest extent during basilar membrane displacement to ST, i.e., during the negative phase of the CM response. Because the waveforms are distorted, they were once again low-pass filtered off-line to better display changes in the fundamental component of the response. The plot at the bottom of the figure confirms that the time of IHC depolarization coincides with basilar membrane displacement to ST. This change in response phase is not related to the production of harmonic components because these are removed by filtering.

Inner hair cell measures are compared with those from an OHC and from the OC fluid space at several levels in Fig. 2. The waveforms have again been low-pass filtered to demonstrate changes in the fundamental component of the response. The OC pattern at the top indicates that the peak of the response occurs later in time as sound pressure level increases from 50 to 90 dB. This is consistent with previous demonstrations (Dallos, 1986) where phase lags accumulate with increasing level for inputs below the BF of the cell. A similar pattern is demonstrated for an OHC in the center panel. Although first described in single unit responses (Anderson *et al.*, 1971), this level-dependent phase behavior is thought to originate in nonlinear basilar membrane mechanics (Rhode, 1971; Rhode and Robles, 1974; Sellick *et al.*, 1982; Geisler and Rhode, 1982; Nuttall and Dolan, 1996; Ruggero *et al.*, 1997). The IHC responses at the bottom also contain an accumulating phase lag but only for

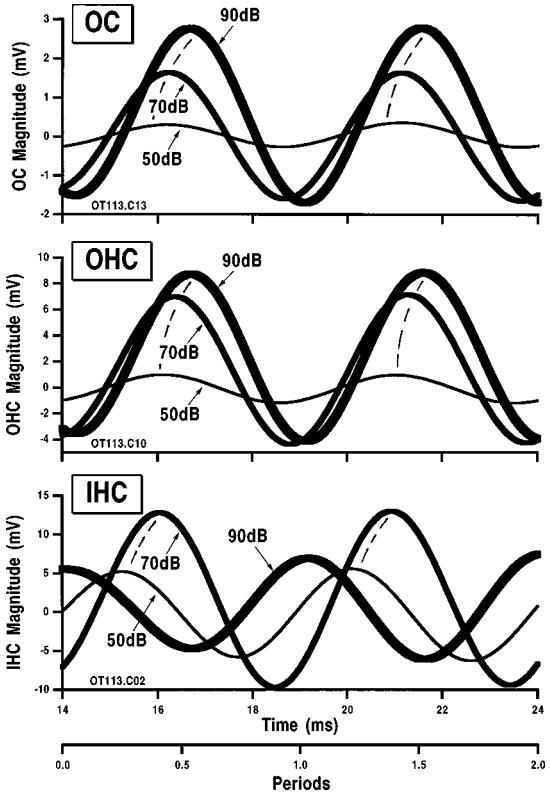

FIG. 2. Low-pass filtered waveforms are shown for 200 Hz at 50, 70, and 90 dB. Responses were also collected at 30 dB but these were nearly in phase with those at 50 dB and are, therefore, omitted for clarity. The top panel provides the OC response; the middle panel, the OHC response, and the lower panel, the IHC response. A vertical dashed line connects the peaks of the functions to highlight the accumulating phase lag observed with increasing intensity. In addition, increasing level is indicated by increasing line thickness. The data in Figs. 1 and 2 were obtained from the same preparation.

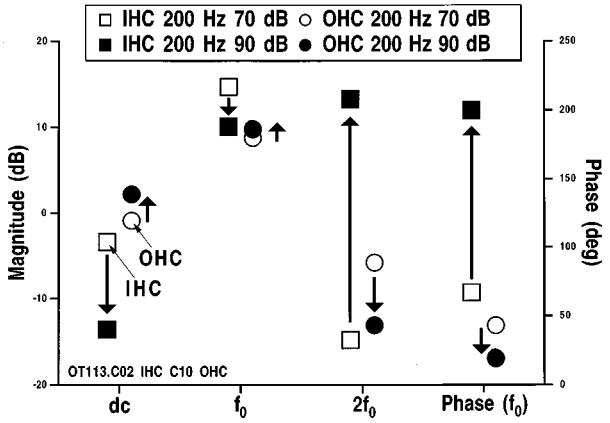

FIG. 3. This graph documents changes in magnitude and phase obtained when the input sound pressure level at 200 Hz increases from 70 (open symbols) to 90 (closed symbols) dB. Magnitudes are plotted on the left ordinate where 0 dB corresponds to a 5-mV peak. In addition to the fundamental, magnitude changes for the dc and second harmonic components are provided. The phase shift at the fundamental is also included and plotted using the right ordinate. These data are for the same OHC (circles) and IHC (squares) responses plotted in Fig. 2.

increases from 50 to 70 dB. As intensity increases from 70 to 90 dB, a phase lead develops and response magnitude decreases relative to the measurements made at lower levels. This IHC behavior is reminiscent of the notch pattern demonstrated in single units where rate decreases are associated with a near 180° phase reversal over a narrow, high-level intensity range (Kiang *et al.*, 1969; Kiang and Moxon, 1972; Allen, 1983; Liberman and Kiang, 1984; Kiang *et al.*, 1986; Ruggero and Rich, 1989; Kiang, 1990; Ruggero *et al.*, 1996; Cai and Geisler, 1996). Absence of this behavior in basilar membrane mechanics (Ruggero *et al.*, 1986, 1991, 1997) is consistent with the lack of a phase reversal in OC and OHC measures.

Although the waveforms in Fig. 2 were low-pass filtered to emphasize alterations in the fundamental component of the response, magnitude changes are also observed for the dc and for the second harmonic. These features are included in Fig. 3 for the OHC (circles) and IHC (squares) responses plotted in Fig. 2. The abscissa represents the dc, the fundamental (f_0), the second harmonic ($2f_0$) and the phase at the fundamental. The phase values are plotted using the ordinate on the right. As indicated in Fig. 3, the magnitude of the IHC response at the fundamental decreases as the input increases from 70 (open symbols) to 90 (closed symbols) dB. The reduction in the dc receptor potential is approximately twice that for the ac response which is consistent with the square law relationship between the two components (Goodman *et al.*, 1982; Russell and Sellick, 1983; Patuzzi and Sellick, 1983; Russell and Cody, 1985; Dallos, 1985). In contrast to decreases in the dc and the fundamental, the magnitude of the second harmonic exhibits a large increase. Although distortion in the acoustic signal is only 40 dB down for an input at 200 Hz, the IHC response at $2f_0$ is 16 dB greater than estimates based on distortion in the sound. The increase in the second harmonic content of the IHC response is unusual because even-order distortion products produced by the hair cell transducer, i.e., the second harmonic and the dc response, are expected to exhibit similar features (Dallos, 1973). The phase at the fundamental also exhibits a large shift as expected from the waveforms in Fig. 2. These IHC response patterns contrast with those for the OHC (circles) recorded in the same electrode track. In other words, all four measures show opposing behaviors in outer versus inner hair cell responses. As sound pressure increases, fundamental and dc OHC responses increase. The reduction in the OHC response at $2f_0$ probably relates to notches in this component consistent with observations published elsewhere (Dallos and Cheatham, 1989a,b). The phase lag recorded in the OHC with increasing level is consistent with similar behavior reported for inputs below BF (Dallos, 1986; Cheatham and Dallos, 1989).

Although we have commented on these response patterns before (Dallos *et al.*, 1986; Dallos and Cheatham, 1989a, b), the previous illustrations were at 700 and 800 Hz. Thus, Fig. 4 provides another example for a fundamental at 140 Hz because this frequency is closer to the ones used in several single unit experiments. These input–output functions illustrate the magnitude notch (left panel) and the large phase change (right panel) for the IHC but not the OC response. Individual response waveforms at 75, 89, and 92 dB are highlighted in Fig. 5. Corresponding values were plotted with enlarged symbols in Fig. 4. In all panels, three responses are plotted: the recorded IHC receptor potential, its

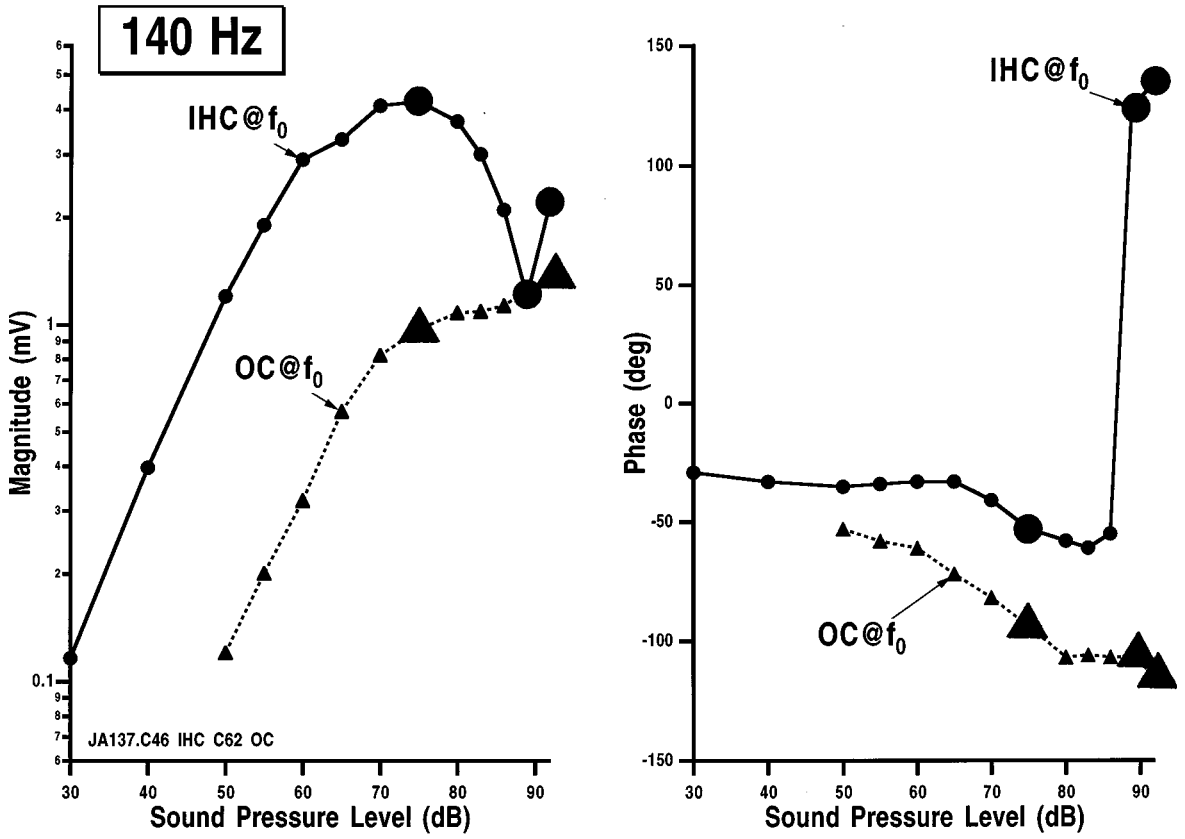

FIG. 4. Input–output functions are plotted here for IHC (solid lines) and OC (dotted lines) responses at 140 Hz. Both magnitude and phase data are provided for the fundamental component (f_0) of the response. The reference for the phase data is arbitrary. Companion waveforms for the responses plotted with enlarged symbols are shown in Fig. 5.

low-pass version (IHCLP), and the extracellular, OC response that has also been low-pass filtered (OCLP). Again, the positive (negative) phase of the OC response is associated with basilar membrane displacement to SV (ST). At 75 dB, shown at the top, both IHC functions plotted with solid and dotted lines peak near basilar membrane velocity to SV as indicated by the symbols on the OC waveform. The depolarizing phase of this response is shaded to emphasize that positive potentials induce transmitter release. Waveforms at 89 dB, provided in the center, indicate a reduction in the fundamental (solid lines), as expected from the magnitude notch in the input–output function in Fig. 4. The unfiltered IHC response (dotted lines), however, displays complexities associated with nonlinear responses. At this level, in the notch region, there are three depolarizations in a single period, with the two largest occurring near basilar membrane velocity to SV and near displacement to ST. This temporal pattern suggests that neural period histograms should contain at least two peaks per cycle. At 92 dB, shown at the bottom, only one depolarization occurs per cycle and the IHC responds near, but slightly leading, displacement to ST.

Additional response patterns from the same IHC are provided in Fig. 6 at 800 Hz which is just below BF. Input–output functions are plotted for both the fundamental (filled circles) and the average (AVE) voltage gradient (open triangles) because the latter may provide the best measure of the driving force for transmitter release (Cheatham and Dallos, 1993). These functions both exhibit magnitude notches implying that nonmonotonicities should also be reflected at the single unit level. It is also noted that responses above the notch are slightly larger than those below (see also Figs. 10–12 in Cheatham and Dallos, 1989). Also plotted in Fig. 6 are input–output functions for the second (filled squares) and third (open circles) harmonics. Notice that the second harmonic peaks in the region of the magnitude notch in the fundamental. This large increase for the second harmonic is similar to that documented in Fig. 2 for a fundamental at 200 Hz. Finally, above the notch, responses for the third harmonic exceed those for the second.

Companion waveforms corresponding to the enlarged symbols in Fig. 6 are provided in Fig. 7. When 800 Hz is presented at 60 dB, the IHC responds during basilar membrane displacement to SV. This is again demonstrated by circles placed on the OC waveform (dashed lines) at the time that the IHC is maximally positive. The phase lead between IHC and OC responses is no longer expressed at this higher input frequency. This is similar to previous results in both first (Sellick and Russell, 1980; Russell and Sellick, 1983; Patuzzi and Yates, 1987; Cody and Mountain, 1989) and third (Dallos and Santos-Sacchi, 1983) turns of the guinea pig cochlea. At 80 dB, in the region of the magnitude notch, the phase of depolarization for the unfiltered IHC response (dotted lines) is slightly leading velocity to ST. Finally, at higher levels, shown at the bottom, response phase changes further and a single phase of depolarization coincides with ST displacement. However, depending on their threshold,

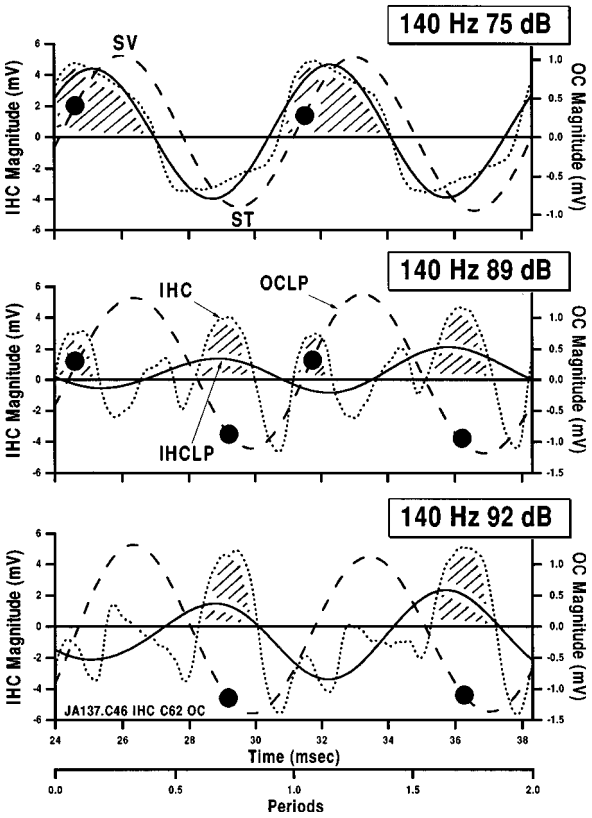

FIG. 5. Individual waveforms for 140 Hz at 75, 89, and 92 dB are plotted here for the IHC (dotted lines) and for the low-pass filtered IHC (solid lines) and OC responses. Circles on the OC waveforms (dashed lines) indicate the time or times of IHC depolarization. Filtered OC waveforms are plotted using the ordinate on the right.

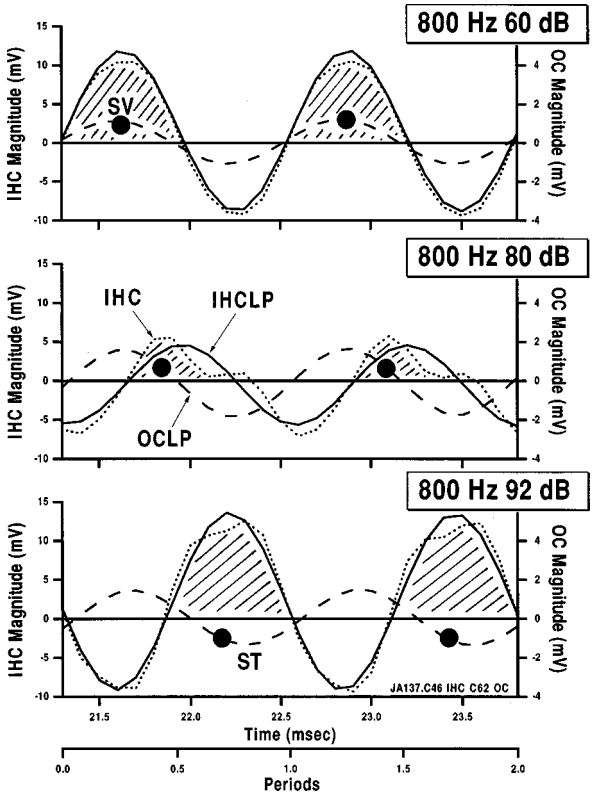

FIG. 7. This plot is similar to Fig. 5 except that these waveforms are for 800 Hz at 60, 80, and 92 dB. Shaded regions indicate the positive IHC depolarizations that are thought to result in transmitter release. Large symbols placed on the OC waveform designate the phases of IHC depolarization relative to position of the basilar membrane. A low-pass filter with cutoff at 850 Hz was used to obtain the filtered responses.

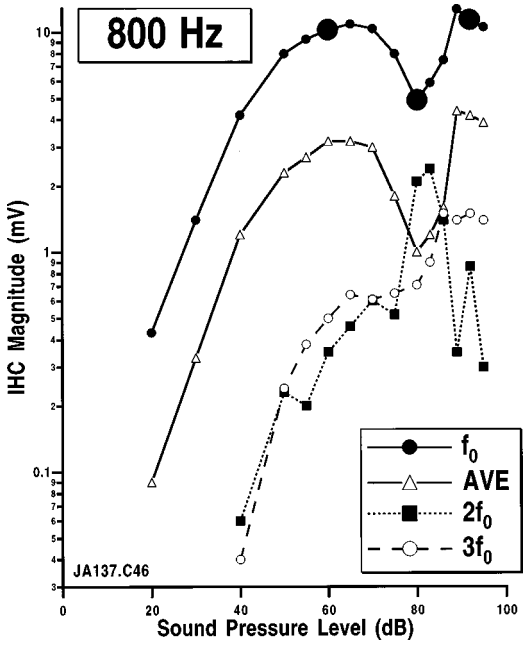

FIG. 6. An IHC input–output function for a fundamental at 800 Hz (solid lines, filled circles) is plotted along with functions for the average (AVE) response (solid lines, open triangles) recorded in the cell and for the second (dotted lines, filled squares) and third (dashed lines, open circles) harmonics. Companion waveforms corresponding to the levels plotted with enlarged symbols are included in Fig. 7.

single units might be expected to respond closer to ST velocity.

Figure 8 provides another example of the response waveforms recorded in the region of the magnitude notch, again for an input at 800 Hz. This cell displayed input–output functions similar to those plotted here in Fig. 6 (see Dallos and Cheatham, 1989b, Fig. 5B). At the top of the figure, the IHC response (dotted lines) is plotted along with a low-pass version from the OC (OCLP) to emphasize the fundamental component of the response and position of the basilar membrane. Symbols indicate that the two phases of IHC depolarization occur near basilar membrane displacement to SV and ST, i.e., near the phases of excitation for responses below and above the notch, respectively. In the lower panel, the low-pass OC response is replotted along with the fundamental and second harmonic components recorded in the IHC. Responses at the fundamental were obtained by low-pass filtering (IHCLP) the waveforms at 850 Hz; the second harmonic by band-pass filtering (IHCBP) the IHC response around 1600 Hz. In the notch region represented here, the IHC response at the fundamental peaks near basilar membrane velocity to ST, while the second harmonic peaks coincide with basilar membrane displacement to SV and ST. This suggests that the two phases of depolarization recorded in the notch, and displayed at the top of the figure, are associated with basilar membrane displacement, because the response is dominated by energy at a frequency which is two times the

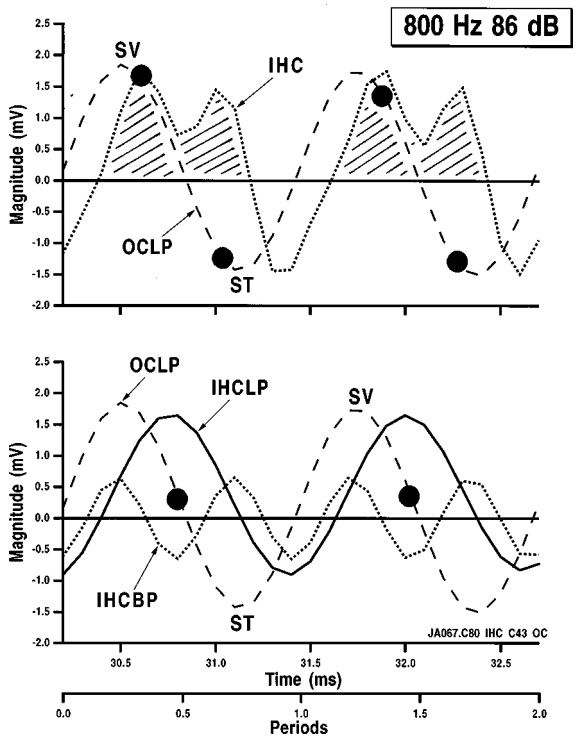

FIG. 8. This plot provides another example of waveforms recorded in the notch region where the fundamental is at a minimum; the second harmonic, a maximum. The IHC responses were recorded for 800 Hz at 86 dB. At the top of the figure, a low-pass filtered OC response (OCLP, dashed lines) is provided to show the fundamental where the positive phase of the response is associated with basilar membrane displacement to SV. The other function is the unfiltered IHC response (dotted lines). In the lower panel, the low-pass filtered OC response is replotted along with the low-pass filtered (IHCLP, solid lines) and the band-pass filtered (IHCBP, dotted lines) IHC responses. The latter has a pass band between 1500 and 1700 Hz to include the second harmonic.

fundamental. In this case, the two peaks of depolarization straddle the fundamental peak which is near ST velocity. Consequently, the presence of multiple components can influence the time or times of hair cell depolarization.

III. DISCUSSION

A. The frequency and level dependence of response phase

Electrophysiological results from the apex (Dallos and Santos-Sacchi, 1983; Dallos, 1985, 1986) and base (Sellick and Russell, 1980; Nuttall *et al.*, 1981; Patuzzi and Yates, 1987) of the cochlea indicate that IHCs respond when the basilar membrane is moving to SV, i.e., for velocity to SV. This response phase is observed for low level, low-frequency inputs, consistent with the presumption that their hair bundles are not firmly attached to the overlying tectorial membrane (Lim, 1972). At somewhat higher frequencies, IHCs respond when the basilar membrane is maximally displaced to SV (Fig. 7; Russell and Sellick, 1983; Patuzzi and Yates, 1987; Cody and Mountain, 1989), reflecting the possibility that movements of the hair bundle become entrained to the displacement pattern of the basilar membrane (Freeman and Weiss, 1990). In addition to this frequency dependence, it is also demonstrated that response phase depends on stimulus level in the region around BF. As sound pressure increases from low to moderate levels, a phase lag accumulates for inputs below BF. Although not shown here, a phase lead for inputs above BF has been documented elsewhere (Dallos, 1986; Cheatham and Dallos, 1989). The most parsimonious explanation for this behavior assumes that damping is intensity dependent. In other words, that bandwidth changes with increasing level from a narrowly tuned/under damped configuration to one that is broadly tuned and highly damped. Network analysis (Bode, 1945) also indicates that phase lags (leads) should accumulate below (above) BF as input level increases.

In addition to this phase nonlinearity expressed in the region around BF, level-dependent changes in response phase are also exhibited at moderate levels where single units fire more than once per cycle in response to low-frequency inputs below ~1000 Hz. This response pattern is thought to relate to the presence of energy at frequencies that are multiples of the fundamental. In other words, when IHC responses at harmonic frequencies are comparable in size to those at the fundamental (Dallos *et al.*, 1986; Cody and Mountain, 1989), additional peaks should occur during a single period of a low-frequency input. Thus, neural peak splitting probably relates to the presence of higher order distortion products generated by the IHC itself and/or present at the input to the cell. Because of the summation of both even- and odd-order harmonic components with the fundamental, individual peaks are not necessarily 180° apart (Johnson, 1980; Cai and Geisler, 1996). It is also envisioned that multiple-peaked histograms will only be observed for low-frequency inputs due to the filtering of harmonic components by the IHC's basolateral membrane at higher fundamental frequencies.

Although the distortion product hypothesis is the most reasonable, it is also possible that multiple firings occur even with an undistorted receptor potential. If the stimulus half-period is longer than the refractory period, then more than one peak could develop per cycle. In other words, when the refractory period ends before the stimulating half-cycle finishes, the opportunity exists for additional spikes to be generated. The timing of these peaks, however, should occur at multiples of the refractory period and not at multiples of the fundamental period. Consequently, the accuracy of the timing of spike discharges, based on this mechanism, will not be as precise as that based on the presence of distortion products. Because double-peaked histograms are observed at moderately high levels, the absolute and not the relative refractory period should determine the time interval between peaks. In other words, the levels at which multiple firings are recorded are probably high enough to compensate any threshold increases caused by the relative refractory period. It is emphasized that this possibility will only apply to very low fundamental frequencies. For example, if the absolute refractory period is ~1 ms and if the stimulus half-period is 2 ms, as it would be for an input at 250 Hz, then multiple firings are possible. However, if the input is 500 Hz, then the absolute refractory period and the stimulus half period are equal. In this case, a second spike would not be generated within a given cycle due to this mechanism.

A third phase behavior is expressed at high stimulus

levels where the time of depolarization changes relative to that obtained at lower levels. This large phase shift is sometimes associated with a magnitude minimum at the fundamental and is thought to be the IHC counterpart of similar features observed in the auditory nerve (Kiang *et al.*, 1969; Kiang and Moxon, 1972; Allen, 1983; Liberman and Kiang, 1984; Kiang *et al.*, 1986; Ruggero and Rich, 1989; Kiang, 1990; Ruggero *et al.*, 1996; Cai and Geisler, 1996). Because IHC data are not routinely collected at high levels, the details of this behavior, referred to here as Nelson's Notch, are only demonstrated in Figs. 4 and 6.

The data in Fig. 4 indicate that the magnitude notch does not result from extracellular responses commensurate with those recorded intracellularly (Gifford and Guinan, 1983). The same conclusion was also reached by Liberman and Kiang (1984) and by Kiang *et al.* (1986) based on observations that high-level neural responses remain unchanged in the presence of OHC damage. These arguments are supported by results in Fig. 2 where this phenomenon was not demonstrated in OC (Cody and Mountain, 1989; Dallos and Cheatham, 1989b) or OHC responses, implying that basilar membrane mechanics may not be the source of this behavior (Ruggero *et al.*, 1986, 1991, 1997). The absence of Nelson's Notch in OHCs and in OC responses could relate to the fact that the tallest OHC stereocilia are firmly imbedded in the overlying tectorial membrane (Kimura, 1966; Hunter-Duvar, 1978). This suggests that multiple modes of excitation are less likely for OHCs that depolarize at a phase near basilar membrane displacement to SV, independent of level (see Fig. 2). In contrast, the stereocilia of IHCs, if not free standing (Lim, 1972), are at least less firmly attached to the tectorial membrane (TM) with the result that the dynamic relationship between tectorial membrane and reticular lamina can influence how and when IHCs are stimulated as suggested by Zwislocki (1986).

It is acknowledged that the data reported here differ from those in gerbil (Zwislocki and Smith, 1989; Zwislocki, 1990) and in guinea pig (Kössl and Russell, 1992; Russell and Kössl, 1992). In the guinea pig experiments, recordings from the base of the cochlea indicate that phase reversals occur in outer but not inner hair cells for inputs approximately 1/2 octave below and above BF. The behavior below BF occurs at a location where the tip and tail of the tuning curve meet. This frequency dependence suggests that this behavior may not be the same as that referred to here as Nelson's Notch. In addition, the gerbil results are only available at one high and one low level. Consequently, it is not known whether the phase change is rapid and whether or not a notch also occurs in the magnitude of the fundamental response. Because any given set of parameters results in the expression of one or more of the phase nonlinearities described here, caution should be used when comparing results obtained using a variety of paradigms. This is because it is difficult to choose stimulus parameters that selectively feature one nonlinearity in the absence of all others. In some cases, the rapid phase changes that characterize the notch pattern are not always fully expressed. For example, when very low-frequency inputs are employed, the velocity dependence of IHC depolarization can influence the measurement resulting in high-level phase shifts that are considerably less than one half-cycle. If inputs are also affected by the phase nonlinearity expressed around BF, then the lead/lag transition in this region may also modify the phase changes associated with the notch behavior especially in single units with low BFs.

B. Nelson's notch and the two-factor cancellation hypothesis

The rapid, high level magnitude and phase changes observed in apical IHCs are expressed in the fundamental component of the response. This characteristic aspect was shown by low-pass filtering the averaged response waveforms to remove energy at the higher harmonics. These observations provide support for the two-factor cancellation hypothesis (Liberman and Kiang, 1984; Kiang, 1990; Lin and Goldstein, 1995) which suggests that two excitatory inputs interact to produce the cancellation notch. At low levels, input to the cell appears to be dominated by one component (I) while at high levels, a second component (II), which is out of phase, controls the input to the IHC.

The schematic in Fig. 9 illustrates the two-factor cancellation hypothesis (Liberman and Kiang, 1984; Kiang, 1990; Lin and Goldstein, 1995) and shows the two components presumed to interact at the input to the IHC transducer. Component I is vulnerable, sensitive, and nonlinear. The nonlinearity is simulated by a quadratically growing second harmonic. This choice is based on measurements in the OC fluid space where the second harmonic is usually larger than is the third (Dallos and Cheatham, 1989b). In contrast to component I, component II is robust and insensitive. The insensitivity is represented here by a threshold element, i.e., a smooth half-wave rectifier designated as F_1, that allows component II to be expressed only at relatively high levels. In other words, component I dominates the input at low levels; component II, at high levels. In the transition region, the two out-of-phase components interact. Although the input to the transducer (F_2) is strongly level dependent, the transducer itself is assumed to remain stable.

The waveforms on the right of Fig. 9 show responses obtained at the output of the transducer. The sinusoidal stimulus is also included and plotted with dashed lines. The solid curve in panel A is the response produced by component I. At high levels, component II dominates the response plotted in panel C. Comparison of panels A and C indicates that only one phase of depolarization is produced when a single component dominates the input to the transducer. The timing of these depolarizations, however, is out of phase. In the transition region when neither component dominates the input to the transducer, the response plotted in panel B is observed. In this case, two positive peaks develop within a single fundamental period corresponding to the preferred phases for components I and II, respectively. The response in panel B reflects cancellation of the fundamental at the input to the transducer with the result that the second harmonic associated with component I provides the only input.

The presence of two phases of excitation per fundamental period in panel B is consistent with the IHC waveforms plotted in Figs. 5 and 8 and with the double-peaked histo-

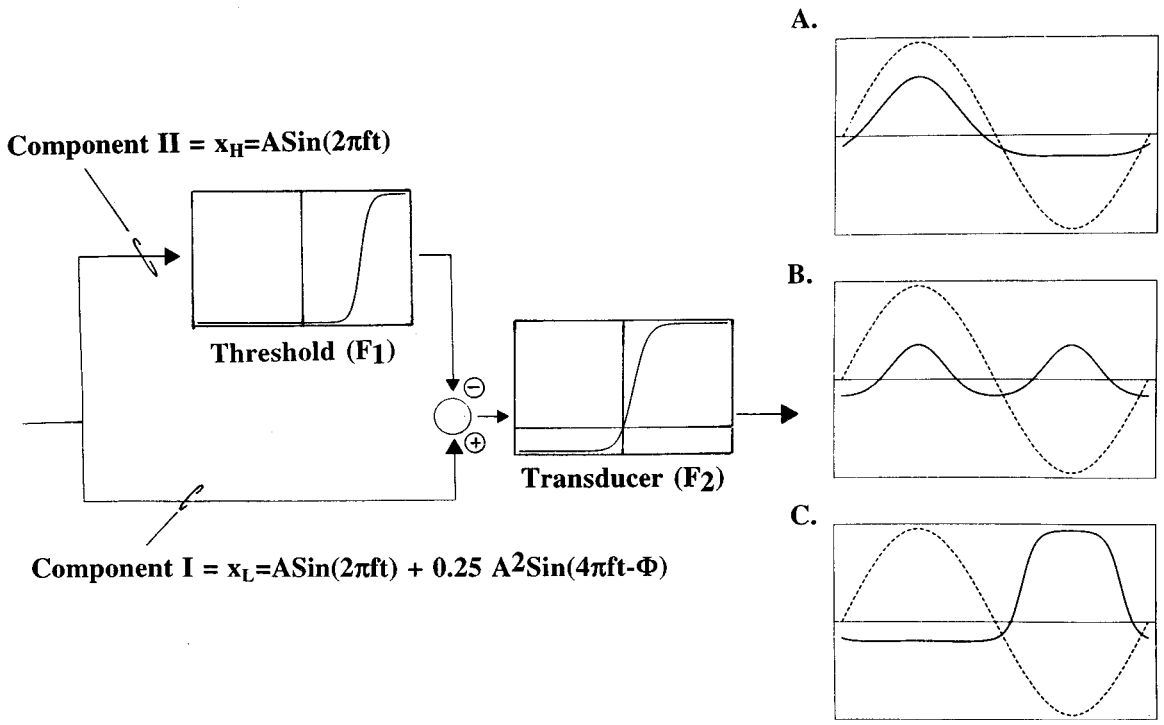

FIG. 9. The schematic on the left displays the two excitatory inputs thought to underlie Nelson's Notch. Component I represents an input containing second harmonic distortion added in a phase of $\pi/2$ relative to the fundamental. Due to incorporation of F_1, component II appears at the input to the IHC only at high levels. A summing device precedes the simulated IHC transducer function and adds components I and II in phase opposition. The waveforms on the right represent responses at the output of the transducer (F_2) depicted in the schematic. In panel A, at the top, component I dominates at low and moderate levels. The sinusoidal input is included for reference and plotted with dashed lines. At high levels, represented at the bottom in panel C, component II dominates the input to the transducer. In the center, when neither component dominates, the two fundamental components cancel because they are similar in size. The second harmonic associated with component I remains because it has an insufficiently large out-of-phase counterpart. The model results shown in Figs. 9 and 10 are based on the equations provided in the Appendix.

grams recorded in single unit responses in the region of the notch when the fundamental is reduced (Ruggero and Rich, 1989; Kiang, 1990; Ruggero *et al.*, 1996; Cai and Geisler, 1996). These bimodal histograms exhibit maxima at times corresponding to single-peaked responses obtained at stimulus levels below and above the transition region where the response is dominated by components I and II, respectively. This is consistent with model results plotted in Fig. 9 and with results in Fig. 8 where IHC depolarizations occur near basilar membrane displacement to SV and to ST in the region of the magnitude notch. However, if the notch behavior is recorded at very low fundamental frequencies, then the two phases of IHC depolarization occur near SV velocity, reflecting the velocity dependence of the IHC transducer as in Fig. 5, and ST displacement.

The two-factor cancellation hypothesis suggests that the two peaks of excitation relate to the existence of the harmonic components as indicated in Figs. 3 and 6. In other words, it is possible that a second harmonic is present mechanically at the input to the IHC in the fluid movements driven by the differential motion between reticular and tectorial plates. If the mechanical input to the IHC at high levels does contain second harmonic components, then IHCs would exhibit two depolarizations per cycle and single units would be expected to fire twice per cycle in the region of the notch when energy at the fundamental is reduced significantly by cancellation. It should be mentioned, however, that third harmonic components could also be present at the input to the IHC. Because these inputs are higher than inputs at the second harmonic frequency, they are more likely to be attenuated by filtering associated with resistances and capacitances in the hair cell's basolateral membrane. This may account for the preponderance of double-peaked histograms recorded in the notch region at the single unit level.

The possibility that harmonic components are present at the input to the IHC is illustrated in Fig. 10A where input–output functions are plotted for the signal measured at the output of the transducer depicted in Fig. 9. Notice that the fundamental and dc responses exhibit magnitude notches at high levels. More importantly, however, the second harmonic peaks in the region of this notch and declines in magnitude at higher levels. These model results are similar to those for the IHC responses plotted in Fig. 6 and represented in Fig. 3. Because the fundamental is reduced in the region of the notch, dc and harmonic components produced by the transducer should also be reduced. Consequently, the peak in the second harmonic is probably not associated with the IHC transducer. As the two-factor cancellation hypothesis suggests, the second harmonic peak could reflect the response of the IHC to an input at twice the fundamental frequency. This component, presumably present mechanically at the input to the cell, is produced by a nonlinear process occurring prior to the transducer, implying that the IHC responds as if stimulated by a single-tone input at the second harmonic frequency. This scenario is consistent with single unit experiments where introduction of a stimulus at the frequency of

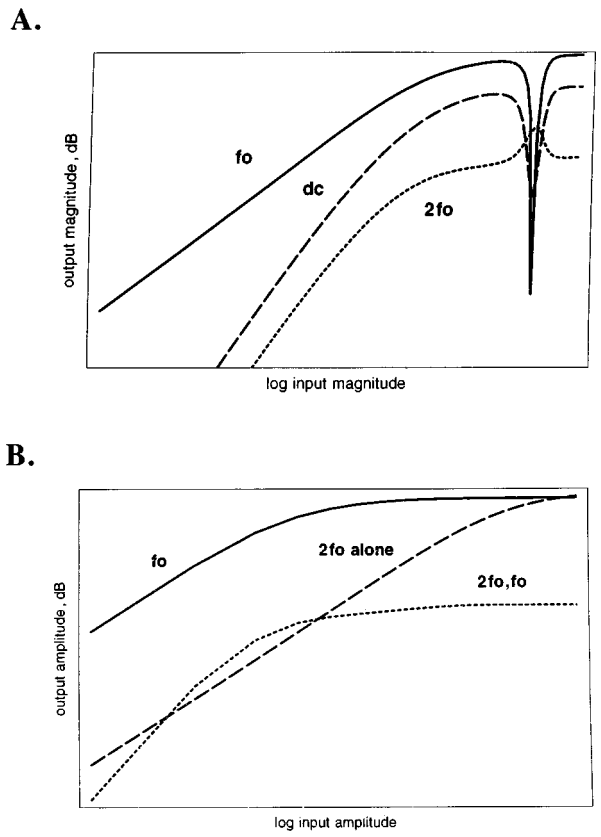

FIG. 10. In this figure, the output of the transducer (F_2) depicted in Fig. 9 is plotted versus input level. Functions in panel A are included for dc (dashed line) as well as ac components at the fundamental (solid line) and second harmonic (dotted line) frequencies. In panel B, input–output functions for the fundamental and second harmonic components are provided. The fundamental for component I alone is plotted with a solid line as a function of input amplitude. When the second harmonic content of component I, i.e., $0.25A^2$ Sin$(4\pi ft)$, is the sole input to the transducer, the resulting output is shown by the dashed line. In contrast, when this second harmonic is fed through the transducer function together with the larger fundamental (i.e., $2f_0, f_0$), it is reduced as shown by the function plotted with the dotted line. Consequently, when the two primaries associated with components I and II cancel one another forming the notch, the second harmonic increases as demonstrated in panel A.

the second harmonic changes double-peaked into single-peaked histograms (Kiang, 1990). In other words, cancellation of the component at $2f_0$ results in a very small response at the fundamental.

To provide further insight into the relationship between fundamental and harmonic components, and more specifically the second harmonic peak in the region of the fundamental notch, additional modeling results are provided in Fig. 10B. The solid curve shows the input-output function at the fundamental for component I alone. This function does not exhibit a notch because no out-of-phase component II is included. The dotted curve indicates that the second harmonic associated with component I saturates at a lower amplitude than the fundamental. However, when the second harmonic is presented alone at the input to the transducer, it saturates at a higher level as indicated by the function plotted with dashed lines. This difference is thought to occur because the distortion product is reduced by the fundamental when they are both affected by the same nonlinearity, as envisioned by Engebretson and Eldredge (1968). These model results suggest that the second harmonic reaches its maximum value in the region of the notch (see Figs. 3 and 6) because the canceled fundamental can no longer interfere with the response to the second harmonic that appears mechanically at the input to cell. This explanation is consistent with the observation that interference tones near BF are especially effective at reducing inputs that are above BF. In fact, this arrangement is depicted in another publication (Cheatham and Dallos, 1990, Fig. 9A) where 910 Hz produces a 12-dB decrease in a 1480-Hz probe when both are presented at the same sound pressure level. This case is similar to that in Fig. 6 where the fundamental at 800 Hz interferes with the second harmonic at 1600 Hz.

Support for the idea that the second harmonic exists mechanically at the input to the IHC comes from ac recordings in the OC fluid space. These measurements are known to reflect OHC receptor currents (Dallos and Cheatham, 1976) and to contain a mixture of nonlinear distortion components (Cody and Mountain, 1989; Dallos and Cheatham, 1990; Geisler *et al.*, 1990). This rich spectral content is not surprising given the nonlinear basilar membrane responses recorded from both the base and apex of the cochlea (Rhode, 1971; Sellick *et al.*, 1982; Nuttall and Dolan, 1996; Ruggero *et al.*, 1997; Cooper and Rhode, 1998). These results suggest that mechanical distortion is intimately related to the mechanisms responsible for frequency selectivity. Because tuning is broad at high input levels, multiple components can interact in complicated ways. In addition, the use of inputs below BF, allows energy at harmonic frequencies to be favorably influenced by the shape of the tuning curve so that the IHC can be more sensitive to higher harmonics than to the fundamental.

The current injection experiments of Cody and Mountain (1989) also suggest that double-peaked histograms reflect the harmonic content of the mechanical input to IHCs. Unfortunately, it is not known whether these results were affected by contributions from voltage-dependent channels in the IHC's basolateral membrane. For example, in the current injection experiments, introduction of a -1 nA current hyperpolarized the cell to -74 mV, a level where channels in the cell's basolateral membrane should be inactivated (Kros, 1996) as stated by Cody and Mountain. However, acoustic stimulation produced a large response, on the order of ~ 28 mV peak-to-peak. This suggests that during the combined electric and acoustic stimulation, the impedance change in the IHC could possibly reflect contributions from the apical transducer as well as from voltage-dependent channels in the cell's basolateral membrane. Consequently, additional experimental evidence is required to ascertain the origin of harmonic components recorded in the IHC responses that determine postsynaptic activity.

Data presented in Fig. 6 indicate that the second harmonic decreases and the third harmonic increases at high levels above the notch region. This may indicate that the set point of the IHC moves to a place along the transducer function where the slope is steeper, i.e., the cell depolarizes slightly. A shift in the set point would increase gain and favor the production of odd versus even harmonics. This possibility is consistent with the observation that responses for odd harmonics exceed those for evens and with the ob-

servation that the fundamental response above the notch is larger than that below (see also Figs. 10–12, Dallos and Cheatham, 1989b).

Finally, the presence of harmonics at the input to the IHC could influence the degree to which notches are observed in single unit, rate-intensity functions (Kiang, 1990). If harmonic components are present, then the fundamental could exhibit cancellation but the average voltage might not show a notch. This is because the harmonic components present mechanically at the input to the cell, are not canceled because they have no out-of-phase counterparts. In fact, if the fundamental is well below BF, then the harmonics at the input could produce a sizable IHC response simply because they are closer to BF. Figure 10(B) also implies that cancellation at the fundamental can enhance energy at harmonic frequencies in the region of the notch.

C. Speculations on the nature of components I and II

Available IHC and neural data suggest that response phase changes rapidly by nearly 180° at high levels as the dominant input to the IHC shifts from component I to II. Because the phase shift is not confined to inputs near BF, it is unlikely that it can be attributed to operation of the cochlear amplifier, i.e., to OHCs in the BF region. For similar reasons, a resonant tectorial membrane model (Zwislocki and Kletsky, 1979; Allen, 1980) is also inadequate to explain the phase shift because the postulated resonance is assumed to track the BF established by basilar membrane mechanics. Consequently, it is assumed that the low level response, i.e., component I, reflects a ter Kuile (1900)/Davis (1965) mechanism in which motion of the basilar membrane to SV results in deflection of inner and outer hair cell stereocilia in the excitatory direction away from the modiolus. This motion pattern is depicted in panel A of Fig. 11. In this schematic, it is assumed that the organ of Corti complex rotates about a pivot point at the osseous spiral lamina, i.e., at the foot of the inner pillar. Because the radial motion of the reticular lamina is toward the modiolus when the basilar membrane is displaced to SV, the bases of the stereocilia are displaced in this same direction. In contrast, the tectorial membrane does not exhibit significant radial movement (Hu *et al.*, 1998) or, at the very least, this movement is much less than the radial movement of the reticular lamina. In other words, the tectorial membrane movement, which is governed by the attached outer hair cell stereocilia, is predominately up and down. In panel B, for small basilar membrane movements to ST, the opposite displacement pattern occurs. In this case, when the basilar membrane moves down, the reticular lamina and the base of the hair bundle move radially toward the spiral ligament. Because the tectorial membrane simply moves down, the stereocilia are deflected in the inhibitory direction. Ciliary rotation occurs because of the direct attachment of the tallest OHC stereocilia to the tectorial membrane (Kimura, 1966) and the probable viscoelastic coupling of the IHC stereocilia (Billone and Raynor, 1973; Freeman and Weiss, 1990).

At high levels of stimulation, large basilar membrane displacements to ST result in a direct coupling between IHC stereocilia and the tectorial membrane at Hensen's stripe, as in panel C. It is possible that this exaggerated motion relates to the more linear behavior of basilar membrane mechanics below BF (Rhode, 1971; Sellick *et al.*, 1982; Nuttall and Dolan, 1996; Ruggero *et al.*, 1997). Because highly compressive responses are observed only at BF, responses below BF can be larger by as much as an order of magnitude. Again, it is assumed that downward displacements of the basilar membrane are associated with radial movements of the reticular lamina toward the spiral ligament and that any

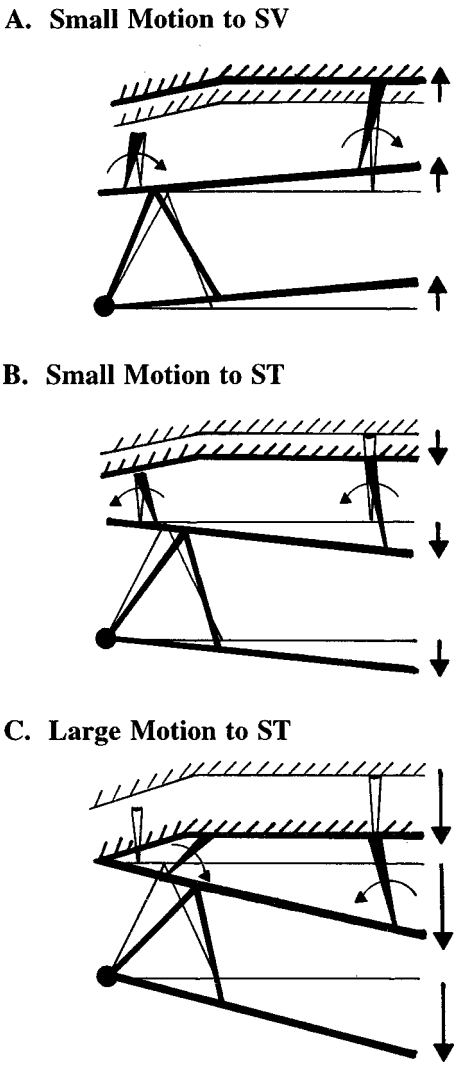

FIG. 11. In this geometrical model of the organ of Corti complex, the tunnel of Corti is represented as a triangle. The stylized cilium on the left is associated with an IHC, that on the right, with an OHC. Three horizontal lines denote the basilar membrane, the reticular lamina and the tectorial membrane, respectively. The latter is also crosshatched for emphasis. Panel A depicts small basilar membrane movement upward to SV; Panel B, small downward movement to ST. Large downward movement to ST is shown in panel C. In all panels, it is assumed that the organ pivots around the attachment point of the basilar membrane at the osseous spiral lamina. Thin lines and open cilia depict the position of the organ of Corti complex at rest while bold lines and filled cilia indicate changes in position for both large and small displacements of the basilar membrane. The direction of motion is indicated by the arrows. The predominate up and down movement of the tectorial membrane is driven by the attached outer hair cell stereocilia. The slanted portion of the tectorial membrane on the left represents Hensen's stripe. All displacements are grossly exaggerated for clarity and structures are not drawn to scale.

radial motion of the tectorial membrane is much less than that at the reticular lamina.

Panel C indicates that large movements of the basilar membrane to ST push the hair bundle of IHCs toward the spiral ligament due to the sideways forcing action of Hensen's stripe. This presumably depolarizes the cell and increases discharge rate at the single unit level. Outer hair cell and basilar membrane (Ruggero *et al.*, 1997) responses, however, do not change their response phase, consistent with the presumption that OHC stereocilia continue to be deflected in the inhibitory direction for large as well as small displacements to ST. In contrast to panels A and B, where ciliary motion for inner and outer hair cells is in the same direction, that in panel C is in opposing directions. In other words, large movements to ST are excitatory for IHCs; inhibitory for OHCs. The simple, geometrical model shown in Fig. 11 demonstrates that the phase shift associated with Nelson's Notch may relate to the possibility that a direct contact occurs between IHC stereocilia and the tectorial membrane at Hensen's stripe for high-level inputs. This hypothesis is reminiscent of Crane's IHC-TM connect–disconnect model (1983) of mechanical interactions within the organ of Corti complex. It is also consistent with Zwislocki's (1986) suggestion that Nelson's Notch is a reflection of nonlinear coupling between the tectorial membrane and the organ of Corti complex.

IV. CONCLUSION

The term peak splitting has sometimes been used to describe the near phase reversal and the notch in discharge rate observed in single unit responses at high stimulus levels. Hair cell data, however, suggest that this terminology is confusing. In fact, the results presented here indicate that the IHC correlates of the rapid phase shift and rate decrease are recorded in the fundamental component of the receptor potential. This implies that these features are not associated with harmonic distortion produced by the IHC transducer. The reason that double-peaked histograms are recorded in the notch region probably reflects cancellation at the fundamental with the result that an input at the second harmonic stimulates the IHC directly and drives transmitter release as suggested by the two-factor cancellation hypothesis (Liberman and Kiang, 1984; Kiang, 1990; Lin and Goldstein, 1995). Although the term peak splitting is appropriate when describing multiple-peaked histograms, it should not be used to describe interactions between the two excitatory processes that are thought to underlie the notch behavior. This is because peak splitting can occur at moderate levels as a result of distortion produced by the IHC transducer while the double-peaked histograms associated with Nelson's Notch probably reflect nonlinearities present at the input to the IHC transducer. In other words, a split peak is correlated with the rapid phase change but not necessarily causally related to it.

ACKNOWLEDGMENTS

Jonathan Siegel is acknowledged for suggesting that the notch behavior should be investigated in the average voltage recorded inside the IHC. We are also grateful to Gulam Emadi for providing the computer programming to accomplish this endeavor. This work was supported (in part) by research Grant No. 5 R01 DC00089 from the National Institute on Deafness and Other Communication Disorders, the National Institutes of Health.

APPENDIX

The simulations shown in Figs. 9 and 10 are based on the following model. Two inputs converge on a common transducer function, (F_2), representing the mechano-electric transduction process of the IHC. These two inputs are preferentially expressed at low (component I$=x_L$) and high (component II$=x_H$) levels. The low-level signal, assumed to contain significant second harmonic content, is expressed as

$$x_L = A\ \mathrm{Sin}(2\pi ft) + 0.25A^2\ \mathrm{Sin}(4\pi ft - \Phi). \tag{A1}$$

Notice that in this formulation, the second harmonic grows as the square of the amplitude. The high-level signal is represented as a simple sinusoid,

$$x_H = A\ \mathrm{Sin}(2\pi ft), \tag{A2}$$

where A is amplitude. Before appearing at the IHC transducer, this signal is weighted by a threshold function, F_1, where

$$F_1 = 2\left(\frac{1}{1+\exp[-15(x_H-0.85)]} - \frac{1}{1+\exp[12.75]}\right). \tag{A3}$$

In the argument of the transducer function, F_2, the two input signals, x_L and $F_1 x_H$, are subtracted such that

$$x = x_L - F_1 x_H. \tag{A4}$$

The expression for the IHC transducer function, F_2, is

$$F_2 = -\left(\frac{1}{1+\exp[10(x-0.15)]} - \frac{1}{1+\exp[-1.5]}\right). \tag{A5}$$

The schematic in Fig. 9 incorporates the $F_1(x_H)$ and $F_2(x)$ functions as computed from the above expressions. The functions plotted with solid lines on the right-hand-side of Fig. 9 are obtained with numerical values of $\Phi = \pi/2$ and amplitude $A = 0.3$ in panel A, $A = 0.72$ in panel B, and $A = 0.82$ in panel C.

Allen, J. B. (**1980**). ''Cochlear micromechanics—A physical model of transduction,'' J. Acoust. Soc. Am. **68**, 1660–1670.

Allen, J. B. (**1983**). ''A hair cell model of neural response,'' in *Mechanics of Hearing*, edited by E. de Boer and M. A. Viergever (Delft U.P., Delft, The Netherlands), pp. 193–202.

Anderson, D. J., Rose, J. E., Hind, J. E., and Brugge, J. F. (**1971**). ''Temporal position of discharges in single auditory nerve fibers within the cycle of a sine-wave stimulus: Frequency and intensity effects,'' J. Acoust. Soc. Am. **49**, 1131–1139.

Billone, M., and Raynor, S. (**1973**). ''Transmission of radial shear forces to cochlear hair cells,'' J. Acoust. Soc. Am. **54**, 1143–1156.

Bode, H. (**1945**). *Network Analysis and Feedback Amplifier Design* (van Nostrand, New York).

Cai, Y., and Geisler, C. D. (**1996**). ''Temporal patterns of the responses of auditory-nerve fibers to low-frequency tones,'' Hearing Res. **96**, 83–93.

Cheatham, M. A., and Dallos, P. (**1989**). ''Two-tone suppression in inner hair responses,'' Hearing Res. **40**, 187–196.

Cheatham, M. A., and Dallos, P. (**1990**). ''Comparison of low- and high-side two-tone suppression in inner hair cell and organ of Corti responses,'' Hearing Res. **50**, 193–210.
Cheatham, M. A., and Dallos, P. (**1993**). ''Longitudinal comparisons of IHC ac and dc receptor potentials recorded from the guinea pig cochlea,'' Hearing Res. **68**, 107–114.
Cody, A. R., and Mountain, D. C. (**1989**). ''Low-frequency responses of inner hair cells: evidence for a mechanical origin of peak splitting,'' Hearing Res. **41**, 89–99.
Cooper, N. P., and Rhode, W. S. (**1998**). ''Apical cochlear mechanics: a review of recent observations,'' in *Psychophysical and Physiological Advances in Hearing*, edited by A. R. Palmer, A. Rees, A. Q. Summerfield, and R. Meddis (Whurr, London), pp. 11–18.
Crane, H. D. (**1983**). ''IHC-TM connect-disconnect and mechanical interaction among IHCs, OHCs, and TM,'' in *Hearing Research and Theory, Vol. 2* (Academic, New York), pp. 125–171.
Dallos, P. (**1973**). *The Auditory Periphery* (Academic, New York).
Dallos, P. (**1985**). ''Response characteristics of mammalian cochlear hair cells,'' J. Neurosci. **5**, 1591–1608.
Dallos, P. (**1986**). ''Neurobiology of cochlear inner and outer hair cells: Intracellular recordings,'' Hearing Res. **22**, 185–198.
Dallos, P., and Cheatham, M. A. (**1976**). ''Production of cochlear potentials by inner and outer hair cells,'' J. Acoust. Soc. Am. **60**, 510–512 (L).
Dallos, P., and Santos-Sacchi, J. (**1983**). ''Ac receptor potentials from hair cells in the low-frequency region of the guinea pig cochlea,'' in *Mechanisms of Hearing*, edited by W. R. Webster and L. M. Aitkin (Monash U.P., Clayton, Australia), pp. 11–16.
Dallos, P., and Cheatham, M. A. (**1989a**). ''Cochlear nonlinearities reflected in inner hair cell responses,'' in *Mechanics of Hearing*, edited by D. T. Kemp and J. P. Wilson (Plenum, London), pp. 197–204.
Dallos, P., and Cheatham, M. A. (**1989b**). ''Nonlinearities in cochlear receptor potentials and their origins,'' J. Acoust. Soc. Am. **86**, 1790–1796.
Dallos, P., and Cheatham, M. A. (**1990**). ''Effects of electrical polarization on inner hair cell receptor potentials,'' J. Acoust. Soc. Am. **87**, 1636–1647.
Dallos, P., Schoeny, Z. G., and Cheatham, M. A. (**1971**). ''On the limitations of cochlear-microphonic measurements,'' J. Acoust. Soc. Am. **49**, 1144–1154.
Dallos, P., Billone, M. C., Durrant, J. D., Wang, C.-y., and Raynor, S. (**1972**). ''Cochlear inner and outer hair cells: Functional differences,'' Science **177**, 356–358.
Dallos, P., Santos-Sacchi, J., and Flock, Å. (**1982**). ''Intracellular recordings from cochlear outer hair cells,'' Science **218**, 582–584.
Dallos, P., Oesterle, E., and Cheatham, M. A. (**1986**). ''Harmonic components in hair cell responses,'' in *Auditory Frequency Selectivity*, edited by B. C. J. Moore and R. D. Patterson (Plenum, London), pp. 73–80.
Davis, H. (**1965**). ''A model for transduction action in the cochlea,'' in *Cold Spring Harbor Symposium on Quantitative Biology*, edited by L. Frisch (Cold Spring Harbor Laboratory, Cold Spring, NY), Vol. 30, pp. 181–190.
Engebretson, A. M., and Eldredge, D. H. (**1968**). ''Model for the nonlinear characteristics of cochlear potentials,'' J. Acoust. Soc. Am. **44**, 548–554.
Flock, Å. (**1971**). ''Sensory transduction in hair cells,'' in *Handbook of Sensory Physiology, Volume I*, edited by W. R. Loewenstein (Springer-Verlag, New York), pp. 396–441.
Freeman, D. M., and Weiss, T. F. (**1990**). ''Hydrodynamic forces on hair bundles at high frequencies,'' Hearing Res. **48**, 31–36.
Geisler, C. D., and Rhode, W. S. (**1982**). ''The phases of basilar-membrane vibrations,'' J. Acoust. Soc. Am. **71**, 1201–1203.
Geisler, C. D., Yates, G. K., Patuzzi, R. B., and Johnstone, B. M. (**1990**). ''Saturation of outer hair cell receptor currents causes two-tone suppression,'' Hearing Res. **44**, 241–256.
Gifford, M. L., and Guinan, Jr., J. J. (**1983**). ''Effects of crossed-olivocochlear bundle stimulation on cat auditory nerve fiber responses to tones,'' J. Acoust. Soc. Am. **74**, 115–123.
Goodman, D. A., Smith, R. L., and Chamberlain, S. C. (**1982**). ''Intracellular and extracellular responses in the organ of Corti of the gerbil,'' Hearing Res. **7**, 161–179.
Hu, X., Evans, B. N., and Dallos, P. (**1998**). ''Direct visualization of organ of Corti kinematics in a hemicochlea,'' J. Neurophysiol. (submitted).
Hunter-Duvar, I. (**1978**). ''Electron microscopic assessment of the cochlea,'' Acta Oto-Laryngol. **351**, 1–44.
Johnson, D. H. (**1974**). ''The response of single auditory-nerve fibers in the cat to single tones: Synchrony and average discharge rate,'' Ph. D. Thesis, Massachusetts Institute of Technology, Cambridge, MA.
Johnson, D. H. (**1980**). ''The relationship between spike rate and synchrony in responses of auditory-nerve fibers to single tones,'' J. Acoust. Soc. Am. **68**, 1115–1122.
Kiang, N. Y.-s. (**1990**). ''Curious oddments of auditory-nerve studies,'' Hearing Res. **49**, 1–6.
Kiang, N. Y.-s., and Moxon, E. C. (**1972**). ''Physiological considerations in artificial stimulation of the inner ear,'' Ann. Otol. Rhinol. Laryngol. **81**, 714–730.
Kiang, N. Y.-s., Baer, T., Marr, E. M., and Demont, D. (**1969**). ''Discharge patterns of single auditory-nerve fibers as functions of tone level,'' J. Acoust. Soc. Am. **46**, 106A.
Kiang, N. Y.-s., Liberman, M. C., Sewell, W. F., and Guinan, Jr., J. J. (**1986**). ''Single unit clues to cochlear mechanisms,'' Hearing Res. **22**, 171–182.
Kimura, R. S. (**1966**). ''Hairs of the cochlear sensory cells and their attachment to the tectorial membrane,'' Acta Oto-Laryngol. **61**, 55–72.
Kössl, M., and Russell, I. J. (**1992**). ''The phase and magnitude of hair cell receptor potentials and frequency tuning in the guinea pig cochlea,'' J. Neurosci. **12**, 1575–1586.
Kros, C. J. (**1996**). ''Physiology of mammalian cochlear hair cells,'' in *The Cochlea*, edited by P. Dallos, A. N. Popper, and R. R. Fay (Springer-Verlag, New York), pp. 318–385.
Kuile, E. ter (**1900**). ''Die übertragung der energie von der grundmembran auf die haarzellen,'' Pflugers Arch. Ges. Physiol. Menschen Tiere **79**, 146–157.
Le Page, E. L. (**1987**). ''Frequency-dependent self-induced bias of the basilar membrane and its potential for controlling sensitivity and tuning of the mammalian cochlea,'' J. Acoust. Soc. Am. **82**, 139–154.
Liberman, M. C., and Kiang, N. Y.-s. (**1984**). ''Single neuron labelling and chronic cochlear pathology. IV. Stereocilia damage and alterations in rate- and level-functions,'' Hearing Res. **16**, 75–90.
Lim, D. J. (**1972**). ''Fine morphology of the tectorial membrane: Its relationship to the organ of Corti,'' Acta Oto-Laryngol. **96**, 199–215.
Lin, T., and Goldstein, J. L. (**1995**). ''Quantifying 2-factor phase relations in nonlinear responses from low characteristic-frequency auditory-nerve fibers,'' Hearing Res. **90**, 126–138.
McGee, J., Walsh, E. J., Gorga, M. P., Farley, G. R., and Javel, E. (**1982**). ''Population study of nonmonotonic response-intensity curves in auditory nerve fibers,'' J. Acoust. Soc. Am. Suppl. 1 **71**, S18.
Nuttall, A. L., and Dolan, D. F. (**1996**). ''Steady-state sinusoidal velocity responses of the basilar membrane in guinea pig,'' J. Acoust. Soc. Am. **99**, 1556–1565.
Nuttall, A. L., Brown, M. C., Masta, R. I., and Lawrence, M. (**1981**). ''Inner hair cell responses to velocity of basilar membrane motion in the guinea pig,'' Brain Res. **211**, 171–174.
Patuzzi, R. B., and Sellick, P. M. (**1983**). ''A comparison between basilar membrane and inner hair cell receptor potential input–output functions in the guinea pig cochlea,'' J. Acoust. Soc. Am. **74**, 1731–1741.
Patuzzi, R. B., and Yates, G. K. (**1987**). ''The low-frequency response of inner hair cells in the guinea pig cochlea: Implications for fluid coupling and resonance of the stereocilia,'' Hearing Res. **30**, 83–98.
Rhode, W. S. (**1971**). ''Observations of the vibration of the basilar membrane in squirrel monkey using the Mössbauer technique,'' J. Acoust. Soc. Am. **49**, 1218–1231.
Rhode, W. S., and Robles, L. (**1974**). ''Evidence from Mössbauer experiments for nonlinear vibration in the cochlea,'' J. Acoust. Soc. Am. **55**, 588–596.
Ruggero, M. A., and Rich, N. C. (**1983**). ''Chinchilla auditory-nerve responses to low frequency tones,'' J. Acoust. Soc. Am. **73**, 2096–2108.
Ruggero, M. A., and Rich, N. C. (**1987**). ''Timing of spike initiation in cochlear afferents: Dependence on site of innervation,'' J. Neurophysiol. **58**, 379–403.
Ruggero, M. A., and Rich, N. C. (**1989**). ''Peak-splitting: Intensity effects in cochlear afferent responses to low frequency tones,'' in *Cochlear Mechanisms—Structure, Function and Models*, edited by J. P. Wilson and D. T. Kemp (Plenum, London), pp. 259–266.
Ruggero, M. A., Robles, L., and Rich, N. C. (**1986**). ''Basilar membrane mechanics at the base of the chinchilla cochlea. II. Responses to low-frequency tones and relationship to microphonics and spike initiation in the VIII-nerve,'' J. Acoust. Soc. Am. **80**, 1375–1383.
Ruggero, M. A., Rich, N. C., and Robles, L. (**1991**). ''Comparison of cochlear-nerve and basilar-membrane responses to low-frequency tones: Absence of macromechanical basis for ''peak splitting,'' Abs. Assoc. Res. Otolaryngol. p. 78.

Ruggero, M. A., Rich, N. C., Shivapuja, B. G., and Temchin, A. N. (**1996**). ''Auditory-nerve responses to low-frequency tones: Intensity dependence,'' Aud. Neurosci. **2**, 159–185.
Ruggero, M. A., Rich, N. C., Recio, A., Narayan, S. S., and Robles, L. (**1997**). ''Basilar-membrane responses to tones at the base of the chinchilla cochlea,'' J. Acoust. Soc. Am. **101**, 2151–2163.
Russell, I. J., and Ashmore, J. F. (**1983**). ''Inner hair cell receptor potentials investigated during transient asphyxia: A model for hair cell coupling,'' in *Hearing—Physiological Bases and Psychophysics*, edited by R. Kinke and R. Hartmann (Springer-Verlag, Berlin), pp. 10–16.
Russell, I. J., and Cody, A. R. (**1985**). ''Transduction in cochlear hair cells,'' in *Peripheral Auditory Mechanisms*, edited by J. B. Allen, J. L. Hall, A. Hubbard, S. T. Neely, and A. Tubis (Springer-Verlag, New York), pp. 349–360.
Russell, I. J., and Kössl, M. (**1992**). ''Modulation of hair cell voltage responses to tones by low frequency biasing of the basilar membrane in the guinea pig cochlea,'' J. Neurosci. **12**, 1587–1601.
Russell, I. J., and Sellick, P. M. (**1983**). ''Low-frequency characteristics of intracellularly recorded receptor-potentials in guinea-pig cochlear hair cells,'' J. Physiol. (London) **338**, 179–206.
Sellick, P. M., and Russell, I. J. (**1980**). ''Responses of inner hair cells to basilar membrane velocity during low frequency auditory stimulation in the guinea pig cochlea,'' Hearing Res. **2**, 439–446.
Sellick, P. M., Patuzzi, R., and Johnstone, B. M. (**1982**). ''Measurement of basilar membrane motion in the guinea pig using the Mössbauer,'' J. Acoust. Soc. Am. **72**, 131–141.
Viemeister, N. F. (**1988**). ''Intensity coding and the dynamic range problem,'' Hearing Res. **34**, 267–274.
Weiss, T. F., Peake, W. T., and Sohmer, H. S. (**1969**). ''Intra-cochlear responses to tones,'' Massachusetts Institute of Technology Quarterly Progress Report **94**, 305–316.
Zwislocki, J. J. (**1986**). ''Are nonlinearities observed in firing rates of auditory-nerve afferents reflections of a nonlinear coupling between the tectorial membrane and the organ of Corti?,'' Hearing Res. **22**, 217–211.
Zwislocki, J. J. (**1990**). ''Active cochlear feedback: Required structure and response phase,'' in *The Mechanics and Biophysics of Hearing*, edited by P. Dallos, C. D. Geisler, J. W. Matthews, M. A. Ruggero, and C. R. Steele (Springer-Verlag, New York), pp. 114–120.
Zwislocki, J. J., and Kletsky, E. J. (**1979**). ''Tectorial membrane: A possible effect on frequency analysis in the cochlea,'' Science **204**, 639–641.
Zwislocki, J. J., and Smith, R. L. (**1989**). ''Phase reversal in outer hair cell responses at high sound intensities,'' in *Cochlear Mechanics: Structure, Function and Models*, edited by J. P. Wilson and D. T. Kemp (Plenum, London), pp. 163–168.

Are inner or outer hair cells the source of summating potentials recorded from the round window?

John D. Durrant[a)]
Departments of Communication Science & Disorders and Otolaryngology, University of Pittsburgh, Pittsburgh, Pennsylvania 15260

Jian Wang, D. L. Ding, and Richard J. Salvi
Hearing Research Laboratory, State University of New York at Buffalo, Buffalo, New York 14214

(Received 19 September 1997; revised 18 March 1998; accepted 20 March 1998)

The relative contribution of inner hair cells (IHCs) and outer hair cells (OHCs) to the production of the summating potential (SP) is unresolved in the literature. Since OHCs in the base of the cochlea have been reported to produce little dc receptor potential except at very high sound pressure levels [I. J. Russell and P. M. Sellick, J. Physiol (London) **284**, 261–290 (1983)], the IHCs appear to be the dominant source of the SP. However, results of intracochlear recordings are conflicting, although deriving from measurements in different turns of the cochlea [e.g., I. J. Russell and P. M. Sellick, J. Physiol. (London) **284**, 261–290 (1983) versus P. Dallos and M. A. Cheatham, *Sensory Transduction* (1992)]. To determine which type of hair cells is the dominant source of the SP recorded at the round window, we used carboplatin to selectively destroy IHCs or a combination of IHCs and OHCs in the chinchilla. Related work, using measurements of distortion product otoacoustic emissions and cochlear potentials to assess the functional status of the OHCs served to validate this animal model [Trautwein *et al.*, Hearing Res. **96**(1-2), 71–82 (1996)]. The SP, cochlear microphonic (CM), and compound action potential (CAP) were recorded from the round window, and cochleograms were determined using well-established histological methods. The results were reasonably distinctive among three groups of ears—control (from untreated normal chinchillas), IHC–loss (extensive IHC loss with minor or no loss of OHCs), and IHC–OHC loss (total IHC loss plus extensive loss of OHCs over the basal half of the cochlea). Ears of chinchillas in the IHC loss group had a decrease of over 50% in SP output compared to control ears with the exact reduction depending somewhat upon the stimulus conditions. Ears in the IHC+OHC loss group, nevertheless, showed even further reduction in SP output which was clearly attributable to destruction of OHCs in the cochlear base. It was concluded that, although the IHCs are responsible for a greater contribution of dc-receptor potential to the SP recorded at the round window, a significant contribution is made by the OHCs, as well. The results suggest, specifically, that the round window ''sees'' SP output roughly in inverse proportion to the IHC:OHC. Lastly, the complexity of SP production, as recorded from the round window, precludes a completely straightforward interpretation of the SP:CAP in clinical ECochG. © *1998 Acoustical Society of America.* [S0001-4966(98)01507-0]

PACS numbers: 43.64.Ld, 43.64.Jb, 43.64.Nf [RDF]

INTRODUCTION

The objective of this investigation was to shed light on a long-standing question in the field of electrocochleography (ECochG)—which receptors, inner hair cells (IHCs) or outer hair cells (OHCs), are the source of the summating potential (SP)? In research, the round-window site is often used to record the SP and cochlear microphonic (CM) since it minimizes damage to the cochlea and the technique is well suited for recordings via permanent in-dwelling electrodes (i.e., for repeated measurements in unanesthetized animals). Clinical recordings, although made from more remote sites (e.g., promontory or tympanic membrane) presumably derive from the round window.[1] Consequently, this question also has direct clinical relevance since the SP is valued in the differential diagnosis of Meniere's disease. The SP and CM recorded from the round window, however, are heavily weighted toward the base of the cochlea (Dallos, 1973). Furthermore, the gross CM is generated primarily by OHCs (Dallos and Wang, 1974). Since basal turn OHCs have been reported to produce little dc receptor potential (Cody and Russell, 1985; Russell and Sellick, 1983), it is unclear how they could equally contribute to the SP. These results suggest basal-turn IHCs to be the dominant source of the SP recorded at the round window.

Researchers, however, have vacillated as to whether IHCs or OHCs are primarily responsible for the SP in general. Davis and his co-workers (1958a, b) first suggested that the IHCs produce SP− and the OHCs produce SP+. In their scheme, SP− refers to the potential recorded in scala vestibuli or scala media when the stimulus is near the best frequency of the recording site. In scala tympani and on the round window, this potential is manifested as SP+ (Dallos, 1973). On the basis of hair-cell lesion studies with strepto-

a)Electronic mail: durrant@csd.upmc.edu

mycin, Davis and his colleagues (1958b) concluded that the IHCs are the dominant source of the SP.

Johnstone and Johnstone (1966), using a nonlinear model of hair-cell transduction, attributed the SP to dc distortion generated by IHCs and OHCs. In contrast to Davis, they suggested that the OHCs were responsible for the SP− recorded in scala vestibuli (or SP+ when recorded in scala tympani or from the round window). This two-polarity model ultimately was shown to conflict with results of intracellular recordings of dc-receptor potentials from cochlear hair cells (Russell and Sellick, 1983; Sellick and Russell, 1979; discussed below).

In critically assessing all available SP research at the time and relying extensively upon his own observations, Dallos (1973) proposed the OHCs as the primary generators of SP. His hypothesis was based on unpublished work with Goran Bredberg in which they destroyed hair cells in the guinea pig with kanamycin. Both polarities of the differentially recorded SP appeared to be correlated strongly with OHC damage, but the SP only weakly reflected the status of the IHCs. The CM input–output functions recorded in the basal turn of animals with selective OHC loss showed a 30-dB loss in sensitivity. The SP input–output function showed a comparable shift along the SPL axis; however, the slopes of the functions were steeper than normal. Consequently, the maximum SP output was not shifted as dramatically as the reduction in sensitivity. Dallos suggested that, beyond 100 dB SPL, the IHCs would begin to contribute significantly, but at more moderate levels of stimulation ''the outer hair cells produce the overwhelming amount of summating potential just as they produce the overwhelming amount of cochlear microphonic'' (Dallos, 1973, p. 375). Dallos and Cheatham (1976) provided further support for the dominance of the OHCs. When recorded in the apex of the guinea pig cochlea, SP output was found to be essentially unchanged with complete destruction of IHCs by kanamycin. Thus, Davis and Dallos arrived at opposite conclusions regarding the source of the SP.

There has yet to be published a peer-reviewed report directly corroborating or refuting either Davis' or Dallos' models. Nevertheless, there have been investigations which have direct bearing on this issue. In attempting to account for two-tone suppression, Geisler and his associates (1990) suggested that nonlinear electromechanical transduction resulted in interference with OHC receptor currents that lead to the suppression of the extracellular SP. This model assumes that the OHCs make a substantive contribution to production of the SP. Fujita (1990), investigating a strain of golden hamsters with abnormally oriented stereocilia on first row OHCs, reported that the SP and auditory brain-stem response (ABR) were normal, but the CM and AP were significantly reduced. These results suggest that, at least, first row OHCs make little contribution to the SP. Harvey and Steel (1992) characterized the round-window-recorded SP in the developing mouse. They suggested that IHCs in the base of the cochlea were the generators of the ''fast'' component of SP+ whereas both IHCs and OHCs seemed to contribute to the ''slow'' SP+ component. They attributed the SP− to the recruitment of more apical generators with increasing sound intensity. Klis and Rebillard (1995), finally, examined SPs and distortion product otoacoustic emissions (namely DPOAEs at $2f1\text{-}f2$) after intracochlear perfusion with ouabain. The DPOAEs at 6.6 and 8 kHz were markedly reduced while SP at 4 or 8 kHz exhibited only modest reduction. Of course, DPOAEs are assumed to be generated by the OHCs. They concluded that the two measures do not arise from the same nonlinear processes.

Intracellular hair-cell recordings have provided a critical link between unit dc-receptor potentials and the SP (i.e., a gross extracellular potential, as traditionally defined and conventionally recorded), so the results of this kind of study also are germane. Russell and Sellick's (1983) recordings in the base of the cochlea revealed a relatively large dc potential in IHCs at low-to-moderate intensities. A dc potential could be recorded only from OHCs at relatively high intensities. However, more recent intracellular recordings from hair cells in the apical three coils of the guinea pig cochlea in Dallos' laboratory (Dallos and Cheatham, 1992; Cheatham, 1993) indicate that a substantial dc receptor potential can be measured in both IHCs and OHCs over a wide dynamic range. Since there are over three times as many OHCs as IHCs, the OHCs would appear to be the predominant SP generator, as Dallos (1973) had contended earlier.

Recently, an animal model has been described which offers a unique opportunity to test the specific contribution of IHCs to the production of the SP (Takeno *et al.*, 1994; Wake *et al.*, 1993, 1994). Using moderate doses of carboplatin, it is possible to selectively destroy almost all of the IHCs in chinchillas while retaining nearly a full complement of functional OHCs (Trautwein *et al.*, 1996; Hofstetter *et al.*, 1997a, b). With higher doses of carboplatin, it is possible to destroy progressively both IHCs and OHCs. We used this animal model to test which theory of generation of the SP, at least as recorded at the round window, is correct.

I. METHODS

A. Subjects

Normal, healthy chinchillas 1–2 years of age and weighing between 350 and 600 g were used as subjects. Two groups of animals were studied—the control group and the experimental or treated group. The control group comprised 15 chinchillas untreated and free of middle ear disease. The experimental group consisted of animals who were part of a larger investigation designed to investigate the functional impact of carboplatin-induced hair cell lesions (Hofstetter *et al.*, 1997a, b; Wang *et al.*, 1997) but in whom the SP was the focus. For 22 ears of the carboplatin-treated animals complete data sets–SP input–output functions measured at multiple frequencies and cytocochleograms—were available. Animals in the experimental group were treated with one of four doses of carboplatin (Bristol Myers-Squibb) administered intraperitoneal, as follows:

38 mg/kg, single dose, $n=1$ ear,

63 mg/kg, double dose*, $n=6$ ears,

75 mg/kg, double dose*, $n=8$ ears,

100 mg/kg, double dose*, $n=7$ ears (*24 h between doses).

These doses were chosen based upon previous experience. The lower (total) doses above were observed to be capable of destroying selectively approximately 25%–30% of the IHCs, whereas the higher doses destroyed nearly all of the IHCs plus a substantial proportion of the OHCs in the basal half of the cochlea (Hofstetter *et al.*, 1997a). However, other relevant data, including some observations that have been reported previously (Trautwein *et al.*, 1996), are described below to put the current results into perspective. Procedures for all measurements reported are summarized in the subsections to follow.

B. Otoacoustic emission analysis

Although not of primary interest in this project, DPOAE measurements were incorporated in earlier validation studies. Briefly, DPOAEs were recorded in awake chinchillas using a low-noise microphone (Etymotic ER10B) coupled to two earphones (Etymotic ER2), before and >1.5 months following carboplatin treatment. The primary tones, $f1$ and $f2$, were presented at a $f2/f1$ ratio of 1.2. The level of the primaries, $L1$ and $L2$, were equal and varied from 0–80 dB in 5-dB steps.

C. Electrophysiology

Chinchillas were anesthetized using sodium pentobarbital (40 mg/kg, i.p., supplemental doses given as needed to maintain an areflexive state), tracheotomized, mounted in a head holder, and maintained at 37 °C body temperature with a heating pad (Trautwein *et al.*, 1996; Wang *et al.*, 1997). The middle ear was opened, and a silver ball electrode was placed on the round window and cemented into place. A second electrode was placed in the neck muscles and served as ground. The pickup of the round window electrode was amplified ($5000–10\,000\times$) and filtered to measure the SP (1–100 Hz), CM (100–30 000 Hz), and compound action potential (CAP; 100–3000 Hz). The output of the recording amplifier was delivered in parallel to an oscilloscope and an analog-to-digital converter (16 bits) on a signal processing board (Spectrum Signal Processing TMS320C25) mounted in the back plane of a personal computer. The output of the recording amplifier was digitized (50 kHz, 50 ms for SP, 30 ms for CM, and 10 ms for CAP), averaged ($N=100$), and stored on disk for later analysis. The SP magnitude was calculated as the voltage difference between the prestimulus baseline and the maximum dc voltage between 10 and 30 ms after stimulus onset. The CM amplitude was measured as the maximum peak-to-peak voltage at 10–20 ms after stimulus onset. Lastly, the CAP magnitude was measured between the peak of $N1$ and the prestimulus baseline.

Acoustic signals were digitally synthesized (16-bit D/A converter, 100 kHz), low-pass filtered (20 000 Hz), and led to a computer-controlled attenuator (127.5-dB range, 0.5-dB step) followed by a power amplifier and sound transducer (Etymotic ER2 mounted in a brass ear piece). A probe tube microphone (Etymotic ER7) was used to calibrate the sound pressure level near the tympanic membrane. Short-duration tone bursts with alternating phase (1-ms rise–fall time, cosine ramp, 2 ms duration, 20/s) were used to measure the CAP input/output functions at 0.25, 0.5, 1, 2, 4, and 8 kHz. Long-duration tone bursts were used to measure input–output functions of the CM (1-ms rise–fall time, cosine ramp, 20-ms duration, 10/s, constant starting phase) and SP (1-ms rise–fall time, 40-ms duration, 10/s, alternating starting phase).

D. Histology

Cytocochleograms were determined via histological procedures routinely employed in the Auditory Research Laboratory at SUNY Buffalo, as described by Hofstetter *et al.* (1997b). Briefly, at the end of the physiological experiments, the anesthetized animals were perfused intracardially with saline (phosphate buffer pH 7.4 at 37 °C), followed by 2.5% glutaraldehyde in veronal acetate buffer. Each bulla was quickly removed and opened. The stapes was removed, the round window was opened, and 2.5% glutaraldehyde in veronal acetate buffer (pH 7.2) was perfused through the round window. The cochleae were stored overnight in the fixative. Some cochleae were subsequently postfixed and stained with osmium tetroxide and then dehydrated through a graded series of ethanol with a final concentration of 70%. The remaining cochleae were perfused with Ehrlich's haemotoxylin solution and then immersed in the same solution for 5 min at room temperature. If the staining was too dark, the cochleae were differentiated with 0.5% hydrochloric acid, then washed with distilled water for 15 min. The bone surrounding each cochlea was removed, and the organ of Corti was carefully dissected out in half turns and mounted in glycerin on glass slides. The sensory epithelium was viewed with a differential interference contrast microscope (Zeiss Standard, $400\times$), and the number of missing IHCs and OHCs were counted over 0.24-mm intervals along the entire length of the basilar membrane. Sensory cells were counted as present if the cell body and the cuticular plate were present. Cytocochleograms, *per se*, were obtained by plotting the percent IHC and OHC loss as a function of percent total distance from the apex of the cochlea. Cochlear position was transformed to frequency using a frequency-place map (Greenwood, 1990). (This research was approved by the Institutional Animal Care and Use Committee at SUNY Buffalo and carried out in accordance with NIH guidelines.)

E. DPOAE, CM, and CAP—Effects of hair cell lesions

Although the preparation was described previously (Trautwein *et al.*, 1996), it is worthwhile to summarize the typical histological findings and functional effects, as manifested by the OAE, CM, and CAP. The highly selective nature of the IHC lesions is illustrated by the cytocochleogram in Fig. 1. In this case, nearly all of the IHCs are missing throughout the cochlea while most of the OHCs are present. The pattern of hair cell loss is typical of that seen with low-to-moderate doses of carboplatin (38–125 mg/kg total dose). All of the IHC lesions in the present study exceeded 72% loss, except for one animal with an IHC lesion of 36%. Figure 2 shows the precarboplatin and postcarboplatin DPOAE input/output functions at 8 kHz for the animal whose coch-

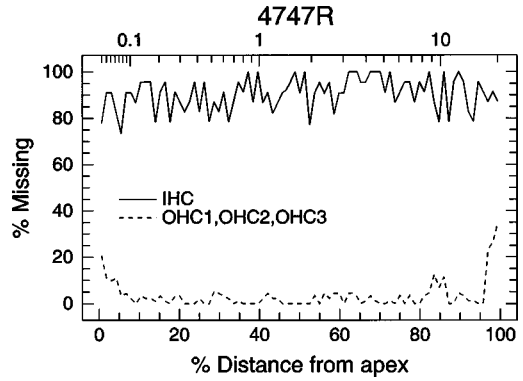

FIG. 1. Cytocochleogram from a carboplatin treated chinchilla (75 mg/kg, 2×i.p.) that developed massive IHC loss, but little OHC loss—percent OHC and IHC loss as a function of percent distance from the apex of the cochlea. Cochlear frequency-place map shown on top axis (Greenwood, 1990).

leogram is shown in Fig. 1. Identification of seemingly intact OHCs histologically, of course, does not assure functional integrity, but the DPOAE input/output functions are completely normal in the face of massive IHC loss. As reported previously, animals with massive IHC loss (~80%–90%) and minor OHC loss (~5%–20% loss) also show a significant reduction in CAP magnitude (Fig. 3); however, CM amplitudes are nearly normal (Fig. 4).

The magnitude of the hair cell lesion increased with carboplatin dose, as noted above (Trautwein *et al.*, 1996; Hofstetter *et al.*, 1997a). Increasing doses of carboplatin (150–200 mg/kg, total dose) not only caused massive IHC loss throughout the cochlea, but often resulted in substantial OHC loss (i.e., over 20%). In general, the hair cell lesions tended to decrease along a base-to-apex gradient, an effect that was more evident in the pattern of OHC loss in our treated ears. Figure 5 shows one case in which there was a nearly total loss of IHCs plus extensive loss of OHCs over the basal two-thirds of the cochlea. Figure 6 shows the precarboplatin and postcarboplatin DPOAE input/output functions at 8 kHz for the animal whose cochleogram is shown in Fig. 5. The postcarboplatin DPOAEs were undetectable; the measured

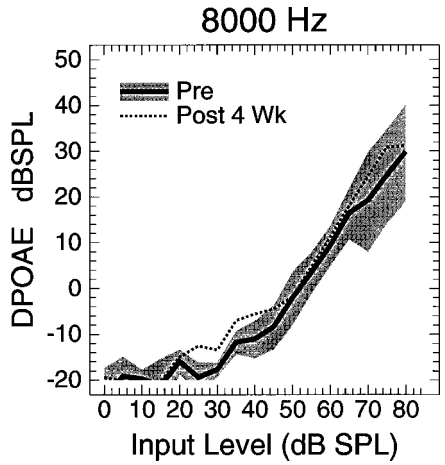

FIG. 2. Mean ($n=4$) precarboplatin (shaded area shows 95% confidence interval) and postcarboplatin DPOAE input/output functions at 8 kHz from the animal whose cochleogram is shown in Fig. 1.

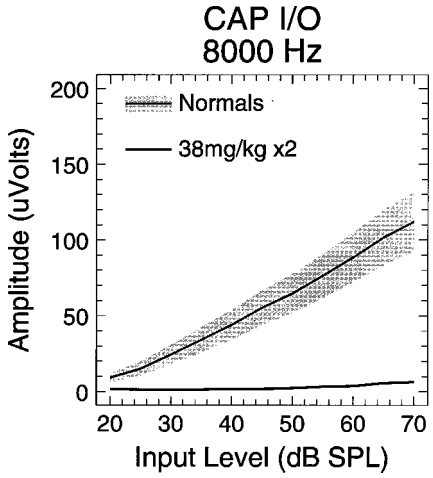

FIG. 3. Average CAP input/output functions at 8 kHz from normal control animals and a group of carboplatin-treated chinchillas that developed massive IHC loss, but minimal OHC loss. Shaded area shows 95% confidence interval around the mean values of controls [adapted from Trautwein *et al.* (1996)].

values were at the noise floor of the measurement system. Complete OHC loss in the basal half of the cochlea thus eliminated the high-frequency DPOAEs. However, low-frequency DPOAEs were almost normal since most of the OHCs were present in the apical half of the cochlea. In addition (not shown), the CAP was eliminated, and the CM was reduced significantly, following the results of Trautwein *et al.* (1996).

II. RESULTS

Inspection of the data from ears of animals in the experimental group suggested a dichotomy of SP findings according to whether or not the OHCs were essentially intact over the basal 40% of the cochlea. The OHCs were considered to be ostensibly intact if there was less than 20% loss. There were 14 ears meeting this criterion but demonstrating essentially total loss of IHCs throughout the cochlea. Consequently, this subgroup is referred to as the IHC loss group.

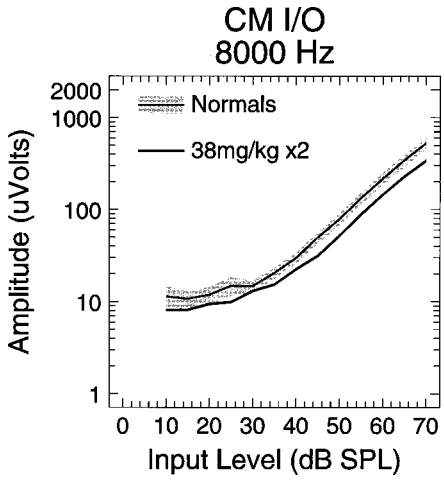

FIG. 4. The CM input/output functions at 8 kHz from normal control animals and the group of carboplatin-treated chinchillas shown in Fig. 3. Shaded area shows 95% confidence interval around mean values of controls [adapted from Trautwein *et al.* (1996)].

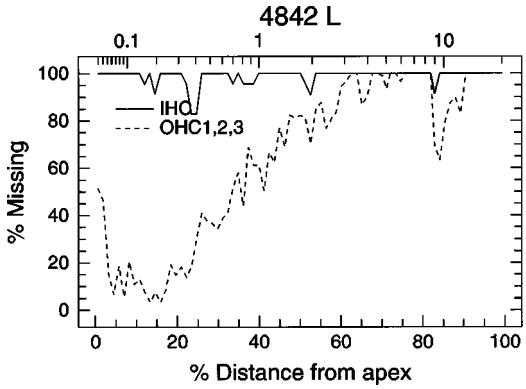

FIG. 5. Cytocochleogram from a carboplatin treated chinchilla (100 mg/kg, 2×, i.p.) that developed massive IHC loss and significant OHC loss over the basal two-thirds of the cochlea. Percent OHC and IHC loss as a function of percent distance from the apex of the cochlea. Cochlear frequency-place map shown on top axis (Greenwood, 1990).

The remainder ($N=8$) had 20%–100% loss of OHCs over 40% or more of the cochlea from the base as well as complete loss of IHCs; this group is referred to as the IHC–OHC loss group. Lesions in the basal 40% of the cochlea encompass the 2.8–20-kHz region of the chinchilla cochlea, and the round window overlooks the vicinity of 10 kHz (from our observations; see also Greenwood, 1990). Figure 7 compares the average SP input/output functions at 2, 4, 8, and 16 kHz among the ears/groups—IHC loss, IHC–OHC loss, and control. In the IHC loss group, SP output was reduced significantly, relative to the control ears, at all frequencies, and the input/output functions were shifted to higher intensities by 20–40 dB. However, the slope of the input/output function showed relatively little change at most frequencies. The largest magnitude reductions occurred at the lowest frequency tested (2 kHz) where the magnitude was reduced by a factor of 10. At higher frequencies (8 and 16 kHz), the magnitude was reduced by a factor of 2 to 4 depending on the level and frequency of the stimulus. Destruction of IHCs plus 20% or more of OHCs resulted in a further decrease in SP magnitude and altered the shape of the input/output function (Fig. 7, dotted line). At low-to-moderate intensities (<65 dB SPL), the slope of the input/output function was relatively shallow and the magnitude seldom exceeded 3 μV. However, at higher intensities, the slope of the input/output function increased abruptly and the magnitude increased from 7–11 μV.

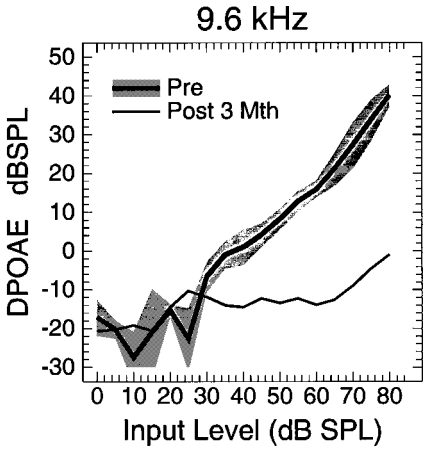

FIG. 6. Mean ($n=4$) precarboplatin (shaded area shows 95% confidence interval) and postcarboplatin DPOAE input/output functions at 8 kHz from the animal whose cochleogram is shown in Fig. 1. Postcarboplatin DPOAEs were equal to the noise floor of the measurement system and were unmeasurable after the carboplatin treatment.

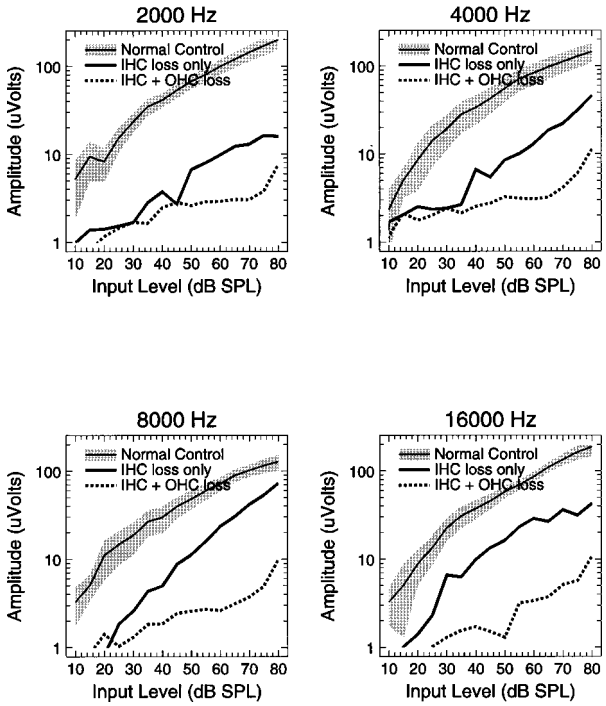

FIG. 7. Mean SP input/output functions from normal control animals (shaded area represents 95% confidence interval), the IHC loss group and the IHC+OHC loss group. Stimulus frequency indicated above each panel.

Table I shows the means and standard deviations of the maximum SP voltages in the three groups of animals and the mean IHC and OHC loss for each group. The mean maximum SP voltage in the control group was 182 μV. In the IHC loss group, the mean IHC loss was 90% and the OHC loss was 7%. The mean maximum SP voltage in this group was 82 μV. In the IHC+OHC loss group, the mean maximum voltage was 11 μV, and the IHC and OHC losses were 99% and 61%, respectively. This decrease in SP magnitude thus was associated with a 54% increase in OHC loss, but only a 9% increase in IHC loss.

The trends observed in all normal and treated animals have been summarized in Fig. 8 by plotting the maximum SP magnitude at 8 kHz versus the percent total hair cell loss (IHC+OHC) in the basal 40% of the cochlea. Since carboplatin generally destroys IHCs before damaging the OHCs, an overall hair cell loss of 25%–30% represents essentially selective loss of IHCs (i.e., with only minor losses of OHCs).

TABLE I. The SP amplitude and IHC and OHC loss.

Group	SP (mean±1 s.d.)	IHC loss (mean±1 s.d.)	OHC loss (mean±1 s.d.)
Normal	182±31 μV	0%	0%
IHC loss	82±37 μV	90%±17%	7%±5%
IHC+OHC loss	11±7 μV	99%±1%	61%±22%

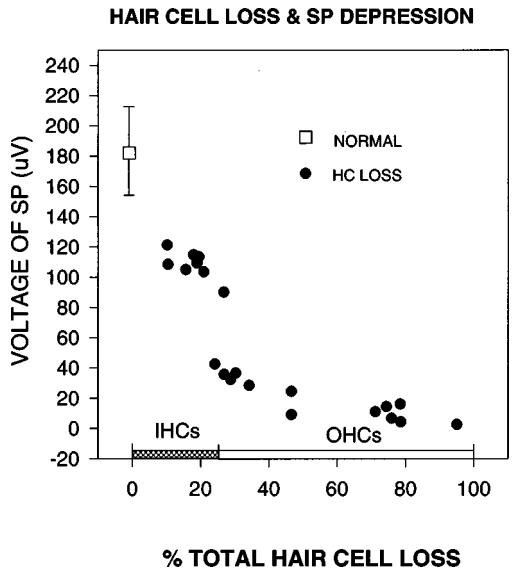

FIG. 8. Maximum SP magnitude at 8 kHz from all carboplatin-treated ears as a function of total hair cell loss (IHC+OHC). Mean SP magnitude (square) and standard deviation (vertical bars) for normal controls shown in upper left corner of figure. Shaded area on abscissa shows 25% percent hair cell loss; this represents mainly IHC loss. Lesions greater than 25%–30% represents mainly OHC loss (see text for details).

Hair cell losses exceeding 25%–30% thus reflect destruction incurred almost exclusively by OHCs.

To assess the hypothesis that IHCs contribute significantly to SP output at the round window, all available data (including control and experimental group animals, SP data at 8 kHz, for a total $N=44$ ears) were scrutinized for the significance of a nearly intact IHC population for near-normal SP output. The results are summarized in a contingency table (Table II). The criteria here are $>60\%$ IHC loss and <120 μV SP output. The results are significant at $p \leqslant 0.05$ level (Fisher exact test). However, the results above shown in Figs. 7 and 8 suggest a significant contribution of OHCs, namely that a nearly intact OHC population, in the face of extensive IHC lesions, is essential for substantive production of SP at the round window. Table III is a contingency table of the frequency of occurrence of $\leqslant 10\%$ versus $>10\%$ losses of OHCs for the criteria of ''SP absent'' (virtually) versus ''SP present;'' the latter was defined as SP>20 μV. The results are clearly significant.

III. DISCUSSION

While our results demonstrate the importance of the IHCs in the production of the SP, our results do not preclude a significant contribution of the OHCs to the SP recorded from the round window. A comparison of the SP input/output functions from normal animals and animals with 90% IHC loss and minimal OHC loss (7%) (see Table I) allows one to estimate the relative contribution of IHCs and OHCs. The IHCs appear to be the dominant generator of the SP at low and moderate intensities. At 50 dB SPL, the IHCs contribute at least 70% or more of the SP magnitude while at higher intensities the IHC contribution remains at more than 50%. Because 10% of the IHCs were present in the IHC loss group (Fig. 7), our estimate of the IHC contribution to the SP could be an underestimate, depending upon their functional state and location in the cochlea (in deference to longitudinal attenuation of the cochlear fluids). Thus, it would appear that OHCs contribute no more than one-third to one-half of the SP recorded from round window. The OHC contribution to the SP, in contrast to the CM, is roughly proportional to the inverse of the OHC–IHC ratio.

TABLE II. Dependence of SP normal output on IHCs ($N=44$ ears).

		Hair cell loss	
		Low	High ($>60\%$)
SP	$\geqslant 120$ μV	18	1
	<120 μV	4	21

TABLE III. Dependence of SP presence on OHCs ($N=44$ ears).

		Hair cell loss	
		Low	High ($>10\%$)
SP	>20 μV	31	0
	absent	0	13

Although destroying the IHCs throughout the cochlea causes a clearly significant reduction, the next major decrease in round-window-recorded SP is related to the loss of OHCs in the base of the cochlea. Since the average OHC loss in the basal 40% of the cochlea was approximately 60%, the most parsimonious explanation for the residual SP ($\leqslant 11$ μV) might be that it is arises from surviving OHCs in the base of the cochlea. However, the abrupt increase in the slope of the SP around 60 dB SPL (e.g., Fig. 7, 4000 Hz) may indicate involvement of a new source of dc-receptor potentials. The observation of large numbers of surviving OHCs in the apical half of the cochlea, even after the highest doses of carboplatin used in this study, suggests increasing contribution from OHCs from more apical turns at high SPLs. Nevertheless, the extracellular dc-receptor potentials from these ''remote'' generators will be subject to the longitudinal attenuation of the cochlear fluids.

The apparent hierarchy of these classes of SP generators—basal IHCs, basal OHCs, and apical OHCs—is similar to the scheme suggested by Harvey and Steel (1992) based on developmental data from the mouse. The significance of contributions of apical SP generators is also consistent with Dallos and Cheatham's observations (Dallos and Cheatham, 1992; Cheatham, 1993) of substantial dc-receptor potentials in OHCs of all turns apical to the first turn. Although contributions distant to the best-frequency of the recording site also are associated with polarity reversals (Dallos, 1973), the stimulation and recording parameters used in this study rarely lead to the reversals of SP polarity.

In summary, although our results are compatible with measurements showing substantial dc-receptor potentials from OHCs (Cheatham, 1993; Dallos, 1986), they are not consistent with Dallos's theory that OHC output dominates SP production in general, at least not in the basal/high-frequency end of the cochlea as ''viewed'' from the round window. Our findings are consistent with results of Russell

and Sellick (1983) suggesting a strong contribution of dc-receptor potentials from IHCs to SP production. Yet, massive IHC lesions failed to eliminate SP at the round window. It thus would appear that neither the model suggested by Russell and Selick's nor Dallos and Cheatham's findings from intracellular recordings is completely correct. The same conclusion applies to the earlier theories of Davis and Dallos, respectively.

The potential clinical importance of these findings seems self-evident. Interpretation of the SP relies not only upon the absolute magnitude of the SP, but its magnitude relative to the CAP. Current theory dictates that the CAP represents excitation of the auditory nerve fibers activated largely by the IHCs, although facilitated by the OHCs at low sound levels. The results of the present study show that selective destruction of IHCs significantly reduces the magnitude of the SP; however, a substantial SP can still be recorded when the CAP is very small (i.e., due to the IHC loss). The ratio of the SP to CAP actually should be increased in ears with selective IHC damage. Consequently, the status of the SP:CAP may not be interpreted unequivocally in all cases, particularly in the absence of clearly normal or enhanced SP.

Clinical ECochG has been used extensively in the diagnosis of Meniere's disease (specificity over 90%), but the sensitivity of the test may barely exceed 50% (e.g., see Pou *et al.*, 1996). At the same time, the underlying mechanism(s) of the effect(s) of hydrops continue to be debated. The disease itself is notorious for its dynamic behavior and may not represent a homogeneous clinical entity. It is conceivable that underlying such dynamics and/or heterogeneity are differential involvement of IHCs and OHCs which might explain the volatility of the SP or the SP:CAP. By obtaining additional measurements, such as DPOAEs and CM, to assess the functional integrity of OHCs, it may be possible to assess the relative contribution of IHCs and OHCs to the disease process (Brown *et al.*, 1989; Dallos and Cheatham, 1976; Hofstetter *et al.*, 1997b).

ACKNOWLEDGMENTS

Work supported in part by NIH grant from NIDCD, R01 DC0016, R.J.S. principal investigator.

[1]This assumption, particularly as it pertains to humans, has yet to be assessed critically. Kiang suggested a model for electrocochleography wherein the round window is considered a natural sink for current from unit action potentials, producing the compound response typically recorded via ECochG or at the round window (Kiang *et al.*, 1976). This, however, does not address the SP. Still, it seems reasonable that the round window, being a membrane, would offer a lower resistance than, say, the oval window, given the stapes and spiral ligament over this window and the additional volume of perilymph in the vestibule between the oval window and scala vestibuli. (The round window membrane, of course, is in direct contact with the scala tympani.) In general, the electrical pathway to the promontory and more remote sites is provided presumably by the middle ear mucosa. Durrant and Ronis (1975) and Durrant *et al.* (1977) studied the issue of the relation of remotely recorded cochlear potentials to intracochlear recordings in the guinea pig. Collectively, the results of these works suggest that ECochG via electrodes on the eardrum or promontory ostensibly sees the round window or, effectively, scala tympani of turn I. The situation, nevertheless, is complex enough to lead to subtle but systematic phase changes in the CM between ''promontory'' and ST. (Note: the promontory site in human only can be approximated in the guniea pig.) Therefore, the assumed linkage of clinical ECochG to the round window, while common and logical, perhaps should not be taken completely for granted.

Brown, A. M., McDowel, B., and Forge, A. (**1989**). ''Acoustic distortion products can be used to monitor the effects of chronic gentamicin treatment,'' Hearing Res. **42**, 143–156.

Cheatham, M. A. (**1993**). ''Cochlear function reflected in mammalian hair cell responses,'' Prog. Brain Res. **97**, 13–19.

Cody, A. R., and Russell, I. J. (**1985**). ''Outer hair cells in the mammalian cochlea and noise-induced hearing loss,'' Nature (London) **315**, 662–665.

Dallos, P. (**1973**). *The Auditory Periphery: Biophysics and Physiology* (Academic, New York).

Dallos, P. (**1986**). ''Neurobiology of cochlear inner and outer hair cells: intracellular recordings,'' Hearing Res. **22**, 185–198.

Dallos, P., and Cheatham, M. A. (**1976**). ''Production of cochlear potentials by inner and outer hair cells,'' J. Acoust. Soc. Am. **60**, 510–512.

Dallos, P., and Cheatham, M. A. (**1992**). ''Cochlear hair cell function reflected in intracellular recordings *in vivo*,'' *in Sensory Transduction*, edited by D. C. Corey and S. Roper (Society of General Physiologists) (Rockefeller University Press, New York), Vol. 47, pp. 371–393.

Dallos, P., and Wang, C. Y. (**1974**). ''Bioelectric correlates of kanamycin intoxication,'' Audiology **13**, 277–289.

Davis, H., Deatherage, B. H., Eldredge, D. H., and Smith, C. A. (**1958a**). ''Summating potentials of the cochlea,'' Am. J. Physiol. **195**, 251–261.

Davis, H., Deatherage, B. H., Rosenblut, B., Fernandez, C., Kimura, R., and Smith, C. A. (**1958b**). ''Modification of cochlear potentials by streptomycin poisoning and by extensive venous obstruction,'' Laryngoscope **68**, 596–627.

Durrant, J. D., and Ronis, M. L. (**1975**). ''Remote extracochlear versus intracochlear recordings in guinea pig,'' Ann. Otol. Rhinol. Laryngol. **84**, 88–94.

Durrant, J. D., Burns, A., and Ronis, M. (**1977**). ''Electrocochleographic studies in animals,'' Adv. Oto-Rhino-Laryngol. **22**, 14–23.

Fujita, H. (**1990**). ''Mutant golden hamsters with an abnormal outer hair cell stereociliary arrangement,'' Hearing Res. **44**(1), 63–69.

Geisler, C. D., Yates, G. K., Patuzzi, R. B., and Johnstone, B. M. (**1990**). ''Saturation of outer hair cell receptor currents causes two-tone suppression,'' Hearing Res. **44**, 241–256.

Greenwood, D. D. (**1990**). ''A cochlear frequency-position function for several species—29 years later,'' J. Acoust. Soc. Am. **87**, 2592–2604.

Harvey, D., and Steel, K. P. (**1992**). ''The development and interpretation of the summating potential response,'' Hearing Res. **61**(1-2), 137–146.

Hofstetter, P., Ding, D. L., and Salvi, R. J. (**1997a**). ''Magnitude and pattern of inner and outer hair cell loss in chinchilla as a function of carboplatin dose,'' Audiology **36**, 301–311.

Hofstetter, P., Ding, D., Powers, N., and Salvi, R. J. (**1997b**). ''Quantitative relationship between carboplatin dose, inner and outer hair cell loss and reduction in distortion product otoacoustic emission amplitude chinchillas,'' Hearing Res. **112**, 199–213.

Johnstone, J. R., and Johnstone, B. M. (**1966**). ''Origin of summating potential,'' J. Acoust. Soc. Am. **40**, 1405–1413.

Kiang, N. Y. S., Moxon, E. C., and Kahn, A. R. (**1976**). ''The relationship of gross potentials recorded form the cochlea to single unit activity in the auditory nerve,'' in *Electrocochleography*, edited by R. J. Ruben, C. Elberling, and G. Salomon (University Park, Baltimore), pp. 95–115.

Klis, S. F., and Rebillard, G. (**1995**). ''A comparison of the effect of cochlear perfusion with ouabain on summating potentials and distortion product otoacoustic emissions in the guinea pig,'' European Archives of Oto-Rhino-Laryngology **252**, 405–408.

Pou, A. M., Hirsch, B. E., Durrant, J. D., Gold, S. R., and Kamerer, D. B. (**1996**). ''The efficacy of tympanic electrocochleography in the diagnosis of endolymphatic hydrops,'' Am. J. Otology **17**(4), 607–611. Erratum: Am. J. Otol. **17**(6), 918 (1996).

Russell, I. J., and Sellick, P. M. (**1983**). ''Intracellular studies of hair cells in the mammalian cochlea,'' J. Physiol. (London) **284**, 261–290.

Sellick, P. M., and Russell, I. J. (**1979**). ''Two-tone suppression in cochlear hair cells,'' Hearing Res. **1**, 227–236.

Takeno, S., Harrison, R., Mount, R., Wake, M., and Harada, Y. (**1994**). ''Introduction of selective inner hair cell damage by carboplatin,'' Scanning Microsc. **8**, 97–106.

Trautwein, P., Hofstetter, P., Wang, J., Salvi, R., and Nostrant, A. (**1996**). ''Selective inner hair cell loss does not alter distortion product otoacoustic emissions,'' Hearing Res. **96**(1-2), 71–82.

Wake, M., Takeno, S., Ibrahim, D., and Harrison, R. (**1994**). ''Selective inner hair cell ototoxicity induced by carboplatin,'' Laryngoscope **104**, 488–493.
Wake, M., Takeno, S., Ibrahim, D., Harrison, R., and Mount, R. (**1993**). ''Carboplatin ototoxicity: an animal model,'' J. Laryngol. Otol. **107**, 585–589.
Wang, J., Powers, N. L., Hofstetter, P., Trautwein, P., Ding, D., and Salvi, R. J. (**1997**). ''Effect of selective IHC loss on auditory nerve fiber threshold, tuning, spontaneous and driven discharge rate,'' Hearing Res. **107**, 67–82.

Influence of centrifugal pathways on forward masking of ventral cochlear nucleus neurons

Susan E. Shore
Department of Otolaryngology, Medical College of Ohio, Toledo, Ohio and Kresge Hearing Research Institute, University of Michigan Medical School, Ann Arbor, Michigan 48109

(Received 8 October 1997; revised 9 March 1998; accepted 10 March 1998)

When responses to one part of a sequence of auditory signals reduce the responses to a subsequent portion of the signal, ''forward masking'' results. Although forward masking occurs in the auditory nerve, that observed in the ventral cochlear nucleus (VCN) more closely resembles psychophysical forward masking. In contrast to the auditory nerve in which the amount of forward masking is proportional to the amount of excitation produced by the masker, most VCN neurons show a poor correlation between forward masking and excitation produced by the masker, indicating a more complex interaction between responses to adjacent signals. This study tested the hypothesis that one component of forward masking is produced by inputs from centrifugal neural connections to the VCN. The centrifugal pathways were interrupted with knife-cut lesions medial to the CN. Responses of single units obtained 60 minutes after the lesions were compared to those obtained before the lesions. In primarylike, sustained chopper and on units the lesions resulted in a reduction in forward masking and enhanced recovery. In contrast, lesions resulted in increased masking in primarylike-notch and low-intensity chopper units. The relationship between masker-elicited excitation and forward masking became more monotonic for transient choppers and on units, approaching that observed for auditory nerve fibers. These effects are probably the result of removal of both inhibitory and excitatory inputs, ultimately reflecting a balance of excitation and inhibition to each neural population in the VCN.
[S0001-4966(98)06306-8]

PACS numbers: 43.64.Qh, 43.64.Wn, 43.66.Dc [RDF]

INTRODUCTION

Psychophysical forward masking occurs when responses to one part of a sequence of auditory signals reduce the responses to a subsequent portion of the signal. While forward masking is observed in both the auditory nerve and the cochlear nucleus (CN), that observed in the ventral CN (VCN) more closely resembles the psychophysical forward masking. Like auditory nerve, VCN units respond with lower firing rates to the second of two stimuli separated by a time interval. However, the manner in which VCN units recover from forward masking differs from auditory nerve, and between VCN unit classes (Boettcher *et al.*, 1990; Shore, 1995). In auditory nerve the amount of forward masking is proportional to the amount of excitation produced by the masker, while most VCN neurons show a poor correlation between forward masking and masker-elicited excitation.

In the auditory nerve the decrement in response to a probe stimulus following the masker has been ascribed to the process of adaptation. Adaptation in sensory receptors is a decline in receptor excitation in the presence of an ongoing stimulus. Adaptation is not present in the auditory receptor hair cell (Goodman *et al.*, 1982; Russell and Sellick, 1978) but does occur in auditory nerve fibers. In response to long tone bursts, auditory nerve fibers initially respond with a high ''onset'' firing rate which declines, first rapidly, then more slowly to a steady-state level (Kiang *et al.*, 1965; Smith, 1979; Smith *et al.*, 1983a; Harris and Dallos, 1979). These two phases of decay have been termed ''rapid'' and ''short-term'' adaptation, respectively, and occur within the first hundred milliseconds of stimulation. After stimulation there is also a decrement in spontaneous activity that reflects a decrease in excitability. This takes several hundred milliseconds to fully recover, at least twice as long as the adaptive process itself (Smith, 1977, 1979; Harris and Dallos, 1979). It has generally been assumed that auditory nerve adaptation is a synaptic phenomenon (Furakawa and Matsuura, 1978; Furakawa *et al.*, 1978, 1979; Smith and Brachman, 1982; Eggermont, 1985; Shore and Nuttall, 1984). In some systems, however, membrane kinetics at the post-synaptic site also play an important role in adaptation (Eggermont, 1985) and should be considered when interpreting forward masking effects.

Although some features of psychophysical forward masking studies are replicated in auditory nerve responses, there are three ways in which masking at these two levels differ: First, greater amounts of forward masking occur psychophysically; second, substantially larger dynamic ranges are observed in psychophysical studies; and third, masker frequency-dependent effects are measured psychophysically which are not observed in auditory nerve responses (Abbas, 1979; Smoorenburg and Kloppenburg, 1986; Smith *et al.*, 1983b; Turner *et al.*, 1994). These differences between auditory nerve and psychophysical results suggest a central contribution to psychophysical forward masking.

Studies of forward masking in the CN indicate that further modification of responses to sequential stimuli takes place in these higher-order neurons (Boettcher *et al.*, 1990; Kaltenbach *et al.*, 1993; Shore, 1995). While the shape and

time course of forward masking recovery functions are similar to auditory nerve for some primarylike and chopper units, other VCN cells recover at variable rates. On units and many transient-chopper units consistently show greater amounts of masking than auditory nerve and more variable recovery rates which could be the result of inhibitory modulations (Boettcher *et al.*, 1990; Shore, 1995). In addition, dorsal CN unit responses show a strong dependence on masker frequency not predicted by the auditory nerve responses (Abbas, 1979; Kaltenbach *et al.*, 1993).

Like auditory nerve, many primarylike units in the VCN show decrements in probe responses proportional to the response-rate increments to the masker. For other units, however, the relationship between masker rate-level functions and probe rate-decrement functions differs from that seen in auditory nerve (Shore, 1995). For some VCN units the decrements in response to the probe saturate when the response to the masker saturates, resulting in a small dynamic range of masking. Other units show continued masking even after the response rate to the masker has saturated, resulting in an increased dynamic range of masking (Shore, 1995).

The CN receives information from higher centers. Synaptic endings from noncochlear sources (Cant and Morest, 1978, 1979; Cant, 1981) arise predominantly in the superior olivary complex, but also the inferior colliculus and contralateral CN (Van Noort, 1969; Elverland, 1977; Cant and Gaston, 1982; Adams, 1983; Adams and Warr, 1976; Covey *et al.*, 1984; Shore *et al.*, 1991, 1992). The projections run in the acoustic striae and trapezoid body and as collaterals of the olivocochlear bundle to all areas of the VCN (Adams, 1983). These pathways run parallel to the ascending pathways, presumably in order to enhance or attenuate incoming sensory information from the auditory nerve. It recently has become apparent that this system is very complex, with an intricate topographic organization. Because many VCN projection neurons receive descending information from their target neurons, some consider these projections to be feedback in nature (Spangler and Warr, 1991).

More than half of axosomatic endings on bushy cells in the anteroventral CN are noncochlear, contradicting the commonly held view that these cells are largely relay neurons (Pickles, 1988). A large proportion of their synapses have either flattened or pleomorphic vesicles, usually associated with synaptic inhibition, and contain either glycine or GABA and in some cases both (Cant and Morest, 1978; Altschuler *et al.*, 1993; Saint Marie *et al.*, 1991, 1993). Large numbers of these putative inhibitory synapses are strategically placed on cell bodies and axon hillocks of bushy and stellate cells to affect the output of these projection cells (Saint Marie *et al.*, 1991, 1993). Projections from periolivary regions appear to use glycine, GABA and also acetylcholine as transmitters (for review see Potashner *et al.*, 1993; Saint Marie *et al.*, 1993; Godfrey *et al.*, 1978, 1988). Thus, the anatomical substrates are in place for this system to be at least partly inhibitory, but results of previous physiological studies have been inconclusive regarding an inhibitory influence. Early studies showed that electrical stimulation of some regions of the superior olivary complex (SOC) inhibited CN units but stimulation of other parts of the SOC produced excitation and release of acetylcholine (Comis, 1970; Comis and Davies, 1969; Comis and Whitfield, 1968). This is consistent with observations of ChAT activity and immunoreactivity in SOC and CN (Godfrey, 1993). Long latency, inhibitory responses in the VCN have also been reported in response to electrical stimulation of the crossed olivocochlear bundle and the ventral acoustic stria, which are within the temporal ranges utilized in this study (Bourk, 1976) and are consistent with descriptions of GABAergic and glycinergic noncochlear inputs (Adams and Mugnaini, 1984; Altschuler *et al.*, 1993; Caspary, 1986; Godfrey *et al.*, 1988; Potashner *et al.*, 1993; Saint Marie *et al.*, 1993; Wenthold and Martin, 1984).

The aim of this study was to test the hypothesis that centrifugal pathways modulate forward masking, recovery rates and masker-probe relationships in VCN units. Centrifugal pathways were severed at the dorsal, ventral and intermediate acoustic stria, before they enter the CN. Similar cuts have previously been shown to be effective in eliminating centrifugal inputs to the CN, resulting in decreases in the release and uptake of GABA and glycine, decreased concentrations of GABA and decreased activities of choline acetyltransferase and acetylcholinesterase in the VCN (Godfrey *et al.*, 1983, 1988; Potashner *et al.*, 1985; Staatz-Benson and Potashner, 1988). Four major effects were observed: (a) Decreased masking for primarylike, sustained chopper, and on units at masker-probe intervals less than 100 ms. (b) Delayed recovery from forward masking for on, sustained, and transient chopper units. (c) Increased masking for primary-with-notch and low-intensity chopper units at masker-probe intervals less than 100 ms. (d) An increase in the correlation between increments in firing rate to the masker and decrements in firing rate to the probe for transient chopper and on units. These changes appear to be predominantly the result of removal of centrifugal inhibition. However, enhanced masking in primarylike-notch and low-intensity chopper units suggests predominantly excitatory input from the removed centrifugal pathways to these units. Thus, the difference in masking seen before and after the lesions represents the sum of the disconnected excitatory and inhibitory influences of these pathways.

I. METHODS

Procedures used in this study are in accordance with NIH guidelines for the use of animals. Healthy, pigmented guinea pigs weighing between 200 and 300 g, with normal Preyer reflexes, were used in this study. The animals were initially injected with ketamine (Ketaset, 120 mg/kg) and Rompun (16 mg/kg) intramuscularly. Anesthesia was maintained with 1/2 dose supplements of ketamine at approximately 60 minute intervals or when needed. Rectal temperature was maintained at 38 °C. After placing the tracheotomized animal in a stereotaxic headholder, the CN was exposed by removing the occipital bone, entering the posterior fossa and aspirating a small portion of the cerebellum overlying the cochlear nucleus until the dorsal CN was visible. Data were used only from animals in which single unit thresholds after lesions fell within the sound pressure level boundaries previously established for unlesioned guinea pigs (Shore, 1995).

A. Single unit recording and data analysis

Single VCN units were isolated using glass micropipettes filled with 2M NaCl. The electrode tips were beveled until the tip impedances were between 9 and 12 megohms. With the aid of a dissecting microscope, the electrode was placed onto the lateral surface of the dorsal CN and advanced in a dorsocaudal-to-rostroventral direction using an hydraulic microdrive operated outside the soundproof (IAC) booth. To avoid confusion among electrode tracts, only 1-to-3 electrode penetrations were made in each animal. At the end of each track, the electrode was withdrawn to the location of the last neuron studied and 5 μA of positive current was applied to the recording electrode for 15 minutes. This produced a mark which could usually be seen after the tissue was sectioned and stained. Because many of the cuts resulted in blood accumulation in the VCN adjacent to the lesions, reconstruction of many electrode tracks became difficult. Those units which were successfully localized were all in the VCN. Signals were amplified with a P15 Grass Instrument preamplifier with a bandpass of 300–3000 Hz and coupled to an operational amplifier to provide a total gain of 1000. Search stimuli were either clicks or 25 ms tone bursts which elicited multi-unit background firing. Once a unit was isolated, its threshold, characteristic frequency (CF) and tuning curve were determined audiovisually, that is, using an audible increase in firing rate combined with a just noticeable increase in the number of spikes observed on the oscilloscope trace. Unit responses were digitized with 10 μs resolution and stored on line. Post-stimulus time histograms to 100 stimuli were displayed during the experiment and were saved for later examination using a Domain Series 3000 computer. Units were classified using PSTHs and inter-spike interval histograms according to the criteria used by Godfrey *et al.* (1975) and Rhode *et al.* (1983). Test stimuli were 25 ms tone bursts, 2 ms rise–fall times, 10/s. Response classes identified were: Primarylike (PL); Primarylike with notch (PL–N); Chopper with sustained chopping throughout the stimulus (CS); Chopper with chopping activity which changed to irregular activity after 3 or 4 chopper peaks, i.e., Transient Chopper (CT); chopping only observed at low intensity stimulation, changing to irregular activity at higher intensities, i.e., Low Intensity Chopper (CL); Onset with low-level later activity, with little or no spontaneous activity (On).

B. Method for interrupting centrifugal input to the VCN

To investigate the effects of interrupting centrifugal inputs to the VCN on spontaneous discharge rate and sound-evoked forward masking functions of VCN neurons, an approximately 5 mm long rostral-caudal knife cut was directed through the cerebellum and brain stem to a position just medial to the CN with the aim of eliminating input from the SOC, the contralateral CN and the inferior colliculus.

Single units were recorded before and 60 minutes after the lesions. An attempt was made after the lesions to access the same region recorded before the cut, based on stereotaxic coordinates. Responses from units of the same class obtained before and after the cuts were compared with each other. Since it was not possible to record from the same unit before and after the lesions, mean data were also obtained across animals for units in each class. Because the before-cut data showed the same trends seen in the normative data of Shore (1995), the after-cut data were also compared with the previously obtained normative data. Statistical significances of mean differences between groups were assessed using Student's *t* test.

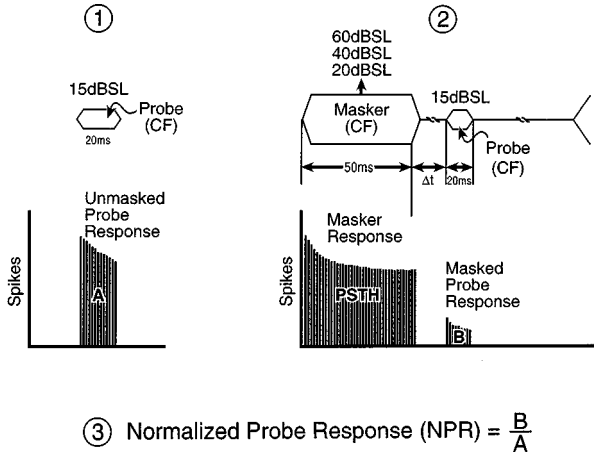

FIG. 1. The forward-masking protocol and analysis used in this study. See Sec. I.

In some cases, the lesions also included a small medial portion of the DCN in addition to centrifugal input. The possible effects of removing some DCN input to VCN were not separately assessed in this study. Discrete chemical lesions, involving specific nuclei, are the subject of an ongoing study to determine more specific effects of different regions of input to the VCN.

C. Forward masking protocol and analysis

The masker, a 50 ms CF tone burst, presented at 20, 40 or 60 dB above the unit's threshold (dB SL), was followed by a 20 ms, 15 dB SL, CF tone burst probe stimulus (Fig. 1). The separation between the end of the masker and the beginning of the probe (delta *t*) varied between 5 and 200 ms. The interval between the end of the probe and the beginning of the following masker was at least 300 ms. A control probe stimulus alone (1) preceded each masker-probe sequence (2) and was used as a reference against which to compare masked probe responses. Firing rates to the masker and the probe were calculated from the PSTHs using an interactive computer program. Both the average rate and the initial peak rate (onset rate) were measured. The onset rate occurs during the initial 2 ms of the PSTH and is equivalent to ''rapid adaptation'' (Smith, 1977). The onset component of the response has been shown in auditory nerve (Smith and Brachman, 1980) and cochlear nucleus cells (Shore, 1995) to have a larger dynamic range than the average rate and might be important in processing stimuli which change rapidly over time, such as speech. The normalized probe response rate (NPR, 3) was calculated by dividing the masked probe rate (B) by the unmasked probe rate (A). A ratio of 1 indicates

TABLE I. Number of units in each class.

	PL	PL-N	C	On	Total
Recovery functions					
Before cut	20	9	31	10	70
After cut	8	6	24	4	42
M-P interactions					
Before cut	9	12	46	15	82
After cut	12	19	50	11	92

full recovery from the masker to pre-masker response rate. NPR was then plotted as a function of the masker-probe interval (delta-*t*).

To determine the relationship between increments in firing rate to the masker and decrements in firing rate to the probe, both were plotted as a function of masker intensity. Masker rate was normalized by dividing by the masker rate obtained 10 dB above the unit's threshold, and probe rate was divided by the response rate to a nonmasked probe presented 15 dB above threshold.

II. RESULTS

The results of this study are based on 43 animals. Data were obtained from 172 units in normal animals and 134 units after lesions. For generating recovery functions, data for 42 of the post-lesion units were compared with normative data previously published (70 units in 25 animals; Shore, 1995). Masker-probe interactions, thresholds and spontaneous rate were measured in the other 92 post-cut units and compared with 82 pre-cut units from the current study. Table I shows the number of units in each class for the recovery and masker probe interaction experiments.

A. Forward masking recovery functions

The following descriptions of individual and mean data were obtained from units after lesions similar to that shown in Fig. 2. In each case, the lesion runs medial to the VCN along its entire rostral-caudal extent, effectively eliminating most of the input from centrifugal inputs to the VCN, as well as, in some cases (not shown), a small portion of the input from the medial portion of DCN.

1. Individual unit data

After lesions, the onset and average rate recoveries often were affected differently: Figure 3 shows the normalized probe rate (NPR) for a CS unit before (Fig. 3A and B) and one obtained 60 minutes after a lesion (Fig. 3C and D). For the lowest masker sound level (20 dB) the unit recorded after the lesion showed a greater reduction in masking of onset rate than average rate compared to the normal. A greater reduction in masking of the average rate suggests that the removed centrifugal inputs provided a rapid inhibitory input to this chopper unit. At the highest masker level (60 dB SL), however, average rate was more affected than onset rate by the lesion, suggesting a delayed inhibitory input at this sound level. The apparent level-dependent effects of the lesions will be considered elsewhere. The remainder of this paper will report results for 20 dB SL maskers only.

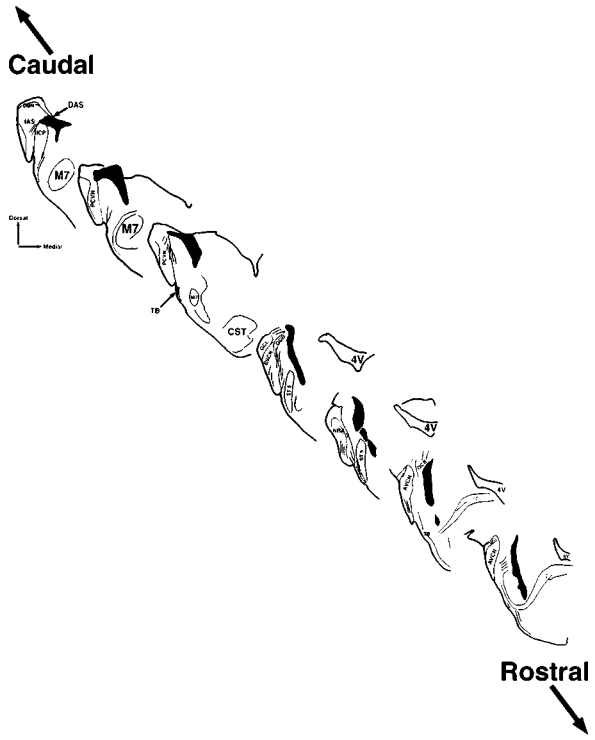

FIG. 2. Camera lucida drawings of 40 μm transverse brainstem sections from a guinea pig in which a knife lesion was made to remove all centrifugal input to the VCN. The lesion is indicated by the shaded area running in a dorso-ventral direction. DCN: Dorsal cochlear nucleus. IAS: Intermediate acoustic stria. M7: Motor nucleus of the 7th cranial nerve. PVCN: Posteroventral cochlear nucleus. CST: Corticospinal tract. GCL: granule cell layer. OCB: olivocochlear bundle. 4V: fourth ventricle. AVCN: anteroventral cochlear nucleus. ST5: spinal tract of the fifth cranial nerve. TB: trapezoid body. NRA: nerve root area.

2. Mean data

Although there was variability among units for the recovery functions, there were also changes associated with the lesions which were widely demonstrated across the various units tested. Mean recovery functions were therefore generated for the six categories of units (see Sec. I): PL, PL-N, CS, CT, CL and ON. Mean onset and average recovery functions for each unit type are shown in Fig. 4 for the 20 dB masker level before and after the lesions:

PL units recorded after lesions showed significantly less forward masking than normal (Fig. 4A and B). The differences from normal occurred at delta-*t* values below 100 ms. At longer intervals recovery time remained the same. For onset rate, the NPR at 5 ms was 0.5, compared with an NPR of 0.05 for normal, indicating a reduction in masking of almost 50% after removal of centrifugal inputs to the CN (assuming recovery at NPR=1 to be 100% recovery). For average rate, the reduction in masking after lesions from an NPR of 0.25 to 0.5 (25%), was less prominent and partly a reflection of the onset rate which is included in the average rate estimate. This difference may indicate that centrifugal input to PL units is fast acting, occurring within the first 2 ms after probe onset.

ON units showed similar changes to those exhibited for PL units at short delta-*t* values, but also showed changes for later delta-*t* values. Following the cuts there was an approxi-

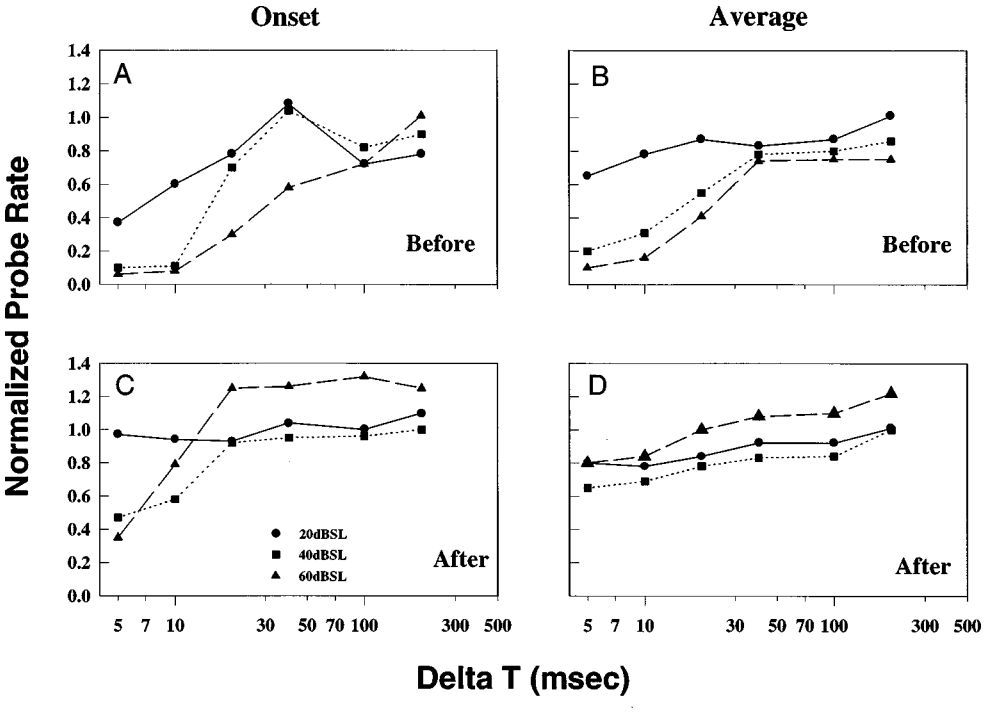

FIG. 3. Recovery of onset (left) and average (right) firing rate in response to the probe (Normalized probe rate, NPR) after forward masking with a 50 ms, CF masker. Masker level: 20, 40 and 60 dB SL. Probe level: 15 dB SL. Two chopper units in AVCN are shown: One before a lesion similar to that shown in Fig. 2 (A and B; CF 4.3 kHz), and one after the lesion (C and D; CF 12.5 kHz).

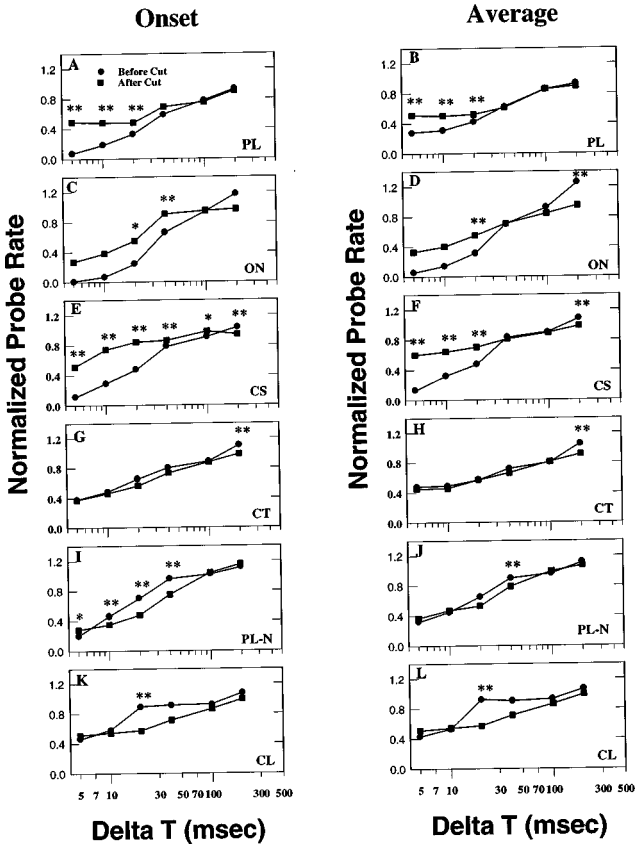

FIG. 4. Mean onset and average recovery functions for each unit type: PL; ON; CS; PL-N; CL; CT. $^{**}p<0.01$. NPR—normalized probe rate. Delta-*t*—masker-probe interval. Masker level—20 dB SL in all cases.

mately 30% increase in onset and average NPR that occurred at a delta-*t* of 5 ms (0.3 compared with 0.0 in the normal; Fig. 4C and D). A significant delay in full recovery of NPR is seen for average rate. In other words, On units did not show the ''overshoot'' or enhanced recovery which occurred before the lesions.

CS units demonstrated comparable decreases in forward masking for onset and average rates after lesions. These differences were more pronounced for delta-*t* values below 40 ms. At a delta-*t* of 5 ms, NPR was 0.55 (onset) and 0.6 (average) after cuts compared with 0.1 (onset and average) for the normal (Fig. 4E and F). Thus, a 40%–50% reduction in masking over that in normal animals was observed after the lesions, reflecting predominantly inhibition from centrifugal input to these units.

CT units showed no difference in recovery after lesions except at a delta-*t* value of 200 ms where a small decrease in masking was seen for onset and average rates at a delta-*t* value of 200 ms (Fig. 4G and H).

PL-N units, in contrast to PL, ON, and CS units, showed more masking following the lesions after an initial small decrease in masking. The primary increases in masking occurred in the onset portion of the response for delta-*t* values between 10 and 100 ms (Fig. 4I and J). Full recovery occurred at the normal time.

CL units, like PL-N units, showed initial (before 10 ms) small decreases, followed by larger increases in masking after lesions. The major changes in NPR occurred at delta-*t* values above 10 ms. Comparable changes were seen for onset and average rates (Fig. 4K and L).

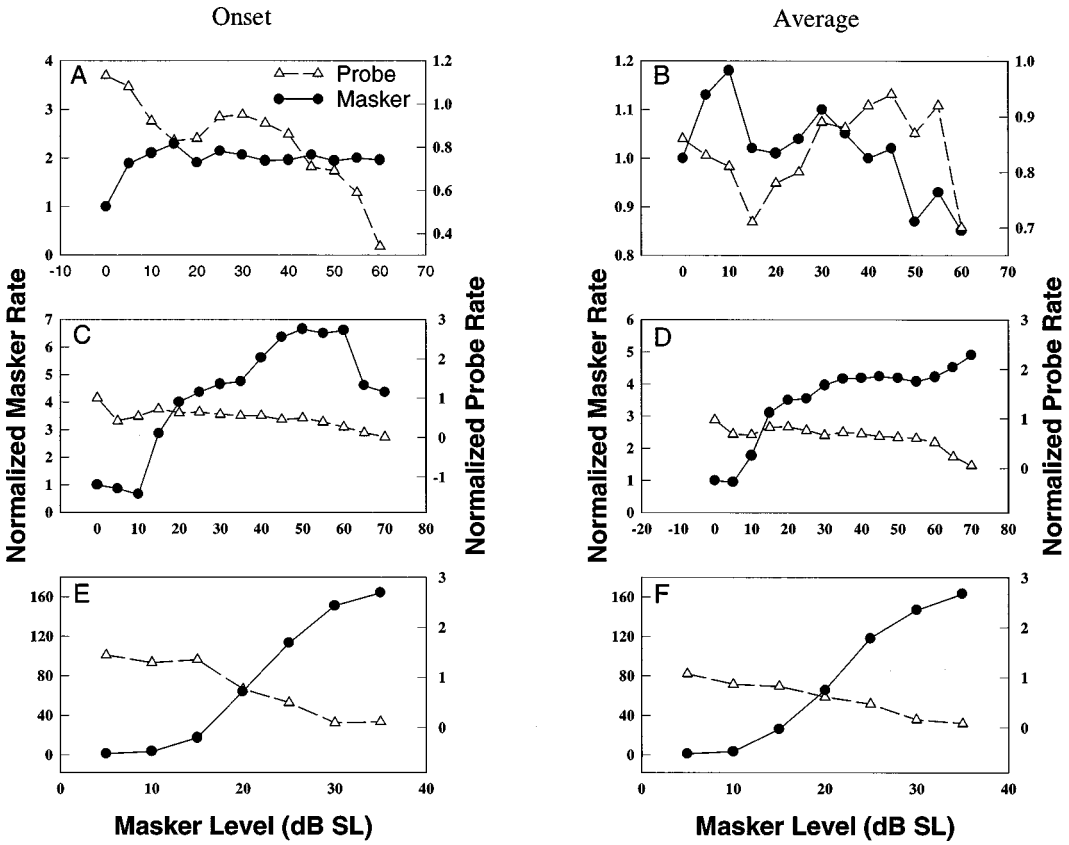

FIG. 5. Rate-level functions for three units in AVCN. Normalized probe rate (NPR) and normalized masker rate (NMR) are plotted as a function of masker level. Maskers were 50 ms CF tonebursts. Masker-probe interval (delta-*t*) was 40 ms. A and B: Responses obtained from a low-CF, primarylike unit before a lesion. C–F: Responses obtained from two low-CF, primarylike units after a lesion similar to that shown in Fig. 2.

B. Rate level functions in response to the probe and the masker

Removal of centrifugal input to the CN also affected rate-level functions in response to the masker and probe. Responses from a low-CF PL unit before lesioning the centrifugal inputs (Fig. 5A and B) showed rate-level functions for masker and probe which were nonmonotonic and uncorrelated. Responses from units after lesioning often showed more monotonic and highly (negatively) correlated rate-level functions (Fig. 5C through F), suggesting a role for the centrifugal inputs in producing the nonmonotonicities observed before the lesion.

Because of the high variability between units for response rate at different levels, mean rate-level functions were not generated. Rather, correlation coefficients (R) were calculated between the rate level functions to the masker and to the probe as a quantitative measure of the relationship between masker-evoked and probe-evoked firing rate. Correlation coefficient values across the whole population of units tested are shown in Fig. 6. The most negative values of R indicate a high negative correlation between firing rates to the masker and firing rates to the probe. Across the whole population, the percentage of units with high negative R values increased after the cuts for both onset and average rate, indicating a stronger negative relationship between firing rate to the masker and firing rate to the probe. Thus, the suggestion in the individual unit data (previous section) of an increase in monotonicity between masker-evoked firing rate and probe-evoked firing rate following the lesions is borne out in the mean data. The actual R values broken down for each unit class are shown in Fig. 7. The decreased R values after lesions shown in Fig. 6 appear to derive mainly from the CT and ON groups. No significant differences in R are seen for the other groups. Because of averaging, the few positive correlations seen in Fig. 6 are not apparent in Fig. 7, but individual unit group analysis shows that the predominant unit type presenting with positive correlations between masker-evoked rate and probe-evoked rate is the CT group.

C. Effects of lesions on spontaneous activity

The spontaneous rate of auditory nerve fibers has been correlated with numerous factors, including the excitation state of the fiber (Liberman, 1982). The spontaneous rates of CN units appear to be determined to a large extent by the spontaneous rates of the innervating auditory nerve fibers (Leake and Snyder, 1989; Liberman, 1991, 1993), but might also be influenced by descending innervation. Thus, the units' spontaneous rates were measured before and after lesions (Table II). The percentages of high (>18 spikes/s), medium (0.5–18 spikes/s) and low (<0.5 spikes/s) spontaneous rates among the population of units changed from 59–high; 33–medium; and 8–low; to 74–high; 26–medium and 0–low after lesions. Note that no low SR units were seen in

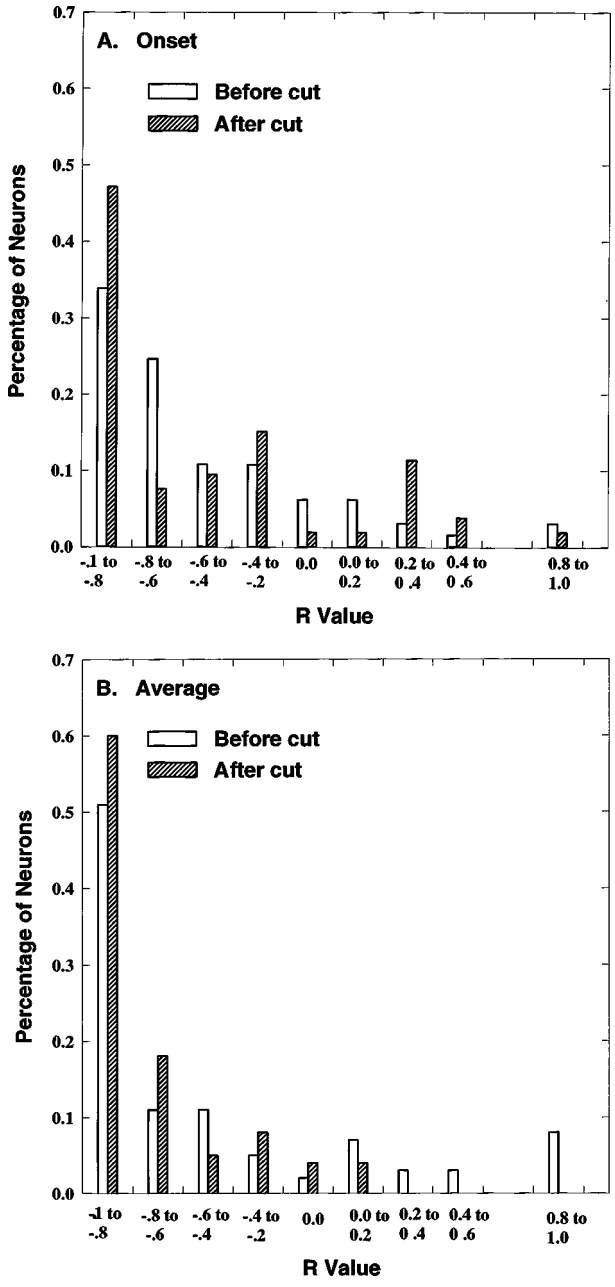

FIG. 6. Correlation coefficients (R) between firing rates to the masker and firing rates to the probe for the populations of units tested before and after lesions. A: Onset rate; B: Average rate. More negative values indicate a strong negative correlation between masker-evoked rate increments and probe-evoked rate decrements.

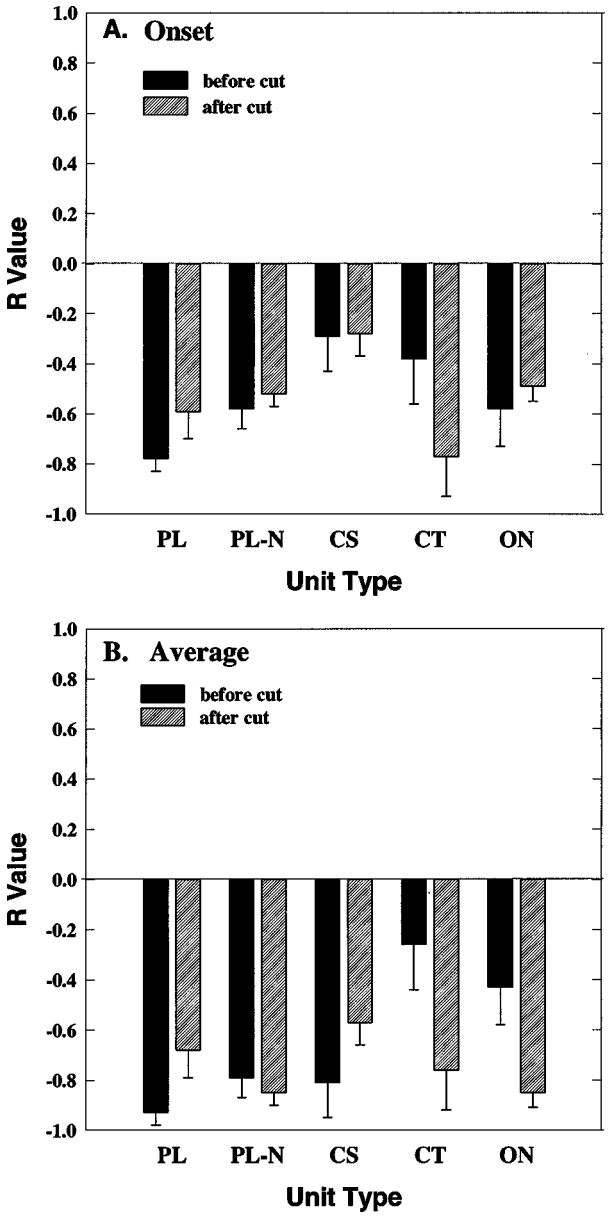

FIG. 7. Mean R values (correlation coefficients) for six classes of VCN units. Correlations were made between normalized probe rate (NPR) and normalized masker rate (NMR) values as a function of masker level. A value of -1 indicates perfect dependence (negative) of NPR on NMR. A: Average rate. B: Onset rate.

the post-lesion condition (Table II). Thus the overall spontaneous rate shows a tendency to increase after removal of centrifugal input which is especially evident for the CS group. The results support the idea of a tonic inhibition imposed by the centrifugal inputs, at least to some groups of neurons in the CN.

D. Effect of lesions on threshold

The thresholds of units obtained after lesions remained unchanged (Fig. 8). The distribution of low, medium and high threshold units after lesions overlaps that in the normal population (t-test not significant). The unchanged thresholds suggest that performing these types of lesions do not compromise the viability of the CN units from which recordings were made.

TABLE II. Percentages of units in high, medium, and low spontaneous rate groups before and after lesions.

	PL	PL-N	C	ON	X
Before lesion					
High SR	50	75	60	25	59
Medium SR	41	17	25	67	33
Low SR	9	8	8	8	8
After lesion					
High SR	50	83	89	40	74
Medium SR	50	17	11	60	26
Low SR	0	0	0	0	0

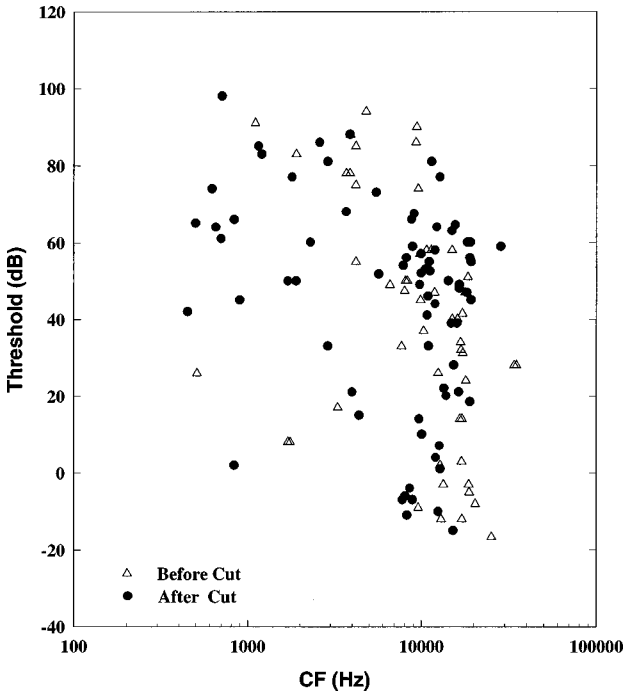

FIG. 8. Threshold values for units tested before and after lesions removing centrifugal input to the VCN.

III. DISCUSSION

A. The influence of centrifugal input to the VCN on forward masking functions

The results of this study suggest that centrifugal pathways play a role in the generation of forward masking in the VCN by providing both inhibitory and excitatory inputs differentially to each cell class in the VCN. There is some evidence for a gradation of the relative strengths of inhibitory inputs relative to excitatory inputs on VCN cell types as follows: CS>ON>PL>CT>PL-N>CL reflecting a balance of inhibitory versus excitatory terminals and their locations on each cell type.

For PL, CS and ON units, masking was reduced compared to that before the cuts, suggesting a predominantly inhibitory centrifugal input. It is noteworthy that removal of centrifugal inputs did not eliminate masking altogether; that remaining is presumably due to a balance of remaining efferents, excitatory and inhibitory, intrinsic connections and adaptation (Snyder and Leake, 1988; Shore *et al.*, 1991, 1992; Saint Marie *et al.*, 1991). The results also suggest that the removed centrifugal inputs had a longer lasting inhibitory effect on ON units than PL or CS units.

In the case of PL-N and CL units, removal of centrifugal inputs had an apparent inhibitory effect resulting in more forward masking after the lesions. This contrasting increase in masking after cuts for PL-N and CL units could thus indicate that these units receive more excitatory than inhibitory centrifugal inputs. One component of the descending pathways, the olivocochlear bundle (OCB), has been shown to lower thresholds of CN neurons and facilitate recovery, thus enabling neurons to fire faster (Comis and Whitfield, 1968; Starr and Wernick, 1968; Comis and Davies, 1969; Comis, 1970; Brown and Buchwald, 1976). More specifically, the medial OCB (MOC) sends collateral inputs to the VCN which have a synaptic morphology suggestive of excitatory input (Brown *et al.*, 1988; Benson and Brown, 1990). Recent evidence suggests that neurons in the small cell cap region of the CN receive excitatory inputs from the OCB (Brown *et al.*, 1988; Benson and Brown, 1990; Brown, 1993; Kim *et al.*, 1995). The neurotransmitter involved in these facilitatory effects is likely to be ACh which, besides being the neurotransmitter used by the MOC (Altschuler and Fex, 1986), has also been implicated as an important neurotransmitter of the descending projections from the vicinity of the superior olivary complex (Godfrey *et al.*, 1983; Martin and Dickson, 1983; Martin *et al.*, 1982; Osen and Roth, 1969). ACh concentrations in CN are reduced by more than 80% after sections of the centrifugal pathways (Godfrey *et al.*, 1983). In addition, the cholinergic innervation derives in part from an intrinsic component (Godfrey *et al.*, 1990). Previous work showed the low-intensity choppers (CL), located in the small cell cap area of the VCN, to have responses which were significantly less affected by a forward masker than core VCN units (Shore, 1995). In the present study removal of centrifugal inputs to the VCN resulted in an increase in masking of CL units in contrast to ON, CS and PL units, which showed less masking after lesions. These neurons may correspond to the small cell cap neurons described by Kim *et al.* (1995). The presence of different types of ACh receptors together with findings that iontophoretic applications of ACh on CN neurons can have excitatory and inhibitory effects suggests that ACh release can bring about multiple post-synaptic effects (Comis and Whitfield, 1968; Caspary *et al.*, 1983).

B. Interaction of masker and probe firing rate

Removal of centrifugal input to the VCN produced more monotonic rate-level functions in response to the masker as well as a more correlated relationship between masker-evoked and probe-evoked firing rates especially for CT and ON units, approaching that seen in auditory nerve fibers. The nonmonotonicities observed in responses of CN units by other investigators have been attributed to inhibitory inputs, either intrinsic or extrinsic to the CN (e.g., Young, 1984; Shofner and Young, 1985). The present results are consistent with centrifugal inputs to CT and ON units being inhibitory. Furthermore, for ON units the inhibition appears to be focused on the initial, onset portion of the response, whereas the entire response of CT units is affected. Primarylike, PL-N and CS units showed little change in correlation between masker-evoked and probe-evoked firing rates before and after lesions. In general, these unit types showed more highly correlated functions in the normal state. The results obtained from the recovery functions are consistent with the correlation data only for the ON group of units. There were no significant differences in correlation of probe-evoked and masker-evoked firing rate for the PL-N or CS groups and a small tendency for the correlation to decrease after the lesions for the PL group. In addition, while the CT group showed little change in recovery functions following lesions, there was a significant increase in correlation. These discrepancies may indicate that the two different measures, recovery

from forward masking and relationship between masker-evoked and probe-evoked firing rate, are indicators of different underlying processes.

Pharmacological applications of GABA demonstrate an inhibitory effect in CN units consistent with the suggestion in the data that the removed centrifugal input to PL, CS and ON units is predominantly inhibitory. Iontophoretic applications of GABA and glycine appear to regulate discharge rate and dynamic range within the excitatory response areas of primarylike neurons in AVCN (Caspary *et al.*, 1993). Onset and chopper units in PVCN also show a shift in their rate-intensity functions which is blocked by both the $GABA_A$ and the $GABA_B$ antagonists (Martin and Dickson, 1983; see Caspary, 1993 for review). Of particular interest is the finding that blocking $GABA_A$ receptors with bicuculline increases specifically the post-onset discharge within the response (Palombi and Caspary, 1992). Assuming the pharmalogical effects are similar for single and two tone experiments, these results suggest that the $GABA_A$ receptor may not be involved in the present effects which always affect the onset portion of the response. Primarylike and chopper units in AVCN show greater changes in tone-evoked and spontaneous activity with applications of glycine than GABA (Caspary *et al.*, 1979; Caspary, 1986). These responses are abolished by strychnine. In view of these arguments it seems more likely that the neurotransmitter involved in forward masking is glycine.

On the other hand, applications of GABA emphasize the response to stimulus onset by more strongly inhibiting spontaneous activity, and may improve the transmission of acoustic signals in constant background noise (Ebert and Ostwald, 1995). The functional significance of recent findings that GABA and glycine are co-contained in VCN terminals (Altschuler *et al.*, 1993) is not known. Allosteric modulation of glycine receptors by GABA is one possibility. Alternatively, both transmitters could act independently to selectively filter auditory information depending on the signal and neural networks involved. The interesting possibility exists that these two transmitters may act synergistically to produce temporally delayed or prolonged inhibition in these cells. This idea is supported by the observation that the onset and steady-state portions of the responses of CN cells behave differently as intensity is increased (Shore, 1995). One transmitter could have a longer action than the other so that the target neuron may respond only to the onset or to the later portion of the signal. GABA and glycine may also have a role in producing the adapted portion of the response. Ongoing pharmacological studies in our laboratory are currently addressing this question more directly.

C. Tonic inhibitory or excitatory activity from centrifugal inputs

While the lesions may have interesting effects on forward masking as demonstrated in the results, there is a possibility that they may also reduce tonic inhibitory or excitatory activity in the VCN neurons. Although not significant, there was a tendency for SR to increase among units after lesions. Thus, the responses to tones used to characterize units could change. However, several recent studies have emphasized the important role of intrinsic membrane conductances in shaping the temporal response properties of neurons in the CNS including the CN (Oertel, 1983; Wu and Oertel, 1984; Manis, 1990; Manis and Marx, 1991; Feng *et al.*, 1994). This, together with the patterns of auditory nerve input onto the three major cell types in the VCN, is a major determinant of the response patterns seen in the VCN. It was assumed here that membrane conductances would preserve the temporal discharge characteristics distinctive to at least the three major cell types in VCN, i.e., PL, CS and ON. This is supported by our results which indicate the presence of the three major types of VCN units and a further distinction between the CS and CT categories after the cuts.

D. Onset versus average rate

Following the removal of centrifugal input, PL and ON units showed greater reductions in masking for the onset compared to the average rate portions of the responses (Fig. 4). This was especially evident for delta-*t* values below 40 ms. Evans (1996) suggests that GABAergic inhibition in ON units in the PVCN may produce the rapid-adaptation component of their responses that can be abolished by applications of bicuculline. Our results suggest, however, that if GABAergic inhibition is responsible for determining the onset characteristics of some ON cells as suggested by Evans (1996), it is intrinsic to the CN. If the inhibition originated central to the CN, the lesions would abolish most ON responses. This is not the case because ON responses were consistently observed following the cuts. Our results would be consistent with lesion-induced release from inhibition in these units.

E. Relationship to psychophysical findings

The effects of a preceding stimulus on detection thresholds in humans have been well documented (Widin and Viemeister, 1979; Jesteadt *et al.*, 1982; Zeng *et al.*, 1991). In general, the timecourse of recovery of threshold is from 100 to 300 ms, correlating well with auditory nerve fibers (Harris and Dallos, 1979; Salvi *et al.*, 1986), and many VCN cells (Boettcher *et al.*, 1990; Shore, 1995). However, the timecourse for recovery of intensity difference limens is slower, sometimes greater than 400 ms (Zeng *et al.*, 1991). Some neurons in CN show greater amounts of masking and slower recoveries than auditory nerve fibers (Boettcher *et al.*, 1990; Shore, 1995), more consistent with the discrimination effects seen psychophysically (Zeng *et al.*, 1991). Many VCN cells, especially those with low spontaneous rates (Shore, 1995), have not recovered by 300 ms after the masker and may therefore contribute to the slower recovery observed for intensity difference limens. Because many of the VCN units in this study recovered more quickly following lesions, centrifugal inputs to the CN may play an important role in determining the intensity difference limens observed psychophysically.

IV. CONCLUSIONS

This study tested the hypothesis that a component of forward masking is produced by inputs from centrifugal neu-

ral connections to the VCN. The centrifugal pathways were interrupted with knife lesions medial to the CN. Responses of single units obtained 60 minutes after the lesions were compared to those obtained before the lesions. Following the lesions recovery from forward masking was facilitated in PL, CS and ON units. In contrast, recovery from masking was delayed in PL-N and CL units. The relationship between masker excitation and masking became more monotonic for CT and ON units, approaching that observed for auditory nerve fibers. These effects appear to be the result of removal of both inhibitory and excitatory inputs to different neural populations in the VCN and provide some evidence for a gradation in the relative strengths of inhibition relative to excitation for each cell type as follows: CS>ON>PL>CT >PL-N>CL.

ACKNOWLEDGMENTS

The author wishes to thank Jaspaul Jawanda and Wenje Li for excellent technical assistance and Sanford Bledsoe and Richard Altschuler for unlimited use of their facilities. I am grateful to Dr. Donald Godfrey who provided valuable guidance throughout the project as well as Ray Meddis and John Middlebrooks who provided very helpful suggestions on an earlier version of this manuscript. This project was supported by the Deafness Research Foundation and NIH Grant Nos. DC00172 and 2P01DC00078-32.

Abbas, P. J. (**1979**). ''Effects of stimulus frequency on adaptation in auditory-nerve fibers,'' J. Acoust. Soc. Am. **65**, 162–165.

Adams, J. C. (**1983**). ''Cytology of periolivary cells and the organization of their projections in the cat,'' J. Comp. Neurol. **183**, 519–538.

Adams, J. C., and Mugnaini, E. (**1984**). ''GAD-like immunoreactivity in the ventral cochlear nucleus,'' Soc. Neurosci. Abst. **10,** 393.

Adams, J. C., and Warr, W. B. (**1976**). ''Origins of axons in the cat's acoustic striae determined by injection of horseradish peroxidase into severed tracts,'' J. Comp. Neurol. **170**, 107–121.

Altschuler, R. A., and Fex, J. (**1986**). ''Efferent neurotransmitters,'' in *Neurobiology of Hearing: The Cochlea*, edited by R. A. Altschuler, R. P. Bobbin, and D. W. Hoffman (Raven, New York), pp. 383–396.

Altschuler, R. A., Juiz, J. M., Shore, S. E., Bledsoe, S. C., Helfert, R. H., and Wenthold, R. J. (**1993**). ''Inhibitory amino acid synapses and pathways in the ventral cochlear nucleus,'' in *The Mammalian Cochlear Nuclei: Organization and Function*, edited by M. A. Merchan, J. M. Juiz, D. A. Godfrey, and E. Mugnaini (Plenum, New York).

Benson, T. E., and Brown, M. C. (**1990**). ''Synapses formed by olivocochlear axon branches in the mouse cochlear nuclear,'' J. Comp. Neurol. **295**, 52–70.

Boettcher, F. A., Salvi, R. J., and Saunders, S. S. (**1990**). ''Comparison of single unit ''Forward Masking'' effects in the cochlear nucleus and auditory nerve,'' Hearing Res. **48**, 125–144.

Bourk, T. R. (**1976**). ''Electrical responses of neural units in the anteroventral cochlear nucleus of the cat,'' Doctoral dissertation, Massachusetts Institute of Technology, Cambridge, MA.

Brown, M. C. (**1993**). ''Fiber pathways and branching patterns of biocytin-labeled olivocochlear neurons in the mouse brainstem,'' J. Comp. Neurol. **337**, 600–613.

Brown, K. A., and Buchwald, J. S. (**1976**). ''Response decrements during repetitive tone stimulation in the surgically isolated cochlear nucleus,'' Exp. Neurol. **53**, 663–669.

Brown, M. C., Berglund, A. M., Kiang, N. Y. S., and Ryugo, D. K. (**1988**). ''Brainstem branches from olivocochlear axons in cats and rodents,'' J. Comp. Neurol. **82**, 491–498.

Cant, N. B. (**1981**). ''The fine structure of two types of stellate cells in the anterior division of the anteroventral cochlear nucleus of the cat,'' Neuroscience **6**, 2643–2655.

Cant, N. B., and Gaston, K. C. (**1982**). ''Pathways connecting the right and left cochlear nuclei,'' J. Comp. Neurol. **212**, 313–326.

Cant, N. B., and Morest, D. K. (**1978**). ''Axons from non-cochlear sources in the anteroventral cochlear nucleus of the cat. A study with the rapid Golgi method,'' Neuroscience **3**, 1003–1029.

Cant, N. B., and Morest, D. K. (**1979**). ''The bushy cells in the anteroventral cochlear nucleus of the cat. A study with the electron microscope,'' Neuroscience **2**, 1925–1945.

Caspary, D. M. (**1986**). ''Cochlear nuclei: Functional neuropharmacology of the principal cell types,'' in *Neurobiology of Hearing: The Cochlea*, edited by R. Altschuler, R. Bobbin, and D. Hoffman (Raven, New York), pp. 303–332.

Caspary, D. M., Havey, D. C., and Feingold, C. L. (**1979**). ''Effects of iontophonetically applied glycine and GABA on neural response patterns in the cochlear nuclei,'' Brain Res. **172**, 179–185.

Comis, S. D. (**1970**). ''Centrifugal inhibitory processes affecting neurones in the cat cochlear nucleus,'' J. Physiol. (London) **210**, 751–760.

Comis, S. D., and Davies, W. E. (**1969**). ''Acetylcholine as a transmitter in the cat auditory system,'' J. Neurochem. **16**, 423–429.

Comis, S. D., and Whitfield, I. C. (**1968**). ''Influence of centrifugal pathways on unit activity in the cochlear nucleus,'' J. Neurophysiol. **31**, 62–68.

Cooke, M. P. (**1986**). ''A computer model of peripheral auditory processing incorporating phase-locking, suppression and adaptation effects,'' Speech Commun. **5**, 261–281.

Covey, E., Jones, D. R., and Casseday, J. H. (**1984**). ''Projections from the superior olivary complex to the cochlear nucleus in the tree shrew,'' J. Comp. Neurol. **226**, 289–305.

Ebert, U., and Ostwald, J. (**1995**). ''GABA can improve acoustic contrast in the rat ventral cochlear nucleus,'' Exp. Brain Res. **104**, 310–322.

Eggermont, J. J. (**1985**). ''Peripheral auditory adaptation and fatigue: A model oriented review,'' Hearing Res. **18**, 57–71.

Elverland, H. H. (**1977**). ''Descending connections between the superior olivary and cochlear nuclear complexes in the cat studied by autoradiographic and horseradish peroxidase methods,'' Exp. Brain Res. **27**, 397–412.

Evans, E. F. (**1996**). ''Inhibition and signal processing in the cochlear nucleus,'' in *Acoustic Signal Processing in the Central Auditory System*, edited by J. Syka (Plenum, New York), p. 13.

Feng, J., Kuwada, S., Ostapoff, E. M., Batra, R., and Morest, D. K. (**1994**). ''A physiological and structural study of neuron types in the cochlear nucleus. I. Intracellular responses to acoustic stimulation and current injection,'' J. Comp. Neurol. **346**, 1–18.

Fuller, J. H., and Shlag, J. D. (**1976**). ''Determination of antidromic excitation by the collision test: problems of interpretation,'' Brain Res. **112**, 283–298.

Furakawa, T., and Matsuura, S. (**1978**). ''Adaptive rundown of excitory post-synaptic potentials at synapses between hair cells and eighth nerve fibers in the goldfish,'' J. Physiol. (London) **276**, 193–210.

Furakawa, T., Harashida, Y., Masuura, S. (**1978**). ''Quantal analysis of the size of excitatory post-synaptic potentials at synapses between hair cells and afferent nerve fibers in goldfish,'' J. Physiol. (London) **276**, 211–226.

Furakawa, T., Masuura, S., and Hwang, J. C. (**1979**). ''Peripheral adaptation with built-in mechanisms for dynamic response in the auditory organ,'' in *Integrative Control Functions of the Brain*, Vol. II (Elsevier, Kodansha), pp. 93–94.

Godfrey, D. A. (**1993**). ''Comparison of quantitative and immunohistochemistry for choline acetyltransferase in the rat cochlear nucleus,'' in *The Mammalian Cochlear Nuclei: Organization and Function*, edited by M. A. Merchan, J. M. Juiz, D. A. Godfrey, and E. Mugnaini (Plenum, New York).

Godfrey, D. A., Beranek, K. L., Carlson, L., Parli, J. A., Dunn, J. D., and Ross, C. D. (**1990**). ''Contribution of centrifugal innervation to choline acetyl-transferase activity in the cat cochlear nucleus,'' Hearing Res. **49**, 259–280.

Godfrey, D. A., Carlson, L., Parli, J. A., and Ross, C. D. (**1988**). ''Distribution of choline acetyltransferase activity in the trapezod body of the rat,'' Soc. Neurosci. Abstr.

Godfrey, D. A., Carter, J. A., Lowry, O. H., and Matschinsky, F. M. (**1978**). ''Distribution of gamma-aminobutyric acid, glycine, glutamate and aspartate in the cochlear nucleus of the cat,'' J. Histochem. Cytochem. **26**, 118–126.

Godfrey, D. A., Kiang, N. Y. S., and Norris, B. E. (**1975**). ''Single unit activity in the posteroventral cochlear nucleus of the cat,'' J. Comp. Neurol. **162**, 247–268.

Godfrey, D. A., Park, J. L., Rabe, J. R., Dunn, J. D., and Ross, C. D. (**1983**).

''Effects of large brain stem lesions on the cholinergic system in the rat cochlear nucleus,'' Hearing Res. **11**, 133–156.
Goodman, D. A., Smith, R. L., and Chamberlin, S. C. (**1982**). ''Intracellular and extracellular responses in the organ of Corti of the gerbil,'' Hearing Res. **7**, 161–179.
Harris, D. M., and Dallos, P. (**1979**). ''Forward masking of auditory nerve fiber responses,'' J. Neurophysiol. **42**, 1083–1107.
Jesteadt, W., Bacon, S. P., and Lehman, J. R. (**1982**). ''Forward masking as a function of frequency, masker level and signal delay,'' J. Acoust. Soc. Am. **71**, 950–962.
Kaltenbach, J. A., Meleca, R. J., Falzarano, P. R., Myers, S. F., and Simpson, T. H. (**1993**). ''Forward masking properties of neurons in the dorsal cochlear nucleus: Possible role in the process of echo suppression,'' Hearing Res. **67**, 35–44.
Kiang, N. Y. S. (**1965**). ''Stimulus coding in the auditory nerve and cochlear nucleus,'' Acta Oto-Laryngol. **59**, 186–200.
Kim, D. O., Parham, H., Zhao, H., and Ghoshal, S. (**1995**). ''The olivocochlear feedback gain control subsystem: Ascending input from the small cell cap of the cochlear nucleus,'' in *Active Hearing*, edited by A. Flock, X. Dottoson, and M. Ulfendahl (Pergamon, New York), pp. 31–51.
Leake, P. A., and Snyder, R. L. (**1989**). ''Topographic organization of the central projections of the spiral ganglion in cats,'' J. Comp. Neurol. **281**, 612–629.
Liberman, M. C. (**1982**). ''Single-neutron labeling in the cat auditory nerve,'' Science **216**, 1239–1241.
Liberman, M. C. (**1991**). ''Central projections of auditory nerve fibers of differing spontaneous rate. I. Anteroventral cochlear nucleus,'' J. Comp. Neurol. **313**, 240–258.
Liberman, M. C. (**1993**). ''Central projections of auditory nerve fibers of differing spontaneous rate, II. Posteroventral and dorsal cochlear nucleus,'' J. Comp. Neurol. **327**, 17–36.
Manis, P. B. (**1990**). ''Membrane properties and discharge characteristics of guinea pig dorsal cochlear nucleus neurons studied *in vitro*,'' J. Neurosci. **10**, 2338–2351.
Manis, P. B., and Marx, S. O. (1991). ''Outward currents in isolated ventral cochlear nucleus neurons,'' J. Neurosci. **11**, 2865–2880.
Martin, M. R., and Dickson, J. W. (**1983**). ''Lateral inhibition in the anteroventral cochlear nucleus of the cat. A microiontophoretic study,'' Hearing Res. **9**, 35–41.
Martin, M. R., Dickson, J. W., and Fex, J. (**1982**). '' Bicuculline, Strychnine and depressant amino acid responses in the anteroventral cochlear nucleus of the cat,'' Neuropharm. **21**, 201–207.
Oertel, D. (**1983**). ''Synaptic response and electrical properties of cells in brain slices of the mouse anteroventral cochlear nucleus,'' J. Neurosci. **3**, 2043–2053.
Osen, K. K., and Roth, K. (**1969**). ''Histochemical localization of cholinesterases in the cochlear nuclei of the cat with notes on the origin of acetylcholinesterase-positive afferents and the superior olive,'' Brain Res. **16**, 165–185.
Palombi, P. S., and Caspary, D. M. (**1992**). ''The GABA-A receptor antagonist bicuculline alters the response properties of posteroventral cochlear nucleus neurons,'' J. Neurophysiol. **67**, 738–746.
Pickles, J. O. (**1988**). *An Introduction to the Physiology of Hearing* (Academic, New York), 2nd ed., p. 165.
Potashner, S. J., Benson, C. G., Ostapoff, E. M., Lindberg, N., and Morest, D. K. (**1993**). ''Glycine and GABA: transmitter candidates of projections descending to the cohlear nucleus,'' in *The Mammalian Cochlear Nuclei: Organization and Function*, edited by M. A. Merchan, J. M. Juiz, D. A. Godfrey, and E. Mugnaini (Plenum, New York).
Relkin, E. M., and Doucet, Jr. (**1991**). ''Recovery of auditory neurons from prior stimulation,'' Abstr. Neurosci. 362.5, p. 874.
Rhode, W. S., Smith, P. H., and Oertel, D. (**1983**). ''Physiological response properties of cells labeled intracellularly with horseradish peroxidase in cat dorsal cochlear nucleus,'' J. Comp. Neurol. **213**, 426–447.
Ritz, L. A., and Brownell, W. E. (**1982**). ''Single unit analysis of the posteroventral cochlear nucleus of the decerebrate cat,'' Neuroscience **7**, 1995–2010.
Russell, I. J., and Sellick, P. M. (**1978**). ''Intracellular studies of haircells in the mammalian cochlea,'' J. Physiol. **284**, 261–290.
Saint Marie, R. L., Benson, C. G., Ostapoff, E. M., and Morest, D. K. (**1991**). ''Glycine immunoreactive projections from the dorsal to the anteroventral cochlear nucleus,'' Hearing Res. **51**, 11–28.
Saint Marie, R. L., Ostapoff, E. M., Benson, C. G., Morest, D. K., and Potashner, S. J. (**1993**). ''Non-cochlear projections to the ventral cochlear nucleus: are they mainly inhibitory?'' in *The Mammalian Cochlear Nuclei: Organization and Function*, edited by M. A. Merchan, J. M. Juiz, D. A. Godfrey, and E. Mugnaini (Plenum, New York).
Salvi, R. J., Saunders, S. S., Ahroon, W. A., Shivapuja, B. G., and Arehole, S. (**1986**). ''Psychophysical and physiological aspects of auditory temporal processing in listeners with noise-induced sensorineural hearing loss,'' in *Basic and Applied Aspects of Noise-Induced Hearing Loss*, edited by R. J. Salvi, D. Henderson, R. P. Hamernik, and V. Colletti (Plenum, New York), pp. 179–184.
Shofner, W. P., and Young, E. D. (**1985**). ''Excitatory/inhibitory response types in the cochlear nucleus: Relationships to discharge patterns and response to electrical stimulation in auditory nerve,'' J. Neurophysiol. **54**, 917–936.
Shore, S. E. (**1995**). ''Recovery of forward-masked responses in ventral cochlear nucleus neurons,'' Hearing Res. **82**, 31–43.
Shore, S. E., and Nuttall, A. L. (**1984**). ''The effects of cochlear hypothermia on compound action potential tuning,'' J. Acoust. Soc. Am. **77**, 590–598.
Shore, S. E., Helfert, R. H., Bledsoe, Jr., S. C., Altschuler, R. A., and Godfrey, D. A. (**1991**). ''Descending projections to the guinea pig cochlear nucleus,'' Hearing Res. **52**, 255–268.
Shore, S. E., Helfert, R. H., Bledsoe, Jr., S. C., Altschuler, R. A., and Godfrey, D. A. (**1992**). ''Connections between cochlear nuclei in guinea pig,'' Hearing Res. **62**, 16–26.
Smith, R. L. (**1977**). ''Short-term adaptation in single auditory nerve fibers: Some post-stimulatory effects,'' J. Neurophysiol. **40**, 1098–1112.
Smith, R. L. (**1979**). ''Adaptation, saturation, and physiological masking in single auditory-nerve fibers,'' J. Acoust. Soc. Am. **65**, 166–178.
Smith, R. L., and Brachman, M. L. (**1980**). ''Operating range and maximum response of single auditory nerve fibers,'' Brain **184**, 499–505.
Smith, R. L., and Brachman, M. L. (**1982**). ''Adaptation in auditory nerve fibers: A revised model,'' Biol. Cybern. **44**, 107–120.
Smith, P. H., and Rhode, W. S. (**1989**). ''Structural and functional properties distinguish two types of multipolar cells in the ventral cochlear nucleus,'' J. Comp. Neurol. **282**, 595–616.
Smith, R. L., Brachman, M. L., and Goodman, D. A. (**1983a**). ''Adaptation in the auditory periphery,'' Ann. (N.Y.) Acad. Sci. **40**, 79–119.
Smith, R. L., Frisina, R. D., and Goodman, D. A. (**1983b**). ''Intensity functions and dynamic responses from the cochlea to the cochlear nucleus,'' in *Hearing–Physiological Bases and Psychophysics*, edited by R. Klinke and R. Hartmann (Springer-Verlag, New York), pp. 112–118.
Smoorenburg, G. F., and Kloppenburg, B. A. M. (**1986**). ''Single unit tuning curves measured with psychoacoustic masking paradigms, in *Auditory Frequency Selectivity*, edited by B. C. Moore and R. D. Patterson, NATO ASI series A, Vol. 119 Life Sciences (Plenum, New York).
Snyder, R. L., and Leake, P. A. (**1988**). ''Intrinsic connections within and between cochlear nucleus subdivisions in cat,'' J. Comp. Neurol. **278**, 209–255.
Spangler, K. M., and Warr, W. B. (**1991**). ''The descending auditory system,'' in *Neurobiology of Hearing: The Central Auditory System*,'' edited by R. A. Altschuler (Raven, New York).
Staatz-Benson, C., and Potashner, S. J. (**1988**). ''Uptake and release of glycine in the guinea pig cochlear nucleus after axotomy of afferent or centrifugal fibers,'' J. Neurochem. **51**, 370–379.
Starr, A., and Wernick, J. S. (**1968**). ''Olivocochlear bundle: Effects on spontaneous and tone-evoked activities of single units in cat cochlear nucleus,'' J. Neurophysiol. **31**, 549–564.
Tolbert, L. P., and Morest, D. K. (**1982**). ''The neuronal architecture of the anteroventral cochlear nucleus of the cat in the region of the cochlear nerve root: Electron microscopy,'' Neuroscience **7**, 3053–3068.
Turner, C. N., Relkin, E. M., and Doucet, J. (**1994**). ''Psychophysical and physiological forward masking studies: Probe duration and risetime effects,'' J. Acoust. Soc. Am. **96**, 795–800.
Van Noort, J. (**1969**). *The Structure and Connections of the Inferior Colliculus: An Investigation of the Lower Auditory System* (Proefschrift, Leiden, van Gorcum and Co., New York).
Wenthold, R. J., and Martin, M. R. (**1984**). ''Neurotransmitters of the auditory nerve and central auditory system,'' in *Hearing Science: Recent Advances*, edited by C. Berlin (College-Hill, San Diego), pp. 341–369.
Westerman, L. A., and Smith, R. L. (**1984**). ''Rapid and short-term adaptation in auditory nerve response,'' Hearing Res. **15**, 249–260.

Wickesberg, R. E., and Oertel, D. (**1990**). ''Delayed frequency specific inhibition in the cochlear nucleus of mice: A mechanism for monaural echo suppression,'' J. Neurosci. **10**, 1762–1768.
Widin, G. P., and Viemeister, N. F. (**1979**). ''Short-term spectral effects in puretone forward masking,'' J. Acoust. Soc. Am. **66**, 396–399.
Winter, I. M., Robertson, D., and Cole, K. S. (**1989**). ''Descending projections from auditory brainstem nuclei to the cochlea and cochlear nucleus of the guinea pig,'' J. Comp. Neurol. **280**, 143–157.
Winter, I. M., and Palmer, A. R. (**1993**). ''Best frequency (BF) threshold reductions caused by off-BF non-excitatory tones in onset units of the cochlear nucleus,'' Abstracts of the Association for Research in Otolaryngology, p. 123.
Winter, I. M., Robertson, D., and Yates, G. K. (**1990**). ''Diversity of characteristic frequency rate-intensity functions in guinea pig auditory nerve fibers,'' Hearing Res. **45**, 191–202.
Wu, S. H., and Oertel, D. (**1984**). ''Intracellular injection with horseradish peroxidase of anteroventral cochlear nucleus,'' J. Neurosci. **4**, 1577–1588.
Young, E. D. (**1984**). ''Response characteristics of neurons of the cochlear nuclei, in *Recent Advances in Hearing Sciences*, edited by C. I. Berlin (College Hill, San Diego, CA).
Zeng, F. G., Turner, C. W., and Relkin, E. M. (**1991**). ''Recovery from prior stimulation II: effects upon intensity discrimination,'' Hearing Res. **55**, 223–230.

The magical "wave" seven, plus or minus two?[a)]

Willy Wong[b)] and Shuji Mori
Faculty of Engineering, Toyama Prefectural University, Toyama, Japan

(Received 24 November 1997; revised 24 February 1998; accepted 10 April 1998)

The idea of the magical number seven has been with us for over 40 years now. During this time, it has been studied extensively by both psychologists and other sensory scientists. One might be skeptical about any new results and ask ''What more possibly can we say about this topic?'' However, in this paper, an attempt is made to refine the interpretation of the magical number by demonstrating that it is not so much a number, but actually a ''wave.'' That is, independent of both experimental fluctuations and statistical bias, the magical number takes on a continuum of possible values. This prediction, made theoretically, is supported by existing experimental data. While this prediction does not amount to any significant change to the understanding of the magical number, it may however provide a criterion to judge the acceptability of any theory that purports to explain the magical number phenomenon. © *1998 Acoustical Society of America.*
[S0001-4966(98)04707-9]

PACS numbers: 43.66.Ba [RVS]

INTRODUCTION

Information theory has been applied extensively to the study of sensory perception. One example is in the exploration of sensory performance relating to how human subjects are limited in their ability to classify single-dimensional stimuli. Information transmitted to a subject is defined as the difference between the input (or stimulus) information and the information loss due to errors in classification (equivocation). In general, increasing the amount of stimulus information results in an increase in transmitted information up to an asymptotic value as shown in Fig. 1. This graph is well-known and has been documented many times, most prominently by Miller (1956).

The purpose of this paper is to question the exact form of this graph. In Fig. 1, the graph shows that transmitted information rises as a monotonic function of the stimulus information. This idealized graph is supported by experimental measurements—up to a point. More precisely, however, one observes small differences in the experimental curve which deviate from the monotonic function shown in Fig. 1. These differences can be observed, for example, in the studies by Pollack (1952) and by Garner (1953); see Figs. 2 and 3. Taken literally, the data points in the graphs show both an apex and a nadir corresponding to critical points in the curve. In the past, these deviations have been attributed to both random error and statistical bias. However, we stand to demonstrate in this paper that these points are not due to any random or statistical process but are actually inherent to the properties of the magical number.

While the exact form of the curve is probably of little interest to sensory researchers (given that both the experimental fluctuations and the statistical bias will in general exceed the magnitude of these deviations), we feel that these critical points do however provide indirect evidence that a comprehensive sensory theory accounting for the magical number must incorporate the idea that a subject utilizes a set of criteria along a decision axis to produce his or her response in an absolute identification experiment.

The second point of the paper is to demonstrate the relationship between two studies which attempt to explain the magical number phenomenon: the intensity resolution studies by Durlach and Braida beginning in 1969 and our recently proposed theory (Wong and Mori, 1998). We shall demonstrate that the two theories are actually compatible, if not identical, our theory being, in a sense, a subset of the Durlach and Braida model. However, despite the relative simplicity of our theory, it confers an advantage over the model of Durlach and Braida when studying the magical number. One can, from our approach, quite easily ascertain the perceptual characteristics underlying the magical number as well as understand the origin of the critical points observed in both Figs. 2 and 3. These issues will be fully elaborated upon in the Discussion.

We begin by reviewing several key concepts from our proposed theory of the magical number.

I. A CONCEPTUAL APPROACH TO THE MAGICAL NUMBER

In a previous paper (Wong and Mori, 1998), we introduced a new approach to understanding the magical number. Primarily because it attempts only to deal with the nature of the magical number itself, it is simpler than many of the earlier theories proposed in other studies (e.g., Durlach and Braida, 1969; Luce *et al.*, 1976; Laming, 1984; Marley and Cook, 1984). The entire theory is based on only a single parameter and was developed by extending the Garner and Hake (1951) information theoretical approach to the absolute identification process.

An absolute identification experiment involves a task whereby a subject is required to classify a single presentation

[a)]This paper was presented at the Technical Committee for Psychological and Physiological Acoustics Meeting, Acoustical Society of Japan on December 12, 1997 in Kumamoto, Japan.

[b)]Current address: Cavendish Laboratory, University of Cambridge, Electronic mail: ww209@phy.cam.ac.uk

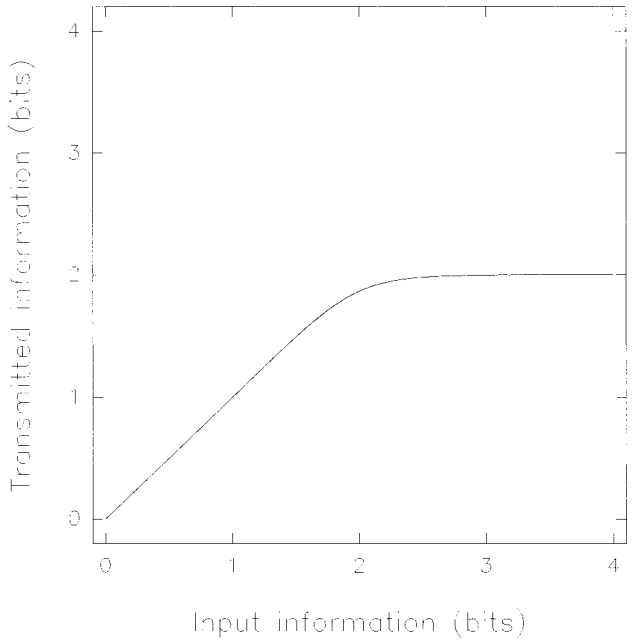

FIG. 1. Schematic diagram showing how transmitted information varies with input information for a human subject. Input information is defined as the base 2 logarithm of the total number of stimulus categories used in the experiment.

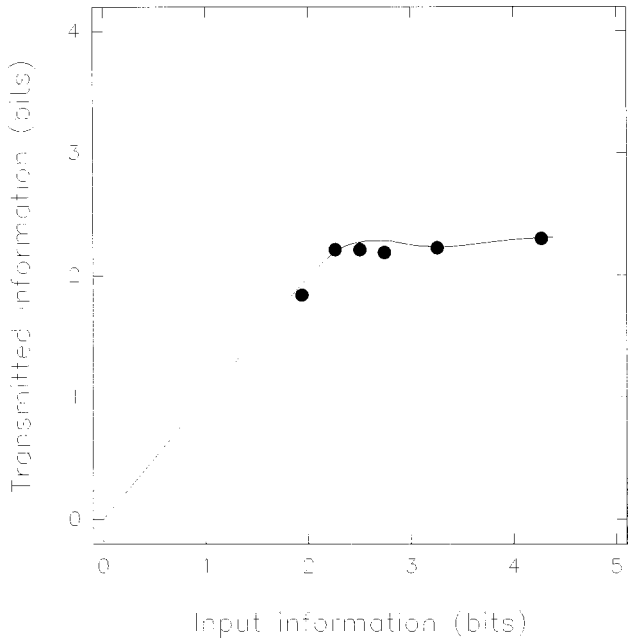

FIG. 3. Data of Garner (1953) from an absolute identification experiment on loudness. Smooth curve was obtained from a single parameter fit from the theory. Please see text for details.

of a stimulus into a pre-assigned category scheme. The stimuli are drawn randomly from a unidimensional continuum. For example, in the absolute identification of loudness, stimuli are drawn from equally spaced categories spanning a fixed stimulus range measured in decibels. The subject's task is to identify, as best as possible, to which category the presented stimuli belong. We shall only consider the case where the categories are nonoverlapping and where there are the same number of input and response categories.

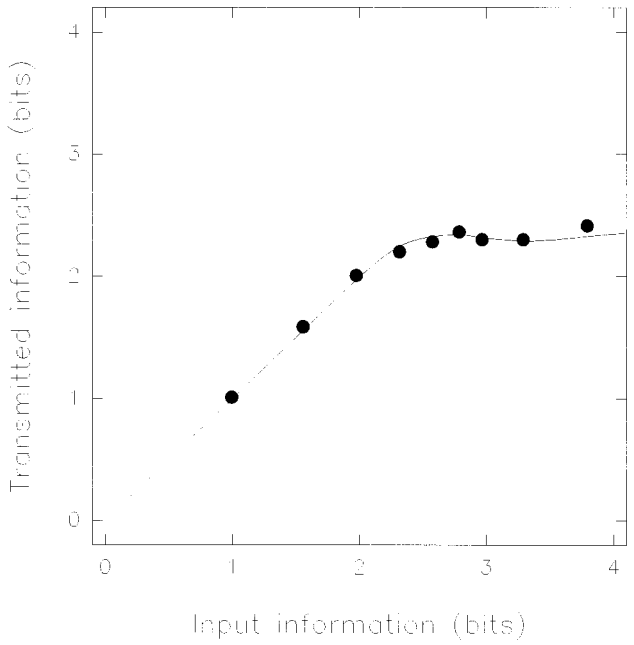

FIG. 2. Data of Pollack (1952) from an absolute identification experiment on pitch. Smooth curve was obtained from a single parameter fit from the theory. Please see also Fig. 3.

A single presentation and classification (i.e., response) constitutes one trial in an experiment. Data collected from sequential trials can be tabulated in a confusion matrix formed by taking input/response pairs obtained from each trial. Correct hits form the diagonal of this matrix. When a large number of trials have been collected, following Garner and Hake (1951), the amount of information required to make one classification can be calculated from the matrix. Denoting the input as x (drawn from an ensemble of possible inputs X) and the response as y (from an ensemble of possible responses Y), the transmitted information can be calculated from the expression for mutual information as introduced by Shannon (1948),

$$I_t = H(X) - H(X|Y). \tag{1}$$

The first term represents the input or stimulus information and the second term represents information loss due to errors in response. It can be demonstrated that

$$I_t = H(X) - H(X|Y) = H(Y) - H(Y|X), \tag{2}$$

where the transmitted information is now calculated with reference to the response information.

The first term of this equation represents the Shannon information associated with the probability of response independent of the input. In the case where the input x is uniformly distributed, one would expect that the response y to be near-uniformly distributed except near the edges where the subject would have a higher proportionality of correct hits due to the usual anchor or edge effects. This is usually what is observed experimentally. If the range of the experiment is large enough, we can ignore the edge effects in our calculation. Thus the Shannon information or entropy associated with a uniform response distribution over an m category experiment is

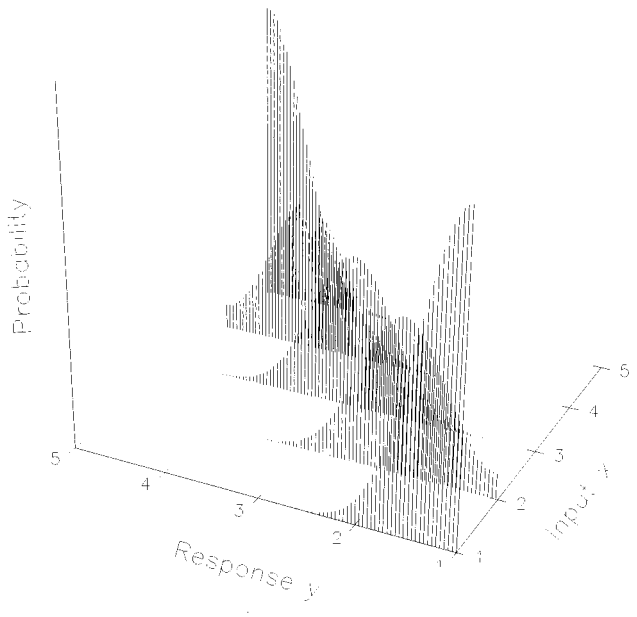

FIG. 4. Schematic diagram illustrating a typical confusion matrix. Response probability is plotted as a function of the input and the response. The response probability along each row is normally distributed with a fixed value of variance to a good approximation except for the first and last rows.

$$H(Y) \simeq \ln(m). \tag{3}$$

We shall continue to use natural logarithms for the remainder of the paper. To convert from natural units to bits, one simply divides the value of information in natural units by ln(2).

The second term is somewhat more difficult to explain. $H(Y|X)$ represents the information loss due to errors in the response (for example, a stimulus from category #3 is classified as category #4). In general, one would expect this error to be normally distributed. That is, y is normally distributed about x so long as there is no drift in the subject's response. This is commonly observed in experiments where the categories are measured in logarithmic physical units (i.e., dB for loudness, log Hz for pitch, etc.). Each row of the categorical matrix shows a characteristic normallike distribution centered along the main diagonal with approximately the same variance, except of course in the first and last rows where the response is strongly influenced by edge effects. This is shown schematically in Fig. 4. It can be demonstrated through a chi-squared analysis of real data that the value of σ_{eff}^2 (properly speaking, the sample variance) is constant for each row apart from the two exceptional rows (Norwich, 1997).

When an experiment is carried over a large number of categories, the response distribution along each row will tend toward a continuous normal distribution. This is the limit that we are interested in. Assuming that the range is sufficiently large, we turn to Shannon (1948) who demonstrated that the entropy of a normal distribution is given by the succinct expression

$$H = \tfrac{1}{2} \ln(2\pi e \sigma_{\text{eff}}^2). \tag{4}$$

σ_{eff}^2 is the variance observed in each row. Notice that the value of entropy is dependent only on the variance and not the mean of the distribution.

Let us now return to $H(Y|X)$ in Eq. (2). $H(Y|X)$ is just the average row entropy of the confusion matrix. Since σ_{eff}^2 is constant for all rows except for the first and last, this implies that the row entropy is constant. Therefore, in the large range limit, we can ignore the contributions from the first and last rows to write

$$H(Y|X) = \tfrac{1}{2} \ln(2\pi e \sigma_{\text{eff}}^2), \tag{5}$$

and

$$I_t = \ln(m) - \tfrac{1}{2} \ln(2\pi e \sigma_{\text{eff}}^2). \tag{6}$$

This equation is derived in greater detail in Wong and Norwich (1997) and has been demonstrated to work quite well for values of $m \gtrsim 10$.

Next, we address the issue of how σ_{eff}^2 changes with the number of categories m. The confusion matrix represents an artificial categorization of the stimulus continuum into discrete components. The subject is required to respond using the preassigned category scheme and yet we must keep in mind that the subject's underlying response need not follow this same format. It would seem reasonable to assume that the underlying response is continuous and normally distributed.

Equation (5) demonstrates that the row entropy is, to a good approximation, dependent only on the variance. Since the variance is approximately constant, we conclude that the row entropy can be calculated solely from a single, representative row of the matrix. Thus we need only to concern ourselves with how this row can be obtained from the underlying continuous response distribution. For simplicity, we choose the middle row of the matrix defined by category $\#(m+1)/2$. Since this number is an integer, m can only take on odd values, a restriction to be kept in mind as we proceed.

We denote the underlying response distribution as $P(y)$ where y is the continuous response variable with variance σ^2. The range of the experiment is fixed at $R = 2a$. It is convenient to set the mean of $P(y)$ equal to zero since the mean does not play a part in the calculation of information [cf. Eq. (6)]. This distribution is plotted in Fig. 5. We have illustrated the case where there are only three categories in the experiment. The ticks on the lower axis show the placement of these categories.

To calculate the probability of response for each category, we introduce a set of criteria (e.g., Treisman, 1985). If no systematic bias is introduced into the subject's response, we might set the criteria at the midway points between adjacent categories. These are shown by the dotted lines in Fig. 5. Let us denote the probability for responding with the kth category as $g(k)$. $g(k)$ is calculated from integrating the underlying probability distribution $P(y)$ between adjacent criteria. Thus the probability that the subject responds with category #1 (given a stimulus from category #2) is obtained by integrating $P(y)$ between $-a$ and $-a/2$, etc. For further details, the reader is referred to Wong and Mori (1998). The variance of the discrete response is then calculated using the standard formula,

$$\sigma_{\text{eff}}^2 = \sum_{k=1}^{m} \left(k - \frac{m+1}{2} \right)^2 g(k). \tag{7}$$

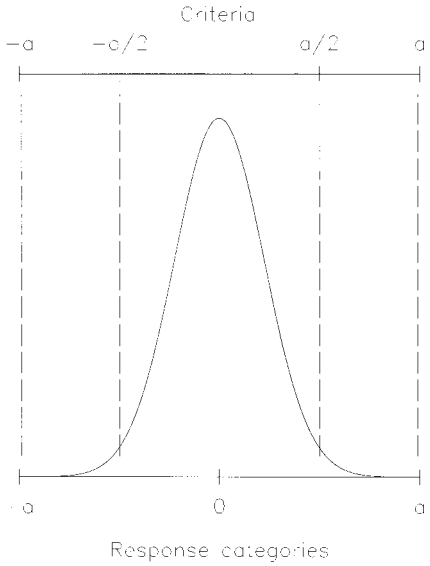

FIG. 5. The continuous distribution of response for an experiment consisting of three categories. The placement of the categories is shown on the lower axis while the criteria are shown on the upper axis. $R=2a$ defines the total stimulus range of the experiment.

In the case where m is large, Eq. (7) takes on a very simple and intuitive form. Calculating an asymptotic expansion for large values of m and assuming that the range is large ($\sqrt{2}\sigma/a \ll 1$), it can be shown that

$$\sigma_{\text{eff}} \simeq m\sigma/R, \tag{8}$$

the standard equation relating continuous to discrete probability distributions (please see Appendix 1 of Wong and Mori, 1998). This equation works best for $m \gtrsim 10$. In writing Eq. (8), we must be careful not to confuse σ_{eff} with σ. σ_{eff} is the standard deviation of response along each row of the confusion matrix while σ is the standard deviation of the underlying continuous response distribution illustrated in Fig. 5. Substituting Eq. (8) into Eq. (6) we find

$$I_t = \ln(R) - \tfrac{1}{2}\ln(2\pi e\sigma^2) = \ln(R/\sigma) - \tfrac{1}{2}\ln(2\pi e). \tag{9}$$

As expected, this is the information associated with a continuous system.

This work forms the core of our recent paper (Wong and Mori, 1998) and the interested reader is referred to this article. We conclude this section with two calculations from the same paper. Recall that Figs. 2 and 3 show, respectively, the results of an absolute identification experiment in pitch (Pollack, 1952) and in loudness (Garner, 1953). These two experiments were used to evaluate the theory. In both experiments, however, m extended to values below the restricted range of our theory (m must be larger than 10). In order to overcome this limitation, we did the following. Returning to Eq. (5), instead of evaluating a close-formed expression for the equivocation entropy, we replaced it with the unevaluated entropy of the middle row to obtain

$$H(Y|X) = -\sum_{k=1}^{m} g(k)\ln g(k). \tag{10}$$

Note that in the limiting case of large m, we can approximate the sum by an integral and replace $g(k)$ with $P(y)$ (the continuous normal distribution). The right-hand sides of Eqs. (5) and (10) would then be identical.

Finally, we calculate the equivocation from Eq. (10) using $\sigma/a = 9.4\times10^{-2}$ for pitch and $\sigma/a = 9.8\times10^{-2}$ for loudness to obtain the two smooth curves shown in Figs. 2 and 3. While the theoretical prediction is in close agreement with the data, but this is not the interesting feature of the graphs. What is surprising is that the theoretical information curves show both a nadir and an apex in agreement with experimental data, but in contrast to the monotonic behavior of the idealized curve shown in Fig. 1. Moreover, the theoretical curves appear to increase even beyond the 16–20 category limit contrary to common expectation.

This discovery prompted us to carefully examine our theory because we had taken certain approximations in developing our equations (e.g., we had made no provisions to account for edge effects). It was of particular interest to see if the critical points would remain when the additional factors were taken into consideration. Thus we turned our attention to the more complete study of Durlach and Braida (1969).

II. A COMPARISON WITH DURLACH AND BRAIDA (1969)

Durlach and Braida (1969) detailed the development of a model for intensity resolution based on certain ideas of Thurstonian scaling. Their decision model is similar to the one discussed in the previous section where the response is represented by a normal distribution along a decision axis. They did, however, considered the case of m individual normal distributions corresponding to the m categories or stimuli of the experiment. The distributions are identical in variance but are each shifted according to the stimulus value (or, equivalently, the category value). Likewise, they introduced a set of criteria placed midway between adjacent categories. The probability of response (analogous to our $g(k)$ function introduced in the last section) is then calculated by integrating the normal distribution between adjacent criteria.

In Figs. 1 and 2 of their 1969 paper, they show calculations from their model predicting how mutual information (I_t) would change for different values of m (Durlach and Braida used the symbol N) and Δ'. Δ' is simply the stimulus range divided by the standard deviation of the distribution. Thus using the symbology introduced in the previous section, we write

$$\Delta' = R/\sigma = 2a/\sigma. \tag{11}$$

In a following paper (Braida and Durlach, 1972), they demonstrated that their model for calculating I_t is in close agreement with measured data.

Recall that the subject's response in both the first and the last rows of the matrix are strongly influenced by edge effects (cf. Fig. 4). In the original Durlach and Braida model no attempt was made to account for these effects, although recently they have proposed an updated treatment incorporating an extensive model for the response near the boundaries of the matrix (Braida and Durlach, 1988). We shall take a simpler approach than one they have introduced in order to keep the calculations as simple as possible.

Let us consider the following response distribution,

$$P(y)=\frac{1}{\sqrt{2\pi\sigma^2}}\,e^{-(y-x)^2/2\sigma^2}+\frac{1}{\sqrt{2\pi\sigma^2}}\,e^{-(-y-x+2a)^2/2\sigma^2}+\frac{1}{\sqrt{2\pi\sigma^2}}\,e^{-(-y-x-2a)^2/2\sigma^2},\tag{12}$$

where x is the stimulus value, y is the response value and a is half the range. We can simplify this expression by defining the function

$$N(y)=\frac{1}{\sqrt{2\pi\sigma^2}}\,e^{-(y-x)^2/2\sigma^2}\tag{13}$$

to obtain

$$P(y)=N(y)+N(-y+2a)+N(-y-2a).\tag{14}$$

A plot of $P(y)$ shows that it is a normalized Gaussian distribution reflecting at both boundaries, $y=-a$ and $y=a$. In fact, Fig. 4 was generated using $P(y)$ so that Eq. (14) appears to be in good qualitative agreement with real data. All that we have done, in writing Eq. (14), is to reflect the part of the distribution which lies outside of the range $[-a,a]$ to provide a first-order approximation to edge effects (Wong and Norwich, 1997). We shall now calculate the mutual information as predicted by the Durlach and Braida model using the response distribution given by Eq. (14).

In Figs. 6 and 7, two graphs from Durlach and Braida (1969, Figs. 1 and 2) are recalculated using the response distribution given in Eq. (14). The results do not differ substantially (recall that in their 1969 paper no attempt was made to account for edge effects). The interesting thing to observe in Fig. 7 is that the critical points (the nadir and apex) also appear in our modification of the Durlach and Braida model. Thus we can conclude that the critical points are probably not the consequence of edge effects since, as demonstrated in the previous section, computation with our own theory (no provision for edge effects) resulted in the same form of curve (cf. Figs. 2 and 3).

For completeness we show in Figs. 8 and 9 predictions made by our theory bearing in mind that only odd values of m can be used in the calculations (recall that the middle row is defined by the category $(m+1)/2$). As expected, the results from the Durlach and Braida approach and the results from our own approach come closest for large values of Δ' when the edge effects can be effectively ignored. Furthermore, in the limit of $m=$ ''∞'' when the standard deviation of response σ_{eff} can be approximated by the simple expression given in Eq. (8), the equation for transmitted information takes on a particularly simple form [cf. Eq. (9)] which we have plotted in both Figs. 6 and 8 with the dotted line. The number of stimuli is increased indefinitely until the system is effectively continuous. We see that edge effects, as quantified at least by the response distribution given in Eq. (12), do not much affect the value of the magical number (defined as the limit of large m and Δ').

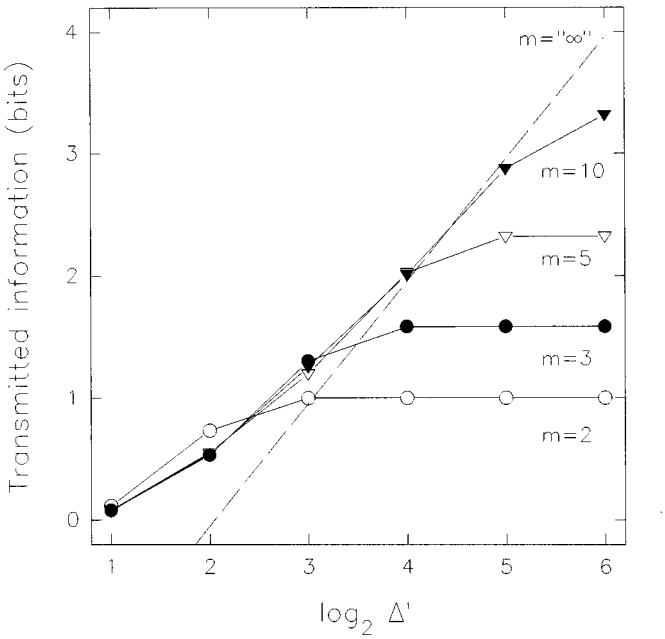

FIG. 6. Figure 1 from Durlach and Braida (1969) was recalculated using the response distribution given in Eq. (14). The dotted line shows the limit where the number of categories becomes indefinitely large and the stimulus input is almost continuous. Please see also Fig. 7.

III. DISCUSSION

A. The magical number or magical wave?

The fluctuations in the value of transmitted information as shown by Figs. 2 and 3 are not at least according to theory attributable to experimental errors or statistical bias. This leads to several possibilities. First, we ask the question of whether the existing experimental studies have adequately

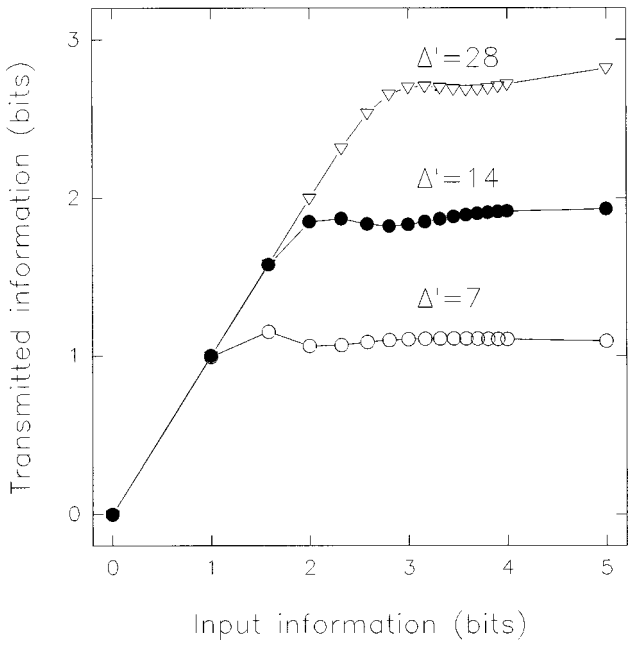

FIG. 7. Figure 2 from Durlach and Braida (1969) was recalculated using the response distribution given in Eq. (14). The results of the recalculation do not differ appreciably although the surprising feature of this graph is that the Durlach and Braida model also predicts the critical points in the transmitted information curve. Please see also Fig. 6.

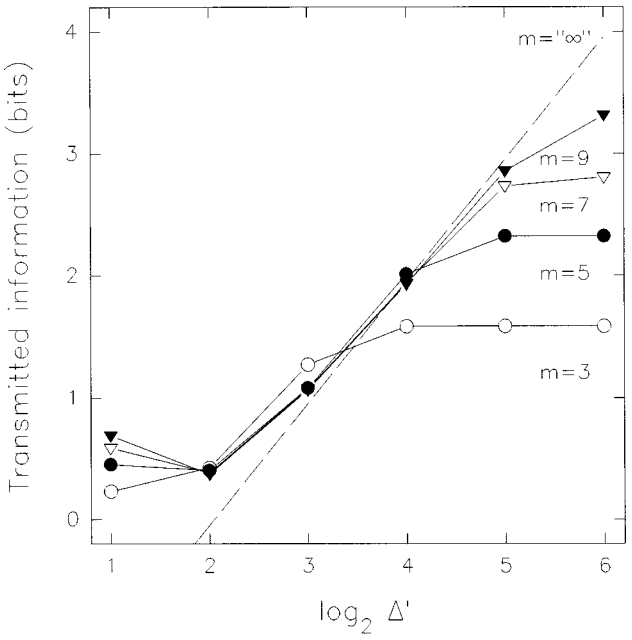

FIG. 8. Figure 6 recalculated with Eq. (10) using the approach detailed in Sec. I (for full details please refer to Wong and Mori, 1998). The calculations from the Durlach and Braida approach and the calculations from our own approach come closest when Δ' is large. The dotted line shows the prediction of Eq. (9) where the number of stimulus categories are increased indefinitely and the system becomes effectively continuous. Please see also Fig. 9.

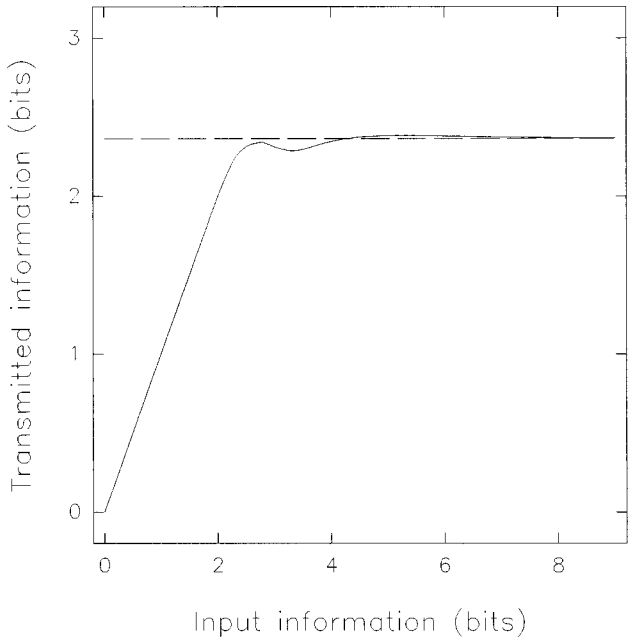

FIG. 10. The transmitted information curve is calculated to $m=512$ categories using the value of σ/a obtained from pitch (please see Fig. 2). While it is unlikely that a human subject can ever distinguish between so many different categories, this exploration serves to demonstrate whether existing experimental studies have adequately explored the large category limit defining the magical number. Since the theoretical curve does not change appreciably outside the 16–20 category limit, further experiments are probably not necessary.

explored the upper region defining the magical number. In principle, the information curve may reach other critical points that take on values which are higher than the asymptote. This question can of course be answered by conducting further experiments. It is also possible, however, for us to first explore this region theoretically to see if it is likely that further experimentation is required.

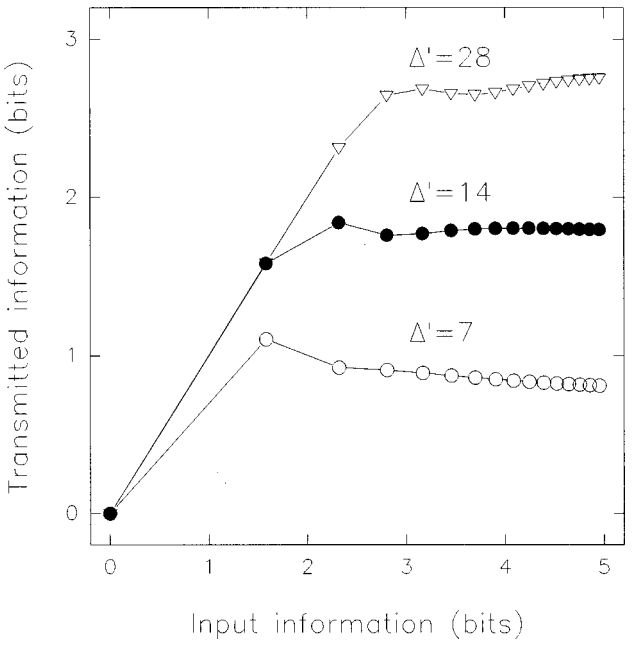

FIG. 9. Figure 7 recalculated with Eq. (10) using the approach detailed in Sec. I (for full details please refer to Wong and Mori, 1998). We see that the calculations from the Durlach and Braida approach and the calculations from our own approach come closest when Δ' is large. The critical points observed in the information curve are similar to the ones found in Figs. 2 and 3. Please see also Fig. 8.

While such calculations can be carried out with the Durlach and Braida model, the complexity of the calculations pose a serious computational problem. However, we can make the same calculation rather quickly using the Wong and Mori approach since the two methods detailed in this paper are identical in the limit of large $\Delta'=R/\sigma$ (the magical number limit). The results are shown in Fig. 10. I_t is calculated to $m=512$ categories using the value of $\sigma/a=0.094$ obtained from pitch (please see Fig. 3) keeping in mind that it is unlikely that a human subject can distinguish between so many different categories even at a large range. The horizontal line shows the prediction of the asymptote by Eq. (9). We observe that the transmitted information as predicted theoretically does not appear to change significantly outside the 16–20 category limit of the earlier studies. Beyond four stimulus categories, the difference of about 0.1 bits of information between the highest and the lowest portion of the information ''wave'' can be easily masked by experimental error or statistical bias. Nevertheless, Fig. 10 demonstrates that it is certainly possible that some point along the information curve can exceed the value of transmitted information at the asymptote.

B. Critical points: A necessary condition for a valid theory?

Since the shape of the transmitted information graph failed to lead to any new interpretation of the magical num-

ber, we now turn to an entirely different approach to understanding the significance behind the critical points, one that may even lead to a general principle of human perception. We begin by looking for the essential feature underlying the magical number phenomenon. Since the model of Durlach and Braida is too intricate to provide a simple answer to this question, we return to the approach detailed in Sec. I keeping in mind that edge effects do not play a prominent role in determining the value of the magical number.

We recall that the critical points in Figs. 2 and 3 appear in the range of 8–12 categories. Let us return to Eq. (6). Although Eq. (6) was derived with the restriction that m be greater than ten categories, we shall nevertheless use this equation keeping in mind that it is only a very crude approximation. Thus we can write down the difference in information between two values of m as

$$\Delta I_t = \Delta(\ln m) - \Delta(\ln \sigma_{\text{eff}}). \tag{15}$$

Around the critical point, the value of ΔI_t hardly changes (corresponding to the first derivative of I_t equalling zero) and Eq. (15) simplifies to be

$$\left.\frac{\Delta \ln \sigma_{\text{eff}}}{\Delta \ln m}\right|_{m=m_c} \sim 1. \tag{16}$$

That is, near the critical point ($m=m_c$) the slope of the standard deviation of response calculated from the matrix plotted against the number of categories on a full-logarithmic plot is approximately equal to one.

This result can also be demonstrated on a linear graph. In Fig. 11, σ_{eff} vs m is plotted (S-shaped curve). σ_{eff} was calculated at each value of m and a cubic spline was then introduced to plot the curve. The straight line corresponds to the asymptotic behaviour of σ_{eff} [cf. Eq. (8)]. The distinctive shape of this curve is the primary reason why the information curve shows a bump. For example, if σ_{eff} approached the asymptotic straight line from the bottom rather than crossing over and approaching from the top, the information curve would increase monotonically to an asymptote without showing the characteristic ''wavelike'' behavior.

The important feature of this demonstration is not the actual shape of the curve itself but rather what the shape of the curve is telling us: Fig. 11 appears to indicate that any theory of the magical number must be based upon the notion of criteria and a continuous distribution of response. We now present an argument for this assertion.

Recall that the S-shaped curve in Fig. 11 was obtained through a choice of only a single parameter σ (the standard deviation of continuous response). With this value of σ, we constructed a continuous normal distribution which we then partitioned into the discrete categories of response. σ_{eff} is then calculated from the resulting distribution at each value of m [cf. Eq. (7)]. By intuition, such a complex curve would require at least two parameters to create in an *ad hoc* mathematical fashion. Even if the same curve can be ''modeled'' by another technique, it would be reasonable to assume that this model would require the use of at least two parameters.

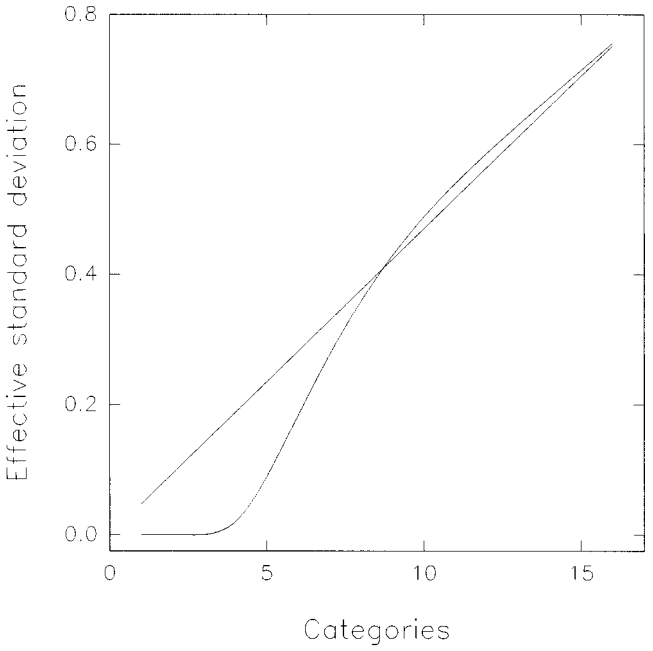

FIG. 11. σ_{eff} plotted as a function of the total number of stimulus categories m using Eq. (7). The distinctive shape of this curve is the primary reason why the information curve shows a bump.

Recall that Occam's Razor (or the Law of Parsimony) dictates that preference should be given to the simpler of two explanations.

Consequently, if experimental measurements of σ_{eff} are in agreement with the theoretical curve shown in Fig. 11, we can likely conclude that the process underlying the absolute identification process is due to a categorization of an underlying response distribution. Any theory that purports to explain absolute identification phenomena must involve these features otherwise the critical points in the information curve will not appear. While it would be of some value to perform direct measurements of σ_{eff}, there is already quite a bit of indirect evidence in the existing literature. The critical points in the transmitted information graphs have been observed in nearly all sensory modalities (in audition, Figs 2 and 3, and in other modalities, i.e., Beebe *et al.*, 1955; Klemmer and Frick, 1953).

C. Assessing the Wong and Mori (1998) approach

In Sec. I, we provided a brief mathematical introduction to our theory of the magical number. We now leave the mathematics behind in order to evaluate the theory as a whole and to contrast it to the approach of Durlach and Braida (1969). In particular, we ask the question: Given that our theory is, in a sense, a subset of the Durlach and Braida model, what is the advantage of having a new theoretical approach which is less general than its predecessors?

To answer this question, we must first understand the difference in philosophy between the two approaches. While both studies are classified as being ''theoretical,'' their aims and goals are different in many ways. For example, the work of Durlach and Braida can be characterized as one in which the goal is to develop an all-encompassing model of intensity

resolution that can predict sensory performance and response in a highly accurate manner. The scope of their work is not limited to that of absolute identification or the magical number alone, embracing many other sensory phenomena including magnitude estimation and discrimination.

By contrast, as mentioned in the Introduction, our approach is one that is tailored specifically to understanding the perceptual features behind the magical number. Detail and accuracy of calculations are sacrificed in order to uncover the underlying simplicity of the sensory process. From this perspective, we might conclude that the principal achievement of our approach lie not in the numerical curve fits shown in Figs. 2 and 3, but in the derivation of the analytical expression Eq. (9). This equation demonstrates that the magical number (I_t evaluated at large R and large m) is a logarithmic function of $\Delta' = R/\sigma$, a result illustrated by the dotted lines in both Figs. 6 and 8. In the case of loudness, for example, if an experiment is carried over the maximum physiological range of hearing (i.e., between the minimum audible intensity and the threshold of pain), Eq. (9) shows that the magical number is defined by the logarithm of the ratio between the audible range and the standard deviation of response (minus a numerical constant). This particularly simple result could only be derived when the problem was stripped to its core leaving only the essential components defining the limits to absolute identification performance. In particular, we recall the main features of our theory where the contributions of edge effects are ignored and the entire categorical matrix is calculated from a single response distribution defined by the middle row of the matrix alone.

While our approach can be characterized as one of simplification, the design of our sensory system need not comply with this desire. And yet when such approximations and simplifications can be demonstrated, this would indicate that there is an underlying simplicity to the laws of perception. Take, for example, the derivation of Eq. (8) [and consequently Eq. (9)]. This derivation requires the use of the critical approximation $\sqrt{2}\sigma/a \ll 1$ (please see Appendix 1 of Wong and Mori, 1998 for further details). Using the two experimental results shown in Figs. 2 and 3, we can quickly see that this approximation is satisfied: $\sqrt{2}\sigma/a = 0.13$ for pitch and $\sqrt{2}\sigma/a = 0.14$ for loudness. Despite the difference in modality (pitch versus loudness), the two parameters are almost of identical numerical value. We have also found this condition to be satisfied by other sensory modalities as well (e.g., taste, please see Wong and Mori, 1998). In fact, a simple calculation with Eq. (9) would demonstrate that even if the magical number is as low as two categories ($I_t = 1$ bit of information), $\sqrt{2}\sigma/a \simeq 0.35$ and the approximation would still hold. Certainly this would suggest that Eq. (9) is an equation characteristic of all sensory modalities.

The analytical expression of Eq. (9) permits us to calculate the magical number once the value of R/σ has been determined. For example, using $\sigma/a = 0.098$ obtained from Fig. 3, we can estimate the value of the magical number for loudness to be $e^{1.60} \simeq 4.9$ categories in agreement with Garner's estimate (Garner, 1953) without going through any elaborate calculations. Furthermore, the simplicity of Eq. (9) also permits us to better understand the origin of the critical points observed in the transmitted information curve. This would not be possible with Eq. (10) alone.

Throughout the paper we have been dealing with measurements of unbiased information. In reality, such values are rather difficult to estimate at large numbers of categories. Although various investigators have proposed different techniques to estimate the informational bias (e.g., Miller and Madow, 1954; Carlton, 1969), a viable method is still lacking to this day. In fact, our theory of the magical number evolved from an earlier study which aimed to overcome the statistical bias through computer simulation (Wong and Norwich, 1997). While Eq. (9) can only be used under circumstances that are impractical from an experimental point of view (large values of m), we maintain that this is perhaps its most useful attribute—to predict the unbiased value of asymptotic transmitted information. Having observed the compatibility of the theory with experimental data at small values of m (cf. Figs. 2 and 3), Eq. (9) is merely an extrapolation of the theory to the limit of large m. This theoretical calculation can help guide the experimental determination of the magical number particularly when the bias cannot be estimated.

While the use of Eq. (9) is restricted to large values of m, one can always use Eq. (10) in place of Eq. (5) when m is less than 10. We recall that the development of Eq. (10) has lead to the prediction of the critical points shown in Figs. 2 and 3 where previously such deviations were attributed to both experimental error and statistical bias. The utility of Eq. (10) has also allowed us to calculate rather quickly the transient behavior of the information curve to very large numbers of categories $m = 512$. An equivalent calculation using the model of Durlach and Braida with the response distribution given by Eq. (12) would take months rather than minutes to complete the entire curve in Fig. 10.

Finally, it has been pointed out that Luce *et al.* (1976) detail some limitations to the Durlach and Braida model. Certainly these comments apply to our own theory as well. While we are very interested in how the ''attention band model'' relates to the developments of this paper, we leave the larger discussion to a dedicated future publication. Both theoretical and experimental work is proceeding at this point. However, it suffices to say that many of the limitations pointed out by Luce *et al.* relate to differences of how transmitted information varies with stimulus range. Since this paper is concerned primarily with how transmitted information varies with the number of stimulus categories at a fixed range, we leave discussion of this matter to a future publication.

IV. CONCLUSIONS

We have reviewed a prediction we made in an earlier study (Wong and Mori, 1998) that the transmitted information does not rise as a monotonic function of the input information as commonly assumed. A recalculation with the model of Durlach and Braida (1969) also yielded similar results. The transmitted information curve was shown to rise to an asymptote with increasing number of stimulus categories although the curve goes through a series of critical points like the motion of a damped oscillator. The value of

transmitted information at these critical points can even exceed the asymptotic value. While these deviations do not amount to any significant changes to our ideas of the magical number, they have nevertheless been observed in many experimental studies across different sensory modalities. Most importantly, however, these predictions appear to indicate that any theory of the magical number must involve the idea that the subject utilizes a set of criteria to determine his or her response.

ACKNOWLEDGMENTS

We would like to thank reviewers Monita Chatterjee and David Eddins for their many helpful and encouraging remarks. *WW* would like to acknowledge the support of the Japan Society for the Promotion of Science for his visiting fellowship to Japan. Both authors acknowledge the support of an operating grant from the Japanese Ministry of Education, Science and Culture (Nos. 09710054 and 97183).

Beebe-Center, J. G., Rogers, M. S., and O'Connell, D. N. (**1955**). ''Transmission of information about sucrose and saline solutions through the sense of taste,'' Journal of Psychology **39**, 157–160.

Braida, L. D., and Durlach, N. I. (**1972**). ''Intensity perception. II. Resolution in one-interval paradigms,'' J. Acoust. Soc. Am. **51**, 483–502.

Braida, L. D., and Durlach, N. I. (**1988**). ''Peripheral and central factors in intensity perception,'' in *Auditory Function: Neurobiological Bases of Hearing*, edited by G. M. Edelman, W. E. Gall, and W. M. Cowan (Wiley, New York), pp. 559–583.

Carlton, A. G. (**1969**). ''On the bias of information estimates,'' Psychol. Bull. **71**, 108–109.

Durlach, N. I., and Braida, L. D. (**1969**). ''Intensity perception: I. Preliminary theory of intensity resolution,'' J. Acoust. Soc. Am. **46**, 372–383.

Garner, W. R. (**1953**). ''An information analysis of absolute judgments of loudness,'' J. Exp. Psychol. **46**, 373–380.

Garner, W. R., and Hake, H. W. (**1951**). ''The amount of information in absolute judgments,'' Psychol. Rev. **58**, 446–459.

Klemmer, E. T., and Frick, F. C. (**1953**). ''Assimilation of information from dot and matrix patterns,'' J. Exp. Psychol. **45**, 15–19.

Laming, D. (**1984**). ''The relativity of 'absolute' judgments,'' British Journal of Mathematical and Statistical Psychology **37**, 152–183.

Luce, R. D., Green, D. M., and Weber, D. L. (**1976**). ''Attention bands in absolute identification,'' Percept. Psychophys. **20**, 49–54.

Marley, A. A. J., and Cook, V. T. (**1984**). ''A fixed rehearsal capacity interpretation of limits on absolute identification performance,'' British Journal of Mathematical and Statistical Psychology **37**, 136–151.

Miller, G. A. (**1956**). ''The magical number seven plus or minus two: Some limits on our capacity for processing information,'' Psychol. Rev. **65**, 81–97.

Miller, G. A., and Madow, W. G. (**1954**). ''On the maximum likelihood estimate of the Shannon-Wiener measure of information,'' AFCRC-TR-54-75 (Operational applications laboratory, Air Force Cambridge Research Center).

Norwich, K. H. (**1997**). Private communication. Unpublished calculations.

Pollack, I. (**1952**). ''The information of elementary auditory displays,'' J. Acoust. Soc. Am. **24**, 745–749.

Shannon, C. E. (**1948**). ''A mathematical theory of communication,'' Bell Syst. Tech. J. **27**, 379–423.

Wong, W., and Mori, S. (**1998**). ''A conceptual approach to the magical number 7,'' Biol. Cybern. (in press).

Wong, W., and Norwich, K. H. (**1997**). ''Simulation of human sensory performance,'' Biosystems **43**, 189–197.

On loudness at threshold[a)]

Søren Buus and Hannes Müsch
Northeastern University, Communication and Digital Signal Processing Center, Department of Electrical and Computer Engineering (409 DA), 110 Forsyth Street, Boston, Massachusetts 02115

Mary Florentine
Northeastern University, Communication Research Laboratory, Department of Speech-Language Pathology and Audiology (133 FR), 100 Forsyth Street, Boston, Massachusetts 02115

(Received 15 September 1997; revised 15 January 1998; accepted 17 April 1998)

Absolute thresholds for and loudness matches between pure tones and four- and ten-tone complexes were used to assess the form of the function relating loudness to sensation level, SL, at low and moderate levels. The components of the tone complexes had equal SLs and were separated by one, two, four, or six critical bands. Six listeners with normal hearing were tested. The thresholds for the multitone complexes indicate that they generally can be detected even when the level of a single component is a few dB below the threshold. The average detection advantage is consistent with predictions for multiple observations in independent, frequency-selective auditory channels, but differences among listeners are apparent. The loudness matches also vary somewhat among listeners. Five of the six listeners matched tone complexes composed of subthreshold components to a pure tone a few dB above threshold. This indicates that the loudness of tones at or even below threshold is greater than zero for these five listeners. A simple model of loudness summation was used to obtain loudness functions from the individual listeners' loudness matches. The slopes of the loudness functions [log(loudness) plotted as a function of log(intensity)] generally exceed unity at low levels and are near 0.2 at 40 dB SL. This shallow slope at moderate levels agrees with loudness functions derived from data on temporal integration of loudness. The average loudness function derived from the present data also is in good agreement with a variety of previous data obtained by magnitude estimation, magnitude production, ratio production, and measurements of binaural loudness summation. [S0001-4966(98)05807-X]

PACS numbers: 43.66.Cb, 43.66.Ba [RVS]

INTRODUCTION

This paper seeks to determine the form of the loudness function at low levels and whether the loudness at threshold is greater than zero. Although these problems have been investigated extensively, a review of the literature reveals continued disagreement about the solution.

For levels well above threshold, most investigators agree that the loudness function for a mid-frequency tone may reasonably be approximated by a power function of intensity with an exponent of about 0.3 (e.g., Stevens, 1955; ISO R 131, 1959; Hellman and Zwislocki, 1963; for review, see Hellman, 1991). However, the exponent may be somewhat lower at moderate levels and somewhat higher at high levels (Florentine *et al.*, 1996; Buus *et al.*, 1997). Likewise, the loudness function [log(loudness) plotted as a function of SPL] undoubtedly becomes steeper at low levels (e.g., Fletcher and Munson, 1933; Knauss, 1937; Luce, 1959; Stevens, 1959; Zwislocki and Hellman, 1960; Scharf and Stevens, 1961; Lochner and Burger, 1961; Hellman and Zwislocki, 1961, 1964), but many different expressions to account for this steepening of the loudness function continue to be used.

Knauss (1937) suggested that loudness at low levels should be proportional to the stimulus intensity, which was also maintained by Zwislocki (1965). According to Knauss (1937), the loudness, N, might be calculated as

$$N = 10^{-3}(10^{-5/2} I/I_0 + 1)^{-2/3} I/I_0, \tag{1}$$

where I is the stimulus intensity and I_0 is the reference intensity ($=10^{-12}$ W/m^2). Zwislocki (1965) suggested that loudness can be modeled as a power function of the total intensity of the stimulus and an internal noise, which accounts for absolute threshold, from which is subtracted the activity due to the internal noise alone, such that the loudness becomes zero when no stimulus is present. Accordingly, loudness may be calculated as

$$N = k_0([1 + c(I/I_{\text{th}})]^{0.27} - 1), \tag{2}$$

where k_0 is a scale factor, c is the signal-to-noise ratio at threshold, and I_{th} is the intensity for the stimulus at threshold. It is important to note that the proportionality between loudness and intensity near threshold predicts that the loudness of a stimulus at threshold, or even below it, is greater than zero.

[a)]Parts of this paper were presented at the 11th International Symposium on Hearing, August 1997, Grantham, England [S. Buus *et al.*, in *Psychophysical and Physiological Advances in Hearing*, edited by A. R. Palmer, A. Reese, A. Q. Summerfield, and R. Meddis (Whurr, London, 1998)] and at the 133rd meeting of the Acoustical Society of America, June 1997, State College, Pennsylvania [S. Buus *et al.*, J. Acoust. Soc. Am. **101**, 3170 (A) (1997)].

In contrast, other investigators have assumed that loudness goes to zero at threshold. Zwicker's (1958; Zwicker and Fastl, 1990) model of loudness summation calculates the loudness within a critical band, N', as

$$N' = k_1([0.5 + 0.5(E/E_{\text{th}})]^{0.23} - 1), \tag{3}$$

where E is the excitation power of the stimulus and E_{th} is the excitation power at threshold. This expression is similar to Zwislocki's (1965), except that it yields a specific loudness of zero when the stimulus is at threshold. Luce (1959) and Stevens (1959, 1966) suggested that loudness should be a power function of the difference between the intensity of the stimulus and its intensity at threshold, such that the loudness could be calculated as

$$N = k_2((I - I_{\text{th}})/I_{\text{th}})^{0.3}, \tag{4}$$

where k_2 is a scale factor. Scharf and Stevens (1961; Scharf, 1978, 1997) suggested that an adequate description of the loudness function could be achieved by subtracting the sound pressure at threshold from that of the stimulus such that the loudness could be calculated as

$$N = k_2((p - p_{\text{th}})/p_{\text{th}})^{0.6}, \tag{5}$$

where p is the rms sound pressure of the stimulus, and p_{th} is the rms sound pressure at threshold. Zwislocki and Hellman (1960; see also Lochner and Burger, 1961) suggested that the threshold correction should be made on the loudness instead of the stimulus magnitude and calculated loudness as

$$N = k_2((I/I_{\text{th}})^{0.3} - 1). \tag{6}$$

These four expressions yield loudness functions with very steep slopes near threshold, whereas those by Knauss (1937) and Zwislocki (1965) approach a slope near unity for log(loudness) as a function of log(intensity).

Whether the loudness at threshold is zero or greater than zero and which, if any, of these expressions provides a correct description of loudness at low levels appear to be unresolved questions. Moore and Glasberg (1986) used an expression similar to Eq. (3) to calculate the specific loudness in their modification of Zwicker's (1958) loudness-summation model, but used an expression similar to Eq. (6) in a more recent version (Moore and Glasberg, 1996). Humes and Jesteadt (1991) also favored Eq. (6) in their review, whereas Scharf (1997) used Eq. (5) to describe loudness of a 1-kHz tone. On the other hand, Hellman and Meiselman (1990) concluded that Zwislocki's (1965) expression provides the best fit to the data. Finally, Moore *et al.* (1997) recently presented a new version of the loudness-summation model in which the specific loudness at threshold is greater than zero, but decreases somewhat faster than Zwislocki's (1965) expression as the stimulus level decreases below threshold.

Clearly, no consensus exists on the form of the loudness function at low levels. Therefore, the present experiment seeks to examine further the loudness function at low levels. To avoid biases that may affect magnitude estimation at low levels (Poulton, 1989), the loudness function will be derived from measurements of loudness summation for multitone complexes. Another advantage of this approach is that it offers a possibility to assess the form of the loudness function at levels near threshold, and even a few dB below it. A tone complex generally will be audible even if the components are a few dB below their individual thresholds (e.g., Green *et al.*, 1959; Buus *et al.*, 1986). Because the loudnesses of individual components in separate auditory channels reasonably can be assumed to add perfectly as long as the component level is near threshold, experiments with tone complexes allow the loudness of subthreshold components to be determined.

Fletcher and Munson (1933) used loudness-balance measurements between a pure tone and tone complexes to determine the form of the loudness function, but they only obtained a small number of loudness matches at low levels, which are the focus of the present paper. Moreover, the components of their complexes were uniformly spaced on a linear frequency scale, which in many cases caused multiple components to be within the bandwidth of a single auditory channel as determined by modern measurements of frequency selectivity (for reviews, see Scharf, 1970; Buus, 1997; Moore, 1997). Scharf (1959) also measured loudness summation at low levels, but it is difficult to derive loudness functions from his measurements because they do not include conditions that allow the effects of mutual masking among the components of the tone complexes to be assessed. Thus it appears that additional measurements will be useful for determining the form of the loudness function at low levels.

I. METHOD

A. Stimuli

Tones at or near 1600 Hz were matched in loudness to tone complexes centered near 1600 Hz. The stimulus duration was 500 ms measured between the half-amplitude points of the 20-ms raised-cosine rise and fall. Different numbers of components and different frequency separations between the components were used to assess the effect of mutual masking among the components and to assess the consistency in the data. The tone complexes consisted of either four or ten components. The frequency separations were one, two, four, or six critical bands (cf. Scharf, 1970; Zwicker and Fastl, 1990) for the four-tone complexes and one or two critical bands for the ten-tone complexes. Component frequencies were chosen on the critical-band scale rather than on the more modern auditory-filter-bandwidth scale (ERB scale; e.g., Glasberg and Moore, 1990) to increase the probability that the components were processed by independent auditory channels. To minimize the number of possible component frequencies, the complexes with a 1-Bark frequency separation were centered (on the critical-band rate scale) at 12 Barks (1720 Hz) instead of the nominal center frequency of 11.5 Barks (1600 Hz). Accordingly, the component frequencies were at 17 critical-band centers between 2.5 and 20.5 Bark. The corresponding frequencies are 250, 450, 570, 700, 840, 1000, 1170, 1370, 1600, 1850, 2150, 2500, 2900, 3400, 4000, 4800, and 7000 Hz.

In some cases, a listener's threshold was found to have a pronounced peak or valley at one or two of these component

frequencies. In these cases, attempts were made to shift the component frequency between 40 and 100 Hz to obtain a relatively smooth threshold curve. The frequency shift increased with frequency and was chosen not to exceed 0.25 Barks. If a shifted frequency produced a smoother threshold curve, it was used in place of the nominal frequency; if it did not, the nominal frequency was retained. If the 1600-Hz component was shifted, as it was for listeners L2, L4, and L5, the pure tone was shifted by the same amount. This procedure was adopted to reduce the possibility that the relation between sensation level, SL, and loudness would be distorted by the components being located at pronounced peaks or valleys in the threshold curve (cf. Kemp, 1979; Cohen, 1982).

The level of the fixed single tone in the loudness-balancing experiment ranged from 1 to 60 dB SL. The component level in the fixed complex ranged from -3 to 20 dB SL for the four-tone complexes and -5 to 20 dB SL in the ten-tone complexes. However, not all listeners could be tested at the lowest level. All components in a complex were set to the same sensation level, which is a simple way to make them approximately equally loud.[1] Hellman and Zwislocki (1961) found that presenting the stimuli at equal SL rather than at equal SPL reduced the variability among listeners' loudness judgments, especially at low levels. Moreover, the absolute threshold curve may be considered an equal-loudness contour and, at low loudness levels, the standard equal-loudness contours are close to constant SLs (ISO, 1987). At the highest component SLs used for the complexes in the present experiment, the components at the lowest frequencies are likely to be somewhat louder than higher-frequency components, but the effect should be negligible. At 20 dB SL, the loudness level of any tone between 1 and 6 kHz is within 1 phon of that for a 1600-Hz tone. Thus only a few components of the complexes with wide frequency separations are likely to show any appreciable deviation from equal loudness and even then the effect on the total loudness will be small. The worst case appears to be the four-tone complex with a frequency separation of 6 Barks. At 20 dB SL, the ISO (1987) loudness level at 1600 Hz is 5 phons less than at 250 Hz and 2 phons less than at 7000 Hz. Consequently, the loudness of the equal-SL complex may be about 20% above that for a complex with four components whose loudness is equal to that of a component at 1600 Hz. This deviation corresponds to about a 2-dB change in the overall level of the complex, which is comparable to the standard error of individual listeners' loudness matches.

B. Apparatus

A PC-compatible computer with a signal processor (TDT AP2) generated the stimuli through a 16-bit D/A converter (TDT DD1) with a 50-kHz sample rate. It also sampled the listeners' responses and executed the adaptive procedure. The output of the D/A was attenuated (TDT PA4), lowpass filtered (TDT FT5, $fc = 20$ kHz, 135 dB/octave), attenuated (TDT PA4), and led to a headphone amplifier (TDT HB6), which fed one earphone of the Sony MDR-V6 headset. The listeners were seated in a sound attenuating booth. For routine calibration, the output of the headphone amplifier was led to a 16-bit A/D converter (TDT DD1), such that the computer could sample the waveform, calculate its spectrum and rms voltage, and display the results before each set of matches. The SPLs reported below presume a frequency-independent output of 116 dB SPL for an input of 1 V rms.[2]

C. Procedure

1. Absolute thresholds

To obtain a reference for setting the sensation levels, absolute thresholds were measured for each of the 17 component frequencies using an adaptive procedure in a two-interval, two-alternative forced-choice paradigm. Each trial contained two observation intervals, which were marked by lights. The pause between them was 450 ms. The signal was presented in either the first or the second observation interval with equal *a priori* probability. The listener's task was to indicate which interval contained the signal by pressing a key on a small computer terminal. Two hundred milliseconds after the listener responded, the correct answer was indicated by a 200-ms light. Following the feedback, the next trial began after a 200-ms delay.

The level of the signal initially was set approximately 15 dB above the listener's threshold. It decreased following three consecutive correct responses and increased following one incorrect response. The step size was 5 dB until the second reversal after which it was reduced to 2 dB. Reversals occurred when the direction of change of the signal level changed from increasing to decreasing or *vice versa*. This procedure converges on the signal level yielding 79.4% correct responses (Levitt, 1971).

A single threshold measurement was based on three interleaved adaptive tracks. On each trial, the track was selected at random among the tracks that had not yet terminated, which they did after five reversals. The threshold for one track was calculated as the average signal level at the fourth and fifth reversals and one threshold measurement was taken as the average threshold across the three tracks. At least three such threshold measurements (for a total of at least nine tracks) were obtained for each listener and frequency. The average across all measurements was used as the reference to set the sensation level of the single tone and the components of the complex in the subsequent experiments.

To determine the lowest level to be tested for each of the complexes, the thresholds for the complexes were also measured using the procedure described above. For these measurements, all components increased and decreased together so their SLs (*re*: threshold for each component presented alone) always were equal.

2. Loudness matches

In the second part of the experiment, each tone complex was matched in loudness to the 1600-Hz tone using an adaptive procedure with a two-interval, two-alternative forced-choice paradigm. On each trial, the listener heard a pure tone and a tone complex presented in random order with a 600-ms pause between them. The listener's task was to indicate

which sound was louder by pressing a key. The response initiated the next trial after a 400-ms delay. The level of the variable sound initially was set about 10 dB above the expected equal-loudness level and was adjusted according to a simple up-down procedure (Jesteadt, 1980; Florentine *et al.*, 1996). If the listener indicated that the variable sound was the louder one, its level was reduced, otherwise it was increased. The step size was 5 dB until the second reversal after which it was reduced to 2 dB. This procedure converges to the 50% point on the psychometric function (Levitt, 1971).

To reduce biases that may occur when only a single fixed sound is presented in a series of trials, six to ten interleaved adaptive tracks were used to obtain concurrent loudness matches at three to five levels with both the pure tone and the tone complex varied. On each trial the track for that trial was selected at random from all tracks that had not yet terminated, which they did after nine reversals. The equal-loudness level for one track was calculated as the average of the levels of the last four reversals. Three such matches were obtained for each listener and condition.

Using concurrent tracks with the fixed stimuli presented at different levels produced a random variation in overall loudness, which forced the listeners to base their responses only on loudness judgments of the two sounds presented in the trial. [For further discussion of roving-level loudness matching procedures, see Buus *et al.* (1997).] Because no more than five levels could be tested concurrently, the complete range of fixed levels was divided into a low and a high range. The highest level in the low range and the lowest level in the high range were identical to check if the range of loudnesses presented affected the loudness matches.

D. Listeners

Four female and two male listeners were tested on all conditions. All were university students (18 to 27 years old) with no history of hearing difficulties and had extensive experience in loudness-matching experiments. Their audiometric thresholds were 10 dB HL or less between 0.25 and 8 kHz, except that thresholds were 15 dB HL at 4 and 8 kHz for L5 and at 2 kHz for L6. All listeners were paid to participate in the experiments. Listener L6 is the second author.

II. RESULTS

A. Thresholds

Figure 1 shows the absolute thresholds for the listeners. As indicated by the filled circles, the thresholds for the frequencies used for loudness matching generally form reasonably smooth functions, although threshold differences exceeding 5 dB between adjacent frequencies occasionally are present. These rapid changes of threshold occur primarily between 1 and 3 kHz and at the extreme frequencies. No attempts were made to shift the extreme frequencies because variations in cochlear sensitivity at these frequencies are difficult to separate from variations in the real-ear frequency response of the earphone.

As indicated by the unfilled circles and *X*'s, which show tone frequencies that were not used as components in the tone complexes, small frequency shifts often, but not always, were sufficient to smooth the threshold curve substantially. (Results are not shown for a few frequencies that were tested only in a single threshold measurement; a complete set of thresholds was not obtained because the initial measurement indicated a threshold as extreme as that for the frequency to be replaced.) In some cases, no frequency less than 0.25 Barks from the nominal frequency was found that would produce a smoother threshold curve. In these cases, the nominal component frequency was retained.

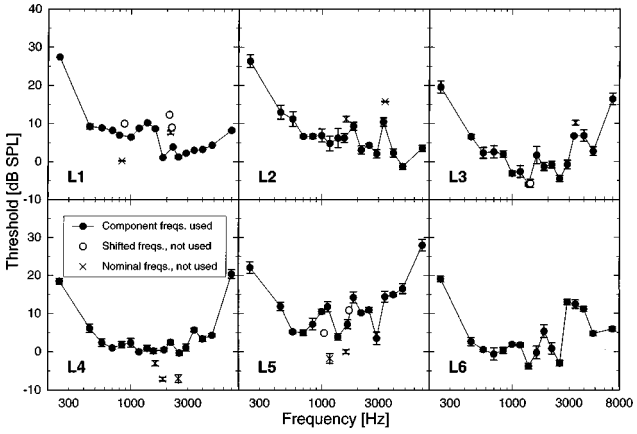

FIG. 1. Absolute thresholds for the individual components of the tone complexes. Each panel shows thresholds as a function of frequency for one listener. The filled circles show thresholds for components used to form the tone complexes for each listener. The unfilled circles show thresholds at additional frequencies, which were investigated in an attempt to reduce the possible influence of the threshold microstructure on loudness (see text for details), but which were not used to form the tone complexes. The *X*'s show nominal component frequencies that were not used in the complexes because their thresholds deviated substantially from those at adjacent frequencies and because a nearby frequency was found to produce a smoother threshold function. The error bars show plus and minus one standard error of the mean.

The thresholds for the tone complexes are shown in Table I. The thresholds are stated in terms of the SL of a single component within the complex and indicate the improvement in threshold obtained due to the availability of signal energy in independent auditory channels (see Buus *et al.*, 1986 for further discussion). If the auditory system uses an optimally weighted sum of the energies in each auditory channel to detect the tone complexes, signal-detection theory predicts that the threshold should be $5\log(n)$ dB lower for an n-tone complex than for a single component in isolation. Thus the expected thresholds are -3 dB SL for the four-tone complexes and -5 dB SL for the ten-tone complexes. The thresholds for listeners L1, L5, and L6 are close to this expectation, whereas they are lower for listener L2 and higher for listeners L3 and L4. The four four-tone complexes generally yield quite similar thresholds as do the two ten-tone complexes, although some exceptions are apparent. Nevertheless, the average data across the six listeners closely follow the predictions for an optimal decision rule. The average thresholds are close to -3 dB SL for all four-tone complexes and close to -5 dB SL for both ten-tone complexes.

TABLE I. Thresholds for the tone complexes in terms of dB SL for a single component. The first column shows the number of components and the second column shows their frequency separation in Barks. The next six columns show the thresholds and, in parentheses below them, the standard errors. The final column shows the averages and, in parentheses below them, the standard deviations across the six listeners. The rows marked ''Average'' show the averages across the four four-tone complexes and across the two ten-tone complexes.

Number of components	Δf	L1	L2	L3	L4	L5	L6	Average (s.d.)
4	1	−2.9 (0.85)	−2.8 (0.32)	0.7 (0.43)	−2.0 (0.50)	−2.9 (0.51)	−4.2 (0.30)	−2.4 (1.64)
4	2	−3.7 (0.99)	−5.7 (0.73)	0.9 (0.66)	−1.5 (0.38)	−3.1 (0.74)	−2.4 (0.41)	−2.6 (2.21)
4	4	−2.8 (0.42)	−6.6 (0.96)	0.3 (1.07)	−0.7 (0.62)	−2.8 (0.38)	−3.8 (0.57)	−2.7 (2.41)
4	6	−2.1 (0.60)	−5.8 (0.25)	−2.5 (1.42)	−0.4 (0.67)	−4.4 (0.38)	−4.2 (0.49)	−3.2 (1.91)
4	Average	−2.9	−5.2	−0.2	−1.1	−3.3	−3.6	−2.7 (1.81)
10	1	−4.8 (0.87)	−7.3 (0.75)	0.1 (0.43)	−2.3 (0.46)	−4.7 (0.33)	−4.8 (0.22)	−4.0 (2.55)
10	2	−3.3 (1.07)	−8.6 (0.45)	−3.0 (0.55)	−2.7 (0.42)	−5.4 (0.46)	−5.3 (0.59)	−4.5 (2.20)
10	Average	−4.0	−8.0	−1.5	−2.5	−4.5	−5.0	−4.2 (2.25)

B. Loudness matches

The loudness-balance results for all listeners and tone complexes are shown in Fig. 2. Generally, the data obtained with the pure tone varied and with the tone complex varied appear to follow a single function, which is reasonably summarized by the polynomials.[3] This shows that the roving-level procedure was successful in reducing biases that affect measurements with traditional adaptive procedures (see also Buus *et al.*, 1997). The average standard errors were 1.6 dB when the tone complex was varied and 2.4 dB when the pure tone was varied. These relatively small standard errors show that reliable loudness matches clearly can be obtained for both four- and ten-tone complexes, even when their components are below their thresholds in isolation. It should be noted that a few matches at low levels show large standard errors, because the variable stimulus occasionally migrated below threshold. Data for which the pure-tone level was less than −2 dB SL were omitted from the model fits, which are discussed later. Because only three points for L4 were omitted, the effect on the analysis was negligible.

Further indication of the reliability of the data comes from the finding that the conditions that were included in both the low and the high ranges of the roving-level procedure yielded very similar results in the two level ranges. No consistent differences are apparent in Fig. 2. The difference between the results obtained in the high and low ranges averages 0.4 dB (s.d.=1.7 dB) across all conditions with the complex varied and 0.75 dB (s.d.=4.3 dB) across all conditions with the tone varied. A five-way [Range (two levels: high or low)×Variable (two levels: tone or complex) ×Complex (six levels: four four-tone complexes and two ten-tone complexes)×Repetition (three levels)×Listener (six levels)] analysis of variance for repeated measures (Data Desk 6.0, Data Description, Inc., Ithaca, NY, 1997) showed that the effect of range and all interactions with it were not significant ($p>0.05$). Thus the range of levels encompassed by our roving-level procedure does not appear to affect the loudness matches, at least for the relatively low levels used in the present experiment.

Five of the six listeners consistently match complexes in which the components are below their individual thresholds with pure tones that are a few dB above thresholds. For these listeners, four or ten below-threshold components clearly add to produce a loudness greater than zero, which indicates that the loudness at and even below threshold must be greater than zero. One listener, L4 who showed only a small detection advantage for the tone complexes, did not produce consistent loudness matches in which the component level of a complex was 0 dB SL or less, except for the ten-tone complex with a frequency separation of 1 Bark. For this listener, loudness may be zero at threshold.

The ten-tone complexes are matched to tones at higher levels than are the four-tone complexes, which is expected because the overall level and the total bandwidth are larger for the ten-tone complexes than for the four-tone complexes. In addition, the level of the matching pure tone generally increases with increasing frequency separation of the complexes with component levels well above thresholds. However, this holds only up to a frequency separation of 4 Barks. As shown in the rightmost panels, the loudness-matching functions for the four-tone complexes with frequency separation of 4 Barks are nearly identical to those with a frequency separation of 6 Barks for all listeners. This indicates that mutual masking probably does not affect the loudness of these complexes consisting of widely separated components. It also indicates that loudness was approximately indepen-

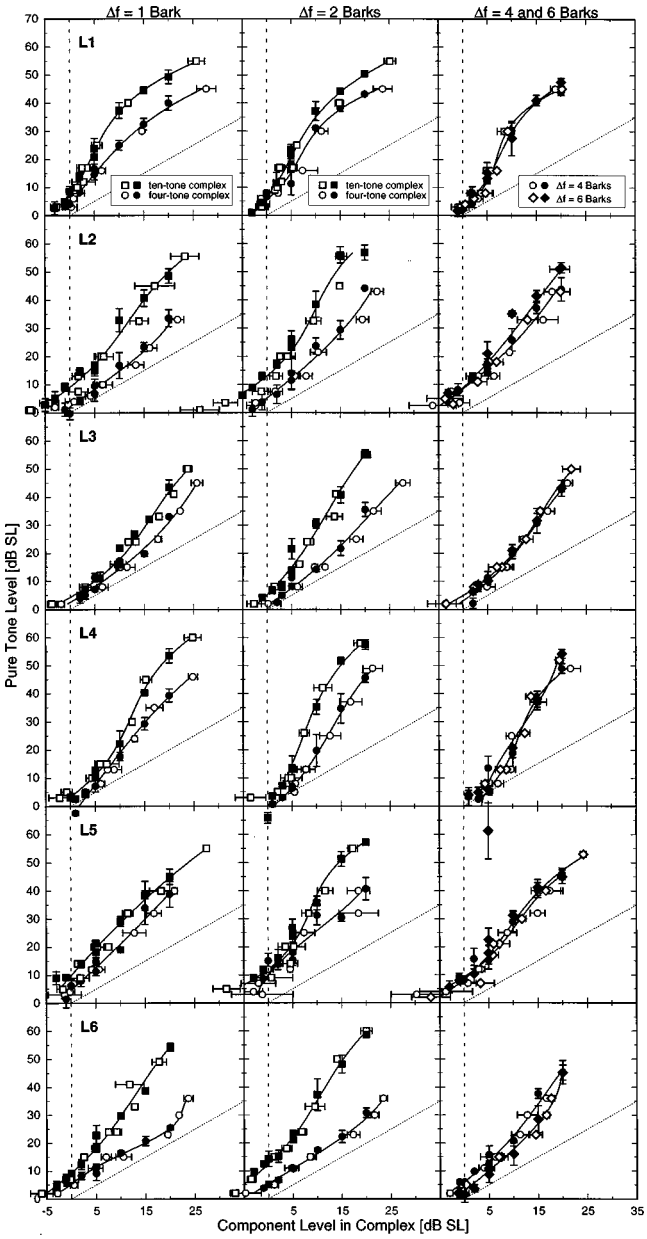

FIG. 2. Loudness balances between a tone near 1600 Hz and four- or ten-tone complexes centered near 1600 Hz. The sensation level of the pure tone is plotted as a function of the sensation level of a single component within the equally loud tone complex. Filled symbols show results obtained when the tone was varied and unfilled symbols show results obtained when the tone complex was varied. The error bars indicate the range of plus and minus one standard error of the mean for three repetitions. The solid lines show polynomial fits to the data, which were used to summarize the data. Each row of panels shows results for a single listener. The left column of panels shows results for four- (circles) and ten-tone (squares) complexes with components 1 Bark apart. The middle column of panels shows results for four- (circles) and ten-tone (squares) complexes with components 2 Barks apart. The right column of panels shows results for four-tone complexes with components 4 (circles) and 6 (diamonds) Barks apart. The dashed vertical lines mark threshold (0 dB SL) for the individual components in the tone complex. The dotted sloping lines indicate equal sensation levels for the tone and the components in a tone complex.

dent of the frequency for our equal-SL components, because different sets of component frequencies in the 4- and 6-Bark frequency separations appear to produce approximately the same loudnesses.

According to Fletcher's (Fletcher and Steinberg, 1924; Fletcher and Munson, 1933) assumption that additivity is a fundamental property of the loudness scale, the loudness of the multitone complexes should be equal to the sum of the loudnesses of their components, provided that mutual masking among the components is absent. Thus the SL difference between the pure tone and an equally loud multitone complex indicates the change in level necessary to increase loudness by a factor of 4 for the four-tone complexes and a factor of 10 for the ten-tone complexes. This indicates that the slope of the loudness function is approximately inversely proportional to the SL difference, at least for complexes at low levels. To obtain preliminary estimates of the form of the loudness function, the SL differences—as calculated from the polynomials fitted to the data in Fig. 2—are shown in Fig. 3.[3]

Mutual masking ought to be absent for even the narrowest frequency separation when the components in the complexes are at 0 dB SL. Therefore, within a particular listener the component SL difference for all four-tone complexes should be the same; the two ten-tone complexes also should yield the same SL difference, which should be $\log(10)/\log(4)=1.66$ times that obtained for four-tone complexes if all the measurements reflect a single function of loudness versus sensation level. Although the data scatter somewhat around this ideal, the deviations rarely exceed 3 dB. For the four-tone complexes, the SL differences at threshold average 3.9 dB for L1, 6.2 dB for L2, 3.0 dB for L3, 8.0 dB for L5, and 5.1 dB for L6 (L4 could not be tested with a component level of 0 dB). The average across these five listeners is 5.2 dB, which is in excellent agreement with the slightly negative loudness summation obtained by Scharf (1959) for 5-dB-SL pure-tone comparisons at 1 and 2 kHz. For the ten-tone complexes, the averages are 6.8 dB for L1, 11.0 dB for L2, 4.8 dB for L3, 10.9 dB for L5, and 10.9 dB for L6, which yields an average of 8.9 dB. The ratio of the average SL differences for four- and ten-tone complexes is 1.69—very close to the expected ratio of 1.66.

The finding that the SL differences are slightly less than the 6- and 10-dB differences that would result if loudness were proportional to intensity indicates that, for these listeners with greater-than-zero loudness at threshold, the loudness grows slightly faster than proportionally with the intensity of the tone. A simple prediction for the exponent is about 1.14 ($[10\log(4)\text{ dB}]/5.2\text{ dB}=1.15$ for the four-tone complexes and $[10\log(10)\text{ dB}]/8.9\text{ dB}=1.13$ for the ten-tone complexes). For individual listeners, exponents predicted in this simple manner range from 0.84 for L5 to 2.05 for L3.

Because mutual masking appears to be absent even at 20 dB SL for the four-component complexes with frequency separations of 4 and 6 Barks, the SL differences obtained for a component level of 20 dB SL can be used to obtain a rough estimate of the slope of each listener's loudness function between 20 and 45 dB SL. Averaged across the 4- and 6-Bark frequency separations, the SL difference is 25.8 dB for L1, 29.0 dB for L2, 23.8 dB for L3, 31.6 dB for L4, 26.4 dB for L5, and 25.2 dB for L6. The corresponding slopes (local exponents) are 0.23, 0.21, 0.25, 0.19, 0.23, and 0.24. On the average, the SL difference is 27.0 dB, corresponding to a slope of about 0.22. Thus it appears that loudness functions

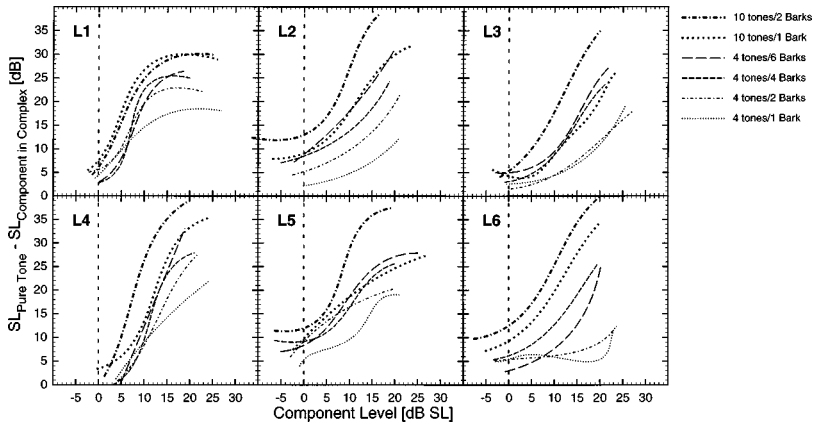

FIG. 3. Sensation-level differences between a pure tone and individual components of an equally loud tone complex plotted as a function of the sensation level of the components in the tone complex. Each panel shows data for an individual listener. The lines are calculated from the polynomials fitted to the raw data (see Fig. 2). Thin lines are for four-tone complexes and thick lines for ten-tone complexes. Separate functions are shown for component separations of 1 (dotted lines), 2 (dash-dotted lines), 4 (short-dashed lines), and 6 Barks (long-dashed lines).

at these moderate levels for all the listeners are shallower than the slope of about 0.3 generally thought to describe the loudness of a mid-frequency tone well above threshold.

The standard errors of the estimate of the SL difference for a single listener and tone complex average about 1.4 dB and the 95% confidence interval is about 3.1 dB. Thus the standard errors for within-listener averages at 0 dB SL are about 0.7 dB for four-tone complexes and 1 dB for ten-tone complexes. It follows that the estimates of the slope of the loudness function at threshold for individual listeners should have a standard error of about 10%–15% of the slope, but because the SL differences are small when the slope is steep, the error may be somewhat larger for listeners with steep loudness functions at threshold. These relatively small standard errors indicate that differences among listeners are likely to be highly significant. In fact, a three-way analysis of variance (number of components×frequency separation ×listener) for repeated measures on the SL differences obtained for the five listeners tested with the components of the complexes set to 0 dB SL shows significant effects of number of components $[F(1,4)=53.7,\ p<0.002]$ and of listener $[F(4,4)=16.6,\ p<0.01]$. Frequency separation and interactions with it were not significant, which supports the assumption that setting the components to the same SL resulted in the loudness being approximately independent of component frequency near threshold.

III. GENERAL DISCUSSION

A. Thresholds of multitone complexes

Most investigators agree that tone complexes composed of equally detectable components can be detected when the individual components would not be audible, even if the components excite independent auditory channels (e.g., Green, 1958; Green *et al.*, 1959; Spiegel, 1979, 1981; Buus *et al.*, 1986; van den Brink and Houtgast, 1990; Langhans and Kohlrausch, 1992; Grose and Hall, 1997). Presumably, this detection advantage results because stimulation of multiple auditory channels allows the listener to make multiple observations, which reduces the relative variance of the decision variable (e.g., Green, 1958; Buus *et al.*, 1986).

The studies cited above investigated detection of tone complexes presented in noise, but there is little reason to believe that multiple observations in independent auditory channels should not be effective in the quiet. However, the few data available are somewhat contradictory. Gässler (1954) found that adding tones further than a critical band below the highest-frequency tone in a multitone complex did not reduce threshold in terms of level per tone. This indicates that the listeners in Gässler's experiments did not take advantage of multiple observations, but based their detection on a single channel. Higgins and Turner (1990) obtained results similar to Gässler's when they added tones below an 1100-Hz tone presented in the quiet. When the tone complexes were presented in noise, tone complexes with components added below 1100 Hz also yielded results similar to Gässler's, but tone complexes with components added symmetrically around the 1100-Hz tone yielded results in agreement with multiple observations in independent frequency selective channels. However, differences between the two conditions were present primarily at medium bandwidths, where the two sets of stimuli are very similar. Thus the differences may be due to variability in the measurements. Recent data obtained in uniformly masking noise show no difference between stimuli in which components were added below, symmetrically around, or above a 2-kHz initial frequency (Kohlrausch and Langhans, 1991).

The present data for detection of multitone complexes in the quiet encompassed much wider bandwidths than those used by Gässler (1954) and Higgins and Turner (1990). Moreover, the present study used only a single component in each critical band and the levels of the components were set to ensure equal detectability, whereas the previous studies used closely spaced equal-amplitude components, which is unlikely to produce equal detectability in all critical bands. Thus the present data are likely to provide a clearer indication of listeners' ability to use multiple observations for detection of tone complexes in the quiet. The average thresholds were -2.7 dB (*re*: the threshold of a single component) for four-tone complexes and -4.2 dB for ten-tone complexes, which is close to the values of -3 and -5 dB predicted for multiple observations in four or ten independent

auditory channels. Thus it appears that multiple observations in independent auditory channels are effective for detection of multitone complexes in the quiet, as well as in noise. However, considerable differences were apparent among individual listeners. Listeners L3 and L4 showed only very small detection advantages for the multitone complexes, whereas listener L2 showed a larger-than-predicted detection advantage. Thus it is likely that the auditory processes responsible for detection of multiple simultaneous components differ among listeners and that the differences among the few available studies on detection of multitone complexes in the quiet reflect, at least in part, differences among individual listeners.

B. Loudness function at low levels

The primary purpose of the present study was to investigate the form of the loudness function at low levels as derived from the measurements of loudness balance between tone complexes and a pure tone. As indicated by the simple analysis in the Results section, it appears that loudness at threshold was greater than zero for five of the six listeners, but may be equal to zero for one listener, L4, who showed only a small detection advantage for multiple tones and could not be tested with complexes whose components were set to 0 dB SL. In addition, the data for four-tone complexes with widely separated components indicated that the slope of the loudness function at levels between 20 and 45-to-50 dB SL may be shallower than the slope of 0.3 commonly assumed to describe the loudness function [log(loudness) plotted as a function of log(intensity)] for a mid-frequency tone.

In the following, a simplified loudness summation model will be used to obtain a more precise description of the loudness functions for the individual listeners. This model also provides further indications of the internal consistency in the data, because it uses a single loudness function to account for the data. The total loudness of a complex is assumed to be the sum of loudnesses of the individual components, except that mutual masking reduces the total loudness as the level increases. Moreover, all components in a complex are assumed to have the same loudness. Accordingly, an n-tone complex with components spaced by Δf and component levels of SL should yield a total loudness, $N_n(\mathrm{SL},\Delta f)$ of

$$N_n(\mathrm{SL},\Delta f)=N_1(\mathrm{SL})(1+(n-1)r(\mathrm{SL},\Delta f)), \tag{7}$$

where $N_1(\mathrm{SL})$ is the loudness function for a pure tone (which is assumed to be the same for all components) and $r(\mathrm{SL},\Delta f)$ is a function that accounts for the loudness reduction due to mutual masking. In other words, the total loudness is equal to the loudness of a single tone plus that from $n-1$ tones reduced by some amount indicated by the loudness-reduction function $r(\mathrm{SL},\Delta f)$, which varies between unity at low levels and may approach zero at high levels. This approach is similar to that used by Fletcher and Munson (1933), but is somewhat simpler because we used components that reasonably could be assumed to be equally loud.

Calculations with an excitation-pattern model similar to that described by Zwicker (1958) verified that the loudness of tone complexes with components set to the same SL was well described by Eq. (7). They also indicated that $r(\mathrm{SL},\Delta f)$ could reasonably be approximated by a lowpass two-line function of SL. The function was equal to unity (no loudness reduction) at low levels, but decreased at a fixed rate above some critical sensation level, which depended only on the frequency separation of the components. That is,

$$r(\mathrm{SL},\Delta f)=\begin{cases}1, & \mathrm{SL}\leqslant \mathrm{SL}_{\mathrm{critical}}(\Delta f),\\ (1-A[\mathrm{SL}-\mathrm{SL}_{\mathrm{critical}}(\Delta f)], & \mathrm{SL}>\mathrm{SL}_{\mathrm{critical}}(\Delta f).\end{cases} \tag{8}$$

In agreement with the inspection of the raw data, the excitation-pattern model and fits to the individual data indicated that the critical levels for Δf's of four and six Barks were higher than the component levels used in the present experiment. Thus $r(\Delta f,\mathrm{SL})$ was determined by three parameters: the slope above the critical level, A, and the critical levels for Δf's of one and two Barks.

Because the data indicated considerable differences among the low-level slopes of the loudness functions for individual listeners, the loudness function used in the model should permit the slope at low levels to vary independently from the slope well above threshold. To fulfill this requirement, Zwislocki's (1965) loudness function was modified by adding a parameter that provided independent control of the asymptotic slope at subthreshold levels. Accordingly, the model calculated the loudness of a pure tone as

$$N_1(\mathrm{SL})=k([1+(C\cdot 10^{\mathrm{SL}/10})^D]^{B/D}-1), \tag{9}$$

where B, C, and D are free parameters and k is a scale factor that does not affect the predictions of the model. In this expression, C may be considered the signal-to-noise ratio at threshold, B is the asymptotic slope of the loudness function at high levels, and D is the asymptotic slope at low levels. It should be noted that this loudness function forces the loudness to be greater than zero at threshold in accord with the data for five of the six listeners. However, the loudness at threshold may be made arbitrarily small by using appropriate values for the parameters C and D. Thus Eq. (9) should be able to provide an adequate description of the loudness function for L4 for whom loudness at threshold may be zero.

As shown in Fig. 4, the model provides good fits to the data for the individual listeners, except perhaps for L1 with the two-Bark frequency separation.[4] The generally good fits indicate a high degree of internal consistency in the data and that the equal-SL components provided an adequate approximation to equal loudness for the components in the tone complexes, because all the loudness matches for one listener are essentially predicted by a single loudness function that depends only on the SL of the tone. The rms error across all listeners and conditions was 3.3 dB for predictions of the pure-tone levels and 1.8 dB for predictions of component levels, which is slightly larger than the 2.4- and 1.6-dB rms errors of the data. As evident in Fig. 4, most of the increased error of the predictions appears to reflect relatively small, but systematic, errors at high levels. At least in some cases, this

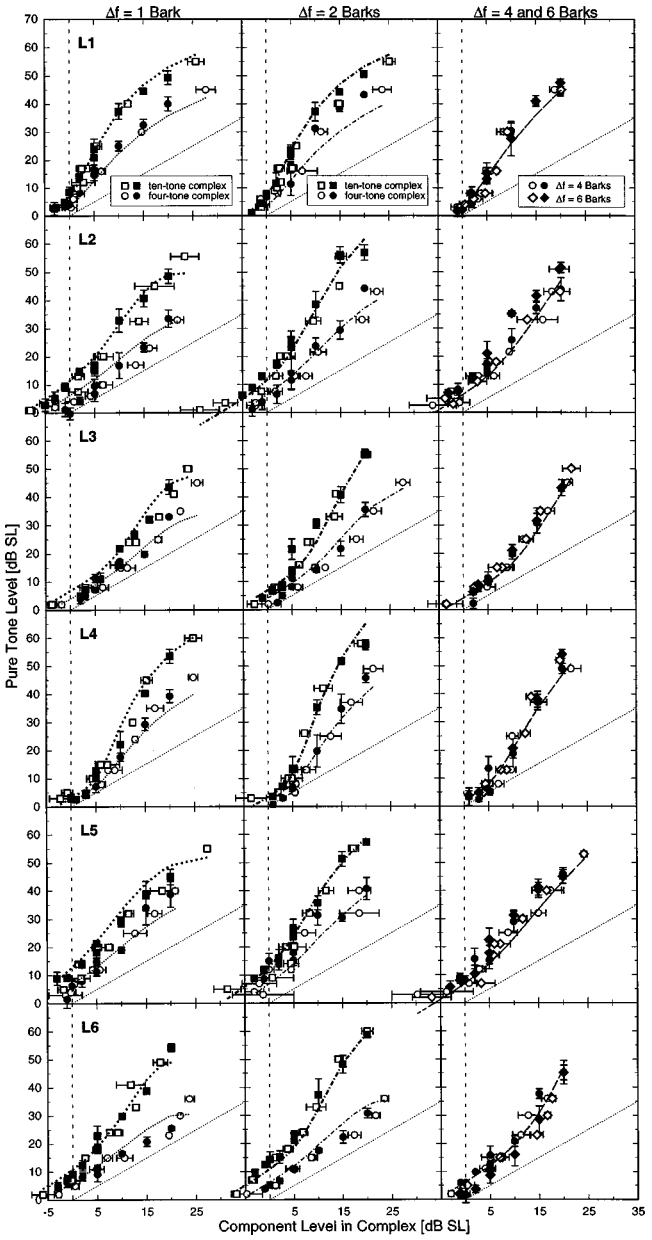

FIG. 4. Predictions of the simple model of loudness summation are compared to the data, which are replotted from Fig. 2, but data omitted from the model fits are not shown. The figure is plotted in the same manner as Fig. 2, except that the various lines show the loudness matches predicted by the model. Thin lines are for four-tone complexes and thick lines for ten-tone complexes. Separate functions are shown for component separations of 1 (dotted lines), 2 (dash-dotted lines), 4 (short-dashed lines), and 6 Barks (long-dashed lines), but generally only one function is visible in the rightmost panels because the model makes identical predictions for the 4- and 6-Bark frequency separations.

error appears to result from the monotonically decreasing slope of the model loudness function, which forces the slope to become unrealistically small at high levels.

The parameters of the loudness functions providing the best fits to the data are shown in Table II. The estimated signal-to-noise ratios at threshold, 10 log(C), vary across listeners. Zwislocki (1965) argued that 10 log(C) should average -4 dB in normal listeners (see also Hellman and Meiselman, 1990). Our average of -7.6 dB is somewhat lower. The difference reflects, at least in part, that Zwislocki's estimate is for thresholds obtained with classical procedures such as Békésy tracking, which yield thresholds corresponding to a higher criterion than that imposed by the forced-choice adaptive procedure used in the present experiment (e.g., Marshall and Jesteadt, 1986). In addition, the estimate of 10 log(C) is rather indirect, because it is determined primarily by the form of the loudness-matching function. Thus, the relatively wide range of values obtained for 10 log(C) may indicate that the form of the transition between the steep low-level slope and the shallow moderate-level slope may differ somewhat across listeners.

TABLE II. Parameter values for the loudness function in the model fitted to individual listeners and the resulting slopes (local exponents) at 0 and 40 dB SL. The second column shows the high-level asymptotic exponent, B, of the modified power function, the third column shows the low-level asymptotic exponent, D, and the fourth column shows the model estimate of the signal-to-noise ratio in dB within the critical band for a tone at absolute threshold, 10 log(C). Listener L4 was omitted in averaging D and the slope at 0 dB, because her values represent an extrapolation of the data.

Listener	B	D	10 log(C) [dB]	Slope at 0 dB SL	Slope at 40 dB SL
L1	0.16	2.31	−1.8	2.04	0.21
L2	0.067	1.09	−8.1	1.03	0.17
L3	0.071	1.52	−11.1	1.50	0.19
L4	0.094	3.03	−6.0	3.01[a]	0.18
L5	0.13	1.04	−6.6	0.96	0.21
L6	0.0001	1.21	−11.9	1.00	0.16
Average	0.09	1.43[b]	−7.6	1.31[b]	0.19

[a]Extrapolated value.
[b]Without L4.

The asymptotic exponents at high levels show considerable scatter among the listeners and appear to be unrealistically small in several cases, which probably reflects that few matches yielded tone levels above 50 dB SL. Thus the asymptotic slope was essentially free to assume any value that provided a good fit to the data at moderate levels. In fact, the slopes around 40 dB SL show relatively little variation among listeners and are in reasonable agreement with the rough estimates discussed earlier. The slopes in Table II are slightly lower than the rough estimates, because the rough estimate is an average slope for levels between 20 and 45-to-50 dB SL. The middle of this range is somewhat below the 40 dB SL used to calculate the slopes in Table II. The asymptotic exponents at low levels all are greater than unity. The slopes at 0 dB SL are in good agreement with the simple predictions discussed earlier and all except one are equal to or larger than unity. Overall, it is clear that the important features of the model loudness functions relate very directly to the loudness matches.

The average slope of 0.19 at 40 dB SL agrees with the mid-level exponents of about 0.2 estimated by Florentine *et al.* (1996) and Buus *et al.* (1997) based on loudness matches between tones of different durations. This slope is considerably shallower than the slope of 0.3 generally assumed to describe loudness of a mid-frequency tone at moderate and high levels. Because a considerable body of data shows that a slope of 0.2 would grossly underestimate the loudness of high-level tones, the slope of the loudness func-

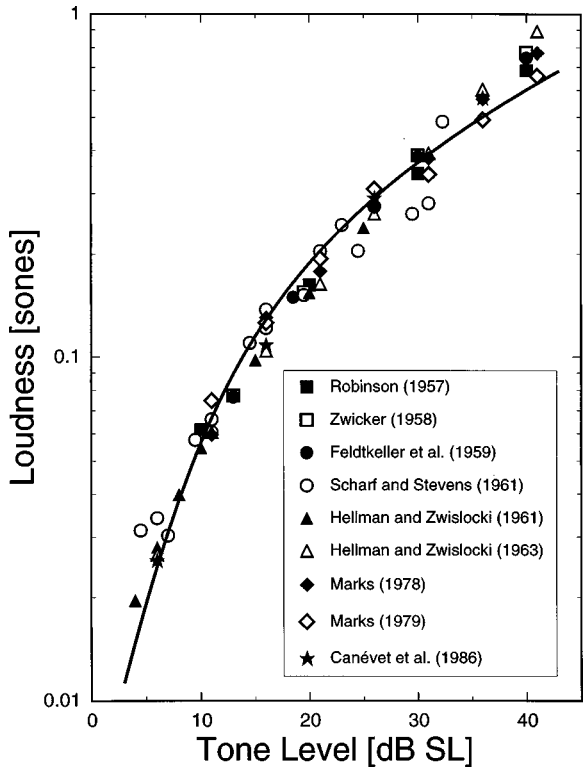

FIG. 5. An average loudness function derived from the present loudness-matching data is compared to previous data obtained by magnitude estimation, magnitude production, ratio production, and measurements of binaural loudness summation (Robinson, 1957; Zwicker, 1958; Feldtkeller *et al.*, 1959; Scharf and Stevens, 1961; Hellman and Zwislocki, 1961, 1963; Marks, 1978, 1979; Canévet *et al.*, 1986). The loudness in sones is plotted on a logarithmic scale as a function of sensation level. The thick line shows the loudness function obtained in the present study. The symbols show loudness estimates from previous studies as indicated in the legend.

tion must increase at higher levels. Thus the shallow slope of the loudness function for tones at moderate levels obtained in the present study offers indirect support for the contention that the slope of the loudness function varies nonmonotonically with level and is shallower at moderate levels than at low and high levels (Fletcher and Munson, 1933; Florentine *et al.*, 1996; Buus *et al.*, 1997).

The low-level slopes obtained in the present study are somewhat steeper than those obtained from Zwislocki's (1965) loudness function, which yields an asymptotic exponent of unity and a slope of 0.89 at 0 dB SL. Thus this function may not give an entirely accurate description of loudness near threshold, although it provides a good approximation to the present data. It is noteworthy that Moore *et al.* (1997) recently revised their loudness-summation model to use a loudness function that yields a greater-than-zero loudness at threshold and has a slope of 1.5 below threshold. This loudness function is in close agreement with that derived from the present data.

To provide a comparison with previous data, an average loudness function is shown in Fig. 5 together with data obtained by magnitude estimation, magnitude production, ratio production, and measurements of binaural loudness summation. The loudness function was obtained from Eq. (9) with $k=0.44$, $B=0.11$, $C=-6$ dB, and $D=1.4$. These parameters are close to the average parameters, but B, C, and D were modified slightly to obtain slopes equal to the average slopes of 1.31 at 0 dB SL and 0.19 at 40 dB SL; k was chosen to obtain a monaural loudness of 0.5 sones at 36 dB SL (corresponding to a binaural loudness of 1 sone at 40 dB SPL in a free field). Clearly, the loudness function derived from the present loudness-matching data is in good agreement with the previous data.

IV. SUMMARY

The present paper used loudness balance between tone complexes with components set to equal SL and pure tones to assess the form of the loudness function for tones at low and moderate levels. A simplified loudness-summation model was used to derive loudness functions from the loudness-balance data for each listener. Absolute thresholds for all component tones and the various tone complexes were also measured. The results show:

(1) Most listeners can detect multitone complexes with components set to levels below the threshold for individual components. The average detection advantage is consistent with predictions for multiple observations in independent, frequency-selective auditory channels, but differences among listeners are apparent.
(2) Loudness at threshold is greater than zero for five of the six listeners tested, but may be zero for one listener.
(3) The slopes of the loudness functions [log(loudness) plotted as a function of log(intensity)] generally exceed unity at low levels.
(4) The slopes of the loudness functions are near 0.2 at 40 dB SL in good agreement with loudness functions derived from data on temporal integration of loudness.

ACKNOWLEDGMENTS

The authors thank Monica Robinson and Heidi Anderson for help with data collection and analysis. Bertram Scharf and two anonymous reviewers gave helpful comments on an earlier version of this manuscript. This research was supported by NIH/NIDCD Grant No. R01DC02241.

[1]Although equal SL may not produce exactly equal loudness if the tones are at peaks or valleys in the fine structure of the threshold curve, we believe that errors resulting from this procedure, if any, are relatively minor. Studies on the relation of the threshold microstructure to loudness note that a constant SPL tone is considerably less loud at peaks than at valleys in the threshold curve (e.g., Kemp, 1979; Cohen, 1982). This finding is qualitatively consistent with the assumption that equal SL produces nearly equal loudness. In fact, further analysis of Kemp's (1979) data shows that equal SL is close to equal loudness for tone levels below about 25 dB SL, except for a few unsystematic deviations that may reflect variability in individual listeners' judgments. Second, component frequencies were selected to reduce the chance that they were at peaks or valleys in the threshold curve, which should reduce loudness differences between equal SL tones. Third, the loudness of the complexes near threshold should be the sum of the loudnesses of the four or ten components. Therefore, any loudness differences between the equal SL components are likely to average out. As discussed later in the paper, a model in which a single function of SL describes the loudness of any component provides a good account of the data. This finding supports the assumption that equal loudness is well approximated by equal SL, at least for the relatively small range of low component levels used in the present study.

[2]Because the real-ear response of earphones varies considerably and unpredictably across listeners, we have chosen to ignore details in the calibration.

The calibration of 116 dB SPL for an input of 1 V yields thresholds that agree reasonably with those reported by other investigators. Moreover, the calibration is uncritical in the present study, because specifying the tone levels in terms of dB SL in effect provides a separate calibration for each listener and frequency.

[3]The polynomials in Figs. 2 and 3 were obtained by fitting polynomials to the complex-tone levels as a function of the pure-tone level. Third-order polynomials were used for all the data except L6's data for the four-tone complexes with a one-Bark frequency separation, which were fitted with a fifth-order polynomial to obtain a monotonic function. Because the polynomials are used only to obtain visual summaries of the data, the coefficients are not important.

[4]The relatively large error of the model fit to L1's data for the two-Bark frequency separation may indicate that the two-line loudness-reduction function is not a good approximation for this listener and frequency separation.

Buus, S. (**1997**). ''Auditory masking,'' in *Encyclopedia of Acoustics, Vol. 3*, edited by M. J. Crocker (Wiley, New York), pp. 1427–1445.

Buus, S., Florentine, M., and Poulsen, T. (**1997**). ''Temporal integration of loudness, loudness discrimination, and the form of the loudness function,'' J. Acoust. Soc. Am. **101**, 669–680.

Buus, S., Schorer, E., Florentine, M., and Zwicker, E. (**1986**). ''Decision rules in detection of simple and complex tones,'' J. Acoust. Soc. Am. **80**, 1646–1657.

Canévet, G., Hellmann, R. P., and Scharf, B. (**1986**). ''Group estimation of loudness in sound fields,'' Acustica **60**, 277–282.

Cohen, M. F. (**1982**). ''Detection threshold microstructure and its effect on temporal integration data,'' J. Acoust. Soc. Am. **71**, 405–409.

Feldtkeller, R., Zwicker, E., and Port, E. (**1959**). ''Lautstärke, Verhältnislautheit und Summenlautheit,'' Frequenz **13**, 108–117.

Fletcher, H., and Munson, W. A. (**1933**). ''Loudness, its definition, measurement and calculation,'' J. Acoust. Soc. Am. **5**, 82–108.

Fletcher, H., and Steinberg, J. C. (**1924**). ''The dependence of the loudness of a complex sound upon the energy in the various frequency regions of the sound,'' Phys. Rev. **24**, 306–317.

Florentine, M., Buus, S., and Poulsen, T. (**1996**). ''Temporal integration of loudness as a function of level,'' J. Acoust. Soc. Am. **99**, 1633–1644.

Gässler, G. (**1954**). ''Über die Hörschwelle für Schallereignisse mit verschieden breitem Frequenzspektrum,'' Acustica **4**, 408–414.

Glasberg, B. R., and Moore, B. C. J. (**1990**). ''Derivation of auditory filter shapes from notched-noise data,'' Hearing Res. **47**, 103–138.

Green, D. M. (**1958**). ''Detection of multiple component signals in noise,'' J. Acoust. Soc. Am. **30**, 904–911.

Green, D. M., McKey, M. J., and Licklider, J. C. R. (**1959**). ''Detection of a pulsed sinusoid in noise as a function of frequency,'' J. Acoust. Soc. Am. **31**, 1446–1452.

Grose, J. H., and Hall, J. W. (**1997**). ''Multiband detection of energy fluctuations,'' J. Acoust. Soc. Am. **102**, 1088–1096.

Hellman, R. P., and Zwislocki, J. J. (**1961**). ''Some factors affecting the estimation of loudness,'' J. Acoust. Soc. Am. **33**, 687–694.

Hellman, R. P., and Zwislocki, J. J. (**1963**). ''Monaural loudness function at 1000 cps and interaural summation,'' J. Acoust. Soc. Am. **35**, 856–865.

Hellman, R. P., and Zwislocki, J. J. (**1964**). ''Loudness function of a 1000-cps tone in the presence of a masking noise,'' J. Acoust. Soc. Am. **36**, 1618–1627.

Hellman, R. P., and Meiselman, C. H. (**1990**). ''Loudness relations for individuals and groups in normal and impaired hearing,'' J. Acoust. Soc. Am. **88**, 2596–2606.

Hellman, R. P. (**1991**). ''Loudness scaling by magnitude scaling: Implications for intensity coding,'' in *Ratio Scaling of Psychological Magnitude: In Honor of the Memory of S. S. Stevens*, edited by G. A. Gescheider and S. J. Bolanowski (Erlbaum, Hillsdale, NJ), pp. 215–228.

Higgins, M. B., and Turner, C. W. (**1990**). ''Summation bandwidths at threshold in normal and hearing-impaired listeners,'' J. Acoust. Soc. Am. **88**, 2625–2630.

Humes, L. E., and Jesteadt, W. (**1991**). ''Models of the effects of threshold on loudness growth and summation,'' J. Acoust. Soc. Am. **90**, 1933–1943.

ISO (**1959**). ISO/R-131-1959 (E) ''Expression of the physical and subjective magnitudes of sound'' (International Organization for Standardization, Geneva).

ISO (**1987**). ISO-226-1987 ''Acoustics—Normal equal-loudness level contours'' (International Organization for Standardization, Geneva).

Jesteadt, W. (**1980**). ''An adaptive procedure for subjective judgments,'' Percept. Psychophys. **28**, 85–88.

Kemp, D. T. (**1979**). ''The evoked cochlear mechanical response and the auditory microstructure—Evidence for a new element in cochlear mechanics,'' in *Models of the Auditory System and Related Signal Processing Techniques*, edited by M. Hoke and E. de Boer, Scand. Audiol. Suppl. **9**, 35–47.

Knauss, H. P. (**1937**). ''An empirical formula for the loudness of a 1000-cycle tone,'' J. Acoust. Soc. Am. **9**, 45–46.

Kohlrausch, A., and Langhans, A. (**1991**). ''Zusammenhang zwischen der Bandbreite von Testsignalen und ihren Mithörschwellen in Rauschmaskierern,'' Fortschr. Akustik, DAGA-91.

Langhans, A., and Kohlrausch, A. (**1992**). ''Spectral integration of broadband signals in diotic and dichotic masking experiments,'' J. Acoust. Soc. Am. **91**, 317–326.

Levitt, H. (**1971**). ''Transformed up-down procedures in psychoacoustics,'' J. Acoust. Soc. Am. **49**, 467–477.

Lochner, J. P. A., and Burger, J. F. (**1961**). ''Form of the loudness function in the presence of masking noise,'' J. Acoust. Soc. Am. **33**, 1705–1707.

Luce, R. D. (**1959**). ''On the possible psychophysical laws,'' Psychol. Rev. **66**, 81–95.

Marks, L. E. (**1978**). ''Binaural summation of the loudness of pure tones,'' J. Acoust. Soc. Am. **64**, 107–113.

Marks, L. E. (**1979**). ''A theory of loudness and loudness judgments,'' Psychol. Rev. **86**, 256–285.

Marshall, L., and Jesteadt, W. (**1986**). ''Comparison of pure-tone audibility thresholds obtained with audiological and two-interval forced-choice procedures,'' J. Speech Hear. Res. **29**, 82–91.

Moore, B. C. J. (**1997**). ''Frequency selectivity and pitch perception,'' in *Encyclopedia of Acoustics, Vol. 3*, edited by M. J. Crocker (Wiley, New York), pp. 1447–1460.

Moore, B. C. J., and Glasberg, B. R. (**1986**). ''The role of frequency selectivity in the perception of loudness, pitch, and time,'' in *Frequency Selectivity in Hearing*, edited by B. C. J. Moore (Academic, London), pp. 251–308.

Moore, B. C. J., and Glasberg, B. R. (**1996**). ''A revision of Zwicker's loudness model,'' Acustica **82**, 335–345.

Moore, B. C. J., Glasberg, B. R., and Baer, T. (**1997**). ''A model for the prediction of thresholds, loudness, and partial loudness,'' J. Audio Eng. Soc. **45**, 224–240.

Poulton, E. C. (**1989**). *Bias in Quantifying Judgments* (Erlbaum, Hillsdale, NJ).

Robinson, D. W. (**1957**). ''The subjective loudness scale,'' Acustica **7**, 217–233.

Scharf, B. (**1959**). ''Critical bands and the loudness of complex sounds near threshold,'' J. Acoust. Soc. Am. **33**, 365–370.

Scharf, B. (**1970**). ''Critical bands,'' in *Foundations of Modern Auditory Theory, Vol. 1*, edited by J. V. Tobias (Academic, New York), pp. 157–202.

Scharf, B. (**1978**). ''Loudness,'' in *Handbook of Perception: Vol. 4. Hearing*, edited by E. C. Carterette and M. P. Friedman (Academic, New York), pp. 187–242.

Scharf, B. (**1997**). ''Loudness,'' in *Encyclopedia of Acoustics, Vol. 3*, edited by M. J. Crocker (Wiley, New York), pp. 1481–1495.

Scharf, B., and Stevens, J. C. (**1961**). ''The form of the loudness function near threshold,'' *Proceedings of the 3rd International Congress on Acoustics* (Elsevier, Amsterdam), pp. 80–82.

Spiegel, M. F. (**1979**). ''The range of spectral integration,'' J. Acoust. Soc. Am. **66**, 1356–1363.

Spiegel, M. F. (**1981**). ''Thresholds for tones in maskers of various bandwidths and for signals of various bandwidths as a function of signal frequency,'' J. Acoust. Soc. Am. **69**, 791–795.

Stevens, S. S. (**1955**). ''The measurement of loudness,'' J. Acoust. Soc. Am. **27**, 815–827.

Stevens, S. S. (**1959**). ''Tactile vibration: Dynamics of sensory intensity,'' J. Exp. Psychol. **59**, 210–218.

Stevens, S. S. (**1966**). ''Power-group transformations under glare, masking, and recruitment,'' J. Acoust. Soc. Am. **27**, 725–735.

van den Brink, W. A. C., and Houtgast, T. (**1990**). ''Spectro-temporal integration in signal detection,'' J. Acoust. Soc. Am. **88**, 1703–1711.

Zwicker, E. (**1958**). ''Über psychologische und methodische Grundlagen der Lautheit,'' Acustica **8**, 237–258.
Zwicker, E., and Fastl, H. (**1990**). *Psychoacoustics. Facts and Models* (Springer-Verlag, New York).
Zwislocki, J. J. (**1965**). ''Analysis of some auditory characteristics,'' in *Handbook of Mathematical Psychology*, edited by R. D. Luce, R. R. Bush, and E. Galanter (Wiley, New York), pp. 1–97.
Zwislocki, J. J., and Hellman, R. P. (**1960**). ''On the ''psychophysical law'','' J. Acoust. Soc. Am. **32**, 924.

Discrimination of frequency glides with superimposed random glides in level

Brian C. J. Moore and Aleksander Sek[a)]
Department of Experimental Psychology, University of Cambridge, Downing Street, Cambridge CB2 3EB, England

(Received 8 December 1997; revised 9 January 1998; accepted 7 April 1998)

These experiments were designed to test the hypothesis that glides in frequency are detected and discriminated by monitoring changes in excitation level on the low-frequency side of the excitation pattern. Thresholds were measured for detecting an increase in the extent of a frequency glide, for various standard extents (transition spans). The center frequency of each stimulus was roved, to prevent subjects from using the start or endpoint frequencies of the stimuli as cues. The level was either fixed at 70 dB SPL, or changed linearly in dB/s by an amount that varied randomly in extent and direction, keeping the level at the midpoint of the glide at 70 dB SPL. These random changes in level were intended to disrupt cues based on monitoring changes in excitation level on one side of the excitation pattern. For some conditions, performance was too good to be explained by subjects monitoring the start or endpoint frequencies of the stimuli. Performance was also too good to be explained in terms of the discrimination of changes in excitation level on one side of the excitation pattern. Thresholds, expressed as a proportion of the equivalent rectangular bandwidth (ERB) of the auditory filter, did not vary greatly with center frequency (0.5, 2, or 6 kHz), suggesting that discrimination did not depend strongly on information derived from phase locking. Glide duration (50 or 400 ms) and glide direction (upward or downward) also had little effect. Thresholds increased with increasing standard transition span, when that span was increased beyond 0.5 ERB. It is concluded that changes in glide extent *per se* can be discriminated, but this is not done by monitoring just one side of the excitation pattern.
[S0001-4966(98)03907-1]

PACS numbers: 43.66.Fe, 43.66.Hg, 43.66.Ba [RVS]

INTRODUCTION

Traditionally, there have been two classes of theory to explain the ability to discriminate frequency changes in sinusoids. One class assumes that frequency discrimination is based on changes in the place distribution of activity in the auditory system. For example, Zwicker (1956, 1970) proposed a model for the detection of frequency modulation (FM) based on the concept of the excitation pattern. He suggested that FM could be detected if it resulted in a change in the amount of excitation greater than 1 dB at any point on the excitation pattern; the change in excitation level was assumed to be greatest on the steeply sloping low-frequency side of the excitation pattern. We have proposed a similar model, but one in which information is combined from all points of the excitation pattern (Moore and Sek, 1994). Zwicker's model has also been applied to the discrimination of successive tone pulses differing in frequency (pulsed tones discrimination) (Moore, 1973; Freyman and Nelson, 1986). Although these models are based on excitation patterns derived from psychoacoustic data, it is generally assumed that the excitation pattern is related to a rate-place representation in the peripheral auditory system, i.e., it is related to the driven neural firing rate as a function of characteristic frequency, and does not depend on neural synchrony (phase locking) to the fine structure of the stimulus.

The slope of the excitation pattern at a given center frequency is closely related to the bandwidth of the auditory filter at that center frequency (Glasberg and Moore, 1990). Hence, models based on excitation patterns generally make the prediction that the threshold for detection of a frequency change at a given center frequency should be a constant proportion of the critical bandwidth or the equivalent rectangular bandwidth (ERB) of the auditory filter at that center frequency, regardless of the center frequency. Data on the frequency discrimination of pulsed tones generally do not conform well to this prediction (Moore, 1974; Moore and Glasberg, 1986, 1989; Sek and Moore, 1995). However, the prediction holds reasonably well for the detection of FM (Zwicker, 1956; Zwicker and Fastl, 1990), especially when the modulation is at a rate of 10 Hz or higher (Sek and Moore, 1995; Moore and Sek, 1996b).

The alternative class of theory assumes that frequency discrimination is based on information contained in the temporal patterns of firing in the auditory nerve (phase locking) (Siebert, 1970; Goldstein and Srulovicz, 1977). However, phase locking to sinusoids appears to break down above 4–5 kHz in the mammalian auditory nerve (Johnson, 1980; Palmer, 1995), so this mechanism probably does not work over the whole audible frequency range.

Moore and Sek (1995, 1996b; Sek and Moore, 1995) have proposed that the mechanisms involved in frequency discrimination vary depending on the exact nature of the stimuli. They suggested, following Moore (1973), that the

[a)]On leave from Institute of Acoustics, Adam Mickiewicz University, Matejki 48/49, 60-769 Poznan, Poland.

frequency discrimination of pulsed tones depends mainly upon the use of phase locking information for frequencies up to about 4–5 kHz; above that frequency, only place information is available. For FM detection, the dominant mechanism was argued to depend on modulation rate; for very low modulation rates (around 2 Hz), a mechanism based on phase locking appears to be dominant, for carrier frequencies up to about 5 kHz. For higher modulation rates (above 10 Hz), a place mechanism appears to be dominant, for all carrier frequencies. For a review of the evidence supporting these ideas see Moore and Sek (1996a).

To explain why phase locking information is used for low modulation rates but not for higher ones, Moore and Sek (1995) suggested that the mechanism based on phase locking may show a form of ''sluggishness'' akin to the sluggishness that has been observed in binaural processing of phase locking information (Grantham and Wightman, 1978, 1979). The mechanism based on phase locking appears to sample the frequency at different instants in time, and it may be ineffective at high modulation rates because the stimuli change frequency too rapidly or spend insufficient time at frequency extremes.

The mechanisms underlying the detection and discrimination of frequency glides remain unclear. Dooley and Moore (1988a) measured thresholds for the detection of frequency glides in 500-ms tones over a wide range of center frequencies (500–8000 Hz). They compared the thresholds with the predictions of Zwicker's (1956) model. They used the excitation-pattern model of Moore and Glasberg (1987) to calculate the changes on the low-frequency sides of the excitation patterns produced by glides in frequency at threshold values. The changes varied somewhat with center frequency, and were somewhat smaller than the smallest detectable change in level. However, they concluded that ''the discrepancies are not large enough to provide strong evidence against the model.''

Madden and Fire (1996) measured thresholds for detecting frequency glides and for discriminating frequency glides of different extents (referred to as transition spans), using 50-ms tone glides. The thresholds were roughly a constant proportion of the ERB of the auditory filter over a range of center frequencies from 500 to 6000 Hz. They took this as support for an excitation-pattern model. In a second study (Madden and Fire, 1997), they used both a 50-ms duration and a 400-ms duration. Following the ideas about the sluggishness of the temporal mechanism described above, they suggested that a temporal mechanism might be able to track glides of long duration, since they have a relatively gradual rate of change of frequency, whereas it might not be able to track rapid frequency glides. However, they found that thresholds were roughly a constant proportion of the ERB of the auditory filter at both durations, over a wide range of center frequencies. They concluded that the results for both durations were consistent with a mechanism that monitors the changes in excitation level at the most steeply sloping part of the excitation pattern evoked by the stimuli (the low-frequency side).

One puzzling aspect of the results of Madden and Fire (1997) is that the thresholds were not affected by duration. As they pointed out, the 400-ms stimuli remain near their start and endpoint frequencies for a longer time than the 50-ms stimuli. This extra time should allow more accurate sampling of the start and endpoint frequencies whatever mechanism is involved. Perhaps the lack of a duration effect reflects the operation of a mechanism that is specifically concerned with the discrimination of rates of change of frequency, rather than merely taking ''snapshots'' of the endpoints (Dooley and Moore, 1988a, b). If glide rate discrimination obeys Weber's law (Dooley and Moore, 1988b), then glide duration should have little effect on performance as a change in duration would change the glide rate of the two stimuli to be discriminated by the same factor.

In the present paper, we describe a replication and extension of the results of Madden and Fire (1996, 1997). The main new feature of our experiment was that we included conditions where large glides in level were superimposed on the stimuli. The glides in level varied randomly in direction (increasing versus decreasing level) and in extent from one stimulus to the next. This was expected to disrupt markedly the usefulness of cues based on monitoring changes in excitation level on one side of the excitation pattern. The rationale is similar to that used previously in tests of the excitation-pattern model as applied to the frequency discrimination of pulsed tones; in those experiments, random differences in level were applied to each stimulus (Emmerich *et al.*, 1989; Moore and Glasberg, 1989). Similarly, to test excitation-pattern models for the detection of FM, amplitude modulation with random modulator phase has been superimposed on the FM to be detected (Grant, 1987; Moore and Glasberg, 1989; Moore and Sek, 1996b).

To understand the rationale in the present experiments, consider the task of discriminating an upward frequency glide of fixed extent (standard) from an upward glide of greater extent (signal). According to an excitation-pattern model this could be done by monitoring the low-frequency side of the excitation pattern; the signal glide would give a larger decrease in excitation level than the standard glide. In a two-interval forced-choice task, the signal would be identified as the stimulus giving the larger decrease in excitation level. The large superimposed random glides in level would be expected to disrupt such a cue for two reasons. First, on some trials, the decrease in excitation level on the low-frequency side of the excitation pattern would be larger for the standard stimulus than for the signal stimulus. Second, discrimination of changes in level appears roughly to follow Weber's law, at least for reasonably large glide extents (Dooley and Moore, 1988b). Hence, discrimination of the changes in excitation level produced by the frequency glides would be harder simply because these were superimposed on large changes in level produced by the level glides.

I. EXPERIMENT 1

A. General method

The method and stimuli were chosen to be very similar to those of Madden and Fire (1996, 1997), so that the results would be directly comparable. Thresholds for detecting frequency glides and for discriminating frequency glides of dif-

ferent extent were measured using 50-ms and 400-ms glides. Conditions were run both without and with superimposed random glides in level.

B. Procedure and stimuli

A two-alternative forced-choice task was used. In the glide detection task, the ''standard'' stimulus was a sinusoid of constant frequency and the ''signal'' stimulus was a sinusoid with gliding frequency whose direction (upward or downward) was fixed within a block of trials. In the glide discrimination task, the ''standard'' stimulus was a frequency glide of fixed extent (transition span), and the ''signal'' stimulus was a frequency glide of greater extent. Again, the direction of the glide was fixed within a block of trials. Subjects were required to identify the interval containing the signal stimulus. The transition spans are specified on an ERB scale, using the equation relating number of ERBs to frequency given by Glasberg and Moore (1990):

$$\text{Number of ERBs} = 21.4 \log_{10}(4.37F + 1),$$

where F is frequency in kHz.

Nominal center frequencies of 500, 2000, and 6000 Hz were used. The standard stimulus had an overall extent of 0, 0.5, 1.0, and 2.0 ERBs, the same as used by Madden and Fire (1996, 1997). The glides were linear on a linear frequency scale. However, for the limited transition spans used, the result is not very different from glides that are linear on an ERB scale. For example, for the 2000-Hz center frequency, the 2-ERB standard glide went from 1773 to 2253 Hz. At its midpoint in time, this glide had a frequency of 2013 Hz, which is very close to the frequency of 2000 Hz that would have occurred for a glide that was uniform on an ERB scale.

On average, the center frequencies of the standard and signal stimuli were equal within a given block of trials. However, the actual center frequency of each stimulus was randomized over a range of ± 1 ERB (total range of 2 ERBs, uniform distribution) to reduce the ability of subjects to perform the task by comparing the start or endpoint frequencies of the standard and signal stimuli. If the frequency change in the signal interval is greater than that in the standard interval by ΔF, then the start and endpoint frequencies in the signal and standard intervals differ, by $0.5\Delta F$. Following arguments given by Green (1988, pp. 19–20), if the center frequency of each stimulus is randomly varied over a range R, then the change in start or endpoint frequency required to give 70.7% correct, assuming perfect resolution of frequency, is $0.235R$. Therefore, given the 2-ERB randomization range used, the smallest possible threshold (expressed as ΔF) that could be achieved by monitoring the start or endpoint frequency is $0.47 \times 2 = 0.94$ ERBs.

The transition span of the standard stimulus was fixed in ERBs, not in Hz. Thus if on a particular trial the actual center frequency was lower than the nominal center frequency, the transition span in Hz was also lower than the nominal value.

Three conditions were run. In one, the level of all stimuli was fixed at 70 dB SPL. This condition was similar to those used by Madden and Fire (1996, 1997). In a second condition, glides in level were superimposed on all stimuli, keeping the level of the midpoint of each glide at 70 dB SPL. The glides were linear in dB/s and the total glide extent for each stimulus was chosen randomly from the ranges 10 to 20 dB, and -10 to -20 dB. In other words, the glides could be either increases or decreases in level, and their absolute value was between 10 and 20 dB. The third condition was similar, except that the absolute values of the total glide extents were in the range 30–40 dB.

Thresholds were measured using a two-down one-up adaptive procedure that estimates the 70.7% correct point on the psychometric function. Denote the difference in frequency extent between the standard and signal stimulus by ΔF. At the start of a run, the value of ΔF was chosen on the basis of pilot trials to be large enough to make the task reasonably easy. The value of ΔF was changed by a factor of 1.5 until four reversals occurred. Thereafter it was changed by a factor of 1.25 and eight further reversals were obtained. The threshold for a run was estimated as the geometric mean value of ΔF at the last eight reversals. Four runs were obtained for each condition. Subsequently, runs were rejected in cases where the standard deviation of the logarithm of the values of ΔF at the last eight reversals was greater than 0.25. This happened in nine cases out of 1728. Therefore, thresholds reported are usually based on four runs, but occasionally on only three.

Stimuli were generated using a Tucker-Davis array processor (TDT-AP2) in a host PC, and a 16-bit digital to analog converter (TDT-DD1) operating at a 50-kHz sampling rate. They were attenuated (TDT-PA4) and sent through an output amplifier (TDT-HB6) to a Sennheiser HD414 earphone. This earphone is designed to mimic the free-field response of the ear. The response at the eardrum is not flat, but it does vary smoothly with frequency. It is possible that, in the condition with no glides in level in the electrical signal, the frequency glides resulted in glides in level in the acoustic signal that provided usable detection cues. However, the superimposed large glides in level in the other conditions would have prevented such cues from being useful.

On each trial, two successive stimuli were presented, the signal and the standard. The order of the two stimuli in each pair was random. Each stimulus had a steady state duration of either 50 or 400 ms. Additional raised-cosine rise/fall times of 5 ms were used. The frequency glide started at the start of the 5-ms onset ramp and finished at the end of the 5-ms offset ramp. The time interval between the stimuli was 500 ms. Lights were used to mark the observation intervals and to provide feedback. Subjects were allowed as long as they wanted to make a response. The next trial began one second after a response had been made. Subjects were tested individually in a double-walled sound-attenuating chamber.

C. Subjects

Three subjects were tested. One was author AS. The other two subjects were paid for their services. All subjects had absolute thresholds less than 20 dB HL at all audiometric frequencies and had no history of hearing disorders. All had previous experience in psychoacoustic tasks. They were given practice in all conditions until their performance ap-

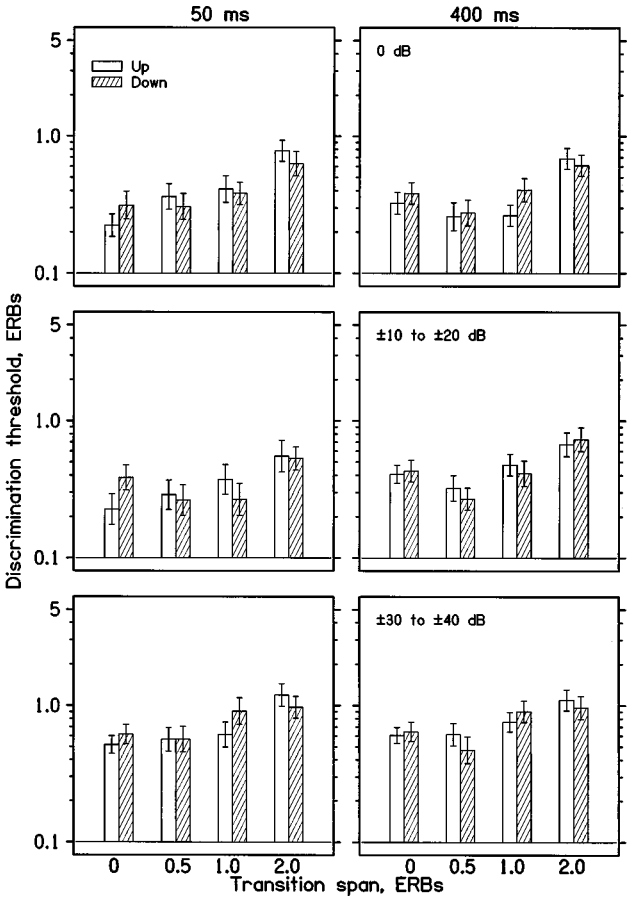

FIG. 1. Results of experiment 1 showing thresholds for discriminating frequency glides expressed in ERBs, averaged across subjects and center frequencies. Thresholds are shown on a logarithmic scale, with an arbitrary baseline of 0.1 ERBs. Thresholds are plotted for each standard transition span, for the 50-ms duration (left panels) and the 400-ms duration (right panels). Each row shows results for one range of the random glides in level. Open bars and shaded bars show thresholds for upward and downward frequency glides, respectively. Error bars indicate ± one standard error across subjects.

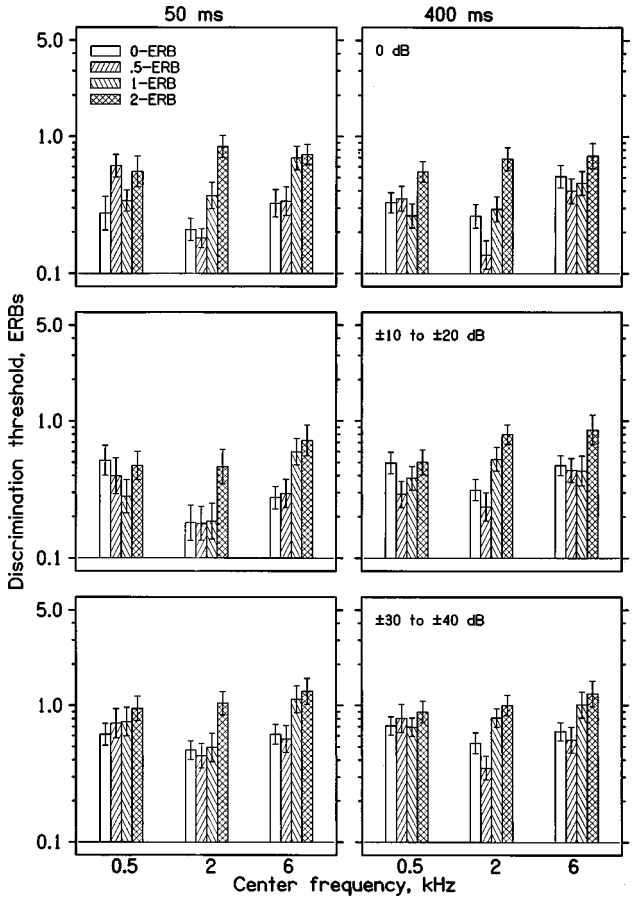

FIG. 2. Results of experiment 1, averaged across subjects and glide directions. Thresholds are plotted for each center frequency, for the 50-ms duration (left panels) and the 400-ms duration (right panels). Each row shows results for one range of the random glides in level. The shading of the bars indicates the standard transition span, as indicated in the key in the top left panel. Error bars indicate ± one standard error across subjects.

peared to be stable; this took between 10 and 15 h. The thresholds gathered during the practice sessions were discarded.

D. Results

The standard deviation of the threshold estimates (across the four runs for a given condition and subject) was roughly a constant proportion of the mean threshold value. Hence, in what follows, geometric means are used throughout, and analyses of variance (ANOVAs) are based on the logarithms of the threshold values. Also, thresholds will be plotted on logarithmic scales. The pattern of results was similar across subjects, so only data averaged across subjects (geometric means) will be presented. We consider first whether there are systematic differences between thresholds for up glides and for down glides. Madden and Fire (1997) reported higher thresholds for 50-ms down glides than for 50-ms up glides, although they offered no explanation for this. They pointed out that the results of previous studies on glide detection are inconsistent in whether they found an effect of glide direction. Figure 1 shows thresholds from the present experiment for each transition span. They are expressed as a proportion of the ERB at each center frequency (i.e., as number of ERBs), and averaged across center frequencies. The left column shows results for the 50-ms glides, and the right column shows results for the 400-ms glides. The three rows show results for the three different amount of random level glide: 0 (top), ± 10 to ± 20 dB (middle) and ± 30 to ± 40 dB (bottom). There is no clear effect of glide direction at either duration, regardless of the amount of superimposed level glide, although there is a slight trend for better performance with up glides for the transition span of 0. The geometric mean thresholds across all center frequencies, transition spans, amounts of glide and durations were 0.47 ERBs for up glides and 0.48 ERBs for down glides.

Figure 2 shows the thresholds averaged across values for up glides and down glides. The left column shows results for the 50-ms glides, and the right column shows results for the 400-ms glides. The three rows show results for the three different amounts of random level glide: 0 (top), ± 10 to ± 20 dB (middle) and ± 30 to ± 40 dB (bottom). Each group of four bars represents one center frequency. The different transition spans are represented by the individual bars within each group of four. The results when no glides in level were applied (top panels) are similar to those reported by Madden

and Fire (1997), except that overall our subjects performed slightly more poorly than theirs. This might reflect individual differences, or it might reflect the fact that we roved the center frequency of the stimuli over a greater range than they did; we used a 2-ERB range, which corresponds to about 25% of the center frequency, whereas they used a range of 10% of the center frequency. As noted earlier, in our experiment the smallest possible threshold that could be achieved by monitoring the start or endpoint frequency is 0.94 ERBs. Most of the thresholds were below that limit, indicating that the task was not performed by monitoring the start or endpoint frequency. The effect of altering the rove range is examined in experiment 2.

Thresholds did not differ systematically for transition spans of 0 and 0.5 ERBs. On average, they increased slightly for a transition span of 1 ERB, and increased more for a span of 2 ERBs. There was no clear effect of duration. There was a trend for performance to be better at 2 kHz than at 0.5 or 6 kHz, especially for the 0- and 0.5-ERB transition spans. A similar trend was observed by Madden and Fire (1996). The introduction of moderate glides in level (middle row) had no overall effect on the thresholds. However, the introduction of larger glides in level (bottom panel) led to thresholds that were markedly higher.

To assess the statistical significance of these effects, a within-subjects analysis of variance (ANOVA) was conducted on the logarithms of the threshold values, with factors duration, direction of frequency glide, center frequency, transition span, and amount of level glide. The main effects of duration and direction of frequency glide were not significant at the 0.05 level. The main effect of transition span was highly significant; $F(3,6)=50.4$, $p<0.001$. *Post hoc* tests showed that mean thresholds did not differ significantly for the 0- and 0.5-ERB spans. The mean threshold was greater for the 1-ERB span than for the 0- and 0.5-ERB spans ($p<0.01$) and was greater for the 2-ERB span than for the 1-ERB span ($p<0.001$). The main effect of amount of glide in level was highly significant; $F(2,4)=175.8$, $p<0.001$. *Post hoc* tests showed that mean thresholds did not differ significantly for the condition with no glides in level and the condition with moderate glides in level. The mean threshold for the condition with large glides in level was significantly greater than for the two other conditions ($p<0.001$). The main effect of center frequency was significant; $F(2,4)=57.1$, $p<0.001$. *Post hoc* tests showed the performance was significantly better at 2 kHz than at 0.5 kHz ($p<0.01$) and at 6 kHz ($p<0.001$). Performance was also significantly better at 0.5 kHz than at 6 kHz ($p<0.05$).

Three of the two-way interactions were significant. The interaction between transition span and center frequency [$F(6,12)=44.9$, $p<0.001$] reflects the fact that, for the 0- and 0.5-ERB transition spans, performance was better at 2 kHz than at the other two frequencies, whereas for the larger transition spans there was little effect of center frequency. The interaction between amount of glide in level and duration [$F(2,4)=39.4$, $p=0.002$] reflects the fact that, performance was slightly better for the shorter duration with the moderate glides in level, but this was not true for when there were no glides or large glides in level. The interaction between transition span and duration [$F(3,6)=31.0$, $p<0.001$] reflects the fact that performance was slightly better for the 50-ms duration for the 0-ERB transition span, but not for the other spans. However, it should be noted that each of these interactions accounted for only a small proportion of the variance in the data (4% or less).

E. Discussion

Consistent with the results of Madden and Fire (1996, 1997), thresholds expressed in ERBs did not vary greatly with center frequency. Nevertheless, average thresholds at 2 kHz were significantly lower than at the two other center frequencies, and average thresholds at 0.5 kHz were lower than at 6 kHz. These effects of frequency would not be predicted by excitation-pattern models. Contrary to what might be expected on the basis of excitation-pattern models, the addition of random glides in level of moderate extent had very little effect on performance. Performance worsened only when very large random glides in level were used, and even then it worsened by an average factor less than two.

The Appendix describes how to calculate the amount of disruption of performance that would be expected on the basis of an excitation-pattern model, assuming perfect resolution of intensity changes. It shows that the *extra* change in excitation level produced by the larger frequency glide in the signal interval would have to be at least 5.9 dB to achieve 70.7% correct for the two conditions in which random glides in level were present. Assuming excitation-pattern slopes corresponding to the average values published by Glasberg and Moore (1990), this requires a value of ΔF of about 0.34 ERBs. For a center frequency of 2 kHz, and for the condition with random glides in level of ± 10 to ± 20 dB, thresholds for the two smaller transition spans (0 and 0.5 ERBs) were smaller than this, at about 0.25 ERBs. This makes it unlikely that subjects performed the task simply by monitoring changes in excitation level on the low-frequency side of the excitation pattern. However, if subjects had excitation patterns with steeper slopes than the average values assumed in the method of Glasberg and Moore, then changes in excitation level might have provided usable cues. For the other center frequencies and spans, and for all center frequencies and spans with the larger level glides, thresholds were greater than 0.34 ERBs. Thus in these cases, we cannot rule out the possibility that subjects performed the task by monitoring changes in excitation level on the low-frequency side of the excitation pattern.

However, the calculations in the Appendix assumed perfect resolution of changes in excitation level. In practice, resolution is far from perfect. The thresholds for detecting frequency glides (i.e., for a transition span of 0) in the *absence* of level glides were about 0.2 to 0.5 ERBs. This corresponds to changes in excitation level of about 3.5 to 8.5 dB. Thus when random glides in level were present, limitations in the resolution of changes in excitation level would have led to thresholds considerably higher than those associated with a change in excitation level of 5.9 dB.

Further analysis leads to the conclusion that performance was not based on the detection of changes in excitation level on one side of the excitation pattern, at least for the

condition in which moderate glides in level were used. Denote the threshold measured with no glide in level by ΔF_0. This is the extra change in frequency in the signal interval needed for $P=0.707$ correct, which corresponds to a detectability index, d', of 0.76. Assume now that random glides in level between ± 10 and ± 20 dB are superimposed, and the proportion correct is measured with ΔF fixed at ΔF_0. On half of the trials (corresponding to the combination of cases 1 and 2 in the Appendix) performance will be at chance ($P=0.5$). On the other half of the trials, performance can be no better than $P=0.707$; in practice it would be lower than $P=0.707$ correct because of the random size of the added level glides. Therefore, the highest possible proportion correct is

$$P=(0.5\times 0.5)+(0.5\times 0.707)=0.603.$$

This corresponds to a value of d' of 0.36, less than half the value when no glides in level were present. To restore the value of P to 0.707, one would expect to have to increase the value of ΔF, by an amount depending on the slope of the psychometric function. We were unable to find data on psychometric functions for frequency glide detection. However, data on the frequency discrimination of pulsed tones and the detection and discrimination of frequency modulation suggest that d' is proportional to ΔF raised to a power between 1 and 2 (Jesteadt and Sims, 1975; Moore and Sek, 1992, 1994, 1995). Thus we would expect to have to increase the value of ΔF by a factor between about 1.4 and 2. In fact, thresholds were almost the same when no level glides were present and when level glides between ± 10 and ± 20 dB were present; the overall geometric mean threshold was 0.385 for the former and 0.389 for the latter. Thus moderate glides in level did not disrupt performance as much as would be predicted if subjects performed the task by monitoring changes in excitation level on the low-frequency side of the excitation pattern. We can conclude that an excitation-pattern model based on this assumption is not tenable.

II. EXPERIMENT 2

A. Rationale

The thresholds for our subjects were somewhat higher than those reported by Madden and Fire (1997). As noted earlier, this might reflect the fact that we roved the center frequency of the stimuli over a greater range than they did; we used a 2-ERB range, which corresponds to about 25% of the center frequency, whereas they used a range of 10% of the center frequency. To assess whether this explanation was plausible, experiment 2 examined the effect of altering the rove range of the center frequency. A second reason for performing this experiment was to assess whether subjects make use of the start and/or endpoint frequencies of the stimuli when they provide reliable cues, i.e., when the center frequency is not roved or is roved over a very small range. If this is the case, then even a moderate rove range of the center frequencies of the stimuli should affect performance. On the other hand, if subjects make use of frequency changes *per se*, then roving the center frequency over a moderate range should have little effect on performance.

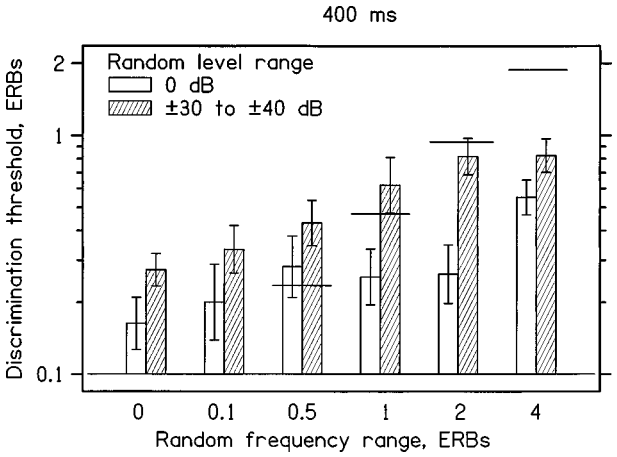

FIG. 3. Results of experiment 2, averaged across subjects and glide directions. Thresholds are plotted for each range over which the center frequency was randomly varied. Open bars show thresholds with the level fixed and shaded bars show thresholds with glides in level varying randomly over the range ± 30 to ± 40 dB. Horizontal lines indicate the best performance that could be achieved based on the start or endpoint frequencies of the stimuli. The lines are not shown for the rove ranges of 0 and 0.1 ERBs, as they would fall below the arbitrary baseline of 0.1. Error bars indicate $\pm$ one standard error across subjects.

B. Method

The procedure and the method of stimulus generation were the same as for experiment 1. Thresholds for detecting upward and downward frequency glides were measured using a carrier frequency of 2 kHz and a standard transition span of 1 ERB. The stimuli were either fixed in level at 70 dB SPL, or had random glides in level of ± 30 to ± 40 dB. The center frequency of the stimuli was randomly varied within an overall range of 0, 0.1, 0.5, 1, 2, or 4 ERBs (rectangular distribution). The rove range was fixed within a block of trials, but varied across blocks. Three subjects were used. Two were the same as for experiment 1. The new subject had extensive experience in similar tasks. All had audiometric thresholds better than 20 dB HL at all audiometric frequencies. The new subject was trained for about 10 h, after which performance appeared to be stable.

C. Results

The pattern of results was similar across subjects. Also, thresholds were similar for up glides and down glides. Figure 3 shows the thresholds for each rove range of the center frequency, averaged across subjects and glide directions and expressed as a proportion of the ERB. The horizontal lines show the thresholds that would be expected if subjects made optimal use of the start or endpoint frequencies; these lines are not shown for rove ranges of 0 and 0.1 ERBs, since they would fall below the value of 0.1 used as the baseline. Open bars show thresholds when the level was constant. For this condition, the mean threshold increased when the rove range in center frequency was increased from 0 to 0.5 ERBs, but remained almost constant when the range was increased from 0.5 to 2 ERBs; this last value is the same as used in experiment 1. The mean threshold roughly doubled when the rove range in center frequency was increased from 2 to 4 ERBs. For rove ranges up to 0.5 ERBs, thresholds are higher than

the limit that would be expected if subjects made optimal use of the start or endpoint frequencies. For rove ranges of 1–4 ERBs, thresholds are clearly below that limit. The fact that performance did not worsen markedly when the rove range was increased from 0.5 to 2 ERBs suggests that subjects were not using the start or endpoint frequencies when the rove range was 0.5 ERBs, even though these frequencies potentially provided useful cues.

The results when the random glides in level were present (shaded bars) tend to show a progressive increase in threshold with increasing rove range of the center frequency beyond 0.1. The thresholds increased by a factor of about 2.4 when the rove range was increased from 0.1 to 2 ERBs. For rove ranges up to 1 ERB, thresholds are higher than the limit that would be expected if subjects made optimal use of the start or endpoint frequencies. For rove ranges of 2 and 4 ERBs, thresholds are below that limit. Thus for the smaller rove ranges, subjects might have been making use of the start and/or endpoint frequencies.

A within-subjects ANOVA was conducted on the logarithms of the thresholds, with factors rove range of center frequency, amount of glide in level, and glide direction. The main effect of rove range of center frequency was highly significant; $F(5,10)=20.3$, $p<0.001$. The main effect of amount of glide in level was also significant; $F(1,2)=23.0$, $p=0.041$. The main effect of glide direction was not significant. The interaction of rove range of center frequency and amount of glide in level approached, but did not reach significance at the 0.05 level; $F(5,10)=2.75$, $p=0.082$. *Post hoc* tests showed that, when no glides in level were present, thresholds increased significantly when the rove range in center frequency was increased from 0 to 0.5 ERBs ($p<0.02$), but did not change significantly over the range 0.5 to 2 ERBs. When glides in level were present, thresholds increased significantly when the rove range in center frequency was increased from 0 to 1 ERB ($p<0.002$), from 0.1 to 1 ERB ($p<0.01$), and from 0.5 to 2 ERBs ($p<0.01$).

The results when the level was constant are broadly consistent with earlier work. Madden and Fire (1996) measured thresholds for the detection and discrimination of 50-ms frequency glides which were either fixed in center frequency or roved in center frequency over a range of 0.1 of the center frequency. They found significantly higher thresholds for the latter. Madden and Fire (1997) mentioned a pilot experiment in which they found an effect of rove range for longer signals, again using a rove range of either 0 or 0.1 of the center frequency. Our results showed that performance worsened somewhat, relative to the no-rove condition, when the center frequency was roved by a small amount, but it did not worsen as the rove range was increased from 0.5 to 2 ERBs.

Part of the motivation for this study was to assess whether the difference in performance of our subjects and those of Madden and Fire (1997) could be explained by our use of a greater rove range for the center frequency. The results of experiment 2 suggest that the difference cannot be explained in this way; when no glides in level were present, thresholds were very similar for rove ranges from 0.5 to 2. Probably, individual differences are the source of the discrepancy across studies. Madden (personal communication) has indicated that two of the subjects of Madden and Fire (1997) had thresholds similar to the mean values of our subjects, while two had smaller thresholds.

In summary, when no glides in level were present, the mean threshold increased slightly when the rove range in center frequency was increased from 0 to 0.5 ERBs, but remained almost constant when the range was increased from 0.5 to 2 ERBs. These results suggest that subjects were not using the start or endpoint frequencies when the rove range was 0.5 ERBs, even though these frequencies potentially provided useful cues. When glides in level were present, the thresholds increased more progressively with increasing rove range of the center frequency. For rove ranges up to 1 ERB, subjects may have been using the start and/or endpoint frequencies of the glides as cues. However, for the rove ranges of 2 and 4 ERBs, thresholds were too low to be explained in this way.

III. EXPERIMENT 3

A. Rationale

In experiment 3, we modified the stimulus conditions to make it much more difficult for subjects to perform well by monitoring changes in excitation level on one side of the excitation pattern. Two modifications were made. First, the glides in level were made to vary randomly over the range -20 to $+20$ dB or -40 to $+40$ dB. In other words, unlike in experiment 1, the range of random glides in level included small glides. Secondly, the adaptive procedure was changed from a two-down one-up procedure tracking 70.7% correct to a three-down one-up procedure tracking 79.4% correct. Following arguments given by Green (1988, pp. 19–21), it can be shown that the *extra* change in excitation level produced by the larger frequency glide in the signal interval would have to be at least 14.3 dB for the ± 20-dB range of level glides and 28.7 dB for the ± 40-dB range of level glides. The experiment was intended to provide a more stringent test of the simple excitation-pattern model.

B. Method

The procedure was similar to that of the previous two experiments except that a three-down one-up adaptive tracking rule was used. The steady state duration of the stimuli was 400 ms and center frequencies of 0.5, 2, and 6 kHz were used. The standard transition span was either 0 or 2 ERBs. Only upward glides in frequency were used. Based on the results of experiment 2, the rove range in center frequency was chosen to be 4 ERBs (± 2 ERBs around the nominal value), to make it very difficult for subjects to perform the task by monitoring the start or endpoint frequencies of the stimuli. In one set of conditions, there were no glides in level; all stimuli had a level of 70 dB SPL. In the other two sets of conditions, glides in level ranging randomly from -20 to $+20$ dB or from -40 to $+40$ dB were used. The glides were linear in dB/s, and the level at the center of each glide was 70 dB SPL. The subjects were the same as for experiment 2.

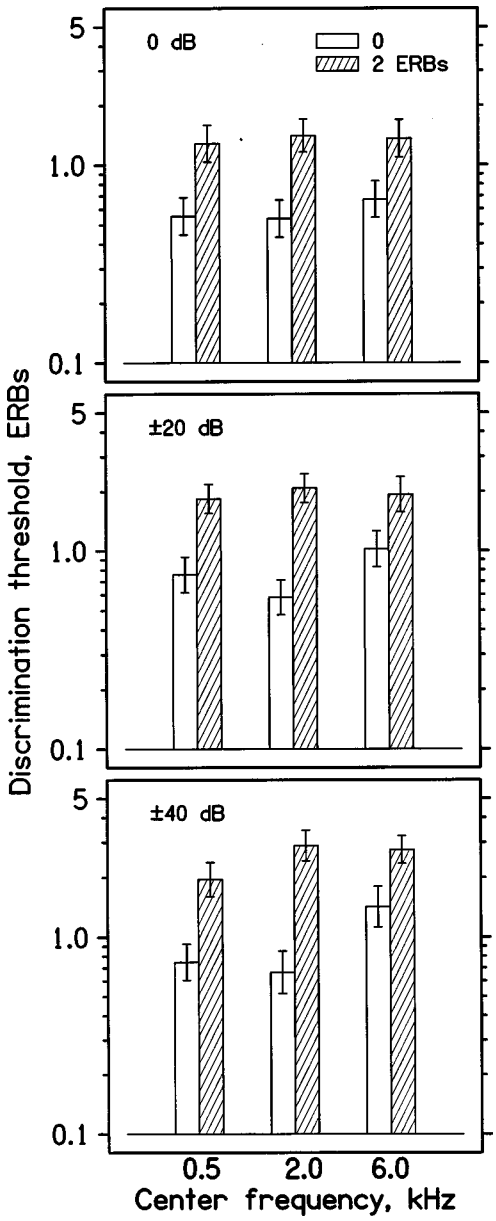

FIG. 4. Results of experiment 3, averaged across subjects. Thresholds are plotted for each center frequency. Each panel shows results for one range of the random glides in level. The shading of the bars indicates the standard transition span, as indicated in the key in the top panel. Error bars indicate ± one standard error across subjects.

C. Results

The pattern of results was similar across subjects. Geometric mean thresholds across subjects are shown in Fig. 4. Each panel shows results for one range of the random glides in level. Thresholds were clearly higher for the larger standard transition span (shaded bars) for all ranges of the random glides in level. Thresholds generally increased with increasing range of the random glides in level, although the increase in threshold was small for the 0-ERB standard transition span for the frequencies of 0.5 and 2 kHz. A within-subjects ANOVA was conducted on the logarithms of the thresholds with factors: standard transition span, center frequency, and range of the random glides in level. The main effect of transition span was highly significant, and accounted for most of the variance in the data; $F(1,2) = 135.2$, $p = 0.007$. The main effect of center frequency was significant; $F(2,4) = 17.08$, $p = 0.011$. This reflects the fact that performance was somewhat worse at 6 kHz than at the two lower center frequencies, although this occurred only for the 0-ERB transition span. The main effect of the range of the random glides in level was also significant; $F(2,4) = 16.77$, $p = 0.011$, reflecting the fact that performance worsened as the range increased. The interaction of transition span and center frequency was significant; $F(2,4) = 40.22$, $p = 0.002$. This reflects the fact that, for the 0-ERB transition span, performance was worse at 6 kHz than at the two lower frequencies, whereas for the 2-ERB span it was not.

We will consider separately the results for the 0-ERB and 2-ERB standard transition spans. For the former, all thresholds are smaller than would be expected if subjects based their performance on monitoring the start or endpoint frequencies of the stimuli. Given that the center frequency was roved over a 4-ERB range, the lowest possible threshold that could be achieved in this way is 1.88 ERBs. Therefore, we can be confident that performance was based on the changes in the stimuli, rather than on their start or endpoint frequencies.

Consider now the effect of introducing the random glides in level. As described earlier, if performance were based on the detection of changes in excitation level on one side of the excitation pattern, the *extra* change in excitation level produced by the larger frequency glide in the signal interval would have to be at least 14.3 dB for the ±20 dB range of level glides and 28.7 dB for the ±40 dB range of level glides. Based on the excitation-pattern model of Glasberg and Moore (1990), these correspond to extra changes in frequency of 0.82 and 1.65 ERBs, respectively. For the ±20-dB range of level glides, the threshold is close to the theoretical limit at a center frequency of 0.5 kHz, but is slightly below that limit at 2 kHz. The threshold is above the theoretical limit at 6 kHz. For the ±40-dB range of level glides, the thresholds are clearly lower than the theoretical limit at 0.5 and 2 kHz. Thus in these two cases we can confidently conclude that performance was not based on monitoring changes in excitation level on one side of the excitation pattern. At 6 kHz, the threshold (1.42 ERBs) is still somewhat below the theoretical limit. Therefore, it appears that, for all three center frequencies, performance for the 0-ERB standard transition span was not based on monitoring changes in excitation level on one side of the excitation pattern, at least when large glides in level were present.

Consider now the results for the 2-ERB standard transition span. In the absence of glides in level, thresholds for all three center frequencies were smaller than would be expected if subjects based their performance on monitoring the start or endpoint frequencies of the stimuli. When glides in level were present, thresholds were close to the theoretical limit of 1.88 ERBs for the ±20-dB level glides, and generally above that limit for the ±40-dB level glides. Thus performance *could* have been based on monitoring the start and/or endpoint frequencies of the stimuli. However, the limit of 1.88 ERBs represents what could be achieved if resolution of the start or endpoint frequencies of the stimuli were perfect. In fact, such resolution would be far from per-

fect, especially when the level was roved over a large range (Henning, 1966; Emmerich *et al.*, 1989). Thus it seems very unlikely that performance was based on monitoring the start and/or endpoint frequencies of the stimuli, especially for the ±20-dB level glides.

Thresholds in the presence of the random glides in level were generally above the theoretical limits that would be expected if performance were based on the detection of changes in excitation level on one side of the excitation pattern. Thus for the 2-ERB standard transition span when random glides in level were present, the simple excitation-pattern model cannot be ruled out.

IV. GENERAL DISCUSSION

The results of experiment 1 showed that the detection and discrimination of frequency glides was not affected by the addition of random glides in level over the range ±10 to ±20 dB. The results of experiment 3 showed that, for a transition span of 0 ERBs, performance was better than would be expected if subjects made optimal use of the start or endpoint frequencies of the stimuli, and was also better than would be expected if subjects made optimal use of changes in excitation level on one side of the excitation pattern. It can be concluded that, at least for these conditions, subjects were discriminating the glides in frequency *per se*, but they were not doing this by monitoring changes in excitation level on just one side of the excitation pattern.

It is possible that performance depended somewhat on the use of temporal information (phase locking). If this were the case, we would expect thresholds in ERBs to increase markedly for the center frequency of 6 kHz, since phase locking is very weak or absent at that frequency (Johnson, 1980; Palmer, 1995). Thresholds in tasks thought to depend on phase locking, such as the frequency discrimination of pulsed tones, show a marked increase at high frequencies (Henning, 1966; Moore, 1973; Sek and Moore, 1995). Two of the subjects of experiment 3 had taken part in other experiments measuring frequency discrimination of pulsed tones. Their thresholds in ERBs were, on average, a factor of 4.5 larger at 6 kHz than at 2 kHz. The results of our experiments did generally show higher thresholds at 6 than at 2 kHz, but the difference was not very large. The largest difference was in experiment 3 for the 0-ERB standard transition span with random level glides in the range ±40 dB, where the threshold was a factor of 2.1 larger at 6 kHz than at 2 kHz. The corresponding factor with the smaller range of glides in level was 1.76. In experiment 1, the effect of center frequency was somewhat smaller, although mean thresholds were significantly lower at 2 kHz and at 0.5 kHz than at 6 kHz.

It is possible, then, that information derived from phase locking had some influence on the results for the two lower center frequencies. We described in the introduction the concept that the mechanism based on phase locking is sluggish and cannot track rapid changes in frequency. If phase locking information was being used in the glide-discrimination task, one would expect it to play a greater role for small standard transition spans than for large spans, since the rate of change of frequency is smaller for the former. The results of experiment 3 provide some support for this idea, especially when large random glides in level were present. Thresholds for the 0-ERB standard transition span increased markedly at 6 kHz, whereas thresholds for the 2-ERB standard span did not change markedly with frequency. The results of experiment 1 showed comparable effects of transition span; for the 0- and 0.5-ERB spans, thresholds tended to be lower at 2 kHz than at 6 kHz, whereas for the 2-ERB span, thresholds varied little with center frequency.

If performance was based mainly on place information, derived from the excitation pattern, then information from the two sides of the excitation pattern must have been compared; otherwise the random glides in level would have had larger effects. Such a comparison would allow changes in frequency to be dissociated from changes in level. For example, a frequency increase would lead to a decrease in excitation level on the low-frequency side of the pattern and an increase on the high-frequency side. An increase in level would lead to an increase in excitation level on both sides of the excitation pattern.

A model incorporating these concepts was proposed by Demany and Semal (1986), as an elaboration of a model of Hartmann and Klein (1980); these models were intended to account for the perception of AM and FM at low rates. Demany and Semal proposed that the peripheral excitation pattern was transformed by processes such as saturation and lateral inhibition into a central excitation pattern with sharp edges. This pattern was assumed to be defined by the tonotopic coordinates of its two edges, labeled as a and b. The separate perceptual attributes of pitch and loudness were extracted from the values of a and b; pitch was assumed to be related to the point midway between a and b, while loudness was assumed to be related to the distance between a and b. In principle, this model could account for our finding that moderate random glides in level had little or no effect on the ability to detect and discriminate glides in frequency.

It should be noted that changes in frequency cannot always be distinguished from changes in level. For example, Moore and Sek (1995) measured psychometric functions for the detection of AM or FM using carrier frequencies of 125, 1000, and 6000 Hz, and modulation rates of 2, 5, and 10 Hz. Then, pairs of values of AM and FM were selected that would be equally detectable, and psychometric functions were measured for the discrimination of AM from FM. For carrier frequencies of 125 and 1000 Hz, the ability to discriminate AM from FM was always poorest at the highest modulation rate (10 Hz); at this rate some subjects were essentially unable to discriminate AM from FM when the detectability of the modulation was relatively low (d' of 1.16 and below). For a modulation rate of 2 Hz, and when the detectability of the modulation was moderate (d' up to about 2), some subjects discriminated the type of modulation as well as they detected the modulation. For a carrier frequency of 6000 Hz, the effect of modulation rate varied across subjects, but there was still a trend for poorer discrimination of modulation type at the highest modulation rate.

In the present experiments, it appears that subjects were partly able to distinguish glides in frequency from glides in level, at least in some conditions, as moderate random glides

in level had little effect on the detection and discrimination of frequency glides. In this context it is noteworthy that, in experiment 1, the duration of the glides had little effect. Shorter durations were associated with greater rates of change of frequency. One might have expected, based on the effect of modulation rate described above, that introducing random glides in level would have a greater effect for the shorter duration. The results do not support this expectation (see Fig. 2).

In experiment 1, increasing the standard transition span from 0 ERBs to 2 ERBs resulted in an increase in threshold by an average factor of 1.9. In experiment 3, the average factor was 2.5. Madden and Fire (1996, 1997) found that thresholds were about a factor of 2 larger for a transition span of 2 ERBs than for a span of 0 ERBs. Tyler *et al.* (1983) also found larger thresholds for a gliding frequency standard than for a fixed standard. The increases in threshold with increasing transition span are consistent with the idea that, for transition spans above a certain value, Weber's law, or something close to it, may apply to glide discrimination (Dooley and Moore, 1988b). In other words, the threshold change in glide extent increases in proportion with the standard transition span. Data for larger transition spans are needed to establish how accurately this holds.

V. CONCLUSIONS

(1) Subjects could detect and discriminate glides in frequency when the start and endpoint frequencies of the stimuli were made unreliable cues, by roving of the center frequency. The results suggest that subjects were not using the start or endpoint frequencies when the rove range was 0.5 ERBs, even though these frequencies potentially provided useful cues. Subjects appear to be sensitive to the glide extent or glide rate.

(2) The addition of glides in level varying randomly in direction and extent impaired the detection and discrimination of frequency glides when the glides in level were very large. However, glides in level of moderate extent had little or no effect on performance. In some conditions, thresholds were lower than the best that could be achieved by monitoring changes in excitation level on one side of the excitation pattern.

(3) Thresholds did not differ significantly for upward and downward glides in frequency.

(4) As found by Madden and Fire (1997), thresholds did not change significantly with duration (50 or 400 ms).

(5) For small standard transition spans, thresholds expressed in ERBs tended to be slightly lower at 0.5 and 2 kHz than at 6 kHz, which may indicate a role for phase locking information at lower frequencies when the rate of change of frequency is small. For the 2-ERB standard transition span, thresholds did not vary markedly with center frequency (0.5, 2, or 6 kHz), which is broadly consistent with the idea that performance was based on some aspect of the excitation pattern.

(6) Thresholds increased when the standard transition span was increased from 0.5 to 2 ERBs.

ACKNOWLEDGMENTS

This work was supported by the Wellcome Trust and by the MRC. We thank Brian Glasberg for advice on statistics and Hedwig Gockel for mathematical tips. Tom Baer, Brian Glasberg, Hedwig Gockel, John Madden, and two anonymous reviewers provided helpful comments on an earlier version of this paper.

APPENDIX: CALCULATION OF THE DISRUPTION TO PERFORMANCE EXPECTED FROM AN EXCITATION PATTERN MODEL

This Appendix describes the disruption of performance that would be expected on the basis of an excitation-pattern model when large glides in level, as used in experiment 1, are superimposed on the glides in frequency. Assume that the task was performed by monitoring the low-frequency sides of the excitation patterns evoked by the stimuli. Consider the task of detecting or discriminating an upward glide in frequency. An appropriate decision rule is: select the interval giving the larger decrease in excitation level. The question addressed next is: how well could subjects perform using such a rule when random glides in level were superimposed on all stimuli? The analysis given below assumes perfect resolution of changes in excitation level. In other words, the analysis is intended to determine the best performance that could be obtained if there were no internal source of variability.

The larger frequency transition in the signal interval leads, on average, to a larger decrease in excitation level in the signal interval. We denote this *extra* decrease in excitation level by X. We assume that the changes in excitation level produced by the glides in level are large compared with X; this assumption turns out to be reasonable. Four cases can be considered, each of which has a probability of occurrence of 0.25.

Case 1: The glide in level is upward in the signal interval and downward in the standard interval. In this case the subject is always wrong.

Case 2: The glide in level is downward in the signal interval and upward in the standard interval. In this case the subject is always correct.

Case 3: The glide in level is upward in both intervals. In this case, the probability of being correct depends on the value of X and on the range, R, over which the glide in level was randomly varied. In our experiment, R was always 10 dB; the range was either 10–20 dB or 30–40 dB. Following arguments given by Green (1988, pp. 19–20), the probability, P, of being correct is

$$P = X/R + 0.5 - 0.5(X/R)^2.$$

Case 4: The glide in level is downward in both intervals. This is similar to case 3, and the probability of being correct is the same.

Since each of the four cases has a probability of occurrence of 0.25, the overall probability of being correct is:

$$P = 0.25\{0 + 1 + X/R + 0.5 - 0.5(X/R)^2 + X/R + 0.5 - 0.5(X/R)^2\}$$
$$= 0.5 + 0.5X/R - 0.25(X/R)^2.$$

Given that our adaptive procedure tracked the 70.7% correct point on the psychometric function (i.e., $P = 0.707$), and that $R = 10$ dB, it can readily be shown that $X = 5.9$ dB. In summary, the *extra* decrease in excitation level produced by the larger frequency glide in the signal interval would have to be at least 5.9 dB to achieve 70.7% correct for the two conditions in which random glides in level were present.

We now have to consider what value of ΔF would be needed to produce such a change. To estimate this, we used the method for calculating excitation patterns described by Glasberg and Moore (1990). To produce a change of 5.9 dB on the low-frequency side of the excitation patterns calculated in this way requires a value of ΔF of about 0.34 ERBs.

Demany, L., and Semal, C. (**1986**). ''On the detection of amplitude modulation and frequency modulation at low modulation frequencies,'' Acustica **61**, 243–255.

Dooley, G. J., and Moore, B. C. J. (**1988a**). ''Detection of linear frequency glides as a function of frequency and duration,'' J. Acoust. Soc. Am. **84**, 2045–2057.

Dooley, G. J., and Moore, B. C. J. (**1988b**). ''Duration discrimination of steady and gliding tones: a new method for estimating sensitivity to rate of change,'' J. Acoust. Soc. Am. **84**, 1332–1337.

Emmerich, D. S., Ellermeier, W., and Butensky, B. (**1989**). ''A reexamination of the frequency discrimination of random-amplitude tones, and a test of Henning's modified energy-detector model,'' J. Acoust. Soc. Am. **85**, 1653–1659.

Freyman, R. L., and Nelson, D. A. (**1986**). ''Frequency discrimination as a function of tonal duration and excitation-pattern slopes in normal and hearing-impaired listeners,'' J. Acoust. Soc. Am. **79**, 1034–1044.

Glasberg, B. R., and Moore, B. C. J. (**1990**). ''Derivation of auditory filter shapes from notched-noise data,'' Hearing Res. **47**, 103–138.

Goldstein, J. L., and Srulovicz, P. (**1977**). ''Auditory-nerve spike intervals as an adequate basis for aural frequency measurement,'' in *Psychophysics and Physiology of Hearing*, edited by E. F. Evans and J. P. Wilson (Academic, London).

Grant, K. W. (**1987**). ''Frequency modulation detection by normally hearing and profoundly hearing-impaired listeners,'' J. Speech Hear. Res. **30**, 558–563.

Grantham, D. W., and Wightman, F. L. (**1978**). ''Detectability of varying interaural temporal differences,'' J. Acoust. Soc. Am. **63**, 511–523.

Grantham, D. W., and Wightman, F. L. (**1979**). ''Detectability of a pulsed tone in the presence of a masker with time-varying interaural correlation,'' J. Acoust. Soc. Am. **65**, 1509–1517.

Green, D. M. (**1988**). *Profile Analysis* (Oxford U.P., Oxford).

Hartmann, W. M., and Klein, M. A. (**1980**). ''Theory of modulation detection for low modulation frequencies,'' J. Acoust. Soc. Am. **67**, 935–946.

Henning, G. B. (**1966**). ''Frequency discrimination of random amplitude tones,'' J. Acoust. Soc. Am. **39**, 336–339.

Jesteadt, W., and Sims, S. L. (**1975**). ''Decision processes in frequency discrimination,'' J. Acoust. Soc. Am. **57**, 1161–1168.

Johnson, D. H. (**1980**). ''The relationship between spike rate and synchrony in responses of auditory-nerve fibers to single tones,'' J. Acoust. Soc. Am. **68**, 1115–1122.

Madden, J. P., and Fire, K. M. (**1996**). ''Detection and discrimination of gliding tones as a function of frequency transition and center frequency,'' J. Acoust. Soc. Am. **100**, 3754–3760.

Madden, J. P., and Fire, K. M. (**1997**). ''Detection and discrimination of frequency glides as a function of direction, duration, frequency span and center frequency,'' J. Acoust. Soc. Am. **102**, 2920–2924.

Moore, B. C. J. (**1973**). ''Frequency difference limens for short-duration tones,'' J. Acoust. Soc. Am. **54**, 610–619.

Moore, B. C. J. (**1974**). ''Relation between the critical bandwidth and the frequency-difference limen,'' J. Acoust. Soc. Am. **55**, 359.

Moore, B. C. J., and Glasberg, B. R. (**1986**). ''The role of frequency selectivity in the perception of loudness, pitch and time,'' in *Frequency Selectivity in Hearing*, edited by B. C. J. Moore (Academic, London).

Moore, B. C. J., and Glasberg, B. R. (**1987**). ''Formulae describing frequency selectivity as a function of frequency and level and their use in calculating excitation patterns,'' Hearing Res. **28**, 209–225.

Moore, B. C. J., and Glasberg, B. R. (**1989**). ''Mechanisms underlying the frequency discrimination of pulsed tones and the detection of frequency modulation,'' J. Acoust. Soc. Am. **86**, 1722–1732.

Moore, B. C. J., and Sek, A. (**1992**). ''Detection of combined frequency and amplitude modulation,'' J. Acoust. Soc. Am. **92**, 3119–3131.

Moore, B. C. J., and Sek, A. (**1994**). ''Effects of carrier frequency and background noise on the detection of mixed modulation,'' J. Acoust. Soc. Am. **96**, 741–751.

Moore, B. C. J., and Sek, A. (**1995**). ''Effects of carrier frequency, modulation rate and modulation waveform on the detection of modulation and the discrimination of modulation type (AM vs FM),'' J. Acoust. Soc. Am. **97**, 2468–2478.

Moore, B. C. J., and Sek, A. (**1996a**). ''The detection of frequency modulation,'' in *Recent Trends in Hearing Research*, edited by H. Fastl, S. Kuwano, and A. Schick (Oldenburg University, Oldenburg).

Moore, B. C. J., and Sek, A. (**1996b**). ''Detection of frequency modulation at low modulation rates: Evidence for a mechanism based on phase locking,'' J. Acoust. Soc. Am. **100**, 2320–2331.

Palmer, A. R. (**1995**). ''Neural signal processing,'' in *Hearing*, edited by B. C. J. Moore (Academic, San Diego).

Sek, A., and Moore, B. C. J. (**1995**). ''Frequency discrimination as a function of frequency, measured in several ways,'' J. Acoust. Soc. Am. **97**, 2479–2486.

Siebert, W. M. (**1970**). ''Frequency discrimination in the auditory system: Place or periodicity mechanisms,'' Proc. IEEE **58**, 723–730.

Tyler, R. S., Wood, E. J., and Fernandes, M. A. (**1983**). ''Frequency resolution and discrimination of constant and dynamic tones in normal and hearing-impaired listeners,'' J. Acoust. Soc. Am. **74**, 1190–1199.

Zwicker, E. (**1956**). ''Die elementaren Grundlagen zur Bestimmung der Informationskapazität des Gehörs,'' Acustica **6**, 356–381.

Zwicker, E. (**1970**). ''Masking and psychological excitation as consequences of the ear's frequency analysis,'' in *Frequency Analysis and Periodicity Detection in Hearing*, edited by R. Plomp and G. F. Smoorenburg (Sijthoff, Leiden).

Zwicker, E., and Fastl, H. (**1990**). *Psychoacoustics—Facts and Models* (Springer-Verlag, Berlin).

Release from masking due to spatial separation of sources in the identification of nonspeech auditory patterns

Gerald Kidd, Jr., Christine R. Mason, Tanya L. Rohtla, and Phalguni S. Deliwala
Department of Communication Disorders, Boston University, 635 Commonwealth Avenue, Boston, Massachusetts 02215

(Received 8 April 1997; revised 23 December 1997; accepted 2 March 1998)

A nonspeech pattern identification task was used to study the role of spatial separation of sources on auditory masking in multisource listening environments. The six frequency patterns forming the signal set were comprised of sequences of eight 60-ms tone bursts. Bursts of masking sounds were played synchronously with the signals. The main variables in the study were (1) the difference in spatial separation in the horizontal plane between signals and maskers and (2) the nature of the masking produced by the maskers. Spatial separation of signal and masker ranged from 0–180 degrees. The maskers were of two types: (1) a sequence of eight 60-ms bursts of Gaussian noise intended to produce predominantly peripherally based ''energetic masking'' and (2) a sequence of eight 60-ms bursts of eight-tone complexes intended to produce primarily centrally based ''informational masking.'' The results indicated that identification performance improved with increasing separation of signal and masker. The amount of improvement depended upon the type of masker and the center frequency of the signal patterns. Much larger improvements were found for spatial separation of the signal and informational masker than for the signal and energetic masker. This was particularly apparent when the acoustical advantage of the signal-to-noise ratio in the more favorable of the two ears (the ear nearest the signal) was taken into account. The results were interpreted as evidence for an important role of binaural hearing in reducing sound source or message uncertainty and may contribute toward solving the ''cocktail party problem.'' © *1998 Acoustical Society of America.* [S0001-4966(98)03506-1]

PACS numbers: 43.66.Pn, 43.66.Dc, 43.66.Ba [RHD]

INTRODUCTION

In noisy environments binaural cues are thought to provide a significant advantage when the task of the listener is to attend to a particular sound source in the presence of competing sources. When the signal is separated spatially from the masker(s), interaural differences in time of arrival and intensity of the waveforms can provide cues that improve detection or recognition performance relative to the circumstance in which the sounds come from the same direction or when only monaural listening is available (e.g., Hirsh, 1950; Plomp, 1976; Saberi *et al.*, 1991; Gilkey, 1995). One well-known acoustical factor in such conditions is the ''head shadow effect.'' If the masker and signal originate from the same location, the signal-to-noise ratio is roughly the same in both ears. However, if the signal and masker are spatially separated, the signal-to-noise ratio will be better in the ear nearer the signal source, particularly in the higher frequencies (e.g., Shaw, 1974). The head shadow effect can provide a substantial improvement in performance in detection or recognition tasks. A second factor is ''binaural interaction''—as often inferred from studies of the ''masking-level-difference'' or ''intelligibility-level-difference''—in which the inputs from the two ears are processed in the central nervous system to improve the effective signal-to-noise ratio of the neural representation reaching the brain. Although masking- and intelligibility-level-differences may be 10–15 dB or more in optimal conditions, studies of binaural analysis applied to free-field listening consistently find relatively small effects (2–5 dB for speech) after accounting for the head shadow effect (e.g., Zurek, 1993; Plomp and Mimpen, 1981; Bronkhorst and Plomp, 1989). This suggests that binaural interaction is relatively unimportant in real-world sound reception. Thus, it is possible to argue that the large subjective advantage of binaural hearing often reported in noisy, multisource environments–sometimes called the ''cocktail party effect'' (cf. Cherry, 1953; Pollack and Pickett, 1958; Yost, 1991)—in reality is due primarily to head shadow or to nonauditory factors and that binaural mechanisms *per se* contribute relatively little [Zurek (1993), p. 274, argues that both psychoacoustic and acoustic factors contribute about equally to an average binaural advantage of about 5 dB for typical listening conditions; see also the recent review by Yost (1997)].

An implicit point in studying the processing of sounds in multisource environments is that the sounds interfere with one another. The performance on detection, discrimination, or identification tasks for a signal occurring in isolation is usually better than when it occurs in the presence of competing sounds. One sound may mask another sound because it dominates the neural representation of the stimulus in the auditory periphery. This process has been termed ''energetic'' or peripheral masking and has been studied extensively. In particular, many studies of binaural processing of sounds in multisource environments have used maskers such as Gaussian noise that produce masking that is thought to be primarily peripheral in origin. Likewise, models of binaural interaction usually assume that central processing of the inputs from the two ears improves the effective signal-to-noise

ratio of signals that are masked in the auditory periphery (cf. Colburn, 1995; Colburn and Durlach, 1978)—in essence, by reducing energetic masking.

During the past 20 years, many studies have demonstrated large masking effects that do not appear to be due to peripherally based energetic masking. Interference in detection, discrimination, or identification tasks can be produced when the signal is embedded in a sequence of masker tones (e.g., Watson *et al.*, 1975, 1976; Leek and Watson, 1984) or is played simultaneously with the masker (e.g., Kidd *et al.*, 1986; Neff and Green, 1987; Kidd *et al.*, 1994) under conditions of high uncertainty. The effects on performance may be quite large, exceeding a 40-dB threshold shift in some conditions for detection tasks and an order of magnitude in the size of the difference limen for discrimination tasks. These studies of ''informational masking'' (cf. Watson, 1987) are characterized by large intersubject differences (e.g., Neff and Dethlefs, 1995) and subject performance can vary considerably with training (e.g., Leek, 1987).

Studies of the effects of spatial separation of sources on sound identification in multisource environments have used maskers that were broadband Gaussian noise, Gaussian noise that was filtered or shaped in a particular way (e.g., ''speech-shaped noise''), or actual speech from one or more talkers (cf. Yost *et al.*, 1996). The procedures employed were not intended specifically to produce a high degree of stimulus uncertainty. We would argue that in these studies the masking that occurred was either predominantly peripherally based energetic masking, or was a combination of energetic and informational masking in proportions that cannot be ascertained. The latter is the case for most speech-masking conditions in which the signal and masker have similar bandwidths (and often similar long-term averaged spectra) but vary from moment to moment in the degree to which they overlap in the frequency domain. The only attempt we are aware of to quantify the relative amounts of energetic and informational masking was for the tone-in-noise detection task (Lutfi, 1990).

In the present study, we examined the hypothesis that the large binaural advantage commonly thought to occur in noisy listening environments is due in part to a reduction in informational masking. This could be the case if the perception that a desired sound source is spatially distinct from competing sources reduces uncertainty along one or more stimulus dimensions. In order to test this hypothesis, we constructed maskers designed to produce large amounts of informational masking with little concomitant energetic masking in a nonspeech pattern identification task (Kidd *et al.*, 1995b). The main experimental variables were the degree of spatial separation in the horizontal plane of signal and masker and whether the masker was the type causing peripherally based energetic masking or centrally based informational masking. Based on previous work, our expectation was that the advantage in identification performance due to spatial separation of sound sources would result primarily from the head shadow effect for the Gaussian noise masker. However, there might be an additional advantage for the informational masker if spatial separation of sources reduces listener uncertainty.

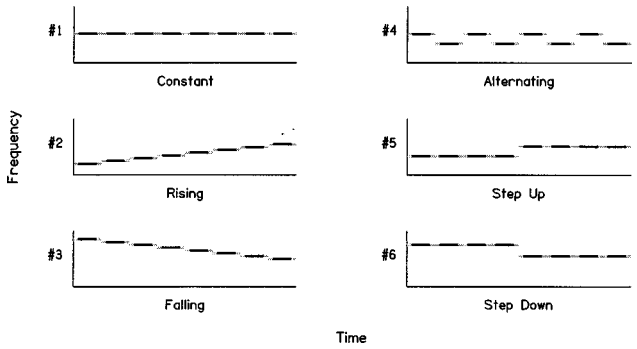

FIG. 1. Schematic of the six signal patterns in sound spectrogram form.

I. METHODS

A. Subjects

Three listeners with prior experience in psychoacoustic experiments, including author TR, served as subjects. Their ages ranged from 24–29 years. All three listeners had normal hearing as determined from audiometric assessment.

B. Stimuli

The stimuli were generated digitally and played through 16-bit digital-to-analog converters (Tucker-Davis Technology) at a rate of 50 000 samples per second, then low-pass filtered at 20 000 Hz. The signals were sequences of tones arranged in six frequency patterns. The signal-tone sequences were comprised of eight 60-ms bursts, including 10-ms cosine-squared rise/decay times with no delay between bursts, resulting in a total pattern length of 480 ms. The six frequency patterns were: (1) constant; (2) rising; (3) falling; (4) alternating; (5) one-step up; and (6) one-step down and are illustrated schematically in Fig. 1.

The signal patterns (and informational maskers, as described below) were generated from 16 eight-frequency bands spaced equally on a logarithmic scale. The center frequencies of the bands ranged from 215–6112 Hz. The width of the frequency bands was 14% of the center frequency. On each trial 1 of the 16 possible bands was selected at random to contain a signal pattern. The pattern—one of the six shown in Fig. 1—was then generated from the eight frequencies available within that band. Signal level was equal for tones in a pattern. The overall level was selected randomly on each trial among a set of levels chosen to generate identification-level functions.

The maskers were sequences of eight 60-ms bursts played synchronously with the signal bursts. There were two types of maskers: independent samples of Gaussian noise bandpass filtered from 200–6500 Hz at a spectrum level of 32 dB and multitone complexes generated to have features similar to the signal patterns in that they were comprised of sets of narrow-band tone sequences. We chose this multitone masker because earlier work from our laboratory (Kidd and Mason, 1997) indicated that it produced large amounts of informational masking for identification, significantly greater masking, in fact, than that produced by the ''multiple-bursts different'' masker used in the earlier pattern-identification experiment (Kidd *et al.*, 1995b). We have designated this

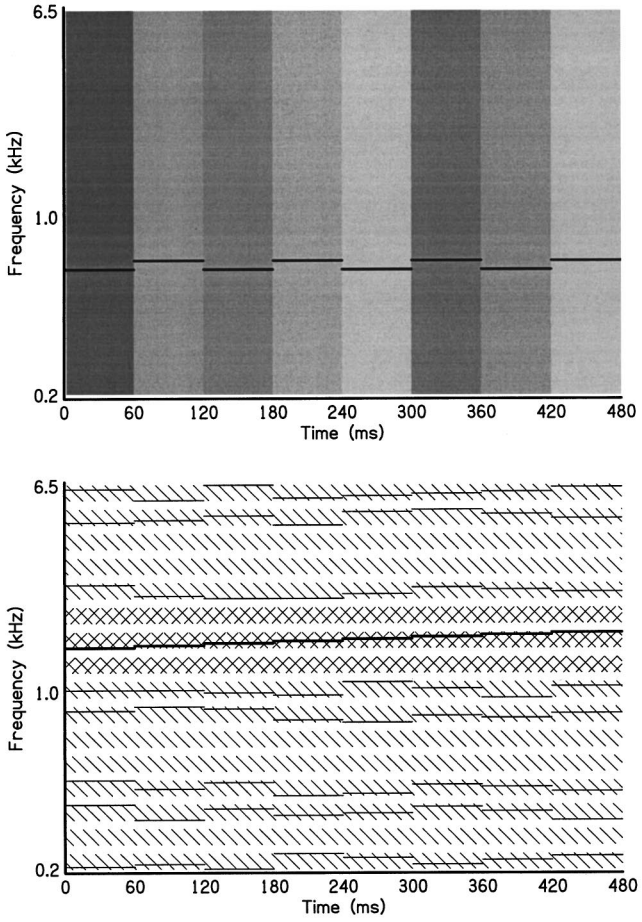

FIG. 2. Schematic of the two multiburst maskers. The top panel shows a sequence of Gaussian-noise masker bursts (BBN). The shading indicates the different bursts. A signal pattern (#4) is shown embedded in the noise. The lower panel shows a sequence of bursts of the MBDN multitone masker. The 16 eight-frequency bands are represented by the diagonal hatching. The medium solid lines represent masker tones. The heavy lines in the cross-hatched band are a signal pattern (#2). The adjacent cross-hatched bands are a ''protected region'' that cannot contain maskers.

masker ''multiple-bursts different-narrow-band'' (MBDN). The MBDN masker was constructed from the same set of 16 bands as the signals. On each trial, the band containing the signal and the two adjacent bands were excluded from selection as masker bands. Eight of the 13 remaining bands were randomly chosen to contain masker tones. For that burst sequence, all of the masker tones fell within the selected bands. Within each masker band, the frequency was a random sample on each burst from among the eight possible frequencies. This resulted in a masker comprised of eight narrow-band tone sequences. The level of the tones in a given masker band was constant and chosen at random from a uniform range from 50–70 dB SPL. These two maskers—Gaussian noise (referred to as ''BBN'') and MBDN—are illustrated schematically in Fig. 2 in spectrogram form.

C. Procedures

The stimuli were presented through seven loudspeakers located 5 ft from the listener roughly at head height (when seated) and separated by 30 degrees azimuth extending from directly in front of the listener (0 degrees) to the listener's right (+90 degrees) and left (−90 degrees). The listeners were asked to maintain a head position directly facing 0 degrees but were not constrained otherwise. The impulse responses of the individual speakers were measured and digital corrections applied to the stimuli to obtain flat frequency responses. The listening environment was quiet but not anechoic (e.g., the floor was carpeted and the subject was surrounded by cloth panel dividers and foam-covered walls; the measured reverberation time was roughly $\frac{1}{4}$ s).

In the identification task, a one-interval six-alternative forced-choice (1I-6AFC) procedure was used in which the six stimulus alternatives were the six patterns. Thus, chance performance was about 16.7%. The signals were chosen randomly, with replacement, on each trial throughout a block of trials. Signal level was mixed throughout each trial block, which consisted of 50–80 trials depending on the number of levels that were tested in that condition. Response feedback was given following each trial. An illustration similar to Fig. 1 identifying the stimulus set was positioned above the response keys. The locations of the signal and, when present, the masker were chosen pseudorandomly on every presentation from among the seven speakers. The pseudorandom selection procedure chose signal and masker locations according to equal probability of occurrence for angular separation (i.e., a separation of 180 degrees was as likely as that of 30 degrees, although there were only 2 possibilities for signal and masker for 180 degrees and there were 14 for 30 degrees). The locations of the masker and signal were cued by a visual map on the computer screen prior to each trial.

The listeners were highly practiced (a minimum of several hundred trials per condition) prior to collection of the data presented here. There were three experimental conditions: identification in ''quiet'' (no added masker) measured for each speaker location, and the two masked conditions—BBN and MBDN—in which signal and masker location/spatial separation was varied. The data plotted represent roughly 100 trials per point for the identification-level functions for each condition.

II. RESULTS

In order to evaluate the effects of signal frequency, the 16 frequency bands from which the signals were drawn were divided into four groups or ''bins'' of four bands each. For *post hoc* analysis, the data were pooled within each bin. To compare performance across different conditions, the decibel values corresponding to the 60% correct point on the identification-level functions were estimated. We chose that point because it is roughly the middle of the range between chance and perfect performance and because it allows more direct comparison with the results of our previous binaural identification work (cf. Kidd *et al.*, 1995b). The estimates were obtained by fitting straight lines to the rising portions of the middle of the functions.

A. Performance in quiet

In the quiet condition, no systematic effect of speaker location was observed, so the results were averaged across locations. The sound pressure levels corresponding to the

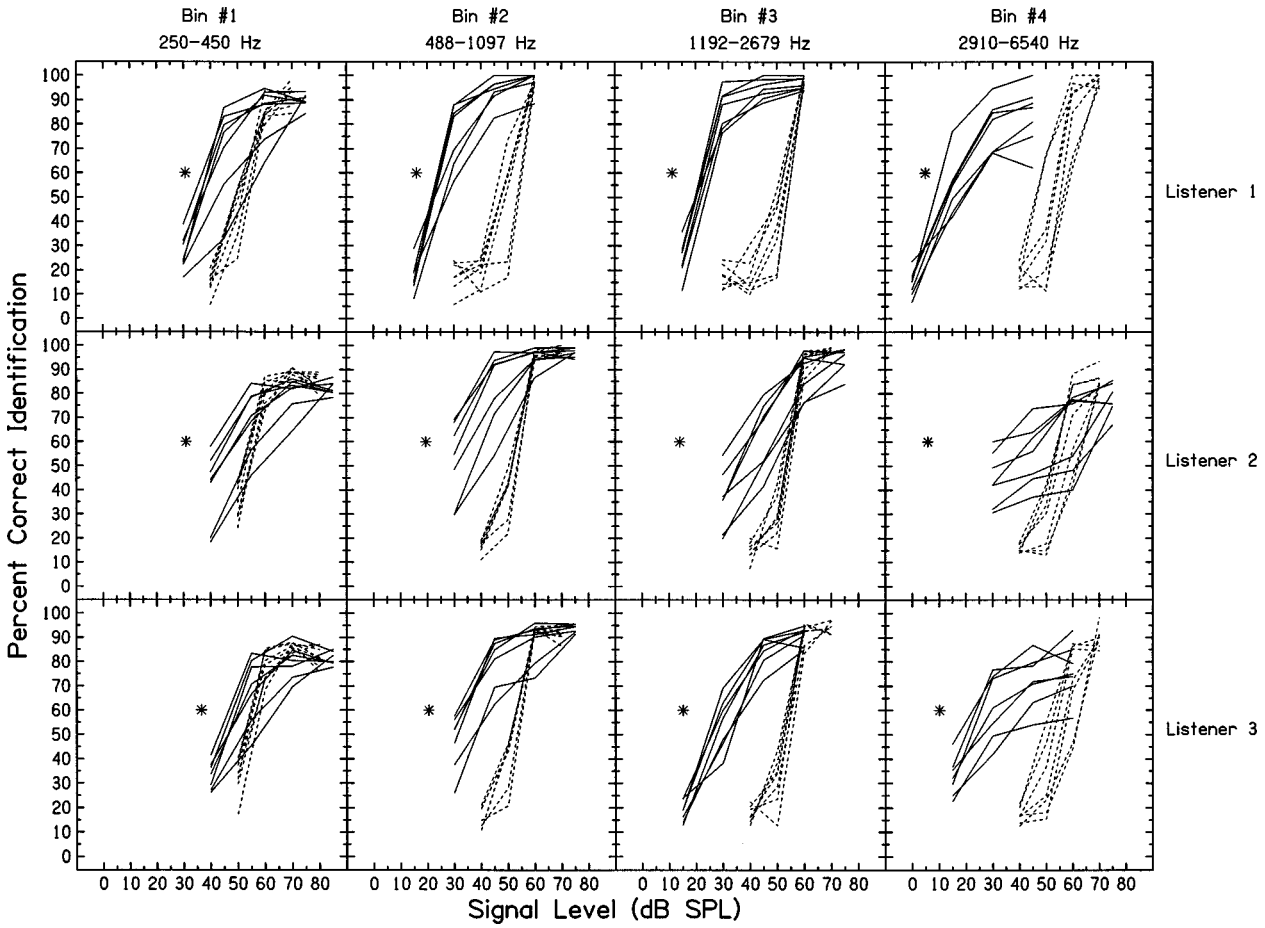

FIG. 3. Identification-level functions for the three listeners. The dashed lines show the data obtained with the BBN masker and the solid lines show the data obtained with the MBDN masker. The four bins are data pooled from different signal frequencies ranging from the lower four bands (bin 1) to the higher four bands (bin 4). The asterisk shows the level corresponding to 60% correct performance in quiet.

60% correct points on the identification-level functions, and the slopes of the fitted functions, were computed. The 60% correct points of the functions vary with frequency as would be expected from the form of the audibility curve measured in the sound field (e.g., Robinson and Dadson, 1956). For the lowest frequency region, the 60% correct points of the identification-level functions are about 31–36 dB SPL and decline to about 6–10 dB SPL in the highest frequency region. On average, the slopes of the fitted functions range from about 3%/dB in the lowest frequency bin to about 5%/dB in the highest frequency bin. Subjects achieved near-100%-correct performance in this task in quiet at moderate levels.

B. Performance in BBN and MBDN maskers

The results from the masked conditions also take the form of identification-level functions. The slopes and orderliness of the functions vary markedly according to the type of masker. This point is illustrated in Fig. 3. The parameter plotted in the figure is degree of spatial separation between masker and signal. Because of the number of functions displayed in each panel, we did not attempt to identify the angular separations. In general, though, the functions are ordered from left to right according to decreasing angular separation. A detailed analysis of the functions is given below.

Both maskers shifted the identification-level functions to the right along the level axis relative to the quiet condition (the midpoint of the function in quiet is shown by the asterisk at the left of each panel). However, the slopes of the identification-level functions were shallower—often much shallower—for the MBDN masker (solid lines) than for the BBN masker (dashed lines). This finding is consistent with that reported in the earlier study by Kidd *et al.* (1995b) although it is even more striking here, possibly because of the greater uncertainty in this task due to randomization in frequency of both the signal and the masker. In some cases, particularly for the highest frequency bin, performance appeared to reach an asymptote at percent correct values well below 100%. In the plots that follow the comparisons of performance are based on the decibel values corresponding to the 60% correct points. Because the slopes of the functions are so different for the two masker types the magnitude of the improvement may vary considerably depending on the level of performance at which a comparison is made. In some cases such comparisons are not even possible (e.g., high percent correct values were not obtained in the MBDN masker even at the highest signal level). There were a few

TABLE I. Sound pressure levels corresponding to 60% correct from the straight-line fits used to summarize the data (see text) for the BBN and MBDN conditions. The slopes of the fitted functions are also given in %/dB SPL. The values are for angular separations of signal and masker in the azimuthal plane. The 16 signal frequency bands were pooled to form four bins ranging from low (bin 1) to high (bin 4) frequencies (see text).

		BBN								MBDN							
Bin	Deg	Listener 1		Listener 2		Listener 3		Average (s.e.)		Listener 1		Listener 2		Listener 3		Average (s.e.)	
No.	sep.	60% Pt	Slope	60% Pt	Slope	60% Pt	Slope	60% Pt	Slope	60% Pt	Slope	60% Pt	Slope	60% Pt	Slope	60% Pt	Slope
	0	56.1	5.85	56.4	5.53	58.4	5.11	57.0(0.71)	5.50(0.22)	58.9	1.58	67.3	1.43	63.9	1.45	63.4(2.42)	1.49(0.05)
	30	55.1	5.03	57.1	4.37	56.9	4.38	56.4(0.64)	4.59(0.22)	50.6	1.72	60.0	1.86	60.0	1.54	56.9(3.15)	1.71(0.09)
	60	52.9	3.14	56.6	4.62	55.5	4.15	55.0(1.09)	3.97(0.44)	42.4	2.02	51.3	0.90	50.7	2.47	48.1(2.86)	1.80(0.47)
1	90	52.5	3.47	55.1	4.99	55.3	5.37	54.3(0.87)	4.61(0.58)	40.3	3.49	50.7	1.35	53.1	1.57	48.0(3.95)	2.14(0.68)
	120	53.5	3.30	54.3	3.71	54.9	4.00	54.2(0.41)	3.67(0.20)	37.2	2.95	44.2	1.13	46.7	2.80	42.7(2.84)	2.29(0.58)
	150	52.6	4.05	53.9	4.47	56.7	3.88	54.4(1.20)	4.13(0.17)	39.0	3.28	46.0	2.11	49.5	3.23	44.8(3.09)	2.87(0.38)
	180	52.4	3.39	54.3	4.51	54.6	4.58	53.8(0.71)	4.16(0.39)	38.7	4.24	41.2	1.75	48.0	2.94	42.6(2.80)	2.97(0.72)
	0	55.4	7.94	55.1	7.53	55.4	7.22	55.3(0.12)	7.56(0.21)	33.4	2.11	46.6	1.90	48.7	1.33	42.9(4.78)	1.78(0.23)
	30	54.9	7.50	54.9	6.57	54.9	6.54	54.9(0.02)	6.87(0.32)	31.8	2.84	42.6	2.14	45.9	1.21	40.1(4.27)	2.06(0.47)
	60	51.2	4.34	53.4	5.43	53.4	4.82	52.6(0.74)	4.86(0.32)	28.5	2.09	36.1	1.52	34.7	2.88	33.1(2.36)	2.16(0.39)
2	90	49.8	3.81	52.4	4.53	53.0	4.96	51.8(0.99)	4.43(0.33)	24.3	4.86	32.1	2.47	32.8	1.45	29.8(2.74)	2.93(1.01)
	120	48.6	3.64	53.3	5.20	53.4	5.05	51.8(1.58)	4.63(0.50)	24.9	4.50	28.8	2.08	31.2	2.10	28.3(1.84)	2.89(0.80)
	150	50.1	4.07	53.3	5.61	53.0	4.59	52.1(1.01)	4.76(0.45)	23.9	4.61	23.9	1.53	31.1	1.14	26.3(2.38)	2.42(1.10)
	180	50.2	3.80	53.2	5.58	53.0	4.66	52.1(0.96)	4.68(0.51)	24.8	4.74	25.9	1.96	33.4	2.36	28.0(2.68)	3.02(0.87)
	0	55.3	7.87	56.3	7.03	56.7	7.08	56.1(0.41)	7.33(0.27)	26.2	4.33	52.4	1.84	37.8	1.94	38.8(7.57)	2.70(0.81)
	30	55.3	8.11	55.4	7.04	55.0	7.22	55.2(0.10)	7.46(0.33)	24.9	3.96	52.6	1.61	35.7	2.15	37.7(8.07)	2.57(0.71)
	60	54.3	6.46	55.3	6.39	54.4	5.86	54.7(0.31)	6.24(0.19)	23.6	2.83	47.2	1.39	34.3	2.19	35.0(6.81)	2.14(0.42)
3	90	52.8	4.07	54.7	6.83	55.4	5.80	54.3(0.78)	5.57(0.81)	23.6	4.41	40.7	1.98	32.0	2.03	32.1(4.91)	2.81(0.80)
	120	50.8	4.14	53.2	5.41	54.4	5.80	52.8(1.06)	5.11(0.50)	22.7	4.29	32.8	1.27	33.1	2.46	29.6(3.43)	2.67(0.88)
	150	50.3	3.49	53.7	6.05	53.8	5.64	52.6(1.17)	5.06(0.80)	22.5	4.22	38.5	1.71	30.4	2.34	30.5(4.63)	2.76(0.75)
	180	51.0	3.86	54.7	6.61	53.3	5.09	53.0(1.07)	5.19(0.80)	22.0	4.68	41.4	1.96	31.2	2.34	31.5(5.60)	3.00(0.85)
	0	59.9	3.80	63.7	3.47	61.6	4.00	61.7(1.12)	3.76(0.16)	24.0	2.06	68.5	0.90	57.5	0.71	50.0(13.4)	1.22(0.42)
	30	60.5	4.25	63.7	3.48	61.8	3.40	62.0(0.93)	3.71(0.27)	25.4	1.49	69.2	0.72	47.1	1.04	47.2(12.6)	1.08(0.22)
	60	58.9	4.37	62.3	3.28	58.4	5.29	59.9(1.21)	4.31(0.60)	24.8	1.95	57.6	0.82	34.9	1.21	39.1(9.68)	1.33(0.33)
4	90	53.4	3.90	58.9	2.39	57.4	4.75	56.6(1.64)	3.68(0.69)	18.3	2.27	44.7	1.16	37.8	0.92	33.6(7.90)	1.45(0.41)
	120	52.3	3.81	54.1	3.48	54.0	3.43	53.5(0.58)	3.57(0.12)	19.5	2.33	29.5	0.40	29.5	1.66	26.2(3.35)	1.47(0.56)
	150	50.3	3.79	53.7	3.28	52.5	3.29	52.1(0.99)	3.45(0.17)	17.9	2.28	44.3	0.85	27.7	1.13	29.9(7.72)	1.42(0.44)
	180	49.1	3.81	53.9	3.62	51.8	3.31	51.6(1.40)	3.58(0.15)	14.1	2.65	32.1	0.62	23.4	1.35	23.3(5.19)	1.54(0.59)

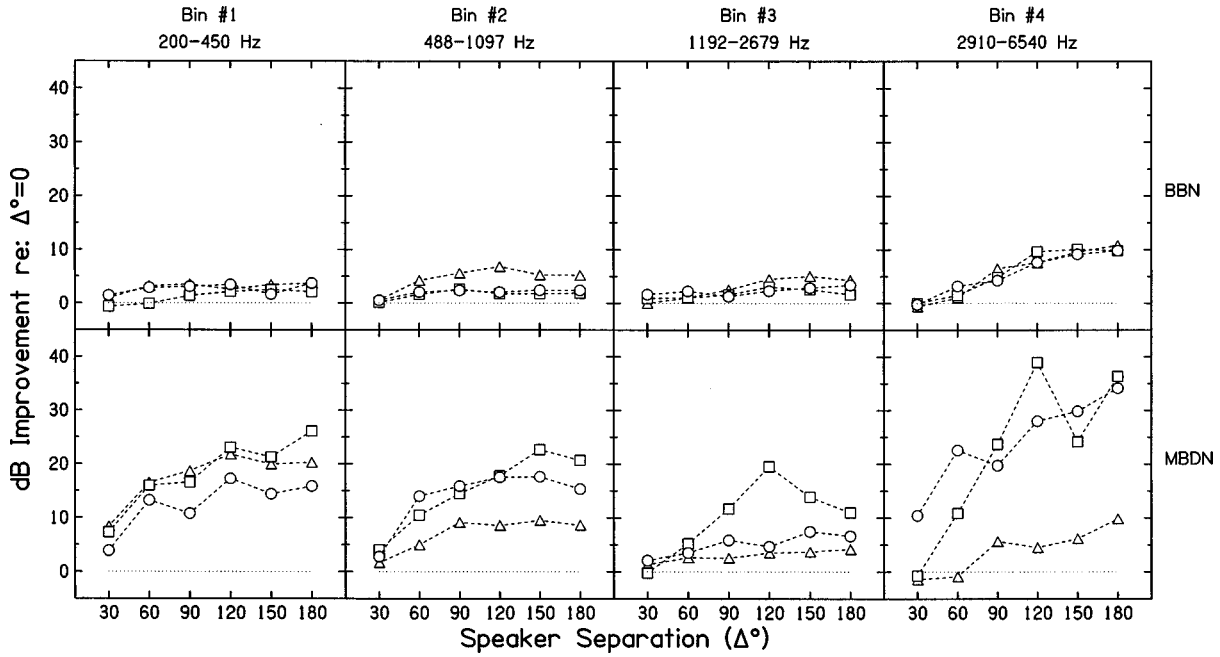

FIG. 4. Improvements in performance at the 60% correct points on the identification-level functions as the spatial separation of signal and masker was varied. The reference is the condition where signal and masker originated from the same location. The upper panel shows the results for the BBN masker and the lower panel shows the results for the MBDN masker. The data from subject 1 are plotted as triangles, from subject 2 as squares and from subject 3 as circles.

instances where we encountered difficulties in deciding which points to include in the straight-line fits. However, the various rules that were tried for including points yielded only slight differences in midpoints that did not affect the conclusions drawn from the data.

The sound pressure levels corresponding to the 60% points from the fitted functions and the slopes of the functions are contained in Table I. For the BBN masker, the 60% points of the functions fell within a 12-dB range for all listeners and conditions. The 180-degree separation produced the lowest levels, which were about the same for all four frequency bins, and the highest levels were obtained for the smaller separations for the highest frequency bin. The slopes of the functions were steepest for the middle two bins and the smaller spatial separations with identification performance increasing about 6%–7%/dB, and were shallowest for most separations of the high-frequency bin with performance increasing about 3%–5%/dB.

For the MBDN masker, there was a much greater range of 60% points—about 40 dB—and generally shallower slopes. Averaged across the three listeners, the highest midpoint was about 64 dB SPL for the lowest frequency bin and 0-degree separation while the lowest midpoint was about 24 dB SPL for the highest frequency bin and 180-degree separation. On average, the slopes of the functions ranged from about 0.78% to 2.66%/dB. Although these three listeners' were quite similar for quiet and BBN conditions, large individual differences were apparent for the MBDN condition.

The improvement in performance measured at the 60% correct point on the identification-level functions is plotted in Fig. 4 as a function of the angular separation between signal and masker. The reference condition is 0-degree separation. For the BBN masker the results were quite consistent across listeners. Small improvements were observed with increasing signal-masker spatial separation through the lower three signal bins. On average, the largest improvement across the three listeners was less than 5 dB in all cases. For the highest frequency bin, more of an effect was observed with improvement increasing steadily with separation up to about 10 dB.

For the MBDN masker, much larger improvements were found in general and there were greater differences in performance between listeners. The largest improvement due to spatial separation for listener 1 occurred for the lowest frequency bin, while for listeners 2 and 3 the largest improvement was found for the highest frequency bin. Some of the advantages were quite large: for the lowest frequency bin the average improvement for the 180-degree separation was just over 20 dB, while listeners 2 and 3 demonstrated advantages in excess of 30 dB for the larger separations in the highest frequency bin. For all three subjects, the least improvement with spatial separation of sources occurred for frequency Bin #3. This result is likely due to the poorer localization accuracy typically found in the mid-frequencies where neither time of arrival nor intensity differences are particularly strong (e.g., Mills, 1972).

For the 30-degree separation condition, the data were examined for differences in performance as a function of the absolute azimuth of the signal. For the BBN masker, no difference was found for any frequency bin except for subject 1 who showed a small advantage for 0 degree azimuth at the highest frequency. For the MBDN masker, performance was generally better when the signal was played from the front than from the sides, although the functions were noisy and the differences between subjects were substantial. This general trend is also consistent with expectations based on the dependence of the minimum audible angle on azimuth [cf. Perrott (1984) for estimates of the minimum audible angle for concurrent stimuli].

To summarize, the listening advantage provided by spatial separation of masker and signal varied according to the type of masker. For Gaussian noise maskers, the obtained advantages were less than 5 dB for signal frequencies below about 3000 Hz, increasing to as much as 10 dB for higher signal frequencies. For the MBDN masker much larger advantages were found in most cases, often exceeding 20 dB for some subjects, and were apparent at high *and* low signal frequencies.

C. Role of head shadow effect

Part of the improvement found with increasing separation between signal and masker is due to the favorable signal-to-noise ratio in the ear nearest the signal. To estimate the influence of this factor on the improvements found in the preceding section, acoustic measurements of the ''head shadow effect'' were obtained.

Golay Code sequences of 512 20-μs digitally generated clicks were presented from each loudspeaker [the general procedures are described in more detail by Kulkarni (1992)]. A Convolvotron signal processing system (Crystal River Engineering) was used for digital-to-analog conversion, analog-to-digital-conversion, and computation of impulse responses. With the exception of the D/A source, the clicks were played through the instrumentation used in the experiments. The peak-equivalent sound pressure level was 80 dB.

The stimuli were measured by $\frac{1}{2}''$ Etymotic microphones mounted at the entrance of the ear canals of each listener. The microphones were held in place by custom-fit ear molds that occluded the canals. The outputs of the microphones were sent to a preamplifier and antialiasing filter, then to the inputs of two A/D channels of the Convolvatron. Each measurement consisted of 32 averages of the Golay sequences from which 1024-tap impulse responses were computed. The head shadow estimate was found by taking the difference in the log-magnitude spectra from the two ears. Measurements were made for each speaker location. Note that the microphone placement was at the entrance of the blocked ear canal and thus does not include the ear canal transfer function.

Results of these measurements are shown in Fig. 5. The figure plots the difference in level between the two microphones as a function of frequency for all three listeners for the ± 90-degree speaker locations averaged together. The magnitude of the differences found for the other speaker locations decreased as the angle approached 0 degrees.

It is relatively straightforward to apply these measurements to the data obtained in the BBN masker. The curves reflect the improvement in signal-to-noise ratio as a function of frequency expected in the nearer of the two ears of the listener. Consider the case when both the signal and the masker originate from the same speaker: $+90$ degrees, for example. Regardless of the signal-to-noise ratio, it is about the same in each ear within the ''critical band'' containing the signal. Now, if the signal remains in the speaker at $+90$ degrees and the noise is moved to the speaker at -90 degrees, the noise is attenuated by the amount plotted in Fig. 5 at each frequency in the ear nearest $+90$ degrees while the signal is attenuated the same amount for its frequency in the opposite ear. The identification-level function should shift

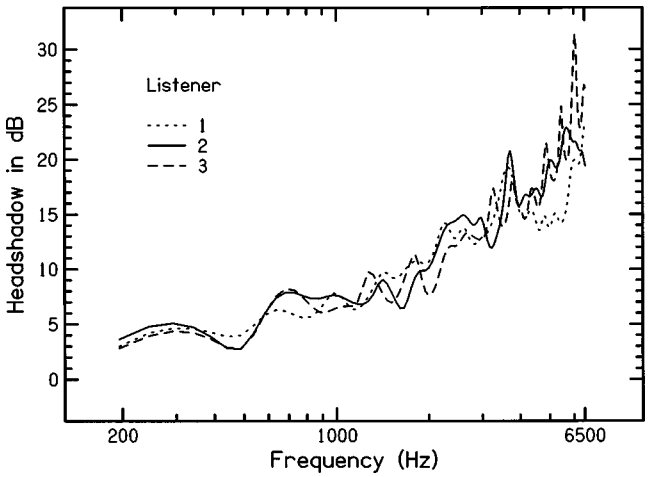

FIG. 5. Estimates of the ''head shadow effect''—the decibel difference in level at the two ears as a function of frequency—for individual listeners averaged across the two 180-degree speaker separations.

along the abscissa by roughly the amount of the attenuation of the masker at the signal frequency. Using that approximation, it appears that most, if not all, of the advantage observed with increasing spatial separation of signal and BBN masker can be attributed to head shadow.

For the MBDN masker, the same frequency-dependent attenuation of the masker relative to the signal in the near ear has a more complicated effect. This is primarily because the masking is not due to the signal-to-noise ratio in the frequency region around the signal but rather to interference produced by components remote in frequency from the signal. Consider first when the signal is in the higher frequencies. Most of the components of the masker would be lower in frequency than the signal (although some components could be two bands away on either side of the signal) and thus would fall in frequency regions where there is less of a head shadow effect. Thus, it is hard to account for the large improvements found for listeners 2 and 3 in the high frequency bin based on head shadow. For the same reasons, it could be argued that the head shadow effect contributed to the large advantages found at the low signal frequencies because most of the masker components would fall higher in frequency than the signal and would be subject to larger amounts of attenuation at the nearer ear. However, even for the low frequency bin, it is unclear whether head shadow has any significant effect. This is because we do not know much about the effects of proximity of masker components in producing informational masking, or, especially, how the amount of masking is influenced by the shape of the masker spectrum or the number of components/MBDN bands. We do know that informational masking increases with increasing number of masker tones in a detection task up to 10–20 components (Neff and Green, 1987; Neff, 1995), although large amounts of masking are found in some conditions for as few as 2–4 masker tones. Also, Neff *et al.*'s work (1993) examining the effect of widening the ''protected region'' (our term meaning the frequency band from which masker tones were excluded) around the signal suggests that, for listeners demonstrating large amounts of informational masking, proximity of masker components is not a critical

factor. Moreover, when they restricted the masker components to the frequency region above, or below, the signal, the amount of masking was not greatly reduced. In the context of the present study, where frequency components remote from the signal frequency were attenuated due to head shadow, Neff *et al.*'s results are relevant and may be viewed as supporting a minor role of head shadow, although clearly there were important procedural differences between studies (e.g., detection versus identification; fixed versus random signal frequency). Further, because the slopes of the identification-level functions in the present study were so shallow for the informational masker, changes on the order of 10–15 dB typically do not produce large changes in performance (see Fig. 3 and Table I). Thus, we conclude that the head shadow effect was not primarily responsible for the advantages found for spatial separation of sources for the MBDN masker, particularly at the lower frequencies.[1]

III. DISCUSSION

The results described above suggest that the magnitude of the listening advantage for the task of identification provided by spatial separation of sound sources depends on the type of masking the listener experiences. When one sound masks the other sound principally by dominating the pattern of excitation such that the peripheral neural representation of the signal is obscured by that of the masker, the listening advantage is largely a consequence of acoustical factors. The signal-to-noise ratio is improved due to the filtering of the masker by the head as it is received in the ear nearest the signal source. Overlayed on that effect is binaural analysis, which, for these conditions at least, probably contributed only slightly to the observed advantage and likely was a factor only for the lower signal frequencies. However, it should be noted that even a small signal-to-noise improvement for a Gaussian noise masker may produce substantial improvements in percent correct identification performance based on the relatively steep slopes observed for the identification-level functions.

When the masking one sound produces on another sound is informational in nature, large advantages due to spatial separation of sources are possible. These advantages do not appear to be based purely on the acoustic filtering of the head or on within-channel binaural analysis mechanisms (e.g., equalization-cancellation, cf. Colburn and Durlach, 1978).

Informational masking is usually attributed to ''uncertainty'' (e.g., Watson, 1987; Leek *et al.*, 1991) and occurs despite a sufficiently robust representation of the signal in the auditory periphery for solving the task (e.g., Kidd *et al.*, 1994; also Neff and Detleffs, 1995). Presumably, the observer is uncertain about the exact content of the stimulus even though the critical elements of the stimulus are audible. Because the signals and MBDN maskers used in this study were drawn from the same set of frequencies, the first tone in each narrow-band sequence could be either the beginning of a signal pattern or part of the masker. As the burst sequence progresses, the likelihood of the hypothesis that the elements falling within a given frequency band forms a signal may change, with some hypotheses becoming more likely and others less likely. It would happen very infrequently that a masker band actually contained a signal pattern because there are 8^8 possible combinations of frequencies in each sequence per band. However, if we assume that there is some noise in the coding of the elements in the periphery and that the listener is tolerant of approximations to patterns (cf. Kidd *et al.*, 1995a), it is not surprising that confusions occur, i.e., that a masker band sounds enough like a signal pattern to elicit an incorrect response. Further, if the listener adopts the strategy of focusing attention on only one frequency region, performance would be at chance, so attention must rapidly switch or be divided among frequency bands. In the attempt to adequately evaluate more than one plausible-sounding narrow-band stimulus, the listener may be unable to discern enough of the signal pattern to correctly identify it. Spatial separation of sources can greatly reduce the uncertainty of the listener about where in frequency attention should be focused. In these experiments, whenever a single narrow-band sound originates from a different spatial location than the remaining frequency sequences, it is always a signal.

Studies of the effects of spatial separation of sources in speech recognition tasks have sometimes used speech as both signals and maskers. On the one hand, these studies are clearly relevant to the current study in that the listener must attend to and extract information from a target source while ignoring one or more other sources that may be highly distracting or confusing to the listener, potentially producing large amounts of informational masking. Depending on the procedures used, the maskers may be very similar to the targets which are distinguishable by various factors that are part of the experimental design (e.g., voice characteristics of the talker, the message being conveyed, etc.). On the other hand, as mentioned in the Introduction, the broadband nature of speech likely also causes large amounts of energetic masking which makes it difficult to attribute the observed effects to one process or the other and the magnitude of the advantage observed may depend on the exact procedures used.

Yost *et al.* (1996) studied the effect of spatial separation of sources on word recognition and localization accuracy in a sound-field listening environment. They measured performance in three conditions: ''normal listening,'' in which subjects were seated in the center of a semicircle of loudspeakers and made judgments about sounds played from the speakers; a condition in which recordings of the stimuli were made through the two channels of KEMAR located in the center of the sound field and subsequently played via headphones to subjects for judging; and a one-headphone condition in which a recording was made using a single microphone located in the sound field and later played monaurally to listeners. They found a small but significant improvement in word recognition for spatially separated sources in the two conditions providing binaural information (''normal'' and KEMAR conditions) relative to the one-headphone condition—especially when there were three, rather than two, simultaneous talkers. For example, the amount of the advantage in identification of letters and numbers (the ''let'' condition in Yost *et al.*'s analysis) for the normal condition compared to the one-headphone condition was less than 5%

for single talkers, slightly less than 10% for two talkers, but more than 35% for three talkers. Localization of sources was at chance for the one-headphone condition and much better than chance for the binaural conditions.

Yost *et al.* concluded that ''there is not a large advantage provided by spatial listening when there are two sound sources...'' but that ''when the sound field becomes more complex with three concurrent sounds, spatial cues appear to play a greater role...'' (p. 1034).

In the Yost *et al.* study the fact that speech was masking speech probably means that energetic masking contributed significantly to the results so, from that perspective, relatively small improvement due to spatial separation of sources would be expected except at the higher frequencies where head shadow would be substantial. However, it should also be noted that uncertainty was minimal: the listener was allowed to listen repeatedly to the stimulus until ready to register a response. Also, the listener was permitted to move his or her head as desired. It is possible that larger advantages due to spatial separation might have resulted if the two-source listening task was more uncertain. It is tempting to explain the larger binaural advantages found for three simultaneous sources by asserting there was greater uncertainty for the listeners than that which occurred for two sources. However, we have no directly relevant data or way of measuring uncertainty that would test that speculation.

A recent study by Koehnke *et al.* (1997) also examined the advantage due to spatial separation of sources in a multisource environment. In their study, two or three simultaneous talkers were presented to listeners via headphones. One talker was the ''target'' and the other talker(s) were ''jammers.'' The spatial locations of the talkers were simulated by applying transfer functions obtained from microphones located in the two ears of KEMAR. Both the test materials and the maskers were sentences. They found improvements in intelligibility at the 50% correct point of up to 15 dB for two sources separated by 180 degrees and 8 dB for three sources separated by 90 degrees relative to listening conditions where the stimuli were mixed and played monaurally. They noted that both head shadow and binaural analysis contributed to the listening advantages, but did not specify how much of the improvement was due to each factor separately.

Yost (1997) has reviewed the substantial body of literature concerning the ''cocktail party problem'' (Cherry, 1953). He points out that the binaural advantage generally declines with increasing signal-to-noise ratio for a variety of tasks. Specifically, the improvement in frequency and intensity discrimination [e.g., Gebhardt *et al.*, 1972; Henning, 1973], speech recognition (Levitt and Rabiner, 1967; Carhart *et al.*, 1968)], and loudness perception (Townsend and Goldstein, 1972) all decline to essentially no advantage once the level of the stimulus is 10–20 dB above masked threshold. Here, though, the advantage due to spatial separation of sources does not decline appreciably with level for the informational masker over a wide range of levels. Further, most identification-level functions for signals embedded in Gaussian noise extend over a relatively narrow range of 10–20 dB unless the signals are complex and have information distributed over a broad range of frequencies. Even then, though, for any given narrow frequency region performance asymptotes quickly as signal-to-noise ratio increases. In the conditions tested in this study performance increases with increasing signal-to-noise ratio much more gradually, suggesting that informational masking, and the factors that cause release from informational masking, operate well above threshold (cf. Kidd *et al.*, 1995b). As Yost points out, little of the work done on the cocktail-party problem has been designed to mimic real-world listening environments. We certainly would not claim that the current experiments are any less artificial or ''laboratory-like'' than earlier work or that there is a simple extrapolation from the identification of nonspeech patterns to the recognition of speech. However, to the extent that uncertainty is a factor in communication situations like those Cherry and others envisioned when framing the cocktail party problem, the present study may indicate one possible binaural solution.

IV. SUMMARY AND CONCLUSIONS

(1) Spatial separation of signal and masker in the horizontal plane improves the identification of nonspeech auditory patterns.
(2) Larger improvements were found for informational maskers than for energetic maskers, especially after the head shadow effect was taken into account. The magnitude of the improvement for the informational masker in some cases was greater than 30 dB, although the individual differences between subjects also were much greater.
(3) The binaural advantage for informational masking, unlike that for energetic masking, is present over a wide range of levels above masked threshold.
(4) The mechanism of masking for the two types of maskers is assumed to be different; thus, the reason for the improvement due to spatial separation is probably different as well. For the energetic masker (BBN), after accounting for the head shadow effect, the improvement due to binaural analysis is relatively small, consistent with studies of free-field intelligibility-level-differences for speech (e.g., Bronkhorst and Plomp, 1988; Zurek, 1993). However, the large advantage found for the informational masker likely is due to a reduction in uncertainty due to perceptual segregation of the sound sources. This large effect may be responsible for the powerful subjective impression of a binaural advantage in the ''cocktail party effect.''

ACKNOWLEDGMENTS

This work was supported by Grant No. DC00100 from NIH/NIDCD, by the ONR-managed MURI Grant No. Z883402, by the Dudley Allen Sargent and Sargent Accelerated Research Award funds, and by the Boston University Hearing Research Center. The authors wish to express their thanks to Peter Chiu, Monica Hawley, Abhijit Kulkarni, and Susan Turney for their assistance with various aspects of this

project. We also are grateful to A. W. Bronkhorst, H. Steven Colburn, and an anonymous reviewer for helpful comments on an earlier version of the manuscript.

[1]We have recently measured identification-level functions for MBDN maskers shaped according to the head-shadow curves shown in Fig. 5 and presented together with the signals at 0 degree azimuth. The preliminary results suggest that the amount of improvement in performance due to the head shadow effect may be roughly comparable for the BBN and MBDN maskers. That is, very small improvements are found at low frequencies increasing to improvements of 10–15 dB at high frequencies.

Bronkhorst, A. W., and Plomp, R. (**1988**). ''The effect of head-induced interaural time and level differences on speech intelligibility in noise,'' J. Acoust. Soc. Am. **83**, 1508–1516.

Bronkhorst, A. W., and Plomp, R. (**1989**) ''Binaural speech intelligibility in noise for hearing-impaired listeners,'' J. Acoust. Soc. Am. **86**, 1374–1383.

Carhart, R., Tillman, T. W., and Dallos, P. J. (**1968**). ''Unmasking for pure tones and spondees: interaural phase and time disparities,'' J. Speech Hear. Res. **11**, 722–734.

Cherry, E. C. (**1953**). ''Some experiments on the recognition of speech with one and two ears,'' J. Acoust. Soc. Am. **25**, 975–979.

Colburn, H. S. (**1995**). ''Computational models of binaural processing,'' in *Auditory Computation*, edited by H. Hawkins and T. McMullin (Springer-Verlag, New York), pp. 332–400.

Colburn, H. S., and Durlach, N. I. (**1978**). ''Models of binaural interaction,'' in *Handbook of Perception, Vol. IV Hearing* (Academic, New York), pp. 467–518.

Gebhardt, C. J., Goldstein, D. P., and Robertson, R. M. (**1972**). ''Frequency discrimination and the MLD,'' J. Acoust. Soc. Am. **51**, 1228–1232.

Gilkey, R. A. (**1995**). ''Effects of frequency on free-field masking,'' Hum. Factors **37**, 835–843.

Henning, G. B. (**1973**). ''Effect of interaural phase on frequency and amplitude discrimination,'' J. Acoust. Soc. Am. **54**, 1160–1178.

Hirsh, I. J. (**1950**). ''The relation between localization and intelligibility,'' J. Acoust. Soc. Am. **22**, 196–200.

Kidd, Jr., G., and Mason, C. R. (**1997**). ''Pattern-like maskers increase informational masking in a nonspeech identification task,'' Program of the 20th Midwinter Research Meeting of the Association for Research in Otolaryngology.

Kidd, Jr., G., Mason, C. R., and Dai, H. (**1995a**). ''Discriminating coherence in spectro-temporal patterns,'' J. Acoust. Soc. Am. **97**, 3782–3790.

Kidd, Jr., G., Mason, C. R., and Green, D. M. (**1986**). ''Auditory profile analysis of irregular sound spectra,'' J. Acoust. Soc. Am. **79**, 1045–1053.

Kidd, Jr., G., Mason, C. R., and Rohtla, T. L. (**1995b**). ''Binaural advantage for sound pattern identification,'' J. Acoust. Soc. Am. **98**, 1977–1986.

Kidd, Jr., G., Mason, C. R., Deliwala, P. S., Woods, W. S., and Colburn, H. S. (**1994**). ''Reducing informational masking by sound segregation,'' J. Acoust. Soc. Am. **95**, 3475–3480.

Koehnke, J., Durlach, N. I., and Zurek, P. M. (**1997**). ''Further results on the cocktail party effect'' (under review).

Kulkarni, A. (**1992**). ''Auditory Imaging in a Virtual Acoustical Environment,'' unpublished Master's thesis, Dept. of Biomedical Engineering, Boston University.

Leek, M. R. (**1987**). ''Directed attention in complex sound perception,'' in *Auditory Processing of Complex Sounds*, edited by W. A. Yost and C. S. Watson (Erlbaum, Hillsdale, NJ), pp. 278–288.

Leek, M. R., and Watson, C. S. (**1984**). ''Learning to detect auditory pattern components,'' J. Acoust. Soc. Am. **76**, 1037–1044.

Leek, M. R., Brown, M. E., and Dorman, M. F. (**1991**). ''Informational masking and auditory attention,'' Percept. Psychophys. **50**, 205–214.

Levitt, H., and Rabiner, L. R. (**1967**). ''Binaural release from masking for speech and gain in intelligibility,'' J. Acoust. Soc. Am. **42**, 601–608.

Lutfi, R. A. (**1990**). ''How much masking is informational masking?,'' J. Acoust. Soc. Am. **80**, 2607–2610.

Mills, A. (**1972**). ''Auditory localization,'' in *Foundations of Modern Auditory Theory*, edited by J. V. Tobias (Academic, New York), Vol. II.

Neff, D. L. (**1995**). ''Signal properties that reduce masking by simultaneous, random-frequency maskers,'' J. Acoust. Soc. Am. **98**, 1909–1920.

Neff, D. L., and Dethlefs, T. M. (**1995**). ''Individual differences in simultaneous masking with random-frequency, multicomponent maskers,'' J. Acoust. Soc. Am. **98**, 125–134.

Neff, D. L., Dethlefs, T. M., and Jesteadt, W. (**1993**). ''Informational masking for multicomponent maskers with spectral gaps,'' J. Acoust. Soc. Am. **94**, 3112–3126.

Neff, D. L., and Green, D. M. (**1987**). ''Masking produced by spectral uncertainty with multicomponent maskers,'' Percept. Psychophys. **41**, 409–415.

Perrot, D. R. (**1984**). ''Concurrent minimum audible angle: A re-examination of the concept of auditory spatial acuity,'' J. Acoust. Soc. Am. **75**, 1201–1206.

Plomp, R. (**1976**). ''Binaural and monaural speech intelligibility of connected discourse in reverberation as a function of azimuth of a single competing sound source (speech or noise),'' Acustica **34**, 200–211.

Plomp, R., and Mimpen, A. M. (**1981**). ''Effect of the orientation of the speaker's head and azimuth of a noise source on the speech reception threshold for sentences,'' Acustica **48**, 325–328.

Pollack, I., and Pickett, J. M. (**1958**). ''Stereophonic listening and speech intelligibility against voice babble,'' J. Acoust. Soc. Am. **30**, 131–133.

Robinson, D. W., and Dadson, R. S. (**1956**). ''A re-determination of equal loudness relations for pure tones,'' Br. J. Appl. Phys. **7**, 166–181.

Saberi, K., Dostal, L., Sadraladabai, T., Bull, V., and Perrott, D. A. (**1991**). ''Free-field release from masking,'' J. Acoust. Soc. Am. **90**, 1355–1370.

Shaw, E. A. G. (**1974**). ''Transformation of sound pressure level from the free field to the eardrum in the horizontal plane,'' J. Acoust. Soc. Am. **56**, 1848.

Townsend, T. H., and Goldstein, D. P. (**1972**). ''Suprathreshold binaural unmasking,'' J. Acoust. Soc. Am. **51**, 621–624.

Watson, C. S. (**1987**). ''Uncertainty, informational masking and the capacity of immediate auditory memory,'' in *Auditory Processing of Complex Sounds*, edited by W. A. Yost and C. S. Watson (Erlbaum, Hillsdale, NJ), pp. 267–277.

Watson, C. S., Kelly, W. J., and Wroton, H. W. (**1976**). ''Factors in the discrimination of tonal patterns. II. Selective attention and learning under various levels of uncertainty,'' J. Acoust. Soc. Am. **60**, 1176–1186.

Watson, C. S., Wroton, H. W., Kelly, W. J., and Benbasset, C. A. (**1975**). ''Factors in the discrimination of tonal patterns. I. Component frequency, temporal position and silent intervals,'' J. Acoust. Soc. Am. **57**, 1175–1185.

Yost, W. A. (**1991**). ''Auditory image perception and analysis,'' Hearing Res. **56**, 8–18.

Yost, W. A., Dye, Jr., R. H., and Sheft, S. (**1996**). ''A simulated 'Cocktail Party' with up to three sound sources,'' Percept. Psychophys. **58**, 1026–1036.

Yost, W. A. (**1997**). ''The cocktail party problem: Forty years later,'' in *Binaural and Spatial Hearing in Real and Virtual Environments*, edited by R. A. Gilkey and T. R. Anderson (Erlbaum, NJ), pp. 329–348.

Zurek, P. (**1993**). ''Binaural advantages and directional effects in speech intelligibility,'' in: *Acoustical Factors Affecting Hearing Aid Performance*, edited by G. A. Studebaker and I. Hochberg (Allyn and Bacon, Boston), pp. 255–276.

High-frequency audibility: Benefits for hearing-impaired listeners

Cynthia A. Hogan
Otolaryngology Division, Department of Surgery, University of Rochester, Rochester, New York 14642

Christopher W. Turner
Department of Speech Pathology and Audiology, Wendall Johnson Center, University of Iowa, Iowa City, Iowa 52242

(Received 18 February 1997; accepted for publication 27 March 1998)

The present study was a systematic investigation of the benefit of providing hearing-impaired listeners with audible high-frequency speech information. Five normal-hearing and nine high-frequency hearing-impaired listeners identified nonsense syllables that were low-pass filtered at a number of cutoff frequencies. As a means of quantifying audibility for each condition, Articulation Index (AI) was calculated for each condition for each listener. Most hearing-impaired listeners demonstrated an improvement in speech recognition as additional audible high-frequency information was provided. In some cases for more severely impaired listeners, increasing the audibility of high-frequency speech information resulted in no further improvement in speech recognition, or even decreases in speech recognition. A new measure of how well hearing-impaired listeners used information within specific frequency bands called ''efficiency'' was devised. This measure compared the benefit of providing a given increase in speech audibility to a hearing-impaired listener to the benefit observed in normal-hearing listeners for the same increase in speech audibility. Efficiencies were calculated using the old AI method and the new AI method (which takes into account the effects of high speech presentation levels). There was a clear pattern in the results suggesting that as the degree of hearing loss at a given frequency increased beyond 55 dB HL, the efficacy of providing additional audibility to that frequency region was diminished, especially when this degree of hearing loss was present at frequencies of 4000 Hz and above. A comparison of analyses from the ''old'' and ''new'' AI procedures suggests that some, but not all, of the deficiencies of speech recognition in these listeners was due to high presentation levels. [S0001-4966(98)02507-7]

PACS numbers: 43.66.Sr, 43.66.Ts, 43.71.Gv, 43.71.Ky [JWH]

INTRODUCTION

High-frequency sensorineural hearing loss is the most common configuration and type of hearing loss seen in the audiology clinic. Usually, the client with this configuration of hearing loss presents with complaints of difficulty understanding or recognizing conversational speech, particularly if the speaker is talking softly or if there is any background noise. A hearing aid is the preferred form of ''treatment'' for a sensorineural hearing loss because this type of loss is not remediable with medication or surgery. The primary goal of current hearing aid fitting strategies is to make the speech signal audible in those regions where the sensitivity is reduced, and in the case of high-frequency hearing loss this means providing high-frequency amplification. Although it is known that amplification can, to a large extent, overcome the audibility deficits accompanying hearing loss, we also know that an increase in audibility does not always provide a complete restoration of speech recognition for all hearing-impaired listeners. Furthermore, it remains unclear as to how the degree of hearing loss relates to the potential improvement in speech recognition provided by increased high-frequency audibility.

In order to investigate the effects of speech audibility upon speech recognition by the hearing-impaired listener, the Articulation Index (AI) (ANSI, 1969a; ANSI, R1997; French and Steinberg, 1947) has been used as a measure of speech audibility, permitting researchers to begin to more directly link speech recognition errors to reduced audibility. The AI appears to provide good prediction of speech recognition scores for normal-hearing listeners and those with mild and moderate hearing loss (e.g., Ching *et al.*, 1997; Dubno *et al.*, 1989b; Humes *et al.*, 1986; Kamm *et al.*, 1985; Pavlovic and Studebaker, 1984; Zurek and Delhorne, 1987). However, the AI tends to overpredict the performance of those hearing-impaired subjects with severe high-frequency hearing loss (e.g., Ching *et al.*, 1998; Dubno *et al.*, 1989a; Kamm *et al.*, 1985; Pavlovic, 1984). For these listeners, the AI method predicts a better score for a given degree of audibility than the hearing-impaired listener actually obtains.

To better predict the effects of sensorineural hearing loss that lie beyond the audibility deficits, Pavlovic (1984) has incorporated suprathreshold low- and high-frequency ''proficiency factors'' into AI calculations. The proficiency factor is a weighting factor that attempts to quantify the reduced benefit of making speech signals audible for some hearing-impaired listeners. His results suggested that some high-frequency hearing-impaired subjects were experiencing other deficits, in addition to threshold elevation, that contributed to their speech understanding difficulties. Ching *et al.* (1998)

used a number of corrections to improve the predictability of speech recognition using the AI. They concluded that predictions based on improvements in audibility were inaccurate. In addition, they found that additional modifications to the calculations, including standardized and individualized modifications, improved prediction of performance, but did not account for the variance observed in the data. In contrast, Zurek and Delhorne (1987) and Humes and Roberts (1990) have concluded that the difficulty of hearing-impaired listeners in understanding speech was primarily the result of inaudibility (or threshold elevation). It is clear that hearing-impaired listeners are a heterogeneous group, and that restoring the audibility of speech signals does not always return their speech recognition to within normal limits.

Several studies have investigated the benefits of additional high-frequency amplification for speech understanding using various amounts and types of amplification. Pascoe (1975) demonstrated an improvement in speech recognition with the addition of high-frequency information for high-frequency hearing loss listeners. Skinner *et al.* (1982) and Sullivan *et al.* (1992) reported that the addition of suprathreshold, high-frequency information (i.e., increasing signal bandwidth) resulted in an improvement in recognition performance for their high-frequency hearing-impaired subjects. The recognition scores were highly correlated with AI for each condition for the two listeners tested in the Skinner *et al.* (1982) study (i.e., as audibility increased the word recognition score also increased) indicating that increases in audibility did result in increases in the recognition score. However, recognition performance was still below that predicted for normal-hearing listeners.

Contrary to the above findings, Murray and Byrne (1986) found that additional high-frequency information was not judged to be beneficial by high-frequency hearing-impaired listeners when asked to judge ''pleasantness.'' They concluded that perhaps because of the severity of the high-frequency hearing loss present the listeners experienced distortion of the speech signal within the auditory system when presented with the high-frequency amplification. They suggested that a lower cutoff frequency (i.e., narrower bandwidth) for amplification may be preferable for some high-frequency hearing-impaired listeners, while others may benefit from the extension of amplification into the high frequencies. Rankovic (1991) found that when audibility was maximized (Almax condition), listeners with normal low-frequency sensitivity sloping to a high-frequency hearing loss performed more poorly than in conditions where audibility was less than the maximum possible. In other words, although Almax provided for the greatest amount of high-frequency audibility for the high-frequency hearing loss listeners, it did not always provide the highest recognition score.

The present study is an effort to determine the extent that listeners with high-frequency hearing loss can improve speech recognition when high-frequency audibility is systematically increased. Also of interest is whether there is a way to predict the benefit of high-frequency audibility and whether or not the severity of high-frequency hearing loss is a predictive factor. In addition, this study investigates whether benefit of high-frequency audibility is dependent on frequency region. It is hypothesized that as the degree of high-frequency hearing loss increases, listeners will obtain less improvement in speech recognition performance with the addition of high-frequency audibility, and that this benefit is also frequency dependent. The present study was therefore designed specifically to address several questions still unanswered to date.

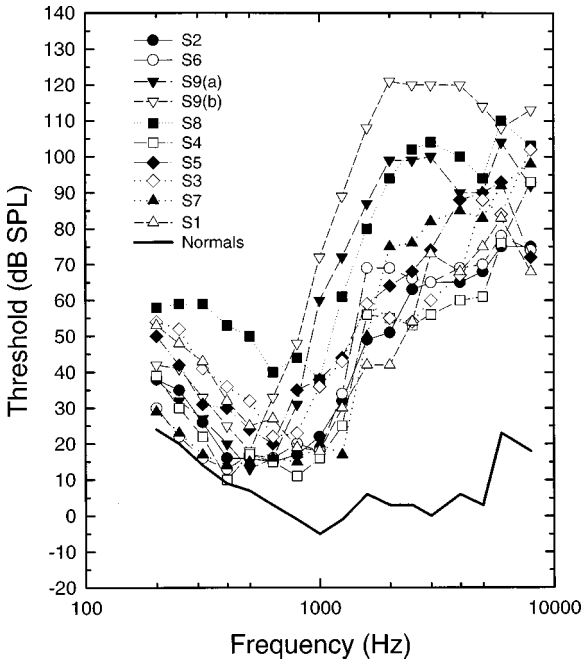

FIG. 1. Individual audiograms of the hearing-impaired listeners (various symbols) and the average thresholds for the normal-hearing group (heavy solid line).

(1) Does increasing audibility in regions of hearing loss improve speech recognition performance in hearing-impaired listeners as much as normal-hearing listeners?
(2) Is there a way to predict benefit of high-frequency audibility, and is severity of the high-frequency hearing loss a factor?
(3) Does benefit depend on the frequency region of hearing loss?

I. METHODS

A. Subjects

Fourteen adults participated in this study. Five subjects (four females and one male) with a mean age of 21 years (ranging from 19 to 24 years) had normal-hearing sensitivity with pure-tone hearing thresholds better than 20 dB HL (*re*: ANSI S3.6, 1969b) from 250 through 8000 Hz. Nine subjects (four females and five males) with a mean age of 63 years (ranging from 33 to 77 years) had relatively normal hearing thresholds or minimally impaired sensitivity (35 dB HL or better) at 250 and 500 Hz and varying degrees of hearing loss for higher frequencies. Sensitivity thresholds for the subjects are displayed in Fig. 1. The threshold average for the normal group is plotted as the heavy solid line, while each symbol and broken line represents the thresholds of one of the hearing-impaired subjects. One hearing-impaired sub-

ject [S9(a)/S9(b)] had a decrease in hearing sensitivity between the two days in which speech recognition data was collected in this study. All speech recognition testing for subject S9(a) at a presentation level of 100 dB was completed on day 1. All testing for subject S9(b) at a presentation level of 105 dB was completed on day 2. Of the nine hearing-impaired listeners, five [S4, S6, S5, S8, and S9(a)/S9(b)] had been using a hearing aid fit to the test ear prior to data collection. A sixth subject, S2, was fit with a hearing aid midway through data collection, and therefore had very little prior experience with amplification and would not be considered an experienced hearing aid user. All subjects were native speakers of English and one ear served as the test ear for the study. The test ear was selected arbitrarily as the subjects had symmetrical hearing loss.

B. Stimuli

1. Threshold stimuli

Thresholds were obtained at the 17 frequencies that correspond to the center frequency of each one-third octave band from 200 through 8000 Hz. These frequencies were chosen in order to assist in calculating AI for each subject. Each pure-tone stimulus (200 ms in duration including a 20-ms onset and 20-ms offset) was stored on a Macintosh IIx and routed through a 16-bit digital-to-analog converter (DigiDesign). Pure-tone levels were expressed as the output of the Sennheiser HD 25 SP headphone as developed in an NBS-9/A coupler. The thresholds obtained in the Sennheiser HD 25 SP earphone in dB SPL were converted to dB HL (ANSI S3.6, 1969b) using correction factors determined from averaged results of a group of normal-hearing young adults who were tested with both the standard TDH-59 and Sennheiser HD 25 SP earphones. These thresholds in dB HL were used in some aspects of the data analysis (see below).

2. Speech recognition stimuli

In an effort to investigate the effects of filtering and amplifying various features of speech and reduce the effects of potentially confounding contextual cues that are present in sentences or continuous discourse on recognition of speech, nonsense syllables were used in this study. A recording of 258 nonsense syllables was used (NST, UCLA version), consisting of 12 lists, 6 lists of Consonant–Vowel (CV) construction and 6 lists of Vowel–Consonant (VC) construction, 3 CV lists and 3 VC lists per speaker (one male and one female speaker). The phonemes (consonant sounds) in each CV and VC list are paired with one of three vowels: (/a/, /i/, or /u/). The 23 phonemes are /b/, /t/, /d/, /dʒ/, /ʒ/, /f/, /g/, /k/, /l/, /m/, /h/, /n/, /p/, /r/, /s/, /ʃ/, /ɸ/, /ð/, /v/, /w/, /y/, and /z/. The frequency importance function required for AI calculations has been previously developed for these particular stimuli (Dirks *et al.*, 1990b, 1990a). The greatest weights for these stimuli are given to the one-third octave bands from 1600 through 5000 Hz, making these stimuli particularly sensitive for use in an investigation of a listener's ability to use high-frequency speech information for improving speech recognition ability. The stimuli were transferred from a DAT recording and stored in digital form on a Macintosh IIx computer. The stimuli were played through a 16-bit, digital-to-analog converter at a sampling rate of 44.1 kHz.

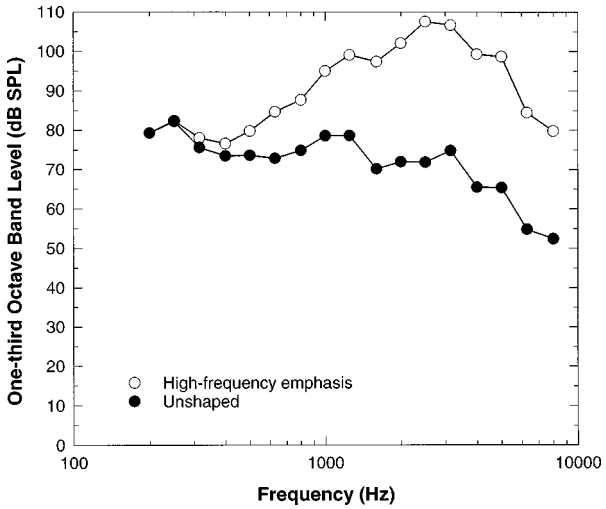

FIG. 2. Spectrum of the NST stimuli at the output of the Sennheiser earphone before (filled circles) and after (open circles) processing through the Spectrum Shaper.

The subjects were selected on the basis of normal low-frequency sensitivity and high-frequency sensorineural hearing loss. In order to increase high-frequency audibility for the hearing-impaired subjects, high-pass amplification was provided with an Orban spectrum shaper (model 672A). The ''shaped'' spectrum was selected as the maximum high-frequency gain the equipment would provide rather than being selected on the basis of one of the clinical prescriptive formulas. The resulting spectrum provided gain in the region of the hearing-impaired subjects' hearing loss as do most of the prescriptive methods, and probably was closest to an NAL-R (Byrne and Dillon, 1986) prescription fit. Figure 2 shows the one-third octave band long-term average spectrum [root mean square (rms) as a function of frequency] of the NST syllables after passing through the spectrum shaper (open circles), as well as unshaped NST syllables (filled circles). Only the ''shaped'' stimuli were used in the speech recognition task in this study.

To evaluate the result of improving high-frequency audibility in specific frequency bands, the speech stimuli were presented to the subjects under numerous filtered conditions. The NST syllables were low-pass filtered through both channels in series of a KEMO Variable Filter (VBF8.04) with a combined measured rejection slope of 60 dB/octave. The low-pass cutoff frequencies were selected to correspond to the upper-frequency boundaries of one-third octave bands (i.e., 4500, 3500, 2800, 2250, 1800, 1400, 1120, 900, 700, 560, and 440 Hz) corresponding to the one-third octave bands with center frequencies of 4000, 3150, 2500, 2000, 1600, 1250, 1000, 800, 630, 500, and 400 Hz, respectively. Use of these cutoff frequencies, along with the steep filtering characteristics of the low-pass filter, simplified the calculation of AI for each condition. Figure 3 shows the NST stimuli's long-term speech spectrum as a function of each of 12 possible low-pass cutoff frequency. A minimum of seven low-pass filter cutoff frequencies (4500 through 1120 Hz), in addition to a broadband condition (9000-Hz cutoff), were

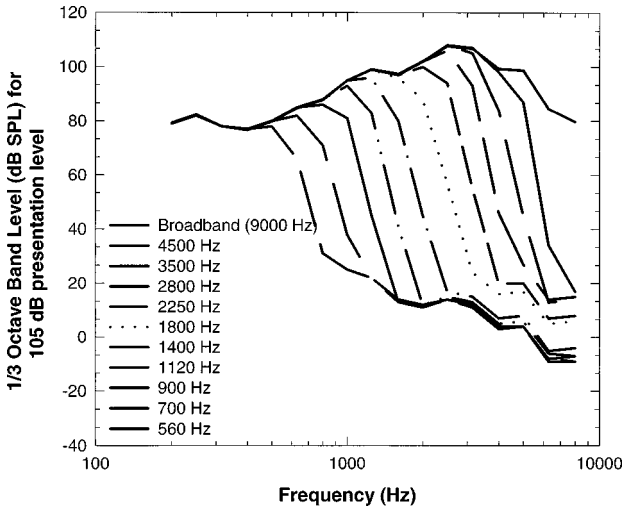

FIG. 3. Spectrum of the NST stimuli for a presentation level of 105 dB SPL at each of 12 low-pass cutoff frequencies (560 through 9000 Hz from left to right, respectively).

used for each listener at each of two or three presentation levels. The number of filter settings selected for data collection varied by subject. Low-frequency cutoffs were added when a listener's score continued to be greater than 30%–40% (with the exception of S5 who completed fewer conditions than the other subjects). The stimuli were delivered via a Sennheiser HD 25 SP earphone with a supra-aural cushion to the test ear of each listener. Therefore, both speech levels and pure-tone threshold levels were referenced to the same NBS-9/A calibration system, to further simplify AI calculations. There was no audible distortion observed at the earphone when speech was sent through the entire system.

C. Procedures

1. Threshold testing

The pure-tone stimuli were generated from the Macintosh IIx computer and attenuated via a Wilsonics programmable attenuator (model PATT). Thresholds were obtained in a two-up, one-down, four-alternative forced-choice adaptive procedure with threshold defined as the 70.7% point (Levitt, 1971) in the psychometric function for each subject using 2-dB steps.

2. Speech recognition testing

Listeners were instructed to respond following each NST stimulus by pushing numbered buttons that corresponded to the phoneme he/she heard. The listeners were provided with a list of the 23 possible phonemes and corresponding button numbers. They were also given a list of examples of each of the consonant sounds used in English words. If the subject was uncertain of a stimulus, he/she was instructed to guess.

The filtered NST syllables were presented at a minimum of two levels, and in one case three levels, to each subject, such that the maximum presentation level was chosen in order to maximize audibility (AI) yet remain comfortable for the listener. The second and/or third presentation level was chosen to be less intense than the first. The overall levels for presentation of the NST stimuli varied from 40 dB SPL to 60 dB SPL for the normal-hearing listeners and 65 to 105 dB for the hearing-impaired listeners. The presentation level, as used in this paper, represents the overall rms level in the broadband condition, therefore, as the bandwidth changed with cutoff frequency, the overall rms level of each filtered condition decreased relative to the overall rms level in the broadband condition at the same presentation level. Thus each one-third octave band level remained constant compared with the same one-third octave band level in the broadband condition at a given presentation level. Each subject was provided with three CV lists as practice. They were tested in the broadband condition initially to demonstrate that they were able to correctly use the phoneme symbols which corresponded to each phoneme. Following completion of the broadband condition at a given presentation level, the remaining cutoff frequencies were randomized. The full 12-list test was presented at each cutoff frequency. Syllables within each of the 12 lists were also randomized. An overall percent correct score based upon the 258 items was obtained in each condition. Each percent correct score was then converted to a Rationalized Arcsine Transform Unit (RAU) (Studebaker, 1985). The RAU transformation equalizes the variances of scores across the range of performance.

3. Audibility calculations

Articulation Index calculations were completed for each listener using two methods. It has been shown that speech presented at very high levels provides less information than speech at normal speaking levels (Studebaker and Sherbecoe, 1995). In order to make speech audible to hearing-impaired listeners one must, by necessity, present speech at high levels. Therefore, some of the problems that hearing-impaired listeners might experience in speech recognition may be due to the high presentation levels of speech, in addition to any cochlear damage present. The ANSI (R1997) version of the AI[1] takes the effect of high presentation levels into account, whereas the ANSI (1969a) version does not. Thus analyzing our data with both procedures and comparing the results may provide insight into the underlying causes of the speech recognition deficits of the hearing-impaired listeners.

The one-third octave band method was used and the Frequency Importance Function developed for these stimuli was used (Dirks *et al.*, 1990b). The pure-tone thresholds obtained at the center frequency of each one-third octave band were not converted to one-third octave band values. The assumption was made that the peaks were +12 dB relative to the root mean square level. No corrections were made for speech masking nor were proficiency or desensitization factors applied.

II. RESULTS

A. Speech recognition results for listeners with normal hearing

The speech recognition tests were administered at two presentation levels and a minimum of seven cutoff frequen-

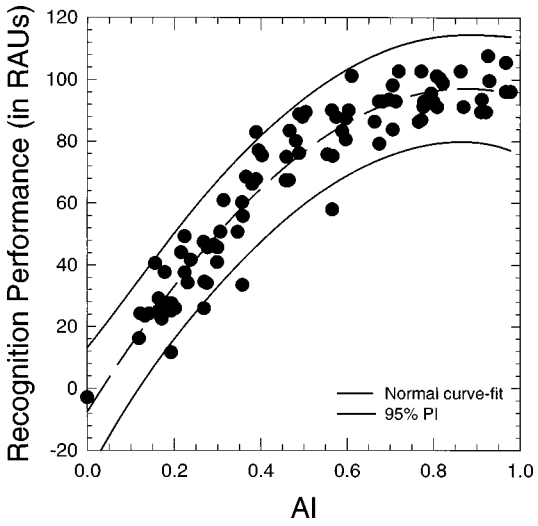

FIG. 4. Recognition performance (in RAU) is plotted as a function of audibility (AI) for NST stimuli for the five normal-hearing listeners. The dashed line represents the second order polynomial regression; the solid lines represent plus and minus two standard deviations.

cies plus the broadband condition. The results of the normal-hearing listeners, recognition performance (in RAUs) plotted as a function of degree of audibility (AI), are shown in Fig. 4. The data points represent the results obtained at two presentation levels (45 and 55 dB SPL for four listeners and 40 and 60 dB SPL for the fifth listener) and numerous low-pass filter cutoff frequencies for the five normal-hearing listeners. The new ANSI standard for calculation of AI (R1997) was also calculated, however, because the normal-hearing listeners did not listen to speech under conditions of loud presentation levels, there were no differences in AIs calculated by each method. Figure 4 clearly shows that as audibility (AI) increased, recognition performance increased. The group data were fit with a second-order polynomial regression (least squares regression) line (dashed line in Fig. 4). The correlation coefficient of the regression line for the normal-group data was $R^2 = 0.912$. The 95% prediction intervals are represented by the solid lines in Fig. 4.[2]

B. Speech recognition results for hearing-impaired listeners

The raw data for the hearing-impaired listeners are found in Table I. The percent correct score is shown for each condition completed by each hearing-impaired listener. The results for each of the hearing-impaired listeners were plotted as recognition score (in RAUs) as a function of audibility (AI). Results for each of the listeners at a given presentation level were also fit with a second-order polynomial regression.

In the three panels of Fig. 5, recognition performance (RAU) is plotted as a function of audibility (AI, calculated with the old AI method (1969a) and the new Al method (R1997) for each of three hearing-impaired listeners S3, S7, and S8, along with the normal-hearing average results and the corresponding 95% prediction intervals as shown in Fig. 4. Listener S3 has a mild high-frequency hearing loss, listener S7 has a moderate high-frequency hearing loss, and listener S8 has a severe high-frequency hearing loss. The different symbols represent results for the old AI calculation (filled circles) and the new AI calculation (open squares). As a given symbol is followed from left to right within a panel, each additional data point represents the result obtained when the next higher-frequency one-third octave band was added to the speech signal. This increase in bandwidth resulted in an increase in high-frequency audibility and therefore an increase in AI. If performance increased as audibility increased, then it suggests that the listener was able to use the additional high-frequency information. However, if performance remained the same as audibility increased, it indi-

TABLE I. The recognition score (percent correct) for the hearing-impaired listeners is listed at each presentation level for each cutoff frequency condition the listener completed. In addition, the final column notes whether a listener was using a hearing aid fit to the test ear. An asterisk indicates that the subject was fit with a hearing aid to the test ear while the data was being collected.

Subject	9 kHz	4.5 kHz	3.5 kHz	2.8 kHz	2.25 kHz	1.8 kHz	1.4 kHz	1.12 kHz	0.9 kHz	0.7 kHz	0.56 kHz	0.44 kHz	HA in test ear
S1 @ 75 dB	77.9	80.2	76.0	74.0	72.9	57.3	46.5	38.4					no
S1 @ 85 dB	80.6	76.7	77.9	77.1	73.2	64.7	45.7	38.8					no
S1 @ 90 dB	81.4	79.4	73.2	77.9	76.0	62.0	49.2	45.3	36.4				no
S2 @ 75 dB	77.1	68.6	70.9	71.7	64.0	64.0	48.4	45.0	29.8	27.1			yes*
S2 @ 85 dB	77.9	81.0	80.5	79.8	77.5	67.0	54.3	55.8	45.3	36.0	27.5		yes*
S3 @ 80 dB	92.2	91.1	91.5	89.1	84.5	70.5	52.3	53.5	38.0				no
S3 @ 90 dB	86.0	88.8	90.7	81.8	84.9	72.1	54.3	53.1	37.6				no
S4 @ 75 dB	71.7	73.2	73.6	67.8	72.7	55.4	50.8	45.0	43.4	35.3	23.6		yes
S4 @ 85 dB	75.2	75.6	66.6	65.9	65.1	57.4	49.6	52.7	39.1	37.9	30.2		yes
S5 @ 85 dB	73.6	79.8	72.5	77.5	74.0	65.1	50.8	53.9					yes
S5 @ 95 dB	81.8		79.8	81.4	83.7	72.9	56.2	53.8	52.7				yes
S6 @ 85 dB	76.7	78.7	75.6	70.5	76.0	65.0	60.8	60.0	50.0	42.2	37.6		yes
S6 @ 95 dB	78.7	76.0	70.9	77.5	74.8	70.5	63.0	60.0	51.4	42.6	38.3	34.9	yes
S7 @ 75 dB	67.4	65.1	58.9	57.4	60.5	52.7	48.1	41.1	33.7	28.7			no
S7 @ 95 dB	65.8	64.0	64.0	63.2	60.1	51.6	44.2	40.7	36.4	31.4			no
S8 @ 95 dB	62.0	59.3	64.7	62.0	60.1	59.7	56.6	48.4	39.5	33.7	36.0		yes
S8 @ 100 dB	54.3	59.3	58.9	58.3	59.7	52.3	49.6	40.3	45.0	32.2			yes
S9(a) @ 100 dB	40.7	39.1	42.6	44.2	48.4	46.9	49.2	47.3	43.7	39.1	40.7		yes
S9(b) @ 105 dB	37.2	39.8	40.3	41.1	48.4	44.5	48.8	51.1	47.3	39.9	44.2		yes

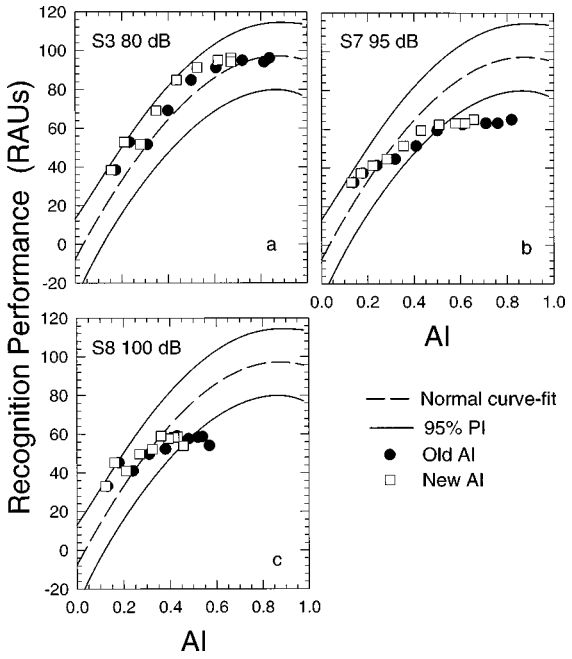

FIG. 5. Recognition performance (RAU) is plotted as a function of audibility (AI) for NST stimuli for three hearing-impaired listeners. Each panel shows the results obtained for one listener; presentation level is in the upper left corner of each panel. The dashed line represents the regression line for the normal-hearing listeners and the solid lines represent the 95% prediction interval.

cates that the listener was not able to make use of the additional high-frequency information. Finally, if the function rolled over, i.e., performance decreased as audibility increased, then this indicates that the additional audible speech information served to reduce speech recognition.

For the most part, the performance of the three hearing-impaired listeners falls within the prediction interval of the normal-hearing listeners. Listener S3's results fall well within the interval, while results for listeners S7 and S8 fall below predicted scores at high AI's when the old AI measure was used (filled circles). When results are plotted as a function of the new AI (open squares), AI is less than that calculated using the old AI (filled circles) and this shifted the data to the left in the figure. With this shift, the data for the hearing-impaired listeners was better predicted by the normal prediction intervals. Maximum AIs for the hearing-impaired listeners was limited because of the degree of the hearing loss and the limits of the equipment. The maximum performance scores for mildly impaired listener S3 (Fig. 5, panel a) were similar to those of the normal-hearing group, even when the maximum AI was less. The maximum performance scores for moderately impaired listener S7 (Fig. 5, panel b) and severely impaired listener S8 (Fig. 5, panel c) were less than those seen for normal-hearing listeners (Fig. 4) or for hearing-impaired listener S3 (Fig. 5, panel a).

In panel a of Fig. 5, it can be seen that the addition of the high-frequency bands resulted in an increase in performance score across most of the range of AI for listener S3. For listeners S7 and S8, however, the addition of audible information high-frequency information did not provide an improvement in performance score, but rather the scores remained relatively stable, with relatively flat functions at mid and high AIs. In other words, these moderately and severely impaired listeners benefited very little from the addition of audible high-frequency information for the recognition of the NST stimuli. As seen in panel c, the addition of audible information in the highest-frequency bands at a presentation level of 100 dB for S8 even resulted in a slight decrease in score (rollover).

C. Quantitative description of speech recognition results

1. Efficiency

Thus far the results for the hearing-impaired listeners have been primarily reported in descriptive terms. It would be beneficial if a more quantitative measure could be applied to the data. In addition, it is also possible to examine the present data for relations between degree of hearing loss for a given listener at a given frequency and the listener's recognition performance when speech is added to those same frequencies. Such data may provide clinical usefulness in fitting hearing aids. Therefore, an ''efficiency'' measure was designed for this purpose.

Efficiency was defined to be a measure of how well the hearing-impaired listeners used speech information presented at audible levels and at various frequencies compared to the normal-hearing listeners. Recall that the data points (performance score plotted as a function of audibility using the new AI) for each hearing-impaired listener at each presentation level were fit with a second-order polynomial regression line (as the normal-group data were). As the data for a given presentation level is followed from left to right in Fig. 5, remember that audibility (AI) was incrementally increased, corresponding to the addition of another one-third octave band of speech information. If the hearing-impaired listener was able to use this increment in speech audibility from that band to improve his/her speech recognition score as well as the normal-hearing group used the same increment in audibility, then the efficiency was defined as equal to one. If the hearing-impaired listener was unable to use that information as well as the normal-hearing listeners to improve their score, then the efficiency should be less than one. If recognition performance decreased with the additional bandwidth (rollover), then the efficiency would be a negative number. The efficiency of a hearing-impaired listener's performance was therefore computed as the hearing-impaired listener's change in recognition score for a given audibility increment divided by the normal group's change in score for the same increment in audibility. The equation is as follows:

$$\text{efficiency} = \frac{\Delta\ \text{score}/\Delta\ \text{AI(hearing-impaired)}}{\Delta\ \text{score}/\Delta\ \text{AI(normal group)}}.$$

These calculations were made between the two consecutive values of AI that correspond to the upper and lower cutoff frequencies representing the addition of an individual one-third octave band for the hearing-impaired listener. The recognition scores for the calculations were obtained from each hearing-impaired listener's regression lines. Figure 6 shows an example of one efficiency calculation for one hearing-impaired listener. The normal-group regression line (solid line) and the second order polynomial regression line

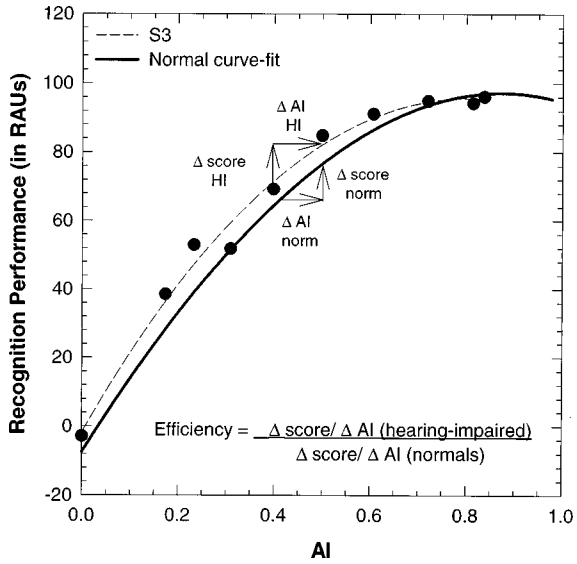

FIG. 6. Normal-group regression line (solid line) and regression line for hearing-impaired listener S3 (dashed line) are plotted to demonstrate the measures used in the calculation of Efficiency.

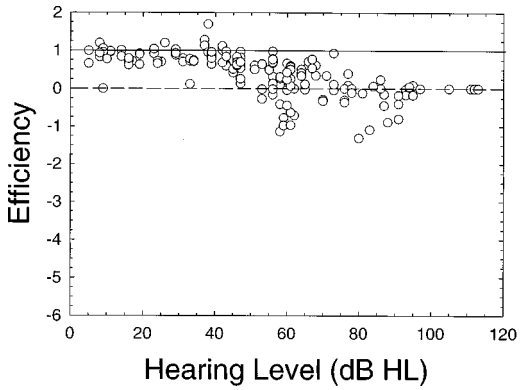

FIG. 7. Efficiency, calculated using the new ANSI method for calculation of AI (R1997), is plotted as a function of threshold for all of the hearing-impaired listeners (open circles). The solid line at an efficiency of one indicates performance equal to that of the normal-hearing group. The dashed line at an efficiency of zero indicates no benefit from the addition of the corresponding speech information.

(dashed line) for mildly impaired listener S3 at a presentation level of 90 dB (filled circles) are shown. Efficiency was calculated at the two points on S3's regression line that correspond to the recognition performance at the upper cutoff frequencies corresponding to the 1600 and 2000 Hz center-frequency one-third octave bands. The first point on the regression line (at an AI of 0.363) is S3's score (70.93 RAUs), while the second point (at an AI of 0.463) represents S3's score (82.38 RAUs) when the cutoff frequency was increased by one-third octave band. Therefore, as audibility (AI) was increased by 0.100, S3's recognition performance increased by 11.45 RAUs. Over the same increase in audibility for the normal-hearing group, the recognition performance increased by 12.38 RAUs. The resultant efficiency was 0.925 (11.45/12.38). S3's score increased almost as much as the score of the normal-hearing group, suggesting that S3 benefited nearly as much as did the normal-hearing listeners when high-frequency bands were added to the speech signal.

Both the ANSI (1969a) and ANSI (R1997) procedures were used in the analysis. The efficiency measure calculated using the 1969 procedure addresses the question of how well a hearing-impaired listener uses audible speech compared to a normal-hearing listener listening at normal speaking levels (this may be the question of interest for a clinical fitting a hearing aid). An efficiency measure calculated using the 1997 procedure addresses the question of how well a hearing-impaired listener uses audible speech compared to a normal-hearing listener listening at the same high presentation levels. A comparison of the two analyses can thus separate the contributions of both high presentation levels and cochlear damage to the speech recognition deficits of the impaired listener.

2. Efficiency as a function of threshold

Of particular interest is the effect that the degree of hearing loss at a particular frequency has on efficiency for that frequency region. Is poorer efficiency associated with more hearing loss while better efficiency is associated with better hearing or less hearing loss (as proposed generally by Pavlovic, 1984)? Recall that there was a measured degree of hearing loss at the test frequency associated with each one-third octave band and a corresponding calculation of efficiency for the addition of each one-third octave band for each hearing-impaired listener. Figure 7 shows efficiency of the hearing-impaired listeners plotted as a function of hearing threshold in dB HL corresponding to the efficiency calculated for that particular band. Efficiencies in this figure were calculated based on AIs using the new method (ANSI R1997). The solid line at an efficiency of one indicates no difference between the performance of the normal-hearing group and hearing-impaired listener. An efficiency of zero (dashed line) indicates an inability of the hearing-impaired listener to use the additional one-third octave band information.

The data of Fig. 7 show that as hearing loss increased, efficiency decreased. In general, as might be expected, when the listener's thresholds were within the normal-hearing range (e.g., thresholds less than 30 dB HL), there was little difference between their efficiency in using audible speech information and the efficiency of the normal-hearing listeners, with most of the data points falling around an efficiency of one. However, as threshold increased beyond 55 dB HL, all listeners performed below an efficiency of one. Again, an efficiency between zero and one indicates that the hearing-impaired listener was not obtaining benefit equivalent to the normal-hearing group with the additional high-frequency information, but was getting some benefit (improvement in score). Interestingly, some listeners obtained a negative efficiency, meaning that performance *decreased* as audible high-frequency information was added to the speech signal. This is a reflection of the rollover in the function, as in the example of one listener (panel c) in Fig. 5. Rollover was seen when the speech recognition score decreased for some of the hearing-impaired listeners as audibility increased, resulting in a negative change in performance from the first point to the second point in the efficiency calculation. The majority of negative efficiency values observed in conjunction with the more severe hearing losses represented rollover.

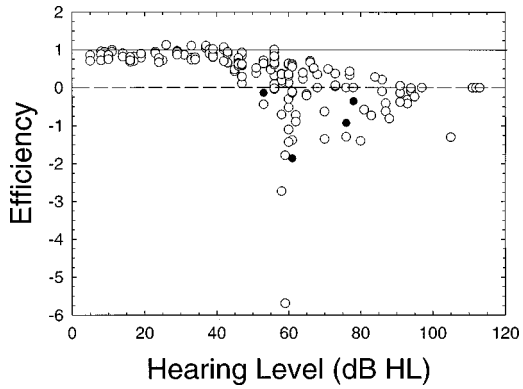

FIG. 8. Efficiency, calculated using the old ANSI method for calculation of AI (1969a), is plotted as a function of threshold for all of the hearing-impaired listeners (open circles). The filled circles were derived from regression lines that showed rollover when the actual data points did not show rollover (see text). The solid line at an efficiency of one indicates performance equal to that of the normal-hearing group. The dashed line at an efficiency of zero indicates no benefit from the addition of the corresponding speech information.

Figure 8 shows efficiency of the hearing-impaired listeners plotted as a function of hearing threshold corresponding to the efficiency calculated for that particular band when AI was calculated using the old ANSI method (1969a) for speech at a high presentation level. There are several data points (filled circles) that should be viewed with caution as they were derived from second order polynomial regression lines for two listeners that showed rollover when in fact the data points did not show real rollover. These results show that as hearing loss increased, efficiency decreased. As seen in the results calculated with the new ANSI (R1997) method (Fig. 7), when the thresholds were essentially normal, the efficiency was close to one, indicating that the hearing-impaired listeners were using the audible speech information as well as the normal-hearing listeners in region of normal/near normal hearing. As threshold increased above 55 dB HL, all listeners performed below an efficiency of one, suggesting that the listener was getting some benefit of increasing high-frequency audibility, but not as much as the normal-hearing listeners. Although the pattern of results is similar to the pattern using the new ANSI method for AI calculation, the efficiencies were generally greater with the new method, although still were not equal to one. Thus use of the old ANSI method resulted in more negative efficiencies and the range of efficiencies was greater, from $+1.81$ to -5.68 compared with a range of $+1.72$ to -1.34. The large negative efficiency values (those less than negative two) resulted when a hearing-impaired listener's function demonstrated a large decrease in score at the same point at which there was a small increase in score for the normal-hearing group. These results suggest that the hearing-impaired listeners were not using the audible high frequency information as well as the normal-hearing listeners to improve their speech recognition scores.

3. Efficiency as a function of frequency

We have just seen that when hearing loss increased beyond approximately 55 dB HL, efficiency tended to be less than one. However, Figs. 7 and 8 do not indicate if this effect is frequency dependent. The six panels of Fig. 9 show the efficiency calculated for the one-third octave bands with center frequencies of 1000, 1600, 2500, 3150, 4000, and 8000 Hz for each of the hearing-impaired listeners. Efficiency is plotted as a function of threshold (in dB HL) at each of the one-third octave center frequency. These data were calculated using the new ANSI method for calculation of AI (R1997) and correspond to the data plotted in Fig. 7. The number of data points on each panel varies due to the total number of conditions the hearing-impaired listeners completed. The results in Fig. 9 show efficiencies for lower frequencies (1000 and 1600 Hz) clustered around one, where the listeners generally had normal or near normal hearing at these frequencies. As seen in Fig. 7, as hearing loss (threshold) increased, efficiency decreased. It does appear that there is a tendency for efficiency for a given degree of hearing loss to be dependent on frequency, particularly in the higher frequencies. At a given hearing level, as frequency increases, the efficiency tends to decrease. For example, at a threshold of approximately 55 dB HL, the average efficiency for the 1600 Hz one-third octave band is slightly less than one, but at 4000 Hz, efficiencies for the same degree of hearing loss are generally clustered around zero. For a given degree of hearing loss in the lower-frequency bands, the hearing-impaired listeners appear to be using audible speech information as efficiently as the normal-hearing group, but at

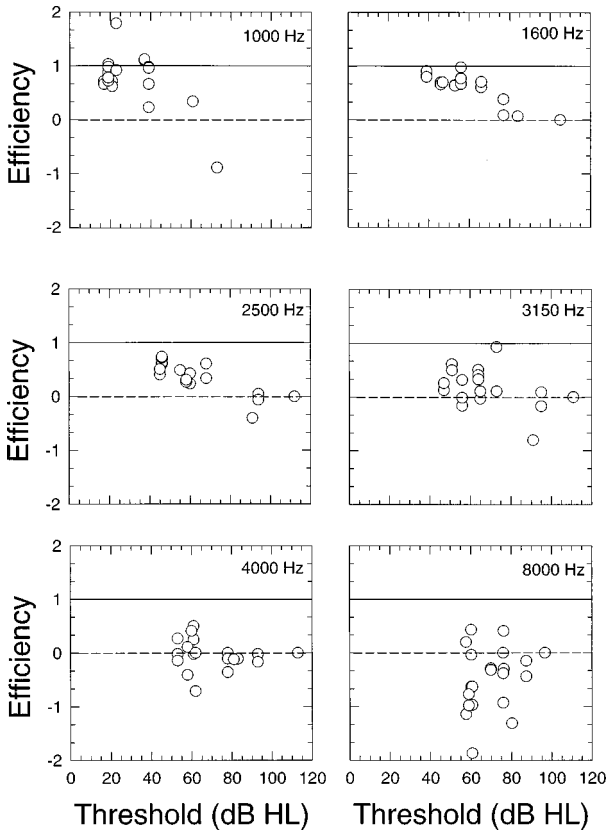

FIG. 9. Each panel represents the efficiency (open circles) within a one-third octave band (1000, 1600, 2500, 3150, 4000, and 8000 Hz) for the hearing-impaired listeners. Efficiency is plotted as a function of threshold. The solid line at one indicates performance equal to that of the normal-hearing group. The dashed line at zero indicates no benefit.

the higher frequencies, not only are they using the information less efficiently than the normal-hearing listeners, the information often appears to be detrimental to their performance while the degree of hearing loss (in dB HL) is equivalent. Note that the negative efficiencies are observed primarily for hearing losses greater than 55 dB HL *and* at frequencies of 4000 Hz and above. It should also be noted, however, that there were no hearing losses less than 40 dB HL at frequencies above 2000 Hz.

III. DISCUSSION

The purpose of this study was to investigate the effect of increasing audibility in high-frequency regions for normal-hearing and high-frequency hearing-impaired listeners on speech recognition scores. An additional purpose was to determine whether there was some way to predict benefit of high-frequency audibility, whether the severity of the high-frequency hearing loss was a factor, and whether any effects were dependent on the frequency of hearing loss.

The normal-hearing listeners demonstrated an increase in recognition score as audibility increased. In the present study, listeners with mild high-frequency hearing loss (i.e., listener S3, Fig. 5, panel a) performed similarly to the normal-hearing listeners, while those listeners with moderate high-frequency hearing loss (i.e., listener S7, Fig. 5, panel b) performed more poorly than the normal-hearing or mildly impaired listeners. Generally, listeners with more severe high-frequency hearing loss (i.e., listener S8, Fig. 5, panel c) performed more poorly than the normal-hearing, mildly impaired, or moderately impaired listeners. In agreement with several previous investigations (i.e., Ching *et al.*, 1997, 1998; Dubno *et al.*, 1989a; Kamm *et al.*, 1985; Pavlovic, 1984; Turner and Robb, 1987), these results suggest that audibility alone is not adequate to account for poorer recognition ability of listeners with moderate or severe high-frequency hearing loss. Comparisons of results plotted as a function of the old AI calculation (1969a) and the new AI calculation (R1997) show that at a given condition, the new AI was less than that calculated with the old AI. Although use of the new AI calculation resulted in more hearing-impaired data falling within the prediction intervals developed on normal-hearing listeners, the performance of the hearing-impaired listeners, particularly those with moderate and severe hearing loss, almost always fell at or below the lower boundary of normal performance. In particular, as hearing loss increased above approximately 55 dB HL listeners were not as efficient as the normal-hearing listeners in using high-frequency information to improve speech recognition performance (Fig. 7). In addition, the results point to a dependence on frequency of hearing loss, in that the hearing-impaired listeners were not using the high-frequency information (particularly in the 4000- and 8000-Hz bands) to improve their score, in some cases when the hearing loss was less than 55 dB HL (Fig. 9).

Two of the mildly, two of the moderately and both severely impaired listeners showed some degree of rollover; their results demonstrated a decrease in performance as audibility increased, consistent with those of Rankovic (1991, 1997). In the present case, audibility increases were obtained by extending the high-frequency cutoff of the speech band. In terms of practical implications, the goal of providing amplification to a hearing-impaired listener with a hearing aid is to provide audibility of the speech signal within the impaired frequency region. However, if the results of the present study were used as a guide, perhaps the high-frequency band(s) that caused a decrease in recognition performance should not be amplified by a hearing aid for these hearing-impaired listeners. This is consistent with the results of Murray and Byrne (1986), who found that increased bandwidth was not always best for listeners with severe high-frequency hearing loss, but that there were instances where a narrower bandwidth resulted in better recognition performance and judgments of pleasantness. In particular, a greater number of negative efficiencies were often observed in this study for hearing losses greater than 55 dB HL (see Fig. 7). In a practical sense, as flexible, programmable hearing aids become clinically available, changing the upper cutoff frequency to eliminate information in the bands found to be detrimental to performance for some listeners with high-frequency hearing loss may be both possible and beneficial to the listener. Eliminating amplification within frequency regions that cause a decrease in performance score might help those listeners to improve their ability to recognize speech. The present results suggest that clinicians should use some caution in providing amplification above 4000 Hz when the hearing loss in those regions is greater than 55 dB HL.

Rankovic (1997) suggested that high presentation levels for speech resulted in rollover. In the present study, the primary purpose was to investigate the effect of improving high-frequency audibility on performance in hearing-impaired listeners and comparing those effects to normal-hearing listeners. It was necessary to use high presentation levels for the hearing-impaired listeners in order to maximize audibility (AI) in the regions of hearing loss. Unfortunately, there appears to be a diminishing return in amplifying high-frequency speech information, in that as amplification is provided in high-frequency regions of moderate to severe impairment, particularly when hearing loss exceeds 55 dB HL, the result may be a decrease in speech recognition performance. A comparison of Figs. 7 and 8 show that the high presentation levels used for the hearing-impaired listeners in this study account for only some of the poorer efficiencies observed. Clearly the effects of cochlear damage upon speech recognition for listeners with more severe hearing losses are real. In terms of clinical purposes, this distinction is unimportant, since for listeners with severe hearing losses, low presentation levels of speech are not an option.

In the present study efficiency decreased as hearing loss increased, particularly when the hearing loss exceeded 55 dB HL, with many negative efficiencies when threshold was worse than 55 dB HL. Van Tasell (1993) suggested that difficulties in speech recognition increased as hearing loss increased beyond 60 dB HL because damage in the cochlea (inner ear) at hearing levels above 60 dB HL was not limited to the outer hair cells, but rather also affected the inner hair cells (Liberman and Dodds, 1984). In addition, Killion (1997) has suggested that sensitivity loss only is the result of outer hair cell loss while inner hair cell loss contributes to

loss of ''clarity.'' It is possible that the lower efficiencies observed for these greater hearing loss regions are the result of stimulating areas within the cochlea that have damage at the inner hair cell level.

ACKNOWLEDGMENTS

This research was supported by NIDCD Grant No. RO1 DC00377 and a Research and Creative Project Grant from the Graduate School, Syracuse University. The authors would like to thank Dave Fabry, Lenore Holte, and Beth Prieve for their contributions to the design of the study and analysis of the results; Amy Horwitz, Pamela Souza, and Karen Doherty for their support; Rebecca Waite and Holly Hutta for their help in data collection; Joe Walton who read an earlier version of this manuscript; and Dianne Van Tasell and one anonymous reviewer for their helpful comments and suggestions.

[1]In the new ANSI AI standard the Articulation Index is now called the Speech Intelligibility Index (SII), however, for the purposes of the present paper, we use the term ''new'' AI or new AI for the SII.

[2]We attempted to describe the data with the equation of Fletcher and Galt (1950), which was specifically developed for fitting AI data such as these. Although their equation worked well for normal-hearing data, it was clearly inadequate for fitting the data of our hearing-impaired listeners.

ANSI (**1969a**). ANSI S3.5-1969, ''American National Standard Methods for the Calculation of the Articulation Index'' (American National Standards Institute, New York).

ANSI (**1969b**). ANSI S3.6-1969, ''American National Standard Specifications for Audiometers'' (American National Standards Institute, New York).

ANSI (**R1997**). ANSI S3.5-1995, ''American National Standard Methods for the Calculation of the Speech Intelligibility Index'' (American National Standards Institute, New York).

Byrne, D., and Dillon, H. (**1986**). ''The National Acoustic Laboratories' (NAL) new procedure for selecting the gain and frequency response of a hearing aid,'' Ear Hear. **7**, 257–265.

Ching, T., Dillon, H., and Byrne, D. (**1997**). ''Prediction of speech recognition from audibility and psychoacoustic abilities of hearing impaired listeners,'' in *Modeling Sensorineural Hearing Loss*, edited by W. Jesteadt (Erlbaum, Mahwah, NJ).

Ching, T., Dillon, H., and Byrne, D. (**1998**). ''Speech recognition of hearing-impaired listeners: Predictions from audibility and the limited role of high-frequency amplification,'' J. Acoust. Soc. Am. **103**, 1128–1140.

Dirks, D. D., Dubno, J. R., Ahlstrom, J. B., and Schaeffer, A. B. (**1990b**). ''Articulation index importance and transfer functions for several speech materials,'' American Speech–Language–Hearing Association **32**, 91.

Dirks, D. D., Dubno, J. R., and Bell, T. S. (**1990a**). ''Problems in the predictions of speech recognition among hearing-impaired listeners,'' J. Acoust. Soc. Am. Suppl. 1 **88**, S32.

Dubno, J. R., Dirks, D. D., and Ellison, D. E. (**1989a**). ''Stop-consonant recognition for normal-hearing listeners and listeners with high-frequency hearing loss. I: The contribution of selected frequency regions,'' J. Acoust. Soc. Am. **85**, 347–354.

Dubno, J. R., Dirks, D. D., and Schaefer, A. B. (**1989b**). ''Stop-consonant recognition for normal-hearing listeners and listeners with high-frequency hearing loss. II: Articulation index predictions,'' J. Acoust. Soc. Am. **85**, 355–364.

Fletcher, H., and Galt, R. H. (**1950**). ''The perception of speech and its relation to telephony,'' J. Acoust. Soc. Am. **22**, 89–151.

French, N. R., and Steinberg, J. C. (**1947**). ''Factors governing the intelligibility of speech sounds,'' J. Acoust. Soc. Am. **19**, 90–119.

Humes, L. E., and Roberts, L. (**1990**). ''Speech-recognition difficulties of the hearing-impaired elderly: The contributions of audibility,'' J. Speech Hear. Res. **33**, 726–735.

Humes, L. E., Dirks, D. D., Bell, T. S., Ahlstrom, C., and Kincaid, G. E. (**1986**). ''Application of the articulation index and the speech transmission index to the recognition of speech by normal-hearing and hearing-impaired listeners,'' J. Speech Hear. Res. **29**, 447–462.

Kamm, C. A., Dirks, D. D., and Bell, T. S. (**1985**). ''Speech recognition and the articulation index for normal- and hearing-impaired listeners,'' J. Acoust. Soc. Am. **77**, 281–288.

Killion, M. (**1997**). ''The SIN report: Circuits haven't solved the hearing-in-noise problem,'' The Hearing Journal **50**, 28–30,32,34.

Levitt, H. (**1971**). ''Transformed up-down methods in psychoacoustics,'' J. Acoust. Soc. Am. **49**, 467–477.

Liberman, M. C., and Dodds, L. W. (**1984**). ''Single-neuron labeling and chronic cochlear pathology. III. Stereocilia damage and alterations of threshold tuning curves,'' Hearing Res. **16**, 55–74.

Murray, N., and Byrne, D. (**1986**). ''Performance of hearing-impaired and normal hearing listeners with various high-frequency cutoffs in hearing aids,'' Aust. J. Audiol. **8**, 21–28.

Pascoe, D. P. (**1975**). ''Frequency responses of hearing aids and their effects on the speech perception of hearing-impaired subjects,'' Ann. Otol. Rhinol. Laryngol. **84, Suppl. 23**, 5–40.

Pavlovic, C. V. (**1984**). ''Use of the articulation index for assessing residual auditory function in listeners with sensorineural hearing impairment,'' J. Acoust. Soc. Am. **75**, 1253–1258.

Pavlovic, C. V., and Studebaker, G. A. (**1984**). ''An evaluation of some assumptions underlying the articulation index,'' J. Acoust. Soc. Am. **75**, 1606–1612.

Rankovic, C. M. (**1991**). ''An application of the articulation index to hearing aid fitting,'' J. Speech Hear. Res. **34**, 391–402.

Rankovic, C. M. (**1997**). ''Prediction of speech reception by listeners with sensorineural hearing loss,'' in *Modeling Sensorineural Hearing Loss*, edited by W. Jesteadt (Erlbaum, Mahwah, NJ).

Skinner, M. W., Karstaedt, M. M., and Miller, J. D. (**1982**). ''Amplification bandwidth and speech intelligibility for two listeners with sensorineural hearing loss,'' Audiology **21**, 251–268.

Studebaker, G. A. (**1985**). ''A 'rationalized' arcsine transform,'' J. Speech Hear. Res. **12**, 455–462.

Studebaker, G. A., and Sherbecoe, R. L. (**1995**). ''Speech recognition at higher than normal speech and noise levels,'' J. Acoust. Soc. Am. **97**, 3358.

Sullivan, J. A., Allsman, C. S., Nielsen, L. B., and Mobley, J. P. (**1992**). ''Amplification for listeners with steeply sloping, high-frequency hearing loss,'' Ear Hear. **13**, 35–45.

Turner, C. W., and Robb, M. P. (**1987**). ''Audibility and recognition of stop consonants in normal and hearing-impaired subjects,'' J. Acoust. Soc. Am. **91**, 1566–1573.

Van Tasell, D. J. (**1993**). ''Hearing loss, speech, and hearing aids,'' J. Speech Hear. Res. **36**, 228–244.

Zurek, P. M., and Delhorne, L. A. (**1987**). ''Consonant reception in noise by listeners with mild and moderate sensorineural hearing impairment,'' J. Acoust. Soc. Am. **82**, 1548–1559.

Modulation detection interference in cochlear implant subjects

Louise M. Richardson, Peter A. Busby, and Graeme M. Clark
Department of Otolaryngology, University of Melbourne, 384–388 Albert Street, East Melbourne, 3002, Victoria, Australia

(Received 20 December 1996; accepted for publication 27 March 1998)

The aim of this study was to determine whether detection thresholds for amplitude modulated signals on a single electrode were influenced by a masking modulation on a second electrode in cochlear implant users. Data were collected from four post-linguistically deafened subjects using the Cochlear Limited prosthesis. Investigated were the effects of the spatial separation between test and masker electrodes, 0 to 5 electrodes (0 to 3.75 mm), and the amount of masking modulation: 24%, 48%, 72%, and 96% above detection thresholds. Initially, modulation detection thresholds for stimulation on a single electrode without masking modulation were obtained for a set of six electrodes in the middle of the array. Modulation detection thresholds on a fixed test electrode were then obtained with unmodulated and modulated masking on a second electrode, which was one of the six electrodes in the initial study. In both studies, thresholds were measured for modulated pulse duration at the modulation frequencies of 10–200 Hz. In the first study, the shape of the detection thresholds as a function of modulation frequency, the temporal modulation transfer function, generally resembled a low-pass filter for two subjects. For the other two subjects, the functions were relatively flat across modulation frequencies. In the second study, unmodulated masking resulted in a small elevation in detection thresholds across electrodes. Modulation detection interference (MDI), the difference between thresholds for the modulated maskers and the unmodulated masker, was greater for larger amounts of masking modulation than for smaller amounts of masking modulation. For three of the four subjects, MDI was higher for smaller spatial separations between the two electrodes than for larger spatial separations suggesting that a portion of MDI may be due to overlap of neural excitation distributions produced by stimulation on two electrodes in close proximity on the array. [S0001-4966(98)01707-X]

PACS numbers: 43.66.Ts, 43.64.Me, 43.66.Mk [JWH]

INTRODUCTION

Temporal variations in amplitude are a common feature of many complex sounds such as speech. One important measure of temporal resolution has been detection thresholds for amplitude modulated stimuli. Typically, detection thresholds have been plotted as a function of modulation frequency to form the temporal modulation transfer function. For normally hearing listeners, the transfer functions have resembled a low-pass filter with a cutoff frequency of about 70 Hz, as detection thresholds are relatively constant for modulation frequencies below about 70 Hz and then increase at 3–6 dB/oct for higher modulation frequencies (Bacon and Viemeister, 1985; Formby, 1985; Viemeister, 1979). The shape of the transfer function has, in general, been similar for normally hearing subjects and hearing-impaired listeners with cochlear losses (Bacon and Viemeister, 1985; Bacon and Gleitman, 1992; Formby, 1986).

Temporal modulation transfer functions have recently been reported for electric stimulation in post-linguistically deafened cochlear implant subjects (Busby *et al.*, 1993; Cazals *et al.*, 1994; Shannon, 1992). In these studies, modulation detection thresholds were measured using stimulation on a single electrode. Most transfer functions for electric stimulation have resembled a low-pass filter with a cutoff frequency of 50–150 Hz, which tended to be higher than that recorded for acoustic stimulation in normally hearing subjects. Also, the slope of the function at modulation frequencies above the cutoff frequency has tended to be steeper than that found for normally hearing subjects. There has been, however, some variation in the shape of the transfer function across subjects. For instance, Shannon (1992) reported some cases where the transfer function resembled a bandpass filter with cutoff frequencies of 80 and 140 Hz. Busby *et al.* (1993) reported transfer functions which were flat for one of the four post-linguistically deafened subjects tested, as the very low detection thresholds did not vary over the range of modulation frequencies tested: 4–250 Hz. Transfer functions which did not markedly vary across modulation frequencies were also recorded by Cazals *et al.* (1994), although these were primarily found in cases where the detection thresholds were considerably elevated. In addition, Busby *et al.* (1993) recorded transfer functions which had an additional low-pass filter with a cutoff frequency of 4–5 Hz in two prelinguistically deafened subjects. For the third prelinguistically deafened subject tested, the transfer function resembled a filter with two pass bands at 4–5 and 100–125 Hz. Finally, it has also been shown that modulation discrimination thresholds, when using a 50% modulation reference signal, were generally similar to the modulation detection thresholds (Busby *et al.*, 1993).

For acoustic stimulation in normally hearing subjects, it has been shown that modulation detection and discrimination thresholds are elevated by the presence of a second modu-

lated signal, described by Yost and Sheft (1989) as modulation detection/discrimination interference (MDI). In general, MDI appears to be relatively unaffected by the distance between the two carrier frequencies, indicating across-channel processes unrelated to critical-band or auditory filter processing (Yost and Sheft, 1989, 1994). Similar findings have been recorded with hearing-impaired listeners with cochlear losses, suggesting that MDI is unaffected by any differences in the size of the critical-band between normally hearing and hearing-impaired subjects (Grose and Hall, 1994). Evidence for across-channel processing also comes from dichotic studies, where thresholds were elevated when the test and masker signals were presented to opposite ears. These dichotic MDI effects, however, have generally been less than those for monotic presentations (Bacon and Opie, 1994; Mendoza *et al.*, 1995b; Yost and Sheft, 1990). Furthermore, Sheft and Yost (1997) examined MDI under a variety of dichotic conditions and found that although binaural stimulus parameters can affect MDI, the amount of reduction in interference due to variations in these parameters would not be substantial. These studies suggest that MDI possibly arises from some form of perceptual grouping or fusion of the test and masker modulations, presumably located central to the peripheral auditory filters. Consequently, a number of studies have examined whether MDI is influenced by variations in the degree of similarity between the test and masker signals. For instance, it appears that phase differences between the modulated signals do not markedly influence MDI (Bacon and Konrad, 1993; Moore *et al.*, 1991; Moore and Shailer, 1994; Yost and Sheft, 1989, 1994). Similarly, it appears that the amount of MDI reduces with increases in the difference between the modulation frequencies of the test and masker, although the effect was relatively broad (Bacon and Opie, 1994; Yost *et al.*, 1989). Also, the degree of similarity in envelope patterns for noise modulated maskers has only minimal effects on MDI (Moore *et al.*, 1995).

There has been, however, some evidence suggesting that within-channel processes may influence MDI in some instances. Some studies have shown that the amount of MDI increases as the difference between the test and masker carrier frequency decreases (Mendoza *et al.*, 1995b; Yost and Sheft, 1989). In addition, there has been a tendency for the amount of MDI to be greater for masking carrier frequencies above the test carrier frequency than for masking carrier frequencies below the test carrier frequency (Bacon and Moore, 1993; Mendoza *et al.*, 1995b). These effects have been partially attributed to within-channel processes such as peripheral interactions on the high-frequency side of the excitation pattern produced by the test signal. Note that the frequency proximity effects have also been recorded using contralateral maskers, suggesting that across-channel processes also contributed to MDI in these cases (Mendoza *et al.*, 1995b).

The purpose of this study using electric stimulation in cochlear implant subjects was to determine whether detection thresholds for a modulated signal on a single electrode are elevated by unmodulated and modulated masking signals on a separate electrode on the electrode array. The subjects were implanted with the Cochlear Limited multiple-electrode prosthesis. Investigated were the effects of the amount of masking modulation and the spatial separation between the two electrodes. It was hypothesised that since an important factor influencing MDI appears to be across-channel processes which are primarily independent of peripheral neural excitation sites in the cochlea, then the results for electric stimulation may be similar to those found for acoustic stimulation. However, the peripheral excitation processes for electric stimulation markedly differ from those for acoustic stimulation. One important difference is that neural excitation distributions produced by electric stimulation in the cochlea are considerably larger than those produced by acoustic stimulation. Therefore, it is possible that MDI for electric stimulation may show a greater influence of within-channel processes than acoustic stimulation.

Indirect evidence of the size of the neural excitation distributions produced by electric stimulation using the Cochlear Limited prosthesis has been shown in studies of loudness summation and forward masking (Lim *et al.*, 1989; Tong and Clark, 1986). Tong and Clark (1986) reported that loudness summation increased in an orderly manner with increases in spatial separation between two electrodes of 0 to 4 electrodes (0 to 3 mm) while loudness summation was complete for larger spatial separations of 5 to 8 electrodes (3.75 to 6 mm), suggesting very little overlap in the neural excitation distributions at these larger spatial separations. The results of a forward masking study with one of these two subjects were consistent with the loudness summation data in that the amount of masking decreased with increases in spatial separation between the masker and probe electrodes. In a separate study of forward masking in one subject, Lim *et al.* (1989) also showed a decrease in the amount of masking as the spatial separation between masker and probe electrodes was increased, and the amount of masking decreased more rapidly in an apical direction from the masker electrode than in a basal direction. In addition, both the amount of masking and the spread of the neural excitation increased with increases in the electric stimulation level of the masker. Therefore, it is possible that broad neural excitation patterns may be produced by both unmodulated and modulated maskers presented at suprathreshold levels, and that MDI may vary as a function of the amount of modulation masking and spatial separation between the masker and test electrodes.

I. METHOD

A. Subjects and electric stimulation hardware

A summary of the histories of the four postlinguistically deafened subjects is shown in Table I. Prior to implantation, all subjects had a profound-to-total bilateral sensorineural hearing loss. During surgery, the 22 electrode array of the Cochlear Limited prosthesis was successfully inserted into the scala tympani and the receiver–stimulator package was placed in the temporal bone (Clark *et al.*, 1987). Power and data were delivered via an external induction coil. The subjects were selected on the basis of their availability for this study and all have participated in previous psychophysical studies.

The residual auditory neurons were stimulated using biphasic pulses with the same electric current and pulse dura-

TABLE I. Summary of subject histories.

Subject	Age (years)	Age at confirmation of profound-to-total hearing loss (years)	Cause of deafness	Duration of implant use (years)
P1	64.3	46	acoustic trauma	12.7
P2	51.1	27	acoustic trauma	6.9
P3	49.5	41	unknown progressive and acoustic trauma	7.5
P4	58.8	35	otosclerosis	7.2

tion in the two phases. Bipolar stimulation was used for all subjects and was produced by passing an electric current between two electrodes separated by one electrode for P2, two electrodes for P1 and P4, and three electrodes for P3. These bipolar modes of stimulation correspond to ''BP+1,'' ''BP+2,'' and ''BP+3'' in the Cochlear Limited clinical procedures, respectively. It was necessary to use the wider bipolar modes so that the current levels were well within the operating range of the prosthesis when using a pulse duration of 100 μs/phase. The term ''electrode'' describes the basal member of the bipolar pair, and electrodes were numbered 22-1 in an apical-basal direction, consistent with the Cochlear Limited notation.

B. Procedure

Two studies were conducted. The first study measured detection thresholds for modulated pulse duration on a single electrode without masking modulation on a second electrode. Data were collected for a series of six electrodes in the middle of the array, electrodes 10, 11, 12, 13, 14, and 15. The second study measured detection thresholds for modulated pulse duration on a test electrode (electrode 10) with unmodulated and modulated masking on one of a series of second electrodes (electrodes 10 to 15). In both studies, detection thresholds were measured for the modulation frequencies of 10, 20, 50, 75, 100, 150, and 200 Hz. All stimuli were 500 ms in duration and the pulse rate was 600 pulses/s. This pulse rate was used to ensure that stimulation using two electrodes (study 2) was within the hardware limits of the Cochlear prosthesis. Note that it was not possible to use modulation frequencies higher than 200 Hz because of the limitations imposed by using pulsatile stimulation. For the modulation frequency of 200 Hz, the modulation period was equal to only three pulses at 600 pulses/s. Pulse duration was modulated rather than current amplitude as finer control of stimulus charge is achieved by using pulse duration. Also, previous studies of modulation detection for cochlear implant subjects have reported a similar pattern of results to normally hearing subjects when using modulated pulse duration (Busby *et al.*, 1993; Shannon, 1992).

In the first study, which measured detection thresholds for modulated pulse duration on a single electrode, the reference stimulus was an unmodulated signal with a pulse duration of 100 μs/phase and the comparison stimulus was a sinusoidally modulated signal around the reference pulse duration of 100 μs/phase. The modulating sinusoid started at the reference pulse duration in a positive-going direction. A schematic example of the stimuli is shown in Fig. 1(A), where the modulation frequency of the comparison is 75 Hz and the modulation depth is 48 μs/phase. The depth of modulation on the comparison stimulus was adaptively varied to obtain the detection threshold. The current level for each electrode was adjusted to a comfortable listening level using a single-interval ascending–descending technique (Busby *et al.*, 1994). These levels were obtained using an unmodulated signal with a pulse duration of 100 μs/phase. Current was increased until stimulation became too loud or uncomfortable, and it was then decreased to a comfortable listening level.

The second study measured detection thresholds for modulated pulse duration on the test electrode (electrode 10) with unmodulated and modulated masking on a second electrode. The reference stimulus was an unmodulated signal with a pulse duration of 100 μs/phase on the test electrode, and an unmodulated or sinusoidally modulated signal around the reference pulse duration of 100 μs/phase on the masker electrode. The comparison stimulus was a sinusoidally modulated signal around the reference pulse duration of 100 μs/phase on the test electrode, and an unmodulated or sinusoidally modulated signal around the reference pulse duration of 100 μs/phase on the masker electrode. The modulation frequencies on the test and masker electrodes were the same and in phase. In the schematic example shown in Fig. 1(B), the modulation frequency is 75 Hz, the masking modulation depth is 72 μs/phase, and the modulation depth on the test electrode in the comparison is 48 μs/phase. The depth of modulation on the test electrode in the comparison stimulus was adaptively varied to obtain the detection threshold. Nonsimultaneous stimulation was used where interleaved pulses were delivered to each electrode at 600 pulses/s, giving a total pulse rate of 1200 pulses/s. The leading electrode was the test electrode (electrode 10).

The masking electrode was one of the series of electrodes used in the first study: electrodes 15 to 10. Therefore, the spatial separations between the two electrodes corresponded to 5 to 0 electrodes (3.75 to 0 mm). The masker electrodes were apical to the test electrode as the forward masking study by Lim *et al.* (1989) indicated that the overlap in neural excitation distributions decreased more rapidly in the apical direction than in the basal direction. The inclusion of the unmodulated masker was to measure the amount of masking produced by stimulation on the second electrode which was unrelated to the modulation. Data were collected for four depths of masking modulation: 24%, 48%, 72%, and 96% above the modulation detection thresholds, as determined in the first study. The actual depth of masking modu-

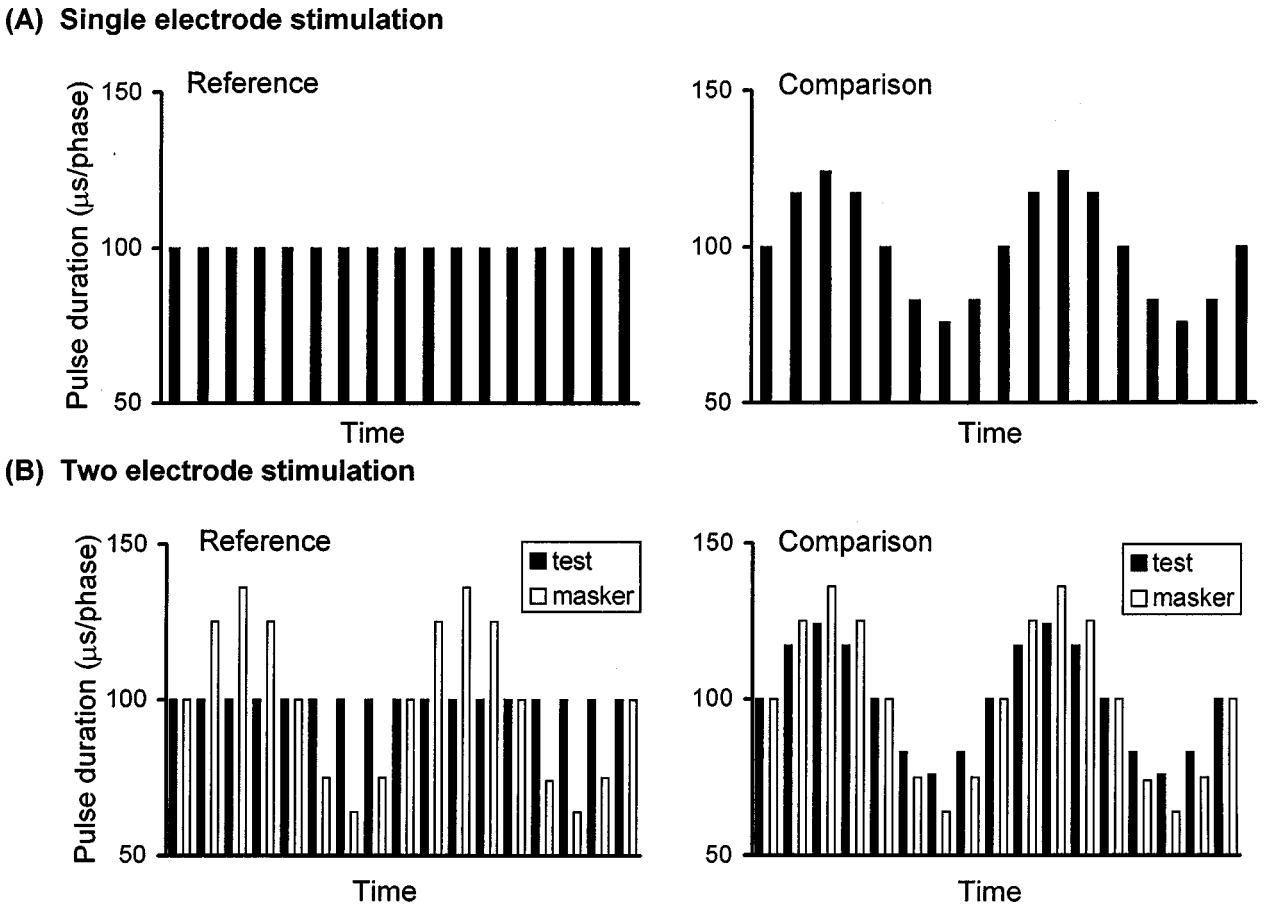

FIG. 1. Schematic examples of the stimuli. (A) Shows the reference and comparison stimuli for single electrode stimulation. Shown are 600 pulses/s stimuli with no modulation in the reference stimulus and two cycles of a 75-Hz modulated signal, with a modulation depth of 48 μs/phase, in the comparison stimulus. (B) Shows the reference and comparison stimuli for two electrode stimulation. The test electrode is unmodulated in the reference stimulus and modulated, using a 75-Hz modulation at a depth of 48 μs/phase, in the comparison stimulus. The masking modulation on the masker electrode has the same modulation frequency (75 Hz) and modulation depth (72 μs/phase) in the reference and comparison stimuli.

lation, therefore, varied for each of the different electrodes and modulation frequencies used because thresholds were not equal across electrodes and modulation frequencies. These percent depths of modulation were selected so that they were integer multiples of 0.8 μs/phase, which was the smallest unit size of pulse duration used in this study.

Initially, data were collected at all spatial separations using the unmodulated and the 24% modulation maskers. However, it was not possible to collect data for all combinations of spatial separations and depths of modulation because of time limitations for subject testing. For the larger modulation depths (48%, 72%, and 96%), data were collected for the spatial separations of 0, 1, 3, and 5 electrodes (0, 0.75, 2.25, and 3.75 mm).

The current levels for the two electrodes were adjusted to a comfortable listening level using the method described by Tong and Clark (1986). Initially, the current levels for each electrode were set at the comfortable listening levels used in the first study. When using a modulated masker, the current level on the masker electrode was reduced so that the loudness of the test and masker electrodes, when stimulated separately, were the same. The reduction in current levels when modulation was applied to the masker electrodes ranged from 0 to 0.28 dB across patients and electrodes, which was equivalent to 0 to 2 current level steps. These dB values were calculated using calibration tables supplied by Cochlear Limited. The reduction in current levels was generally larger for greater amounts of modulation on the masker electrode. The current levels on the test and masker electrodes were then reduced in equal steps so that the overall loudness of the two electrodes when stimulated together was at a comfortable listening level. Figure 2 shows the amount of reduction, in dB, on the test electrode (electrode 10) for the different spatial separations and amounts of masking modulation. The reductions on the masker electrodes were very similar to those on the test electrode, with minor variations in dB values due to different current levels on the different electrodes. In general, less reduction was used for masker electrodes close to the test electrode, and the amount of reduction did not essentially vary for separations of greater than 3 electrodes (2.25 mm). Note that these reductions were equivalent to 3–8 current level steps. For two subjects (P2 and P3), a greater amount of reduction was used for the larger amounts of masking modulations, above 72% for P2 and above 48% for P3. These findings were also consistent with previous results on loudness summation (Tong and Clark, 1986), as described in the Introduction.

An adaptive four-interval forced choice procedure was used to obtain the detection thresholds in both studies. Each trial consisted of four intervals separated by 500 ms. Three

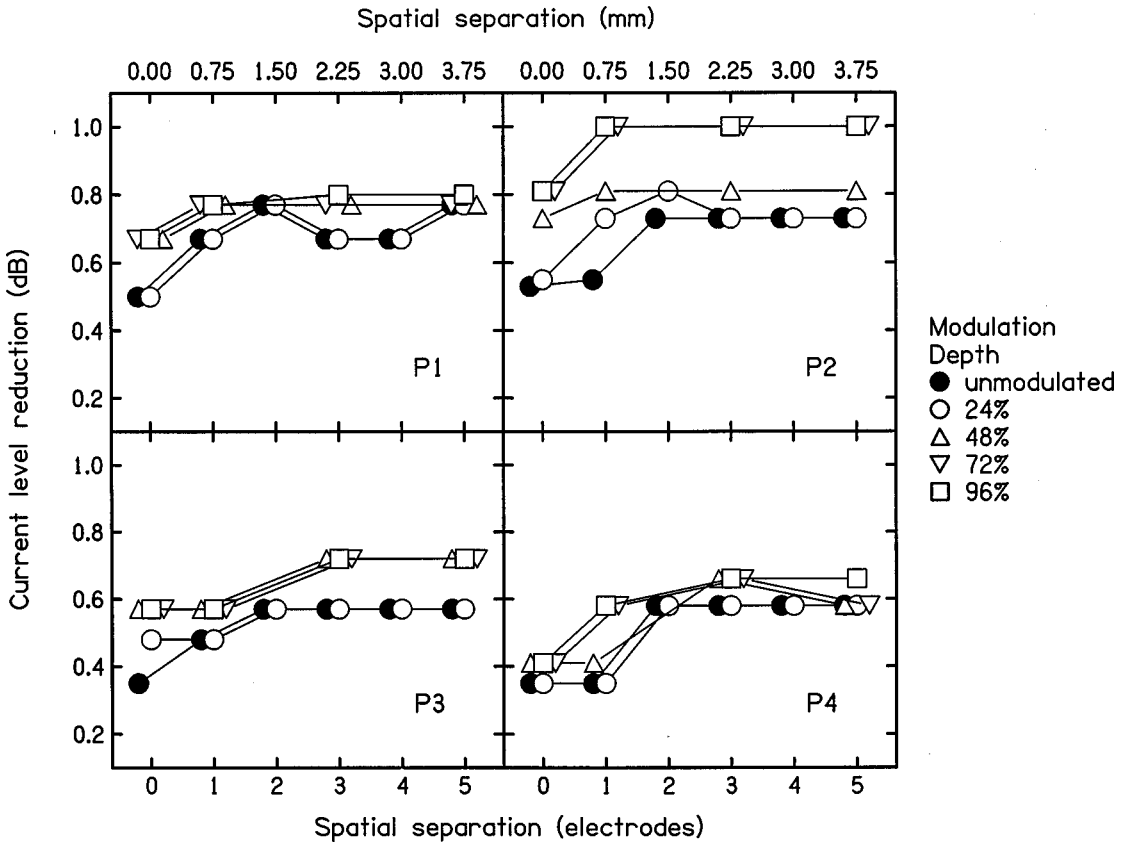

FIG. 2. The amount of reduction (dB) on the test electrode (electrode 10), when using two electrode stimulation, for different spatial separations and amounts of masking modulation.

of the intervals were the reference stimulus and one was the comparison stimulus. The interval with the comparison was randomly selected in each trial. Each interval was cued by a number (1–4) graphically displayed on a computer screen. The subject responded verbally by selecting the number corresponding to the comparison in each trial. Feedback was provided after each trial by flashing the number corresponding to the comparison on the screen. The comparison was chosen to be clearly different from the reference at the beginning of the adaptive procedure. The modulation depth of the comparison was reduced after two consecutive correct responses, increased after two consecutive incorrect responses, and remained unchanged after two consecutive trails consisting of one correct and one incorrect response. This procedure converged on the 50% correct point on the psychometric function (Busby *et al.*, 1993). The stepsize of change to the comparison modulation depth was 0.8 μs/phase for the last six reversals. Each run was terminated after ten reversals and the average of the last six was taken as the result. A single limen was obtained for each data point.

II. RESULTS

The modulation detection thresholds for stimulation on a single electrode with no masking (study 1) were generally similar for P1, P2, and P3, but were elevated for P4. There were also small, but significant, differences in thresholds across electrodes for P1 and P3 but not for P2 and P4. Figure 3 shows the detection thresholds for the six electrodes (electrodes 10 to 15) expressed as 20 log m, where m is the differential threshold/reference pulse duration (Busby *et al.*, 1993). For P1, P2, and P3, two sets of data were collected for electrodes 11 and 13. This second set of data was obtained at the conclusion of the second study to confirm the initial set. The error bars in Fig. 3 show the range of thresholds, although in a number of instances these error bars are not visible because the range was within the symbol size. For P1, P2, and P3, the average thresholds across electrodes and modulation frequencies were -40.8, -36.3, and -43.4 on the log scale, corresponding to 0.99, 1.74, and 0.72 μs/phase, respectively. For P4, the average threshold was larger, -24.7 on the log scale which corresponded to 6.55 μs/phase. As far as differences across electrodes are concerned, the data for each subject were separately submitted to a one-way analysis of variance. *Post hoc* analyses of the means using the Tukey test were used to determine which electrodes contributed to the significant effects. For P1, a significant difference ($p=0.001$) in thresholds was recorded across electrodes, which was due to poorer thresholds for electrodes 12 and 14 than for electrodes 11 and 13. These differences, however, were only 5.1 to 5.3 dB, which corresponded to 0.66 to 0.68 μs/phase. For P3, a significant difference ($p<0.001$) in thresholds was recorded across electrodes, which was due to poorer thresholds for electrodes 10 and 11 than for electrodes 14 and 15, and poorer thresholds for electrode 13 than for electrode 15. Again these differences were small, 3.4 to 6.2 dB, which corresponded to 0.27 to 0.47 μs/phase. No significant differences in thresholds across electrodes were recorded for P2 ($p=0.965$) and P4 ($p=0.068$).

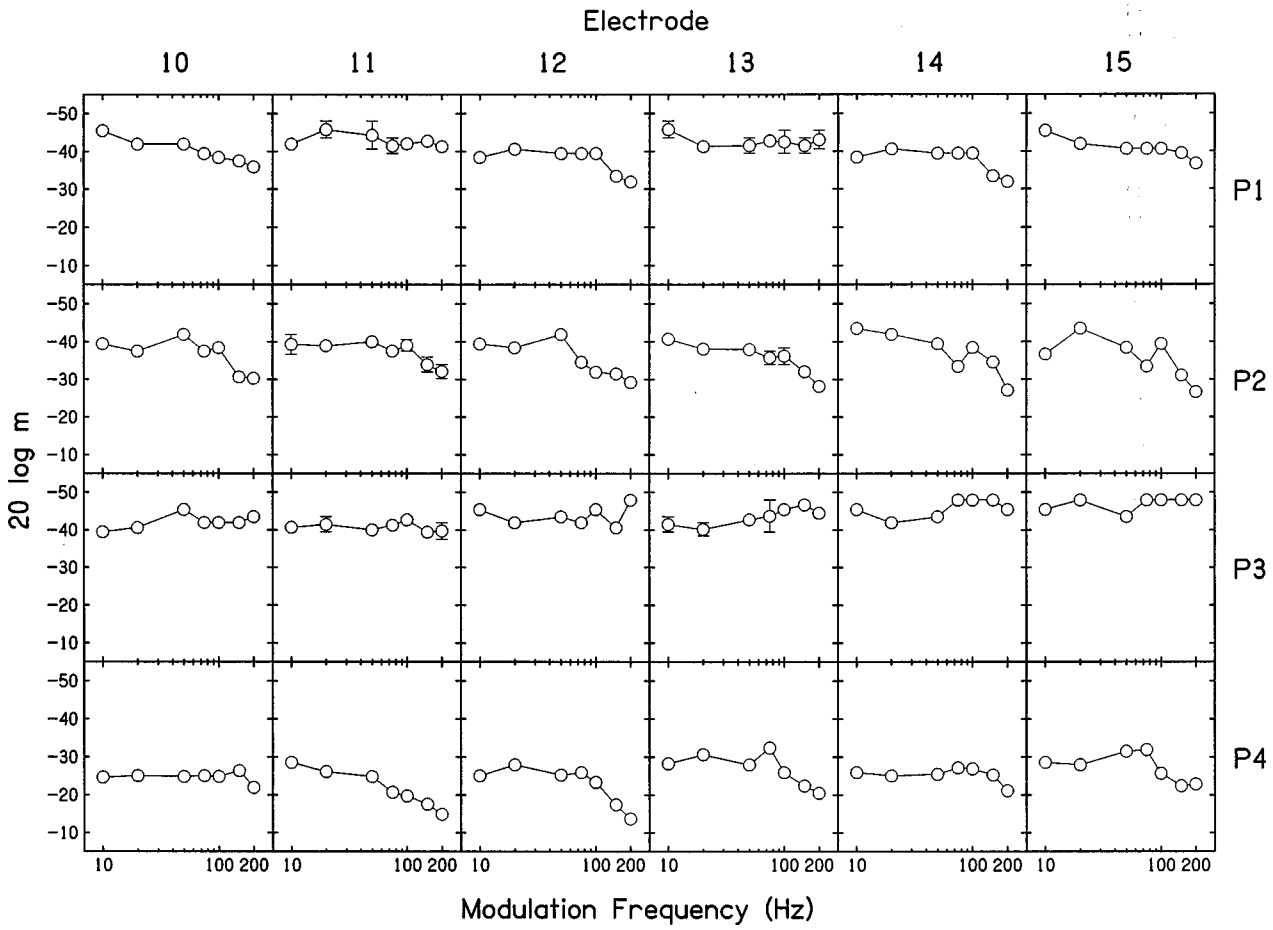

FIG. 3. Modulation detection thresholds for stimulation on a single electrode with no masking.

The shape of the threshold curve as a function of modulation frequency, the temporal modulation transfer function, resembled a low-pass filter for P2 and P4 in most instances. For P1 and P3, the functions in most cases had no clear low-pass filter shape. In those cases where there was a discernible low-pass filter shape, the cutoff frequency (3-dB-down point) was estimated using the procedure described by Shannon (1992). The location of the peak sensitivity was determined by visual inspection of the data (Fig. 3) and a linear regression line (dB×log modulation frequency axes) was fitted to the sloping portion of the transfer function. The 3-dB-down point from peak sensitivity was calculated from the regression line. The average 3-dB-down point was 103.6 Hz (s.d.=26.2 Hz) across patients and electrodes.

Figure 4 shows the modulation detection thresholds for stimulation on the test electrode (electrode 10) with the unmodulated and 24% modulation maskers on the second electrode (study 2), in addition to the detection thresholds for electrode 10 with no masking on the second electrode (study 1). To determine whether thresholds varied across the three conditions shown in Fig. 4, the data for each subject and electrode were separately analysed using a one-way analysis of variance. *Post hoc* analyses of the means using the Tukey test were used to determine which conditions contributed to the significant effects. The three types of significant differences ($p<0.05$) recorded were: thresholds all three conditions were different from each other and ordered from unmasked, unmodulated masker, and 24% modulation masker (UM$<$0$<$24); the masked thresholds were poorer than the unmasked thresholds but there was no difference between thresholds for the unmodulated and 24% modulated maskers (UM$<$0,24); and thresholds for the 24% modulated masker were poorer than the unmasked thresholds (UM$<$24). Nonsignificant differences ($p>0.05$) were recorded on three electrodes for P4 (n.s.).

The general trend was that thresholds were elevated by the presence of the unmodulated and 24% modulated maskers, with the exception of P4 (Fig. 4). For P1 and P3, masked thresholds were significantly poorer than the unmasked thresholds for all electrodes, and thresholds for the 24% modulated masker were significantly poorer than those for the unmodulated masker for three (P1) and four (P3) electrodes. For P2, masked thresholds were significantly poorer than the unmasked thresholds for three electrodes, with no significant difference between thresholds for the unmodulated and 24% modulated maskers, while for the other three electrodes, thresholds for the 24% modulation masker were significantly poorer than the unmasked thresholds. For P4, masked thresholds were significantly poorer than the unmasked thresholds at a spatial separation of 0 electrodes (0 mm), with no significant difference between thresholds for the unmodulated and 24% modulated maskers, and thresholds for the 24% modulated masker were significantly poorer than the unmasked thresholds for the two adjacent spatial

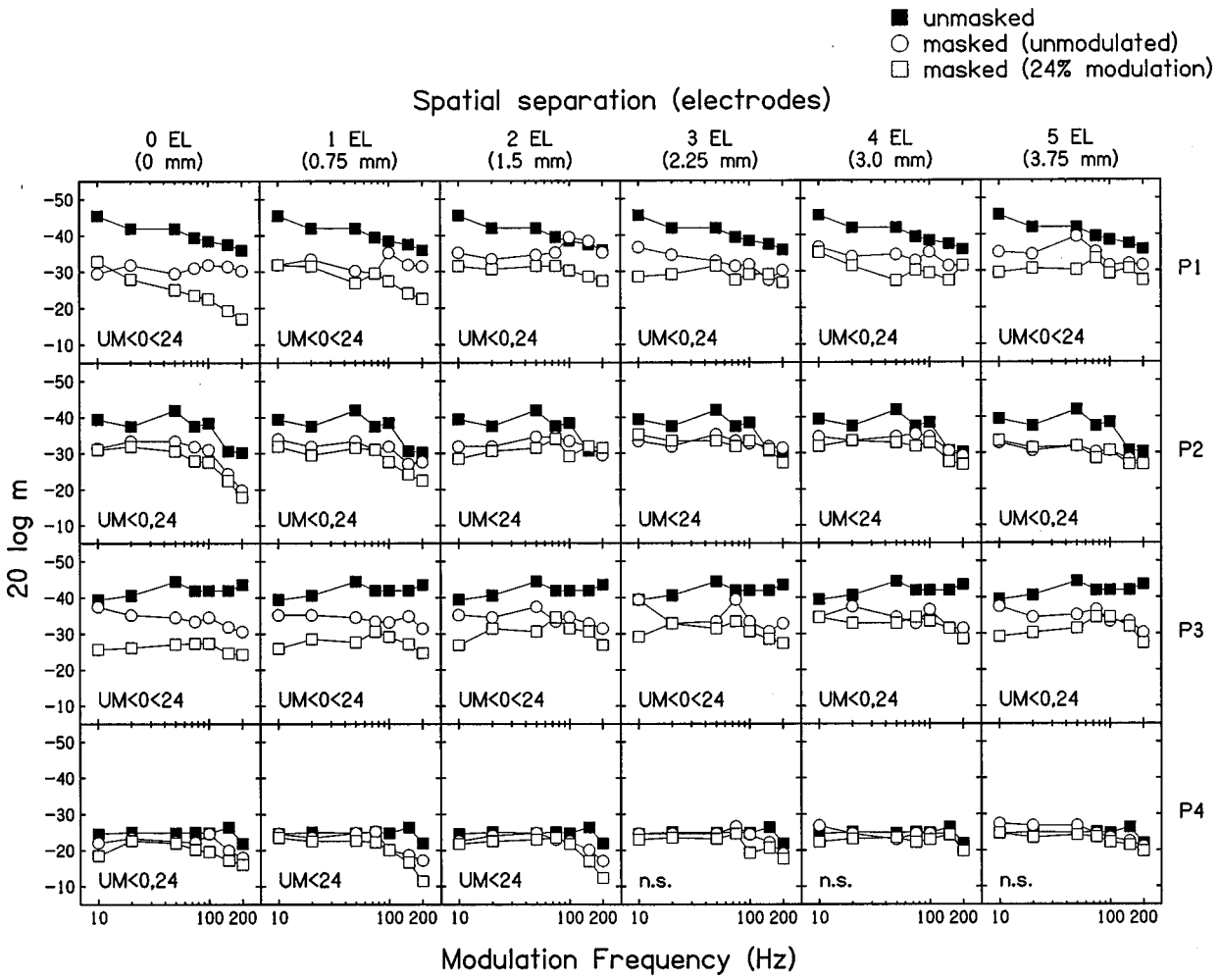

FIG. 4. Modulation detection thresholds for stimulation on the test electrode (electrode 10) with unmodulated and 24% modulation masking on the second electrode. Also shown on each graph are the detection thresholds for electrode 10 with no masking on the second electrode.

separations, 1 and 2 electrodes (0.75 and 1.5 mm). At larger spatial separations for P4, there were no significant differences in thresholds across modulation conditions. Differences in the mean elevations in thresholds, averaged across modulation frequencies and spatial separations, were consistent with these findings. The mean elevations due to the presence of the unmodulated masker were larger for P1 and P3 than for the other two subjects, with the smallest elevation for P4: 7.0 dB for P1, 5.0 dB for P2, 7.9 dB for P3, and 1.6 dB for P4. The mean elevations due to the 24% modulation masker were 11.6 dB for P1, 6.5 dB for P2, 12.3 dB for P3, and 3.4 dB for P4.

Figure 5 shows the mean threshold elevation and MDI values, averaged across modulation frequencies, for each subject and spatial separation between test and masker electrodes. The threshold elevation values were calculated by subtracting the masked thresholds for the unmodulated and modulated maskers (study 2) from the thresholds with no masking modulation (study 1), indicating the effects of both unmodulated and modulated masking on detection thresholds. The MDI values were calculated by subtracting the masked thresholds for the modulated maskers (24% to 96% modulation) from the masked thresholds for the unmodulated masker (study 2), indicating the effects of masking by modulated signals on detection thresholds, and is equivalent to MDI reported for acoustic stimulation (Yost and Sheft, 1989). The values on 20 log *m* scale were used in these calculations. Note that there were no consistent differences in the threshold elevation and MDI values related to modulation frequency.

In order to determine whether the threshold elevation and MDI values differed across spatial separations and masking modulation depths, the data for each subject were separately analysed using a two-way analysis of variance. In these analyses, data for the unmodulated and 24% modulation maskers at the spatial separations of 2 and 4 electrodes (1.5 and 3.0 mm) were excluded as there were no corresponding data for the 48% to 96% modulation maskers. Significant differences ($p<0.001$) were recorded for the main effects of spatial separation and masking modulation depth in almost all cases, the one exception was the MDI data for P4 where there was no significant difference ($p=0.791$) between spatial separations. In addition, significant interactions ($p<0.008$) between spatial separation and masking modulation depth were recorded for P1, P2, and P3 in the threshold elevation data, and P2 in the MDI data. *Post hoc* analyses of the means using the Tukey test were used to determine which modulation depths and spatial separations contributed

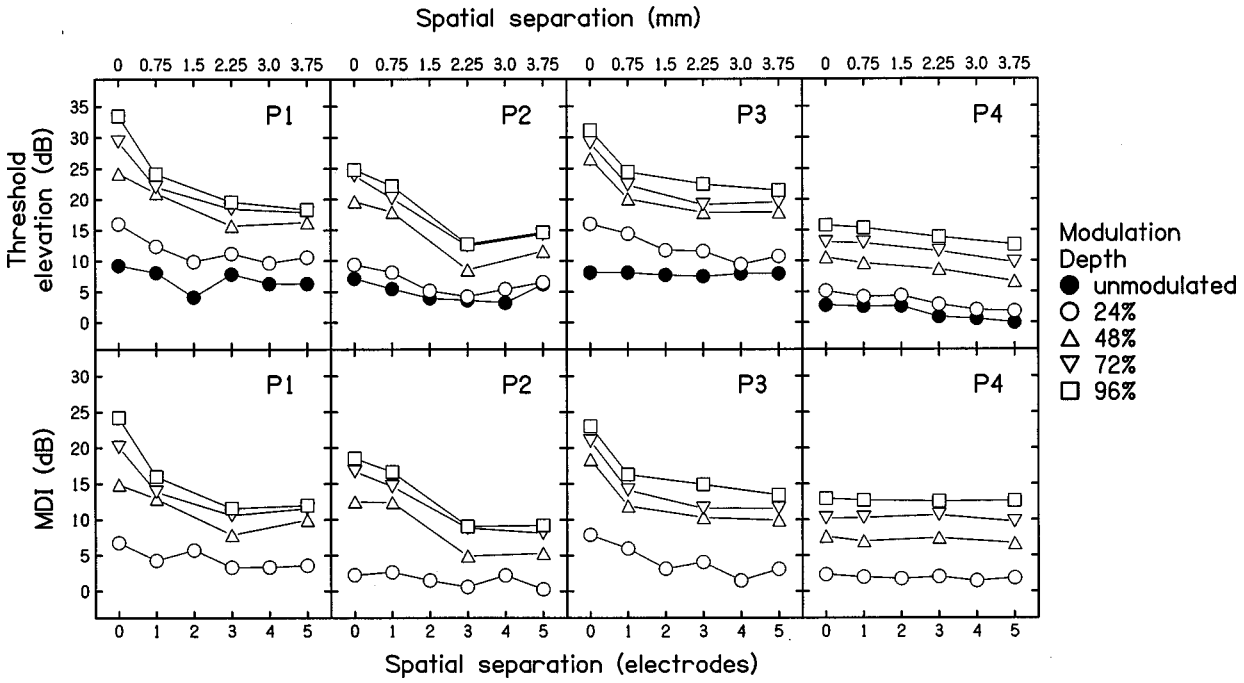

FIG. 5. Mean threshold elevation and MDI values. Data were averaged across modulation frequencies for each subject and spatial separation. The threshold elevation values were calculated by subtracting masked thresholds (unmodulated and modulated) from the unmasked thresholds. The MDI values were calculated by subtracting the masked thresholds for the modulated maskers from the masked thresholds for the unmodulated masker.

to these significant effects, using a $p<0.05$ criterion.

For all four subjects, threshold elevation and MDI values were higher for larger amounts of masking modulation, 48% and above, than for smaller amounts, less than 24%. In general, there were no differences in threshold elevation and MDI values between the unmodulated and 24% modulation maskers, and between the 72% and 96% modulation maskers. Threshold elevation values for the unmodulated and 24% modulation maskers were not significantly different from each other with two exceptions, P1 and P3 at a spatial separation of 0 electrodes (0 mm). With four exceptions, the threshold elevation values for the 48% modulation masker were significantly higher than those for the unmodulated and 24% modulation maskers. These exceptions were P2 at spatial separations of 3 and 5 electrodes (2.25 and 3.75 mm), where there were no significant differences between values for the unmodulated, 24%, and 48% modulation maskers. Also for P1 and P3 at a spatial separation of 3 electrodes (2.25 mm) and P3 at a spatial separation of 1 electrode (0.75 mm), there were no significant differences between values for the 24% and 48% modulation maskers. Threshold elevation values for the 48% modulation masker were not significantly different from those for the 72% and 96% modulation maskers, with two exceptions. These were for P1 at a spatial separation of 0 electrodes (0 mm), where the values for the 96% modulation masker were significantly higher than those for the 48% modulation masker, and for P4, where the values for 48%, 72%, and 96% modulation maskers were all significantly different from each other. Threshold elevation values were significantly higher for the 72% and 96% modulation maskers than for the unmodulated and 24% modulation maskers in all instances.

The pattern of results was generally similar for the MDI values. For all subjects, values for the 72% and 96% modulation maskers were significantly higher than those for the 24% modulation masker. Note that values for the 96% modulation masker were significantly higher than those for the 48% modulation masker in all cases, differing from the findings for the threshold elevation values. There were also some additional individual differences in the MDI data. For P2 at the spatial separations of 0 and 3 electrodes (0 and 2.25 mm), values for the 72% modulation masker were significantly higher than those for the 48% modulation masker. For P4, values for the 96% modulation masker were significantly higher than those for the 72% modulation masker, and values for the 72% modulation masker were significant higher than those for the 48% modulation masker.

As far as differences in threshold elevation and MDI values as a function of spatial separation are concerned, values for the 48% to 96% modulation maskers were generally higher for smaller spatial separations than for larger separations (Fig. 5). The exception was for P4, where there were no significant differences in MDI values across spatial separations. Visual inspection of the data and the results of the statistical analyses suggested that the effects of spatial separation on threshold elevation and MDI values mainly differed for the 48% to 96% modulation maskers. For these larger modulation maskers, there was an initial rapid decrease in threshold elevation and MDI values with increases in spatial separation, followed by minor variations in values for larger spatial separations. The location of this ''knee-point'' was at a spatial separation of 1 electrode (0.75 mm) for P1 and P3, and at 3 electrodes (2.25 mm) for P2. Using data for 96% modulation masker, the mean increase in MDI values between the knee-point and a spatial separation of 0 electrodes was 8.1 dB, averaged across P1–P3 with a range

of 6.7 to 9.5 dB. For P4, there was a gradual decrease in threshold elevation values with increases in spatial separation.

In the case of threshold elevation values for P1, P2, and P3, there were no significant differences across spatial separations for the unmodulated and 24% modulation maskers. For larger amounts of modulation masking for these three subjects, threshold elevation values at spatial separations less than the knee-point were significantly higher than those at spatial separations equal to and greater than the knee-point, and values at spatial separations equal to and greater than the knee-point were typically not significantly different. For example, in the results for P3 at the 48%, 72%, and 96% modulation maskers, there were significant differences between the spatial separations of 0 and 1 electrode (0 and 0.75 mm), 0 and 3 electrodes (0 and 2.25 mm), and 0 and 5 electrodes (0 and 3.75 mm). There were no significant differences between the spatial separations of 1, 3, and 5 electrodes (0.75, 2.25, and 3.75 mm). Therefore, the knee-point for P3 was at a spatial separation of 1 electrode (0.75 mm). The knee-points for P1 and P2 were at the spatial separations of 1 and 3 electrodes (0.75 and 2.25 mm), respectively. For P4, there was a gradual reduction in threshold elevation values with increases in spatial separation, where values for the spatial separation of 0 electrodes (0 mm) were significantly higher than those for the separations of 3 and 5 electrodes (2.25 and 3.75 mm), and the values for the spatial separation of 1 electrode (0.75 mm) were significantly higher than those for the spatial separation of 5 electrodes (3.75 mm).

For the MDI values, visual inspection of the data suggested that the effects of spatial separation were very similar to those for the threshold elevation data. However, it was not possible to statistically determine the locations of the knee-points for the different modulation maskers as there were no significant interactions between spatial separation and masking modulation depth, the one exception was for P2. For this subject, the location of the knee-point was at a spatial separation of 3 electrodes (2.25 mm), the same spatial separation as was found in the analysis of the threshold elevation data. For P1 and P3, values across all modulation maskers for the spatial separation of 0 electrodes (0 min) were significantly higher than those for spatial separations of 1, 3, and 5 electrodes (0.75, 2.25, and 3.75 mm) and there were no significant differences in values for these three larger spatial separations, with two exceptions. For P1, the values at the spatial separation of 1 electrode (0.75 mm) were significantly higher than those at the spatial separation of 3 electrodes (2.25 mm), while for P3, values at the spatial separation of 1 electrode (0.75 mm) were significantly higher than those at the spatial separation of 5 electrodes (3.75 mm). This suggested a knee-point at a spatial separation of 1 electrode (0.75 mm) for these two subjects, consistent with the findings for the threshold elevation data. For P4, there were no significant differences in MDI values across spatial separations.

Figure 6 shows the mean threshold elevation (upper graph) and MDI (lower graph) values, averaged across subjects. The threshold elevation values were averaged across all spatial separations as there were no significant differences related to spatial separation, giving a mean value of 5.75 dB.

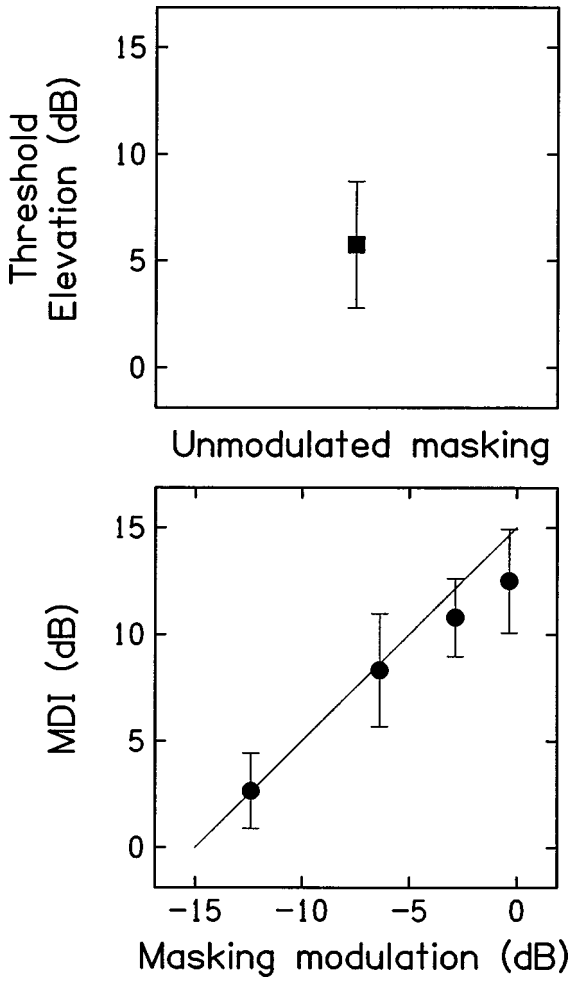

FIG. 6. Mean threshold elevation (upper graph) and MDI (lower graph) values. Data were averaged across subjects and nonsignificant spatial separations. In the case of threshold elevation values, all spatial separations were included as there were no significant differences across spatial separations. For MDI values, these were averaged across those spatial separations at the knee-point and greater to show MDI with a minimal influence of spatial separation.

The MDI values were averaged across those spatial separations at the knee-point and greater in order to show MDI with minimal influences of spatial separation. The masking modulation depths (24% to 96%) have been converted to dB to show the growth of MDI as a function of dB masking modulation. The solid line in the lower graph indicates a linear relationship between masking modulation and MDI. The average MDI data from our subjects lies close to this line except at the higher masking modulations, 72% and 96%, where the increase in MDI was less than the increase in masking modulation.

III. DISCUSSION

The absolute modulation detection thresholds for stimulation on a single electrode, without the presence of masking modulation (Fig. 3) were similar to those reported by Shannon (1992) and Busby *et al.* (1993) but tended to be better than those reported by Cazals *et al.* (1994), indicating some between-subject, and possibly across-device, variability in modulation detection thresholds. Also, there were minor but

significant differences in threshold values across electrodes for two of our subjects. These differences, however, may not be of any marked importance as they were between 0.27 and 0.68/μs phase, which was within the step size of the adaptive procedure (0.8 μs/phase). It is possible that these differences may be related to differences in the size of the dynamic range, as seen in some of the data from Shannon (1992), although this was not investigated in our study. In further studies, it would be useful to examine the relationships between modulation detection thresholds, the size of the dynamic range, and the location of the stimulated electrode. For two of the subjects, the shape of the transfer functions generally resembled a low-pass filter, while for the other two subjects, there was no clear low-pass filter shape for most electrodes. The average 3-dB-down point, 103 Hz, was lower than that reported by Shannon (1992), 149 Hz, but was within the range of values recorded, 79–250 Hz.

In general, modulation detection thresholds were elevated by the presence of unmodulated and modulated maskers, and masked thresholds increased with increases in the amount of masking modulation (Fig. 6). The mean elevation in thresholds due to the unmodulated masker, averaged across subjects and spatial separations, was 5.75 dB. This was greater than that found for acoustic stimulation in normally hearing subjects, which has generally not exceeded 3 dB (Bacon and Moore, 1993; Bacon and Opie, 1994; Bacon *et al.*, 1995; Mendoza *et al.*, 1995b; Yost and Sheft, 1990; Yost and Sheft, 1994). Using the averaged data beyond the knee-points in the masking profiles (Fig. 6), the amount of MDI for electric stimulation was similar to that for acoustic stimulation. For 96% modulation masking, the mean MDI value using electric stimulation was 12.5 dB, which was within the range recorded using acoustic stimulation for 100% modulation masking, 6 to 16 dB (Bacon and Konrad, 1993; Bacon and Opie, 1994; Grose and Hall, 1994; Hall and Grose, 1991; Mendoza *et al.*, 1995b; Yost and Sheft, 1989). Also, the increase in MDI from 24% to 96% masking modulation was 9.9 dB using electric stimulation (Fig. 6), which was at the upper limit of the range recorded for acoustic stimulation, 4 to 10 dB for an increase in masking modulation from 25% to 100% (Bacon and Konrad, 1993). Mendoza *et al.* (1995a) also recorded an increase of around 7 dB as masking modulation was increased from 20% to 80%, using randomly amplitude modulated acoustic stimuli. Our findings indicate that, at least where there was a minimal influence of spatial separation, MDI for electric stimulation appears to be similar to that for acoustic stimulation. Therefore, it is possible that central mechanisms which may underlie MDI, such as perceptual grouping or fusion based on the common amplitude modulation, are unaffected by differences in the method of peripheral stimulation, electric and acoustic.

For three of the four subjects (P1–P3), there was a marked effect of spatial separation on threshold elevation and MDI values at masking modulations of 48% and greater, as values increased with decreases in the spatial separation between the test and masker electrodes (Fig. 5). An initial hypothesis was that MDI variations as a function of spatial separation could be related to the overlap of neural excitation patterns in the cochlea produced by stimulation of two sites in close proximity on the array, as shown in loudness summation and forward masking studies (Lim *et al.*, 1989; Tong and Clark, 1986). This would be roughly analogous to the within-channel effects on MDI for acoustic stimulation (Bacon and Konrad, 1993). Also, we hypothesized that broader neural excitation patterns would be produced by increases in the amount of masking modulation. The data from P1–P3 were generally consistent with these two hypotheses in that MDI increased with decreases in the spatial separation between test and masker electrodes and that this effect appeared to be greater with increases in the amount of masking. The mean increases in MDI for P1–P3 between the knee-points and a spatial separation of 0 electrodes were 6 and 8 dB, at 48% and 96%, respectively. These values were larger than the increases in MDI for acoustic stimulation between the most proximal masking signals and more distal frequencies, which have been around 1 to 5 dB for a 50% masking modulation (Bacon and Konrad, 1993; Bacon and Moore, 1993; Bacon *et al.*, 1995) and 2 to 5 dB for a 100% masking modulation (Mendoza *et al.*, 1995b; Yost *et al.*, 1989). The greater contribution of within-channel processes to MDI for electrical stimulation may be due to the larger neural excitation distributions produced by electrical stimulation, in comparison to acoustical stimulation, and thus broader neural excitation distributions produced by stimulation on two electrodes in close proximity on the array.

It would also be expected that the location of the knee-point for the threshold elevation and MDI data (Fig. 5) would be at similar spatial separations as the current level reduction data (Fig. 2), as both sets would be influenced by the extent of overlap in neural excitation patterns produced by stimulation on the two electrodes. While the knee-points in the current level reduction data were within 1 electrode of those for the threshold elevation and MDI data, there was not a one-to-one correspondence in locations. The locations of the knee points for the current level reduction data were partially influenced by the amount of masking modulation and were located at spatial separations of 1–2, 1–2, and 2–3 electrodes, for P1, P2, and P3, respectively (Fig. 2). The location of the knee-point for the threshold elevation and MDI data were at spatial separations of 1, 3, and 1 electrode for P1, P2, and P3 (Fig. 5). More importantly, there was a clear knee-point in the current level reduction data for P4 at spatial separations of 2–3 electrodes (Fig. 2), but there was no corresponding knee-point in the threshold elevation and MDI data (Fig. 5) for this subject. However, it should be noted that the current level reduction data were not equivalent to measures of loudness summation as the reductions in current level were to ensure that stimulation was not uncomfortably loud. It is likely, however, that the spread of neural excitation in the cochlea was a common mechanism in both measures, but that loudness summation would more accurately show this spread of excitation.

In addition to the lack of effect of spatial separation in the threshold elevation and MDI data for P4 (Fig. 5), the unmasked thresholds for stimulation on a single electrode were also poorer for this subject (Fig. 3), indicating a reduced sensitivity to amplitude modulation. It is possible that

the lack of any marked effects of spatial separation on threshold elevation and MDI could be related to this reduced sensitivity. For modulated maskers, the amount of modulation on the test and masker electrodes was larger for P4 than for the other three subjects, which may have produced a much greater spread of neural excitation. Thus any decrease in MDI with increases in spatial separation between test and masker electrodes may be hidden by this greater spread of neural excitation for P4.

In further studies, it would be important to examine the influences of variations in the characteristics of the masking modulations on MDI using electric stimulation. In the current study, the modulation frequency and the phase of the test and masking modulations were the same. Therefore, it would be useful to determine whether MDI would vary with differences in these modulation parameters. If MDI using electric stimulation is influenced by tuning to modulation frequency and phase, then MDI may be reduced by variations in these parameters. This would differ from findings using acoustic stimulation where modulation frequency and phase have not had marked effects on MDI (Bacon and Opie, 1994; Moore *et al.*, 1991; Yost and Sheft, 1994). It would also be important to further study the effects of overlap in neural excitation distributions produced by stimulation on two electrodes. This can be investigated by measures of MDI using masker electrodes located both apical and basal to the test electrode, to examine any asymmetry effects, and by measures of the effects of mode of stimulation, as wider modes of stimulation may produce a broader spread of MDI with respect to spatial separation. These studies, in addition to those of forward masking and loudness summation, would provide important information about the perception of complex stimulation patterns using multiple-electrode cochlear implants.

ACKNOWLEDGMENTS

This work was supported by the Research Council of Australia Special Research Centre ''The Human Communication Research Centre'' at the Department of Otolaryngology, the National Health and Medical Research Council of Australia, and the Cooperative Research Centre for Cochlear Implant, Speech and Hearing Research. The authors wish to thank Mark Harrison for technical support and staff at the Cochlear Implant Clinic at the Royal Victorian Eye and Ear Hospital for their assistance.

Bacon, S. P., and Gleitman, R. M. (**1992**). ''Modulation detection in subjects with relatively flat hearing losses,'' J. Speech Hear. Res. **35**, 642–653.

Bacon, S. P., and Konrad, D. (**1993**). ''Modulation detection interference under conditions favouring within- or across-channel processing,'' J. Acoust. Soc. Am. **93**, 1012–1022.

Bacon, S. P., and Moore, B. C. J. (**1993**). ''Modulation detection interference: Some spectral effects,'' J. Acoust. Soc. Am. **93**, 3442–3453.

Bacon, S. P., and Opie, J. M. (**1994**). ''Monotic and dichotic modulation detection interference in practised and unpractised subjects,'' J. Acoust. Soc. Am. **95**, 2637–2641.

Bacon, S. P., and Viemeister, N. F. (**1985**). ''Temporal modulation transfer functions in normal-hearing and hearing-impaired listeners,'' Audiology **24**, 117–1134.

Bacon, S. P., Moore, B. C. J., Shailer, M. J., and Jorasz, U. (**1995**). ''Effects of combining maskers in modulation detection interference,'' J. Acoust. Soc. Am. **97**, 1847–1853.

Busby, P. A., Tong, Y. C., and Clark, G. M. (**1993**). ''The perception of temporal modulations by cochlear implant patients,'' J. Acoust. Soc. Am. **94**, 124–131.

Busby, P. A., Whitford, L. A., Blamey, P. J., Richardson, L. M., and Clark, G. M. (**1994**). ''Pitch perception for different modes of stimulation using the Cochlear multiple-electrode prosthesis,'' J. Acoust. Soc. Am. **95**, 2658–2669.

Cazals, Y., Pelizzone, M., Saudan, O., and Boex, C. (**1994**). ''Low-pass filtering in amplitude modulation detection associated with vowel and consonant identification in subjects with cochlear implants,'' J. Acoust. Soc. Am. **96**, 2048–2054.

Clark, G. M., Blamey, P. J., Busby, P. A., Dowell, R. C., Franz, B. K., Musgrave, G. N., Nienhuys, T. G., Pyman, B. C., Roberts, S. A., Tong, Y. C., Webb, R. L., Kuzma, J. A., Money, D. K., Patrick, J. F., and Seligman, P. M. (**1987**). ''A multiple-electrode intracochlear implant for children,'' Acta Oto-Laryngol. **113**, 825–828.

Formby, C. (**1985**). ''Differential sensitivity to tonal frequency and the rate of amplitude modulation of broadband noise by normally hearing listeners,'' J. Acoust. Soc. Am. **78**, 70–77.

Formby, C. (**1986**). ''Modulation detection by patients with eighth-nerve tumors,'' J. Speech Hear. Res. **29**, 413–419.

Grose, J. H., and Hall, J. W. (**1994**). ''Modulation detection interference (MDI) in listeners with cochlear hearing loss,'' J. Speech Hear. Res. **37**, 680–686.

Hall, J. W., and Grose, J. H. (**1991**). ''Some effects of auditory grouping factors on modulation detection interference (MDI),'' J. Acoust. Soc. Am. **90**, 3028–3035.

Lim, H. H., Tong, Y. C., and Clark, G. M. (**1989**). ''Forward masking patterns produced by intracochlear electrical stimulation of one and two electrode pairs in the human cochlea,'' J. Acoust. Soc. Am. **86**, 971–980.

Mendoza, L., Hall, J. W., and Grose, J. H. (**1995a**). ''Modulation detection interference using random and sinusoidal amplitude modulation,'' J. Acoust. Soc. Am. **97**, 2487–2492.

Mendoza, L., Hall, J. W., and Grose, J. H. (**1995b**). ''Within- and across-channel processes in modulation detection interference,'' J. Acoust. Soc. Am. **97**, 3072–3079.

Moore, B. C. J., Glasberg, B. R., Gaunt, T., and Child, T. (**1991**). ''Across-channel masking of changes in modulation depth for amplitude- and frequency-modulated signals,'' Q. J. Exp. Psychol. **43A**, 327–347.

Moore, B. C. J., Sek, A., and Shailer, M. J. (**1995**). ''Modulation discrimination interference for narrow-band noise modulators,'' J. Acoust. Soc. Am. **97**, 2493–2497.

Moore, B. C. J., and Shailer, M. J. (**1994**). ''Effects of harmonicity, modulator phase, and number of masker components on modulation discrimination interference,'' J. Acoust. Soc. Am. **95**, 3555–3560.

Shannon, R. V. (**1992**). ''Temporal modulation transfer functions in patients with cochlear implants,'' J. Acoust. Soc. Am. **92**, 2156–2164.

Sheft, S., and Yost, W. A. (**1997**). ''Binaural modulation detection interference,'' J. Acoust. Soc. Am. **102**, 1791–1798.

Tong, Y. C., and Clark, G. M. (**1986**). ''Loudness summation, masking, and temporal interaction for sensations produced by electric stimulation of two sites in the human cochlea,'' J. Acoust. Soc. Am. **79**, 1958–1965.

Viemeister, N. F. (**1979**). ''Temporal modulation transfer functions based upon modulation thresholds,'' J. Acoust. Soc. Am. **66**, 1364–1380.

Yost, W. A., and Sheft, S. (**1989**). ''Across-critical-band processing of amplitude-modulated tones,'' J. Acoust. Soc. Am. **85**, 848–857.

Yost, W. A., and Sheft, S. (**1990**). ''A comparison among three measures of cross-spectral processing of amplitude modulation with tonal signals,'' J. Acoust. Soc. Am. **87**, 897–900.

Yost, W. A., and Sheft, S. (**1994**). ''Modulation detection interference: Across-frequency processing and auditory grouping,'' Hearing Res. **79**, 48–58.

Yost, W. A., Sheft, S., and Opie, J. (**1989**). ''Modulation interference in detection and discrimination of amplitude modulation,'' J. Acoust. Soc. Am. **86**, 2138–2147.

Amplitude and period discrimination of haptic stimuli

Martha A. Rinker and James C. Craig
Department of Psychology, Indiana University, Bloomington, Indiana 47405

Lynne E. Bernstein
House Ear Institute, Los Angeles, California 90057-1902

(Received 22 January 1997; accepted for publication 26 March 1998)

As part of a project to examine the ability of the hand to receive speech information, the present study examined subjects' ability to discriminate finger movements along the dimensions of amplitude and period (movement duration). The movements consisted of single-cycle, sinewave movements and single-cycle, cosine movements presented to the index finger. Difference thresholds were collected using an adaptive, two-interval, temporal forced-choice procedure. Amplitudes from 6 to 19 mm were examined, and the difference thresholds ranged from 10% to 18%. The thresholds were unaffected by the period of the movement. Periods from 3000 to 111 ms (0.33–9 Hz) were examined, and thresholds ranged from 6% to 16%. The thresholds were unaffected by the amplitude of the movement. Further measurements in which period was varied in the amplitude discrimination task and amplitude was varied in the period discrimination task indicated that subjects were not using peak velocity as the basis for discrimination. These measurements were collected using a display specifically designed for the examination of haptic stimulation and capable of presenting controlled patterns of movement and vibration to the fingers. © *1998 Acoustical Society of America.* [S0001-4966(98)02407-2]

PACS numbers: 43.66.Wv, 43.66.Ts [JWH]

INTRODUCTION

In determining the sensory capacity of any system, it is necessary to provide measurements of sensitivity along a number of stimulus dimensions. In haptic perception, the ability to move the fingers and to sense changes in their movement is a key aspect in the sensory and manipulative capacities of the hand. The present study examined subjects' ability to discriminate movements along the dimensions of amplitude and period for sinusoidal finger movement. In the amplitude discrimination measurements, the task was to report which of two finger movements had a larger peak-to-peak amplitude. In the period discrimination measurements, the task was to report which of the two movements had a shorter period. These amplitude and period discrimination measurements were collected using a display specifically designed for the examination of haptic stimulation and capable of presenting controlled patterns of movement and vibration to the fingers (Eberhardt *et al.*, 1994). The device was designed such that in contacting it, subjects had to actively follow the patterns of movement.

One of the most significant examples of the perceptual capacities of the hand is the use of the Tadoma method of speech communication. In Tadoma the human face serves as an active, haptic display from which an observer, typically a deaf–blind individual, receives speech information by monitoring haptic cues (predominately kinesthetic and tactile cues) and air flow generated during speech (Reed *et al.*, 1985). Tadoma users place their thumb upon a talker's lips and fan the other four fingers across the talker's face and neck. The movements of the lips and jaw as well as vibrations resulting from the production of speech are monitored using the fingers. By means of the Tadoma method, well-trained, deaf–blind individuals can comprehend slow-to-normal rates of speech (Reed *et al.*, 1982). The successful use of Tadoma demonstrates that the haptic system can process a considerable amount of information about movement and vibration.

In studying the perceptual capabilities of the hand, a major issue is the extent to which one chooses to impose movement on a passively receptive hand or allows the subject to actively explore the object or display. The question as to whether active versus passive presentation may improve perceptual abilities is a complicated one (Loomis and Lederman, 1986). In studies examining this issue, researchers have attempted to provide meaningful distinctions among the types of information available in tactile perception, movement perception, and haptic perception, which includes both tactile and movement perception. Gibson (1962, 1966) focused on the distinction between active and passive touch, emphasizing his belief that the processes of touch are different depending on the method by which the information is obtained. According to Gibson (1962), active touch provides a perception of, or information about, the object in the environment that is being touched, whereas passive touch produces a perception of the events occurring at the sensory surface of the skin. Katz (1989) also focused on the difference between active and passive touch and discussed the importance of active touch or motion of the hand and fingers in achieving the rich, complex perceptions that are possible through touch. Kalaska (1994) argued for the use of actively produced movements in the study of proprioceptive mechanisms citing evidence such as the modulation by active movements of both ascending proprioceptive signals and tactile signals (Chapman, 1994).

Although acknowledging that active movement is more characteristic of perceptual processing by the hand, researchers have an understandable need to provide precise stimulus control, not always possible with the unconstrained move-

 0001-4966/98/104(1)/453/11/$15.00

ments of the hand. Therefore there are a large number of studies that have examined sensitivity to passive movements of single joints (Clark and Horch, 1986; Hall and McCloskey, 1983; Gandevia *et al.*, 1983) and factors affecting sensitivity such as stimulus velocity (e.g., Hall and McCloskey, 1983) or selective changes in peripheral input (Clark *et al.*, 1983, 1979). At the other end of the active–passive continuum are studies in which active movements produced by the subject are the focus of investigation. Tasks such as movement reproduction and matching the position of two limbs provide information about the acuity of the actively engaged proprioceptive system (e.g., Lloyd and Caldwell, 1965). Still other studies have produced considerable information about the patterns of coordinated, active movements unconstrained by external stimuli (e.g., Schoner and Kelso, 1988).

In the present study we chose a middle ground in which the subject actively followed the movement of the device, but these movements were constrained. This choice was based in part on the capabilities of Tadoma users to understand speech. The face can be considered a display that requires the user to actively follow its movements, and the user's movements are constrained to some extent by the facial movements. A potential benefit of such a display is that it may reveal perceptual abilities not seen under passive presentation. One cost of active movement on the part of the subject is a reduction of stimulus control, and the possibility that the subject's movement may alter the movement of the display.

There have been a number of displays designed to present speech information via the skin. For the most part these displays have used arrays of stimulators applied to passive areas of skin (Weisenberger and Miller, 1987) and thus do not engage kinesthetic receptors. In a review of tactile communication of speech, Kirman (1973) pointed out that displays that present spatial patterns of stimulation to a fixed location on the skin are not taking advantage of the full information gathering potential of the hand. The spatiotemporal presentation of tactile stimulation in conjunction with the kinesthetic input that results from positional changes in the fingers provides a richer stimulation than a simple, spatial array.

To provide a more controlled source of kinesthetic and tactile stimulation and to emulate the kind of stimulation provided by the face, Tan *et al.* (1989) designed an artificial Tadoma system, a mechanical face. Using this display, they made a series of measurements of subjects' sensitivity to movements generated by the face and calculated the amount of information transmitted for various combinations of movement. When using this artificial face, the hand is positioned as it would be in natural Tadoma. Difference thresholds for displacement were measured for a number of different movements, in–out movement of the upper lip, in–out movement of the lower lip, up–down movement of the lower lip, and up–down movement of the lower jaw. The maximum displacements presented were 6 mm for upper lip in–out movement, 7 mm for lower lip in–out movement, 7 mm for lower lip up–down movement, and 24 mm for jaw up–down movement. The difference threshold was determined for each type of movement presented by itself (fixed background condition) and presented in the presence of random variations in the amplitudes of the other three types of movement (roving background condition). Weber fractions were found to be much smaller in the fixed background condition (8.3%–10.6%) as compared to the roving background condition (15.1%–46.1%).

Following up on this work, Tan (1996) developed a multifinger, positional display that presents stimulation to the thumb, index, and middle fingers. Tan demonstrated that an impressive rate of information transmission is possible using both tactile and kinesthetic stimulation. Using stimuli that consisted of combinations of low-frequency, kinesthetic stimulation (2–6 Hz) as well as tactile stimulation at middle (15–44 Hz) and high frequencies (150 and 300 Hz), Tan estimated an information transfer rate of approximately 12 bits/s, a rate that is estimated to be close to the information transfer rate achieved with the use of natural Tadoma.

Rather than focusing on the perception of movements at individual finger joints (e.g., Hall and McCloskey, 1983), the emphasis in the present study is consistent with the use of the hand in Tadoma and with Gibson's focus on the hand as a ''perceptual system'' for active touch. The nature of the display that was used in the present study required that subjects, as in the Tan (1996) study, actively and purposefully attempt to move with the movement of the display. In fact, their active involvement in following and monitoring the movement of the display was required for them to maintain contact with the display and to perform the task. Other than positioning the subject's wrist and palm on top of a hand rest, the subject's hand and fingers were not physically restrained as they followed the movement of the display. The movements produced by the observer were more complicated than single joint movements examined in many studies of kinesthesis.

A possible future use for the current display involves the presentation of motions related to the articulatory gestures associated with speech production. Using the display, representations of lip, tongue, and jaw movements or positions could be haptically monitored by a deaf or deaf–blind observer. For this reason, movement parameters for the current study were chosen to fall within the range of amplitudes and frequencies of movements associated with the articulatory gestures of speech. A number of different studies have provided measurements of jaw and lip movement resulting from very slow rates of speech to the highest repetition rate physically possible. Depending upon the articulator, the subject's task, individual differences, and so forth, some representative values of frequencies associated with speech movement ranged from 0.8 to 8 Hz and amplitudes ranged from 0.2 to 23.3 mm (Kelso *et al.*, 1985; Nelson *et al.*, 1984; Ohala, 1975). In the present study, the periods of movement ranged from 3000 to 111 ms (which correspond to frequencies from 0.33 to 9 Hz) and the amplitudes ranged from 6 to 19 mm.

The current study consisted of three experiments. Measurements were made of the difference threshold for amplitude (experiment 1) and period (experiment 2) for sinusoidal finger movements. Having established the range of difference thresholds for amplitude and period, some of the cues

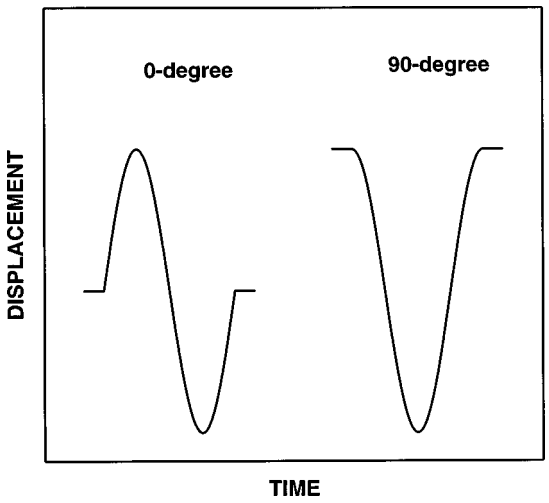

FIG. 1. The pattern of movement for the 0-degree and 90-degree waveforms. The horizontal lines before the onset and after the offset of movement show the starting displacements for the two movements.

that subjects might use in making these discriminations were examined in experiment 3.

I. GENERAL METHODS

Similar methods and testing procedures were used in all three experiments and are described below. All subjects were undergraduates selected from a pool of subjects who were paid employees of the laboratory. All subjects were right handed.

The system used to generate the finger movements consisted of a generic 486 personal computer, custom microcontroller and servoamplifier circuits, and, as actuator, the head-positioning motor from a Micropolis 1355 hard disk drive. An arm (nominally horizontal) was mounted to the motor's rotor. A 1.4×1.9-cm finger plate on which was glued a plastic washer was mounted to the distal arm end. This served as the finger rest. Rotor-to-plate separation was 9.4 cm. The plate moved primarily in the vertical direction, with a maximum plate displacement of about 5 cm. A positional error feedback servoamplifier was used to control the actuator. Absolute position was obtained by connecting the slider of a high-quality linear potentiometer (ETI LCP-12A-25) to the arm. As the motor moved, the potentiometer generated a feedback signal that caused deviations in the movement waveform (due to loading) to be compensated for by additional opposing force. Additional details of the construction and capabilities of the system may be found in Eberhardt *et al.* (1994) and Eberhardt *et al.* (1998).

Two standard waveforms were used, the ''0-degree'' and ''90-degree'' waveforms. The 0-degree waveform was one cycle of a sine function. The 90-degree waveform was one cycle of a sine function shifted 90 degrees in phase, a cosine function (as shown in Fig. 1). The amplitudes and periods tested are reported within each experiment.

In all experiments, the subjects participated in preliminary sessions in which they were familiarized with each task. Subjects practiced maintaining contact with and following the stimulator during its entire movement cycle. Subjects also had to learn to avoid applying excessive force on the contactor. When the force to the contactor exceeded the capacity of the feedback circuit to compensate, a light was illuminated. Subjects had little difficulty maintaining an appropriate amount of force against the display and following the contactor. As will be discussed, however, subjects could and did produce alterations in the amplitude of the movement. During the initial preliminary sessions, the subjects' view of the contactor was unobstructed. During subsequent testing, a curtain blocked their view of the contactor and their hands. Although no obvious sounds were generated by the stimulator, subjects wore ear plugs to eliminate any possible auditory cues.

A two-alternative, temporal forced-choice paradigm was used to determine difference thresholds. This procedure was combined with a fast adaptive procedure and converged on 71% correct performance (Levitt, 1971). For example, at the beginning of an amplitude discrimination run, the comparison stimulus was set at an amplitude level that was 40% greater than the standard amplitude. The difference between the standard and comparison amplitude was then decreased following two successive correct responses and increased following one incorrect response. An amplitude reversal of the comparison stimulus took place after either of the following sequences of responses: (1) an incorrect response following two successive correct responses or (2) two successive correct responses following an incorrect response. A block of trials was completed after 14 reversals had occurred. The initial step size, that is, the magnitude of the increase or decrease in the comparison value, was set at 6% of the standard value. After the first reversal, the step size was 4% of the standard amplitude. The step size was then reduced by half after each subsequent reversal until the value was 0.5% of the standard value. Threshold was determined by averaging the comparison amplitudes of the last ten reversals in the run.

The tracking procedure for period discrimination was similar. At the beginning of a run, the period of the comparison was 29% shorter (higher in frequency) than the standard period. The period of the comparison was increased (moved closer to the standard) following two, successive correct responses and decreased (moved further from the standard) after each incorrect trial. Step size was based on the period of the movement, using the percentages listed above for amplitude discrimination.

Subjects were seated comfortably with their right arms elevated slightly and supported by an arm rest on a table in front of them. The right index finger was placed on the contactor of the stimulator. Subjects were informed that two movements separated by 600 ms would be presented to their index finger. Depending upon the task, they were instructed to respond orally ''one'' if the first interval contained the larger movement (or shorter period) and to respond ''two'' if the second interval contained the larger movement (or shorter period). For all measurements subjects were provided with a verbal description of the task, a visual illustration of the stimuli, and sample blocks of trials (continued until the subject indicated that they understood the task). Trial-by-trial feedback was provided orally.

TABLE I. Stimulus conditions for the main sets of measurements in experiments 1 and 2.

Measurement	Discrimination	Amplitude (mm)	Period (ms)	Waveform
		Experiment 1		
Set 1	amplitude	6.3, 11.8, 19.2	1000	0-degree
Set 2	amplitude	6.3, 11.9, 19.3	1000	90-degree
Set 3	amplitude	11.9	1000, 333, 167	90-degree
		Experiment 2		
Set 1	period	11.8	3000, 1000, 333	0-degree
Set 2	period	11.8	333, 167, 111	0-degree
Set 3	period	11.9	1000, 333	90-degree
Set 4	period	6.3, 11.9	1000	90-degree

II. EXPERIMENT 1

In experiment 1, subjects' sensitivity to changes in amplitude of finger motion was examined. The experiment consisted of three sets of measurements with two different waveforms. The purpose was to obtain amplitude difference thresholds across a range both of amplitudes (sets 1 and 2) and of movement periods (set 3). For these measurements, two sinusoidal movements, differing in amplitude, were delivered to the right index finger (see Fig. 1). Subjects indicated which of the two movements had the larger amplitude. In sets 1 and 2, all movements were at a single period, 1000 ms. Each stimulus in the first set of measurements was one cycle of a sine function (0-degree waveform). Each stimulus in the second set was an offset cosine function (90-degree waveform, see Fig. 1). For the 0-degree waveform, the movement began at the point of maximum velocity in the sine function. Subjects commented that cues associated with the onset of movement such as velocity, acceleration, or jerk appeared to be useful in discriminating between the two movements. The higher amplitude stimulus, the comparison, always had the higher stimulus onset velocity, acceleration, and jerk. The 90-degree waveform, in which movement onset occurred at a point of minimum velocity, was examined to see whether onset characteristics affected performance. In set 3, a single amplitude of the 90-degree waveform was tested at three different periods of movement, 167, 333, and 1000 ms. With changes in period, a number of aspects of the waveform change such as peak velocity and acceleration. The purpose of set 3 was to determine whether sensitivity to amplitude differences remained constant across a range of periods.

A. Methods

Six subjects were tested in the first set of measurements, five in the second set of measurements, and five in the third set of measurements. Subjects were selected on the basis of availability, so that some subjects participated in more than one set of measurements. Table I shows the stimuli used in all three sets. For example, in the amplitude discrimination task of set 1, three standard amplitudes (6.3, 11.8, 19.2) were tested at a period of 1000 ms (1 Hz) using the 0-degree waveform. Due to a calibration error, the size of the two larger standard amplitudes was 0.1 mm larger for the 90-degree waveform compared to the 0-degree waveform.

For sets 1 and 2, each testing session consisted of two to three blocks of trials. Subjects completed six blocks of trials at each standard amplitude for the 0-degree waveform and four blocks of trials at each standard for the 90-degree waveform. The order of presentation varied randomly with the restriction that all three amplitudes of movement had to be presented before one of them was presented again. In set 3, each testing session consisted of two to three blocks of trials, and subjects completed seven blocks of trials at each period of movement. The order of presentation varied randomly with the restriction that all three periods of movement had to be presented before one of them was presented again.

B. Results

The results are reported both as the absolute difference between the amplitude of the standard and comparison, the difference threshold (DL), and as the relative change in amplitude (Weber fraction). The Weber fraction was calculated by dividing the DL by the standard amplitude and multiplying this value by 100 to obtain the percentage change. The upper function in Fig. 2 shows the DL for the 6.3-, 11.8-, and 19.2-mm standards from set 1. It appears that the DL increases at each successive increase in the amplitude of the standard. As would be expected from the set 1 data in Fig. 2, a two-way, repeated measures analysis of variance (amplitude×block) revealed a main effect of amplitude [$F(2,10)=13.35$, $p<0.01$]. No practice effect was found.

The results of the second set of measurements (90-degree waveform) are shown as the lower function in the upper panel of Fig. 2. The results are very similar to the 0-degree results. A two-way repeated measures analysis of variance (amplitude×block) revealed a main effect of amplitude [$F(2,8)=27.43$, $p<0.001$]. Although there was no overall effect of practice, an amplitude by block interaction reflected an improvement in the last two blocks of trials at the 19.3-mm standard [$F(6,24)=2.66$, $p<0.05$].

The fact that the absolute difference in amplitude increases as the amplitude of the standard increases suggests that subjects may be discriminating relative rather than absolute changes in amplitude. Therefore the data were replotted in the lower panel of Fig. 2 with the difference between the standard and comparison amplitudes shown as the percentage change from the standard amplitude (Weber fraction). The Weber fraction also varied as a function of amplitude, decreasing as amplitude increases. For the set 1 data, a two-way repeated measures analysis of variance

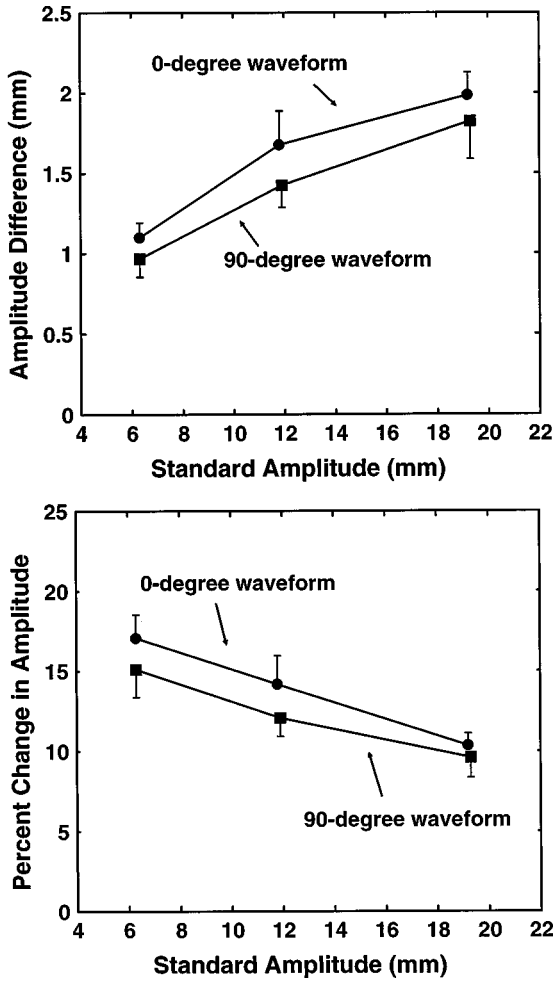

FIG. 2. The top panel shows the difference in amplitude between the standard and comparison (DL) for the 0-degree (set 1) and 90-degree (set 2) waveforms of experiment 1 as a function of the standard amplitude. The bottom panel shows the DLs replotted as Weber fractions. Error bars represent one standard error of the mean.

(amplitude×block) revealed a main effect of standard amplitude [$F(2,10)=9.60$, $p<0.01$]. The set 2 data are shown as the lower function in Fig. 2. Similar to the set 1 results, a two-way repeated measures analysis of variance revealed a main effect of amplitude [$F(2,8)=24.66$, $p<0.001$].

The difference between performance for the 0-degree and 90-degree waveforms suggests that the DL and Weber fraction may be smaller for the 90-degree waveform. However, because of subject differences and the slight difference in amplitude between 90-degree and 0-degree data sets, an additional set of measurements was conducted to compare directly performance on the two waveforms. A single, standard amplitude (11.9 mm, 1 Hz) was tested with both waveforms. Five subjects completed eight blocks of trials for each waveform. A two-way, repeated measures analysis of variance (waveform×block) showed a main effect of waveform [$F(1,4)=39.02$, $p<0.01$]. The DL and Weber fraction were larger for the 0-degree waveform (2.2 mm or 18.3%) than the 90-degree waveform (1.3 mm or 11.2%). These values can be compared to the standard amplitude of 11.9 mm shown in Fig. 2.

In set 3, the Weber fractions for the 1000-, 333-, and 167-ms periods were 12.9%, 11.8%, and 12.6%, respectively. The corresponding DLs were 1.53, 1.39, and 1.45 mm. The repeated measures analysis of variance (period ×block) on either the Weber fraction or the DL showed no main effect of either period [$F(2,8)=0.97$, $p>0.05$] or block [$F(6,24)=0.62$, $p>0.05$].

C. Discussion

The results demonstrate that subjects are able to discriminate the amplitude of actively followed movement. The range of Weber fractions across subjects and across the three standard amplitudes and across the two waveforms was 17% with a low of 5% and a high of 22%. The individual subjects in the Tan *et al.* (1989) study showed a smaller range of Weber fractions (6.1%) across subjects and across displacements with a low of 5.5% and a high of 11.6%. Tan *et al.* also reported that the Weber fraction (calculated as the displacement amplitude divided by the reference amplitude) was ''roughly independent'' of the reference displacement. Unlike their conclusion, we did not find that Weber fractions remained constant across the standard displacements. This discrepancy, however, might be accounted for by differences between the two mechanical displays, as well as the technique used to determine threshold.

Nominal (intended) amplitudes were calculated based on displacement with a 7-g, static load placed upon the contactor of the stimulator to simulate finger load. If subjects resisted the device, they could deform and reduce the amplitude of the movement. Subjects' resistance to the movement would vary the pressure exerted against their fingerpads, as well as the actual excursion of the fingerpad. To evaluate the degree that subjects altered the nominal amplitude of the movement, the feedback signal was digitized for each stimulus presentation of the 90-degree waveform in set 2. This servocontrol feedback data provided a measure of the actual excursions of the finger that were then compared to the nominal excursion.

This analysis indicated that subjects' interactions with the display added variations in the amplitude to the nominal amplitude. At smaller nominal amplitudes, this variation was proportionally larger relative to the standard as compared to the variation at the larger standard amplitudes. This proportionally larger variation may adversely affect performance to a greater extent at the smaller as compared to the larger standard amplitudes. This variation, added by the subjects, may have contributed to the rise in the Weber fraction as the standard amplitude decreased. This interpretation is consistent with the data shown in the lower panel of Fig. 2, where percent change is greater for smaller amplitudes and declines with increasing amplitude. Also, considering the addition of subject-generated ''noise'' to the stimuli, the present results provide a conservative estimate of the subjects' discrimination ability. If the amount of variability added by the subject were reduced, perhaps through extensive practice or greater resistance to positional change in the contactor, and active following was still maintained, then lower thresholds for movement may be found.

The direct comparison of the 90-degree and 0-degree waveforms using 11.9-mm, 1000-ms period movements

demonstrated that the DL was greater for the 0-degree as compared to the 90-degree waveform. All subjects showed higher average thresholds for the 0-degree waveform as compared to the 90-degree waveform. This result, which is in the opposite direction to that suggested by the subjects' comments, indicates that cues associated with onset may be potent stimuli, but may in fact, be detrimental to performance. Although testing at a wider range of amplitudes and frequencies is needed before a firm conclusion can be drawn, the present data offer no evidence that onset cues aid discrimination. As noted in the previous paragraph, subjects' interactions with the display added variations in amplitude to the nominal amplitude. An interesting possibility, not explored in the current measurements, is that differences in performance between the 0-degree and 90-degree waveforms might be related to differential interactions with the display.

The amplitude discrimination results of set 3 showed that across the three periods of movement tested (1000, 333, 167 ms) sensitivity to changes in amplitude was independent of the period of movement. Rabinowitz (1993), testing a substantially larger range of frequencies (2–32 Hz), did report a slight decrease in the JND for amplitude discrimination with increasing frequency. In the present study changing the period from 1000 to 167 ms changes a number of cues that could affect sensitivity, such as peak velocity or acceleration, however, the DLs remained unchanged. However, it is possible that if we had tested over a larger range of periods, a decrease in the DL may have been found.

III. EXPERIMENT 2

In experiment 2 measurements were made of the DLs for period in a manner that paralleled the amplitude measurements in experiment 1. The purpose was to obtain period DLs across a range of periods (sets 1, 2, and 3), to obtain DLs across different amplitudes (set 4), and to determine whether period DLs were affected by variations in movement duration (set 5). Table I shows the stimuli used in the first four sets of measurements. In all measurements, two sinusoidal movements differing in period were delivered sequentially to the right index finger. Subjects indicated which interval they perceived to contain the shorter period of movement. As in experiment 1, two types of sinusoidal movement were presented, 0-degree (sets 1 and 2) and 90-degree (sets 3, 4, and 5). The five sets of measurements differed in the periods of the standard movements tested. In sets 1, 2, and 3 all measurements were made at a single amplitude of movement (11.9 mm). Set 4 differed from the other three sets in that a single standard period (1000 ms) was tested at two different amplitudes of movement (6.3 and 11.9 mm). With changes in amplitude, a number of aspects of the waveform change, such as peak velocity and acceleration. The purpose of set 4 was to determine whether sensitivity to period differences remained constant across different amplitudes. In a fifth set of measurements the overall duration of movement was varied to determine whether sensitivity to period differences was impaired by irrelevant variations in movement duration. In these measurements, the duration of one of the movements was lengthened randomly by increments of up to 400 ms producing a movement composed of more than a single cycle, but less than two complete cycles and thus separating period from overall duration.

A. Methods

Six subjects participated in the first set of measurements, five in the second, five in the third, five in the fourth, and six in the fifth. Subjects were selected on the basis of their availability, so that some participated in more than one of the five sets of measurements. The subjects' task was to select the temporal interval that contained the shorter-period movement. Subjects were instructed to respond ''one'' if the first interval contained the shorter-period movement or ''two'' if the second interval contained the shorter-period movement. Testing sessions consisted of two to three blocks of trials. In sets 1, 2, and 3, each standard period had to be tested before one of them could be presented again. In set 4, the two amplitudes were tested on alternating blocks of trials. The number of measurements completed at each standard period in sets 1, 2, and 3 were six, six, and five, respectively. In set 4, 15 blocks of trials were completed at each amplitude of movement.

In set 5, the overall duration of movement was changed on a random basis to examine the extent to which the DL for period was affected. Two 11.9-mm, 90-degree movements were presented on each trial. The standard period was 1000 ms. Two duration conditions, the ''single'' and the ''delta *t*'' conditions, were tested. The single condition was identical to the procedure described in the first four sets of measurements reported above, that is, each movement consisted of a single cycle of the 90-degree waveform. In the delta *t* condition, the duration of either the comparison or the standard movement was incremented by 100, 200, or 400 ms producing a movement that was longer than a single cycle but less than two complete cycles. The time increment was always added to the second interval of movement, and the placement of the standard and comparison was varied on a trial-to-trial basis such that the duration of the comparison was longer on approximately half of the trials and the duration of the standard was longer on the remaining trials. The three time increments were presented randomly on a trial-by-trial basis. Subjects were informed that an additional increment of time would be added to one of the two movements on each trial. They were instructed to respond with the interval containing the shorter period movement and ignore overall duration. After the subject responded, feedback was provided and the contactor was returned to the original starting position. Six subjects completed ten blocks of trials for each condition.

B. Results

All of the reported DLs (absolute differences in period between the standard and comparison) and Weber fractions (relative differences in period calculated by dividing the DL by the standard period and multiplying by 100 to get the percent change) are based on the movement's period. The DLs for each standard period in set 1 are shown in Fig. 3. The results of an analysis of variance were consistent with the trend shown for the set 1 data, that is, discriminability declined with increasing period. A two-way, repeated mea-

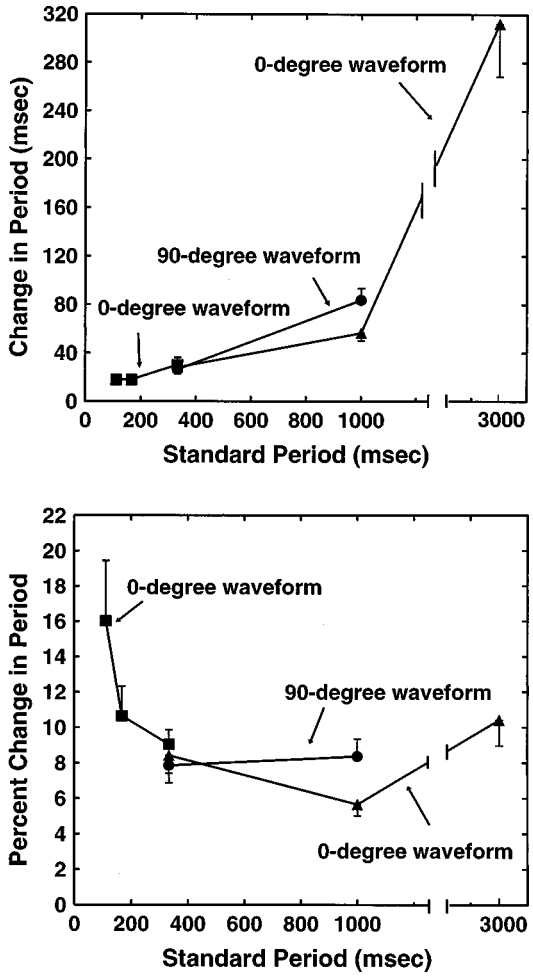

FIG. 3. The top panel shows the period difference in ms between the standard and comparison (DL) as a function of the period of the standard. The results from sets 1, 2, 3, and 4 of experiment 2 are shown. The bottom panel shows the DLs replotted as Weber fractions. Error bars represent one standard error of the mean.

sures analysis of variance (period×block) revealed a main effect of period [$F(2,19)=40.89$, $p<0.0001$]. The results from set 2 and set 3, also shown in Fig. 3, were similar to the results of set 1. The analysis of variance for set 2 (period×block) showed a main effect of period [$F(2,8)=20.57$, $p<0.001$], and the analysis of variance for set 3 (period×block) showed a main effect of period [$F(1,4)=27.82$, $p<0.01$].

As with the amplitude data, the fact that the DL increased as the period of the standard increased suggests that subjects might be discriminating relative rather than absolute changes in period. To examine this possibility, the DLs from all three sets were replotted as Weber fractions in the lower panel of Fig. 3. The data from sets 1 and 2 present a similar picture; Weber fractions appear to change as a function of period. For sets 1 and 2, a two-way repeated measures analysis of variance (period×block) revealed a main effect of standard period [$F(2,10)=6.08$, $p<0.05$] and [$F(2,8)=16.80$, $p<0.01$], respectively. Unlike set 1, the set 3 data showed no main effect of period [$F(1,4)=0.12$, $p>0.05$]. These results are, however, consistent with those found in set 1. In set 1 the percent change from the standard period showed a significant overall effect of the standard period, but a *post hoc* analysis (Tukey HSD) found no significant difference between the Weber fractions for the 1000- and 333-ms standard periods.

In set 4, the Weber fractions for the 6.3-mm and 11.9-mm movements were 9.4% and 8.0%, respectively. The corresponding DLs were 94 and 80 ms. A repeated measures analysis of variance (amplitude×block) did not show a main effect of amplitude [$F(1,4)=6.13$, $p>0.05$] or block [$F(2,14)=1.10$, $p>0.05$]. There was, however, an amplitude by block interaction [$F(14,56)=1.94$, $p<0.05$]. The Weber fraction for the 11.9-mm amplitude was consistent with the measurements in data sets 1, 2, and 3.

For set 5, the Weber fraction (and DL) in the single period condition was 7.4% (74 ms) and in the delta *t* condition was 8.6% (86 ms). A repeated measures analysis of variance (condition×block) showed no significant effect of condition [$F(9,45)=0.91$, $p>0.05$]. It should be noted that these measurements do not rule out the use of overall duration in the previous single-cycle measurements (sets 1–4) in which the overall duration and period were identical. These results suggest that when overall duration and period are not identical (set 5) subjects do not have to rely solely upon overall duration as a cue in this particular period discrimination task. These measurements do not, however, eliminate the possible use of temporal cues other than the overall duration such as the period of the movement or the time it takes for the finger to move from its highest to its lowest point.

C. Discussion

For the discrimination measure common to all three sets of data (the 333-ms standard), the Weber fractions were within 1% of each other. For the 1000-ms standard, tested in set 1 (0-degree), set 3 (90-degree), and set 4 (90-degree) performance was within 4%. The data suggest that performance on the period discrimination task is not greatly affected by the phase of the waveform. The Weber fractions measured here tended to increase as the period became shorter. Rabinowitz (1993) reported that the Weber fraction (delta f/f) was ''roughly 0.1'' at frequencies of 4 and 8 Hz. Within the range common to the measurements of Rabinowitz, the current difference thresholds are quite similar. Although Rabinowitz did not find a change in the Weber fraction up to 8 Hz, it is possible that at higher frequencies the Weber fraction may rise, as it did at the 111-ms period (9 Hz) movement in the current measurements.

Measured as the DL, performance was poorer at the longer periods and improved with the shorter periods. The largest absolute change in period was required for the 3000-ms standard, where the DL was more than 310 ms. The amount of time required to complete a single trial at this standard period was 6600 ms. After the delivery of the movement in the first temporal interval, subjects had to wait longer for the second movement to reach completion compared to the amount of time required for the shorter period standards. It is possible that the memory requirements for this longer stimulus trial played a role in the lower performance level.

The results of set 4 showed that across the two amplitudes tested, 6.3 and 11.9 mm, sensitivity to changes in period was independent of amplitude. Whereas changes in amplitude produce corresponding changes in the peak velocity and acceleration of both the standard and the comparison, sensitivity remains unchanged.

There are a number of cues that subjects might be using to discriminate between the two periods of movement. Overall duration of movement is an obvious one. The literature on the perception of temporal intervals has shown that the difference threshold for two time intervals varies considerably based on the nature of the task, the instructions given to the subject, and the type of stimulus occurring within the time interval (Woodrow, 1951). The values for difference thresholds for time perception, however, are in the range of the DLs for period discrimination results in the present study (Woodrow, 1951). If subjects were using the duration of movement in each interval as the basis for discriminations, they were being very effective, that is, their performance was at the lower end of the values reported by Woodrow (1951) (7%–14%). In addition, subjects were making these discriminations under conditions in which the onsets and offsets of the movement interval were either abrupt (0-degree waveform) or gradual (90-degree waveform). Subjects performed the task well, even under the less than ideal conditions (i.e., the less clear temporal boundaries) presented by the 90-degree waveform.

An additional possibility is that subjects were making a judgment of perceived intensity. It was noted informally that, at a given amplitude, short-period movements were perceived as ''stronger'' than long-period movements when period differences were large. If subjects were sensitive to smaller differences in perceived intensity produced by period differences of the magnitude used here, it is possible that subjects were discriminating movements on the basis of perceived intensity.

IV. EXPERIMENT 3

Experiment 3 examined some possible cues that subjects might use in discriminating differences in amplitude and differences in period. The purpose of these measurements was to determine whether amplitude DLs are increased by irrelevant variations in the period of movement and the accompanying irrelevant changes in velocity (set 1), and to determine whether period difference thresholds are increased by irrelevant variations in amplitude and the accompanying irrelevant changes in velocity (set 2). Several stimulus dimensions vary directly with the amplitude and period of a sinusoidal motion. For example, peak velocity, peak acceleration, and average acceleration increase with increasing amplitude. For the sake of simplicity, all of these potential cues will be referred to as velocity cues. During the amplitude discrimination measurements of experiment 1, subjects commented that they sometimes correctly selected the comparison stimulus because it was the one that moved faster. If velocity cues were the sole or even the main cue in discriminating amplitude, then reducing the effectiveness of these cues should reduce performance.

Set 1 examined amplitude discrimination and set 2 examined period discrimination. To reduce the effectiveness of velocity cues in the amplitude discrimination task, the amplitude differences were presented via two periods of movement. On half of the trials, the standard was presented at a period of 1000 ms (1 Hz) and the comparison was presented at a period of 500 ms (2 Hz). On the remaining trials, the standard was presented at 500 ms and the comparison was presented at 1000 ms. On each trial, the periods of the standard and comparison motions were determined randomly, so that period itself was an unreliable cue for the difference in amplitude. The movement presented at the shorter period had a higher peak velocity and peak acceleration, that is, unless the longer period movement was large enough in amplitude to compensate for the velocity differences resulting from the difference in period. On the trials in which the comparison (larger amplitude movement) was presented at 500 ms and the standard (smaller amplitude movement) was presented at 1000 ms, the comparison movement should always have a higher peak velocity and peak acceleration. If subjects based their decision on peak velocity or acceleration, they would be correct on these trials. On the remaining half of the trials, in which the standard was presented at the shorter period of 500 ms (2 Hz) and the comparison was presented at 1000 ms (1 Hz), the amplitude of the 1000-ms comparison would have to be twice that of the 500-ms standard for the two movements to have equivalent peak velocities. In this case, the only way a response based on velocity would be correct is if the amplitude of the 1000-ms comparison was more than twice the amplitude of the 500-ms standard. If subjects based their amplitude discrimination judgments solely on the basis of velocity cues, then the Weber fraction would have to be more than 100%.

A parallel set of measurements was carried out with a period discrimination task. In these measurements, the standard and comparison were presented at two different amplitudes. Subjects were instructed to respond to the period of the movement and ignore differences in amplitude. On each trial, the amplitude of movement in the first temporal interval was 6.3 mm and the amplitude of movement in the second interval was 11.9 mm. The comparison (shorter period movement) and the standard were randomly paired with the two amplitudes. As in the amplitude discrimination task, the effectiveness of velocity cues would be reduced since velocity varies with amplitude as well as period.

A. Methods

Five subjects were tested in set 1 and set 2. The stimuli for sets 1 and 2 are described in Table II. In the amplitude measurements subjects selected the temporal interval (1 or 2) that contained the larger amplitude motion regardless of the period of the motion. Two period conditions were presented. In the ''same period'' condition, the periods in the first and second temporal intervals were identical (1000 ms). In the ''mixed period'' condition, the period in the first temporal interval was 1000 ms, and the period in the second temporal interval was 500 ms. The ''mixed period'' condition and the ''same period'' condition were presented on alternate blocks of trials. The placement of the standard in the first or second

TABLE II. Stimulus conditions for main measurements in experiment 3.

Measurement	Discrimination	Amplitude (mm)	Period (ms)	Waveform
Set 1	amplitude (same period)	11.9	1000	90-degree
	amplitude (mixed period)	11.9	1000/500[a]	90-degree
Set 2	period (same amplitude)	6.3	1000	90-degree
	period (mixed amplitude)	6.3/11.9[b]	1000	90-degree

[a]Movement was presented at two different periods on each trial.
[b]Movement was presented at two different amplitudes on each trial.

temporal interval was randomly determined on a trial-by-trial basis. Over a block of trials, the standard was presented at the shorter period on approximately half of the trials and at the longer period on the remaining half of the trials. Subjects were instructed to report the interval containing the larger amplitude movement and to ignore any difference in period. Nine blocks of trials were completed for each condition.

For the period discrimination measurements (set 2), the subjects' task was to report the temporal interval that contained the shorter period of motion regardless of the amplitude of the motion. Two amplitude conditions were tested. In the ''same amplitude'' condition, the amplitude within the first and second temporal interval was identical, 6.3 mm. In the ''mixed amplitude'' condition, the amplitude of the motion in the first temporal interval was 6.3 mm and the amplitude of the movement in the second temporal interval was 11.9 mm. As was the case in the previous period discrimination tasks, the placement of the standard period in the first or second temporal interval was randomly determined on a trial-by-trial basis. The shorter period movement was presented at the higher amplitude on approximately half of the trials and at the lower amplitude on the remaining trials. The ''mixed amplitude'' condition and the ''same amplitude'' condition were presented on alternate blocks of trials. Seven blocks of trials were completed for each condition.

B. Results

1. Set 1

The results are presented in the first and second columns of Table III. This table shows the amplitude DLs for the ''same period'' and ''mixed period'' conditions. A two-way, repeated-measures analysis of variance (period condition×block) on the DLs showed no effect of period [$F(1,4)=1.84$, $p>0.05$]. As expected, no significant effect of period was found when the data were reanalyzed in terms of the Weber fractions [$F(1,4)=1.84$, $p>0.05$]. It appears there was no difference in the performance level for the ''same'' and ''mixed'' period conditions. The irrelevant variation caused no change, that is, it did not harm performance, suggesting that subjects did not have to rely on these variations to make their discriminations.

TABLE III. Difference thresholds for ''Same'' and ''Mixed'' conditions in sets 1 and 2 from experiment 3.

	Amplitude discrimination at 11.9 mm		Period discrimination at 1000 ms	
Condition	mm	%	ms	%
Same	1.3	11.2	86	8.6
Mixed	1.7	14.4	82	8.2

The main question this experiment was designed to address was whether velocity cues were the primary cues that subjects were using. Although velocity cues do not appear to be the major cues in amplitude discrimination, it is possible that velocity affects subjects' responses. A more detailed analysis of the results was carried out to determine if the differences in period in the ''mixed'' condition had any effect on amplitude discrimination. Specifically we asked whether subjects were more likely to select the shorter period movement. This analysis showed that, although there was no change in overall sensitivity, subjects' responding was biased by the velocity of the movement, and that they were more likely to respond with the second interval (the interval containing the shorter period). Such a response bias was not present in the ''same'' condition. As noted in experiment 2, movements differing in period may also differ in perceived intensity. The response bias observed here (the tendency to choose the interval containing the shorter period) is consistent with responding to the signal with the greater perceived intensity.

2. Set 2

The results are shown in the third and fourth columns of Table III. This table shows the period DLs and Weber fractions for the ''same amplitude'' and ''mixed amplitude'' conditions. A two-way, repeated-measures analysis of variance (amplitude condition×block) on DLs revealed no effect of amplitude [$F(1,4)=0.18$, $p>0.05$]. As expected, no significant effect of amplitude was found when the data were reanalyzed as Weber fractions [$F(1,4)=0.18$, $p>0.05$]. It appears there was no difference in the performance level for the ''same'' and ''mixed'' amplitude conditions; and, as with amplitude discrimination, period discrimination appears not to depend upon velocity cues.

Paralleling the amplitude discrimination analysis in set 1, we asked whether subjects were more likely to select the higher amplitude movement in the mixed condition. Similar

to the set 1 data, the analysis showed that, although there was no overall change in sensitivity, subjects' responding was biased by the velocity of the movement. They were more likely to respond with the second interval (the interval containing the larger amplitude).

The results of the amplitude and period discrimination measurements of experiment 3 suggest that subjects are not basing their decision solely on velocity cues. However, the velocity cues do affect performance in that subjects are more likely to be correct on trials composed of particular amplitude and period combinations. As the data demonstrate, subjects have a tendency to take velocity cues into account, but in this particular case their influence is not large enough to alter the overall level of performance.

V. GENERAL DISCUSSION

These measurements are part of a project exploring the ability of subjects to perform discriminations of active finger movements. The goal of this project is to determine both the sensitivity of the hand to various stimulus dimensions and the cues subjects use to discriminate between stimuli along these dimensions. There are a number of stimulus dimensions that subjects might be using to discriminate period and amplitude differences. The results from experiment 3 indicate that, although velocity cues may affect the discriminability of changes in period and amplitude, they are clearly not necessary for the discriminations. Once velocity cues are excluded, potential cues in amplitude discrimination include the distance moved by the finger as well as tactile cues arising from the fingerpad's contact with the contactor. In the period discrimination when velocity cues are eliminated, available cues include the period of the movement, tactile cues, and differences in perceived intensity.

As noted, one cue available in both the amplitude and period measurements is the tactile component of the movement. A specific tactile cue may be generated because of the way in which the contactor of the display rotates about a center axis. The movement of the finger is in a slight arc rather than a true vertical excursion. When the contactor moves upward from its horizontal resting position, the finger extends to follow the contactor and might slip very slightly. As the finger moves back to horizontal, the finger retracts slightly. The arc of the movement is such that a 14-mm excursion (measured as vertical excursion only) results in a 1-mm horizontal extension or retraction of the finger. The rate of slip would be higher for a shorter period of movement compared to a longer period of movement, and the amount of slip might correspond to the amplitude of the movement such that more slip would occur at larger amplitudes of motion. This tactile stimulation provided by the slip could provide a cue that subjects are able to use in the amplitude discrimination task (Srinivasan *et al.*, 1990). Another tactile cue might be the pressure exerted by the contactor as it moves against the finger at the onset of the movement.

The present results indicate that subjects' sensitivity relative to changes in amplitude and period of finger movement is similar to the differential sensitivity determined for other somatosensory stimuli. For example, the difference limen for vibratory amplitude using a two-interval, forced-choice tracking procedure varies from approximately 12% to greater than 25% for frequencies in the range of 25 to 250 Hz (Gescheider *et al.*, 1990). In the current study, difference thresholds for amplitude were in the range of 10% to 18%. In a frequency discrimination task Rothenberg *et al.* (1977) presented sinusoidal vibrations varying from 20 to 225 Hz to the forearm and found Weber fractions ranging from 13% to about 26%. These values are below those found by Goff (1967) for sinusoidal stimuli presented to the fingers (20% to approximately 57%). The period discrimination values in the current study ranged from 6% to 16% for periods in the range of 3000 to 111 ms (0.33 to 9 Hz).

The results from both the amplitude and period measurements show that, with some exceptions, neither absolute nor relative sensitivity remains constant throughout the dynamic range of these stimuli. In other words, it is not possible to quote a single value for either amplitude discrimination or for period discrimination that holds for the range of stimuli that one encounters in speech production. Although the present results do provide a range of values for period and amplitude discrimination, the practical consequences of a lack of any constant value for either period or amplitude discrimination is the necessity of additional measurements to determine discriminability at particular amplitude or period combinations.

The current device was designed to require subjects to actively follow the movement of the display rather than having the fingers passively moved. Although the version of the device used in the current measurements was limited somewhat in stiffness or resistance to deformation by the subject's finger, subsequent versions have a higher degree of stiffness. Using a display that requires subjects to actively follow the movement of the stimulator may be a possible benefit for perception. Movements and muscle contractions have been shown to enhance kinesthetic acuity (Gandevia *et al.*, 1992). Studies have also shown higher accuracy in a limb-position, matching task when the limb is actively placed (Clark and Horch, 1986). Additional information, such as that resulting from the efferent signals needed to follow along with the display movement and the monitoring of the display movement in an effort to maintain contact with it, may permit subjects to discriminate the amplitude and period of the movement better than they might during passive movement. It is also possible that the reverse would happen, that having to actively monitor and follow the display diverts attention from the discrimination task and impedes performance. Due to the design of the current display, however, it was not possible for an active versus a completely passive comparison to be performed. The current display does, however, allow the amount of resistance to be varied. Thus it will be possible to examine how changes in the resistance affect discriminability.

One potential use for a final version of the current display would be as a haptic display for the transmission of speech information. The movements presented on the display would be transformations of acoustic or physiological speech signals. The haptic cues for the speech segments may be the result of combinations of different amplitudes and frequencies of motion. For example, if the frequency or period of

jaw movement were higher for one of two segments, and the distance the jaw traveled was the same for both segments, then frequency, acceleration, velocity, and impulse would all be dimensions that might be the basis for identifying a particular segment.

VI. CONCLUSIONS

Difference thresholds for large amplitude (6.3–19.3 mm) and long-period (0.33–9 Hz) finger movements were measured. Four major conclusions from these measurements are: (1) Neither amplitude discrimination thresholds nor period discrimination thresholds were constant across the range of standards tested. Amplitude DLs ranged from 10% to 18%, and period DLs ranged from 6% to 16%. (2) In a period discrimination task, varying the duration of movement such that period and overall duration do not coincide did not increase DLs for the period of movement. (3) Amplitude DLs for an 11.9-mm standard movement did not vary significantly over a period range of 1000 to 167 ms (average DLs ranged from 11.8% to 12.9%), and period DLs for a 1000-ms standard movement did not vary significantly when tested at amplitudes of 6.3 and 11.9 mm (average DLs were 9.4% and 8.0%, respectively). (4) Amplitude DLs appear to be remarkably resistant to irrelevant variations in period and period DLs appear to be remarkably resistant to irrelevant variations in amplitude. Although performance was stable under these limited variations in the irrelevant parameters, further work is required to determine whether these conclusions would hold over a larger range of amplitudes and frequencies.

ACKNOWLEDGMENTS

The authors thank Roger P. Rhodes for his assistance in conducting these experiments. The authors also thank Silvio Eberhardt, David Coulter, John Jordan, and Yulin Chen for technical assistance. Reprint requests should be addressed to M.A. Rinker, Department of Speech and Hearing Science, 1070 Carmack Rd., Ohio State University, Columbus, OH 43210-1002 (electronic mail: rinker.13@osu.edu). This work was supported in part by research Grant No. DC-01577 from the National Institute on Deafness and Other Communication Disorders, National Institutes of Health, to the third author. The research was also supported by research Grant No. DC-00095 from the National Institute on Deafness and Other Communication Disorders, National Institutes of Health, to the second author.

Chapman, C. E. (**1994**). ''Active versus passive touch: factors influencing the transmission of somatosensory signals to primary somatosensory cortex,'' Can. J. Physiol. Pharmacol. **72**, 558–570.

Clark, F. J., Burgess, R. C., and Chapin, J. W. (**1983**). ''Humans lack a sense of static-position of finger,'' Soc. Neurosci. Abstracts **9**, 1033.

Clark, F. J., and Horch, K. W. (**1986**). ''Kinesthesia,'' in *Handbook of Perception and Human Performance: Sensory Processes and Perception*, edited by K. R. Boff, L. Kaufman, and J. P. Thomas (Wiley, New York), pp. 1–62.

Clark, F. J., Horch, K. W., Bach, S. M., and Larson, G. F. (**1979**). ''Contributions of cutaneous and joint receptors to static knee-position sense in man,'' J. Neurophysiol. **42**, 877–888.

Eberhardt, S. P., Bernstein, L. E., Barac-Cikoja, D., Coulter, D. C., and Jordan, J. (**1994**). ''Inducing dynamic haptic perception by the hand: System description and some results,'' Proc. Am. Soc. Mech. Eng. **55**, 345–351.

Eberhardt, S. P., Bernstein, L. E., Coulter, D. C., Jordan, J., and Chen, Y. (**1998**). ''Motion and vibration transmission for studying haptic perception by the hand'' (in preparation).

Gandevia, S. C., Hall, L. A., McCloskey, D. I., and Potter, E. K. (**1983**). ''Proprioceptive sensation at the terminal joint of the middle finger,'' J. Physiol. (London) **335**, 507–517.

Gandevia, S. C., McCloskey, D. I., and Burke, D. (**1992**). ''Kinaesthetic signals and muscle contraction,'' Trends Neurosci. **15**, 62–65.

Gescheider, G. A., Bolanowski, S. J., Verrillo, R. T., Arpajian, D. J., and Ryan, T. F. (**1990**). ''Vibrotactile intensity discrimination measured by three methods,'' J. Acoust. Soc. Am. **87**, 330–338.

Gibson, J. J. (**1962**). ''Observations on active touch,'' Psychol. Rev. **69**, 477–491.

Gibson, J. J. (**1966**). *The Senses Considered as Perceptual Systems* (Houghton Mifflin, Boston).

Goff, G. D. (**1967**). ''Differential discrimination of frequency of cutaneous mechanical vibration,'' J. Exp. Psychol. **74**, 294–299.

Hall, L. A., and McCloskey, D. I. (**1983**). ''Detection of movements imposed on finger, elbow, and shoulder joints,'' J. Physiol. (London) **335**, 519–533.

Kalaska, J. F. (**1994**). ''Central neural mechanisms of touch and proprioception,'' Can. J. Physiol. Pharmacol. **72**, 542–545.

Katz, D. (**1989**). *The World of Touch*, translated by L. E. Krueger (Erlbaum, Hillsdale, NJ). (Original work published 1925.)

Kelso, J. A. S., Vatikiotis-Bateson, E., Saltzman, E. L., and Kay, B. (**1985**). ''A qualitative dynamic analysis of reiterant speech production: Phase portraits, kinematics, and dynamic modeling,'' J. Acoust. Soc. Am. **77**, 266–280.

Kirman, J. H. (**1973**). ''Tactile communication of speech: A review and an analysis,'' Psychol. Bull. **80**, 54–74.

Levitt, H. (**1971**). ''Transformed up-down methods in psychoacoustics,'' J. Acoust. Soc. Am. **49**, 467–477.

Lloyd, A. J., and Caldwell, L. S. (**1965**). ''Accuracy in active and passive positioning of the leg on the basis of kinesthetic cues,'' J. Comp. Physiol. Psychol. **60**, 102–106.

Loomis, J. M., and Lederman, S. J. (**1986**). ''Tactual Perception,'' in *Handbook of Perception and Human Performance: Cognitive Processes and Performance*, edited by K. R. Boff, L. Kaufman, and J. P. Thomas (Wiley, New York), pp. 1–41.

Nelson, W. L., Perkell, J. S., and Westbury, J. R. (**1984**). ''Mandible movements during increasingly rapid articulations of single syllables: Preliminary observations,'' J. Acoust. Soc. Am. **75**, 945–951.

Ohala, J. J. (**1975**). ''The temporal regulation of speech,'' in *Auditory Analysis and Perception of Speech*, edited by G. Fant and M. A. A. Tatham (Academic, London).

Rabinowitz, W. M. (**1993**). RLE Progress Report, Number 136, Jan.–Dec. 1993.

Reed, C. M., Durlach, N. I., and Braida, L. D. (**1982**). ''Research on tactile communication of speech: A review,'' Monogr. **20**, American Speech, Language, and Hearing Association (ASHA).

Reed, C. M., Rabinowitz, W. M., Durlach, N. I., Braida, L. D., Conway-Fithian, S., and Schultz, M. C. (**1985**). ''Research on the Tadoma method of speech communication,'' J. Acoust. Soc. Am. **77**, 247–257.

Rothenberg, M., Verrillo, R. T., Zahorian, S. A., Brachman, M. L., and Bolanowski, S. J. (**1977**). ''Vibrotactile frequency for encoding speech,'' J. Acoust. Soc. Am. **62**, 1003–1012.

Schoner, G., and Kelso, J. A. S. (**1988**). ''Dynamic pattern generation in behavioral and neural systems,'' Science **239**, 1513–1520.

Srinivasan, M. A., Whitehouse, J. M., and LaMotte, R. H. (**1990**). ''Tactile detection of slip: Surface microgeometry and peripheral neural codes,'' J. Neurophysiol. **63**, 1323–1332.

Tan, H. Z. (**1996**). ''Information transmission with a multi-finger tactual display,'' Ph.D. thesis, Department of Electrical Engineering and Computer Science, MIT.

Tan, H. Z., Rabinowitz, W. M., and Durlach, N. I. (**1989**). ''Analysis of a synthetic Tadoma system as a multidimensional tactile display,'' J. Acoust. Soc. Am. **86**, 981–988.

Weisenberger, J. M., and Miller, J. D. (**1987**). ''The role of tactile aids in providing information about acoustic stimuli,'' J. Acoust. Soc. Am. **82**, 906–916.

Woodrow, H. (**1951**). ''Time Perception,'' in *Handbook of Experimental Psychology*, edited by S. S. Stevens (Wiley, New York), pp. 1224–1236.

Phonation onset: Vocal fold modeling and high-speed glottography

Patrick Mergell[a)]
Department of Phoniatrics and Pedaudiology, University Erlangen-Nuremberg, Bohlenplatz 21, D-91054 Erlangen, Germany

Hanspeter Herzel[b)]
Institute for Theoretical Biology, Humboldt University Berlin, Invalidenstr. 43, D-10115 Berlin, Germany

Thomas Wittenberg,[c)] Monika Tigges,[d)] and Ulrich Eysholdt[e)]
Department of Phoniatrics and Pedaudiology, University Erlangen-Nuremberg, Bohlenplatz 21, D-91054 Erlangen, Germany

(Received 3 February 1997; accepted for publication 16 March 1998)

Phonation onset is discussed in the framework of dynamical systems as a Hopf bifurcation, i.e., as a transition from damped to sustained vocal fold oscillations due to changes of parameters defining the underlying laryngeal configuration (e.g., adduction, subglottal pressure, muscular activity). An analytic envelope curve of the oscillation onset is deduced by analyzing the Hopf bifurcation in mathematical models of the vocal folds. It is governed by a single time constant which can be identified with the physiological parameter *phonation onset time*. This parameter reflects the laryngeal state prior to phonation and can be used as a quantitative classification criterion in order to assess the phonation onset in clinical diagnosis. The extraction of the phonation onset time from simulated time series using a simplified two-mass model and from digital high-speed videos is described in detail. It shows a good agreement between theory and measurement. © *1998 Acoustical Society of America.* [S0001-4966(98)06106-2]

PACS numbers: 43.70.Aj, 05.45.+b [AL]

INTRODUCTION

The analysis of the voice onset has received much attention in phonetics and in speech pathology. The voice onset time (VOT) extracted from spectrograms of speech signals is an important measure serving to distinguish linguistic categories of stop-consonants. It is defined as the time interval between the noise pulse due to the stop release and the phonation onset (Lisker and Abramson, 1964). We refer to the phonation onset as the amplitude growth of the vocal fold oscillation, considering the voice as a product of the complete source-articulator system and phonation as the primary glottal signal. In clinical practice, the assessment of the phonation onset can be used as a diagnostic tool in order to detect vocal dysfunctions. It is a critical phase during phonation because it depends on the precise coordination between subglottal pressure and the glottal impedance.

The studies by Peters *et al.* (1986) and by Cooke *et al.* (1997) document that the timing of the voice onset is a substantial physiological feature for the discrimination of different voice onset qualities as they are perceived by experts. The vocal fold kinematics during voice onset can be subdivided into the process of vocal fold adduction and the phonation onset. Cooke *et al.* (1997) showed that the transition between the two processes is continuous. We assume that the adduction process and the phonation onset time can be treated separately as a first approximation. The degree of adduction as well as the growth of oscillation amplitude are smooth nonlinear functions describing the asymptotic transition from an initial to a final state. Therefore, it is difficult to define a nonambiguous time measure. Conventionally, the process duration is defined as the time interval between two threshold crossings. Peters *et al.* (1986) transformed the speech signals of voice onsets into a root mean square amplitude envelope by averaging over time windows of 40 ms. They introduced a predictor for the abruptness of the phonation onset which is given by the duration of the amplitude envelope growth from 10% to 90% of its saturation level. Cooke *et al.* (1997) defined the degree of adduction as the distance between the vocal processes. Thus, they determined the duration of the adduction as the time interval between 80% and 20% of the initial distance or between 80% of the initial distance and the onset of vocal fold vibration. Werner-Kukuk and von Leden (1970) analyzed vocal initiation (synonymous to our definition of phonation onset) by means of high-speed cinematography and by classifying the different onset types using the qualities soft, hard, and breathy. By counting the number of oscillation cycles during the time of growth from zero to maximum amplitude (without giving explicit thresholds), they found that the oscillation amplitude in soft and breathy phonation onsets reached its maximum gradually. In contrast, the amplitude was increasing much faster in hard phonation. Moreover, they observed that the ventricular folds move considerably during hard phonation onsets whereas they remain nearly immobile during soft and

[a)]Electronic mail: mergell@phoni.med.uni-erlangen.de
[b)]Electronic mail: herzel@itb.biologie.hu-berlin.de
[c)]Electronic mail: wittenberg@phoni.med.uni-erlangen.de
[d)]Electronic mail: tigges@phoni.med.uni-erlangen.de
[e)]Electronic mail: eysholdt@phoni.med.uni-erlangen.de

breathy phonation onsets. Since the choices of the data processing and the thresholds are somewhat arbitrary, it is difficult to compare the results from different studies as long as the dynamic behavior of the process under investigation is unknown or as long as the thresholds are not standardized. In our approach, the data processing and the definition of the phonation onset time is nonambiguous.

In the past, one central goal of model analysis was the determination of the critical subglottal pressure for the start of self-sustained oscillations. The change in the dynamic behavior is based on a Hopf bifurcation (Bergé *et al.*, 1984; Berry *et al.*, 1996). At a critical pressure value, a stable equilibrium state of the system, i.e., the rest position, becomes unstable and the dynamics undergo a change from a fixed point to a limit cycle attractor. For pressure values beyond the threshold, the vibration amplitude at phonation onset is growing from an initial to a saturation value.

Steinecke and Herzel (1995) analyzed the Hopf bifurcation in the simplified two-mass model by calculating Hopf bifurcation diagrams numerically. The critical subglottal pressure of the model is given by $P_{th} \approx 2.4$ cm H_2O for standard phonation conditions which is comparable with experimental measurements ($P_{th} \approx 3-4$ cm H_2O) (Titze, 1994). Titze (1988) deduced a threshold pressure approximation for the excitation of small amplitudes of mucosal surface waves. The simple formula predicts a linear growth of the phonation threshold pressure with the tissue damping coefficient, the fundamental frequency, and the prephonatory glottal halfwidth at the Hopf bifurcation. Experiments with a physical model of the mucosa confirmed these results (Titze *et al.*, 1995). Moreover, Verdolini *et al.* (1990) observed for dry tissue hydration conditions (i.e., for high tissue damping) an increased phonation threshold pressure. Other corresponding clinical investigations are based on voice range profile measurements or phonetograms (Titze, 1992; Wendler *et al.*, 1996). This examination method is appropriate to detect qualitative differences in healthy voices as well as dysfunctions in pathological voices. The voice range profile separates the plane spanned by the fundamental frequency and the sound pressure level axes into two regions: the phonation region and the aphonia region. The lower border of the phonation region shows the individual dependence of the phonation threshold pressure on the fundamental frequency and therefore gives a measure of phonatory effort.

As yet, there is no quantitative description relating direct measurements of the vocal fold dynamics during phonation onset with a quantitative physiological theory. Since the phonation onset is based on a transient oscillation of the vocal folds, the analysis by means of conventional examination methods (Colton and Woo, 1995) fails: The trigger time and the duration of one apparent vibratory cycle in video stroboscopy is longer than the phonation onset time. Electroglottography provides a complex signal that is proportional to the vocal fold contact area and can hardly be related to the original onset oscillation signal. Speech signals include the vocal tract resonances requiring inverse filtering in order to recover the glottal airflow function. The resulting information about the left and the right vocal fold oscillation is mixed and cannot be decomposed. Photoglottography allows a direct measurement but it also provides only mixed information since the signal is proportional to the glottal area. Besides high-speed cinematography only high-speed kymography (Svec and Schutte, 1996) resolves the oscillation onsets of the left *and* the right vocal fold. In principle, the theory of phonation onset can be compared to any measurement of glottal amplitude curves. High-speed recordings, however, allow a direct comparison of model simulations with left and right vocal fold oscillation amplitudes. Hence, we combine in this paper vocal fold modeling and high-speed glottography (HGG) (Wittenberg *et al.*, 1995; Eysholdt *et al.*, 1996) in order to give an objective insight in the physical mechanism of the phonation onset.

I. PARAMETRIZATION OF THE PHONATION ONSET

A. Analytical envelope solution

It is impossible to find an explicit solution for the dynamics of the mass distribution in the vocal folds. Therefore, we simply assume that the real glottal system obeys a set of coupled differential equations, i.e., its essential features can be simulated by means of any adequate mass–spring model from the literature. We chose a representative coordinate (e.g., a point at the midglottal vocal fold border) and we write its oscillatory solution as a function of time t in a universal way

$$x(t) = r(t)\sin\,\phi(t), \tag{1}$$

where $\phi(t)$ is the phase and $r(t)$ corresponds to the envelope function of the oscillation describing the series of oscillation maxima and minima. We are interested in the growth of $r(t)$, starting from a small initial value. Near a Hopf bifurcation, the dynamical equation of the chosen vocal fold coordinate can be written as (Titze, 1988; Jackson, 1989; Verhulst, 1990)

$$\ddot{x} + x = F(x,\dot{x}), \tag{2}$$

where $F(x,\dot{x})$ is a nonlinear driving force. Using Eq. (1) and a Taylor expansion of Eq. (2), ϕ-averaging over one oscillation period gives the differential equation of the envelope

$$\dot{r} = a_0 + a_1 r + a_2 r^2 + a_3 r^3 + \mathcal{O}(r^4), \tag{3}$$

where a_i are Taylor coefficients (Jackson, 1989; Verhulst, 1990). Since amplitude growth and saturation are mainly governed by the linear and odd nonlinear terms, one can transform Eq. (3) into the normal form of the Hopf bifurcation

$$\dot{r} = ar + br^3 + \mathcal{O}(r^5). \tag{4}$$

This procedure is rather general and can be applied to any specific biomechanical vocal fold model. Assuming $b<0$ and dropping the higher-order terms $\mathcal{O}(r^5)$, Eq. (4) has a simple solution that reads

$$r(t) = \pm\left(\left[\frac{1}{r_0^2} + \frac{b}{a}\right]e^{-2at} - \frac{b}{a}\right)^{-1/2}, \tag{5}$$

where $r_0 = r(0)$ is the initial amplitude.

We emphasize that the derivation of Eq. (4) has a universal character. It is generally valid in a close vicinity of the Hopf bifurcation where the amplitudes are small in the sense that the dynamics is governed by lower-order nonlinear terms. However, the approximations leading to the solution in Eq. (5) have to be verified in complex biomechanical models.

B. General features of the envelope solution

For further consideration, we chose the positive branch of Eq. (5), i.e., the series of oscillation maxima. The following derivations can be carried out analogously for the negative branch, i.e., the series of oscillation minima, by transforming $r(t) \rightarrow -r(t)$. With $t \rightarrow \infty$, we get the saturation amplitude, i.e., the amplitude of the limit cycle attractor

$$r_\infty = \lim_{t \rightarrow \infty} r(t) = \sqrt{-\frac{a}{b}}. \tag{6}$$

For small values of $r(t \rightarrow 0)$ we can neglect the cubic term in Eq. (4) ($ar \ll br^3$) and we simply find an exponential law

$$r(t) \sim r_0 e^{at}. \tag{7}$$

Hence, for $a<0$, the oscillation will be damped out. In this case, more energy is dissipated in the tissue than is transferred from the airflow into the vocal folds. The inverse situation is given for $a>0$, where the amplitude is growing exponentially from cycle to cycle. As the amplitude increases ($t \rightarrow \infty$), the nonlinear term controlled by the parameter $b<0$ in Eq. (4) becomes more and more dominant and enforces a saturation behavior that can be written as

$$r(t) \sim r_\infty \left(1 - \frac{1}{2} \left[\left(\frac{r_\infty}{r_0} \right)^2 - 1 \right] e^{-2at} \right). \tag{8}$$

In order to give a more concrete idea of the physiological meaning of the parameter a, we briefly discuss its relation to the phonation threshold pressure. Mergell (1998) has calculated the parameter a for the simplified two-mass model by Steinecke and Herzel (1995) which reads

$$a = \beta (P_s - P_{th}), \tag{9}$$

where P_s is the subglottal pressure, P_{th} is the phonation threshold pressure for a certain larynx configuration, and β is a proportionality factor. Hence, the parameter a vanishes when P_s becomes P_{th} whereas the oscillation amplitude is growing exponentially for $P_s > P_{th}$ and damped for $P_s < P_{th}$.

Using Eq. (4) we describe the phonation onset as a Hopf bifurcation characterized by an exponential growth that in turn is delimited by a cubic nonlinearity (Bergé *et al.*, 1984). The change of dynamics from a fixed point to a limit cycle is a steady process that occurs above a critical pressure value (supercritical Hopf bifurcation, compare Fig. 1). In some situations, however, jumps of the amplitudes and hysteresis have been observed near phonation onset (Titze *et al.*, 1995; Berry *et al.*, 1996). Such a behavior can be described by using positive values of b and the incorporation of higher nonlinearities (compare to Fig. 2). The corresponding subcritical Hopf bifurcation exhibits parameter regions in which phonation intervals (limit cycle) and aphonia (steady state) coexist (Bergé *et al.*, 1984; Herzel *et al.*, 1994). In this case, the minimal pressure to sustain phonation is different from the threshold pressure for a transition from a steady state to a limit cycle. At both thresholds, the onset and the offset of vocal fold oscillations happen abruptly. In the intermediate region, jumps from one dynamic regime into the other can be observed. Two threshold pressures have been calculated for vocal fold models by Lucero and Gotoh (1993) and Lucero (1993). Hysteresis has also been found in recent excised larynx experiments (Berry *et al.*, 1996) and in a physical model of the mucosa (Titze *et al.*, 1995).

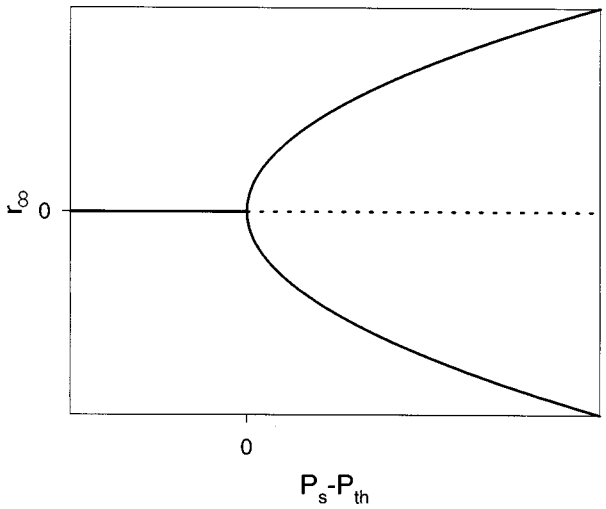

FIG. 1. Hopf bifurcation based an the equation $\dot{r} = ar + br^3$, $b<0$. $r_\infty = \pm\sqrt{-a/b}$ defines the saturation value of the envelope curve. At $P_s = P_{th}$ the fixed point solution is replaced by a stable limit cycle. Since the bifurcation branches start above the critical pressure P_{th}, i.e., $P_s > P_{th}$, the bifurcation is called supercritical. Solid lines indicate that the equilibrium solution is stable, dotted lines mark unstable solutions. Note that $(P_s - P_{th}) \sim a$.

Since it is not possible to give a simple solution of the

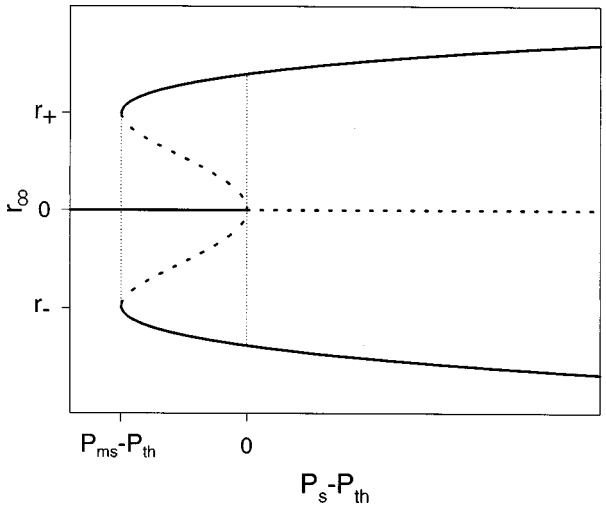

FIG. 2. Hysteresis in the case of a subcritical bifurcation, where the branches exist already below the critical pressure P_{th}, i.e., $P_{ms} < P_s < P_{th}$. $(P_{ms} - P_{th}) \sim -(b^2/4c)$, where P_{ms} is the minimum pressure required to sustain phonation. The underlying equation is given by $\dot{r} = ar + br^3 + cr^5$, $b>0$, $c<0$. $r_\pm = \pm\sqrt{-b/2c}$.

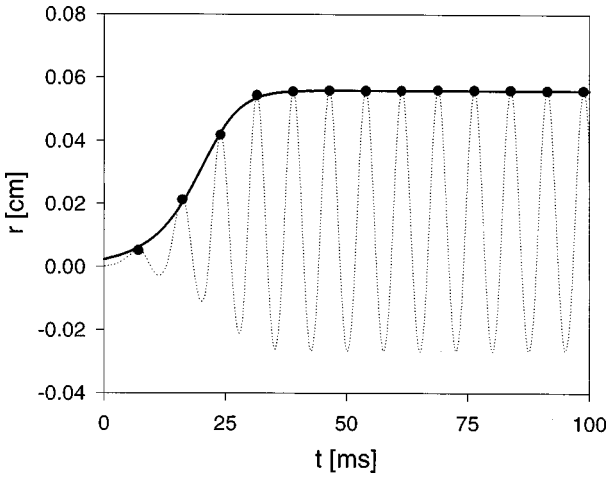

FIG. 3. Simulation of a phonation onset using the simplified two-mass model by Steinecke and Herzel. The dotted curve shows the oscillation amplitude. The series of oscillation maxima that define the envelope curve are marked with filled circles. The solid line represents the performed fit to the maxima taking the parametrization from Eq. (10). $\tau=(7.1\pm0.1)$ ms.

normal form including higher than third-order terms, and since we assume that most of observed phonation onsets are produced in a P_s region, where hysteresis is not essential, we forgo a quantitative discussion of the subcritical case shown in Fig. 2.

C. Definition of the phonation onset time

By introducing the ratio $\zeta=(r_0/r_\infty)^2$, we get the parametrization from Eq. (5)

$$r(t)=r_0([1-\zeta]e^{-2at}+\zeta)^{-1/2}. \tag{10}$$

Note that this solution contains beside the initial amplitude r_0 and the saturation amplitude r_∞ only one single free parameter a.

Our aim is to extract a unique definition of the phonation onset time from this expression. We present two ways to define the characteristic time constant based on the presented theory.

(1) By means of a nonlinear curve fit with the parametrization given in Eq. (10) one can determine r_0, r_∞, and a. In Fig. 3 this method is demonstrated. The fit has been performed to the series of maximum amplitudes extracted from a simulated vocal fold oscillation. It will be shown that an adequate definition of the phonation onset time is given by $\tau=a^{-1}$.

(2) A very simple and robust method is to chose two different threshold fractions S' and S of the saturation amplitude and to define the phonation onset time as the difference between the respective durations of amplitude growth. The duration of growth from the initial amplitude r_0, e.g., the first oscillation maximum of the phonation onset, to an arbitrary fraction S, e.g., $S=70\%$, of the saturation amplitude r_∞ is given by

$$\tau_s=\frac{1}{2a}\ln\left[\frac{\zeta^{-1}}{S^{-2}-1}\right], \tag{11}$$

and therefore we find

$$\tau_{s,s'}=\tau_s-\tau_{s'}=\frac{1}{2a}\ln\left(\frac{S'^{-2}-1}{S^{-2}-1}\right)=\frac{Z(S,S')}{a}. \tag{12}$$

At this point, it becomes clear that any time interval of amplitude growth is proportional to $\tau=1/a$ and the prefactor is determined by the chosen thresholds S and S'. Fulfilling the condition

$$S'=\frac{1}{\sqrt{e^2(S^{-2}-1)+1}}, \tag{13}$$

where e is the Euler number, we can find values S' and S for which $Z(S,S')$ is unity and therefore $\tau=a^{-1}$. Hence, the inverse of the parameter a can be directly identified with the phonation onset time and the dependencies on initial and saturation amplitude have been eliminated. This result is a consequence of the fact that a is invariant under scaling and time translation of the envelope curve $r(t)$. For centering the threshold crossings around the half-saturation amplitude we set $S'=0.5-p$ and $S=0.5+p$. Solving Eq. (13), we find $p=0.178$ and therefore $S'=32.2\%$ and $S=67.8\%$.

We summarize that the parameter a can be determined easily by defining two arbitrary amplitude thresholds and applying Eq. (12) or by a curve fit. The time interval a^{-1} can be interpreted as the duration of amplitude growth from 32.2% to 67.8% of the saturation amplitude. Hence, the unique definition of the phonation onset time is

$$\tau=\frac{1}{a}. \tag{14}$$

This definition has general character since it describes the phonation onset mechanism in a universal way, i.e., as a supercritical Hopf bifurcation.

II. SIMULATIONS OF THE TWO-MASS MODEL

Our computer simulations are performed with a simplified two-mass model which is considered to be an adequate choice in order to study the basic features of phonation onset. For a detailed description of the model and its limitations, the reader is referred to the original paper by Steinecke and Herzel (1995). Essential physiological parameters varied in phonation are the glottal rest area a_0 and the subglottal pressure P_s. For a constant set of model parameters, the phonation onset time has been extracted from simulated time series by using the method shown in Fig. 3. Figures 4 and 5 show the relations between τ and these quantities in the employed model. The phonation onset time grows with decreasing subglottal pressure (Fig. 4) and increasing glottal rest area (Fig. 5). This is in agreement with the result given by Titze (1988) predicting an increase of the phonation threshold pressure for an increasing glottal rest area. It also explains that in laryngeal nerve paralyses higher subglottal pressures are required in order to compensate a glottal chink due to the impaired adduction muscles (Smith *et al.*, 1992).

In Fig. 6 we demonstrate how to extrapolate the phonation onset time data in order to determine the phonation threshold pressure using Eq. (9). Hence, measuring the phonation onset time, we indirectly obtain information about the threshold pressure.

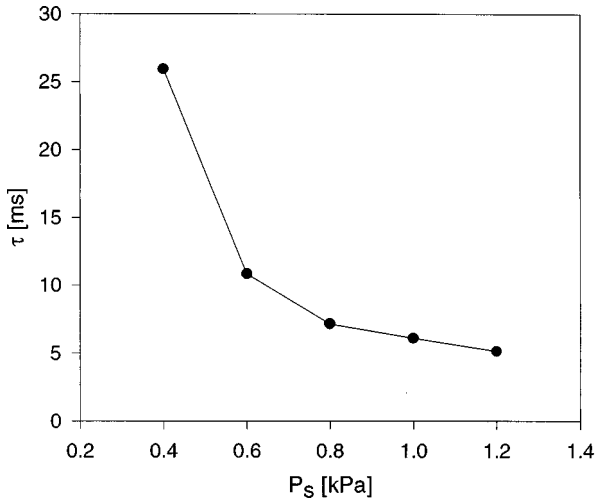

FIG. 4. Phonation onset time in the two-mass model as a function of subglottal pressure. The equations and the parameters are taken from Steinecke and Herzel (1995).

Our model simulations show that the phonation onset time which is inversely proportional to $P_s - P_{th}$ increases with the fundamental frequency according to several experimental and theoretical studies (Titze, 1994). Figure 7 shows the Hopf bifurcation obtained by linear stability analysis and verified with model simulations. The threshold pressure is presented as a function of the parameter q, scaling linearly the natural frequencies ($f_{i,\mathrm{nat}} = \sqrt{k_i/m_i}$) of the model masses which is near to the fundamental frequency. The scaling is simply performed by

$$m_i' = \frac{m_i}{q}, \quad k_i' = q k_i \rightarrow f_{i,\mathrm{nat}}' = q f_{i,\mathrm{nat}}, \tag{15}$$

where m_i and k_i are mass and stiffness coefficients. In the two-dimensional bifurcation diagram, the threshold curve separates the parameter plane into the regions of sustained phonation and aphonia (compare the voice range profile measurement). Since the threshold curve exhibits a minimum, we state that there exists an optimal relation between

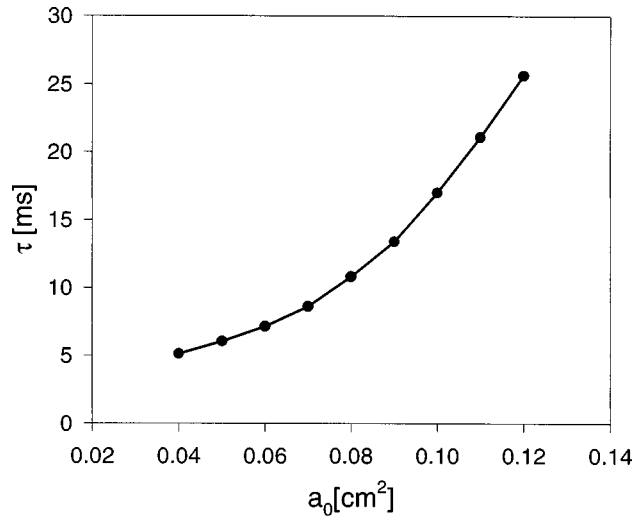

FIG. 5. Phonation onset time in the two-mass model as a function of glottal rest area ($P_s = 8$ cm H_2O).

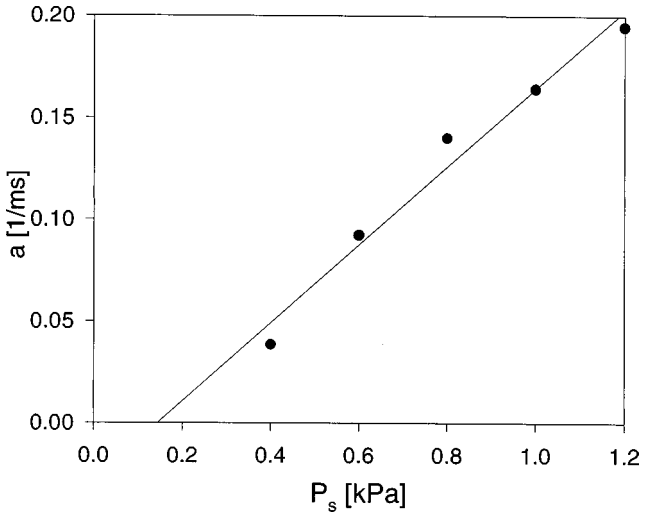

FIG. 6. The parameter $a = 1/\tau$ in the two-mass model as a function of the subglottal pressure. This figure suggests that the phonation threshold pressure can be determined by the extrapolation of onset time data to $a = 0$, where $P_s = P_{th}$.

fundamental frequency and subglottal pressure for a given laryngeal configuration. The phonation onset time decreases with increasing distance from the bifurcation curve towards the phonation region. Hence, the measurement of the phonation onset time provides the same information as the lower border of the voice range profile.

III. APPLICATION TO HIGH-SPEED GLOTTOGRAPHY

Semiautomatic motion analysis software was applied to extract the glottal geometry from high-speed sequences (Wittenberg *et al.*, 1995). As a first step, the glottal area is separated from its laryngeal environment for each digitized image (128 pixel×128 pixel, 0.1 mm/pixel). Starting a search from a reference point on the principal glottal axis in perpendicular direction, the vocal fold oscillation amplitude is determined via gray scale edge detection in each high-speed

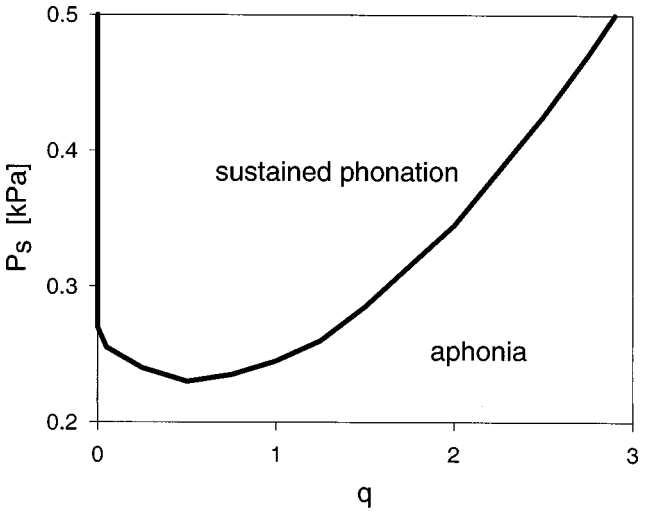

FIG. 7. Two-dimensional Hopf bifurcation diagram in the two-mass model. The phonation threshold pressure curve subdivides the parameter plane into two stability regions. Aphonia corresponds to a stable fixed point, i.e., the vocal folds stay in rest position. Across the threshold curve a dynamical change occurs and sustained phonation sets in.

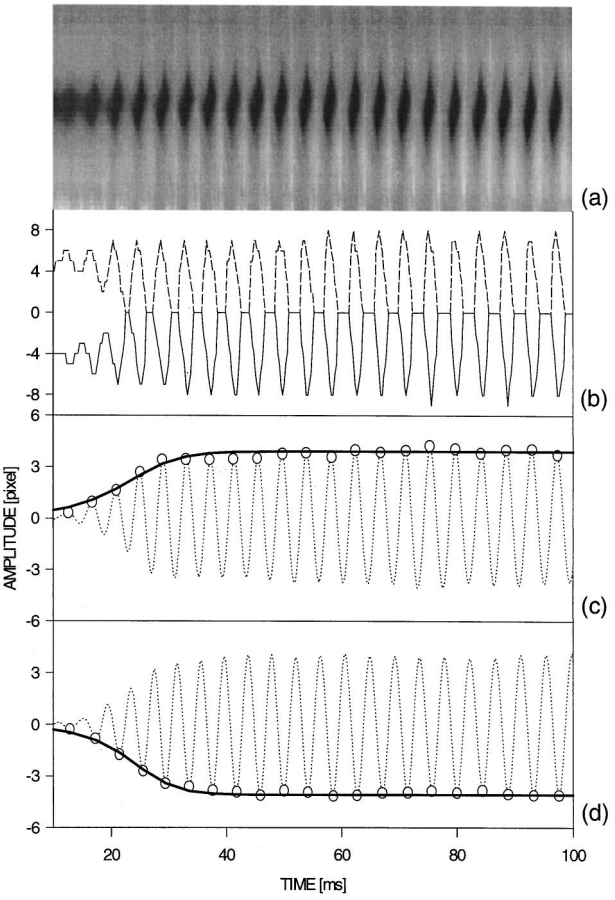

FIG. 8. (a) High-speed kymogram of a phonation onset. (b) Corresponding high-speed glottograms, $F_0 = 233$ Hz. (b) Fit to the onset envelope curve of the left vocal fold oscillation. From the fit (solid line) to the maxima (circles) of the filtered raw data we extract $\tau = (7.5 \pm 1.2)$ ms. (d) Fit to the onset envelope curve of left vocal fold oscillation: $\tau = (6.4 \pm 1.0)$ ms.

video frame. For a subsequent analysis, the resulting time series from the left and the right midglottal vocal fold oscillation have been bandpass filtered to reduce the spectral components related to artifacts and noise. We used a Hamming window with the passband $0.9f_0 < f < 1.1f_0$, where f_0 is the fundamental frequency. Figure 8 shows the application of the presented formalism to digital high-speed sequences. In order to exemplify how high-speed data are processed, we now discuss the required steps. According to Wittenberg (1997), the sequence of midglottal scan lines which are extracted transversely to the principal glottal axis from subsequent high-speed video frames is called digital high-speed kymogram. Figure 8(a) shows the kymogram of a phonation onset. The corresponding time series yielded by image processing are shown in Fig. 8(b). The raw data are filtered and the derived oscillation envelope curve is fit to the oscillation extrema. Considering the envelope curves of the left [Fig. 8(c)] and the right [Fig. 8(d)] oscillation onset, we state that the presented data can be described excellently by the fits. A detailed statistical study of phonation onsets in 52 subjects with functional dysphonia has been carried out by Wittenberg *et al.* (1997).

IV. DISCUSSION

In this work, we have studied primarily the growth of the vocal fold amplitudes during the phonation onset. The characterization of the whole kinematics of the voice onset additionally requires quantitative models of the adduction process and of the vocal tract dynamics.

The phonation onset could be described as a supercritical Hopf bifurcation. We isolated the central quantitative measure characterizing the phonation onset, i.e., the phonation onset time. It has been defined as the duration of amplitude growth from 32.2% to 67.8% of the saturation amplitude. In our calculations we assumed that prior to phonation onset induced by a constant subglottal pressure, the larynx is set into an initial rest state, i.e., all laryngeal parameters are supposed to be constants of time during phonation onset. This assumption is reasonable despite the observation by Cooke *et al.* (1997) stating that the transition between the growth of the vocal fold oscillation amplitude and the adduction process is continuous. Since, generally, the adduction duration is about a factor of 10 higher than the phonation onset time [compare Cooke *et al.* (1997)], we can omit the change of glottal area during phonation onset in a first approximation.

In contrast, any specific laryngeal parameter setting has its own phonation onset features, i.e., phonation onset time and saturation amplitude. It must be distinguished between parameter variations due to inter- and intraindividually changing glottal configurations, and those caused by explicit dependence on time during phonation onset which have been excluded from the present discussion. Analyzing the two-mass model, we found that the phonation onset time increases with decreasing subglottal pressure, increasing fundamental frequency and glottal rest area. Moreover, we presented a method for the determination of the subglottal threshold pressure from phonation onset time measurements. Future work will be dedicated to a more extensive analysis of high-speed data from phonation onsets in an analogous way.

Since the presented theory relates direct measurements of vocal fold oscillations with biomechanical model simulations, it permits a rough reconstruction of a given internal laryngeal configuration. In particular, the combination of mathematical models with quantitative analysis and direct observation of vocal fold vibrations can be helpful for the diagnosis of functional dysphonia because the underlying laryngeal processes as well as pathological tissue and innervation changes are detectable only in the complex vocal fold oscillation patterns.

ACKNOWLEDGMENTS

This work has been supported by the Deutsche Forschungsgemeinschaft. We thank I. R. Titze and D. Berry at the National Center for Voice and Speech in Iowa City for many fruitful discussions.

Bergé, P., Pomeau, P., and Vidal, C. (**1984**). *Order within Chaos* (Wiley Hermann).

Berry, D. A., Herzel, H., Titze, I. R., and Story, B. H. (**1996**). ''Bifurcations in excised larynx experiments,'' J. Voice **10**, 129–138.

Colton, R. H., and Woo, P. (**1995**). ''Measuring vocal fold function,'' in *Diagnosis and Treatment of Voice Disorders*, edited by J. S. Rubin, R. T. Sataloff, G. S. Korovin, and W. J. Gould (Igaku-Shoin, New York), pp. 290–315.

Cooke, A., Ludlow, C. L., Hallet, N., and Selbie, W. S. (**1997**). ''Characteristics of vocal fold adduction related to voice onset,'' J. Voice **11**, 12–22.

Eysholdt, U., Tigges, M., Wittenberg, T., and Pröschel, U. (**1996**). ''Direct evaluation of high-speed recordings of vocal fold vibrations,'' Folia phonatr. Logop. **48**, 163–170.

Herzel, H.-P., Berry, D. A., Titze, I. R., and Saleh, M. (**1994**). ''Analysis of vocal disorders with methods from nonlinear dynamics,'' J. Speech Hear. Res. **37**, 1008–1019.

Jackson, E. A. (**1989**). *Perspectives of Nonlinear Dynamics* (Cambridge U.P., Cambridge).

Lisker, L., and Abramson, A. (**1964**). ''A cross-language study of voicing in initial stops: Acoustical measurements,'' Word **20**, 384–422.

Lucero, J. C. (**1993**). ''Dynamics of the two-mass model of the vocal folds: Equilibria, bifurcations, and oscillation region,'' J. Acoust. Soc. Am. **94**, 3104–3111.

Lucero, J. C., and Gotoh, T. (**1993**). ''On the threshold pressure and the minimum sustaining pressure in the vocal fold oscillation,'' J. Acoust. Soc. Jpn. **14**, 213–214.

Mergell, P. (**1998**). Ph.D. thesis, Technische Universität Berlin.

Peters, H. F. M., Boves, L., and van Dielen, I. C. H. (**1986**). ''Perceptual judgement of abruptness of voice onset in vowels as a function of the amplitude envelope,'' J. Speech Heas. Dis. **51**, 299–308.

Smith, M. E., Berke, G., Gerrat, B. R., and Kreiman, J. (**1992**). ''Laryngeal paralyses: Theoretical considerations and effects on laryngeal vibration,'' J. Speech Hear. Res. **35**, 545–554.

Steinecke, I., and Herzel, H. (**1995**). ''Bifurcations in an asymmetric vocal fold model,'' J. Acoust. Soc. Am. **97**, 1874–1884.

Svec, J. G., and Schutte, H. K. (**1996**). ''Videokymography: High-Speed Line Scanning of Vocal Fold Vibration,'' J. Voice **10**, 201–205.

Titze, I. R. (**1988**). ''The physics of small-amplitude oscillation of the vocal folds,'' J. Acoust. Soc. Am. **83**, 1536–1551.

Titze, I. R. (**1992**). ''Acoustic Interpretation of the Voice Range Profile (Phonetogram),'' J. Speech Hear. Res. **35**, 21–34.

Titze, I. R. (**1994**). *Principles of Voice Production* (Prentice-Hall, Englewood Cliffs, NJ).

Titze, I. R., Schmidt, S. S., and Titze, M. R. (**1995**). ''Phonation threshold pressure in a physical model of the vocal fold mucosa,'' J. Acoust. Soc. Am. **97**, 3080–3084.

Verdolini, K., Titze, I. R., and Druker, D. G. (**1990**). ''Changes in Phonation Threshold Pressure with Induced Conditions of Hydration,'' J. Voice **4**, 142–151.

Verhulst, F. (**1990**). *Nonlinear Differential Equations and Dynamical Systems* (Springer-Verlag, Berlin).

Wendler, J., Seidner, W., Kittel, G., and Eysholdt, U. (**1996**). *Lehrbuch der Phoniatrie und Pädaudiologie* (Georg Thieme, Stuttgart).

Werner-Kukuk, E., and von Leden, H. (**1970**). ''Vocal initiation: High speed cinematographic studies on normal subjects,'' Folia Phoniatr. **22**, 107–116.

Wittenberg, T. (**1997**). ''Automatic motion extraction from laryngeal kymograms,'' in *Advances in Quantitative Laryngoscopy*, edited by T. Wittenberg, P. Mergell, M. Tigges, and U. Eysholdt (Verlag Phoniatrie, Göttingen), pp. 21–28.

Wittenberg, T., Moser, M., Tigges, M., and Eysholdt, U. (**1995**). ''Recording, processing, and analysis of digital high-speed sequences in glottography,'' Mach. Vision Appl. **8**, 399–404.

Wittenberg, T., Mergell, P., Tigges, M., and Eysholdt, U. (**1997**). ''Quantitative characterization of functional voice disorders using motion analysis of highspeed video and modeling,'' Proc. ICASSP-97, Munich, Germany.

Vocal tract area functions for an adult female speaker based on volumetric imaging

Brad H. Story
National Center for Voice and Speech, WJ Gould Voice Research Center, Denver Center for the Performing Arts, Denver, Colorado 80209

Ingo R. Titze
National Center for Voice and Speech, WJ Gould Voice Research Center, Denver Center for the Performing Arts, Denver, Colorado 80209 and Department of Speech Pathology and Audiology, University of Iowa, Iowa City, Iowa 52242

Eric A. Hoffman
Division of Physiologic Imaging, Department of Radiology, University of Iowa College of Medicine, Iowa City, Iowa 52242

(Received 25 September 1997; accepted for publication 7 April 1998)

Magnetic resonance imaging (MRI) was used to acquire vocal tract shapes of ten vowels /i, ɪ, ɛ, æ, ʌ, ɑ, ɔ, o, ʊ, u/ and two liquid approximants /ɝ, l/ for a 27-year-old adult female. These images were complemented with additional images acquired with electron beam computed tomography (CT) of /i/ and /ɑ/. Each 3-D shape was condensed into a set of cross-sectional areas of oblique sections perpendicular to the centerline of the vocal tract's long axis, resulting in an ''area function.'' Formant frequencies computed for each area function showed reasonable similarity to those determined from the natural (recorded) speech of the imaged subject, but differences suggest that some of the imaged vocal tract shapes were articulated differently during imaging than during recording of natural speech, and also that imaging procedures may have compromised some accuracy for a few shapes. The formant calculations also confirmed the significant effect that the piriform sinus can have on lowering the formant frequencies. A comparison is made between area functions derived using both MRI and CT methods for the vowels /i/ and /ɑ/. Additionally, the area functions reported in this study are compared with those from two previous studies and demonstrate general similarities in shape but also obvious differences that can be attributed to anatomical differences of the imaged subjects and to differences in imaging techniques and image processing methods. [S0001-4966(98)03807-7]

PACS numbers: 43.70.Aj, 43.70.Jt [AL]

INTRODUCTION

The use of magnetic resonance imaging (MRI) has, in recent years, become a viable option by which to study speech production. In particular, it is well suited for volumetric imaging in which the entire head and neck tissue surrounding the vocal tract is captured as a set of image slices (in the axial, sagittal, or coronal planes). The 3-D vocal tract shape can be reconstructed from this image set by separating the air in each slice from the tissue and bone. Since one of the primary goals of vocal tract imaging is to obtain the information necessary to accurately model speech production, particular interest is in reducing the 3-D vocal tract shape to cross-sectional areas extending from the glottis to the lips to generate an ''area function.'' Note that even though the 3-D shape is reduced to an area function, the areas are measured directly from the imaged head and neck volume rather than from a rule-based conversion of midsagittal dimensions to area (e.g., Mermelstein, 1973). The main disadvantage of using MRI to study speech is that acquisition of enough image slices to capture a single volume of the vocal tract space typically requires several minutes of scanning. This currently restricts volumetric studies to single phonemic configurations rather than continuous speech. Nonetheless, much can be learned from static vocal tract shapes as is evidenced by the extensively used area function data in Fant (1960) and recent MRI-based studies reported by Baer *et al.* (1991) and Yang and Kasuya (1994) for vowels; Dang *et al.* (1994) for nasals and the nasal tract; Dang and Honda (1997) for piriform sinuses; Story *et al.* (1996b) for vowels and consonants; and the extensive work on fricatives, liquid approximants, and vowels by Narayanan *et al.* (1995, 1997a), Alwan *et al.* (1997) and Narayanan *et al.* (1997b).

This study is part of a continuing effort to collect comprehensive sets of phonemic vocal tract shapes (vowels and consonants) and corresponding area functions from a small number of subjects; Story *et al.* (1996b) reported area functions for 18 vocal tract configurations of one male subject. The point is to generate speaker-specific area function inventories that can be used to model the entire spectrum of speech sounds of a particular person. Such an inventory would retain that part of a speaker's identity which is vocal tract dependent, making it useful for understanding which components of the vocal tract shape contribute to the unique sound of an individual as well as providing the basis for simulating or synthesizing speaker-specific speech. Some

TABLE I. List of imaged phonemes and example words.

Phonetic symbol	Example
i	heat
ɪ	hit
ɛ	head
æ	hat
ʌ	ton
ɑ	hot
ɔ	paw
o	hoe
ʊ	hood
u	who
ɝ	earth
l	lump

limited success in synthesizing sentence level speech with the male area functions of Story *et al.* (1996b) was reported in Titze *et al.* (1997). Ideally, such inventories would exist for many diverse speakers such as males and females of different regional, racial, and language backgrounds. Continued vocal tract imaging projects may eventually realize an extensive, diverse database of comprehensive area function sets, and corresponding audio recordings for a variety of speakers, providing a resource for speech researchers.

The specific aim of this paper is to report vocal tract area functions corresponding to ten vowels (/i, ɪ, ɛ, æ, ʌ, ɑ, ɔ, o, ʊ, u/) and two liquid approximants, /ɝ/ and /l/, of one adult female subject. In addition to using MRI, electron-beam computed tomography (CT) was used to acquire additional image sets for /i/ and /ɑ/. The advantage of CT relative to MRI is that it gives a more distinct air-tissue interface, images teeth, and requires far less scan time; its disadvantage is the exposure to ionizing radiation, hence the reason for imaging only two vowels. The data obtained with CT are useful for: (1) measuring the volume of the teeth; this information is used to correct the MRI image sets since MRI poorly images teeth; (2) accurately measuring the length and cross-sectional area of the piriform sinuses; and (3) a cross-comparison of vocal tract shapes imaged with two independent imaging systems.

The paper will first focus on presenting the area function data and making comparisons between MRI and CT and also to other recent MRI-based studies. The accuracy of the area functions is then assessed by comparing the formant frequencies derived from acoustic modeling and those measured from the recorded speech of the subject.

I. IMAGE ACQUISITION AND ANALYSIS

A. Scanning parameters and protocol

Volumetric imaging of the vocal tract was performed using MRI for 22 different phonemic vocal tract shapes of one female subject and also for the nasal tract and trachea. However, only a subset, listed in Table I, will be reported here. At the time of scanning, the subject (DJ) was a 27-year-old female with no history of speech or voice disorders and is native to the state of Texas in the southern United States. She did not, however, have a pronounced Texas accent. She also had no history of specialized vocal or speech training (e.g., phonetics, singing, dramatic arts, public speaking, etc.). The subject was 5-ft 2-in. tall and weighed approximately 120 pounds. Additionally, the vowels /i/ and /ɑ/ were imaged with CT for the same subject.

Prior to any of the imaging sessions, the subject participated in two practice/training sessions in which she lay supine on a comfortable cushion and practiced sustaining the phonemes listed in Table I; concentration on maintaining a steady vocal tract shape was emphasized. The example words (Table I) were helpful in eliciting the appropriate vowel sound. Such practice sessions are regarded by the authors as being an essential orientation for the subject.

The MR images were acquired using a General Electric Signa 1.5-Tesla scanner. The image acquisition mode and pulse sequence parameters were identical to those used in Story *et al.* (1996b). A 24 slice series of 5-mm-thick contiguous, parallel, axial sections extended from just superior to the hard palate down to about the first tracheal ring. The field of view (slice dimensions) for each slice was 24 cm×24 cm which, with a pixel matrix of 256×256, gives a pixel dimension of 0.938 mm/pixel. Each series of image slices was gathered in such a way that the first 12 slices span the entire volume of the head and neck but with a 5-mm gap between each slice. The next 12 slices also span the entire volume with a 5-mm interslice gap but this acquisition begins with a 5-mm offset relative to the first 12 slices. Thus the acquisition of the last 12 slices fills the gaps between the first 12, resulting in a contiguous 24 slice series. This procedure is called an interleaved acquisition.

After the subject had been positioned in the MR scanner (see Story *et al.*, 1996b, for more details), the image acquisition protocol proceeded as follows. For a specific phoneme, the corresponding example word (see Table I) was spoken to the subject over an intercom. The subject then was asked to produce a sustained version of the phoneme that the investigators verified before beginning the actual image acquisition. When the subject was ready she began phonation. At this time the MR technologist started scanning and after 8 s the scan was paused to allow the subject to breathe. The scanning was continued when the subject resumed phonation. The scanning time required for each image set (i.e., for one phoneme) was 4 min and 48 s which required on the order of 36 repetitions of each phoneme. Thus with pauses for respiration between repetitions, each image set took about 10–15 min to complete. Because of the potential for vocal and general physical fatigue, the experiment was separated into two sessions which occurred different days.

All CT images were obtained using an Imatron C-150 scanner (Boyd and Lipton, 1983) (Imatron Corp., South San Francisco). For a single volume scan of the vocal tract, a series of 3-mm-thick contiguous, parallel, axial images were acquired with the same superior/inferior extent as for the MRI. The axial images captured the full A-P (anterior–posterior) and lateral extent of the airway within each slice. The field of view was 18 cm with a pixel matrix of 512 ×512. This provided ''*x*'' and ''*y*'' pixel dimensions in the axial plane of 0.352 mm. The time required to scan the desired 40 slice volume using the CT was approximately 20 s, which was too long to comfortably phonate without strain.

TABLE II. Comparison of electron beam computed tomography (CT) and magnetic resonance imaging (MRI) with specific regard to this study.

Imaging parameter	CT	MRI
Field of view (cm)	18×18	24×24
In-plane matrix (pixels)	512×512	256×256
In-plane resolution (cm/pixel)	0.0392	0.0938
Cross-sectional area of one pixel (cm^2)	0.0015	0.0088
Slice thickness (cm)	0.3	0.5
Teeth	yes	no
Scan time for one volume (min)	0.33	4.8
~No. of repetitions to complete scan	2	36

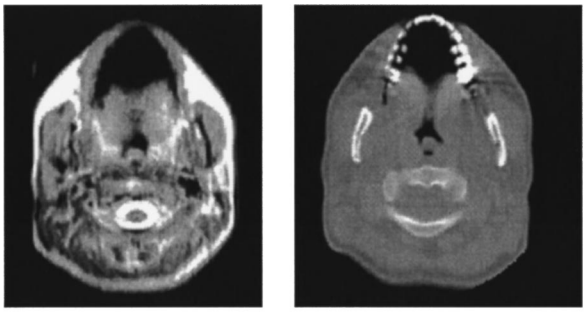

FIG. 1. Axial slices through the oral cavity for the vowel /ɑ/: (a) MRI; (b) CT.

Thus the subject phonated for 10 s at the end of which scanning was halted to allow for respiration and then restarted. (A recently updated version of the CT scanner is now able to acquire 140 slices in 15 s.)

The use of two entirely independent imaging modalities to acquire vocal tract shapes for the same two vowels allows for cross checking the validity of each measured area function; any gross measurement errors in using either method should be apparent in the comparison. Another aspect of using two methods of imaging is that separate productions of the same vowel are captured at different times and on different days, thus allowing for an evaluation of measurement repeatability. Also, because the image acquisition time for CT is on the order of seconds rather than minutes, the CT-based tract shapes are much closer to being a ''snapshot'' of the vowel rather than a long-term average over many repetitions.

Table II summarizes the measurement parameters of both imaging systems; it should be noted that these comparisons strictly apply to this study only and should not be considered as a general comparison of the two imaging systems. The in-plane dimensions of each CT slice are sampled by twice as many pixels as the MRI which, with their respective fields of view, gives pixel dimensions of 0.0392 cm/pixel and 0.0938 cm/pixel for CT and MRI, respectively. This means that the minimum measurable cross-sectional area in any given CT slice is 0.0015 cm^2 while for MRI the minimum is nearly six times greater at 0.0088 cm^2. These differences are especially important when small areas are measured. For example, an area of 0.2 cm^2 would be sampled by 133 pixels in an CT slice but by only 22 pixels in an MRI slice. Thus if the algorithm which segments the air from tissue were to miss, say, one pixel, the MRI-based measurement would be in error by nearly 5% while an error of less than 1% would result from an CT-based measurement. The thickness of each axial slice is also finer at 3 mm for CT than the 5 mm used to obtain the MR images, giving the inferior–superior dimension in the CT image set greater spatial resolution than the MRI-based set. Also note that the teeth are captured by the CT but not by MRI, which means that the MR images must be corrected for the presence of the teeth.

Another important comparison is the amount of time required to scan the vocal tract volume for each phonemic configuration. With CT, the scan time is 0.33 min (20 s) which can be completed with only two repetitions of a given phoneme. In contrast, the MR scanner needed 4.8 min to capture the desired volume requiring the subject to perform about 36 repetitions. Thus with finer spatial resolution, capture of the teeth, and significantly less scan time, CT should provide the more accurate image sets from which area functions can be determined.

It should also be noted that the wearing of ear plugs and the intense sound of the MR scanner required the subject to phonate at a much higher intensity level than would be typical for conversational speech. In contrast, the CT scanner is relatively quiet, allowing the subject to phonate at a more comfortable intensity. Thus the MR images must be considered as representing ''loud'' speech while the CT represents a more conversational level of loudness.

B. Image analysis

The analysis of all image sets was performed with VIDA (Volumetric Image Display and Analysis) which is a general image display and quantitation package (Hoffman *et al.*, 1992; see also the Internet web page at http://everest.radiology.uiowa.edu). The image analysis process is the same as was used in our previous work which can be found in Story (1995) and Story *et al.* (1995, 1996a,b). Thus detailed explanations of the entire image analysis will not be repeated here.

Figure 1(a) and (b) show an axial slice through the oral cavity for the vowel /ɑ/ using MRI and CT, respectively. In the MR slice [Fig. 1(a)], black space exists for air, teeth, and blood while in the CT slice [Fig. 1(b)] black space denotes only air; note that the teeth are visible in the CT slice. The image analysis process included three main steps. The first step is the segmentation of the airway in each slice (like those in Fig. 1) from the surrounding tissue including an account of the space occupied by teeth; note that the dimensions of the teeth can be obtained from the CT images and used to correct the MR image sets (Story *et al.*, 1996a,b). Step two is the three-dimensional reconstruction of the airway by shape-based interpolation (Raya and Udupa, 1990; see also Story *et al.*, 1996b, p. 541), such as those shown in Figs. 2–3 and 6–10.

Because the image sets were gathered in an interleaved fashion, any change in position of the subject's body (most importantly the head and neck) from the beginning to the end of scanning one vocal tract shape will be reflected as an offset of the two interleaved halves of the image set. A sig-

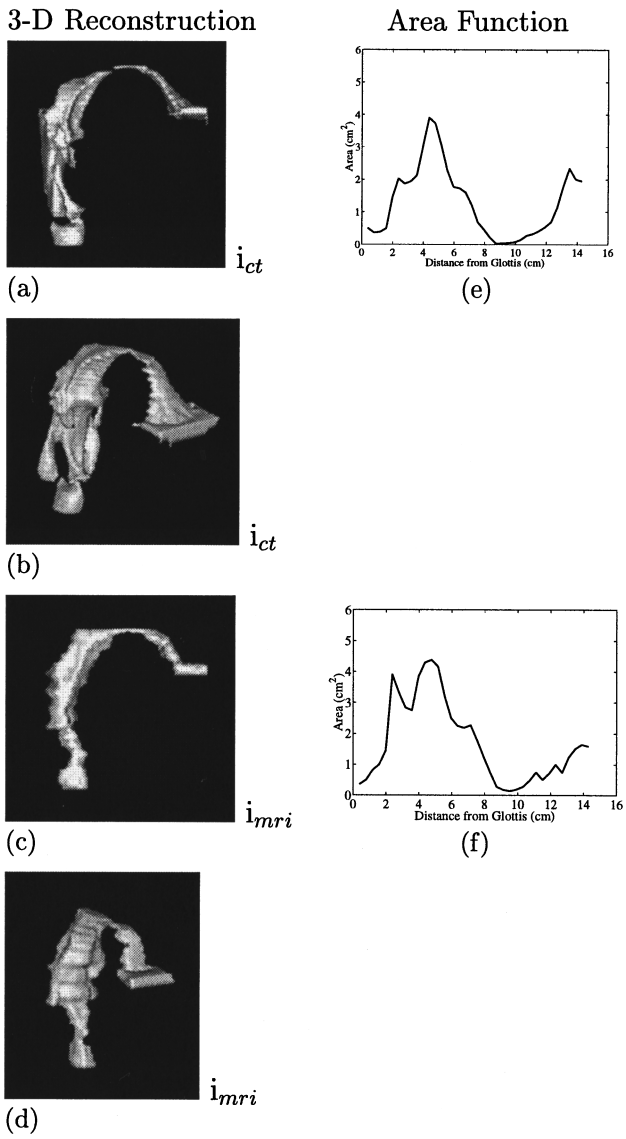

FIG. 2. 3-D reconstructions and area functions for /i/: (a) CT-based /i/—sagittal projection; (b) CT-based /i/—rotated and tilted; (c) MRI-based /i/—sagittal projection; (d) MRI-based /i/—rotated and tilted; (e) area function for CT-based /i/; (f) area function for MRI-based /i/.

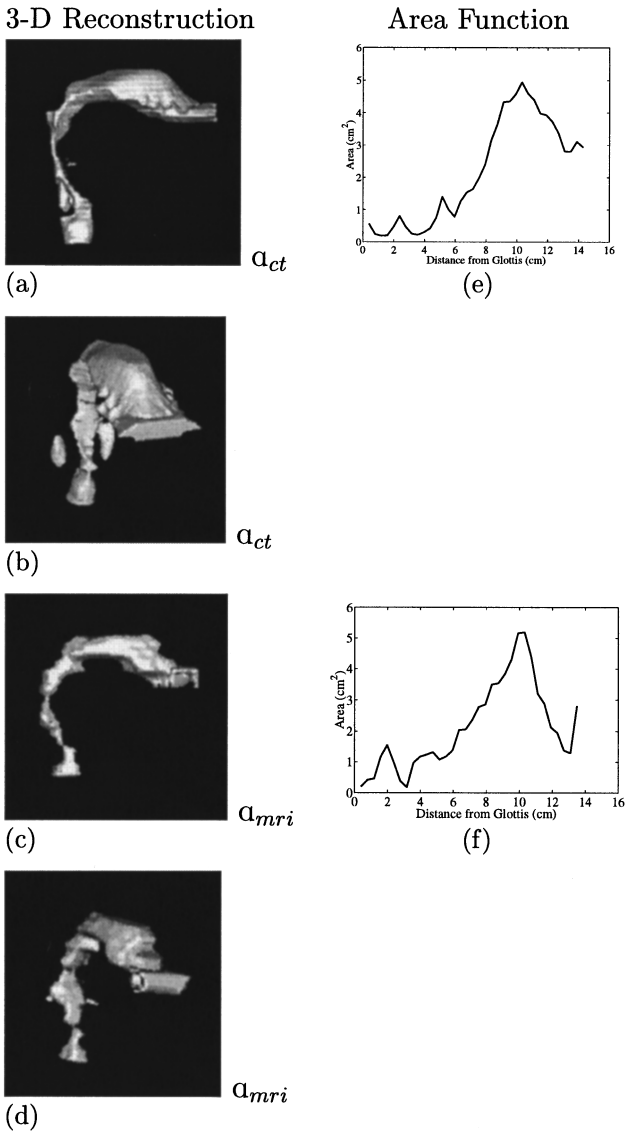

FIG. 3. 3-D reconstructions and area functions for /ɑ/: (a) CT-based /ɑ/—sagittal projection; (b) CT-based /ɑ/—rotated and tilted; (c) MRI-based /ɑ/—sagittal projection; (d) MRI-based /ɑ/—rotated and tilted; (e) area function for CT-based /ɑ/; (f) area function for MRI-based /ɑ/.

nificant offset of this type will create a rippled texture in the superior/inferior dimension of the 3-D reconstructed shapes. Prior to the image analysis process for each shape, an assessment was made as to whether such an offset had occurred. This assessment was made by reformatting the axial image sets so that a midsagittal slice could be viewed. Any offset was clearly indicated in this plane if sharp discontinuities existed in the contour of the spine or other identifiable boundaries. If present, the offset was corrected by moving one-half of the image set (every other slice) relative to the other until the discontinuities were as smooth as possible. This correction was performed on the vowels /ɑ/, /ɔ/, and /æ/. Even after correction, the rippled effect can be seen in the oral cavity of the /ɔ/ (see Fig. 7). Such an effect was observed only in the /m/ and /n/ of the Story *et al.* (1996b) and no correction was applied in that case. The problem came to light only when a reconstruction of the /ɑ/, the first shape analyzed, yielded a highly rippled structure. A small amount of rippling can be seen in many of the uncorrected surface rendered shapes, usually in the pharyngeal region. The deviation in these cases was regarded as too small to be effectively corrected.

The final step is determination of the area function. The glottal end point of the vocal tract was measured directly from the 3-D vocal tract reconstruction by first finding the interpolated axial slice in the glottal region with the smallest area. The end of the vocal tract was then set to be the area in the next superior slice. The area at the lips was also determined from the 3-D reconstruction but from a measurement of the coronal slice at the termination of the vocal tract. The cross-sectional areas between the end points were determined by finding the centerline through the 3-D reconstruction with an iterative bisection algorithm (see Story *et al.*, 1996b, p. 542) and then measuring the areas of oblique sections calculated to be locally perpendicular to the centerline. Thus the collection of these areas extending from just above

the glottis to the lips comprises the area function. However, area functions produced by this process have variable linear distances between consecutive cross-sectional area values (areas were separated by 0.2–0.4 cm of vocal tract length). For acoustic modeling purposes it is often convenient if each area function is discretized at equal length intervals. The type of acoustic model used in a later section of this paper (wave-reflection type) to compute the vocal tract formants, requires that the length of the final area function be an even integer multiple of the length interval. The wave-reflection model dictates that the length of each finite section of the area function be equal to the speed of sound divided by two times the sampling frequency. For this study (also for Story *et al.*, 1996b), the length interval was chosen to be 0.396 825 cm which results from a sampling frequency of 44.1 kHz and a speed of sound equal to 350 m/s. Thus each ''raw'' area function produced by the image analysis was transformed to meet these demands by first normalizing it to a discrete length that was closest to the measured length. Following length normalization, the area function was converted to the equal length interval representation by fitting it with a cubic spline and then sampling the resulting curve at the desired equally spaced intervals.

II. RESULTS

In this section, the 3-D images and area functions for the /i/ and /ɑ/ vowels are first presented such that the comparison between CT and MRI can be readily observed. Measurements of piriform sinuses from the CT image sets and the MRI-based images and area functions of the vowels and liquids follow in succeeding sections.

A. Vowels /i/ and /ɑ/: CT and MRI

Two projections of the reconstructed 3-D vocal tract shapes are shown for the CT and MRI versions of /i/ and /ɑ/, along with their area functions in Figs. 2 and 3, respectively. The a, b, and e parts of each figure correspond to CT, while the c, d, and f correspond to MRI. The first picture for each case [Figs. 2(a), (c) and 3(a), (c)] is a sagittal projection followed by a rotated and tilted view [Figs. 2b, (d) and 3(b), (d)] allowing for a better perspective of the 3-D shape. The most inferior point of each vocal tract reconstruction is the uppermost section of the trachea which then narrows in the glottal region before widening into the pharyngeal cavity. The tract then bends into the oral cavity, finally terminating at the lips (most anterior point). The greater spatial resolution of the CT images relative to those from MRI is apparent in the reconstructions where more of the fine structure of the pharyngeal walls and the oral cavity can be seen. Note the impressions into the airway made by the teeth in the /ɑ/. Above the trachea, the CT-based reconstructions become small in the region of the glottis and then widen for a short distance into the laryngeal ventricle. The fingerlike extensions that hang down below the pharynx are the piriform sinuses; note that the right piriform sinus of the /ɑ/ [Fig. 3(b)] is disconnected from the main vocal tract.

In the MRI-based reconstructions, the laryngeal ventricle appears to be absent. Movement artifact in the glottal region could have obscured some of the detail of this region, but also the enviroment of the MR-scanner required loud phonations which could possibly lead to a reduced ventricular area. Such a relationship between phonation and ventricular area can be observed in van den Berg (1958, p. 232) where laryngeal x-ray tomograms of a bass vocalist, phonating with an /ɑ/ vowel at a fundamental frequency of 173 Hz, showed a smaller ventricular space for a 75-dB production than for one at 55 dB. Vennard (1967, pp. 90–92), in summary of the van den Berg (1958) tomograms and similar additional tomograms from Landeau and Zuili (1963), states: ''*in soft tones and falsetto tones the ventricles are the largest. In medium tones they are smaller, and in loud high chest tones they are often obliterated*.''

In some of the MR image sets, the piriform sinuses appeared to be disconnected from the main vocal tract and it was not clear whether this was due to movement artifact or if the sinuses were truly decoupled. The CT reconstructions indicate a well-defined sinus structure but also show the possibility of decoupling from the main vocal tract. It was decided to use only the higher resolution measurements of the piriform space from the CT images and to not analyze them at all in the MR images. Thus the piriform sinuses are absent in all of the MRI-based 3-D reconstructions.

For each of the area functions, the leftmost area represents a point just above the glottis and the lip termination is at the right side of the graph. Since the area functions were discretized at equal length intervals of 0.396 cm, the first area begins at that distance. None of the area functions in this paper include the cross-sectional area of the piriform sinuses; their measurements are presented in the next section.

As expected, the vocal tract reconstructions and area functions from both CT and MRI show the opposing configurations of the pharyngeal and oral cavities for these two vowels; i.e., large pharynx and constricted oral cavity for the /i/, constricted pharynx, and large oral cavity for /ɑ/. However, due to the presence of the laryngeal ventricle, the CT area functions begin with an area of about 0.5 cm^2 and then decrease before increasing again at about 2 cm above the glottis. In contrast, the MRI-based area functions begin with small areas and increase with distance from the glottis. For all four area functions, the area begins to increase at about 2–3 cm above the glottis, which is approximately where the piriform sinuses join the main vocal tract tube. Each of these area functions, as well as the other vowels in this study, are tabulated in numerical form in Table III.

The CT and MRI versions of the /i/ vowel have comparable back-cavity maximum areas of about 4 cm^2 at similar distances above the glottis. Likewise, the frontal cavity areas (11–15 cm) are also quite similar. The minimum area in both cases occurs at around 9 cm from the glottis, but in the CT area function this minimum is less than 0.1 cm^2 which is unrealistically small for a vowel; the smallest area in the MRI /i/ is 0.14 cm^2. The likely origin of this small area comes from a limitation of imaging in only the axial plane. For vocal tract shapes with a highly constricted, but open, front cavity, most notably an /i/, the thickness of an axial slice (3 mm for CT, 5 mm for MRI) may contain contributions of both tissue and air. The result is a gray-scale value

TABLE III. Area functions for ten vowels (subject DJ). Column 1 indicates the section number, each of which represents a length of 0.396 825 cm. Column 2, labeled ''dist.'' is the distance from the glottis in centimeters. For each vowel, section 1 is the glottal end of the vocal tract and the final section is the termination at the lips. The ''ct'' subscript indicates area functions derived from electron beam computed tomography. All areas are given in cm^2.

Section	dist.	i	i_{ct}	ɪ	ɛ	æ	ʌ	ɑ	$ɑ_{ct}$	ɔ	o	ʊ	u
1	0.40	0.36	0.50	0.21	0.18	0.26	0.18	0.20	0.56	0.82	0.17	0.07	0.22
2	0.79	0.50	0.36	0.14	0.15	0.19	0.29	0.42	0.24	1.11	0.18	0.10	0.48
3	1.19	0.82	0.38	0.40	0.55	0.70	0.51	0.46	0.19	0.95	0.81	0.07	0.81
4	1.59	1.00	0.49	0.51	0.92	1.23	0.94	1.17	0.20	0.70	0.65	0.05	0.90
5	1.98	1.45	1.45	0.82	0.49	1.14	0.43	1.55	0.46	0.44	0.61	0.18	1.20
6	2.38	3.90	2.03	0.72	0.53	1.03	0.37	0.99	0.80	0.45	0.46	0.43	3.13
7	2.78	3.33	1.87	0.88	0.50	1.10	0.42	0.38	0.47	0.38	0.44	0.75	2.71
8	3.17	2.84	1.94	1.01	0.46	1.27	0.27	0.18	0.25	0.36	0.61	0.47	1.75
9	3.57	2.75	2.13	0.91	1.35	1.78	0.51	0.97	0.22	0.56	0.67	0.29	2.01
10	3.97	3.84	3.02	1.55	1.16	1.94	0.60	1.17	0.30	1.01	0.97	0.11	2.20
11	4.37	4.30	3.90	1.70	1.54	1.80	1.00	1.24	0.42	0.95	1.19	0.32	2.16
12	4.76	4.38	3.73	1.86	1.31	2.16	0.48	1.32	0.75	0.79	0.66	0.58	2.56
13	5.16	4.16	3.05	1.36	1.03	2.78	0.21	1.08	1.40	0.68	0.37	1.11	2.61
14	5.56	3.22	2.27	1.14	1.38	3.01	0.28	1.18	1.01	0.33	0.46	0.84	2.34
15	5.95	2.50	1.77	1.67	1.67	3.00	0.62	1.38	0.78	0.88	1.33	0.17	2.05
16	6.35	2.25	1.73	1.93	1.45	2.98	0.84	2.04	1.26	2.06	2.00	0.39	1.21
17	6.75	2.19	1.60	1.79	1.26	2.92	0.92	2.06	1.54	2.41	1.81	0.81	0.80
18	7.14	2.27	1.21	1.57	1.22	3.27	1.15	2.36	1.64	2.47	1.77	1.03	0.74
19	7.54	1.78	0.68	1.46	1.29	3.80	1.47	2.78	1.98	3.10	2.24	1.02	1.36
20	7.94	1.25	0.46	1.22	1.27	3.79	2.00	2.86	2.40	4.01	2.43	1.04	1.18
21	8.33	0.74	0.21	1.28	1.28	4.03	2.32	3.50	3.16	4.43	2.87	1.42	1.05
22	8.73	0.28	0.03	1.22	1.45	3.46	2.71	3.54	3.65	5.15	4.24	1.93	0.78
23	9.13	0.18	0.04	1.31	1.83	3.06	2.64	3.84	4.33	5.61	4.63	2.10	0.78
24	9.52	0.14	0.05	1.23	1.46	2.75	2.74	4.31	4.35	6.07	4.95	2.21	1.17
25	9.92	0.19	0.07	1.13	1.26	3.89	2.26	5.16	4.58	6.62	4.92	2.53	1.47
26	10.32	0.28	0.14	1.20	1.25	2.91	2.14	5.19	4.94	7.15	4.76	2.82	2.00
27	10.71	0.48	0.27	0.98	1.77	3.22	1.96	4.39	4.59	8.05	5.34	2.80	2.50
28	11.11	0.75	0.32	1.47	1.60	3.82	2.02	3.20	4.39	8.38	5.43	2.46	2.92
29	11.51	0.51	0.41	1.70	1.52	3.90	1.83	2.89	3.98	8.13	4.75	2.32	3.10
30	11.90	0.71	0.53	0.97	1.80	3.43	1.25	2.13	3.93	8.10	4.26	2.46	2.98
31	12.30	1.00	0.69	0.86	2.14		1.35	1.95	3.72	8.64	2.97	2.09	3.40
32	12.70	0.74	1.14	1.20	1.59		1.90	1.38	3.37	6.02	1.99	2.57	3.61
33	13.10	1.24	1.80	1.18			1.70	1.29	2.81	3.32	1.33	1.76	2.97
34	13.49	1.51	2.34	1.34			1.69	2.81	2.81	2.26	1.45	1.37	2.74
35	13.89	1.65	2.01						3.11	1.94	1.60	1.09	1.79
36	14.29	1.59	1.95						2.94	1.58	1.39	1.16	0.87
37	14.68												0.44
38	15.08												0.18

that is some ''average'' of air and tissue which could be above or below the established gray-scale threshold for air (i.e., air may be included as tissue or vice versa). For an /i/ at its most constricted point, the airspace between the tongue surface and the hard palate may not span an axial distance of more than one image slice. Thus if both tissue and air contribute to the gray-scale value of the slice, the error in area measurement in this particular location of the vocal tract could be quite large. This same problem may also exist in the MRI-based /i/ (in fact, it is potentially more of a problem because of the thicker slices), but apparently the production in this case was more open than the CT version giving a more reasonable minimum area. Also, since the MRI /i/ was acquired with an undesired, but necessary, loud vocal production (i.e., increased subglottal pressure), a slightly more open vocal tract shape might be expected to avoid turbulence generation due to increased supraglottal pressure behind the constriction (Schulman, 1989). However, it will be shown in a later section on acoustic modeling that both of these /i/ area functions produce first formants ($F1$) well below those measured from the subject's recorded speech, suggesting that the minimum area is too small in both cases. These small constriction areas also indicate that the subject may have produced a somewhat extreme version of /i/, possibly due to her articulatory adaptation to the supine position; she may have used more linguopalatal bracing and also exaggerated the tongue root retraction relative to speaking in an upright position.

For the /ɑ/, the CT and MRI cases show many similarities but also some important differences. The CT /ɑ/ is apparently a more extreme production than its MRI counterpart with a more open oral cavity and constricted pharynx. Such a production would likely have a lower tongue position than in the MRI /ɑ/. Both area functions have nearly the same maximum area ($\sim 5\ cm^2$) occurring in the oral cavity at about 10 cm from the glottis, but beyond the maximum, the area in the MRI /ɑ/ rapidly decreases to about $1.3\ cm^2$ before rising to almost $3\ cm^2$ at the lips. The CT /ɑ/ also decreases from the maximum but more gradually and only to a value just below $3\ cm^2$. The pharyngeal areas also differ between the two /ɑ/'s. Between 1 and 7 cm from the glottis the MRI /ɑ/ has areas that are about 1.1–2 times larger than the CT /ɑ/. The

length of the CT /ɑ/ is also about 0.8 cm longer than the MRI.

In general, the differences observed between the CT and MRI versions of the /i/ and /ɑ/ area functions seem to be largely due to the subject's variation in producing these vowels rather than any significant differences between imaging methods.

B. Piriform sinuses

Measurements of the piriform sinuses were performed on the CT-based reconstructions of the /i/ and /ɑ/ because of the higher spatial resolution relative to MRI. As mentioned previously, the piriform sinuses can be seen in 3-D form in Figs. 2(a) and (c) and 3(a) and (c) where they are the finger-like extensions that hang down below the pharynx. Axial slices through the piriform sinus region for both the /i/ and /ɑ/ are shown in Fig. 4(a) and (b), respectively; the slices marked 1–6 represent those that contain the sinus cavities, the dark areas to the left and right of the epilaryngeal tube (the center dark area). In each case, the slice labeled ''1'' contains the connection of the sinuses to the epilaryngeal tube (although the right sinus in the /ɑ/ never connects) and each consecutive slice represents a descent of 3 mm toward the glottis. For both vowels, the cross-sectional area of the main vocal tract changes abruptly between slices 1 and 2 as the sinuses connect. This is reflected by the sharp area increase observed 2–3 cm above the glottis in the /i/ and /ɑ/ area functions of Figs. 2 and 3.

Figure 5 shows area functions for the left and right sinuses of each vowel. The x-axis on each graph represents the distance from the entrance of each sinus (the connection point to the main vocal tract). For the /i/, the right sinus connects to the main tract 2 cm above the glottis and the left connection is at a distance of 1.8 cm. The left sinus connection for the /ɑ/ occurs at 2 cm and the right sinus does not connect at all. In each case, the left sinus is shorter than the right. In general, the cross-sectional areas are nearly twice as large for the sinuses in the /i/ versus those from the /ɑ/, apparently due to the pharyngeal widening of the /i/.

The length and area measurements of the piriform sinuses are somewhat smaller than those reported by Dang and Honda (1997). The one female subject in their study showed piriform sinus lengths of 1.7–1.8 cm and volumes ranging from 0.921 to 1.159 cm^2. Also the difference between piriform configuration for different vowels was quite small. In contrast, the subject in the present study (DJ) has piriform lengths of 1.1–1.5 cm and volumes on the order of 0.8 cm^2 (left side) for the /i/ and 0.25 cm^2 for the /ɑ/ (left side).

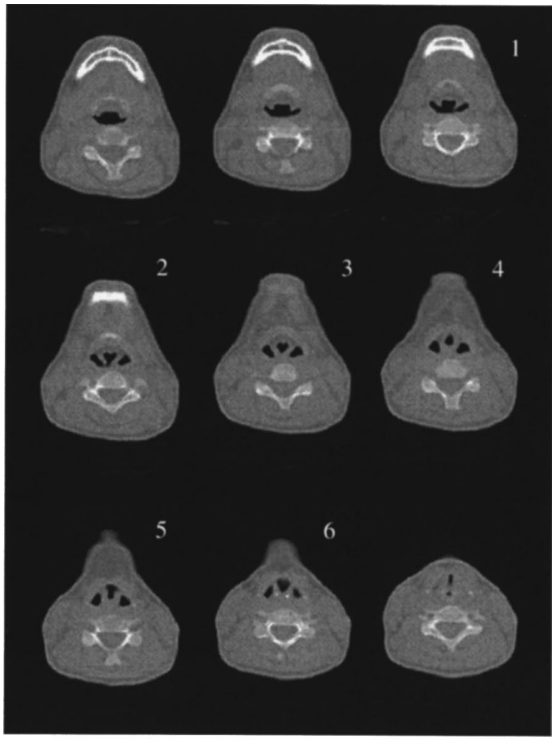

(a)

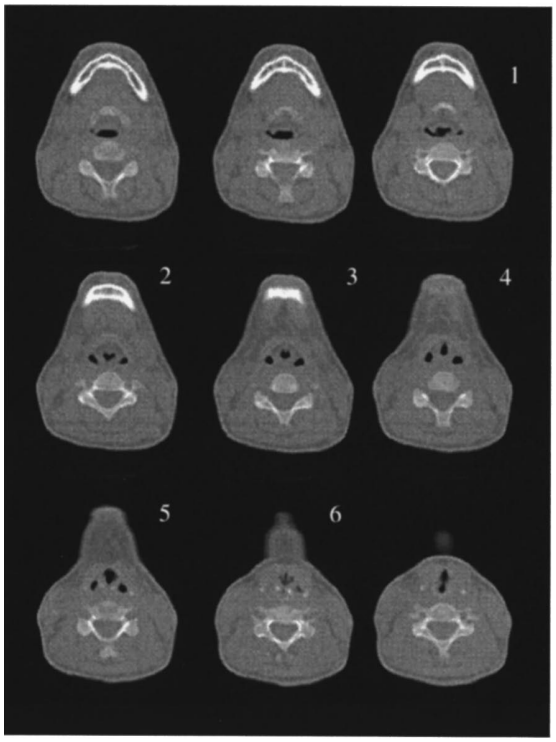

(b)

FIG. 4. Series of axial slices acquired with CT showing the piriform sinuses: (a) from the /i/ image set; (b) from the /ɑ/ image set.

C. MRI-based vowels

Sagittal projections of the 3-D vocal tract reconstructions and their corresponding area functions are shown in Figs. 6, 7, and 8 for the MRI-based vowels; even though presented previously, the /i/ and /ɑ/ are also included here for continuity. The figures are grouped to show a progression of vocal tract shapes that first exhibit a constricted oral section, then a constricted pharyngeal region, and finally a constricted midsection of the vocal tract. The numerical versions of each area function are given in Table III for the ten vowels.

The four vocal tract reconstructions and area functions in Fig. 6 show the tightly constricted oral cavity and wide

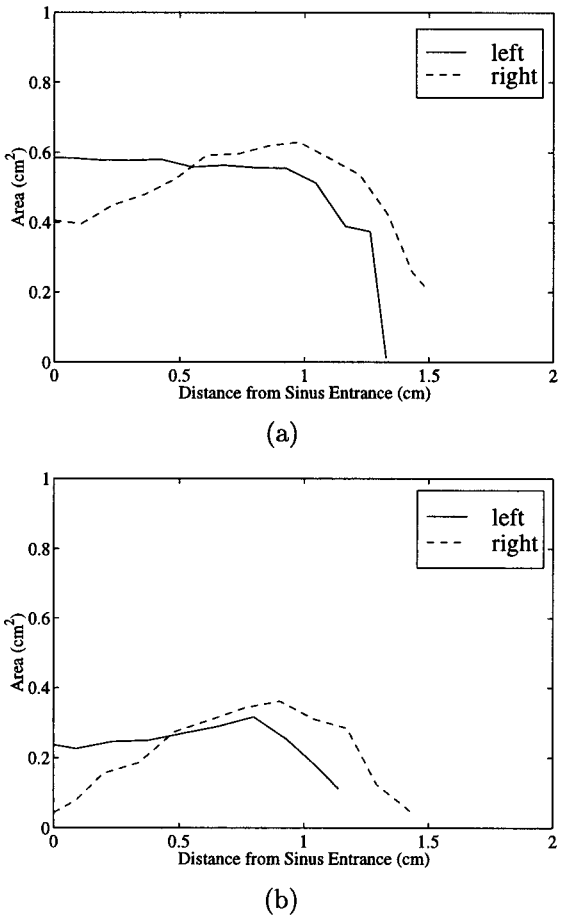

FIG. 5. Area functions for left (solid) and right (dashed) piriform sinuses. The leftmost point on each graph is the connection to the main vocal tract: (a) for /i/; (b) for /ɑ/.

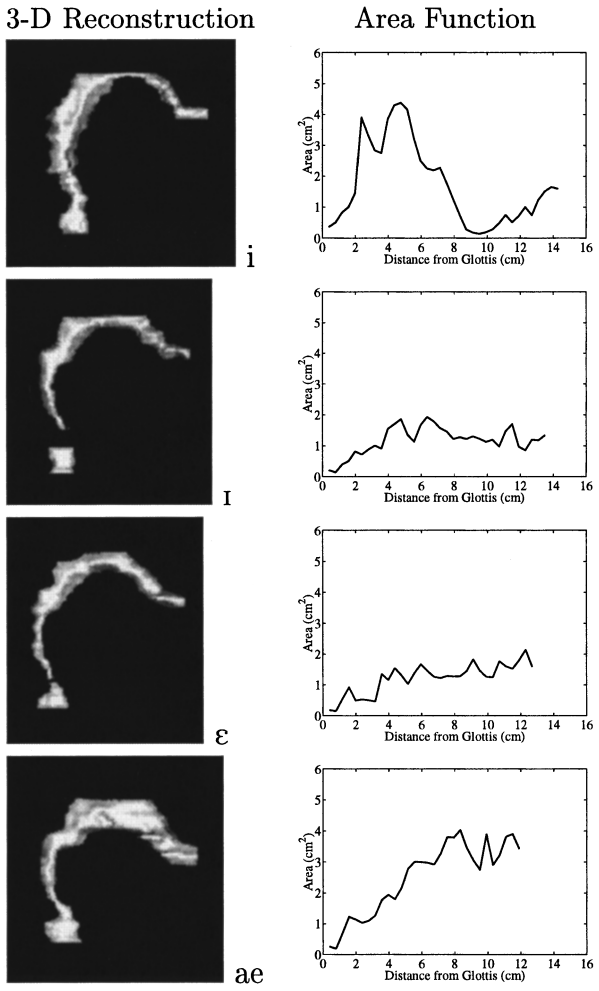

FIG. 6. 3-D reconstructions and area functions for /i/, /ɪ/, /ɛ/, and /æ/.

pharynx of the /i/ give way to increasingly larger oral cavities but shrinking pharyngeal cavities for /ɪ/, /ɛ/, and /æ/. The /ɪ/ contains a break in the airway in the region of the glottis because of blurring, presumably caused by motion artifact. However, because these obscured slices occurred mainly in the glottal region, the area function is still believed to be complete; i.e., the first cross-sectional area is just above the glottis.

The difference in area functions for /i/ and /ɪ/ is quite dramatic. The /i/ pharynx is large and the constriction is tight while the /ɪ/ shows a large reduction in pharyngeal area and a relatively open oral cavity. The /ɛ/ is quite similar to the /ɪ/ in all regions of the area function but a careful examination of both the 3-D reconstructions and the area functions shows that the pharyngeal section (from about 2 cm to 8 cm above the glottis) for /ɪ/ is generally larger than for the /ɛ/. Above the 8-cm point, areas for /ɪ/ show a general decrease while for /ɛ/ area tends to increase. It should also be noted that for both vowels, nearly the entire area function is less than 2.0 cm^2. In contrast, the /i/ had a maximum area of 4.5 cm^2. The male area functions reported by Story *et al.* (1996b) for these three vowels showed a more gradual transition from a wide pharynx and constricted oral cavity for /i/ to a shrinking pharynx and widening oral cavity for /ɪ/ and /ɛ/.

For /æ/, the area gradually increases throughout the entire length of the vocal tract, reaching a peak value of 4 cm^2. The /æ/ maintains the characteristics of both a widened pharynx and a widened oral cavity, giving it a typical hornlike shape and indicating that it is a transition between the front and back vowel categories.

The /ʌ/, /ɑ/, and /ɔ/ are shown in Fig. 7 where all three exhibit a constricted pharynx and a widened oral cavity that grows progressively larger throughout these vowels. The area functions show that the epilarynx and lower pharynx (0 cm to 6 cm above the glottis) for the /ʌ/ and /ɔ/ are both less than 1 cm^2 in area, while the /ɑ/ is slightly more enlarged in this region with areas greater than 1 cm^2. Above a point about 6 cm from the glottis all three vowels have increased cross-sectional areas. The /ʌ/ reaches a peak value of 2.74 cm^2, while the /ɑ/ and /ɔ/ attain peak areas of 5.2 cm^2 and 8.64 cm^2, respectively. The maximum area for the /ɔ/ vowel is the largest in the entire set of area functions. Note that the vertical scale for the /ɔ/ area function extends from 0 to 10 cm^2 while all others are set to a range of 0 to 6 cm^2.

Reconstructions and area functions for /o/, /ʊ/, and /u/ are grouped together in Fig. 8 because they are traditionally thought of as vowels which divide the vocal tract into two distinct chambers separated by a tight constriction. However, only the /u/ seems to exhibit this characteristic and even here the middle section is not highly constricted. A few of these vowel shapes seem to show more similarity to those in the

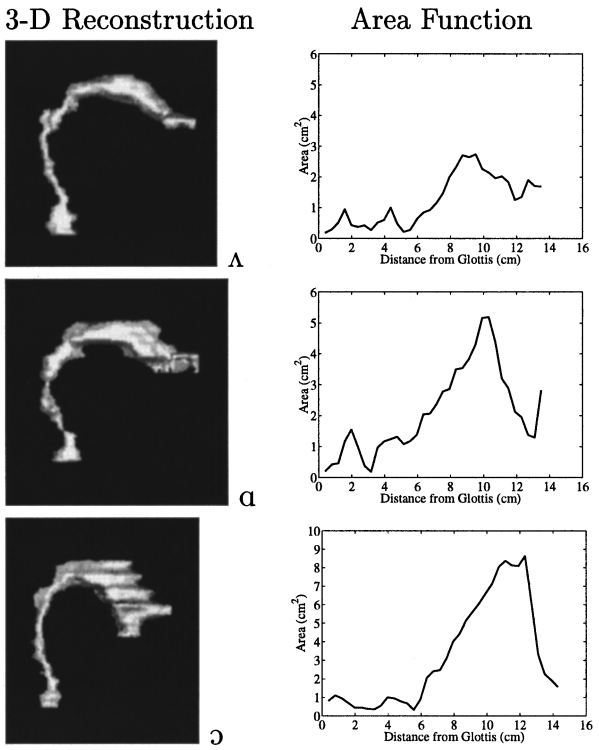

FIG. 7. 3-D reconstructions and area functions for /ʌ/, /ɑ/, and /ɔ/.

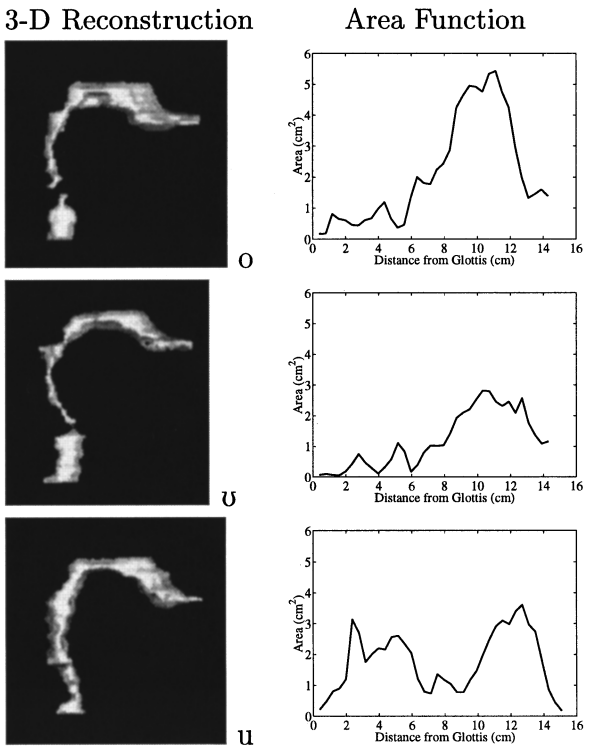

FIG. 8. 3-D reconstructions and area functions for /o/, /ʊ/, and /u/.

previous figure (Fig. 5). In particular, the /o/ is similar to the /ɑ/ and the /ʊ/ similar to the /ʌ/ in the sense that the pharyngeal sections are comparably constricted and the oral cavities similarly enlarged. They are also similar in terms of absolute area measurements where the peak cross-sectional areas for /o/ and /ɑ/ are 5.43 cm^2 and 5.19 cm^2, respectively, while the /ʊ/ and /ʌ/ have respective peak areas of 2.82 cm^2 and 2.74 cm^2. The main differences within these two pairs of vowels is the location of the pharyngeal constrictions. For example, the /o/ has a distinct constriction at about 5.2 cm above the glottis while the /ɑ/ has comparable constriction 3 cm above the glottis. Likewise, the /ʊ/ contains pharyngeal constrictions at locations 4 cm and 6 cm from the glottis and /ʌ/ has similar constrictions at 3 cm and 5 cm above the glottis. The /u/ demonstrates a constriction at a distance 7–9 cm above the glottis which is nearly the midpoint of the vocal tract. On either side of the constriction are two similarly sized cavities resulting from the widened pharyngeal and oral spaces. The lack of a tightly constricted midsection in the /u/ could again be partially due to the loud speech condition necessitated by the MR scanner, where the subject may have opened the tract to avoid turbulence generation (Schulman, 1989).

It is useful to compare some of the area functions in this study to those previously reported for other female subjects. Figure 9 shows the area functions (given in Table III) of our subject (DJ) for the vowels /i, ɑ, u/ together with the area functions of the same vowels from two female subjects, one reported by Yang and Kasuya (1994) and the other by Narayanan *et al.* (1997b). Narayanan *et al.* (1997b) reported area functions for two female subjects but their subject PK was chosen for comparison because she had a vocal tract most similar in size to DJ. In a very gross sense, the general shape of each vowel is similar across the three studies but large differences are apparent. For all of the vowels, the Yang and Kasuya (1994) and Narayanan *et al.* (1997b) area functions show larger areas at the glottal end (epilarynx) than for the DJ versions; note, however, that epilaryngeal areas for the Narayanan *et al.* (1997b) are all smaller than in the Yang and Kasuya (1994) data. Measurement of areas in this region of the vocal tract can be influenced by motion artifact due to the close proximity to the vibrating vocal folds, as well as the method by which the airways are segmented from the surrounding tissue. As was discussed in Secs. II A and II B, the airway in the epilaryngeal region was segmented as being separate from the piriform sinuses to the point where they couple to the main vocal tract. Yang and Kasuya (1994) did not specifically discuss whether the contribution of the piriform sinuses was included or excluded in their reported area functions. Narayanan *et al.* (1997b) did segment the main vocal tract separately from the piriform sinuses but measured the tract area in this region directly from the axial slices (according to Narayanan *et al.*, 1995). In contrast, the method used in this study measured areas from oblique sections perpendicular to the vocal tract centerline throughout the tract, with the exception of the glottal and lip termination areas. As mentioned by Narayanan *et al.* (1995), the area measured directly from the axial plane may differ from those measured from oblique sections by approximately the cosine of the angle between planes. Thus the measurement technique and the particular subject likely account for the differences. It might also be noted here that Högberg's (1995) study of male and female area functions derived from midsagittal x-ray projections, reveal a narrowing of the epilarynx as distance is increased from the glottis. Fant's (1960) area functions also indicate such a narrowing. This characteristic

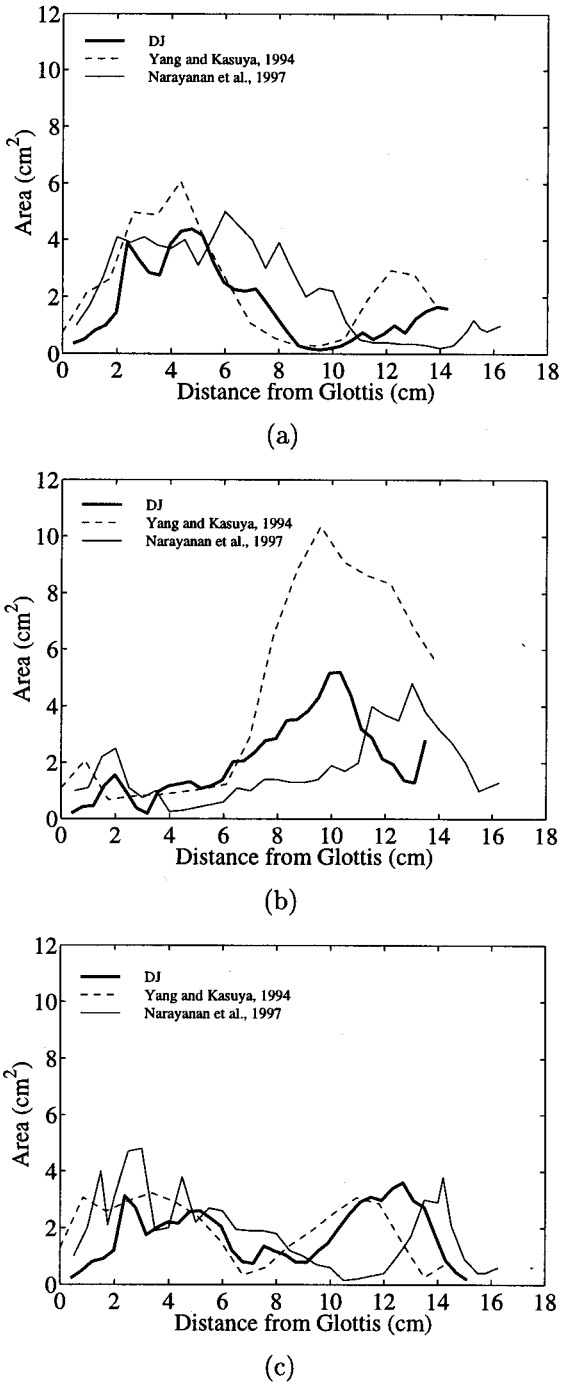

FIG. 9. Comparison of area functions for subject DJ (thick line) with estimated area functions from Yang and Kasuya (1994) (dashed) and Narayanan *et al.* (1997b) (subject PK) (thin line): (a) /i/; (b) /ɑ/; (c) /u/.

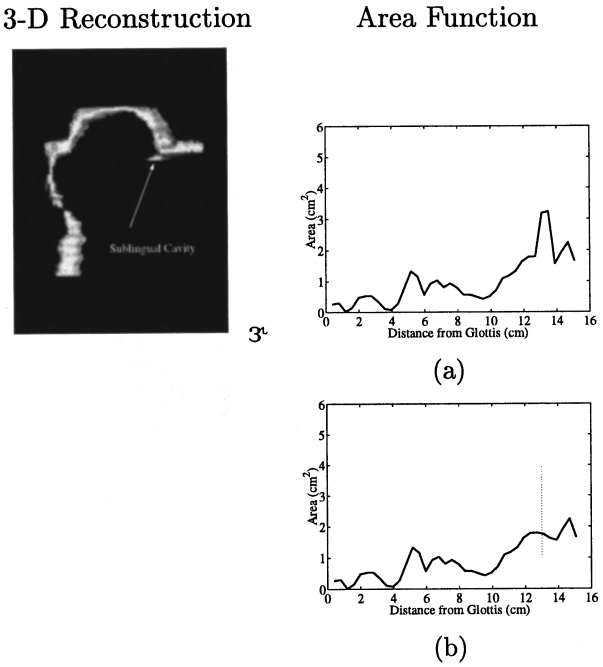

FIG. 10. 3-D reconstruction and area functions for /ɝ/: (a) sublingual cavity is included in the area function; (b) sublingual cavity not included in the area function.

was observed in the area functions for the CT-based /i/ and /ɑ/ (Figs. 2, 3) but does not occur in any of the area functions based on MRI, including those from Yang and Kasuya (1994) and Narayanan *et al.* (1997b). Furthermore, such a narrowing of the epilaryngeal tube is not observed in MRI-based area functions reported for male subjects by Baer *et al.* (1991), Yang and Kasuya (1994), Story *et al.* (1996b), or Narayanan *et al.* (1997b). As mentioned earlier, this may be due to the fact that subjects need to phonate loudly during a MR image acquisition in order to hear themselves resulting in a reduction of the ventricular space. In contrast, the environment for collecting sagittal x-ray projection images is more conducive to conversational levels of vocal intensity.

Throughout the rest of the vocal tract, the areas are comparable across all three studies. The exception is the oral cavity of the Yang and Kasuya /ɑ/ which exceeds 10 cm^2. Narayanan *et al.*'s (1997b) subject has the longest vocal tract of the three subjects and most of this length appears to be in the pharyngeal cavity. The /i/ and /u/ both exhibit widened back cavities that extend to about 10 cm from the glottis. Likewise, oral cavity widening for the /ɑ/, is prominent only beyond the 10-cm point. In addition, the constriction locations in the /u/ for DJ and Yang and Kasuya (1994) are located at nearly the midpoint of their respective tract lengths while the Narayanan *et al.* (1997b) data shows this constriction to be at about 70% of the distance from the glottis to the lips.

D. Liquids /ɝ/ and /l/

The /ɝ/ shape is differentiated from the other tract shapes by the presence of a small sublingual cavity which is indicated in the reconstruction of /ɝ/ in Fig. 10. This cavity is often assumed to act as a sidebranch resonator, and as such should be specified separately from the area function. However, a case can also be made that its length is small enough (less than a centimeter) that its effect as a sidebranch would be primarily at high frequencies (greater than 10 kHz). Thus two area functions for /ɝ/ are shown in Fig. 10 and given numerically in Table IV. The uppermost figure is the case where the contribution of the sublingual cavity has been included in the area function (this is the cause of the sharp area increase at the 13-cm point), while the graph just below it gives the area function without the sublingual cavity. In this second case, the sublingual cavity is a sidebranch that

TABLE IV. Area functions for /ɜ˞/ and /l/. As in Table III, column 1 indicates the section number, each of which represents a length of 0.396 825 cm and column 2, labeled ''dist.'' is the distance from the glottis in centimeters. The third and fourth columns give the /ɜ˞/ with and without the sublingual cavity added to the area function, respectively (this affects only sections 33 and 34). Column 5 gives the areas measured for /l/ extending from the glottis to the lingual contact with the alveolar ridge (sections 1–29) and the front cavity (sections 33–36). The right (rp) and left (lp) lateral passages are given in columns 6 and 7. All areas are given in cm^2.

Section	dist	$ɜ˞_a$	$ɜ˞_b$	l_a	l-rp	l-lp
1	0.40	0.27	0.27	0.18		
2	0.79	0.30	0.30	0.32		
3	1.19	0.02	0.02	0.60		
4	1.58	0.15	0.15	1.12		
5	1.98	0.48	0.48	0.41		
6	2.38	0.53	0.53	0.49		
7	2.77	0.53	0.53	0.41		
8	3.17	0.34	0.34	0.29		
9	3.56	0.11	0.11	0.23		
10	3.96	0.08	0.08	0.72		
11	4.36	0.28	0.28	1.13		
12	4.75	0.80	0.80	0.93		
13	5.15	1.33	1.33	0.75		
14	5.54	1.16	1.16	0.49		
15	5.94	0.57	0.57	0.34		
16	6.34	0.93	0.93	0.75		
17	6.73	1.03	1.03	1.24		
18	7.13	0.81	0.81	1.68		
19	7.52	0.93	0.93	2.26		
20	7.92	0.80	0.80	2.12		
21	8.32	0.57	0.57	2.29		
22	8.71	0.57	0.57	2.26	0.07	
23	9.11	0.50	0.50	2.20	0.06	0.09
24	9.50	0.43	0.43	2.31	0.13	0.10
25	9.90	0.51	0.51	2.22	0.22	0.07
26	10.30	0.71	0.71	2.02	0.28	0.20
27	10.69	1.09	1.09	1.65	0.25	0.20
28	11.09	1.18	1.18	0.75	0.11	0.13
29	11.48	1.33	1.33	0.29	0.09	0.04
30	11.88	1.64	1.64		0.11	0.07
31	12.28	1.78	1.78		0.18	0.12
32	12.67	1.79	1.79		0.25	0.28
33	13.07	3.19	1.75	0.79		
34	13.46	3.24	1.62	1.49		
35	13.86	1.56	1.56	1.52		
36	14.26	1.93	1.93	1.71		
37	14.65	2.24	2.24			
38	15.05	1.65	1.65			

couples to the main area function at a distance 13.1 cm from glottis (indicated by the vertical dotted line) with a length of 0.75 cm. The sidebranch is approximated as two discrete sections with length 0.396 cm and cross-sectional areas of 1.5 cm^2 and 0.5 cm^2. In either case, the area function shows a constriction occurring in the epilaryngeal region (1 cm above glottis) and another in the pharynx (4 cm above glottis). A depression in the area function occurs about 9.5–10 cm from the glottis, which is the apparent location of the oral constriction. The ''bunched'' tongue /r/ reported for a female subject (PK) by Alwan *et al.* (1997) indicates constriction locations similar to the /ɜ˞/ reported here. However, the magnitude of the cross-sectional areas are, in general, larger in the Alwan *et al.* (1997) data. While the appropriate characteristics of an /ɜ˞/ are present, it must be noted that the subject had difficulty in producing it. Even after several preimaging practice sessions she still felt that this shape was foreign to her as a phonetic element. Thus the information regarding this tract shape may have been compromised by her unfamiliarity with it.

The /l/ is shown in Fig. 11 from both a sagittal view and a rotated and tilted perspective to give an indication of the lateral air flow and acoustic path around the tongue. The contact of the tongue with the roof of the oral cavity is indicated by the gap between the oral section and the lip section. The lateral pathways connecting these two cavities is, however, difficult to understand. From the surface renderings, the lateral pathways appear to connect to the vocal tract at a point in the posterior oral cavity. Such a connection point would imply that the subject pressed the tongue against the alveolar ridge and extended the contact against the teeth posteriorly to at least the bicuspids. A configuration like this would have most of the oral cavity space behind the tongue acting as a sidebranch resonator. The area function was de-

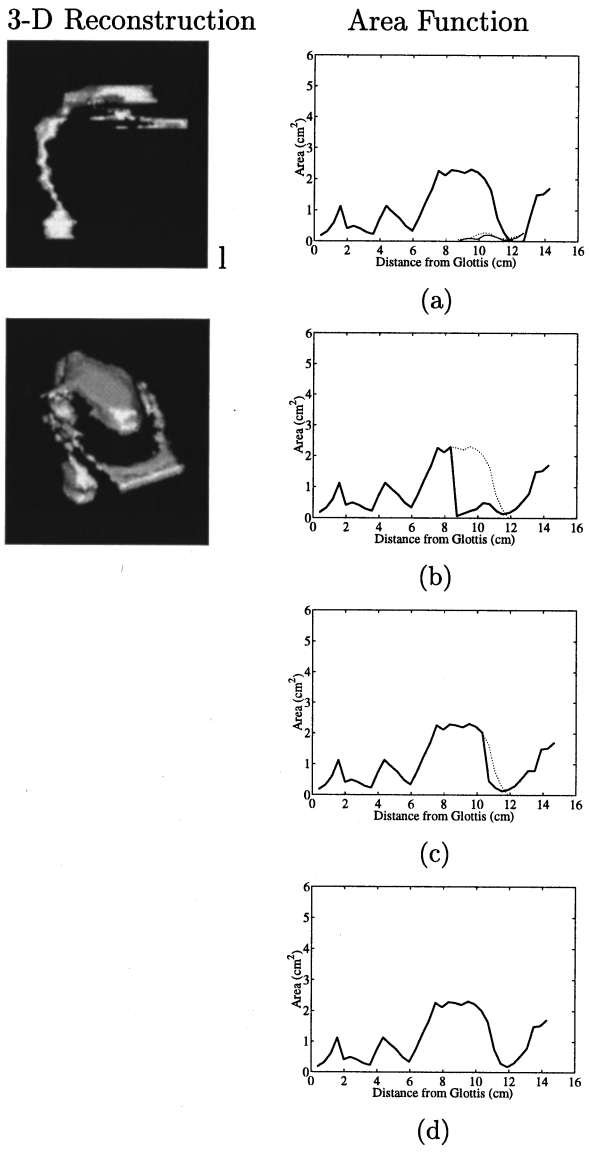

FIG. 11. 3-D reconstruction and area functions for /l/: (a) area function extending from just above the glottis to the point of lingual contact with the alveolar ridge and also for the frontal cavity; the lateral passages are represented by the thin (right path) and dotted (left path) lines; (b) modification of the /l/ such that the main area function is given by the thick line and the resulting sidebranch cavity is shown with the dotted line; the back and front cavities are connected by the sum of the left and right lateral passages; (c) a second modification where the volume of sidebranch cavity is reduced; the main area function is given by the thick line, sidebranch by the dotted, and back and front cavities are again connected by the sum of the left and right lateral passages; (d) a third modification where the back and front cavities of the area function in (a) are simply connected by the portion of the lateral pathways between them; thus no sidebranch is present.

termined from just above the glottis to the point of lingual contact with the alveolar ridge and also for the frontal cavity as shown graphically by the thick line in Fig. 11(a) and numerically in Table IV. The areas comprising the left and right lateral pathways were measured from coronal sections of the 3-D reconstruction beginning from their most posterior point and continuing anteriorly until they merge with the frontal cavity. They are also shown graphically in Fig. 11(a) by the thin (right path) and dotted (left path) lines and numerically in Table IV.

In order to appropriately model the lateral passages and the sidebranch cavity directly posterior to the tongue/palate contact, a modified configuration of the /l/ area function, shown in Fig. 11(b), was developed in similar fashion to Fant (1960) and Fant and Båvegård (1997). This figure gives the area function just as in Fig. 11(a) up to the point where the lateral pathways are present (Section 22 in Table III). From this point to the posterior side of the frontal cavity, the main area function is the sum of the left and right lateral paths. However, because of the difficulty in determining where in the back cavity the lateral pathways actually connected, two additional alternative area functions are given in Fig. 11(c) and (d). In Fig. 11(c), the lateral path connection is moved closer to the lips, bringing much of the sidebranch in Fig. 11(b) back into the main vocal tract area function. Finally, in Fig. 11(d) the back and front cavities of the area function are simply connected by the portion of the pathways between them; thus no sidebranch resonator is present.

Vocal tract shapes for lateral approximants are known to have two primary allophonic variations, a prevocalic /l/ called the light variant and a post vocalic or syllabic /ɫ/ called the dark variant (Espy-Wilson, 1992; Ladefoged, 1993; Narayanan *et al.*, 1997a). The lateral produced by DJ was elicited in a prevocalic context with the example word ''lump'' (see Table I) making it the light variant. A comparison to the ''light'' /l/ reported for subject PK in Narayanan *et al.* (1997a) shows similarities both in area and length for the cavities just posterior and anterior to the lingual-alveolar contact; however, the area function in the lower pharynx again shows smaller areas for DJ.

III. COMPARISON OF NATURAL AND COMPUTED FORMANTS

A method by which to assess the accuracy of the measured area functions is to compute their acoustic characteristics and compare them to those same characteristics measured from the subject's real speech. Toward this goal it would seem most appropriate to record the speech sounds of the subject as they are scanned. Baer *et al.* (1991) did attempt such a recording with an electret microphone with some success, but in general the MR examination room is magnetically and acoustically hostile to audio recording systems. The large magnetic fields prohibit the use of high quality condenser microphones and the intense sounds produced during scanning by the switching magnetic fields would give an acoustic recording with much higher levels of interfering noise than those of the desired signal. In lieu of attempting to record in this enviroment, a high quality audio recording was made in an anechoic chamber. All of the speech sounds corresponding to the vowels and liquids in Table I were recorded.

A. Audio recording and formant analysis

The subject was asked to lay in a supine position on the suspended floor of an anechoic chamber. Ear plugs were used to create similar acoustic feedback conditions and elicit loud vocal productions like those experienced in the MR scanner, but no attempt was made to replicate the scanner's acoustic signal. A microphone (AKG CK22) was located 0.5 m from the subject's mouth at 45 degrees off-axis. The mi-

crophone signal was preamplified with a Symmetrix SX202 preamp and recorded with a Panasonic SV-3700 DAT recorder with a sampling frequency of 44.1 kHz. The speech sounds were sustained for several seconds and each was repeated three times. The data were later transferred in digital form from the DAT recorder to a Macintosh Quadra 950 via an Audiomedia sound card and later downsampled to 22.05 kHz.

For each of the three repetitions of a given speech sound, a frame-based LPC (linear predictive coding) analysis was used to extract the first three formant locations ($F1$, $F2$, and $F3$) at intervals of 25 ms. For each frame, an LPC spectrum (autocorrelation method—Markel and Gray, 1976) was computed using 16 coefficients and a peak picking algorithm with parabolic interpolation (Titze *et al.*, 1987) was used to find estimates for $F1$, $F2$, and $F3$. Finally, the mean and standard deviation were computed for each formant throughout the series of analysis frames (across all repetitions). As a check on the validity of the LPC analysis, each recorded sound was also viewed spectrographically and the formants were determined visually with a cursor. The LPC derived formants were, in all cases, close to those from the spectrogram.

The voice fundamental frequency (F_0) was also determined across all repetitions of each recorded sound. This was done by applying a zero-crossing method (Titze *et al.*, 1987) to a low-passed (below $F1$) version of the recorded sound.

B. Formant frequency calculation

The formant frequencies associated with the vowels and liquids from MRI as well as the two vowels from CT were computed with a wave-reflection analog vocal tract model (Liljencrants, 1985; Story, 1995) which included energy losses due to the yielding properties of the vocal tract walls, fluid viscosity, and radiation from the mouth. The model was sampled at a frequency of 44.1 kHz and each finite section of the area function represented by a tube length of 0.396 cm. The frequency response of each area function was determined by exciting the vocal tract at the closed glottal end with a one sample impulse and computing the Fourier transform of the output (the impulse response). The first three formants were determined by the same peak picking method used in the LPC analysis of the recorded speech. Since it is well known that the presence of the piriform sinuses can lower the formant frequencies (Fant, 1960; Lin, 1990; Story, 1995; Dang and Honda, 1997), the frequency response was computed twice for each area function; once with an acoustic side branch representing the piriform sinuses and once without. The sidebranch was coupled to the main vocal tract at section 4 (1.58 cm from the glottis) of each area function. Since only a single side branch was implemented to represent both piriform sinuses, the cross-sectional areas used were the sum of an averaged version (across two vowels) of the data given in Fig. 5. Additional sidebranch shunts were implemented to compute the formant locations for the /ɝ/ and /l/ as discussed in a previous section.

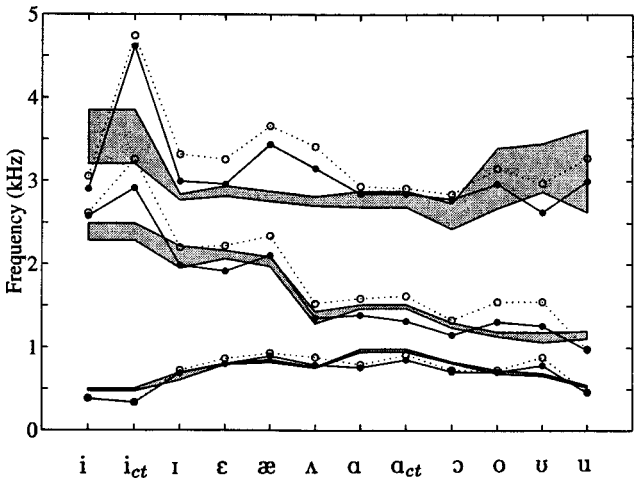

FIG. 12. Comparison of formant locations for $F1$, $F2$, and $F3$ computed for the area functions in Table III and extracted from LPC spectra of the natural speech. The gray bands depict plus and minus one standard deviation from the mean of the natural speech formants. The solid circles represent computed formants for each vowel *with* the piriform sidebranch while the open circles represent the same vowels *without* the piriform.

C. Natural versus synthesized formants: Vowels

Figure 12 shows a comparison of the first three formant locations extracted from the recorded speech and those computed for each corresponding vowel area function. The gray bands represent plus and minus one standard deviation from the mean of the natural speech formants. The open circles show the computed formant locations for each vowel without a piriform side branch while the solid black circles indicate the formants when the sidebranch was connected. [Note that the computed formants for the CT version of /i/ and /ɑ/ are also included in this graph; the natural speech formants for these two vowels were duplicated for comparison purposes.] A tabular representation of the data in Fig. 12 is provided in Table V in which each column shows relevant information for one vowel. The percentage error (given in Hz) for the computed formants relative to the mean natural speech formants is also given; a negative error indicates the computed value was below the measured value and above it for a positive error.

For the recorded speech, the variability grows progressively larger from the first formant to the third as indicated by the magnitude of the standard deviations (width of the gray bands in Fig. 12). The third formant is highly variable for the /i, o, ʊ, u/ which might suggest some unsteadiness of the tongue during productions where the tongue is raised or arched. How DJ's measured vowel formants fit into a more global view of vowel production can be partially assessed by comparing them to formant frequencies averaged over a large number of female speakers reported by Childers and Wu (1991) and Hillenbrand *et al.* (1995) (these studies will henceforth be referred to as CW and HGCW, respectively). DJ's $F1$ frequencies are nearly all higher than those given by these two studies while her $F2$ and $F3$ frequencies are observed to be either higher or lower depending on the particular vowel. It is also noted that DJ's mean F_0 of 274 Hz is more than 50 Hz higher than the mean F_0's in both CW and HGCW. Both DJ's relatively high $F1$ frequencies and mean

TABLE V. Measured and computed formants for the ten vowels given in Table III. Each measured formant (denoted by superscript ''N'') is the mean across several seconds of recording (three repetitions) and sd is the standard deviation. For the columns with i_{ct} and α_{ct}, the natural speech formants are the same as for the MRI-based i and ɑ. The computed formant values (denoted by ''C'') are given for cases with and without the piriform sinus sidebranch where np means ''no piriform'' and p means with piriform. The Δ's represent the percent error of the computed formants relative to the mean value of the natural speech formants [e.g., $\Delta 1 = 100(F1^C - F1^N)/F1^N$].

	i	i_{ct}	ɪ	ɛ	æ	ʌ	ɑ	α_{ct}	ɔ	o	ʊ	u
F_0	315		280	272	274	255	249		266	264	267	296
$F1^N$	489		649	799	837	759	961		817	706	675	533
sd	±16		±47	±6	±17	±6	±18		±8	±20	±15	±14
$F2^N$	2387		2079	2112	2028	1360	1488		1264	1157	1122	1152
sd	±103		±132	±49	±57	±74	±23		±32	±26	±60	±44
$F3^N$	3526		2799	2874	2814	2756	2779		2574	3030	3157	3122
sd	±325		±35	±61	±60	±56	±96		±155	±359	±289	±495
$F1^C_p$	382	335	686	802	897	791	757	849	707	704	786	454
np	386	336	721	863	933	884	792	909	727	730	883	463
$F2^C_p$	2577	2913	1983	1914	2105	1353	1385	1313	1146	1306	1259	970
np	2615	3255	2197	2219	2338	1528	1585	1613	1327	1546	1548	981
$F3^C_p$	2899	4612	2990	2957	3436	3149	2846	2842	2776	2962	2625	2997
np	3054	4741	3313	3255	3660	3412	2933	2909	2835	3147	2972	3273
Δ1 p	−21.9	−31.6	5.7	0.3	7.1	4.2	−21.2	−11.6	−13.5	−0.2	16.4	−14.8
np	−21.1	−31.2	11.1	8.0	11.5	16.6	−17.5	−5.4	−11.0	3.4	30.8	−13.0
Δ2 p	8.0	22.0	−4.6	−9.3	3.8	−0.5	−6.9	−11.8	−9.3	12.8	12.2	−15.8
np	9.6	36.4	5.7	5.1	15.3	12.4	6.6	8.4	4.9	33.6	38.0	−14.9
Δ3 p	−17.8	30.8	6.8	2.9	22.1	14.3	2.4	2.3	7.8	−2.3	−16.8	−4.0
np	−13.4	34.5	18.3	13.3	30.1	23.8	5.6	4.7	10.1	3.8	−5.9	4.8

F_0 could be indicative of her small physical size in terms of possibly shorter than average vocal tract length and vocal folds. It is also possible that, at least in part, high F_0's could result from large subglottal pressures (Titze, 1989) due to phonations that were almost certainly louder than those recorded by CW and DGCW; high $F1$'s may result from an articulatory adaptation that attempts to maintain appropriate phonetic distances between F_0 and $F1$ (Schulman, 1989).

In Fig. 13, mean values of $F1$ and $F2$ taken from CW and HGCW as well as those measured for subject DJ are plotted for the vowels /i, æ, ɑ, u/. This figure clearly shows a rightward shift in $F1$ of DJ's vowels relative to the other studies and also indicates a slight compression in the range of $F2$. The exception is the /æ/ which is closely matched to that from CW but is still shifted to the right relative to the /æ/ reported by HGCW. In contrast, the /ɑ/, while being quite distant from the average given by CW, is similar to the /ɑ/ reported by HGCW. If DJ's formants are compared with the scatter plot of all the collected data for females given in CW (see their p. 1854) (HGCW also gave a scatter plot but did not separate the men, women, and children), it can be seen that DJ's /i/ would be at the extreme right edge of the /i/ formant space and may be classified by some listeners as an /ɪ/. Likewise, the other vowels, with the exception of /æ/ and /ʌ/, all seem to fall along the edges of their respective $F1-F2$ formant spaces. DJ's tendency to use an extreme part of the formant space is likely due to factors such as her relatively small physical size (5 ft 2-in. tall, 120 pounds), regional background (Texas), and general speaking style, but, as was mentioned previously, could also be partially due to the loud speech condition under which her speech sounds were recorded.

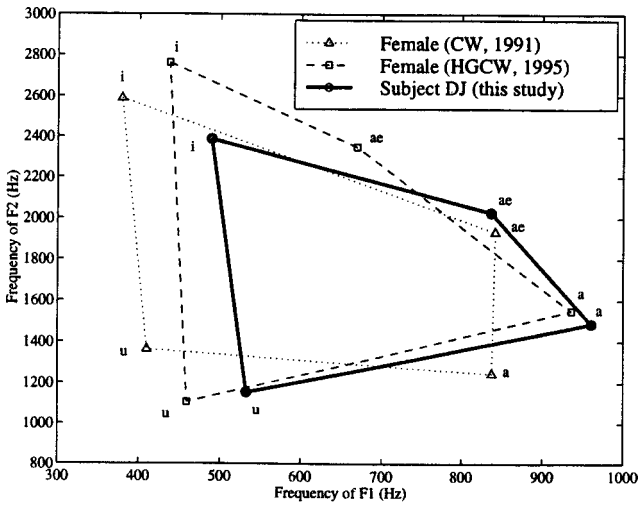

FIG. 13. Comparison of $F1$ and $F2$ of the vowels /i/ (upper left), ''ae'' =/æ/ (upper right), ''a''=/ɑ/ (lower right), and /u/ (lower left), for subject DJ with previously published values from Childers and Wu (1991) and Hillenbrand *et al.* (1995).

The computed formants in Fig. 12 show the significant role the piriform sinuses can play in determining the actual formant location. The piriform side branch has the effect of always decreasing the frequency value of the formants, however the amount of decrease is dependent on the vocal tract shape; e.g., for $F1$ of the two /i/ vowels the sidebranch has almost no effect but for the /ʌ/ there is nearly a 100-Hz difference between the sinus/no sinus conditions. It is also noted that the sidebranch has its greatest effect in $F2$ and $F3$. In fact, many of the $F2$'s for the sinus/no sinus conditions straddle the band of variation of the natural speech, meaning that finer adjustment of the amount of coupling and cross-sectional areas of the piriform sinus could bring most

of the $F2$'s close to the measured mean values.

The computed $F1$'s given in Table V show that 5 (/ɪ, ɛ, æ, ʌ, o/) out of the 12 vowels *with* the piriform sidebranch differ from the measured $F1$'s by less than 10%, while 4 others have errors less than 20%. The two versions of the /i/ have the worst $F1$ matches with errors of −21.9% and −31.6% for MRI and CT, respectively. The MRI /ɑ/ also is poorly matched with a −21.2% error. For $F2$ and $F3$, there are seven vowels that differ by less than 10%; /i, ɪ, ɛ, æ, ʌ, $ɑ_{mri}$/ in $F2$ and /ɪ, ɛ, ɔ, o, u, $ɑ_{mri}$, $ɑ_{ct}$/ in $F3$. When the formants were computed *without* the piriform sidebranch, the absolute percent differences relative to the recorded speech are generally larger, with a few exceptions. For example, the $F1$'s for the two /i/'s, two /ɑ/'s, /ɔ/, and /u/ show less error without the piriform than with it; this is also true for $F2$ of the two /ɑ/'s, /ɔ/, and /u/. The error with the piriform shunt for several vowels is negative (formants too low) and positive without it (formants too high) showing, as did Fig. 12, that varying the size of piriform sinus could ''tune'' these vowel shapes to have formants closely in line with those measured from the recorded speech. This effect is observed for $F1$ and $F3$ of /o/ and $F2$ of /ɪ, ɛ, ɔ, o, $ɑ_{mri}$, $ɑ_{ct}$/.

The large errors between natural speech and computed formants observed for the two /i/'s apparently results from a more extreme /i/ production during imaging than during the audio recording session; the possibly extreme production of this vowel was discussed in Sec. II A. Based on the formants for the recorded and computed /i/ and /ɪ/, it can be speculated that DJ's vocal tract shape during the recorded /i/ is likely to be somewhere between that measured for /i/ and /ɪ/. That is, a slightly reduced pharyngeal space and increased oral constriction area. While this may partially explain the discrepancy between the natural and computed formants, it is interesting to note that both of the measured /i/ area functions have formants more closely aligned with the CW and DGCW studies than did the subject's real speech.

Both versions of the /ɑ/ produced $F1$'s below that of the recorded speech, with the CT-based /ɑ/ (without a piriform sidebranch) producing the closest match which was within 52 Hz of the natural speech. In Sec. II A, the CT-based /ɑ/ was suggested to be a more extreme production than its MRI-based counterpart. However, calculation of the formants suggests the subject used an even more extreme vocal tract shape for producing the vowel during recording; this is also indicated by the previous comparison of the recorded natural speech formants to the CW and DGCW studies.

D. Natural versus synthesized formants: Liquids

The natural and computed formants for several possible configurations of /ɝ/ and /l/ are shown in Fig. 14. The subscripts [(a)–(d)] refer to the area functions given in Figs. 10 and 11. The (e) and (f) versions of the /l/ are similar to the (d) except that the connection between front and back cavities is by only the right or left pathway, respectively. As before, the gray bands represent plus and minus one standard deviation from the mean of the measured natural speech formants while the open and solid circles are the formants computed with and without the piriform sidebranch, respectively. The formants measured from the recorded speech have been

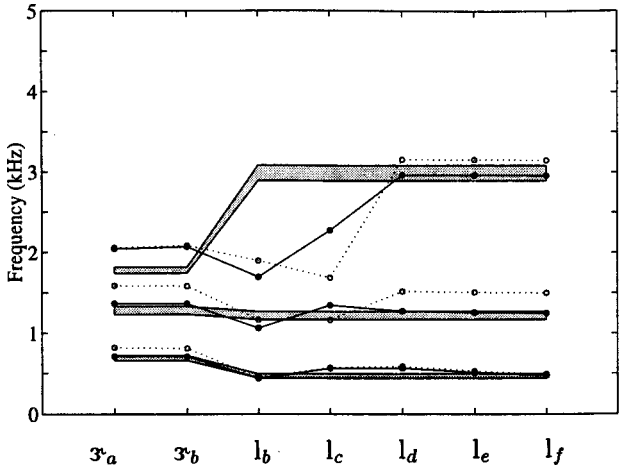

FIG. 14. Comparison of formant locations for $F1$, $F2$, and $F3$ computed for the area functions in Table IV (/ɝ/ and /l/) and extracted from LPC spectra of the natural speech. The gray bands depict plus and minus one standard deviation from the mean of the natural speech formants. The solid circles represent computed formants for each vowel *with* the piriform sidebranch while the open circles represent the same vowels *without* the piriform. The /$ɝ_a$/ and /$ɝ_b$/ correspond to the area functions listed under the same symbols in Table IV. The /l_b/, /l_c/, /l_d/, /l_e/, and /l_f/ correspond to the various /l/ configurations discussed in the text.

replicated for the various configurations of the two liquids. These data are also given in Table VI in similar fashion to that for the vowels.

The first /ɝ/ is the case with the sublingual cavity added directly to the area function and thus, no sublingual sidebranch is present. For the second /ɝ/, the sublingual cavity was represented as a separate sidebranch (see Sec. II C for exact cross-sectional areas). For both cases, the piriform shunt imposes a significant downward shift of $F1$ and $F2$ toward those of the natural speech but produces almost no shift in $F3$. There is little difference between the two /ɝ/'s with $F1$ and $F2$ differing from natural speech by about 3% and 6.5%, respectively. $F3$ for both cases is about 270 too high which is likely caused by the lack of a pronounced constriction in the oral cavity.

The formants for the first /l/ configuration (l_b) correspond to the area function and sidebranch cavity shown in Fig. 11(b), and are all lower than those for the /ɝ/. This is in large error relative to the measured natural formants and it is also well known that one of primary acoustic differences between /ɝ/ and /l/ is that $F3$ is higher for /l/ than for /ɝ/ (Fant, 1960; Espy-Wilson, 1992). Thus the /l_b/ configuration is a poor representation of the /l/. The /l_c/ [see Fig. 11(c)] has a much shorter sidebranch behind the apical closure, but its length is similar enough to that of the piriform sidebranch that they apparently interact to produce a higher $F2$ and $F3$ with the piriform than without it; recall that for all other cases the presence of piriform shunt lowers formants. In either case, the $F3$ is still much lower than for the natural speech. The third case of /l_d/ [shown in Fig. 11(d)] has no post-apical shunt but just connects the back and front vocal tract cavities with the sum of portions of the right and left pathways between them. The computed formants with the piriform shunt are now more similar to those of the natural speech, but $F1$ still differs by more than 20%. In the /l_e/ and

TABLE VI. Measured and computed formants for /ɝ/ and /l/. Each measured formant (denoted by superscript ''N'') is the mean across several seconds of recording (three repetitions) and sd is the standard deviation. The natural speech formants are only listed once each for /ɝ/ and /l/ in columns 2 and 4. The computed formant values (denoted by ''C'') are given for cases with and without the piriform sinus sidebranch where np means ''no piriform'' and p means with piriform. The Δ's represent the percent error of the computed formants relative to the mean value of the natural speech formants. The /ɝ$_a$/ and /ɝ$_b$/ correspond to the area functions listed under the same symbols in Table IV. The /l$_b$/, /l$_c$/, /l$_d$/, /l$_e$/, and /l$_f$/ correspond to the various /l/ configurations discussed in the text.

	ɝ$_a$	ɝ$_b$	l$_b$	l$_c$	l$_d$	l$_e$	l$_f$
F_0	76		261				
$F1^N$	691		464				
sd	±31		±27				
$F2^N$	1282		1217				
sd	±49		±50				
$F3^N$	1783		2986				
sd	±37		±98				
$F1_p^C$	712	710	435	561	563	509	475
np	820	811	445	570	587	527	488
$F2_p^C$	1370	1365	1063	1347	1273	1256	1246
np	1589	1584	1164	1163	1519	1506	1498
$F3_p^C$	2048	2072	1696	2276	2963	2959	2955
np	2064	2087	1898	1689	3154	3151	3148
Δ1 p	3.0	2.7	−6.4	20.8	21.1	9.6	2.2
np	18.6	17.3	−4.1	22.7	26.3	13.4	5.2
Δ2 p	6.9	6.5	−12.7	10.6	4.6	3.2	2.4
np	24.0	23.6	−4.3	−4.5	24.8	23.7	23.1
Δ3 p	14.9	16.2	−43.2	−23.8	−0.8	−0.9	−1.0
np	15.8	17.0	−36.4	−43.4	5.6	5.5	5.4

/l$_f$/ configurations, the back and front tract cavities are connected by only the right or left pathway, respectively. The errors are further reduced for both these cases with the /l$_f$/ giving respective $F1$, $F2$, and $F3$ differences of only 2.2, 2.4, and −1.0. In fact, this last case is the best match of computed to natural speech formants in the entire area function set. Thus for subject DJ, the most appropriate /l/ model is simply an area function comprised of three parts: (1) the portion extending from the glottis to the lingual contact with the alveolar ridge; (2) the highly constricted pathway connected back and front cavities; and (3) the front cavity.

E. Summary

As an assessment of area function accuracy, the comparison of natural and computed formants suggests that they are, in general, reasonable representations of subject DJ's vowels and liquids. They do, however, produce formants that lie mostly at the extremes of the vowel spaces reported for females by Childers and Wu (1991) and Hillenbrand *et al.* (1995) suggesting that DJ may not be an ''average'' female speaker. Many of the differences between computed and natural formants were less than 10% which can be largely attributed to slight differences in vocal tract shape during audio recording than during scanning. Also, a closed glottis was assumed for the formant calculations while it is possible that the measured natural speech formants were partially influenced by incomplete glottal closure. The larger errors, such as for the two /i/'s, indicate a significantly different articulatory configuration during the recording and scanning sessions.

Comparisons of computed and measured natural speech formants in other MRI vocal tract studies have yielded errors of similar magnitudes to those reported here. The computed formants of many of Baer *et al.*'s (1991) area functions differed from natural speech by about 15%–30% with one as high as 70% and some as low as 1%. Percentage differences between the Story *et al.* (1996b) area function formants and natural speech ranged from less than 1% up to 43%, but with the majority less than 10%. Yang and Kasuya's (1994) data showed several area functions with formant errors less than 5% while Narayanan *et al.*'s (1997b) three female vowels differed from natural speech by mostly 10%–30% but with a high of 65% and a low of 3.5%.

For potential future use of DJ's area functions to synthesize speech, it would be possible to make use of either a manual or automatic optimization scheme which could ''tune'' each area function to coincide more closely with the measured formants. As examples, a manual optimization based on sensitivity functions (Fant and Pauli, 1975) was performed on a male /ɝ/ in Story (1995) and an automatic method has been reported by Beautemps *et al.* (1995).

ACKNOWLEDGMENTS

The authors would like to thank Steve Baker for his technical expertise and willingness to do late night scanning as well as the staff of the Division of Physiologic Imaging at the University of Iowa for allowing generous use of equipment and software. Two anonymous reviewers are also gratefully acknowledged for their helpful comments on an earlier version of this paper. This study was supported by

Grant No. R01 DC02532-02 from the National Institutes on Deafness and Other Communication Disorders.

Alwan, A. A., Narayanan, S. S., and Haker, K. (**1997**). ''Toward articulatory-acoustic models for liquid approximants based on MRI and EPG data. Part I. The rhotics,'' J. Acoust. Soc. Am. **101**, 1078–1089.

Baer, T., Gore, J. C., Gracco, L. C., and Nye, P. W. (**1991**). ''Analysis of vocal tract shape and dimensions using magnetic resonance imaging: Vowels,'' J. Acoust. Soc. Am. **90**, 799–828.

Beautemps, D., Badin, P., and Laboissière, R. (**1995**). ''Deriving vocal-tract area functions from midsagittal profiles and formant frequencies: A new model for vowels and fricative consonants based on experimental data,'' Speech Commun. **16**, 27–47.

Boyd, D. P., and Lipton, M. J. (**1983**). ''Cardiac computed tomography,'' Proc. IEEE **71**, 298–307.

Childers, D. G., and Wu, K. (**1991**). ''Gender recognition from speech. Part II: Fine analysis,'' J. Acoust. Soc. Am. **90**, 1841–1856.

Dang, J., and Honda, K. (**1997**). ''Acoustic characteristics of the piriform fossa in models and humans,'' J. Acoust. Soc. Am. **101**, 456–465.

Dang, J., Honda, K., and Suzuki, H. (**1994**). ''Morphological and acoustical analysis of the nasal and the paranasal cavities,'' J. Acoust. Soc. Am. **96**, 2088–2100.

Espy-Wilson, C. Y. (**1992**). ''Acoustic measures for linguistic features distinguishing the semivowels /w j r l/ in American English,'' J. Acoust. Soc. Am. **92**, 736–757.

Fant, G. (**1960**). *The Acoustic Theory of Speech Production* (Mouton, The Hague).

Fant, G., and Båvegård, M. (**1997**). ''Parametric model of VT area functions: vowels and consonants,'' STL-QRSR, KTH, 1, 1–20.

Fant, G., and Pauli, S. (**1975**). ''Spatial characteristics of vocal tract resonance modes,'' in Proc. Speech Comm. Sem. 74., Stockholm, Sweden, Aug 1–3, 121–132.

Hillenbrand, J., Getty, L. A., Clark, M. J., and Wheeler, K. (**1995**). ''Acoustic characteristics of American English vowels,'' J. Acoust. Soc. Am. **97**, 3099–3111.

Hoffman, E. A., Gnanaprakasam, D., Gupta, K. B., Hoford, J. D., Kugelmass, S. D., and Kulawiec, R. S. (**1992**). ''VIDA: An environment for multidimensional image display and analysis,'' SPIE Proc. Biomed. Image Proc. and 3-D Microscopy, 1660, San Jose, CA, 10–13 February.

Högberg, J. (**1995**). ''From sagittal distance to area function and male to female scaling of the vocal tract,'' STL-QPSR, KTH, 4, 11–53.

Ladefoged, P. (**1993**). *A Course in Phonetics*, 3rd ed. (Harcourt Brace College, Fort Worth).

Landeau, M., and Zuili, H. (**1963**). ''Vocal emission and tomograms of the larynx,'' National Assoc. of Teachers of Singing Bulletin, February.

Liljencrants, J. (**1985**). ''Speech synthesis with a reflection-type line analog,'' DS Dissertation, Dept. of Speech Comm. and Music Acoust., Royal Inst. of Tech., Stockholm, Sweden.

Lin, Q. (**1990**). ''Speech production theory and articulatory speech synthesis,'' Ph. D. dissertation, KTH, Stockholm, Sweden.

Markel, J. D., and Gray, A. H. (**1976**). *Linear Prediction of Speech* (Springer-Verlag, New York).

Mermelstein, P. (**1973**). ''Articulatory model for the study of speech production,'' J. Acoust. Soc. Am. **53**, 1070–1082.

Narayanan, S. S., Alwan, A. A., and Haker, K. (**1995**). ''An articulatory study of fricative consonants using magnetic resonance imaging,'' J. Acoust. Soc. Am. **98**, 1325–1347.

Narayanan, S. S., Alwan, A. A., and Haker, K. (**1997a**). ''Toward articulatory-acoustic models for liquid approximants based on MRI and EPG data. Part I. The laterals,'' J. Acoust. Soc. Am. **101**, 1064–1077.

Narayanan, S. S., Alwan, A. A., and Song, Y. (**1997b**). ''New results in vowel production: MRI, EPG, and acoustic data,'' Proc. of 1997 European Speech Proc. Conf., Rhodes, Greece, Sept. 1997, Vol. 2, 1007–1009.

Raya, S. P., and Udupa, J. K. (**1990**). ''Shape-based interpolation of multidimensional objects,'' IEEE Trans. Med. Imaging **9**, 32–42.

Schulman, R. (**1989**). ''Articulatory dynamics of loud and normal speech,'' J. Acoust. Soc. Am. **85**, 295–312.

Story, B. H. (**1995**). ''Physiologically-based speech simulation using an enhanced wave-reflection model of the vocal tract,'' Ph.D. dissertation, University of Iowa.

Story, B. H., Hoffman, E. A., and Titze, I. R. (**1995**). ''Speech simulation based on MR images of the vocal tract,'' SPIE Medical Imaging—Physiology and Function from Multidimensional Images 2433, 179–190.

Story, B. H., Hoffman, E. A., and Titze, I. R. (**1996a**). ''Vocal tract imaging: A comparison of MRI and CT,'' SPIE Medical Imaging—Physiology and Function from Multidimensional Images 2709, 209–222.

Story, B. H., Titze, I. R., and Hoffman, E. A. (**1996b**). ''Vocal tract area functions from magnetic resonance imaging,'' J. Acoust. Soc. Am. **100**, 537–554.

Titze, I. R. (**1989**). ''On the relation between subglottal pressure and fundamental frequency in phonation,'' J. Acoust. Soc. Am. **85**, 901–906.

Titze, I. R., Horii, Y., and Scherer, R. C. (**1987**). ''Some technical considerations in voice perturbation measurements,'' J. Speech Hear. Res. **30**, 252–260.

Titze, I. R., Wong, D., Story, B., and Long, R. (**1997**). ''Considerations in voice transformation with physiologic scaling principles,'' Speech Commun. **22**, 113–123.

van den Berg, J. (**1958**). ''Myoelastic-aerodynamic theory of voice production,'' J. Speech Hear. Res. **1**, 227–244.

Vennard, W. (**1967**). *Singing, the Mechanism and the Technic* (Carl Fischer, New York).

Yang, C-S, and Kasuya, H. (**1994**). ''Accurate measurement of vocal tract shapes from magnetic resonance images of child, female, and male subjects,'' Proc. of ICSLP 94, 623–626, Yokohama, Japan.

Dynamic specification of coarticulated German vowels: Perceptual and acoustical studies

Winifred Strange[a)]
Communication Sciences and Disorders, University of South Florida, Tampa, Florida 33620-8150

Ocke-Schwen Bohn[b)]
Englisches Seminar, Universität Kiel, 24098 Kiel, Germany

(Received 29 July 1997; accepted for publication 11 March 1998)

To examine the generality of Strange's Dynamic Specification Theory of vowel perception, two perceptual experiments investigated whether dynamic (time-varying) acoustic information about vowel gestures was critical for identification of coarticulated vowels in German, a language without diphthongization. The perception by native North German (NG) speakers of electronically modified /dVt/ syllables produced in carrier sentences was assessed using the ''silent-center'' paradigm. The relative efficacy of static target information, dynamic spectral information (defined over syllable onsets and offsets together), and intrinsic vowel length was investigated in listening conditions in which the centers (silent-center conditions) or the onsets and offsets (vowel-center conditions) of the syllables were silenced. Listeners correctly identified most vowels in silent-center syllables and in vowel-center stimuli when both conditions included information about intrinsic vowel length. When duration information was removed, errors increased significantly, but performance was relatively better for silent-center syllables than for vowel-center stimuli. Acoustical analyses of the effects of coarticulation on target formant frequencies, vocalic duration, and dynamic spectro-temporal patterns in the stimulus materials were performed to elucidate the nature of the dynamic spectral information. In comparison with vowels produced in citation form /hVt/ syllables by the same speaker, the coarticulated /dVt/ utterances showed considerable ''target undershoot'' of formant frequencies and reduced duration differences between tense and lax vowel pairs. This suggests that both static spectral cues and relative duration information for NG vowels may not remain perceptually distinctive in continuous speech. Analysis of formant movement within syllable nuclei corroborated descriptions of German vowels as monophthongal. However, an analysis of first formant *temporal* trajectories revealed distinct patterns for tense and lax vowels that could be used by listeners to disambiguate coarticulated NG vowels. [S0001-4966(98)05306-5]

PACS numbers: 43.71.An, 43.71.Es, 43.71.Hw, 43.70.Fq [AL]

INTRODUCTION

Previous studies have investigated the role of dynamic (time-varying) spectral information in the specification of American English (AE) vowels when they are produced in syllables, phrases, and sentence length utterances (cf. Strange, 1989a, Huang, 1991). In general, both acoustic and perceptual studies support the conclusion that distinctive patterns of formant *movement* throughout consonant–vowel–consonant (CVC) syllables provide important information for the differentiation of coarticulated AE vowels (cf. Hillenbrand *et al.*, 1995; Jenkins *et al.*, 1994; Jenkins and Strange, in press; Parker and Diehl, 1984; Strange, 1989b; Verbrugge and Rakerd, 1986). However, interpretations of the perceptual results and hypotheses about the exact nature of the relevant dynamic information differ (Strange, 1989a; Andruski and Nearey, 1992). In order to examine the generality of the perceptual results and to assess alternative hypotheses about the nature of the dynamic information, the present study investigated the perception of coarticulated (North) German vowels.

For AE vowels, dynamic spectral information includes distinctive patterns of formant movement into and out of the vocalic nucleus of vowels (Lehiste and Peterson, 1961; Jenkins *et al.*, 1994) as well as formant movement within vocalic nuclei which characterizes the diphthongization of many so-called single-target AE vowels (Andruski and Nearey, 1992; Hillenbrand *et al.*, 1995; Jenkins *et al.*, 1994). (These sources of information are discussed further below.) The perceptual importance of such information has been demonstrated using the ''silent-center'' paradigm, in which naturally produced CVC syllables are electronically modified in order to manipulate the availability of dynamic spectral information, (static) formant target information (traditionally considered the primary information for vowel identity), and intrinsic vowel duration (considered secondary or redundant information for the differentiation of English vowels) (Jenkins *et al.*, 1983).

In general, identification of AE vowels in *silent-center* (SC) syllables (in which the vocalic nuclei are attenuated to silence) is no less accurate (and sometimes more accurate)

a)Electronic mail: strange@luna.cas.usf.edu
b)Now at Engelsk Institut, Aarhus Universitet, 8000 Aarhus C, Denmark.

than for *vowel-center* (VC) stimuli (in which vocalic nuclei are presented with onsets and offsets removed) when information about the intrinsic duration of the vowels is available (Jenkins *et al.*, 1983; Strange *et al.*, 1983; Strange, 1989b). When intrinsic duration differences are removed, errors on both SC syllables and VC stimuli increase. For fixed-duration SC syllables, errors increase primarily for intrinsically short vowels (Strange *et al.*, 1983; Strange, 1989b; see also Parker and Diehl, 1984). For fixed-duration VC stimuli, vowel perception is disrupted to an even greater extent, especially for long vowels. That is, when extracted from syllable contexts, static formant targets alone are not *sufficient* to differentiate AE vowels perceptually.

This pattern of results for AE vowels has been replicated several times using the productions of different speakers, with vowels in different consonantal contexts, and for syllables spoken in sentence context as well as in lists. These perceptual findings have led to the development of a theory of the perception of coarticulated vowels which has been referred to as Dynamic Specification Theory (Strange, 1989a). This approach starts with the conception of vowels as *gestures* with intrinsic timing characteristics (Fowler, 1980; Browman and Goldstein, 1991). That is, it is assumed that the underlying articulatory specification of each vowel gesture includes not only a distinctive postural target (specification of jaw opening and tongue body constriction location and degree), but also a distinctive ''style of movement'' toward and away from that vocal tract target. While these vowel gestures are specified independently of preceding and following consonant gestures, there is considerable temporal overlap (coproduction) of movements associated with the consonant and vowel gestures when producing syllables at normal to rapid rates (as well as possible vowel-to-vowel coarticulation). Thus the formant trajectories of a CVC syllable are a joint function of both consonant and vowel gestures. However, perceptual studies using the silent-center methodology indicate that onsets and offsets of CVC syllables containing different stop consonants (but the same vowel) may be recombined with little or no loss in accuracy of vowel identification (Strange, 1987; Strange and Jenkins, 1988). This suggests that at least some parameters of formant trajectories specified over syllable onsets and offsets are *intrinsic to the vowel* and remain invariant over different consonantal contexts, at least within a single manner class of consonants.

Two types of dynamic spectral information might be used in the perception of coarticulated American English (AE) vowels (Jenkins *et al.*, 1994; Strange, 1989b). First, vowels may be differentiated in terms of temporal characteristics of their formant trajectories (Lehiste and Peterson, 1961). The trajectories of ''tense'' (long) vowels tend to have longer nuclei and shorter offglides, relative to the total duration of the syllable. In contrast, ''lax'' (short) vowels have proportionally shorter nuclei and longer offglides. There are no systematic differences in the relative timing of onglides for tense and lax vowels. Thus two temporal trajectory patterns can be defined for AE vowels: a tense vowel pattern with temporally symmetrical onglides and offglides, and a lax vowel pattern with an asymmetric temporal pattern in which offglides are longer than onglides (Jenkins *et al.*, 1994). Perceptual studies using synthetic speech materials have demonstrated that temporal parameters of formant trajectories can influence the perception of vowels in CVC syllables (Huang, 1985, 1986; DiBenedetto, 1989). Thus relationships between rates of formant movement at syllable onsets and offsets may provide distinctive information that can be used by listeners to identify vowels in SC syllables.

A second source of dynamic spectral information is the formant movement within the vocalic nuclei of CVC syllables associated with the diphthongization of many vowels in Canadian and American dialects of English (Nearey, 1989; Nearey and Assmann, 1986; Strange, 1989a; see also Miller, 1991). According to Nearey's Compound Target Theory (Nearey, 1989; Nearey and Assmann, 1986; Andruski and Nearey, 1992), Canadian (and AE) vowels can be differentiated by contrasting patterns of *vowel-inherent spectral change* (VISC) in vocalic nuclei, defined over two points: the *target* (which occurs early in the nucleus) and the *offglide* (which specifies the direction and extent of formant movement from the target) Andruski and Nearey (1992) suggested further that VISC information *alone* was sufficient to account for the perception of AE vowels in SC syllables. They reported on a set of studies in which perception of vowels in natural SC /bVb/ syllables, ''minimalist'' synthetic /bVb/ syllables, and fixed-duration vocalic centers of synthetic syllables was compared. Since there were no significant overall differences in identification accuracy across conditions (error rates were 34%, 31%, and 29%, respectively) and the pattern of errors was similar, they concluded that listeners were using the same VISC information to identify vowels in all three conditions. (Note, however, that error rates were relatively high overall.)

Andruski and Nearey's interpretation of the SC syllable studies suggests that the perceptual importance of dynamic spectral information for vowel identification may be restricted to the diphthongized vowels of American and Canadian English. If, on the other hand, Strange's more general interpretation of the studies has validity, we might expect that dynamic spectral information plays a relatively important role in the perception of vowels even for languages which have little or no diphthongization of so-called single-target vowels. We would expect that for other languages which have large vowel inventories resulting in acoustic ambiguity of static target information in continuous speech, vowel gestures would be further differentiated by distinctive styles of movement. These dynamic differences would result in distinctive time-varying articulatory and acoustic patterns often described by linguists in terms of the features of tenseness and/or length. For some languages, differences in vowel gestures might *not* include differential patterns of diphthongization within the vowel nucleus. In order to investigate the generality of the findings that dynamic spectral information is important in the perception of coarticulated vowels, and to shed further light on the nature of the dynamic spectral information, it was important to replicate the studies of silent-center syllables using a language with a large vowel inventory whose vowels differ in tenseness and/or length, but

which have little or no diphthongization of single-target vowels. German is such a language.

Standard German is usually described as having at least 14 monophthongs /i, ɪ, e, ɛ, ɑ, a, y, ʏ, ø, œ, u, ʊ, o, ɔ/, and 3 true diphthongs /a͡ɪ, a͡ʊ, ɔ͡ɪ/. Unlike English, German does not use diphthongization to differentiate this relatively large set of monophthongs. There is general agreement that the 14 monophthongs can be grouped into 7 contrasting pairs /i–ɪ/, /e–ɛ/, /ɑ–a/, /y–ʏ/, /u–ʊ/, /o–ɔ/, /ø–œ/, but German phoneticians and phonologists differ with respect to the feature(s) used to differentiate these pairs. Traditionally, German scholars have used the terms *close* versus *open*. For instance, /i/ is the close and /ɪ/ the open member of the /i–ɪ/ pair (Siebs, 1969). Other features used to describe these German vowel pairs are *tense* versus *lax* and *long* versus *short* (e.g., tense or long /i/ versus lax or short /ɪ/) (Moulton, 1962; Kohler, 1977). In acoustic terms, the members of each pair differ in that the close, tense, long vowel occupies a more peripheral portion of the acoustic vowel space than the more central, open, lax, short vowel, except for the pair /ɑ–a/, which has very similar static formant targets. (See Sec. IV for a more detailed description of German vowel acoustics and articulation.)

North German (NG) vowels were examined in the present study because the similarities and differences between NG and AE vowels allowed us to address some of the issues raised above. In both languages, tense–lax pairs differ both temporally and spectrally. However, there are two important differences between AE and NG vowels: (1) the duration contrast within tense–lax pairs is reportedly larger in German than in English (Barry, 1974a, b; Bethge, 1963; Iivonen, 1983, 1987; Weiss, 1972, 1976; Bohn and Flege, 1990, 1992), and (2), German monophthongs are considered nondiphthongal.

The few studies examining the perception of German vowels by native speakers have concentrated primarily on the question of the relative importance of spectral (static target information) versus duration information in vowel identification. Weiss (1976, see also Weiss, 1974; Wangler and Weiss, 1975) had a ''human synthesizer'' (i.e., a skilled phonetician) produce 300 tokens of German vowels which differed in vowel spectrum and duration. The unedited /bVtən/ tokens were categorized by native German listeners with different dialect backgrounds and different amounts of English language experience. One important result of the Weiss (1976) study was that the use of the spectral vs duration cues was a function of vowel height. All listeners relied more on duration differences (and less on spectral differences) to identify low vowels, whereas high vowels were predominantly identified on the basis of spectral properties. Sendlmeier (1981) also examined the effect of temporal manipulations on the identification of German vowels, using edited natural tokens of German vowels in monosyllabic words. His results were in good agreement with those of Weiss (1976; see also Heike, 1970, 1972; Lindner, 1976). Sendlmeier concluded that ''there is no uniform answer to the question of the perceptive, and thus phonological relevance of duration of German vowels'' (Sendlmeier, 1981, p. 291).

The purpose of the present research was to replicate the ''silent-center'' studies of AE syllables, using a corpus of NG vowels spoken in sentence length utterances by a single speaker and listeners who were native speakers of North German. Two perceptual studies were completed to explore the relative contribution of dynamic spectral information, static target information, and intrinsic duration information, to the perception of the 14 German monophthongs produced in stressed /dVt/ syllables in a fixed carrier sentence. The first perceptual study examined whether information in silent-center syllables was sufficient to maintain highly accurate identification of German vowels. The second perceptual study explored the relative contribution of intrinsic duration information to the identification of coarticulated German vowels produced in sentence length utterances. Finally, an acoustic study was undertaken to assess the effects of coarticulation on three types of information for the identification of the vowels of this speaker: target formant frequencies, vocalic duration, and dynamic spectro-temporal patterns.

I. VERIFICATION OF STIMULI

A. Methods

The speech materials were recorded by the second author, a phonetically trained male native speaker of German who was 37 years old at the time of the recordings. The speaker had spent his entire childhood and all but five years of his adult life in Northern Germany (Kiel, Schlewig-Holstein). His accent in German is typical of native speakers from the Kiel region (i.e., North German). The 14 monophthongs of NG were produced in four blocks of 15 utterances in which the 14 vowels occurred in different random orders. (The first utterance in each block of 15 was repeated at the end to control for differences in intonation associated with list-final position; this utterance was discarded.) The vowels were produced in /dVt/ syllables in the sentence, ''Ich habe /dVt/ gesagt'' (''I said dVt'') at the speaker's self-selected normal rate of speaking. The speaker was instructed to use normal stress and not to ''overarticulate'' the target syllables. Stimulus materials were recorded on a Tascam 22-2 high fidelity tape recorder in an IAC sound chamber with a Shure Spher-o-dyne microphone. After recording, the speaker listened to all productions and rejected a few because of poor articulation or voice quality. All tokens used in the perceptual studies were considered ''good'' instances of the vowels by the speaker.

The last three blocks of sentences were digitized on a DEC Vaxstation II/GPX minicomputer at a 20-kHz sampling rate with 12-bit resolution after low-pass filtering at 9.8 kHz and 6 dB/oct pre-emphasis. (The first block of trials was discarded because they were recorded at a lower amplitude than subsequent utterances.) Only slight modifications in input intensity were made across the utterances within each block. When intensity was modified, the entire sentence was amplified or attenuated so that the intensity of the target syllable remained in its original relationship to the carrier sentence. Thus the relative intensity of the target syllables varied naturally across the 14 vowels. From the digitized waveforms, measurements of target syllable duration, voice

onset time (VOT) and fundamental frequency ($F0$) were used to make the final selection of two instances of each of 14 vowels. Utterances were chosen which had the shortest values of VOT and stable $F0$ (i.e., no pitch breaks or perturbations). The final corpus consisted of all 14 utterances of the third block, 6 utterances from the second block, and 8 utterances from the fourth block.

The 28 sentences containing 2 instances of each of 14 vowels were arranged in 4 different random sequences, converted to analog signals, with de-emphasis and anti-aliasing filtering and recorded on audio tape. The response interval between utterances was 4, with an 8-s interval between blocks of 14 utterances. Thus the listening test consisted of 112 trials in which each utterance occurred 4 times and each target vowel occurred 8 times.

The listening test was presented to a group of 15 native speakers of NG who participated as unpaid volunteers. The mean age of the 14 female and 1 male subjects was 23 years (s.d.=2.7). The subjects were recruited from introductory English linguistics courses at the Kiel University and had received either no training or minimal training in phonetics. A background questionnaire was administered to confirm that each subject met the following selection criteria: no history of hearing loss, native speaker of NG (i.e., subject spent childhood and most of her/his adult life in Northern Germany, and one or both parents were North Germans), limited exposure during adulthood to native English speakers (i.e., less than a total of one year in English-speaking countries). All 15 subjects met the criteria.

The test was conducted in the Language Laboratory of Kiel University. Each subject received 10 numbered answer sheets each of which contained 14 lines with the 15 response alternatives in Standard German orthography. Because German orthography is largely phonemic it was possible to spell the test syllables in a way that made letter-sound correspondences unambiguous. Each line listed the response alternatives in the following order: *diet*, *ditt*, *deht*, *dett*, *däht*, *daht*, *datt*, *düht*, *dütt*, *döht*, *dött*, *duht*, *dutt*, *doht*, *dott*. The vowels in these syllables are /i, ɪ, e, ɛ, ɛː, ɑ, a, y, ʏ, ø, œ, u, ʊ, o, ɔ/.[1]

Before testing began, subjects were familiarized with the task in three steps. In step, 1, the experimenter (a 33-year-old male native speaker of North German) pronounced the 14 vowels in isolation and in /dVt/ syllables. The experimenter then produced 14 randomized utterances of ''ich habe /dVt/ gesagt'' and indicated after each utterance which alternative he had intended on the response form displayed on an overhead projector. In step 2, 28 recorded sentences with dVt syllables (2 instances of each of the 14 vowels) were presented in random order to subjects with an audio cassette tape player and loudspeaker. The utterances had been spoken by a 31-year-old female native speaker of North German. The subjects used the first two pages of the answer sheet to mark their responses. After each block of 14 stimuli, the experimenter indicated on the displayed response form which responses the speaker had intended. Step 3 consisted of the presentation of the first 28 sentences of the listening test. The stimuli were presented via a Revox A77 reel-to-reel tape recorder and passed through the Language Laboratory's Conrac Electron SLA S4 system to Conrac Electron MKK 300 headphones, which were connected to individual listening stations in the laboratory. The subjects just listened to these sentences without marking answers; no feedback was given.

Following this familiarization, the listening test was presented (8 blocks of 14 trials each) using the same equipment as in step 3 of the familiarization. Subjects responded by putting a diagonal line through the syllable they had heard. After the experiment, subjects responded to a questionnaire regarding language background and exposure and training in linguistics/phonetics.

B. Results

The results from this preliminary experiment indicated that the vowel productions of the speaker provided a very good match to the vowel systems of the subjects. Thirteen of 15 subjects made no errors on the 112-trial test; the 2 remaining subjects made a total of 3 errors. These errors all involved the response category *däht*, which was not present in the stimulus material.

II. IDENTIFICATION OF GERMAN VOWELS IN SILENT-CENTER SYLLABLES

The purpose of the first perceptual study was to determine whether the identity of German monophthongs was maintained when listeners were presented silent-center (SC) syllables in which intrinsic durations and dynamic spectral information were preserved, but vocalic nuclei were attenuated to silence. Performance on vowel-center (VC) stimuli, which preserved target information and intrinsic duration differences, was compared with that on the SC syllables. Finally, two control conditions were included—syllable onsets (Initials) and syllable offsets (Finals)—to insure that vowel identity was not adequately specified in either portion of the SC syllables alone, but rather was defined by relational parameters specified over both portions taken together.

If, as predicted by the Dynamic Specification Theory, dynamic spectral information is important for the perception of German vowels, we would expect a pattern of results across the four conditions similar to that found for English vowels. That is, vowels in SC syllables would be identified with relatively high accuracy, not less and possibly more accurately than in the VC condition. Both conditions would yield much better performance than Initials and Finals conditions, which were expected to yield very high error rates.

A. Methods

1. Stimulus conditions

Four modified stimulus conditions were generated from the digitized sentence corpus described above, using waveform editing techniques. First, each target syllable was divided into onset, center, and offset portions. Several different criteria have been used in previous studies of English vowels to determine what proportions of each syllable were included in each of these portions. Differing from previous studies, the criterion of a fixed number of pitch periods was not adopted because variation in VOT and $F0$ would have led to considerable variation in both the absolute and proportional

TABLE I. Average and range in durations of onset, center, and offset portions of tense (long) vowels and lax (short) vowels. Absolute durations (in ms), number of pitch periods included in each portion, and proportions of total syllable duration are given. Averages represent the mean of 14 instances (7 vowels×2 repetitions).

Portion[a]	Tense vowels		Lax vowels	
	Mean	Range	Mean	Range
Onsets				
Absolute (ms)	31.1	(27–36)	26.1	(21–32)
VOT	14.5	(11–17)	16.4	(13–22)
No. pitch periods	1.9	(1–2)	1.2	(1–2)
% total syllables	26%	(19–34)	26%	(24–36)
Centers				
Absolute (ms)	63.6	(34–113)	39.8	(26–53)
No. pitch periods	7.2	(4–12)	4.6	(3–6)
% total syllables	50.4%	(36–64)	44.6%	(37–55)
Offsets				
Absolute (ms)	27.1	(21–36)	22.9	(14–30)
No. pitch periods	2.7	(2–3)	2.4	(2–3)
% total syllables	22.4%	(17–27)	22.2%	(18–32)
Syllable duration (ms)	122.4	(90–176)	88.2	(69–108)

[a]Note: Percentages of onset, center, and offset portions do not sum to 100% because they represent *averages* of 14 syllables.

durations of onset and offset portions. Rather, a variable number of pitch periods was retained in order to minimize the differences in absolute durations of onset and offset portions as much as possible, while silencing the entire vocalic nucleus of each syllable. As in the Strange (1989b) study, a minimum of three pitch periods defined the center portions.

Table I gives the average and range in absolute durations, number of pitch periods, and proportions of total syllable duration for onset portions, center portions, and offset portions of tense and lax vowels, separately. As these data indicate, there was a large range in the absolute duration of the center portions, due to the large variation in overall duration across the 14 vowels (69–176 ms). In addition to a larger contrast between some tense–lax vowel pairs than is the case for English, syllable durations also varied considerably more with vowel height than in English.

a. Silent-center (SC) syllable condition. SC syllables were generated by attenuating to silence the center portion of each of the 28 target syllables, while leaving onset and offset portions in their original temporal position. (Since portions were defined in terms of pitch periods, all silences began and ended at the zero crossing between pitch periods, thus avoiding the generation of perceptible transients.)

b. Vowel centers (VC) condition. These stimuli were the converse of the SC syllables. They were generated by attenuating to silence both onset and offset portions, leaving the centers in their original temporal positions in the sentences. Onsets were silenced from immediately before the initial consonant burst to the end of the onset portion; offset portions were silenced from the beginning of the offset portion to the end of the final /t/ burst.

c. Control conditions. The Initials (I) stimuli were generated by silencing both center and offset portions of each target syllable. The Finals (F) stimuli were generated by silencing both onset and center portions of each syllable.

Separate listening tests were recorded for each stimulus condition. A test consisted of four blocks of the 28 utterances containing the modified syllables in their original sentence contexts. The same random sequences and interstimulus intervals as were used for the verification test described above were employed for these listening tests. Thus the only difference between conditions was in which portions of the target syllables were silenced. In a test, each of the 28 utterances occurred 4 times; each of the 14 vowels occurred 8 times, for a total of 112 trials.

2. Subjects, procedures, and equipment

Subject recruitment and selection criteria were the same as for the verification experiment. All subjects were native speakers of NG; exposure to, and knowledge of, languages other than German did not differ appreciably for the subjects across these groups and the previous group. The group of 57 subjects (44 females, 13 males) had a mean age of 24 years (s.d.=3.1). Subjects were randomly assigned to the four conditions (18 subjects in SC, 15 subjects in VC, 14 subjects in I, and 10 subjects in F). The data for five subjects were later discarded; three because of failure to meet dialect criteria, one for failure to meet the minimal English experience criterion, and one for errors in using the response form during familiarization. Thus 16, 14, 13, and 9 subjects remained in SC, VC, I, and F conditions, respectively.

Procedures and equipment were the same as in the verification experiment with unmodified syllables, with one exception. During step 3 of familiarization, each group of subjects listened with no feedback to 28 sentences containing the modified syllables on which they were subsequently tested. Before listening, the subjects were told that the syllables had been modified ''in some way.''

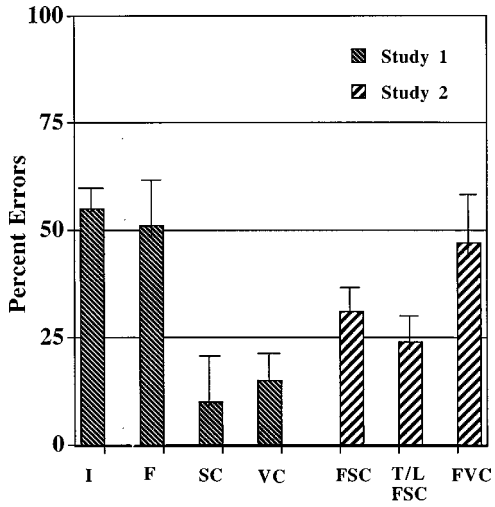

FIG. 1. Overall errors in vowel identification in Initials (I), Finals (F), Silent-Center syllables (SC), and Vowel-Centers (VC) conditions of study 1 (left 4 bars) and Fixed duration SC (FSC), Tense/Lax Fixed duration SC (T/LFSC) and Fixed duration VC (FVC) conditions of study 2 (right three bars). Errors are expressed as percentages of opportunities; brackets indicate 1 standard deviation.

B. Results and discussion

Performance was scored in terms of the number of identification errors, where an error was defined as a response other than the intended vowel of the original utterance or an omission. Because subjects were instructed to respond on every trial even if they had to guess, there were very few omissions. Figure 1 (left 4 bars) presents the overall results for the four stimulus conditions, expressed as the percentage of errors (out of 112 opportunities) averaged across subjects within each group. As the figure shows, overall performance in SC and VC conditions was much better than in I and F control conditions. A one-way ANOVA for independent groups verified that groups differed significantly, $F(3,48) = 52.912$, $p < 0.001$. Pairwise comparisons (Least Significant Differences) revealed that the SC and VC groups made significantly fewer errors than the other two groups ($p < 0.01$), but did not differ significantly from each other ($p > 0.05$).

The overall error rate of 10% in the SC condition was significantly higher than for the unmodified syllables (median errors for unmodified syllables=0), but vowel identity was nevertheless well maintained in most cases, despite the drastic modifications of the acoustic syllables. In addition, the distribution of scores for the SC subjects was highly skewed (mode=3% errors, median=8% errors), suggesting that for some subjects at least, silencing the vocalic nuclei had no detrimental effect on their ability to identify the vowels accurately.

Table II presents the errors for each vowel (expressed as a percentage of opportunities) pooled over subjects in each group. The most frequent error responses are given in parentheses for vowels which had 10% or greater errors. In the SC condition, error rates varied across vowels from 0% to 34%, with only 5 of the 14 vowels yielding error rates of greater than 10%. The high front lax vowels /ɪ, ʏ/ were confused most often with their mid front lax counterparts /ɛ, œ/, while the mid front tense /e/ was misidentified as the high tense /i/. The two other vowels showed tense–lax confusions (/o–ʊ/ and /ɑ–a/). Four of these five vowels were identified more accurately in the VC condition.

TABLE II. Mean errors (in percent) on tense and lax vowels in Silent-Center Syllables (SC), Vowel-Center (VC), Initials (I), and Finals (F) modified conditions. Modal error responses are given in parentheses for error rates exceeding 10%.

	Conditions			
	SC	VC	I	F
Tense vowels				
i	2	11 (ɪ)	13 (ɪ)	79 (ɪ)
e	23 (i)	41 (ɪ)	95 (ɪ)	100 (ɪ)
ɑ	15 (a)	7	86 (a)	90 (a)
y	0	10 (ʏ)	28 (ʏ)	68 (ʏ)
ø	10 (y,ʏ)	35 (ʏ)	94 (ʏ)	100 (ʏ)
u	1	6	13 (ʊ)	44 (ʊ)
o	13 (ʊ)	2	100 (ʊ)	100 (ʊ)
Overall tense	9.2%	16.0%	61.3%	83.0%
Lax vowels				
ɪ	22 (ɛ)	0	21 (ɛ)	4
ɛ	8	29 (ɪ)	76 (ɪ)	46 (œ,ɪ)
a	1	11 (œ)	20 (ɑ)	10 (ɑ)
ʏ	34 (œ)	10 (ɪ)	60 (ʊ,œ)	14 (ʏ,œ)
œ	7	15 (ʏ)	86 (ʏ)	26 (ʏ,ø)
ʊ	0	14 (ʏ)	13 (u)	7
ɔ	5	23 (a)	60 (ʊ)	18 (o,ʊ,œ)
Overall lax	11.0%	14.6%	48.0%	17.9%

In the VC condition, 8 of the 14 vowels were misidentified more than 10% of the time. In some cases, the modal error response differed from the SC condition. Tense vowels were most often misidentified as lax vowels, while lax vowels produced errors in vowel height, rounding, and frontness. These differences in type of vowel error in SC and VC conditions suggest that syllable onsets and offsets together provided *different* information than did vocalic nuclei, even though both were sufficient, in conjunction with intrinsic duration information, to specify vowel identity most of the time.

The extremely high error rates in both I and F conditions demonstrated that neither onsets alone nor offsets alone were sufficient to maintain vowel identity. As the modal error responses suggest, the lack of duration information may have accounted for many of the errors on tense vowels (this is discussed further in Sec. IV).

The overall pattern of performance in this study was strikingly similar to that reported by Strange and her colleagues for AE vowels (Strange *et al.*, 1983; Strange, 1989b). As was found for English vowels, accurate perception of vowels in SC syllables demonstrates that dynamic spectral information, in conjunction with intrinsic duration differences, is *sufficient* to specify German monophthongs in most cases. Static target information, specified by formant relationships in vocalic nuclei, is not necessary for accurate perception of the vowels. The similarity in results for English and German vowels argues indirectly against the notion that SC syllables containing English vowels are well identi-

fied *only* because they preserve diphthongal patterns of formant movement. The results in this study do reinforce the hypothesis that dynamic spectral parameters defined over syllable onsets and offsets provide perceptually relevant information about underlying differences in the ''style of movement'' of tense and lax vowels. This is also suggested by the error patterns on SC syllables; the most common errors in this condition were tense–tense and lax–lax confusions. Before exploring further the nature of the dynamic spectral information available in the SC syllables, another perceptual study was performed to investigate the relative contribution of intrinsic duration information to the identification of German vowels.

III. ROLE OF DURATION IN PERCEPTION OF GERMAN VOWELS

In study 2, the effects on vowel identification of modifying duration information were investigated by assessing performance in three additional conditions: (1) Fixed-duration SC (Fixed SC) syllables in which differences in duration of all 28 SC syllables were neutralized by adjusting the silent intervals between onsets and offsets; (2) Tense–Lax Fixed duration SC (Tense/Lax Fixed SC) syllables, in which duration varied across SC syllables containing vowel pairs which differed in height, but within each tense–lax pair, durations were equated; and (3) Fixed duration Vowel Centers (Fixed VC) in which the center portions of all 28 stimuli were trimmed to approximately the same (short) duration. For the Fixed SC condition, neither static target information nor any intrinsic duration information was available, leaving only dynamic spectral information. For the Fixed VC condition, only static target information remained. For the Tense/Lax Fixed SC condition, duration information about vowel height remained, as well as dynamic spectral information. However, static target information and duration information about tense–lax contrasts was not available. Comparisons of relative accuracy of vowel identification in these conditions allowed us to assess the contribution of intrinsic duration information to differentiation of tense–lax vowel pairs, and also to investigate the relative efficacy of dynamic spectral information vs static target information when intrinsic duration information about tense–lax contrasts and vowel height was not available.

Since vowel duration is considered important in the differentiation of at least some NG vowel pairs, we predicted that performance in all three new conditions would be relatively worse than for comparable conditions in English vowel studies. Nevertheless, we predicted that performance in the Fixed SC syllable and Tense/Lax Fixed SC syllable conditions would be significantly better than in the Fixed VC condition, just as in the English vowel studies.

A. Methods

1. Stimulus conditions

a. Fixed SC syllables. In the previous study of English vowels in sentence context (Strange, 1989b), Fixed SC syllables were generated by separating the onset and offset portions of all SC syllables with a silent interval that was equal to the average silent interval of all syllables in the SC syllables. Using this technique, all syllables containing intrinsically short vowels were lengthened, while all syllables containing intrinsically long vowels were shortened, although the amount of shortening and lengthening varied somewhat as a function of vowel height. This resulted in all syllables in the Fixed SC syllable condition having approximately the same duration. For the present study, this same procedure was used to create Fixed SC syllables. All syllables were adjusted to a duration of 106 ms (± 3 ms). However, since differences in duration for high versus low German vowels were proportionally greater than the differences between most tense–lax pairs, this procedure resulted in some of the high tense vowels actually being lengthened rather than shortened, while some of the low lax vowels were actually shortened or lengthened very little.

b. Tense/lax fixed SC syllables. First, the average duration of the four syllables containing each tense–lax vowel pair (two tokens of each vowel) was computed; then silent intervals in the four SC syllables were adjusted so that all four syllables were equated in duration. Thus the 2 /dit/ syllables and the 2 /dɪt/ syllables were all equal in duration, but were shorter than the /dɑt/ and /dat/ syllables. (For the average vowel durations, see Table V).

c. Fixed VC stimuli. These stimuli were generated by silencing all but the middle 4 pitch periods (approximately 36 ms) of each of the 28 dVt syllables. These four pitch periods were the same as those included in the VC stimuli, except for the shortest stimulus (which included only three pitch periods in the center portion). All 28 Fixed VC stimuli contained the portion of the vocalic nucleus in which formants reached maxima or minima most closely approximating ''canonical'' vowel targets (see Sec. IV).

Three separate listening tests were recorded using the same procedures as in study 1. The modified stimuli were imbedded in their original sentences, and recorded in the same random sequences as before. Thus each of the 28 stimuli occurred 4 times, for a total of 112 trials (8 trials $\times 14$ vowels).

2. Subjects, procedures, and equipment

Subject recruitment and selection criteria were the same as for study 1. The group of 43 subjects (31 females, 12 males) had a mean age of 23 years (s.d.$=1.5$). Subjects were randomly assigned to the three conditions (15 subjects in Fixed SC syllables, 14 subjects in Tense/Lax Fixed SC syllables, and 14 subjects in Fixed VC condition). Data for 4 subjects were later discarded because of failure to meet the dialect or language criteria, resulting in 13, 14, and 12 participants in the three groups. Procedures and equipment were the same as in the previous experiment.

B. Results and discussion

As expected, overall identification accuracy in all three conditions was poorer than for SC and VC conditions in study 1. Figure 1 (right 3 bars) presents the overall error rates and Table III gives the error rates for individual vowels and the modal error response(s) for vowels with 10% or greater errors.

TABLE III. Mean errors (in percent) on tense and lax vowels in Fixed duration Silent-Center Syllables (Fixed SC), Tense/Lax Fixed duration Silent Center syllables (Tense/Lax Fixed SC), and Fixed duration Vowel Center (Fixed VC) conditions. Modal error responses in parentheses for vowels with greater than 10% errors.

	Conditions		
	Fixed SC	Tense/Lax fixed SC	Fixed VC
Tense vowels			
i	1	1	28 (ɪ)
e	55 (i,ɪ)	46 (i)	93 (ɪ)
ɑ	94 (a)	68 (a)	88 (a)
y	1	9	45 (ʏ)
ø	56 (ʏ)	32 (ʏ)	98 (ʏ)
u	0	0	21 (ʊ)
o	74 (ʊ)	29 (ʊ)	91 (ʊ)
Overall tense	40.1%	26.4%	66.3%
Lax vowels			
ɪ	57 (ɛ)	43 (ɛ)	11 (i)
ɛ	1	12 (ɪ,e)	28 (ɪ)
a	1	11 (ɑ)	28 (œ)
ʏ	68 (œ)	67 (œ)	43 (ɪ)
œ	1	12 (ø)	36 (ɛ)
ʊ	1	2	24 (ʏ)
ɔ	1	3	22 (a)
Overall lax	18.6%	21.4%	27.4%

As these data show, performance was best for the Tense/Lax Fixed SC syllables ($\bar{x}=24\%$ errors) in which dynamic spectral information and duration information about vowel height (but not tense–lax contrasts) were present. Errors were somewhat greater for the Fixed SC syllables ($\bar{x}=31\%$ errors) in which only dynamic spectral information distinguished the vowels. However, performance in this condition was still better than for the Fixed VC condition ($\bar{x}=47\%$ errors) which contained only static target information. A one-way ANOVA for independent groups indicated that these group differences were statistically significant, $F(2,36)=23.82$, $p<0.001$. Pairwise comparisons (Least Significant Differences) indicated that performance was significantly poorer in the Fixed VC condition than in both of the other conditions ($p<0.01$). Performance was also significantly poorer for the Fixed SC syllables than for the Tense/Lax Fixed SC syllables ($p<0.05$).

These results confirmed the prediction that modified syllables containing only static target information would be identified very poorly. In fact, a comparison of the performance of the Fixed VC group with the I and F groups of study 1 revealed no significant differences, $F(2,31)=1.67$, $p=0.21$. That is, vowel identification was no better when subjects were presented the portion of the vocalic nucleus in which formants approach canonical targets than when they were presented either syllable onsets (burst plus 1–2 pitch periods) or offsets (2–3 pitch periods plus silence and final consonant burst).

As shown in Table III, errors on all 14 vowels of the Fixed VC condition exceeded 10%. The pattern of error responses indicates that mid and low tense vowels (with the longest original durations) were misidentified most often and modal errors were of spectrally adjacent lax vowels. This pattern of errors is very similar to that found in the Initials and Finals conditions of study 1 (see Table II), which suggests that the shortened durations accounted for the identification pattern. Note, however, that many of the lax vowels in the Fixed VC condition were also misidentified at relatively high rates. Thus we can conclude that static spectral information in the center of these syllables was not sufficient to differentiate coarticulated German vowels.

The types of errors found in identification of vowels in the two SC syllable conditions in which duration information was disrupted show a different pattern of confusions. For the Fixed SC syllables, six vowels yielded error rates of greater than 10%. However, only three of the tense vowels were misidentified as spectrally similar lax vowels; modal error responses for the other three vowels were the same as those found in the SC condition of study 1, although the overall number of such errors increased. The pattern of errors for vowels in the Tense/Lax Fixed SC syllables was similar to the Fixed SC syllables, although errors were distributed somewhat more broadly over vowel types, with 9 of the 14 vowels yielding error rates of greater than 10%. Again, modal errors on these vowels consisted of both tense–lax confusions and errors in vowel height. Because of the way in which these stimuli were made, tense–lax confusions tended to be more symmetrical than in the Fixed SC condition, resulting in relatively more errors for some lax vowels and fewer errors for some tense vowels in the Tense/Lax Fixed SC syllables than in the Fixed SC syllables.

The overall pattern of results found in this study is similar to that reported earlier for AE vowels (Strange, 1989b; see also Strange *et al.*, 1983; Jenkins *et al.*, 1983). As found here, elimination of duration information led to an increase in identification errors for English vowels. The poorer performance in the Fixed VC condition relative to the VC, SC, Fixed SC, and Tense/Lax Fixed SC conditions in the present study is also comparable to the results for AE vowels, and reinforces the claim that static target information, as given by the spectral pattern in syllable centers, is not adequate to differentiate coarticulated NG vowels perceptually. The fact that Fixed VC stimuli were perceived more poorly than Fixed SC syllables, neither of which contained distinctive duration information, suggests that dynamic spectral information defined over syllable onsets and offsets is *more* efficacious than static target information in the perceptual specification of coarticulated German vowels. That is, syllable onsets and offsets together provide perceptually important information about German vowels, independent of information provided by intrinsic duration differences.

IV. ACOUSTICAL ANALYSES

Acoustical analyses were conducted to elucidate the nature of the dynamic information that may have been used by listeners to differentiate the German vowels. Specifically, temporal and spectral parameters of the formant trajectories of the stimulus corpus used in the perceptual study were compared with a set of /hVt/ syllables produced as citation-form utterances by the same speaker. The latter corpus was also used to determine if the vowels of this speaker contained any vowel ''diphthongization,'' independent of for-

mant movement associated with coarticulation with initial and final consonants. In addition, it provided a set of ''canonical'' formant values for his vowel space, from which to determine whether there was target undershoot in the coarticulated vowels spoken in /dVt/ syllables in sentence length utterances. Finally, a comparison of the relative durations of CVC syllables spoken in lists versus sentences was performed to determine the extent to which intrinsic vowel length differences found in citation-form utterances were maintained in utterances produced at a speaking rate and in a style more closely resembling continuous speech.

In contrast to American English, the monophthongs of Standard German (SG) are not considered to be diphthongized (Moulton, 1962; Scherer and Wollmann, 1972). We know of no acoustical analyses of SG vowels that have examined the extent to which formants move throughout vocalic nuclei, probably because auditory judgments yield the impression that SG vowels are indeed ''steady state.'' Several studies have shown that the duration contrast in German tense/lax pairs may be quite large when the vowels are produced in isolated monosyllables. For example, Iivonen (1987) reported that tense vowels were more than twice as long as lax vowels for speakers from various German dialect regions. Iivonen (1987, 1989a, b) also indicated that the spectral contrast between vowels in tense/lax pairs was small for speakers of Southern varieties of SG, but quite large for speakers of Central and Northern varieties. As in AE, tense vowels were more peripheral in the acoustic vowel space than lax vowels, which were centralized in Northern and Central varieties of SG.

We are not aware of any studies which directly examined the effects of speech style (citation form versus sentence context) on the duration or the spectrum of vowels. However, a number of studies have shown that the duration of German vowels is affected by factors such as phonetic context (Meyer, 1904), the number of syllables in the word (Meyer, 1904; Dinnsen and Garcia-Zamor, 1971; Rietveld, 1975) and word stress (Rietveld, 1975; Ramers, 1988; Jessen, 1993). The studies of Rietveld and Ramers, who both recorded speakers of SG from the Cologne/Bonn area, suggest that the duration contrast for tense/lax vowel pairs in stressed monosyllables is drastically reduced, if not neutralized, in unstressed syllables.

In the present study, four types of acoustic information were investigated:

(1) Static ''target'' information was assessed by comparing $F1/F2/F3$ formant values of the /dVt/ stimuli with the speaker's ''canonical'' target values, as measured from productions of the vowels spoken in citation-form /hVt/ syllables. Of interest was the extent to which target ''undershoot'' in the sentence length utterances reduced the separation of vowel categories in the acoustic vowel space. Such a reduction might account for the increase in identification errors for stimuli in which only the center portions of the vocalic nuclei of the syllables were presented.

(2) Relative durations of the /dVt/ syllables were compared with those of citation-form /hVt/ syllables to examine whether the *proportional* differences associated with the tense–lax distinction and with vowel height shown in citation-form (''careful'') style speech were maintained in sentential utterances. Since instructions had encouraged the trained speaker to produce the sentences at a rate appropriate for communicating with a competent speaker of German in quiet conditions, the sentences were thought to represent a style of speech that was somewhere between the speaker's ''casual'' style and his ''careful'' style.

(3) Formant change within the vocalic nuclei of the /dVt/ syllables was compared with formant movement patterns in the citation-form /hVt/ syllables to determine if formant movement in the /dVt/ stimuli could be attributed to diphthongization of the vowels by this speaker, or if it reflected only the coarticulatory influence of initial and final alveolar stop consonants.

(4) $F1$ temporal trajectories of the /dVt/ syllables were analyzed to see if distinctive ''tense'' and ''lax'' patterns were present in the stimuli employed in the previous perceptual study.

A. Methods

1. Stimulus conditions

In addition to the stimuli recorded for the perceptual experiments (described above) a second set, recorded in the same session, included 4 repetitions of each of the 14 vowels produced in /hVt/ syllables spoken in citation form. Each utterance was preceded by a number identifier spoken in German (e.g., ''Nummer eins (pause) [hit]; Nummer fünf (pause) [hat];...''). For each repetition of the set of 14 utterances, the vowels were produced in a different random order to control for possible sequence effects and the first utterance was repeated at the end of the list to control for list intonation effects. (The last utterance was not used.) During recording, the sets of /dVt/ sentence stimuli and /hVt/ citation stimuli were interspersed with sets of other sentence stimuli not used in this study. The speaker for both sets was the second author. (See Sec. I for further details.)

2. Procedures

Recording and digitization procedures were described in Sec. I. Measurements of duration were made to the nearest 1 ms from digital waveform displays. Syllable durations for the /dVt/ stimuli were defined as the interval from the beginning of the release burst of the initial /d/ to the beginning of closure for the final /t/ (i.e., the beginning of silence). Thus this measure included the period of aspiration preceding the onset of periodic sound (i.e., voice-onset-time). Durations for the /hVt/ stimuli were defined as the interval between the onset of periodic sound to the closure for the final /t/ (i.e., it did not include the voiceless /h/).

Spectral analysis was performed using the LPC and DFT algorithms available in the Interactive Laboratories Systems (ILS) computer software. For the /dVt/ stimuli, formant trajectories were computed manually from LPC spectra (14 coefficients) using a 9-ms Hamming window placed over each glottal period such that the beginning of the window coincided with the beginning of the period. Missing information due to merged formants or other obvious peak picking errors was supplied by computing DFT spectra (2048 points) start-

ing at the same location and manually setting a cursor at the apparent peak in the spectrum. Approximately 3% of the measurements were derived from DFT spectra.[2]

For the /hVt/ stimuli, target formant frequencies were defined as the values obtained by averaging the values derived from the two LPC spectra closest to the one-third temporal point in the vocalic nucleus. Upon inspection of wideband spectrograms of the utterances, the one-third point was chosen to insure that any formant movement associated with the final /t/ did not influence this measurement. For these stimuli, LPC spectra showed more merging of formants or obvious errors, especially in the estimation of $F2$ values for /u, ʊ, o/; thus, 11% of formant frequencies had to be estimated from DFT spectra (11% for $F1$, 21% for $F2$, and 0% for $F3$). For /dVt/ stimuli, static formant values were derived by averaging the two spectral sections closest to the one-half point. For long, tense vowels, these targets were within the quasi-steady-state portion of the syllable nucleus. For the short, lax vowels, however, formants often moved rapidly throughout the entire vocalic nucleus. For these vowels, the static measures taken at midpoint almost always contained formant maxima/minima representing the articulatory position closest to canonical targets. The portion of each syllable from which these static measures were obtained was included in the Fixed VC stimuli of the second perceptual study (see Sec. III). $F1$ and $F3$ values were all computed from LPC spectra, while 11% of $F2$ values were derived from DFT spectra because of merging with $F1$ in the LPC analysis.

$F1$ temporal trajectories of the /dVt/ syllables were characterized by segmenting each syllable into onglide, nucleus, and offglide portions. The interval between the beginning and end of the quasi-steady-state portion (<9-Hz change in $F1$ frequency of adjacent pitch periods) was defined as the nucleus, with preceding and following portions designated onglide and offglide, respectively. When no steady-state existed, the duration of the nucleus was recorded as 0 and the onglide and offglide durations were established by determining the temporal location of the $F1$ maximum frequency. For one repetition of each of the vowels, /y, ø, e/, $F1$ formant values did not change throughout the entire vocalic nucleus; for these tokens, onglide and offglide durations were considered 0. Durations of onglides, offglides, and nuclei were then converted into proportions of total syllable duration (including voice-onset-time).

B. Results

1. Static target information

Canonical targets for this speaker were defined as the values at the one-third temporal midpoint of each citation-form /hVt/ syllable. Table IV presents frequency values for the first three formants, averaged over the four tokens of each vowel. Figure 2 presents the averaged $F1$ and $F2$ data. Superimposed on this ''target vowel space'' are the average values for the two tokens of each vowel derived from the /dVt/ syllables produced in sentence context. As the figure clearly shows, there was an overall reduction in acoustic differentiation of the coarticulated vowels produced in the carrier sentence. For all vowel categories except /y, ɛ, ɑ/, either $F1$ or $F2$ or both show acoustic undershoot or centralization of the /dVt/ syllables relative to /hVt/ target values. Average $F1$ frequencies were lower than canonical values for the lax vowels /ɪ, ʏ, œ, ɔ, ʊ, a/ and for /ø/, while average $F2$ values were lower for the front unrounded vowels /i,e,ɪ/ and higher for the back rounded vowels /u, ʊ, ɔ, o/. Average $F3$ values were higher in /dVt/ syllables than in /hVt/ syllables for 8 of the 14 vowels, reflecting the coarticulatory influence of the high $F3$ value for the initial (and final) alveolar consonant. Thus front rounded vowels in /dVt/ syllables were displaced toward canonical values for front unrounded vowels.

For some vowel categories, it appeared that formant values at /dVt/ syllable midpoint were actually closer to the canonical values of a different vowel category. Linear discriminant analysis was employed to quantify these trends (Klecka, 1980). Formant frequencies for the four citation-form instances of each vowel were converted to Barks and $F1$, $F2$, and $F3$ values entered as discriminating variables in a linear discriminant analysis (Stat Soft, Inc., 1991). Classification of individual vowels on the basis of the canonical discriminant functions derived from this corpus was nearly perfect (only one instance of /œ/ was misclassified as /ʏ/. However, when Bark-transformed $F1/F2/F3$ values for the

TABLE IV. Target formant frequencies (Hz) measured in the steady-state portion of the citation-form /hVt/ syllables (one-third of the way through the vocalic portion of each syllable).

Vowels	$F1$	$F2$	$F3$
/i/	250	2131	2888
/ɪ/	422	1860	2211
/e/	307	2080	2358
/ɛ/	451	1663	2176
/a/	632	1275	2140
/y/	300	1571	2007
/ʏ/	457	1437	2044
/ø/	327	1412	1866
/œ/	553	1455	1978
/u/	298	670	2028
/ʊ/	440	844	2130
/o/	344	649	2335
/ɔ/	615	905	2012
/ɑ/	624	1041	2189

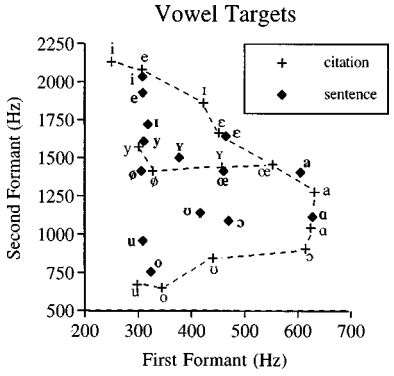

FIG. 2. Average formant frequencies (in Hz) of citation-form /hVt/ utterances (crosses), with average formant frequencies of the /dVt/ syllables superimposed (filled diamonds).

two instances of each vowel produced in /dVt/ context were classified using the canonical discriminant functions derived from the /hVt/ corpus, correct classification decreased to only 64% (18/28 instances). Classification errors were not evenly distributed across vowel categories. Both instances of each of the six unrounded vowels /i, ɪ, e, ɛ, ɑ, a/ and of /y/ were correctly classified, whereas one or both instances of the remaining rounded vowels /ʏ, ø, œ, u, ʊ, o, ɔ/ were misclassified. As the figure suggests, the mid front rounded vowels /ø/ and /œ/ were misclassified as high front rounded vowels /y/ and /ʏ/, respectively, due primarily to the lowering of their $F1$ (as well as raising of $F3$) relative to canonical values. The back rounded vowels /u, ʊ, o, ɔ/ were misclassified as /ʊ, ʏ, u, and ɑ or a/, respectively, due to their relatively high $F2$ values. For /u/ and /o/, $F3$ values were also higher in /dVt/ context than in /hVt/ context. Finally, one instance of /ʏ/ was misclassified as /ɛ/, due to $F2/F3$ raising relative to canonical values. Of the ten misclassifications of /dVt/ utterances, only three involved tense–lax confusions, despite the fact that duration information was not provided as one the classification variables.

These data indicate that static target information in these coarticulated syllables, as given by the formant values at syllable midpoint, may have been impoverished in two respects. First, target undershoot, especially for the short, lax vowels, decreased overall acoustic differentiation of the vowels in the formant space. Second, effects of coarticulation with alveolar consonants led to mid-syllable formant values for the back and front rounded vowels being displaced towards adjacent canonical vowel categories such that they were miscategorized when information about consonantal context was not taken into account. Thus when short portions of syllable nuclei are excised from coarticulated syllables (as in the Fixed VC condition of the perceptual study), vowel identification may be relatively poor even for lax vowels, if listeners identify the stimuli on the basis of stored representations of ''canonical'' vowel targets.

To address this issue further, a separate discriminant analysis was performed on the /dVt/ corpus, using the Bark-transformed values of $F1$, $F2$, and $F3$ for the 28 stimuli. Results of classification on the basis of the linear discriminant functions established for this corpus yielded 100% correct identification. Of course, this analysis must be interpreted with caution because of the small number of instances of each vowel category, but as a descriptive device it shows that the 14 vowel categories remained separable in $F1/F2/F3$ space despite the overall reduction in differentiation due to target undershoot associated with the coarticulatory influence of initial and final alveolar consonants on midsyllable formant frequencies.

2. Relative duration information

Table V presents the average durations of the four tokens of each vowel produced in citation-form /hVt/ syllables (above) and two tokens produced in /dVt/ syllables in sentence context (below). Looking first at the citation-form utterances, it is apparent that absolute duration differences varied systematically with tenseness, vowel height, and rounding. Averaging over all vowels within each category, tense vowels were 70% longer than lax vowels. Tense high vowels were shorter in absolute duration than tense mid vowels, with the tense low vowel longest. Within high and mid groups, front unrounded vowels tended to be shorter than front and back rounded vowels. There was a much smaller range of average durations for the lax vowels. However, the high vowels tended to be shorter than mid and low vowels and unrounded vowels tended to be shorter than the rounded vowels.

TABLE V. Average durations (in ms) of citation-form /hVt/ (above) and sentence-context /dVt/ syllables (below).

Vowel pair	Tense	Lax	Ratio T/L
	Citation /hVt/		
/i–ɪ/	130	85	1.53
/y–ʏ/	160	103	1.55
/u–ʊ/	161	101	1.59
/e–ɛ/	163	94	1.73
/ø–œ/	172	118	1.46
/o–ɔ/	195	101	1.94
/ɑ–a/	197	91	2.17
Overall average	168	99	1.70
	Sentence /dVt/		
/i–ɪ/	97	70	1.39
/y–ʏ/	103	80	1.28
/u–ʊ/	96	78	1.24
/e–ɛ/	120	93	1.28
/ø–œ/	127	99	1.28
/o–ɔ/	144	104	1.40
/ɑ–a/	172	95	1.81
Overall average	123	88	1.38

To determine whether these trends were systematic, a 7 (vowel pairs) by 2 (tense–lax) ANOVA for independent groups was conducted. Both main effects and the interaction were highly significant [Pairs: $F(6,42)=6.99$, Tenseness: $F(1,42)=302.07$; Pairs×Tenseness$(6,42)=4.56$; $p<0.001$ for all comparisons]. *Post hoc* pairwise comparisons of tense vowels showed that /i/ was significantly shorter than /ø, o, ɑ/, $p<0.02$. Planned comparisons among mean durations of high, mid, and low tense vowels indicated that high tense vowels were, on average, significantly shorter than mid and low tense vowels, $F(2,25)=9.66$, $p<0.001$. As a group, mid tense vowels did not differ significantly from the low tense vowel, nor were any of the pairwise comparisons significant. Within lax vowels, only the vowels /ɪ/ vs /œ/ differed significantly in duration ($p<0.05$). Average differences between high, mid, and low lax vowels were not statistically reliable ($p>0.20$).

Looking next at the vowels spoken in the continuous speech context, the average data illustrate that relative duration differences between tense and lax vowels decreased for all seven pairs (overall average tense/lax ratio=1.38) in comparison with citation-form utterances (overall average tense–lax ratio=1.70). With the exception of the low vowel pair, tense vowels ranged from only 24% to 40% longer than their lax vowel counterparts. This was due to the disproportionate shortening, relative to their citation-form durations, of the coarticulated tense vowels. As the table shows, average ab-

solute reductions in tense vowel duration (/hVt/–/dVt/) ranged from 33 to 65 ms, except for /ɑ/. In contrast, syllable durations for /dVt/ syllables containing lax vowels decreased only from 1 to 24 ms relative to citation-form values, except for /ɔ/ and /a/, which were actually slightly longer on average than citation-form syllables.

To assess these differences statistically, a 2 (tense–lax)×2(citation-sentence) mixed design ANOVA was performed, using the mean duration of each vowel in each context as the sampling variable and treating context as a repeated measures factor. Both main effects and the interaction (contexts within tense–lax) were highly significant [Tenseness: $F(1,12)=26.69$; Context: $F(1,12)=65.75$; Interaction: $F(1,12)=25.55$, all $p<0.001$]. That is, tense vowels were, on average, longer than lax vowels, vowels in citation form were, on average, longer than vowels in sentence context, and tense vowels were shortened relatively more than lax vowels in the sentence-context syllables.

These results indicate that relative duration information for spectrally similar tense and lax vowels was reduced for vowels produced at speaking rates more closely approximating continuous speech conditions. For this speaker, then, vowels produced in continuous speech context were less differentiated acoustically than citation-form utterances, both in terms of static spectral values and relative duration differences.

3. Vowel-inherent spectral change (VISC)

One purpose for investigating formant trajectories of the /dVt/ syllables, as compared with citation-form /hVt/ syllables produced by the same speaker, was to determine if formant movement throughout the vocalic nucleus of the more rapidly produced syllables could be attributed to coarticulatory influences alone, or whether it also reflected some diphthongization of the single target vowels by this speaker. In order to quantify formant movement which might be considered ''inherent'' to the vowel, changes in $F1$ and $F2$ frequencies from a point 25% through the vocalic duration to the 75% point in each /hVt/ syllables were computed and transformed into a percentage change score: [(value at 75% pt–value at 25% pt)/(value at 25% pt)] X 100).[3] These differences (including the sign) were then averaged over the four instances of each vowel (as presented in Table VI Part A).

As the table indicates, formant movement throughout the middle half of /hVt/ syllables containing long tense vowels was slight, with no change greater than 10%—the figure Nearey used to characterize significant VISC in Canadian English vowels produced in citation-form /bVb/ syllables (Andruski and Nearey, 1992; but see Jenkins *et al.*, 1994). In fact, average $F2$ movement of tense vowels did not exceed 5% in any case, while $F1$ movement varied from less than 1% to 8%. Thus it can be concluded that none of this speaker's tense vowels showed any systematic diphthongization.

As shown in Table VI Part A, several of the /hVt/ syllables containing lax vowels showed significant formant movement across the middle half of their vocalic nuclei. Average $F1$ values decreased for all but /hɪt/, with four vowels showing changes of greater than 5% (2 vowels >10% change). Inspection of the formant trajectories suggested that these decreases in $F1$ could be attributed to the fact that the 75% point in these very short syllables was located in the final /t/ transitional portion of the syllables. Likewise, average movement of $F2$, which exceeded 5% for 4 of the seven lax vowels, appeared to reflect the influence of the final /t/. That is, the front unrounded vowels /ɪ, ɛ/ showed decreases, while the back vowels /ʊ, ɔ/ showed increases, suggesting that $F2$ values for the lax vowels converged on a value for /t/ of about 1500 Hz.

TABLE VI. Percentage change in formant frequencies over the middle half of citation-form /hVt/ syllables (A) and from the end of the Initial portion to the beginning of the Final portion of SC dVt syllables (B). (See text for explanation.) Values exceeding 5% are given in boldface.

Tense	$F1$ change	$F2$ change	Lax	$F1$ change	$F2$ change
		A. Citation-form /hVt/ syllables			
/i/	**−7.8**	0.2	/ɪ/	1.0	**−7.7**
/e/	−0.8	−0.1	/ɛ/	−1.7	**−6.8**
/y/	4.5	0.2	/ʏ/	**−6.3**	1.9
/ø/	0.8	0.8	/œ/	**−17.4**	3.8
/u/	**−5.7**	2.0	/ʊ/	**−5.4**	**64.7**
/o/	3.8	**5.0**	/ɔ/	**−20.1**	**25.5**
/ɑ/	−3.0	1.9	/a/	−2.4	1.8
		B. Sentence /dVt/ syllables			
/i/	−0.5	**7.1**	/ɪ/	2.0	−2.4
/e/	0.5	**8.5**	/ɛ/	**12.8**	−3.8
/y/	−1.0	−0.8	/ʏ/	**−5.2**	−1.6
/ø/	0.3	−0.2	/œ/	**16.0**	−4.9
/u/	−0.2	**−11.1**	/ʊ/	4.4	−4.8
/o/	1.6	**−18.7**	/ɔ/	**−13.8**	**−10.0**
/ɑ/	**32.1**	**−5.5**	/a/	**16.5**	0.1

In examining patterns of formant movement in the /dVt/ syllables, it was expected that syllables containing lax vowels would again reflect coarticulatory influences. However, the direction of movement might differ for /dVt/ and /hVt/ syllables as a function of differences in place-of-articulation of the initial consonant. In addition, syllables containing tense vowels with reduced durations might also show formant movement reflecting coproduction of consonants and vowel. Table VI Part B presents the patterns of frequency change in $F1$ and $F2$ change from the first to the second point, again expressed as a percentage, with the sign indicating the direction of change. Ten of the 14 vowels showed an average change exceeding 5% in $F1$ or $F2$ or both (7 syllables showed >10% average change of one or both formants). Change in $F1$ was present for syllables containing five lax vowels and the tense vowel /ɑ/. Note, however, that in four cases, the formant frequency increased, rather than decreased as observed in the /hVt/ syllables (compare Table VI Parts A and B). In the same way, for the five vowels showing greater than 5% average change in $F2$ frequency, the direction of change in /dVt/ syllables was either opposite that observed in /hVt/ syllables, or occurred for vowels that showed no significant $F2$ movement in /hVt/ syllables. In general, then, spectral change occurring across the silenced portion of the /dVt/ syllables was not predictable from formant movement patterns displayed in citation-form syllables. Therefore, it can be assumed that trajectory patterns reflected

TABLE VII. $F1$ temporal trajectories: (A) Average durations (ms) of $F1$ onglide, nucleus, and offglide portions of /dVt/ syllables. (B) Relative durations (percent of total syllable duration from initial stop burst to /t/ closure).

	Onglide[a]		Nucleus		Offglide	
Vowel type	Mean	Range	Mean	Range	Mean	Range
			A. Absolute durations (ms)			
Tense	16	(0–47)	96	(72–123)	11	(0–35)
Lax	38	(23–54)	33	(8–52)	18	(0–32)
			B. Relative durations (percent)			
Tense	12	(0–28)	79	(49–100)	9	(0–24)
Lax	44	(23–57)	36	(10–57)	20	(0–34)

[a]Onglide durations were measured from the /d/ release burst to the first pitch period of the quasi-steady-state nucleus, and thus, included voiceless portions in which $F1$ was not excited by periodic sound (voice-onset time). See Table I for average values of voice-onset time.

coarticulatory effects rather than diphthongization intrinsic to the vowels.

The formant movement in the /dVt/ syllables can be explained by considering the location of the measurement points relative to the complete formant trajectories of each syllable (see Sec. II for a detailed description). In most cases, the portion silenced in the SC syllables (and retained in the VC stimuli) included portions of the relatively rapid initial and final transitions associated with the consonants. This was true of almost all syllables containing lax vowels, because of their very short durations and lack of steady-state nuclei. In addition, many of the tense vowels had initial or final transitions that exceeded the length of the initial and final portions of the SC syllables. Therefore initial and final formant transitions were ''interrupted'' at different points when they were not temporally symmetrical (see below).

In summary, it can be concluded that the ''single-target'' vowels of this NG speaker were not diphthongized even when produced in relatively slow syllables produced in lists. Formant movement within the central part of the /hVt/ syllables, when it occurred, was due to the coproduction of the vowel and the final alveolar stop consonant. Even for these slowly articulated syllables, the influence of the final consonant began quite early in the syllables containing lax vowels. When the vowels were coarticulated with initial and final alveolar stop consonants in syllables produced in a carrier sentence, formant trajectories showed continuous movement throughout the vocalic nuclei except for the longest tense vowels and the vowels whose $F2$ target values were near the $F2$ value for the alveolar stop. This formant movement in coarticulated syllables is not inherent to the vowel in that it varies both in direction and extent as a function of the consonantal context. It, therefore, cannot provide invariant information about vowel identity.

4. F1 temporal trajectories

Strange and her colleagues and others have hypothesized that $F1$ temporal trajectories provide distinctive acoustic information for AE vowels. $F1$ trajectories were therefore investigated in the present study to explore whether NG vowels might be distinguished by similar temporal patterns. Table VII summarizes the data for the /dVt/ syllables employed in the perceptual studies; averages durations of onglide, nucleus, and offglide portions of $F1$ trajectories tense and lax vowels are shown in A (ranges shown in parentheses). Following Lehiste and Peterson (1961), these temporal data were then converted to proportions of total syllable duration for each stimulus by dividing the duration of each portion by the total duration. These relative durations, averaged for tense and lax vowels, respectively, are given in B (ranges in parentheses).

What is immediately apparent are the clear differences in duration of nuclei for tense versus lax vowels. Whereas tense vowels had considerable quasi-steady-state $F1$ portions (mean=96 ms), lax vowels were characterized by very short $F1$ steady states (mean=33 ms), even for the high vowels with low $F1$ target frequencies. The latter pattern is due not only to the fact that syllable durations were relatively short, but also to the fact that the absolute durations of $F1$ onglides and offglides were longer (mean=38 ms and 18 ms, respectively) than for $F1$ onglides and offglides of tense vowels (mean=16 ms and 11 ms, respectively). It can be inferred from these data that the opening and closing gestures associated with tense vowels were more rapid than those associated with lax vowels.

When temporal patterns of $F1$ trajectories are represented in terms of *relative* durations of onglides and offglides (Table VII Part B), a distinct pattern emerges. Tense vowels were characterized by temporally more symmetrical $F1$ trajectories, with very short and approximately equal length onglides and offglides (12% and 9%, respectively). Only 7 of the 14 syllables containing tense vowels had numerically longer onglides than offglides (mean=17 ms); 4 had longer offglides than onglides (mean=13 ms) and 3 were equal in duration (no change in $F1$ throughout the entire vocalic portion of the syllable). In contrast, syllables containing lax vowels had temporally more asymmetrical trajectories, and relatively longer onglides and offglides (44% and 20%, respectively). For 12 of the 14 lax vowels of this speaker's productions, onglides were numerically longer than offglides (mean=25 ms); both tokens of /dɔt/ showed the opposite pattern of temporal asymmetry (mean=7 ms). In all cases, spectrally similar tense and lax vowel pairs were well differentiated by $F1$ temporal trajectory patterns. To the extent that these patterns are recoverable from the SC syllables, $F1$ temporal trajectories may provide information that disambiguates tense and lax vowels with similar static target information.

C. Discussion

The results of this investigation of four perceptually relevant acoustic parameters of German coarticulated vowels can be summarized as follows:

(1) Static target information, given by the formant frequencies in a single spectral cross section within the vocalic nuclei of /dVt/ syllables produced in sentences, was impoverished, due to reduced acoustic differentiation and target undershoot, especially of the front and back

rounded vowels, as compared with canonical values attained from the speaker's citation-form /hVt/ syllables.

(2) Relative duration differences between spectrally similar tense and lax vowels were also reduced in rapidly spoken /dVt/ syllables, as compared with the citation-form utterances, largely due to the disproportionate reduction in the durations of the tense vowels in coarticulated syllables.

(3) Formant movement within the vocalic nuclei of the /dVt/ syllables could be attributed to coproduction of vowel and consonants, rather than to diphthongization of NG vowels by this speaker. For lax vowels, and some tense vowels, the influence of the consonants was seen throughout the entire vocalic nucleus.

(4) An analysis of $F1$ temporal trajectories of the /dVt/ syllables revealed distinct patterns associated with tense and lax vowels. In addition to differences in the length of quasi-steady-state portions, tense and lax vowels also differed in the relative durations of $F1$ onglide and offglide portions. Whereas syllables containing tense vowels tended to have symmetrical patterns with relatively rapid and approximately equal length $F1$ onglides and offglides, syllables containing lax vowels tended to have asymmetrical $F1$ temporal trajectories, with onglides more than twice as long as offglides, on average.

These results confirm expectations that NG monophthongs do not contain any of the vowel-inherent spectral change associated with several American and Canadian English vowels. While the present study included only one phonetically trained speaker, impressionistic phonetic descriptions of German suggest that vowels produced by other speakers will reveal similar patterns. With respect to the interpretation of the perceptual studies of German SC syllables reported here, the acoustic data confirm that dynamic spectral information is important in the perceptual specification of coarticulated vowels even for a language with no diphthongization of single-target vowels.

The finding that vowel duration differences were significantly reduced in syllables produced in sentence context (except for the low vowel pair /ɑ–a/) suggests that, in phonetic/phonological analyses of North German, vowel ''quantity'' (length) should be considered redundant with or secondary to ''vowel quality'' (tongue and jaw position) features for contrasts between tense/lax pairs of mid and high vowels (see also Jessen, 1993). It is interesting to note that the overall proportional difference between tense and lax vowels in this speaker's German /dVt/ utterances ($T/L = 1.38$) was not greater than that reported for American English vowels. For instance, Peterson and Lehiste (1960) report an overall difference between ''long'' and ''short'' vowels of 1.33. More recently, Crystal and House (1988) measured segmental durations in AE vowels spoken in continuous speech corpora. For stressed syllables ending in voiceless stops with no pause following the syllable, the ratio of long to short vowels was 1.64.

In light of these results, it is noteworthy that vowel duration appears to be more important perceptually for identification of German coarticulated vowels than it is for the identification of AE vowels. This is probably due to the fact that durational differences for high versus low vowels are proportionally greater for German vowels than for AE vowels, as well as to the fact that duration is the primary acoustic ''cue'' for the /ɑ–a/ vowel pair.

The finding that the $F1$ temporal patterns were distinctive for tense and lax vowels in German is similar to that reported for AE vowels. In both languages, the long, tense vowels are characterized by relatively symmetrical temporal trajectories with relatively rapid onglides and offglides (Huang, 1985, 1986; Jenkins *et al.*, 1994; Lehiste and Peterson, 1961). In contrast, $F1$ temporal trajectories for syllables containing lax vowels are asymmetrical. However, unlike AE in which offglides are relatively longer than onglides (Jenkins *et al.*, 1994; Lehiste and Peterson, 1961), the opposite pattern characterized six of the seven German lax vowels. In an earlier study, Fliflet (1962) reported relatively rapid onglides and offglides for tense vowels and slower onglides and offglides for lax vowels produced by German speakers from the Kiel area. He did not mention, however, whether the trajectories were symmetrical or asymmetrical.

It is premature to conclude on the basis of the vowels spoken in a single CVC context by a single speaker that these $F1$ temporal trajectories provide reliable (and possibly invariant) information for the identification of German vowels. However, the present findings do allow us to speculate that these relational parameters could have provided perceptually relevant information in SC syllable conditions in the perceptual study. For the most part, errors in these modified conditions were lax–lax errors and tense–tense errors, even when tense–lax syllable duration differences were removed (in the Tense/Lax Fixed SC condition).

V. GENERAL DISCUSSION AND CONCLUSIONS

The main purpose of these studies was to test the generality of the claim of Dynamic Specification Theory that time-varying acoustic patterns (formant trajectory parameters) which specify underlying dynamic characteristics of vowel gestures are critically important for perception of coarticulated vowels. German vowels were chosen to test the generality of this model of vowel perception because its vowel inventory is large, leading to a crowded acoustic vowel space and considerable overlap of static spectral targets, and because German vowel pairs are distinguished on the basis of their tenseness/length. However, unlike American English, German vowels are described as having little or no diphthongization.

Results of study 1 revealed that perception of German vowels in silent-center syllables was highly accurate, despite drastic reduction in the vocalic information (only 9–19 ms of voiced onset transitions and 18–30 ms of offset transitions remained). Identification of these silent-center syllables was much better than when either onset portions alone or offset portions alone were presented, confirming that neither portion by itself contained adequate information for accurate vowel identification. As has been reported for English vowels, performance on silent-center syllables was not significantly worse (and was numerically slightly better) than performance on vowel-center stimuli. In addition, when errors

were made, the error responses differed in these two conditions, suggesting that syllable onsets and offsets together provided *different* information than did the vocalic nuclei (see also Fox, 1989).

In the second perceptual study, the relative contribution of intrinsic duration information was addressed. As expected, perceptual errors increased for stimuli in which all syllable duration differences were removed. However, vowels in the Fixed SC syllable condition were more accurately identified than vowels in the Fixed VC condition. That is, dynamic spectral information alone was better than static target information alone in specifying vowel identity. Nevertheless, errors were three times greater on Fixed SC syllables than on SC syllables with duration information intact. Errors on both lax and tense vowels increased in the absence of duration information, but the pattern of confusions was similar in both SC conditions. Low and mid tense vowels were misidentified as spectrally similar lax vowels; front unrounded and rounded high lax vowels were misidentified as mid unrounded and rounded vowels, respectively. For the rounded vowels, this may have been due to the fact that the coarticulated high lax vowels were acoustically more similar to ''canonical'' mid vowel targets. The finding that mid and low tense vowels were most affected by removal of duration information corroborates earlier studies of German vowels (Weiss, 1976; Sendlmeier, 1981) which reported that duration manipulations affected the perceived identity of low vowels the most and high vowels the least.

Identification of vowels in Tense/Lax Fixed SC syllables, in which only the duration differences between tense–lax vowel pairs were equated, was significantly better than in Fixed SC syllables. We can conclude that duration information was used by listeners in identifying vowel height in the former condition. Errors were reduced, relative to the fixed-duration condition, especially for /ɑ, o, ø/. This was probably due to the fact that the durations of syllables containing these tense vowels were closer to the original durations (see Table III). It appears that mid and low tense German vowels must be ''long'' (relative to other vowels in the same overall context) to be accurately identified.

The effect of removing syllable duration information on the pattern of errors in identifying German vowels in silent-center syllables differs somewhat from that found for AE vowels. For the latter, shortening syllables containing long vowels did not increase identification errors, while lengthening syllables containing short vowels produced a significant increase in errors (Strange, 1989b). The differences between the pattern of errors for German and English vowels in these SC syllable conditions may be due, in part, to the fact that many of the tense (long) vowels of English are produced with considerable diphthongization. Thus even when SC syllables containing these vowels are shortened, formant movement information remains available (Andruski and Nearey, 1992). In contrast, German tense vowels are produced without diphthongization; thus duration information may be relatively more important for maintaining the identity of nonhigh tense vowels. However, this does not explain the cross-language difference in the role of duration in differentiating German /ɑ–a/ versus English /ɑ–ʌ/, since both the English vowels are monophthongal (Andruski and Nearey, 1992). Again, previous research on German vowels and the acoustic analyses suggest that static spectral differences between /a/ and /ɑ/ are small in North German, whereas English /ɑ/ and /ʌ/ may be spectrally more distant.

In summary, then, the perceptual differentiation of coarticulated North German vowels is dependent on both temporal information (intrinsic vowel duration) and on dynamic spectral information specified over the onsets and offsets of the CVC syllable. Spectrally similar tense–lax pairs are distinguished by both kinds of information. Intrinsic duration information is especially important for the differentiation of low vowels. In addition, relative duration differences (as well as target formant frequencies) are used by North German perceivers in distinguishing vowel height.

The finding that static targets are not sufficient to differentiate German or English vowels is compatible with both Nearey's Compound Target model and Strange's Dynamic Specification model of vowel perception. However, the German data cast some doubt on Andruski and Nearey's explanation for *why* SC syllables containing American and Canadian English vowel are perceived well. According to their account, silent-center syllables preserve differential diphthongization patterns associated with spectrally adjacent tense and lax vowels of these dialects of English. By their account, the direction and extent of movement of the first and second formants are ''computed'' by a comparison of the formant values at the end of the initial portion (target value) and those at the beginning of the final portion (offglide value), and serve to differentiate vowels with similar $F1/F2$ targets. Thus the relationship between only two points of the formant trajectories (target and offglide) are considered relevant.

In tests of this account (Andruski and Nearey, 1992; Nearey and Assmann, 1986; Nearey, 1995), Nearey and his colleagues have employed either carefully articulated isolated vowels or vowels produced in citation-form bVb syllables. Thus formant movement from the end of the initial portion to the beginning of the final portion of silent-center syllables was probably a function of the diphthongal pattern of the vowel in their stimuli. However, in CVC syllables spoken more rapidly in a carrier sentence, such as the ones used in the present study and in previous studies of AE vowels by Strange and colleagues (Strange, 1989b; Strange and Jenkins, 1988; Jenkins *et al.*, 1994), there is more temporal overlap of consonantal and vowel gestures (and more tongue coarticulation with alveolar and velar consonants). As a result, changes in formant frequencies across the silent portions of the SC syllables can be present because the ''cut points'' occur during the initial and final transitions (i.e., the opening and closing gestures). Differences in formant frequencies across the silent portion of the SC syllables therefore do not necessarily reflect diphthongization *per se*, but rather may be due to differences in rates of transitions of onsets and offsets (cf. Jenkins *et al.*, 1994). In the present study, the extensive acoustic comparisons of the stimuli used in the perceptual studies with the same speaker's vowels produced in citation-form /hVt/ syllables allowed us to determine if formant movement from the end of the initial portion

to the beginning of the final of the SC syllables (when it occurred) was due to diphthongization of vowel nuclei or to onset/offset temporal patterns. We concluded that movement across the portion of the syllables silenced in the SC conditions was not due to diphthongization of the vowels.

Recent data from acoustical and perceptual studies of American English vowels argue against a Target+Offglide account of the dynamic information available in silent-center syllables. In a replication and extension of the work of Verbrugge and Rakerd (1986) and Andruski and Nearey (1992), Jenkins and colleagues (Jenkins *et al.,* 1994) showed that vowels in ''hybrid'' dVd SC syllables (recombined from the utterances of a man and woman) were identified no less accurately than control SC syllable stimuli, despite the fact that the direction and extent of formant movement across initial and final portions was drastically different for hybrid and control stimuli (see Figs. 2 and 3 of Jenkins *et al.,* 1994). (Although Andruski and Nearey did not provide similar acoustical comparisons of their stimuli, we can assume that VISC information was similarly disrupted in their hybrid syllables.) The lack of an increase in identification errors for hybrid syllables (and the similar pattern of errors, when they occurred, for both control and hybrid syllables) argues against the claim that VISC information *alone* accounts for the perception of SC syllables. In addition, the finding that initial and final portions of CVC syllables in which the consonants differed could be cross spliced with no increase in identification errors on SC syllables also argues against the sufficiency of target+offglide information, since again, the direction and extent of formant movement differs from the original syllables (see Strange, 1987).

The pattern of results demonstrated here for North German vowels is compatible with the Dynamic Specification account which claims that temporal trajectories may provide important dynamic information for the perception of both German and English vowels. Further studies are needed to establish the generality of these perceptual results with German vowels. To the extent that the phenomena remain robust over different contexts and speakers, as they do for English vowels, they provide support for the generality of the Dynamic Specification account of perception of coarticulated vowels. For languages with large vowel inventories, we speculate that differences in the ''style of movement'' associated with vowel gestures serve to maintain the distinctiveness of phonetic categories in the face of the ambiguity of ''target'' information for vowels as they are produced in continuous speech. The exact nature of those differences in style of movement and the acoustic parameters which specify those differences perceptually must be explored in future studies using a variety of languages.

ACKNOWLEDGMENTS

This research was supported by a grant to the first author from National Institute for Deafness and Other Communication Disorders (NIDCD-DC00323) ''Vowel Perception.'' The manuscript was completed when the first author was a Visiting Researcher at ATR Human Information Processing Research Laboratories. The authors with to thank James J. Jenkins for helpful comments on earlier drafts of the manuscript, Anders Lofquist and two anonymous reviewers for comments on later version of the manuscripts, Desiderio Saludes and Xiange Ling for their assistance in generating stimulus materials, Patrick Jung for assistance in testing German subjects, Sonja Trent for assistance in data reduction and analysis, and John Pruitt for assistance in statistical analysis. Portions of this research were reported at the November, 1991 meeting of the Acoustical Society of America [J. Acoust. Soc. Am. **90**, 2253 (A) (1991)]. Requests for reprints should be addressed to the first author.

[1]Although /ɛ:/ was not included in the stimulus set because it is a ''hypercorrect'' vowel for North Germans, we included it as a response alternative because Sendlmeier (1981) reported that speakers who do not themselves use this vowel may nevertheless have it as a perceptual category.

[2]Although DFT spectra were computed over larger segments of the syllable than were LPC spectra, most missing formant data occurred in the center portions of syllables containing long, back vowels where formants were moving most slowly. Comparison of LPC and DFT formant values using these parameters were closely matched for vowels which did not show merged formants.

[3]Hillenbrand *et al.* (1995) measured at 20% and 80% points in /hVd/ syllables; Andruski and Nearey (1992) measured at a fixed duration (40 ms) from onset and offset of /bVb/ syllables. As described in the Methods Sections, the 25%–75% points were selected to minimize the influence of consonants while maximizing the proportion of the syllable nucleus over which formant movement might be detected.

Andruski, J. E., and Nearey, T. M. (**1992**). ''On the sufficiency of compound target specification of isolated vowels and vowels in /bVb/ syllables,'' J. Acoust. Soc. Am. **91**, 390–410.

Barry, W. J. (**1974a**). ''*Perzeption und Produktion im sub-phonemischen Bereich: Eine kontrastive Untersuchung an intersprachlichen Minimalpaaren des Deutschen und Englischen* (Niemeyer, Tübingen).

Barry, W. J. (**1974b**). ''Language background and the perception of foreign faccent,'' J. of Phonetics **2**, 65–89.

Bethge, W. (**1963**). ''Beziehungen der Generation zur Quantität in den deutschen Mundarten,'' Phonetica **9**, 200–208.

Bohn, O.-S., and Flege, J. E. (**1990**). ''Interlingual identification and the role of foreign language experience in L2 vowel perception,'' Applied Psycholinguistics **11**, 303–328.

Bohn, O.-S., and Flege, J. E. (**1992**). ''The production of new and similar vowels by adult German learners of English,'' Studies in Second Language Acquisition **14**, 131–158.

Browman, C., and Goldstein, L. (**1991**). ''Gestural structures: Distinctiveness, phonological processes and historical change,'' in *Modularity and the Motor Theory of Speech Perception*, edited by I. G. Mattingly and M. Studdert-Kennedy (Erlbaum, Hillsdale, NJ).

Crystal, T. H., and House, A. S. (**1988**). ''The duration of American-English vowels: An overview,'' J. of Phonetics **16**, 263–284.

DiBenedetto, M-G. (**1989**). ''Frequency and time variations of the first formant: Properties relevant to the perception of vowel height,'' J. Acoust. Soc. Am. **86**, 67–77.

Dinnsen, D., and Garcia-Zamor, M. (**1971**). ''The three degrees of vowel length in German,'' Papers in Linguistics **4**, 111–126.

Fliflet, A. L. (**1962**). ''Gespannte und ungespannte Vokale,'' Studia Linguistica **16**, 24–28.

Fowler, C. A. (**1980**). ''Coarticulation and theories of extrinsic timing,'' J. of Phonetics **8**, 113–133.

Fox, R. A. (**1989**). ''Dynamic information in the identification and discrimination of vowels,'' Phonetica **46**, 97–116.

Heike, G. (**1970**). ''Lautdauer als Merkmal der wahrgenommenen Quantität, Qualität und Betonung im Deutschen,'' in *Proceedings VIth ICPhS Prague*, 1967, edited by B. Hala, M. Romportl, and P. Janota (Academia, Prague), pp. 433–437.

Heike, G. (**1972**). ''Quantitative und qualitative Differenzen von Realisationen im Deutschen,'' in *Proceedings VII ICPhS, Montreal*, edited by A. Rigault and R. Charbonneau (Mouton, The Hague), pp. 725–729.

Hillenbrand, J., Getty, L. A., Clark, M. J., and Wheeler, K. (**1995**). ''Acoustic characteristics of American English vowels,'' J. Acoust. Soc. Am. **97**, 3099–3111.

Huang, C. (**1985**). ''Perceptual correlates of the tense/lax distinction in general American English,'' Masters thesis, MIT, Cambridge, MA.
Huang, C. (**1986**). ''The effect of formant frequency trajectory and spectral shape on the tense/lax distinction in American vowels,'' Proceedings of ICASSP 86, the IEEE–IECEJ–ASJ International Conference on Acoustics, Speech and Signal Processing, Tokyo, Japan, 8–11 April 1986, pp. 893–896.
Huang, C. (**1991**). ''An acoustic and perceptual study of vowel formant trajectories in American English,'' Report 563, Research Laboratory of Electronics, MIT, Cambridge, MA.
Iivonen, A. K. (**1983**). ''Zur Frage der regionalen Variation der hochdeutschen Vokale,'' Neuphilologische Mitteilungen **84**, 45–52.
Iivonen, A. K. (**1987**). ''Monophthonge des gehobenen Wienderdeutsch,'' Folia Linguistica **21**, 293–336.
Iivonen, A. K. (**1989a**). ''Regional differences in the realization of Standard German vowels,'' Mimeographed Series of the Institute of Phonetics, University of Helsinki **15**, 4–20.
Iivonen, A. K. (**1989b**). ''Regionally determined realization of the Standard German vowel system,'' Mimeographed Series of the Institute of Phonetics, University of Helsinki **15**, 21–28.
Jenkins, J. J., and Strange, W. (**in press**). ''Perception of dynamic information for vowels in syllable onsets and offsets,'' Percept. Psychophys.
Jenkins, J. J., Strange, W., and Miranda, S. (**1994**). ''Vowel identification in mixed-speaker silent-center syllables,'' J. Acoust. Soc. Am. **95**, 1030–1043.
Jenkins, J. J., Strange, W., and Edman, T. (**1983**). ''Identification of vowels in ''vowelless'' syllables,'' Percept. Psychophys. **34**, 441–450.
Jessen, M. (**1993**). ''Stress conditions on vowel quality and quantity in German,'' Working Papers of the Cornell Phonetics Laboratory **8**, 1–27.
Klecka, W. R. (**1980**). *Discriminant Analysis* (Sage, Newbury Park).
Kohler, K. J. (**1977**). *Einführung in die Phonetik des Deutschen* (Schmidt, Berlin).
Lehiste, I., and Peterson, G. E. (**1961**). ''Transitions, glides, and diphthongs,'' J. Acoust. Soc. Am. **33**, 268–277.
Lindner, G. (**1976**). ''Urteilsveränderung bei Vokalkürzung,'' Zeitschrift fur Phonetik, Sprachwissenschaft und Kommunikationsforschung **29**, 407–414.
Meyer, E. S. (**1904**). ''Zur Vokaldauer im Deutschen,'' in *Nordiska Studier tillegnade Adolf Noreen* (K. W. Appelberg, Uppsala), pp. 347–356.
Miller, J. D. (**1991**). ''Auditory-perceptual interpretation of vowels and diphthongs: A progress report,'' J. Acoust. Soc. Am. **89**, 1997(A).
Moulton, W. G. (**1962**). *The Sounds of English and German* (University of Chicago Press, Chicago).
Nearey, T. (**1989**). ''Static, dynamic, and relational factors in vowel perception,'' J. Acoust. Soc. Am. **85**, 2088–2113.
Nearey, T. (**1995**). ''Evidence for the perceptual relevance of vowel-inherent spectral change for front vowels in Canadian English,'' in *Proceedings XIIIth International Congress Phonetics Science*, edited by K. P. Branderud **2**, 678–681.
Nearey, T., and Assmann, P. (**1986**). ''Modeling the role of inherent spectral change in vowel identification,'' J. Acoust. Soc. Am. **80**, 1297–1308.
Parker, E. M., and Diehl, R. L. (**1984**). ''Identifying vowels in CVC syllables: Effects of inserting silence and noise,'' Percept. Psychophys. **36**, 369–380.
Peterson, G. E., and Lehiste, I. (**1960**). ''Duration of syllable nuclei in English,'' J. Acoust. Soc. Am. **32**, 693–703.
Ramers, K. H. (**1988**). *Vakalquantität und-qualität im Deutschen* (Niemeyer, Tübingen).
Rietveld, A. C. M. (**1975**). ''Untersuchung zur Vokaldauer im Deutschen,'' Phonetica **31**, 248–258.
Scherer, G., and Wollmann, A. (**1972**). *Englische Phonetik und Phonologie* (Schmidt, Berlin).
Sendlmeier, W. F. (**1981**). ''Der Einfluss von Qualität und Quantität auf die Perzeption betonter Vokale des Deutschen,'' Phonetica **38**, 291–308.
Siebs, T. (**1969**). *Deutsche Aussprache* (de Gruyter, Berlin), 19th ed.
Stat Soft, Inc. (**1991**). Statistica 3.1.
Strange, W. (**1987**). ''Information for vowels in formant transitions,'' J. Mem. Lang. **26**, 550–557.
Strange, W. (**1989a**). ''Evolving theories of vowel perception,'' J. Acoust. Soc. Am. **85**, 2081–2087.
Strange, W. (**1989b**). ''Dynamic specification of coarticulated vowels spoken in sentence context,'' J. Acoust. Soc. Am. **85**, 2135–2153.
Strange, W., and Jenkins, J. J. (**1988**). ''Context-independent dynamic information for vowel identification,'' J. Acoust. Soc. Am. Suppl. 1 **84**, S159.
Strange, W., Jenkins, J. J., and Johnson, T. L. (**1983**). ''Dynamic specification of coarticulated vowels,'' J. Acoust. Soc. Am. **74**, 695–705.
Verbrugge, R., and Rakerd, B. (**1986**). ''Evidence of talker-independent information for vowels,'' Lang. Speech **29**, 39–57.
Wängler, H-H., and Weiss, R. (**1975**). ''Experimental approach to the study of vowel perception in German,'' Phonetica **32**, 180–199.
Weiss, R. (**1972**). ''Perceptual parameters of vowel duration and quality in German'' in *Proceedings VIIth ICPhS, Montreal*, edited by A. Rigault and R. Charbonneau (Mouton, The Hague), pp. 633–636.
Weiss, R. (**1974**). ''Relationship of vowel length and quality in the perception of German vowels,'' Linguistics **123**, 59–70.
Weiss, R. (**1976**). *The Perception of Vowel Length and Quality in German. An Experimental Phonetic Investigation* (Buske, Hamburg).

Importance of tonal envelope cues in Chinese speech recognition

Qian-Jie Fu[a)]
Department of Auditory Implants and Perception, House Ear Institute, 2100 West Third Street, Los Angeles, California 90057 and Department of Biomedical Engineering, University of Southern California, Los Angeles, California 90089

Fan-Gang Zeng
Department of Auditory Implants and Perception, House Ear Institute, 2100 West Third Street, Los Angeles, California 90057 and Department of Electrical Engineering, University of Southern California, Los Angeles, California 90089

Robert V. Shannon
Department of Auditory Implants and Perception, House Ear Institute, 2100 West Third Street, Los Angeles, California 90057 and Department of Biomedical Engineering, University of Southern California, Los Angeles, California 90089

Sigfrid D. Soli
House Ear Institute, 2100 West Third Street, Los Angeles, California 90057

(Received 8 May 1997; revised 21 January 1998; accepted 31 March 1998)

Recent studies have shown that temporal waveform envelope cues can provide significant information for English speech recognition. This study investigated the use of temporal envelope cues in a tonal language: Mandarin Chinese. In this study, the speech was divided into several frequency analysis bands; the amplitude envelope was extracted from each band by half-wave rectification and low-pass filtering and was used to modulate a noise of the same bandwidth as the analysis band. These manipulations preserved temporal and amplitude cues in each frequency band, but removed the spectral detail within each band. Chinese vowels, consonants, tones and sentences were identified by 12 native Chinese-speaking listeners with 1, 2, 3, and 4 noise bands. The results showed that the recognition score of vowels, consonants, and sentences increased monotonically with the number of bands, a pattern similar to that observed in English speech recognition. In contrast, tones were consistently recognized at about 80% correct level, independent of the number of bands. This high level of tone recognition produced a significant difference in the open-set sentence recognition between Chinese (11.0%) and English (2.9%) for the one-band condition where no spectral information was available. The data also revealed that, with primarily temporal cues, the falling–rising tone (tone 3) and the falling tone (tone 4) were more easily recognized than the flat tone (tone 1) and the rising tone (tone 2). This differential pattern in tone recognition resulted in a similar pattern in word recognition: words having either tone 3 or 4 were more likely to be recognized while words having tone 1 and 2 were not. The quantitative role of tones in Chinese speech recognition was further explored using a power-function model and found to play a significant role in relating phoneme recognition to sentence recognition. [S0001-4966(98)02607-1]

PACS numbers: 43.71.Es, 43.71.Hw [WS]

INTRODUCTION

Traditionally, spectral information in speech sounds has been regarded as the most important cue for speech recognition, while the temporal waveform envelope of the speech sounds has been considered largely a redundant cue. The view that the temporal envelope plays an insignificant role in speech recognition may originate in Licklider's classic experiment, in which speech sounds were infinitely clipped in amplitude, resulting in a flat temporal envelope, but still maintained a high degree of intelligibility (Licklider and Pollack, 1948). However, the importance of temporal information has not always been neglected; for example, Fletcher (1995) attributed high intelligibility of whispered speech sounds, at least partially, to their ''manner of starting and stopping.'' More recent studies have found that, in the absence of spectral cues, temporal envelope cues alone can produce significant consonant recognition (Rosen, 1992; Van Tasell *et al.*, 1987). Shannon *et al.* (1995) systematically studied the trade-off between the spectral and temporal envelope cues. In their study, temporal envelopes of speech sounds were extracted from one to four broad frequency bands, and used to modulate noises of the same bandwidths. This manipulation preserved temporal envelope cues in each band but restricted the listener to severely degraded spectral information. Shannon *et al.* found that identification of consonants, vowels, and sentences improved monotonically as the number of bands was increased, and near perfect speech recognition was achieved with only four bands of modulated noise.

[a)]Electronic mail: qfu@hei.org

 0001-4966/98/104(1)/505/6/$15.00

The present study extends the Shannon *et al.* study to a tonal language, i.e., Mandarin Chinese speech. Tones are important in Chinese speech recognition because the tonality of a monosyllable is lexically meaningful (e.g., Liang, 1963; Wang, 1989; Lin, 1988). There are four tonal patterns in Mandarin Chinese, which are characterized by their fundamental frequency ($F0$) contours. Tone 1 has a flat $F0$ pattern, tone 2 has a rising $F0$ pattern, tone 3 has a falling–rising $F0$ pattern, and tone 4 has a falling $F0$ pattern. For example, the same syllable /ma/ can mean ''mother,'' ''linen,'' ''horse,'' or ''scold'' for the tone pattern 1, 2, 3, or 4, respectively.

Although the $F0$ pattern is the dominant cue for tone recognition, other acoustic cues can contribute to tone recognition. For example, Liang (1963) found that 94.6% correct tone recognition can be achieved with the speech high-pass filtered at 300 Hz. He argued that this high level of tone recognition in the high-pass filtered speech is due to the residue pitch, extracted from the harmonic information and termed as the ''phenomenon of the missing fundamental'' (Schouten *et al.*, 1962). Liang also found that 64.0% tone recognition can be achieved in whispered speech in which neither fundamental frequency nor the harmonic fine structure was present. The whispered speech results indicated that the temporal envelope could also encode information for tone recognition. However, other studies found that tonal contrasts were not well preserved in whispered speech (Abramson, 1972; Howie, 1976). Whalen and Xu (1992) used signal-correlated-noise stimuli (Schroeder, 1968) to further study the contribution of both amplitude contour and duration to tone recognition. To produce signal-correlated-noise stimuli, a speech signal is digitized and the sign of approximately half of the samples, chosen at random, is flipped, resulting in a new stimulus that has a flat spectrum but exactly the same temporal envelope as the original speech signal. The original $F0$ pattern, spectral fine structure, and the spectral envelope are completely absent in the signal-correlated-noise stimulus. Under these conditions, Whalen and Xu found that about 70% recognition level of tones can be achieved. These results clearly demonstrated that the $F0$ pattern is not the only cue in tone recognition; other acoustic cues, including amplitude contour and duration, can also play a significant role.

The major goal of this study was to investigate the use of temporal envelope cues in a tonal language, specifically in Mandarin Chinese at word and sentence levels. The same approach as in the Shannon *et al.* study was used to manipulate the relative distribution of temporal and spectral information. In the present study, the amount of spectral information in speech was increased systematically by changing the number of bands from one, two, and three to four. The amount of temporal envelope information in speech was manipulated by changing the cutoff frequency of envelope extraction filters. Rosen (1992) defined three main temporal features: envelope (2–50 Hz), periodicity (50–500 Hz), and fine-structure (500–10 000 Hz). Two low-pass filters with cutoff frequencies of 50 and 500 Hz were used for envelope extraction to evaluate the relative contribution of both temporal envelope and periodicity information to speech recognition. Recognition of Chinese vowels, consonants, and sentences was measured in 12 native Chinese-speaking listeners as a function of the number of noise bands. In addition, recognition of four tones in standard Chinese was measured and correlated to recognition of Chinese sentence recognition.

I. METHODS

A. Subjects

Twelve native Chinese-speaking listeners, including seven men and five women, ranging in age from 25 to 35 years old, participated in this study. All listeners were recruited from the University of Southern California and were paid for their services. All listeners had pure-tone thresholds better than 15 dB HL at octave frequencies from 250 to 4000 Hz in both ears.

B. Stimuli

The tape-recorded test data were derived from the ''Chinese minimal auditory capability test'' developed by Beijing Union Hospital in P. R. China (Zhang *et al.*, 1988). The test stimuli were spoken by an adult male speaker. The test materials included 21 initial consonants, 35 final vowels, 4 tones, and 200 daily-life sentences. The letter and its associate IPA for all 21 initial consonants and 35 final vowels used in the present study are listed in Appendix A. All materials were divided into four test groups with each containing vowel, consonant, tone, and sentence recognition. Similar to the study of Shannon *et al.* (1995), the tape-played sound was digitized at a 10-kHz sampling rate and passed through a pre-emphasis filter to whiten the spectrum (low pass below 1200 Hz, -6 dB/octave). Then the signal was split into several analysis frequency bands (24 dB/octave, elliptical bandpass filter) and the amplitude envelope from each band was extracted by half-wave rectification and low-pass filtering (elliptical IIR filters with cutoff frequencies of 50 and 500 Hz, -6 dB/octave). The speech envelope was used to amplitude modulate a wide-band white noise, which was then spectrally limited by the same bandpass filter as in the original analysis band. These manipulations preserved band-specific temporal envelope cues, but removed totally the spectral details within each band. The resulting modulated noises from each band were summed, amplified (CROWN D75), and then presented to the listeners through TDH-49 headphones. The overall levels were calibrated for each combination of parameters to produce an average A-weighted output level of 75 dB for continuous speech. All these manipulations were implemented on a real-time signal processing system. In the present study, the one, two, three, or four analysis bands, each combined with the 50- or 500-Hz envelope filters, produced a total of eight conditions. The total bandwidth was from 100 to 4000 Hz. The corner frequencies for the one-band processor were 100 and 4000 Hz. The corner frequencies for the two-band processor were 100, 1500, and 4000 Hz. The corner frequencies for the three-band processor were 100, 800, 1500, and 4000 Hz. The corner frequencies of the four-band processor were 100, 800, 1500, 2500, and 4000 Hz.

C. Procedures

For the consonant, vowel, and tone tests, a four-alternative, forced-choice procedure was used in which both the pinyin[1] and its corresponding Chinese character were shown on the choice list. One test session consisted of 4 blocks, each of which had 10 trials for consonant, vowel, tone recognition, and 20 trials for sentence recognition. A sample block is shown in Appendix B. The stimulus in consonant, vowel and tone tests was a single syllable, consisting of an initial consonant and a following vowel with a tone. In each trial of the consonant test, four-alternative syllables, which had the same following vowel and tone, were included in the choice list. The listener was asked to identify the consonant by marking the syllable containing the consonant that was presented. Because not all combinations of the initial consonant and the following vowel were lexically meaningful, the vowel and tone varied from trial to trial to accommodate the meaning of Chinese words. The same was true for consonants and tones in the vowel recognition test, and for consonants and vowels in the tone recognition test. In the daily-life ''open-set'' sentence recognition test, the listener was asked to write down as many words as were recognized in each sentence. Each test block included 20 sentences, and each sentence had 2–8 key words, resulting in a total of 100 key words. Sentences were presented without repetition. The recognition score was calculated based on the percentage of the total number of key words correctly recognized. All subjects received extensive training, including familiarization with the testing environment and the speech quality of all eight experimental conditions via 15-min casual conversation with experimenter through the real-time processing system, and informal tests of sample materials. The sample materials were not included in the formal tests. The sequence of these eight experimental conditions were randomized and counterbalanced across subjects. No feedback was provided regarding the correct answer in any test.

II. RESULTS AND DISCUSSION

Figure 1 shows the averaged recognition results from 12 subjects as a function of the number of noise bands. Results from four different tasks, including consonant, vowel, tone, and sentence recognition, are presented in panel A, B, C, and D, respectively. The two temporal envelope filter cutoff frequencies, 50 and 500 Hz, are represented by the short dashed line and the solid line, respectively. As a comparison, panels A, B, and D also show our previous results of English vowel, consonant, and sentence recognition obtained with the envelope filter frequency at 500 Hz (the long dashed line, Shannon *et al.*, 1995). Figure 1A shows that, as the number of bands was increased from one to four, the recognition score of Chinese consonants increased monotonically from 50.1% to 84.7% for the 500-Hz envelope filtering condition and increased from 45.0% to 79.8% for the 50-Hz filtering condition. A two-way, repeated-measures analysis of variance (ANOVA) was performed, with the number of bands and the low-pass envelope filters as within-subjects factors. This analysis showed a significant effect of the number of bands

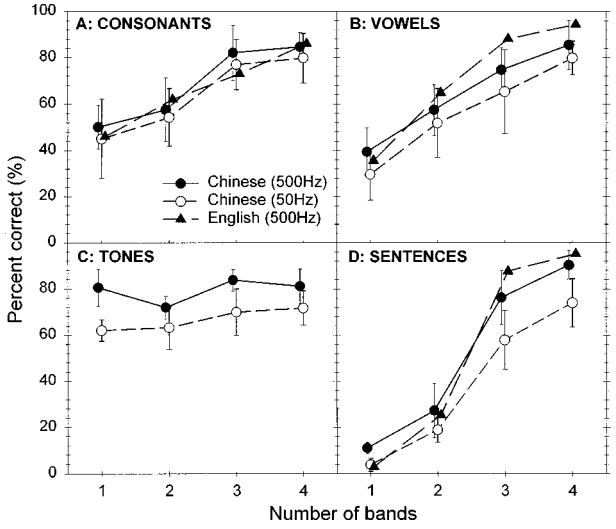

FIG. 1. Speech recognition as a function of the number of noise bands. A: consonants; B: vowels; C: tones; D: sentences. The conditions included English with the envelope filter frequency at 500 Hz (▲), Chinese with the envelope filter frequency at 500 Hz (●) and at 50 Hz (○).

$[F(3,57)=19.45, p<0.001]$ but no significant difference between the 500- and 50-Hz condition $[F(1,57)=1.34, p>0.05]$.

Figure 1B shows Chinese vowel recognition as a function of the number of bands. The recognition score of Chinese vowels increased monotonically from 39.4% in the one-band condition to 85.6% in the four-band condition for the 500-Hz condition and increased from 29.6% to 79.9% for the 50-Hz condition. A similar two-way ANOVA showed a significant effect of the number of bands $[F(3,57)=35.09, p<0.001]$ but no significant effect of the envelope filters $[F(1,57)=3.84, p>0.05]$.

Figure 1C shows Chinese tone recognition as a function of the number of bands. In contrast to the Chinese consonant and vowel results, the two-way ANOVA showed no significant effect of the number of bands $[F(3,57)=2.15, p>0.05]$ but a significant effect of the envelope filters $[F(1,57)=26.54, p<0.001]$. The percent correct score of tone recognition averaged across four band conditions was 80.8% in the 500-Hz filtering condition and 66.9% in the 50-Hz filtering condition.

Figure 1D shows Chinese sentence recognition as a function of the number of bands. Similar to consonant and vowel recognition patterns, the recognition score of Chinese sentences increased monotonically from 11.0% in the one-band condition to 90.4% in the four-band condition for the 500-Hz condition and increased from 3.8% to 74.0% accordingly for the 50-Hz condition. The two-way ANOVA showed both significant effects of the number of bands $[F(3,55)=17.08, p<0.001]$ and the envelope filters $[F(1,55)=138.49, p<0.001]$.

The present results showed several interesting similarities as well as differences between Chinese and English speech recognition with primarily temporal cues. First, both Chinese and English consonant, vowel, and sentence recognition improved monotonically as a function of the number of bands. No significant effect was observed between the

50-Hz and 500-Hz cutoff frequencies of the envelope filter in Chinese consonant and vowel recognition, similar to English consonant and vowel recognition (Shannon *et al.*, 1995). Second, different from consonant, vowel, and sentence results, tones were consistently recognized at an 80.8% correct level in the 500-Hz filtering condition and 66.9% correct level in the 50-Hz filtering condition, independent of the number of bands. Third, a significant effect of the envelope filters was observed in Chinese sentence recognition but not in English sentence recognition. In particular, for the one-band, 500-Hz filtering condition, where no spectral information was available, Chinese produced a significantly higher score in sentence recognition (11.0%) than English (2.9%) [$t(17)=4.71$, $p<0.001$].

The similar effect of the envelope filter cutoff frequency on Chinese tone and sentence recognition suggested a possibly important role for tonal envelope cues in Chinese speech recognition. Two approaches were used to address the possible relationship between Chinese tone and sentence recognition. First, a qualitative relationship between tone recognition and sentence recognition was investigated based on the results from the 500-Hz condition. Results showed that different tones had different recognition scores. As shown in the solid line of Fig. 2(A), the recognition scores of the falling-rising tone (tone 3) and the falling tone (tone 4) were almost twice as high as those of the flat tone (tone 1) and the rising tone (tone 2) in the one-band condition. This result was consistent with an earlier finding (Whalen and Xu, 1992) and might be explained by the differences in the amplitude contour (Fu *et al.*, 1995). Our acoustic analysis showed that the amplitude envelope was highly correlated with $F0$ contour for the falling–rising tone and falling tone, and this correlation was likely responsible for the high recognition score of these two tones. However, tone 1 and tone 2 did not seem to have amplitude envelopes that were highly correlated to their respective $F0$ contours. If tone recognition had played an important role in sentence recognition, then words with tone 3 and tone 4 would be more easily recognized than words with tone 1 and tone 2. The dashed line in Fig. 2(A) shows the distribution patterns of tones (right y axis) for correctly recognized words in sentence recognition for the one-band condition. Indeed, most of the words that were correctly recognized in sentence recognition had either tone 3 or tone 4. Figure 2(B) shows the recognition score of the individual tones and the distribution tonal patterns of the correctly recognized words in sentence recognition for the four-band condition. Although the difference was smaller between tones for the four-band condition than the one-band condition, the recognition scores of tone 3 and tone 4 were still significantly higher than those of tone 1 and tone 2, resulting in a similar tonal distribution pattern of the correctly recognized words. These results indicated that tone played a greater role in sentence recognition when no spectral information was available, and became less important when more spectral information was available.

A quantitative relationship among Chinese vowel, consonant, tone, and sentence recognition scores was also assessed using a power-function model (Boothroyd and Nittrouer, 1988; Rabinowitz *et al.*, 1992). The power-function

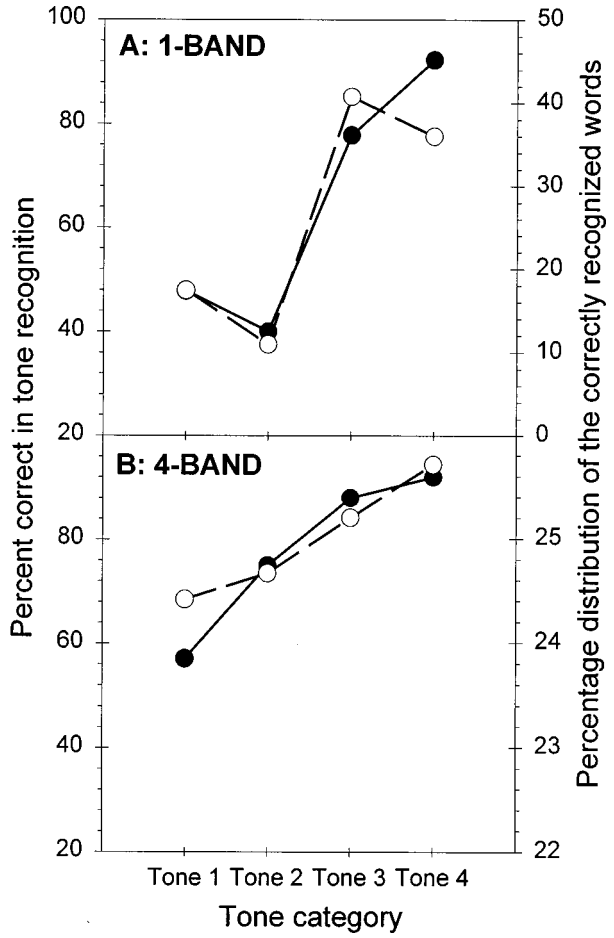

FIG. 2. (A) Percent correct of tone recognition in the one-band condition (●). The tonal distribution pattern of the correctly recognized words in sentence recognition for the one-band condition (○). (B) Percent correct of tone recognition in the four-band condition (●). The tonal distribution pattern of the correctly recognized words in sentence recognition for the four-band condition (○).

model, based on the original work by Fletcher (1995), could account for the benefit of sentence context (factor k) and the relation between word and phoneme recognition (factor j). First, the sentence context factor is represented in the following equation:

$$p_s = 1-(1-p_w)^k, \tag{1}$$

where p_s is the recognition probability for words in sentences, p_w is the recognition probability for isolated words, and the exponent k is the sentence context factor.

Second, the recognition probability for an isolated CVC word is represented as follows:

$$p_w = p_p^j, \tag{2}$$

where p_p is the recognition probability for the individual phonemes and p_w is the recognition probability for the isolated words, j has a value between 2 and 3, reflecting the fact that, due to language constraints, only 2–3 phonemes must be recognized for correct recognition of isolated CVC words.

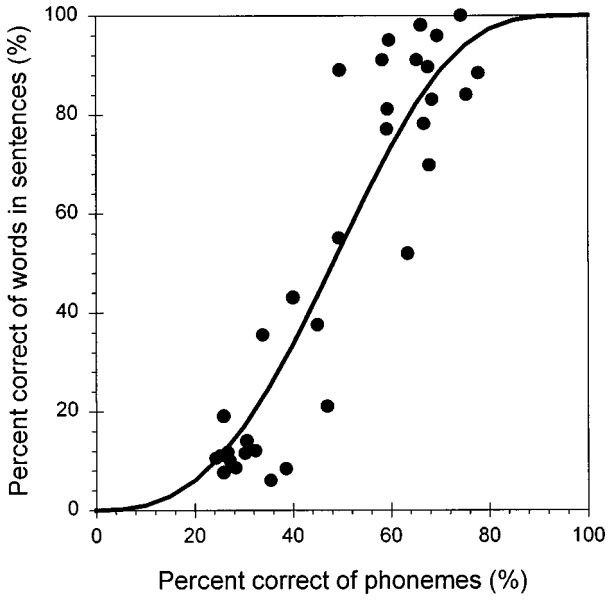

FIG. 3. The relationship between sentence and phoneme recognition based on a power-function model. Symbols showed experimental data and the solid line represented the predicted relationship between the recognition probability of phonemes and sentences.

Finally, we combine Eqs. (1) and (2) to obtain the relation between the recognition probability for words in sentences and phonemes:

$$p_s = 1 - (1 - p_p^j)^k. \tag{3}$$

Because no comparable results were available in Chinese materials, the present study used the same $k(4.5)$ and $j(2.67)$ values as in English materials (Rabinowitz *et al.*, 1992). Different from the previous study, the recognition probability for phonemes was calculated by combing the recognition probability for vowels, consonants, and tones:

$$p_p = p_c^{w_c} p_v^{w_v} p_t^{w_t}, \tag{4}$$

where p_c, p_v, and p_t are the recognition probability of consonants, vowels, and tones, and w_c, w_v, and w_t are weighting parameters. Figure 3 shows the best fitting power-function (the solid line) in relating the recognition probability of phonemes to the recognition probability for words in sentences[2] ($r = 0.92$). The weights for consonants, vowels, and tones were 0.64 (s.e.$=0.13$), 0.71 (s.e.$=0.13$), and 0.79 (s.e.$=0.18$), respectively. A one-way ANOVA showed no significant difference between the weights [$F(2,96) = 0.26$, $p > 0.05$]. These results suggested an approximately equal contribution of consonants, vowels, and tones to Chinese sentence recognition under the present conditions.

III. CONCLUSIONS

High-level performance of Mandarin Chinese speech recognition was achieved with primarily temporal envelope cues, extending previous results obtained with English speech. Due to the tonal nature of Chinese speech, several significant differences were also observed between English and Chinese speech recognition. In contrast to the recognition of consonants, vowels, and sentences, which increased monotonically as a function of the number of bands, tones were recognized at an 80% correct level in the 500-Hz envelope filter condition, independent of the number of bands. This high level of tone recognition produced a significant difference in the open-set sentence recognition between Chinese (11.0%) and English (2.9%) for the one-band condition where no spectral information was available. The analysis of tone recognition and the tone distribution pattern for words in sentence recognition indicated a high correlation between tone recognition and sentence recognition. The present study also used a power-function model to reveal that, with temporal envelope cues, tones contribute to Chinese speech recognition with temporal envelope cues in a similar way to consonants and vowels.

ACKNOWLEDGMENTS

Portions of this paper were presented at the 129th Meeting of the Acoustical Society of America. We are grateful to all subjects for their participation in our experiments and to Alena Wilson for editing the manuscript. We also thank Dr. Winifred Strange, Dr. Adrian Fourcin, Dr. Xu Yi, and an anonymous reviewer for their helpful comments. Research was supported in part by NIH (DC-02267 and DC-01526).

APPENDIX A: A LIST OF CONSONANTS AND VOWELS

A Chinese single syllable consists of an initial consonant and a following vowel with a tone. There are 21 initial consonants and 35 final vowels used in the present study. The letter and its associated IPA symbol are shown as follows:

(1) 21 initial consonants
b[p], p[p^h], m[m], f[f], d[t], t[t^h], n[n], l[l], g[k], k[k^h], h[x], j[tɕ], q[$tɕ^h$], x[ɕ], zh[tʂ], ch[$tʂ^h$], sh[ʂ], r[ʐ], z[ts], c[ts^h], s[s]

(2) 35 final vowels
(a) 6 simple vowels
a[a], o[o], e[ɤ], i[i], u[u], ü[y]
(b) 13 complex vowels
ai[aɪ], ei[eɪ], ao[aʊ], ou[oʊ], ia[ia], ie[iɛ], iao[iɑʊ], iou[iəʊ], ua[ua], uo[uo], uai[uaɪ], uei[ueɪ], üe[yɛ]
(c) 16 compound nasal vowels
an[an], en[ən], ang[ɑŋ], eng[əŋ], ong[oŋ], ian[iɛn], in[in], iang[iɑŋ], ing[iŋ], ion[iʊŋ], uan[uan], uen[uən], uang[uɑŋ], ueng[ʊəŋ], üan[yɛn], ün[yn].

APPENDIX B: SAMPLE TEST MATERIALS

One test block of vowel recognition is shown.

Trial 1:	ba(3)	ben(3)	bi(3)	biao(3)
	把	本	笔	表
Trial 2:	du(2)	di(2)	de(2)	die(2)
	读	敌	得	迭
Trial 3:	gai(3)	gan(3)	guo(3)	guang(3)
	改	敢	果	广
Trial 4:	ji(1)	jiang(1)	jian(1)	jia(1)
	鸡	将	尖	家
Trial 5:	le(4)	liang(4)	li(4)	lue(4)
	乐	亮	利	略
Trial 6:	men(2)	mian(2)	mi(2)	mao(2)
	门	棉	迷	毛
Trial 7:	she(4)	shu(4)	shi(4)	shang(4)
	射	树	是	上
Trial 8:	hun(1)	hua(1)	he(1)	hei(1)
	昏	花	喝	黑
Trial 9:	ye(3)	yu(3)	yi(3)	yao(3)
	也	雨	以	咬
Trial 10:	rong(2)	ren(2)	ru(2)	ran(2)
	容	人	如	然

[1]Pinyin transcription is a phonemic spelling system for Mandarin. The pinyin of a single syllable consists of an initial consonant and a following vowel with a tone. In this paper, the four tones are represented by the tone mark ''1'' for the high tone, ''2'' for the rising tone, ''3'' for the falling–rising tone, and ''4'' for the falling tone.

[2]The relation between the phoneme recognition probability and the sentence recognition probability can also be predicted by a linear function (slope $=1.65$, $r=0.90$). However, the power function model is based on the combination of the two relations [factor j and k, Eq. (3)]. Each relation can not be well predicted by a linear function. Besides, if there were more data in the two extreme conditions, the relation would be more like a power function instead of a linear function.

Abramson, A. S. (**1972**). ''Tonal experiments with whispered Thai,'' in *Papers in Linguistics and Phonetics to the Memory of Pierre Delattre*, edited by A. Valdman (Mouton, The Hague), pp. 31–44.

Boothroyd, A., and Nittrouer, S. (**1988**). ''Mathematical treatment of context effect in phoneme and word recognition,'' J. Acoust. Soc. Am. **84**, 101–114.

Fletcher, H. B. (**1995**). ''The speaking mechanism,'' in *Speech and Hearing in Communication*, edited by J. B. Allen (Acoustical Society of America, Woodbury, NY), Chap. 2, p. 16.

Fu, Q.-J., Zeng, F.-G., Shannon, R. V., and Soli, S. (**1995**). ''Chinese Speech Recognition only Using Amplitude Envelope Cues,'' 1995 Conference on Implantable Auditory Prostheses, abstract booklet, 61.

Howie, J. M. (**1976**). *Acoustical Studies of Mandarin Vowels and Tones* (Cambridge U. P., Cambridge, England).

Liang, Z.-A. (**1963**). ''The auditory perception of Mandarin Tones,'' Acta Phys. Sin. **26**, 85–91.

Licklider, J. C. R., and Pollack, I. (**1948**). ''Effects of differentiation, integration, and infinite peak clipping on the intelligibility of speech,'' J. Acoust. Soc. Am. **20**, 42–51.

Lin, M.-C. (**1988**). ''The acoustic characteristics and perceptual cues of tones in Standard Chinese,'' Chinese Yuwen **204**, 182–193.

Rabinowitz, W. M., Eddington, D. K., Delhorne, L. A., and Cuneo, P. A. (**1992**). ''Relations among different measures of speech reception in subjects using a cochlear implant,'' J. Acoust. Soc. Am. **92**, 1869–1881.

Rosen, S. (**1992**). ''Temporal information in speech: acoustic, auditory and linguistics aspects,'' Philos. Trans. R. Soc. London, Ser. B **336**, 367–373.

Schouten, J. F., Ritsma, R. J., and Cardozo, B. L. (**1962**). ''Pitch of the residue,'' J. Acoust. Soc. Am. **34**, 1418–1424.

Schroeder, M. R. (**1968**). ''Reference signal for signal quality studies,'' J. Acoust. Soc. Am. **44**, 1735–1736.

Shannon, R. V., Zeng, F.-G., Kamath, V., Wygonski, J., and Ekelid, M. (**1995**). ''Speech Recognition with Primarily Temporal Cues,'' Science **270**, 303–304.

Van Tasell, D. J., Soli, S. D., Kirby, V. M., and Widin, G. P. (**1987**). ''Speech waveform envelope cues for consonant recognition,'' J. Acoust. Soc. Am. **82**, 1152–1161.

Wang, R.-H. (**1989**). ''Chinese phonetics,'' in *Speech Signal Processing*, edited by Y. B. Chen and R.-H. Wang (University of Science and Technology of China Press), Chap. 3, pp. 37–64.

Whalen, D. H., and Xu, Y. (**1992**). ''Information for Mandarin Tones in the amplitude contour and in brief segments,'' Phonetica **49**, 25–47.

Zhang, H., Zhao K. L., and Wang, Z. Z. (**1988**). ''MACC: Chinese Minimal Auditory Capability Test,'' Beijing Union Hospital, Beijing, P. R. China.

Exploration of the perceptual magnet effect using the mismatch negativity auditory evoked potential

Anu Sharma[a] and Michael F. Dorman
Department of Speech and Hearing Science, Arizona State University, Tempe, Arizona 85287-0102

(Received 28 May 1997; revised 27 February 1998; accepted 28 February 1998)

The goals of this study were (i) to assess the replicability of the ''perceptual magnet effect'' [Iverson and Kuhl, J. Acoust. Soc. Am. **97**(1), 553–561 (1995)] and (ii) to investigate neurophysiologic processes underlying the perceptual magnet effect by using the mismatch negativity (MMN) auditory evoked potential. A stimulus continuum from /i/ to /e/ was synthesized by varying F_1 and F_2 in equal mel steps. Ten adult subjects identified and rated the goodness of the stimuli. Results revealed that the prototype was the stimulus with the lowest F_1 and highest F_2 values and the nonprototype stimulus was close to the category boundary. Subjects discriminated stimulus pairs differing in equal mel steps. The results indicated that discrimination accuracy was not significantly different in the prototype and the nonprototype condition. That is, no perceptual magnet effect was observed. The MMN evoked potential (a preattentive, neurophysiologic index of auditory discrimination) revealed that despite equal mel differences between the stimulus pairs the MMN was largest for the prototype pair (i.e., the pair that had the lowest F_1 and highest F_2 values). Therefore the MMN appears to be sensitive to within category acoustic differences. Taken together, the behavioral and electrophysiologic results indicate that discrimination of stimulus pairs near a prototype is based on the auditory structure of the stimulus pairs. © *1998 Acoustical Society of America.* [S0001-4966(98)03007-0]

PACS numbers: 43.71.Es, 43.71.An, 43.64.Qh [WS]

Prototype theories have been used in cognitive psychology to explain aspects of human perception and categorization. Generally, these theories contend that cognitive categories are organized around ideal ''representatives'' or prototypes that are stored in memory. These prototypes then serve as reference points for evaluating other items related to that category. Recent studies in speech perception have used the concept of ''phonetic prototypes'' to explain perception *within* phonetic categories (Samuel, 1982; Grieser and Kuhl, 1989; Kuhl, 1991). For example, Samuel (1982) and Miller *et al.* (1983) reported that prototypical stop consonants were better as adaptors in selective adaptation experiments than nonprototypes. Miller (1977) and Repp (1977) found that prototypical stop consonants were more efficient as dichotic competitors than less prototypical ones.

Kuhl (1991) has claimed that prototypes account for the differences in the discrimination of stimulus pairs, separated by equal mel differences, within vowel categories. The outcome that stimulus pairs near a prototype are more difficult to discriminate than pairs further away from the prototype has been dubbed the ''perceptual magnet effect.'' Kuhl argues that discrimination is poor around a prototype because perceptual space around the prototype is ''shrunk.'' The perceptual magnet effect is not found with Rhesus monkeys (Kuhl, 1991) which suggests that phonetic processes, in contrast to acoustic processes, are central to the effect.

Studies by other investigators have provided less conclusive data regarding the existence of a perceptual magnet in speech perception. Sussman and Laucker-Morano (1995) and Lively (1993, 1996) both failed to replicate Kuhl's (1991) findings. Both sets of investigators found that Kuhl's prototype stimulus was, in fact, not the best rated exemplar of the /i/ category and the nonprototype stimulus was not identified as an /i/ for the most part. Both studies also failed to convincingly demonstrate the magnet effect when using more appropriate stimuli as prototypes and nonprototypes and when manipulating variables such as (i) the type of discrimination task (e.g., AX vs 4IAX), (ii) the analysis procedure (generalization scores versus *d*-prime) and (iii) subject characteristics (naive versus trained subjects). These studies concluded that within-category vowel discrimination was more likely governed by the auditory structure of the stimulus rather than the ''magnet''-like effects of phonetic prototypes. This is consistent with results from previous studies showing that the auditory properties of vowels are perceptually salient (Studdert-Kennedy, 1993).

Recently, Iverson and Kuhl (1995) attempted to verify the findings of Kuhl (1991). A stimulus continuum varying from /i/ to /e/ in equal mel steps was created which encompassed the original prototype and nonprototype stimuli in Kuhl (1991). Iverson and Kuhl (1995) found that the original prototype stimulus was not the best rated exemplar of the category and that the original nonprototype stimulus lay on the phonetic boundary, i.e., was identified as /i/ only 55% of the time. However, Iverson and Kuhl (1995) found that subjects had greater difficulty discriminating stimuli that were more prototypical than those that were less prototypical. These results supported the hypothesis that prototypes act as perceptual magnets and ''shrink'' the surrounding perceptual space. The results from a recent study by Aaltonen *et al.* (1997), which examined the perceptual magnet effect for Finnish vowels using behavioral and electrophysiologic mea-

[a]Electronic mail: anu.sharma@asu.edu

sures, gave only equivocal support to Kuhl's theory. Aaltonen *et al.* (1997) found that subjects fell into two groups based on their ability to label vowels consistently: good and poor categorizers. Good categorizers showed a perceptual magnet effect, whereas poor categorizers did not.

The data reviewed above indicate a lack of consensus as to whether within-category vowel discrimination is governed by properties of the auditory system or by higher level phonetic processing, i.e., the effects of phonetic prototypes. In order to better understand within-category vowel perception, we have examined within-category vowel discrimination using the mismatch negativity (MMN) evoked potential. The MMN is an event-related potential that is elicited by an acoustic change occurring in a sequence of repetitive stimuli (Näätänen *et al.*, 1978). A sizable literature suggests that the MMN is a *preattentive*, neurophysiologic index of auditory discrimination. For example, when attention is focused on one ear in a dichotic listening task, the MMN can be elicited in the unattended ear (Näätänen, 1982, 1990, 1992; Näätänen *et al.*, 1993; Paavilainen *et al.*, 1993). MMN responses have also been elicited in humans during sleep (Alho *et al.*, 1990; Cheour-Luhtanen *et al.*, 1995) and in anesthetized animals (Csépe *et al.*, 1987, 1990; Javitt *et al.*, 1992; Steinschneider *et al.*, 1994; Karmos *et al.*, 1993; Kraus *et al.*, 1994). The generators for the MMN include auditory thalamic and cortical areas (Kraus *et al.*, 1995; Alho, 1995; Csépe, 1995).

The MMN can be elicited using speech signals in which the voice-onset time, starting frequencies and duration of F_2/F_3 and steady-state formants change (Aaltonen *et al.*, 1987; Sams *et al.*, 1990; Sharma *et al.*, 1993; Kraus *et al.*, 1993; Kraus *et al.*, 1994a; Maiste *et al.*, 1995; Sandridge and Boothroyd, 1996). Given that the MMN appears to reflect sensory discrimination, it is an interesting tool with which to study within-category vowel discrimination.

The goals of the present study were (i) to determine whether the perceptual magnet effect could be replicated and (ii) to use the MMN to investigate neurophysiologic processes underlying within-category vowel perception.

I. BEHAVIORAL EXPERIMENT

A. Method

1. Subjects

Ten English speaking adults with normal hearing (aged 20–39 years; six females and four males) were paid $5/h for their participation. All were native speakers of English who reported no formal training in phonetics. Subjects reported no history of speech or hearing problems.

2. Stimuli

The stimuli were 13 tokens of the vowel /i/. This stimulus continuum included Kuhl's (1991) prototype and nonprototype stimuli. Stimulus 5 was Kuhl's original prototype and stimulus 9 was Kuhl's original nonprototype.

The five-formant vowel stimuli were synthesized using the Klatt (1980) synthesizer. The values of the first two formants varied in equal steps along the mel scale (Fant, 1973). The mel scale is linear at low frequencies and logarithmic at higher frequencies and is used to equate the magnitude of a perceived pitch change at different frequencies. The third through fifth formants were steady state. F_1 varied from 197 to 429 Hz (259 to 515 mels) and F_2 varied from 1925 to 2489 Hz (1803 to 1548 mels), F_3 was 3010 Hz, F_4 was 3300 Hz and F_5 was 3850 Hz. F_0 rose from 112 to 130 Hz over the first 35 ms and dropped to 92 Hz for the remainder of the vowel. With the exception of overall vowel duration, stimulus parameters were based on those reported by Iverson and Kuhl (1995). In this study, vowel duration was 140 ms compared to 435 ms in Iverson and Kuhl (1995). The stimuli were equated in intensity (within 1 dB of each other) and presented to the subjects at 75 dB SPL, binaurally under headphones (Senheiser, 410).

3. Procedures

In the identification portion of the experiment subjects were asked to listen to the sounds under headphones and to classify each sound either as /i/ (as in the sound HE) or not /i/. Subjects were asked to indicate their responses by clicking with the mouse on panels marked HE and NOT-HE appearing on the computer screen. Each subject was given an initial practice session in which he or she heard each stimulus once. Next, eight repetitions of each of the 13 stimuli were presented to the subject in a random order.

Following the identification task subjects were asked to rate how good an example each stimulus was of the /i/ category from a scale of 1 (poorest) to 7 (best). The rating scale was based on the one used by Kuhl (1991) and Iverson and Kuhl (1995). Subjects were encouraged to use the entire rating scale. Subjects indicated their responses by clicking on panels labeled 1 through 7 which appeared on the computer screen. Subjects completed an initial practice trial with each of the 13 tokens presented in a random order. After the practice, subjects completed the experimental session in which they heard eight repetitions of each of the 13 tokens in a random order.

Anticipating the results of the rating experiment, three pairs of stimuli were chosen for the discrimination experiment (viz., stimlulus pairs 1–3, 3–5, and 5–7). The acoustic difference (in mels) was equal for each pair. Based on preliminary data it was anticipated that stimulus pairs 1–3 and 3–5 would represent the prototype and nonprototype conditions, respectively. It is worth noting that Iverson and Kuhl (1995) report that discrimination was significantly better for Kuhl's original prototype when it was paired with adjacent stimuli (along the continuum) that were less prototypical, than when it was paired with adjacent stimuli that were more prototypical. Given that our stimulus 5 was modeled after Kuhl's original prototype, we anticipated that the 3–5 and 5–7 conditions in our study would simulate Iverson and Kuhl's ''more prototypical'' and ''less prototypical'' comparisons, respectively.

An AX discrimination task was employed. On each trial subjects heard two stimuli with an interstimulus interval

TABLE I. Mean scores for identification and rating experiments.

Stimulus number	Percent /i/ identification	Goodness rating
1	100	6.2
2	100	6.2
3	99	6.0
4	98	6.0
5	95	5.8
6	95	5.3
7	75	4.2
8	56	3.0
9	20	1.9
10	6	1.8
11	1	1.6
12	3	1.4
13	0	1.4

(ISI) of 250 ms. Subjects were asked to determine whether the stimuli in the pair were ''same'' or ''different.'' Subjects indicated their responses by clicking on panels labeled ''same'' or ''different'' on the computer screen. Correct answer feedback was not provided. The presentation of stimulus pairs was randomized within the test and across subjects. The direction of vowel change was counterbalanced across different trials. For each pair, an initial practice session of 20 trials was presented (ten same and ten different trials). The experimental session consisted of a total of 100 trials (50 same and 50 different) for each stimulus pair.

B. Results and discussion

Table I shows the identification and rating results averaged across all subjects. Kuhl (1991) defines the prototype and the nonprototype as those stimuli that are given the highest and lowest rating scores, respectively. Additionally, she states that it is critical that both the prototype and nonprototype are easily identified as members of the same vowel category. In this study, subjects identified stimuli 1 through 6 as /i/ at least 95% of the time. Stimuli at the beginning of the continuum received the highest (100%) identification scores. The highest rating (6.2 out of 7) was given to stimuli 1 and 2. Of the two, stimulus 1 was selected to serve as the prototype stimulus for this study. Stimulus 5 (Kuhl's prototype) is a good exemplar of the category but is not the prototype. Since stimulus 9 (Kuhl's nonprototype) was identified as an /i/ only 20%, it is not a suitable nonprototype. On the other hand, stimulus 7 which had 75% identification and 4.2 rating scores fit the definition of a nonprototype.

Stimuli with the lowest F_1 and highest F_2 values were given the highest ratings and as F_1 and F_2 values changed systematically along the continuum, stimuli were given correspondingly lower goodness ratings. The mean rating scores were significantly correlated with increasing F_1 values (Spearman $r=+1.0$; $p<0.001$) and decreasing F_2 values (Spearman $r=-1.0$; $p<0.001$). The overall pattern of identification and rating results is consistent with that reported by Iverson and Kuhl (1995), despite the difference in vowel duration between the two studies.

Results of the discrimination experiment were analyzed using d-prime (Kaplan *et al.*, 1978; MacMillan and Creelman, 1991). Mean d-prime scores for all three pairs are shown in Fig. 1. A one way, repeated measures ANOVA revealed a significant main effect of stimulus pair ($F=5.08$, $p<0.02$). *Post hoc* tests (Student Neuman Kuels) indicated that discrimination for stimulus pair 3–5 was significantly poorer than for the 1–3 and 5–7 pairs ($p<0.05$). However, discrimination was not significantly different between the 1–3 and 5–7 pairs ($p>0.05$). Therefore the results of the behavioral experiment show that the position of sounds within the stimulus category influences their perception. Overall, discrimination at the two ends of the continuum was better than in the middle.

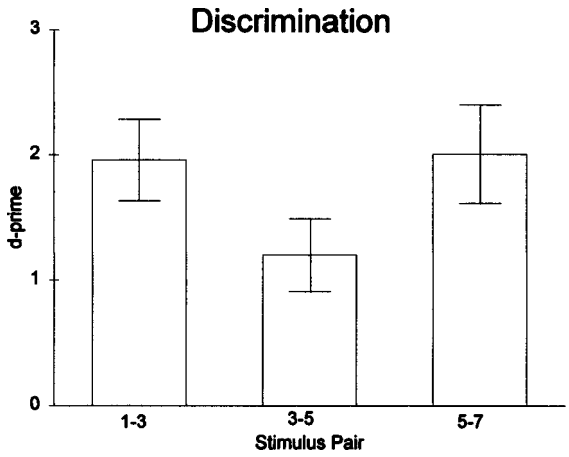

FIG. 1. Mean d-prime scores for the discrimination experiment. Subjects were significantly poorer at discriminating the 3–5 pair compared to the other two pairs ($p<0.05$). Discrimination was not significantly different for the 1–3 and 5–7 pairs ($p>0.05$). Error bars indicate ± 1 standard error.

In summary, the overall trend of our identification and rating results is consistent with Iverson and Kuhl's (1995) findings. Furthermore, if we consider the discrimination results for Kuhl's ''prototype'' (stimulus 5) and the nonprototype (stimulus 7), the outcome is also similar to Iverson and Kuhl (1995). That is, given equal acoustic differences it is easier to discriminate stimuli in the nonprototype (5–7) condition than in the ''prototype'' (3–5) condition. On the other hand, when we compare the true prototype (stimulus 1) and the nonprototype (stimulus 7), we find that the discrimination is similar for the prototype (1–3) and nonprototype (5–7) conditions. This result does not duplicate a magnet-like effect for the prototype and is consistent with the findings of Lively (1993, 1996) and Sussman and Laucker-Morano (1995).

II. ELECTROPHYSIOLOGIC EXPERIMENT

A. Method

1. Subjects

The subjects were the same as those used in the behavioral experiment. Subjects were seated in a sound booth. To control for arousal and to minimize subjects attention to the test stimuli, subjects watched a videotaped movie of their choice. Video tape audio levels were kept below 40 dB SPL-A. Subjects were asked to ignore the vowel stimuli that were presented through insert earphones at 75 dB SPL in the right ear.

2. Stimuli

The stimuli were the same as those used in the behavioral discrimination experiment, i.e., stimulus pairs 1–3, 3–5 and 5–7. The MMN was elicited using an oddball paradigm in which repetitive presentations of a ''standard'' stimulus were occasionally replaced with a ''deviant'' or ''target'' stimulus. For the 1–3 pair, stimulus 1 was the standard and stimulus 3 was the deviant. For the 3–5 pair, stimulus 3 was the standard and 5 was the deviant. For the 5–7 pair, stimulus 7 was the standard and stimulus 5 was the deviant. The presentation of standard and deviant stimuli was not counterbalanced within a stimulus pair. The stimuli were presented at an offset-to-onset ISI of 510 ms. The deviant stimulus had a probability of occurrence of 15%. The order of the conditions was counterbalanced across subjects.

3. Procedures

Procedures used to record and analyze the MMN were similar to those used previously (Sharma *et al.*, 1993; Kraus *et al.*, 1995). Auditory evoked potentials were recorded using a NeuroScan Inc. data acquisition system. Stimuli were delivered to the right ear using insert earphones. Electrodes were placed on the midline (Fz, Cz and Pz), over each hemisphere (F3, F4, C3, C4) and at the mastoids. The reference electrode was on the nose and the ground was on the forehead. Eye movements were monitored with a bipolar electrode montage (supraorbital to lateral canthus). Averaging was suspended when the eye channel registered blinks. The recording window included a 100 ms prestimulus period and 500 ms of post-stimulus time. Evoked responses were bandpass filtered from 0.1 to 100 Hz. In each condition, 2000 sweeps of the response to the standard and 300 sweeps of the response to the deviant stimulus were collected.

a. Individual data analysis. Responses that were judged noisy or that were greater than 100 uV were rejected offline. For each subject, sweeps were averaged to compute an individual average waveform for the standard and deviant stimuli. Because the MMN is by definition, a potential elicited only by the deviant stimulus, MMN component was measured from a difference wave computed by subtracting the standard from the deviant response. This procedure serves to isolate the MMN component from other obligatory evoked potential components such as N1 and P2 (Kraus *et al.*, 1995). For each subject, the morphologies of the individual standard, deviant and difference waves were assessed relative to previously described morphologies of speech-evoked potentials (Kraus *et al.*, 1993). The MMN was identified visually (in the difference wave) as a relative negativity following the N1 peak (seen in the standard and deviant waves). The point of maximum negativity of the MMN component was noted and the adjacent relative positive peaks were selected as the MMN onset and offset. The MMN duration was defined as the offset minus the onset latency for each subject. To measure the area of the MMN, a line was drawn from the onset to the offset of the MMN in the difference wave. The enclosed area of the difference waveform was measured as ms $\times$ uV. Duration and area measurements were computed from responses at the Fz electrode since MMN is maximally recorded at frontocentral electrodes (Näätänen, 1992; Sandridge and Boothroyd, 1996).

b. Group data analysis. For each condition, a grand average standard, deviant and difference waveform was computed by averaging across all subjects. A point-to-point *t* test of the values contributing to the waveforms determined the period over which the grand averages were significantly different from zero at the $p<0.05$ level. A significant negativity (seen in the grand average difference wave) following the N1peak (seen in the grand average standard and deviant waves) was defined as the group MMN.

B. Results and discussion

The MMN elicited in response to the 1–3 pair was longer in duration and larger in area than in the other two conditions. This trend was consistent across all the electrode sites except at the mastoids where no MMNs were observed in any of the stimulus conditions. Figure 2 shows the grand average difference waves from the three stimulus conditions at electrode site Fz. Mean values for MMN duration are seen in Fig. 3 (top panel). A one way, repeated measures ANOVA (computed on the duration values taken from the averaged difference waves of individual subjects) showed a significant main effect of stimulus condition ($F=8.7$, $p<0.002$). *Post hoc* tests (Student Neuman Kuels) revealed that MMN duration was significantly longer in the 1–3 condition compared to 3–5 and 5–7 conditions ($p<0.05$). MMN duration was not significantly different for the 3–5 and 5–7 conditions ($p>0.05$). As can be seen in Fig. 3 (bottom panel), similar results were obtained for MMN area. A second one way, repeated measures ANOVA (computed on the area values taken from the averaged difference waves of individual subjects) showed a significant main effect of stimulus condition ($F=4.77$, $p<0.02$). *Post hoc* tests (Student Neuman Kuels) revealed that MMN area was significantly larger in the 1–3 condition compared to the 3–5 and 5–7 conditions ($p<0.05$). The MMN area was not significantly different for the 3–5 and 5–7 conditions ($p>0.05$).

In summary, the results of the electrophysiological experiment showed that the MMN was significantly larger for the 1–3 pair compared to the other two pairs. That is, for equal mel differences between standard and deviant stimuli, larger MMNs were elicited for the stimulus pair with the highest F_2 and lowest F_1 values. These results are consistent with those of Aaltonen *et al.* (1997) who found that for a continuum varying in equal F_2 steps (for the Finnish vowel /i/), the MMN was largest for stimulus pairs which had the highest F_2 values.

III. GENERAL DISCUSSION

Our results show that the vowel /i/ category exhibits an internal structure based on its acoustic properties. Results of the identification and rating experiments showed that certain tokens were perceived to be better exemplars of the category than others. This internal structure appears to be based on physical parameters of the vowels. Stimuli with the lowest F_1 and highest F_2 values were ranked as the best exemplars.

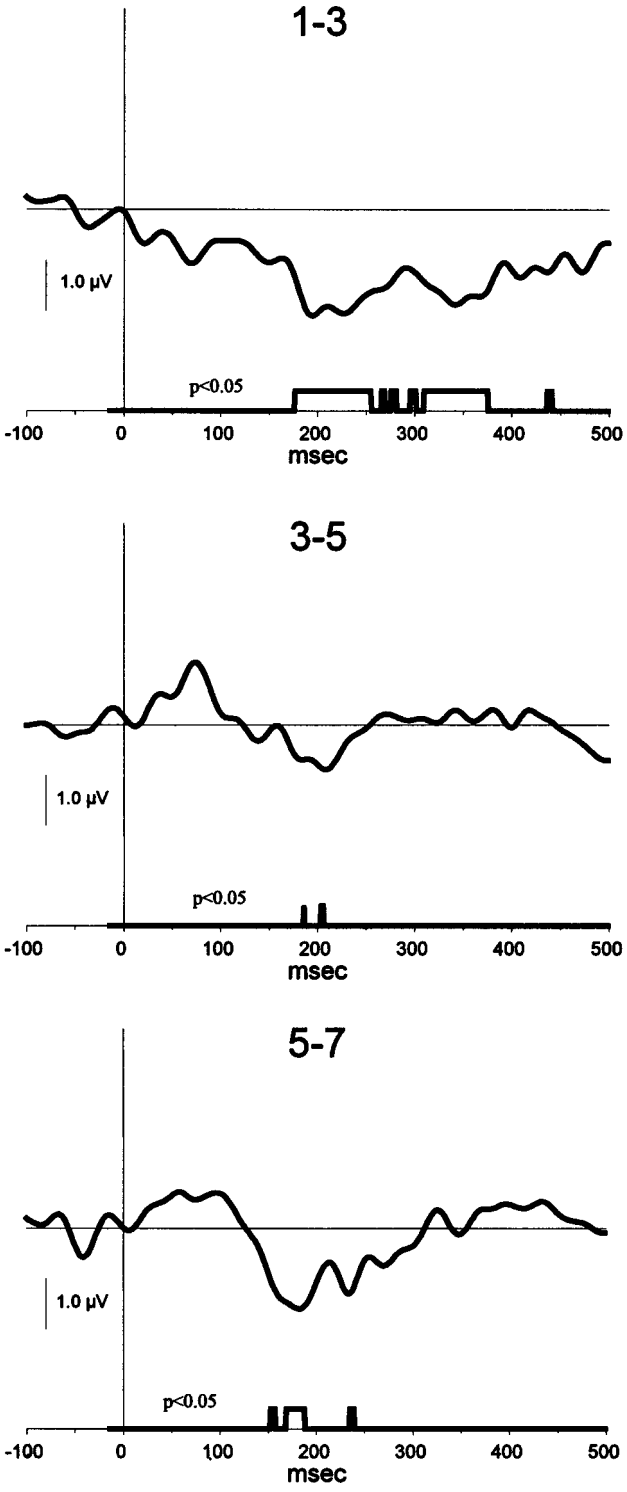

FIG. 2. Grand average (across subjects) difference waves in the three stimulus conditions. The MMN response is seen in the difference wave as a deflection below the zero line. The boxes on the x-axis under the difference waves indicate the latency ranges over which a significant mismatch response occurred ($p<0.05$).

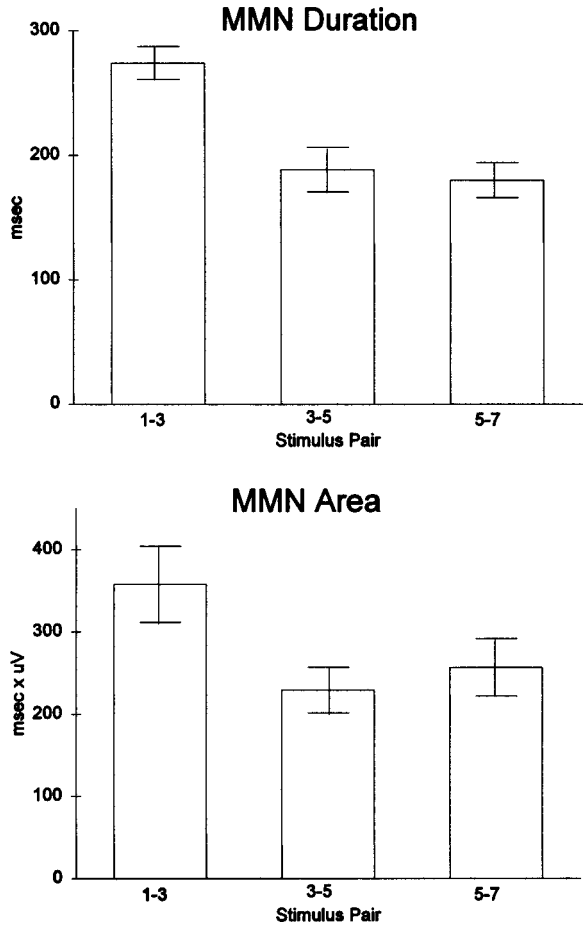

FIG. 3. The top panel shows the mean MMN duration and the bottom panel shows the mean MMN area in the three stimulus conditions. MMN duration and area were significantly larger in the 1–3 condition compared to the other two ($p<0.05$). MMN area and duration were not significantly different for the 3–5 and 5–7 stimulus conditions ($p<0.05$). Error bars indicate ± 1 standard error.

As F_1 and F_2 values changed systematically along the continuum, stimuli were given correspondingly lower goodness ratings. As a result the ''true'' prototype and nonprototype (stimulus 1 and 7, respectively) fell at the two ends of the category. The overall pattern of our identification and rating results is similar to Iverson and Kuhl's (1995) findings using a comparable stimulus continuum.

If we consider our results with respect to Kuhl's original, but not ''true'' prototype (i.e., stimulus 5), we were able to duplicate Iverson and Kuhl's (1995) findings, i.e., the 3–5 pair was significantly more difficult to discriminate than the 5–7 pair. Because the MMN was not significantly different for the 3–5 and 5–7 stimulus pairs, it appears that the behavioral discrimination differences between these pairs were not due to inherent acoustic differences. Rather, the enhanced discrimination for the nonprototype condition is probably the result of phonetic processing of some sort. Possibly stimulus 7 is close enough to the category boundary that it has an /I/-like quality and it is this quality that makes the 5–7 pair easy to discriminate.

When the ''true'' prototype was used we did not find evidence for a perceptual magnet effect. Discrimination for the 1–3 pair (true prototype condition) was not significantly different from the 5–7 pair (nonprototype condition). Moreover, discrimination of the 1–3 pair was better than discrimination of the 3–5 pair. This result is consistent with the studies of Lively (1996) and Sussman and Laucker-Morano (1995) who failed to demonstrate a convincing perceptual magnet effect using appropriate prototype and nonprototype stimuli.

In the present study, the MMN response to the 1–3 pair was larger than the response to the two other pairs. This implies that the enhanced behavioral discrimination for the 1–3 pair, when compared to the 3–5 pair, is likely due to underlying acoustic factors. It is difficult to compare our results with previous studies of the perceptual magnet effect in English. Lively (1996) and Kuhl (1991) did not report results for specific pairs of stimuli, rather their results were collapsed across all stimuli in an orbit. Sussman and Laucker-Morano (1995) and Iverson and Kuhl (1995) tested discrimination for specific pairs of stimuli, however, they did not test discrimination for stimulus pairs that would be comparable to our 1–3 pair.

Given that our 1–3 pair had the highest F_2 and lowest F_1 values, our findings of enhanced discrimination for this pair are comparable to those from a recent study by Aaltonen *et al.* (1997). In that study Finnish listeners' identification, rating and discrimination was assessed for stimuli falling along an /i/ continuum varying in F_2 in equal mel steps. Aaltonen and colleagues classified their subjects into two groups based on individual rating scores. Subjects in their ''High P'' group had judged individual prototypes to be at the high F_2 end of the category and nonprototypes to be at the category boundary. For subjects in their ''Low P'' group, essentially the opposite category structure was seen. Aaltonen *et al.* (1997) found that regardless of the location of subjects' individual prototypes and nonprototypes along the continuum, the largest MMNs were elicited for stimuli with the highest F_2 values. Therefore they concluded that the perceptual magnet effect was indicated for the Low P group (whose nonprototypes were at the high F_2 end) and not for the High P group (whose prototypes were at the high F_2 end).

Unlike Aaltonen *et al.* (1997) our subjects showed a consistent pattern of goodness ratings in which stimuli at the high F_2 (and low F_1) end of the continuum were given relatively higher ratings compared to stimuli near the category boundary. Therefore based on goodness ratings, our subjects as a whole were comparable to the High P group in Aaltonen *et al.* (1997). In that study, based on measures of category consistency and boundary width, the High P group was judged to consist of ''poor'' or inconsistent categorizers. However, in the present study, all listeners had sharp boundaries and small boundary widths, similar to subjects who were classified as ''good'' or consistent categorizers by Aaltonen *et al.* (1997). Given then, that our subjects are at least partially comparable to the High P group of Aaltonen *et al.* (1997) the electrophysiologic findings of the two studies appear consistent. That is, in this study and for the High P group of Aaltonen *et al.* (1997), the MMN was larger for the prototype as opposed to the nonprototype.

It should be noted that in this study a potentially important variable, the interstimulus interval (ISI), differed between the behavioral and electrophysiologic discrimination experiments. This occurred because parameters for the behavioral experiment were primarily selected to be consistent with the Iverson and Kuhl (1995) study which we were trying to replicate, while variables for the electrophysiologic experiment were chosen to optimize the MMN recordings. As a result, the ISI in the behavioral discrimination experiment (250 ms) was shorter than the ISI in the MMN experiment (510 ms). ISI is considered an important variable in behavioral discrimination experiments because a short ISI may allow subjects to rely more on acoustic (compared to phonetic) cues (Pisoni, 1973). However, changes in ISI do not appear to influence MMN results in a comparable fashion. Previous studies in which the MMN was elicited at varied ISI have shown that the MMN primarily reflects changes in acoustic (physical) parameters of the stimulus (Aaltonen *et al.*, 1987; Sams *et al.*, 1990; Sharma *et al.*, 1993; Maiste *et al.*, 1995). In those studies, even though behavioral discrimination was enhanced across phonetic categories, the MMN did not show this effect. This suggests that the MMN appears to reflect acoustic processing regardless of ISI. Therefore it is unlikely that the overall pattern of the present MMN findings would be different if the ISI in the electrophysiologic experiment could have been shortened to match the ISI of the behavioral experiment.

Some investigators (e.g., Sussman and Laucker-Morano, 1995; Polka and Bohn, 1996) have reported that direction of change of the vowel formants may affect discrimination results. In our behavioral experiment, the order of presentation of stimuli within a pair was counterbalanced and therefore the direction of vowel change was not an issue. In the electrophysiologic experiment, stimulus presentation within pairs was not counterbalanced. For pairs 1–3 and 3–5, the deviant stimulus had a higher F_1 and lower F_2 than the standard, however, for the 5–7 pair the deviant stimulus had a lower F_1 and higher F_2 than the standard. Therefore it is possible that the opposite directions of formant change may be a potentially confounding variable. However, it should be emphasized that one of the most important results of this study which argues against the existence of a perceptual magnet effect is that for pairs with the same direction of formant change the MMN was larger for the more prototypical pair (1–3) compared to the less prototypical pair (3–5).

In summary, taken together the behavioral and electrophysiologic results show that discrimination within the vowel /i/ category depends on both acoustic and phonetic factors. Towards the nonprototype end of the category, discrimination was enhanced due to phonetic processing (presumably due to proximity to the category boundary), while the enhanced discrimination seen at the ''true'' prototype end was influenced by the underlying auditory properties of vowels. Further research is necessary to determine the specific attributes of an auditory stimulus which account for discrimination peaks within a phonetic category.

Aaltonen, O., Eerola, O., Hellstrom, C., Uusipaikka, E., and Lang, A. (**1997**). ''Perceptual magnet effect in the light of behavioral and psychophysiological data,'' J. Acoust. Soc. Am. **101**, 1090–1103.

Aaltonen, O., Niemi, P., Nyrke, T., and Tuhkanen, M. (**1987**). ''Event-related brain potentials and the perception of a phonetic continuum,'' Biol. Psychol. **24**, 197–207.

Alho, K. (**1995**). ''Cerebral generators of mismatch negativity (MMN) and its magnetic counterpart (MMNm) elicited by sound changes,'' Ear Hear. **16**, 38–50.

Alho, K., Sainio, K., Sajaniemi, N., Reinikainen, K., and Näätänen, R. (**1990**). ''Event-related brain potential of human newborns to pitch change

of an acoustic stimulus,'' Electroencephalogr. Clin. Neurophysiol. **77**, 155–155.
Cheour-Luhtanen, M., Alho, K., Kujala, T., Sainio, K., Reinikainen, K., Renlund, M., Aaltonen, O., Eerola, O., and Näätänen, R. (**1995**). ''Mismatch negativity shows discrimination of speech stimuli in newborns,'' Hearing Res. **82**, 53–58.
Csépe, V. (**1995**). ''On the origin and development of the Mismatch Negativity,'' Ear Hear. **16**, 91–104.
Csépe, V., Karmos, G., and Molnár, M. (**1987**). ''Evoked potential correlates of stimulus deviance during wakefulness and sleep in the cat-animal model of mismatched negativity,'' Electroencephalogr. Clin. Neurophysiol. **66**, 571–578.
Csépe, V., Karmos, G., and Molnár, M. (**1990**). ''Subcortical evoked potential correlates of early information processing: Mismatch negativity in cats,'' in *Dynamics of Sensory and Cognitive Processing by the Brain*, edited by E. Basar and T. Bullock (Springer-Verlag, Berlin), pp. 279–289.
Fant, G. (**1973**). *Speech Sound and Features* (MIT, Cambridge, MA).
Grieser, D., and Kuhl, P. K. (**1989**). ''Categorization of speech sounds by infants: Support for speech sound prototypes,'' Dev. Psychol. **25**, 577–588.
Iverson, P., and Kuhl, P. (**1995**). ''Mapping the perceptual magnet effect for speech using signal detection theory and multidimensional scaling,'' J. Acoust. Soc. Am. **97**, 553–561.
Javitt, D., Schroeder, C., Steinschneider, M., Arezzo, J., and Vaughan, Jr., H. (**1992**). ''Demonstration of mismatch negativity in monkey,'' Electroencephalogr. Clin. Neurophysiol. **83**, 87–90.
Kaplan, H. L., Macmillan, N. A., and Creelman, C. D. (**1978**). ''Tables of d' for variable-standard discrimination paradigms,'' Behav. Res. Methods Instrum. **10**, 796–813.
Karmos, G., Winkler, I., Molnar, M., and Csépe, V. (**1993**). ''Animal model of middle latency auditory evoked responses-intracortical generators of the mismatch negativity,'' in *New Developments in Event Related Potentials*, edited by H. Heinze, G. Mangun, and T. Munte (Birkhauser, Boston), pp. 95–102.
Klatt, D. H. (**1980**). ''Software for a parallel/cascade formant synthesizer,'' J. Acoust. Soc. Am. **67**, 971–995.
Kraus, N., McGee, T., Carrell, T., King, C., Littman, T., and Nicol, T. (**1994a**). ''Discrimination speech-like contrasts in the auditory thalamus and cortex,'' J. Acoust. Soc. Am. **96**, 2758–2768.
Kraus, N., McGee, T., Carrell, T., and Sharma, A. (**1995**). ''Neurophysiologic bases of speech discrimination,'' Ear Hear. **16**, 19–37.
Kraus, N., McGee, T., Carrell, T., Sharma, A., and Nicol, T. (**1993**). ''Speech-evoked cortical evoked potentials,'' J. Am. Acad. Audiol. **4**, 238–248.
Kraus, N., McGee, T., Littman, T., Nicol, T., and King, C. (**1994b**). ''Nonprimary auditory thalamic representation of acoustic change,'' J. Neurophysiol. **72**, 1270–1277.
Kuhl, P. K. (**1991**). ''Human adults and human infants show a 'perceptual magnet effect' for the prototypes of speech categories, monkeys do not,'' Percept. Psychophys. **50**, 93–107.
Lively, S. E. (**1993**). ''An examination of the perceptual magnet effects,'' J. Acoust. Soc. Am. **93**, 2423.
Lively, S. E. (**1996**). ''On prototypes and phonetic categories: A critical assessment of the perceptual magnet effect in speech perception,'' Research Report, Indiana University (unpublished).
Macmillan, N. A., and Creelman, C. D. (**1991**). *Detection Theory: A User's Guide* (Cambridge U.P., New York).
Maiste, A., Wiens, A., Hunt, M., and Picton, T. (**1995**). ''Event-related potentials and the categorical perception of speech sounds,'' Ear Hear. **16**, 68–90.
Miller, J. L. (**1977**). ''Properties of feature detectors for VOT: The voiceless channel of analysis.'' J. Acoust. Soc. Am. **62**, 641–648.
Miller, J. L., Connine, C. M., Schermer, T. M., and Kluender, K. R. (**1983**). ''A possible auditory basis for internal structure of phonetic categories,'' J. Acoust. Soc. Am. **73**, 2124–233.
Näätänen, R. (**1982**). ''Processing negativity: An evoked-potential reflection of selective attention,'' Psychol. Bull. **92**, 605–640.
Näätänen, R. (**1990**). ''The role of attention in auditory information processing as revealed by event-related potentials and other brain measures of cognitive function,'' Behav. Brain Sci. **13**, 201–288.
Näätänen, R. (**1992**). *Attention and Brain Function* (Erlbaum, Hillsdale, NJ).
Näätänen, R., Gaillard, A., and Mäntysalo, S. (**1978**). ''Early selective attention effect on evoked potential reinterpreted,'' Acta Psychol. **41**, 313–329.
Näätänen, R., Jiang, D., Lavikainen, J., Reinikainen, K., and Paavilainen, P. (**1993**). ''Event-related potentials reveal a memory trace for temporal features,'' NeuroReport **5**, 310–312.
Paavilainen, P., Titinen, H., Alho, K., and Näätänen, R. (**1993**). ''Mismatch negativity to slight pitch changes outside strong attentional focus,'' Biol. Psychol. **37**, 23–41.
Pisoni, D. B. (**1973**). ''Auditory and phonetic memory codes in the discrimination of consonants and vowels,'' Percept. Psychophys. **13**, 253–260.
Polka, L., and Bohn, O. S. (**1996**). ''A cross-language comparison of vowel perception in English-learning and German-learning infants,'' J. Acoust. Soc. Am. **100**, 577–592.
Repp, B. H. (**1977**). ''Dichotic competition of speech sounds: The role of acoustic stimulus structure,'' J. Exp. Psychol. **3**, 37–50.
Sams, M., Aulanko, R., Aaltonen, O., and Näätänen, R. (**1990**).''Event-related potentials to infrequent changes in synthesized phonetic stimuli,'' J. Cogn. Neurosci. **2**, 344–357.
Samuel, A. G. (**1982**). ''Phonetic prototypes,'' Percept. Psychoacoustics **31**, 307–314.
Sandridge, S. A., and Boothroyd, A. (**1996**). ''Using naurally produced speech to elicit the Mismatch Negativity,'' J. Am. Acad. Audiol. **7**, 105–112.
Sharma, A., Kraus, N., McGee, T., Carrell, T., and Nicol, T. (**1993**). ''Acoustic versus phonetic representation of speech as reflected by the mismatch negativity event-related potential,'' Electroencephalogr. Clin. Neurophysiol. **88**, 64–71.
Steinschneider, M., Schroeder, C. E., Arezzo, J. C., and Vaughan, Jr., H. G. (**1994**). ''Speech-evoked activity in primary auditory cortex: Effects of voice onset time,'' Electroencephalogr. Clin. Neurophysiol. **92**, 30–43.
Studdert-Kennedy, M. (**1993**). ''Discovering phonetic function,'' J. Phon. **21**, 147–155.
Sussman, J., and Lauckner-Morano, V. (**1995**). ''Further tests of the 'perceptual magnet effect' in the perception of [i]: Identification and change/no-change discrimination,'' J. Acoust. Soc. Am. **97**, 539–551.

The perception of speech gestures

Aimée M. Surprenant[a)]
Department of Psychological Sciences, Purdue University, West Lafayette, Indiana 47907-1364

Louis Goldstein
Haskins Laboratories New Haven, Connecticut 06510 and Yale University, New Haven, Connecticut 06520

(Received 2 April 1996; revised 4 March 1998; accepted 31 March 1998)

Two experiments examined the effects of temporal overlap of speech gestures on the perception of stop consonant clusters. Sequences of stop consonant gestures that exhibit temporal overlap extreme enough to potentially eliminate the acoustic evidence of (at least) one of the consonants were obtained from x-ray microbeam data. Subjects were given a consonant monitoring task using stimuli containing stop sequences as well as those containing single stops. Results showed that (1) the initial consonant in the stop sequences was detected significantly less often than in the single stops; (2) bilabial gestures were considerably more effective at obscuring a preceding alveolar than the reverse; and (3) the detection rate correlated with an index of overlap between lip and tongue tip gestures. Experiment 2 employed stimuli that were truncated during the closure for the critical stop or stop sequence, so as to eliminate any information occurring in the acoustic signal at the stop release. This experiment showed that removing release information decreased detectability of the consonants generally. However, consistent with the observed gestural patterns, removing the release did not decrease detection of the alveolar stop when it was the first consonant of a sequence, indicating that there was no information about the alveolar stop present in acoustic realization of the second stop release. These experiments show that certain gestural patterns actually produced by English speakers may not be completely recoverable by listeners, and further, that it is possible to relate recoverability to particular metric properties of the gestural pattern. © *1998 Acoustical Society of America.* [S0001-4966(98)02707-6]

PACS numbers: 43.71.Es, 43.71.An [WS]

INTRODUCTION

The observation that the acoustic properties of phonological units vary considerably as a function of phonetic context has been the basis for a great deal of research in both speech perception and production. In speech, phonological units are produced in overlapping time frames (Liberman *et al.*, 1967; Fowler, 1986) and, as a result of this coproduction, the acoustic signal bears a complex relation to the perceived units. Because of the lack of context-invariant correspondence between the signal and the percept, some theories of speech perception have looked to places other than an acoustic description of the speech signal to find the invariants that allow us to achieve a stable percept in the face of such contextual dependence. In particular, the revised motor theory of speech perception (Liberman and Mattingly, 1985, p. 2) has identified the ''intended phonetic gestures of the speaker, represented in the brain as invariant motor commands,'' as the units of speech perception.

Although the exact processes whereby the listener recovers the abstract gestures from the speech signal have not been specified in detail, the general idea is that the listener uses (innately specified) phonetic knowledge to find a gestural pattern that could have given rise to a particular acoustic input to the speech system. One question that can be posed from this perspective is, what acoustic conditions are necessary for a gesture to be (correctly) recovered? In the extreme, it is obvious that some evidence of a gesture in the acoustic signal is necessary in order for it to be recovered. As Mattingly (1981) has argued, it is possible to view the syllabic organization of speech gestures as a means by which gestures can be overlapped substantially (so as to maximize ''parallel transmission'') while still ensuring recoverability. However, it remains a question exactly how subtle the local acoustic consequences of a gesture can be and still lead to correct interpretation.

There do seem to be circumstances in which the listener may fail to recover the gestures intended by (and indeed produced by) the talker. Such circumstances may occur in informal or casual speech, which has traditionally been described as exhibiting deletion or assimilation of consonants in sequences (Brown, 1977). Browman and Goldstein (1990) have presented articulatory movement data showing that, in at least some of these cases, the gesture for a putatively deleted consonant is, in fact, produced by the talker, but is overlapped by surrounding consonant gestures to such an extent that it is perceptually ''hidden.'' An example they present is the final [t] in ''perfect,'' when produced in the fluent phrase ''perfect memory.'' X-ray evidence in this case revealed motion of the tongue tip toward the alveolar ridge and then away from it, comparable in magnitude to the motion found in examples in which the [t] was completely audible (when there was a prosodic boundary between ''perfect'' and ''memory''). In the fluent phrase, the closing and releasing motions of the tongue tip occur while the vocal tract is completely closed by the overlapping dorsal ([k]) and

[a)]Electronic mail: aimee@psych.purdue.edu

labial ([m]) closure gestures. Browman and Goldstein (1991) have hypothesized that recovery failures of this kind (and others) can ultimately lead to ''listener-based'' historical sound changes (of the kind proposed by Ohala, 1981). If such perceptual ''hiding'' of overlapped gestures can be demonstrated systematically, it can provide evidence relevant to theories of speech perception that use the gesture as the unit of perception. In particular, it suggests that there are limiting cases where the nature of the acoustic output resulting from a pattern of overlapping gestures is such that recovery of the gestures by the listener is difficult, if not impossible.

The assimilations and deletions reported for fluent speech have primarily been observed by phoneticians through ''careful listening.'' Taking the deletion of [t] in ''perfect memory'' as an example, what such listening actually reveals is that there is no local information in the signal that sounds like the formation or release of a tongue tip constriction. However, the word ''perfect'' might still be expected to sound completely normal to a naive listener, in context, and thus it is possible that the listeners are still recovering the ''hidden'' gesture, perhaps using knowledge of higher-order gestural dependencies. For example, the precise degree of temporal overlap between the dorsal and labial gestures (and their relations to other gestures in the utterance) might be different if the intended utterance had no tongue tip closure gesture at all (i.e., had the speaker intended to say ''perfeck memory''). If that were the case, listeners *could* infer the existence of the tongue tip gesture from the pattern of overlap, even if there was no local acoustic indication of its formation or release. One way to see whether a potentially ''hidden'' gesture is actually recovered or not is to present listeners with utterances that differ minimally in whether that gesture is part of the ''intended'' phonetic structure of the speaker, and see if listeners can distinguish them.

Such a study was undertaken by Byrd (1992). She used the Haskins gestural model (Browman and Goldstein, 1990; Saltzman and Munhall, 1989; Rubin *et al.*, 1981) to create sets of stimuli that varied in the amount of overlap between two consonant gestures across a word boundary (''bad ban'' and ''bab dan''). The overlap between C_1 and C_2 was varied over 11 steps from 34% to 107% (the latter indicating that C_2 actually preceded C_1 slightly). These stimuli were presented to subjects in a forced-choice identification task in order to assess the perceptual effects of the overlap between gestures. The effect of overlap on the identification of a consonant was measured in two contexts, bilabial#alveolar (''ba$\underline{b}$ $\underline{d}$an'') and alveolar#bilabial (''ba$\underline{d}$ $\underline{b}$an''). The size of the gestures was held constant in all cases. The results showed that as the amount of overlap increased, identification of C_1 was significantly reduced (C_1 was perceived as assimilated to C_2). This effect was stronger and appeared with a smaller amount of overlap in the [db] condition compared to the [bd] condition. It appears that the tongue tip gesture was more easily hidden by the subsequent labial gesture than vice versa. In a second condition, Byrd (1992) found similar results when the stimuli were truncated during the medial stop closure. However, in this truncated case, the effects were weaker and occurred only with a greater amount of overlap compared to the condition where the context word was present. The stronger effects obtained in the two-word condition are consistent with other results (Repp, 1978; Dorman *et al.*, 1979; Ohala, 1990) showing that, as stop closure duration in a VC_1C_2V decreases, only one consonant is perceived, and that CV information dominates over VC information in determining the identification of that consonant.

Byrd's experiment demonstrates that gestures may, in fact, fail to be recovered under conditions of extreme overlap. However, her study employed synthetic speech generated by a gestural model (as is true of similar experiments in German by Geumann and Kröger, 1995), and it is not clear that her stimuli preserve subtleties of gestural organization, from which listeners might recover an overlapped gesture, as discussed above. Nolan (1992) used naturally produced materials for a perceptual study of assimilation. He examined electropalatographic (EPG) production data for utterances with sequences of alveolar-velar consonants across word boundaries, such as ''road collapsed.'' In addition to examples produced with complete alveolar closure, he found examples in which the EPG indicated that the tongue tip gesture is reduced in magnitude so as to no longer produce a complete closure (''residual-alveolar'') and examples in which the tongue tip gesture is so reduced that there is no apparent tongue tip contact at all (''zero-alveolar''). Listeners were asked to identify these utterances and a set of control utterances in which the tongue tip gesture is not part of the phonetic intent (e.g., ''rogue collapsed''). Listeners correctly identified the ''residual-alveolar'' utterances with a greater than chance frequency, although the error rate was higher than for the examples with complete alveolar closure. ''Zero-alveolar'' utterances were not distinguished from the controls. Thus it appears that a tongue tip gesture is not recovered by the listener when it is reduced in magnitude by a certain degree. However, although Nolan suggested that there is a continuous change from full to nonexistent gestures, due to limitations of the contact measures employed, he was unable to systematically demonstrate continuous changes in perception with changes in degree of closure of the tongue tip. In addition, Nolan did not measure temporal overlap of the gestures involved, and thus, the study has nothing to say about the possibility of gestural hiding.

Taken together, the experiments by Nolan (1992) and Byrd (1992) indicate that the perceived assimilation can result from the failure to recover an intended gesture and that recoverability may be affected by at least two factors, the size of the gesture and the amount of overlap between two adjacent gestures. The two experiments reported here combine both factors and investigate listeners' responses to stimuli with naturally produced consonant sequences that show substantial gestural overlap. The stimuli, taken from an x-ray microbeam study, were chosen in order to maximize variation in overlap as well as in the size of the relevant gesture. X-ray data provide a means for quantifying the production data more precisely than would be possible in electropalatographic studies. The experiments were also designed to test the hypothesis (Browman and Goldstein, 1990, 1992; Byrd, 1992) that tongue tip gestures are more sensitive

to such hiding than lip gestures, a hypothesis that could account for the fact (Byrd, 1992) that in the phonology of many languages, coronal consonants assimilate more commonly to noncoronals than vice versa.

I. EXPERIMENT 1

The purpose of experiment 1 was to explore how the detection of a stop consonant gesture is affected by its size (as actually produced by a speaker) and the degree to which it is overlapped by a subsequent stop gesture. We compared the detection of stop consonant gestures when they are followed by a second (partially overlapping) stop gesture (''stop sequence'' condition) to the detection of stop gestures not immediately followed by another stop (''single stop'' condition) and then performed statistical analyses to investigate the potential contributions of gesture magnitude and overlap to the detectability scores. Natural speech tokens that were tracked by x-ray microbeam technology were used to measure the actual movements of the articulators.

A. Methods

1. Subjects

Subjects were 22 Purdue University undergraduates who volunteered to participate in exchange for credit in introductory psychology courses. Data from two subjects were discarded because they were not native speakers of American English.

2. Stimuli

The stimuli for the perceptual experiments were utterances for which articulatory data had been collected using the NIH x-ray microbeam system at the University of Wisconsin (Nadler *et al.*, 1987). Gold pellets were placed in a number of locations on the subject's tongue, jaw, and lips. The subject (a male student at the University of Wisconsin, who grew up in California) then read a set of three-word sentences (printed in normal English orthography), each starting with the word ''my'' and followed by a CVC word such as ''top.'' The CVC words had either voiceless labial (''p'') or voiceless alveolar (''t'') stops as the final consonant. The third word was a two-syllable verb (or nonsense verb) ''_uddles'' with the blank being filled by ''p,'' ''t,'' ''c,'' ''h.'' The subject was prompted to place contrastive accent on one of the three words of the phrase, by means of a contextualizing sentence that was displayed to the subject, but not read aloud, and by capitalizing the to be accented word. In the course of the experiment, all three stress patterns were recorded. Each phrase was produced five times in succession by the same male speaker and the movements of the pellets in relation to the fixed parts of the vocal tract were tracked by the system and synchronized with the acoustic signal. Analysis of gestural magnitude in these utterances, and in particular, the difference in magnitude between the initial and final C's in the CVC word can be found in Browman and Goldstein (1995).

The stimuli for the present study were chosen to compare perception of stimuli in which the oral gesture for a final stop is overlapped in time by the oral gesture for the stop consonant that begins the following word (''stop sequence context'') with stimuli in which there is no oral stop gesture at the beginning of the following word, and therefore the final stop gesture is not overlapped by another stop (''single stop context''). In addition, they were designed to compare the effect of overlap of labials on alveolars to the effect of alveolars on labials (e.g., ''tot puddles'' versus ''top tuttles''). All three stress patterns were used. The stimuli chosen for each monitoring condition are shown in Table I above. An equal number of stimuli that lacked the target (*Absent* column in Table I) were chosen as filler items. They also occurred in two forms: those involving a stop consonant sequence (''cuddles''), and those involving a single stop (''huddles'').

TABLE I. Stimuli used in the experiments. The stimuli for experiment 2 were identical to those of experiment 1 except that the stimuli were truncated during the acoustic closure following the initial CVC word.

Target		Present	Absent
''t''	stop sequence	tot puddles	top cuddles
	single stop	tot huddles	top huddles
''p''	stop sequence	top tuddles	tot cuddles
	single stop	top huddles	tot huddles

To choose particular stimulus tokens from the recorded x-ray material we examined the movements of pellets on tongue tip and lips, in particular, the vertical position of the tongue tip pellet (tongue tip height) and the vertical distance between the upper and lower lip pellets (lip aperture). Movements of these parameters have been used (Browman and Goldstein, 1988, 1995) to infer the timing (and size) of tongue tip closure gestures (e.g., in ''tot''), and bilabial closure gestures (e.g., in ''puddles''). An example of an output from the x-ray microbeam system is given in Fig. 1. The top of the figure shows the time functions of tongue tip height and lip aperture, while the bottom shows the two-dimensional positions of the relevant pellets) at a particular point in time (shown by the arrow just below the time axis),

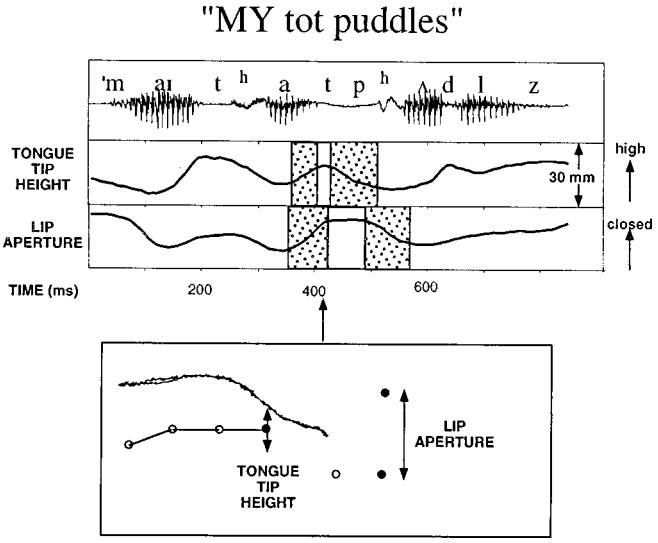

FIG. 1. An example of the output from the x-ray microbeam system. See text for further explanation.

with respect to a tracing of the subject's hard palate. The relevant pellets (one on the tongue tip and one on each lip) are represented by filled circles. The unfilled ones represent other pellets on the tongue and lower teeth. The subject was saying ''MY tot puddles.'' For both the tongue tip and lip closure gestures, three kinematic events associated with each gesture are shown. The first event, closing movement, is marked by the first shaded region; the second, held constriction peak or plateau, is the clear region between the two shaded regions; and the third, opening movement, is marked by the second shaded region. Note that, in this example, the closing movements of the two gestures overlap almost completely. For the perceptual experiment, we chose those three tokens (of the five produced in succession for each stress pattern) that exhibited a range of variation in both the magnitude of the tongue tip gesture (amount of movement shown by the closing and opening events) and degree of overlap between tongue tip and lip closing movements.

Stimuli were digitized from videotape (recorded during the x-ray session) onto an Apple Macintosh computer, using eight-bit digitization and a sampling rate of 22 kHz. The initial word (''my'') was excised (up to the silence for the initial stop in the CVC word) resulting in stimuli that ranged from approximately 600 to 800 ms in length.

The two monitoring conditions (monitor for ''t'' or ''p'') were blocked and presented in a counterbalanced order to each subject. Three different tokens of each of the four utterances for each of three different stress patterns were selected and presented four times for a total of 144 trials in each condition, half of which contained the target and half of which did not.

3. Apparatus

Stimuli were presented by an Apple Macintosh IIci computer, and played through Sony MDR-V5 headphones. Subjects were permitted to adjust the level of the sounds, during the practice phase, to a comfortable setting. Subjects responded by pressing a button on an external hardware box.

4. Procedure

The task used in this experiment was a phoneme monitoring (vigilance) task in which subjects were asked to press a button as quickly as possible when they heard a specific consonant. This task has been used extensively to explore the time course of word recognition (Foss and Blank, 1980; Marslen-Wilson and Tyler, 1980). The dependent variable in this type of experiment is usually response time. However, because we were mainly interested in determining whether the listeners heard the target, accuracy, rather than speed, was stressed to the subjects.

The targets (''t'' and ''p'') were presented in blocks and subjects were instructed to monitor for a different target after the first block. The following instructions were read to the subjects:

''You will be hearing nonsense utterances that consist of two words. What we would like you to do is to press a button as quickly as you can when you hear the sound (''tee as in tot''/''pee as in top''). You will be hearing only four possible sounds (t condition—tot puddles, top cuddles, tot huddles, top huddles; p condition—top tuddles, tot cuddles, top huddles, tot huddles). If you do not hear the sound (''tee''/''pee'') in the sequence, just don't press the button and wait for the next trial. If you do hear it, press the button as quickly as you can. Half of the sounds will have a (''tee''/''pee'') in them and half will not.''

In the ''t'' condition, subjects were given the following additional instructions:

''There will be a ''tee'' sound beginning each utterance but you are to ignore that and decide if there was a ''tee'' anywhere else in the word.''

There were ten practice trials before each block. On any given trial a message appeared in the center of the screen informing the subject that a trial was about to begin. After 100 ms, a letter appeared in the middle of the screen as a reminder of the target, and the stimulus was presented over the headphones. Subjects either pressed a button indicating that they had heard the target or waited for the next trial. Two seconds later the next trial began. The stimuli were presented in a new random order for each subject and the two target conditions were blocked and counterbalanced across subjects.

5. Stimulus measurements

For each stimulus token, the magnitude of the gestures and the amount that they overlapped were measured, so that these variables could be used as predictors of subjects' perceptual responses. The measurements were based on the three kinematic events associated with each gesture, as shown in Fig. 1. These events were detected automatically by finding curve extrema (peaks and valleys) with a noise band of 1 mm, that is, extrema plateaux within which the pellets move less than 1 mm. In Fig. 1, the held constriction peaks for tongue tip height and lip aperture were plateaux detected in this way. The closing movement for a stop gesture begins at the right edge of the preceding vowel's plateau and continues to the left edge of the constriction plateau for the stop gesture. The opening movement begins at the right edge of the stop's constriction plateau and continues to the left edge of the plateau for the following vowel. Once these events had been detected, the eleven magnitude and overlap measures listed in Table II were calculated. The first nine characterize properties of the individual gestures, and the last two characterize the temporal overlap between the gestures.

B. Results

The data were analyzed in two ways. First, we divided responses into categories of ''correct'' and ''incorrect'' based on what the speaker was asked to produce (and presumably intended to produce). Thus, if the speaker in the x-ray microbeam study was reading ''tot puddles,'' the ''correct'' response in the ''t'' condition would be a button press, i.e., the consonant was detected. Then, a simple analysis of variance was performed on the number of correct detections. This analysis is presented in the next section. However, given that we have measurements on continuous movements of the gestures, we can also use correlation analyses to relate

TABLE II. Gestural variables correlated with perceptual responses.

Lip Aperture (LA)	Vertical distance between upper and lower lips during constriction plateau (mm)
Δ Lip Aperture Closing (Δ LA Closing)	Change in Lip Aperture from beginning of closing movement to constriction plateau (mm)
Δ Lip Aperture Opening (Δ LA Opening)	Change in Lip Aperture from constriction plateau to the end of opening movement (mm)
Duration of LA Constriction Plateau (LA Duration)	Time from end of LA closing movement to the beginning of LA opening movement (ms)
Tongue Tip Height (TT)	Vertical position of tongue tip during constriction plateau (mm)
Δ Tongue Tip Closing (Δ TT Closing)	Change in tongue tip height from beginning of closing movement to constriction plateau (mm)
Δ Tongue Tip Opening (Δ TT Opening)	Change in tongue tip height from constriction plateau to end of opening movement (mm)
Duration of TT Constriction Plateau (TT Duration)	Time from end of TT closing movement to the beginning of TT opening movement (ms)
Duration of Cl Closing Movement	Time from beginning of closing movement (TT or LA, as appropriate) to constriction plateau (ms)
Closing Lag	Time between end of TT closing movement and end of LA closing movement (ms)
Opening Lag	Time between beginning of TT opening movement and beginning of LA opening movement (ms)

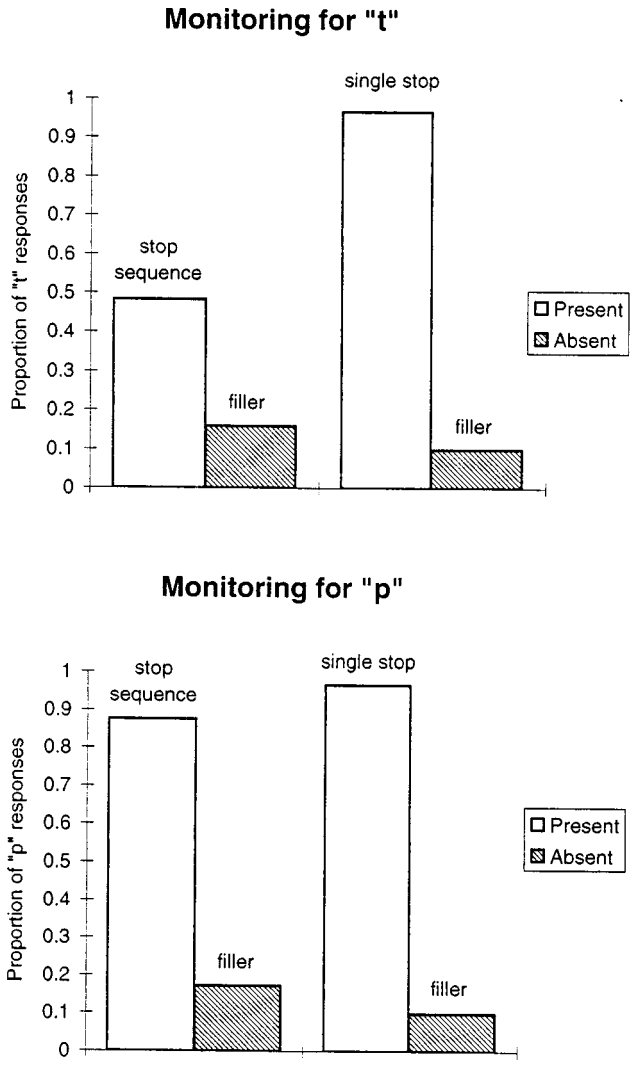

FIG. 2. Proportion of ''t'' (top panel) and ''p'' (bottom panel) responses as a function of presence or absence of the target for experiment 1.

the relative sizes of the gestures and the amount of their overlap to the consonant monitoring responses. These analyses are reported in the subsequent section.

1. Analysis of variance

Overall, subjects were performing the basic task accurately. Figure 2 shows the mean proportion of consonants detected as a function of utterance type for the ''t'' and ''p'' conditions. In addition, the figure shows the proportion of consonants incorrectly detected when the stimulus was not present (filler). As is evident in the top panel of the figure, the proportion of ''t'' responses to stop sequences was substantially lower than to the single stop stimuli. This difference is much smaller in the ''p'' condition (bottom panel). In both conditions there were few false alarms to the filler items.

With these data, we can perform a signal detection analysis. However, because in some conditions we have a large number of perfect discriminations which produce a false alarm rate of 0 or a hit rate of 1.0, or both, we used the nonparametric analog of d', A' (Pollack, 1970). This measure ranges from 0 to 1 where chance responding is 0.5. The resulting A' data were analyzed by means of analysis of variance, with factors corresponding to condition (''t'' vs ''p''), context (''stop sequence'' versus ''single stop''), accent, and order of production.

When the to-be-detected consonant was actually present, subjects responded more than when it was not present [$F(1,19)=95.31$, MSe$=0.05$, $p<0.01$]. In addition, the overall detectability (A') in the ''p'' condition (0.93) was greater than in the ''t'' condition (0.83), $F(1,19)=42.46$, MSe$=0.04$, $p<0.01$. That main effect is largely due the interaction of context and condition [$F(1,19)=41.09$, MSe $=0.04$, $p<0.01$]: In the ''p'' condition, there was a small effect of context with an A' of 0.89 for the stop sequence items compared to 0.70 for the stop sequence items in the ''t'' condition. In both conditions A' was 0.96 for the single stop targets.

For the present purposes, the main variable of interest is the difference in responses to the stop sequences compared to the single stops. Planned contrasts show that the effect of context was statistically significant in both the ''p'' [$F(1,19)=16.71$, MSe$=0.02$, $p<0.01$] and the ''t'' [$F(1,19)=91.22$, MSe$=0.06$, $p<0.01$] conditions. In addition, item analyses (see Clark, 1973, for a rationale and formulas for using MinF') show both effects to be reliable [''p''—$F(1,38)=6.33$, $p<0.05$; ''t''—$F(1,38)=61.46$, $p<0.01$] although the MinF' was reliable only in the ''t''

TABLE III. Experiment 1. Spearman's correlation coefficients for ranked data (r_s) between gestural variables and detections of the target (**$p<0.05$; *$p<0.10$). First row—''tot puddles,'' second row—''top tuddles.''

	LA	Δ LA closing	Δ LA opening	LA duration	TT	Δ TT closing	Closing duration	Δ TT opening	TT duration	Closing lag	Opening lag
t	−0.19	−0.76**	0.71**	0.07	0.52	−0.10	−0.23	0.63*	0.46	0.64*	0.74**
p	−0.01	0.26	−0.05	0.36	0.20	0.17	0.15	0.21	0.09	0.45	0.19

condition [''p''—Min$F'(1,54)=3.76$, $p=0.06$; ''t''—Min$F'(1,54)=35.37$, $p<0.01$].

Each token was spoken by the subject in the x-ray microbeam study in three possible stress patterns; either the initial, the middle, or the final word of the phrase was stressed (''MY,'' ''CVC,'' or ''_UDDLES''). Although we had made no *a priori* predictions about the effect of stress pattern on detection of a particular consonant, the interactions of condition, stress and context were interesting. There was a main effect of stress, with detectability increasing as the stress moved from the first to the last word [$F(2,19)=14.41$, MSe$=0.02$, $p<0.05$]. All of the two-way interactions with stress were reliable and can be interpreted by examining the three-way interaction of condition, stress, and context [$F(2,38)=10.16$, MSe$=0.02$, $p<0.05$]. This interaction can be attributed to the effect of stress being different for the ''t'' and the ''p'' conditions. In both conditions, there was a ceiling effect for the single stop stimuli with all stress conditions having an A' greater than 0.95. However, in the stop sequence conditions, when the target was ''t,'' there was an increase in detectability from the first to the final word stressed (0.64, 0.65, 0.81, respectively) but when the target was ''p'' that increase occurred when the second word was stressed (0.83, 0.94, 0.91). The reduced effect of context, resulting in increased detectability, for ''t'' when the final word is stressed could be due to the fact that, in the production subject's data, final alveolar stops are sharply reduced in magnitude when accent is on the first or second words, but they are not as reduced when the accent is on the final word (Browman and Goldstein, 1995).

The final variable of interest was the order in which the tokens were initially produced. Each phrase was produced five times in rapid succession and, because deletions and assimilations generally increase in rapid speech (Browman and Goldstein, 1995), it is likely that the amount of assimilation or consonant deletion increased from the first utterance to the last. The main effect of order was statistically significant with detections decreasing as the utterance was pronounced in the beginning to the end of the trial [$F(2,38)=3.65$, MSe$=0.02$, $p<0.05$]. The three-way interaction among condition, context and order was also reliable [$F(2,38)=3.67$, MSe$=0.07$, $p<0.05$]. As with the stress variable, there was a ceiling effect in the single stop condition, with delectability greater than 0.95 for all orders of pronunciation. For the stop sequence conditions, detectability decreased with order of pronunciation for the ''t'' (0.78, 0.66, 0.66) condition but not for the ''p'' condition (0.90, 0.88, 0.89).

One other effect was statistically significant: There was a reliable three-way interaction involving context, stress, and order [$F(2,38)=4.23$, MSe$=0.02$, $p<0.01$] due primarily to a lack of effect of stress and order in the single stop conditions.

2. Correlational analyses

The analyses reported above indicate that alveolar stops were detected significantly less often in the stop sequence condition than in the single stop condition. Given the availability of articulatory data on different tokens used in the experiment, we wanted to see to what extent variation in the detectability of these alveolar consonants in the stop sequence condition could be predicted from variation in the gestural pattern: the spatial extent of the alveolar gesture, the spatial extent of the overlapping labial gesture, and the degree of overlap between the two.

Each token of ''tot puddles'' was analyzed separately and gestural extent and overlap was characterized in terms of the factors in Table II. These factors were correlated, using Spearman's correlation coefficient for ranked data (r_S) with the mean number of target detections for each utterance. The correlations between the detection of the target and articulatory factors for the utterances containing ''t'' are shown in the top line of Table III. It is evident that factors characterizing the size of both gestures and the degree of overlap help determine detectability, although the correlations reach significance only for the three largest correlations: Opening Lag (the time between the beginning of lowering of the tongue tip and the beginning of opening of the lips—$r_S=0.74$, $p<0.05$), Δ LA closing (the change in lip aperture from the beginning of the closing movement to the constriction plateau—$r_S=-0.76$, $p<0.05$), and Δ LA opening (the change in lip aperture from the constriction plateau to the end of the opening movement—$r_S=0.71$, $p<0.05$).

The significant correlation of Opening Lag and detection supports the role of gestural overlap in detectability. The longer this interval (indicating greater separation, and thus less overlap between the gestures), the greater the detectability of the target. The correlations involving lip aperture are also consistent with the hypothesis that the tongue tip gesture may be ''hidden'' by the lip gesture. The change in lip aperture (LA) during lip closing correlated negatively with detectability: larger lip movements resulted in reduced detectability. The change in LA during opening also correlated with detectability, but with the opposite sign. The reason for the reversal of sign seems to be that the value of LA attained during the ''p'' closure is fairly stable across all tokens, and that differences in LA change are associated with different values of LA during the preceding and following vowels. The LA during the vowels of the words ''tot'' and ''puddles'' are negatively correlated with one another because of stress: when stress is on ''tot'' LA is much wider

for the vowel in ''tot'' than for the vowel in ''puddles.'' The reverse is true when ''puddles'' is stressed. Thus if larger changes of LA during the closing movement help to reduce detectability of ''t,'' then changes of LA during opening will, necessarily, be correlated positively with detectability.

The size of the tongue tip gesture, as measured by the height of the tongue tip at gesture peak (TT—$r_s = 0.52$, $p = 0.14$), or by the change in tongue-tip height during opening (Δ TT Opening—$r_s = 0.63$, $p = 0.06$), also showed substantial positive correlations with target detection, although these did not reach significance. The larger the tongue tip gesture, the greater the likelihood of it being perceived.

Correlational analyses of ''p'' responses with properties of the gestures in ''top tuddles'' utterances (shown in the second line of Table III) were not very revealing. This is because the range of responses was quite restricted (0.74–0.98). The comparable range for the proportion of ''t'' responses is 0.18–0.74. The actual Spearman rank-order correlations of each factor and number of responses are included in Table III; none were even marginally reliable.

C. Discussion

Experiment 1 showed, using natural speech tokens, that a stop gesture was less likely to be detected when it was followed by an overlapping stop gesture than when there was no following stop. This result, by itself, is consistent with previous studies which show that the release a of stop gesture is more perceptually informative than its closing movement (Malecot, 1958; Wang, 1959; Repp, 1978; Fujimura *et al.*, 1978; Dorman *et al.*, 1979; Ohala, 1990). In addition, however, for the t#p condition of the present experiment, we were able to use correlations between articulatory measures and detection rates to show that token-to-token variation in detectability was related to the degree of overlap of the two closure gestures and to the size of the potentially interfering (or ''hiding'') closing movement for the second stop. The greatest predictor of detection of a final ''t'' was the time between the end of the tongue tip closure and the end of the lip closure. In other words, the larger the temporal distance between the gestures in production (as indexed by this measure), the more likely the first was to be detected. The size of the lip gesture (Δ LA Closing, Δ LA Opening) also correlated significantly with detectability of ''t.''

It is worth considering why it is that Opening Lag is the overlap index that best predicts detectability (better than Closing Lag). This correlation would seem to point to the perceptual importance of the tongue tip opening movement, yet this is not likely the case for these stimuli, since in every case the tongue tip gesture is always acoustically ''unreleased.'' That is, there is no release burst associated with the lowering of the tongue tip. This is due to the fact that for every stimulus the beginning of tongue tip lowering occurs during the held LA constriction, that is, when the lips are closed. In fact, virtually all of the TT opening is completed by the time the lips begin to open. Thus the perceptually relevant information for the tongue tip gesture in this context must be the closing movement of the tongue tip. (This will be tested directly in experiment 2, in which the stimuli are truncated during the acoustic closure, so that only the closing movements can be perceptually relevant.) Detectability may be hindered to the extent to which lip closure is also taking place during this tip closing interval, and so the ideal predictor of detectability ought to be how much acoustically relevant lip closure is taking place during the tip closure interval. Since the onsets of tongue tip and lip movements are generally synchronous, the length of time between end of closing movements (Closing Lag) might have been expected to be a good approximation to this ideal predictor. However, the movement data show that the end of closing movement is ambiguous for LA. There is typically a long shallow slope atop the lip plateau, and the automatically determined point for the end of closing movement can be located at a variety of points along that plateau. On the other hand, the beginning of lip opening is clear in these signals, and well captured by the automatically determined point. Thus if there is a systematic relation between the time of opening of the lips and the ''true'' (and acoustically relevant) end of the lip closing movement (not an unreasonable assumption), Opening Lag may be providing a better measure of acoustically relevant overlap during the tip closing interval than is Closing Lag.

Another important finding of the present experiment is the asymmetry between the t#p and p#t utterances. The effect of a following stop on detectability was much greater for the t#p utterances. Byrd (1992) reports a similar finding with her synthesized stimuli, although the extent of the asymmetry does not appear to be as strong as in the present experiment. A number of explanations for such an asymmetry can be considered. One possible explanation that Byrd gives is that the formant frequencies that result (just before complete closure) from exactly simultaneous lip and tongue tip constrictions are closer to those that result from a lip closure alone than those that result from a tongue tip closure alone. This explanation cannot be tested directly here, as we have no stimuli in which the two gestures are perfectly synchronous.

Browman and Goldstein (1990) suggest an explanation for this asymmetry based on the kinematic properties of tongue tip and lip gestures. In particular, they note that tongue tip gestures have been found (e.g., by Kuehn and Moll, 1976) to involve higher velocities of movement than lip or tongue dorsum gestures and they hypothesize that a faster gesture might be easier to hide perceptually. However, Kuehn and Moll's observations of nonsense VCVC utterances do not appear to extend to the contexts tested here, as the mean of the average closing velocities for the tongue tip in t#p utterances was 141 mm/s, and that for Lip Aperture in p#t utterances was 198 mm/s.

Another hypothesis for this asymmetry implicates the role of acoustic closure duration. As is well known (see, e.g., Repp, 1978; Dorman *et al.*, 1979; Ohala, 1990), when closure durations of VCCV utterances are (artificially) shortened beyond the values typically observed in natural speech, listeners report hearing only a single consonant, usually the second of the two. Thus it would be important to determine if the t#p and p#t utterances in the present experiment differed in closure duration. However, the average closure du-

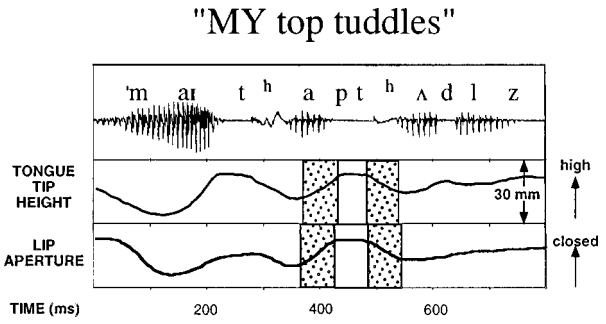

FIG. 3. Example of a token of ''MY top tuttles.'' See text for further explanation.

ration was, in fact, about the same in the p#t (87 ms) and the t#p (85 ms) utterances.

Another possible explanation implicates the role of overlap during the release phase of the two closure gestures. As noted above, in the t#p stimuli the tongue tip release movement is already completed by the time of release of the lips. This can be seen in the example token shown in Fig. 1. However, the parallel state of affairs does not hold for the p#t stimuli. Figure 3 shows the time functions of tongue tip height and lip aperture in an example token of ''MY top tuddles.'' Here, the lips are just starting to open as the tongue tip is lowered. Thus there is potential lip information available at the release of p#t stimuli, but no tongue tip information available at the release of t#p stimuli. To the extent that this is a contributing factor to the obtained asymmetry, we would expect that if the stimuli were truncated during the closure, the asymmetry between the conditions would be reduced, as the p#t condition responses would become less detectable (because information at release is removed). Experiment 2 tests this prediction.

II. EXPERIMENT 2

Experiment 2 was an exact replication of experiment 1 with one change: The utterances were truncated at the closure at the end of the CVC word. As argued above, the release information explanations for the order asymmetry obtained in experiment 1 would predict that the asymmetry will be reduced when the stimuli are truncated.

A. Methods

1. Subjects

Twenty different Purdue University undergraduates volunteered to participate in exchange for credit in introductory psychology courses. All were native speakers of American English.

2. Stimuli

The stimuli for experiment 2 were identical to those of experiment 1 except that they were truncated during the closure interval at the end of the CVC word. This was done by digitally cutting the stimulus in this silent interval, resulting in stimuli that ranged from approximately 200 to 300 ms in duration.

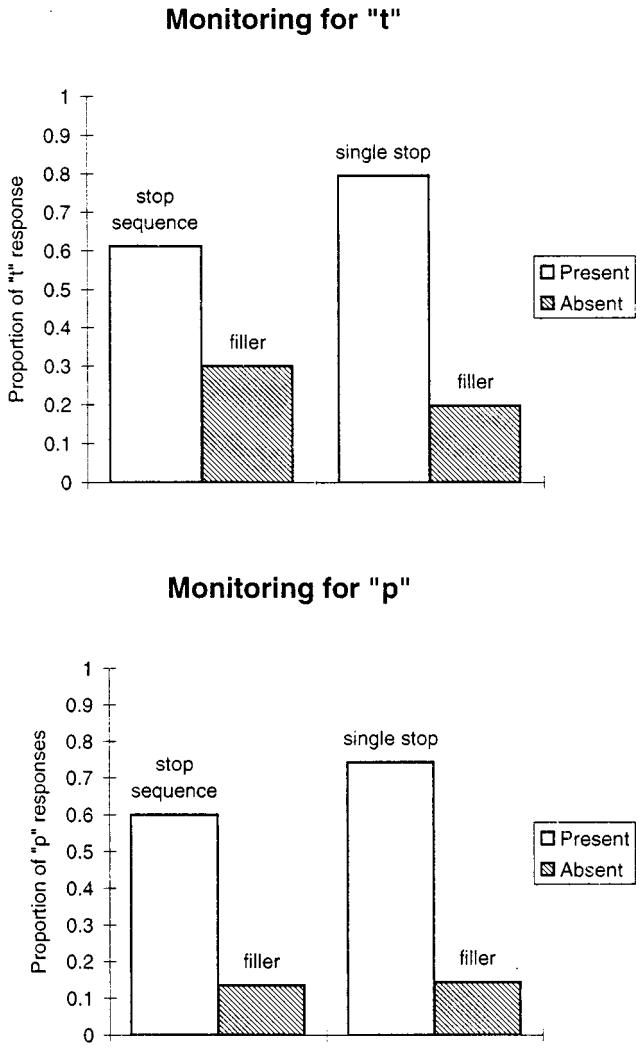

FIG. 4. Proportion of ''t'' (top panel) and ''p'' (bottom panel) responses as a function of presence or absence of the target for experiment 2.

B. Results

1. ANOVAs

As in experiment 1, we first divided responses into categories of ''correct'' and ''incorrect'' based on what the speaker was asked to produce (and presumably intended to produce). Thus if the speaker in the x-ray microbeam study was reading ''tot puddles,'' the ''correct'' response in the ''t'' condition would be a button press, i.e., the consonant was detected. Although subjects were performing the basic task accurately (see Fig. 4), there were more false alarms to the filler utterances (dark bars), especially in the ''t'' condition (top panel) than in experiment 1.

As in the previous experiment, we transformed the hits and false alarms into A' for the statistical analyses. Unlike in experiment 1, there was no reliable difference overall between ''t'' and ''p'' responses [$F(1,19)=4.00$, MSe$=0.07$, $p=0.06$]. The main effect of context was significant [$F(1,19)=38.2$, MSe$=0.05$, $p<0.01$] as was the interaction of context and condition [$F(1,19)=5.9$, MSe$=0.05$, $p<0.05$]. Looking at the means, it seems that the size of the context effect was still larger in the ''t'' condition (0.70, 0.84) than in the ''p'' condition (0.78, 0.84). The difference

TABLE IV. Experiment 2. Spearman's correlation coefficients for ranked data (r_s) between gestural variables and detections of the target (**$p<0.05$; *$p<0.10$). First row—''tot [puddles],'' second row—''top [tuddles].''

	LA	Δ LA closing	Δ LA opening	LA duration	TT	Δ TT closing	Δ TT opening	Closing duration	TT duration	Closing lag	Opening lag
t	−0.23	−0.62*	0.54	0.17	0.51	−0.03	0.60*	−0.19	0.26	0.41	0.82**
p	−0.07	0.70**	−0.63*	0.46	−0.05	0.49	−0.37	−0.20	−0.50	−0.71**	−0.46

in the size of the context effect is, however, much smaller than for experiment 1 (see below). In addition, item analyses show context to be significant for both conditions [''p''—$F(1,38)=5.28$, $p<0.05$; ''t''—$F(1,38)=18.37$, $p<0.01$] although the MinF' was reliable only in the ''t'' condition [''p''—Min$F'(1,54)=3.64$, $p=0.06$; ''t''—Min$F''(1,54)=10.98$, $p<0.01$].

There was a main effect of stress [$F(2,38)=7.51$, MSe $=0.05$, $p<0.05$] with detections increasing from the first to the second word stressed but no appreciable difference between the second and third word stressed (0.75, 0.82, 0.81). As in experiment 1, there was little effect of stress on detection of the single stop stimuli (0.81, 0.84, 0.89 for the three stress levels) but there was an increase in detection as a function of stress for the stop sequence stimuli (0.68, 0.80, 0.73). This is evident in the interaction of context and stress [$F(4,76)=2.80$, MSe$=0.02$, $p<0.05$]. There was also an interaction of stress and production order with the largest effect of order being on the initial stress pattern with decreasing effects of order on the second and third position stress patterns. Finally, there was a three-way interaction of condition, overlap, and stress [$F(2,38)=9.34$, MSe$=0.05$, $p<0.05$]. Inspection of the means reveals that this is due to an actual decrease in detectability of the ''p'' segment in the single stop condition as compared to the stop sequence context when the stress is on the word ''top'' in the stimulus.

Finally, there was a main effect of order with detections decreasing from the first to the third repetition produced [$F(2,38)=8.08$, MSe$=0.04$, $p<0.05$]. In addition to the effects described above, pronunciation order also interacted with the monitoring condition [$F(2,38)=17.80$, MSe $=0.03$, $p<0.05$] with a larger effect of order emerging in the ''t'' condition than in the ''p'' condition. There was also significant interaction of order and context [$F(2,38)=6.53$, MSe$=0.03$, $p<0.05$] with a larger effect of order on the stop sequence as compared to the single stop stimuli.

In order to test the hypotheses about the basis for the t#p—p#t asymmetry observed in experiment 1, it is useful to compare the results of the two experiments quantitatively. Because the two experiments are identical in design as well as the number of subjects, it is possible to consider them to be two conditions of a between-subjects design and compare the experiments directly in a statistical analysis.

The purpose of the following analysis is to compare the two experiments in terms of the two different types of context and the two monitoring conditions so we collapsed across stress pattern and order. Thus we performed a three-way mixed ANOVA with experiment (between-subjects), monitoring condition (''t,'' ''p''), and context (single stop, stop sequence) as the factors. All of the main effects and interactions were statistically significant with no F value below 5.0 and no p value of less than 0.05. The significant main effect of experiment indicates that subjects performed generally worse in experiment 2, as would be expected based on the removal of release information. However, the effect of experiment was not uniform, as indicated by the significant interactions. It is evident comparing Figs. 2 and 4 that the t#p—p#t asymmetry is weaker in experiment 2 (as predicted by the released information hypothesis), and the significant three-way interaction can be interpreted as confirming this reduction statistically.

To further evaluate the release information hypothesis, we examined the two-way experiment by context interaction separately for ''t'' and ''p'' (which is justified in light of the significant three-way interaction). The two-way interaction was significant in the ''t'' condition [$F(1,38)=8.09$, MSe $=0.007$, $p<0.01$] but did not approach significance in the ''p'' condition [$F(1,38)<1$]. Performance in both contexts of the ''p'' condition fell by the same amount. In the ''t'' condition, however, detection performance decreased only in the single stop context and stayed almost exactly the same in the stop sequence (t#p) context.

This pattern of results can be explained by the fact that release information is removed in experiment 2. Obviously in the single stop condition, releases contain information about the critical consonant, and that information is removed. In addition, according to the release information account of the asymmetry in experiment 1, there is significant information about ''p'' in the p#t releases. This account is strongly supported by the fact that the decrement in performance in experiment 2 is about the same for the p#t condition as it is in the p#h condition: ''p'' release information is important in both cases. Likewise it explains why there is no decrement in the t#p condition, since it hypothesized that there no information about ''t'' in the t#p releases (see Fig. 3).

Finally, the fact that there is still a significant context by condition interaction in experiment 2, even though it is weaker, suggests that other factors, such as the acoustic one hypothesized by Byrd (1992) may also be contributing to an asymmetry between t#p and p#t.

2. Correlational analyses

Table IV shows Spearman's rank order correlations between gestural measurements and the detection of the target consonant. For ''t'' (first row), the pattern of correlations are similar to those in experiment 1, although almost universally smaller in value. The factor showing the largest correlation with the detection of the target is the Opening Lag, as it was in experiment 1. That this factor also showed the largest correlation with detectability in this experiment ($r_s=0.82$,

$p<0.05$), supports the analysis suggested above, that the strong correlation of Opening Lag was not due to any perceptual importance of the relative timing of the gestures' releases, but rather occurred because Opening Lag might capture the amount of acoustically relevant overlap during the gestures' closing phases. In experiment 2, the actual constriction openings are necessarily perceptually irrelevant: The stimulus is cut before either gesture is released. Although listeners only hear the gestures' closing phases, Opening Lag is the largest predictor of perceptual responses.

A closer look at the data reveals that responses to the truncated ''tot p'' in this experiment were highly correlated with the intact ''tot puddles'' in experiment 1 ($r_s=0.92$; $p<0.05$). In contrast, the correlation between responses to ''tot h'' and ''tot huddles'' was -0.42 ($p=0.19$). This is consistent with the view that all of the information relevant to perception of final ''t'' in the context of a following ''p'' is, in fact, in the closing movements, even in the intact forms of experiment 1.

In contrast to experiment 1, there were some reliable correlations between the number of ''p'' responses and the articulatory measurements. In particular, Δ LA Closing was highly correlated with the detectability of the target ($r_s=0.70$, $p<0.05$) indicating that when the movement into the lip gesture is large, detectability of ''p'' increases. The Closing Lag was a reliable predictor of detectability ($r_s=-0.71$, $p<0.05$) showing that the larger the separation between the two gestures, the larger the detectability of the target. The sign is reversed in the Closing Lag factor (compared to the Opening Lag) because the measurement is from the beginning of the TT movement to the beginning of the lip movement. The fact that such correlations only emerge in experiment 2 again supports the hypothesis that lip information is being perceived during the release of p#t stimuli. When such information is removed, and the only information available occurs during the closing movements, the kinematic characterization of the closing gestures and their overlap affect detectability.

C. Discussion

The results of this experiment were consistent with those of experiment 1, especially as regards the perception of a final ''t'' when it is produced in the context of a following overlapping stop. One difference between the experiments is that there were generally fewer correct detections of the target in experiment 2, when the stimuli were truncated during the medial closure(s). This effect was especially evident for the single stop condition, when the final gestures were not followed by an overlapping oral stop beginning the next word, but instead by /h/. The reason for this difference seems straightforward. In experiment 1, there are two sources of information that can lead to the detection of the final stop in these single stop stimuli: the closing movement of the stop gesture, and the opening (or release) movement. In experiment 2, this opening movement has been cut off, and the closing movement is all that is available. Without the opening movement, the amount of information specifying the gesture is reduced, and uncertainty increases. Moreover, the ability of listeners to perceive place information correctly based only on VC movements is relatively poor, as found in the studies listed previously. This would account for the fact that the decrement in performance is primarily observed for the single stops in the ''t'' condition, since it is only these overt finals that have audible opening movements in experiment 1. For stimuli like ''tot puddles,'' the opening movement for the final alveolar stop is almost completely achieved by the time the labial closure begins to open (within 7 ms) so this tongue tip opening information is no more available in experiment 1 than it is in experiment 2 for these stimuli. For the ''p'' condition, decrement occurs in both single stop and stop sequence contexts. This also seems to be explicable on the basis of the timing of the release movements. For overlapped stimuli like ''top tuttles,'' the opening movements for the final labial and the following tongue tip gestures are almost synchronous (the labial leads by a very small amount, about 10 ms), but this means that some of the labial opening information is available to listeners in this condition in experiment 1, but not in experiment 2. Thus for ''p'' stimuli, performance would be expected to be reduced in both single stop and stop sequence contexts.

The differences in results between experiments 1 and 2 cannot be well explained by the hypothesis that listeners are using closure duration as a ''cue'' for whether they hear one or two consonants. That hypothesis might predict an improvement in detectability for the stop sequence condition in experiment 2 over that in experiment 1, as the potentially short closure durations of experiment 1 could bias listeners to hear a single consonant, whose identity would be dominated by the release information. Such an improvement was, in fact, exhibited in Byrd's (1992) study. While it is not clear how to explain this difference between the studies, it should be noted that even in Byrd's study, the asymmetry between alveolar-labial and labial-alveolar sequences is less pronounced when truncated stimuli are employed.

The absence of the opening movements in experiment 2 could also account for the patterns observed in the correlation results. If the t#p stimuli have essentially the same gestural information available to listeners in experiments 1 and 2, as suggested above, then one would expect the same pattern of correlations with the articulatory measures in the two experiments, and that is, indeed, what was found. On the other hand, the gestural information available to the listeners in the p#t condition is different in the two experiments, because lip opening information *is* available to listeners in experiment 1, but not in experiment 2. In the absence of the opening information (and the attendant increase in uncertainty), aspects of the magnitude of the labial closure and the degree of overlap become important determinants of detectability, and this accounts for the significant correlations observed in experiment 2, but not in experiment 1.

III. GENERAL DISCUSSION

These two experiments show a significant reduction in the number of detections of a word-final alveolar consonant if it is partially or completely overlapped by a labial consonant gesture that begins the following word. A final labial does not suffer this decrement in detection to such an extent when overlapped by a following alveolar. This asymmetrical

pattern replicates the perceptual results obtained by Byrd (1992) with synthetic speech and can be used to explain the direction of the assimilation tendencies observed in English and other languages (Browman and Goldstein, 1990; Byrd, 1992). The results of the two experiments combined suggest that one major factor contributing to this asymmetry is that a word-final tongue tip gesture is short in duration and that its release does not, therefore, overlap the release of the following labial. This reduced duration could be viewed as part of a general reduction of the final tongue tip gestures, which involves spatial reduction (Browman and Goldstein, 1995; Byrd, 1996; Giles and Moll, 1975) as well as this temporal reduction.

More generally, the results obtained show that variation in degree of overlap among gestural units has measurable consequences in listeners' ability to detect the presence of those gestures, even when that variation is within the range of natural speech. Detection of final ''t'' is poorer when the tongue tip closing gesture is more overlapped by a following labial closure gesture. Such results provide some realistic boundary conditions for theories that propose that listeners recover the gestures of the talker (e.g., Liberman and Mattingly, 1985; Fowler and Rosenblum, 1991). For his/her part, the talker may respect these limitations on recoverability. Recall that, in general, tokens produced early in the list by the talker exhibited better recognition than those produced late in the list. The talker may ''intend'' to allow more gestural reduction and overlap in circumstances in which the utterance can be assumed (by virtue of repetition) to be redundant (for related views of the role of informational context on production, see Fowler and Housum, 1987; Lindblom, 1990; Sotillo *et al.*, 1995).

Interestingly, the results support the view that gestural overlap can also have beneficial perceptual consequences. The detection of final ''p'' in ''top tuddles'' appears to benefit from the lip release movement that overlaps the tongue tip release for the initial ''t.'' The listener appears to be able to use the acoustic signal at the release of the closure in ''top tuddles'' to provide information about the presence of both a tongue tip gesture and a lip gesture. Such a result is consistent with the ''vector-analysis'' view (e.g., Fowler and Smith, 1986) of how overlapped gestures are decomposed perceptually as well as with motor theory's general claim that the speech system is specifically designed to recover coproduced gestures. However, previous observations have focused on the perception of overlapping consonant and vowel gestures, while the present results argue that similar evidence can be found in the domain of consonant–consonant gesture overlap. It remains for future work to determine in what circumstances overlap can be correctly parsed by listeners (and therefore used beneficially in recovery) and in what circumstances overlap impedes recoverability. The stimuli used in these experiments include examples of both types.

Knowledge of the conditions under which gestural recovery can fail may contribute to an account of the kinds of gestural structures that languages tend to employ in their phonologies (e.g., Mattingly, 1981; Byrd, 1992; Silverman, 1995), as well as to an account of how gestural structures may change over historical time (e.g., ''listener-based'' sound changes, of the kind that have been discussed by Ohala, 1981). Surprisingly, few studies have systematically examined correlations between articulatory variability and perception of speech. These experiments add to the small literature correlating speech production measures with perceptual data. Although it seems obvious that the variability in movements of the vocal tract would be correlated with how gestures are perceived, there are few direct experimental demonstrations of this.

ACKNOWLEDGMENTS

This research was supported by an individual NIH National Research Service Award to the first author and by NICHD Grant No. HD 01994 to Haskins Laboratories. Portions of these experiments were presented at the 125th Meeting of the Acoustical Society of America, Ottawa, Ontario, Canada. Correspondence may be addressed to Aimée M. Surprenant, 1364 Psychological Sciences Bldg., Purdue University, West Lafayette, IN 47907-1364, email: aimee@psych.purdue.edu. The authors wish to thank Dr. Ian Neath for help conducting the experiments and for comments on an earlier version of the manuscript, and Dr. Michael Studdert-Kennedy and Dr. Ignatius Mattingly for their comments.

Browman, C. P., and Goldstein, L. (**1988**). ''Some notes on syllable structure in articulatory phonology,'' Phonetica **45**, 140–155.

Browman, C. P., and Goldstein, L. (**1990**). ''Tiers in articulatory phonology, with some implications for casual speech,'' in *Papers in Laboratory Phonology I: Between the Grammar and Physics of Speech*, edited by J. Kingston and M. Beckman (Cambridge U.P., Cambridge), pp. 341–376.

Browman, C. P., and Goldstein, L. (**1991**). ''Gestural Structures: Distinctiveness, phonological processes, and historical change,'' in *Modularity and the Motor Theory of Speech Perception*, edited by I. G. Mattingly and M. Studdert-Kennedy (Erlbaum, Hillsdale, NJ), pp. 313–338.

Browman, C. P., and Goldstein, L. (**1992**). ''Articulatory phonology: An overview,'' Phonetica **49**, 155–180.

Browman, C. P., and Goldstein, L. (**1995**). ''Gestural syllable position effects in American English,'' in *Producing Speech: Contemporary Issues. For Katherine Safford Harris*, edited by F. Bell-Berti and L. J. Raphael (American Institute of Physics, Woodbury, NY), pp. 19–34.

Brown, G. (**1977**). *Listening to Spoken English* (Longman, London).

Byrd, D. (**1992**). ''Perception of assimilation in consonant clusters: A gestural model,'' Phonetica **49**, 1–24.

Byrd, D. (**1996**). ''Influences on articulatory timing in consonant sequences,'' J. Phonet. **24**, 209–244.

Clark, H. H. (**1973**). ''The language-as-fixed-effect fallacy: A critique of language statistics in psychological research,'' J. Verb. Learn. Verb. Beh. **12**, 335–359.

Dorman, M. F., Raphael, L. J., and Liberman, A. M. (**1979**). ''Some experiments on the sound of silence in phonetic perception,'' J. Acoust. Soc. Am. **65**, 1518–1532.

Foss, D. J., and Blank, M. A. (**1980**). ''Identifying the speech codes,'' Cogn. Psychol. **12**, 1–31.

Fowler, C. (**1986**). ''An event approach to the study of speech perception from a direct-realist perspective,'' J. Phonet. **14**, 3–28.

Fowler, C. A., and Housum, J. (**1987**). ''Talkers' signaling of ''new'' and ''old'' words in speech and listeners' perception and use of the distinction,'' J. Mem. Lang. **26**, 489–504.

Fowler, C. A., and Rosenblum, L. D. (**1991**). ''The perception of phonetic gestures,'' in *Modularity and the Motor Theory of Speech Perception*, edited by I. G. Mattingly and M. Studdert-Kennedy (Erlbaum, Hillsdale, NJ), pp. 33–59.

Fowler, C. A., and Smith, M. (**1986**). ''Speech perception as ''vector analysis'': An approach to the problems of segmentation and invariance,'' in *Invariance and Variability in Speech Processes*, edited by J. Perkell and D. Klatt (Erlbaum, Hillsdale, NJ), pp. 123–136.

Fujimura, O., Macchi, M. J., and Streeter, L. A. (**1978**). ''Perception of stop consonants with conflicting transitional cues: A cross-linguistic study,'' Lang. Speech. **21**, 337–346.

Geumann, A., and Kröger, B. (**1995**). ''Some implications for gestural underspecification as a result of the analysis of German /t/ assimilation,'' in Proceedings of the XIIIth International Congress of Phonetic Sciences, edited by K. Elenius and P. Branderud (ICPhS 95) (KTH and Stockholm University, Stockholm).

Giles, S., and Moll, K. (**1975**). ''Cinefluorographic study of selected allophones of English /l/,'' Phonetica **31**, 206–227.

Kuehn, D. P., and Moll, K. (**1976**). ''A cineradiographic study of VC and CV articulatory velocities,'' J. Phonet. **4**, 303–320.

Liberman, A. M., Cooper, F. S., Shankweiler, D. P., and Studdert-Kennedy, M. (**1967**). ''Perception of the speech code,'' Psychol. Rev. **74**, 431–461.

Liberman, A. M., and Mattingly, I. G. (**1985**). ''The motor theory of speech perception, revised,'' Cognition **21**, 1–36.

Lindblom, B. (**1990**). ''Explaining phonetic variation: A sketch of the H and H theory,'' in *Speech Production and Speech Modeling*, edited by W. J. Hardcastle and A. Marchal (Kluwer Academic, Dordrecht, The Netherlands), pp. 403–439.

Malecot, A. (**1956**). ''Acoustic cues for nasal consonants: An experimental study involving a tape-splicing technique,'' Language **32**, 274–284.

Marslen-Wilson, W., and Tyler, L. K. (**1980**). ''The temporal structure of spoken language understanding,'' Cognition **8**, 1–71.

Mattingly, I. G. (**1981**). ''Phonetic representation and speech synthesis by rule,'' in *The Cognitive Representation of Speech*, edited by T. Myers, J. Laver, and J. Anderson (North-Holland, Amsterdam), pp. 415–420.

Nadler, R. D., Abbs, J. H., and Fujimura, O. (**1987**). ''Speech movement research using the new x-ray microbeam system,'' University of Wisconsin Speech Motor Control Laboratories Preprints, pp. 181–184.

Nolan, F. (**1992**). ''The descriptive role of segments: Evidence from Assimilation,'' in *Papers in Laboratory Phonology II: Gesture, Segment, Prosody*, edited by G. Docherty and D. R. Ladd (Cambridge U.P., Cambridge).

Ohala, J. (**1981**). ''The listener as a source of sound change,'' in *Papers from a Parasession on Language and Behavior*, edited by C. S. Masek, R. A. Hendrick, and M. F. Miller (Chicago Linguistics Society, Chicago), pp. 178–203.

Ohala, J. (**1990**). ''The phonetics and phonology of aspects of assimilation,'' in *Papers in Laboratory Phonology I: Between the Grammar and the Physics of Speech*, edited by J. Kingston and M. E. Beckman (Cambridge U.P., Cambridge), pp. 258–275.

Pollack, I. (**1970**). ''A nonparamentric procedure for evaluation of true and false positives,'' Behav. Res. Methods Instrum. **2**, 155–156.

Repp, B. (**1978**). ''Perceptual integration and differentiation of spectral cues for intervocalic stop consonants,'' Percept. Psychophys. **24**, 471–485.

Rubin, P., Baer, T., and Mermelstein, P. (**1981**). ''An articulatory synthesizer for perceptual research,'' J. Acoust. Soc. Am. **70**, 321–328.

Saltzman, E., and Munhall, K. G. (**1989**). ''A dynamical approach to gestural patterning in speech production,'' Ecol. Psych. **1**, 333–382.

Silverman, D. (**1995**). ''Phasing and recoverability,'' Doctoral dissertation, Department of Linguistics. UCLA.

Sotillo, C., McAllister, J., Bard, E. G., Doherty-Sneddon, G., and Newlands, A. (**1995**). ''Word intelligibility and place assimilation in spontaneous speech,'' in *Proceedings of the XIIIth International Congress of Phonetic Sciences, 2*, edited by K. Elenius and P. Branderud (KTH and Stockholm University, Stockholm, Sweden), pp. 550–553.

Wang, W. S. (**1959**). ''Transition and release as perceptual cues for final plosives,'' J. Speech Hearing Res. **2**, 66–73.

Audiovisual gating and the time course of speech perception

K. G. Munhall
Department of Psychology, Queen's University, Kingston, Ontario K7L 3N6, Canada

Y. Tohkura
ATR Human Information Processing Research Laboratories, Kyoto, Japan

(Received 4 March 1997; revised 27 February 1998; accepted 10 March 1998)

The time course of audiovisual information in speech perception was examined using a gating paradigm. VCVs that evoked the McGurk effect were gated visually and auditorily. The visual gating yielded a McGurk effect that increased in strength as a linear function of amount of visual stimulus presented. The acoustic gating revealed a more nonlinear function in which the VC information was considerably weaker than the CV portion of the VCV. The results suggest that the flow of cross-modal information is quite complex during audiovisual speech perception. © *1998 Acoustical Society of America.* [S0001-4966(98)05406-X]

PACS numbers: 43.71.Ma, 43.71.Es [WS]

INTRODUCTION

Visual and auditory information both contribute to the natural perception of speech [for reviews see Summerfield (1992) and Massaro (1987)]. In noisy conditions, for example, intelligibility increases if the speaker's face can be seen (Sumby and Pollack, 1954) and even under good listening conditions a visual stimulus can influence the identification of an auditory token (McGurk and MacDonald, 1976). In the present paper, we present evidence concerning the time course of both visual and auditory information for consonants. Specifically, we independently gated visual and auditory stimuli that elicit the McGurk effect to examine the temporal development of the audiovisual percept.

The McGurk effect is an audiovisual illusion in which one speech stimulus is presented auditorily (e.g., /bi/) and another is presented in synchrony visually (e.g., /gi/). Subjects frequently report hearing a third sound (e.g., /di/). This effect has been useful as a tool for the study of audiovisual integration in speech perception. While there have been numerous replications of McGurk and MacDonald's original finding (e.g., Green and Kuhl, 1989; Green *et al.*, 1988, 1991; MacDonald and McGurk, 1978; Manuel *et al.*, 1983; Massaro, 1987; Massaro and Cohen, 1983; Munhall *et al.*, 1996; Sekiyama and Tohkura, 1991; Summerfield and McGrath, 1984), a great deal is still unknown about the necessary and sufficient conditions required to produce audiovisual integration in speech. In this paper we explore how auditory and visual information for consonants unfolds over time.

The process of speech perception is necessarily extended in time because the information for individual sounds does not occur at any single instant (Liberman *et al.*, 1967). Both acoustic analyses and perceptual experiments have shown this extended span of perceptual information. From the production side this can be attributed to the overlap of speech gestures (e.g., Öhman, 1967; Fowler, 1977) and to the fact that individual speech gestures take a set amount of time. On the perceptual side, the temporal extent of perceptual processing is partly due to the nature of the information itself and partly due to the time course of the information processing. A number of studies have demonstrated that dynamic information extending over a syllable is important in vowel perception and normalization (Verbrugge *et al.*, 1976; Strange, 1989), auditory speech perception (Remez *et al.*, 1981), visual perception of speech (Rosenblum, 1994) and perhaps audiovisual integration (Munhall *et al.*, 1996).

There are many indications that the dynamic information from the visual and auditory modalities has a complicated timing structure. The visual information itself is asynchronous. The upper lip, lower lip and jaw, for example, have similar time functions but are shifted in phase with respect to each other (Gracco, 1988). In addition, the spans of visual and auditory information are not equal or coincident in time since there is frequently articulator motion before there is an acoustic consequence (Bell-Berti and Harris, 1981). This can be seen in preparatory adjustments for articulation or in the motion during the acoustic silence associated with the production of stop consonants (Löfqvist and Gracco, 1996); the tongue, jaw, and lips move continuously during oral closures. These acoustic/articulatory timing patterns often allow subjects to have access to visual information about place of articulation before the auditory information is available, e.g., before the silent interval for a stop is complete (Cathiard *et al.*, 1996; Green and Gerdman, 1995; Smeele, 1994).

In two experiments, we examined the relative timing of the information in the visual and auditory modalities. Further, we tested whether subjects can make use of the information available within a modality at any point in time. In the experiments we use a gating technique (Grosjean, 1980, 1996) in which increasing larger segments of the target stimulus are presented incrementally across trials. This is done by constructing a continuum in which the duration of the segment of the stimulus starting from the onset is increased in steps up to the full target stimulus duration. The interpretation of the results of gating experiments can be controversial. While some feel that the techniques show continuous perceptual uptake (e.g., Grosjean, 1996) others feel that gating is not an on-line task and that subjects are simply required to guess based on partial information (Cutler, 1995). Our experiments did not address this issue; rather, our aim

was to examine the availability of information in the auditory and visual modalities at a point in time.

In our studies we separately gated the stimuli from the two modalities to study their individual contributions to the percept. In addition, we used stimuli in these gating studies that evoke the McGurk effect. The use of these contradictory stimuli allows us to test the separate contributions of the auditory and visual modalities. In the first experiment, the amount of visual information was varied while in the second experiment the amount of acoustic information was gated. In combination, the two studies allowed a comparison of the time course of audiovisual information available in McGurk stimuli. In particular, the experiments allowed us to compare the shape of gating functions obtained from the two modalities.

The shape of the gating function indicates the impact of equal temporal steps of information on perception and thus can serve as an index of the temporal development of information within a modality. Some theories of cross-modal perception (e.g., Welch and Warren, 1980) require a strong correlation between the information in the two modalities for audiovisual integration to occur, for such a theory to work, the temporal development of information should be similar for vision and audition. Testing this class of models requires that the cross-modal timing of information be specified in order to evaluate the temporal cohesion of the information across the two modalities. This includes determining the onset of information associated with a given segment within a modality as well as determining the time course of information within each modality. While we know that the visual information precedes acoustic information (e.g., Smeele, 1994), we know considerably less about the time course of information development in the two modalities during audiovisual perception. One reason for this is that, with a few notable exceptions (Cathiard *et al.*, 1996; Munhall *et al.*, 1996), the visual stimuli in audiovisual speech perception experiments are never characterized. It is common in the field to be provided only with information about the gender of the speaker and nothing about the dynamics of facial movement (Munhall and Vatikiotis-Bateson, 1998).

In the experiments presented here we provide an estimate of oral kinematics for each of the visual stimuli and we separately gate the auditory and visual tokens. The pattern of response or gating functions produced by subjects was used to estimate the available information within a modality. These gating functions for the two modalities establish the temporal conditions faced by any theory of cross-modal perception.

I. METHODS

A. Subjects

Seventy undergraduate students with self-reported normal hearing and normal or corrected to normal vision served as subjects in the two experiments. All subjects were native speakers of English. Twenty different subjects participated in the experimental conditions of each of the two experiments (40 subjects in total). An additional 20 subjects served in the control or baseline conditions of both experiments: Visual-only (experiment 1) and auditory-only (experiment 2) control conditions. Order of presentation of the two control conditions was balanced across subjects. Ten different subjects participated in a third baseline group in which no gating stimuli were presented. A between subject design was chosen for this experiment because pilot studies have shown that the magnitude of the McGurk effect is greatly influenced by subjects' experience with the auditory stimuli in auditory-only conditions. Thus different subjects were used for the auditory-only and audiovisual gating conditions. All subjects were naive to the purpose of the experiments and hadn't served in a McGurk experiment before.

B. Stimulus materials

In both experiments, natural productions of VCV stimuli by four different talkers were used. The stimuli consisted on a face saying /ægæ/ while the auditory stimuli were recordings of the same talkers saying /æbæ/. The visual stimuli were stored on a videodisc recorded at Queen's University. The auditory stimuli were digitized from the original sound tracts at 22-kHz sampling rate using a 12-bit A/D board (DataTranslation, DT2820).

C. Equipment

Subjects watched the displays on a 20-in. video monitor (Sony PVM 1910) and the videodiscs were played on a Pioneer (model LD-V8000) videodisc player. The acoustic signals were amplified, filtered with a 10-kHz cutoff and played through an MG Electronics Cabaret speaker that was placed directly below the monitor. Custom software was used to control the videodisc trials, play the auditory stimuli synchronously with the video, and record subjects' responses from the keyboard.

D. Synchronization of stimuli

During the development of the experiments, the audio and visual stimuli were synchronized using the original sound track from the visual stimuli. We aligned the timing of the acoustic burst onset of the /g/ from the soundtrack of the /ægæ/ video with the burst onset of the acoustic stimulus, /b/. This timing relation was considered synchronous and the experimental software allowed this timing to be reliably reproduced (approximately 1-ms accuracy).

E. Procedure

The subjects were tested individually in a large laboratory room. Subjects were seated approximately 2 m in front of the video monitor with a keyboard placed in front of them. They were instructed to watch the faces of the speakers and to listen to the acoustic output from the speaker and report what the stimuli sounded like. They responded by choosing one of four labeled keys. Four consecutive keys on the keyboard were labeled B, D, G, and O. Order of key labels was balanced across subjects. The first three labels stand for the stops /b/, /d/, /g/, and the final label stands for ''other.'' ''O'' was used when the subjects could not determine the consonant, when the subjects perceived a consonant other than one

of the voiced stops, or when the did not hear a consonant at all. Following the presentation of instructions, the subjects were given a short practice session to familiarize them with the experimental protocol. The experiments were response paced with a new trial being presented two seconds following the subject's response. Between trials the screen was blackened. In the video gating conditions the screen was blackened at the gated frame and remained black throughout the rest of the trial.

II. EXPERIMENT 1

Previous work on gating audiovisual stimuli (Cathiard *et al.*, 1996; Smeele, 1994) has indicated that the visual component of the stimuli contains strong information for place of articulation and that this information precedes the acoustic information in time. Smeele (1994) found that for CV stimuli the visual information was useful up to 150 ms prior to acoustic onset for the syllable. Similar results have been reported by Cathiard *et al.* (1996). In their study of V–V transitions, subjects were able to use gated visual information for vowel rounding up to 100 ms prior to the acoustic onset of the vowel.

In the first experiment, we explored the time course of the perception of the visual information in McGurk stimuli. The subjects viewed stimuli in which the visual intervocalic consonant was gated. In a typical trial, a subject would view a visual stimulus from stimulus onset to the gate location at which point the screen would go black for the rest of the trial. Different subjects served in the audiovisual and visual only conditions and gate durations were presented in random order.

A. Stimuli

The audio stimulus æbæ was always played in its entirety on each trial. As will be shown in experiment 2, the auditory stimuli were highly intelligible. The visual stimuli were gated in one frame steps from four frames before to four frames after the time of the acoustic burst. One frame equaled approximately 33 ms. In total, nine gate durations were used: From the beginning of the VCV to four, three, two, or one frame before the intervocalic burst, from the beginning of the VCV to (but not including) the intervocalic burst and from the beginning of the VCV to one, two, three, or four frames after the burst. The subjects were shown 160 trials in the experiment [4 talkers×4 repetitions×10 stimuli (9 gated stimuli+ungated stimulus)].

The gates were equal in duration for all talkers independent of the timing of their facial movements. Figure 1 shows the kinematics of oral opening for the four talkers and the location of the gates. In order to estimate the time course of the visual information, frame-by-frame measures of the vertical separation between the lips were recorded using a computerized image measurement system (Tiede, 1994).[1] For all talkers, the lips were in a closed position at the beginning of the trial, followed by a peak opening (approximately frame 15) for the first vowel. The oral aperture closes somewhat for the intervocalic /g/ and opens again for the second vowel (approximately frame 30). Finally, the oral aperture closes after the bisyllable. The vertical line indicates the frame during which oral release occurs. Thus the gated stimuli spanned the minimum aperture for the consonant and the movement toward the peak opening for the second vowel.

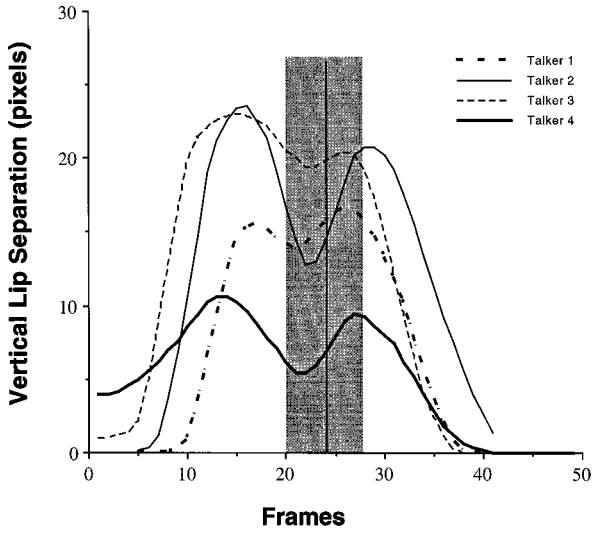

FIG. 1. Vertical separation of the lips in the visual stimuli produced by the four talkers. The vertical line indicates the frame containing the acoustic release burst. The shaded region indicates the range covered by the gating.

B. Results

Four responses were available to the subjects and the overall distribution of these responses can be seen in Fig. 2. The pattern of responses is influenced by the gating time with distinctly different patterns being observed for the four responses. In the audiovisual condition the ''B'' response decreases as the gate moves from four frames before to four frames after the intervocalic burst. ''D'' responses increase over the same interval while ''G'' and ''O'' response rates did not differ as a function of gate. The video-only control conditions are also plotted in each panel of Fig. 2. The ''D'' and ''G'' responses show an increase as a function of gate duration while the ''B'' responses are very infrequent and response rate is not influenced by gating time. The ''O'' decreases as a function of gate duration reflecting subjects' inability to detect a consonant for the early gates.

ANOVAs were computed independently for each response. Main effects of modality (audiovisual versus video-only) were found for three of the response [$F(1,38) = 175.1,\ 9.2,\ 99.8$, $p < 0.01$ for ''B'', ''D'', and ''O'', respectively] indicating that the percentage of ''B'' and ''D'' responses were higher in the audiovisual condition than the visual only. The percentage of ''O'' responses was higher in the visual-only than the audiovisual condition. Modality by gate time interactions were observed for three of the responses [$F(9,342) = 15.8,\ 5.5,\ 21.2$, $p < 0.01$ for ''B'', ''G'', and ''O'', respectively; the gate time factor tests the nine gate times plus the ungated stimulus]. These interactions indicate that the size of the differences between audiovisual and visual-only conditions changed as a function of the gate time. For example, the rate of ''O'' responses is much greater in the visual-only condition at −4 frames than +4 frames (Fig. 2). Trend analyses were carried out to characterized the gating response functions in the audiovisual

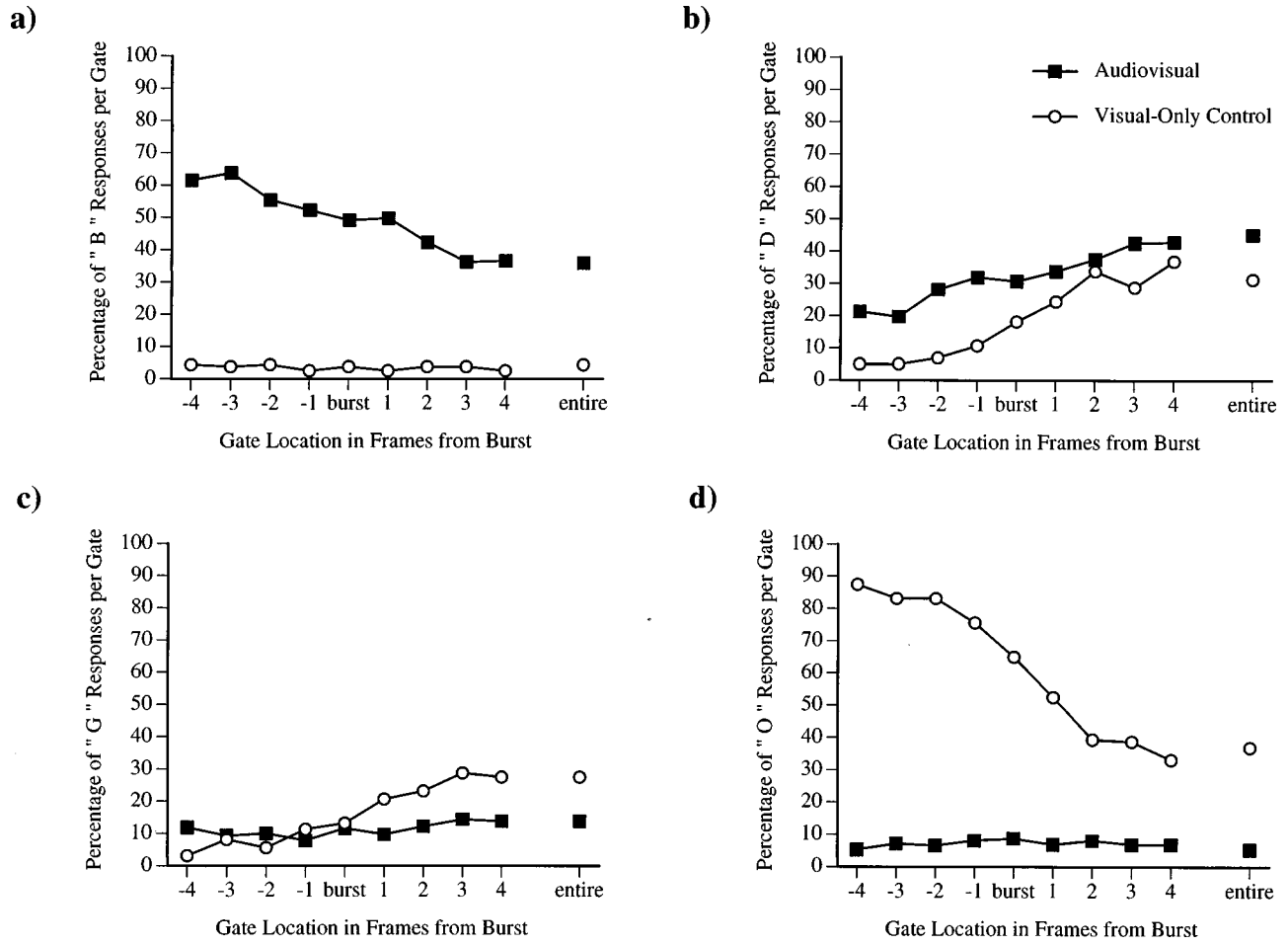

FIG. 2. Percentage of responses as a function of visual gate duration for (a) ''B'' responses, (b) ''D'' responses, (c) ''G'' responses, and (d) ''O'' or other responses. The boxes correspond to the audiovisual condition and the circles to the video-only condition.

condition. The ''B'' and ''D'' response options showed strong linear trends with no quadratic or cubic trends ($p < 0.0001$). The primarily linear functions for the visual conditions reflect the dynamical nature of the visual information. We are unable to determine from the gating technique whether the information is processed continuously (see Cutler, 1995) but it is clear that the information is incremental and is continuously available.

The stimulus set used in the experiment was produced by four different talkers whose tokens differed in the quality of visual and auditory information. Some talkers produce stimuli that yielded much stronger McGurk effects than others (Munhall *et al.*, 1996). By examining the gating functions for each talker we tested whether the average gating time function was observed for the individual talkers (i.e., for different levels of audiovisual integration) and whether the underlying pattern of visual intelligibility for the different talkers influenced the McGurk effect. In the visual only condition the number of reported ''B'' responses was consistently low for all talkers across gate durations [Fig. 3(a)]. The percentage of ''D'' responses [Fig. 3(b)], however, is somewhat higher for talker 1 and especially talker 4. The percentage of ''B'' and ''D'' responses in the audiovisual condition differ markedly for different talkers [Fig. 3(c), (d)]. Stimuli from talkers 2 and 4 evoked fewer ''B'' responses and more ''D'' responses than stimuli from talkers 1 and 3. However, the response functions from all 4 talkers were generally similar; they all showed a large linear trend with no obvious higher order trend.

The two talkers whose stimuli produced the largest McGurk effects (talker 2 and 4) had the largest movement associated with the intervocalic consonant. The decrease in aperture for the /g/ for talkers 1 and 3 was relatively modest compared to talkers 2 and 4. It should be noted that there was a substantial amount of articulator movement prior to the first gate, particularly for talkers 2 and 4. The use of this visual information might account for the substantial McGurk effects produced at the earliest gate. However, there does not seem to be any relationship between key events in the oral kinematics and the shape of the gating function. As can be seen by comparing Figs. 1 and 3, there is not a discontinuity in the response pattern at displacement or velocity peaks.

III. EXPERIMENT 2

In the second experiment, we examined the time course of audiovisual VCV perception by gating the auditory signal (Grosjean, 1980) at the same time points as used in experiment 1 before and after the intervocalic consonant burst. By presenting the auditory stimulus in increments we could assess the timing of the use of auditory information and the role the auditory information played in intermodal percep-

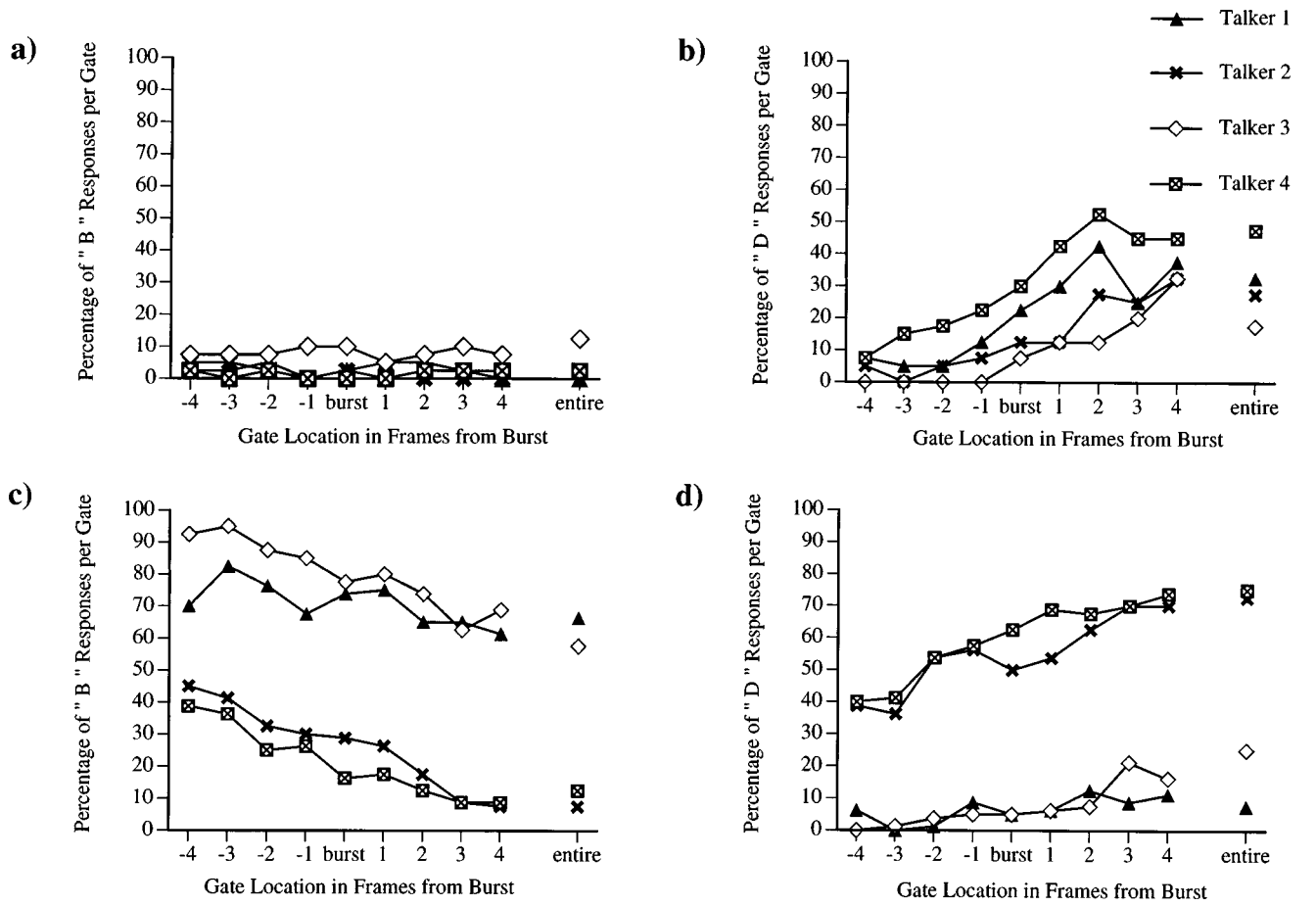

FIG. 3. Percentage of responses as a function of visual gate duration for the stimuli from the four talkers. (a) ''B'' responses in the visual only condition; (b) ''D'' responses in the visual only condition; (c) ''B'' responses in the audiovisual condition; (d) ''D'' responses in the audiovisual condition.

tion. Previous studies have shown that gating technique to be a robust (Cotton and Grosjean, 1984) and valid (Tyler and Wessels, 1985) tool for exploring the auditory perceptual information.

In this experiment we compared the perception of gated auditory stimuli in an auditory-only condition to gated auditory stimuli in an audiovisual condition to examine how the auditory contribution to the perceptual event grew over time. The different gate durations were presented in random order within a modality condition. Different individuals served as subjects in the auditory-only and audiovisual conditions.

A. Stimuli

The video stimuli were played in their entirety on each trial. The auditory stimuli were presented in nine gate durations: From the beginning of the VCV to 120, 90, 60, and 30 ms before the intervocalic burst, from the beginning of the VCV to (but not including) the intervocalic burst and from the beginning of the VCV to 30, 60, 90, and 120 ms after the burst. These gate intervals corresponded approximately to the timing of gates of one frame used in the visual gating in experiment 1.

B. Results

Four responses were available to the subjects and the overall distribution of these responses can be seen in Fig. 4. The pattern of responses is influenced by the gating time with distinctly different patterns being observed for the four responses. In the audiovisual condition the ''O'' response decreased as the gate moved from 120 ms before to 120 ms after the intervocalic burst. The other three responses (''B, D, G'') increased over the same interval with ''B'' and ''D'' increasing more than ''G''. All four responses showed major changes in response rate between the gates at the intervocalic burst and the gate 30 ms later. The auditory-only control conditions are also plotted in Fig. 4. The ''B'' and ''O'' responses showed a similar pattern, while the ''D'' and ''G'' responses were very infrequent and response rate was not influenced by gating time.

ANOVAs were computed independently for each response. Main effects of modality (audiovisual versus audio-only) were found for all four responses [$F(1,38) = 168.1$, 70.2, 18.0, 11.3, $p < 0.01$ for ''B'', ''D'', ''G'', and ''O'', respectively]. Modality by gate time interactions were observed for all four responses [$F(9,342) = 14.2$, 45.8, 4.1, 6.6, $p < 0.01$ for ''B'', ''D'', ''G'', and ''O'', respectively].

Trend analyses were carried out to characterize the gating response functions in the audiovisual condition. Unlike the pattern observed in experiment 1 for visual information, the pattern was significantly nonlinear. Three of four response options (with ''G'' being the exception) showed strong linear and cubic trends ($p < 0.0001$). In large part, this

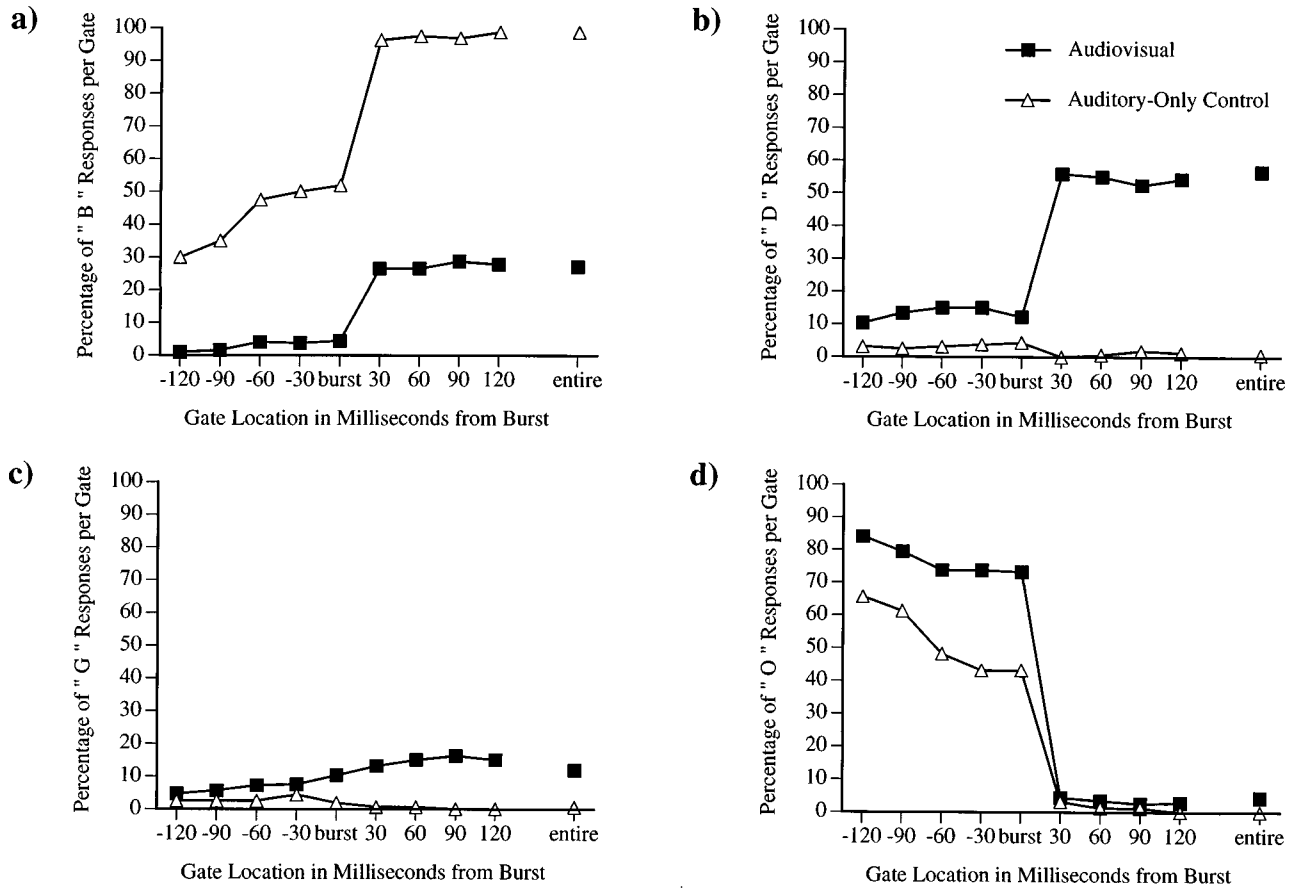

FIG. 4. Percentage of responses as a function of auditory gate duration for (a) ''B'' responses, (b) ''D'' responses, (c) ''G'' responses, and (d) ''O'' or other responses. The boxes correspond to the audiovisual condition and the triangles to the auditory-only condition.

pattern was determined by the particular gate locations used with these stimuli. The gating manipulation in this experiment was carried out using gate steps of equal duration for all four talkers' stimuli, chosen to roughly correspond with the timing of visual gates used in experiment 1 (i.e., approximately 1 video frame). Table I shows the durations of the acoustic intervals in the four talkers' /æbæ/ productions. Two things should be noted about the data in this table. First, the stimuli were not all equal in duration and this means that the gates were not always in equivalent positions. Second, the gates preceding the burst occurred mostly during oral closure for the /b/. Voicing was apparent during all of the talkers' closures but the subjects did not make use of the closure information until the duration of the interval was signaled. Thus, the acoustic stimuli seem to be divided into VC and CV portions by the gating. The one exception to this pattern was talker 3, whose closure was quite short and thus the gates preceding the burst occurred mostly during the first vowel. Interestingly, the percentage of /b/s reported for the auditory only condition of talker 3 showed a distinctly different pattern than the other three talkers [Fig. 5(a)]. However, all talkers showed a similar nonlinear pattern in the audiovisual condition [Fig. 5(b) and (c)]. While the auditory information may contain dynamical cues, it appears to be punctuated by discontinuities that have different degrees of perceptual impact. The visual stimuli in this task provided continuous information over time while auditory perception was marked by instants or time windows of greater or lesser information (cf. Blumstein and Stevens, 1980).

TABLE I. Durations of the acoustic stimuli used in experiments 1 and 2.

Talker	Vowel 1	Closure	VOT	Vowel 2
1	139.8	119.5	11.0	233.3
2	215.8	139.6	7.0	286.9
3	159.1	69.6	4.8	246.9
4	244.9	115.8	5.7	323.9

The pattern of response in the auditory-only condition was consistent with previous findings on the perception of intervocalic consonants [Dorman *et al.*, 1979; Householder, 1956 (cited in Byrd, 1992); Streeter and Nigro, 1979]. While information for the consonant may be present in both VC and the CV portions of the bisyllable, information in the CV portion appears to be much more salient. Subjects did not report a large number of ''B'' responses in the auditory-only condition until they heard the release burst (gate 30 ms after the burst). The discontinuity in the response functions reflect the differential strength of the VC versus CV cues.

The pattern of responses in the audiovisual condition largely mirrored the pattern observed for the auditory only. For example, ''B'' and ''O'' response functions were similar in shape for the audiovisual and auditory-only conditions. The largest difference between the two conditions and the largest interaction effect was observed for ''D'' responses.

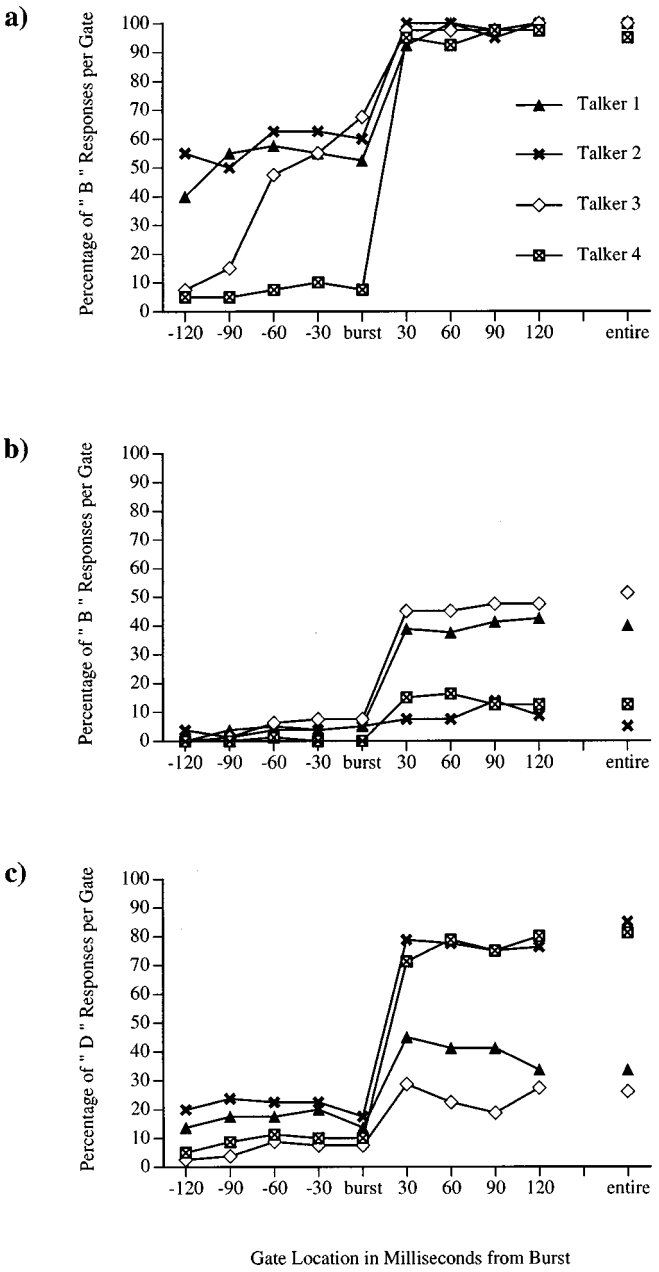

FIG. 5. Percentage of responses as a function of auditory gate duration for the stimuli from the four talkers. (a) ''B'' responses in the auditory only condition; (b) ''B'' responses in the audiovisual condition; (c) ''D'' responses in the audiovisual condition.

This is interesting in that it suggests that until there is sufficient auditory information to support a strong ''B'' response (or at least to support the perception of a consonant) the McGurk effect cannot be observed.

As in experiment 1, we examined the patterns of responses for stimuli produced by the different talkers. Figure 5 shows the percentage of /b/ and /d/ responses for the audiovisual condition and the percentage of /b/ responses for the auditory-only condition. The /b/ responses for the auditory-only condition [Fig. 5(a)] reveal that accuracy for stimuli from all talkers reached ceiling at the first gate beyond the intervocalic burst. While perception of the /b/ varied for different talkers before the burst, there was little difference among the four talkers' asymptotic response levels

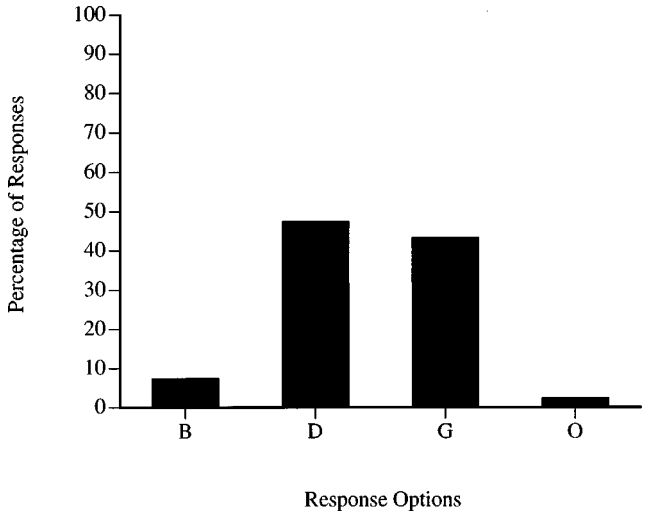

FIG. 6. Percentage of ''B,'' ''D,'' ''G,'' and ''O'' responses in the audiovisual control condition.

following the burst. The differences in perception of /b/ in the auditory-only condition before the burst do not directly account for the talker differences in elicitation of the McGurk effect. Talker 4's stimuli produced by far the lowest perception of /b/ while the stimuli for talker 2 produced the highest perception of /b/. The stimuli for these two talkers showed the strongest McGurk effect overall [Fig. 5(c)].

In Fig. 4, the percentage of ''B'' responses given when the ungated audiovisual stimulus was played is shown. Both the value in this experiment and the value reported for the same condition in experiment 1 are higher than we usually observe for stimuli of this kind. To verify this we tested an additional 10 subjects who were only shown the complete audiovisual McGurk stimuli (i.e., no gated stimuli were presented). Figure 6 shows the average responses for these subjects. The percentage of ''B''s reported by these subjects (7.3%), for example, is much lower than reported in experiments 1 (35.9%) and 2 (27.2%). It would appear either that the gated stimuli induced a bias or that sampling differences produced this pattern of results (see below).

IV. GENERAL DISCUSSION

The data from the two experiments show distinct differences between the visual and auditory signals and how they are processed. The auditory information for the intervocalic consonant appears to be much stronger in the CV portion of the bisyllable than in the VC portion. As a result auditory consonant identification was quite poor until after the intervocalic release burst was heard. The perception of the visual information, on the other hand, was more continuous. The percentage of /b/s reported in the audiovisual condition of the visual gating experiment (exp. 1) changed as a linear function of the amount of the visual stimulus presented. These patterns of results were observed for three groups of subjects and were observed for stimuli produced by four different talkers.

This pattern suggests that visual information unfolds smoothly with the dynamics of articulation but that the acoustic information does not always directly reflect these

smooth kinematics. Rather, the acoustics are punctuated by instants of greater information value. This can occur for a number of reasons. Some acoustic instants may be highly salient because the cues at a point in time are robust. For example, the burst of a stop which extends over a small temporal span is very informative. A second source of nonlinearity in the acoustic information is the perceptual use of temporal intervals. A stretch of silence has little or no information value until it is completed. Only at the end of the interval can the duration indicate the manner and style of articulation.

Previous research on the time course of audiovisual speech perception has indicated that the visual cues for place of articulation can precede the acoustic information by more than 100 ms (e.g., Smeele, 1994). This research, in conjunction with the present findings, suggests that the flow of cross-modal information is quite complex. Information from the visual and auditory modalities is not synchronous and does not unfold continuously at the same rate. Thus it seems unlikely that the perceptual system uses temporal coincidence or any tight cross-modal timing as the basis of audiovisual integration. Studies in which the synchrony of the auditory and visual signals was directly manipulated support this conclusion (e.g., Abry *et al.*, 1996; Massaro and Cohen, 1993; Munhall *et al.*, 1996; Tillman *et al.*, 1984). For example, Munhall *et al.* found that the acoustic signal could be delayed up to 180 ms from normal audiovisual timing without a significant decrease in the strength of the McGurk effect.

While the perceptual system is quite tolerant of desynchrony of audiovisual information, there are limitations. This is particularly true when the acoustic information is advanced in time relative to the visual stimulus. A number of experiments have shown that sound-lead is not tolerated as well as sound-lag (e.g., Abry *et al.*, 1996; Dixon and Spitz, 1980; Munhall *et al.*, 1996; Smeele *et al.*, 1992; Tillman *et al.*, 1984; but cf. Gerdeman, 1994). Abry *et al.* suggest that the tolerance for advancing the sound is limited by the natural audiovisual timing relationship. Articulatory movements naturally precede the acoustics and the sound can be advanced only until the point at which the acoustic information would precede the gestures. This cross-modal timing boundary might suggest a limited perceptual span over which the information from the two modalities must be linked and thus some temporal dependence in cross-modal perception. In our view a more likely explanation is that the limitation is not time *per se* but rather the information processing of the auditory information; visual information might not influence perceptual categorization if the auditory information has reached a criterion threshold. The more natural temporal precedence of visual information may have led to a priming role for the visual signal in normal audiovisual perception. Sams *et al.* (1991) have also concluded that the visual stimuli may prime the auditory stimuli based on their magnetoencephalographic study of the McGurk effect. While auditory segmental context effects (in which later occurring information influences the category judgment for a preceding segment) are numerous (e.g., Mann and Repp, 1980), visual information may not produce similar effects on auditory perception.

Two studies may provide counterevidence to the suggestion that visual information that follows auditory information in time does not produce context effects on auditory perception. Green and Gerdeman (1995) have shown that the magnitude of the McGurk effect is influenced by whether the following visual vowel matches the auditory vowel. Green and Miller (1985) showed that the voicing boundary in an auditory /bi–pi/ continuum was influenced by the visual speaking rate for the bilabial. One of the primary differences between speaking rates was the duration of the visual vowels. However, in both of these studies that were also visual cues for speaking rate or vowel context that preceded the auditory information for the consonant. The visual information for different speaking rates is based in the dynamics of articulation which are apparent throughout the visual syllable. For example, velocities of speech movement can change with speaking rate and peak velocities occur quite early within a gesture. Similarly, the articulation of consonants is influenced quite early by following vowels and therefore, the coarticulation effect reported by Green and Gerdeman (1995) may not be due to visual information that follows the consonant. Thus it is possible to interpret even these studies as instances of visual priming of the auditory judgment.

It should be noted that the pattern of results for the visual gating experiment indicates that the visual information is continuously available and incrementally useful to the perceiver but it does not speak to the issue of the continuity of uptake of the visual information. The gating paradigm requires subjects to guess on the basis of the available information for each gate duration. The observed results do not indicate that the time course of the normal perceptual decision process mirrors the gating function.

The kinematics of the lip movements shown in Fig. 1 represent only a part of the complex visual stimulus provided by the moving face [see Munhall and Vatikiotis-Bateson (1998) for a review of facial dynamics during speech]. It is clear even from this crude measure, however, that the face is continuously varying during speech production. This time-varying visual information signals the rate of speaking (Green, 1987; Green and Miller, 1985), as well as indicating segmental structure and segmental categories (Summerfield, 1987). A number of years ago Remez *et al.* (1981) showed that time-varying acoustic information is sufficient to signal the phonetic structure of an utterance. In a previous paper (Munhall *et al.*, 1996) we suggested that this dynamic information may play a crucial role in audiovisual integration. The complexity of the timing data in the present studies raises the possibility that the dynamic information is extracted separately for each modality before the information from vision and audition is merged. Recently, Green *et al.* (1991) and Massaro (1987) have argued similarly that auditory and visual information is processed to some degree before integration takes place. While Green *et al.* argue only that talker characteristics may be processed, Massaro proposes that the auditory and visual information are completely processed prior to integration.

One of the intriguing observations in these experiments is that subjects who were presented only with complete au-

diovisual VCVs (Fig. 6) showed a stronger McGurk effect than the experimental subjects in the two studies (''entire'' in Figs. 2 and 4). Two possible explanations are available for this finding. First, chance sampling differences may account for the discrepancy between the subjects. Second, the pattern of results may be caused by contextual biasing. In the experimental group that perceived the highest number of /b/s across all gating conditions (subjects in exp. 1), the weakest McGurk effect was found for the ungated stimuli. In the group that perceived the next highest number of /b/s across all gating conditions (exp. 2), an intermediate McGurk effect was observed for the ungated stimuli. Finally, the McGurk-only group (i.e., no gating) that had the least experience with auditory /b/ perceptions overall showed the strongest McGurk effect. While these trends are not conclusive, they are consistent with the idea that exposure to /b/ exemplars may alter or bias responses in the McGurk effect (cf. Case *et al.*, 1995).

ACKNOWLEDGMENTS

This research was funded by NIH Grant No. DC-00594 from the National Institute of Deafness and other Communicative Disorders and NSERC. The authors wish to thank Kerry Green and Eric Vatikiotis-Bateson for helpful comments on an earlier version of this paper.

[1]Use of this measure is a simplification. No single point on the face captures all of the visual information available to a perceiver. A number of recent perceptual studies have demonstrated that the motion of the full face is used in speechreading (Smeele *et al.*, 1995; Guiard-Marigny *et al.*, 1995). In these studies, subjects performed better when more of the facial surface than the lips was visible. Statistical examination of the motion of various regions of the face is consistent with these findings (Vatikiotis-Bateson *et al.*, 1996). When the 3-D motion of markers on the face was used to estimate the rms amplitude of the speech acoustics, the best estimate was achieved using all of the markers including positions at a distance from the lips.

Abry, C., Lallouache, M. T., and Cathiard, M. A. (**1996**). ''How can coarticulation models account for speech sensitivity to audio-visual desynchronization?,'' in *Speechreading by Humans and Machines*, edited by D. Stork and M. E. Hennecke (Springer-Verlag, Berlin).

Bell-Berti, F., and Harris, K. S. (**1981**). ''A temporal model of speech production,'' Phonetica **38**, 9–20.

Blumstein, S. E., and Stevens, K. N. (**1980**). ''Perceptual invariance and onset spectra for stop consonants in different vowel environments,'' J. Acoust. Soc. Am. **67**, 648–662.

Byrd, D. (**1992**). ''Perception of assimilation in consonant clusters: A gestural model,'' Phonetica **49**, 1–24.

Case, P., Tuller, B., Ding, M., and Kelso, J. A. S. (**1995**). ''Evaluation of a dynamical model of speech perception,'' Percept. Psychophys. **57**, 977–988.

Cathiard, M. A., Lallouache, M. T., and Abry, C. (**1996**). ''Does movement on the lips mean movment in the mind?,'' in *Speechreading by Humans and Machines*, edited by D. Stork and M. E. Hennecke (Springer-Verlag, Berlin).

Cotton, S., and Grosjean, F. (**1984**). ''The gating paradigm: A comparison of successive and individual presentation formats,'' Percept. Psychophys. **35**, 41–48.

Cutler, A. (**1995**). ''Spoken word recognition and production,'' in *Speech, Language, and Communication*, edited by J. L. Miller and P. D. Eimas (Academic, San Diego).

Dixon, N., and Spitz, L. (**1980**). ''The detection of audiovisual desynchrony,'' Perception **9**, 719–721.

Dorman, M. F., Raphael, L. J., and Liberman, A. M. (**1979**). ''Some experiments on the sound of silence in phonetic perception,'' J. Acoust. Soc. Am. **65**, 1518–1532.

Fowler, C. A. (**1977**). *Timing Control in Speech Production* (Indiana University, University Club, Bloomington).

Gerdeman, A. (**1994**). ''Temporal incongruity and the McGurk effect,'' unpublished Master's thesis, University of Arizona.

Gracco, V. L. (**1988**). ''Timing factors in the coordination of speech movements,'' J. Neurosci. **8**, 4628–4634.

Green, K. P. (**1987**). ''The perception of speaking rate using visual information from a talker's face,'' Percept. Psychophys. **42**, 587–593.

Green, K., and Miller, J. (**1985**). ''On the role of visual rate information in phonetic perception,'' Percept. Psychophys. **38**, 269–276.

Green, K. P., and Gerdeman, A. (**1995**). ''Cross-modal discrepancies in coarticulation and the integration of speech information: The McGurk effect with mismatched vowels,'' J. Exp. Psychol. **21**, 1409–1426.

Green, K. P., and Kuhl, K. P. (**1989**). ''The role of visual information in the processing of place and manner features in speech perception,'' Percept. Psychophys. **45**, 34–41.

Green, K. P., Kuhl, K. P., and Meltzoff, N. A. (**1988**). ''Factors affecting the integration of auditory and visual information in speech: The effect of vowel environment,'' Paper presented at the meeting of the Acoustical Society of America, Honolulu.

Green, K. P., Kuhl, K. P., Meltzoff, A. N., and Stevens, E. R. (**1991**). ''Integrating speech information across talkers, gender, and sensory modality: Female faces and male voices in the McGurk effect,'' Percept. Psychophys. **50**, 524–536.

Grosjean, F. (**1980**). ''Spoken word recognition processes and the gating paradigm,'' Percept. Psychophys. **28**, 267–283.

Grosjean, F. (**1996**). ''Gating,'' Language and Cognitive Processes **11**, 597–604.

Guiard-Marigny, T., Ostry, D. J., and Benoit, C. (**1995**). ''Speech intelligibility of synthetic lips and jaw,'' *Proceedings of the 13th International Congress of Phonetic Sciences* (Stockholm, Sweden), Vol. 3, pp. 222–225.

Liberman, A., Cooper, F., Shankweiler, D., and Studdert-Kennedy, M. (**1967**). ''Perception of the speech code,'' Psychol. Rev. **74**, 431–461.

Löfqvist, A., and Gracco, V. (**1996**). ''Labial kinematics in stop consonant production,'' J. Acoust. Soc. Am. **99**, 2472 (A).

Mann, V., and Repp, B. (**1980**). ''Influence of vocalic context on perception of the [ʃ]–[s] distinction,'' Percept. Psychophys. **28**, 213–228.

Manuel, S. Y., Repp, B., Studdert-Kennedy, M., and Liberman, A. (**1983**). ''Exploring the McGurk effect,'' J. Acoust. Soc. Am. Suppl. 1 **74**, S66.

MacDonald, J., and McGurk, H. (**1978**). ''Visual influences on speech perception,'' Percept. Psychophys. **24**, 253–257.

Massaro, D. W. (**1987**). *Speech Perception by Ear and Eye* (Erlbaum, Hillsdale, NJ).

Massaro, D. W., and Cohen, M. M. (**1993**). ''Perceiving asynchronous bimodal speech in consonant-vowel and vowel syllables,'' Speech Commun. **13**, 127–134.

McGurk, H., and MacDonald, J. (**1976**). ''Hearing lips and seeing speech,'' Nature **264**, 746–748.

Munhall, K. G., Gribble, P., Sacco, L., and Ward, M. (**1996**). ''Temporal constraints on the McGurk effect,'' Percept. Psychophys. **58**, 351–362.

Munhall, K. G., and Vatikiotis-Bateson, E. (**1998**). ''The moving face during speech communication,'' in *Hearing by Eye, Part 2: The Psychology of Speechreading and Audiovisual Speech*, edited by R. Campbell, B. Dodd, and D. Burnham (Taylor and Francis, Psychology Press, London).

Nusbaum, H. C., and Morin, T. M. (**1992**). ''Paying attention to differences among talkers,'' in *Speech Perception, Production and Linguistic Structure*, edited by Y. Tohkura, E. Vatikiotis-Bateson, and Y. Sagisaka (Ohm-sha, Tokyo).

Öhman, S. (**1967**). ''Numerical model of coarticulation,'' J. Acoust. Soc. Am. **41**, 310–320.

Remez, R., Rubin, P., Pisoni, D., and Carrell, T. (**1981**). ''Speech perception without traditional cues,'' Science **212**, 947–950.

Rosenblum, L. (**1994**). ''How special is audiovisual speech integration?,'' Current Psychology of Cognition **13**, 110–116.

Sams, M., Aulanko, R., Hämäläinin, M., Hari, R., Lounasmaa, O., Lu, S., and Simola, J. (**1991**). ''Seeing speech: Visual information from lip movements modifies activity in the human auditory cortex,'' Neurosci. Lett. **127**, 141–145.

Sekiyama, K., and Tohkura, Y. (**1991**). ''McGurk effect in non-English listeners: Few visual effects for Japanese subjects hearing Japanese syl-

lables of high auditory intelligibility,'' J. Acoust. Soc. Am. **90**, 1797–1805.
Smeele, P. M. T. (**1994**). ''Perceiving speech: Integrating auditory and visual speech,'' unpublished doctoral dissertation, Delft University of Technology.
Smeele, P. M. T., Sittig, A. C., and Van Heuven, V. J. (**1992**). ''Intelligibility of audio-visually desynchronized speech: asymmetrical effect of phoneme position,'' *Proceedings of the International Conference on Spoken Language Processing*, pp. 65–68.
Smeele, P., Hahnlen, L., Stevens, E., Kuhl, P., and Meltzoff, A. (**1995**). ''Investigating the role of specific facial information in audiovisual speech perception,'' J. Acoust. Soc. Am. **98**, 2569(A).
Strange, W. (**1989**). ''Evolving theories of vowel perception,'' J. Acoust. Soc. Am. **85**, 2081–2087.
Streeter, L., and Nigro, G. (**1979**). ''The role of medial consonant transitions in word perception,'' J. Acoust. Soc. Am. **65**, 1533–1541.
Sumby, W. H., and Pollack, I. (**1954**). ''Visual contribution to speech intelligibility in noise,'' J. Acoust. Soc. Am. **26**, 212–215.
Summerfield, Q. (**1987**). ''Some preliminaries to a comprehensive account of audio-visual speech perception,'' in *Hearing by Eye: The Psychology of Lip-Reading*, edited by B. Dodd and R. Campbell (Erlbaum, London), pp. 3–51.
Summerfield, Q. (**1992**). ''Lipreading and audio-visual speech perception,'' Philos. Trans. R. Soc. London, Ser. B **335**, 71–78.
Summerfield, Q., and McGrath, M. (**1984**). ''Detection and resolution of audio-visual incompatibility in the perception of vowels,'' Q. J. Exp. Psychol. **36A**, 51–74.
Tiede, M. (**1994**). Vidiot (Macintosh video analysis software), ATR Laboratories, Kyoto.
Tillman, H. G., Pomino-Marschall, B., and Porzig, H. (**1984**). ''Zum Einfluß visuell dargeborener Sprachbewegungen auf die Wahrnehumung der akustisch kodieten Artikulation,'' Forschungsberichte des Instituts für Phonetik und Sprachliche Kommunikation der Universität München **19**, 318–338.
Tyler, L. K., and Wessels, J. (**1985**). ''Is gating an on-line task? Evidence from naming latency data,'' Percept. Psychophys. **35**, 409–420.
Vatikiotis-Bateson, E., Munhall, K. G., Kasahara, Y., Garcia, F., and Yehia, H. (**1996**). ''Characterizing audiovisual information during speech,'' *Proceedings of the Fourth International Conference on Spoken Language Processing*, ICSLP-96, pp. 1485–1488.
Verbrugge, R., Strange, W., Shankweiler, D., and Edman, T. (**1976**). ''What information enables a listener to map a talker's vowel space?,'' J. Acoust. Soc. Am. **60**, 198–212.
Welch, R. B., and Warren, D. H. (**1980**). ''Immediate perceptual response to intersensory discrepancy,'' Psychol. Bull. **88**, 638–667.

Acceptability for temporal modification of single vowel segments in isolated words[a)]

Hiroaki Kato[b),c)] and Minoru Tsuzaki
ATR Human Information Processing Research Laboratories, Hikaridai, Seikacho, Kyoto, 619-0288, Japan

Yoshinori Sagisaka[c)]
ATR Interpreting Telecommunications Research Laboratories, Hikaridai, Seikacho, Kyoto, 619-0288, Japan

(Received 3 December 1996; accepted for publication 20 March 1998)

Few perceptual studies of the temporal aspects of speech have investigated the influence of changes in segmental durations in terms of acceptability. Aiming to contribute to the assessment of rules for assigning segmental durations in speech synthesis, the current study measured the perceptual acceptability of changes in the segmental duration of vowels as a function of the segment attributes or context, such as base duration, temporal position in a word, vowel quality, and voicing of the following segment. Seven listeners estimated the acceptability of word stimuli in which one of the vowels was subjected to a temporal modification from −50 ms (for shortening) to +50 ms (for lengthening) in 5-ms steps. The temporal modification was applied to vowel segments in 70 word contexts; their durations ranged from 35–145 ms, the mora position in the word was first or third, the vowel quality was /ɑ/ or /i/, and the following segment was a voiced or an unvoiced consonant. The experimental results showed that the listeners' acceptable range of durational modification was narrower for vowels in the first moraic position in the word than for those in the third moraic position. The acceptable range was also narrower for the vowel /ɑ/ than for the vowel /i/, and similarly narrower for vowels followed by unvoiced consonants than for those followed by voiced consonants. The vowel that fell into the least vulnerable class (the third /i/, followed by a voiced consonant) required 140% of the modification of that which fell into the most vulnerable class (the first /ɑ/, followed by an unvoiced consonant) to yield the same acceptability decrement. In contrast, the effect of the original vowel duration on the acceptability of temporal modifications was not significant despite its wide variation (35–145 ms). [S0001-4966(98)01107-2]

PACS numbers: 43.72.Lc, 43.71.Gv, 43.66.Mk [JLH]

INTRODUCTION

Rules to assign segmental duration have been proposed for speech synthesis to replicate the segmental durations found in naturally spoken utterances (Allen *et al.*, 1987; Carlson and Granström, 1986; Campbell, 1992; Fant and Kruckenberg, 1989; Higuchi *et al.*, 1993; Kaiki and Sagisaka, 1992; Klatt, 1979; Riley, 1992; van Santen, 1994; Takeda *et al.*, 1989). Each of the segmental durations realized by such durational rules generally has a certain amount of error compared with the corresponding naturally spoken duration. The effectiveness of a durational rule should be evaluated by how well these errors would be accepted by human listeners, who are the final recipients of synthesized speech in general. However, in almost all previous cases, the average of the absolute error of each segmental duration from its standard has been adopted as the measure for objective evaluation.

One possible problem with this measure is that it gives every segment the same weight in the error evaluation. In other words, it neglects factors which may affect the perception of segmental duration, such as (1) interactions among errors in different segments (Kato *et al.*, 1997) and (2) variations in segment attributes (Bochner *et al.*, 1988; Carlson and Granström, 1975; Huggins, 1972; Klatt and Cooper, 1975). If the perceptual sensitivity to durational modification largely depends upon these factors, the reliability of the traditional measure, which gives every segment the same weight, should be seriously reconsidered. At the same time, if such a segmental effect on perceptual evaluation could be quantitatively specified, we could obtain a more valid (closer to human evaluation) measure than the traditional one to evaluate durational rules. In the previous study (Kato *et al.*, 1997), we focused on the first factor, i.e., interactions among errors, and investigated to what degree a temporal modification in one segment is compensated by a modification in an adjacent segment. As a result, the amount of perceptual compensation was found to be inversely correlated with the difference in loudness between the two segments of interest. The current study looks at the second factor and examines whether the attributes and context of individual segments affect the perceptual sensitivity to durational modification, and, if so, how large these effects are.

[a)]Part of this work was presented at the Second International Conference on Spoken Language Processing in 1992 (Proceedings of ICSLP-92, pp. 507–510).

[b)]Electronic mail: kato@hip.atr.co.jp
[c)]The first and third authors are also with Graduate School of Science and Technology, Kobe University, Rokkodaicho, Nada, Kobe, 657-8501, Japan.

A. Factors affecting perceptual evaluation for changes in segmental durations

First, we will consider factors affecting auditory sensitivity to durational changes. It is widely acknowledged that the absolute just noticeable differences (jnd's) of auditory duration will increase with an increase in the base duration for stimuli ranging in the duration of speech segments (e.g., from 50–300 ms) (Abel, 1972a, 1972b; Creelman, 1962; Fujisaki *et al.*, 1975; Small and Campbell, 1962). According to these studies, although the relative jnd's or Weber fractions, i.e., the proportions of jnd's to their corresponding base durations, may decrease slightly with an increase in the base duration of this range, the absolute jnd's still keep increasing. Abel (1972a), for example, suggested that the absolute jnd was roughly proportional to the square root of the base duration. An analogous tendency was also observed for durational jnd's of vowel segments (Bochner *et al.*, 1988). Bochner *et al.* have shown that jnd's tended to increase with an increase in the base duration of six vowels (75–170 ms) which were presented in isolation or in a consonant–vowel–consonant (CVC) sequence. Klatt and Cooper (1975), on the other hand, have reported absolute jnd data for vowel or syllable nucleus durations that did not appear to depend on the base durations. Their target was the stressed vowel /i/ in the word ''deal(er)'' embedded in various sentences; the duration of the syllable nuclei which included the target vowels ranged from 165–340 ms. The jnd's varied almost independently from the durations of the syllable nucleus, i.e., the base durations.[1] These jnd studies on vowel or syllable nucleus durations cannot be directly compared to each other, owing to differences in the range of stimulus duration and in the stimulus context that embedded the target duration. The influence of base duration on temporal sensitivity, particularly for a speech segment, therefore warrants testing by further systematic studies.

In addition to the factor of base duration, three factors have been reported which could affect auditory sensitivity to durational modifications in speech segments. The first factor is the temporal position in a word; Klatt (1976) reported that the durational jnd was smaller for segments in the first syllable of a two-syllable word than for segments in word-final syllables. The second factor is the effect of the following word; the jnd for vowel duration was smaller at the sentence end than elsewhere in the sentence (Klatt, 1976). Klatt suggested that this effect probably involved a backward recognition masking (Massaro and Cohen, 1975); i.e., if other words follow the crucial segment, the jnd will increase. The third factor, which has been mentioned by both Huggins (1972) and Carlson and Granström (1975), is the type of segment. They reported that their subjects were more sensitive to durational changes in vowel segments than to those in consonant segments. This third factor, however, did not appear to be significant in Fujisaki *et al.*'s experiments (Fujisaki *et al.*, 1975); the jnd obtained was almost equal for all types of segments, regardless of whether the crucial segment was a vowel or a consonant. Fujisaki suggested that such disagreement was probably due to whether durational differences served as cues for the phonemic distinctions; the segmental durations investigated by Fujisaki *et al.* were phonemic in Japanese while those tested by the other studies were not phonemic (Carlson and Granström, 1975, commentary section).

Although jnd's can be precisely defined in psychoacoustical terms, acceptability is another useful measure for evaluating errors in durational rules. This measure can be considered more practical than jnd's, because there are many cases in which we can accept two tokens as natural utterances even though they are clearly discriminable. This acceptability measure, however, has seldom been investigated, except for several pioneering studies (Sato, 1977; Hoshino and Fujisaki, 1983; Sagisaka and Tohkura, 1984). Sato (1977) investigated the acceptability of temporal modifications in vowel segments within isolated words. The acceptable modifications reported ranged from 15–30 ms and were smaller for word-initial segments than for word-medial or -final segments. This kind of positional effect is consistent with that observed for durational jnd's by Klatt and Cooper (1975). Hoshino and Fujisaki (1983) used vowel or consonant segments and reported that shortening modifications were more acceptable than lengthening modifications. Sagisaka and Tohkura (1984) used sentence stimuli in which every segmental duration was subjected to a random modification and reported that the acceptable modification size was about 30 ms.

Since these studies on acceptability evaluation were rather elementary and were primarily designed to measure the rough range of acceptable modification that could be instantly applied to their own durational rules, the number of speech samples employed in each study was not very large. Sato's study used four words, all starting with the same phoneme sequence (*saka*, *sakana*, *sakanaya*, and *sakanayasan*), Hoshino *et al.* used three nonsense words (*hatapaka*, *hatabaka*, and *hapakka*), and Sagisaka *et al.* used two sentences. Consequently, one should be prudent in generalizing the tendencies observed in these studies. Also, they did not provide any information to evaluate whether or not the factors affecting temporal jnd's would also affect acceptability, except for the factor of temporal position in a word.

B. Factors to be tested in the study

Based upon the above background discussions, the current study was designed to provide a direct and reliable test as to whether segment attributes or context affect the acceptability of durational modifications in speech segments. For this purpose, we limited the number of factors to be tested and their constituent levels in order to obtain sufficient data for each level of the factors. The tested factors were chosen from the factors themselves or from relevant factors that were reported as being effective in previous jnd or acceptability studies. Some of the chosen factors are also important in view of the control of segmental durations for speech synthesis (Crystal and House, 1988; Klatt, 1979; van Santen, 1992; Kaiki and Sagisaka, 1992), so experiments using these factors are of practical benefit for establishing durational rules based on perceptual characteristics.

Original duration. We should first examine the factor of the base or original duration because this is crucial for evaluating segmental errors in that it determines the unit in

which the errors should be considered, i.e., absolute duration (e.g., milliseconds) or relative duration (e.g., percent). To test this factor, a wide variety of durations are necessary for the test segments of the original materials. Therefore, the segments to be tested were chosen from vowel segments, which generally have the widest durational dispersion in spoken Japanese (Sagisaka and Tohkura, 1984). We then examined the following three factors.

Temporal position within a word. The tendency for a word-initial segment to be more susceptible to temporal modifications than a word-medial or -final segment was previously observed both in the jnd study (Klatt and Cooper, 1975) and in the acceptability study (Sato, 1977). They found this positional effect only in a single-stimulus context for each study. Thus, we included this factor to test whether it is statistically robust.

Vowel quality. The factor of phoneme difference was suggested in previous jnd studies (Carlson and Granström, 1975; Huggins, 1972). Although the contrast observed was that between vowels and consonants, we employed the contrast between two different vowels because the current study treated only vowel segments owing to the requirement of a wide durational variation. Vowel quality is, indeed, a major control factor in terms of durational rule (Peterson and Lehiste, 1960; Umeda, 1975; Sagisaka and Tohkura, 1984).

Voicing of the following consonant. Klatt *et al.* (1975) suggested the backward influence of words immediately following the segment in question. In accordance with this suggestion, the factor of the following segment was examined in the current study. To obtain enough samples to allow reliable statistical analyses for each of the constituent levels, we focused on the contrast between voiced and unvoiced consonants. The voicing of postvocalic consonants is acknowledged as a control factor for vowel durations in many languages (Delattre, 1962; Luce and Charles-Luce, 1985).

I. METHOD

A. Subjects

Seven adults with normal hearing participated in the experiment. All of them were native speakers of Japanese.

B. Stimuli

The original material was taken from the same speech database as reported in our previous paper (Kato *et al.*, 1997). The current study modified only one segment within a word while the previous study additionally modified either the preceding or following segment.

Seventy words were selected from the ATR speech database (Kurematsu *et al.*, 1990). All of them were commonly used four-mora Japanese words,[2] excluding words with doubled vowels, geminated consonants, or moraic nasals,[3] which have a heterogeneous syllable structure and, thus, may disturb the temporal regularities observed in open syllable sequences. The selected words were spoken naturally in isolation by one male speaker and were digitized at a 12-kHz sampling frequency and with 16-bit precision.

One segment out of four vowel segments in each stimulus word was subjected to durational modification. Each segmental duration of these target vowels was manually measured from the spectrographic images by well-trained labelers. The measured durations of the target vowels ranged from 35–145 ms as shown in Fig. 1. The three factors other than original duration were represented in the selected materials by the following three contrastive aspects of the target vowels: (1) the temporal position in a word was either the first or third moraic position, (2) the vowel quality was either /ɑ/ or /i/, the lowest or highest vowel in Japanese, and (3) the following consonant was either voiced or unvoiced. Table I shows the number of target vowels with these contrasts. The 70 selected tokens are listed in the Appendix (Table AI) with the attributes of each of the target vowels.

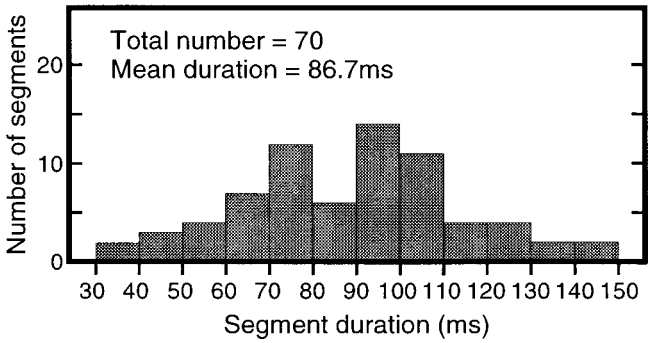

FIG. 1. Histograms in 10-ms bins showing the distribution of the segmental durations of the original vowel materials. Each duration was manually measured from spectrograms by trained labelers.

The temporal modifications were made by a cepstral analysis and resynthesis technique with the log magnitude approximation (LMA) filter (Imai and Kitamura, 1978), and were carried out at a 2.5-ms frame interval. The duration change was achieved by deleting or doubling every *n*th frame in the synthesis parameters throughout the whole vowel.

Each target vowel duration was shortened or lengthened over a range that extended from −50 ms to +50 ms from the original duration in 5-ms steps, resulting in 21 different modification steps. Since 5 of the 70 target durations were less than 50 ms, i.e., their modification did not reach −50 ms, their modification steps were less than 21. In total, 1452 word stimuli were prepared.[4] As a result of a preliminary listening, it was confirmed that there was no phonemic shift in either the target vowels or the surrounding phonemes caused by these manipulations.

C. Procedures

The prepared stimuli were first recorded onto a digital audiotape (DAT) through a D/A converter (MD-8000 mkII,

TABLE I. The number of selected vowel segments which fell into each of the cells defined by the factors to be tested. The number of segments followed by voiced consonants are in parentheses.

	First mora	Third mora	Total
/ɑ/	21 (15)	22 (12)	43 (27)
/i/	14 (10)	13 (10)	27 (20)
Total	35 (25)	35 (22)	70 (47)

PAVEC) and a low-pass filter (FV-665, NF Electronic Instruments, $fc = 5700$ Hz, -96 dB/oct) with a DAT recorder (DTC-55ES, SONY), and then presented diotically to the subjects through headphones (SR-Λ Professional, driven by SRM-1 MkII, STAX) in a sound-treated room. A 4-s interval was inserted after each presentation for the subjects' response. The average presentation level was 73 dB (A weighted) which was measured with a sound level meter (type 2231, Brüel & Kjær) mounted on an artificial ear (type 4153, Brüel & Kjær).

The subjects were told that each stimulus word was possibly subjected to a temporal modification. Their task was to evaluate how acceptable each stimulus was, as an exemplar of the token of that stimulus on a seven-point rating scale ranging from -3 to 3, where -3 corresponds to ''quite acceptable'' and 3 corresponds to ''unacceptable.'' [5] The subjects were asked to limit their responses to the temporal aspect of the stimuli, as much as possible. A total experimental run for each subject was comprised of ten sessions. Seven of the 70 tokens were chosen for each session, and 4 repetitions of their 21 modified versions were randomly presented in the session. Thus, each subject evaluated each stimulus four times in total. Each of the seven tokens within a session was carefully picked from each constituent level of the factors to be tested, assuring that the seven tokens were as uniformly distributed as possible throughout the levels; the primary criterion was the uniformity in the variation of the original duration.

II. RESULTS

A. Measure of acceptability

Figure 2 shows the obtained evaluation scores pooled over all subjects and all target vowels, plotted as a function of change in the duration of the target vowels. As seen in the figure, the evaluation score had a general inclination; i.e., the bottom of the scatter plot, the most acceptable point, is located around the center of the horizontal axis, and the score increases in an accelerated manner from that bottom point as the absolute change increases. The subjects' sensitivity to durational modification can be represented by the sharpness of the rise from the bottom point. Although a similar inclination was observed in all individual plottings obtained for each combination of subjects and target vowels, the size of the horizontal or vertical shift of the bottom point varied depending on the subject or target. These bottom point shifts can be regarded as subject response biases.[6] To parametrize the subjects' sensitivity or the vulnerability of the target vowels irrespective of these response biases, a parabolic regression as generally formulated below was applied to this plot (superimposed in Fig. 2),[7]

$$\text{Evaluation score} = \alpha(\Delta T - \beta)^2 + \gamma, \tag{1}$$

where ΔT is the change in duration; the unit of ΔT is not relative duration but milliseconds. This regression was the best fitted polynomial function to this plot on the basis of the F-ratio criterion, i.e., the second order model achieved the smallest probability of the null hypothesis [$F(2,10231) = 1699.4$, $p < 0.0001$]. The coefficient of the second-order

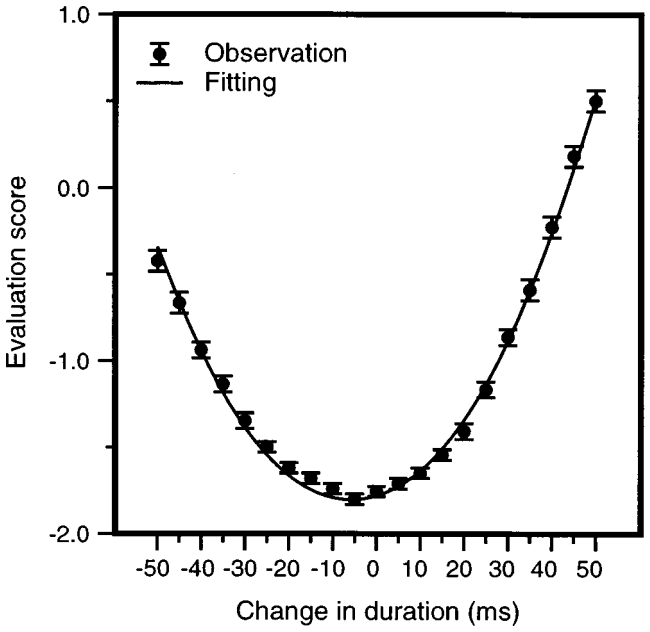

FIG. 2. Evaluation scores of acceptability pooled over stimuli and subjects as a function of change in the duration of vowel segments. Each point consists of 1960 observations (70 stimuli×7 subjects×4 observations). The error bars show the standard errors. A fitting curve by the second-order polynomial regression is superimposed. The curve is formulated as $y = 0.000743(x + 5.68)^2 - 1.77$.

term or α of this parabolic curve shows the rate of change in the evaluation score with a change in durational modification; both horizontal and vertical response biases can be separated out as β and γ. As derived from Eq. (1), α represents the average decrement[8] of the acceptability for a certain size of temporal modification, and also the width between the longer and shorter limits of the temporal modification which yields a certain amount of acceptability decrement, i.e., an acceptable range. Thus, α indicates the vulnerability of the vowel durations from the temporal modification. Therefore, we adopted the second-order polynomial coefficient of the fitting curve as the object variable of the current study and refer to it as a vulnerability index or simply α, hereafter.

We then applied a parabolic fitting to the evaluation scores for each of the 70 target vowels and each of the seven subjects, obtaining 490 fitting curves. Figure 3 shows typical examples of individual fittings illustrating the difference in the acceptability change between two different targets. Prior to the statistical analyses, we dropped unreliable data (fitting curves) on the basis of two criteria: (1) a fitting curve in which α was not positive was dropped because it suggests that the subject probably sensed no durational change for that particular token, and (2) a fitting curve in which the axis was extremely remote (more than six times sigma) from the distribution center of the entire data was dropped. Thus, ten fitting curves were excluded, i.e., seven eliminations due to the first criterion, one elimination due to the second, and two eliminations due to both criteria, resulting in 480 fitting curves. Thus, the object variable of this study consists of 480 α scores.

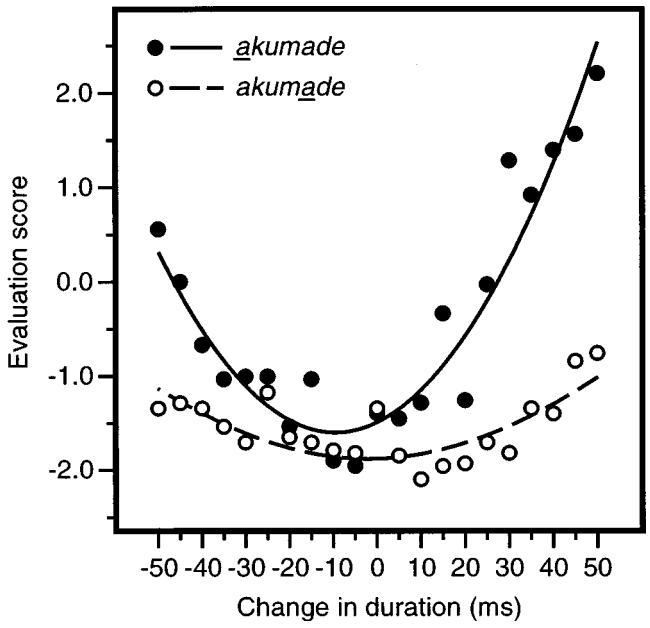

FIG. 3. An example illustrating a difference in acceptability change between two different vowels. The vowels which were subjected to durational modification are marked with underlines in the legend. The scatter plots show that the evaluation score varies according to the durational change more drastically for the first vowel of the word *akumade* (to the bitter end) (filled circles) than for the third vowel of the same word (open circles). The two regression curves trace this tendency. These are formulated as $y=0.00116(x+9.48)^2-1.44$ (solid line), and $y=0.000322(x+2.02)^2-1.84$ (dashed line).

B. Effect tests

First, the effect of the original segmental duration on the vulnerability index was tested. The Pearson's product-moment correlation coefficient was extremely small ($r=0.0189$) (e.g., McCall, 1980) and the general linear model (SAS Institute, Inc., 1990) with subject as the random factor showed no significant effect [$F(1,6)=0.127$, $p>0.73$]. [A more tolerant criterion, the Spearman's rank correlation test, also showed no significant effect ($\rho=0.077$).] To examine these analyses more specifically, we further computed correlations between the original duration and the vulnerability index within each of the seven subjects. As shown in Table II, the absolute values of the correlation coefficients were fairly small and their signs did not agree with each other, i.e., four positive correlations and three negative ones.

Next, the effects of the other three factors on the vulnerability index were tested. A three-way factorial ANOVA of repeated measures was performed with position in a word, vowel quality, and voicing of the following consonant as the main factors, and with subject as the blocking factor. The main effects of position in a word, vowel quality, and voicing of the following consonant were significant [$F(1,42)=22.5$, $p<0.001$; $F(1,42)=16.3$, $p<0.001$; $F(1,42)=30.9$, $p<0.001$, respectively]. As shown in Fig. 4(a)–(c), the vulnerability index was greater for vowels at the first moraic position in a word than those at the third moraic position. It was also greater for the vowel /ɑ/ than for the vowel /i/, and similarly greater for vowels followed by unvoiced consonants than for those followed by voiced conso-

TABLE II. The correlation coefficients between the original duration and the vulnerability index (α) for each of the seven subjects, in terms of either Pearson's product-moment correlation or Spearman's rank correlation analysis.

Subject ID	Pearson's r	Spearman's ρ
1	0.25	0.31
2	0.081	0.17
3	−0.17	−0.12
4	0.31	0.36
5	−0.27	−0.21
6	0.17	0.23
7	−0.060	−0.041

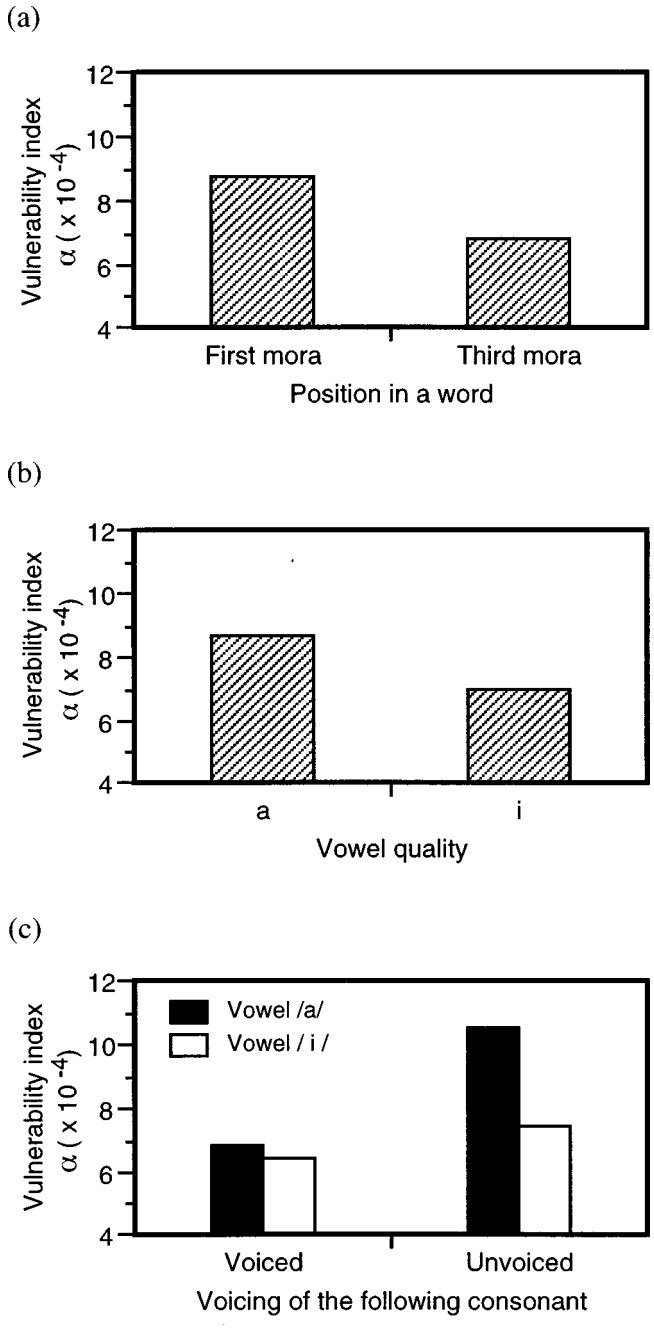

FIG. 4. The least squares means of the vulnerability index (α), the second-order polynomial coefficient of the fitting curve, for each level in the factors of (a) temporal position in a word, (b) vowel quality, and (c) voicing of the following consonant; they were calculated in the ANOVA procedure. A larger α implies a narrower acceptable range.

nants. There was a significant interaction between the factors of vowel quality and voicing of the following consonant [$F(1,42)=10.7$, $p<0.003$]; the effect of voicing of the following consonant was larger for the vowel /ɑ/ than for the vowel /i/. No other interaction was significant.

The target vowel that fell into the most vulnerable (i.e., susceptible to durational modification) combination of these three factors was /ɑ/ followed by an unvoiced consonant at the first moraic position in a word. That which fell into the least vulnerable combination was /i/ followed by a voiced consonant at the third moraic position in a word. The ratio of the averaged α score of the most vulnerable targets to that of the least vulnerable targets was 1.96. This means that the least vulnerable targets required 140% of the temporal modification of the most vulnerable targets to yield the same acceptability decrement. In other aspects, a certain modification size which was evaluated as acceptable for one vowel, say 50 ms, could become unacceptable for another vowel depending on the vowel's attributes and context.

III. DISCUSSION

The primary purpose of the current study was to test whether or not the segment attributes or context affect the perceptual sensitivity to modifications in vowel durations, and, if so, how large these effects are. The results showed that the vulnerability index (α score) was affected by the three experimental factors: (1) position, (2) quality, and (3) voicing. This indicates that perceptual acceptability changes as a function of temporal modification at a different rate depending on the attributes and context of the segment, such as its temporal position in the word, its vowel quality, and the voicing of the following consonant. In contrast, the original vowel duration had no significant effect on the vulnerability index despite its wide variation, i.e., 35–145 ms. The following two subsections will try to provide perceptual implications for each of the test factors that did or did not yield a significant effect, in relation to previous studies on auditory temporal perception.[9]

A. Original duration

The present results revealed that the original vowel duration had no significant linear relation with the vulnerability index. This implies that the absolute acceptable range depends little on the original vowel duration. This result appears to disagree with the result of Bochner *et al.*'s (1988) study and agrees with that of the study of Klatt and Cooper (1975). Bochner *et al.* reported that the absolute jnd of the vowel duration increased with an increase in the original vowel duration. Klatt *et al.*, on the other hand, found no significant correlation between the jnd's of vowel durations and their original durations. The stimulus conditions of these two studies differed from each other principally in two aspects: the range of vowel durations tested, and the context in which the tested vowels were embedded. The range of vowel durations tested in the current study, 35–145 ms, was closer to that of Bochner *et al.*'s study, 75–175 ms, than that of Klatt *et al.*'s study, 165–340 ms, although the current results did not agree with those of Bochner *et al.*'s but with Klatt *et al.*'s. Therefore, the difference in the range of vowel durations is not likely to explain the disagreement between the results of Bochner *et al.*'s study and those of both Klatt *et al.*'s and the current studies.

For the presentation context of the tested vowels, Bochner *et al.* used a monosyllabic context, i.e., CVC or isolated vowel segment. Such a single-nucleus or isolated context is comparable to the stimulus presentations of the previous jnd studies using nonspeech filled durations (Abel, 1972b; Ruhm *et al.*, 1966; Small and Campbell, 1962); they presented single durations in isolation. The results of these nonspeech studies commonly showed a tendency similar to that of Bochner *et al.*'s study, i.e., the jnd's were roughly proportional to the base durations. On the other hand, the current study presented a vowel segment in polysyllabic context, i.e., a four-vowel word. Klatt *et al.* also employed a polysyllabic context, i.e., a sentence. This contrast in presentation context might suggest a general tendency underlying the perception of durational changes; i.e., an isolated or monosyllabic context makes the influence of the base duration effective while a polysyllabic context reduces or hides it. The polysyllabic presentation generally provides widely distributed information that spans a two-segment range or more, which listeners can utilize for their judgment in addition to the target duration itself. Although it is difficult to specify the valid cues in such wider processes owing to the limitation of the stimulus manipulation in the current experiment, it can be assumed that the listeners tended to depend on temporal cues distributed in a range wider than a single segment. The presence of such wide-ranging processes can also be suggested by the temporal compensation phenomena between two consecutive segments as Huggins (1968) and Kato *et al.* (1997) pointed out.

B. Psychophysical implications of the three factors affecting acceptability

The experimental results showed that at least three aspects of vowel segments affect the acceptability evaluation for temporal modifications in the segment: (1) the temporal position within a word, (2) the vowel quality, and (3) the voicing of the following consonant. Implications of these effects are discussed below. The discussions focus on whether the effects could be interpreted within psychophysical or auditory-based knowledge instead of speech-specific features. Psychophysical interpretations tend to provide a wider generalization of the effects than speech-specific ones do; they enable wide applicability in evaluating new materials that have not actually been examined.

1. Positional effect

The effect of the segment's position in the word found in the current study is consistent with that observed in the previous studies on both acceptability estimation (Sato, 1977) and jnd measurement (Klatt and Cooper, 1975). The listeners responded more critically to modifications in word-initial vowels than to those in the following vowels. A positional effect of this sort has also been reported for nonspeech stimuli (Tanaka *et al.*, 1994). Tanaka *et al.* measured temporal jnd's for one of three successive intervals marked by four

click sequences which were devised so as to replicate the temporal structure of a four-mora word. The results showed that the jnd for the first interval of a sequence was significantly smaller than that for the third interval, i.e., the listeners responded more sensitively to a temporal modification at the initial position than to one at the following position. Thus, the positional effect can be explained by a non-speech-specific mechanism.

2. Effect of vowel quality

The modifications in the vowel /ɑ/ had a stronger influence than those in the vowel /i/. In Japanese, the high vowel /i/ has a smaller intrinsic power, which correlates highly with loudness, than the low vowel /ɑ/ has (Mimura *et al.*, 1991) as observed in the contrast between high and low vowels in English (Lehiste and Peterson, 1959). This contrastive property of the power or loudness between these two vowels is likely to explain the effect found. Several studies have reported that the power or intensity of the stimuli affect the discrimination performance for different filled durations (Creelman, 1962; Kato and Tsuzaki, 1994; Tyler *et al.*, 1982).[10] Although their stimuli were not taken from speech, these studies commonly pointed out that a higher intensity level in the stimulus yielded a higher discrimination performance for the stimulus duration. This tendency can qualitatively explain the current effect of vowel quality; i.e., the vowel /ɑ/ was more susceptible to temporal change than the vowel /i/. In the current experiment, the loudness of the target vowel /ɑ/ was found to be, certainly, greater than that of the target vowel /i/. The average loudness of the vowels /ɑ/ and /i/ was 11.6 and 7.3 sone, respectively, which were calculated in accordance with ISO-532B (ISO, 1975) using Zwicker *et al.*'s (1991) algorithm. The difference between these two averages was confirmed to be significant by a Student's t test [$t(68)=6.54$, $p<0.001$].

3. Effect of voicing of the following consonant

The listeners responded more sensitively to a change in duration when the vowel whose duration was to be judged was followed by a voiceless consonant than when it was followed by a voiced consonant. This tendency appears to be consistent with the observation of Klatt and Cooper (1975); their listeners tended to be less sensitive to temporal changes in segments with following words than to those without following words. Klatt *et al.* suggested that the effect found might be due to some sort of backward recognition masking (Massaro and Cohen, 1975). Thus, the subsequent event, the presence of the following word, might disturb the listener's judgment of the target durations by overwriting new information onto the listener's auditory storage before he/she had completed the processing.

The current effect of the following consonant may be partially interpreted by an explanation of this sort, however, a more basic or lower-level influence should also be taken into account because the effect in the current study spans a relatively short range, i.e., a segment period, while that in Klatt *et al.*'s study probably spans a word period. Looking at the change in acoustic features on the vowel-to-consonant boundaries, greater changes are observed for the unvoiced consonant cases than for the voiced consonant cases, in terms of either $F0$, power, or spectrum. Therefore, we can reasonably assume that the offsets of vowels are perceptually more salient when they are followed by unvoiced consonants than when they are followed by voiced consonants. A greater perceptual effect can apparently be assumed for the temporal displacement of a boundary having a greater perceptual salience. This view is consistent with the previous finding that the perceptual salience for a temporal displacement of a segment boundary is high when there is a large loudness difference or jump at the boundary (Kato *et al.*, 1997).

TABLE III. The averages (and standard deviations in parentheses) of the original durations of the tested vowels, in milliseconds, for each of the constituent levels of the three factors: position in a word, vowel quality, and voicing of the following consonant.

Position in a word	
First mora	Third mora
77.1 (23.4)	96.3 (22.8)
Vowel quality	
/ɑ/	/i/
93.4 (22.0)	75.9 (25.7)
Voicing of the following consonant	
Voiced	Unvoiced
82.1 (28.0)	96.1 (12.9)

C. Interactions between original duration and the other three factors

Table III shows the means and standard deviations of the original durations of the vowels tested, for each of the constituent levels of the three factors: position in a word, vowel quality, and voicing of the following consonant. These averaged values suggest that none of the three factors is independent of the original duration. The difference in the average durations between two levels of each factor turned out to be significant as follows:

temporal position within a word: first mora<third mora,
vowel quality: /ɑ/>/i/,
voicing of the following consonant: voiced <unvoiced.[11]

Therefore, one might argue that the observed effects of these three factors are not substantial, and that the current result could be interpreted solely by the factor of original duration without considering the other three factors. In this subsection we will discuss this possibility.

Assuming the influence of the original duration, a shorter original duration was expected to yield a narrower absolute acceptable range. As a matter of fact, the reverse tendency was observed for the factor of vowel quality; the acceptable range was generally narrower for the vowel /ɑ/, which has a longer inherent duration, than for the vowel /i/, which has a shorter inherent duration. A similar discrepancy was found between the expected effect of the original duration and the observed effect in the case of the voicing of the following consonant. Therefore, these two factors may not be interchangeable with the factor of original duration.

The positional effect, on the other hand, appears to be in agreement with the expected effect of the original duration.

TABLE IV. The correlation coefficients between the original duration and the vulnerability index (α) for each of the eight conditions defined by the three factors other than the factor of original duration, i.e., position in a word (1 or 3), vowel quality (a or i), and voicing of the following consonant (v or uv), in terms of either Pearson's product-moment correlation or Spearman's rank correlation analysis.

Condition	Pearson's r	Spearman's ρ
1-a-v	0.043	0.055
1-a-uv	−0.092	−0.052
1-i-v	−0.10	−0.075
1-i-uv	0.082	0.0066
3-a-v	0.067	0.038
3-a-uv	−0.19	−0.10
3-i-v	0.016	0.023
3-i-uv	0.031	0.029

To examine this possibility specifically, the obtained vulnerability indices (α's) were separated into four subsets corresponding to four cells constituting the combination of the factors of vowel quality and voicing of the following consonant, i.e., (/ɑ/, /i/)×(voiced, unvoiced). Thus, no factors other than position and original duration had any influence within each of these subsets. We then applied a linear model onto the α score with either position in a word or original duration as an explanatory variable, for each subset. The results showed that position in a word correlated more highly with the α score than original duration in all subsets. These results support the view that the positional factor is a more plausible explanatory variable than the original duration.

Another problem then arises. As the effects of the three factors other than original duration are large, they may obscure a genuine effect of original duration. To test this possibility, we computed correlations between original duration and the α score within each of the eight conditions defined by the factors of position in a word, vowel quality, and voicing of the following consonant. The results showed that there is no condition where original duration has a significant effect in terms of both linear correlation and rank correlation as shown in Table IV.

Although these discussions may not be enough to reject the possibility of an influence of the original duration, they are enough to show that the difference in original duration cannot provide a consistent explanation of the observed tendencies in the vulnerability indices.

IV. SUMMARY

Acceptability of temporal unnaturalness was measured for word stimuli in which one of the vowel durations was systematically changed. The changes in acceptability depended on at least three factors: (1) the temporal position of the modified vowel within the word, (2) the quality of the modified vowel, and (3) the voicing of the consonant preceded by the modified vowel. For a given amount of modification, the listeners evaluated the modification of vowels at the third mora position in the word as more acceptable than the modification of those at the initial mora position in the word. They also evaluated the modification of /i/ segments as more acceptable than that of /ɑ/ segments, and they evaluated the modification of vowels followed by a voiced consonant as more acceptable than those followed by an unvoiced consonant. The original duration of the target vowel itself had no systematic effect on the rate of acceptability change.

The primary impact of the current study is that the least vulnerable vowel, the third /i/ followed by a voiced consonant, required 140% of the temporal modifications or durational errors required by the most vulnerable vowel, the first /ɑ/ followed by an unvoiced consonant, to yield the same acceptability decrement. These results suggest that the traditional measure for durational rules, the average acoustic error, is insufficient in terms of perceptual evaluation, i.e., acceptability rating. We expect a more valid (closer to human perception) measure for durational rules to be achieved by taking into account the perceptual factors suggested in the present study as weighting values in the error evaluation.

ACKNOWLEDGMENTS

We are grateful to Noriko Yoshikawa for running the experimental procedures, and to the listeners involved in the experiment. We would like to thank Nick Campbell and Hideki Kawahara for their many helpful comments and suggestions on early versions of this paper. We would also like to thank Yoh'ichi Tohkura for his continuous encouragement and the initial impetus for the current study.

APPENDIX: SEGMENTAL PROPERTIES AND α SCORE OF EACH TESTED VOWEL

Table AI shows the word texts used in the experiment in alphabetical order, and the position in a word, vowel quality, voicing of the following consonant, duration, and mean of vulnerability indices for each of the tested vowel segments.

TABLE AI. Words used in the experiment in alphabetical order, and the position in a word, vowel quality, voicing of the following consonant, duration, and mean of vulnerability indices (α's) for each of the tested vowel segments. The transcription of Japanese text is based on the Hepburn system. The vowels whose durations were subjected to modification are marked with boldface.

Text	Position	Vowel	Following consonant	Duration (ms)	$\alpha(\times 10^{-4})$
akumade	1	a	uv	102.5	11.56
akum**a**de	3	a	v	100	3.22
atsumaru	1	a	uv	102.5	7.85
b**a**kugeki	1	a	uv	105	12.93
b**a**rabara	1	a	v	95	4.96
barab**a**ra	3	a	v	80	3.42
ch**i**jimeru	1	i	v	70	5.61
fumik**i**ri	3	i	v	75	5.67
g**a**kureki	1	a	uv	100	12.83
hanah**a**da	3	a	v	70	4.87
h**a**nareru	1	a	v	55	6.01
h**a**rahara	1	a	v	75	7.78
harah**a**ra	3	a	v	75	3.40
h**a**rigane	1	a	v	65	5.20
hatar**a**ki	3	a	uv	130	6.26
hatsur**a**tsu	3	a	uv	115	8.65
h**i**rogaru	1	i	v	65	6.64
h**i**romeru	1	i	v	55	4.97
horob**i**ru	3	i	v	102.5	8.87

TABLE AI. (*Continued*.)

Text	Position	Vowel	Following consonant	Duration (ms)	$\alpha(\times 10^{-4})$
imas**a**ra	3	a	v	90	6.72
iriguchi	1	i	v	95	4.88
kakur**i**tsu	3	i	uv	95	6.99
kakuj**i**tsu	3	i	uv	90	6.48
k**a**nashimu	1	a	v	55	9.76
kasan**a**ru	3	a	v	120	8.83
k**a**tameru	1	a	uv	77.5	10.55
ketob**a**su	3	a	uv	92.5	9.65
k**i**nodoku	1	i	v	57.5	5.92
kogat**a**na	3	a	v	75	6.91
korog**a**su	3	a	uv	95	10.51
kotog**a**ra	3	a	v	135	5.19
kurush**i**mu	3	i	v	60	5.35
m**a**monaku	1	a	v	70	6.10
m**a**rumeru	1	a	v	120	8.89
matag**a**ru	3	a	v	125	5.87
m**i**kakeru	1	i	uv	80	7.64
m**i**nogasu	1	i	v	60	10.37
m**i**tomeru	1	i	uv	85	10.12
m**i**tsumeru	1	i	uv	90	6.45
muras**a**ki	3	a	uv	95	8.32
n**a**gedasu	1	a	v	110	10.25
n**a**nishiro	1	a	v	100	13.56
n**a**raberu	1	a	v	90	7.45
n**a**ruhodo	1	a	v	95	8.69
n**i**semono	1	i	uv	75	7.54
nokog**i**ri	3	i	v	145	4.90
osam**a**ru	3	a	v	140	3.60
rokug**a**tsu	3	a	uv	105	12.41
s**a**bireru	1	a	v	85	7.40
s**a**kasama	1	a	uv	80	14.23
sashid**a**su	3	a	uv	100	10.32
setsur**i**tsu	3	i	uv	105	6.80
sh**i**baraku	1	i	v	37.5	8.36
sh**i**mekiri	1	i	v	40	5.21
shimek**i**ri	3	i	v	70	3.00
sh**i**mekiru	1	i	v	35	6.73
shimij**i**mi	3	i	v	65	7.19
sh**i**nabiru	1	i	v	47.5	8.56
shinab**i**ru	3	i	v	90	7.29
tachim**a**chi	3	a	uv	110	8.39
t**a**dachini	1	a	v	45	9.99
t**a**matama	1	a	v	60	8.95
tamat**a**ma	3	a	v	75	6.88
tanoshimi	3	i	v	70	4.99
tanoshimu	3	i	v	65	7.02
tomok**a**ku	3	a	uv	90	9.07
tonik**a**ku	3	a	uv	90	9.17
uragiru	3	i	v	125	5.72
z**a**razara	1	a	v	117.5	7.67
zaraz**a**ra	3	a	v	105	2.42

[1]Although the authors of the original reference did not mention this irrelevancy explicitly, our analysis of their data showed no significant correlation between the base duration and the absolute jnd. The Pearson product moment was very small ($r=0.011$). The linear regression also turned out to be not effective [$F(1,5)=0.0007$, $p=0.98$].

[2]To maximize freedom in word selection, we chose the materials from the four-mora words which are lexically the most frequent in contemporary Japanese (Yokoyama, 1981).

[3]In the orthography, each of them has a separate character with the same status as the CV units.

[4]They were (20 modification steps+1 unmodified)×70 vowels−18 (incomplete steps for the target vowels whose durations were less than 50 ms).

[5]If listeners were asked to estimate ''naturalness,'' they might tend to use such a strict criterion that one could not maintain an effective evaluation for the whole range of temporal modification to be tested. To obtain information for a reasonably wide range of modifications, we chose the ''rating of acceptability'' over the ''rating of naturalness.''

[6]The horizontal value of the bottom point reflects the amount of modification required to obtain the most preferred duration of the target vowel from its original, as-produced, duration. The vertical value of the bottom point reflects the score which the subject gave to his/her best duration. These two aspects might be influenced by factors that are difficult to control in experiments, i.e., subjects' response biases.

[7]Although we could choose fitting functions other than polynomial fittings and/or could rescale the vertical axis to obtain an interval scale, we adopted the parabolic fitting on the raw evaluation scores because of the advantage of its directly reflecting the subjects' responses and its goodness of fitting.

[8]As we assigned a larger evaluation score to a more unacceptable or less acceptable impression, an increment of the evaluation score implies a decrement of the acceptability.

[9]Most of the studies included in the current discussion were based on measurements of duration discriminability. Although discriminability studies may not be directly compared with acceptability studies in general, the vulnerability index used in the current study has been reported to reflect, to some extent, the variation in duration discrimination thresholds or jnd's (Kato *et al.*, 1992). We, therefore, recognize that it is valuable to discuss the agreements and discrepancies between the current results of acceptability tests and the previous results of jnd studies.

[10]For auditory intervals filled with noise or pure tones, the discrimination performance for stimulus duration does not appear to be affected by a change in intensity, as long as the stimulus whose duration is to be judged is presented in isolation and is clearly audible (Allan, 1979; Abel, 1972a; Creelman, 1962). However, it has been reported to be affected if the duration to be judged was not clearly marked (Creelman, 1962; Tyler *et al.*, 1982) or if it was presented between preceding and following sounds just as a speech segment in a word is usually surrounded by other segments (Kato and Tsuzaki, 1994).

[11]Although the duration of a vowel or syllable nucleus in English is generally shorter when it is followed by an unvoiced segment than when it is followed by a voiced segment (Peterson and Lehiste, 1960), a vowel duration in Japanese has no clear tendency of this sort. The reverse tendency has even been reported by Campbell and Sagisaka (1991); they showed that vowels followed by unvoiced consonants are longer than those followed by voiced consonants, as a result of the statistical analysis of a spoken Japanese database comprised of 503 sentences.

Abel, S. M. (**1972a**). ''Discrimination of temporal gaps,'' J. Acoust. Soc. Am. **52**, 519–524.

Abel, S. M. (**1972b**). ''Duration discrimination of noise and tone bursts,'' J. Acoust. Soc. Am. **51**, 1219–1223.

Allan, L. G. (**1979**). ''The perception of time,'' Percept. Psychophys. **26**, 340–354.

Allen, J., Hunnicutt, M. S., and Klatt, D. H. (**1987**). *From Text to Speech: The MITalk System* (Cambridge U.P., Cambridge, UK).

Bochner, J. H., Snell, K. B., and MacKenzie, D. J. (**1988**). ''Duration discrimination of speech and tonal complex stimuli by normally hearing and hearing-impaired listeners,'' J. Acoust. Soc. Am. **84**, 493–500.

Campbell, W. N. (**1992**). ''Multi-level timing in speech,'' doctoral dissertation, University of Sussex, Brighton, UK.

Campbell, W. N., and Sagisaka, Y. (**1991**). ''Moraic and syllable-level effects on speech timing,'' Acoustical Society of Japan, Trans. Tech. Committee Speech SP90-107, pp. 35–40.

Carlson, R., and Granström, B. (**1975**). ''Perception of segmental duration,'' in *Structure and Process in Speech Perception*, edited by A. Cohen and S. Nooteboom (Springer-Verlag, Berlin), pp. 90–106.

Carlson, R., and Granström, B. (**1986**). ''A search for durational rules in a real-speech database,'' Phonetica **43**, 140–154.

Creelman, C. D. (**1962**). ''Human discrimination of auditory duration,'' J. Acoust. Soc. Am. **34**, 582–593.

Crystal, T. H., and House, A. S. (**1988**). ''Segmental durations in connected-speech signals: Current results,'' J. Acoust. Soc. Am. **83**, 1553–1573.

Delattre, P. C. (**1962**). ''Some factors of vowel duration and their cross-linguistic validity,'' J. Acoust. Soc. Am. **34**, 1141–1143.

Fant, G., and Kruckenberg, A. (**1989**). ''Preliminaries to the study of Swedish prose reading and reading style,'' Royal Institute of Technology, Speech Transmission Lab. Q. Prog. Status Report 2/1989, pp. 1–83.

Fujisaki, H., Nakamura, K., and Imoto, T. (**1975**). ''Auditory perception of duration of speech and non-speech stimuli,'' in *Auditory Analysis and Perception of Speech*, edited by G. Fant and M. A. A. Tatham (Academic, London), pp. 197–219.
Higuchi, N., Shimizu, T., Kawai, H., and Yamamoto, S. (**1993**). ''Control of phoneme duration based on the movement of speech organs,'' J. Acoust. Soc. Jpn. (E) **14**, 281–283.
Hoshino, M., and Fujisaki, H. (**1983**). ''A study on perception of changes in segmental durations,'' Acoustical Society of Japan, Trans. Tech. Committee Speech S82-75, pp. 593–599 (in Japanese with English abstract and English figure captions).
Huggins, A. W. F. (**1968**). ''The perception of timing in natural speech: Compensation within the syllable,'' Language and Speech **11**, 1–11.
Huggins, A. W. F. (**1972**). ''Just noticeable differences for segment duration in natural speech,'' J. Acoust. Soc. Am. **51**, 1270–1278.
Imai, S., and Kitamura, T. (**1978**). ''Speech analysis synthesis system using the log magnitude approximation filter,'' The Transactions of the Institute of Electronics and Communication Engineers **J61-A**, 527–534 (in Japanese with English figure captions).
ISO (**1975**) ISO 532-1975 (E). ''Acoustics—Method for calculating loudness level'' (International Organization for Standardization, Geneva).
Kaiki, N., and Sagisaka, Y. (**1992**). ''The control of segmental duration in speech synthesis using statistical methods,'' in *Speech Perception, Production and Linguistic Structure*, edited by Y. Tohkura, E. Vatikiotis-Bateson, and Y. Sagisaka (IOS, Amsterdam), pp. 391–402.
Kato, H., and Tsuzaki, M. (**1994**). ''Intensity effect on discrimination of auditory duration flanked by preceding and succeeding tones,'' J. Acoust. Soc. Jpn. (E) **15**, 349–351.
Kato, H., Tsuzaki, M., and Sagisaka, Y. (**1992**). ''Acceptability and discrimination threshold for distortion of segmental duration in Japanese words,'' in *Proceedings of International Conference on Spoken Language Processing* (University of Alberta, Edmonton, AB), pp. 507–510.
Kato, H., Tsuzaki, M., and Sagisaka, Y. (**1997**). ''Acceptability for temporal modification of consecutive segments in isolated words,'' J. Acoust. Soc. Am. **101**, 2311–2322.
Klatt, D. H. (**1976**). ''Linguistic uses of segmental duration in English: Acoustic and perceptual evidence,'' J. Acoust. Soc. Am. **59**, 1208–1221.
Klatt, D. H. (**1979**). ''Synthesis by rule of segmental durations in English sentences,'' in *Frontiers of Speech Communication Research*, edited by B. Lindblom and S. Öhman (Academic, London), pp. 287–299.
Klatt, D. H., and Cooper, W. E. (**1975**). ''Perception of segment duration in sentence contexts,'' in *Structure and Process in Speech Perception*, edited by A. Cohen and S. G. Nooteboom (Springer-Verlag, Berlin), pp. 69–89.
Kurematsu, A., Takeda, K., Sagisaka, Y., Katagiri, S., Kuwabara, H., and Shikano, K. (**1990**). ''ATR Japanese speech database as a tool of speech recognition and synthesis,'' Speech Commun. **9**, 357–363.
Lehiste, I., and Peterson, G. E. (**1959**). ''Vowel amplitude and phonemic stress in American English,'' J. Acoust. Soc. Am. **31**, 428–435.
Luce, P. A., and Charles-Luce, J. (**1985**). ''Contextual effects on vowel duration, closure duration, and the consonant/vowel ratio in speech production,'' J. Acoust. Soc. Am. **78**, 1949–1957.
Massaro, D. W., and Cohen, M. M. (**1975**). ''Perceptual auditory storage in speech recognition,'' in *Structure and Process in Speech Perception*, edited by A. Cohen and S. G. Nooteboom (Springer-Verlag, Berlin), pp. 226–245.
McCall, R. B. (**1980**). *Fundamental Statistics for Psychology* (HBJ, New York), 3rd ed.
Mimura, K., Kaiki, N., and Sagisaka, Y. (**1991**). ''Statistically derived rules for amplitude and duration control in Japanese speech synthesis,'' in *Proceedings of Korea-Japan Joint Workshop on Advanced Technology of Speech Recognition and Synthesis*, pp. 151–156.
Peterson, G. E., and Lehiste, I. (**1960**). ''Duration of syllable nuclei in English,'' J. Acoust. Soc. Am. **32**, 693–703.
Riley, M. (**1992**). ''Tree-based modelling of segmental durations,'' in *Talking Machines: Theories, Models, and Designs*, edited by G. Bailly, C. Benoît, and T. R. Sawallis (Elsevier, Amsterdam), pp. 265–273.
Ruhm, H. B., Mencke, E. O., Milburn, B., Cooper, W. A., and Rose, D. E. (**1966**). ''Differential sensitivity to duration of acoustic signals,'' J. Speech Hear. Res. **9**, 371–384.
Sagisaka, Y., and Tohkura, Y. (**1984**). ''Phoneme duration control for speech synthesis by rule,'' The Transactions of the Institute of Electronics and Communication Engineers **J67-A**, 629–636 (in Japanese with English figure captions).
SAS Institute, Inc. (**1990**). *SAS/STAT User's Guide, Version 6* (SAS Institute, Cary, NC), 4th ed., Vol. 2.
Sato, H. (**1977**). ''Segmental duration and timing location in speech,'' Acoustical Society of Japan, Trans. Tech. Committee Speech S77-31, pp. 1–8 (in Japanese with English abstract and English figure captions).
Small, A. M., and Campbell, R. A. (**1962**). ''Temporal differential sensitivity for auditory stimuli,'' Am. J. Psychol. **75**, 401–410.
Takeda, K., Sagisaka, Y., and Kuwabara, H. (**1989**). ''On sentence-level factors governing segmental duration in Japanese,'' J. Acoust. Soc. Am. **86**, 2081–2087.
Tanaka, M., Tsuzaki, M., and Kato, H. (**1994**). ''Discrimination of empty duration in the click sequence simulating a mora structure,'' J. Acoust. Soc. Jpn. (E) **15**, 191–192.
Tyler, R. S., Summerfield, Q., Wood, E. J., and Fernandes, M. A. (**1982**). ''Psychoacoustic and phonetic temporal processing in normal and hearing-impaired listeners,'' J. Acoust. Soc. Am. **72**, 740–752.
Umeda, N. (**1975**). ''Vowel duration in American English,'' J. Acoust. Soc. Am. **58**, 434–445.
van Santen, J. P. H. (**1992**). ''Contextual effects on vowel duration,'' Speech Commun. **11**, 513–546.
van Santen, J. P. H. (**1994**). ''Assignment of segmental duration in text-to-speech synthesis,'' Comput. Speech Lang. **8**, 95–128.
Yokoyama, S. (**1981**). ''Occurrence frequency data of a Japanese dictionary,'' Bulletin of the Electrotechnical Laboratory **45**, 395–418.
Zwicker, E., Fastl, H., Widmann, U., Kurakata, K., Kuwano, S., and Namba, S. (**1991**). ''Program for calculating loudness according to DIN 45631 (ISO 532B),'' J. Acoust. Soc. Jpn. (E) **12**, 39–42.

Characterizing the clarinet tone: Measurements of Lyapunov exponents, correlation dimension, and unsteadiness

Teresa D. Wilson
4558 Ave. A, #209, Austin, Texas 78751

Douglas H. Keefe
Boys Town National Research Hospital, 555 North 30th Street, Omaha, Nebraska 68131

(Received 19 December 1997; revised 1 April 1998; accepted 2 April 1998)

The clarinet tone is produced by a self-sustained oscillation involving nonlinearity between the flow through the reed and the mechanical response of the reed, and acoustic coupling via the air column response. Regimes of oscillation include periodic, biperiodic, and other quasi-periodic signals, yet even a nominally periodic tone has small, but perceptually and musically important, deviations that are obscured in a conventional power spectrum. Such deviations may be due to the nonlinear dynamics underlying sound production or to perturbations in the performer's control of the instrument via changes in lip embouchure, blowing pressure, and vocal tract configuration. Techniques based upon experimental nonlinear dynamics and short-time signal processing are applied to the acoustic signal measured within the clarinet mouthpiece to assess the role of these additional deviations on sound production. These include the Lyapunov exponent, correlation dimension, and a normalized period-synchronous energy variance, termed unsteadiness. Normal tones and multiphonics are indistinguishable with respect to their Lyapunov exponents. The largest exponent is small and positive, indicating a small amount of information loss each cycle. The information in clarinet tones diminishes at rates ranging from 10 to 60 bits/s. Unsteadiness accounts for the variations in correlation dimension for normal tones but not for multiphonics. These measures may be useful in the study of more subtle aspects of tone production in wind instruments.
 [S0001-4966(98)03507-3]

PACS numbers: 43.75.Ef [WJS]

INTRODUCTION

Reed-driven wind instruments including the clarinet rely on the nonlinear valving action of the reed on the air flow. The reed motion is strongly coupled to the acoustic responses of the air column and the player's vocal tract in terms of the pressure difference acting across the reed. Periodic or biperiodic attractors are established in which the steady blowing pressure contributed by the player is converted into a nonlinear, phase-locked oscillation. Techniques devised in experimental nonlinear dynamics are well-suited for the study of wind-instrument sound generation.

In addition to the nonlinear attributes associated with the analytically tractable models of the interactions of the reed, air-column, and vocal-tract oscillators on the air flow entering the wind instrument, there exist other processes influencing sound generation that add further degrees of freedom to the dynamical system. Focusing attention on the clarinet, such processes include the possible motion of the lip and embouchure, involuntary muscle movements in the lip, and air-flow turbulence through the reed opening and mouthpiece. The stable pressure waveform and its perturbation by the presence of these additional degrees of freedom constitute the physical correlate to what we think of as a natural clarinet tone. The musical expressiveness of wind instruments is related to such departures from strictly periodic oscillations. The research presented in this report investigates quantitative descriptions of sound produced within a clarinet mouthpiece using signal processing techniques from experimental nonlinear dynamics and short-time analyses. The purpose is to objectively assess the role of these additional degrees of freedom on sound production.

Techniques from nonlinear dynamics have been applied to the analysis of wind-instrument sounds. Using a simplified model of the cane-reed instrument, McIntyre *et al.*,[1] Maganza *et al.*,[2] and Brod[3] showed that the nonlinear flow function through the reed tip could be put in the form of an iteration equation and that wind instruments should undergo a Feigenbaum-type route to chaos, with a cascade of period doublings. Maganza *et al.* performed experiments on both a plastic tube and a real clarinet without a mouthpiece and observed period doubling for both resonators. Gibiat[4] repeated Maganza's experiment and created phase space representations and Poincaré sections of actual wind-instrument tones. He observed period doubling and tripling and found that multiphonics are biperiodic with closed-curve Poincaré sections and spectra that are linear combinations of two frequencies. Keefe and Laden[5] found that multiphonics have a broadband spectral component not present for normal tones. They calculated correlation dimensions for clarinet and saxophone multiphonics and suggested that the fractional correlation dimensions they found may imply a strange attractor for these multiphonics. Kobata and Idogawa[6] and Idogawa *et al.*[7] created phase space representations and calculated correlation dimensions for sounds from an artificially blown clarinet using an E3 (written) fingering. They observed periodic, biperiodic, and one triperiodic oscillation, as well as one possibly chaotic oscillation that had a broadband spectral

component. They found fractional correlation dimensions even for periodic tones.

In addition to the sound produced by the nonlinear processes that control the oscillation, there is also a noise component present in a tone. There have been a few attempts to study and characterize this noise. Chafe[8,9] and Cook[10] have studied noise in synthesized instrument tones and in the voice. They found that when pulsed noise is added in sync with the nonlinear control mechanism, it creates more ''well-incorporated'' noise in synthesized sounds. Schumacher and Chafe[11] and Schumacher[12] used the norm difference method to detect noise features such as low-amplitude subharmonic oscillations. It appears that an acoustic characterization of the noise in real wind instruments is necessary to produce authentic synthesized sounds. When the noise is not present, the sound has a ''fixed'' quality since the ''controlled randomness'' of the minute changes that occur during actual performance are not present.[13]

Previous researchers have reported that wind-instrument sounds have fractional dimension and have speculated on the possible presence of chaos in such sounds. If an attractor exists, a calculation of the Lyapunov exponent (LE) tests whether or not a system is chaotic, i.e., whether or not there is a sensitive dependence on initial conditions. A technique to measure the LE is described below and used to interpret the process of sound production in the clarinet.

The concept of a regime of oscillation is constructed upon the idealized case of a periodic sound, whose partials are exactly harmonic. The existence of additional degrees of freedom produces deviations from periodicity. The approach developed by Bouasse and Benade emphasizes that wind instrument sounds may vary in fundamental frequency but that the presence of phase-locking keeps the partials harmonically related on a short-time basis. This suggests that variations in the short-time energy may conveniently be studied after removing the short-time variations in the period. This is analogous to the pitch synchronous spectrum analysis technique developed to analyze voiced speech.[14] Our emphasis is to relate the fluctuations in period-synchronous signal energy, which we term *unsteadiness*, to measurements of dimension and LE, so that we can characterize the fine structure of the clarinet tone.

The purely physics approach to the study of clarinet tones might well focus on tones produced using an artificial blowing apparatus, but our more interdisciplinary interest is the study of clarinet tones produced by performers. Each performer participating in this study was a professional clarinetist, and each was capable of an exceedingly high control over the various technical and musical aspects of tone production.

The next section describes the data analyzed and the experimental set up. Section II, defines the nonlinear dynamics concepts and describes the numerical methods used to calculated the correlation dimension, the Lyapunov exponents, and the unsteadiness. Section III presents the results of the analysis on measured clarinet tones. Section IV is a discussion of the results, and Sec. V describes our conclusions.

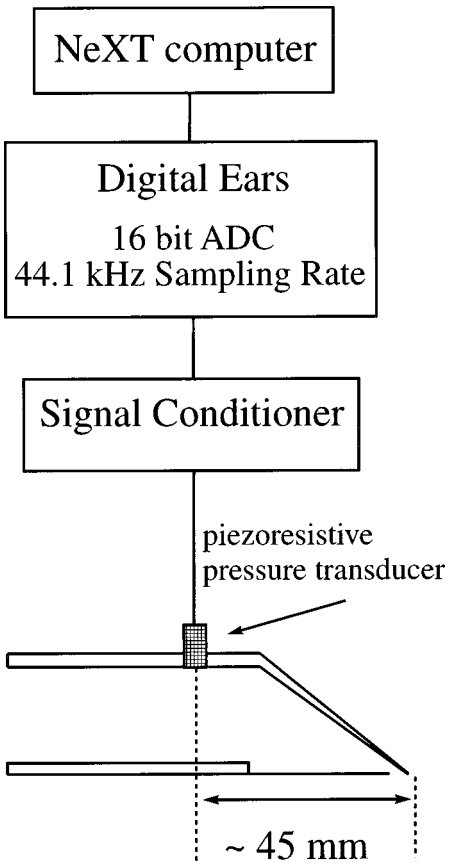

FIG. 1. Experimental setup.

I. EXPERIMENTAL METHODS

The data used in the analysis were pressure time series measured inside the mouthpiece of a clarinet (Fig. 1). A piezoresistive transducer (Endevco model 8510B-2, o.d. 3.8 mm) was inserted into a hole drilled into the top surface of a mouthpiece about 45 mm from the mouthpiece tip. The transducer was inserted so that it was flush with the inner mouthpiece wall, and the outside surface was sealed with wax. A professional-level clarinetist was asked to play a musically steady normal tone or a multiphonic for 5–10 s. The signal from the transducer passed through a signal conditioner and into the Digital Ears 16-bit analog-to-digital converter, which sampled the signal at a rate of 44.1 kHz. A NeXT computer stored the data as a sound file.

The pressure measured at this position is not the input pressure (in the linear approximation) at the tip of the mouthpiece. While this discrepancy affects the interpretation of spectra, it is irrelevant to the signal processing techniques of primary interest.

II. NUMERICAL METHODS

The nonlinear dynamic quantities calculated were the Lyapunov exponents, the correlation dimension, and a measure of the unsteadiness, to be defined below.

A. Lyapunov exponents

After an initial transient, an invariant set of trajectories is attained in the phase space of the dynamical system. This

invariant set is an attracting set if a sufficiently small perturbation in any trajectory in the invariant set asymptotically converges back to the invariant set. Any attracting set that is physically observable is an attractor. The geometrical structure of the attractor can often be classified in terms of its representation in phase space, whereas its temporal structure is assessed in terms of the Lyapunov exponent. That is, two points on a trajectory may be close in phase space, but remote in time.

The Lyapunov exponents are measures of the dynamical or time evolution properties of the attractor. As an initial ball of radius ϵ evolves in phase space, it becomes an ellipsoid with each axis of radius $\epsilon 2^{\lambda_i t}$. The Lyapunov exponents λ_i give the amount of exponential convergence or divergence in that direction of phase space, and there is one exponent for each direction in phase space. The exponents are in units of bits per second due to the use of base two. A Lyapunov exponent of zero implies that direction of phase space is in the direction of no expansion or contraction along the trajectory. An exponent that is less than zero means two nearby trajectories will converge. An exponent greater than zero implies that two nearby trajectories, produced as a result of an arbitrary small shift in the initial conditions, will diverge. For a dissipative system such as a musical instrument, the sum of all exponents must be less than zero, implying overall convergence. If one exponent is greater than zero, trajectories are diverging while at the same time converging to a finite attractor surface, and the result is a chaotic system. A positive Lyapunov exponent is sufficient proof that the attractor of a system is chaotic. To the extent that a clarinet multiphonic forms an attractor in the strict mathematical sense, a calculation of its Lyapunov exponents assesses whether chaos exists, as possibly suggested by the fractional correlation dimensions previously reported for multiphonics.

The method used for calculating Lyapunov exponents generally follows that of Eckmann *et al.*,[15] but some changes have been introduced to improve the accuracy of the method. The main idea of this method is to follow the evolution of neighboring points on the attractor to determine the convergence or divergence along each direction in phase space. It is described in some detail because of its unfamiliarity in the musical acoustics literature.

For a continuous system, the evolution of an initial point $\mathbf{x}(0)$ in phase space is determined by a differential equation

$$d\mathbf{x}(t)/dt = \mathcal{F}(\mathbf{x}(t)), \tag{1}$$

where $\mathcal{F}$ is some function. In the discrete case a (different) function $\mathbf{F}$ gives the values of an initial point $\mathbf{x}(t_i)$ at discrete intervals of time $t_i + n\tau$, where τ is the time between points on the trajectory, and i and n are both integers. The time variable may be omitted for simplicity, and the point is identified by its index $i+n$. The differential equation in Eq. (1) for the continuous-time system may be written as an iteration equation for the corresponding discrete-time system:

$$\mathbf{x}_{i+n} = \mathbf{F}(\mathbf{x}_i). \tag{2}$$

This equation provides the means for calculating the state vector at future times in terms of the vector at the current time.

The Lyapunov exponents of the system are calculated based on the assumption that the distance between two points initially close together will grow or decrease exponentially with time. If two points in phase space $\mathbf{x}(t_1)$ and $\mathbf{x}(t_2)$ are initially a distance $\delta\mathbf{x}(t_0)$ apart, then the distance $\delta\mathbf{x}(t)$ between the two points at any later time t will be

$$\delta\mathbf{x}(t) = \mathbf{H}\delta\mathbf{x}(t_0), \tag{3}$$

where $\mathbf{H}$ is the flow matrix of dimension $d \times d$ describing the system. The eigenvalues γ_k of this equation are the square roots of the eigenvalues of $\mathbf{H}\mathbf{H}^T$, where the superscript T stands for transposition. These eigenvalues γ_k are assumed to vary exponentially with time:

$$\gamma_k = 2^{\lambda_k (t - t_0)}, \tag{4}$$

where λ_k is the kth Lyapunov exponent and $k = 1,2,\ldots,d$. Finding the Lyapunov exponents is equivalent to finding the eigenvalues of the flow equation, and the exponents are calculated from

$$\lambda_k = \log_2 \gamma\kappa/(t - t_0), \tag{5}$$

in the limit that $(t - t_0)$ is very large.

In practice, the use of the eigenvalues of the flow equation leads to numerical problems in the limit that $(t - t_0)$ becomes large. First, following an initial error vector $\delta\mathbf{x}(t_0)$ for a long time $(t - t_0)$ does not give a good estimate of the *local* values of the Lyapunov exponents on the attractor, which is what is desired. The direction of contraction or expansion for each exponent varies with position on the attractor. The flow equation can only be followed for short time intervals before this directional information is lost. Second, the errors due to noise and finite numerical precision build up until they prevent the determination of most of the exponents.

These difficulties are avoided by decomposing the evolution described by the flow matrix $\mathbf{H}$ into smaller evolution steps by using the iteration equation [Eq. (2)]. After one iteration, the distance between two points $\mathbf{x}_i$ and $\mathbf{x}_j$ that are initially close together is

$$\mathbf{x}_{i+n} - \mathbf{x}_{j+n} = \mathbf{F}(\mathbf{x}_i) - \mathbf{F}(\mathbf{x}_j), \tag{6}$$

which, after linearization, becomes

$$\mathbf{x}_{i+n} - \mathbf{x}_{j+n} = \mathbf{T}(\mathbf{x}_i - \mathbf{x}_j), \tag{7}$$

where $\mathbf{T}$ is the Jacobian matrix of the function $\mathbf{F}$. The evolution of an initial distance $(\mathbf{x}_i - \mathbf{x}_j)$ after a time Kn can be found by applying the Jacobian matrix $\mathbf{T}$ to this initial separation distance K times. The flow matrix $\mathbf{H}$, which is a series of such evolution steps, can then be represented as a product of Jacobian matrices:

$$\mathbf{H} = \mathbf{T}_{i+(K-1)n}\mathbf{T}_{i+(K-2)n}\cdots\mathbf{T}_{i+n}\mathbf{T}_i, \tag{8}$$

where the subscript i specifies that the Jacobian represents the evolution in the neighborhood of the initial point $\mathbf{x}_i$.

Two methods have been formulated to calculate the eigenvalues of $\mathbf{H}$: Gram–Schmidt orthonormalization used by Sano and Sawada[16] and QR decomposition used by Eckmann *et al.*[15] The algorithm followed here uses QR decomposition because it gives more nearly orthogonal vectors.[17]

QR decomposition takes any matrix **A** and decomposes it into two matrices, **Q** and **R**:

$$\mathbf{A}=\mathbf{QR}, \tag{9}$$

with the properties that **Q** is an orthogonal matrix (i.e., $\mathbf{Q}^T=\mathbf{Q}^{-1}$), and **R** is upper triangular with nonzero diagonal elements if **A** has nonzero diagonal elements. For any invertible matrix, this decomposition is unique.

QR decomposition is used iteratively by defining a matrix $\mathbf{A}_{K+1}$ as the product of the current Jacobian $\mathbf{T}_{i+Kn}$ and the previous $\mathbf{Q}_K$. The QR decomposition for iteration $K+1$ is

$$\mathbf{A}_{K+1}=\mathbf{T}_{i+Kn}\mathbf{Q}_K=\mathbf{Q}_{K+1}\mathbf{R}_{K+1}. \tag{10}$$

The reason for doing such multiplication and decomposition will become clear shortly. One can then solve for matrix $\mathbf{T}_{i+Kn}$ by multiplying by the inverse of $\mathbf{Q}_K$:

$$\mathbf{T}_{i+Kn}=\mathbf{Q}_{K+1}\mathbf{R}_{K+1}\mathbf{Q}_K^{-1}. \tag{11}$$

The flow matrix is then written as

$$\begin{aligned}\mathbf{H}&=\mathbf{T}_{i+(K-1)n}\mathbf{T}_{i+(K-2)n}\cdots\mathbf{T}_i\\&=\mathbf{Q}_K\mathbf{R}_K\mathbf{Q}_{K-1}^{-1}\mathbf{Q}_{K-1}\mathbf{R}_{K-1}\mathbf{Q}_{K-2}^{-1}\cdots\mathbf{Q}_1\mathbf{R}_1\mathbf{Q}_0^{-1}\\&=\mathbf{Q}_K\mathbf{R}_K\mathbf{R}_{K-1}\cdots\mathbf{R}_1\mathbf{Q}_0^{-1}\\&=\mathbf{Q}_K\mathbf{R}\mathbf{Q}_0^{-1},\end{aligned} \tag{12}$$

where **R** is the product $\mathbf{R}_K\mathbf{R}_{K-1}\cdots\mathbf{R}_1$. Since **R** is the product of upper triangular matrices, it is itself upper triangular.

It is the eigenvalues of $\mathbf{HH}^T$ that are of interest and

$$\begin{aligned}\mathbf{HH}^T&=\mathbf{Q}_K\mathbf{R}\mathbf{Q}_0^{-1}\mathbf{Q}_0\mathbf{R}^T\mathbf{Q}_K^{-1}\\&=\mathbf{Q}_K\mathbf{R}\mathbf{R}^T\mathbf{Q}_K^{-1}.\end{aligned} \tag{13}$$

Note that the choice of $\mathbf{Q}_0$ is arbitrary and is chosen to be the identity matrix. This shows that $\mathbf{HH}^T$ and $\mathbf{RR}^T$ are related by a similarity transformation, and therefore the eigenvalues of $\mathbf{HH}^T$ are the eigenvalues of $\mathbf{RR}^T$.[18] Since **R** is upper triangular, $\mathbf{RR}^T$ is also upper triangular, and the eigenvalues of an upper triangular matrix are just the diagonal elements of the matrix. Therefore, the eigenvalues of $\mathbf{RR}^T$ are R_{kk}^2, where R_{kk} is the kth diagonal element of **R**, and $k=1,2,...,d$. The Lyapunov exponents are then calculated from

$$\begin{aligned}\lambda_k&=\left(\frac{1}{t}\right)\log_2 R_{kk}\\&=\left(\frac{1}{t}\right)\log_2\left(\prod (R_{kk})^i\right)\\&=\left(\frac{1}{t}\right)\sum \log_2(R_{kk})^i,\end{aligned} \tag{14}$$

where $(R_{kk})^i$ is the kth diagonal element of the matrix $\mathbf{R}_i$, the product and sum range over $i=1,2,...,K$, and t is equal to the total time evolution Kn.

Following Eckmann *et al.*, the implementation of this method is an algorithm with three main steps: (a) reconstruct the attractor; (b) solve for the Jacobian of the system; and (c) calculate the Lyapunov exponents.

(a) *Reconstruct the attractor*. The input to the program is a one-dimensional time series $(x_1,x_2,\ldots,x_N)$ in uncalibrated, raw units measured at intervals of time τ. The sampling frequency is $1/\tau$. The input time series is the digitized pressure waveform measured inside the clarinet mouthpiece. In order to create a multi-dimensional attractor from one-dimensional data, one must ''reconstruct'' the attractor[19] by embedding the attractor in a d_E-dimensional space: one defines a d_E-dimensional vector

$$\mathbf{x}_i=(x_i,x_{i+1},\ldots,x_{i+d_E-1}) \tag{15}$$

for some initial point x_i. Since the LE algorithm follows the evolution of points nearby to this initial point, the next step is to look for neighboring points $\mathbf{x}_j$ in phase space that are within a radius $r>0$ of $\mathbf{x}_i$. In order for a point to qualify as a neighbor of $\mathbf{x}_i$, it must satisfy the condition

$$|x_{i+\alpha}-x_{j+\alpha}|\leqslant r, \tag{16}$$

for $\alpha=0,1,...,d_E-1$. Points that are close in time may not be (phase-space) neighbors in this sense, and neighbors need not be close in time. In addition, the evolved neighbors after a time m_{ev} must also be near the so-called evolved initial point:

$$|x_{i+\alpha+m_{ev}}-x_{j+\alpha+m_{ev}}|\leqslant r. \tag{17}$$

The program allows for a further check that

$$|i-j|>n_{\min}, \tag{18}$$

where $n_{\min}$ is some minimum distance (measured in samples) in the time series. If two points are too close to each other and on the same orbit, i.e., within $n_{\min}$ samples, they will be correlated in time and will provide no information on the LE.

In a modification to the standard algorithm, special attention has been devoted to choosing the ''best'' possible neighbors for a particular point. In order to avoid searching the entire file for neighbors at each iteration, the original time series is sorted. The initial point is located in the sorted list, and the program checks neighboring points at increasing distances from the initial point out to the radius r of the ball being searched. First, the maximum component difference (MCD) for the vector associated with that neighbor must be less than the radius of the ball that defines the set of neighbors:

$$\text{MCD}=\text{MAX}\{|x_{i+\alpha}-x_{j+\alpha}|\}\leqslant r,\quad \alpha=0,1,...,d_E-1. \tag{19}$$

If this is true, the index j and its associated MCD are stored in a list of possible neighbors. After all points in the ball of radius r have been checked, the list of possible neighbors is sorted according to increasing MCD. The points in this sorted list are checked (going from smallest MCD to largest MCD) to make sure all components of the evolved vector are within the ball. If this is true, the point with the smallest MCD is added to the list of neighbors. The purpose of using the MCD in finding neighbors is to choose the nearest possible neighbors to the initial point. The points in the sorted list are checked until the number of neighbors M reaches the minimum of the two quantities $2d_E$ and d_E+4, $\text{MIN}(2d_E,d_E+4)$. If the entire ball is searched and still not

enough neighbors are found, the point and its neighbors are accepted if at least d_E neighbors have been found. If fewer than d_E neighbors were found, the initial point is rejected, and the process is repeated with the next point in the time series. This method of searching for neighbors differs slightly from that used by Eckmann *et al.* They checked the points in the order of increasing first component only, not the MCD, so the neighbors they chose were not necessarily the nearest. We found the method of Eckmann *et al.* gave less than acceptable results. The results of the Lyapunov exponent calculation improved using the MCD.

(b) *Solve for the Jacobian of the system*. Once enough neighbors are found, one can solve for the Jacobian $\mathbf{T}$ in the equation

$$\mathbf{T}(\mathbf{x}_i-\mathbf{x}_j)=\mathbf{x}_{i+m_{ev}}-\mathbf{x}_{j+m_{ev}}, \tag{20}$$

which is similar in form to Eq. (7) such that $\mathbf{T}$ is a $d_E\times d_E$ matrix. Often the vectors $\mathbf{x}_j-\mathbf{x}_i$ do not span a d_E-dimensional space, and $\mathbf{T}$ cannot be completely determined. The dimension of the phase space embedding can be reduced by dropping some of the components from the original embedded vectors. The point $\mathbf{x}_i$ becomes

$$\begin{aligned}\mathbf{x}_i&=(x_i,x_{i+m_{\text{delay}}},\ldots,x_{i+(d_M-1)m_{\text{delay}}})\\&=(x_i,x_{i+m_{\text{delay}}},\ldots,x_{i+d_E-1}),\end{aligned} \tag{21}$$

where m_{delay} is the delay between the remaining components, and d_M is the dimension of the new vector. d_M is related to d_E by

$$d_M=(d_E-1)/m_{\text{delay}}+1\leqslant d_E. \tag{22}$$

$\mathbf{T}$ is now a $d_M\times d_M$ matrix.

Theoretically, d_M should be slightly larger than the dimension of the phase space of the attractor (and thus the expected number of exponents) in order to accurately determine all of the exponents. However, any value of d_M that is greater than the dimension of the attractor phase space will give a singular Jacobian $\mathbf{T}$ since $\mathbf{T}$ will not be well-defined in all directions of the phase space. Noise and finite data resolution will desingularize $\mathbf{T}$ but will also produce a set of false exponents that may be confused with the true exponents. The false exponents will have different characteristics depending on the relative size of the noise present. If the noise is not small compared to the precision and density of the data, the false exponents will all be negative. If the noise is small, the false exponents will be positive and larger than the largest true exponents since the original data have more nonlinearity than the approximation of the flow map used to fit the data. In the present case, the noise is large relative to the data precision, and it is expected that all false exponents will be negative. This means that the largest (positive) exponent will be a true exponent and it can be used as a measure of the rate of information loss. We are only concerned with this largest LE.

The phase space vector $\mathbf{x}_i$ defined in Eq. (15) is reconstructed based upon the temporally adjacent samples to x_i, that is, with single-sample spacing. It is recognized in the literature on calculating the dimensionality of an attractor from a time series that it may be advantageous to reconstruct an attractor using a multiple-sample spacing, based upon an effective down-sampling by a factor m_S. The reconstructed attractor becomes the vector

$$\mathbf{x}_i=(x_i,x_{i+m_S},\ldots,x_{i+(d_E-1)m_S}). \tag{23}$$

The neighbor search uses these vectors consisting of every other m_Sth point. Introducing the delay m_{delay} creates the vectors used to solve for $\mathbf{T}$:

$$\mathbf{x}_i=(x_i,x_{i+m_Sm_{\text{delay}}},\ldots,x_{i+m_S(d_M-1)m_{\text{delay}}}). \tag{24}$$

This representation generalizes that of Eq. (21). The corresponding evolved vector then becomes

$$\mathbf{x}_{i+m_{ev}}=(x_{i+m_{ev}},x_{i+m_Sm_{\text{delay}}+m_{ev}},\ldots,x_{i+m_S(d_M-1)m_{\text{delay}}+m_{ev}}). \tag{25}$$

Taking $m_S>1$ has the effect of artificially increasing the sample time if m_{ev} is set equal to m_S. The value for m_S was usually chosen to be near the first minimum in the mutual information.[20] Mutual information gives the number of bits that can be predicted after a time delay d if the current state is known. A minimum in the mutual information translates into a maximum of information gain between the two states.

Up until this point, all calculations use integer arithmetic to minimize computation time and storage. The remainder of the algorithm uses floating point arithmetic.

Eckmann *et al.* used a least squares algorithm to solve for $\mathbf{T}$, but the algorithm here uses singular value decomposition (SVD). SVD was found to be more reliable than the least squares technique in the time series we analyzed.

The matrix equation to be solved is, from Eq. (20),

$$\sum_l \mathbf{T}_{kl}(\mathbf{x}_i-\mathbf{x}_j)_l=(\mathbf{x}_{i+m_{ev}}-\mathbf{x}_{j+m_{ev}})_k. \tag{26}$$

T_{kl} is the (k,l) component of $\mathbf{T}$, $(\mathbf{x}_i-\mathbf{x}_j)_l$ is the lth component of $(\mathbf{x}_i-\mathbf{x}_j)$, and $(\mathbf{x}_{i+m_{ev}}-\mathbf{x}_{j+m_{ev}})_k$ is the kth component of $(\mathbf{x}_{i+m_{ev}}-\mathbf{x}_{j+m_{ev}})$. The sum is over $l=1,\ldots,d_M$. This equation is solved once for each row k of $\mathbf{T}$; there are M equations to solve simultaneously, where M is the number of neighbors $\mathbf{x}_j$ of the initial point $\mathbf{x}_i$. SVD is applied once to the matrix formed by the M difference vectors $(\mathbf{x}_i-\mathbf{x}_j)$, and the decomposition is back-substituted d_M times to solve for the entire matrix $\mathbf{T}$, one row at a time.

(c) *Calculate the Lyapunov exponents*. The current Jacobian $\mathbf{T}_{i+Km_{ev}}$ is decomposed as described earlier using a QR decomposition routine:[21]

$$\mathbf{T}_{i+Km_{ev}}\mathbf{Q}_K=\mathbf{Q}_{K+1}\mathbf{R}_{K+1}. \tag{27}$$

Then the diagonal elements of $\mathbf{R}_{K+1}$ are used to compute the current values of the Lyapunov exponents:

$$\lambda_k=\frac{1}{Km_{ev}\tau}\sum \log_2(R_{kk})^i, \tag{28}$$

where the sum is for $i=1,2,\ldots,K$, and the number of exponents is $k=1,2,\ldots,d_M$.

If there are negative diagonal elements in $\mathbf{R}$ (which is sometimes the case), then the signs of that row of $\mathbf{R}$ and of the corresponding column of $\mathbf{Q}$ are changed to make that

diagonal element of **R** positive. This sign change has no effect on the decomposition since the product **QR** is unchanged.

This algorithm was tested on a sine wave and the Lorenz and Rössler attractors. The periodic system of a sine wave has two Lyapunov exponents, both equal to 0.0. This algorithm gave values for the exponents of 0.01 ± 0.04 and -0.05 ± 0.04 bits/s. It reliably reproduced the positive exponents of the Lorenz attractor to within 5% and of the Rössler attractor to within 7%. The results presented below report only the largest exponent, since that one determines if the system is chaotic. It will be positive for a chaotic attractor or zero for a nonchaotic attractor, assuming that an attractor exists.

The parameters m_{delay}, m_S, and m_{ev} were varied until a scaling region was found, that is, a region in parameter space where the exponents stayed fairly constant. These were taken to be the final values of the exponents, and the optimum ranges of the parameters for the test systems are discussed below.

The final values of the Lyapunov exponents converged after about $K=5000$ iterations. The time step corresponding to one iteration is $m_{ev}=m_S m_{\text{delay}}\tau$, where $\tau=1/44\,100$s, so the minimum sound file length necessary is $5000m_{ev}$, which is around a few seconds, for clarinet tones, depending on the values of m_S and m_{delay} chosen. Once the exponents had converged, there was still a small variation about the converged values, and so the exponents from the last 500 iterations were averaged to obtain the final values.

There was some variation with the initial starting point, but it was small.

For the test systems, the results were fairly insensitive to the value of d_M, as long as d_M was greater than or equal to the expected number of exponents, which was 2 for the sine wave and 3 for the Lorenz and Rössler systems.

In the code to find the nearest neighbors, $n_{\min}$ was set equal to 5. $r_{\max}$ ranged over 2%–4% of the maximum extent of the attractor, depending on whether enough neighbors were found within the smaller radius. $r_{\min}$ was equal to one discrete step of the 16-bit analog-to-digital converter.

The exponents usually converged for a range of values of m_{delay} and d_M. m_{delay} was varied over 1–6 and d_M over 3–8 to find a scaling region. If m_{ev} (and therefore m_{delay}) was too large, a lack of neighbors would prevent a determination of the exponents. If not enough neighbors could be found for a significant number of points (usually 20% for the test systems), the algorithm could not determine the correct values of the exponents.

The best results on these test cases were obtained with $m_{ev}=m_{\text{delay}}=m_S=1$. Eckmann *et al.* state that m_{delay} should be greater than 1 in order to make $d_M<d_E$ and to correctly determine all the exponents. The advantage in using an embedding dimension larger than the matrix dimension is that the neighbors, which are chosen in the d_E-dimensional space, will more likely be close to the initial point, since more components are being compared. Taking a smaller d_M will then reduce the number of false exponents.

For the clarinet tone analyses, m_{delay} was set equal to m_{ev} for the best results, as was done by Eckmann *et al.* and Sano and Sawada.

B. Correlation dimension

The correlation dimension[22] is a geometric measure of the attractor that tells how strongly points on the attractor are spatially correlated with one another in phase space. The correlation function $C(R)$ is defined as the average fraction of points within a radius R. $C(R)$ scales as

$$C(R)\sim R^D, \tag{29}$$

and D is the *correlation dimension*. $D=1$ for a periodic system (e.g., the one-dimensional simple harmonic oscillator), $D=2$ for a biperiodic system, $D=3$ for a triperiodic system, and D is fractional for a chaotic system, although fractional values for D do not always imply chaotic systems. The method used to calculate the correlation dimension is described by Keefe and Laden.[5] The correlation function is calculated as R varies over a range of values, and the correlation dimension is calculated as the slope of the $\log C$ vs $\log R$ curve. In practice, this must be done for several values of the embedding dimension, and usually there is some range of $\log C$ values for which the slope converges to the same value for some range of embedding dimensions. The range of $\log C$ values is a ''scaling region.'' An estimate of the correlation dimension D is the average value of the slope in the scaling region, and the standard error reported is one-half the range in slopes as the embedding dimension is varied.

C. Unsteadiness

A quantitative measure of unsteadiness was defined for comparison with the LE and correlation dimension measures. Other researchers have studied unsteadiness by looking at period-to-period variations of the waveform.[9–11] The technique applied here follows a similar approach and involves period-synchronous averaging of long waveform durations. The standard deviation of this average waveform can then be used to define an unsteadiness associated with the oscillation. Another way to approach this method is from the viewpoint of phase portraits. When the phase portraits are inspected, the trajectory has a finite width to it because the oscillation does not follow the same path every time but varies.

Period-synchronous averaging involves averaging the pressure values at the same relative phase in each period. For present purposes, a ''period'' is defined as the time between successive zero crossings of the waveform with similar polarity, after the dc component has been subtracted, and is equivalent to making one loop around the attractor of a periodic system. This method uses period-by-period resampling to remove any variability due to unsteadiness of the period length, i.e., frequency modulation, and the unsteadiness that is left is due only to amplitude modulation.

A single measure of unsteadiness over one period can be determined by averaging the standard deviation over the entire period and dividing by the root-mean-squared (rms) energy of the average waveform to get a normalized unsteadiness that is expressed as a fraction of the total wave energy:

$$\text{Unsteadiness}=\langle\sigma\rangle/\text{rms}. \tag{30}$$

Theoretically, a strictly periodic tone with unsteadiness equal to zero should have a correlation dimension $D=1.0$, and a

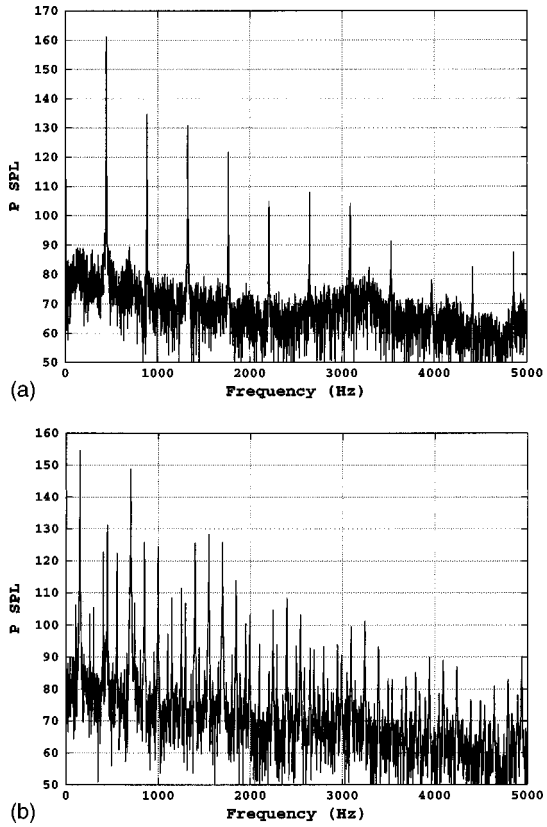

FIG. 2. Mouthpiece pressure spectra for: (a) normal tone B4; (b) multiphonic E3&G5.

strictly biperiodic tone with unsteadiness equal to zero should have $D=2.0$.

This unsteadiness was calculated for overlapping 32 768-sample segments of the pressure time series at intervals of 16 384 samples in order to get a graph of unsteadiness versus time. In order to compare the change in the unsteadiness with time and the change in the correlation dimension with time, a ''short-time correlation dimension'' was calculated for each 32 768-sample segment. This short-time correlation dimension gives a value of the correlation dimension D over a particular span of time, were an attractor to exist in that time span. If an attractor does not exist, then the short-time correlation dimension gives a nonrigorous estimate of the dynamical complexity over the signal duration used.

III. RESULTS

This section presents results for the spectral characteristics of the tones studied, the phase space representations, the correlation dimension, the Lyapunov exponents, and the unsteadiness.

A. Spectral characteristics

Figure 2 shows the mouthpiece pressure spectra for (a) the normal tone B4 and (b) the multiphonics E3&G5. Multiphonics are denoted by the approximate pitch of each of the separately audible tones present. Thus the multiphonic E3&G5 has audible tones near E3 and G5 (written), in the ANSI pitch class terminology such that middle C on the piano is C4. Both spectra were calculated from a 32 768-sample section of the pressure time series. The noise level was similar for both normal tones and multiphonics. There was no significant high-level broadband component to the mouthpiece pressure spectra of clarinet multiphonics as was observed by Keefe and Laden for saxophone multiphonics based upon pressure measurements at a location external to the instrument.

The normal tone spectrum [Fig. 2(a)] has spectral peaks at multiples of the fundamental frequency (440 Hz for B4). The multiphonics spectrum [Fig. 2(b)] has strong peaks at 148 Hz and 698 Hz, the fundamental frequencies of the two audible pitches E3 and G5. In addition, there are peaks at sum and difference frequencies of these two fundamental frequencies. All peak frequencies can be expressed as a multiple of a single basis frequency, which is 21.2 Hz for the section shown.

B. Phase space representations

Phase space portraits of a system are created by plotting each point in the time series versus the point n samples later in the time series. For a suitable delay n, a picture of the system dynamics is produced.

Figure 3(a) shows the phase portrait for the normal tone B4 shown in Fig. 2(a) and the phase portrait is a circle, or limit cycle, since a normal tone is a periodic oscillation. This phase portrait is plotted for 1000 samples, corresponding to approximately nine periods of oscillation. The deviations from the average trajectory are small, indicating that the tone is nominally stationary. Figure 3(b) shows the phase portrait for the multiphonic E3&G5 shown in Fig. 2(b), and it is a torus, implying a biperiodic system. There are 5000 samples plotted in this figure. All but one of the multiphonics studied had toroidal phase portraits. The one exception was a multiphonic played at a *forte* dynamic level, and its phase portrait had no obvious structure.

After the attractor has been embedded in a phase space of appropriate dimension, it can be strobed to produce a cross-sectional view of the attractor known as a Poincaré section.[4] Figure 4 shows the Poincaré section of the multiphonic in Fig. 3(b) and shows that the Poincaré section of a torus is two circles when the slice is taken across the entire attractor. In this view, some folding of the circles is apparent. Except for two cases discussed in the next section, Poincaré sections of other multiphonics were qualitatively similar in that they described biperiodic spectra in agreement with the findings of Gibiat.

C. Correlation dimension

For the normal clarinet tones studied, the correlation dimension D ranged over 1.0–1.1 with a standard error of less than 0.02 for each D value. For all the multiphonics except two (discussed below), the correlation dimension was 2.0–2.3 with a standard error of less than 0.2. If these small fractional values are truncated, these results indicate that the normal tones studied are periodic systems, and the multiphonics are biperiodic. The phase portraits of these tones and

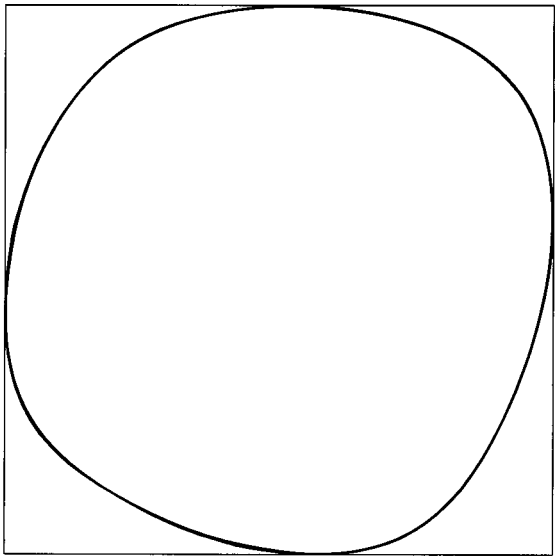

FIG. 3. Phase space portraits for: (a) normal tone B4; (b) multiphonic E3&G5.

multiphonics support this conclusion. The phase portraits of the normal tones were all circles, and those of the multiphonics were all 2-tori.

One multiphonic was played at both a *piano* and a *forte* dynamic level. The value of the correlation dimension varied over 3.4–3.6 for the *piano* multiphonic and over 4.0–4.3 for the *forte* multiphonic as the performer attempted to hold the multiphonic steady over its duration after the onset. The three-dimensional Poincaré section of the *piano* multiphonic shows a torus (Fig. 5), whereas the three-dimensional Poincaré section of the *forte* multiphonic showed no obvious structure. Figure 6 shows the mouthpiece pressure spectra from 32 768-sample sections of (a) the *piano* and (b) *forte* multiphonics. The 32 768-sample section of the *piano* multiphonic shown had $D \approx 3.4$, and the 32 768-sample section of the *forte* multiphonic had $D \approx 4.0-4.1$. The overall noise level is higher for the *forte* multiphonic (b). The four lowest-frequency large spectral peaks correspond approximately to

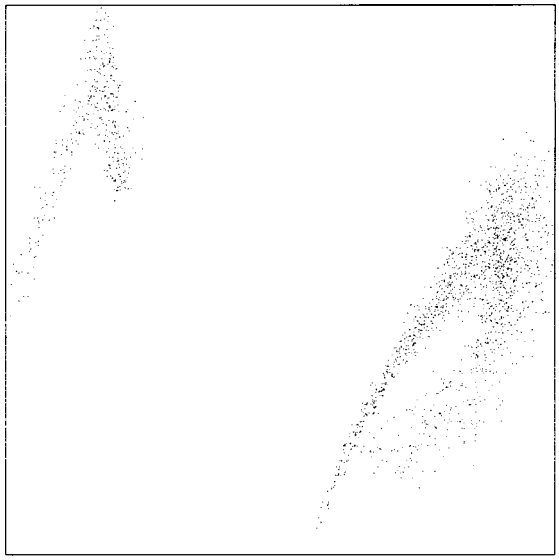

FIG. 4. Poincaré section for E3&G5.

the fundamental frequencies of the pitches D#4, G5, C#6, and F#6, respectively, although the frequencies were slightly different for the *piano* and *forte* dynamic levels: 277, 684, 1011, and 1287 Hz for *piano* and 280, 682, 1024, and 1304 Hz for *forte*. The differences in pressure level at these peaks between *forte* and *piano* were +4.7, −2.3, +7, and +4.4 dB, respectively. As the dynamic level increased, the peak levels increased at three of the peaks and decreased at one (corresponding to G5). The peak at the fundamental frequency of approximately E7 showed the greatest increase. There was a 17.7 dB increase at the peak at 2606 Hz for *piano* and 2575 Hz for *forte*.

D. Lyapunov exponents

The parameter values necessary to define a scaling region were slightly different for the clarinet pressure time

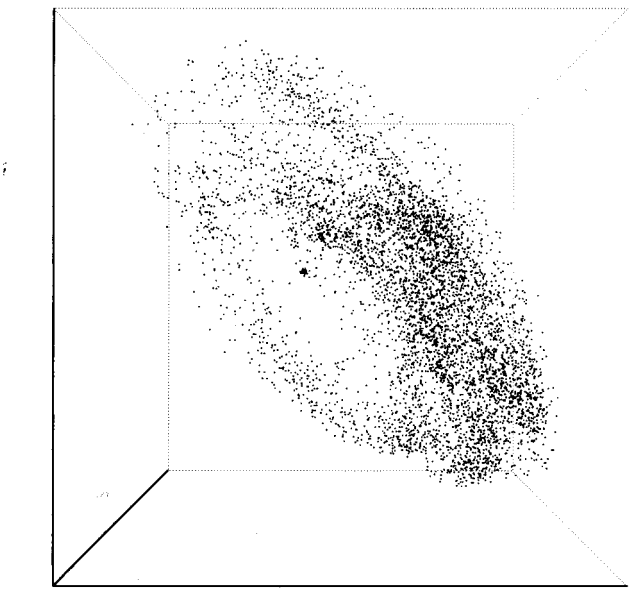

FIG. 5. Three-dimensional Poincaré section for triperiodic multiphonic.

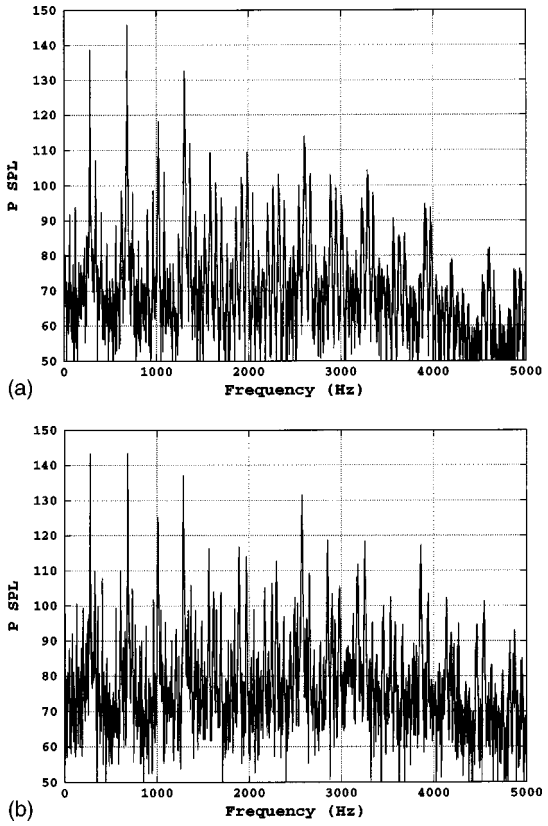

FIG. 6. Mouth pressure spectra for multiphonic played at two dynamic levels: (a) *piano*; (b) *forte*.

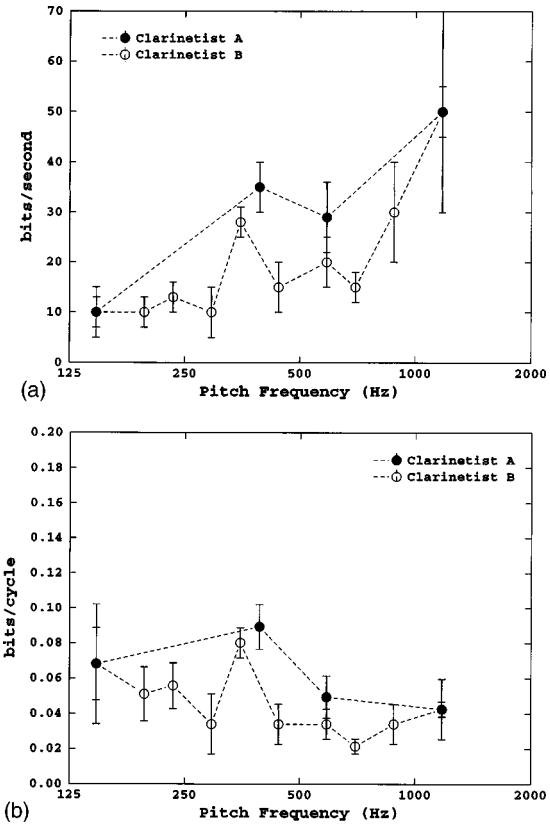

FIG. 7. Normal tones: Largest Lyapunov exponent versus sounding frequency (Hz), such that the Lyapunov exponent is plotted in units of bits/s (a), and bits/cycle (b).

series than for the test systems. The matrix dimension d_M had to be larger than 3, and the exponents converged more uniformly for larger values of d_M, up to 8, which was the largest value used. The embedding delay m_{delay} had to be larger than one, whereas for the test systems results were best for $m_{\text{delay}} \sim 1$. Values of $m_{\text{delay}} = 2-6$ gave a fairly well-defined scaling region. The sampling delay m_S was taken to be the first minimum in the mutual information, whereas for the test systems it had to be less than the mutual information minimum. The evolution step is $m_{ev} = m_{\text{delay}} m_S$, and thus varies with m_{delay}. The exclusion range $n_{\min}$ was taken to be 5. The minimum radius for the shell of neighbors was taken to be 1 and the maximum radius ranged from 2%–4% of the entire attractor extent, depending on how easily neighbors were found at the smaller radius. Only the largest Lyapunov exponent will be shown for the experimental data; the next largest exponent often did not converge and was difficult to distinguish from false exponents.

Figure 7(a) shows the largest Lyapunov exponent λ_1 calculated for the normal tones in bits/s as a function of the fundamental frequency of the clarinet tone. The filled and open circles represent tones played by two different performers. The error bars estimate the range in values over the scaling region. The tones in the low to middle portion of the chalumeau register (147–349 Hz) all have $\lambda_1 \approx 10$ bits/s. The throat tones (370–415 Hz) have a much larger λ_1 of approximately 30 bits/s. The tones in the clarion register (above 440 Hz) have a wider spread of λ_1 over 15–30 bits/s. The only altissimo tone recorded (E6, 1175 Hz) had a large value of λ_1 of 50 bits/s for both performers. The exponents calculated for the two performers agreed for the lowest (E3) and highest (E6) notes and were within the uncertainty for the rest of the notes. It is useful to re-express the LE values in units of bits/cycle by dividing the LE value in bits/s by the sounding frequency in Hz. This gives the rate of information loss in each cycle of oscillation. Although it is difficult to determine whether the LE is constant for these limited results, the LE values are in the range of 0.02–0.08 bits/cycle. The trend for increasing LE (in bits/s) with increasing sounding frequency is readily apparent in Fig. 7(a), whereas the LE (in bits/cycle) has no clear linear trend with increasing sounding frequency [Fig. 7(b)].

The Lyapunov exponent was calculated for four multiphonics. Table I lists the four multiphonics, the fingerings used to produce them, and the largest LE for each. For the multiphonics studied, the LE was in the range 10–60 bits/s with an uncertainty of 5–15 bits/s. These values are within the range of the values obtained for the normal tones.

The exponents were calculated for only four multiphonics because it was especially difficult to determine the exponents for multiphonics. A long (generally at least 5 s), steady

TABLE I. Largest Lyapunov exponent for various multiphonics.

Multiphonic	Fingering	Largest LE (bits/s)
E3&G5	E3	20±5
C4&C7	G3+*LH* C#/G# key	60±10
D#4&C#6	C#6 without RK	30±15
F#4&A#5	B♭5	10±5

data time series is necessary to find enough nearby neighbors and to allow the exponents to converge to their final values. Multiphonics are difficult to hold steady for a long time period, and this presents a problem.

E. Unsteadiness

The correlation dimension for normal tones and multiphonics was not a pure integer, as expected for periodic or multiperiodic systems, but often had a fractional part. A fractional correlation dimension can be associated with a chaotic system, but the normal tones and multiphonics studied did not have chaotic phase portraits, as inferred by qualitative inspection.

Since the phase portraits of these systems suggest periodic or multiperiodic systems, it may be that the fractional values of the correlation dimensions are not due to the presence of chaos, but to some other factor. One possibility is that the underlying system does not reside on a well-defined attractor, so that the apparent fractional dimensionality is produced by fluctuations in the player's control of the oscillation or due to other aeroacoustic factors, observed as a slight unsteadiness in the tone. This unsteadiness could be due, for example, to an independent noise source, or to time-varying control variables such as blowing pressure and reed parameters.

To investigate the relation between the unsteadiness in the tone and the correlation dimension, the measure of the unsteadiness defined in Sec. III C was calculated for these normal tones and multiphonics.

The unsteadiness was calculated for overlapping 32 768-sample segments of the pressure time series at intervals of 16 384 samples in order to get a graph of unsteadiness versus time. A short-time correlation dimension was also calculated for the same 32 768-sample segments. Figure 8 plots the short-time correlation dimension and the unsteadiness as a function of time for the normal tone (written) B4. This was one of the more audibly unsteady normal tones. There is a strong degree of correlation between the unsteadiness as defined above and the short-time correlation dimension for this normal tone and for other normal tones analyzed. Amplitude modulation accounts completely for the variation in short-time correlation dimension with time. The unsteadiness is almost exactly equal to the difference between the calculated short-time correlation dimension and the ideal correlation dimension of a limit cycle ($D=1.0$). There were similar strong correlations between the unsteadiness and the short-time correlation dimension for other normal tones.

Figure 9 shows the short-time correlation dimension and unsteadiness plotted as a function of time for the multiphonic D#4&C#6. The ''period'' for this multiphonic was taken to be the common basis frequency (139.6 Hz) of the two main oscillation frequencies (277.2 Hz and 976.4 Hz). There is no obvious relationship between the correlation dimension and this measure of unsteadiness for this multiphonic. Clearly, amplitude modulation does not account for the fractional value of the correlation dimension of the multiphonics tested.

One problem with calculating this unsteadiness for multiphonics is that the pressure waveforms are so complex and the basis period is so long, that it is difficult to choose the

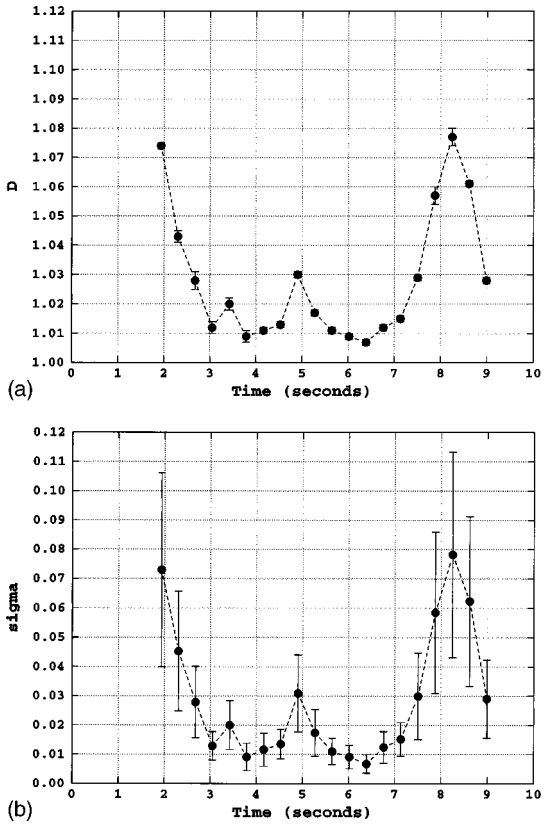

FIG. 8. Correlation dimension (a) and unsteadiness, denoted sigma, (b) versus time for normal tone B4.

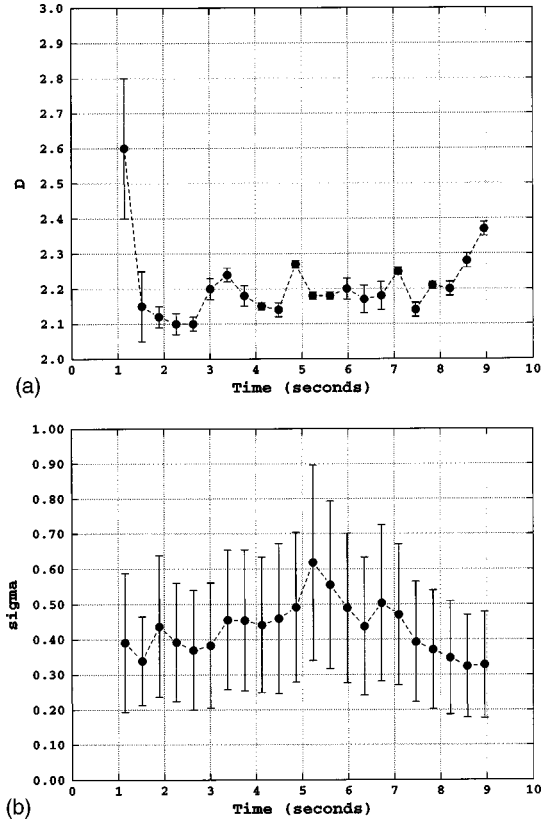

FIG. 9. Correlation dimension (a) and unsteadiness, denoted sigma, (b) versus time for multiphonic D#4&C#6.

''beginning'' of the waveform at the same point in the waveform for each 32 768-sample section. If the starting point of the waveform is incorrectly chosen, then this could lead to errors in the period-synchronous averaging.

A similar comparison of the unsteadiness with the Lyapunov exponent could not be made because the method used to calculate the Lyapunov exponent requires a long-time average, and the exponent has not converged over the short-time scales used to calculate the correlation dimension.

IV. DISCUSSION

Even though multiphonics sound quite different from normal tones, the analysis of the largest Lyapunov exponents shows that their values for multiphonics are indistinguishable from their values for normal tones. This indicates that both types of oscillation have comparable rates of information loss, and suggests that the primary mechanism underlying information loss is common to both classes of tones.

The largest Lyapunov exponents for these normal tones and multiphonics are positive, which would indicate that they are chaotic if the underlying system trajectories truly reside on an attractor. If the systems are chaotic, then it follows from the roughly equal Lyapunov exponent values that normal tones have approximately the same sensitivity to initial conditions as do multiphonic tones. However, the phase space portraits of normal tones and multiphonics appear to be those of essentially periodic and multiperiodic systems, not chaotic systems. Much more likely is that the theoretical construct of an attractor is only approximately realized in clarinet tone production. The existence of an attractor assumes that the control variables of the system, such as the reed parameters and blowing pressure in the case of wind instruments, remain constant. If these parameters vary due to the unsteadiness of the performer, or if hydrodynamical turbulence in the airflow within the reed aperture is significant, then the attractor may not be well-defined, and the significance of the Lyapunov exponents (and correlation dimensions) calculated from the phase space embedding becomes ambiguous. They remain an effective way to characterize the dynamical complexity of musical instrument tones, but the experimenter may have great difficulty in determining whether fractional correlation dimensions and positive Lyapunov exponents suggest the presence of chaos or nonstationarity.

Period variations, as determined by the measure of unsteadiness defined, accounted for the temporal variations in short-time correlation dimension for normal tones. The increase in ''size'' of the attractor given by the difference between the measured correlation dimension and the correlation dimension for a strictly periodic tone ($D=1$) is due to the ''size'' of the unsteadiness expressed as a fraction of the steady, periodic portion of the oscillation. The region in phase space occupied by the system increases, causing an increase in the correlation dimension.

There was no similar relation between the unsteadiness and the correlation dimension for multiphonics. Practical problems of calculating the unsteadiness include choosing the same starting point in the waveform each time, since multiphonic waveforms are more complex than normal tones and the basis period is extremely long. Perhaps another measure of unsteadiness that is easier to apply to multiphonics would solve this problem. Amplitude modulation, which the measure of unsteadiness here does not include, may account for some of the variability present in multiphonics.

One triperiodic and one quadperiodic multiphonic were observed. The triperiodic multiphonic had $D \approx 3.4-3.6$ and the three-dimensional Poincaré section was a torus. The conclusion is that this multiphonic cannot be described as a biperiodic system but is actually triperiodic. The only other known mention of a triperiodic state is in Idogawa *et al.*[7] They analyzed a triperiodic state produced on an artificially blown clarinet and found $D=3.2-3.3$. The quadperiodic multiphonic analyzed here had $D \approx 4.0-4.3$, indicating a system in a four-dimensional phase space. The three-dimensional Poincaré section of this multiphonic had no obvious structure, which is to be expected when observing a four-dimensional system in a three-dimensional phase space. This observation of a quadperiodic multiphonic broadens the dynamical class of sounds that clarinet multiphonics are known to produce.

Musical instrument sounds have complicated patterns of AM and FM related to modulations of the performer's control systems. The period-synchronous analyses of normal clarinet tones measured the amplitude modulation (AM) after discarding the frequency modulation (FM) component, and the result was very similar to the short-time correlation dimension measurement. It follows that the short-time correlation dimension is insensitive to FM. This is not a surprising result, since it measures the effective dynamical dimension of a system without specific reference to the temporal axis. For example, the correlation dimension of a time-reversed system is identical to that of the original system. A variation in FM is akin to a ''stretching'' of the rate at which the system moves along a given trajectory. This stretching does not alter the geometry of the trajectory in its phase space. In contrast, the Lyapunov exponent is profoundly sensitive to the direction of time, insofar as time reversal transforms diverging pairs of trajectories into converging pairs, and vice versa. The LE should be sensitive to FM as the rate of divergence or convergence of trajectories are influenced by the temporal stretching of the trajectories. Because the LEs of normal and multiphonic tones are comparable in value, the simplest explanation is that the loss of information quantified in the largest LE is due to perturbations in the performer's control systems, i.e., fluctuations in the embouchure control variables and the blowing pressure. Similar measurements using clarinet tones produced using an artificial blowing machine would be useful in understanding these processes and the extent to which the concept of an attractor is physically realizable in describing wind instrument tones.

Positive LEs in clarinet tones are, in this view, not an indication of chaos but rather an outgrowth of instabilities in the control parameters that prevent the system trajectories from ever converging to an attractor. Even when a clarinetist sustains a single tone, there are inherent performance fluctuations that render the resulting acoustic signal unpredictable after a sufficient length of time. It is interesting to note that the throat tones had larger LEs than adjacent tones,

which is consistent with the statement that the throat tones are less well-centered. The quality of a centered tone may be due to the extent to which short-term predictability is maintained. This quality is not accounted for in terms of standard spectral analyses. An electrical oscillator is adept at producing tones with long-term predictability, and this is usually considered undesirable by listeners. Either too much or too little predictability is bad. The natural instability of wind-instrument tones are the physical correlate to musical expressiveness, and the measures studied in this research may have relevance to a better understanding of this subjective microstructure of musical tone.

V. CONCLUSIONS

Lyapunov exponents have been calculated for clarinet tones and multiphonics performed by highly skilled clarinetists. Normal tones and multiphonics are indistinguishable with respect to their Lyapunov exponents. The largest exponent is small and positive, indicating a small amount of information loss each cycle. Unsteadiness, defined in terms of the cumulative standard deviation over a single ''period'' of the waveform using a period-synchronous analysis, accounted for the temporal variations in short-time correlation dimension for normal tones but not for multiphonics. Even when musicians are asked to play the steadiest possible tones, our results support the view that the clarinet tone may only be approximated as the output of a limit cycle. Nonstationary behavior eliminates long-term predictability while maintaining short-term predictability.

[1] M. E. McIntyre, R. T. Schumacher, and J. Woodhouse, ''On the oscillations of musical instruments,'' J. Acoust. Soc. Am. **74**, 1325–1345 (1983).

[2] C. Maganza, R. Caussé, and F. Laloë, ''Bifurcations, period doublings and chaos in clarinetlike systems,'' Europhys. Lett. **1**, 295–302 (1986).

[3] K. Brod, ''Die Klarinette als Verzweigungssystem: Eine Anwendung der Methode der iterierten Abbildungen,'' Acustica **72**, 72–78 (1990).

[4] V. Gibiat, ''Phase space representations of acoustical musical signals,'' J. Sound Vib. **123**, 529–536 (1988).

[5] D. H. Keefe and B. Laden, ''Correlation dimension of woodwind multiphonic tones,'' J. Acoust. Soc. Am. **90**, 1754–1765 (1991).

[6] T. Kobata and T. Idogawa, ''Pressure in the mouthpiece, reed opening, and air-flow speed at the reed opening of a clarinet artificially blown,'' J. Acoust. Soc. Jpn. (E) **14**, 417–428 (1993).

[7] T. Idogawa, T. Kobata, K. Komuro, and M. Iwaki, ''Nonlinear vibrations in the air column of a clarinet artificially blown,'' J. Acoust. Soc. Am. **93**, 540–551 (1993).

[8] C. Chafe, ''Pulsed noise in self-sustained oscillations of musical instruments,'' in *Proceedings IEEE International Conference on Acoustics, Speech, and Signal Processing*, Albuquerque, NM (IEEE, New York, 1990), pp. 1157–1160, Vol. 2.

[9] C. Chafe, ''Pulsed noise and microtransients in physical models of musical instruments,'' Technical Report STAN-M-65, Center for Computer Research in Music and Acoustics, Department of Music, Stanford University, 1990.

[10] P. R. Cook, ''Noise and aperiodicity in the glottal source: A study of singer voices,'' Technical Report STAN-M-75, Center for Computer Research in Music and Acoustics, Department of Music, Stanford University, 1991.

[11] R. T. Schumacher and C. Chafe, ''Characterization of aperiodicity in nearly periodic signals,'' in *Proceedings IEEE International Conference on Acoustics, Speech, and Signal Processing*, Albuquerque, NM (IEEE, New York, 1990), Vol. 2, pp. 1161–1164.

[12] R. T. Schumacher, ''Analysis of aperiodicities in nearly periodic waveforms,'' J. Acoust. Soc. Am. **91**, 438–451 (1992).

[13] E. M. Richards, *The Clarinet of the Twenty-First Century* (E & K Publishers, Fairport, NY, 1992).

[14] M. V. Mathews, J. E. Miller, and E. E. David, Jr., ''Pitch synchronous analysis of voiced sounds,'' J. Acoust. Soc. Am. **33**, 179–186 (1961).

[15] J.-P. Eckmann, S. O. Kamphorst, D. Ruelle, and S. Ciliberto, ''Liapunov exponents from time series,'' Phys. Rev. A **34**, 4971–4979 (1986).

[16] M. Sano and Y. Sawada, ''Measurement of the Lyapunov spectrum from a chaotic time series,'' Phys. Rev. Lett. **55**, 1082–1085 (1985).

[17] J.-P. Eckmann and D. Ruelle, ''Ergodic theory of chaos and strange attractors, reviews of modern physics,'' Rev. Mod. Phys. **57**, 617–656 (1985).

[18] G. Strang, *Linear Algebra and its Applications* (Harcourt Brace Jovanovich, San Diego, 1988).

[19] N. H. Packard, J. P. Crutchfield, J. D. Farmer, and R. S. Shaw, ''Geometry from a time series,'' Phys. Rev. Lett. **45**, 712–716 (1980).

[20] A. Fraser and H. L. Swinney, ''Independent coordinates for strange attractors from mutual information,'' Phys. Rev. A **33**, 1134–1140 (1986).

[21] W. H. Press, *Numerical Recipes in C: The Art of Scientific Computing* (Cambridge U.P., New York, 1992).

[22] P. Grassberger and I. Procaccia, ''Measuring the strangeness of strange attractors,'' Physica D **9**, 189–208 (1983).

Detection of ultrasonic tones and simulated dolphin echolocation clicks by a teleost fish, the American shad (*Alosa sapidissima*)

David A. Mann[a] and Zhongmin Lu
Department of Zoology, University of Maryland, College Park, Maryland 20742

Mardi C. Hastings
Department of Mechanical Engineering, The Ohio State University, Columbus, Ohio 43210

Arthur N. Popper[b]
Department of Zoology, University of Maryland, College Park, Maryland 20742

(Received 21 January 1998; accepted for publication 4 April 1998)

The authors previously reported that American shad (*Alosa sapidissima*) can detect sounds from 100 Hz to 180 kHz, with two regions of best sensitivity, one from 200 to 800 Hz and the other from 25 to 150 kHz [Mann *et al.*, Nature **389**, 341 (1997)]. These results demonstrated ultrasonic hearing by shad, but thresholds at lower frequencies were potentially masked by background noise in the experimental room. In this study, the thresholds of the American shad in a quieter and smaller tank, as well as thresholds for detecting simulated echolocation sounds of bottlenosed dolphins was determined. Shad had lower thresholds for detection (from 0.2 to 0.8 kHz) in the quieter and smaller tank compared with the previous experiment, with low-frequency background noise but similar thresholds at ultrasonic frequencies. Shad were also able to detect echolocation clicks with a threshold of 171 dB *re*: 1 μPa peak to peak. If spherical spreading and an absorption coefficient of 0.02 dB/m of dolphin echolocation clicks are assumed, shad should be able to detect echolocating *Tursiops truncatus* at ranges up to 187 m. The authors propose that ultrasonic hearing evolved in shad in response to selection pressures from echolocating odontocete cetaceans. © *1998 Acoustical Society of America.* [S0001-4966(98)02907-5]

PACS numbers: 43.80.Lb, 43.66.Dc, 43.66.Gf [FD]

INTRODUCTION

Investigations of the distribution of blueback herring (*Alosa aestivalis*), a member of the teleost taxonomic order Clupeiformes (herrings, sardines, and shads), demonstrated that these fish would swim away from ultrasonic echosounders used to quantify fish abundance, suggesting that at least some species of clupeids may be able to detect ultrasound (Nestler *et al.*, 1992). It was also shown that high-intensity pulsed ultrasound could be used to repel several clupeid species including alewives (*Alosa pseudoharengus*) (100 and 125 kHz at 195 dB *re*: 1 μPa at 1 m), blueback herring (110 and 140 kHz at $>$180 dB *re*: 1 μPa at 1 m), and American shad (*Alosa sapidissima*) (122–128 kHz at 190 dB *re*: 1 μPa at 1 m) (Dunning *et al.*, 1992; Nestler *et al.*, 1992; Ross *et al.*, 1993, 1996) from the cold water intakes of power plants. In addition, Kraus *et al.* (1997) showed that sounds produced by pingers attached to large fishing nets to repel dolphins may also repel the clupeids that are being sought with the nets. Similarly, it has been shown that cod (*Gadus morhua*) will respond to sound from 38-kHz echosounders, and behavioral tests have demonstrated that they can detect this frequency but with poor auditory sensitivity (194 dB *re*: 1 μPa) (Astrup and Møhl, 1993, 1998).

Other than the data for cod, the results with clupeids were in sharp contrast to more quantified behavioral studies of hearing in fishes, which demonstrated that all other teleosts, including the herring (*Clupea harengus*), had substantial decrements in hearing above 500 to 1500 Hz, and this led to the conclusion that these fishes could not detect sounds higher than 1–3 kHz (Enger, 1967; Fay, 1988; Popper and Platt, 1993). It should be noted that the earlier investigators never tested higher frequency sounds on the premise that since thresholds were already getting poor at the highest frequencies tested, they would not improve at even higher frequencies.

We recently presented initial data showing that the American shad (*Alosa spaidissima*) can detect pure tones from sonic (0.2 kHz) to ultrasonic frequencies (180 kHz) (Mann *et al.*, 1997). The thresholds at the lowest frequencies, however, may have been masked by low-frequency noise from a recirculating water pump in a reservoir adjacent to the large tank in which the experiments were conducted. In this report, we present data on hearing thresholds from 0.2 to 100 kHz determined in a smaller tank and quieter environment and demonstrate the ability of American shad to detect simulated dolphin echolocation clicks.

I. METHODS

A. Experimental setup

Fish were obtained from the PEPCO Chalk Point Generating Station (Chalk Point, MD) aquaculture facility and held at the University of Maryland, College Park (UMD) fish

[a]Current address: Tucker-Davis Technologies, 4550 NW 6th Street, Gainesville, FL 32609.
[b]Correspondence and requests for materials should be addressed to A.N.P. (Electronic mail: popper@zool.umd.edu).

 0001-4966/98/104(1)/562/7/$15.00

colony. Fish ranged in size from 90- to 104-mm standard length. All procedures were approved by the Animal Care and Use Committee of the University of Maryland, College Park.

Previous threshold determinations for pure tones (Mann *et al.*, 1997) and the current thresholds for clicks were measured in a relatively large round fiberglass tank (122-cm diameter $\times$ 70-cm water depth). Fish were placed 20 cm from the center of the tank and 35 cm from the bottom and surface. The ultrasonic transducer was placed 15 cm from the fish and at the same depth as the fish. Pure-tone thresholds reported here were measured in a smaller rectangular tank ($40 \times 40 \times 50$ cm) located in a soundproof room. Each fish was placed 17.5 cm from the center of the tank and 15 cm from the bottom and surface. The transducer was located 30 cm from the fish. The transducer cables were electrically shielded, and the low-frequency transducer was shielded by a grounded metal mesh.

In all cases, fish were held in a modified 50-ml plastic conical tube, which allowed movements of only about 5 mm (numerous holes in the tube walls allowed for water circulation for respiration). This kept the fish in approximately the same position relative to the sound field (but see Discussion) and prevented them from moving about and shaking out the electrodes used to record cardiac and muscle activity (see below).

B. Sound stimuli

Pure tones at and below 12.8 kHz were digitally generated by Tucker-Davis Technologies, Inc. (TDT) equipment that had a 50-kHz sampling rate and a 50-ms rise-fall time. The digital sample was bandpass filtered between 50 Hz and 15 kHz (TDT model PF4 filter), attenuated by a programmable attenuator (TDT model PA4), amplified by a power amplifier, and played through an underwater speaker (University Sound UW-30). Tone frequencies above 12.8 kHz were generated by a function generator (Wavetek model 182A) that was triggered by a programmable trigger (TDT model TG6). A 50-ms rise-fall time was produced for all signals by passing the signal through a Colbourn Instruments Rise-Fall module. This signal was then attenuated with TDT equipment and played through either the amplifier and a UW-30 speaker (25 kHz) or an ITC-1042 underwater transducer without further amplification (50 kHz, 80 kHz, 100 kHz).

Click trains were generated by using the programmable trigger to repeatedly trigger the function generator to generate one cycle at 100 kHz. This caused the transducer to resonate at its natural frequency (80 kHz). The click train was composed of 8 clicks with a 50-ms interclick interval.

C. Calibration

To calibrate the system, an LC-10 hydrophone (calibrated sensitivity of -208.6 dB *re*: 1 V/μPa; ± 3 dB 0.1–180 kHz, omnidirectional) was positioned in the fish holder without the fish. The hydrophone output was analyzed by a digital oscilloscope (LeCroy 9310AM), with sampling at 250 kHz for signals 25 kHz and lower and at 1 MHz for signals above 25 kHz. Spectral analyses were performed with a Hanning window on the digitized hydrophone signal and were based on 50 000 points. Amplitudes of tones were calculated in dB *re*: 1 μPa from spectral analyses performed with the oscilloscope's internal FFT. Amplitudes of clicks were measured from the time waveform sampled at 1 MHz and calculated in dB *re*: 1 μPa peak to peak (p-p).

Click sound-pressure levels were measured as peak-to-peak values, rather than rms levels, because they are very short duration signals with exponential decays, and the duration over which to integrate the energy is not easily selected. Since the thresholds for tones and clicks were referenced to different values, they are not directly comparable.

Background noise was measured with a B&K 8103 hydrophone (calibrated charge sensitivity of 0.096 pC/Pa) connected to a charge amplifier scaled to 20 Pa/V. The output was analyzed with a digital oscilloscope (Hewlett-Packard 54542) with a built-in FFT. Spectrum levels at all frequencies were always at least 15 dB below threshold in both tanks.

D. Classical conditioning

Fish were anesthetized with 0.1 mg/L MS-222 (Sigma), an anesthetic for cold-blooded vertebrates. A wire electrode was inserted just below the skin on the fish's ventral surface, and the fish was then inserted into the conical tube in which it stayed for the duration of the testing. The signal from the electrode was filtered from 30 to 1000 Hz and amplified $50\times$ with a Grass P5 amplifier and then sampled by the TDT system at 50 kHz. The fish were respirated throughout the experiment by a flow-through water system. They were allowed to recover for at least 30 min before testing began to enable them to acclimate to the enclosure and to allow the anesthetic to wear off.

Fish were trained using classical conditioning of heart rate or muscle activity. Fish were presented with a test tone for 5 s, followed by a brief 1-V ac electric shock that was delivered across a pair of wire electrodes located on either side of the fish, with a spacing of 10 cm. The shock duration was 50 ms. Suppression of heart rate was determined by comparing the interheartbeat interval (IHBI) during the test tone, with the IHBI 5 s prior to the test tone [Fig. 1(B)]. A detection was considered to have occurred if the mean peristimulus IHBI was more than three standard errors greater than the prestimulus mean IHBI. Tone presentations and heartbeat monitoring were automated with TDT equipment (Lu *et al.*, 1996).

Fish often showed increased peristimulus muscle activity that was greater in amplitude than the heart rate and that would not allow automatic detection of heartbeat intervals. This muscle activity also provided a reliable method to determine thresholds. In these cases, detection responses were based on the total energy in the signal prestimulus and peristimulus. A detection occurred if the peristimulus energy was 120% or more of the prestimulus energy. Fish were included in the study only if the false detection rate was 5% or less, determined from running 20 control trials with no stimulus. Thresholds were almost identical for both measures.

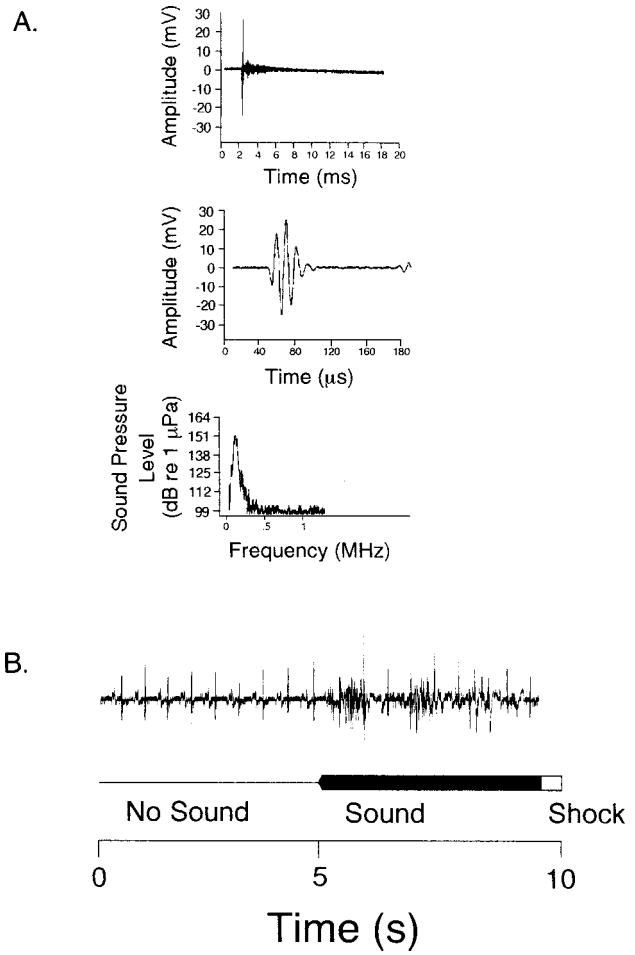

FIG. 1. (A) Click time waveform and power spectra measured at the position of the fish in the tank. The top panel shows a single click (183 dB *re*: 1 μPa p-p) generated by pulsing an ITC-1042 underwater transducer, followed by echos from the foam-lined tank wall. The middle panel shows the click on an expanded time axis, and the bottom panel shows the power spectrum of this click with a peak energy at 80 kHz. (B) Example traces of American shad cardiac and swimming muscle responses to presentation of sound paired with shock. After a 5-s control period with no sound, a click train is played for 5 s, ending with an electrical shock. Individual spikes are heartbeats, which slow down in the presence of the sound. The noise signal that begins after 5 s is the swimming muscle response.

E. Threshold determination

Thresholds were determined with a modified staircase method (e.g., Jacobs and Tavolga, 1968). The first three trials were a binary search designed to rapidly identify the approximate amplitude of the threshold (Lu *et al.*, 1996). With the use of this paradigm, if detection occurred on the first trial, the amplitude on the second trial was set at half the difference between the first trial amplitude and a minimum amplitude (50 dB). If detection did not occur on the first trial, then the amplitude on the second was half the difference between the first trial amplitude and a maximum amplitude of 160 dB. If detection occurred on the first trial and not on the second, then the third trial amplitude was halfway between that of the first and second trials. The binary search was used over the first three trials to rapidly approach threshold.

After the first three trials, amplitude changes were made in 4-dB steps. If a fish did not detect the sound on a previous trial, the amplitude was increased 4 dB. If the fish detected the sound on the previous trial, the amplitude was decreased 4 dB. Intertrial intervals were randomly selected between 3 and 5 min, with an average of 4 min. Trials were continued until a plateau was reached where there were alternations between detection and no detection responses. The threshold was defined, as determined in dB, as the average of at least six amplitudes at which there was a change from detection to no detection and or no detection to detection responses. One threshold from each of five or more fish was used to calculate the mean threshold at each frequency. For the click stimulus, the mean threshold was calculated using the thresholds from four fish.

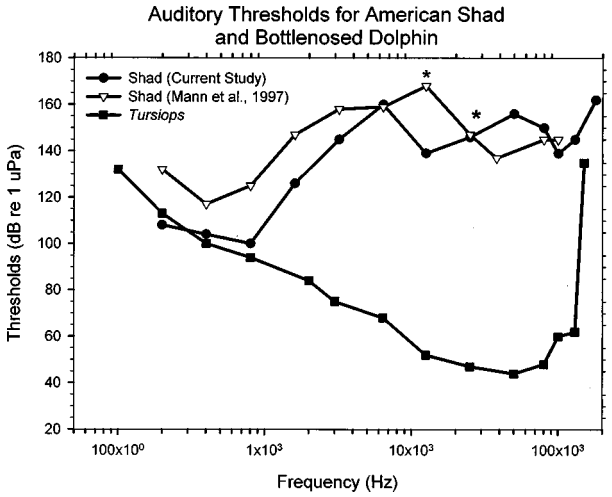

FIG. 2. Mean auditory thresholds of the American shad (standard error in Table I) for both the previous (Mann *et al.*, 1997) and current study up to 100 kHz along with additional data at higher frequencies. For comparisons, data are shown for the bottlenosed dolphin, *Tursiops truncatus* (Johnson, 1967). Asterisks indicate frequencies where some shad did not respond to the highest sound levels that could be produced in the experimental setup (see Table I for details).

II. RESULTS

A. Pure-tone thresholds and masking

One concern with previous ultrasound studies was the possibility of there being lower frequency sound associated with the ultrasound presentations and that the fish were detecting and responding to these lower frequency sounds rather than to the ultrasonic spectral peak. Accordingly, in our experiments, we measured the frequency spectrum of the signal and found no significant lower frequency sounds associated with our ultrasound presentations [see Fig. 1(A)].

American shad had the best sensitivity to sound between 0.2 and 0.8 kHz, with a threshold near 100 dB *re*: 1 μPa, as shown in Fig. 2 (see also Table I). The thresholds shown in the figure were somewhat poorer at 1.6 kHz, with poorest sensitivity from 3.2 to 12.5 kHz. At ultrasonic frequencies (25 to 100 kHz), the thresholds were about 147 dB *re*: 1 μPa. Note that in this and the previous study, some shad could detect sound at 12.5 and 25 kHz while some could not (asterisks in Fig. 2), suggesting some intraspecific variation in hearing capabilities.

As a control to rule out possible artifacts, such as low-frequency sound or electrical noise, four goldfish were

TABLE I. Auditory thresholds for the American had.

Pure tones	Current study		Previous study with low-frequency background noise (Mann *et al.*, 1997)		
Frequency	Mean threshold±SE dB *re*:1 μPa	*n*	Mean threshold±SE dB *re*:1 μPa	*n*	*t* text *P* value
200	108±3	7	132±13	5	0.016
400	104±5	5	117±11	6	0.175
800	101±3	8	126±8	6	0.003
1600	126±11	8	147±7	6	0.062
3200	145±7	6	159±4 (149±7)[a]	4 (2)[a]	0.057
6400	160±5	5	159±4 (176)[a]	5 (1)[a]	0.562
12 500	139 (149±8)[a]	1 (4)[a]	168 (168±5)[a]	1 (5)[a]	NA
25 000	146±9 (169±2)[a]	3 (4)[a]	147±10 (146±2)[a]	2 (3)[a]	NA
38 000	-	-	137±7 (146)[a]	3 (2)[a]	NA
50 000	156±2	8	-	-	NA
80 000	150±3	12	145±4	8	0.828
100 000	139±20	2	146±5	7	0.295

	Mean threshold±SE dB *re*: 1 μPa p-p	*n*
50 μs click, 80-kHz peak frequency	171±2 dB	4

[a]Data for maximum levels we could produce, at which some fish could not detect the sound.

trained using identical procedures to detect a 0.8-kHz tone at 130 dB *re*: 1 μPa. Several previous studies demonstrated that goldfish are sensitive to sound up to about 3 kHz (Fay, 1988), and one study suggested that they can detect sound up to 15 kHz (Offutt, 1968), although this has never been replicated. None of the four goldfish tested could detect 80-kHz tones at the maximum amplitude possible with our system (160 dB *re*: 1 μPa), a signal that could readily be detected by all shad used in this and our previous study (Mann *et al.*, 1997). This suggests that ultrasound detection by the American shad was not artifactual.

B. Echolocation click thresholds

American shad could also detect simulated bottlenosed dolphin echolocation click trains, which had eight clicks, a 50-ms interclick interval, 50-μs click duration, and a peak frequency at 80 kHz [Fig. 1(A)]. [Natural bottlenosed dolphin clicks are 50- to 80-μs duration, 115-kHz peak frequency, and 50- to 150-ms interclick interval (Au, 1993).]. The threshold for these clicks was about 171±2 dB p-p (Table I).

III. DISCUSSION

A. Threshold calibration

In this paper, we present auditory thresholds for the American shad determined in a relatively quiet environment. The thresholds, at low frequencies, are lower than those determined in a somewhat larger tank that had a recirculating pump running adjacent to it (Mann *et al.*, 1997), indicating that the earlier thresholds may have been masked. Still, it is important to point out that there is some variability in our data that may not just reflect interanimal differences at threshold. Instead, variation may also reflect the nature of the experimental setup.

In our experiments, we placed the fish in a small holding chamber and then positioned the chamber in our experimental tank. The fish could move a few millimeters in any direction in the holding chamber, and while we took care in positioning the fish in the same place for each experiment, there was no doubt some variation in the precise position of the fish in the tank relative to the sound source. The significant point here is that standing waves in the tank could create steep sound-pressure gradients, especially at lower frequencies. Thus the actual sound pressure impinging upon the fish could vary over a very small distance. This would have changed the exact sound level of the stimulus from one fish to the next and potentially even for a single fish if it moved any distance in the restraining tube. While we might have been able to determine this pressure gradient using multiple hydrophones, this would have not necessarily given useful information since the pressure gradient itself is affected by the fish and its position and the chamber in which the fish was placed and its position.

Thus while we suggest that the thresholds we present are valid, there is the caveat that we could not calibrate the precise sound that was present at the fish. Of course, there is the other caveat, as discussed below, that we are not even positive of the receptor being used by the fish. Until we know the receptor, we cannot know where to calibrate the sound along the fish's body.

B. Comparison with other species and masking

The only earlier study on the hearing ability of a clupeid proposed a tentative audiogram from 0.03 to 4 kHz for the herring (*Clupea harengus*) based on the responses of single neurons in the medulla oblongata (Enger, 1967). In that study, herring showed the greatest sensitivity from 0.03 to 1 kHz, with a threshold of 80 dB *re*: 1 μPa (Enger, 1967). The data for the herring agree with the low-frequency results for the shad in that both studies found best sensitivity at low frequencies. However, the herring thresholds were about 20 dB lower than those of American shad. This difference could be caused by several factors including species differences, the size of the fish tested (we tested small fish), differences in the experimental acoustic environment, or the differences in using behavioral and physiological measures. In contrast, our data at the higher frequencies are quite similar to experiments done on several species of *Alosa* in open pens that showed that the fish would respond and swim away from 125-kHz noises as low as 145 dB *re*: 1 μPa (e.g., Dunning *et al.*, 1992; Nestler *et al.*, 1992; Ross *et al.*, 1993, 1996), a threshold that is very similar to that determined in our setup for the American shad.

The low-frequency bandwidth of best hearing of the American shad is nearly as wide as that of fish traditionally classified as ''hearing specialists,'' including goldfish, carp,

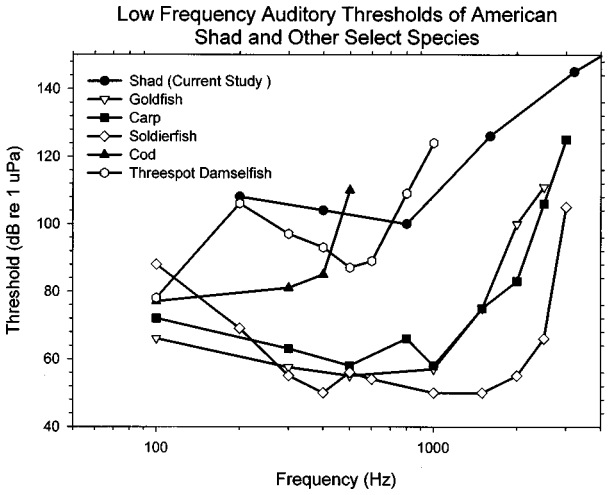

FIG. 3. Comparison of behaviorally determined auditory thresholds of American shad (up to 4 kHz) with behavioral thresholds for several other species of fish including carp (*Cyprinis carpio*) (Popper, 1972), cod (*Gadus morhua*) (Chapman and Hawkins, 1973), goldfish (*Carassius auratus*) (Popper, 1971), soldierfish (*Myripristis kuntee*) (Coombs and Popper, 1979), and threespot damselfish (*Eupomacentrus planiformes*) (Myrberg and Spires, 1980).

and some squirrelfish (Fig. 3) (reviewed in Fay, 1988). The low-frequency bandwidth of American shad is also substantially wider than that of other fishes without hearing specializations (Fig. 3). Yet our data indicate that the absolute thresholds for shad detecting low-frequency sounds is higher than those of goldfish by as much as 50 dB. It is likely, therefore, that while the shad can be classified as a ''hearing specialist'' based on its extraordinarily wide bandwidth of hearing, in the lower frequency range in which other specialists hear very well, shad are not very sensitive. Clearly, the overall bandwidth of the American shad is far wider than any other species tested to date. Thus while we would not consider American shad a hearing specialist in terms of having both wide bandwidth and excellent sensitivity, it is indeed a ''specialist'' in that it has an extraordinarily wide bandwidth of sensitivity, even compared with echolocating bats and dolphins (Fay, 1988).

Ultrasound detection is not yet widely known among fishes. While cod can detect ultrasound with poor sensitivity (Astrup and Møhl, 1993), we could not get goldfish to respond to ultrasound at the highest amplitudes we could generate. Thus our results suggest that at least some hearing specialists, such as the goldfish, may have evolved excellent low-frequency hearing but not the ability to detect ultrasound.

C. Potential mechanisms of ultrasound detection

The question arises as to how American shad detect ultrasound. At this point, it is not possible to stipulate the detection mechanism, but the parsimonious argument is that the ear is involved. We make this suggestion for two reasons. First, all other animals (vertebrate and invertebrate) that detect ultrasound have evolved mechanisms for detection that use the ear. Thus it is reasonable to suggest that evolution would act on an existing relatively high-frequency mechanotransducer to produce ultrasonic hearing rather than produce a totally new system or take advantage of other low-frequency mechanotransducers (e.g., touch receptors) to detect ultrasound.

The second argument is based on the observation that all members of the taxonomic order in which shad reside, the Clupeiformes, have a unique ear structure in which a pair of thin air-filled tubes project from the swimbladder to terminate in air chambers that are connected with the utricles of the inner ear (Wohlfahrt, 1936, 1938). While past investigators have not speculated on the use of the specialized ear for ultrasound detection, the special function of this ear was generally suggested to enhance hearing but in the sonic, and possibly infrasonic, ranges (e.g., Wohlfahrt, 1936, 1938; Enger, 1967; Denton and Gray, 1979; Denton *et al.*, 1979; Popper and Platt, 1979; Blaxter *et al.*, 1981; Platt and Popper, 1981).

In the specialized clupeid ear, the air bubble, located in the auditory bulla, is separated by a thin membrane from a more dorsal fluid-filled chamber that leads into the utricular chamber. In the herring, the membrane is attached to the utricular sensory macula by an elastic thread (Blaxter *et al.*, 1981). The fluid space of the bulla is also separated by a thin membrane from the fluid-filled canals of the lateral line (Denton and Gray, 1979). The membrane that lies between the air cavity and fluid space of the auditory bulla of the sprat (*Sprattus sprattus*) and herring was found to be the most responsive to pressure oscillations from 0.014 Hz to 1 kHz, with decreasing sensitivity up to 10 kHz (the highest frequency tested) by Denton *et al.* (1979). However, since this work was done in a freshly dead animal and since the bulla was exposed, it is very possible that the *in vivo* response of the membrane may actually be to much higher frequencies since postmortem effects result in substantial lowering of resonance frequencies of fish air bubbles, even within a few minutes of death (Cox and Rogers, 1987).

We also argue for involvement of the ear since the sensory epithelium of the clupeid utricle is highly derived and is virtually unique among all vertebrates that have been studied (Popper and Platt, 1979; Platt and Popper, 1981a, b). In fact, there are several characteristics of the utricle that are of interest and are reminiscent of possible adaptations for high-frequency hearing in mammals. In particular, the utricular sensory epithelium is divided into three parts, and two of these, the anterior and middle maculae, sit over the fluids of the ear (O'Connell, 1955; Popper and Platt, 1979; Best and Gray, 1980). In contrast, the posterior macula, the single macula of utricles of all other fishes, and the saccule and lagena maculae of clupeids and other fishes, all sit on rigid structures. As a result, the likely mechanism of stimulation of the suspended parts of the utricular epithelium is different than the other otolithic endorgans (e.g., Best and Gray, 1980). It is possible that the suspension of the utricular maculae might be analogous to the suspension of the organ of Corti found in mammals. Moreover, the thickness of the membrane supporting the suspended macula varies along the length of the receptor (Best and Gray, 1980), as it does in the organ of Corti (e.g., Echteler *et al.*, 1994), suggesting that different regions of the epithelia respond to different frequencies.

Despite our suggestion of the involvement of the ear in ultrasound detection, it is still possible that other mechanisms are involved that do not require the ear. Dunning *et al.* (1992) suggested that the fish could be detecting cavitation produced by the high-intensity sounds, but our calculations at the frequencies tested indicate that cavitation effects would not have taken place even at the highest sound amplitudes used in our investigation. It is also possible that the signals were stimulating other receptors, such as those in the skin. Specialized skin receptors for detection of high frequencies are not known for any animal, and so if the shad were using such receptors, it is likely that they were using generalized receptors that were overstimulated by the ultrasound. If that were the case, however, we would have expected a similar response from our ''control'' animals, goldfish, when they were stimulated with the highest intensity ultrasound at 80 kHz.

Clearly, physical studies on the responses of the bulla to sound from low to ultrasonic frequencies and on the neurophysiology of the ear are needed to test the hypothesis that the auditory bullae are responsible for the ability of shad to detect ultrasound.

D. Echolocation click detection

American shad were also able to detect simulated dolphin echolocation clicks with a 50-ms interclick period at a threshold of 171 dB *re*: 1 μPa p-p. Based on this threshold, shad are likely to be able to detect the echolocation clicks of odontocetes, which are typically high-frequency and high-intensity short-duration sounds [e.g., *Tursiops truncatus*: 220 dB *re*: 1 μPa, p-p source level (SL), 50- to 80-μs duration; *Phocoena phocoena*: 162 dB *re*: 1 μPa, p-p SL, 130- to 260-μs duration] (Au, 1993). If spherical spreading and an absorption coefficient of 0.02 dB/m are assumed, shad should be able to detect echolocating *Tursiops truncatus* at a range of 9–187 m for clicks from 190 to 220 dB *re*: 1 μPa p-p SL. Of course, it is possible that the thresholds for actual echolocation clicks might be somewhat poorer than for the artificial clicks used in these experiments because of auditory system summation (Fay and Coombs, 1983). Moreover, it should be noted that while the emitted sound levels of other smaller porpoises, such as the harbor porpoise, are of lower amplitude than that of *Tursiops*, the duration of the signals for these species is longer (Au, 1993). Thus, as demonstrated by Au, the total energy in these signals is about the same or more than that in *Tursiops*, suggesting that American shad could detect the signal if there is any temporal summation.

Tursiops truncatus are able to detect a water-filled 7.62-cm-diameter steel sphere at 113-m distance (Au, 1993). Given that the target strength of a school of shad is much higher than that of the steel sphere, it is likely that an echolocating dolphin could detect a school of shad before they were able to detect the echolocation clicks. Still, the shad should be able to detect a dolphin at a sufficient distance to enable them to take evasive actions.

Indeed, this observation in American shad is reminiscent of the results of studies showing that moths (and many other insect species) perform an elaborate behavioral evasive repertoire when they detect bat cries (Roeder, 1962; Hoy, 1992), and there is evidence that clupeids undergo an escape response when they detect ultrasonic clicks (Nestler *et al.*, 1992). In fact, in preliminary experiments in which ultrasonic tones or clicks were played into a tank containing free-swimming American shad, they immediately grouped together on the side of the tank opposite the transducer (unpublished observations, Mann *et al.*).

It is of interest to note that one difference between the results from moths and from American shad is the bandwidth of the detection ability of the two animals. Moths hear only a very narrow range of frequencies that is related to the range of frequencies in the echolocation sounds of their bat predators (e.g., Hoy, 1992). In contrast, the ultrasonic hearing bandwidth of American shad is very wide and sensitivity is about equally good across most of this ultrasonic range. However, examination of the echolocation behavior of *Tursiops* and other echolocating odontocetes demonstrates the selective pressures that must have been operative in the evolution of the wide bandwidth of the American shad. The echolocation sounds vary in different echolocating species (Au, 1993) and so it is likely that shad have evolved a wide hearing bandwidth to avoid predation by more than one species [e.g., *Delphinus delphinus*, common dolphin, 23–67 kHz, *Phocoena phocoena*, Harbor porpoise, 120–140 kHz (Au, 1993)]. Thus if the detection bandwidth of American shad (or any other clupeid) were narrow, they would not be able to detect more than one dolphin species, but with a wide bandwidth, the shad are presumably able to detect predators no matter what frequencies are used in the echolocation signal.

Two additional questions arise. First, is it likely that other species of fish can detect ultrasound, and second, how did ultrasound detection arise in fishes? It is well known that a number of taxonomically distinct groups of insects have separately evolved the ability to detect echolocation sounds of bats (Hoy, 1992). If ultrasound detection evolved several times in insects because of the strong pressures of a bat predator, it might be possible that other teleost species, unrelated to clupeids but that are also preyed upon by odontocetes, could have evolved ultrasound detection. Cod fall into this category (Astrup and Møhl, 1993, 1998). Thus it may be fruitful to examine other species to determine whether ultrasound detection is more ubiquitous among fishes than is now known.

The origin of ultrasound detection by clupeids is not something that can be easily determined. Clupeids evolved long before cetaceans, and all extant clupeids have the auditory bullae, suggesting that it too existed before there were odontocetes (Barnes *et al.*, 1985; Nelson, 1994). Many clupeids migrate from the ocean to freshwater to spawn and thus would have encountered shallow waters where higher frequency sounds propagate far better than lower frequencies (Rogers and Cox, 1988). If this were the case, then it is possible that clupeid ancestors, as the goldfish, might have evolved mechanisms to enhance relatively high-frequency hearing compared with fishes that lived in deeper waters. Thus the clupeid utricle was already specialized for detection of relatively high frequencies and that once they moved out into the oceans and encountered odontocetes, they were al-

ready preadapted to deal with the evolving dolphin echolocation system. In essence, the production of ultrasound by odontocetes and the further broadening of the clupeid bandwidth might have happened concurrently.

ACKNOWLEDGMENTS

We thank P. Kerlin and P. Willenborg of Potomac Electric Power Company (PEPCO) for supplying the shad, C. Derenburger and J. Finneran for help with tank acoustics and hydrophone calibration, C. Moss and W. Wilson for the loan and help with the digital oscilloscope, and W. Au for discussions on generating clicks. We also thank D. Dunning, J. Nestler, and C. Schilt for discussions on their ultrasound experiments, A. Read for discussions on dolphin feeding, and W. W. L. Au, R. R. Fay, and W. N. Tavolga for their comments on an earlier draft of this manuscript. This work was supported by Grant No. 1 BN96-311354 from the National Science Foundation and by training Grants No. T32 DC-00046 and No. F32 DC-00248 from the National Institute of Deafness and Other Communicative Disorders of the National Institutes of Health.

Astrup, J., and Møhl, B. (**1993**). ''Detection of intense ultrasound by the cod, *Gadus morhua*,'' J. Exp. Biol. **182**, 71–80.

Astrup, J., and Møhl, B. (**1998**). ''Discrimination between high and low repetition rates of ultrasonic pulses by the cod,'' J. Fish Biol. **52**, 205–208.

Au, W. W. L. (**1993**). *The Sonar of Dolphins* (Springer-Verlag, New York).

Barnes, L. G., Domning, D. P., and Ray, C. E. (**1985**). ''Status of studies on fossil marine mammals,'' Mar. Mam. Sci. **1**, 15–53.

Best, A. C. G., and Gray, J. A. B. (**1980**). ''Morphology of the utricular recess in the sprat,'' J. Mar. Biol. Assoc. U.K. **60**, 703–715.

Blaxter, J. H. S., Denton, E. J., and Gray, J. A. B. (**1981**). ''The auditory bullae-swimbladder system in late stage herring larvae,'' J. Mar. Biol. Assoc. U.K. **61**, 315–326.

Chapman, C. J., and Hawkins, A. D. (**1973**). ''A field study of hearing in the cod, *Gadus morhua L.*,'' J. Comp. Physiol. **85**, 147–167.

Coombs, S., and Popper, A. N. (**1979**). ''Hearing differences among Hawaiian squirrelfishes (Family Holocentridae) related to differences in the peripheral auditory system,'' J. Comp. Physiol. **132**, 203–207.

Cox, M., and Rogers, P. H. (**1987**). ''Automated noninvasive motion measurement of auditory organs in fish using ultrasound,'' J. Vibration, Acoustics, Stress, and Reliability in Design **109**, 55–59.

Denton, E. J., and Gray, J. A. B. (**1979**). ''The analysis of sound by the sprat ear,'' Nature (London) **282**, 406–407.

Denton, E. J., Gray, J. A. B., and Blaxter, J. H. S. (**1979**). ''The mechanics of the clupeid acousticolateralis system: frequency responses,'' J. Mar. Biol. Assoc. U.K. **59**, 27–47.

Dunning, D. J., Ross, Q. E., Geoghegan, P., Reichle, J., Menezes, J. K., and Watson, J. K. (**1992**). ''Alewives avoid high-frequency sound,'' N. Am. J. Fish. Manage. **12**, 407–416.

Echteler, S. M., Fay, R. R., and Popper, A. N. (**1994**). ''Structure of the mammalian cochlea,'' in *Comparative Hearing: Mammals*, edited by R. R. Fay and A. N. Popper (Springer-Verlag, New York), pp. 134–171.

Enger, P. S. (**1967**). ''Hearing in herring,'' Comp. Biochem. Physiol. **22**, 527–538.

Fay, R. R. (**1988**). *Hearing in Vertebrates: A Psychophysics Databook* (Hill-Fay, Winnetka, IL).

Fay, R., and Coombs, S. (**1983**). ''Neural mechanisms in sound detection and temporal summation,'' Hearing Res. **10**, 69–92.

Hoy, R. R. (**1992**). ''The evolution of hearing in insects as an adaptation to predation by bats,'' in *The Evolutionary Biology of Hearing*, edited by D. B. Webster, R. R. Fay, and A. N. Popper (Springer-Verlag, New York), pp. 115–130.

Jacobs, D. W., and Tavolga, W. N. (**1968**). ''Acoustic frequency discrimination in the goldfish,'' Anim. Beh. **16**, 67–71.

Johnson, C. S. (**1967**). ''Sound detection thresholds in marine mammals,'' in *Marine Bio-Acoustics II*, edited by W. N. Tavolga (Pergamon, Oxford), pp. 247–260.

Kraus, S. D., Read, A. J., Solow, A., Baldwin, K., Spradlin, T., Anderson, E., and Williamson, J. (**1997**). ''Acoustic alarms reduce porpoise mortality,'' Nature (London) **388**, 525.

Lu, Z., Popper, A. N., and Fay, R. R. (**1996**). ''Behavioral detection of acoustic particle motion by a teleost fish (*Astronotus ocellatus*): sensitivity and directionality,'' J. Comp. Physiol. A **179**, 227–233.

Mann, D. A., Lu, Z., and Popper, A. N. (**1997**). ''Ultrasound detection by a teleost fish,'' Nature (London) **389**, 341.

Myrberg, Jr., A. A., and Spires, J. Y. (**1980**). ''Hearing in damselfishes: an analysis of signal detection among closely related species,'' J. Comp. Physiol. **140**, 135–144.

Nelson, J. S. (**1994**). *Fishes of the World* (Wiley, New York).

Nestler, J. M., Ploskey, G. R., Pickens, J., Menezes, J., and Schilt, C. (**1992**). ''Responses of blueback herring to high-frequency sound and implications for reducing entrainment at hydropower dams,'' N. Am. J. Fish. Manage. **12**, 667–683.

O'Connell, C. P. (**1955**). ''The gas bladder and its relation to the inner ear in *Sardinops caerulea* and *Engraulis mordax*,'' Fish. Bull. **56**, 505–533.

Offutt, G. C. (**1968**). ''Auditory response in the goldfish,'' J. Aud. Res. **8**, 391–400.

Platt, C., and Popper, A. N. (**1981a**). ''Otolith organ receptor morphology in herring-like fishes,'' in *Vestibular System: Function and Morphology*, edited by T. Gualterotti (Springer-Verlag, New York), pp. 64–74.

Platt, C., and Popper, A. N. (**1981b**). ''Structure and function in the ear,'' in *Hearing and Sound Communication in Fishes*, edited by W. N. Tavolga, A. N. Popper, and R. R. Fay (Springer-Verlag, New York), pp. 3–38.

Popper, A. N. (**1971**). ''The effects of size on the auditory capacities of the goldfish,'' J. Aud. Res. **11**, 239–247.

Popper, A. N. (**1972**). ''Pure-tone auditory thresholds for the carp *Cyprinus carpio*,'' J. Acoust. Soc. Am. **52**, 1714–1717.

Popper, A. N., and Platt, C. (**1979**). ''The herring ear has a unique receptor pattern,'' Nature (London) **280**, 832–833.

Popper, A. N., and Platt, C. (**1993**). ''Inner ear and lateral line of bony fishes,'' in *The Physiology of Fishes*, edited by D. H. Evans (CRC, Boca Raton, FL), pp. 99–136.

Roeder, K. D. (**1962**). ''The behavior of free flying moths in the presence of artificial ultrasonic pulses,'' Anim. Behav. **10**, 300–304.

Rogers, P. H., and Cox, M. (**1988**). ''Underwater sound as a biological stimulus,'' in *Sensory Biology of Aquatic Animals*, edited by J. Atema, R. R. Fay, A. N. Popper, and W. N. Tavolga (Springer-Verlag, New York), pp. 131–149.

Ross, Q. E., Dunning, D. J., Menezes, J. K., Kenna, Jr., M. J., and Tiller, G. W. (**1996**). ''Reducing impingement of alewives with high-frequency sound at a power plant intake on Lake Ontario,'' N. Am. J. Fish. Manage. **16**, 548–559.

Ross, Q. E., Dunning, D. J., Thorne, R., Menezes, J. K., Tiller, G. W., and Watson, J. K. (**1993**). ''Response of alewives to high-frequency sound at a power plant intake on Lake Ontario,'' N. Am. J. Fish. Manage. **13**, 291–303.

Wohlfahrt, T. A. (**1936**). ''Das Ohrlabyrinth der Sardine (*Clupea pilchardus* Walb.) und seine Beziehungen zur Schwimmblase und Seitenlinie,'' Z. Morphol. Oekol. Tiere **31**, 371–410.

Wohlfahrt, T. A. (**1938**). ''Von den Ohren der Fische. Die Beziehungen des innneren Ohres zur Schwimmblase besonders bei heringsartigen Fischen,'' Aurder Natur, Leipzig **15**, 82–87.

One tone, two ears, three dimensions: A robotic investigation of pinnae movements used by rhinolophid and hipposiderid bats

V. A. Walker,[a] H. Peremans, and J. C. T. Hallam
Department of Artificial Intelligence, University of Edinburgh, Forrest Hill, 5, Edinburgh EH1 2Q1, United Kingdom

(Received 25 June 1997; revised 10 October 1997; accepted 5 March 1998)

Bats, which echolocate using broadband calls, are believed to employ the passive acoustic filtering properties of the head and pinnae to provide spectral cues which encode 3-D target angle. Microchiropteran species whose calls consist of a single, constant frequency harmonic (i.e., some species in the families *Rhinolophidae* and *Hipposideridae*) may create additional acoustic localization cues via vigorous pinna movements. In this work, two types of echolocation cues generated by moving a pair of receivers aboard a model sensor head are investigated. In the first case, it is supposed that a common 3-D echolocation principle employed by all bats is the creation of alternative viewing perspectives, and that constant frequency (CF) echolocators use pinna *movement* rather than *morphology* to alter the acoustic axes of their perceptual systems. Alternatively, it is possible rhinolophids and hipposiderids move their ears to create dynamic cues—in the form of frequency and amplitude modulations—which vary systematically with target elevation. Here the use of binaural and monaural timing cues derived from amplitude modulated echo envelopes are investigated. In this case, pinna mobility provides an echolocator with a mechanism for creating dramatic temporal cues for directional sensing which, unlike interaural timing differences, do not degrade with head size. [S0001-4966(98)04306-9]

PACS numbers: 43.80.Lb, 43.80.Jz, 43.64.Bt [FD]

INTRODUCTION

Sound converging on a receiver from different positions in the field will be characteristically delayed and attenuated as a result of its unique travel paths. Likewise, sound originating from a single location, but received at different positions in the field, can be characterized by particular delay and intensity *differences*. By employing two laterally separated receivers, animals lateralize[1] sound based on interaural disparities of intensity (IID), arrival time (ITD) and/or phase. The relative magnitudes and, therefore, the relative importance of these effects varies with sound frequency, and the acoustic properties and dimensions of the head and pinnae of an animal.

Although an ITD can provide a relatively large head with precise angle-to-target measurements, it is an inherently less flexible mechanism because the calibration constant—i.e., the speed of sound—is fixed by the environment. In contrast, intensity is an adjustable calibration constant: it can be manipulated by characteristics of the receiver such as pinna size and orientation. Using IIDs, even small binaural receiving systems can enjoy the stereo effects of large heads.

It is widely assumed that this is the strategy of echolocating bats. The heads of bats are small and maximum ITDs are less than 50 μs. In contrast, bat heads can generate large IIDs: measured IIDs are typically 25–30 dB [see review in Pollak and Park (1996)]. Moreover, binaural neurons in the bat's auditory system are most sensitive to IIDs (Pollak, 1988). If bats, like many other mammals, have a minimally detectable intensity difference of approximately 1 dB, most species studied should detect differences of between 1 and 5 degrees in the lateral position of pure-tone sources at relevant frequencies (Obrist *et al.*, 1993).

While the placement of two receivers on opposite sides of an acoustic perceptual system generates IIDs that are powerful lateralization cues, adding pinnae to receivers creates directional cues which enable animals—using only two ears—to ''project'' a sound source out to a well-defined location having attributes of front–back–above–below as well as right–left. Bat pinnae are well developed and may even exceed the dimensions of the head. The variety of actual pinnae shapes, sizes, and mobility within *Microchiroptera* suggest that, just as there are a variety of different approaches to calling in echolocation, there are also a variety of approaches to reception.

Most bats which employ broadband calls appear to hold their pinnae in a fixed orientation relative to the head during echolocation and may localize targets in three dimensions by comparing IIDs across different frequencies (Grinnell and Grinnell, 1965; Lawrence and Simmons, 1982; Fuzessery *et al.*, 1992; Obrist *et al.*, 1993). That is, they exploit the fact that both the size of their ''acoustic magnifying glass'' (i.e., the region of highest listening sensitivity) and its orientation in space changes with frequency, due to the passive acoustic properties of the head and pinnae.

Directional cues naturally occurring in the echo power spectrum will not be available to bats echolocating with a single constant frequency (CF) call e.g., many species in the

[a]Electronic mail: ashley@dai.ed.ac.uk

 0001-4966/98/104(1)/569/11/$15.00

families *Rhinolophidae* and *Hipposideridae*. Members of both families echolocate using the second CF harmonic and are distinguished by the lack of a tragus and highly mobile pinnae. Some rhinolophid and hipposiderid bats independently rotate their pinnae, like two opposing antennae, during echolocation. The mobility of the pinnae may be employed in search-related tasks. However, these bats appear to investigate potential targets more systematically via vertical arc scanning motions. One such movement appears to be made for each CF echolocation pulse/echo—with the right and left pinnae moving along equal and oppositely signed arcs during one pulse/echo, and reversing this motion during the next pulse/echo, and so on (Möhres, 1953; Schneider and Möhres, 1960; Griffin *et al.*, 1962; Pye *et al.*, 1962; Pye and Roberts, 1970; Gorlinsky and Konstantinov, 1978; Mogdans *et al.*, 1988).

Functions which have been suggested for the ear movements include: scanning to obtain bearing information via the inherent directionality of the pinnae (Möhres, 1953; Schnitzler, 1973), scanning to measure echo amplitude in spite of the directionality of the pinnae (Pye, 1967), and the production of local Doppler shifts to increase the effective directionality of the pinnae (Pye and Roberts, 1970). Behavioral studies confirm the importance of ear movements in target localization: immobilization of the pinnae causes disorientation and a loss of localization acuity (particularly in the vertical direction) in *Rhinolophus ferrumequinum* (Schneider and Möhres, 1960; Gorlinsky and Konstantinov, 1978; Mogdans *et al.*, 1988). However, there have been no studies (to our knowledge) which have directly tested the accuracy and feasibility of specific theories. Here we investigate, using a computational methodology, the information content of two types of intensity cues generated by receivers scanning so as to mimic the pinna movements of rhinolophid and hipposiderid bats.

In Sec. II A, we explore the possibility that a CF emitting echolocator may use pinna *movement* rather than *morphology* to exploit the same localization principle believed to be employed in broadband echolocation, i.e., the use of more than one SONAR horizon[2] along which to localize sound. By moving a single, fixed-width acoustic magnifying glass to a series of different orientations during reception, rhinolophids and hipposiderids may provide themselves with additional viewing perspectives across which to sample and compare IID values in the same way that broadband emitting bats may compare IIDs across frequencies.

In Sec. II B, we investigate the possibility that the pinnae may be scanned to create dynamic intensity cues, rather than other measurement perspectives. In this regard, we explore the generation and use of novel timing cues. For example, pinnae sweeping vertically across a target set up amplitude modulation patterns in returning echoes which change systematically with target elevation (Schnitzler, 1973). Monaurally, target elevation is encoded in the temporal disparity between echo arrival time and echo amplitude peak time. Binaurally, target elevation is encoded in the temporal disparity between echo peak times in the right and left ears. This, in turn, gives rise to IID rates of change which also characterize target elevation. Unlike ITDs, the resolvability of timing cues generated in this sensory context are determined by the sensitivity and speed of the ears (*millisecond* cues), rather than the size of the head (*microsecond* cues).

Given the fine frequency discrimination of some rhinolophids and hipposiderids, it is natural to suppose that the movement of the ears plays a role in producing local Doppler shifts which aid in both target separation and localization (Pye and Roberts, 1970). However, the present transducer mountings and the speed of the servo-motors controlling the receiver's motion do not facilitate the generation of sufficient Doppler shifts to investigate frequency cues with our current equipment.

In the next section, we begin with an overview of the modelling methodology employed in this work (Sec. I A), and a discussion of both the key assumptions underlying model (Sec. I B) and the hardware and software components used in the implementation of the model (Sec. I C). Section I D provides a description of the experiments. Following the presentation of the results (Sec. II), we discuss this work in the context of related investigations (Sec. III).

I. METHODOLOGY

A. The computational approach

In order to describe how the neuronal systems of echolocating bats can effectively use various parameters of echoes for the localization of targets, investigations should proceed along three research frontiers: neurophysiological, behavioral, and computational. Electrophysiological recordings of neural responses to auditory stimuli reveal how given cues are processed in the nervous system of bats. Test stimuli for these investigations may be obtained from behavioral experiments with bats and/or theoretical studies. In the case of the former, the response of bats to systematic variation of target properties demonstrates whether they can use particular acoustic cues. (To this end, field studies indicate which cues seem to be the most important for bats under natural conditions.) Likewise, a computational approach may be employed to generate hypotheses for neurophysiological tests. In this case, analysis of echoes by physical measurements and theoretical considerations reveals how echoes are formed and, therefore, which echo parameters may characterize the invariant properties of a target.

Here the computational approach is taken in an investigation of the acoustic cues created by the pinna motion of rhinolophid and hipposiderid bats. Moreover, the sufficiency of those cues to engender a binaural echolocation system with robust and accurate spatial percepts is tested aboard a robotic sensor head. This artificial echolocation system mimics the external auditory apparatus of a bat using functionally analogous transducers and electromechanical motion control circuitry.

The robot used in these studies possesses no other sensory modalities or environmental knowledge. Moreover, because this model inhabits the same environment as the animal, we make no simplifying assumptions about target types, environmental noise, or acoustic clutter. In this regard, such a model facilitates examination of more realistic environ-

mental interactions than are possible using mathematical models and computer simulations.

From our results, we do not infer a particular use of cues by bats. Rather, our aim is to generate hypotheses for neurophysiological studies by demonstrating that certain plausible cues are sufficient to account for behavior.

B. Assumptions

Any computable representation of a biological system requires simplification, which, in turn, implies a number of assumptions about what are the relevant factors to represent, and what constitutes a satisfactory way to represent them. The assumptions made regarding the pinnae and their motion are enumerated below.

1. Pinna morphology

The ears of bats are complex physical structures and local effects involving reflections from pinna folds and crenellations are likely to generate important acoustic cues. However, in this work, we ignore local effects and employ only the global directionality brought about by diffraction across the opening of the pinnae. We adopt an assumption common in pinna modeling; that the opening of the pinna experiences sound diffraction similar to a single, circular aperture (Fletcher and Thwaites, 1979; Guppy and Coles, 1988; Kuc, 1994). Across a limited range of frequencies, the directivity characteristics of the main sensitivity lobe of a *circular piston* (receiving in an infinite baffle) can be related to the diffraction limits imposed by the effective radius of the pinna opening in relation to sound wavelength (Guppy and Coles, 1988; Kuc, 1994). In what follows, a piston receiver (and emitter) is employed, due to the availability of a *physical* model, i.e., the electrostatic Polaroid series 7000 transducer (Biber *et al.*, 1980).

2. Directionality

The radius of the Polaroid transducer used in these investigations ($a=11.3$ mm) is larger than that of a typical rhinolophid or hipposiderid pinna opening and, therefore, the beam width of the model pinna is narrower than that of a bat. Moreover, due to external constraints, emitting and receiving transducers are mounted at a common elevation aboard a relatively large head (see Fig. 1) such that the resulting directionality of the model sensor head is less circularly symmetric than that of a bat. However, within the frontal sound field of both the model sensor head and those of bats echolocating at their dominant CF; similar high-resolution IID profiles arise: 0.3–0.9 degrees dB^{-1} robot (measured over the effective range of the system), 0.6 degrees dB^{-1} *Rhinolophus rouxi*, *R. clivosus*, *R. eloquens*, *Asellia tridens*, and *Hipposideros lankadiva* (Obrist *et al.*, 1993). Where we believe differences in beam widths are significant, simulation results using a model head based on an average *R. ferrumequinum* pinna width ($a=4.5$ mm) and call frequency (83 kHz) are shown.

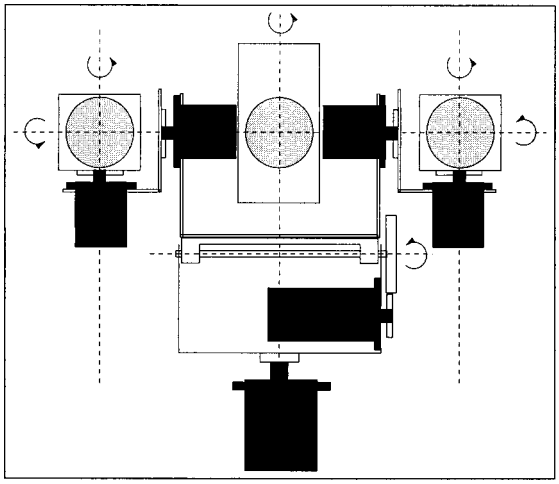

FIG. 1. **Robot sensor head**. The robotic sensor head consists of a central transmitter (fixed to the head) flanked by two independently orientatable receivers. Transducers are shown in grey, motors in black, and pan and tilt axes are indicated via arrows. All transducers are mounted in a common elevation plane and laterally separated by 8 cm.

3. Pinna motion

Qualitative observation of additional head movements, pinna rotations, and changes in pinna shape have been associated with the systematic vertical pinna scanning behavior employed by rhinolophids and hipposiderids (Möhres, 1953; Schneider and Möhres, 1960; Pye *et al.*, 1962). These additional motions may allow a bat to change the size as well as the orientation of its acoustic magnifying glass. Indeed, neurophysiological studies have confirmed that both the orientation and size of the spatial response area of an auditory neuron depends upon the orientation of a bat's pinnae (Neuweiler, 1970; Sun and Jen, 1987). Nevertheless, here we investigate only changes in the vertical orientation of the pinnae.

4. Synchronization of sound and movement

Ear movements appear to take place before the production of a pulse (Pye and Roberts, 1970), therefore, it is speculated that movements may actually be synchronized with the arrival of (previous) echoes. In this investigation, maximal use of the receiver motion is made by ensuring that the receivers are at their extreme orientations before echo reception and are moving throughout its duration. Because the servo-motors controlling the motion of the receivers move relatively slowly (approximately 300 degrees s^{-1} at peak speed), this necessitated a long (>60 ms) call.

5. Call structure

The echolocation calls of rhinolophids and hipposiderids contain multiple harmonics, and the long CF portion of each harmonic may be preceded and followed by brief (<5 ms), 10–30-kHz-wide frequency-modulated (FM) sweeps. However, because vocal track processes largely strip the fundamental and third harmonics, we assume that the bulk of the information used by these bats during echolocation is gained from the dominant harmonic CF portion of the signal. Therefore, we work with CF signals at the most efficient frequency

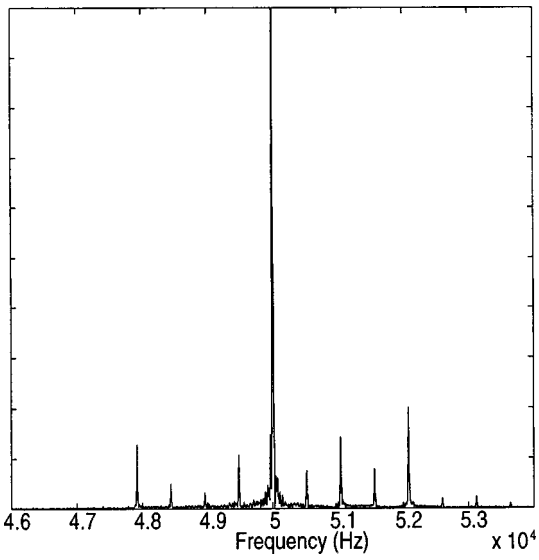

FIG. 2. **Spectrum of fan echo**. Measured frequency spectrum of amplitude and frequency modulated echo from seven-blade fan rotating at approximately 70 Hz.

for our transducer (50 kHz). (Where simulation results are used, we employ the 83-kHz dominant CF frequency of *R. ferrumequinum*.)

6. Information content per echo/ear movement

We assume that the information available in a single echo contains complete (though, probably, imperfect) localization information. This, in turn, implies that the pinnae need only make one sweep (rather than, for example, a full down-and-up cycle) to generate acoustic cues. This assumption is in keeping with the widely held assumption that bats employing broadband sounds *simultaneously* sample target location along a number of SONAR horizons within the beam of a single echo. More convincing, perhaps, is the fact that rhinolophids and hipposiderids emit pulses in groups containing as few as a single pulse/movement (Pye *et al.*, 1962).

7. Target separation

Implementation of sensing strategies in a noisy, acoustically cluttered environment introduces the need for some means by which to separate target echoes from reflections off other objects and, in the case of long signals, from the overlapping emission. Isolating a target in the time domain was not possible in the cluttered laboratory, given the length of the signal. Instead, isolation in the frequency domain was achieved by employing an oscillating target. As in many behavioral studies, a fan target was used to amplitude and frequency modulate the CF call signal (von der Emde and Schnitzler, 1986; Nitsche, 1987; Ostwald *et al.*, 1988). This target (i.e., a pentium heat-sink fan consisting of seven blades rotating at approximately 70 Hz) sets up a pattern of side bands at approximately 500-Hz intervals on either side of the 50-kHz emitted frequency. The resulting acoustic target ''signature,'' an example of which is shown in Fig. 2, is easily separable from energy at 50 kHz—which mainly contains reflections from background structures.

C. The computational architecture

The robotic sensor head is described briefly below, and in more detail in Peremans *et al.* (1997).

1. Hardware

The sensor head has six degrees of freedom, as indicated in Fig. 1, allowing panning and tilting of the neck, and independent panning and tilting of each receiver. The motors driving the different axes are standard radio-control model servos. Control signals, i.e., pulse-width-modulated signals, are generated by a transputer.

A transmitter module has inputs for frequency and amplitude modulations to be imposed on a carrier wave. Alternatively, the FM signal generation part of the transmitter module can be bypassed and a digitally generated signal fed directly into the power amplifier. This latter strategy is employed in the work reported here to create a 50-kHz echolocation signal with well-defined phase characteristics.

Echo detection and amplification is performed by the receiver modules mounted behind their associated transducers. The output signals from the receivers are sampled at 200 kHz. All further processing of the received signals is performed on a transputer-based multiprocessor.

2. Signal processing

The signal processing operations performed upon the received echoes are based upon a simple model of cochlear filtering. Received signals are filtered by narrow ($Q>100$) bandpass filters centered at behaviorally relevant frequencies. Bandpass-filtered signals are full-wave rectified and then smoothed using a lowpass filter (i.e., a second-order Butterworth filter).

Computation constraints restricted the number of possible filters to two and, therefore, the acoustic signature of the fan target (see Fig. 2) was captured by a set of filters centered at 51 and 52 kHz. Additional filters would improve the signal-to-noise ratio and facilitate the detection of this target in an environment containing other reflectors with periodic motion. However, additional filters were not necessary in this localization task. By not admitting sound at 50 kHz, we reject reflections from stationary objects and the relatively loud call energy.

3. 3D echo simulator

A simulation tool was developed to test algorithms before implementation on the robotic sensor head. The 3D echo simulator mimics the functionality of the robotic model except that it operates in a noise- and clutter-free world where the user can define sensor head attributes (e.g., transducer size, call frequency) and target types arbitrarily (Walker, 1997). Because the simulator allows us to vary the morphology of the sensor head, results generated in simulation are juxtaposed with measured results where their use provides a more meaningful comparison with the small heads of bats (i.e., in Sec. II B 1).

Unless otherwise stated, the reader can assume that results shown were collected from the robotic sensor head operating in an acoustically cluttered laboratory.

D. Experimental descriptions

In the experiments reported in the following section, a reflecting target (see Sec. I B 7) was placed at a series of bearings covering the frontal sound field in 2-degree increments. For each target position, the sensor head emitted an echolocation pulse and the receivers were moved in opposing vertical arcs during echo reception.

The target range in all experiments was $r = 0.3$ m. It was necessary to fix the target range because IIDs vary with target range as well as bearing for a system with large interaural dimensions. By working with targets at a particular range, IIDs measured by our sensor head depend only upon target bearing (for a given receiver orientation) as they would for the small heads of bats.

The results shown in Sec. II A were obtained by stepping the receivers through extrema angles of ± 12 degrees in 6-degree increments. This angular excursion was used because the -20-dB measured beam width of the Polaroid transducer (i.e., the level at which the first null in the directivity pattern begins to appear) is approximately 24 degrees. Thus, for each target position, five IIDs were computed from the maximum intensity of the processed signals emerging from the right and left filter banks at each SONAR horizon. In this way, five IID maps were built up to describe the frontal sound field as heard from each SONAR horizon. The number of maps necessary was empirically determined as described in Sec. II A. Less symmetrical pinna would require fewer listening perspectives. It is possible that as few as two different SONAR horizons, e.g., measured at the beginning and end points of the pinna scan, could achieve the same effect as we demonstrate.

The results given in Sec. II B are based upon continuous vertical motion of the receivers which generates amplitude modulations in the returning echo envelopes. Elevation angle was derived from the modulation patterns (as described below) and azimuth was calculated independently from IIDs.

In Sec. II B 2, target elevation was derived from the time at which peaks occur in amplitude-modulated echo envelopes and azimuth was calculated from an interaural comparison of the peak intensity values. In Sec. II B 1, the continuous difference between right and left echo envelopes (i.e., rates of change of IIDs) are computed. Here, results are presented for a small simulated sensor head whose dimensions and frequency are based on those typical of *R. ferrumequinum*. In the simulation, pinnae were snapped into opposite extreme orientations (right pinna up, left pinna down) at the time of call emission, and then moved, with a sinusoidal velocity profile, through opposing vertical arcs of 30 degrees centered on the horizontal mid-line. This particular angular excursion was used because the beam width of the main sensitivity lobe of the simulated pinnae is approximately 30 degrees. This value corresponds well with peak-to-peak scan amplitudes (measured at the tip of the ear of *R. ferrumequinum*) which can exceed 1 cm—describing an arc of about 30 degrees (Pye and Roberts, 1970).

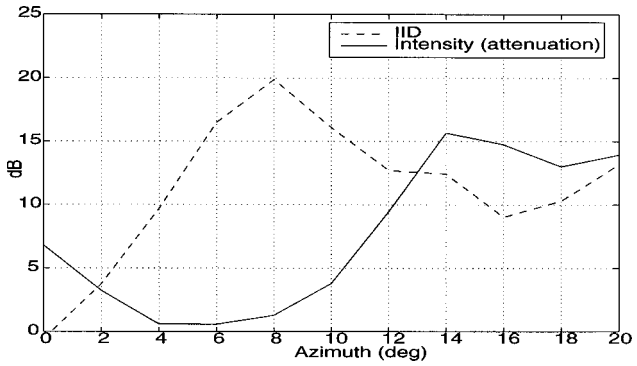

FIG. 3. **IIDs and overall intensity attenuation**. The IID values and intensity attenuation (with respect to peak intensity) measured across half of the frontal sound field. [Data taken from the SONAR horizon (0° elevation plane) of Fig. 4, *Column 1* (c).]

II. RESULTS

In the following sections, we examine the accuracy with which targets can be localized using either static (Sec. II A) or dynamic (Sec. II B) cues.

A. Static approach: IID "Maps"

By placing two receivers on the opposite sides of a head, a tone can be lateralized (approximately). To localize a tone more specifically, the SONAR horizon can be tilted and another measurement taken. This might be achieved by rotating the head. Alternatively, opposing pinnae motions might be employed to achieve similar effects. As shown in Fig. 4, *Column 1* (a)–(c), vertical arc scanning movements of the pinnae tilt the SONAR horizon.

Figure 3 shows IIDs measured along the SONAR horizon of the robotic sensor head. Across those angles where the IID curve rises, resolution is high (<0.5 degrees dB^{-1}). However, the IID curve is nonmonotonic; the same IID may represent both a medial and lateral azimuth position. Additional ambiguities arise along the vertical midline and in the periphery, where the 0-dB IID value effectively codes for all angular positions. Moreover, additional ambiguities arise due to resolution limitations and measurement noise.

These ambiguities arise within each SONAR horizon; however, they can be eliminated by combining results across alternative SONAR horizons. Figure 4, *Column 2* (a)–(e) shows how the mapping of IIDs onto representative spatial regions changes as the SONAR horizon is rotated (in 6-degree increments) via receiver movements. There, populations of cells—coding for IIDs varying from 20 dB (white) to -20 dB (black)—are laid out on iso-frequency grids depicting the angular positions in space which give rise to them. Receiver motion causes the region with the steepest IID slope (i.e., the SONAR horizon) to tilt—increasing measurement resolution in each spatial region through which it moves.

Columns 3 and 4 of Fig. 4 demonstrate how repositioning the pinnae during echo reception can break the symmetry inherent in the binaural receiving system and overcome limitations due to noise and measurement resolution. In the construction of this demonstration, a test target was placed at an

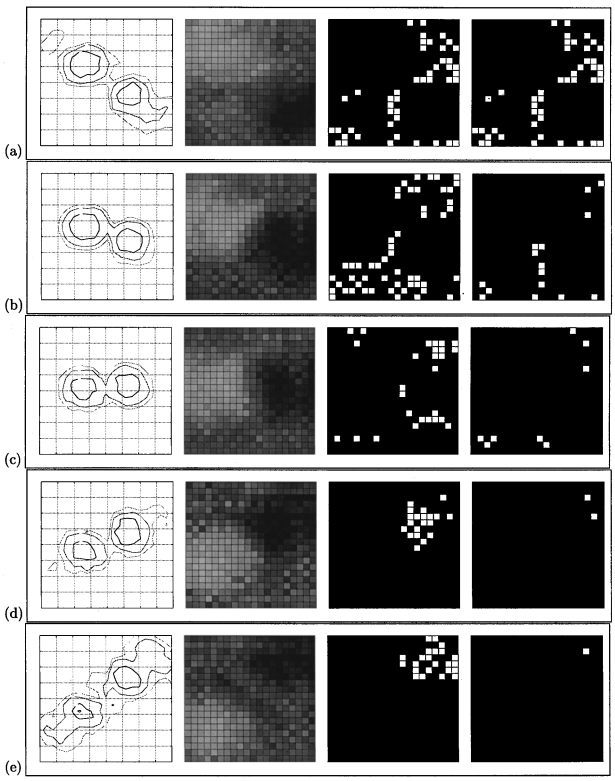

FIG. 4. **Binaural directionality plots, IID maps, and target resolution**. *Column 1 (left)*: Rotation of the SONAR horizon due to movement of the receivers (right, left): (a) (+12 degrees, −12 degrees), (b) (+6 degrees, −6degrees), (c) (0 degrees, 0 degrees), (d) (−6 degrees, +6 degrees), (e) (−12 degrees, +12 degrees). Intensity values measured from reflections off a target located at indicated angular positions in the ipsilateral frontal sound field of each receiver. Iso-intensity contours are −3 dB (inner), −7 dB (middle), and −10 dB (outer). Axes cover ±20 in both azimuth and elevation, in 5-degree increments. *Column 2*: Measured IID values. White denotes +20 dB, black −20 dB. Axes cover ±20 in both azimuth and elevation, each cell represents 2 degree. *Column 3*: Hypothesized target bearings shown as cells whose IID values match (matches within 95% of the best match shown) that of the test target [true bearing (14 degrees, 14 degrees)]. *Column 4*: Hypothesis resolution through cumulative tallying of votes in *Column 3*. (a)–(d) Hypotheses within 95% of most likely hypothesis. (e) Overall single best hypothesis.

arbitrarily chosen angular position in the frontal sound field, i.e., (14-azimuth, 14-degree elevation). The receivers were then rotated through each of the five orientations and, in each orientation, a new IID measurement was collected during reflection of a single pulse. A comparison was then made between each new IID value and those stored in the corresponding memorized IID map. Figure 4, *Column 3* (a)–(e) shows the results of that comparison as a locus of possible target bearings whose characteristic IID values best match that of the test target.

Notice that when the SONAR horizon runs nearly perpendicular to the target [as in Fig. 4, *Column 3* (a) and (b)], a small IID is generated which makes the target appear to be located between the receivers and/or in the acoustic ''blind'' spot directly above or below the emitter. In these receiver orientations, there is little measurement sensitivity in the area where the target lies and, due to noise, the locus of possible target positions is wide and messy. The cluster of possibilities tightens as the SONAR horizon is rotated toward the target. Around 0° [Fig. 4, *Column 3* (c)], a ring of possibilities is generated in which the azimuth position of the target is perceived to be in the right portion of the sound field. When the horizon starts to align itself with the target [Fig. 4, *Column 4* (d) and (e)], target localization is good and a small cluster of possible target bearings is generated.

Column 4 of Fig. 4(a)–(e) shows how ambiguities may be reduced across a series of measurements by combining hypotheses generated at each orientation. Each succeeding map [from (a)–(e)] takes the hypotheses of the previous map and combines its own by simply adding the maps (i.e., tallying the votes). Shown are the bearings receiving votes within 95% of the best hypothesis—except the last map (e), which shows the single hypothesis receiving the most votes. Notice how, in the first three movements, the symmetries are broken. The final orientations serve to remove uncertainty due to noise and resolution limitations.

Across the whole frontal sound field (±20-degree azimuth, ±20-degree elevation), the average azimuth error is 6 degrees, while the average elevation error is 4 degrees. The difference in accuracy arises because the directionality is naturally sharper in the vertical direction (see Fig. 4, *Column 1*) due to the transducer mountings.

In this approach, localization accuracy varies with target position. The angular positions through which the SONAR horizon sweeps yield the best localization results because sensitivity is highest there. For targets lying along the SONAR horizon, the average azimuth error is 2 degrees and the average elevation error is less than 1 degree. By contrast, accuracy is low along the vertical mid-line (average error is 6 degrees in both azimuth and elevation) because the system confuses low IID values generated along the mid-line between the receivers with those arising due to low absolute signal values in the periphery (blind spots).

The use of additional measurement orientations would improve results by increasing the likelihood of the SONAR horizon landing on the target. In simulation, the number of maps was manipulated and a probabilistic measurement integration scheme was implemented so that the remaining ambiguity could be monitored during each stage of the map integration process. In this scheme, the probability that a particular cell (of a particular map) gave rise to a given measurement was computed across all possible target bearings and a Bayesian strategy was used to combine maps. The entropy of the probability distribution defined over the possible target positions was used as a measure of the remaining ambiguity. Using five maps, the entropy decreased steadily across the comparison—suggesting that more maps could yield better accuracy. Doubling the number of maps (i.e., moving through receiver orientations in 3-degrees increments) drove the average error to below 1 degree in both azimuth and elevation and nearly halved the average entropy.

Very few maps may be needed for an echolocator with less symmetric pinnae; however, this approach does require a motor control/proprioception system able to reposition the pinnae with some accuracy. In the next subsection, we explore dynamic approaches that rely upon the inherent motion and signal dynamics.

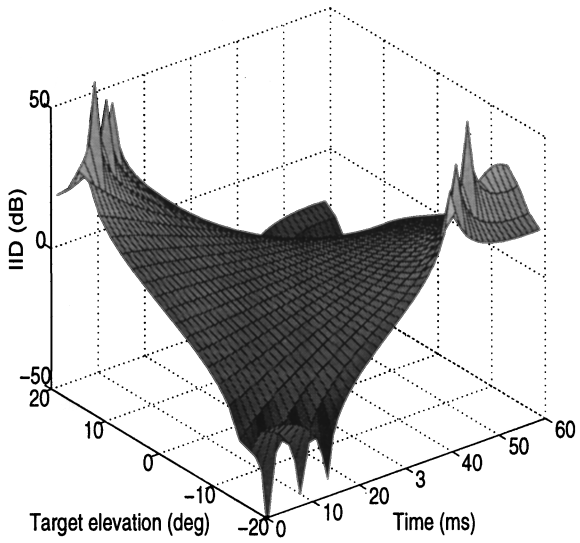

FIG. 5. **IID as a function of time and target elevation (simulated)**. Simulated time history of IID values (''IID slopes'') for simulated pinnae moving through 30 degrees elevation arcs. (Pinnae are modelled as piston receivers of radius $a=4.5$ mm, based on a typical *R. ferrumequinum* pinna width.) During each trial, the simulated target was positioned within the 0 degrees azimuth plane at the indicated elevation. (The movement of the ears produced no Doppler effect.)

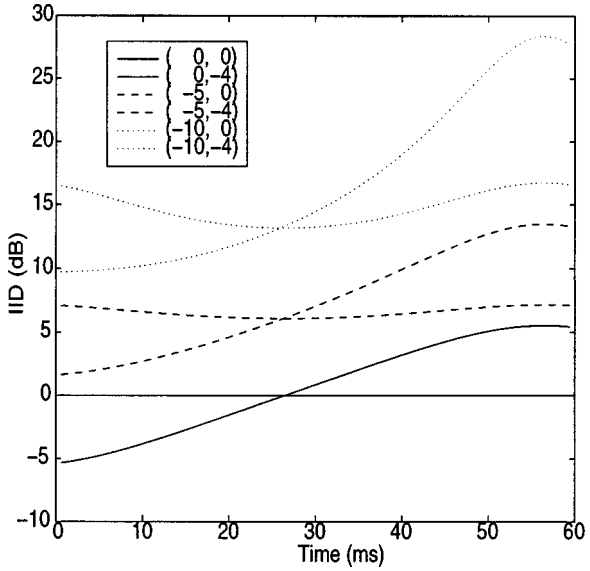

FIG. 6. **IID as a function of time and target position (simulated)**. The IID slopes and offsets for simulated pinnae moving through 30 degrees elevation arcs. The azimuth orientation of the acoustic axes (-15 degrees (right), $+15$ degrees (left)) is held constant throughout the scan. Target (azimuth, elevation) pairs are indicated.

B. Dynamic approach: Temporal cues

1. IID rates of change

Figure 5 illustrates the *change in IID* simulated by scanning a pair of ears (the size of *R. ferrumequinum*) continuously during echo reception. When a target is positioned at a negative elevation, the right pinna hears a weak reflection at the beginning of the reception interval and sound intensity increases smoothly as it is scanned downwards (i.e., toward the target). Because the opposite trend is present in the left ear, the IID (right minus left) increases over time. The IID profile is steepest when the target is located in an extreme elevation position (± 15 degrees) and, as the target is brought to the horizontal mid-line (around which the pinnae scan), response peaks in each ear overlap increasingly, thereby flattening the slope. At 0-degree elevation, IIDs are constant across the duration of the measurement.

Monotonicity of the IID profile is broken if the target moves outside the central elevation region as shown for target positions $>|15|$-degree elevation. Here the roughening of the IID profile occurs as the first zero in a receiver's directivity pattern sweeps past the target. Similar effects would be encountered if the target moved to the azimuthal periphery, or if the ears are driven to widely diverging orientations such that the main lobes of their sensitivity beams no longer overlap.

In the approach outlined here, azimuth information might be derived from IID values themselves. As shown in Fig. 6, the family of slopes representing different target elevations is centered on 0 dB for targets at 0-degree azimuth; however, as the target moves to other azimuth positions, this IID offset changes. By rotating the pinnae outwards (and holding them there throughout the sweep), an echolocator can increase the interaural intensity differences encoding target azimuth. In the simulation, the acoustic axes[3] of the right and left transducers were rotated outward from the middle of the sound field by $|15|$-degree azimuth into their respective ipsilateral sound fields. This yields an approximately 0.7-degree dB^{-1} offset. By contrast, in preliminary studies with the acoustic axes pointing directly forward, the simulator predicted that pinnae the size of *R. ferrumequinum* would only afford a 2.5-degree dB^{-1} resolution.

From Fig. 6 we can see that the straightforward use of a single slope value to represent elevation independently of azimuth is possible in the middle of the frontal sound field; however, this assumption breaks down as the target moves laterally such that response in one receiver predominantly determines the IID values along the slope. At 5-degree azimuth, IID slopes (based on a first-order approximation) only deviate from those at 0 degrees by 9%; however, when a target moves out to an azimuth angle of 10 degrees deviations increase to 30%.

It is possible to construct a calibration factor to correct for this systematic variation, but a simpler strategy (for an echolocation system with a mobile head) might be to limit sensing to a narrow region of the frontal sound field were the approximation is reasonable. Such a region could be determined from the overall signal intensities, which, due to the effects of the directional emission, are stable across the middle of the frontal sound field. As shown for the robotic sensor head in Fig. 3, by sensing only within the angular cone where overall signal levels are high (e.g., 8 degrees for the robotic sensor head), the potential medial-lateral ambiguity in single-tone lateralization may be eliminated as well. Another way to minimize the dependence of elevation cues on target's azimuth is to employ temporal cues to encode elevation as described in the next section.

2. Peak delays

The IID slopes arise because echo amplitudes peak at different times in right and left receivers moving through

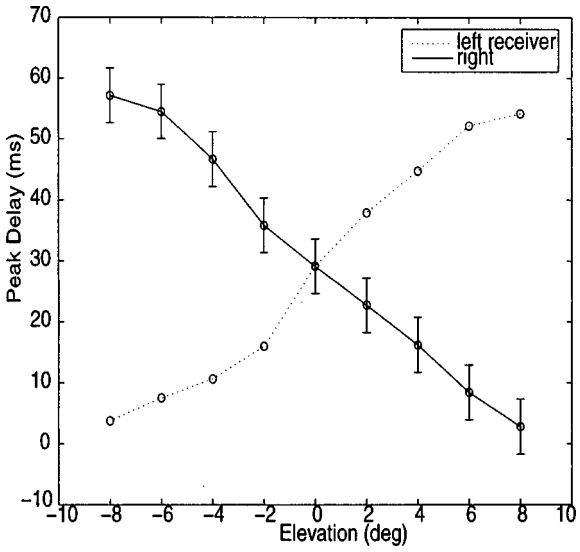

FIG. 7. **Average peak delay**. Measured peak delay in each receiver as a function of target elevation (i.e., values averaged across all target azimuth positions). Error bars (only shown for the right receiver) indicate the average variance in each elevation measurement.

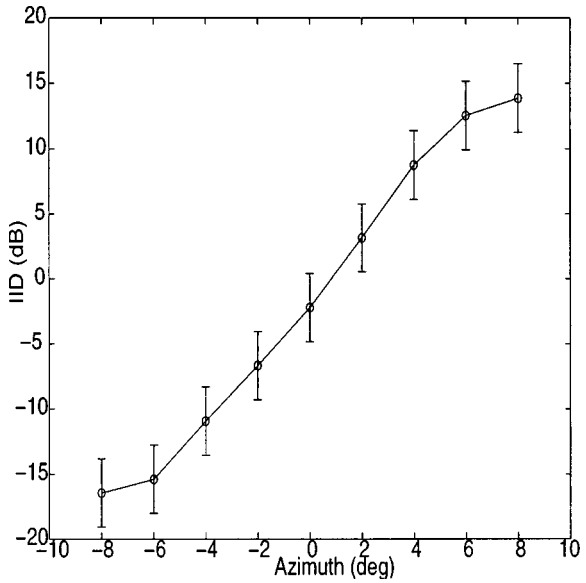

FIG. 8. **Average IID**. Measured IID as a function of target azimuth (i.e., values averaged across all target elevation positions). Error bars indicate the average variance in each azimuth measurement.

opposing vertical arcs. This fact suggests that an echolocator with mobile pinnae might represent target elevation via interaural (peak) timing differences (ITD_{peaks}). Alternatively, this information can be derived from monaural timing cues, i.e., the delay between echo arrival time and echo peak time in each ear. Although the peak echo intensity *value* reflected from a target at any particular elevation will vary with target azimuth, the *peak delay* time depends predominantly on the speed of the pinnae and the vertical angle between target and pinnae start orientation. The *difference* in monaural peak delay values encoding adjacent target elevation angles is determined by the motion of an acoustic axis and, therefore, can be understood simply as a delay-per-degree transformation (if the velocity of the receivers is sufficiently linear).

Figure 7 shows this transformation as the delay profile for right and left receivers averaged across different target azimuth angles. A straight line approximation to the curves yields a 1 degree per 3-ms transformation, i.e., a 3-ms resolution encoding adjacent elevation angles. This figure is based on receivers scanning over 16 degrees in 60 ms and may suggest temporal resolution greater than that available to a bat. (Rhinolophids and hipposiderids may scan their pinnae over twice this angular extent in less than half of this time.) However, scan rates and, therefore, elevation resolution can be manipulated explicitly.

Along the contours of Fig. 7, the average separation between measured peak delay values encoding adjacent target elevations is 6.0 ms (per 2 degrees). As the average variation of each measurement is nearly half of this (i.e., 3.3 ms, as shown via the error bars), it is possible to determine a target's elevation position with an accuracy of within ± 2-degree elevation.

Figure 8 shows the variation in IID values with target azimuth (across all elevations). As IIDs change continuously throughout the scan, we adopted the simple approach of comparing the peak intensity values in each receiver. Values encoding each azimuth are averaged across all elevations, and the error bars indicate the average variation in each measurement due to noise and differences in target elevation. As shown, this use of IIDs to determine target azimuth position independently of elevation has an accuracy of approximately ± 2-degree azimuth across the center of the frontal sound field where IIDs vary monotonically. Naturally, angular resolution is highest in the front of the sound field where IIDs change most rapidly.

Using this decoupled strategy of measuring azimuth via IIDs and elevation via monaural peak delays (with interaural confidence checks were possible) can provide unambiguous, high-resolution 3D angular cues across a limited region of the frontal sound field. Outside of this region, targets can still be detected, and behavioral mechanisms may be used to bring the target into the optimized environment of the front-center sound field for analysis.

III. DISCUSSION

A. Static cues

Auditory cues give rise to strong spatial percepts and, yet, the surface of the auditory sensor, unlike, for example, the visual sensor, is not laid out topographically with respect to space. Because of this, it is intriguing to ask whether (and, if so, where) in the auditory system a spatial map may be assembled.

Patterns of response across iso-frequency populations of neurons with particular aural preferences and different IID sensitivities may provide a substrate on which spatial maps are formed. For example, of particular interest is a ventromedial population of binaural cells in the 60-kHz contour of the central nucleus of the inferior colliculus (ICc) (observed in *P. parnellii*) in which IIDs are generated via a subtractive process wherein supra-threshold sounds originating in the excitatory (contralateral) ear evoke a certain discharge rate which is inhibited by sound presented to the ipsilateral ear when the resulting IID exceeds a certain threshold level

(Wenstrup *et al.*, 1986, 1988). Moreover, the representation of different thresholds by these ''excitatory–inhibitory'' (EI) neurons is topographically organized within this region such that neurons with high positive inhibitory thresholds (requiring a louder ipsilateral than contralateral stimulus to produce inhibition) are located in the dorsal EI region and progressively shift to lower inhibitory thresholds among ventral EI neurons [see review in Pollak and Park (1996)].

The IIDs created by the acoustic properties of the ears (and head) combined with the topographic representation of the inhibitory thresholds within EI neurons suggests that the position of a target in space may be represented (at least partially) as the position of a border separating a region of discharging cells from a region of inhibited cells [see review in Pollak and Park (1996)]. Such an organization might host the representation of space across the frontal sound field; however, as demonstrated in the example of Fig. 4, an isofrequency IID value may code for several distinct regions of space.

In broadband-emitting bats, ambiguities may be eliminated by combining hypothesized target bearings across different frequencies (Grinnell and Grinnell, 1965; Lawrence and Simmons, 1982; Fuzessery *et al.*, 1992; Obrist *et al.*, 1993). In other words, a single pair of ears contains several acoustic magnifying glasses whose width (or focal power) and axis of orientation vary with frequency. If each magnifying glass points at the frontal sound field, but focuses on different spatial regions, ambiguities might be eliminated in the response accumulated across a series of IID maps. [Exploitation of alternative measurement perspectives is an auditory mechanism which may be employed by both active and passive listeners. Extensive studies with the barn owl have shown that neurons in the optic techtum integrate interaural phase and intensity cues (which may individually be ambiguous) such that their receptive fields are restricted to a single region of space for broadband stimuli (Brainard *et al.*, 1992).]

In these terms, the pinnae of rhinolophids and hipposiderids contain a single, fixed-width acoustic magnifying glass which has very fine spatial resolution [0.6 degrees dB^{-1} at the dominant echolocation frequency in several species (Obrist *et al.*, 1993)]. By actively moving the magnifying glass, these bats may collect measurements in series rather than in parallel, but otherwise may integrate IIDs sampled from different regions of space in much that same way as broadband-emitting bats are believed to do. Thus, when viewed as a mechanism for the maintenance of maximal spatial sensitivity to a small area of the frontal auditory space, ear movements may provide these bats with versatility in maximizing the spatial sensitivity of individual neurons during echolocation.

In support of this hypothesis, it is interesting to note that when deprived of the use of the muscles which move the pinnae relative to the head, *R. ferrumequinum* become disoriented and lose localization acuity until they learn to compensate by moving the head vigorously (Schneider and Möhres, 1960; Mogdans *et al.*, 1988)—a trick which may tilt the SONAR horizon in much the same way as pinna movement. *Pteronotus parnellii*, another predominantly CF echolocator, has relatively immobile pinnae, but has been observed to move its head in much this same way when emitting CF pulses (Pye and Roberts, 1970; Schnitzler, 1970). Rapid movement of the ears is used by other Phyllostomidae/Mormoopidae, but the movements appear to be elicited by external sounds, unrelated to the emission of their short broadband pulses (Pye and Roberts, 1970).

B. Dynamic cues

In rhinolophids, neurons sensitive to target motion have been observed (Schlegel, 1980; Neuweiler, 1980). Although most superior olivary, lemniscal, and collicular neurons faithfully encode the angular position of a target irrespective of target velocity, some neurons encode target motion by increasing discharge rates proportional to speed and/or direction of motion. (In this study, a ''target'' was a sound source simulated by periodically amplitude modulating pure tone intensities diametrically in ipsi- and contralateral earphones so as to appear to move horizontally around the head of the bat at speeds from $4-1000$ degrees s^{-1}.) Some of these neurons only respond when the target sweeps through a narrow angular sector with a marked best angle. In other neurons, the representation of azimuth angle is lost because units extract only dynamic features.

If neurons exist to represent moving targets measured by stationary pinnae, then the apparent motion of a stationary target, as measured by moving pinnae, may provide a strong directional cue which an animal can learn to associate with target angle.

C. Target ''recognition''

In any realistic localization experiment, some means of isolating the target echo (from other overlapping sound) must be introduced. In these experiments, ''target recognition'' came for free, so to speak, because the system was tuned to respond only to targets which fluttered at the particular oscillation rate of the fan target. Other reflectors did not generate energy in the necessary frequency channels for them to be localized. [Additional narrow bandpass filters may be used to distinguish between several oscillating targets on the basis of their side-band profiles (Walker *et al.*, 1998).] The cochleae of rhinolophids contain a region of heightened sensitivity just above the dominant echolocation call frequency which appears to facilitate detection of modulated echoes reflected from fluttering targets (Neuweiler, 1970).

This mechanism also provides the binaural echolocator with a natural means for overcoming the correspondence problem—which may be particularly acute in a system with mobile transducers scanning through different regions of space.

IV. CONCLUSION

Much work in echolocation has addressed the role of spectral cues in 3D target localization. In contrast, we present models which demonstrate how a binaural echolocation system can localize targets using a single CF signal. We explore two ways in which pinna movements may be used to

compensate for a lack of bandwidth and allow hipposiderids and rhinolophids to confine echo analysis to the narrow window of the acoustic fovea, where the abundance of neural processing in the frequency range of the echolocation signal facilitates fine target analysis (Schuller and Pollak, 1979).

We investigated the hypothesis that all bats employ a common strategy of sampling discrete regions of space within the beam of a single echolocation pulse. Due to the fact that the acoustic axes of the ears point in different directions at different frequencies, broadband-emitting bats may sample different regions of space by altering the operating frequency of their auditory systems. In contrast, rhinolophids and hipposiderids hold that parameter largely constant but may achieve the same overall effect by actively altering the position of their receivers. We showed that, for a binaural echolocation system with similar IID resolution to that of many rhinolophid and hipposiderid species, combining IID values from several viewing perspectives can be used to disambiguate target position—without recourse to additional coding mechanisms.

We also investigated the creation and use of dynamic cues. Across a limited region of the frontal sound field, accurate (± 2 degrees) elevation measurements can be made by sweeping the ears through opposing elevation arcs and measuring the time of the peak in the amplitude-modulated echoes returning from stationary targets. Thus, just as pinna size and shape create dramatic binaural intensity differences, pinna mobility can allow some echolocators to derive dramatic temporal cues for localization, i.e., cues dependent upon pinna speed (millisecond cues) rather than interaural distance (microsecond cues).

Because rhinolophids and hipposiderid bats perform fine frequency analysis, it is likely that Doppler cues created by the ears also play a role in localization. Movements of the ear relative to the target will frequency modulate the reflected echo which, in turn, may aid in separation and provide directional cues through the cosine law (Pye *et al.*, 1962). Another (complementary) explanation for the exaggerated size of the ear and the use of a high-frequency harmonic for sensing is that these features increase the Doppler effects within scanning pinnae. We hope to explore Doppler effects in future work.

ACKNOWLEDGMENTS

Ashley Walker is funded by a British Council Overseas Research Studentship. Herbert Peremans is supported by a ''Marie Curie'' Fellowship from the European Community. The authors thank the University of Edinburgh for computing and other facilities. In particular, we are grateful to Andrew Haston for construction and maintenance of this experimental hardware, and to Martin Westhead and three anonymous reviewers for providing stimulating feedback on the manuscript.

[1]The term *lateralize* is used to describe the localization of a sound source/reflector within the plane containing the receivers.

[2]Here, the term *SONAR horizon* is used to mean the region in space across which IIDs (at a given frequency) vary most sharply. For example, in Fig. 4 *Column 1* (a)–(e) the SONAR horizon could be drawn as a straight line through the sensitivity peaks of each receiver.

[3]The term *acoustic axis* is used to denote the region of space for which a receiver is maximally sensitive.

Biber, C., Ellin, S., Shenk, E., and Stempec, J. (**1980**). ''The polaroid ultrasonic ranging system,'' in *The 67th Convention of the Audio Engineering Society*.

Brainard, M., Knudsen, E., and Esterly, S. (**1992**). ''Neural derivation of sound source location: Resolution of spatial ambiguities in binaural cues,'' J. Acoust. Soc. Am. **91**, 1015–1027.

Fletcher, N., and Thwaites, S. (**1979**). ''Physical models for the analysis of acoustical systems in biology,'' Q. Rev. Biophys. **12**, 25–65.

Fuzessery, Z., Hartley, D., and Wenstrup, J. (**1992**). ''Spatial processing within the mustache bat echolocating system: possible mechanisms for optimization,'' J. Comp. Physiol. A **170**, 57–71.

Gorlinsky, I., and Konstantinov, A. (**1978**). ''Auditory localization of ultrasonic source by *Rhinolophus ferrumequinum*,'' in *Proc. of the Fourth Int. Bat Research Conf.*, edited by R. Olembo, J. Castelino, and F. Mutere, pp. 145–153.

Griffin, D., Dunning, D., Cahlander, D., and Webster, F. (**1962**). ''Correlated orientation sounds and ear movements of horseshoe bats,'' Nature (London) **196**, 1185–1186.

Grinnell, A., and Grinnell, V. (**1965**). ''Neural correlates of vertical localization in echolocating bat,'' J. Physiol. (London) **181**, 830–851.

Guppy, A., and Coles, R. (**1988**). ''Acoustical aspects of hearing and echolocation in bats,'' in *Animal SONAR Processes and Performance (NATO ASI Series)*, edited by P. Nachtigall and P. Moore (Plenum, New York), pp. 289–294.

Kuc, R. (**1994**). ''Sensorimotor model of bat echolocation and prey capture,'' J. Acoust. Soc. Am. **96**, 1965–1978.

Lawrence, B., and Simmons, J. (**1982**). ''Echolocation in bats: The external ear and perception of the vertical position of targets,'' Science **218**, 481–483.

Mogdans, J., Ostwald, J., and Schnitzler, H. (**1988**). ''The role of pinna movement for the localization of vertical and horizontal wire obstacles in the greater horseshoe bat, *Rhinolophus ferrumequinum*,'' J. Acoust. Soc. Am. **84**, 1676–1679.

Möhres, F. (**1953**). ''Uber die Ultraschallorientierung der Hufeisennasen,'' Z. fuer Vergleichende Physiologie **34**, 547–588.

Neuweiler, G. (**1970**). ''Neurophysiologische Untersuchungen zum Echoortungsystem der Grossen Hufeisennase *Rhinolophus ferrumequinum*,'' Z. fuer Vergleichende Physiologie **67**, 273–306.

Neuweiler, G. (**1980**). ''Auditory processing of echoes: Peripheral processing,'' in *Animal SONAR Systems (NATO ASI Series)*, edited by R. Busnel and J. Fish (Plenum, New York), pp. 519–548.

Nitsche, V. (**1987**). ''Das Unterscheidungsvermögen für Schlagfrequenzen mechanisch stimulierter Flügel in störungsfreier und akustisch gestörter Umgebung bei der FM-CF-FM Fledermaus Rhinolophus ferrumequinum,'' Ph.D. thesis, Fakultät Biologie, München.

Obrist, M., Fenton, M., Eger, J., and Schlegel, P. (**1993**). ''What ears do for bats: A comparative study of pinna sound pressure transformation in chiroptera,'' J. Exp. Biol. **180**, 119–152.

Ostwald, J., Schnitzler, H., and Schuller, G. (**1988**). ''Target discrimination and target classification in echolocating bats,'' in *Animal SONAR Processes and Performance (NATO ASI Series)*, edited by P. Nachtigall and P. Moore (Plenum, New York), pp. 413–434.

Peremans, H., Walker, V., and Hallam, J. (**1997**). ''A biologically inspired sonarhead,'' D. A. I. Technical Report No. 44, University of Edinburgh.

Pollak, G. (**1988**). ''Time is traded for intensity in the bat's auditory system,'' Hearing Res. **36**, 107–124.

Pollak, G., and Park, T. (**1996**). ''The inferior colliculus,'' in *Hearing By Bats*, edited by R. Fay and A. Popper (Springer-Verlag, New York), pp. 296–367.

Pye, J. (**1967**). ''Theories of sonar systems and their application to biological organisms (discussion),'' in *Animal SONAR Systems*, Lab. Physiol. Acoust. CNRS Jouy-en-Josas, pp. 1121–1136.

Pye, J., Flinn, M., and Pye, A. (**1962**). ''Correlated orientation sounds and ear movements of horseshoe bats,'' Nature (London) **196**, 1186–1188.

Pye, J., and Roberts, L. (**1970**). ''Ear movements in a hipposiderid bat,'' Nature (London) **225**, 285–286.

Schlegel, P. (**1980**). ''Single brain stem unit responses to binaural stimuli simulating moving sounds in *Rhinolophus ferrumequinum*,'' in *Animal SONAR Systems (NATO ASI Series)*, edited by R. Busnel and J. Fish (Plenum, New York), pp. 973–975.

Schneider, H., and Möhres, F. (**1960**). ''Die Ohrbewegungen der Hufeisenfledermäuse (Chiroptera, Rhinolophidae) und der Mechanismus des Bildhörens,'' Z. Vergl. Physiol. **44**, 1–40.
Schnitzler, H. (**1970**). ''Echoortung bei der Fledermaus *chilonycteris rubiginosa*,'' Z. Vergl. Physiol. **68**, 25–39.
Schnitzler, H. (**1973**). ''Die Echoortung der Fledermäuse und ihre hörphysiologischen Grundlagen,'' Fortschr. Zool. **21**, 136–189.
Schuller, G., and Pollak, G. (**1979**). ''Disproportionate frequency representation in the inferior colliculus of horseshoe bats: evidence for an 'acoustic fovea','' J. Comp. Physiol. A **132**, 47–54.
Sun, X., and Jen, P. (**1987**). ''Pinna position affects the auditory space representation in the inferior colliculus of the FM bat, *Eptesicus fuscus*,'' Hearing Res. **27**, 207–219.
von der Emde, G., and Schnitzler, H. (**1986**). ''Fluttering target detection in hipposiderid bats,'' J. Comp. Physiol. A **14**, 43–55.
Walker, V. (**1997**). ''An investigation of qualitative echolocation strategies in synthetic bats and real robots,'' Ph.D. thesis, University of Edinburgh.
Walker, V., Peremans, H., and Hallam, J. (**1998**). ''Good vibrations: Exploiting reflector motion to partition an acoustic environment,'' J. Robotics and Autonomous Systems: Special issue on Quantitative Assessment of Mobile Robot Behaviour (in press).
Wenstrup, J., Fuzessery, Z., and Pollak, G. (**1988**). ''Binaural neurons in the mustache bat's inferior colliculus. II. Determinants of spatial responses among 60-kHz EI neurons,'' J. Neurophysiol. **60**, 1384–1404.
Wenstrup, J., Ross, L., and Pollak, G. (**1986**). ''Binaural response organization within a frequency-band representation of the inferior colliculus: implications for sound localization,'' J. Neurosci. **6**, 962–973.

LETTERS TO THE EDITOR

This Letters section is for publishing (a) brief acoustical research or applied acoustical reports, (b) comments on articles or letters previously published in this Journal, and (c) a reply by the article author to criticism by the Letter author in (b). Extensive reports should be submitted as articles, not in a letter series. Letters are peer-reviewed on the same basis as articles, but usually require less review time before acceptance. Letters cannot exceed four printed pages (approximately 3000–4000 words) including figures, tables, references, and a required abstract of about 100 words.

Some considerations concerning replicated spectra

Jamal Assaad and Jean Michel Rouvaen
Institut d'Electronique et de Microélectronique du Nord (IEMN), UMR CNRS 9929, OAE Department, Université de Valenciennes et du Hainaut Cambrésis, le Mont Houy, BP 311, 59304–Valenciennes Cedex, France

(Received 30 July 1996; revised 20 January 1998; accepted 10 February 1998)

The aim of this paper is to clarify the effect replicated sources in two-dimensional radiation problems. In fact, it will be shown that the discrete pressure computed by using the angular spectrum approach is equal to the analytical pressure plus error terms arising from the convolutions of replicated spectra of the original spectrum and the Green's function. A similar result is obtained for the far-field discrete pressure. For the later case, it will be shown that errors can be eliminated by choosing a sampling step smaller to that given by the Nyquist criterion. © *1998 Acoustical Society of America.* [S0001-4966(98)00206-9]

PACS numbers: 43.20.Rz, 43.20.Ye [JEG]

INTRODUCTION

The computed pressure field via angular spectrum decomposition can be found in many papers.[1–5] Moreover, Refs. 1–5 give the description of the angular spectrum approach (ASA). Moreover, they give an extensive review of the literature associated with the concept of ASA. Thus this description will not be recalled here.

I. PRESSURE FIELDS

Figure 1 describes an acoustic harmonic source (or transducer) of width $2A$ mounted in a rigid wall. The length of the transducer (along y axis) is assumed to be infinite. Then the two-dimensional radiation problem will be considered. The harmonic state $\exp(j\omega t)$ will be assumed and retained as reference. The pressure $p(x,z)$ is given by

$$p_n^a(x,z)=\frac{k\rho c}{2}\int_{-\infty}^{+\infty}\nu(x')H_0^{(1)}(kr)dx', \tag{1}$$

where k is the wave number, $\nu(x')$ is the normal velocity in the source plane $z=0$, and $H_0^{(1)}(kr)$ is the zeroth-order Hankel function, x and z are the coordinates of the field point M, and r gives the position of the field point with respect to running point P, i.e., $r=PM=\sqrt{(x-x')^2+z^2}$ ($x'=OP$, see Fig. 1). k is the wave number equal to $2\pi/\lambda$ (λ being the in water wavelength). The upper index a refers to the analytical expression while the lower index n indicates that the corresponding pressure is valuable in the near-field and far-field zones.

The pressure as given by Eq. (1) can be written as [see Eq. (50) in Ref. 6]:

$$p_n^a(x,z)=\frac{k\rho c}{2}\sqrt{\frac{2}{\pi}}\,e^{j\pi/4}\times\int_{-\infty}^{+\infty}\nu(x')\,\frac{\exp(-jk\sqrt{(x-x')^2+z^2})}{\sqrt{k((x-x')^2+z^2)}}\,dx'. \tag{2}$$

Equation (2) can be rewritten as

$$p_n^a(x,z)=\frac{k\rho c}{2}\,\nu(x)*g(x,z), \tag{3}$$

with

$$g(x,z)=\sqrt{\frac{2}{\pi}}\,e^{j\pi/4}\,\frac{\exp[-jk(x^2+z^2)^{0.5}]}{\sqrt{k(x^2+z^2)}}, \tag{4}$$

where $g(x,z)$ is the Green's function.

To use the ASA, the source (Fig. 1) must be sampled. As for signals there are a lot of methods to sample the normal velocity distribution $\nu(x)$ in the source plane $z=0$ (Fig. 1). The classical sampling of $\nu(x)$ is used and can be mathematically described by

$$\nu^c(x)=\Delta d\sum_{i_x=-\infty}^{\infty}\nu(i_x\Delta d)\,\delta(x-i_x\Delta d), \tag{5}$$

where $\delta(x)$ is the Dirac function and Δd is the sampling interval in x. In the above equation, the upper index c refers to the classical sampling. Due to sampling the acoustic pressure is modified to p_n^c:

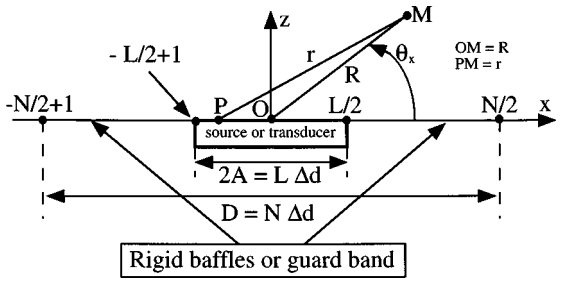

FIG. 1. Geometry and notation used for the calculation of the acoustic field.

$$p_n^c(x,z)=\frac{k\rho c}{2}\,\nu^c(x)*g(x,z). \tag{6}$$

It should be noted that as Δd goes to zero, p_n^c converges to p_n^a. In order to get an expression of p_n^c in terms of p_n^a the FT and its inverse will be applied to Eq. (6), i.e.,

$$p_n^a(x,z)=\frac{k\rho c}{2}\,\mathrm{FT}^{-1}(\mathrm{FT}\nu^c(x)*g(x,z)), \tag{7}$$

which can be rewritten as

$$p_n^a(x,z)=\frac{k\rho c}{2}\,\mathrm{FT}^{-1}(V^c(k_x)*G(k_x,z)), \tag{8}$$

where $V^c(k_x)$ and $G(k_x,z)$ are the FT of $\nu^c(x)$ and $g(x,z)$, respectively. The FT of $\nu^c(x)$ is defined by

$$V^c(f_x)=\int_{-\infty}^{+\infty}\nu^c(x')e^{-j2\pi f_x x'}\,dx', \tag{9}$$

where $k_x=2\pi f_x$. Using Eq. (5), this FT can be computed as

$$V^c(f_x)=V(f_x)*\sum_{i_x=-\infty}^{+\infty}\delta\left(f_x-\frac{i_x}{\Delta d}\right)$$

$$=\sum_{i_x=-\infty}^{+\infty}V\left(f_x-\frac{i_x}{\Delta d}\right). \tag{10}$$

Then the discrete pressure can be expressed in terms of the analytical pressure via the relation:

$$p_n^c(x,z)=\frac{k\rho c}{2}\,TF^{-1}\left\{\sum_{i_x=-\infty}^{i_x=+\infty}V\left(f_x-\frac{i_x}{\Delta d}\right)G(f_x,z)\right\}. \tag{11}$$

The last equation can be also rewritten as

$$p_n^c(x,z)=\frac{k\rho c}{2}\left\{\sum_{i_x=-\infty}^{i_x=+\infty}\left(\nu(x)\times\exp\left[-2j\pi\,\frac{i_x}{\Delta d}\,x\right]\right)^*g(x,z)\right\}. \tag{12}$$

The FT of Green's function is given by

$$G(f_x,z)=2\,\frac{\exp(jzk_z)}{k_z}, \tag{13}$$

with

$$k_z=\sqrt{1-n_x^2}\quad\text{if}\quad k^2\geqslant k_x^2$$

$$=jk\sqrt{n_x^2-1}\quad\text{if}\quad k^2<k_x^2, \tag{14}$$

where n_x is the cosine direction, i.e., $n_x=\cos\theta_x$ ($k_x=kn_x$). R and θ_x are polar coordinates (see Fig. 1). As for three-dimensional case,[4] since G is not bandlimited, we cannot obtain the exact sound field by spatial sampling. In addition, as has been shown in Ref. 5, when the observation point M is in the far-field zone the FT of the Green's function becomes undersampled. Then the computed far-field pressures will contains ripples. Moreover, Eq. (11) indicates that the discrete pressure is equal to the analytical one corrupted by terms which are given by the convolutions of replicated spectra of the original spectrum $V(f_x)$ and Green's function, i.e.,

$$p_n^c(x,z)=p^a(x,z)+\frac{k\rho c}{2}\,\mathrm{TF}^{-1}\times\left\{\sum_{i_x\neq 0}V\left(f_x-\frac{i_x}{\Delta d}\right)G(f_x,z)\right\}. \tag{15}$$

In addition, when Δd goes to zero, the replicated sources will be rejected at the infinity and then will not contribute. Thus when Δd goes to zero, the discrete pressure converges to the analytical pressure. In three-dimensional case Hah *et al.*[4] has derived ''exactly'' the same equation. Moreover, the right hand of Eq. (15) can be computed in the case of piston mode.[4] The above equation contradicts Eq. (1) in Ref. 3 and its related conclusion. In fact, the used relation in Ref. 6 is given by

$$p_n^c(x,z)=\sum_{r=-\infty}^{+\infty}p_n^a(x+rD). \tag{16}$$

Then the authors of Ref. 3 conclude that: this relation can be interpreted in terms of spatial aliasing (time aliasing). The similar formula was derived by Wiliams (Ref. 1 in this paper). The summation in this equation shows that instead of a single source there exist a set of planar sources, each located at a node along an infinite line with internodal distance D. The actual source centers at the origin. The others vibrate in phase and with the same normal velocity distribution as the actual source and they are called replicated sources.

First, in Ref. 3, there is no demonstration concerning the above equation. Second, Williams *et al.*[1] have found the same relation by assuming Δd goes to zero. The authors of Ref. 3 have used this equation for finite Δd values.

II. FAR-FIELD PRESSURE

To get an equivalent relation between the discrete and analytical far-field pressures, it is not so simple to use the limit when $R\to\infty$ of Eq. (12). In fact, to obtain Eq. (11) many integrations have been used and then some mathematical manipulations must be justified. But we can use directly the asymptotic expression of Eq. (1) [see Eq. (61) in Ref. 6 or Eq. (7) in Ref. 5]. This expression is given by

$$p_f^a(R,\theta_x)=p_0\int_{-\infty}^{+\infty}\nu(x')e^{-jkx'\cos\theta_x}\,dx'=p_0V(k_x), \tag{17}$$

with

$$p_0=\frac{k\rho c}{2}\,\tilde{H}(kR)$$

$$\text{and}\quad \tilde{H}(kR)=\sqrt{\frac{2}{\pi kR}}\exp[-j(kR-\pi/4)]. \quad (18)$$

The lower index f indicates that the corresponding pressure is only valuable in the far-field zone. To obtain Eq. (17), the following relation:

$$\frac{e^{-jkr}}{\sqrt{kr}}\rightarrow\frac{\exp[-jkR(1-x'\cos\theta_x)]}{\sqrt{kR}}\quad\text{for}\quad R\gg 2A \quad (19)$$

has been used with $-A<x'<A$, $x=R\cos\theta_x$, and $z=R\sin\theta_x$. Equation (17) can be rewritten as

$$p_f^a(R,\theta_x)=\frac{k\rho c}{2}\,v(x)*\tilde{g}(x,z)\Big|_{x=0} \quad (20)$$

with

$$\tilde{g}(x,z)=\tilde{H}(kR)\exp(-jkx\cos\theta_x). \quad (21)$$

In the following the asymptotic expression $\tilde{g}(x,z)$ will be named the asymptotic Green's function. It is interesting to note that we have

$$v(x)*g(x,z)\rightarrow v(x)*\tilde{g}(x,z)|_{x=0}\ \text{ as }\ R\gg 2A. \quad (22)$$

Similarly and in the same manner as before, we can easily demonstrate that the discrete far-field pressure is given by

$$p_f^c(R,\theta_x)=p_f^a(R,\theta_x)+\frac{k\rho c}{2}\,\mathrm{TF}^{-1}\left\{\sum_{i_x\neq 0}V\left(f_x\,\frac{-i_x}{\Delta d}\right)\tilde{G}(f_x,z)\right\} \quad (23a)$$

or by

$$p_f^c(R,\theta_x)=\frac{k\rho c}{2}\sum_{i_x=-\infty}^{i_x=+\infty}\left(\nu(x)\times\exp\left[-2j\pi\,\frac{i_x}{\Delta d}\,x^*\right]\right)\tilde{g}(x,z)\Big|_{x=0}, \quad (23b)$$

and can easily be computed as

$$p_f^c(R,\theta_x)=\frac{k\rho c}{2}\,\tilde{H}(kR)\times\sum_{i_x=-\infty}^{i_x=+\infty}\left(\int_{-\infty}^{+\infty}\nu(x')e^{-jkx'i_x2n_{\mathrm{up}}}e^{-jkx\cos\theta_x}dx'\right), \quad (24)$$

where $\tilde{G}(f_x,z)$ is the FT of the asymptotic Green's function and given by

$$\tilde{G}(f_x,z)=\tilde{H}(kR)\,\delta(f_x-(\cos\theta_x)/\lambda). \quad (25)$$

To obtain Eq. (24) the following relation: $n_{\mathrm{up}}=\lambda/(2\Delta d)$ has been used. When $\Delta d=\lambda/2$ (Nyquist criterion) we obtain $n_{\mathrm{up}}=1$. It is interesting to note that, contrary to the FT of $g(x,z)$, the FT of $\tilde{g}(x,z)$ is bandlimited, then the sound field can be sampled at a finite step size. In addition, as has been shown in Ref. 5 when the observation point M is in the far-field zone the FT of Green's function becomes undersampled. Then the computed discrete pressures by Eq. (11) will contains ripples. But when Eq. (23) is used, the computed far-field pressures show less ripples. These ripples is found far from the axis of the transducer. In fact, Eq. (23) indicates that the pressure is corrupted by terms which are given by the convolutions of replicated spectra of the original spectrum and the FT of the asymptotic Green's function. These replicated spectral are placed at points given by $i_x/\Delta d$. These points are also given by $i_x(2n_{\mathrm{up}})$ in angular range. As the angular spectrum is, generally, very small for $\cos\theta_x$ values near unity, these replicated sources not play a major role. For this reason results shown by Fig. 3 in Ref. 5 are correct for $n_x<n_{\mathrm{up}}/2$ and for $L_\alpha>1/(2n_{\mathrm{up}})$ $(2A=L_\alpha\lambda)$. If we want to eliminate these ripples a value of $2n_{\mathrm{up}}$ greater than unity is necessary (see Fig. 4 in Ref. 5).

Finally, Eq. (24) can be obtained directly using Eqs. (10) and (17) and can be rewritten as

$$p_f^c(R,n_x)=\sum_{i_x=-\infty}^{+\infty}p_f^a(R,n_x-2i_xn_{\mathrm{up}}). \quad (26)$$

For the piston mode the discrete far-field pressure is then given by

$$p_f^c(R,n_x)=p_0'\sum_{i_x=-\infty}^{+\infty}\mathrm{sinc}(kA(\cos\theta_x-2i_xn_{\mathrm{up}})). \quad (27)$$

Again, it is clear that when n_{up} is chosen increasingly greater than unity, the computed discrete pressure becomes increasingly closer to the analytical pressure over the interval $[-1,1]$.

III. CONCLUSION

Some clarifications have been given for the replicated spectra due to sampling effects. It is shown that, in the far field, Eq. (17) must be used to implement the angular spectrum approach. In fact, the equivalent asymptotic expression for the Green's function is bandlimited and then it can be sampled with a finite step. Finally, it has been shown that when the source is oversampled the computed far-field discrete pressure can become close to the analytical far-field pressure over the interval $[-1,1]$.

[1] E. G. Williams and J. D. Maynard, ''Numerical evaluation of the Rayleigh integral for planar radiators using the FFT,'' J. Acoust. Soc. Am. **72**, 2020–2030 (1982).

[2] P. Wu, R. Kazys, and T. Stepinski, ''Analysis of the numerically implemented angular spectrum approach based on the evaluation of two-dimensional acoustic fields. Part I. Errors due to the discrete Fourier transform and discretization,'' J. Acoust. Soc. Am. **99**, 1339–1348 (1996).

[3] P. Wu, R. Kazys, and T. Stepinski, ''Analysis of the numerically implemented angular spectrum approach based on the evaluation of two-dimensional acoustic fields. Part II. Characteristics as a function of angular range,'' J. Acoust. Soc. Am. **99**, 1339–1348 (1996).

[4] Z. G. Hah and K. M. Sung, ''Effect of spatial sampling in the calculation of ultrasonic fields generated by piston mode,'' J. Acoust. Soc. Am. **92**, 3403–3408 (1992).

[5] J. Assaad and J.-M. Rouvaen, ''Numerical evaluation of the far-field directivity pattern using the fast Fourier transform,'' J. Acoust. Soc. Am. **104**, 72–80 (1998).

[6] J. Assaad, J.-N. Decarpigny, C. Bruneel, R. Bossut, and B. Hamonic, ''Application of the finite element method to two-dimensional radiation problems,'' J. Acoust. Soc. Am. **94**, 562–573 (1993).

A note about acoustic streaming: Comparison of C. E. Bradley's and W. L. Nyborg's theories

Xiaoliang Zhao, Zhemin Zhu, and Gonghuan Du
Institute of Acoustics, Nanjing University, Nanjing 210093, People's Republic of China

(Received 27 August 1997; accepted for publication 18 March 1998)

Some comparisons of C. E. Bradley's and W. L. Nyborg's theories on acoustic streaming are given.
 [S0001-4966(98)03107-5]

PACS numbers: 43.25.Nm [MAB]

C. E. Bradley (1996) derived a system of equations and boundary conditions that describe acoustically driven flow in a very general system.[1] Through careful consideration of boundary condition at the face of the acoustic radiator, he found a new flow driven mechanism. Each of the driven mechanisms was analyzed to determine both the physical origins of them and the structures of the resultant flow. His research is quite useful and necessary, especially in handling the problems of acoustic streaming induced by a radiator whose surface motion is nonrectilinear. Formerly, W. L. Nyborg (1965) published an article on acoustic streaming, in which a system of equations was also established to predict the acoustic streaming field structure.[2] Noting that this article was not cited by Bradley's paper, we compared them in order to understand the complex streaming problems better.

First, both Bradley and Nyborg started their analysis from equations of conservation of mass and momentum in Eulerian coordinates. The difference is that Bradley considered that entropy does not vary under the first-order approximation in the constitutive relations, while Nyborg assumed that $p_1=c^2\rho_1+R\dot{\rho}_1$, in which the second term denotes the ''relaxation.'' If we assume $\mathbf{u}_1$ is represented as the real part of a complex number with time factor $e^{i\omega t}$, the equation in Bradley's paper:

$$\boldsymbol{\nabla}\boldsymbol{\nabla}\cdot\mathbf{u}_1+\frac{\mu}{\rho_0c_0^2}\nabla^2\frac{\partial\mathbf{u}_1}{\partial t}+\frac{\mu_B+(\mu/3)}{\rho_0c_0^2}\boldsymbol{\nabla}\boldsymbol{\nabla}\cdot\frac{\partial\mathbf{u}_1}{\partial t}-\frac{1}{c_0^2}\frac{\partial^2\mathbf{u}_1}{\partial t^2}=\mathbf{0} \tag{1}$$

reduces to

$$[2k^{-2}+ib\beta^{-2}]\boldsymbol{\nabla}\boldsymbol{\nabla}\cdot\mathbf{u}_1+2\mathbf{u}_1=i\beta^{-2}\boldsymbol{\nabla}\times\boldsymbol{\nabla}\times\mathbf{u}_1, \tag{2}$$

where constants β and b are defined as

$$\beta^2=\frac{\omega\rho_0}{2\mu},\quad \mu b=\left[\mu_B+\frac{4}{3}\mu\right]. \tag{3}$$

It is almost the same as Eq. (8) in Nyborg's article, except that $\mu b=[\mu_B+4/3\mu+\rho_0R]$ by Nyborg's definition, in which the relaxation term affects the first-order sound field as would an increase of the bulk viscosity. In addition, the decomposition process (to the first-order velocity field) made by Bradley and Nyborg agree well, i.e., Eqs. (6) and (7) in Bradley's paper are consistent with Eqs. (12) and (13) in Nyborg's article.

Second, both Bradley and Nyborg dealt with the second-order Eulerian time-averaged velocity $\mathbf{u}_{dc}$ or $\mathbf{u}_2$ similarly. An improvement made by Bradley is that he studied the boundary condition of the radiator in detail and deduced that $\mathbf{u}_{dc}$ commonly is not divergence free. Equations (10) and (11) in Bradley's paper are the same as Eqs. (14) and (15) in Nyborg's article. Nyborg assumes $\boldsymbol{\nabla}\cdot\mathbf{u}_2=0$ while Bradley derived

$$\boldsymbol{\nabla}\cdot\mathbf{u}_{dc}=-\frac{1}{\rho_0c_0^2}\boldsymbol{\nabla}\cdot\langle\mathbf{I}\rangle, \tag{4}$$

where $\langle\mathbf{I}\rangle=\langle p_1\mathbf{u}_1\rangle$ is the acoustic intensity. Consequently, Eq. (17) in Bradley's paper also resembles Eq. (16) in Nyborg's article, except that an amendment of $\mathbf{F}$ is made by Bradley due to the divergence of $\mathbf{u}_{dc}$.

Third, the definition of mass-transport in both articles are similar. Nyborg derived the ''net-mass-flow'' velocity for acoustic streaming in accordance with the nonacoustic situation where an incompressible fluid of constant density ρ_0 flows steadily with velocity $\mathbf{U}$. To be specific, he kept the product of $\rho\mathbf{u}$ up to the second order and took time average, then obtained:

$$\int_s\langle\rho_0\mathbf{u}_2+\rho_1\mathbf{u}_1\rangle\cdot d\mathbf{S}=M, \tag{5}$$

where M represents the time-averaged mass flow rate. Assuming that $\mathbf{u}_T=\rho_0^{-1}\langle\rho_1\mathbf{u}_1\rangle$, he defined the mass-transport velocity $\mathbf{U}$ as $\mathbf{U}=\mathbf{u}_2+\mathbf{u}_T$. In Bradley's paper, this process may be found in Sec. III A, though $\mathbf{u}_T$ is not defined.

Last, both Bradley and Nyborg have discussed the Lagrangian velocity field to explain why the Eulerian time-average velocity $\mathbf{u}_{dc}$ or $\mathbf{u}_2$ (with nonslip boundary condition at the rest surface of the boundary) is not the velocity commonly determined in experiment; i.e., Eq. (22) in Bradley's paper is the same as Eq. (40) in Nyborg's article. That is

$$\langle\mathbf{u}(Q,t)\rangle\cong\mathbf{u}_2+\langle\boldsymbol{\xi}_1\cdot\boldsymbol{\nabla}\mathbf{u}_1\rangle. \tag{6}$$

Here $\langle\mathbf{u}(Q,t)\rangle$ is equivalent to $\mathbf{u}_L$, both denoting the time-averaged Lagrangian velocity. Nyborg focused his interest on the rectilinear motion cases, i.e., $\boldsymbol{\xi}_1$ and $\mathbf{u}_1$ are parallel to each other (see p. 282, Ref. 2). He concluded that $\mathbf{U}=\langle\mathbf{u}(Q,t)\rangle$ [Eq. (41a), Ref. 2] under that approximation. Bradley, on the other hand, extended the discussion to nonrectilinear ones and found if the neighboring elliptical motion is not uniform, the time-averaged Lagrangian velocity field $\mathbf{u}_L$ differs from mass-transport velocity $\mathbf{U}$. Otherwise, if

the field is rectilinear or if the field is elliptical but uniform, $\mathbf{u}_L$ and $\mathbf{U}$ are identical. The results they obtained for rectilinear fluid motion cases also agree.

In conclusion, the processes in which Bradley and Nyborg dealt with the acoustic streaming field structure are found to be similar to each other in some respects. Nyborg devoted most of his study to rectilinear fluid motion cases, while Bradley extended the theory to nonrectilinear ones. Comparison of these two articles may give readers a better understanding of acoustic streaming field structure.

[1] C. E. Bradley, ''Acoustic streaming field structure: The influence of radiator,'' J. Acoust. Soc. Am. **100**, 1399–1408 (1996).
[2] W. L. Nyborg, Phys. Acoust. **2** B, 265–331 (1965).

Conformation transition and behavior of the ultrasonic attenuation in cyclohexanol and aqueous solution of cyclohexanol

S. Z. Mirzaev, P. K. Khabibullaev, A. A. Saidov, V. S. Kononenko, and I. I. Shinder
Heat Physics Department, Uzbek Academy of Sciences, Chilanzar C, Katartal 28, Tashkent, 700135, Uzbekistan

(Received 27 October 1997; accepted for publication 6 April 1998)

Experimental results for the absorption of ultrasonic waves in pure cyclohexanol and aqueous solution of cyclohexanol in the frequency range 0.06–150 MHz and at temperatures 30, 40, 50, and 60 °C are reported. The ultrasonic relaxation spectra of pure cyclohexanol investigated show two relaxation processes in contrast to those aqueous solutions of cyclohexanol, which indicate a single relaxation process. One relaxation process is located in the frequency range 0.01–1 MHz and the second in the range 0.8–10 GHz. The process with the lower relaxation frequency has been assigned to the ''chair''–''chair'' molecular conformations. © *1998 Acoustical Society of America.* [S0001-4966(98)04007-7]

PACS numbers: 43.35.Bf [HEB]

INTRODUCTION

Acoustic spectroscopy can be advantageously used to study molecular motions and fast chemical reactions in pure liquids and in liquid mixtures.[1,2] This work is devoted to the experimental study of monomolecular reaction in cyclohexanol and aqueous solution of cyclohexanol. We have investigated the absorption of sound in cyclohexanol, cyclohexanol–water solution over the frequency range of 0.06–150 MHz at various temperatures. The ultra- and hypersonic properties of liquid cyclohexanol have been investigated previously.[3–7] Karpovich[3] investigated the acoustical properties of cyclohexanol at frequencies from 0.2 to 0.6 MHz at 32 °C, and Plass[4] measured the sound absorption from 400 to 1500 MHz at 20 °C. Klyichnikova and others[5] determined the velocity and absorption of hypersound in liquid cyclohexanol at 30 °C at a frequency of 5.3 GHz. Kishimoto and Nomoto[6] studied the absorption of sound in the temperature interval from 10 to 35 °C at 8 MHz. Shakhparonov[7] calculated the thermodynamic parameters on the basis of dielectric data. All the cited works refer either to one fixed frequency and temperature or to very narrow frequency and temperature ranges. References 3–7 therefore do not disclose the possible molecular mechanism of the observed relaxation interval. Cyclohexanol $C_6H_{12}O$ was purchased from Fluka and was used without further purification. Water was distilled and additionally deionized. The experimental apparatus and procedure for measuring the absorption coefficient of sound is described in earlier papers.[8,9]

I. ABSORPTION MEASUREMENTS AND RESULTS

In the present work we measured the velocity of sound c in cyclohexanol at a frequency of 20 MHz and at temperatures of 30, 40, 50, and 60 °C. The experimental values of c are given in Table I. We investigated the absorption coefficient at the indicated temperatures in the frequency range from 60 kHz to 150 MHz. The dependence of α/f^2 on the frequency is shown in Fig. 1, in which it is seen that two pronounced acoustic relaxation intervals are observed in cyclohexanol in the investigated frequency-temperature range. The solid lines represent the calculated relaxation spectra from a double relaxation equation. It is apparent that a double relaxation equation is required to adequately fit the experimental data obtained at 30 and 40 °C. The frequency dependence at all temperatures is givenly the following equation within the experimental error limits:

$$\frac{\alpha}{f^2}=\sum_{i=1}^{2}\frac{A_i}{(1+(\omega\tau_i)^2)}+B, \tag{1}$$

where A_i and τ_i are relaxation amplitude and time of characteristic processes, B is constant, and $\omega=2\pi f$ is the cyclic frequency. The experimental values of A_1, A_2, B, τ_1, τ_2 for cyclohexanol are given in Table I. The first, low-frequency acoustic relaxation interval is from 0.01 to 1 MHz, and the second, high-frequency interval from 0.8 to 10 GHz. It has now been confirmed by spectroscopic methods[10,11] that cyclohexanol molecules exist in two preferred conformations:

TABLE I. The experimental values of A, B and τ, c for pure cyclohexanol Eq. (1).

Temperature °C	Velocity m/s	A_1, 10^{-12} s^2 m^{-1}	A_2, 10^{-15} s^2 m^{-1}	B	$\tau_1\times10^6$ s	$\tau_2\times10^9$ s
30	1448.8	355±54	612	20	3.8±0.34	0.35±0.23
40	1413	280±110	422	19	2.7±1.8	0.11±0.1
50	1377.2	205±34	296	18	2.14±0.1	0.092±.07
60	1341.4	130±3	214	17	1.21±0.1	0.03±0.2

 0001-4966/98/104(1)/585/3/$15.00

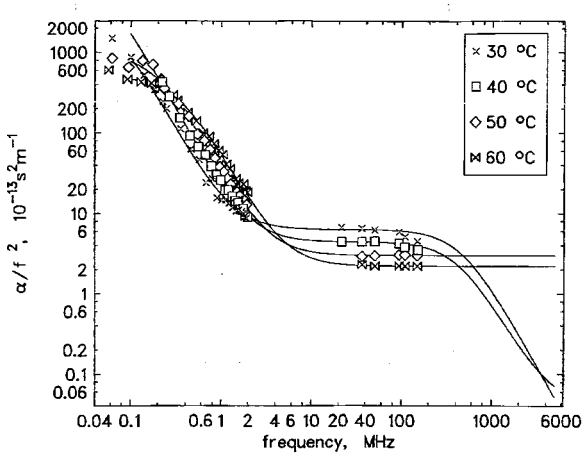

FIG. 1. Ultrasonic absorption as a function of frequency for pure cyclohexanol at 30, 40, 50, and 60 °C. The solid line in the figure represent the calculated (for case i=2) relaxation spectra from Eq. (1).

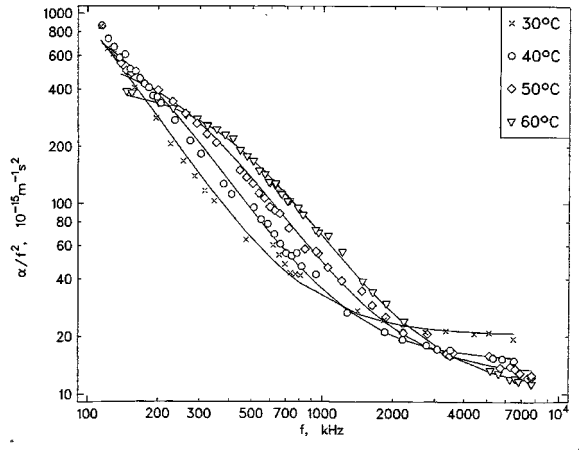

FIG. 2. Ultrasonic absorption as a function of frequency for 1.4 weight % solution cyclohexanol in water at 30, 40, 50, and 60 °C. The solid line in the figure represent the calculated (for case i=1) relaxation spectra from Eq. (1).

(1) the ''chair'' form with an equatorial hydroxyl group; (2) the ''chair'' form with an axial hydroxyl group. It is well known that in the transition of the hydroxyl group from equatorial to axial orientation the lowest-energy intermediate conformation is a ''titled boat'' form. According to Lamb and Sherwood[11] the latter conformation does not exist in sizeable quantities. Consequently, the disturbance of equilibrium between the ''chair'' molecular conformations due to the transmission of a sound wave causes relaxation observed in the low-frequency interval from 10 kHz to 1 MHz. On the basis of the foregoing arguments and the experimental values of A_1, τ_1, c, we determine the difference ΔH_0 between the activation enthalpies of the axial and equatorial groups, the activation enthalpy $\Delta H_{12}^{\neq}$ of the forward reaction, and the activation enthalpy $\Delta H_{21}^{\neq}$ of the reverse reaction.

We employ the expressions[1]

$$\tau = \frac{h}{kT} \exp\left(\frac{\Delta F_{21}^{\neq}}{RT}\right) \tag{2}$$

and

$$\frac{2\mu_{\max}}{\pi} \frac{C_P}{\gamma - 1} \approx R\left(\frac{\Delta H_0}{RT}\right)^2 \exp\left(-\frac{\Delta H_0}{RT}\right) \cdot F, \tag{3}$$

where

$$F = \exp\left(\frac{\Delta S_{21}^{\neq}}{R}\right) \quad \text{and} \quad \mu_{\max} = \frac{A_i \cdot c}{4\pi\tau},$$

and $\Delta F_{21}^{\neq} = \Delta H_{21}^{\neq} - T\Delta S_{21}^{\neq}$ in (3), in which h is Planck's constant, k is Boltzmann's constant, R is the gas constant, and T is the absolute temperature. Here, $\Delta F_{21}^{\neq}$ is the free enthalpy and $\Delta S_{21}^{\neq}$ is the entropy of activation of the reverse reaction, C_P is the specific heat per unit mass at constant pressure, and $\gamma = C_P/C_V$ is the ratio of the specific heats. In practice the values of C_P and γ may not be known with sufficient accuracy, and it is preferable to replace C_P and γ by measured values of the velocity of sound as follows:[1] $c^2 = (\gamma - 1)\, JC_P/\theta\, ^2T$, where $J = 4.187$ J/cal. The quantity $[T^2 C_P \mu_{\max}/(\gamma - 1)] = (TJ/c^2)[C_P/\theta]^2 \mu_{\max}$, and since $[C_P/\theta]^2$ does not usually strongly depend on temperature, the value can be obtained approximately by least-squares method from Eq. (3). The values so obtained are $\Delta H_0 = 1.07$ kcal/mol, $\Delta H_{12}^{\neq} = 5.46$ kcal/mol, $\Delta H_{21}^{\neq} = 6.53$ kcal/mol, $\Delta F_{21}^{\neq} = 10$ kcal/mol, and $\Delta S_{21}^{\neq} = -5.7$ cal/K mol. The energy difference between the axial and equatorial groups has been determined earlier by the NMR method. Values of 1.05 kcal/mol[12] and 1.07 kcal/mol[13] were obtained, which agree with the results of our calculations. The second acoustic dispersion interval is associated with structural relaxation. Clearly, structural relaxation in cyclohexanol, as in other alcohols, is attributable to the formation and destruction of hydrogen bonds between oxygen and hydrogen atoms of the hydroxyl groups. An exact discussion of the relaxation energetics is impossible in the absence of data for GHz frequency region for cyclohexanol. To gain further insight into rotational-isomeric mechanism and possibility of variations of these mechanisms in solutions we investigated the acoustic spectra of cyclohexanol–water solutions. We prepared a solution with concentration 1.4 by weight % cyclohexanol in water. The results of our measurements of the dilute solution of cyclohexanol in the range from 100 kHz to 8 MHz are shown in Fig. 2 in which it is seen that one acoustic relaxation interval is observed in the investigated frequency-temperature range. The experimental values of A, B and τ are given in Table II. The temperature dependencies of the parameters A, B, τ warrant the assumption that the low-frequency relaxation process in a cyclohexanol-water solution is attributable to the same mechanism that occurs in pure cyclohexanol in the frequency interval from 0.01 to 1 MHz. The relative large value of B for aqueous solution of cyclohexanol can be taken as an in-

TABLE II. The experimental values of A, B, and τ for a solution of 1.4 weight % cyclohexanol in water Eq. (1).

T, °C	A, 10^{-12} s^2 m^{-1}	B, 10^{-15} s^2 m^{-1}	$\tau \times 10^6$ s
30	3.65	20	3.7
40	1.2	15	2.9
50	0.61	13	2.1
60	0.41	10	1.3

dication for the existence of a relaxation process at frequencies higher than that used in this study.

[1] J. Lamb, ''Thermal relaxation in liquids,'' in *Physical Acoustics. Principles and Methods* (Academic, New York, 1965), Vol. 2, Pt. A, p. 203.
[2] V. F. Nozdrev, *The Use of Ultrasonics in Molecular Physics* (Pergamon, Oxford, 1965), p. 424.
[3] J. J. Karpovich, ''Investigation of rotational isomers with ultrasound'' Chem. Phys. **22**, 1767 (1954).
[4] K. G. Plass, ''Relaxationen in organischen Flussigkeiten bei 1 GHz,'' Acustica **19**, 236–242 (1967).
[5] T. N. Klyuchnicova, L. V. Lanshina, and K. Parpiev, ''Acoustical properties of certain organic liquids,'' Sov. Phys. Acoust. **18**, 267–269 (1972).
[6] T. N. Kishimoto and O. J. Nomoto, ''Absorption of ultrasonic waves in organic liquids. 1. Liquids with positive temperature coefficient of sound absorption,'' J. Phys. Soc. Jpn. **9**, 620 (1954).
[7] M. I. Shakhparonov, ''Mechanism of low-frequency dielectric relaxation and viscous friction in alcohols and water,'' Dokl. Akad. Nauk SSSR **175**, 1097 (1967).
[8] V. S. Kononenko, ''Precision method for measurements of the ultrasound absorption coefficient in liquids at frequencies of 0.1–20 MHz,'' Sov. Phys. Acoust. **33**, 401–404 (1987).
[9] P. K. Khabibullev, V. S. Kononenko, S. Z. Mirzaev, and A. A. Saidov, ''O mehanizme poglosheniya zvuka v okrestnosti kriticheskoi tochki rasslaivaniya rastvora metanol-n-geptan,'' Dokl. Akad. Nauk Uzbekistan (in Russian) **2**, 14–17 (1995).
[10] S. I. Mizushima, *Structure of Molecules and Rotation* (Academic, New York, 1954).
[11] J. Lamb and J. M. Sherwood, ''Ultrasonic absorption and relaxation in some cyclohexane derivates in the liquid state,'' Trans. Faraday Soc. **51**, 1674 (1955).
[12] J. Reisse, J. C. Celotti, D. Zimmermann, and G. Chiurdoglu, ''Analyse conformationnelle par resonance nucleaire magnetique. 1. Difference d'enthalpie et d'entalpie entre conformeres du cyclohexanol,'' Tetrahedron Lett. **1**, 2145–2150 (1964).
[13] F. A. Anet, ''The use of remote deuteration for determination of coupling constants and conformational equilibria in cyclohexane derivatives,'' J. Am. Chem. Soc. **84**, 1053 (1962).

Vibration of a membrane whose shape is the union of two circles—Method of internal matching

C. Y. Wang
Department of Mathematics, Michigan State University, East Lansing, Michigan 48824

(Received 10 February 1998; accepted for publication 17 April 1998)

The vibration of a membrane shaped like a simply connected figure eight is studied. The domain is simplified to a single circle region using the internal matching method. The results also include the circular membrane with one segment constrained. © *1998 Acoustical Society of America.* [S0001-4966(98)06007-X]

PACS numbers: 43.40.Dx, 43.20.Mv [CBB]

INTRODUCTION

The vibration of membranes is a fundamental topic in the theory of sound.[1] The solution to the resulting Helmholtz equation is also important in the vibration of simply supported plates and in electromagnetic waveguides.[2] Membranes or waveguides of various shapes have been studied by a variety of methods, including conformal mapping, perturbation, point match, variation, boundary element, and direct numerical integration.[3]

The purpose of this paper is twofold. First we introduce the new method of internal matching, which is related to the point-match method. Second, the method is applied to a membrane shaped like the union of two equal circles, the properties of which have never been studied before. The results also include the important case of a circular membrane with one segment constrained.

I. FORMULATION

The governing equation for membrane vibration is the Helmholtz equation

$$\nabla^2 w + k^2 w = 0, \tag{1}$$

where w is the displacement and k is the normalized frequency

$$k^2 = (\text{frequency})^2(\text{length})^2(\text{density})/(\text{tension per length}). \tag{2}$$

Consider the membrane with the shape of the union of two equal disks [Fig. 1(a)] where all lengths are normalized by the radius of the disks. The distance between the disk centers is $2a$. Due to the geometry, existing methods will be tedious, if not impossible, to apply.

We note that there are two axes of symmetry: $\overline{AA}$ and $\overline{BB}$. Any eigenmode would be either symmetrical or antisymmetrical about these axes. Consider only the left disk and let the arc $\overset{\frown}{BPB}$ complete the circle [Fig. 1(b)]. Let P' be the reflection of P, about $\overline{BB}$. Since $\overline{BB}$ is a geometric symmetry line, either

$$w(P) = w(P') \tag{3}$$

or

$$w(P) = -w(P'). \tag{4}$$

Let (r,θ) be polar coordinates with origin at the center of the disk. Then a is the distance from origin to $\overline{BB}$. If point P is at $(1,\theta)$, trigonometry gives P' at (ρ,ϕ) where

$$\rho \equiv \sqrt{1+4a^2-4a\cos\theta}, \tag{5}$$

$$\phi \equiv \tan^{-1}\left(\frac{\sin\theta}{2a-\cos\theta}\right). \tag{6}$$

Now instead of the inconvenient shape of Fig. 1(a) we can study the full circle of Fig. 1(b) with the boundary conditions $w=0$ on the solid boundary and internal matching Eqs. (3) or (4) on the arc $\overset{\frown}{BPB}$.

Since $\overline{AA}$ is also an axis of symmetry, the eigenmode may also be symmetrical or antisymmetrical about $\overline{AA}$. Thus there are four cases. For the SS mode, w is symmetrical to both $\overline{AA}$ and $\overline{BB}$. The complete general solution to Eq. (1) even in θ and bounded at $r=0$ is

$$w(r,\theta) = \sum_{n=0}^{\infty} C_n n!\,\cos(n\theta) J_n(kr), \tag{7}$$

where C_n are coefficients to be determined, J_n are Bessel functions, and the factor $n!$ is to assure C_n has reasonable values for large n. Let $\beta = \cos^{-1} a$. The boundary conditions are

$$w(1,\theta) = 0, \quad \beta < \theta \leqslant \pi, \tag{8}$$

$$w(1,\theta) = w(\rho,\phi), \quad 0 \leqslant \theta < \beta. \tag{9}$$

For the SA mode w is symmetrical to $\overline{AA}$ but antisymmetrical to $\overline{BB}$. Equation (9) is supplanted by

$$w(1,\theta) = -w(\rho,\phi), \quad 0 \leqslant \theta < \beta. \tag{10}$$

For the AS mode we use the solution odd in θ

$$w(r,\theta) = \sum_{n=1}^{\infty} D_n n!\,\sin(n\theta) J_n(kr) \tag{11}$$

and Eqs. (8), (9). For the AA mode Eqs. (11), (8), (10) are solved.

We shall use point match on N points on the half-circle, although it is also possible to use Fourier inversion. Let

$$\theta_j = (j-0.5)\pi/N, \quad \rho_j = \rho(\theta_j), \quad \phi_j = \phi(\theta_j). \tag{12}$$

For the SS mode, truncate Eq. (7) to $N-1$ terms and apply Eqs. (8), (9)

 0001-4966/98/104(1)/588/3/$15.00

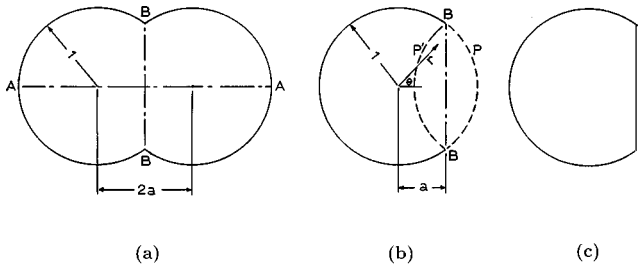

FIG. 1. (a) The membrane shaped like a union of two circles; (b) Solution domain of a single circle; (c) The membrane shaped like a truncated circle.

$$\sum_{0}^{N-1} C_n n! \left[\cos(n\theta_j) J_n(k) - \begin{cases} 0, & \beta < \theta_j \\ \cos(n\phi_j) J_n(k\rho_j), & \beta > \theta_j \end{cases} \right] = 0, \quad j = 1 \text{ to } N. \tag{13}$$

There are N homogeneous equations. For nontrivial C_n the determinant of the coefficients of C_n is set to zero. The eigenvalue k is then obtained by a simple root-finder algorithm. For given geometry or a the fundamental frequency (cutoff frequency) is the lowest k for the SS mode.

After k is obtained, we solve Eq. (13) again with $C_0 = 1$ and the last equation deleted. The solution C_n then gives the eigenmode w from Eq. (7). Accuracy is improved by increasing N. Normally, $N = 30$ is adequate for a 4 digit accuracy.

II. COMPARISON WITH OTHER METHODS

For a membrane with arbitrary shape, direct point match on the boundary is sometimes used.[3] Convergence, however, is not always assured.[4] In the current method, the point match is applied on a circle (although the membrane is not a circle). On a circle Eq. (7) is a standard Fourier series, whose convergence to the correct boundary conditions as $N \to \infty$ is well known. Thus internal point match may have some advantage over direct point match in terms of convergence.

We shall compare some of our results with those obtained by an entirely different method, the variational method. Following Weinstock,[5] the solution to Eq. (1) can be shown to be minimizing the integral

$$I = \int\int (w_x^2 + w_y^2)\, d\sigma \tag{14}$$

with the constraint

$$\int\int w^2\, d\sigma = 1, \tag{15}$$

where σ is the area bounded by the membrane boundary. The function w is then approximated by a set of approximate eigenfunctions which satisfy the zero boundary condition. Minimization of Eq. (14) then yields a characteristic equation for the eigenvalue. However, due to our geometry, it is not possible to find eigenfunctions corresponding to the SS mode which yields the fundamental frequency. For the next mode, the SA mode, or the circular membrane with one segment constrained, one can choose the polynomials

$$w = (1 - x^2 - y^2)(x - a)(b_1 + b_2 x + b_3 x^2 + b_4 y^2) = \sum_{1}^{4} b_i \phi_i(x, y). \tag{16}$$

Then the eigenvalue k is obtained from

$$|\Gamma_{ij} - k\Lambda_{ij}| = 0, \tag{17}$$

where

$$\Gamma_{ij} = \int\int \left(\frac{\partial \phi_i}{\partial x} \frac{\partial \phi_j}{\partial x} + \frac{\partial \phi_i}{\partial y} \frac{\partial \phi_j}{\partial y} \right) d\sigma \tag{18}$$

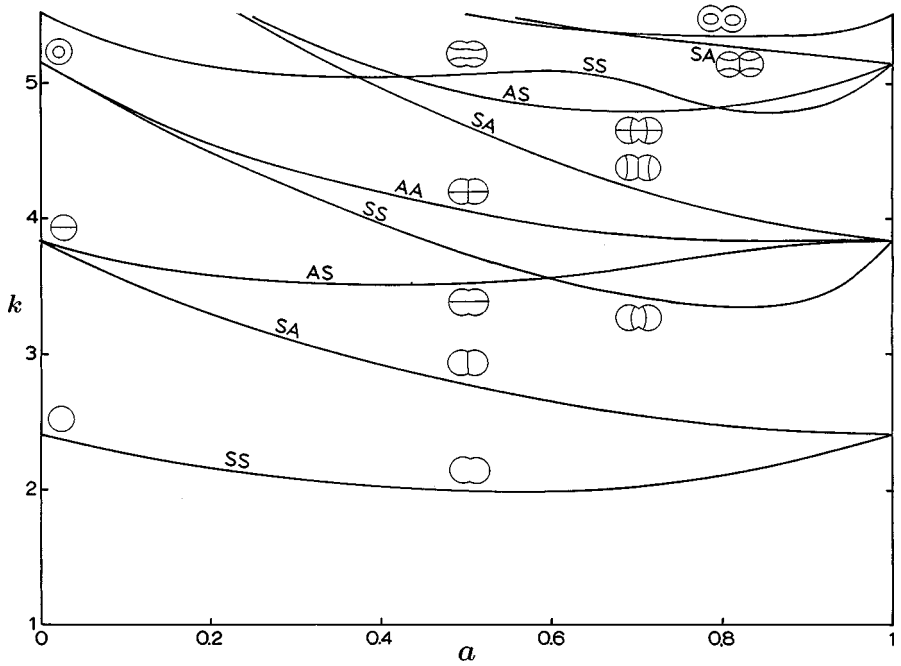

FIG. 2. Vibration frequencies for various modes.

TABLE I. Comparison of eigenvalues of the lowest *SA* mode.

a	0	0.25	0.50	0.75	1
k (variational) (4 terms)	3.833	3.190	2.784	2.538	2.430
k (present) (30 points)	3.832	3.189	2.782	2.525	2.405

and

$$\Lambda_{ij} = \int \int \phi_i \phi_j \, d\sigma. \tag{19}$$

Table I shows a comparison of the results.

We see that the two methods differ by at most 1%, with the largest difference occurring at $a=1$. However, we know when $a=0$ or $a=1$ the boundary is a circle with eigenvalues 3.8317 and 2.4048 (zeroes of J_1 and J_0, respectively). Thus our 30-point internal matching is accurate and slightly better than the 4-term variational method.

Of course, it is possible to include more terms in the variational method. We should note, however, even for 4 terms there are already 32 difficult double integrations to perform, a process much slower than the present method.

III. RESULTS AND DISCUSSION

Figure 2 shows the frequency k as a function of a (half-distance between the disk centers). When $a=0$ the disks overlap, and the frequencies are the same as those of a circular membrane, i.e., the zeros of $J_n(k)$, $k=2.405$, 3.832, 5.136, 5.520, etc. Similarly when $a=1$ the two disks are disjoint and the same frequencies for a circular membrane are recovered.

Consider the lowest frequency for the *SS* mode which is also the fundamental frequency below which no vibration could occur. As a is increased the frequency first decreases, reaches a minimum near $a=0.6$, then increases again. Normally the fundamental frequency decreases with increased area. However, for our geometry when a is near unity the perimeter increases faster than the area, causing an increase in frequency.

The next higher mode is an *SA* mode with zero displacement along $\overline{BB}$ axis. The solution is thus applicable to a circular membrane with one segment constrained or clamped [Fig. 1(c)]. For such a geometry the frequency curves consist of all the *SA* and *AA* modes in Fig. 2.

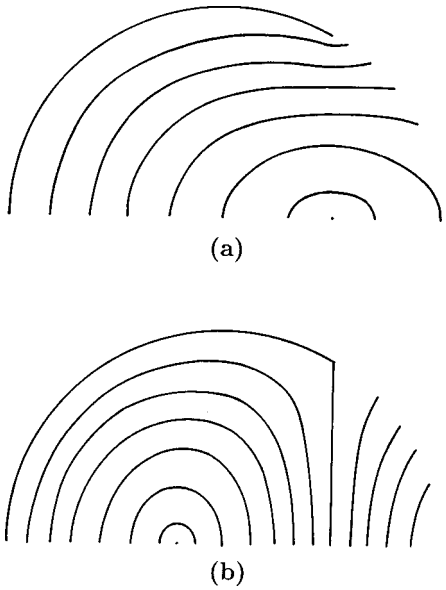

FIG. 3. (a) Displacement profile for the fundamental mode, $a=0.5$; (b) Displacement profile for the second mode, $a=0.5$.

The displacement profile for a fundamental mode is shown in Fig. 3(a). Due to internal matching the figure can be reflected about the $\overline{BB}$ axis. Figure 3(b) shows the next higher mode. One can either reflect about $\overline{BB}$ or regard $\overline{BB}$ as part of the boundary for a truncated circular membrane. Typical stationary ($w=0$) lines for the higher modes are sketched in Fig. 2.

The method of internal matching is found to be simple and accurate. It may be applied to some other geometries such as the symmetrical L-shape membrane studied by Irie *et al.*[6] who used integration of Green's functions. However, Irie's method is inapplicable to the curved geometries considered in this paper. One can of course use finite difference or finite elements, but these methods are not only tedious for curved boundaries but also involve more computations.

[1] Lord Rayleigh, *The Theory of Sound* (Dover, New York, 1945), 2nd ed., Vol. 1.
[2] R. F. Harrington, *Time Harmonic Electromagnetic Fields* (McGraw-Hill, New York, 1961).
[3] F. L. Ng, ''Tabulation of methods for the numerical solution of the hollow waveguide problem,'' IEEE Trans. MMT **22**, 322–329 (1974).
[4] E. M. Sparrow, ''Discussion,'' J. Heat Transfer **88**, 182 (1966).
[5] R. Weinstock, *Calculus of Variations* (McGraw-Hill, New York, 1952).
[6] T. Irie, G. Yamada, and K. Ashida, ''Vibrations of cross-shaped, *I*-shaped and L-shaped membranes and plates,'' J. Acoust. Soc. Am. **72**, 460–465 (1982).

Synchronization of cubic distortion spontaneous otoacoustic emissions

Pim van Dijk[a] and Hero P. Wit
Department of Otorhinolaryngology, University Hospital Groningen, P.O. Box 30.001, 9700 RB Groningen, The Netherlands

(Received 11 December 1997; revised 1 January 1998; accepted 10 March 1998)

A spontaneous otoacoustic emission spectrum may contain equally spaced emission peaks. Then, two peaks, at frequencies, f_1 and f_2, respectively, apparently generate a distortion product at $f_d = 2f_1 - f_2$ [or $2f_2 - f_1$]. For the three emission peaks of nine of such triplets (in six emission spectra), the phases $\phi_1(t)$, $\phi_2(t)$ and $\phi_d(t)$ were computed, respectively. The phase difference $\Delta\phi(t) = \phi_d - (2\phi_1 - \phi_2)$ [or $\Delta\phi = \phi_d - (2\phi_2 - \phi_1)$] tends to lock at a plateau value ϕ_{lock} (modulo 2π), but occasional jumps up or down $n \times 2\pi$ to a neighboring plateau. Apparently, the emission at position $2f_1 - f_2$ [or $2f_2 - f_1$] synchronizes to the cubic distortion product generated by the primaries f_1 and f_2, but occasionally slips out of the synchronized regime. This behavior is consistent with a model consisting of a self-sustained oscillator in the presence of weak noise, driven by a periodic force. © *1998 Acoustical Society of America.* [S0001-4966(98)05206-0]

PACS numbers: 43.64.Jb, 43.64.Kc [BLL-M]

INTRODUCTION

The frequency spectrum of a spontaneous otoacoustic emission (SOAE) may contain several narrow peaks. These peaks display various correlations (briefly reviewed in Van Dijk and Wit, 1998). For example, the emission spectrum may contain equally spaced triplets of peaks, where one of the emission frequencies is apparently generated by cubic distortion of both other emission frequencies (Burns *et al.*, 1984; Jones *et al.*, 1986; Whitehead *et al.*, 1993). The spectral peak corresponding to a distortion product emission peak often displays a secondary ''hump,'' which may indicate that the emission is an ''independent'' emission component, partially synchronized to a weak distortion product generated in the ear by the two ''primary'' emission components (Talmadge *et al.*, 1993). In this paper, we investigate this hypothesis, by comparing the instantaneous phase of distortion product and primary emission peaks.

I. MATERIAL AND METHOD

Spontaneous otoacoustic emission recordings from six human subjects were analyzed. These digitized recordings have been previously described (Van Dijk and Wit, 1990a; Talmadge *et al.*, 1993; Van Dijk and Wit, 1998). The spectrum of each of these recordings contains multiple peaks, corresponding to the spontaneous otoacoustic emission generated in the inner ear. Several equally spaced triplets were present in the SOAE spectra. We considered triplets equally spaced, if the frequency separation between (a) the low- and mid-frequency peak, and (b) the mid- and high-frequency peak, differed 1 Hz or less (Van Dijk and Wit, 1990a). For nine equally spaced triplets, each of the spectral peaks was narrower than 10 Hz (e.g., FWHM$<$10 Hz). These triplets were selected for further analysis.

It is not clear which of the SOAEs in a triplet are the ''primary'' SOAEs and which one is the distortion SOAE. We used the spectral width to identify the distortion SOAE. The spectral width of an SOAE results from random frequency fluctuations. Because the frequency fluctuations of both primary SOAE will cumulate in frequency fluctuation of the distortion SOAE, we assumed the broadest peak to be the distortion emission, while the two narrower peaks are assumed to be the primary SOAEs (Van Dijk and Wit, 1998).

For each triplet, the following analysis was applied: The individual emission peaks in a triplet were isolated by digital bandpass filtering with a zero-phase fourth-order Butterworth filter (width 50 Hz). For details on the filtering procedure, see Van Dijk and Wit (1998). After filtering, an individual emission can be represented by $x(t) = A(t)\cos\phi(t)$. From $x(t)$ and its Hilbert transform $\tilde{x}(t)$, the instantaneous phase follows as $\phi(t) = \arctan[\tilde{x}(t)/x(t)]$ (Bendat and Piersol, 1971).

For each peak in the triplet the phase was computed. The phases of the primaries are $\phi_1(t)$ and $\phi_2(t)$. The phase of the emission at the distortion product position is denoted as $\phi_d(t)$. If a $[2f_1 - f_2]$ emission were generated by a static

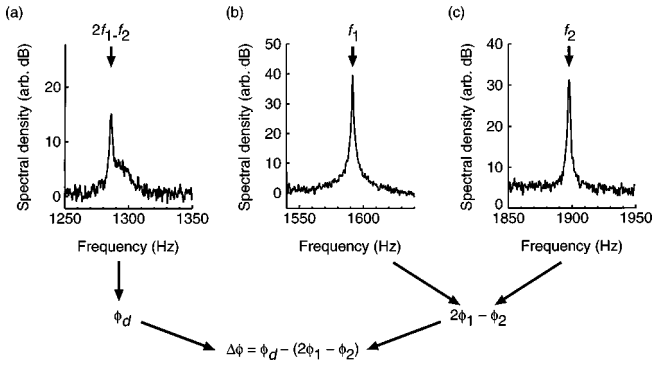

FIG. 1. Frequency spectra of three equally spaced peaks in the SOAE recorded from subject WK. (a) −10 dB SPL @ 1286 Hz; (b) 10 dB SPL @ 1592 Hz; (c) −2.8 dB SPL @ 1898 Hz. For each peak, the instantaneous phase was computed, which was used to calculate the phase difference $\Delta\phi(t)$ [see Fig. 2(a)].

[a]Electronic mail: p.van.dijk@med.rug.nl

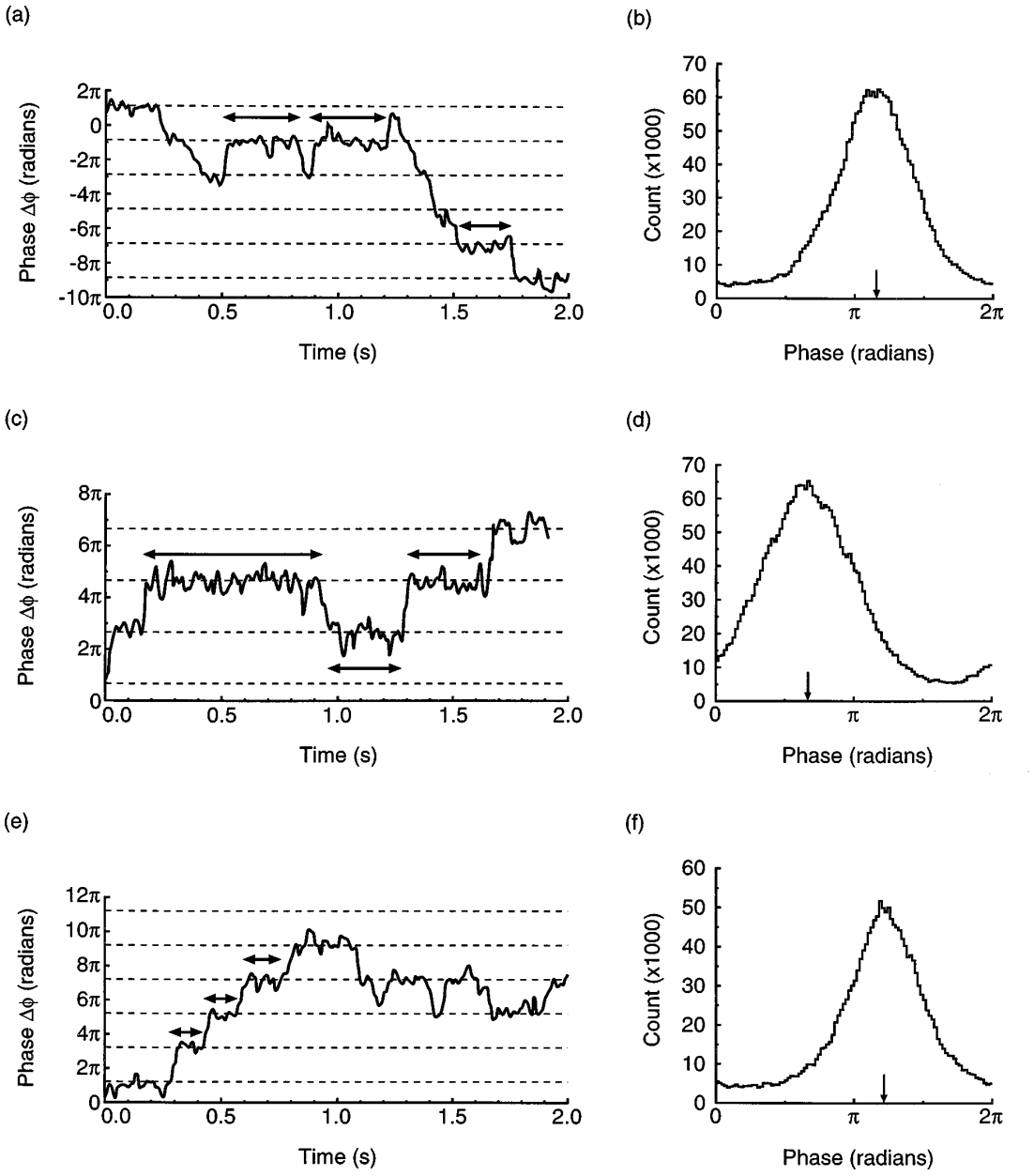

FIG. 2. (a) Small section of the phase $\Delta\phi(t)$ for subject WK (solid curve). The dashed horizontal lines are at $\Delta\phi = 3.57$ modulo 2π. The phase tends to lock at the dashed lines. This is evident as plateaus in the phase curve (a few plateaus were emphasized by a double arrow). Occasionally, the phase slips out of synchronization. Then, the phase jumps to an adjacent dashed line. For the entire recording (181 s), the average number of upward and downward phase jumps was 1.5 and 2.8 jumps/s, respectively. (b) Histogram of $\Delta\phi$ modulo 2π for the entire recording in subject WK. The arrow marks $\Delta\phi = 3.57$. From the phase distribution the synchronization index was computed: $R = 0.57$. (c), (d) Same as panel (a) and (b), but for one of the equally spaced SOAE triplets in subject JH. SOAE center frequencies: 1290 Hz, 1378 Hz, and 1466 Hz. The dashed lines are at $\Delta\phi = 2.07$ modulo 2π. The average number of upward and downward phase jumps was 3.3 and 2.2 jumps/s. Synchronization index: $R = 0.50$. (e), (f) Same as panel (a) and (b), but for the equally spaced SOAE triplet in subject MvD. SOAE center frequencies: 1242 Hz, 1525 Hz, and 1807 Hz. The dashed lines are at $\Delta\phi = 3.85$ modulo 2π. The average number of upward and downward phase jumps was 3.2 and 2.5 jumps/s. Synchronization index: $R = 0.54$.

nonlinear distortion of the primary emissions, it's phase would be given by $2\phi_1(t) - \phi_2(t) + c$, where c is an unknown constant. We computed the phase difference

$$\Delta\phi(t) = \phi_d(t) - [2\phi_1(t) - \phi_2(t)]. \quad (1)$$

For an emission at frequency $2f_2 - f_1$, the phase difference

$$\Delta\phi(t) = \phi_d(t) - [2\phi_2(t) - \phi_1(t)] \quad (2)$$

was computed. Note that from these two equations it follows that $\Delta\phi(t)$ does not depend on which SOAE in a triplet is considered to be the distortion emission.

II. RESULTS

Figure 1 displays FFT spectra of three equally spaced SOAE peaks in subject WK. Panels (b) and (c) show the primary peaks f_1 and f_2, while panel (a) gives the spectrum at position $2f_1 - f_2$. The latter spectrum displays an asymmetry, with a ''shoulder'' at one side: similar asymmetry was observed across subjects for five out of nine investigated triplets.

Figure 2(a) displays a short time interval of the behavior of the phase difference $\Delta\phi(t)$, calculated for the triplet in

TABLE I. Center frequency, level, and full width at half-maximum (FWHM) for the SOAEs included in the present study. Each row contains data for the three SOAEs in an equally spaced triplet. In addition, the synchronization index is displayed. For subject BD, three triplets were included. For subject JH, two triplets were included. For each triplet, the broadest SOAE peak was assumed to correspond to the distortion emission (see bold numbers).

	Center frequency (Hz)			Level (dB SPL)			FWHM (Hz)			Synchronization
Subject	1	2	3	1	2	3	1	2	3	index
BD	1107	1293	1480	0.7	−3.3	−0.3	**6.3**	4.5	5.2	0.11
BD	1380	1566	1752	6.3	11.4	5.2	**6.7**	1.5	1.9	0.69
BD	1480	1752	2024	−0.3	5.2	7.9	**5.2**	1.9	1.3	0.30
JC	2178	2545	2913	−1.4	11.7	5.8	**2.2**	0.8	1.2	0.78
JH	1272	1466	1659	−9.9	−2.9	4.1	**2.2**	0.6	0.4	0.14
JH	1290	1378	1466	−3.5	0.3	−2.9	**1.4**	0.4	0.6	0.50
WK	1286	1592	1898	−10.0	10.0	−2.8	**1.0**	0.2	0.6	0.57
ML	1059	1923	2787	3.2	−3.3	−2.1	0.5	1.6	**2.1**	0.05
MvD	1242	1525	1807	−16.8	10.0	−0.3	1.7	1.5	**1.8**	0.54

Fig. 1. The phase $\Delta\phi$ follows a pattern typical for all investigated triplets: it fluctuates about some value ϕ_{lock}, and occasionally makes a fast transition to some neighboring phase ϕ_{lock} modulo 2π. When locked at a particular phase, the emission is synchronized to the distortion frequency $2f_1 - f_2$. The locking phase ϕ_{lock} presumably depends in a complicated way on the various parameters which describe the triplet of emission generators involved. Consequently, it is expected to be different for different SOAE triplets.

The distortion emission signal may be written as

$$x_d(t) = A_d(t)\cos[\omega_d t - \delta\phi_d(t)], \tag{3}$$

where the center frequency ω_d was explicitly separated from the phase fluctuation component $\delta\phi_d(t)$. Its instantaneous frequency is defined as

$$\omega(t) = \omega_d - \frac{d[\delta\phi_d(t)]}{dt}. \tag{4}$$

A phase jump of the distortion emission phase $\delta\phi_d(t)$ will result in a phase jump of the phase difference $\Delta\phi(t)$. From the relation Eq. (4) between instantaneous frequency $\omega(t)$ and the slope $d[\delta\phi_d(t)]/dt$, it follows that a downward (upward) phase jump reflects a temporal increase (decrease) of the emission frequency. In the example in Fig. 2(a), downward phase shifts are more frequent than upward shift. This indicates that the distortion emission is most likely to jump to a frequency above $2f_1 - f_2$, and explains the shape of the asymmetric peak in Fig. 1(a).

The histogram in Fig. 2(b) displays the distribution of the phase difference $\Delta\phi$ modulo 2π for the triplet of Fig. 1. In the histogram, data for the entire SOAE recording were accumulated. The phase distribution is nonuniform, because the phase behavior illustrated in panel (a) was present throughout the SOAE recording.

Figure 2(c)–(f) displays similar results for two other SOAE triplets. For one of these triplets [see panel (e) and (f), subject MvD] comparison of the spectral widths of the SOAE peaks lead to consider both lowest-frequency SOAEs as primaries (f_1, f_2), while the highest-frequency SOAE was assumed to be near the distortion frequency $2f_2 - f_1$.

The phase locking behavior may be expressed in a synchronization index R, which we computed from the phase distributions.[1] Table I gives an overview of SOAEs included in our study, along with the synchronization index R obtained for each triplet. R ranged from 0.05 to 0.78 across triplets.

III. DISCUSSION

The phase behavior of an SOAE component at a distortion product frequency is consistent with a model consisting of a self-sustained oscillator in the presence of noise, driven by a periodic force (Stratonovich, 1963; for a brief summary of the behavior of such a model system, see Van Dijk and Wit, 1990b). Apparently, the ''primary'' SOAEs internally generate a cubic distortion product. If this distortion is close enough in frequency to an independent spontaneous otoacoustic emission, it acts as a periodic force on the emission generator, and synchronizes the emission to the distortion frequency. However, the synchronized emission occasionally slips out of synchronization, due to noise present in the inner ear. The same behavior has been described for SOAEs synchronized to a cubic distortion product generated by two weak externally applied primary tones (Van Dijk and Wit, 1990b). Our results support the hypothesis that a cubic distortion SOAE corresponds to an ''independent'' SOAE, synchronized to an internally generated weak distortion product.

Burns *et al.* (1984; their Fig. 2) showed that suppression of the higher-frequency SOAE by an external tone may suppress the SOAE at the $2f_1 - f_2$ distortion frequency. This behavior seems not in agreement with the notion of an ''independent'' SOAE. If one of the primaries is suppressed, the synchronization of the emission to the distortion frequency will disappear, but its amplitude is not expected to be suppressed. However, in the Burns *et al.* study, the release from synchronization may have lead to spectral broadening of the distortion SOAE while its amplitude remained unchanged. Possibly, this made it indistinguishable from the noise background. Alternatively, the synchronization behavior which we described was not present in the Burns *et al.* case, and occurs only for triplets consisting of relatively strong SOAEs. Recall that the SOAE triplets in our study were drawn from a population of relatively strong SOAEs (see Van Dijk and Wit, 1998).

Our description of synchronization of an ''independent'' SOAE suggests interpretation of two experimental findings: (1) Burns *et al.* (1984) noted that the levels of cubic distortion SOAE relative to the primaries are 10–15 dB larger than distortions produced by external tones. Evidently, if an ''independent'' SOAE is synchronized to the distortion frequency, the energy emitted at that frequency may be enhanced. (2) The spectral width of a distortion product SOAE is related to the widths of both ''primary'' emissions, but is usually larger than a simple model predicts (Van Dijk and Wit, 1998). The occasional slip out of synchronization may account for the additional broadening of the peak.

In conclusion, for the SOAE triplets we studied, the cubic distortion SOAE may be considered an ''independent'' emission, which is synchronized by a distortion product generated by two ''primary'' SOAEs.

ACKNOWLEDGMENTS

We thank Carrick Talmadge, Glenis Long, and Arnold Tubis at Purdue University for providing some of their emission recordings for analysis. This research was supported by The Royal Netherlands Academy of Sciences and Arts, and the Heinsius Houbolt Fund. The study is part of the research program of our Department: Communication through Hearing and Speech, which is incorporated in the Sensory Systems Group of the Groningen Graduate School for Behavioral and Cognitive Neurosciences (BCN).

[1]The index R is computed similarly to the synchronization index used in auditory physiology (Weiss and Rose, 1988).

Bendat, J., and Piersol, A. (**1971**). *Random Data: Analysis and Measurement Procedures* (Wiley–Interscience, New York).

Burns, E. M., Strickland, E. A., Tubis, A., and Jones, K. (**1984**). ''Interactions among spontaneous otoacoustic emissions. I. Distortion products and linked emissions,'' Hearing Res. **16**, 271–278.

Jones, K., Tubis, A., Long, G. R., Burns, E. M., and Strickland, E. A. (**1986**). ''Interactions among multiple spontaneous otoacoustic emissions,'' in *Peripheral Auditory Mechanisms*, edited by J. B. Allen, J. L. Hall, A. Hubbard, S. T. Neely, and A. Tubis (Springer-Verlag, Berlin), pp. 266–273.

Stratonovich, R. L. (**1963**). *Topics in the Theory of Random Noise, Volume 2* (Gordon and Breach, New York).

Talmadge, C., Long, G., Murphy, W., and Tubis, A. (**1993**). ''New off-line method for detecting spontaneous otoacoustic emissions in human subjects,'' Hearing Res. **71**, 170–182.

Van Dijk, P., and Wit, H. P. (**1990a**). ''Amplitude and frequency fluctuations of spontaneous otoacoustic emissions,'' J. Acoust. Soc. Am. **88**, 1779–1793.

Van Dijk, P., and Wit, H. P. (**1990b**). ''Synchronization of spontaneous otoacoustic emissions to a $2f_1-f_2$ distortion product,'' J. Acoust. Soc. Am. **88**, 850–856.

Van Dijk P., and Wit, H. P. (**1998**). ''Correlated amplitude fluctuations of spontaneous otoacoustic emissions,'' J. Acoust. Soc. Am. **104**, 336–343.

Weiss, T. F., and Rose, C. (**1988**). ''Stages of degradation of timing information in the cochlea: A comparison of hair-cell and nerve-fiber responses in the alligator lizard,'' Hearing Res. **33**, 167–174.

Whitehead, M., Kamal, N., Lonsbury-Martin, B., and Martin, G. (**1993**). ''Spontaneous otoacoustic emissions in different racial groups,'' Scand. Audiol. **22**, 3–10.

Criterion for the minimum source distance at which plane-wave beamforming can be applied

James G. Ryan
Acoustics and Signal Processing, Institute for Microstructural Sciences, National Research Council Canada, Ottawa, Ontario K1A 0R6, Canada

(Received 7 November 1996; accepted for publication 2 April 1998)

An expression is derived which can be used to determine the extent of the near field for a given microphone array size and operating wavelength. This expression is based on the distortion of the near-field array response, and approximates the distance at which the magnitude response error due to plane-wave beamforming is 1 dB. [S0001-4966(98)04607-4]

PACS numbers: 43.72.Kb, 43.38.Hz, 43.38.Si [JLH]

INTRODUCTION

Conventional analysis and synthesis techniques for acoustic arrays are based on the assumption that the distance between the array and the sound source is sufficiently large that only plane-wave propagation need be considered. Under this far-field assumption, the main beam of the array is steered by delaying the individual sensor signals by an amount equal to the propagation delay of a plane wave prior to summing.

There are common applications, however, where the plane-wave assumption can be in error. An example is the deployment of speech-bandwidth microphone arrays in small rooms.[1] Since the size of an array is usually related to its operating wavelength, the aperture of a speech-bandwidth array can be of the same order of magnitude as the distance to the sound source in a small room. In such cases, the sound source is located in the array's near field and wavefront curvature can be detected within the aperture of the array. Delay adjustment can still be used for directing the main beam but the required delays must be adjusted to match the propagation delays of a spherical wave originating at the source location.

Current estimates of the near-field extent for arrays are generally a multiple of the basic parameter L^2/λ, where L is the maximum dimension of the array and λ is the operating wavelength.[2,3] These estimates, however, produce a conservative measure of the near field since they do not account for the wavefront's angle of incidence with the array. For a source located along the endfire direction of a linear array, for instance, the required delays for plane- and spherical-wave beamforming are identical. As a result, no response errors would result from using plane-wave beamforming.

This letter presents an alternate expression to define the near-field to far-field transition region of a linear array in terms of angle of incidence. The expression is derived from considerations of the distortion in the array's response to a single, near-field acoustic source. As will be shown, it provides a reasonable approximation to an equi-error contour line for a linear array with a large number of elements.

I. ARRAY RESPONSE TO A NEAR-FIELD ACOUSTIC SOURCE

Consider an acoustic source located in the near field of an M-element linear array as illustrated in Fig. 1. The source location is described by the polar coordinates r, representing the distance between the source and the coordinate origin, and θ, the angle formed between the line segment r and the positive x axis. The array elements are distributed along the x axis at locations given by x_m.

The response $G(r,\theta)$ of a uniformly weighted delay-and-sum beamformer to a monochromatic spherical wave emitted by the source is given by

$$G(r,\theta)=\sum_{m=0}^{M-1}\frac{e^{-j(kr_m+\omega\tau_m)}}{r_m}, \tag{1}$$

where $\omega=2\pi f$ is the angular frequency, c is the speed of wave propagation, τ_m is the beamformer delay for sensor m, and r_m is the distance between the source location and sensor m:

$$r_m=\sqrt{r^2-2rx_m\cos\theta+x_m^2}. \tag{2}$$

The array response is controlled by adjusting the beamformer delays such that they match the time delays associated with the propagation of a desired wavefront across the array. To focus the array on a near-field point (r',θ'), the required beamformer delays are

$$\tau_m=\frac{r'-r'_m}{c}, \tag{3}$$

where r'_m is the distance from the sensor m to the array focal point and the phase reference is at the coordinate origin. The array response is then

$$G(r,\theta,r',\theta')=\sum_{m=0}^{M-1}\frac{e^{-jk(r_m+r'-r'_m)}}{r_m}.$$

When the source location and the array focal point coincide, the beamformer delays match the propagation delays. Setting $(r,\theta)=(r',\theta')$ yields the spherical-wave beamformer response $G_s(r,\theta)$,

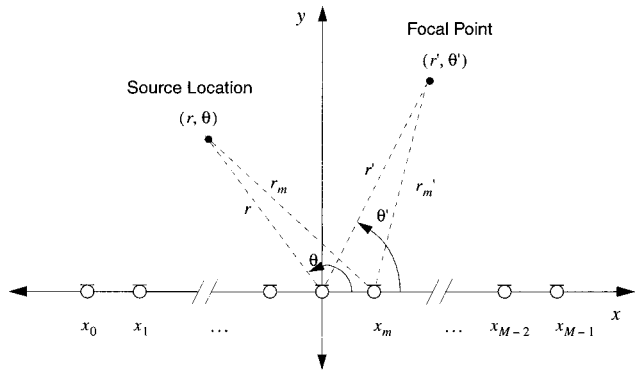

FIG. 1. Sketch of an acoustic source located at (r,θ) in the near field of an M-element linear array which is focused at the point (r°,θ°). The array is located along the x coordinate axis.

$$G_s(r,\theta)=e^{-jkr}\sum_{m=0}^{M-1}\frac{1}{r_m}, \tag{4}$$

so the array output is a scaled and delayed version of the source signal.

If the source distance is neglected in steering the array's main beam, the beamformer delays depend only upon the angle of incidence. The delays required to steer the array for plane waves incident from an angle θ' are

$$\tau_m=\frac{x_m\cos\theta'}{c}, \tag{5}$$

and the corresponding array response is

$$G(r,\theta,\infty,\theta')=\sum_{m=0}^{M-1}\frac{e^{-jk(r_m+x_m\cos\theta')}}{r_m}. \tag{6}$$

Setting $\theta=\theta'$ yields the near-field response for plane-wave beamforming $G_p(r,\theta)$:

$$G_p(r,\theta)=\sum_{m=0}^{M-1}\frac{e^{-jk(r_m+x_m\cos\theta)}}{r_m}. \tag{7}$$

In this case, even though the true source angle θ coincides with the array steering angle θ', the beamformer delays do not exactly match the wave propagation delays and the array response is a linearly distorted version of the source waveform. The severity of the delay mismatch and subsequent response distortion are determined by the source distance r with higher distortion produced for closer source positions.

The distortion in the near-field response due to plane-wave beamforming is described by the response error $\varepsilon(r,\theta)$:

$$\epsilon(r,\theta)=20\log\left|\frac{G_p(r,\theta)}{G_s(r,\theta)}\right|. \tag{8}$$

The response error is the magnitude of the ratio of the plane-wave steered response to the spherical-wave focused response when $\theta=\theta'$ for plane-wave beamforming, and $(r,\theta)=(r',\theta')$ for spherical-wave beamforming. This error function isolates the effects of delay mismatch from those due to spherical-wave spreading through the denominator term $|G_s(r,\theta)|$.

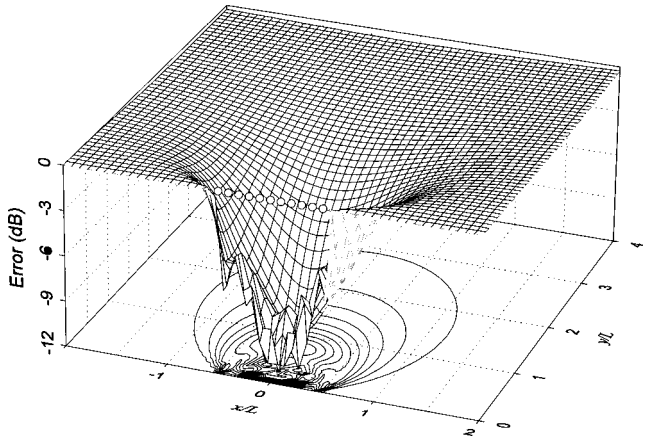

FIG. 2. Error in array response due to plane-wave beamforming for an acoustic source located in the near field of an 11-element linear array with uniform sensor spacing equal to λ/2. The sensor locations are indicated by the small circles along the x axis and the location coordinates are normalized to the array length L.

The response error $\varepsilon(r,\theta)$ has been calculated over a square region in the near field of an 11-element array with uniform sensor spacing of λ/2. The data are plotted in Fig. 2 with the polar location coordinates (r,θ) converted to rectangular coordinates (x,y). All distances are normalized to the array length L and the sensor positions are indicated by a series of small circles located along the x axis.

The plot shows that $\varepsilon(r,\theta)$ depends on both source distance and angle. Neglecting the complicated fluctuations in the immediate vicinity of the sensors, the error is highest for the broadside direction (perpendicular to the array axis), reaching a peak value of approximately -12 dB at a distance equal to $L/4$. For the endfire direction, the error is zero at all distances since the beamformer delays for plane-wave and spherical-wave beamforming are identical. Clearly, a single criterion to describe the near-field extent is insufficient to describe this situation.

II. MINIMUM DISTANCE FOR VALIDITY OF THE PLANE-WAVE ASSUMPTION

To examine the transition between near field and far field, consider the near-field array response for plane-wave beamforming in Eq. (7). Focusing only on the response error due to plane-wave beamforming, let $\theta=\theta'$ as in the numerator of (8). The magnitude of this expression is

$$|G_p(r,\theta)|=\left[\sum_{m=0}^{M-1}\frac{1}{r_m^2}+2\sum_{m=1}^{M-1}\sum_{n=0}^{m-1}\frac{\cos k[r_m+x_m\cos\theta-r_n-x_n\cos\theta]}{r_m r_n}\right]^{1/2}, \tag{9}$$

where r_m is the distance from sensor m to the source position.

As indicated in this expression, the varying distance between the source and the individual array elements results in both phase and amplitude differences at the different array sensors. In determining the onset of response distortion, however, the variations in phase are far more important than the variations in amplitude. Consequently, it is assumed that $1/r_m \approx 1/r$ in the denominator so $|G_p(r,\theta)|$ can be expressed approximately as

$$|G_p(r,\theta)| \approx \frac{1}{r} \cdot \left[M + 2 \sum_{m=1}^{M-1} \sum_{n=0}^{m-1} \cos k[r_m + x_m \cos\theta - r_n - x_n \cos\theta] \right]^{1/2}. \quad (10)$$

For a properly focused array the beamformer delays cancel the propagation delays, the argument of the cosine term is zero, and the array response attains its maximum magnitude. If the delays are maladjusted, however, the cosine argument deviates from zero and the output magnitude will be less than its maximum value. The exact amount by which the magnitude decreases depends on many factors and is very difficult to determine analytically. It is certain, however, that the magnitude will be affected if the absolute value of one of the cosine arguments exceeds $\pi/2$ because the corresponding term in the summation will be negative and will cause a reduction in the magnitude. Although this criterion does not directly relate to the level of reduction in the array's magnitude response it does provide a clear distinction line between terms which contribute to and those which detract from the magnitude response. Furthermore, it will be seen that for arrays with a large number of sensors, the criterion leads to an expression which approximates an equal-magnitude contour in a two-dimensional map of the array response error.

Excessive deterioration of the magnitude response can be avoided if the maximum cosine argument in Eq. (10) is limited to $\pi/2$. Thus the criterion becomes

$$|k[r_m + x_m \cos\theta - r_n - x_n \cos\theta]|_{\max} = \pi/2 \quad \forall m,n, \quad (11)$$

which can be simplified to

$$|\psi(x_m) - \psi(x_n)|_{\max} = \lambda/4 \quad \forall m,n, \quad (12)$$

where

$$\psi(x) = \sqrt{r^2 - 2rx \cos\theta + x^2} + x \cos\theta.$$

The maximum value of $|\psi(x_m) - \psi(x_n)|$ is obtained when $\psi(x_m) = \psi_{\max}$ and $\psi(x_n) = \psi_{\min}$, or vice versa. It is straightforward to show that the maximum value of $\psi(x)$ is attained for $x = L/2$ when $\theta < \pi/2$ and for $x = -L/2$ when $\theta > \pi/2$ where L is the total length of the array. The minimum is attained when $x = 0$, that is,

$$\psi_{\max} = \left[r^2 - rL|\cos\theta| + \frac{L^2}{4} \right]^{1/2} + \frac{L}{2} \cdot |\cos\theta|$$

and

$$\psi_{\min} = r.$$

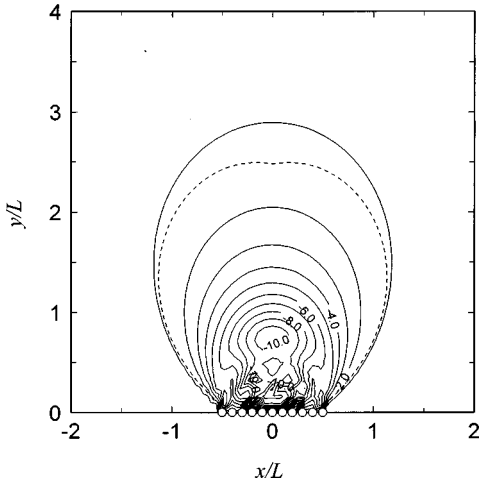

FIG. 3. Extent of the near field according to Eq. (13) superimposed on a contour plot of the same array response error data shown in Fig. 2. The sensor locations are indicated by the small circles along the x axis and the location coordinates are normalized to the array length L.

For an array with an odd number of sensors $M = 2N+1$, then the discrete values of x_m will include both $x = L/2$ and $x = 0$. For an odd number of sensors, the discrete values of x_m includes only $x = L/2$; however, for sensor spacing less than $\lambda/2$ the error made in assuming that $x = 0$ for the sensor closest to the origin will be small.

Substituting these values into Eq. (12) and solving for r yields the following lower bound r_n on the distance at which the plane wave assumption is valid:

$$r_n = \frac{(L \sin\theta)^2}{2\lambda} + \frac{L}{2}|\cos\theta| - \frac{\lambda}{8}. \quad (13)$$

When $\theta = \pi/2$ this estimate of the far-field distance reduces to $(L^2/2\lambda) - \lambda/8$ which, for large arrays, is very nearly equal to the estimate $L^2/2\lambda$ obtained by Steinberg[2] based on an allowable error of 1 dB. This estimate is somewhat less conservative than the estimate $\pi L^2/4\lambda$ obtained by Ziomek.[3] As the incidence angle deviates from $\theta = \pi/2$, however, the near-field extent deviates from $L^2/2\lambda$. At $\theta = 0$, the near-field extent extends only to a distance of $L/2 - \lambda/8$.

As previously discussed, the criterion used to define the near-field extent does not indicate the severity of the error in the array's magnitude response due to the far-field assumption. This error is determined by the number of array elements as well as their spatial distribution. It is possible, however, to illustrate the utility of the near-field expression by comparing it with the response error surface shown in Fig. 2. Figure 3 shows a contour plot of the same data as shown in Fig. 2. The contour line (solid lines) spacing is 1 dB. Again, the array position is indicated by the series of small circles along the x axis ($y = 0$). Superimposed on the contour plot is a graph of the near-field extent according to Eq. (13) (dashed line). It is seen that, for this example, Eq. (13) is a close approximation to the -1-dB contour line. Thus, even though the criterion for defining the near field does not include an indication of error magnitude, the resulting expression does provide a reasonable approximation to an equi-error contour line. For arrays with a large number of sensors, the near-field expression closely approaches the -1-dB con-

tour, whereas for a small number of sensors the near-field extent lies between the -1- and -3-dB contour lines.

III. CONCLUSION

This letter presents an expression for describing the minimum source distance at which plane-wave beamforming can be used without creating excessive response distortion. The expression is shown to provide a good approximation to an equi-error contour line in the array response. The approximation is better for arrays with a larger number of sensors.

[1] F. Pirz, ''Design of a Wideband, Constant Beamwidth, Array Microphone for Use in the Near Field,'' Bell Syst. Tech. J. **58**, 1839–1850 (1979).

[2] B. D. Steinberg, *Principles of Aperture and Array System Design* (Wiley, New York, 1976), Chap. 1, p. 12.

[3] L. J. Ziomek, ''Three Necessary Conditions for the Validity of the Fresnel Phase Approximation for the Near-Field Beam Pattern of an Aperture,'' IEEE J. Ocean Eng. **18**, 73–75 (1993).

Erratum: "Dynamical surface response of a semi-infinite anisotropic elastic media to an impulsive force" [J. Acoust. Soc. Am. 103, 114–124 (1998)]

C. Bescond and M. Deschamps
Laboratoire de Mécanique Physique, Université de Bordeaux I, URA C.N.R.S. n° 867. 351, Cours de la Libération, 33405-TALENCE Cedex, France

(Received 13 February 1997; accepted for publication 15 September 1997)

[S0001-4966(98)00406-8]

PACS numbers: 43.20.Gp, 43.10.Vn [ANN]

In our paper, Fig. 11(a) should be as shown below.

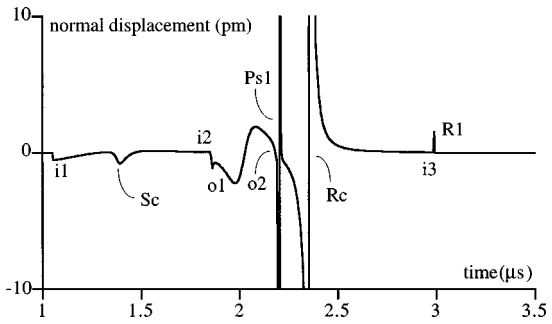

FIG. 11. Waveform calculated for a Dirac temporal excitation at the observation point $\Phi=60°$. (a) Point source. Arrival time: ''in plane'' (i1,i2,i3) and ''out of plane'' (o1,o2) skimming surface waves, Rayleigh wave (R1), Pseudo-surface wave (Ps1).

Erratum: "Acoustic wave scattering from a coated cylindrical shell" [J. Acoust. Soc. Am. 103, 3073(A) (1998)]

Sung H. Ko
Naval Undersea Warfare Center Division, Newport, Rhode Island 02841

(Received 24 April 1998; accepted for publication 24 April 1998)

[S0001-4966(98)06607-7]

PACS numbers: 43.20.Tb, 43.40.Yq, 43.30.Lz, 43.10.Sv [EM]

Instead of Sung H. Ko, the names of the authors should be Sung H. Ko and Bruce E. Sandman.

 0001-4966/98/104(1)/599/1/$15.00